Mechanical Behavior of Salt X

Editors:

J.H.P. de Bresser

M.R. Drury

P. A. Fokker

M. Gazzani

S.J.T. Hangx

A.R. Niemeijer

C.J. Spiers

CRC Press
Taylor & Francis Group

THE MECHANICAL BEHAVIOR OF SALT X

Rock salt formations have long been recognized as a valuable resource - not only for salt mining but for construction of oil and gas storage caverns and for isolation of radioactive and other hazardous wastes. Current interest is fast expanding towards construction and re-use of solution-mined caverns for storage of renewable energy in the form of hydrogen, compressed air and other gases. Evaluating the long term performance and safety of such systems demands an understanding of the coupled mechanical behavior and transport properties of salt. This volume presents a collection of 60 research papers defining the state-of-the-art in the field. Topics range from fundamental work on deformation mechanisms and damage of rock salt to compaction of engineered salt backfill. The latest constitutive models are applied in computational studies addressing the evolution and integrity of storage caverns, repositories, salt mines and entire salt formations, while field studies document ground truth at multiple scales. The volume is structured into seven themes:
- Microphysical processes and creep models
- Laboratory testing
- Geological isolation systems and geotechnical barriers
- Analytical and numerical modelling
- Monitoring and site-specific studies
- Cavern and borehole abandonment and integrity
- Energy storage in salt caverns

The Mechanical Behavior of Salt X will appeal to graduate students, academics, engineers and professionals working in the fields of salt mechanics, salt mining and geological storage of energy and wastes, but also to researchers in rock physics in general.

The Mechanical Behavior of Salt X

Proceedings of the 10th Conference on the Mechanical Behavior of Salt (SaltMech X), Utrecht, The Netherlands, 06-08 July 2022

Editors:

J.H.P. de Bresser
Faculty of Geosciences, Utrecht University (UU), The Netherlands

M.R. Drury
Faculty of Geosciences, Utrecht University (UU), The Netherlands

P.A. Fokker
TNO Energy Transition, Applied Geosciences, Utrecht, The Netherlands

M. Gazzani
Faculty of Geosciences, Utrecht University (UU), The Netherlands

S.J.T. Hangx
Faculty of Geosciences, Utrecht University (UU), The Netherlands

A.R. Niemeijer
Faculty of Geosciences, Utrecht University (UU), The Netherlands

C.J. Spiers
Faculty of Geosciences, Utrecht University (UU), The Netherlands

Cover illustration:
Microstructure of naturally deformed rock salt from the Avery Island salt dome, Louisiana, U.S.A. (images contributed by C.J. Spiers).

The gold-colored image (long-side scale ~0.8 mm) is a   light micrograph of a polished and etched section showing the internal subgrain structure within a single salt grain in the rock. The subgrains plus stress vs. subgrain size relations for salt indicate that deformation involved a component of dislocation creep at a deviatoric stress around 1 MPa.

The blue image (long-side scale 3 mm) is a transmitted light micrograph of a thin section of Avery Island salt that was γ-irradiated to reveal the internal microstructure through radiation damage (precipitation of sodium nano-particles). The section shows evidence for both subgrains and asymmetric crystal overgrowth features (clear zones), suggesting that deformation involved not only dislocation creep but also dissolution-precipitation processes, such as grain boundary migration and/or pressure solution.

All papers published in this volume were peer-reviewed before publication. Original papers and original reviews of previous work were accepted. The Organizing Committee is not responsible for the statements made or for the opinions expressed in this volume.

Although all care is taken to ensure integrity and the quality of this publication and the information herein, no responsibility is assumed by the publishers nor the author for any damage to the property or persons as a result of operation or use of this publication and/or the information contained herein.

Table of contents

Theme 1: Microphysical processes and creep models

Theme 2: Laboratory testing

Theme 4: Analytical and numerical modelling

Theme 5: Monitoring and site-specific studies

Theme 6: Cavern and borehole abandonment and integrity

Foreword

The Tenth Conference on the Mechanical Behavior of Salt (SaltMech X) continues a long-standing tradition, and provides an opportunity to highlight recent developments, in a field that is gaining new impetus through the need for geological storage options posed by the energy transition. Launched in 1981, the SaltMech Conference Series serves to exchange research findings and practical experiences regarding the mechanical behavior of rock salt, in the context of its safe use in mining and as a host rock for energy storage and hazardous waste disposal.

The conference is jointly organized by the *Experimental Rock Deformation Group (HPT Laboratory)*, the *Structural Geology and Electron Microscopy Group* and the *Copernicus Institute for Sustainable Development* at the Faculty of Geosciences at Utrecht University (UU), the Netherlands. The conference is held at Utrecht University's *Utrecht Science Park*, which is also home to the Geological Survey of the Netherlands and TNO's geosciences research. It brings together colleagues with backgrounds in numerous branches of science, engineering, mining, industry and regulation.

The main topics of the conference are grouped together in the following seven themes, which also form the basis for the structure of the proceedings:

- Microphysical processes and creep models
- Laboratory testing
- Geological isolation systems and geotechnical barriers
- Analytical and numerical modelling
- Monitoring and site-specific studies
- Cavern and borehole abandonment and integrity
- Energy storage in salt caverns

We are pleased to issue these conference proceedings in direct relationship to the conference and to be able to make the proceedings available to the largest possible audience via Open Access.

We thank all the authors for their contributions to the conference and proceedings and for their dedicated efforts and commitment to meet the associated deadlines.

Hans de Bresser, UU (NL)

Martyn Drury, UU (NL)

Peter Fokker, TNO (NL)

Matteo Gazzani, UU (NL)

Suzanne Hangx, UU (NL)

André Niemeijer, UU (NL)

Chris Spiers, UU (NL)

Acknowledgements

Sponsors

SaltMech X and the opportunity to publish its proceedings via Open Access would not have been possible without the sponsorship of the companies and institutes listed below, and of the Netherlands *Ministry of Economic Affairs and Climate*. The Organizing Committee is deeply grateful to all for their generous support.

Conference organization

Theme 1: Microphysical processes and creep models

A new rock salt constitutive model with back stress and drag stress hardening

Benjamin Reedlunn

Sandia National Laboratories, P.O. Box 5800, Albuquerque, NM 87112, USA

breedlu@sandia.gov

ABSTRACT: This paper presents a new, largely phenomenological, model for rock salt that includes branches for pressure solution and dislocation glide viscoplasticity. The dislocation glide branch utilizes back stress hardening for heterogeneously distributed dislocations and drag stress hardening for uniformly distributed dislocations. By transitioning between pressure solution at low strain rates, back stress dominated hardening at low to medium strain rates, and drag stress dominated hardening at high strain rates, a single model calibration can capture the behavior of Waste Isolation Pilot Plant salt over strain rates ranging from 10^{-12} to 10^{-4} 1/s, and temperatures from 20 to 60ºC. The same model calibration can also predict the Bauschinger effect (and represent reverse creep). Although room for improvement exists, the model's elegant formulation can capture an assortment of damage-free behaviors

1. Introduction

Rock salt constitutive models are used to simulate the evolution of mines, boreholes, storage caverns for gases and liquids, and nuclear waste repositories in rock salt formations. A wide variety of thermo-mechanical constitutive models have been proposed for rock salt, yet even the damage-free (micro-crack-free) thermoviscoplastic behavior remains difficult to capture. The Munson-Dawson model (Reedlunn et al. 2022), for example, can be calibrated against damage-free constant stress tests with low to medium steady-state strain rates (10^{-12} to 10^{-8} 1/s), but such a calibration fails to represent damage-free constant strain rate tests at high strain rates (10^{-6} to 10^{-4} 1/s). Capturing the damage-free behavior at these high strain rates is important because high strain rates are frequently used to characterize the mechanical behavior of damaged salt (dilated salt with micro-cracks). A constitutive model must first adequately capture damage-free behavior before attempting to represent how damage degrades salt's strength.

This paper presents a new model for the damage-free behavior of salt. Model development was influenced by a variety of models for metals (see J. Chaboche (2008) for a review) and the Aubertin, Yahya, et al. (1999) model for salt. Section 2 defines the new model formulation, Section 3 briefly discusses the formulation, Section 4 details four model calibrations, Section 5 partially validates the model, and Section 6 provides a short summary.

2. Model formulation

Several preliminaries bear mentioning before defining the model formulation. First, compressive strains and stresses are treated as positive. Second, variables represented by capital letters are material constants, while variables represented by lower case letters are functions of other variables. Third, this section presents the model in an infinitesimal strain setting, but one can easily have extended the model into the finite deformation realm using hypoelasticity.

The model additively decomposes the total strain rate $\dot{\varepsilon}$ into an elastic strain rate $\dot{\varepsilon}^{el}$, a thermal strain rate $\dot{\varepsilon}^{th}$ and a viscoplastic strain rate $\dot{\varepsilon}^{vp}$.

$$\dot{\varepsilon} = \dot{\varepsilon}^{el} + \dot{\varepsilon}^{th} + \dot{\varepsilon}^{vp} \tag{1}$$

The elastic behavior utilizes generalized Hooke's law in rate form to relate $\dot{\varepsilon}^{el}$, the fourth-order isotropic elastic stiffness tensor $\boldsymbol{E}$, and the stress rate $\dot{\sigma}$:

$$\dot{\boldsymbol{\sigma}} = \boldsymbol{E} : \dot{\varepsilon}^{el} = \boldsymbol{E} : \left(\dot{\varepsilon} - \dot{\varepsilon}^{th} - \dot{\varepsilon}^{vp} \right) \tag{2}$$

$$\boldsymbol{E} = \left(E_1 - \frac{2}{3} E_2 \right) \boldsymbol{I}_{\otimes} \boldsymbol{I} + 2 E_2 \text{II} \tag{3}$$

where E_1 is the bulk modulus, E_2 is the shear modulus, $\boldsymbol{I}$ is the second-order identity tensor, and II is the fourth-order symmetric identity tensor. The thermal strain portion of the model is simply

$$\dot{\varepsilon}^{th} = -A\dot{\theta}\boldsymbol{I} \tag{4}$$

where A is the coefficient of thermal expansion, and θ is the absolute temperature. The viscoplastic strain rate is additively decomposed into a pressure solution strain rate $\dot{\varepsilon}^{ps}$ and a dislocation glide strain rate $\dot{\varepsilon}^{dg}$

$$\dot{\varepsilon}^{vp} = \dot{\varepsilon}^{ps} + \dot{\varepsilon}^{dg} \tag{5}$$

The $\dot{\varepsilon}^{ps}$ branch captures steady-state viscoplastic behavior at low stresses. This branch utilizes the following flow rule,

$$\dot{\varepsilon}^{ps} = \dot{\bar{\varepsilon}}^{ps} \frac{\partial \tilde{\sigma}^{ps}}{\partial \sigma} \quad , \tag{6}$$

Where $\dot{\bar{\varepsilon}}^{ps}$ and $\tilde{\sigma}^{ps}$ are the equivalent pressure solution strain rate and stress, respectively. Pressure solution viscoplasticity is taken to be independent of the mean stress $\sigma^m = \frac{tr(\sigma)}{3}$ and driven entirely by the deviatoric stress σ^{dev}, so the pressure solution stress is simply

$$\boldsymbol{\sigma}^{ps} = \boldsymbol{\sigma}^{dev} = \boldsymbol{\sigma} - \sigma^m \boldsymbol{I} \tag{7}$$

This stress tensor is reduced to a scalar equivalent (von Mises) pressure solution stress as

$$\tilde{\sigma}^{ps} = \sqrt{\frac{3}{2} \boldsymbol{\sigma}^{ps} : \boldsymbol{\sigma}^{ps}} \tag{8}$$

The equivalent pressure solution strain rate is given by

$$\dot{\bar{\varepsilon}}^{ps} = P_1 \exp\left(-\frac{P_2}{\theta}\right) \frac{\tilde{\sigma}^{ps}}{\theta} \tag{9}$$

where P_j are material constants (Spiers et al. 1990). Eq. (9) assumes any non-zero $\tilde{\sigma}^{ps}$ causes pressure solution flow, such that the pressure solution quasi-static (rate-independent) yield surface is simply a point at $\boldsymbol{\sigma} = 0$.

The dislocation glide branch $\dot{\varepsilon}^{dg}$ dominates transient viscoplastic behavior at low stresses, and all viscoplastic behavior at medium to high stresses. Dislocation glide utilizes the following flow rule

$$\dot{\varepsilon}^{dg} = \dot{\bar{\varepsilon}}^{dg} \frac{\partial \tilde{\sigma}^{dg}}{\partial \sigma} \tag{10}$$

Where $\dot{\tilde{\varepsilon}}^{dg}$ and $\tilde{\sigma}^{dg}$ are the equivalent dislocation glide strain rate and stress, respectively. In contrast to the pressure solution branch and the majority of other salt models, the model assumes dislocation glide is driven by a dislocation glide stress (a.k.a. effective stress)

$$\sigma^{dg} = \sigma^{dev} - b \tag{11}$$

that includes b, a second-order tensor called the back stress (a.k.a. internal stress). With this definition for σ^{dg}, the equivalent (von Mises) dislocation glide stress is

$$\tilde{\sigma}^{dg} = \sqrt{\frac{3}{2}\sigma^{dg} : \sigma^{dg}} \tag{12}$$

Unlike the pressure solution branch, the dislocation glide branch has a finite size, quasi-static, yield surface, defined as

$$g = \tilde{\sigma}^{dg} - G_0 y \tag{13}$$

where G_0 is a material constant and y is an isotropic hardening variable called the drag stress that evolves from a positive initial value Y_0 to some positive value. By default, $G_0 = E_2 \times 10^{-10}/Y_0$, which makes the $g = 0$ surface typically very small relative to $\tilde{\sigma}^{dg}$. The equivalent dislocation glide strain rate is

$$\dot{\tilde{\varepsilon}}^{dg} = \begin{cases} 0 & \text{for } g < 0 \\ G_1 \exp\left(-\frac{G_2}{\theta}\right) \left|\sinh\left(\frac{\tilde{\sigma}^{dg}}{y}\right)\right|^{G_3} & \text{for } g \geq 0 \end{cases} \tag{14}$$

where G_j are material constants. The $g \geq 0$ expression applies for both transient and steady-state creep, but it is motivated by the Garofalo (1963) steady-state creep expression. The drag stress y evolves according to the following differential equation,

$$\dot{y} = Y_1 \left(\frac{Y_1}{y}\right)^{Y_2} \left(1 - \frac{y}{\bar{y}}\right) \dot{\tilde{\varepsilon}}^{dg} \tag{15}$$

where

$$\bar{y} = \frac{\bar{\sigma} - \bar{b}}{\sinh^{-1}\left\{\left[\frac{\dot{\tilde{\varepsilon}}^{dg}}{G_1 \exp\left(-\frac{G_2}{\theta}\right)}\right]^{1/G_3}\right\}} \tag{16}$$

is the drag stress saturation ($\bar{y} \geq Y_0$),

$$\bar{\sigma} = Y_4 \sinh^{-1}\left\{\left[\frac{\dot{\tilde{\varepsilon}}^{dg}}{Y_3 \exp\left(-\frac{G_2}{\theta}\right)}\right]^{\frac{1}{Y_5}}\right\} \tag{17}$$

is the equivalent (von Mises) stress saturation, $\bar{b}$ is the equivalent back stress saturation (discussed below), and Y_j are material parameters. The back stress has a similar, yet different, set of evolution equations. Following Chaboche (1986), b is decomposed as

$$b = \sum_{j=1}^{2} b_j \tag{18}$$

where b_1 is a short range, quickly evolving, back stress and b_2 is a long range, slowly evolving, back stress. Each back stress has an equivalent back stress defined as

$$\tilde{b}_j = \sqrt{\frac{3}{2} b_j : b_j} \tag{19}$$

Each back stress begins at B_{j0}, which must be deviatoric ($\mathrm{tr}(B_{j0}) = 0$) and is set to the zero tensor 0 by default. As deformation proceeds, each back stress evolves according to

$$\dot{b}_j = B_{j1} \left(\frac{2}{3} \dot{\varepsilon}^{dg} - \frac{b_j}{\bar{b}_j} \dot{\bar{\varepsilon}}^{dg} \right) \tag{20}$$

where

$$\bar{b}_j = B_{j2} B_{j3} \tanh\left(\frac{\bar{\sigma}}{B_{j3}} \right) \tag{21}$$

is the jth equivalent back stress saturation and B_{jk} are material constants. Analogous to Eq. (18), the equivalent back stresses can be summed as

$$\tilde{b} = \sum_{j=1}^{2} \tilde{b}_j \quad \text{and} \quad \bar{b} = \sum_{j=1}^{2} \bar{b}_j \tag{22}$$

All materials parameters should be non-negative to obtain typical material behavior. Furthermore, $1 - \sum_{j=1}^{2} B_{j2}$ must be non-negative to ensure $\bar{\sigma} - \bar{b}$ in Eq. (16) is positive.

3. Discussion of model formulation

This section briefly discusses some salient details of the model formulation. A more thorough discussion will be published at a later date.

3.1 Lack of coupling between branches

The model assumes that $\dot{\varepsilon}^{ps}$ and $\dot{\varepsilon}^{dg}$ are largely independent processes because pressure solution occurs along the grain boundaries, while dislocation glide occurs inside the grains. One potential mode of coupling, however, has been experimentally observed for $\theta \geq 75$ ºC: recrystallization by brine-assisted grain boundary migration (Ter Heege et al. 2005). This process consumes grains with high dislocation density, changes the average grain size, and requires significant strain ($\bar{\varepsilon}^{vp} > 10$ %) to be activated. A reduction in dislocation-based hardening could be implicitly captured by calibrating the model against laboratory experiments that include recrystallization, but the model does not attempt to capture the impact of grain size changes on pressure solution viscoplasticity. Omitting this coupling is likely insignificant in many applications since $\bar{\varepsilon}^{vp} > 10$ % tends to occur close to drifts and caverns, where pressure solution creep is not the dominant mechanism.

3.2 Pressure Solution Branch

The pressure solution branch consists solely of steady-state deformation, without any hardening (transient strain), for several reasons. According to classical pressure solution

theory, the increase in salt solubility in a brine film, of 0.1 μm thickness, surrounding a grain, of 10 mm size, due to a 1 MPa increase in $\tilde{\sigma}^{ps}$, at θ = 100 °C would produce a negligible transient creep strain on the order of 10^{-8} (Spiers 2021). Non-classical effects, such as pressure solution-based redistribution of grain boundary stresses, grain coarsening, grain elongation, or other structural changes to grain boundaries, could perhaps create a hardening effect, but a succinct, quantitative, description of such effects is not known to the author. On the other hand, the existence of sub-grains corresponding to low stresses in in-situ deformed samples (Carter et al. 1993) and reverse creep at low stresses (Gharbi et al. 2020) suggest that dislocation glide is active during low stress creep, even if dislocation glide does not dominate the steady-state rate. It, therefore, seems reasonable to assume dislocation glide creep dominates transient creep at low stresses, while pressure solution creep dominates steady-state creep at low stresses.

3.3 Dislocation Glide Branch

Although the dislocation glide branch is largely phenomenological, some loose physical meaning can be attached to the back stresses and drag stress. The back stresses represent hardening due to heterogenously distributed dislocation substructures, such as sub-grains and wavy slip bands produced by dislocation climb and cross-slip, respectively (Carter et al. 1993). These substructures are commonly observed at low to medium strain rates ($10^{-12} \leq \tilde{\varepsilon}^{vp} \leq 10^{-8}$ 1/s) and low to high temperatures ($20 \leq \theta \leq 700°C$). The drag stress represents hardening due to more uniform dislocation distributions, as are observed at higher strain rates (Raj et al. 1989). The motivation behind the name "drag stress" can be seen by inverting the $g \geq 0$ case in Eq. (14) as

$$\tilde{\sigma}^{dg} = y \sinh^{-1}\left\{\left[\frac{\dot{\tilde{\varepsilon}}^{dg}}{G_1 exp\left(-\frac{G_2}{\theta}\right)}\right]^{\frac{1}{G_3}}\right\} \tag{23}$$

in which $\tilde{\sigma}^{dg}$ is equal to y multiplied by a non-linear function of $\dot{\tilde{\varepsilon}}^{dg}$. Thus, y plays a role similar to an evolving dashpot in rheological models. Another important observation is the stresses $\boldsymbol{\sigma}^{dg}$, and $\boldsymbol{b}$ are co-axial along proportional stress paths, such that Eqs. (11) and (12) can be simplified to

$$\tilde{\sigma} = \tilde{b} + \tilde{\sigma}^{dg} \tag{24}$$

Where $\tilde{\sigma} = \sqrt{\frac{3}{2}\boldsymbol{\sigma}^{dev}:\boldsymbol{\sigma}^{dev}}$. Eq. (24) can be seen as decomposing $\tilde{\sigma}$ into a back stress contribution $\tilde{b}$ and a drag stress contribution $\tilde{\sigma}^{dg}$ (see Eq. (23)) when $\dot{\tilde{\varepsilon}}^{dg}$ is controlled, as approximately occurs in a constant strain rate test. Both hardening evolution equations (Eqs. (15) and (20)) conform to the Bailey-Orowan concept, in which the hardening rate is the result of a competition between a strain hardening term and a strain (a.k.a. dynamic) recovery term. Hardening saturates when the hardening and recovery rates balance one another ($\dot{y} = 0$ and $\dot{\boldsymbol{b}}_j = 0$). At hardening saturation, $\tilde{b}_j = \bar{b}_j, y = \bar{y}$, the stresses $\boldsymbol{\sigma}^{dg}$ and $\boldsymbol{b}$ are co-axial (even for non-proportional stress paths), such that Eqs. (14), (16), (17) and (24) combine to give $\tilde{\sigma} = \bar{\sigma}$. Inverting the expression for $\bar{\sigma}$ in Eq. (17) results in the Garofalo (1963) steady-state dislocation glide strain rate expression:

$$\dot{\bar{\varepsilon}}^{dg} = Y_3 \exp\left(-\frac{G_2}{\theta}\right)\left[\sinh\left(\frac{\bar{\sigma}}{Y_4}\right)\right]^{Y_5} \tag{25}$$

One can rearrange Eq. (16) into a form similar to Eq. (24) as

$$\bar{\sigma} = \bar{b} + \bar{\sigma}^{dg} \tag{26}$$

which shows that one must decide how to partition the hardening saturation between back stress and drag stress contributions. The hyperbolic tangent in Eq. (21) assumes back stress contributions dominate at low stresses (low strain rates) and drag stress contributions dominate at high stresses (high strain rates). This critical premise is based on direct measurements of the back stress in single phase metals (Takeuchi et al. 1976, Figure 15), the microstructural observations at the start of this sub-section, and the study discussed in Section 5.

4. Calibration

This section reviews four model calibrations against damage-free axisymmetric compression tests on salt from the Waste Isolation Pilot Plant (WIPP). Attention is focused on calibration performance rather than the calibration procedure.

Many details of the axisymmetric compression tests on WIPP salt can be found in Salzer et al. (2015), Düsterloh et al. (2015), and Reedlunn et al. (2022), but some points are reviewed herein. The specimen grain sizes ranged from 2 to 28 mm, with an arithmetic average of 10 mm. Each test began with a hydrostatic consolidation stage for one to ten days at 20 MPa of pressure. The logarithmic axial strain and logarithmic inelastic volumetric strains at the end of the consolidation stage are denoted as $\varepsilon_{zz}(t_0)$ and $\varepsilon_{vol}^{ie}(t_0)$, respectively, while $\varepsilon_{zz} - \varepsilon_{zz}(t_0)$ and $\varepsilon_{vol}^{ie} - \varepsilon_{vol}^{ie}(t_0)$ are the strain changes thereafter. Each constant stress test involved two non-zero $\bar{\sigma}$ stages. The first creep stage was designed to approach the steady-state strain rate from "above", while the second creep stage was meant to approach the steady-state strain rate from "below", as discussed in Günther et al. (2015). In the constant strain rate tests, the axial engineering strain rate $\dot{e}_{zz}$ was held fixed, not the axial logarithmic strain rate $\dot{\varepsilon}_{zz} = \dot{e}_{zz}/(1 - e_{zz})$, so care was taken to convert between the two strain rate measures as needed. After the consolidation stage, the radial confining pressure was held at $\sigma_{rr} = 10$ or 20 MPa to avoid significant micro-cracking.

(a) Model fit to steady-state strain rate measurements

(b) Back stress and drag stress contributions (the Cal 1A1 and 1A2 $\bar{\sigma}^{dg}$ curves overlap)
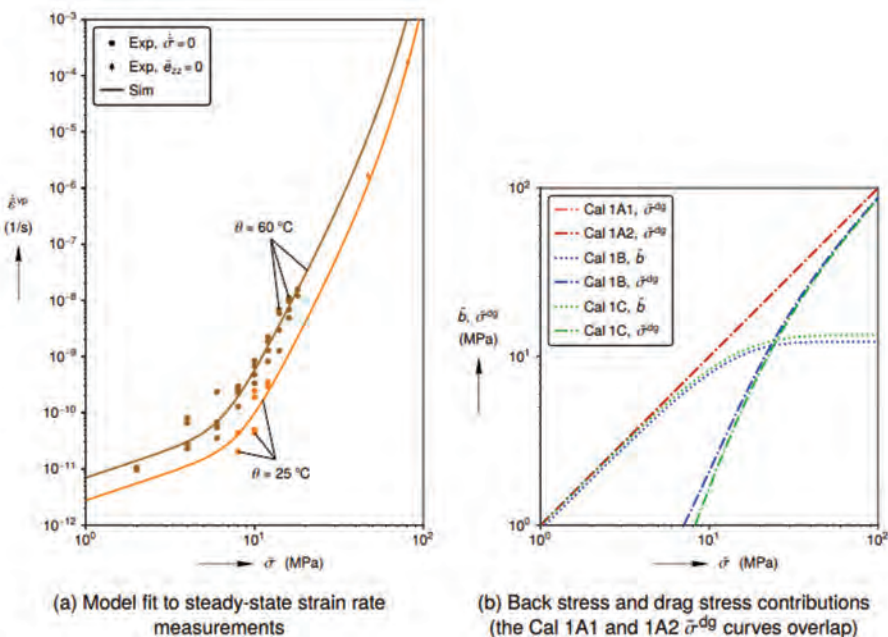
Figure 1: Model behavior at hardening saturation (steady-state)

Despite these confining pressures, some samples still developed significant micro-cracks towards the end of the test, judging by $\varepsilon_{vol}^{ie} - \varepsilon_{vol}^{ie}(t_0)$. Consequently, only stress–strain curve segments corresponding to $\varepsilon_{vol}^{ie} - \varepsilon_{vol}^{ie}(t_0) \geq 0$ (compressive inelastic volume strain) were treated as micro-crack-free and suitable for model calibration. One exception to this rule was made to compute the saturation stress $\bar{\sigma}$ from test A_TUC_TC98, as noted below.

The experimental measurements in Fig. 1a were derived from measuring the steady-state strain rate in constant stress experiments and the saturation stress in two constant strain rate experiments, all with σ_{rr} = 20 MPa. In the faster constant strain rate test, A_TUC_TC98, the maximum stress of 75.2 MPa corresponded to $\varepsilon_{zz} - \varepsilon_{zz}(t_0)$ = 42.2 % and $\varepsilon_{vol}^{ie} - \varepsilon_{vol}^{ie}(t_0)$ = − 0.8 %. As micro-cracking likely affected this maximum stress, the stress–strain slope at the onset of expansion ($\varepsilon_{vol}^{ie} - \varepsilon_{vol}^{ie}(t_0)$ < 0) was linearly extended to $\varepsilon_{zz} - \varepsilon_{zz}(t_0)$ = 42.2 %, resulting in 86.8 MPa, and a micro-crack-free saturation stress was roughly estimated as $\bar{\sigma}$ = (75.2 + 86.8)/2 = 81.0 MPa. The logarithmic scale in Fig. 1a makes a 75.2 to 86.8 MPa uncertainty virtually negligible, so 81.0 MPa was treated as a reliable data point.

Several calibration decisions were made in the absence of specific recent experimental measurements on WIPP salt. (1) The thermoelastic parameters in Table 1 were inherited from Munson et al. (1989). (2) The parameter G_1 was set to 10^9 1/s. (3) The initial drag stress was set to Y_0 = 1.0 MPa, since preliminary simulations showed the model's response was insensitive to Y_0 when $\tilde{\sigma} > 2Y_0$. (4) Back stress hardening prior to testing was neglected ($\mathbf{B}_{j0}$ = **0**). (5) The parameter P_2 was set to 2950 K, based on the granular salt compaction experiments in Spiers et al. (1990). (6) The calibrations focused on the 20 ≤ θ ≤ 60°C temperature range.

With the parameters G_1 and P_2 selected, the strain rate saturation parameters P_1, G_2, Y_3, Y_4, and Y_5 were optimized, in a least squares sense, against the steady-state strain rate measurements. The resulting fits are shown in Fig. 1a and the parameter values are listed in Table 1. All four model calibrations utilize the same steady-state strain rate calibration.

The hardening parameters were fit against the strain vs. time curves from the first stage of the constant stress tests and the stress vs. strain curves from the damage-free portions of the constant strain rate tests. The fitting process minimized a merit function that compared simulations against experimental measurements in an integrated least-squares sense. The resulting parameter sets are listed in Table 1. The performance of each hardening calibration is shown in Figs. 2 and 3. Figure 2a depicts the transient creep strain $\tilde{\varepsilon}^{tr}(t_1)$ after $t_1 \approx 50$ days of creep at various applied stresses and two temperatures. (The transient strain $\tilde{\varepsilon}^{tr} = \tilde{\varepsilon}^{tr}(t)$ is ε_{zz} minus the elastic and accumulated steady-state creep strain.) Fig. 2b depicts the characteristic creep time t^{ch}, which is the time for $\tilde{\varepsilon}^{tr}$ to reach 0.8 $\tilde{\varepsilon}^{tr}(t_1)$. Each simulated curve, for a given temperature, in Fig. 2 was derived from one hundred individual constant stress simulations. Each constant stress simulation utilized a different $\bar{\sigma}$, ranging from 1 to 100 MPa. Values of $\tilde{\varepsilon}^{tr}(t_1)$ and t^{ch} were extracted from each simulated strain history in the same manner as the experiments. Note that salt tends to approach steady-state creep in less time when tested at higher temperatures and stresses than at lower temperatures and stresses, so, by focusing on a fixed time, Fig. 2 plots the transient behavior at various degrees of proximity to true steady-state creep. Although one should be cautious about comparing the transient behavior at different stresses and temperatures in Fig. 2, one can still directly compare experimental measurements and simulations at a given stress and temperature. Finally, the plots in Fig. 3 show the stress vs. strain curves for constant strain

rate experiments and simulations at three different engineering strain rates. Only the $\varepsilon_{vol}^{ie}-\varepsilon_{vol}^{ie}(t_0) \geq 0$ portions of the experimental measurements are shown, which is why some measured responses abruptly terminate.

(a) Transient creep strain at $t_1 \approx 50$ d

(b) Characteristic creep time
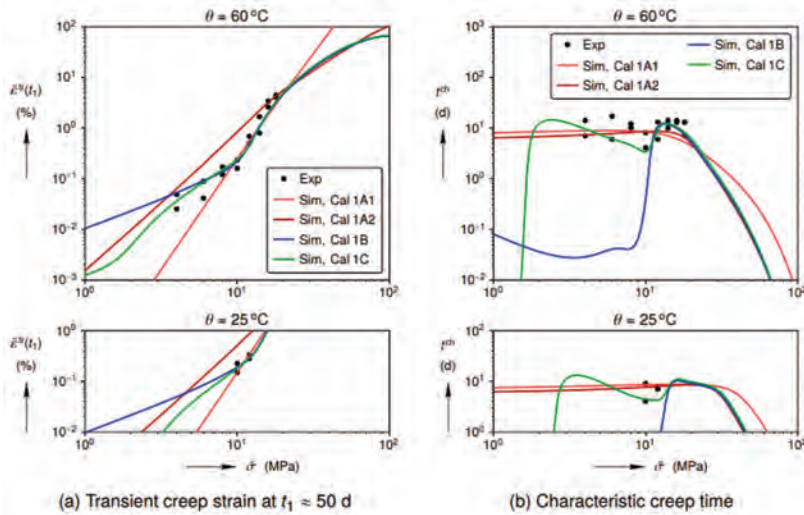
Figure 2: Transient strains and characteristic times from constant stress simulations compared against experimental measurements (first constant stress stage only).

(a) Calibration 1A1
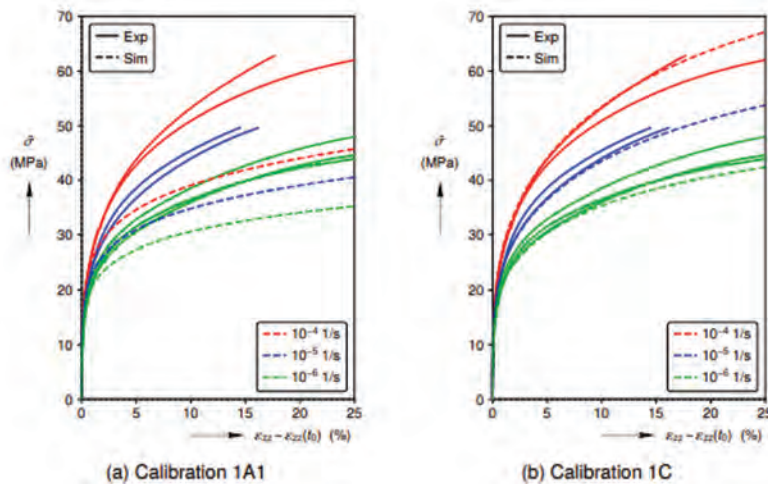
(b) Calibration 1C

Figure 3: Stress–strain curves from room temperature constant strain rate simulations from Calibration 1A1 and 1C compared against experimental measurements. (Constant strain rate simulation results for Calibrations 1A2 and 1B were similar to the Calibration 1C results in (b).)

Calibration 1A1 optimized G_3, Y_1, and Y_2 against the first-stage constant stress tests with $10 \leq \tilde{\sigma} \leq 18$ MPa. The Calibration 1A1 simulations of constant stress tests produce $\tilde{\varepsilon}^{tr}(t_1)$ and t^{ch} values that agree with the experimental measurements (see Figs. 2a and 2b) within the calibration range, but not outside the calibration range. The constant stress simulations at $\tilde{\sigma}$

≤ 6 MPa under-predict the $\tilde{\varepsilon}^{tr}(t_1)$ values (see Fig. 2a), and the constant strain rate simulations substantially under-predict the stresses for $\varepsilon_{zz} - \varepsilon_{zz}(t_0) > 1$ % at all three strain rates (see Fig. 3a). This latter under-prediction is especially problematic because a model that cannot capture damage-free constant strain rate behavior cannot be used to infer the degree of damage in low confining pressure constant strain rate tests.

Calibration 1A2, by contrast, optimized G_3, Y_1, and Y_2 against the constant strain rate tests with $10^{-6} \leq \dot{e}_{zz} \leq 10^{-4}$ 1/s. The back stress evolution rates were again set to zero ($B_{j1} = 0$). The Calibration 1A2 simulations produced stress–strain responses similar to the Calibration 1C responses shown in Fig. 3b as desired, but simulations of the constant stress tests at $\tilde{\sigma} <$ 16 MPa substantially over-predicted $\tilde{\varepsilon}^{tr}(t_1)$ (see Fig. 2a).

Calibration 1B fit G_3, Y_1, Y_2, B_{21}, B_{22}, and B_{23} against the first-stage constant stress tests with $10 \leq \tilde{\sigma} \leq 18$ MPa and the constant strain rate tests with $10^{-6} \leq \dot{e}_{zz} \leq 10^{-4}$ 1/s. The short range back stress evolution rate was set to zero ($B_{11} = 0$). Calibration 1B captured the measured $\tilde{\varepsilon}^{tr}(t_1)$ and t^{ch} values for $10 \leq \tilde{\sigma} \leq 18$ MPa (see Figs. 2a and 2b), and the Calibration 1B stress-strain curves were similar to the Calibration 1C curves (see Fig. 3b). Outside of the calibration range, Calibration 1B reasonably predicted the $\tilde{\varepsilon}^{tr}(t_1)$ values for $4 \leq \tilde{\sigma} \leq 8$ MPa, but underpredicted the t^{ch} measurements by roughly 100× in the same stress range.

Table 1: Calibrations (All calibrations utilize the default values of $G_0 = E_2$ x $10^{10}/Y_0$ and $B_{j0} = 0$)

Type	Parameter	Units	Cal 1A1	Cal 1A2	Cal 1B	Cal 1C
Thermo-elastic	E_1	Pa	20.67×10^9	20.67×10^9	20.67×10^9	20.67×10^9
	E_2	Pa	12.40×10^9	12.40×10^9	12.40×10^9	12.40×10^9
	A	1/K	45×10^{-6}	45×10^{-6}	45×10^{-6}	45×10^{-6}
Pressure Solution	P_1	K/(Pa s)	16.39×10^{-12}	16.39×10^{-12}	16.39×10^{-12}	16.39×10^{-12}
	P_2	K	2.950×10^3	2.950×10^3	2.950×10^3	2.950×10^3
Dislocation Glide	G_1	1/s	1×10^9	1×10^9	1×10^9	1×10^9
	G_2	K	5.585×10^3	5.585×10^3	5.585×10^3	5.585×10^3
	G_3	–	22.03	14.12	8.543	7.973
	Y_0	Pa	1×10^6	1×10^6	1×10^6	1×10^6
	Y_1	Pa	86.08×10^6	221.6×10^6	451.6×10^6	496.7×10^6
	Y_2	–	4.240	2.138	1.035	0.9911
	Y_3	1/s	36.00	36.00	36.00	36.00
	Y_4	Pa	43.50×10^6	43.50×10^6	43.50×10^6	43.50×10^6
	Y_5	–	5.623	5.623	5.623	5.623
	B_{11}	Pa	0	0	0	84.63×10^9
	B_{12}	–	1×10^{-9}	1×10^{-9}	1×10^{-9}	0.2910
	B_{13}	Pa	1×10^9	1×10^9	1×10^9	18.60×10^6
	B_{21}	Pa	0	0	8.303×10^9	5.445×10^9
	B_{22}	–	1×10^{-9}	1×10^{-9}	0.9420	0.7090
	B_{23}	Pa	1×10^9	1×10^9	12.98×10^6	11.29×10^6

Calibration 1C fit G_3, Y_1, Y_2, B_{11}, B_{13}, B_{21}, B_{22}, and B_{23} against the first-stage constant stress tests with $4 \leq \tilde{\sigma} \leq 18$ MPa and the constant strain rate tests with $10^{-6} \leq \dot{e}_{zz} \leq 10^{-4}$ 1/s. Preliminary optimizations that allowed both B_{12} and B_{22} to vary produced $B_{12} + B_{22} \approx 0.999$ (recall $B_{12} + B_{22} > 1$ is prohibited), so $B_{12} = 1 - B_{22}$ was simply enforced for the final Calibration 1C optimization. This most flexible model calibration produced behaviors similar to Calibration 1B, except it more accurately captured the t^{ch} measurements at $4 \leq \tilde{\sigma} \leq 8$ MPa (see Fig. 2b). The relative contributions of the back stresses and drag stress at hardening saturation can be seen in Fig. 1b for each of the calibrations. Calibrations 1A1 and 1A2 do not include back stresses, so the drag stress contribution $\bar{\sigma}^{dg}$ dominates at all applied stresses and strain rates. Calibrations 1B and 1C, however, conform to the assumption

discussed at the end of Section 3.3: $\bar{b}$ dominates at low stresses and $\bar{\sigma}^{dg}$ dominates at high stresses

5. Partial validation

The previous section demonstrated how the drag stress and two back stresses can be used to capture salt's damage-free behavior at different stresses and strain rates. All the calibration experiments, however, involved monotonic proportional stress paths. This section compares model calibrations 1A2, 1B, and 1C against a constant strain rate experiment with a non-monotonic proportional stress path. Such loading direction reversals lead to a temporary reduction in flow strength known as the Bauschinger effect. This effect is frequently attributed to microstructural residual stresses associated with heterogenous dislocation distributions, such as sub-grains (see Mughrabi (1983, Fig. 4)).
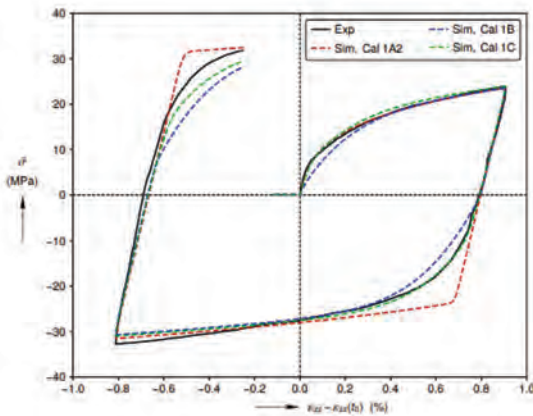
Figure 4: A comparison of three different model calibration stress-strain responses against experimental measurements on artificial rock salt.

The Bauschinger effect has not been studied on WIPP salt, so an experiment on artificial rock salt (Aubertin, Julien, et al. 1999, Fig. 5d) was utilized instead. Fig. 4 displays the artificial rock salt stress–strain response at $|\dot{\varepsilon}_{zz}| = 3.5 \times 10^{-5}$ 1/s, $\sigma_{rr} = 53$ MPa, and $\theta = 20$ ºC, during three stages: axisymmetric compression, axisymmetric extension, and a second axisymmetric compression stage . This artificial rock salt experiment was simulated using slightly modified versions of Calibration 1A2, 1B, and 1C. The elastic moduli E_1 and E_2 were both reduced by a factor of 22.5/31.0 = 0.7258 to properly capture the artificial rock salt's linear elastic behavior, as reported by Aubertin, Yahya, et al. (1999). In addition, the simulated stress difference $\breve{\sigma} = \sigma_{zz} - \sigma_{rr}$ values were scaled by 0.92× to bring the WIPP salt derived predictions more in-line with the artificial salt measurements during the first axisymmetric compression stage.

Fig. 4 also compares the simulated stress–strain responses against the experimental measurements. The (scaled) $\breve{\sigma}$ from Calibration 1A2, which includes only drag stress hardening, matches the experimental measurements nearly exactly during the first axisymmetric compression stage, but fails to capture the Bauschinger effect during the axisymmetric extension and second axisymmetric compression stages. Adding one back stress in Calibration 1B produces a prediction that qualitatively represents the Bauschinger effect, but the prediction is not quite stiff enough at the onset of hardening and re-hardening. Adding a second kinematic hardening back stress causes Calibration 1C to accurately represent the initial hardening during the first axisymmetric compression stage, accurately predict the re-hardening during the axisymmetric extension stage, and come closer to

predicting the re-hardening during the second axisymmetric compression stage. This prediction of the Bauschinger effect is significant because the Calibration 1C back stress was not calibrated against tests with non-monotonic loading, as is often done. Instead, the back stress parameters B_{ij} were calibrated against monotonic loading tests, such that the back stress dominated at low strain rates (low stresses) and played a lesser, yet significant, role at high strain rates (high stresses) (see Fig. 1b). The successful prediction of the Bauschinger effect by Calibration 1C, therefore, validates the hyperbolic tangent in Eq. (21). Although not shown herein, the model can also represent reverse creep during a multistage constant stress experiment. During forward creep at an applied $\tilde{\sigma}$, $\tilde{b}$ evolves to some value $\tilde{b}$ < $\tilde{\sigma}$. Subsequently decreasing $\tilde{\sigma}$ to $\tilde{\sigma}$ < $\tilde{b}$ produces reverse creep (see Eq. (10)).

6. Summary

A new model for the thermo-viscoplastic behavior of damage-free rock salt has been developed, calibrated, and partially validated. The pressure solution branch captured salt's steadystate behavior at low stresses. The dislocation glide branch captured WIPP salt's transient behavior at low stresses, and all observed viscoplastic behavior at medium to high stresses. After calibrating the model against monotonic experiments, the model successfully predicted the Bauschinger effect in a non-monotonic experiment. This result validates a key assumption in the model: the back stress dominates at low strain rates (low stresses) and the drag stress dominates at high strain rates (high stresses). Future work will likely focus on adding damage and healing to the model.

Acknowledgements

References

AUBERTIN, M., JULIEN, M. R., SERVANT, S. & GILL, D. E. 1999. A rate-dependent model for the ductile behavior of salt rocks. Canadian Geotechnical Journal, 36, 4, 660–674.

AUBERTIN, M., YAHYA, O. M. L. & JULIEN, M. 1999. Modeling mixed hardening of alkali halides with a modified version of an internal state variables model. International Journal of Plasticity, 15, 10, 1067–1088.

CARTER, N., HORSEMAN, S., RUSSELL, J. & HANDIN, J. 1993. Rheology of rocksalt. Journal of Structural Geology, 15, 9-10, 1257–1271. 11/12 Utrecht 2022 Chaboche, J.-L. (1986). Time-independent constitutive theories for cyclic plasticity. International Journal of plasticity, 2, 2, 149–188.

CHABOCHE, J. 2008. A review of some plasticity and viscoplasticity constitutive theories. International Journal of Plasticity, 24, 10, 1642–1693.

DÜSTERLOH, U., HERCHEN, K., LUX, K.-H., SALZER, K., GÜNTHER, R.-M., MINKLEY, W., HAMPEL, A., ARGÜELLO JR, J. G. & HANSEN, F. D. 2015. Joint Project III on the comparison of

constitutive models for the thermomechanical behavior of rock salt. III. Extensive laboratory test program with argillaceous salt from WIPP and comparison of test results. Proc. 8th Conference on the Mechanical Behavior of Salt, 13–21.

GAROFALO, F. 1963. An empirical relation defining the stress dependence of minimum creep rate in metals. Trans. AIME, 227, 351–356.

GHARBI, H., BEREST, P., BLANCO-MARTIN, L. & BROUARD, B. 2020. Determining upper and lower bounds for steady state strain rate during a creep test on a salt sample. International Journal of Rock Mechanics and Mining Sciences, 134, 104452.

GÜNTHER, R.-M., SALZER, K., POPP, T. & LÜDELING, C. 2015. Steady-state creep of rock salt: improved approaches for lab determination and modelling. Rock Mechanics and Rock Engineering, 48, 6, 2603–2613.

MUGHRABI, H. 1983. Dislocation wall and cell structures and long-range internal stresses in deformed metal crystals. Acta metallurgica, 31, 9, 1367–1379.

MUNSON, D. E., FOSSUM, A. F. & SENSENY, P. E. 1989. Advances in resolution of discrepancies between predicted and measured in situ WIPP room closures. Tech. rep. SAND88- 2948, Albuquerque, NM, USA: Sandia National Laboratories.

RAJ, S. V. AND PHARR, G. 1989. Creep substructure formation in sodium chloride single crystals in the power law and exponential creep regimes. Materials Science and Engineering: A, 122, 2, 233–242.

REEDLUNN, B., ARGÜELLO, J. G. & HANSEN, F. D. 2022. A Reinvestigation into Munson's Model for Room Closure in Bedded Rock Salt. International Journal of Rock Mechanics and Mining Sciences, 151.

SALZER, K., GÜNTHER, R.-M., MINKLEY, W., NAUMANN, D., POPP, T., HAMPEL, A., LUX, K.-H., HERCHEN, K., DÜSTERLOH, U., ARGÜELLO JR, J. G. & HANSEN, F. D. 2015. Joint Project III on the comparison of constitutive models for the thermomechanical behavior of rock salt. II. Extensive laboratory test program with clean salt from WIPP. Proc. 8th Conference on the Mechanical Behavior of Salt, 3–12.

SPIERS, C. J. 2021. Negligible transient strain due to pressure solution. Personal Communication.

SPIERS, C., SCHUTJENS, P., BRZESOWSKY, R., PEACH, C., LIEZENBERG, J. & ZWART, H. 1990. Experimental determination of constitutive parameters governing creep of rocksalt by pressure solution. Geological Society, London, Special Publications, 54, 1, 215–227.

TAKEUCHI, S. & ARGON, A. 1976. Steady-state creep of single-phase crystalline matter at high temperature. Journal of Materials Science, 11, 8, 1542–1566.

TER HEEGE, J., DE BRESSER, J. & SPIERS, C. 2005. Dynamic recrystallization of wet synthetic polycrystalline halite: dependence of grain size distribution on flow stress, temperature and strain. Tectonophysics, 396, 1-2, 35–57.

Grain-boundary processes and semibrittle behavior of salt-rock

Jihui Ding[1], Frederick M. Chester[1], Judith S. Chester[1], Xianda Shen[2], Chloé Arson[3]*

[1]Center for Tectonophysics, Department of Geology & Geophysics, Texas A&M University, College Station, TX, USA, [2]Department of Civil and Environmental Engineering, Clarkson Univeristy, Potsdam, NY, USA, [4]School of Civil and Environmental Engineering, Georgia Institute of Technology, Atlanta, GA, USA

* jihuiding@gmail.com

ABSTRACT: Grain-boundary microcracking, sliding, indentation, and healing have been shown to impact salt-rock bulk deformation. An improved understanding of the combined action of grain-boundary processes is necessary for accurate interpretation of salt-rock mechanical behavior in both natural and engineering contexts. We prepared granular, low-porosity, work-hardened salt-rocks (~300 ppm water) for triaxial stress-cycling experiments at low confining pressure to investigate semibrittle behavior and effective stress. We used optical microscopy to characterize grain-scale structure. Semibrittle flow involves coupled grain-boundary sliding and wing-crack opening accommodated by indentation via intragranular dislocation glide. Grain-boundary sliding is frictional at higher strain rates, but the associated dispersion of water from fluid inclusions along boundaries can activate linear-viscous, fluid-assisted, diffusional sliding at lower strain rates ($<10^{-8}$ s^{-1}). The combined action of these mechanisms leads to pressure- and time-dependent behaviors including anelasticity and hysteresis. In addition, we conducted cyclic pore- and confining-pressure tests to demonstrate that during semibrittle flow, strength depends on differential pressure consistent with the Terzaghi's effective stress law. This behavior may be explained by combined operation of pressure-independent intracrystalline-plastic mechanisms and transmission of pore pressure at grain boundaries via thin fluid films. Our study indicates coupled microprocesses are key to understanding semibrittle behavior of salt-rocks.

1   Introduction

Transitioning from fossil fuels to renewable energy has become more urgent in combating climate change. Under this context, salt rock formations are receiving renewed interest in storing clean energy medium (e.g., hydrogen) and could play a significant role in enabling large-scale adoption of solar and wind energy. To ensure an efficient and safe operation of salt caverns, we need a complete understanding of salt mechanical behavior at storage conditions. Salt caverns for energy storage typically operate at low pressure (a few to tens of megapascals) and temperature below 90°C (Bérest 2013; Ozarslan 2012; Wang et al. 2018). Under such conditions, brittle processes of fracturing and frictional sliding are expected to occur in addition to viscous processes of crystal-plasticity and pressure solution (Chester 1989; Hunsche & Hampel 1999; Minkley et al. 2015; Munson et al. 1999; Peach & Spiers 1996). The combined operation of brittle and intracrystalline plastic micromechanisms, termed as semibrittle deformation, is inherently complex and requires further investigation. Specifically, more work is needed to elucidate how the combined operation of brittle and viscous microprocesses affects both elastic and inelastic deformation in the semibrittle regime, and whether the simultaneous operation of the different mechanisms is coupled or independent. In addition, continued work is needed to settle the effective stress debate for semibrittle deformation involving simultaneous operation of brittle (pressure dependent) and intracrystalline-plastic (pressure independent) micromechanisms, and possibly large grain-contact area (Beeler et al. 2016; Noda & Takahashi 2016) .

This paper summarizes recent experimental work on deformation mechanisms (Ding et al. 2021b) and the effective stress law (Ding et al. 2021a) for semibrittle deformation of synthetic polycrystalline halite samples. Reagent-grade, granular halite is consolidated to fabricate low porosity, work-hardened aggregates in the laboratory. Stress cycling is employed in triaxial

compression tests to document elastic-plastic and viscoelastic behaviors and change in effective stress states. Microstructural characterization of grain-scale structure facilitates evaluation of deformation mechanisms and associated effective stress coefficient in semibrittle deformation regime.

2 Semibrittle deformation

2.1 Cyclic triaxial compression tests

We fabricated cylindrical synthetic salt-rock samples for the mechanical tests using high-purity (99 wt.%), reagent-grade granular salt. The granular salt was first sieved to produce more uniform grain size distribution of 0.3–0.355 mm and then uniaxially consolidated at a temperature of 150°C and a maximum axial stress of 75 MPa in a custom-made piston cylinder cell (Ding et al. 2016). Fabricated samples were right-circular cylinders (19 mm diameter and 43 mm length) with starting bulk porosity of 5.45% ± 0.06%. Using a Fourier transform infrared (FTIR) spectrometer, initial sample water contents were determined as 301 ± 18 weight ppm (Ding 2019). Because samples were always sealed, their water contents are expected to remain more or less constant during and after tests.

To investigate elastic-plastic and viscoelastic behaviors during semibrittle deformation, we employed triaxial stress-cycling technique that involved both large-and small-load cycles. In large-load cycles, differential stress was cycled between zero and the flow strength, and the sample was deformed permanently by a specified increment of axial shortening before the unload portion of the cycle. In small-load cycles, differential stress was cycled between 0 and ~6.5 MPa and the sample deformed elastically. Each large-load cycle, conducted at a constant strain rate of 3×10^{-6} s^{-1}, was followed by three small-load cycles with decreasing strain rate from 3×10^{-5}, 3×10^{-6}, to 3×10^{-7} s^{-1}. The tests were performed at room temperature and a confining pressure of 1 MPa without pore fluid pressure.
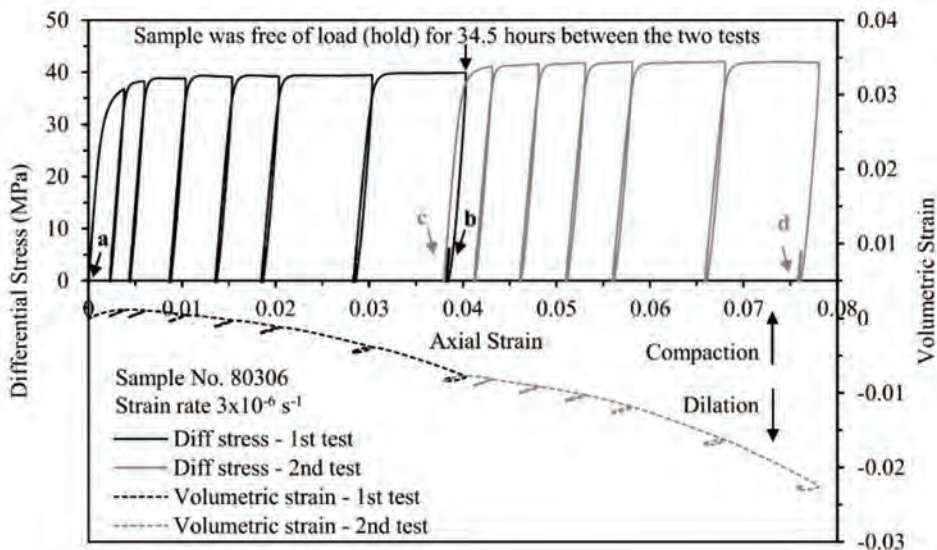
Figure 1: Differential stress and volumetric strain versus axial strain for sample No. 80306. The first and last small-load cycles for each round of cyclic compression test are indicated by letters. Note small-load cycles are not readily seen due to scale and masking by large-load cycle. Figure modified from Ding et al. (2021b).

At room temperature and a confining pressure of 1 MPa, salt rock deforms inelastically at a relatively constant stress of ~40 MPa (Figure 1). Multiple large-load cycles do not alter flow strength. The inelastic deformation is homogeneous across the samples with only a slight barreling in the middle. In the beginning of the deformation experiment the sample compacts slightly and then steadily dilates thereafter, documenting a porosity increase. Small-load cycles reveal characteristic stress-strain behavior.

The first set of small-load cycles, conducted before any inelastic deformation, show linear elastic deformation and the small-load cycles show no apparent change in behavior at different strain rates (Figure 2a). After a total deformation to approximately 3.8% axial strain, the salt rock exhibits different stress-strain behavior at different strain rates (Figure 2b). Small-load cycles progressively develop a nonlinear elastic response with hysteresis that is rate-dependent. Slower loading and unloading lead to more compliant behavior and hysteresis; however, even with hysteresis, the axial strain during a single small load-unload cycle is nearly fully recovered at zero differential load regardless of strain rate. A second-round cyclic loading test was conducted after a 34.5 hour-long hold with no confinement. The behavior during the first small-load cycle (which precedes the first large cycle) shows that the sample recovers to the initial state (i.e., the state prior to initiating the first round of small-load cycling) where hysteresis and rate-dependence are absent (Figure 2c). With continued deformation during the second-round cyclic loading, the sample displays the same evolution as in the first-round of cyclic loading before the hold, that is, increasing rate-dependence and hysteresis with permanent strain (Figure 2d).
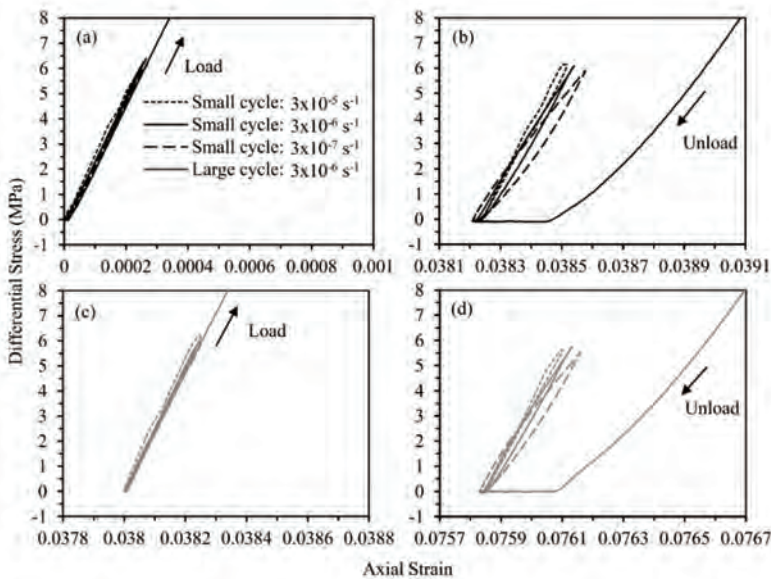
Figure 2: Differential stress versus axial and radial strain of small-load cycles for sample No. 80306. The first (a and c) and last (b and d) small-load cycles for two rounds of cyclic compression tests are shown. Refer Figure 1 for locations of these small-load cycles in the overall stress-strain curve. Loading and unloading directions of large-load cycles are indicated by arrows. Figure modified from Ding et al. (2021b).

2.2   Deformation mechanisms

The synthetic salt rock samples contain work-hardened grains with equant pores (Figure 3a). Grain contacts appear fully closed and are often straight or only slightly curved. The dominant intragranular substructure are the well-developed, dense, arrays of linear etch features, termed slip lines. The wavy slip lines are indications of dislocation glide controlled by cross slip of

screw dislocations (Senseny et al. 1992; Spiers & Carter 1996) and formed during the hot-pressing of salt grains. Recrystallized grains and intragranular cracks are present but uncommon.

Upon triaxial deformation, intracrystalline plasticity through dislocation glide is an active deformation mechanism but a subordinate one, accounting for only ~6% of total axial deformation based upon analysis of microstructure images (Shen et al. 2021b). The dominant micromechanism contributing to strain is cracking-opening and pore closure, leading to dilatancy, and sliding along grain boundaries that allows grain rearrangement (Figure 3b). Grain-boundary opening-mode cracks (gbo cracks) distribute uniformly across samples and preferentially orient parallel or subparallel to differential load axis. The density, aperture, and linking of the gbo cracks increase with increasing inelastic strain and linked crack arrays comprised of several gbo cracks develop at large axial strain (Ding et al. 2017). Moreover, opening cracks produce new porosity that explains the observed dilatancy throughout triaxial deformation (Figure 1). Based on the geometry and distribution of gbo cracks, shear motion can be confidently inferred along adjacent closed grain boundaries (Figure 3b). Here, we refer to the shear motion along grain boundaries with the descriptive term, grain-boundary sliding (gbs), that is, the mechanism of sliding is not implied. The coexistence of intracrystalline plasticity and gbs in deformed salt rocks are also documented by other works (Bourcier et al. 2013a; Bourcier et al. 2013b; Gaye et al. 2014). At low confining pressure, room temperature and moderate strain rate, the observed gbs is likely frictional. For a differential stress of 40 MPa and confining pressure of 1 MPa, shear and normal stress on grain boundaries at angles 45° to the sample axis is sufficient for frictional slip with a coefficient of friction of 0.95, assuming stress homogeneity. Grain boundaries deemed likely to have slipped in the deformed samples, based on linkage to pores or neighboring gbo cracks, have an average orientation of 50.4° to the sample axis. For these and greater angles, frictional sliding on grain boundaries is compatible with the range of friction coefficients observed in shear experiments on granular salt (Chester & Logan 1990), particularly considering the likelihood of significant stress variation at the grain scale. The samples are considered wet with a water content of 301 ppm (Watanabe & Peach 2002) and contain abound fluid inclusions at grain boundaries (Figure 3c). For fine-grained salt-rocks (0.08–2 mm), this water content is sufficient to invoke fluid-assisted grain boundary processes such as grain-boundary migration recrystallization and solution-transfer creep as long as the water is located at the grain boundaries (Shen & Arson 2019a; Spiers & Carter 1996; Ter Heege et al. 2005; Watanabe & Peach 2002). We infer that at low strain rates, gbs is accommodated by water-assisted diffusion once water is distributed along the sliding grain boundaries. The observed hysterisis (Figure 2b and d) also is explained by water-assisted diffusional gbs. Additionally, similar experiments on dry halite aggregates (~ 5 ppm water) do not show the hysteresis (Ding et al. 2021b). The diffusion process is likely localized and serves as an effective accommodation mechanism for gbs (Bos & Spiers 2002; Pennock et al. 2006; Raj & Ashby 1971).
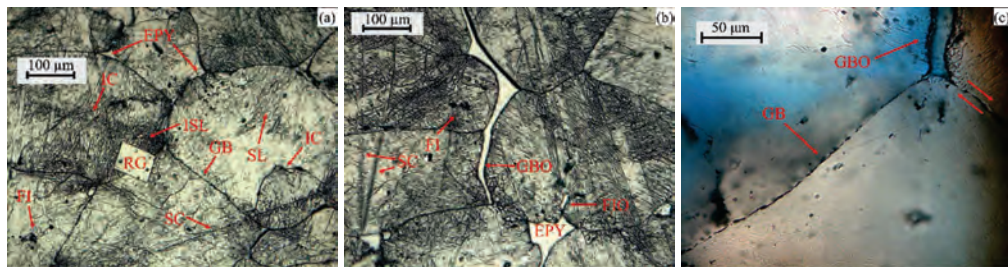
Figure 3: Reflected-light photomicrographs of (a) a synthetic salt rock sample prior to triaxial deformation, (b) a sample after triaxial deformation, and (c) transmitted-light photomicrograph of a sample after triaxial deformation. GB - grain boundary, GBO - grain boundary opening, EPY - epoxy (filling larger pores), RG - recrystallized grain, SL - slip lines, ISL - intersected slip lines, FI - fluid inclusions intersected by the polished surface, FIO - fluid inclusion opening, IC - intragranular cracks, SC - scratch associated with polishing. Paired arrows show inferred

shear motion on grain boundaries associated with grain-boundary opening. For the photos of the triaxially deformed samples, differential load axis is vertical. Figure modified from Ding et al. (2021b).

At test conditions, salt rock samples deform in the semibrittle flow field with a combined operation of intracrystalline-plastic mechanisms, intragranular cracking, gbo cracking, and by frictional gbs at the higher strain rates, and fluid-assisted diffusional gbs at the lower strain rates. While intragranular cracking is subordinate, the displacement along linked arrays of gbs and gbo cracks formed at variably oriented grain-boundaries is the dominant microprocess for grain rearrangement and axial shortening. The gbs shear surface inclined to the load axis and neighboring gbo segments are analogous to the well-known shear and wing crack for failure of brittle materials (Erdogan & Sih 1963; Griffith 1924). For brittle elastic material, the shear displacement on the surface inclined to the loading direction is coupled with the opening and extension of the wing cracks, leading to an elastoplastic behavior. By analogy, for the case of salt-rock at semibrittle flow conditions, frictional gbs is coupled with gbo to produce pressure-dependent plastic behavior. During semibrittle flow at low strain rates, the coupling of gbs by fluid-assisted diffusion processes and gbo by cracking lead to viscoplastic behavior as well as viscoelastic behavior during small stress cycling represented by anelasticity and hysteresis (see also Ding et al. 2021b; Shen et al. 2021a).

In salt caverns, similar conditions of low temperature and effective pressure that promote semibrittle deformation in our experiments may be encountered at cavern walls (Bérest 2013; Brouard et al. 2012; Wang et al. 2018). Inelastic deformation from large stress cycles around salt cavern walls could lead to the development of grain boundary cracking and frictional sliding to redistribute water, which can activate viscous processes. Linking of preferentially opened grain boundaries with shear slipping boundaries can produce linked arrays that, with further stress cycling, could cause instability of cavern wall such as spalling and block fall (Ding et al. 2017). Avoidance of large stress cycling could minimize breakage and activation of frictional sliding with dilatancy from associated opening boundaries, and employing holds to allow stress relaxation and healing of cracked grain boundary could help preserve the integrity of cavern walls. Additionally, as water is almost always present in natural salt rocks (Roedder 1984), elastic deformation may be dependent on loading rate with pronounced hysteresis at low strain rates in between stress cycles. Numerical modeling of salt caverns should consider the time-dependent behavior of salt and the consequent damage and healing processes, which will affect the mechanical behavior and sealing capability of salt caverns (Arson 2020; Shen & Arson 2019b).

3 Effective Stress for Semibrittle Deformation

3.1 Effective stress tests

To understand the effects of pore fluid pressure in controlling semibrittle deformation, we followed a similar approach used by Bishop & Skinner (1977) to test the effective stress law. Rewriting the general effective stress law gives:

$$\sigma^e = P_c - \alpha P_p = \left(P_c - P_p \right) + \left(1 - \alpha \right) P_p , \tag{1}$$

where σ^e is the effective pressure for rock strength, P_c is the confining pressure, P_p is the pore fluid pressure, and α is the effective stress coefficient. In the experiments, the difference between confining pressure and pore pressure was kept small, but the absolute magnitude of pore pressure used was varied between small and large values. When the variation of pore pressure is large enough, then the term $(1 - \alpha) P_p$ on the right side of Equation (1) leads to first-order change in effective stress even if the α is slightly smaller than unity. Both silicon oil and argon gas were used as pore fluid to investigate the effects of pore medium on the effective stress.

After increasing pore pressure by more than two orders of magnitude, the flow strengths of different load cycles differ by less than 2 MPa (Figure 4). When reducing pressures back to starting values, flow stress starts around 3 MPa lower than that of the previous cycle but with a higher hardening rate, so that the final flow stress reaches around 1 MPa less than that of the previous cycle. The same mechanical behavior is observed in the triaxial compression test using argon gas as pore fluid (Figure 5), in which pore pressure was increased by 35 times. At the tested pressure range, the changes of flow strength are within 2 MPa upon changing pore pressure for both liquid and gas pore medium.
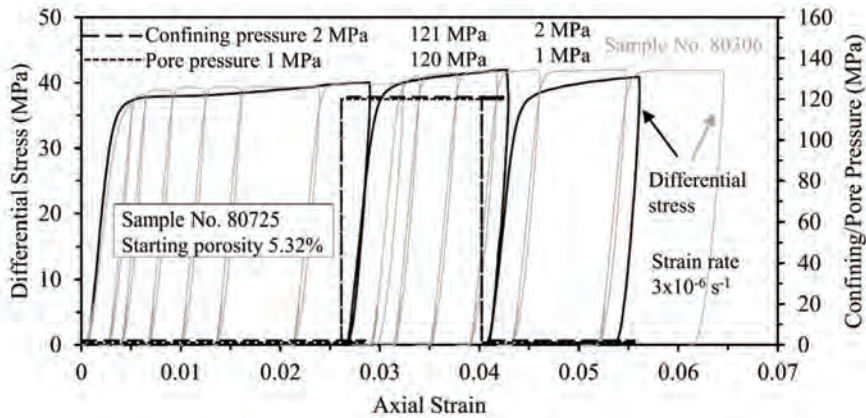
Figure 4: Differential stress versus axial strain for triaxial compression test using silicone oil as pore fluid. Stress-strain curve of sample No. 80306 is shown as a reference. Figure modified from Ding et al. (2021a).
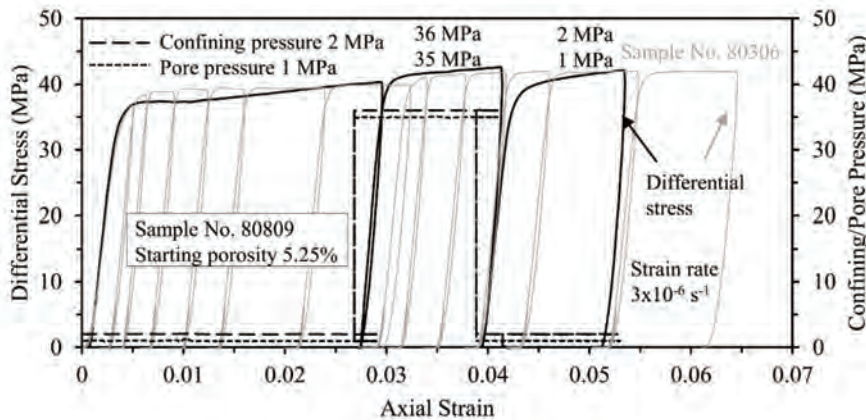
Figure 5: Differential stress versus axial strain for triaxial compression test using argon gas as pore fluid. Stress-strain curve of sample No. 80306 is shown as a reference. Figure modified from Ding et al. (2021a).

3.2 Effective stress coefficient

As shown in Figure 1, the flow strength of semibrittle deformation is not affected by multiple full loading and unloading cycles before the no-load hold period. After the hold, the flow strength increases by 2 MPa. Triaxial compression tests involving confining pressure stepping demonstrates that increasing differential pressure (P_c - P_p) by an increment of 1 MPa leads to progressive increase in flow strength of around 2 MPa over 0.8% axial strain, which can be

identified in the stress-strain curve (Figure 6). Therefore, effective stress for confining and pore pressure cycling tests (Figure 4 and 5) has changed less than 1 MPa. Thus, according to Equation 1, the effective stress coefficient α can be estimated to be > 0.99 for the test using silicone oil and >0.97 for the test using argon gas. This suggests that pore fluid pressure within the samples were adequately controlled throughout testing, and the Terzaghi's effective stress law holds for semibrittle deformation in triaxial compression tests. We suggest that α effectively equals unity during semibrittle deformation for three reasons: the potential to convey pore fluid pressure within thin fluid films along grain contacts; the potential for fluid to invade and pressurize the walls of microcracks during crack propagation; and the pressure-independence of intracrystalline-plastic deformation associated with grain indentation and microscopic asperity yielding. Isostatic consolidation tests on semibrittle salt-rocks also indicate alpha is nearly 1 (Ding et al. 2021a).
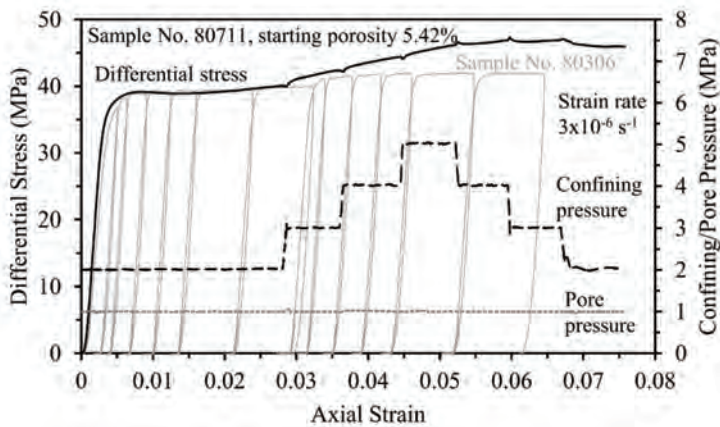
Figure 6: Differential stress versus axial strain for triaxial compression test using silicone oil as pore fluid. Pore pressure was constant at 1 MPa. Confining pressure was stepwise increased from 2 to 5 MPa and decreased back to 2 MPa. Stress-strain curve of sample No. 80306 is shown as a reference. Figure modified from Ding et al. (2021a).

Our effective stress tests reveal that $\alpha = 1$ gives sufficient accuracy for describing shear strength of salt aggregates involving coupled brittle and plastic processes. This may provide a basis for understanding the mechanical behavior for engineered salt structures and salt tectonics involving semibrittle deformation. Analyses of salt structure integrity and stability require knowledge of effective stress states in order to apply pressure-dependent rheological models.

4   Conclusions

Cyclic triaxial compression tests were conducted on low porosity, work-hardened synthetic salt rocks at room temperature and low confinement. Mechanical behavior and microstructures document semibrittle deformation involving grain-boundary opening and sliding, dislocation glide, intragranular cracking. Large stress cycling activates grain-boundary sliding accommodated by frictional processes at high strain rates or accommodated by fluid-assisted diffusion at low strain rates. The coupling of micromechanisms suggests that semibrittle deformation is more appropriately represented as a distinct rheologic zone in deformation-mechanism analysis. For such semibrittle deformation, the effective stress coefficient can be sufficiently treated as unity to describe flow strength. This may be explained by the transmission of pore pressure at grain boundaries and microcracks via thin fluid films and that

the yielding process to form and break contacts is governed by intracrystalline plasticity which is characteristically dependent on shear stress but largely independent of pressure.

Acknowledgements

References

ARSON, C. 2020. Micro-macro mechanics of damage and healing in rocks. *Open Geomechanics*, *2*, 1-41.

BEELER, N. M., HIRTH, G., THOMAS, A. & BÜRGMANN, R. 2016. Effective stress, friction, and deep crustal faulting. *J Geophys Res Solid Earth*, *121*, 1040-1059.

BÉREST, P. 2013. *The mechanical behavior of salt and salt caverns*. Paper presented at ISRM International Symposium - EUROCK 2013, International Society for Rock Mechanics and Rock Engineering, Wroclaw, Poland.

BISHOP, A. W. & SKINNER, A. E. 1977. The influence of high pore-water pressure on the strength of cohesionless soils. *Philosophical Transactions of the Royal Society A*, *284*, 91-130.

BOS, B. & SPIERS, C. J. 2002. Fluid-assisted healing processes in gouge-bearing faults: Insights from experiments on a rock analogue system. *Pure and Applied Geophysics*, *159*, 2537-2566.

BOURCIER, M., BORNERT, M., DIMANOV, A., HÉRIPRÉ, E. & RAPHANEL, J. L. 2013a. Multiscale experimental investigation of crystal plasticity and grain boundary sliding in synthetic halite using digital image correlation. *J Geophys Res Solid Earth*, *118*, 511-526.

BOURCIER, M., DIMANOV, A., HÉRIPRÉ, E., RAPHANEL, J., DESBOIS, G., BOURCIER, M., ET AL. 2013b. Full field investigation of salt deformation at room temperature : cooperation of crystal plasticity and grain sliding.

BROUARD, B., BÉREST, P., DJIZANNE, H. & FRANGI, A. 2012. Mechanical stability of a salt cavern submitted to high-frequency cycles. In P. Bérest, M. Ghoreychi, F. Hadj-Hassen and M. Tijani (Eds.), *The Mechanical Behavior of Salt VII*. Paris, France: Taylor & Francis Group.

CHESTER, F. M. 1989. Dynamic recrystallization in semi-brittle faults. *Journal of Structural Geology*, *11*(7), 847-858.

CHESTER, F. M. & LOGAN, J. 1990. Frictional faulting in polycrystalline halite: Correlation of microstructure, mechanisms of slip, and constitutive behaviour, in A. G. Duba, W. B. Durham, J. W. Handin and H. F. Wang (Eds.), *The Brittle-Ductile Transition in Rocks: The Heard Volume, Geophysical Monograph Series* (Vol. 56, pp. 49-65). Washington, DC: American Geophysical Union.

DING, J. 2019. Grain boundary processes, anelasticity, and test of the effective stress law for semibrittle deformation of synthetic salt-rocks, (Doctoral dissertation). Retrieved from OAKTrust. College Station, TX: Texas A&M University.

DING, J., CHESTER, F. M. & CHESTER, J. S. 2021a. Test of the Effective Stress Law for Semibrittle Deformation Using Isostatic and Triaxial Load Paths. *J Geophys Res Solid Earth*, *126*(5).

DING, J., CHESTER, F. M., CHESTER, J. S., SHEN, X. & ARSON, C. 2017. *Microcrack network development in salt-rock during cyclic loading at low confining pressure*. Paper presented

at 51st U.S. Rock Mechanics/Geomechanics Symposium, American Rock Mechanics Association, San Francisco, CA.

Ding, J., Chester, F. M., Chester, J. S., Shen, X. & Arson, C. 2021b. Coupled brittle and viscous micromechanisms produce semibrittle flow, grain-boundary sliding, and anelasticity in salt-rock. *J Geophys Res Solid Earth*, *126*, e2020JB021261.

Ding, J., Chester, F. M., Chester, J. S., Zhu, C. & Arson, C. 2016. *Mechanical behavior and microstructure development in consolidation of nominally dry granular salt*. Paper presented at 50th U.S. Rock Mechanics/Geomechanics Symposium, American Rock Mechanics Association, Houston, TX.

Erdogan, F. & Sih, G. C. 1963. On the crack extension in plates under plane loading and transverse shear. *Journal of Basic Engineering*, *85*(4), 519-525.

Gaye, A., Bornert, M., Lenoir, N., Sab, K., Dimanov, A., Bourcier, M. 2014. *Micromechanics of halite investigated by 2D and 3D multiscale full-field measurements*. Paper presented at 48th US Rock Mechanics/Geomechanics Symposium, OnePetro.

Griffith, A. 1924. The theory of rupture. In C. B. Biereno and J. M. Burgers (Eds.), *Proceedings of the First International Congress on Applied Mechanic*. Delft, Netherlands: Tech. Boekhandel en Drukkerij. J. Waltman Jr.

Hunsche, U. & Hampel, A. 1999. Rock salt — the mechanical properties of the host rock material for a radioactive waste repository. *Eng Geol*, *52*(3), 271-291.

Minkley, W., Knauth, M., Fabig, T. & Farag, N. 2015. Stability and integrity of salt caverns under consideration of hydro-mechanical loading. In L. Roberts, K. Mellegard and F. Hansen (Eds.), *The Mechanical Behavior of Salt VIII*. Paris, France: Taylor & Francis Group.

Munson, D. E., Chan, K. S. & Fossum, A. F. 1999. *Fracture and healing of rock salt related to salt caverns*. Paper presented at SMRI Spring Meeting, Solution Mining Research Institute, Las Vegas, NV.

Noda, H. & Takahashi, M. 2016. The effective stress law at a brittle-plastic transition with a halite gouge layer. *Geophysical Research Letters*, *43*(5), 1966-1972.

Ozarslan, A. 2012. Large-scale hydrogen energy storage in salt caverns. *International Journal of Hydrogen Energy*, *37*(19), 14265-14277.

Peach, C. J. & Spiers, C. J. 1996. Influence of crystal plastic deformation on dilatancy and permeability development in synthetic salt rock. *Tectonophysics*, *256*, 101-128.

Pennock, G. M., Drury, M. R., Peach, C. J. & Spiers, C. J. 2006. The influence of water on deformation microstructures and textures in synthetic NaCl measured using EBSD. *Journal of Structural Geology*, *28*, 588-601.

Raj, R. & Ashby, M. F. 1971. On grain boundary sliding and diffusional creep. *Metallurgical Transactions*, *2*, 1113-1127.

Roedder, E. 1984. The fluids in salt. *American Mineralogist*, *69*, 413-439.

Senseny, P. E., Hansen, F. D., Russell, J. E., Carter, N. L. & Handin, J. W. 1992. Mechanical behavior of rock salt: Phenomenology and micromechanisms. *Int J Rock Mech Min Sci*, *29*, 363-378.

Shen, X. & Arson, C. 2019a. An isotropic self-consistent homogenization scheme for chemo-mechanical healing driven by pressure solution in halite. *International Journal of Solids and Structures*, *161*, 96-110.

Shen, X. & Arson, C. 2019b. Simulation of salt-cavity healing based on a micro–macro model of pressure solution. *Petroleum Geoscience*, *25*(3), 251-257.

SHEN, X., DING, J., ARSON, C., CHESTER, J. S. & CHESTER, F. M. 2021a. Micromechanical modeling for rate-dependent behavior of salt rock under cyclic loading. *International Journal for Numerical and Analytical Methods in Geomechanics*, *45*(1), 28-44.

SHEN, X., DING, J., LORDKIPANIDZE, I., ARSON, C., CHESTER, J. S. & CHESTER, F. M. 2021b. Fabric evolution and crack propagation in salt during consolidation and cyclic compression tests. *Acta Geotechnica*.

SPIERS, C. J. & CARTER, N. L. 1996. Micorophysics of rocksalt flow in nature. In M. Aubertin and H. R. J. Hardy (Eds.), *Proceedings of the Conference on the Mechanical Behavior of Salt IV.* Clausthal-Zellerfeld, Germany: Trans Tech Publications.

TER HEEGE, J. H., DE BRESSER, J. H. P. & SPIERS, C. J. 2005. Rheological behaviour of synthetic rocksalt: The interplay between water, dynamic recrystallization and deformation mechanisms. *Journal of Structural Geology*, *27*, 948-963.

WANG, T., MA, H. L., SHI, X. L., YANG, C. H., ZHANG, N., LI, J. L. 2018. Salt cavern gas storage in an ultra-deep formation in Hubei, China. *Int J Rock Mech Min Sci*, *102*, 57-70.

WATANABE, T. & PEACH, C. J. 2002. Electrical impedance measurement of plastically deforming halite rocks at 125°C and 50 MPa. *J Geophys Res Solid Earth*, *107*(B1), 2004.

Mechanisms of dilatancy in rock salt at the grain-scale and implications for the dilatancy boundary

B.G.A. van Oosterhout[1], S.J.T. Hangx[1], C.J. Spiers[1]*

[1]HPT laboratory, Department of Earth Sciences, Utrecht University, The Netherlands

* *b.g.a.vanoosterhout@uu.nl*

ABSTRACT: This paper presents an experimental investigation of the dilatancy boundary in rock salt based on triaxial compression tests (room temperature $10^{-5}s^{-1}$) of naturally wet and dried Leinesteinsalz samples. The experiments indicate that dilatancy in the Leinesteinsalz is observed at confining pressures $\leq 15\,MPa$, while at higher confining pressure mechanical behavior is non-dilatant. Two microphysical models were constructed based on mechanisms based on (1) intergranular slip and tensile failure and (2) the opening of voids due to plastic strain misfits between individual grains. A comparison of the experimental data with the first model indicates that slip on grain boundaries can only occur when the friction on the grain boundaries is lowered by the presence of fluid inclusions. The absence of any significant difference between dilatancy in dry and wet Leinesteinsalz eliminates the possibility that dilatancy is controlled by intergranular slip. The second model shows the typical type of behavior observed in the experiment with initial compaction and a later switch to dilatancy as axial strain progresses but fails to show a switch to compaction-only behavior at high confinement. Hence, dilatancy in rock salt is likely to be controlled by the opening of voids related to misfit strains, but the model needs to be modified.

1   Introduction

Natural rock salt formations are characterized by extremely low permeability, high ductility and high sealing capacity, making salt an excellent host rock for geological storage and disposal facilities. Nonetheless, the creation of underground cavities and excavations in rock salt disturbs the original stress state of the rock salt, resulting in an increase in deviatoric stress and a decrease in mean stress around the cavity walls (Tsang et al. 2005). Under these conditions, dense rock salt dilates via microcracking, leading to a positive volume change and an increase in porosity and permeability (Peach et al. 2001). The extent of dilatancy in this excavation disturbed or damage zone (EDZ), as well as the impact of dilatancy on the transport properties, are of key importance for assessing the safety of radioactive waste storage and disposal facilities in salt (Alkan et al. 2007). Recently, the extent of the EDZ has also gained attention in relation to a) the integrity of solution-mined storage caverns for renewably derived hydrogen or compressed air (Khaledi et al. 2016), and b) the long-term fate of abandoned, brine-filled caverns (Bérest & Brouard 2003). It is also of interest in the context of the self-sealing potential of abandoned hydrocarbon wellbores in rock salt caprocks (Orlic & Buijze 2014; Buijze et al. this volume).

The stress conditions at which dilatancy occurs have been measured experimentally and are typically determined based on sample-scale measurements of volumetric strain and permeability (Peach 1991) and/or acoustic phenomena (Popp et al. 2001), made during triaxial tests. In most of these experiments, the onset of dilatancy, or the "dilatancy boundary", is defined as the minimum in the volumetric strain versus axial strain curve (dilatancy defined as positive). The empirically derived relationship indicates that the dilatancy boundary can be represented in differential or equivalent stress (σ_{eq}) vs. mean stress space ($\bar{\sigma}$). However, to date, no microphysical basis for the dilatancy boundary has been proposed that would provide a basis for extrapolation beyond lab conditions and time scales, or to more complex deformation paths.

The present study reports triaxial experiments on Leinesteinsalz samples carried out over a broad range of confining pressure ($2.5 - 40\ MPa$) on both naturally wet rock salt (i.e. with natural brine content) and on artificially dried rock salt. In addition, for the "wet" experiments, permeametry measurements were performed before and after the triaxial experiments. The aim is to test preliminary microphysical models for dilatancy development in deforming rock salt, based on the physical and/or chemical processes playing a role at the grain-scale. Two models are presented here. One is based on microcracks forming as a result of slip on inclined grain boundaries, causing tensile cracks to open on boundaries subparallel to the compression direction. A second model is based on the opening of voids due to plastic misfit strains between individual grains, related to a lack of five easy slip systems.

2   Experimental method

The present approach involved conventional triaxial deformation tests in combination with permeametry was performed on natural Leinesteinsalz samples (Zechstein Z2), at room temperature and relatively rapid strain rates ($4.8 \cdot 10^{-5}\ s^{-1}$). The deformation experiments were performed using the dilatometric triaxial apparatus (designed by H.C. Heard, described in detail by Peach 1991) at systematically varied confining pressures (P_c) ranging from 5 to 22.5 MPa. Confining pressure intervals of 2.5 MPa were explored to locate the transition from non-dilatant to dilatant behavior within that resolution. A first set of experiments was performed with no special sample pre-treatment, (i.e. on samples containing their inherent water content reached under storage conditions). In these runs, a saturated brine pressure of 2.5 MPa was applied to the sample ends and brine permeability measurements were made before and after the deformation experiment. After preparing and sealing the samples, the assembly was placed into the main pressure vessel and the pore fluid system was filled with 100% saturated brine. To close any pre-existing cracks that may have been formed during coring and machining, the confining pressure was first brought up to 25 MPa and maintained for 60 minutes, before lowering to the desired experimental value. The fluid permeability was measured before and after removal of the differential stress in each deformation experiment using transient step permeametry, which entails the measurement of the pressure decay due to flow-through following the application of a fluid pressure difference across the sample ends. This method has been widely described and used successfully for low porosity and low permeability rocks, using gases and liquids (see Peach 1991; Sutherland & Cave 1980; Trimmer 1982). A second set of experiments (two tests) was performed in an identical manner but on samples that were pre-treated and dried under vacuum for a period of two months at $50°C$, without applying brine pressure and without making permeability measurements.

3   Results

The experiments performed to investigate dilatancy in the Leinesteinsalz samples are listed in Table 1, along with the experimental conditions and data on the initial and final state of the samples. The two tests performed to investigate the effect of drying the samples on the dilatancy boundary are listed in the second block of Table 1.

At low confining pressures ($< 10\ MPa$), the volumetric strain curves indicate compaction in the early stages of loading, while at a few percent axial strain ($0 - 3\%$) a clear turn-around point is observed, marking the switch to dilatant behavior. At intermediate confining pressures ($12.5\ MPa - 15\ MPa$), such a turn-around point can still be identified, but the amount of positive volume change after this minimum point is minor (see Table 1). At confining pressures above $15\ MPa$, no turn-around point can be identified, and the mechanical behavior is non-dilatant throughout the entire experiment. The stress-strain curves in all experiments are non-linear from the onset of loading, indicating work hardening plastic flow. The axial strain, volumetric strain and differential stress of this turn-around point are shown in Table 1. Hence, a clear progression from dilatant behavior up to $P_c = 10 - 12.5\ MPa$ to non-dilatant behavior at P_c of

15 MPa and higher. No significant difference between wet and dry dilatancy experiments at the same mean effective stress was observed. This implies that the mechanical behavior of a wet experiments with an applied brine pressure of 2.5 MPa is similar to a dry experiment (without applied brine pressure) at 2.5 MPa lower confining pressure.

Table 1: List of deformation experiments on Leinesteinsalz shortened at strain rates of $4.8 \cdot 10^{-5}$ s^{-1}. σ_{dil}, ε_{ax_dil} and ε_{v_dil} represent the differential stress, axial strain and volumetric strain at the point where dilatancy occurs, ε_{ax_tot} and ε_{v_tot} represent the axial and volumetric strain at the end of the experiment. $\kappa_{initial}$ and κ_{final} represent the permeability, measured within the machine at the imposed confining pressure, before and after the experiment.

Specimen number		P_c (MPa)	P_p (MPa)	σ_{dil} (MPa)	ε_{ax_dil} (%)	ε_{v_dil} (%)	$\varepsilon_{ax\,tot}$ (%)	$\varepsilon_{v\,tot}$ (%)	$\kappa_{initial}$ (m^2)	κ_{final} (m^2)
356/016 TC	Wet	5.0	2.5	13.30	0.36	-0.01	10.04	+2.18	$<10^{-21}$	$3.92 \cdot 10^{-16}$
356/028 TC	Wet	7.5	2.5	25.24	2.40	-0.31	11.62	+0.29	X	X
356/030 TC	Wet	10.0	2.5	26.47	2.83	-0.10*	11.17	+0.03*	$<10^{-21}$	$1.96 \cdot 10^{-18}$
356/024 TC	Wet	12.5	2.5	43.34	7.15	-0.34	12.01	-0.35	$2.07 \cdot 10^{-20}$	$6.54 \cdot 10^{-19}$
356/036 TC	Wet	15.0	2.5	44.61	5.73	-0.21	11.14	-0.24	$1.52 \cdot 10^{-20}$	$2.03 \cdot 10^{-19}$
356/040 TC	Wet	22.5	2.5	n/a	n/a	n/a	12.50	-0.41	$<10^{-21}$	$3.62 \cdot 10^{-20}$
356/037 TC	Wet	40.0	2.5	n/a	n/a	n/a	16.12	-0.53	$<10^{-21}$	$<10^{-21}$
356/033 TC	Dry	2.5	0	7.94	0.21	-0.01	10.48	+1.76	X	X
356/035 TC	Dry	7.5	0	34.38	3.16	-0.16	11.61	+0.27	X	X

*   determined from pore volume change
X   not measured
n/a   not available: no minimum/turn-around point is reached during the experiment

The initial permeability of most samples subjected to permeametry are below the measurable resolution and hence smaller than 10^{-21} m^2. However, for samples 356/024 TC and 356/036 TC a permeability of respectively $2.07 \cdot 10^{-20}$ m^2 and $1.52 \cdot 10^{-20}$ m^2 was determined (see Table 1). At all confining pressures, except at 40 MPa, an increase in permeability was observed after deformation. At 5 MPa, the permeability increased by five orders of magnitude; at 10 MPa, the increase was three orders of magnitude. At 40.0 MPa, the permeability remained below 10^{-21} m^2 (i.e. below the resolution limit) as in the undeformed state.

Based on the experimental results, the switch from non-dilatant to dilatant behavior for Leinesteinsalz can be presented in terms of differential stress vs. increasing confining pressure. Most experiments on dilatancy are performed without applying a pore pressure (e.g. Peach & Spiers 1996; Popp & Kern 2001) and in those experiments the mean effective stress is equal to the mean stress. In order to compare the experimental data in this study with other experimental data on dilatancy, the dilatancy boundary here is shown as a function of mean effective stress ($\left[\frac{\sigma_1+2\sigma_3}{3}\right] - P_f$).

A switch to dilatancy is observed at experiments below 15.0 MPa. At 22.5 MPa and 40.0 MPa no minimum is reached in the external volume change and the change in the internal volume is considered insignificant to define a minimum at 22.5 MPa and absent at 40.0 MPa as well. Therefore, the dilatancy boundary is defined based on the volumetric strain data up to 15.0 MPa confining pressure. Based on the experimental data from this study on Leinesteinsalz, we suggest that the data is described most accurately by a linear dilatancy boundary, given by $\sigma_{eq} = 1.56\bar{\sigma} + 3.47$ (see Figure 1a). Samples 356/033 TC and 356/035 TC were pre-treated and dried under vacuum for a period of two months at 50℃, before

deformation at respectively $2.5\,MPa$ and $7.5\,MPa$. The stress conditions at the absolute minimum in the volumetric strain curve for dry and wet Leinesteinsalz are shown in Figure 1b. Note that for the wet experiments, the assumption is made that pore fluid penetrates the sample pore space. Therefore, the stress evolution paths of the wet experiments at $5.0\,MPa$ and $10.0\,MPa$ coincide with the dry experiments at respectively $2.5\,MPa$ and $7.5\,MPa$.
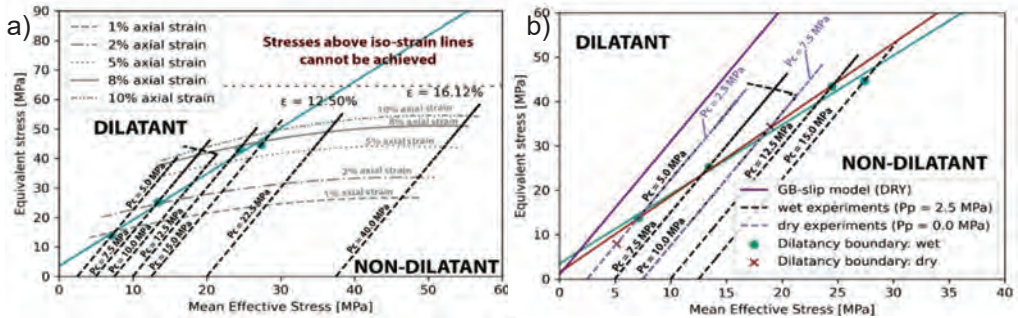
Figure 1: (a) Dilatancy boundary as a function of mean effective stress and Von Mises equivalent stress (differential stress) in "wet" Leinesteinsalz. The stress evolution of the individual experiments, shown in black and the grey envelopes, show the stress supported at different axial strains. (b) Dilatancy boundary in "wet" (green line) vs dry (brown line) Leinesteinsalz. As a reference, the theoretical prediction by the GBFS model for dry rock salt is shown.

Note that in this study, the "wet" experiments are all performed with a pore pressure of $2.5\,MPa$, theoretically lowering the mean effective stress by an equal amount. This relies on the assumption that the pore fluid can penetrate the pore space, requiring interconnection of these pores and is only valid once the rock salt has become dilatant. However, the fluid pressure can force the transfer of intrusion to the cracks and thus serving as an internal drive for the opening and growth of cracks and promote dilatancy (Alkan et al. 2007). Therefore, prior to the dilatancy boundary the pore pressure may already have some effect. Also note that when including the progression of axial strain for all "wet" experiments, it can be observed that the dilatancy boundary crosses the $1-2\%$ axial strain line for the experiment at $5-7.5\,MPa$ confinement and $5-8\%$ strain for $10-12.5\,MPa$ confinement. It is evident that at higher confining pressures the conditions required for dilatancy are not reached in these experiments. Additional strain beyond 10% hardly results in any further increase in differential stress on the rock salt and hence the differential stresses required for dilatancy occur at high confining pressures are not feasible. This is substantiated by the absence of a permeability increase after deformation in rock salt deformed at $40\,MPa$.

4 Models describing dilatancy in rock salt

While a lot of research has been aimed at quantifying dilatancy and the dilatancy boundary for various types of rock salt, at a range of confining pressures and for different deformation rates, relatively little effort has been made to explain why dilatancy occurs at the conditions observed in experiments. Peach & Spiers 1996 and Alkan 2009 have derived models to explain the observed increase in permeability in relation to dilatancy and microcrack linkage, using percolation theory. However, these do not explain under which conditions dilatancy in rock salt occurs, beyond empirical and/or phenomenological model fits. A preliminary attempt is made here to explore microphysical models that can mechanistically account for the onset of dilatancy in deforming rock salt, based on the physical and chemical processes operating at the grain scale.

4.1 Grain boundary frictional slip (GBFS) model

Peach 1991 and Hunsche 1998 have concluded that the dilatancy boundary is only dependent on deviatoric and mean stress and does not significantly vary between different salt types. They and other authors (e.g. Alkan et al. 2009; Popp et al. 2001) accordingly treat the dilatancy boundary as resembling a yield or failure criterion. At differential stresses above this boundary, microcracks are generated, creating excess lateral strains (volumetric strain) and resulting in a rapid increase in permeability. Microstructural evidence suggests that microcracks are generated on grain boundaries that are oriented parallel to σ_1 (Peach 1991, Peach & Spiers 1996). This suggests shear failure or slip on grain boundaries oriented at a favorable angle to σ_1, in combination with tensile opening of grain boundaries oriented subparallel to σ_1, may be responsible for generating dilatant microcracking in rock salt during plastic deformation. In the following, a model is developed to assess this possibility.

As starting point, consider an idealized 2-D rock salt microstructure consisting of hexagonal grains, defined by the apical angle (ψ) and aspect ratio (height/width) ($R = \frac{h}{w}$) (see Figure 2). Given that experiments on dilatancy in general are performed under axi-symmetric conditions ($\sigma_2 = \sigma_3$), we assume that the onset of dilatancy can be treated as a 2D problem (c.f. Coulomb failure). On type A grain boundaries (Figure 2), sliding is expected once the shear stress ($\tilde{\tau}_A$) exceeds a critical grain boundary shear strength and when the normal tensile stress on type D grain boundaries ($\tilde{\sigma}_D$) exceeds the tensile strength ($\tilde{T}_0$). The criterion for shear failure is assumed to be expressible by a coulomb frictional slip criterion expressed by: $\tilde{\tau}_A = \tilde{\mu}\,\tilde{\sigma}_A + S_0$, in which $\tilde{\mu}\,(-)$ is the microscopic, grain boundary friction coefficient, $\tilde{\sigma}_A$ is the normal stress acting on the inclined A-type grain boundaries and S_0 is the grain boundary cohesion.
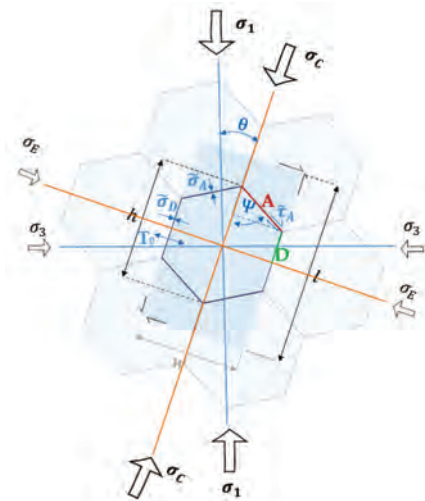
Figure 2: Microstructural model of hexagonal grain used to construct the GBFS-model, the unit cell is shown in shaded blue. The grain shape is defined by the apical angle (ψ) and aspect ratio ($R = \frac{h}{w}$) and its orientation with respect to the largest principal stress is denoted by θ. The grain boundaries along which sliding occurs (type A: $\tilde{\tau}_A = \tilde{\mu}\,\tilde{\sigma}_A + S_0$) and where tensile failure occurs (type D: $\tilde{\sigma}_D = -\tilde{T}_0$) are both indicated in the figure. σ_C, σ_E and are the normal stresses in the rotated axis frame.

Consider the shaded unit cell shown in Figure 2, and assume a compressive stress state $\sigma_1 > \sigma_2 = \sigma_3$ that is uniform for all unit cells and orientated at an angle θ with respect to the microstructure. This state leads to the following criterion for the dilatancy-boundary as defined by the GBFS model when θ is zero:

$$\sigma_1 - \sigma_3 = \left[\frac{(2R\tan(\psi)-1)(\tan(\psi)+\mu)}{\tan(\psi)(1-\mu(\tan(\psi)))} - 1\right]\sigma_3 + \left[\frac{2T_0(R\tan(\psi)-1)(\tan(\psi)+\mu)+S_0(1+\tan^2\psi)}{\tan(\psi)(1-\mu(\tan(\psi)))}\right] \quad (1)$$

in which $R = \frac{h}{w}$.

This dilatancy boundary can be represented by a linear function given by: $\sigma_1 - \sigma_3 = \Lambda\sigma_3 + B_0$, in which Λ is the slope of the dilatancy boundary and B_0 is its intercept. Alternatively, it can be represented by a linear relation between deviatoric stress and means stress, which can be directly compared with the empirical data shown in Figure 1 represented by $\sigma_{eq} = 1.56\bar{\sigma} + 3.47$, or obtained for natural salt and synthetic salt by previous authors (Peach 1991, Peach & Spiers 1996; Popp & Kern 2001 & Alkan et al. 2007).

To investigate whether the GBFS model can indeed describe the empirically derived dilatancy boundary, it is assumed that the tensile strength and the cohesion are both negligible. Realistic grain shapes are expected to have an aspect ratio (R) of 1-1.25 and the minimum friction coefficient ($\tilde{\mu}$) at salt grain boundaries, based on friction experiments by Bos et al. 2000 and Niemeijer & Spiers 2007 is 0.5. Minimizing the length of type D grain boundaries makes it more favorable for microcracking to occur, however it is expected that a grain of which the type D grain boundary $< \frac{w}{4}$ (face D $< \frac{w}{8}$) is unrealistic, as triple junctions of $\sim120°$ are expected from microstructures. Model predictions for this range of parameter values and for $\theta = 0°$ are shown in Figure 3a.

Tilting the grain with respect to the principal stress axes, such that $0 < \theta < 30°$, facilitates slip on inclined grain boundaries (type A) (see Figure 2). At the same time, tensile failure of type D grain boundaries becomes more difficult. For this range in θ, the GBFS criterion (for $S_0, T_0 = 0$) takes the form:

$$\sigma_1 - \sigma_3 = \left[\frac{(2A-2)}{(1+\cos(2\theta)-A+A\cos(2\theta)-B\sin(2\theta))}\right]\sigma_3 \quad (2)$$

In which $A = \frac{(2R\tan(\psi)-1)(\tan(\psi)+\mu)}{\tan(\psi)(1-\mu(\tan(\psi)))}$ and $B = \frac{(2R\tan(\psi)-1)(1-\mu(\tan(\psi))-\tan(\psi)(\tan(\psi)+\mu))}{\tan(\psi)(1-\mu(\tan(\psi)))}$.

When $\theta = 13°$, the slope of the dilatancy boundary is minimal ($\Lambda = 10.0$). This theoretical dilatancy boundary is plotted for $\psi = 60°, \mu = 0.5, R = 1.155$ in equivalent stress ($\sigma_1 - \sigma_3$) vs. mean stress (($\sigma_1 + 2\sigma_3$)/3) space in Figure 3a, alongside the predictions for the same shape where $\theta = 0°$. The empirical criterion shown in Figure 1a, which fits the dilatancy data obtained in our experiments, is added for comparison. Only predictions for unrealistic grain shapes (D $= \frac{w}{16}$, $\psi = 41.6°$, orange hexagon) approach the measured dilatancy boundary; reasonable values for R (≤ 1.25), ψ ($\geq 50°$) and μ (≥ 0.5), at all values of θ predict dilatancy at significantly higher differential stresses than observed experimentally. It can be concluded that the present GBFS-model for solid-solid grain boundary contacts (e.g. assuming dry grain boundaries or grain boundaries where any fluids present do not become over-pressured or wet the grain boundary) cannot account for dilatancy in rock salt.
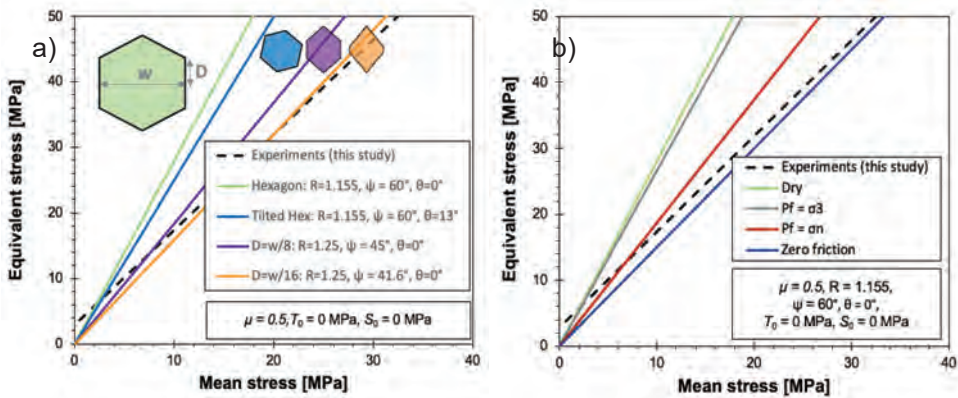
Figure 3: Dilatancy boundaries predicted by the GBFS-model compared to the dilatancy boundary derived from experiments in this study (equivalent stress vs. mean stress), for: (a) dry full solid-solid grain boundary contacts and (b) for grain boundaries containing inclusions taking up a fraction of 0.5 of the grain boundary, with a fluid pressure at respectively σ_3 and σ_n (the local normal stress on face A and D), and considering zero friction due to fluid lubrication. Note that the condition $P_f = \sigma_n$ (red line in b) represents the dilatancy boundary just before the inclusion becomes unstable as it represents the limit fluid pressure above which hydrofracture occurs. Also note that zero friction (blue line in b) does not imply that the intrinsic friction coefficient of the rock salt drops to zero, but that the effective normal stress is zero as the grain boundary is lubricated.

Let us now consider the possible effects of brine present in grain boundaries. There is widespread evidence for the presence of brine inclusions, channels and films in grain boundaries in natural rock salt (e.g. Urai et al. 1986), which may potentially affect grain boundary shear and tensile strength. Experiments on dry versus brine-saturated granular salt have shown that any chemical effect of brine on intergranular friction coefficient is close to negligible (Niemeijer & Spiers 2006). However, when inclusions are present at a pressure larger than 0, the grain boundary contact area decrease and the intrinsic grain boundary stress increases, which does affect the stress required to get dilatancy following the GBFS-model. Based on microstructural evidence (e.g. Urai et al. 1986), here it is assumed that inclusions take up 50% of the grain boundary contact area.

For brine-bearing grain boundaries, two end-member assumptions can be made regarding the brine pressure in inclusion arrays, channels or films: (1) the fluid pressure is equal to σ_3, which is a reasonable approximation for dilated salt near a fluid-filled borehole, assuming that the minimum principal stress (σ_3) normal to the borehole wall is equal to the fluid pressure; and (2) the fluid pressure in individual grain boundaries is equal to the local normal stress on the grain boundary (At face A: $P_f = \tilde{\sigma}_A$, At face D: $P_f = \tilde{\sigma}_D$). which both lower the dilatancy boundary (see Figure 3b). The case where the fluid pressure in the inclusions is equal to the local normal stress on the grain boundary must be considered as an upper limit as the inclusions cannot be stable at higher fluid pressures.

However, when the fluid in grain boundary inclusions or channels does increase beyond this stress the inclusions become over-pressured by compression of the grain boundary structure, reducing the effective normal stress and even "hydrofracturing" solid-solid contact points, then grain boundary frictional strength will be significantly further reduced compared with a dry grain boundary. Similarly, if thin, connected brine films form in grain boundaries due to dissolution of solid-solid contact points, hence spreading of fluid inclusions and associated dynamic wetting of the grain boundaries (see Van Oosterhout et al., this volume), then the effective

normal stress and frictional strength again fall to zero – provided the fluid film is not squeezed out from asperity contacts.

When the fluid inclusions become mobilized, the effective stress on the grain boundary is zero, and the dilatancy boundary (for $S_0, T_0 = 0$) is given by:

$$\sigma_1 - \sigma_3 = [2R\tan(\psi) - 2]\sigma_3 \tag{3}$$

For $\psi = 60°$ and $R = 1.155$, in the absence of an effective stress on the inclined grain boundary (face A), the slope of the dilatancy boundary (Λ) is 2.0 (see Figure 3b). This is very close to the slope of the dilatancy boundary observed in the dilatancy experiments in this study and previous work (e.g. Peach 1991; Peach & Spiers 1996; Popp & Kern 2001 & Alkan et al. 2007). Taking $\psi = 50°$ and $R = 1.25$ (at $\theta = 0°$, which is the most favorable orientated if the grain boundaries are lubricated) in combination with a lubricated grain boundary reduces the slope of the dilatancy boundary even further to $\Lambda = 1.6$. It can be concluded that the current GBFS model is able to explain the observed dilatancy boundary only when the grain boundaries are wetted and there is no grain boundary friction. Therefore, if the GBFS model applies, the dilatancy boundary obtained in our experiments and described in previous work should reflect a dilatancy boundary for "wet" rock salt with wetted grain boundaries. Based on this result, there should be a significant difference in the deviatoric stress required to obtain dilatancy in dried rock salt ($\Lambda > 10.0$) compared with wet rock salt ($\Lambda = 2.0$). However, no such effect is seen in our experimental results (see Figure 1b). The absence of any significant difference in dilatancy development in our dried and wet (undried and brine pressurized) Leinesteinsalz samples accordingly eliminates the possibility that dilatancy is controlled by intergranular slip on wet or dry grain boundaries (see Figure 1b).

4.2   Plastic strain incompatibility model

An alternative approach is that dilatancy in rock salt is caused by the plastic anisotropy of individual grains. While the crystal orientations of halite grains in rock salt are generally uniformly distributed (Kern 1977), favorably orientated grains deform more than unfavorably orientated grains. This indicates that the condition of complete strain compatibility between grains is not satisfied (Wenk et al. 1989) and Taylor's classical model, that requires all crystals to deform at the same rate and therefore to undergo the same shape change as the polycrystal, does not apply for halite. For a polycrystalline aggregate to deform homogeneously, at least five independent slip-systems have to be active to satisfy the Von Mises condition for uniform strain in a polycrystalline aggregate (Von Mises 1928). Carter & Heard (1970) show that in halite at low temperatures, only the $\{110\} < 1\bar{1}0 >$ slip systems are active, meaning that the Von Mises conditions will not be satisfied, and that deformation and stress state will be heterogeneous from grain to grain with voids opening at grain boundaries when pressures are too low to force significant lattice bending or activation of additional slip systems.

Therefore, we have derived an exploratory model which assumes that dilatancy is caused by intergranular void opening related to plastic strain incompatibility (PSI). The PSI model is based on a simplified/idealized microstructure consisting of identical cubic grains of edge size d, subjected to principal stresses $\sigma_1, \sigma_2, \sigma_3$ applied perpendicular to the faces of the cube (see Figure 4). Here axi-symmetric conditions are considered ($\sigma_1 > \sigma_2 = \sigma_3$). The faces, e.g. the grain boundaries normal to the principal stresses, are assumed to have spaced fluid inclusions in island-channel form, of which the islands have an initial thickness ($w_{1,2,3}^0$) and island fraction area ($\alpha_{1,2,3}^0$) under atmospheric conditions (see Figure 4). From the grain boundary microstructure of natural salts, such as the Leinesteinsalz, we take the initial contact area fraction to be around 0.5, while the grain boundary (island-channel) thickness is assumed to be in the range of 0.5-5 μm (based on microstructural observations, e.g. Desbois et al. 2012), the grain size is taken to be 5 mm and the bulk modulus of salt is taken as 30 GPa (Warren, 2016).

It is assumed that individual grains and the grain boundary islands (contact points) deform both elastically and plastically and have the same elastic and plastic properties as the macroscopic aggregate determined from the work-hardening curve obtained in the present study under (near) non-dilatant, room temperature conditions (e.g. at 20 MPa). We describe the stress strain curve obtained at these conditions by $\varepsilon = f_m(\sigma) = A\sigma^n$, with $A = 5.7 \cdot 10^{-7}$ and $n = 3.1$, which gives an accurate fit. It is furthermore assumed that the plastic misfit strain increment (a volumetric strain) is proportional to the plastic axial strain according to the relation $d\varepsilon_v^+ = \beta d\varepsilon_1^{pl}$, in which β represents the misfit factor, which is estimated to be around $0.05 - 0.1$, to account for 2% positive volumetric strain under dilatant conditions at low confinement (2.5 MPa). After applying a confining pressure, axial loading (σ_a) is assumed to cause opening of triangular-sectioned grain boundary voids or cracks, with fixed aspect ratio ($a = \frac{h^+}{\Delta w^+}$), as a result of plastic misfit strain. The cracks are assumed to open on boundaries normal to σ_3 . At the same time, axial loading causes deformation of the islands present in grain boundaries normal to σ_1. The inclusions are assumed to be filled with brine at a pore pressure of 0. The compressive deformation of the islands (process 1) and the crack opening/growth (process 2) are indicated in Figure 4b. At present, any effect of crack closure by plastic intrusion into the opening crack (process 4) is not included in the model.
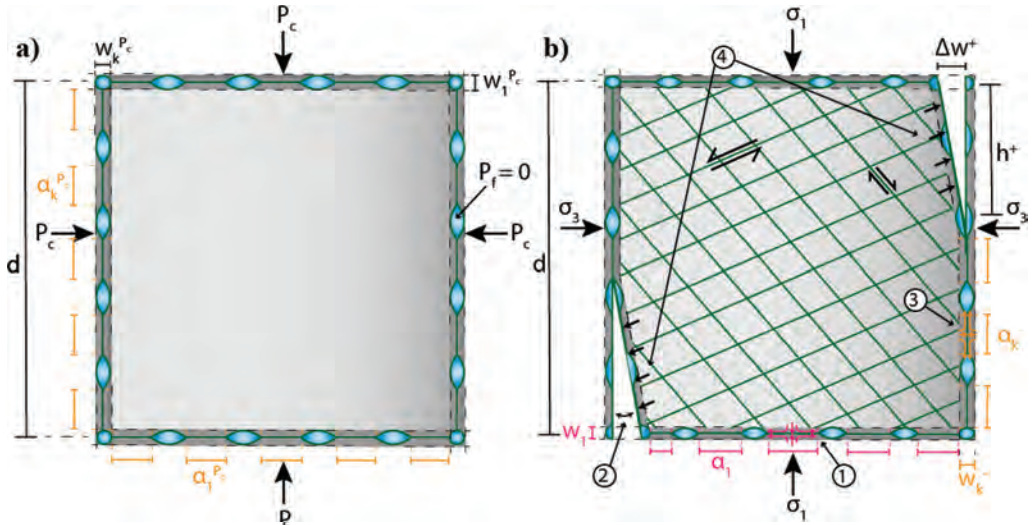
Figure 4: Schematic diagram of an idealized microstructure to illustrate the evolution of plastic strain incompatibility in rock salt under (a) hydrostatic conditions ($\sigma_1 = \sigma_3 = P_c$) and (b) under axial loading conditions $\sigma_1 > \sigma_3 = P_c$.

The stress-strain response as a result of axial loading at differential stress σ_a can now be written as:

$$\varepsilon_a = f_m(\sigma_a) - \left[f_m\left(\frac{\sigma_a + P_c}{\alpha_1}\right) - f_m\left(\frac{P_c}{\alpha_1^{P_c}}\right)\right] \frac{w^{P_c}}{d} \tag{4}$$

in which $\alpha_1^{P_c}$ and α_1 are respectively the strained contact area fractions of the horizontal grain boundaries after applying a confining pressure and axial loading, and w^{P_c} is the width of the grain boundaries after applying a confining pressure. The volumetric strain resulting from axial loading (compaction defined as positive) at differential stress σ_a is subsequently given by the relation:

$$\varepsilon_{va} = \frac{\sigma_a}{3K} + \left[f_m\left(\frac{\sigma_a + P_c}{\alpha_1}\right) - f_m\left(\frac{P_c}{\alpha_1^{P_c}}\right)\right] \frac{w^{P_c}}{d} - \beta[f_m(\sigma_a)] + \frac{w^{P_c}}{d}\left[f_m\left(\frac{P_c}{\alpha_k}\right) - f_m\left(\frac{P_c}{\alpha_k^{P_c}}\right)\right] \tag{5}$$

Here, the first term on the right hand side represent the elastic volumetric compression due to axial loading, the second term the volumetric compression of the grain boundaries normal to σ_1, the third term is the volumetric dilatation due to plastic misfit strains and the fourth term represents the volumetric compression of the grain boundaries normal to σ_3 (which is equal to P_c), in which $\alpha_k{}^{P_c}$ is the contact area fraction of the vertical grain boundaries after applying a confining pressure and $\alpha_k{}^-$ is the contact area fraction of the vertical grain boundaries after dilatant crack opening, corrected for the length of the crack, which in turn is given by:

$$h^+ = d\sqrt{\frac{a\beta[f_m(\sigma_a)]}{2}}$$

(6)

where a is the crack aspect ratio, here taken as 4 on the basis of microstructural observations. The volumetric strain evolution predicted by this set of equations (plus the assumption that all plastic flow occurs at constant volume) for a range of confining pressures is shown in Figure 5. The PSI-model successfully predicts the initial compaction and then dilatant behavior seen in at low confining pressure. However, the transition to non-dilatant behavior observed in experiments at high confining pressure, is not predicted by this model. This is presumably because plastic intrusion into opening cracks is not yet included. Further work on this is underway.
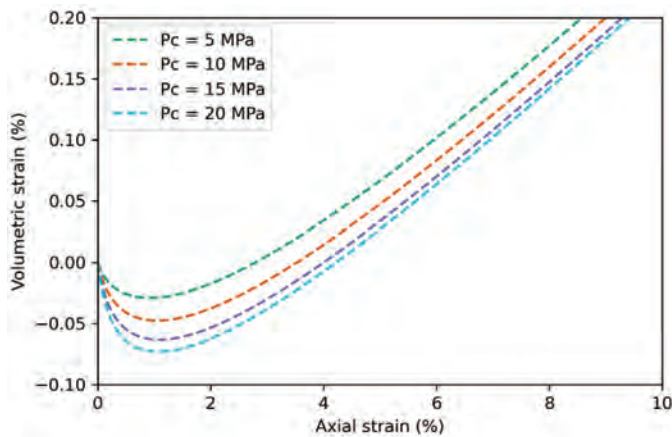
Figure 5: Volumetric strain evolution as a function of axial strain predicted by the PSI model for $P_c = 5 - 20$ MPa.

5   Implications of experimental results on dilatancy in rock salt

The present experimental results confirm earlier work that dilatancy is limited to rock salt subjected to confining pressures at or below $15.0\ MPa$ or mean stresses $< 20.0\ MPa$. Based on the experimental results in this study, a linear dilatancy boundary has been constructed (see Figure 1a). Although, the dilatancy boundary can be extended to higher mean stresses, the strength of the samples measured at different strains, indicates that the differential stresses required to get dilatancy above a mean stress of $20.0\ MPa$ are not supported. Hence, the part of the dilatancy boundary that has a significant meaning is limited to a mean stress of $< 20\ MPa$. Based on the microphysical models described in this study, it can be excluded that frictional sliding in combination with tensile opening (e.g. the GBFS-model) is the sole mechanism governing dilatancy in rock salt. For any realistic grain shape, for full solid-solid contacts dilatancy by the means of frictional sliding will occur at much higher stresses than observed in experiments on dried samples. The PSI-model on the other hand does describe the observed behavior at low confining pressures ($\leq 10\ MPa$). However, it fails to describe a transition to non-dilatant behavior at higher confining pressures ($> 15\ MPa$). Further work on

the PSI-model is required to test whether plastic misfit strains, possibly in combination with local grain boundary slip, can account for the observed microstructural changes associated with dilatancy. At stresses near and certainly above the dilatancy boundary, it is expected that creep processes are accelerated due to the damage and the presence of a connected microcrack network (Alkan et al. 2009). Hampel 2012, describes a composite dilatancy model (CDM) to account for the reduction in load-baring capacity with increasing damage and dilatancy. In addition, they consider the effect of the access of humidity on enhancing creep rates once microcracks are present (see Hampel & Schulze 2017). However, both the influence of damage (δ_{dam}) and humidity (Θ) are modeled by empirical functions, based on an empirical dilatancy boundary given by $\sigma_{eq} = -0.0369 \cdot \bar{\sigma}^2 + 1.9663 \cdot \bar{\sigma} + 1.3001$. The CDM model allows for both the effect of a damage and humidity parameter to be $0 * f(\Theta, \delta_{dam})$ in the non-dilated field and rapidly rises to $1 * f(\Theta, \delta_{dam})$ near and above the dilatancy boundary. In this study, the aim is to derive a microphysical basis for the transition to dilant behavior, which then can be used to account for the microstructural changes associated with dilatancy and directly related to estimate the acceleration of creep in the dilant field. As such, the CDM model does not provide a microphysical basis for dilatancy either. The dilatancy boundary used for the CDM-model deviates to lower differential stresses around a mean effective stress of $15.0 \, MPa$, with respect to the dilatancy boundary obtained from experiments in this study. Hence at mean effective stresses above $15.0 \, MPa$, it is expected that the creep acceleration due to dilatancy based on our dilatancy boundary is modest compared to the CDM model. Although, a quantitative comparison is difficult as the CDM model and its parameters are entwined with the dilatancy boundary of their study.

6   Conclusions

Deformation experiments have been performed to investigate the influence of plastic deformation processes on dilatancy and permeability on natural Leinesteinsalz rock salt. The experiments were carried out in the work hardening flow regime at room temperature at strain rates of $4.8 \cdot 10^{-5} \, s^{-1}$. Two microphysical models were constructed in an attempt to explain the mechanisms causing dilatancy and microcrack development at the grain-scale, based on intergranular slip and plastic strain incompatibility. The principal results and conclusions are summarized below.

- Dilatancy in Leinesteinsalz is observed at confining pressures $\leq 15 \, MPa$. No transition from non-dilated to dilated behavior is observed in experiments $> 15 \, MPa$ and the stress/strain conditions at which dilatancy is expected to occur cannot be reached under conditions relevant for both natural and induced behavior.
- The experiments on Leinesteinsalz indicate that the dilatancy boundary can be described as a linear function of equivalent stress versus mean stress. This linear boundary has no meaning above a mean effective stress of $20 \, MPa$, as the differential stress required for dilatancy is not supported by the sample.
- The GBFS-model cannot explain the observed dilatancy boundary unless grain boundary frictional resistance is zero. This condition can theoretically be achieved if mechanical loading results in coating of the grain boundaries with fluid films. However, the absence of any significant difference between dilatancy in dry and wet Leinesteinsalz eliminates the possibility that dilatancy in rock salt is controlled by intergranular frictional slip and the GBFS-model does not describe the mechanisms associated with dilatancy in rock salt.
- Dilatancy in rock salt is likely to be controlled by the opening of voids related to plastic misfit strains, which are compensated for by closure of voids by plastic compaction at higher confining pressures. Work is in progress to understand and model this better.

Acknowledgements

References

ALKAN, H., CINAR, Y. & PUSCH, G. 2007. Rock salt dilatancy boundary from combined acoustic emission and triaxial compression tests. International journal of rock mechanics and mining sciences, 44(1), 108-119.

ALKAN, H. 2009. Percolation model for dilatancy-induced permeability of the excavation damaged zone in rock salt. *Int. J. Rock Mech. Min. Sci. 46 (4)*, pp. 716–724.

BÉREST, P. & BROUARD, B. 2003. Safety of salt caverns used for underground storage blow out; mechanical instability; seepage; cavern abandonment. *Oil & Gas Science and Technology*, 58.3: 361-384.

BOS, B., PEACH, C.J. & SPIERS, C.J. 2000. Slip behavior of simulated gouge-bearing faults under conditions favoring pressure solution. J. Geophys. Res. Solid Earth 105 (B7), pp. 16699–16717.

CARTER, N.L. & HEARD, H.C. 1970. Temperature and rate dependent deformation of halite. *Am. J. Sci.*

CELIA, M.A., BACHU, S., NORDBOTTEN, J.M., KAVETSKI, D. & GASDA, S.E. 2005. Modeling critical leakage pathways in a risk assessment framework: representation of abandoned wells. In: *Fourth Annual Conference on Carbon Capture and Sequestration DOE/NETL*.

DAVIES, R.J., ALMOND, S., WARD, R.S. JACKSON, R.B., ADAMS, C., WORRALL, F. HERRINGSHAW, L.G., GLUYAS, J.G. & WHITEHEAD, M.A. 2015. Reply: "Oil and gas wells and their integrity: Implications for shale and unconventional resource exploitation". *Mar. Pet. Geol. 59*, pp. 674–675.

DESBOIS, G., URAI, J.L., DE BRESSER, J.H.P. 2012. Fluid distribution in grain boundaries of natural fine-grained rock salt deformed at low differential stress (Qom Kuh salt fountain, central Iran): Implications for rheology and transport properties. *Journal of Structural Geology*, 2012, 43: 128-143.

HAMPEL, A. 2012. The CDM constitutive model for the mechanical behavior of rock salt: Recent developments and extensions. *Mechanical Behavior of Salt VII*, pp. 45-55.

HAMPEL, A. & SCHULZE, O. 2017. The composite dilatancy model: a constitutive model for the mechanical behavior of rock salt. *Mechanical behavior of salt-understanding of THMC processes in salt. CRC Press*, pp. 99-107.

HUNSCHE, U. 1998. Determination of dilatancy boundary and damage up to failure for four types of rock salt at different stress geometries. *Ser. rock soil Mech.*

KERN, H. 1977. Preferred orientation of experimentally deformed limestone marble, quartzite and rock salt at different temperatures and states of stress. *Tectonophysics 39 (1–3)*, pp. 103–120.

KHALEDI, K., MAHMOUDI, E., DATCHEVA, M. & SCHANZ, T. 2015. Stability and serviceability of underground energy storage caverns in rock salt subjected to mechanical cyclic loading. *Int. J. Rock Mech. Min. Sci. 86 (July)*, pp. 115–131.

NIEMEIJER, A.R. & SPIERS, C.J. 2006. Velocity dependence of strength and healing behavior in simulated phyllosilicate-bearing fault gouge. *Tectonophysics 427 (1–4)*, pp. 231–253.

NIEMEIJER, A.R. & SPIERS, C.J. 2007. A microphysical model for strong velocity weakening in phyllosilicate-bearing fault gouges. *J. Geophys. Res. Solid Earth 112 (10)*, pp. 1–12.

ORLIC, B. & BUIJZE, L. 2014. Numerical modeling of wellbore closure by the creep of rock salt caprocks. In 48th US Rock Mechanics/Geomechanics Symposium. OnePetro.

PEACH, C.J., SPIERS, C.J., TRIMBY, P.W. 2001. Effect of confining pressure on dilatation, recrystallization, and flow of rock salt at 150 C. Journal of Geophysical Research: Solid Earth 160(B7), 13315-13328.

PEACH, C.J. 1991. Influence of deformation on the fluid transport properties of salt rocks (Doctoral dissertation, Faculteit Aardwetenschappen der Rijksuniversiteit te Utrecht).

POPP, T., KERN, H., & SCHULZE, O. 2001. Evolution of dilatancy and permeability in rock salt during hydrostatic compaction and triaxial deformation. Journal of geophysical research: Solid Earth, 106(B3), 4061-4078.

SUTHERLAND, H.J. & CAVE, S.P. 1980. Argon gas permeability of new mexico rock salt under hydrostatic compression. *Int. J. Rock Mech. Min. Sci. Geomech. 17 (5)*, pp. 281–288.

TRIMMER, D. 1982. Laboratory measurements of ultralow permeability of geologic materials. Rev. Sci. Instrum. 53 (8), pp. 1246–1254.

TSANG, C.F., BERNIER, F. & DAVIES, C. 2005. Geohydromechanical processes in the excavation damaged zone in crystalline rock, rock salt, and indurated and plastic clays – in the context of radioactive waste disposal. International Journal of Rock Mechanics and Mining Sciences, 42(1), 109–125.

VON MISES, R. 1928. Mechanik der plastischen Formänderung von Kristallen. *Zeitschrift für Angew. Math. und Mech.* pp. 161–185.

WARREN, J.K. 2016. Evaporites: A geological compendium. Springer.

WENK, H.R., CANOVA, G., MOLINARI, A. & MECKING, H. 1989. Texture development in halite: comparison of Taylor model and self-consistent theory. *Acta metallurgica*, 1989, 37.7: 2017-2029.

A review of frictional sliding on brine-penetrated faults in salt

André Niemeijer[1], Martijn van den Ende[2], Chris Marone[3,4], Derek Elsworth[4,] Chris Spiers[1]*

[1]Department of Earth Sciences, Utrecht University, The Netherlands; [2]Université Côte d'Azur, OCA, UMR Lagrange, France; [3]Dipartimento di Scienze della Terra La Sapienza Università di Roma, Italy, [4] Department of Geosciences, Pennsylvania State University, USA

* a.r.niemeijer@uu.nl

ABSTRACT: We review and discuss experimental observations of the frictional sliding of porous, fluid saturated faults in salt. In previous work, granular salt has been used almost exclusively as an analogue for quartz under hydrothermal conditions due to its high solubility at room temperature. However, the frictional behavior of salt itself is of interest, since localized frictional or frictional-viscous shear might occur at low effective stresses, such as those expected if migrating brine permeates localized zones during salt tectonics or after cavern abandonment. Results from slide-hold-slide experiments, performed at room temperature and an effective normal stress of 1, 2.5 and 5 MPa, show that porous/granular faults in salt regain strength within hours. Slip-dependent weakening, velocity-weakening and stick-slip behavior were observed during sliding at constant velocity, implying significant potential for unstable, localized deformation under fluid-saturated conditions. The results demonstrate that localized frictional or frictional-viscous shear of salt could occur in fluid-permeated zones at interfaces between lithologies, is potentially unstable and might provide pathways for fluid expulsion.

1 Introduction

In studies of fault and earthquake mechanics, the transition from brittle to viscous behaviour with increasing depth, i.e. pressure and temperature, is an important topic, because earthquakes are unlikely to nucleate in viscously deforming faults. Fluid-assisted diffusion creep or pressure solution is an important mechanism operating in natural faults at upper- to mid-crustal conditions However, it is challenging to investigate the effects of pressure solution or other viscous mechanisms in natural fault rocks at laboratory time scale. In contrast, pressure solution processes are rapid in salt, even at room temperature, provided that the grain size is small enough. Fine-grained salt has therefore often been used as a rock analogue material to investigate the effects of viscous mechanisms such as pressure solution on fault strength and stability (e.g. Shimamoto 1986; Bos et al. 2000; Niemeijer & Spiers 2006).

In nature, salt is generally considered to be an efficient seal against fluid migration due to its ductile nature under typical stress and strain rate conditions. However, cases of brittle faulting and subsequent fluid infiltration in salt have been reported (Davison 2009; Schléder et al. 2008; Zhuo et al. 2013). Schléder et al (2008) performed detailed microstructural observations of veins in folded rock salt samples retrieved from an exploratory borehole. On the basis of the presence of euhedral to subhedral halite grains, indicating they grew in an open space and the presence of fluid inclusion bands, they concluded that the crack was generated by hydrofracturing of the rock salt due to the development of near lithostatic fluid pressure. Davison (2009) presents several observations of brittle faulting in salt from both outcrops and seismic data and concluded that fracturing and faulting in salt likely only occurs in the presence of high pore fluid pressure. Finally, Zhuo et al. (2013) used the similarity of biomarkers in oil and gas below and above halite beds to conclude that the halite beds in this example did not act as an efficient seal and that hydrocarbons migrated through brittle faults in the halite beds.

Since brittle faulting creates porosity and permeability, understanding the parameters that affect the frictional strength could be important. Here, we present a summary and review of experimental studies of frictional sliding of simulated salt gouges.

2 Experimental approaches

The fault friction experiments reported in this contribution have all been performed on simulated fault gouges sandwiched between different types of forcing blocks. In a seminal study in 1986, Shimamoto reported results from experiments cylindrical specimens of Tennessee sandstone with a pre-cut surface at a 30 ° angle to the central axis, covered with a thin (0.3 mm) layer of fine-grained salt (Figure 1). In these types of experiments, the cylindrical sample assembly is jacketed in a low strength jacket and subjected to variable confining pressures up to several 100s of MPa within an oil- or gas-filled pressure vessel. Shear on the simulated fault is achieved by advancing a piston at a prescribed rate, shortening the assembly. During shortening, the fault area reduces, and confining pressure will need to be adjusted to maintain constant normal stress. Total displacement on the simulated fault is limited to a few mm by the potential rupture of the jacket. Another type of friction test is the double-direct shear set-up inside a biaxial loading frame (Figure 1b). In this set-up, two identical layers of typically fine-grained material (i.e. simulated gouge) are sandwiched by two square stainless steel side blocks (typically 5x5 cm) and one rectangular central block of the same width (typically 5x10 cm). Normal stress is applied using a servo-controlled horizontal ram and shear on the layers is achieved by advancing the central piston at a prescribed rate. The fault area remains constant during shear, but the gouge layer becomes thinner with increasing displacement as gouge material is pushed down out of the fault area. The final type of friction experiments reported here are rotary or ring shear experiments, in which the sample assembly can be ring or cylinder ring shaped (Figure 1c). In the case of experiments using a cylindrical set-up, rocks such as gabbro are typically used as "wall rock" and the gouge layer is confined by an outer Teflon ring.
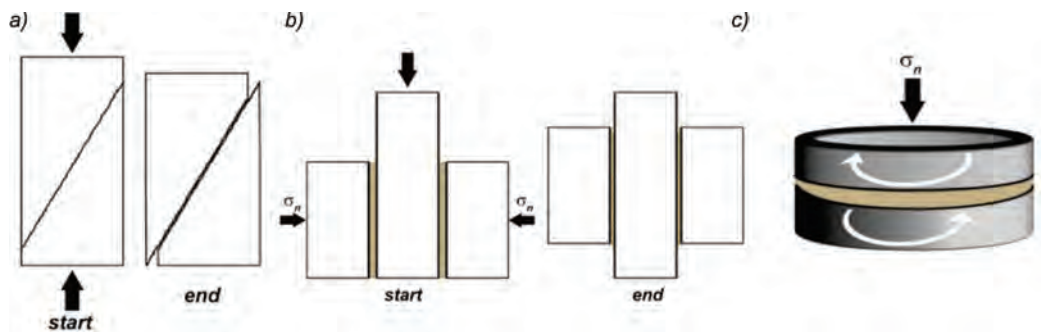
Figure 1: Diagrams of the different configurations used in the experiments reported here to investigate the frictional behaviour of simulated fault gouges. a) Saw-cut set-up, the gouge layer is sandwiched between two half cylinders cut typically at an angle of 25° to the vertical axis. b) Double-direct shear set-up, two gouge layers are sandwiched between roughened blocks, typically made of stainless-steel c) Ring shear set-up, a gouge layer is between two ring-shaped pistons (from Niemeijer et al. 2020).

In the experiments using a ring set-up, stainless rings are used, equipped with O-rings to provide a seal for pore fluids and confined by inner and outer stainless-steel rings. Importantly, in all types of experiments, the forcing blocks ("wall rocks") are artificially roughened to promote slip to occur within the gouge layer. In the case of stainless steel or other metallic forcing blocks, machined regular triangular prisms ("teeth") typically form the roughness. These teeth are regularly spaced and usually have a height of several 100s of

microns. In contrast, forcing blocks made from rocks are roughened by grinding with a sanding paper of specific roughness or by sandblasting. In all experiments, the procedure is to construct a simulated gouge layer by depositing and flattening a prescribed amount of granular salt with a known grain size distribution or fraction. The sample assembly consisting of the forcing blocks with the sandwiched gouge layer is subsequently installed in the deformation apparatus and a constant normal force is applied. In general, the sample is kept under a constant normal stress until changes in the layer thickness (compaction) are too small to measure. At this point, the secondary loading axis is engaged, and the sample is loaded in shear until slip occurs within the gouge layer. In most friction studies, the main interest is in the velocity dependence of sliding friction, expressed as an empirical variable *(a–b)*, which plays a key role in studies of earthquake nucleation using the empirical rate-and-state friction laws (RSF) (Dieterich 1979; Ruina 1983). The value of *(a–b)* is obtained by instantaneously changing the loading velocity and monitoring the change in friction:

$$(a - b) = \frac{\mu_1 - \mu_0}{\ln(v_1/v_0)}$$

where μ_0 is the steady state friction at v_0 and μ_1 is the steady state friction at v_1. In the RSF framework, a slip instability can only occur when *(a–b)* is negative and stable sliding occurs for positive values of *(a–b)*. A common goal of friction studies is thus to measure the variation in the value of *(a–b)* by shearing a sample at constant velocity until a steady state is reached followed by instantaneous changes in the loading velocity, typically at 3-fold increments (e.g. 1-3-10-30-100 µm/s). Often these types of velocity-step sequences are complemented by another procedure, so-called slide-hold-slides. In these, the loading velocity is set to zero for increasingly longer hold times and the peak friction upon re-sliding is determined and plotted as a function of hold time. In this way, a *healing* rate is determined as the loglinear slope through the data, which can be used to empirically extrapolate to natural temporal scales.

3   A note on extrapolation

In nature, seismic slip velocities are typically quoted to be in the order of m/s (Heaton 1990), whereas earthquake nucleation velocities are usually assumed to be on the order of µm/s (Marone 1998). However, it is not exactly known how to translate these to human-induced loading rates that are the consequence of changes in stress state due to the extraction or injection of fluids. A different type of experiment in which the shear stress on the simulated fault is controlled by injecting a fluid would closer mimic these cases (e.g. Scuderi & Collettini 2018). However, we can translate the loading rates shown in Figure 2 to the rates at which shear stress is applied using the stiffness of the experimental apparatuses. The lowest applicable laboratory rate of 0.001 µm/s translates to a stress change of ~0.1 kPa/s or 8.64 MPa per day, which is very high and makes a direct (empirical) extrapolation of laboratory results unreliable. It is therefore critical to identify the rate-controlling deformation mechanisms and use their kinetics to extrapolate laboratory results to nature.
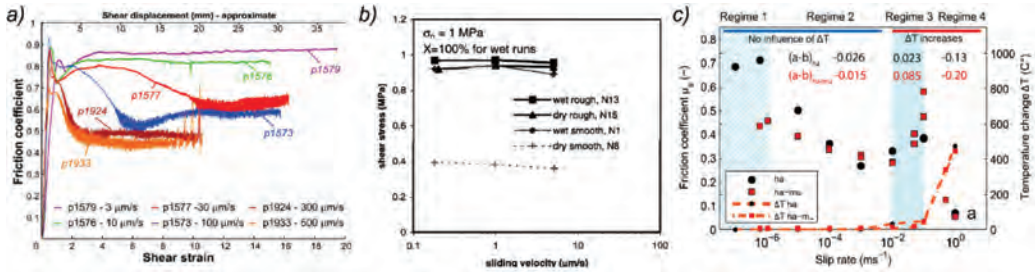
Figure 2: Results from frictional sliding experiments on simulated fault gouges of salt. a) Series of experiments at constant sliding in the presence of saturated brine at 5 MPa effective normal stress and with an initial layer thickness of 5 mm in the double direct shear set-up with steel forcing blocks (from Niemeijer et al 2010) b) Summary of velocity-stepping experiments in a rotary shear set-up with smooth and rough halite (< 3% porosity) wall rocks at 1 MPa effective normal stress in the presence of brine and with an initial layer thickness of 1 mm (from Bos et al. 2000). c) Summary of constant velocity-stepping experiments on 1 mm thick simulated fault gouges of salt (ha) and salt + 20 wt% gouge (ha-mu) at an effective normal stress of 5 MPa in a rotary shear apparatus with gabbro forcing blocks under room-dry conditions (from Buijze et al. 2017).

4   Velocity dependence of sliding strength of granular salt

In Figure 2, we show results from room temperature frictional sliding experiments on wet and room-dry granular salt gouges over a wide range of loading velocities. The steady state sliding strength depends strongly on the presence of a (chemically active) fluid, sliding velocity, displacement and the roughness of the wall rocks. At the lowest sliding velocities investigated (0.01- 10 µm/s), both room-dry and wet salt gouges have high frictional strength, with values between 0.7 to almost 1. Samples deformed dry are slightly weaker, but the difference is small compared to the effect of wall rock roughness and to that of higher slip velocities. Major weakening down to a friction of ~0.4 occurs for dry salt gouges deformed against a smooth wall rock (Figure 2b). A similar amount of weakening is observed for wet gouges deformed one to two orders of magnitude faster (v = 30-500 µm/s, Figure 2a) and even more weakening occurs in dry gouges sheared at 1 mm/s (Figure 2c). A similar observation of a broad velocity weakening was already made in 1986 by Shimamoto in saw-cut experiments on dry salt gouge performed at confining pressures up to 250 MPa. In those high confining pressure experiments, the transition from velocity strengthening to weakening occurred already at a velocity of 0.3 micron/s, which seems to decrease with increasing confining pressure. Note that the layer thickness in these experiments was only 0.3 mm.

It was noted by Shimamoto that some displacement is needed before a steady state mechanical behaviour is reached. This is also the case for wet salt gouges as shown in Figure 2a and was also demonstrated in the studies by Bos et al. (2000) and Buijze et al. (2017). The amount of displacement (or shear strain) needed to reach steady state sliding shortens with increasing sliding velocity and decreasing wall rock roughness (Niemeijer et al. 2010).

5   Failure or peak frictional strength of granular salt

Another interesting feature of the frictional strength of wet granular salt can be seen in Figure 2a. It seems that there can be quite a variability in the peak frictional strength of the gouge layers, which could be related to the loading velocity, but is more likely related to the duration of the pre-shear compaction stage. More detailed observations on this feature were made by Bos & Spiers (2002); Niemeijer et al (2008); van den Ende & Niemeijer (2019), by performing slide-hold-slide experiments on simulated fault gouges of brine-saturated salt. Some of their key results are shown in Figure 3. All three studies demonstrate that the failure strength of the simulated fault increases rapidly with increasing hold duration, particularly in brine-saturated samples. Moreover, the strength recovery is larger when the loading velocity is higher. The volumetric data shown in the bottom panel of Figure 3c indicate that there is a correlation between the strength recovery and the amount of compaction during the hold period. It seems that a higher porosity is sustained during sliding at higher velocity which allows for faster and more compaction during the hold periods, which in turn leads to a higher failure strength upon re-shear.
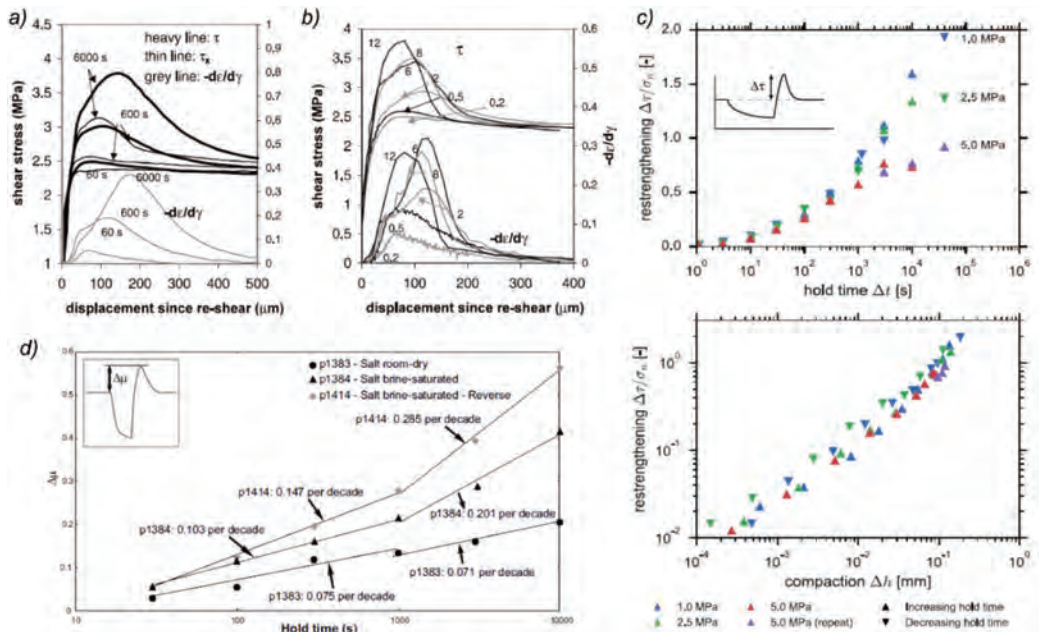
Figure 3. Experimental results of slide-hold-slide experiments on brine-saturated and room-dry salt gouges a), b) Experiments in a rotary shear set-up an effective normal stress of 2.5 MPa (from Bos & Spiers 2002). Sliding velocity was 2 ⬜m/s in the experiments shown in a) with variable hold times, hold time was 600 seconds with variable loading velocities in b). c) Results from the same rotary shear set-up as Bos & Spiers (2002) with a loading velocity of 10 ⬜m/s (from Van den Ende & Niemeijer 2019). Data shows the amount of excess frictional strength developed during the holds relative to the steady state sliding friction. Bottom panel shows the same data but plotted as a function of observed compaction during the hold. d) Results from the double-direct shear configuration at a loading rate of 5 ⬜m/s and an effective normal stress of 5 MPa (from Niemeijer et al. 2008).

The data in the bottom panel of Figure 3c shows a loglinear relation between the strength recovery and the amount of compaction during the hold but this seems to deviate at larger values of compaction. In Figure 4 we can see why this is the case. In the shear stress vs.

normal stress plots for different hold periods, it becomes clear that the intercept at zero normal stress is no longer negligible for hold periods longer than 300 seconds. The slopes (=internal friction) and intercepts (=cohesion) are shown in Figures 4b and 4c, respectively. The strength recovery observed is not only due to the recovery of porosity lost during the hold period, but also due to the development of cohesion, which is likely to be the results of some form of grain boundary (contact) healing. Importantly, this suggests that the reactivation of brittle faults will require substantial shear stress even at zero effective normal stress.
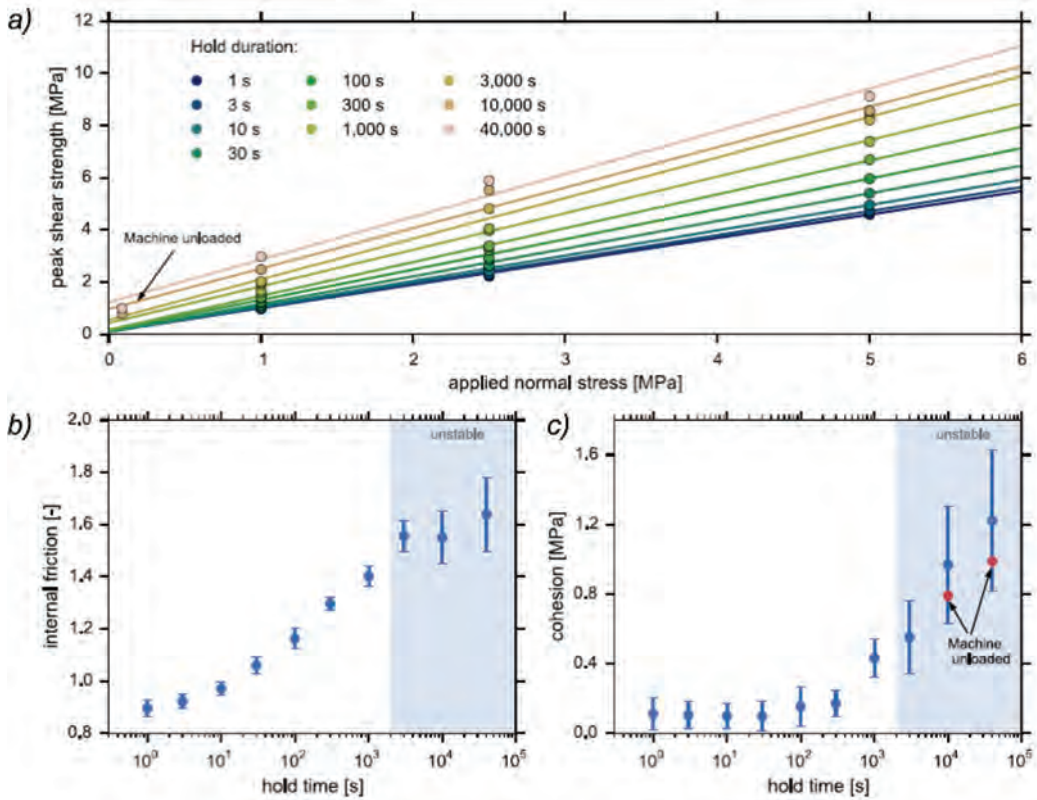
Figure 4: Data derived from slide-hold-slide experiments on brine-saturated salt gouges (from Van den Ende & Niemeijer 2019). a) Peak shear stress upon-research as a function of applied normal stress for different holds b) Values of the slopes (=internal friction) as a function of hold time c) Values of the intercepts (=cohesion) as a function of hold time.

6   Microstructures

In Figure 5, we show some representative microstructures of salt gouges sheared in the presence of saturated brine. Gouges sheared at relatively low velocity (< 10 µm/s) display low porosity domains separated by fractured domains at a low angle to the shear zone

boundary (Riedel shear, Logan et al. 1992). In contrast, gouges sheared at higher velocity show high porosities (estimated ~20-25%), in domains that are either parallel or at low angle to the shear zone boundary. Notably, a boundary parallel domain is present which is characterized by severe grain size reduction compared to the remainder of the gouge layer (boundary shear). Similar microstructures are observed for samples deformed under room-dry conditions or in the presence of a chemically inert conditions for all sliding velocities. The presence of the boundary shear seems to be correlated to the occurrence of frictionally unstable sliding.
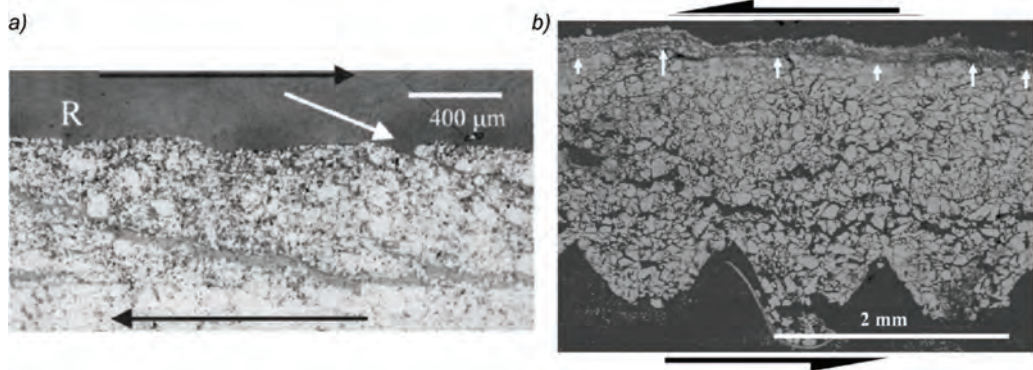
Figure 5: Examples of microstructures obtained in friction experiments on brine-saturated salt gouges. a) Reflected light image of salt gouge deformed at 2 μm/s and 1 MPa normal stress with a smooth halite wall rock (from Bos et al. 2000). White arrow indicates a Riedel shear, shear sense as indicated b) Backscatter Electron image of salt gouge deformed at 100 □m/s and 5 MPa normal stress. White arrows indicate a fine-grained boundary shear. Shear sense as indicated (from Niemeijer et al. 2010).

7　　Summary, implications, and suggestions for future work

The frictional strength of salt gouges is controlled to a large extent by the volumetric behaviour of the gouge layer, i.e. at low sliding velocity in the presence of a chemically active fluid, compaction via pressure solution keeps the porosity of the gouge layer low, forcing localized fracturing of the gouge layer at a low angle to the shear zone boundary. In contrast, in gouges with a relatively lower activity of pressure solution compaction, grain size reduction produces a boundary parallel shear band which causes a weakening of the gouge layer and frictional unstable sliding.

This implies that the brittle reactivation of faults in salt can generate significant porosity and permeability, depending on the nature of the fluids present and on the loading rate. In the presence of brine, such porosity and permeability will be rapidly destroyed due to the fast compaction via pressure solution and the fine grain size produced during sliding.

For future work, it would be useful to establish how fault-parallel and fault-perpendicular permeability of brittle faults in salt evolves with slip and time and to contrast the behaviour of the simulated gouges in the presence of brine vs. that in the presence of H_2 or CO_2 and of mixtures of these.

References

BOS, B., PEACH, C. J. & SPIERS, C. J. 2000. Slip behavior of simulated gouge-bearing faults under conditions favoring pressure solution. Journal of Geophysical Research: Solid Earth, 105, 16699-16717.

BOS, B. & C. J. SPIERS, C. J. 2002. Fluid-assisted Healing Processes in Gouge-bearing Faults: Insights from Experiments on a Rock Analogue System. Pure and Applied Geophysics, 159, 2537-2566.

BUIJZE, L., NIEMEIJER, A. R., HAN, R., SHIMAMOTO, T. & SPIERS, C. J. 2017. Friction properties and deformation mechanisms of halite(-mica) gouges from low to high sliding velocities. Earth and Planetary Science Letters, 458, 107-119.

DAVISON, I. 2009. Faulting and fluid flow through salt. Journal of the Geological Society, 166, 205-216.

DIETERICH, J. H. 1979. Modeling of Rock Friction I. Experimental Results and Constitutive Equations. Journal of Geophysical Research, 84.

HEATON, T. H. 1990. Evidence for and implications of self-healing pulses of slip in earthquake rupture. Physics of the Earth and Planetary Interiors, 64, 1-20.

LOGAN, J. M., DENGO, C. A., HIGGS, N. G. & WANG, Z. Z. 1992. Fabrics of experimental fault zones - their developement and relationship to mechanical behavior. eds. B. Evans & T.-f. Wong. Elseview.

MARONE, C. 1998. Laboratory-derived friction laws and their application to seismic faulting. Annual Review of Earth and Planetary Sciences, 26, 643-696.

NIEMEIJER, A., FAGERENG, Å., IKARI, M., NIELSEN, S. & WILLINGSHOFER, E. 2020. Faulting in the laboratory. In Understanding Faults, 167-220.

NIEMEIJER, A., MARONE, C. & ELSWORTH, D. 2008 Healing of simulated fault gouges aided by pressure solution: Results from rock analogue experiments. Journal of Geophysical Research, 113.

--- 2010 Frictional strength and strain weakening in simulated fault gouge: Competition between geometrical weakening and chemical strengthening. Journal of Geophysical Research, 115.

NIEMEIJER, A. R. & SPIERS, C. J. 2006. Velocity dependence of strength and healing behaviour in simulated phyllosilicate-bearing fault gouge. Tectonophysics, 427, 231-253.

RUINA, A. 1983. Slip Instability and State Variable Friction Laws. Journal of Geophysical Research, 88.

SCHLÉDER, Z., URAI, J. L., NOLLET, S. & HILGERS, C. 2008. Solution-precipitation creep and fluid flow in halite: a case study of Zechstein (Z1) rocksalt from Neuhof salt mine (Germany). International Journal of Earth Sciences, 97, 1045-1056.

SCUDERI, M. M. & COLLETTINI, C. 2018. Fluid Injection and the Mechanics of Frictional Stability of Shale-Bearing Faults. Journal of Geophysical Research: Solid Earth, 123, 8364-8384.

SHIMAMOTO, T. 1986. Transition between frictional slip and ductile flow for halite shear zones at room temperature. Science, 231, 711-714.

VAN DEN ENDE, M. P. A. & NIEMEIJER, A. R. 2019. An investigation into the role of time-dependent cohesion in interseismic fault restrengthening. Sci Rep, 9, 9894.

ZHUO, Q.-G., MENG, F.-W., SONG, Y., YANG, H.-J., LI, Y. & NI, P. 2013. Hydrocarbon migration through salt: evidence from Kelasu tectonic zone of Kuqa foreland basin in China. Carbonates and Evaporites, 29, 291-297.

Microstructural evolution of glacier salt from the Kuh-e-Namak salt diapir, Iran

Julia Schmitz[1], Prokop Závada[2], Janos L. Urai[1]*

[1]Institute of Tectonics and Geodynamics, RWTH Aachen University, 52064 Aachen, Germany; [2]Institute of Geophysics of the Czech Academy of Sciences, Czech Republic;

[*] julia.schmitz@tag.rwth-aachen.de

ABSTRACT: During an extensive field campaign, we have studied the full range of microstructures from the top to bottom of the salt dome and glacier Kuh-e-Namak in Iran. For the studies, the samples were gamma-irradiated, which was followed by the thin section preparation including dry polishing and etching (Schleder and Urai, 2005). Microstructures were studied under reflected and transmitted light. The salt samples are of variable impurity content and capture a sequence of microstructures that reflect the progressive recrystallization from the top part of an extrusive dome down along the slope of an adjacent glacier. The domal coarse-grained halite is typical with relics of rectangular crystals with growth bands and elongated porphyroclasts that are surrounded by parallel zones of recrystallized halite grains. Down along the profile of the glacier, the degree of recrystallization increases, the content of porphyroclasts progressively decreases on behalf of the fine-grained matrix of elongated and strain-free halite grains. The microstructures are interpreted in terms of combined dislocation creep and solution-precipitation creep. Since pressure solution is dominant in salt glaciers at low deviatoric stress, the fine-grained salt deforms much more rapidly than predicted based on dislocation creep allowing the flow of salt glaciers as predicted by Wenkert (1979).

1   Introduction

The rheology of rock salt and its deformation mechanisms play a key role in many applications. Although understanding of salt systems and their deformation increased over the past decades, what allows glacier salt to flow downhill is poorly understood. The most interesting fact about flow in fine-grained salt in salt glaciers (i.e. namakiers, Talbot 1979) and extrusive salt nappes (Schleder & Urai 2007) is that the salt is weakened by the influence of interstitial salt-brine solution enhancing the solution-precipitation (SP) creep with a combination of dislocation creep (DC) (Urai et al. 1986, 2008; Desbois et al. 2010). Therefore, glacier salt was proposed to flow at geologically high strain rates at very low shear stress in, for example, the Zagros Mountains and in central Iran (Talbot 1979; Talbot & Rogers 1980; Talbot 1981; Talbot & Jarvis 1984; Talbot 1998; Talbot et al. 2000; Talbot & Aftabi 2004).

Since salt plays an important role in basin dynamics and the engineering industry like caverns for gas storage or nuclear waste disposal (Langer 1993; Rowan et el. 1999; Littke et al. 2008), understanding of this field example of the deformation and flow of rock salt under low temperatures and low deviatoric stress could contribute to further improvements. Especially for engineering, SP creep and measurements of salt creep at low stresses are important but also controversial (Bérest et al. 2005). Studying salt from a natural laboratory like this salt glacier gives us the result of an experiment that is relevant for salt engineering but cannot be performed in a laboratory. SP creep was already proposed by Wenkert (1979) as the main reason for weakening glacier salt. The inferred low shear stress and high strain rate (<0.25 MPa, 1.1x 10-11 to 1.9 x 10-9 1/s; Jackson, 1985) in salt glaciers are explained as creep resulting from diffusion of ions through an interstitial salt-brine solution. Furthermore, this weakening effect was also observed in experimentally deformed fine-grained wet salt by Urai et al. (1986). Závada et al. (2015) showed with samples from the salt dome and glacier Kuh-e-Namak that solid second phases can enhance the mobility of salt due to increased diffusion rates along the solid inclusion-halite contacts by SP dominated creep. These results are supported by the study of naturally deformed rocksalt-mudrock-tectonite from the subsurface

by Leitner et al. (2011) where the presence of fibrous halite in stress shadows of mudrock clasts was interpreted in terms of SP creep.

This study aims to extend our understanding of the microstructural evidence in halite in terms of deformation and recrystallization processes in salt glaciers. The analyzed samples are from the Kuh-e-Namak (Dashti) diapir in southern Iran and are well studied regarding the flow properties of different rock salt types by Závada et al. (2015). Four samples are compared on basis of grain and subgrain size, microstructural and textural analysis using gamma-irradiated thin sections.

2 Geological setting

The Kuh-e-Namak (Dashti) diapir (28.26°N; 51.70°E) is considered as an exceptional example of the on-shore salt diapirs in Iran due to the high elevation of its apical part (~1550 m a.s.l.), excellent exposure of flow structures in flow-parallel valleys and absence of caprock (the solid residuum of rock salt after dissolution) on steeply dipping glaciers (Fig. 1) (Talbot, 1979). This diapir represents the southernmost exposed salt structure of the Zagros Fold and Thrust Belt that surfaced already in the Late-Cretaceous from within a tensional jog of an en-echelon array of the N-S trending Kazeroun lineament, a major regional fault zone (Talbot & Jarvis 1984; Sepehr & Cosgrove 2005). The diapir stems from the basal source layer of the Infra-Cambrian Hormuz Salt Series originally at a depth of ~6-8 km. The Kuh-e-Namak diapir consists of an elliptical dome of 6 x 1 km elongated in NNE-SSW direction and two glaciers that are generated from both the northern and southern edges of the dome. The dome is located at the crest of the foremost anticline in the fold array of the Zagros Fold and Thrust Belt, where it is cross-cut by the Kazeroun fault. Both glaciers flow down along the flanks of oppositely dipping limbs of the anticline (Fig. 1).
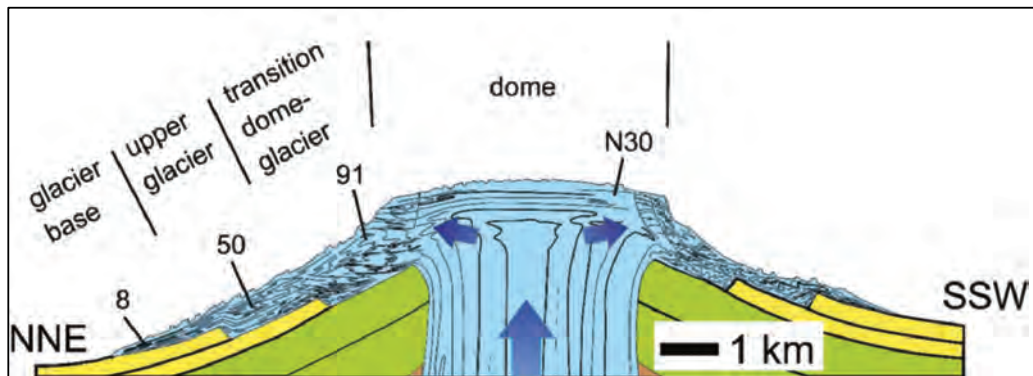
Figure 1: Simplified geological profile of the Kuh-e-Namak diapir in Iran where the four samples and their locations are shown. The salt diapir and glacier (light blue) and the flow directions are indicated by the arrows.

The outcrops reveal rock salt of variable colors, which are rendered by the fragments of the dismembered and comminuted carbonate, anhydrite and siliciclastic interlayers of the Hormuz Salt Series. These colored salt layers are distorted into Z-shaped and recumbent isoclinal folds in the glaciers. The colored rock salt types are divided into two groups, the 'dirty', where the content of insoluble residues is above 5 wt.% (gray, green, magenta and gray) and the 'clean' or translucent types, with the insoluble residues below 1.5 wt.% (red, honey brown, orange and white). While the 'dirty' rock types are in general more fine-grained and display dominantly mylonitic and equigranular microstructures, the 'clean' translucent types are typical with large porphyroclasts of halite and gneissic fabric. Recent estimates of deformation on the Kuh-e-Namak diapir from remote sensing datasets (COSI-Corr method) by Zhang et al. (2021)

identified permanent deformation after the rainfall events that were coupled with dome subsidence and uplift on the flanks of the dome and the glaciers. This latter study also identified a higher deformation rate in domains of the diapir occupied by 'dirty salts' in contrast to stagnant domains of 'clean salts' in agreement with microstructural analysis rheological inferences from Závada et al. (2015). However, the inferred rates of deformation in the order of ~20 m (Zhang et al. 2021) during the rainy season of several months seem unrealistically high.

3 Samples and methods of study

Oriented samples of rock salt were collected in both the domal part and the northern glacier of the Kuh-e-Namak (Fig. 1). According to the described methods by Zavada et al. (2015), four slab cutouts were gamma-irradiated (Urai et al. 1986; Schleder & Urai 2005; 2007; Desbois et al. 2010; Zavada et al. 2012) in the Nuclear Research Reactor of Munich (Germany) at 105 °C with a dose rate of 24-26 kGy/h to a total dose of 7.1-8.1 MGy, resulting in the blue decoration of microstructures. From the gamma-irradiated slab cutouts, thin sections were prepared and dry polished as well as surface etched subsequently (Spiers et al., 1986; Urai et al., 1985; Schleder and Urai, 2007) to show grain boundary and subgrain boundary microstructures. The microstructures were studied and imaged with reflected and transmitted, plane-polarized light microscopy. The halite grain boundaries were manually traced from reflected light micrographs of the irradiated thin sections. Afterwards, the grain and subgrain boundaries were digitalized and then analyzed with ImageJ software to calculate the equivalent circular diameter (ECD) to obtain the differential stress from subgrain piezometry.

4 Results

The following sub-sections describe typical microstructures for the domal part, dome-glacier transition, glacier and base of the glacier. The four samples are almost pure halite (~96 to 98%) with anhydrite and siltstone fragments as the main second solid phases.

4.1 Domal part - N30

The salt sample from the domal part of the diapir displays a "gneissic" fabric (Fig. 2) with a bimodal grain size distribution of sometimes rounded or subhedral large halite grains of up to 10 mm surrounded by fine-grained halite in the matrix. The gamma-irradiated section shows white polygonal subgrain boundaries in most of the halite grains in both, matrix grains and porphyroclasts (Fig. 3a). Many of the halite porphyroclasts are marked by dark blue cores with white substructure-rich rims (Fig. 3a). Some of the porphyroclasts show also substructures in their cores, whereas several grains in the matrix completely consist of subgrains (Fig. 3a). Some subgrains are elongated and terminate at the grain boundaries. Several substructure-poor grains show dark blue colored, less developed polygonal structures. Further, small grains of 0.25 to 2 mm without any subgrains are visible (Fig. 3a). Sub- to euhedral grains bulge into subgrain-rich grains (Fig. 3a). Several porphyroclasts are marked by sub-parallel or orthogonal white lines representing traces of healed intragranular microcracks terminating at the grain boundaries (Fig. 3a). These traces are in some cases more diffuse and can contain arrays of fluid inclusions (Fig. 3b). The grain boundaries have an irregular morphology with frequently sub- to euhedral grain boundary segments (Fig. 3a).

4.2 Domal-glacier transition - 91

The sample from the transition between the extrusive dome and the glacier has in some parts a stronger shaped-preferred orientation (SPO) than the sample from the domal part and shows a mylonitic fabric. The elongated or euhedral porphyroclasts of up to 12 mm are of dark to pale

blue color and surrounded by recrystallized finer-grained halite in the matrix (Fig. 2). The amount of matrix in this sample increased at the expense of the porphyroclasts (Fig. 2). The cores of the elongated clasts are mostly dominated by subgrains (Fig. 3c) and only in a few cases, they are completely free of subgrains. In comparison to the euhedral porphyroclasts, the elongated clasts are surrounded by a white, substructure-rich rim (Fig. 2). Growth bands typically developed in the sub- to euhedral grains of different grain sizes. Substructure-rich grains are also typically truncated by the boundaries of new strain-free grains (Fig. 3c). Common microstructures visible in the porphyroclasts are healed microcracks, fluid inclusion traces, slip and growth bands. From the etched surfaces in reflected light, it can be observed that the vast majority of small grains lack substructures (Fig. 3d). In general, more siltstone fragments are locally present where smaller fragments are aligned along with bands. These siltstone fragments are also accompanied by fibrous halite in their stress shadows (Fig. 3c). Different planar zones can be characterized by coarse-, fine-grained halite and the amount of solid inclusions (Fig. 2). The grain boundaries of the porphyroclasts have an irregular morphology or sub- to euhedral grain boundary segments, whereas the fine-grained matrix has mainly rectangular grain boundaries (Fig. 3d).

4.3   Glacier salt - 50

The glacier material has a strong SPO especially in the fine-grained matrix (Fig. 2) and can be characterized as a mylonitic texture. There are only a few porphyroclasts of up to 4.5 mm visible and most of them are aligned minor bands that consist of coarse-grained halite grains (Fig. 2). A progressive disintegration of the porphyroclasts and increasing content of the fine-grained matrix is visible here. The porphyroclasts are either characterized by a dark blue, substructure-rich core with a white or light blue rim or completely light blue with substructures (Fig. 2). The dark blue cores are patchy and reveal some slip bands. The lighter blue rims are substructure-rich (Fig. 3e). Euhedral, substructure-free and mostly violet halite grains are truncating substructure-free and substructure-rich grains (Fig. 3e). Most of the large solid inclusions show fibrous halite in their stress shadows (Fig. 2). Elongation of the grains as well as core-rim structures can be observed. The grain boundaries have frequently subhedral grain boundary segments (Fig. 3e). A general zonation is visible, where one can differentiate between fine-grained halite, coarse-grained with porphyroclasts and more solid inclusion-rich bands (Fig. 2). The porosity is mainly present in coarse-grained domains or in along the edges of solid inclusions as well as along the fine-grained bands that contain small solid inclusions (Fig. 2). Fine-grained bands contain halite grains more elongated and fibrous patches (Fig. 3f).

4.4   Base of glacier - 8

The sample from the base of the glacier represents a mylonitic to ultra-mylonitic fabric with a strong SPO and an average grain size of 0.322 mm. It consists of a mostly fine-grained matrix with elongated grains and a few elongated, dark blue grains, that likely represent the remains of porphyroclasts (Fig. 3g). Further, some subhedral solid inclusions of anhydrite of up to 1 mm are visible (Fig. 2). The majority of the halite grains are substructure-free (Fig. 3h). Fibrous halite is typically found in the stress shadows of the solid inclusions and the core-mantle structures of porphyroclasts (Fig. 3g). The grain boundaries have an irregular morphology. Solid inclusions are arranged in discrete bands (Fig. 2). In the solid inclusion-rich part of the sample, the halite grains are also more elongated and display a higher SPO than in the coarser grains domains of the same sample.
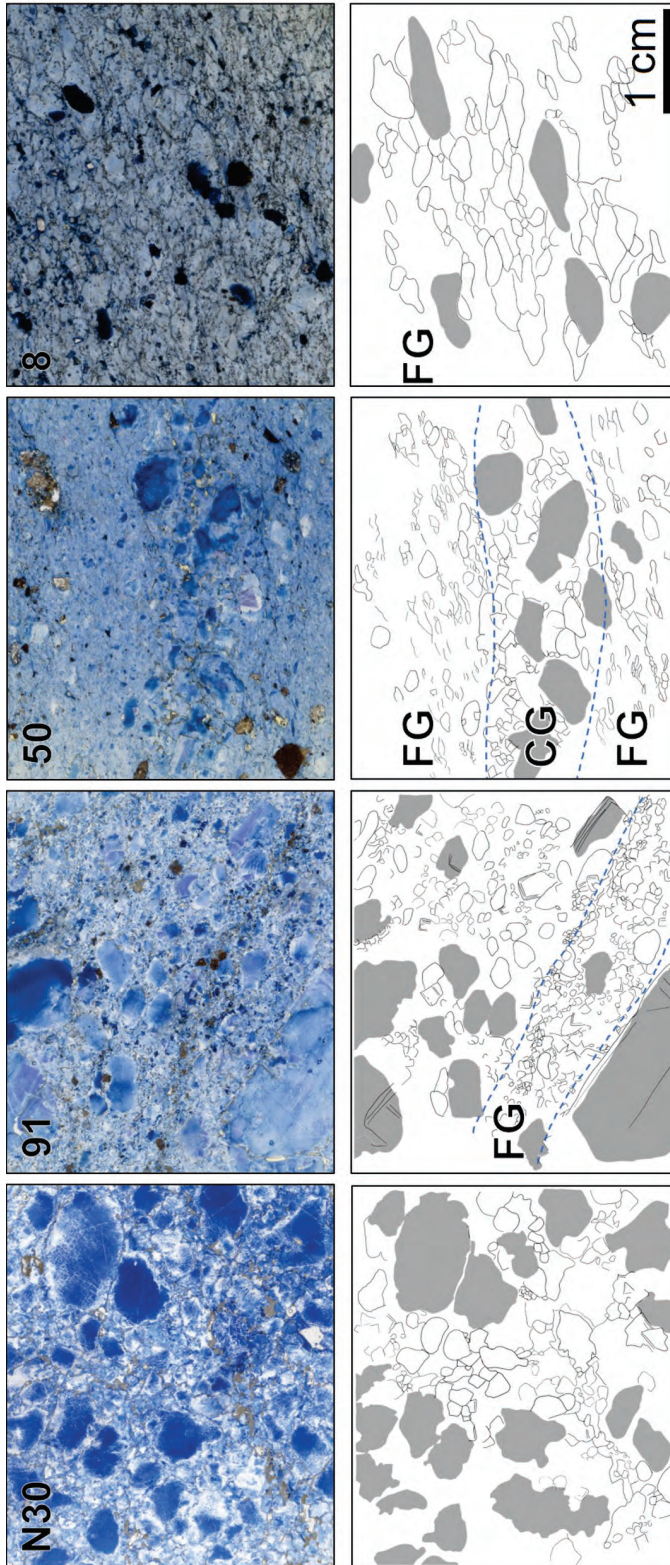
Figure 2: Microstructures under transmitted light (upper row), zonation (blue lines) and segmented porphyroclasts (grey) (lower row) of gamma-irradiated samples (N30, 91, 50 and 8) taken from the salt dome and glacier Kuh-e-Namak. N30 shows gneissic structure, no zonation and large amount of porphyroclasts. 91 shows the original euhedral halite grains surrounded by a zone of fine-grained (FG) recrystallized matrix. 50 has an increased content of fine-grained matrix is visible, whereas the content in coarse-grained (CG) porphyroclasts decreased. 8 shows dominantly the fine-grained recrystallized matrix only with a few porphyroclasts as dark blue patches and no zonation.

4.5 Porosity

The thinsections of the four samples show pores in different sizes and shapes. The largest porosity and also largest pores are present in N30. The amount of porosity and size of the pores decreases down along the profile of the glacier (Table 1, Fig. 2). Possible development of the abundant porosity can be either the leaching by fresh water from rain or another salt phase that dissolved during the thinsection preparation.
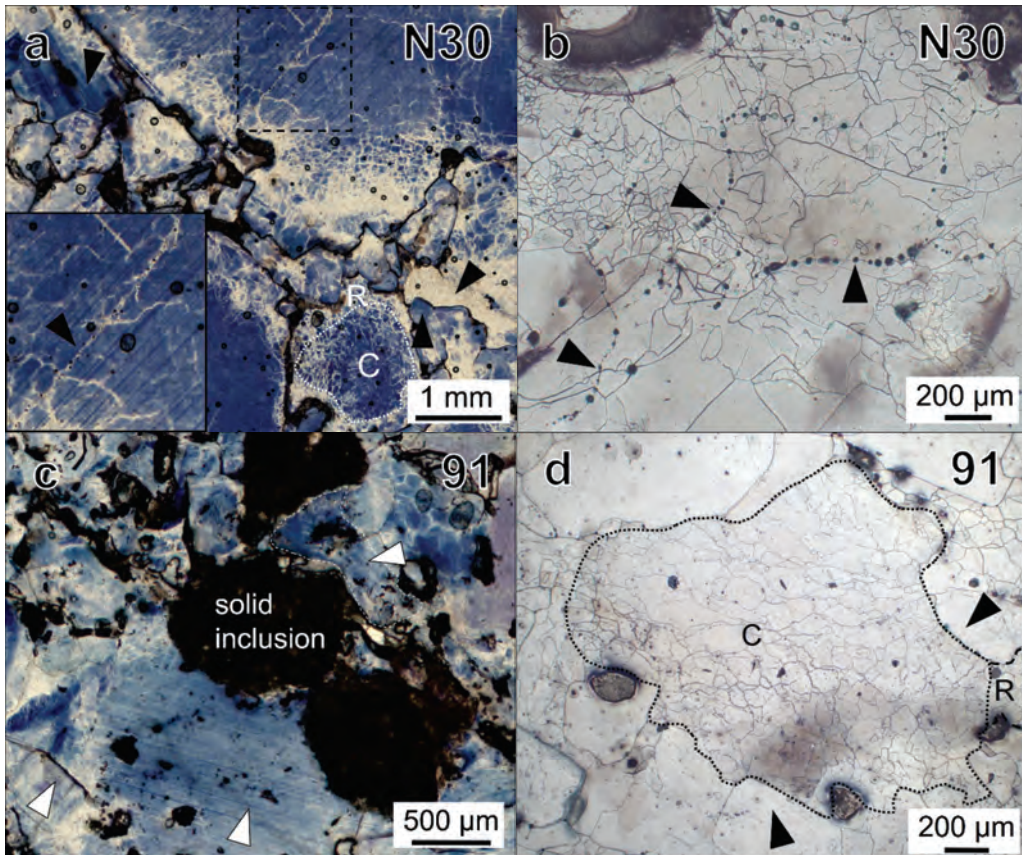
Figure 3: Microstructures of oriented thin sections created from the salt samples in transmitted (a, c,f,g) and reflected (b,d,e,h) light. a Porphyroclasts with substructure-free or-rich core (C) and a rim (R) of white polygons. Glide planes and microcracks are also present as well as sub-to euhedral matrix grains with growth bands overgrowing substructure-rich to almost white grains indicated by black arrows. b Black arrows indicate healed microcracks with fluid inclusions. c Porphyroclast with glide planes is visible which is truncated by a new grain. Solid inclusions show fibrous halite in their stress shadow indicated by white arrow. d Boundaries of sub- to euhedral grain segments of matrix grains consuming a substructure-rich porphyroclast. e Porphyroclast is consumed by subhedral new grain which is then also truncated by a new grain indicated with black arrows. f Fibrous halite in matrix in a more solid inclusion rich part of the section. g Dark blue, substructure-free cores of porphyroclasts with substructure-rich mantle and fibrous halite are surrounded by recrystallized fine-grained matrix. h Most of the halite grains show no subgrains and are recrystallized, whereas some still have subgrains.
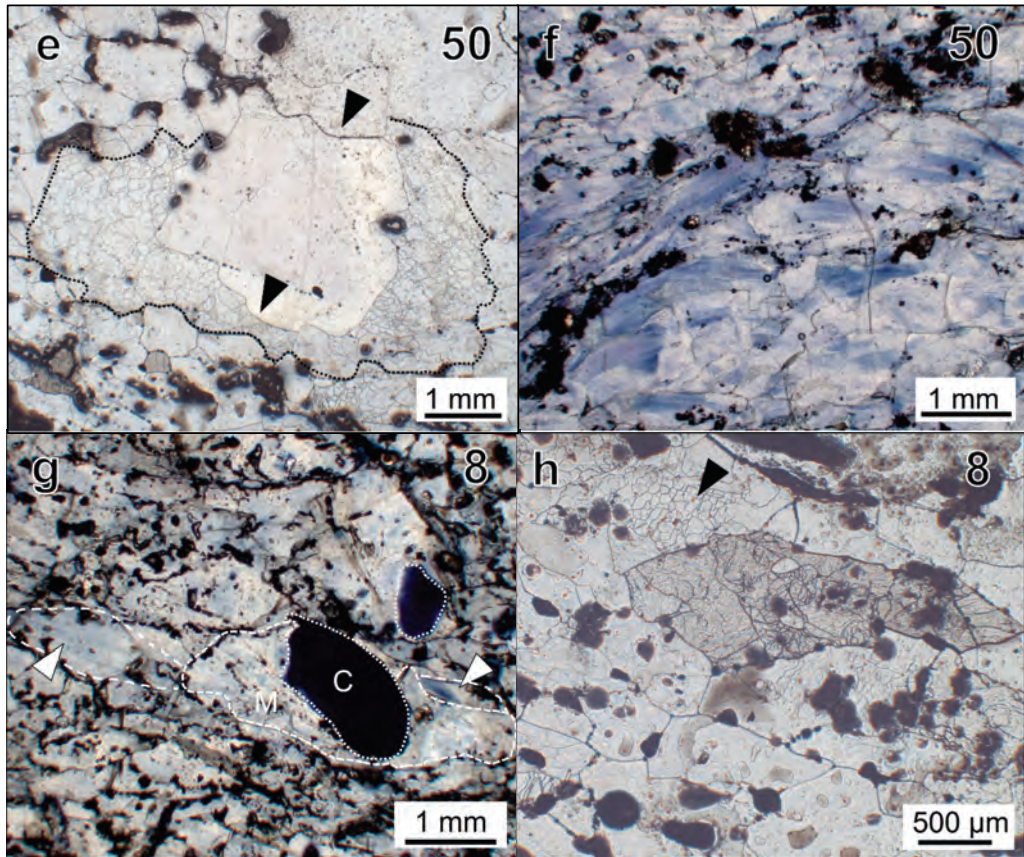
Figure 3: Continued

4.6 Quantitative microstructural analysis

Table 1: Quantitative microstructural analysis performed on grains and subgrains, as well as the share of porphyroclasts and porosity in the samples N30, 91, 50 and 8.

Samples	Grains			Subgrains			Porphyroclasts [%]	Porosity [%]
	N	Grain size	N		Subgrain size	Differential stress (MPa)		
		Mean [µm]			Mean [µm]			
Domal N30	259	342	1459	37.01	4.6	33.73	5
Transition 91	144	342	3430	37.91	4.5	26.76	3
Glacier 50	229	466	1833	32.66	5.1	11.27	2
Base 8	109	322	875	42.09	4.1	8.74	<1

5   Discussion

A previous study focused on the impact of second phases on the rheological properties of the different rock salt types of the Hormuz Salt Formation (Závada et al., 2015) based on microstructural analysis of different rock salt samples from the Kuh-e-Namak in southern Iran. The major aim of our study is to emphasize the microstructural evidence about the evolution and deformation history of the glacier salt as well as the origin of parallel zones of recrystallization.

5.1   Interpretation of deformation and recrystallization based on the microstructural study

The extruding salt at the domal part of the Kuh-e-Namak where the halite grains and porphyroclasts mainly contain subgrains shows evidence for dislocation creep (DC) (Fig. 3a, c,d,e). New grains consuming those subgrain-rich porphyroclasts indicate that the GBM of the matrix grains postdates recovery of the halite upon extrusion from narrow diapiric stem related to the stress drop (Fig. 3a). Microcracks with arrays of fluid inclusions could be attributed to i) temperature changes or ii) sample collection or iii) sample cutting and thick-section preparation. It has to be noted that the salt in this part of the Kuh-e-Namak presents no primary microstructures like chevron crystals. Therefore, we conclude that the salt is already recrystallized after extrusion in the cold diapir stem and only relict grains represent the domal salt from the source layer sequence which is described by Schoenherr et al. (2010). Since the Ara Salt from Oman, described by Schoenherr et al. (2010), is regarded as equivalent to the Hormuz Salt Series, we expect to see similar microstructures below the dome surface if it could be drilled.

The transition and glacier zone samples show the strain fringes of fibrous halite in the stress shadows of solid inclusions or halite porphyroclasts (Fig. 3c, f,g). These strain fringes result from solution-precipitation (SP) creep accompanied by grain boundary sliding (GBS), where the grain dissolution of high stressed contacts is followed by the transport by diffusion in the interstitial brine and precipitation at grain boundaries in stress shadows of adjacent grains or clasts. New grains bulging into subgrain-rich porphyroclasts suggest DC creep accommodated by fluid assisted grain boundary migration (GBM) (Fig. 3d, e). New, strain-free grains with edge-parallel growth bands that frequently are consuming subgrain-rich grains and core-rim structures of porphyroclasts indicate non-conservative GBM (Fig. 3d,e) (Schleder & Urai 2007). Equant recrystallized grains in the matrix can be interpreted as a result of SP creep associated with GBS. Subgrain-rich grains at the base of the glacier still have some evidence for DC creep even if SP creep dominated. Present porosity is due to leaching by freshwater from periodic rainfalls.

In general, the observed microstructures and the interpretation are in good agreement with previous studies of salt glaciers and fountains (Zavada et al. 2015; Desbois et al. 2010; Schoenherr et al. 2010). The average grain and subgrain size of the analyzed samples of 360 µm and 37 µm respectively show some differences to the values of other salt diapirs, e.g. South Oman Basin or domes of the Ghaba Salt Basin. Here, both, the grain and subgrain size, are larger by a factor of almost 10 for the grain and by factor 2 for the subgrain size (Schoenherr et al. 2010) in comparison to the Kuh-e-Namak. Desbois et al. (2010) results are in the same order of magnitude for grain and subgrain size.

The microstructural evolution can be summarized as followed: 1. original salt with primary deposition-related microstructures, 2. Rise through the cold stem of diapir (high stress and flow rate), subgrains development, DC creep dominated, 3. Pressure and flow drop close to the surface, GBM accommodated with microcracking, 4. Grain disintegration by GBM, 5. SP creep in glaciers enhanced by freshwater.

5.2 Parallel zones of recrystallization

The different recrystallization and deformation degrees of the zones in the samples could indicate a connection to the inter-granular solid inclusions and therefore explain the different viscosity contrasts. According to Zavada et al. (2015), the solid phases have a weakening effect on the halite and therefore enhance the SP creep as well as the hardening effect of the intragranular inclusions inhibiting the DC. That results in fine-grained zones with solid inclusions, whereas the coarser-grained zones are solid inclusion-poor and therefore not strongly affected by the weakening effect of these inclusions related to their enhanced effect for SP creep. These small-scale zonations could be upscaled for new models of the flow of halite in salt glaciers.

5.3 Stress calculation

From experimental deformation data, it is known that there is a strong correlation between the subgrain size D and flow stress σ (Carter et al., 1993). For halite this relationship can be written by (Schleder & Urai 2005):

$$D \ (\mu m) = 215 \ \sigma^{-1.15} \ (MPa) \tag{1}$$

With this relationship, an estimation for the paleostress for halite can be calculated. This study suggests high differential stresses of 4.1-5.1 MPa for the halite samples. Additionally, for the base of the glacier, a stress of 0.7 MPa was calculated from the recrystallized grain size. These results are in good agreement with Zavada et al. (2015) results of 3.1-4.6 MPa and 3.1-4.8 MPa for the Qum-Kuh salt fountain (Desbois et al. 2010). However, the slightly larger stresses are still comparable to stresses calculated by Leitner et al. (2011) for a rocksalt-mudrock-tectonite. Such high differential stress does not exist in the glacier, therefore, these high stresses are interpreted to be remains from the flow in the cold diapiric stem (Schoenherr et al., 2010). After that, no recrystallization like DC creep in the glacier occurred, where flow stresses are above 1 MPa (Wenkert 1979; Schleder & Urai 2007). The results are also supported by values for SP creep by Urai et al. (1986).

6   Conclusions

Four samples from the naturally deformed Kuh-e-Namak glacier in SW Iran represent the extruded Infra-Cambrian Hormuz Salt Formation. The samples were studied and grouped into the different locations: domal part, dome-glacier transition, glacier and base of the glacier. The microstructural evidence suggests that:

- Domal salt of gneissic fabric is characterized by dislocation creep, hence power-law creep. The differential stress was between 4.1-5.1 MPa, as deduced from the subgrain size piezometry.

- Glacier salt is of mylonitic fabric and dominated by solution-precipitation creep and grain boundary sliding and therefore close to Newtonian flow. Influence of water-assisted recrystallization is promoted by porosity development due to leaching by freshwater.

- The Kuh-e-Namak glacier is another example of the weakening effect of brine-assisted solution precipitation creep of fine-grained rock salt naturally deformed at low differential stress and shear stress leading to the lateral spreading of the glacier salt.

- The variable content of solid inclusions results in parallel zones of different amount of recrystallization and variation in deformation mechanism, which cause a viscosity contrast. This weakening effect of solid inclusions on halite could therefore enhance the flow of glacier salt.

Acknowledgements

References

Bérest, P., Antoine Blum, P., Pierre Charpentier, J., Gharbi, H., & Valès, F. 2005. Very slow creep tests on rock samples. International Journal of Rock Mechanics and Mining Sciences, 42(4), 569–576.

Carter, N.L, S.T Horseman, J.E Russell, & J Handin, 1993. Rheology of Rocksalt. Journal of Structural Geology 15 (9–10): 1257–71.

Desbois, G., P. Zavada, Z. Schleder, & J.L. Urai, 2010. Deformation and Recrystallization Mechanisms in Actively Extruding Salt Fountain: Microstructural Evidence for a Switch in Deformation Mechanisms with Increased Availability of Meteoric Water and Decreased Grain Size (Qum Kuh, Central Iran). Journal of Structural Geology 32: 580–94.

Jackson, M.P.A. 1985. Natural Strain in Diapiric and Glacial Rock Salt, with Emphasis on Oakwood Dome, East Texas. Bureau of Economic Geology, The University of Texas at Austin, TX.

Langer, M. 1993. Use of solution-mined caverns in salt for oil and gas storage and toxic waste disposal in Germany. Engineering Geology 35, 183-190.

Leitner, C., F. Neubauer, J.L. Urai, & J. Schoenherr, 2011. Structure and Evolution of a Rocksalt-Mudrock-Tectonite: The Haselgebirge in the Northern Calcareous Alps. Structural Geology 33: 970–84.

Littke, R., Bayer, U., Gajewski, D. & Nelskamp, S. 2008. Dynamics of Complex Intracontinental Basins. The Central European Basin System, vol. XXIV, ISBN 978-3-540-85084-7, 519.

Rowan, M.G., Jackson, M.P.A. & Trudgill, B.D. 1999. Salt-related fault families and fault welds in the northern Gulf of Mexico. AAPG Bull. Am. Assoc. Pet. Geol. 83 (9), 1454-1484.

Schleder, Z. & J.L. Urai, 2005. Microstructural Evolution of Deformation- Modified Primary Halite from Hengelo, the Netherlands. International Journal of Earth Sciences 94: 941–56.

Schleder, Z. & J.L. Urai, 2007. Deformation and Recrystallization Mechanisms in Mylonitic Shear Zones in Naturally Deformed Extrusive Eocene-Oligocene Rocksalt from Eyvanekey Plateau and Garmsar Hills (Central Iran). Journal of Structural Geology 29 (2): 241–55.

Schoenherr, J., Z. Schléder, J. L. Urai, R. Littke, & P. A. Kukla, 2010. Deformation Mechanisms of Deeply Buried and Surface-Piercing Late Pre-Cambrian to Early Cambrian Ara Salt from Interior Oman. International Journal of Earth Sciences 99 (5): 1007–25.

Sepehr, M. & Cosgrove, J. W. 2005. Role of the Kazerun fault zone in the formation and deformation of the Zagros fold-thrust belt, Iran, Tectonics 24(5).

Spiers, C.J., J.L. Urai, G.S. Lister, J.N. Boland, & H.J. Zwart, 1986. The Influence of Fluid-Rock Interaction on the Rheology of Salt Rock. Final Report EUR 10399 EN. Utrecht, Netherlands: State University of Utrecht.

Talbot, C.J. 1979. Fold trains in a glacier of salt in southern Iran. Journal of Structural Geology 1 (1), 5-18.

Talbot, C.J., 1981. Sliding and other deformation mechanisms in glacier of salt, S Iran. In: McClay, K.R., Prince, N.J. (Eds.), Thrust and Nappe Tectonics. Geological Society, London, Special Publications, vol. 9, pp. 173-183.

TALBOT, C.J. 1998. Extrusions of Hormuz salt in Iran. In: Blundell, D.J., Scott, A.C. (Eds.), Lyell: the Past is the Key to the Present, vol. 143. Geological Society Special Publication, pp. 315-334.

TALBOT, C.J. & AFTABI, P., 2004. Geology and models of salt extrusion at Qom Kuh, central Iran. Journal of the Geological Society 161, 321-334.

TALBOT, C.J. & JARVIS, R.J., 1984. Age, budget and dynamics of an active salt extrusion in Iran. Journal of Structural Geology 6 (5), 521-533.

TALBOT, C.J., MEDVEDEV, S., ALAVI, M., SHAHRIVAR, H. & HEIDARI, E. 2000. Salt extrusion at Kuh-e-Jahani, Iran, from June 1994 to November 1997. In: Vendeville, B.C., Mart, Y., Vigneresse, J.-L. (Eds.), Salt, Shale and Igneous Diapirs in and around Europe. Geological Society, London, Special Publications, vol. 174, pp. 93-110.

URAI, J.L., Z. SCHLEDER, C.J. SPIERS, & P.A. KUKLA, 2008. Flow and Transport Properties of Salt Rocks. In Dynamics of Complex Intracontinental Basins: The Central European Basin System, 277–90. Springer.

URAI, J.L., C.J. SPIERS, C.J. PEACH, & H.J. ZWART, 1985. A Laboratory Investigation into the Interaction of Recrystallization and Radiation Damage Effects in Polycrystalline Salt Rocks. Report over the Period March- October 1985 EUR 11849 EN. HPT Laboratorium: Instituut voor Aardwetenschappen.

URAI, J.L., C.J. SPIERS, H.J. ZWART, & G.S. LISTER, 1986. Weakening of Rock Salt by Water During Long-Term Creep. Nature 324: 554–57.

WENKERT, D. 1979. The Flow of Salt Glaciers. Geophysical Research Letters 6 (6): 523–26.

ZAVADA, P., G. DESBOIS, A. SCHWEDT, O. LEXA, & J.L. URAI, 2012. Extreme Ductile Deformation of Fine-Grained Salt by Coupled Solution-Precipitation Creep and Microcracking: Microstructural Evidence from Perennial Zechstein Sequence (Neuhof Salt Mine, Germany). Journal of Structural Geology 37: 89–104.

ZAVADA, P., G. DESBOIS, J.L. URAI, K. SCHULMANN, M. RAHMATI, & O. LEXA, 2015. Impact of Solid Second Phases on Deformation Mechanisms of Naturally Deformed Salt Rocks (Kuh-e-Namak, Dashti, Iran) and Rheological Stratification of the Hormuz Salt Formation. Journal of Structural Geology 74: 117–44.

ZHANG, S., JIANG, Q., SHI, C., XU, X., GONG, Y., XI, J., LIU, W. & LIU, B. 2021. Application of Sentinel-1 and-2 Images in Measuring the Deformation of Kuh-e-Namak (Dashti) Namakier, Iran. Remote Sensing. 2021; 13(4):785.

A threshold stress for pressure solution creep in rock salt: Model predictions vs. observations

B.G.A. van Oosterhout[1]*, S.J.T. Hangx[1], C.J. Spiers[1]

[1]HPT-laboratory, Department of Earth Sciences, Faculty of Geosciences, Utrecht University, The Netherlands

* b.g.a.vanoosterhout@uu.nl

ABSTRACT: At low deviatoric stress, flow of rock salt is expected to be controlled by pressure solution creep. This requires a fluid phase to be present in grain boundaries in the form of adsorbed grain boundary films or a dynamically wetting island-channel structure. However, whether such structures can persist at low stress or will be eliminated by healing phenomena is open to question. In this study, a model is derived describing a threshold stress for pressure solution, below which healing occurs, and creep is stopped. The results predict that pressure solution creep in rock salt, at depths up to 3 km, is inhibited below a deviatoric stress of 0.07 to 0.7 or at most 0.90 MPa. When deviatoric stresses in rock salt drop below this threshold stress, a decrease in strain rate from $\sim 10^{-13}$ to 10^{-18} s^{-1} is expected, due to a switch to dislocation creep. The model needs to be tested against CT experiments or optical observations on grain boundary behavior under stress, and against confined creep tests at very low deviatoric stress, as far as technically feasible. If confirmed, the effect of this threshold stress needs to be considered in future numerical studies of flow in rock salt.

1 Introduction

Creep laws for rock salt provide essential input for modelling salt tectonic flow, the long-term evolution of salt-based radioactive waste repositories (Tsang et al. 2005), solution-mined cavern behavior and associated subsidence (Breunese et al. 2003), and closure of uncased (abandoned) wellbores in rock salt (Orlic & Buijze 2014). At laboratory strain rates, temperatures of 20-200°C and differential (deviatoric) stresses in the range 5-25 MPa, deformation of natural rock salt is characterized by power-law dislocation creep with a stress sensitivity (n-value) of typically ~5 (Carter & Hansen 1983; Hunsche & Hampel 1999). However, strain rates inferred from field studies are several orders of magnitude higher than expected from extrapolating laboratory dislocation creep laws to natural, low-stress conditions (Urai et al. 1986; Bérest et al. 2019). This suggests that another mechanism, with a lower stress exponent (n), controls creep in rock salt at deviatoric stresses below 4-5 MPa.

A likely candidate, based on theory and on experiments on synthetic fine-grained (50-200 μm) salt is fluid-assisted grain boundary diffusion creep, or "pressure solution (Spiers et al. 1990). The rate of creep by this linear viscous mechanism (n=1) is inversely proportional to grain size cubed. For this reason, it is extremely slow and difficult to detect in experiments on natural salt (grain size 3-10 mm). Nonetheless, strong evidence for this type of behavior has recently been reported in ultra-long term (years), mostly unconfined creep tests, performed on natural salts at differential stresses down to ~1 or even 0.1 MPa under stable environmental conditions (Bérest et al. 2019; Herchen et al 2018). On the other hand, microstructural observations (Urai et al. 1986; 1987; Peach et al. 2001; Schleder & Urai 2007), thermodynamic arguments (Desbois et al. 2012) and observations on sinking rates of anhydrite rafts or "stringers" in salt formations (Raith et al. 2016) have been taken to imply that a threshold stress of 1-10 MPa exists below which pressure solution does not operate in salt under (confined) subsurface conditions - due to healing of the grain boundary fluid films that make pressure solution possible.

If linear (pressure solution) creep indeed occurs at low deviatoric stresses in the far field around salt caverns, storage facilities and boreholes, then the long-term evolution of these systems

and associated surface and/or environmental effects, will be impacted and need to be evaluated. Both microphysically (Spiers et al. 1990) and experimentally based (Bérest et al. 2019, Herchen et al. 2018) linear creep laws that account for pressure solution already exist and have been applied and tuned in numerical simulations of cavern convergence and subsidence (e.g. Breunese et al 2003). In contrast, no experimental evidence has been found for the existence of a threshold stress below which pressure solution is prevented by grain boundary healing, at least down to a few MPa in confined creep tests at in-situ conditions (Herchen et al. 2018) and to 0.2 MPa in unconfined tests (Berest et al. 2019). Moreover, previous thermodynamic estimates (1-10 MPa - Desbois et al. 2012) are based on a model that is appropriate for quartz but less so for salt. The aim of the present paper is to derive a theoretical criterion for the threshold stress for pressure solution that accounts for the specific properties of rock salt and that can be tested in future via targeted experiments.

2   Previous work

Creep of a dense polycrystalline material by pressure solution requires a fluid phase to be #present in grain boundaries in the form of adsorbed grain boundary films (Rutter 1976) or else a dynamically wetting (non-equilibrium) island-channel network (Lehner 1990) as inferred for wet salt by Spiers et al. (1990) and De Meer et al. (2002) (Figure 1a-c). Pressure solution in such a system is driven by chemical potential gradients around individual grains, set up by gradients in normal stress. It involves three serial processes: (1) dissolution of the solid at grain boundaries under high normal stress, (2) diffusion of dissolved material through the grain boundary fluid, and (3) precipitation of the dissolved solid in grain boundaries under low normal stress or on free pore walls. A key question is whether a dynamically wetted island-channel network or fluid films can persist or will be eliminated by grain boundary healing phenomena (Hickman & Evans 1995). At very low differential stresses, surface energy effects are expected to play a significant role (Heidug 1995), causing such structures to neck-down to form isolated fluid inclusions with lower interfacial area, i.e. causing healing of the grain boundary (Houben et al. 2013) (see Figure 1d) and hence cessation of pressure solution creep at a threshold stress level (De Meer et al. 2002; Desbois et al. 2012; Van Noort et al. 2008).

Assuming a non-equilibrium, grain boundary island-channel structure, and examining competition between surface-energy-driven island growth (grain boundary healing) versus wetting of the grain boundary by undercutting (dissolution) of the islands, Van Noort et al. (2008) proposed a model defining a threshold grain boundary stress for pressure solution in porous quartz aggregates. This was expressed as an effective normal stress $\sigma_{crit} = \sigma_n - P_f$, where σ_n is the total normal stress component on a dissolving grain boundary and P_f is the fluid pressure in the connected island-channel structure. The quartz was assumed to be purely elastic, with dissolution of the load-supporting islands being driven by their average elastic strain energy. Below the "threshold stress" obtained, pressure solution is prevented as the fluid channel network becomes disconnected by surface-energy-driven grain boundary healing. The grain contact threshold stress for pressure solution in quartz, based on the model by Van Noort et al. (2008), is given by the criterion:

$$\sigma_{crit} = 2\alpha \sqrt{\frac{E\gamma_{sl}}{2r}\left(\cos\left(\frac{\theta}{2}\right) - \cos\left(\frac{\theta_{eq}}{2}\right)\right)} \qquad (1)$$

Here α is the total island area fraction of grain boundary occupied by solid island contact, E the Young's modulus of quartz, γ_{sl} is the solid/liquid interfacial energy, r is the radius of interfacial curvature at island margins, θ is the dihedral angle at the contact margin (near 0° in dynamically wetted grain boundaries) and θ_{eq} is the dihedral angle at the contact margin at thermodynamic equilibrium. This criterion predicts grain contact threshold stresses for pressure solution in quartz that match favorably with those associated with cessation of pressure solution in hydrothermal compaction experiments on granular quartz aggregates reported by Niemeijer et al. (2002). Using the model of Van Noort et al. (2008), Desbois et al.

(2012) predicted that grain boundary healing in natural rock salt dominates over dynamic wetting when effective normal contact stresses on grain boundaries (assumed equal to differential stress) fall below 1-10 MPa, with the threshold value depending on the radius of curvature of grain boundary fluid inclusions or channels.
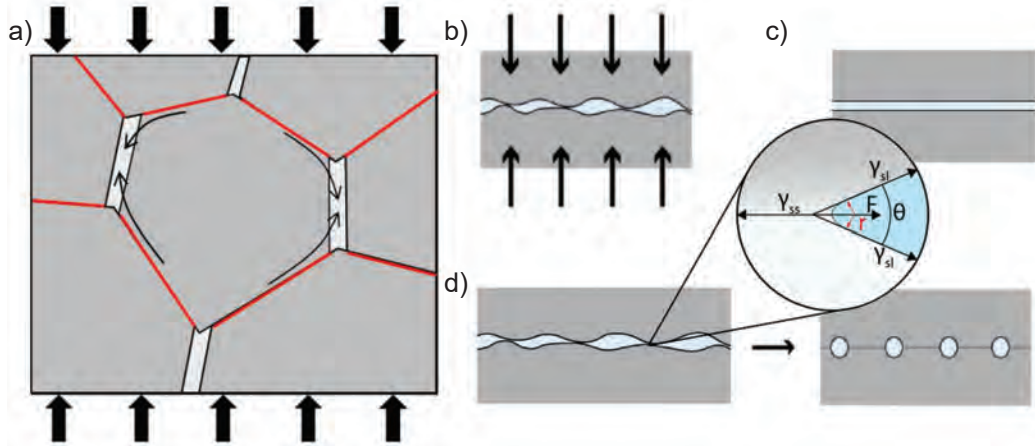
Figure 1: (a) Schematic diagram illustrating pattern of mass transfer involved in creep by pressure solution in a polycrystalline aggregate. Grain boundaries contain a fluid phase. Dissolution occurs at grain boundaries under high normal stress (red) followed by diffusion to and precipitation at grain boundaries under low normal stress (light grey). (b) An island-channel model of a fluid-filled grain boundary. (c) An adsorbed fluid film model of a grain boundary. (d) Necking down (occlusion) of a grain boundary channel network or fluid film to form arrays of disconnected spherical inclusions, by means of surface-energy-driven diffusive mass transport (Houben et al. 2013).

However, Desbois et al. (2012) do not take into account that: (1) stress intensification will occur at the tips of the generally elliptical fluid inclusions and channels found in salt grain boundaries (also ignored by Van Noort et al), (2) the radius of curvature appearing in the Van Noort criterion is the inclusion tip radius r (Figure 1d) as opposed to the much larger inclusion periphery or roof/floor radius, and (3) easy plastic deformation of salt compared with quartz means that the free energy (elastic strain energy) stored in dislocations produced by plastic deformation at island margins contributes to the chemical potential hence solubility of the solid islands, facilitating dissolution. When these three factors are considered, it is expected that a lower threshold stress will emerge for pressure solution in rock salt than predicted by Desbois et al (2012). In the following, we derive a revised expression for the threshold stress in salt, taking these factors into account.

3 Theoretical model

As starting point, consider a representative element of grain boundary (Figure 2) orientated normal to the maximum principal compressive stress (σ_1) in a volume of salt rock deforming by pressure solution but very close to the threshold stress at which grain boundaries heal. Grain boundaries are assumed to possess an island-channel structure that is still just connected. This means that the fluid pressure (P_f) within the channels will be buffered by and roughly equal to the minimum principal stress (σ_3), as grain boundaries generally have low tensile (hydrofracture) strength. The element considered in Figure 2 contains a single representative channel.

Given the above assumptions, the average differential stress experienced by the intervening solid islands (area fraction α) will be equal to $(\sigma_1 - \sigma_3)/\alpha$. With reference to Figure 2, the chemical potential of the solid at any point on a channel surface (or at any point on solid-solution interface) is given by the relation: $\mu_s \equiv \mu_{se} = f_s + P_f\Omega_s + \frac{\gamma_{sl}}{R_s}\Omega_s$ (Heidug 1995). Here μ_{se} is the equilibrium potential of the solute in the solution (by definition identical to the potential of the solid μ_s), f_s represents the Helmholtz free energy of the solid ($Jmol^{-1}$), P_f is the fluid pressure (Pa), Ω_s is the molar volume of the solid (m³ mol⁻¹), γ_{sl} is the interfacial free energy of the solid/liquid interface (Nm^{-1}) and R_s is the minimum principal radius of local interfacial curvature measured in the solid (m). For equilibrium at the triple junction contact between two grains (islands) and a fluid inclusion or channel, the Young-Dupré force balance: $\gamma_{ss} = 2\gamma_{sl}\cos\left(\frac{\theta_{eq}}{2}\right)$ applies, where γ_{ss} is the solid-solid interfacial free energy (Nm^{-1}) and θ_{eq} is the equilibrium dihedral angle. Based on the experiments of Lewis & Holness 1996, the equilibrium dihedral angle in rock salt is $60 - 70°$, for the halite-brine system at typical pressure-temperature conditions down to around $3\,km$ (though the uncertainties may be large, especially considering the effects of anisotropy in halite surface energy - Laporte & Provost 2000). When a fluid inclusion or channel is removed from equilibrium by undercutting of islands at triple junctions, the resulting dihedral angle $\theta \to 0$ and the thermodynamic surface force F (Nm^{-1}) acting on the triple junction or cusp sites A, (Figure 2) can be approximated by $F = 2\gamma_{sl} - \gamma_{ss}$.
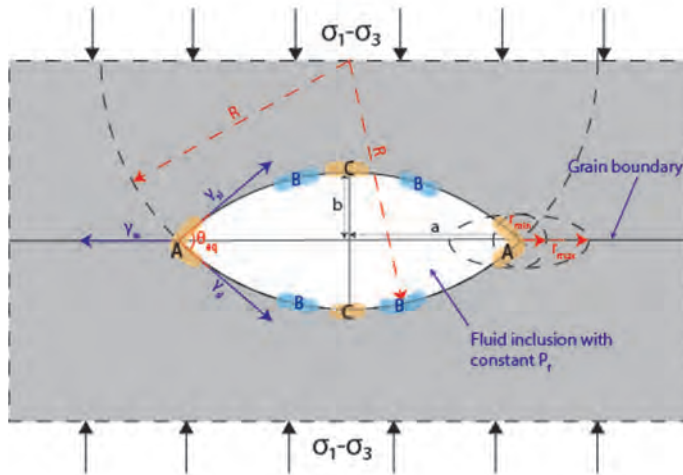
Figure 2: Schematic diagram of an elliptical inclusion or channel close to equilibrium in an element of grain boundary normal to σ_1 in a salt polycrystal where $\sigma_1 > \sigma_3 \approx P_f$. Aspect ratio a/b is defined by the equilibrium dihedral angle. At point A in the solid, there is intense concentration of vertical compressive stress, while at C there is horizontal extension. Point B is a neutral point where there is little or no deformation of the solid, relative to a hydrostatic reference state ($\sigma_1 = \sigma_3 = P_f$).

The above relations for the Young-Dupré Force F and for chemical potential are now applied to determine the chemical potential of the solid at sites A and B (Figure 2). From (2), the chemical potential of the solid at a neutral region B where there is no stress concentration (intermediate between the point of maximum compressive stress concentration at A and the maximum tensile stress at C) is given by $\mu_B = f_B + P_f\Omega_B - \frac{\gamma_{sl}\Omega_B}{R}$, where R is the radius of curvature of the fluid-solid interface measured in the fluid (Figure 2). At region A, the chemical potential is given by: $\mu_A = f_A + P_f\Omega_A - \frac{F\Omega_A}{2r}$ (Van Noort et al. 2008), in which r is the of curvature

within the dissolving cusp region during initiation of island undercutting (see Figure 2). This is taken to be at least equal to the radius of curvature at the tip of an ellipse (r_{min}) and at most to half the inclusion/channel height ($r_{max} = b$), so that: $\frac{b^2}{a} \leq r \leq b$. Assuming, the difference in molar volume between A and B is negligible, the potential difference between A and B is therefore given by:

$$\Delta\mu_{AB} = \mu_A - \mu_B = \Delta f_{AB} - \left(\frac{F}{2r} + \frac{\gamma_{sl}}{R}\right)\Omega_s \tag{2}$$

For dissolution at A (island undercutting and dynamic wetting), $\Delta\mu_{AB} > 0$. Recognizing that $R \gg r$, for typical dihedral angles, and that R/r will increase further as island dissolution proceeds, the criterion for non-equilibrium (dynamic) wetting versus healing of grain boundaries becomes:

$$\Delta f_{AB} > \frac{-F}{2r}\Omega_s = \frac{\gamma_{sl}\left[1 - cos\left(\frac{\theta_{eq}}{2}\right)\right]}{r}\Omega_s \tag{3}$$

To obtain Δf_{AB}, the difference in local stress state between the cusp regions A and the neutral regions B is needed. Assuming that the stress concentration at cusp sites (A) leads to localized work hardening plastic flow, the stress at A can be crudely estimated using the stress intensification factor $\lambda = \left(1 + 2\frac{a}{b}\right)/\alpha$ at the tip of a 2D elliptical hole in an infinite elastic medium due to Inglis (1913), augmented by the additional factor $1/\alpha$ reflecting the effect of island area fraction. Our approximation for the stress at A is hence given by $\lambda\sigma/\alpha$, or $z\sigma$ where σ is the far field differential stress ($\sigma_1 - \sigma_3$) and $z = \lambda/\alpha$. For an equilibrium dihedral angle (θ_{eq}) of 60° (Lewis & Holness 1996), the geometry of Figure 2 under near-equilibrium conditions (near-uniform R) implies a (minimum) aspect ratio $\frac{a}{b}$ of 3.73, so that the stress intensification z at A is (8.46)$/\alpha$ or ~17 for $\alpha = \frac{1}{2}$, for example. During isothermal deformation of a solid, elastic and dislocation stored energy contribute to the local Helmholtz free energy (e.g. Lehner 1990; Peach et al. 2001, Van Noort et al. 2008), so that:

$$\Delta f_{AB} = \Delta f_{elastic} + \Delta f_{dislocations} \approx \left(\frac{(z\sigma)^2}{E} + \rho W\right)\Omega_s \tag{4}$$

where E is the Young's Modulus in Pa, ρ is the dislocation density in m^{-2} and W is the dislocation self-energy in Jm^{-1}. In addition, via: $\rho W = \beta\frac{(z\sigma)^2}{G}$, in which β is constant with a value of approximately one and G is the shear modulus (Hull et al. 2011), so that:

$$\Delta f_{AB} = (z\sigma)^2\left(\frac{1}{E} + \frac{1}{G}\right)\Omega_s \tag{5}$$

Combining this with Eq. (3), the threshold differential stress for non-equilibrium grain boundary wetting, hence pressure solution in rock salt, can now be expressed as:

$$\sigma_{ps} = \sqrt{\frac{EG}{E+G}\frac{\gamma_{sl}}{r}\frac{1 - cos\left(\frac{\theta_{eq}}{2}\right)}{z^2}} \tag{6}$$

This criterion represents an unstable equilibrium state from which the system will always evolve such that grain boundary wetting occurs when $\sigma_1 - \sigma_3 > \sigma_{ps}$ and grain boundary healing occurs when $\sigma_1 - \sigma_3 < \sigma_{ps}$.

4   Model predictions

Suitable parameter values are now inserted into Eq. (6) to predict the threshold stress σ_{ps} for pressure solution in salt rock at depths up to 3 km (lithostatic pressure 65 -70 MPa, 75-110 °C). Bruno et al. (2009) show that the salt-brine interfacial energy at 30 °C is 0.125 Nm^{-1} for (100), 0.270 Nm^{-1} for (110) and ~0.4 Nm^{-1} for (111). In this study, the most favorable value for wetting of 0.125 Nm^{-1} is used. Further, we take $E = 29\ GPa,\ G = 11\ GPa$ (Warren 2016), $\theta_{eq} = 60 - 70°$, and $r = 1 - 100\ \mu m$. The chosen value of z is based on the above analysis of stress intensification at island margin sites (triple junction or cusp region A, Figure 2) and taken as 10-20. The predicted dependence of σ_{ps} on cusp radius r is shown in Figure 3, along with a comparison with the threshold stress estimates by Desbois et al (2012).
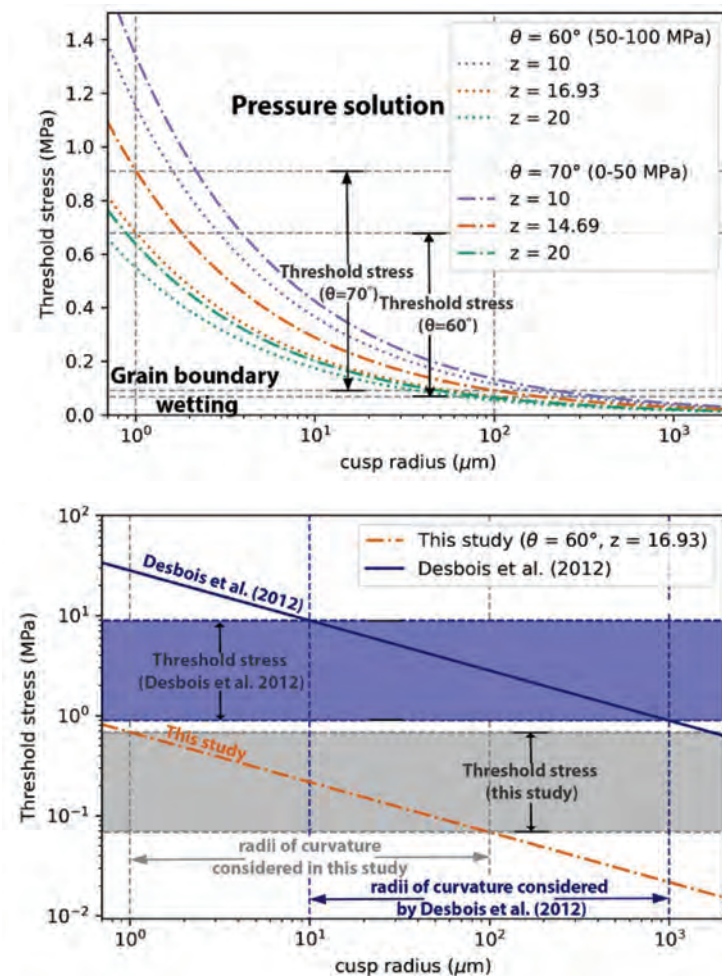
Figure 3: (top Predicted threshold stress for pressure solution vs.(log) cusp radius r for values of z between 10 and 20 and for $\theta_{eq} = 60°$ and 70°. (bottom) Equivalent log-log plot for parameter values expected at $\theta_{eq} = 60°$ and z = 16.93°,plus comparison with the threshold given by Desbois et al. (2012). N.B. The threshold stress is a threshold in differential or deviatoric stress.

Under ambient laboratory conditions, connected grain boundary fluid inclusions, films and channels in the Gorleben and Asse rock salt typically have a measured width (2b in Figure 2)

of 10 to $40\,\mu m$ normal to the grain boundary plane, while some isolated inclusions have diameters of up to $200\,\mu m$ in the Asse rocksalt (Urai et al. 1987; Thiemeyer et al. 2015), These values may be reduced under confined (e.g. in-situ) conditions, though this effect is expected to be minor (no change in order), especially when inclusions are brine filled. For inclusion widths in this full range of 10 to $200\,\mu m$, and corresponding aspect ratios ($\frac{a}{b}$, Figure 2) of 3.17 and 3.73, the relation $\frac{b^2}{a} \leq r \leq b$ given above yields radii of curvature (r) at the cusp between 1 and $100\,\mu m$. For this range in cusp radii, the threshold differential stress for pressure solution predicted by the present theory (Figure 3) is respectively $0.09 - 0.9\,MPa$ at shallow depths ($\theta_{eq} = 70°$, $P_c = 0 - 50\,MPa$) and $0.07 - 0.7\,MPa$ at deeper levels ($\theta_{eq} = 60°$, $P_c = 50 - 100\,MPa$) and assuming elliptical inclusion cross-section and an associated stress intensification z of 10 to 20. This is the stress required to activate grain boundary brine films and hence pressure solution in rocksalt. Note that it is at least one order lower than the estimate of $1 - 10\,MPa$ put forward by Desbois et al (2012) on the basis of the original (elastic) model by Van Noort et al. (2008) coupled with r-values corresponding to inclusion periphery or roof/floor radii (see Figure 3).

5   Comparison with microstructural constraints

The above estimates for the threshold differential stress for pressure solution are now compared with microstructural constraints on the stresses and deformation mechanisms operating during natural salt flow. The in-situ stresses driving flow of rock salt in nature cannot be measured directly. However, they can be estimated using the relationship between steady state flow stress $\sigma = (\sigma_1 - \sigma_3)$ and subgrain diameter d that all crystalline materials exhibit when deformation involves a component of dislocation creep (Twiss 1977). This relationship takes the form $d = K\sigma^{-m}$ where K and m are temperature-insensitive, material parameters (Twiss 1977). It was calibrated for natural and synthetic rocksalt in deformation experiments in the dislocation creep regime by Carter et al. (1993) yielding $K = 215$ and $m = 1.15$ (Urai & Schléder, 2005).

Now, subgrain sizes in naturally deformed rocksalt, from strongly deformed domal to lightly deformed bedded salt, typically vary from 80 to $360\,\mu m$ (e.g. Carter et al. 1982). Values around $200\,\mu m$ (stress ~1 MPa) are common in salt domes and walls, e.g. at Avery Island (Carter et al. 1982) and at Asse, Germany (Urai et al. 1987). Measured subgrain sizes in bedded rocksalt samples from Hengelo (Netherlands) show values in the range $290\,\mu m \pm 143\,\mu m$ to $390\,\mu m \pm 223\,\mu m$ (Schléder & Urai 2005). These data suggest that dislocation creep is active in all of the naturally deformed systems studied to date, although the strain contribution is unconstrained and may be small (a few% strain is sufficient to produce subgrains – e.g. Pennock et al. 2006). Using the above relationship between flow stress and subgrain size, the implication is that differential stresses in natural rocksalt lie between $0.4\ and\ 2.5\,MPa$. At the same time, many naturally deformed salts show evidence not only of dislocation creep (in the form of subgrains) but also of a) dynamic recrystallization involving fluid assisted grain boundary migration by dissolution-precipitation transfer across grain boundary brine films, and b) intergranular precipitation/overgrowth features suggesting pressure solution (Urai et al., 1987; Spiers & Carter, 1998; Schléder & Urai 2005). In addition, combined experimental plus microstructural studies performed on synthetic salt rock (Ter Heege et al. 2005; Pennock et al. 2006) have demonstrated that fluid-assisted dynamic recrystallization tends to occur in or near the transition between dislocation glide/creep and pressure solution. Taken together, the above pieces of evidence indicate that dislocation creep, fluid-assisted recrystallization and pressure solution occur alongside each other during natural salt flow at differential stresses in the range 0.4 to 2.5 MPa. This in turn implies that any threshold stress for pressure solution must lie at lower values, lending support to our model predictions of 0.07 to 0.70 (> 2km) or 0.90 MPa (<2 km) and providing a basis to reject the threshold of 1 to $10\,MPa$ estimated by Desbois et al (2012) as too high.

6 Implications for creep of natural rock salt

To assess the impact of the presently derived threshold for pressure solution on the creep behavior of rock salt at low deviatoric stresses in the further field around salt caverns, storage facilities and boreholes (and in the context of salt tectonic flow), we have added it to a deformation mechanism map for salt constructed using well-known dislocation creep (Hunsche and Hampel, 1999) and pressure solution (Spiers et al., 1990) creep equations (Figure 4). Inspection of Figure 4 shows that at 60-100°C, most natural salts, which have a grain size around $5 - 10\ mm$, are expected to show a transition from dislocation creep to pressure solution at stresses in the range $2 - 8\ MPa$ and strain rates in the range $10^{-11} - 10^{-13}\ s^{-1}$. These stresses fall above but close to those inferred from subgrain sizes measured for dynamically recrystallized salts with active fluid films, such as the Asse material (Urai et al. 1987) but a factor of $10 - 100$ times higher than the threshold stress for pressure solution predicted in this study. On this basis, combined with the microstructural arguments detailed above, we infer that at 2-3 km depth pressure solution can be expected to be active during flow of rock salt at stresses down to threshold values in our predicted range of $0.07 - 0.70\ MPa$. We anticipate that pressure solution strain rates may start to deviate from the Spiers et al. pressure solution law at ~$0.7\ MPa$, dropping to zero below ~$0.07\ MPa$, while dilslocation creep remains active but at rates below $10^{-16} - 10^{-18}\ s^{-1}$, i.e. some 4-6 orders lower than if pressure solution were active (see Figure 4) This effect can be simplified by assuming a mid-range threshold of say $0.2\ MPa$ (horizontal black line in Figure 4b), above which pressure solution creep is unaffected and below which it is inhibited by grain boundary healing, causing an abrupt switch back to dislocation creep at strain rates some four to six orders of magnitude lower than expected for pressure solution at $0.2\ MPa$.
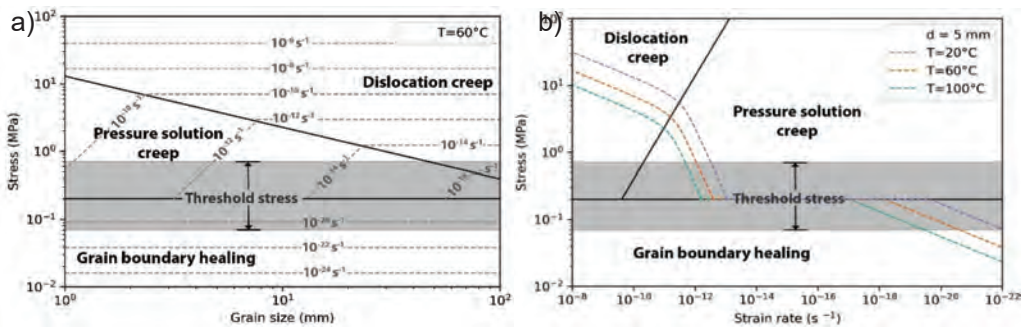
Figure 4: (a) Deformation map for rock salt drawn at a constant temperature of $60\ °C$ in log grain size vs. log stress space. (b) Deformation map at constant grain size (d = 5mm) drawn in log strain rate vs. log stress space. Stresses are differential or deviatoric flow stresses. Creep rates are based on the dislocation creep law by Hunsche & Hampel (1999), and the pressure solution creep equation of Spiers et al. (1990). Below the threshold stress, pressure solution creep is inhibited, healing dominates and strain rates drop by 4-6 orders.

The impact that the threshold behavior captured in Figure 4 will have in numerical models addressing i) salt flow in the far field around solution-mined caverns, storage facilities and boreholes, and ii) the associated long-term system evolution and surface effects, remains to be seen. Qualitatively, though, the threshold can be expected to limit the radial extent of the zone around an opening in which pressure solution is active (depending on cavern pressure). The present threshold stress model is purely theoretical and needs to be tested in future by means of long-term experiments and direct micro-CT or optical observations of grain boundary behavior under increasing normal stress. If proven to exist, long-term, far-field modelling

clearly needs to consider not only pressure solution creep but also the measured value or range of the threshold stress observed.

7 Conclusions

This study has derived a theoretical criterion estimating the differential stress at which surface-energy-driven healing effects dominate over stress-driven dynamic wetting phenomena in brine-bearing grain boundaries in rock salt. Below this threshold stress, grain boundary brine channels disconnect, and pressure solution creep is inhibited. Our main conclusions are as follows:

- When the free energy of dislocations and stress intensification effects around grain boundary fluid inclusions and channels are considered, surface energy effects are expected to prevent pressure solution in salt below a threshold differential stress of 0.07 to at most 0.90 MPa (as opposed to earlier estimates of 1-10 MPa).
- Many naturally deformed rock salts display microstructural evidence for both dislocation creep and dissolution-precipitation mechanisms. Associated subgrain sizes, coupled with experimentally calibrated subgrain size vs. stress relations, imply flow stresses that are higher than the threshold stress derived here. This confirms that pressure solution creep can operate in natural rock salt above the calculated threshold.
- A decrease in strain rates from $\sim 10^{-13}$ to 10^{-18} s^{-1} is expected when deviatoric stresses in rock salt drop below the threshold value. At this point pressure solution creep ceases leaving only dislocation creep to operate at vanishingly low rates.
- The present threshold stress needs to be verified via suitable experiments.
- If verified, the effects of the present threshold stress for pressure solution need to be considered in future numerical studies of flow around salt caverns and storage facilities.

Acknowledgements

References

BÉREST, P., GHARBI, H., BROUARD, B., BRÜCKNER, D. DE VRIES, K., HÉVIN, G., SPIERS, C.J. & URAI, J. 2019. VERY slow creep tests on salt samples. Rock Mechanics and Rock Engineering, 52(9), 2917-2934.

BREUNESE, J.N., DE MEER, S. & KROON, I.C. 2003. Observation and prediction of the relation between salt creep and land subsidence in solution mining. The Barradeel case. In: Proc. SMRI Fall Meeting, Chester: United Kingdom. p. 38-57.

BRUNO, M. AQUILANO, D. & PRENCIPE, M. 2009. Quantum-mechanical and thermodynamical study on the (110) and reconstructed (111) faces of NaCl crystals. Crystal Growth and Design, 9(4), 1912-1916.

CARTER, N.L, & HANSEN, F.D. 1983. Creep of rocksalt. Tectonophysics, 92(4), 275-333.

CARTER, N.L., HORSEMAN, S.T., RUSSELL, J.E. & HANDIN, J. 1993. Rheology of rocksalt. J. Struct. Geol. 15 (9–10), pp. 1257–1271.

DE MEER, S., SPIERS, C.J., PEACH, C.J. & WATANABE, T. 2002. Diffusive properties of fluid-filled grain boundaries measured electrically during active pressure solution. Earth Planet. Sci. Lett. 200 (1–2), pp. 147–157.

DESBOIS, G., URAI, J.L. & DE BRESSER, J.H. 2012. Fluid distribution in grain boundaries of natural fine-grained rock salt deformed at low differential stress (Qom Kuh salt fountain, central Iran) : Implications for rheology and transport properties. Journal of Structural Geology, 43, 128-143.

HEIDUG, W.K. 1995. Intergranular solid-fluid phase transformations under stress: The effect of surface forces. J. Geophys. Res. Solid Earth 100 (B4), pp. 5931–5940.

HICKMAN, S.H. & EVANS, B. 1991. Experimental pressure solution in halite: The effect of grain/interphase boundary structure. J. Geol. Soc. London. 148 (3), pp. 549–560.

HERCHEN, K., POPP, T., DÜSTERLOH, U., LUX, K., SALZER, ET AL. 2018. WEIMOS : Laboratory Investigations of Damage Reduction and Creep at Small Deviatoric Stresses in Rock Salt. pp. 175-192.

HOUBEN, M.E., TEN HOVE, A., PEACH, C.J. & SPIERS, C.J. 2013. Crack healing in rocksalt via diffusion in adsorbed aqueous films: Microphysical modelling versus experiments. Phys. Chem. Earth 64, pp. 95–104.

HULL, D. & BACON, D.J. 2011. Introduction to dislocations (Vol. 37). Elsevier.

HUNSCHE, U. & HAMPEL, A. 1991. Rock salt—the mechanical properties of the host rock material for a radioactive waste repository. Eng. Geol. 52 (3), pp. 271–291.

INGLIS, C.E. 1913. Stresses in a plate due to the presence of cracks and sharp corners. Trans Inst Naval Archit, 55, 219-241.

LAPORTE, D. & PROVOST, A. Equilibrium geometry of a fluid phase in a polycrystalline aggregate with anisotropic surface energies: dry grain boundaries. Journal of Geophyiscal Research: Solid Earth 2000, 105. B11: 25937-25953.

LEHNER, F.K. 1990. Thermodynamics of rock deformation by pressure solution. In: McClay, K.R. (Ed.), Deformation Processes in Minerals, Ceramics and Rocks. pp. 296–331.

LEWIS, S. & HOLNESS, M. 1996. Equilibrium halite-H_2O dihedral angles: High rock-salt permeability in the shallow crust?. Geology 24 (5), pp. 431–434.

NIEMEIJER, A.R., SPIERS, C.J. & BOS, B. 2002. Compaction creep of quartz sand at 400–600 C: Experimental evidence for dissolution-controlled pressure solution. Earth and Planetary Science Letters, 195(3-4), 261-275.

ORLIC, B. & BUIJZE, L. 2014. Numerical modeling of wellbore closure by the creep of rock salt caprocks. In: 48th US Rock Mechanics / Geomechanics Symposium 2014. pp. 1533–1540.

PEACH, C.J., SPIERS, C.J. & TRIMBY, P.W. 2001. Effect of confining pressure on dilatation, recrystallization, and flow of rock salt at 150°C. J. Geophys. Res. 106 (B7), pp. 13,315-13,328.

PENNOCK, G.M., DRURY, M.R., PEACH, C.J. & SPIERS, C.J. The influence of water on deformation microstructures and textures in synthetic NaCl measured using EBSD. Journal of structural geology, 2006, 28.4: 588-601.

RAITH, A.F., STROZYK, F., VISSER, J. & URAI, J.L. 2016. Evolution of rheologically heterogeneous salt structures: a case study from the NE Netherlands. Solid Earth, 2016, 7.1, pp. 67-82.

RUTTER, E.H. 1976. The Kinetics of Rock Deformation by Pressure Solution. Philos. Trans. R. Soc. A Math. Phys. Eng. Sci. 283 (1312), pp. 203–219.

SCHLEDER, Z. & URAI, J.L. 2005. Microstructural evolution of deformation-modified primary halite from the Middle Triassic Röt Formation at Hengelo, The Netherlands. Int. J. Earth Sci. 94 (5–6), pp. 941–955.

SCHLÉDER, Z. BURLIGA, S. & URAI, J.L. 2007. Dynamic and static recrystallization-related

microstructures in halite samples from the Kłodawa salt wall (central Poland) as revealed by gamma-irradiation. Neues Jahrb. für Mineral. - Abhandlungen 184 (August), pp. 17–28.

SPIERS, C.J. & CARTER, N.L. 1998. Microphysics of rocksalt flow in nature. Aubertin, M., and Hardy, H.R. (eds.): The mechanical behavior of salt, proceedings of the 4th conference, Trans Tech. Publ. Series on Rock and Soil Mechanics, 22, 115-128.

SPIERS, C.J., SCHUTJENS, P.M.T.M., BRZESOWSKY ,R.H., PEACH, C.J., LIETZENBERG, J.L. & ZWART, H.J. 1990. Experimental determination of constitutive parameters governing creep of rocksalt by pressure solution. Geological Society, London, Special Publications, 54(1), 215-227.

TER HEEGE, J.H., DE BRESSER, J.H.P. & SPIERS, C.J. 2005. Dynamic recrystallization of wet synthetic polycrystalline halite: Dependence of grain size distribution on flow stress, temperature and strain. Tectonophysics 396 (1–2), pp. 35–57.

THIEMEYER, N. HABERSETZER, J., PEINL, M. ZULAUF, G. & HAMMER, J. 2015. The application of high resolution x-ray computed tomography on naturally deformed rock salt: Multi-scale investigations of the structural inventory. Journal of Structural Geology, 77, 92-106.

TSANG, C.F., BERNIER, F. & DAVIES, C. 2005. Geohydromechanical processes in the Excavation Damaged Zone in crystalline rock, rock salt, and indurated and plastic clays in the context of radioactive waste disposal. International Journal of Rock Mechanics and Mining Sciences, 42(1), 109-125.

TWISS, R.J. 1977. Theory and applicability of a recrystallized grain size paleopiezometer. Pure Appl. Geophys. PAGEOPH 115 (1–2), pp. 227–244.

URAI, J.L., SPIERS, C.J. & ZWART, H.J. & LISTER, G.S. 1986. Weakening of rock salt by water during long-term creep. Nature 324 (6097), pp. 554–557.

URAI, J.L. SPIERS, C.J., PEACH, C.J. FRANSSEN, R.C.M.W. & LIEZENBERG, J.L. 1987. Deformation mechanisms operating in naturally deformed halite rocks as deduced from microstructural investigations. Geologie en Mijnbouw, 66(2), 165-176.

VAN NOORT, R. VISSER, H.J. & SPIERS, C.J. 2008. Influence of grain boundary structure on dissolution-controlled pressure solution and retarding effects of grain boundary healing. Journal of Geophysical Research: Solid Earth, 113 (B3).

WARREN, J.K. 2016. Evaporites: A Geological Compendium, 2nd ed. Springer.

Coupled mechanical-chemical modeling of compaction of salt at the microscale

Mengsu Hu[1], Carl I. Steefel[1], Jonny Rutqvist[1]*

[1]Lawrence Berkeley National Laboratory, USA

* Email: mengsuhu@lbl.gov

ABSTRACT: We have developed a new microscale mechanical-chemical (MC) model that accounts for coupled deformation, dynamic contacts, and reactive transport in granular systems with realistic geometric representations. The MC model was achieved by linking a new microscale mechanical code based on the numerical manifold method (NMM) to the reactive transport model Crunch. Using this first of its kind quantitative microscale model, we show the results of compaction and pressure solution within a halite aggregate. We found that sharp corners of salt grains can dominate the contact dynamics, microfracturing, and pressure solution during the compaction, and thus govern the structural changes and porosity loss of the system. We found that pressure solution, which preferentially dissolves sharp corners and edges, can lead to relatively high porosity loss in the system, thus playing an important role in the creep of salt. Our analysis showed that the dynamic changes of salt granular systems involving grain relocation and pressure solution can occur repeatedly and continuously, thus contributing to longer-term creep of salt at larger scales.

1   Introduction

The creep of salt is the key feature that governs the formation and evolution of salt rocks on the earth. Understanding the creep of salt is essential for effectively predicting the long-term evolution of nuclear waste repositories and strategic storage caverns for oil and gas in salt rocks (Urai et al. 1986). Different underlying mechanisms of creep in different stress/temperature ranges have been theoretically proposed (Urai et al. 1986). Based on laboratory tests micrograph, Urai & Spiers (2007) suggested that grain dislocation, microfracturing and pressure solution (Spiers et al. 1990; Zhang et al. 2007) are mechanisms acting during long-term creep. Identifying these mechanisms has advanced the understanding of salt creep. However, an important scientific question remains:

How does each mechanism quantitatively impact creep in granular systems that involve such complex geometric and multi-physical conditions?

In order to answer this scientific question, we need to use experiments or numerical modeling at relatively small scales- i.e., micro-grain scale or smaller scales to quantify processes that contribute to the creep of salt at larger scales.

Microscale mechanical-chemical modeling is very challenging, and thus has rarely been attempted. Microscale geomaterials (such as grain boundaries and corners) often have complex geometric features. These complex geometric features lead to discontinuities in physical fields (i.e., flow, transport, mechanics) and cannot be simplified easily. Furthermore, microscale multiphysics (flow, transport, chemical reactions and mechanics) are described by a different set of governing equations than what are used for those at larger scales (Hu & Rutqvist 2020a; 2020b; 2021). Among all the challenges, the most challenging aspect for numerical modeling is to calculate when and where contacts occur dynamically among a number of grains that can have arbitrary shapes. This is further complicated by the fact that these grains can move, deform, and in some cases fail or break apart as a result of complex coupled thermal-hydro-mechanical-chemical (THMC) processes.

In this study, we apply a microscale mechanical-chemical (MC) model for the first time to analyze compaction and pressure solution within a halite aggregate in order to understand and quantify mechanisms of creep of salt at the larger scale (Hu et al. 2021). The MC model is a microscale mechanical model based on the NMM (Hu & Rutqvist 2020b) and the reactive transport model Crunch (Steefel et al. 2015) that were developed previously by the authors. We will first briefly introduce the approach of the MC couplings in terms of the physics and geometry. Then we present results of the MC processes of the halite aggregate with a focus on analyses of compaction and pressure solution.

2 Approach: Coupling of Mechanics and Reactive Transport

In order to realize the MC coupling, we sequentially link a mechanical code named numerical manifold method (NMM, Hu & Rutqvist 2020a; 2020b; 2021) to the reactive transport code Crunch (Steefel et al. 2015).

The numerical manifold method (NMM) offers a powerful numerical method for continuum and discontinuum mechanical analysis. Subsequently, the author has developed multi-scale hydro-mechanical models and a series of computer code for fractures and porous media with rigorous geometrical and physical representations (Hu & Rutqvist 2020a; 2020b; 2021). At micro-discontinuum scales, an algorithm was developed that rigorously incorporates contact detection, contact enforcement, and iteration for contact state convergence. Thus, our NMM model can simulate elastic deformation of the solid grains, the failure of the grains, dynamic changes of contact locations and contact states, which includes intergranular frictional sliding (Hu & Rutqvist 2020b).

The Crunch family of codes is Open Source software for calculating chemical reaction and transport (Steefel et al. 2015). With the advanced capabilities of handling reactive transport at the microscale, Crunch explicitly solves for the mass balance of each chemical species affected by transport via advection and diffusion, and by chemical reactions that are described with a variety of rate laws based on thermodynamics and/or kinetics.

2.1 Coupling Physics: Stress-Dependent Solubility Formulation for Crunch

The solubility of halite depends on *both* the solid and aqueous phases, so thermodynamic properties need to be described for each. In this work, we use the minimum principal stress to calculate the pressure-dependent solubility of the halite. Note that minimum principal stress is the maximum compressive stress, which is positive when it is under compression.

The stress effect on mineral solubility can be calculated using thermodynamic pressure as the master variable. From basic thermodynamic principles, the solubility as a function of pressure is given by (Appelo et al. 2014)

$$\ln K_{P,T} = \ln K_{P=1,T} - \Delta V_r \left(\frac{P-1}{RT} \right) \tag{1}$$

where $\ln K_{P,T}$ is the equilibrium constant at the pressure of interest, $\ln K_{P=1,T}$ is the equilibrium constant at 1 atmosphere pressure, ΔV_r is the volume change of reaction (cm^3 mol^{-1}), T is the absolute temperature (°K), and R is the gas constant (82.0574587 cm^3·atm·K^{-1}·mol^{-1}). The volume change of reaction is given by the sum of the apparent partial molar volumes of the ions Na$^+$ and Cl$^-$ in solution minus the molar volume of halite at the pressure of interest (Hu et al. 2021):

$$\Delta V_r = V_{m,Na^+} + V_{m,Cl^-} - V_{Halite} \tag{2}$$

The apparent partial molar volumes are a function of the composition of the solution (Appelo et al. 2014). Over the limited pressure range we consider in the context of pressure solution, the molar volume of the halite can be considered to be constant at 27.1 cm^3 mol^{-1}, which leaves the apparent partial molar volumes of Na$^+$ and Cl$^-$ to be calculated. The apparent partial molar volumes of the ions can be calculated as a function of the thermodynamic pressure (Appelo et al. 2014), which has been implemented into Crunch for the purposes of this study (Hu et al. 2021).

The kinetics of the halite is a function of solubility $K_{P,T}$, which is a function of stress. Using a transition state theory (TST) rate law with a rate constant, k, of 0.254 mol m^{-2} s^{-1}, we obtain:

$$r = -Ak \left(1 - \frac{Q}{K_{P,T}}\right) \tag{3}$$

where Q is the ion activity product:

$$Q = a_{Na^+} a_{Cl^-} \tag{4}$$

The activity of the sodium ion, a_{Na^+}, is defined by the product of the activity coefficient and the concentration:

$$a_{Na^+} = \gamma_{Na^+} C_{Na^+} \tag{5}$$

and the activity of chloride, a_{Cl^-}, is defined similarly.

The rate law in Equation (3) is combined together with the diffusive flux described by Fick's Law, and an accumulation term to yield the reactive transport equations for Na$^+$ and Cl$^-$ linked together by the reaction rate of halite:

$$\frac{\partial(\varphi C_{Na^+})}{\partial t} = \nabla \cdot (\varphi^m D_{Na^+} \nabla C_{Na^+}) - r \tag{6}$$

$$\frac{\partial(\varphi C_{Cl^-})}{\partial t} = \nabla \cdot (\varphi^m D_{Cl^-} \nabla C_{Cl^-}) - r \tag{7}$$

where $\varphi^m D_{Na^+}$ and $\varphi^m D_{Cl^-}$ are the effective diffusivities (Steefel et al. 2015) which are updated due to the change of the porosity as a result of deformation, grain movement, and chemical reaction (Hu et al. 2021).

Examining the Equation (3) in combination with Equations (1-2), we see that the spatially variable solubility $K_{P,T}$ is higher when the compressive stress is higher. In addition to the effect on solubility, which provides the source of the spatially variable chemical potential, rates of reaction typically increase as well. The resulting chemical potential gradients drive diffusion from highly stressed contacts to relatively lower stressed faces.

2.2 Coupling geometry

The challenges of linking of NMM to Crunch are primarily associated with differences of meshes and interpolations in space and time. In particular, NMM uses Lagrangian mesh and allows for boundaries across meshes, while Crunch uses Eulerian mesh that need to conform to boundaries. This makes it challenging to capture large deformation and moving boundaries when contact occurs among interfaces and particles.
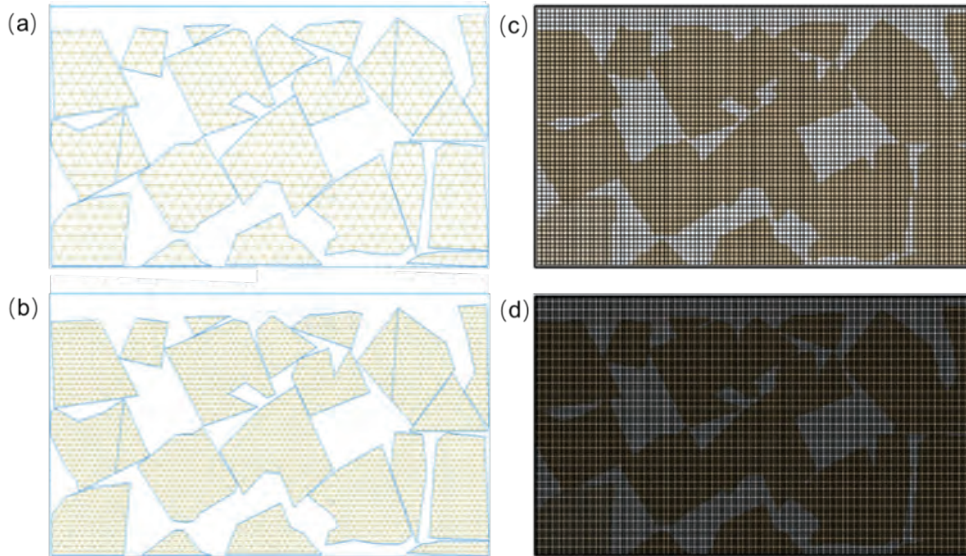
Figure 1. Generated irregular physical (a) coarser and (b) denser meshes in NMM from regular triangular mathematical meshes; Generated rectangular (c) coarser and (d) denser meshes in Crunch (Domain size: 2mm×1.2mm)

In order to overcome the challenges associated with different meshes that are used in NMM (Lagrangiran, unstructured mesh) and Crunch (Eulerian, structured mesh), a new approach has been developed in Crunch to generate mesh automatically. With this approach, when the grain boundaries move due to deformation and/or motion, the Eulerian mesh in Crunch is reconstructed to capture such moving boundaries. In order to transfer interpolation between NMM and Crunch, a mesh mapping algorithm is used to map between the rectangular Crunch grids and the NMM irregular meshes, and a linear interpolation is used to calculate displacements at each cell centers of Crunch and associated stress tensor. In Figure 1, we show an example of generated coarser and denser meshes in NMM and Crunch, respectively. As Crunch requires a much finer mesh to calculate reactive transport accurately, different densities of meshes in Crunch and NMM are used.

The two codes are coupled sequentially. NMM calculates the displacement, strain and stress and updates the geometry each time. The calculated stress and updated geometry is then transferred to Crunch. Crunch uses the stress components to calculate the halite solubility based on the local thermodynamic pressure of the solid and contacting fluid phase, and reaction rate. In turn, chemical dissolution or precipitation calculated by Crunch may lead to changes in the geometry and/or mechanical properties, and those are calculated in NMM. Because mechanical processes (e.g., deformation and movement) occur much faster than chemical reactions and fluid transport, all the components are flexibly treated as coupled or decoupled depending on the rates of processes and the time step chosen.
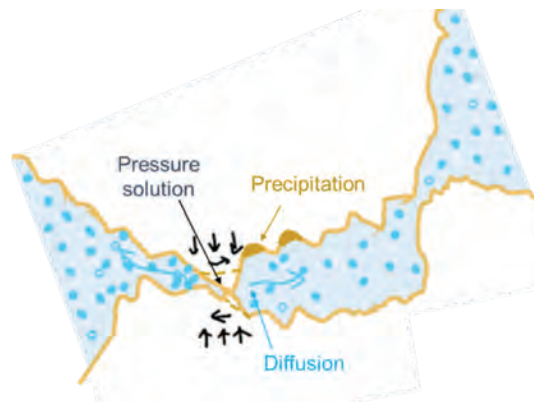
Figure 2. The NMM-Crunch model for pressure solution at two interfaces

With these coupling physics, we can rigorously consider the process of pressure solution, diffusion and precipitation. Figure 2 shows the schematic of the pressure solution model in NMM-Crunch. Note that these interfaces can be boundaries of mineral grains or fractures, and have arbitrary geometry. As shown in Figure 2, pressure solution occurs when the compressive stress at localized contacting surfaces is high, resulting in the dissolution of the halite grain. As a result of the local pressure solution, a chemical potential gradient corresponding to a gradient in concentration is generated and sodium and chloride ions diffuse down the gradient. The sodium and chloride derived from dissolution diffuses to lower stress faces where the solubility is lower and precipitates there. Thus, the dissolution-diffusion-precpitation mechanism provides a mechanism for mass transfer within the pore structure. Results are shown in Section 3.

3 Microscale Modeling of Pressure Solution in Granular Salt

3.1 Model Setup

We apply the MC model to analyze the compaction of halite grains (Hu et al. 2021). We extracted an image of dry compacted salt powder from Spiers et al. (1988, Figure 3.23). The initial domain is 2 mm × 1.5 mm. The idea is to obtain a realistic geometric representation and structure of a halite grain pack. Here, we only consider the grains in light colors and neglect the darker colored powders. This assumption leads to a more challenging problem than the treatment of a continuous heterogeneous porous media because rigorously capturing the contact dynamics and their coupling with deformation and chemical reaction are more complicated. The discontinuous treatment leads to larger porosity change than is the case with a continuous treatment. As a result of this assumption, we obtain a loosely packed halite aggregate with an initial porosity of 0.466.

During all the stages of the modeling, we apply a constant load of 5.25MPa from the top bar (which is located on the top of the granular system) and the outer boundaries of all the other three columns are fixed. In the modeling, we considered the following processes:

- Initial compaction: Responding to the loading, the grain minerals move, deform, and reorganize until mechanical equilibrium is reached.
- Secondary compaction: After reaching equilibrium of initial compaction, high stress at localized areas results in growth of new microfractures and pressure solution. As a result

of microfracturing and pressure solution, secondary compaction is initiated. These processes were considered explicitly with updated geometry.

- MC processes including repeated occurrence of pressure solution and grain relocation at different locations in the system after secondary compaction: After reaching the mechanical equilibrium of secondary compaction, a larger number of halite grains are in contact, resulting in a larger contacting area undergoing higher stress than after the initial compaction. At this stage, chemical reaction becomes more important: dissolution of the halite grains is enhanced due to the increased solubility and reaction rates at these stressed areas. As the stressed areas in the grain pack become more widespread, pressure solution becomes more systematic than localized. With sufficient time, the pressure solution results in dissolution locally of sharp corners and edges of the halite grains, thus triggering further compaction. These complex MC processes were simulated.

In this paper, we only show the results of the MC processes at a later stage—i.e., after the secondary compaction, when pressure solution occurs at more locations across the granular system.

3.2   Results

After reaching equilibrium of secondary compaction, we calculate the minimum principal stress. Because Crunch calculates chemical reaction and transport in the pore spaces as well as in the mineral grains, it needs stress information in both media. Figure 3 shows the result of the interpreted stress from NMM to Crunch using different grids. As we can see, the interpretation is accurate as the stress distribution is identical within the grains, and the stress is zero in the pore space.
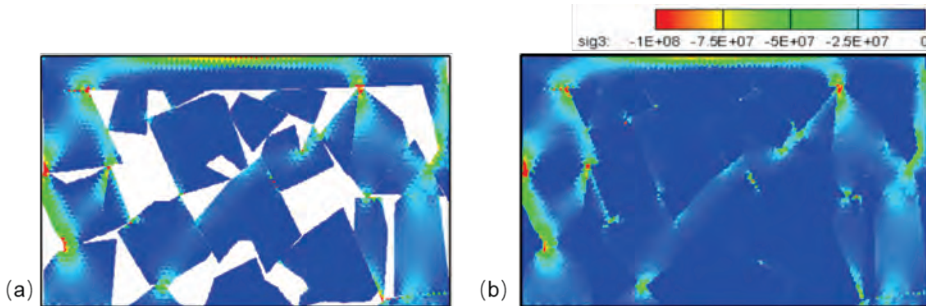
Figure 3. Minimum principal stress after reaching equilibrium of secondary compaction using (a) NMM mesh, and (b) interpolated rectangular mesh for Crunch (Unit: Pa).

As a result of pressure solution, diffusion, and chemical reaction, the system reached an initial quasi-steady state by about 10 hours, with dissolution and precipitation approximately balanced over the domain, although sodium and chloride concentrations continue to evolve slowly over the longer time scale (Figure 4). The quasi-steady state is defined here with respect to the concentration of sodium and chloride in the brine—in contrast, the porosity of the system continues to evolve due to the combination of dissolution and precipitation, but much more slowly.

Since the system is closed, the concentration in the pore fluid gradually increases as the locally highly stressed halite increases the sodium and chloride concentrations in the brine to values well above the normal baseline solubility given by the equilibrium constant at 1 bar pressure (about 6.13M). The gradients in chemical potential that develop (shown as concentration in Figure 4) drive molecular diffusion, thus transferring mass (sodium and chloride) from highly stressed regions to regions of relatively lower stress where halite precipitation can occur.
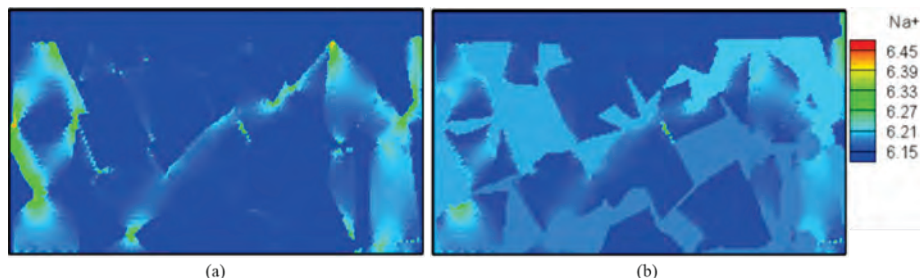
Figure 4. Sodium concentration (mol kgw⁻¹) calculated after (a) 2 hours and (b) 10,000 hours. High concentrations of sodium (and chloride) result from the effects of stress on the halite solubility.

Dissolution rates of halite are shown in Figures 5a (2 hours) and 5b (10,000 hours) while precipitation rates of halite are shown in Figure 5c (2 hours) and 5d (10,000 hours). Dissolution occurs along stressed contacts of the halite grains (compare to Figure 3) where the equilibrium constant for halite (or equivalently, its solubility) has increased. Precipitation occurs primarily in nearby zones (free faces) where the stress is less (see especially Figure 5d). The rates of reaction shown in Figure 5 are far less than the intrinsic mineral dissolution and precipitation rates for halite (order of 0.254 mol m⁻² s⁻¹), suggesting that the overall process of pressure solution in this case is diffusion-limited.
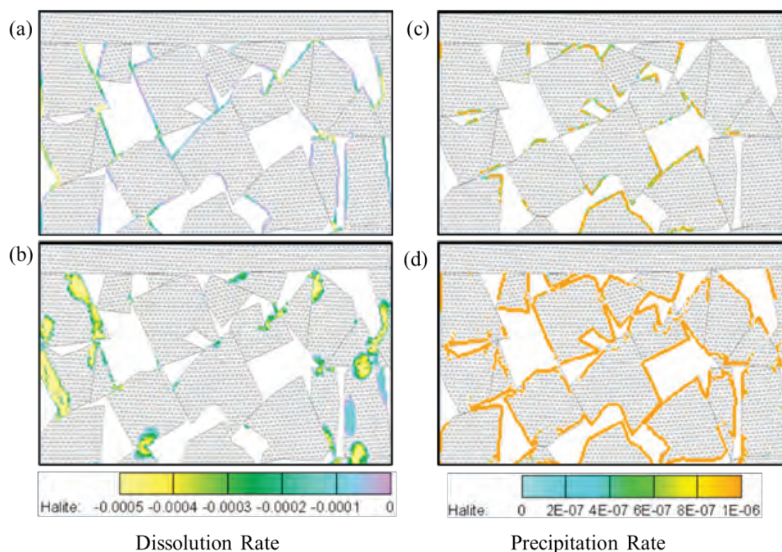
Figure 5. Dissolution rate of halite after (a) 2 hours and (b) 10,000 hours of simulation time, and precipitation rate of halite after (c) 2 hours and (d) 10,000 hours of simulation time (Unit: mol m⁻¹ s⁻¹).

The MC processes of pressure solution in this closed system do not result in significant net porosity change—mass is transferred conservatively within the domain from sites of dissolution at high stress contacts to sites of precipitation at lower stress contacts, except for the effect of the increase of the average concentration of sodium and chloride in the brine as it equilibrates with the stressed halite grains under closed system conditions. Figure 6 summarizes the time evolution of the porosity increase in the system as a result of pressure solution, which can be used to understand the subsequent mechanical compaction that occurs. At 1,000 hours (Figure 6a), the local increase in porosity is still minor, and generally insufficient to change the geometry of the grain pack. However, by 5,000 and 10,000 hours (Figures 6b and 6c), the

porosity increase is locally high enough that geometry of the grain pack is modified and mechanical compaction can continue as sharp corners have been eroded. To result in compaction and creep, the pressure solution process must be sufficient to remove contacting grain corners and edges so that more pore space can be opened up to accommodate more compaction. If and when these corners are removed via pressure solution, the domain can continue to compact beyond the purely mechanical configuration shown in Figure 3.
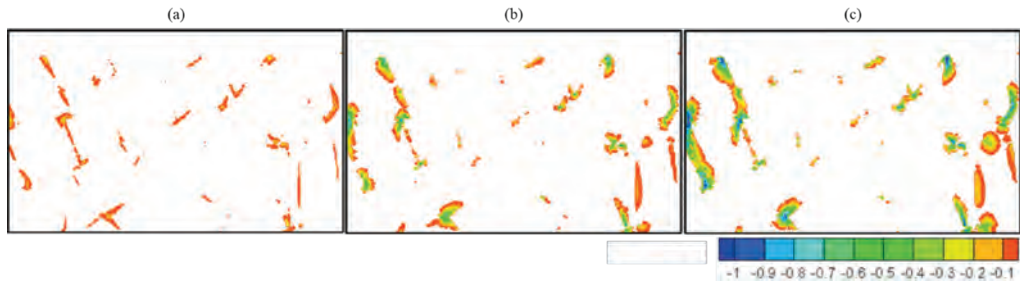
Figure 6. Porosity increase after (a) 1,000, (b) 5,000, and (c) 10,000 hours of simulation time

The calculated porosity increase in Crunch is treated as removal of solid mass in the NMM. Figure 7 shows the result of geometric update in NMM after 10,000 hours of Crunch simulation time. In particular, several sharp corners that underwent high stress are dissolved. These geometric changes with increased porosity and less sharp corners in the system lead to further compaction. In a very short period (0.75 second), the simulation of compaction reaches a new steady state. The calculated stress with NMM mesh and interpolated Crunch mesh is shown in Figure 8.

Figure 7. Geometry and NMM mesh of the halite grains after pressure solution

As is apparent in Figure 8, the high stress is redistributed to corners that are relatively sharp. In addition, the long and thin grain on the upper right of the system tends to fail after pressure solution occurs in the center, leaving a very thin section undergoing high stress. As for the two fractured grains, we can see the two sub-grains on the lower left that were divided by a microfracture are now separated due to the availability of newly created pore space. The left sub-grain is in contact with other grains on the top and bottom, whereas the right sub-grain is stress free as it has more space on the right to accommodate its movement. At this stage, the porosity loss is approximately 4.7%, making the total porosity loss as 35%.Note that the small amount of mass lost at sharp corners as a result of pressure solution can produce a significant reduction in porosity in the system due to the continued mechanical compaction that follows.
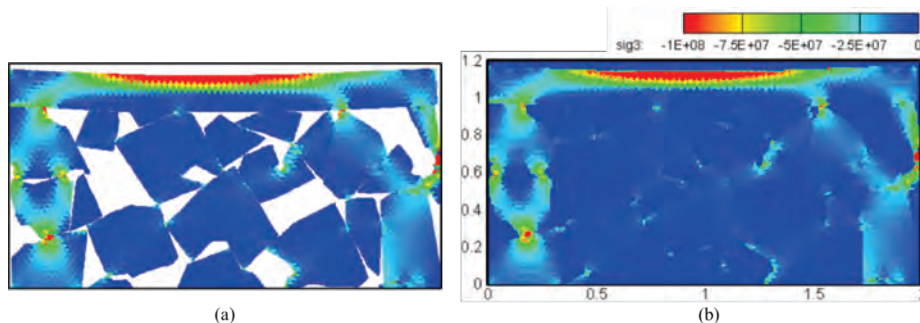
Figure 8. Minimum principal stress of the granular system after reaching equilibrium of compaction (10,000 hours of simulation) due to pressure solution using (a) NMM mesh, and (b) interpolated rectangular mesh for Crunch (Unit: Pa).

4   Conclusions

In order to understand, quantify and provide insights for creep of salt at large scales, we conducted the first-of-its-kind MC analyses of microscale granular salt compaction and pressure solution in this study (Hu et al. 2021). We made use of a previously developed (Hu & Rutqvist 2020b) microscale mechanical model based on the NMM and linked the NMM to the reactive transport code Crunch (Steefel et al. 2015) to conduct the MC analyses. In our simulation, we extracted the geometry of a halite aggregate from an image and explicitly represented the geometry and the structure of the aggregate in both NMM and Crunch with different numerical grids. We show results of compaction due to pressure solution and grain relocation with regorious treatment of the complex coupling physics as well as geometry. By rigorously accounting for pressure solution for a rather long period (10,000 hours), we are able to capture enhanced dissolution of halite grains as removal of solid mass at sharper corners, and thereafter capture the further compaction induced by pressure solution.

Based on our simulations, we found the following phenomena:

- Sharp corners of mineral grains can dominate the structural changes and loss of porosity of the system, which can be further altered by creation of new microfractures and/or pressure solution;
- Sharp corners become the focus of maximum mineral dissolution due to the accumulated high stress at these locations. The localized mineral dissolution creates chemical potential gradients that drive diffusion from the stressed contacts to areas with lower stress where mineral precipitation can occur;
- Pressure solution, which preferentially dissolves sharp corners and edges, can lead to relatively high porosity loss in the system, thus playing an important role in the creep of salt;
- The dynamic changes of salt granular systems involving reorganization of grain aggregates, creation of microfractures and pressure solution can have repeated occurrence, therefore potentially contributing to long-term creep behavior of salt at larger scales.

Thus, our first-of-its-kind MC model provides quantitative descriptions of microscale mechanical and chemical processes including compaction and pressur solution that explain creep of salt (i.e., porosity loss of the granular system) at larger scales. In future, it will be important to investigate how migration of brine inclusions induced by a temperature gradient (Hu and Rutqvist, 2020c) impacts creep. More importantly, a closer collaboration with

laboratory experiments at the microscale will be critical for validating the numerical model as well as for revealing possible undetected mechanisms.

Acknowledgements

References

APPELO, C. A. J., PARKHURST, D. L. & POST, V. E. A. 2014. Equations for calculating hydrogeochemical reactions of minerals and gases such as CO_2 at high pressures and temperatures. Geochimica et Cosmochimica Acta, 125, 49-67.

HU, M. & RUTQVIST, J. 2020a. Numerical Manifold Method Modeling of Coupled Processes in Fractured Geological Media at Multiple Scales. Journal of Rock Mechanics and Geotechnical Engineering, 12(4), 667-681.

HU, M. & RUTQVIST, J. 2020b. Microscale mechanical modeling of deformable geomaterials with dynamic contacts based on the numerical manifold method. Computational Geosciences, 24, 1783–1797.

HU, M. & RUTQVIST, J. 2020c. Finite volume modeling of coupled thermo-hydro-mechanical processes with application to brine migration in salt. Computational Geosciences, 24, 1751–1765.

HU, M. & RUTQVIST, J. 2021. Multi-scale Coupled Processes Modeling of Fractures as Porous, Interfacial and Granular Systems from Rock Images with the Numerical Manifold Method. Rock Mechanics and Rock Engineering. https://doi.org/10.1007/s00603-021-02455-6

HU, M., STEEFEL, C.I. & RUTQVIST, J. 2021. Microscale mechanical-chemical modeling of granular salt: Insights for creep. Journal of Geophysical Research: Solid Earth.

SPIERS, C.J., PEACH, C.J., BRZESOWSKY, R.H., SCHUTJENS, P.M.T.M., LIEZENBERG, J.L. & ZWART, H.J. 1988. Long term rheological and transport properties of dry and wet salt rocks. Report EUR 11848 EN, Commission of the European Communities.

SPIERS, C. J., SCHUTJENS, P. M. T. M., BRZESOWSKY, R. H., PEACH, C. J., LIEZENBERG, J. L. & ZWART, H. J. 1990. Experimental determination of constitutive parameters governing creep of rocksalt by pressure solution. Geological Society, London, Special Publications, 54(1), 215–227.

STEEFEL, C.I., APPELO, C.A.J., ARORA, B., JACQUES, D., KALBACHER, T., KOLDITZ, O., LAGNEAU, V., LICHTNER, P.C., MAYER, K.U., MEEUSSEN, J.C.L. & MOLINS, S. 2015a. Reactive transport codes for subsurface environmental simulation. Computational Geosciences, 19, 445-478.

URAI, J.L., SPIERS, C.J., HENDRIK, J.Z. & LISTER, G.S. 1986. Weakening of rock salt by water during long-term creep. Nature 324:554–557.

URAI, J.L. & SPIERS, C.J. 2007. The effect of grain boundary water on deformation mechanisms and rheology of rocksalt during long-term deformation. Proc. 6th Conf. Mech. Beh. of Salt. Taylor & Francis Group, London, 149–158.

ZHANG, X., PEACH, C.J., GRUPA, J. & SPIERS, C.J. 2007. Stress relaxation experiments on compacted granular salt: effects of water. Proc. 6th Conf. Mech. Beh. of Salt. Taylor & Francis Group, London, 159–165.

Effects of grain size distribution on the permeability of compacting aggregates: results from rock-analogue experiments and microphysical models

André Niemeijer[1,2,3], Derek Elsworth[1,3] and Chris Marone[2,3]*

[1]Department of Energy and Mineral Engineering, The Pennsylvania State University, USA
[2]Department of Geosciences, The Pennsylvania State University, USA
[3]G3 Center and Energy Institute, The Pennsylvania State University, USA

*** *a.r.niemeijer@uu.nl*

ABSTRACT: We investigate the evolution of permeability with porosity and grain size in compacting aggregates of brine-saturated salt. The porosity of aggregates with different initial grain size distributions was reduced by a step-wise application of compactive strain, retaining the effective normal stress <5 MPa. Permeability was measured under measured steady state flow with a pore pressure differential of 0.1 MPa across two granular layers in parallel. We found that permeability decreased with decreasing porosity according to a power law relation, consistent with predictions from capillary models (i.e. Kozeny-Carman Equation), but with an exponent that changes with porosity. The Kozeny-Carman model overestimates observed permeabilities in all experiments by at least one order-of-magnitude as a result of the assumed monodispersed distribution of grain diameters and therefore pore throat sizes. We extend the Kozeny-Carman model using an expression for the tortuosity that is dependent on the actual grain size. The broader grain size distributions, with abundant small grains, returns lower permeabilities than those predicted using the average or median grain size**.**

1. Introduction

Previous work has shown that permeability is strongly related to the porosity and grain size of rock or fault gouge (Bernabé 1995; Bernabé et al. 2003; Zhang et al. 1994a,b; David et al. 1994; Fredrich et al. 2006; Giger et al. 2007). For most materials, it has been shown that permeability varies with porosity with a power law dependence, ϕ^{α}, where α can take values ranging from 21 to 2 (David et al. 1994b; Zhu, et al.1995; Bernabé et al. 2003), depending on the mechanism of porosity-reduction or creation. Bernabé et al (2003) showed that the value of the apparent power exponent α depends significantly on the deformation mechanism that is operating under the experimental conditions. This is most likely the result of changes in effective pathways through the pore or fracture network that are not directly related to changes in the actual porosity. In order to distinguish between these, Bernabé et al (2003) considered the difference between effective porosity and non-effective porosity. Here, effective porosity is defined as porosity that contributes to (i.e. is part of) the effective fluid flow path and non-effective porosity is any part of the void space within a solid. The non-effective porosity can be pore walls, dead-end pores, sealed cracks or otherwise isolated voids. Changes in non-effective porosity will not lead to changes in permeability and therefore should reduce the sensitivity of the porosity dependence of permeability (i.e. α). However, if the effective porosity consists of an array of different-sized pores in series, the permeability will be mostly controlled by the size of the smallest pore. In such a case, a change in porosity that affects all pores equally should lower the permeability more than for an array of single-sized pores. Clearly, the permeability of a rock with varying grain size distributions, and subject to different deformation mechanisms, will change differently with changing porosity.

Here, we present results from an experimental study on powdered samples of rock salt. This study focuses on the effect of time-dependent compaction by pressure solution on the permeability of granular aggregates to assess the effects of initial grain size distribution on the porosity-permeability relation.

2. Background

One of the most widely used models defining permeability of granular aggregates as a function of grain size and porosity, is the Kozeny-Carman (KC) equation (Kozeny 1927; Carman 1937). The KC-model is based on the Poiseuille Equation for the average velocity of an incompressible uniform liquid (Newtonian liquid) in a cylindrical tube of constant radius R:

$$V_{ave} = \frac{1}{8\mu} R^2 \frac{dP}{dx} \tag{1}$$

where V_{ave} is the average flow velocity (m/s), μ is the viscosity of the liquid and dP/dx is the pressure gradient. In order to account for the variation in the size of the flow channels in a natural sample, a characteristic dimension is needed to describe the average size of the flow channel. The hydraulic radius (R_H=cross sectional area of the flow channel/wetted perimeter) is often used and Equation (1) in terms of flow rate becomes:

$$q = C_s \frac{1}{\mu} R_H^2 A_{flow} \frac{dP}{dx} \tag{2}$$

where C_s is a shape factor for the cross section of the tube (1/2 for a circle) and A_{flow} is the cross-sectional area of the tube. Now, for a bundle of fully saturated parallel capillaries of constant but irregular cross section, contributing to a total cross section (see Figure 1), the area of flow passages is given by

$$A_{flow} = \varphi A_{total} \tag{3}$$

The hydraulic radius is given by

$$R_H = \frac{A_{flow}}{P} = \frac{A_{flow}L}{PL} = \frac{V_{water}}{S_0} \tag{4}$$

where P is the wetted perimeter, L is the length of the flow channel in the direction of flow and S_0 is the specific surface area per unit volume of particles. Assuming full saturation of the aggregate, the volume of water is given by

$$V_{water} = \varphi \cdot V_s \tag{5}$$

Combining equations (3), (4) and (5) into (2) gives:

$$q = C_s \frac{1}{\mu} \left(\frac{\varphi \cdot V_s}{S_0} \right)^2 \varphi \cdot A_{total} \frac{dP}{dx} = C_s \frac{1}{\mu} \frac{V_s^2}{S_0^2} \varphi^3 A_{total} \frac{dP}{dx} \tag{6}$$

Now, by analogy with Darcy's law, the hydraulic conductivity is:
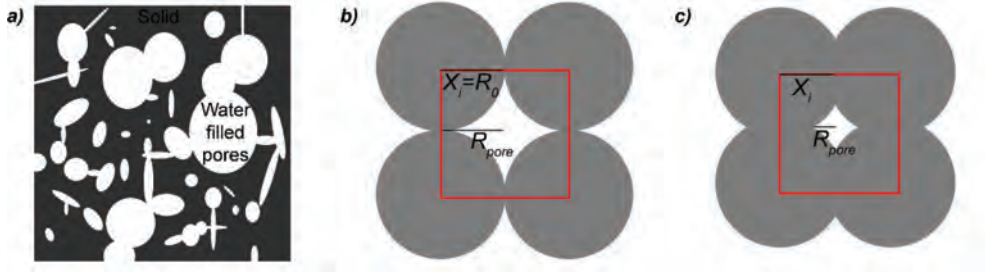
Figure 1: a) Schematic representation of variably shaped pores in natural samples b) Idealized geometry (Simple Cubic packing) at maximum porosity allowing the calculation of the pore radius and area (see e.g. Pluymakers & Spiers 2014) c) the grain aggregate of b) at an arbitrary lower porosity.

$$K_h = C_s \frac{1}{\mu} \frac{V_s^2}{S_0^2} \varphi^3 \tag{7}$$

and the permeability is given by:

$$k = K_h \mu = C_s \frac{V_s^2}{S_0^2} \varphi^3 \tag{8}$$

which is one form of the Kozeny-Carman Equation. Now, C_s can be expressed as a function of the pore shape and tortuosity (effective path length):

$$C_s = \frac{1}{k_0 T^2} \tag{9}$$

where k_0 is a pore shape factor (usually taken as 2.5) and T is the tortuosity (usually taken as $\sqrt{2}$).

In this formulation, the grain size dependence of permeability is expressed through the definition of the hydraulic radius, which can be readily adjusted to fit the experimental data. Moreover, the KC model has so far been mostly applied using a single magnitude for the hydraulic radius and by extension the grain size, whereas natural samples always show a grain size distribution. An aggregate with a distributed grain size will have a lower permeability than an aggregate consisting of single sized grains, as finer grains will occlude the larger pores, thus reducing the effective pore size and increasing the tortuosity. Here, we extend the original KC formulation to accommodate a distributed grain size. To do this, we start again with equation (1), but now using the actual radius of the pore:

$$V_{ave} = \frac{1}{8\mu} R_{pore}^2 \frac{dP}{dx} \tag{10}$$

And the flow rate and permeability will thus be:

$$q = C_s \frac{1}{\mu} R_{pore}^2 A_{pore} \frac{dP}{dx} \tag{11}$$

$$K = C_s R_{pore}^2 \frac{A_{pore}}{A_{total}} \qquad (12)$$

where A_{pore} and A_{total} are defined in Figure 1. We use a simple geometrical model of perfect spheres in simple cubic packing, deforming by intergranular penetration as a result of pressure solution, allowing the contact areas to grow and the pore sizes to decrease (see Figure 1 and Pluymakers & Spiers 2015). We further use a random number generator to generate up to 10000 different grain sizes from a desired grain size distribution and calculate the permeability for each grain size according to (9) and (12). The values for the pore area, total area and pore size are calculated for each magnitude of porosity. To accommodate the increase in tortuosity and decrease in pore size for a broader grain size distribution, we define the tortuosity as:

$$T = \frac{c^2}{x_i^2} \sqrt{2} \qquad (13)$$

where c is the mean grain size of the distribution and x_i is the current grain size. After calculating the permeability for each individual grain size for a given porosity, the bulk permeability is calculated by taking the geometric mean (equivalent to all pores in parallel) and the harmonic mean (equivalent to all pores in series) of the distribution of permeability values.

3. Experimental methods

A series of stress relaxation experiments were performed on simulated fault gouges consisting of granular rock salt in a double-direct shear configuration with a true triaxial pressure vessel (Samuelson et al. 2009). The rock salt was ground and sieved to obtain initial grain sizes in the ranges 38-106, 53-106 and 63-90 µm (see Table 1). The loading platens (Figure 3a) are plumbed to allow pore fluid access. To ensure an even distribution of the pore fluid pressure over the sample area, porous stone plates or sintered stainless steel plates ("frits") were used. The permeability of the frits was tested using a dummy sample of glass beads (d= 0.5 mm and k=10^{-8} m^2) and was found to be higher than the maximum permeability measurable with the diameter of the tubing used (~5x10^{-13} m^2). Samples were prepared by loading the side blocks with approximately 45 grams of material, yielding two layers with an initial thickness of ~ 6 mm. The loaded side blocks were attached to the center block and the entire sample assembly was placed inside a set of rubber membranes (see Samuelson et al. 2009). The sample was sealed by winding steel wire around the three loading blocks, effectively sealing the rubber membrane against the O-rings. The sealed assembly was then placed inside the pressure vessel which is located inside a biaxial loading frame and the sample was compacted under room-dry conditions for 15 minutes at an applied horizontal stress of 5 MPa.

After the completion of dry compaction, the thickness of the sample assembly was measured on the bench and the assembly was returned to the pressure vessel. A horizontal stress of ~0.5 MPa was applied to keep the assembly in place while connecting the fluid inlet and outlet lines to the vessel fittings. Then, the pressure vessel was closed and filled with the confining fluid (XCELTHERM® 600 oil from Radco Industries). At the same time, the horizontal piston was switched to displacement control mode. The desired confining pressure (2 MPa) was applied using the pressure intensifier and servo-controlled at 2 MPa during the entire experiment (variation < 0.05 MPa). At this point, the "zero" load signal and "zero" horizontal position were recorded. Pore fluid was introduced into the system by attaching pore fluid tube A to the pressure vessel and slowly elevating the pressure in intensifier A, so that the applied pore pressure did not exceed 0.1 MPa. After ~ 30 mm of displacement on pore pressure intensifier A, breakthrough occurred of the pore fluid from outlet B. Next, pore

fluid tube B was attached to the vessel and a pore pressure of 0.1 MPa was applied by pressure intensifier A in servo-controlled mode. The sample was subsequently loaded horizontally at such a rate that the normal stress never exceeded 10 MPa until the desired porosity (i.e. horizontal displacement) was achieved. The sample was allowed to relax to hydrostatic stress and a pressure differential was applied across the sample by lowering pore pressure B (usually to 0.05 MPa, i.e. $\Delta P=0.05$ MPa). The flow rate was measured by the movement of both pore pressure intensifiers. Once steady state flow was achieved (as evidenced by equal flow rates in A and B), the pressure differential was maintained for an additional 15-30 mm of displacement on the pore pressure pistons. Then, the valve on pore pressure intensifier B was closed and the sample was again horizontally loaded and allowed to relax.

In this manner, the permeability of the samples was determined for different porosities in a step-wise fashion. At the end of the experiment, the pore pressure and confining pressure were removed, and the sample assembly was flushed with compressed air. The final thickness of the sample assembly was recorded, and the sample was disassembled. The two compacted layers were carefully removed from the loading blocks and flushed with iso-butanol to remove any remaining brine. The samples were then dried at 50 ºC for 24 hours before impregnation with epoxy and subsequent thin sectioning for SEM and microscope analysis.

Table 1: List of all experiments reported here.[1] Porosity determined from measured layer thickness and weight of salt assuming a density of 2.17 g/cm^{3}, [2] Final porosities from displacement of horizontal piston,[3] Final porosity determined using Archimedes method. n.d. means not determined.

Experiment	Grain size (μm)	h_0 (mm)	h_{final} (mm)	ϕ_0[1]	ϕ_{final}[2]	ϕ_{final}[3]
p1327	38-106	10.51	6.66	45.41	16.54	16.9
p1445	38-106	14.06	10.82	36.28	1.72	n.d.
p1490	38-106	15.13	12.29	35.25	8.71	7.2
p1444	53-106	14.04	12.13	32.85	20.19	14.4
p1489	53-106	15.25	12.36	38.33	7.84	11.7
p1498	53-106	14.28	11.93	38.86	11.87	12.0
p1536	53-106	16.95	13.05	40.46	8.12	16.5
p1537	63-90	17.17	13.15	38.48	6.32	12.2

4. 1. Results – Stress relaxation

In Figure 2a, we show the stress relaxation curve for three samples with different initial grain size distributions. In all cases, the applied stress drops rapidly, initially, followed by a more gradual decrease. Stress relaxation rates are highest during the initial part of the experiment (i.e. at high porosities) and for the smallest grain sizes. Moreover, stress relaxes faster for samples with a broader grain size distribution, indicating faster compaction rates for these samples ((Niemeijer et al. 2009). We calculated volumetric strain rates using the elasticity of the samples and the biaxial loading apparatus and show typical results in Figure 2b. The stress dependence of volumetric strain rate is initially high with an exponent of 2 or larger, before decreasing and reaching a value of ~1 in the later stages of the stress relaxation.

4. 2. Results – Permeability

We show the results for flowthrough tests with a constant pore pressure differential in Figure 3a. Upon opening the valve to allow flow, an increase in pore pressure B and a decrease in pore pressure A can be observed, resulting in a lower pressure differential. After an initial transient
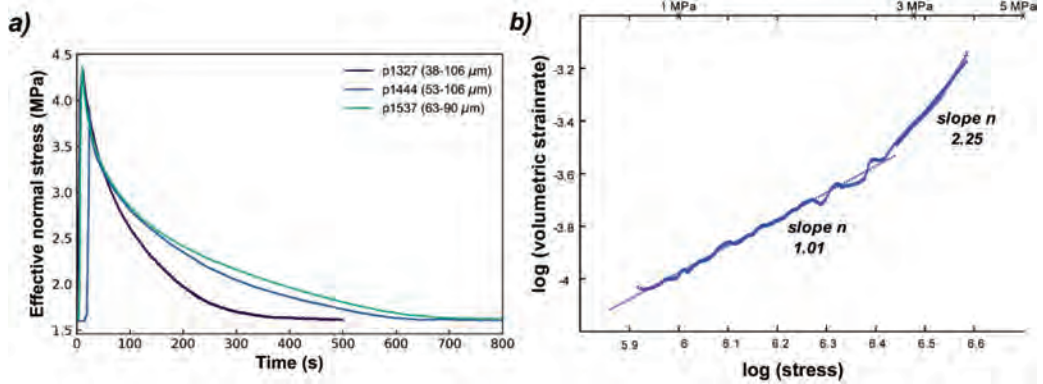
Figure 2 a) Evolution of effective normal stress over time for three experiments with different initial grain size distributions. b) Volumetric strain rate as a function of effective stress during stress relaxation in experiment p1327 (d=38-106 µm, see Table 1).

stage of high flow rates, the flow rate stabilizes, and steady state flow is achieved, which we define as the point at which the flowrates in pistons A & B were within 10% of each other. The duration of the transient stage depended on the storage capacity of the sample and the downstream reservoir and was never longer than ~20 seconds. In calculating flowrates, an averaging window of 5 seconds was used to reduce noise. Permeability was calculated using Darcy' law:

$$k = \frac{Q \cdot l \cdot \mu_f}{A} \Delta P$$
(14)

Here, Q is the flow rate through the sample (m³/s), l is the length of the flow path, in our case the thickness of the sample layers (m), μ_f is the dynamic viscosity of the fluid (N/m²s), A is the sample area (m²) and ΔP is the pressure differential (Pa). Permeability decreases with decreasing porosity for all samples (Figure 3b) and this decrease is largest for the samples with the widest grain size distribution.
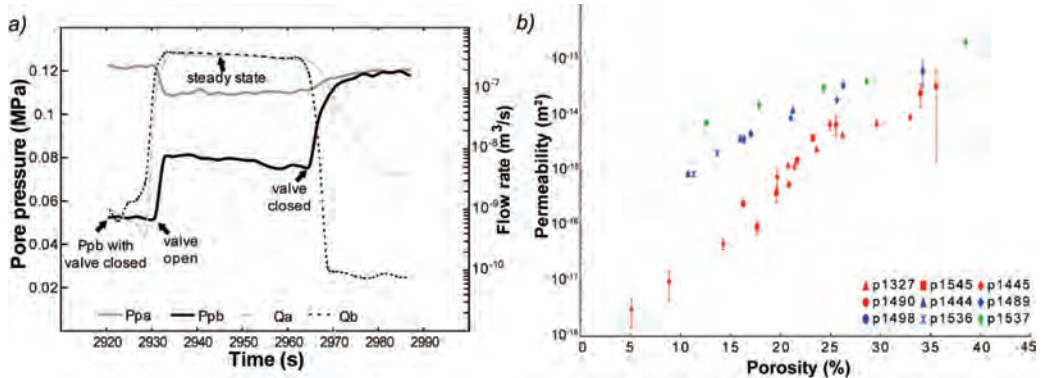
Figure 3: a) Evolution of pore pressure and flowrate as measured in the two fluid intensifiers during a measurement of permeability b) All permeability and porosity data obtained. The grain size fractions used are 38-106 µm (red symbols), 53-106 µm (blue symbols) and 63-90 µm (green symbols).

4.3. Results - Microstructures

In Figure 4a we show a general overview of the microstructure of sample p1327, obtained via X-ray CT scanning using a Zeiss Xradia 610 Versa X-ray microscope. This sample has a final porosity of 16% (see also Table 1), which is also reflected in the microstructure. The final grain size is similar to the initial grain size fractions (38-106 µm) and there is no evidence of intragranular fracturing and grain size reduction. The grain boundaries appear smooth, long and are hard to distinguish. A small number of intact anhydrite grains are randomly distributed throughout the volume. In rare locations, small overgrowths can be observed (Figure 4b).
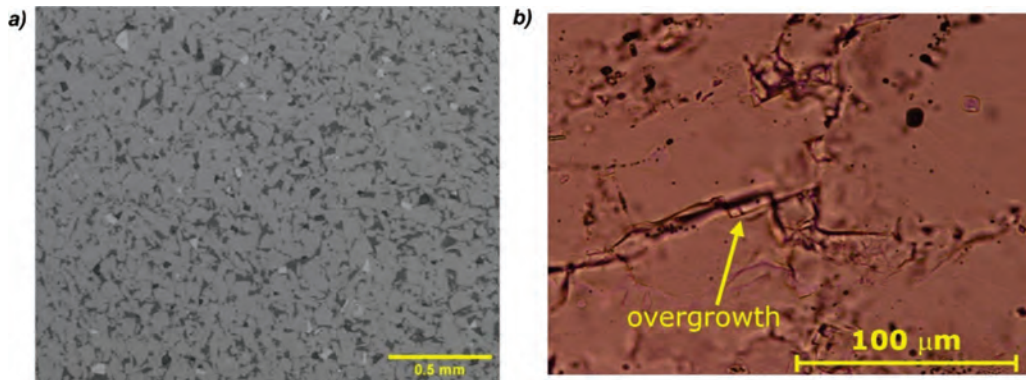
Figure 4: a) X-ray CT image obtained using the Zeiss Xradia 610 microscope of sample p1327. b) Light microscope image of a detail of sample p1327.

5. Discussion

5.1. Deformation mechanism

Under the present experimental conditions, there are a number of possible porosity reducing processes These are 1) cataclasis and associated grain size reduction, grain rotation and rearrangement, 2) dislocation creep and 3) intergranular pressure solution creep. We did not observe significant intragranular fracturing in the final microstructure nor did we observe significant time-dependent porosity reduction during room-dry (~35 % humidity) compaction. Based on these observations, we argue that cataclasis was not a significant porosity reducing process in our samples, although it may play a minor role on the scale of grain contacts.

For pressure solution creep, theory and experiments (Spiers et al. 1989) have demonstrated a stress exponent of 1 for low stress, low strain rate and/or small grain size, whereas the stress

exponent for wet dislocation creep is > 2. The stress exponent we determined is initially >2, indicating some contribution of dislocation creep to the deformation – however, it reduces with ongoing compaction and lower stresses to a value very close to 1. Combining this with the microstructural observations, we conclude that the dominant compaction mechanism was intergranular pressure solution creep with some minor contribution of dislocation creep during initial compaction at high porosity and at correspondingly high stresses at grain-grain contact.

5.2. Effect of porosity and grain distribution on permeability

The data presented in Figure 3b clearly show that permeability of a granular aggregate of salt is dependent on the grain size distribution. Aggregates with a narrow grain size distribution have a permeability that is up to an order of magnitude higher than that of an aggregate with a broad grain size distribution. In Figure 5, we show two realizations of our simple extension to the classical KC model, along with the data of all experiments using a grain size distribution 38-106 μm. For both examples shown, the permeability decreases when a distributed grain size is considered, but it decreases more for a uniform distribution than for a lognormal distribution. This is because the permeability of an aggregate with a lognormal grain size distribution is largely controlled by the most abundant grain size which is the mean grain size. Still, permeability is up to an order of magnitude smaller if we assume that all pores in the distribution are in series (i.e. considering the harmonic mean). Also note that the standard deviation used for this calculation was still relatively small at 15 μm.

In contrast to the KC formulation, our model does not predict a power law dependence of permeability on porosity, i.e.

$$k = k_0 \phi^\alpha$$
(15)

where α is typically 3. At porosities above 10%, our model predicts a slope significantly above 3 (α=4.27) which seems to better fit the data, especially at porosities above 20%. Results from linear regression of some of the experimental data shown in Figure 5 are listed in Table 2. The loglinear fits are not perfect and there is considerable variability in the slopes for the different experiments. This may reflect uncertainties in the actual porosity values in each experiment, such as those due to small discrepancies in the measured amount of material or in measurements of layer thickness. However, the values of α are consistently larger than 6 and the 95% lower bound value is consistently larger than 3. Spiers and coworkers (1989) reported a value for α of 5.02 for samples with porosity in the range 5-40% and using Argon gas permeametry. They were able to also determine the connected porosity which yielded an exponent of 2.89, much closer to that expected from models based on the hydraulic radius. Unfortunately, we were not able to quantify the connected porosity, but it is likely that our large values for α are similarly caused by the presence of non-effective porosity (Bernabé et al. 2003). As already argued by Bernabé and coworkers (2003), it is the change in effective porosity that will change the permeability. It is the ratio of effective over non-effective porosity (defined as ξ by Bernabé et al. 2003) which controls the magnitude of the power law exponent if we consider total porosity only. Our data and especially the trends in individual experiments suggest that this ratio ξ is not constant during compaction of salt aggregates via pressure solution. Ignoring, for now, data at anomalously low porosities of 5 and 10%, the remainder of the data suggest an increase in the power law exponent α. This is in turn suggests a continuous decrease in the ratio of effective over non-effective porosity ξ, which was also observed by Spiers et al. (1989). Our data are not of sufficiently high quality and density to determine whether there is any change in the manner that the non-effective porosity and thus ξ evolves, although the limited data suggest smaller changes with decreasing porosity for narrower grain size distributions and thus a smaller change in non-effective porosity.
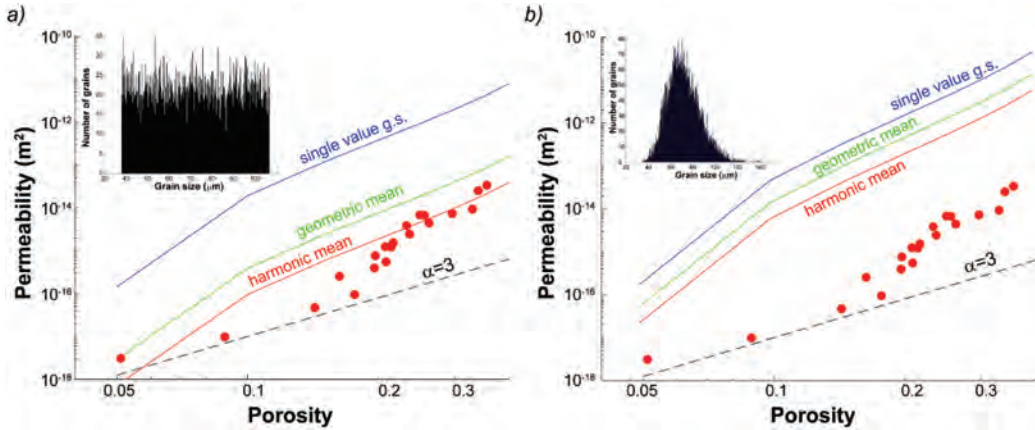
Figure 5: Permeability calculated using Equations 9, 10 and 12, based on SCC packing, evolving through compaction via pressure solution (see Figure 1) for a uniform grain size distribution (a) with minimum and maximum grain sizes of 38 µm and 106 µm, respectively, and a lognormal grain size distribution (b) with a mean grain size of 72 µm and standard deviation of 15 µm. Data points shown are from experiments p1327, p1445, p1490 and p1545.

Table 2: Results of linear regressions on the porosity-permeability data of experiments p1327, p1445, p1490 and p1545 (d=38-106 µm).

Porosity	α	lower 95%	upper 95%	R^2	N	k_0
all	6.27	5.40	7.14	0.93	20	$10^{-10.73}$
> 20%	5.92	4.25	7.60	0.86	13	$10^{-10.88}$
> 10%	6.73	5.46	7.99	0.90	18	$10^{-10.45}$
10-20	5.92	-17.07	28.91	0.38	5	$10^{-10.23}$
20-30	6.95	3.44	10.45	0.76	10	$10^{-11.16}$

6. Summary, limitations, and suggestions for future work

The work presented here demonstrates that it is important to consider the grain size distribution of granular aggregates when modeling the evolution of porosity and permeability with time since permeability at constant porosity is lower in samples with a wider grain size distribution. In fine-grained salt aggregates, compaction *via* pressure solution reduces porosity and permeability rapidly, falling to below 10^{-17} m^2 within a day at room temperature for an average grain size of 72 µm. The relation between permeability and porosity cannot be described by a power law with a single exponent. We posit that this is since not all porosity contributes to the flow network and that the proportion of this non-effective porosity increases with decreasing total porosity. The inability to determine the proportion of non-effective porosity in our sample during the experiments is a severe limitation, which might be solved in future work by employing transient permeametry techniques such as utilizing pressure decay or pressure oscillations. Both methods provide information on the storage capacity of the sample. Ideally, continuous measurements of permeability are desired during ongoing compaction. However, attempts at this resulted in the development of dissolution holes within the sample. Measurements through transient permeametry may prevent the wormholing. Another option is to perform experiments under concurrent X-ray CT, so that the development of porosity may be continuously imaged and quantified.

References

BERNABÉ, Y. 1995. Pore-scale heterogeneity, energy dissipation and the transport properties of rocks. *Geophysical Research Letters,* 22**,** 1529-1532.

BERNABÉ, Y., U. MOK, & B. EVANS, 2003. Permeability-porosity relationships in rocks subjected to various evolution processes. *Pure and Applied Geophysics,* 160**,** 937-960.

CARMAN, P. 1937. Fluid flow through a granular bed. *Trans. Inst. Chem. Eng.,* 15**,** 150-167.

DAVID, C., WONG, T.-F., ZHU, W. & ZHANG, J. 1994. Laboratory measurement of compaction-induced permeability change in porous rocks: implications for the generation and maintenance of pore pressure excess in the crust. *Pure and Applied Geophysics,* 143**,** 425-455.

FREDRICH, J. T., DIGIOVANNI, A. A. & NOBLE, D. R. 2006. Predicting macroscopic transport properties using microscopic image data. *Journal of Geophysical Research,* 111**.**

GIGER, S. B., TENTHOREY, E., COX, S. F. & FITZ GERARLD, J. D. 2007. Permeability evolution in quartz fault gouges under hydrothermal conditions. *Journal of Geophysical Research,* 112**.**

KOZENY, J. 1927. Uber kapillar Leiting der Wasser in Boden. *Sitzungsber. Akad. Wiss. Wien,* 136**,** 271-306.

NIEMEIJER, A., ELSWORTH, D. & MARONE, C. 2009. Significant effect of grain size distribution on compaction rates in granular aggregates. *Earth and Planetary Science Letters,* 284**,** 386-391.

PLUYMAKERS, A. M. H. & SPIERS, C. J. 2015. Compaction creep of simulated anhydrite fault gouge by pressure solution: theory v. experiments and implications for fault sealing. *Geological Society, London, Special Publications,* 409**,** 107-124.

SAMUELSON, J., ELSWORTH, D. & MARONE, C. 2009. Shear-induced dilatancy of fluid-saturated faults: Experiment and theory. *Journal of Geophysical Research,* 114.

SPIERS, C. J., PEACH, C.J., BRZESOWSKY, R.H., SCHUTJENS, P. M., LIEZENBERG, J. L.& ZWART, H. J. 1989. Long-term rheological and transport properties of dry and wet salt rocks. Luxembourg: Commission of the European Communities.

SPIERS, C. J. & SCHUTJENS, P. M. 1990. Densification of crystalline aggregates by fluid-phase diffusional creep. In *Deformation processes in minerals, ceramics and rocks,* eds. Barber & P. G. Meredith. London.

ZHANG, S., COX, S. F. & PATERSON, M. S. 1994a. The influence of room temperature deformation on porosity and permeability in calcite aggregates. *Journal of Geophysical Research,* 99**,** 15761-15775.

ZHANG, S., PATERSON, M. S. & COX, S. F. 1994b. Porosity and permeability evolution during hot isostatic pressing of calcite aggregates. *Journal of Geophysical Research,* 99**,** 15741-15760.

ZHU, W., DAVID, C. & WONG, T.-F. 1995. Network modeling of permeability evolution during cementation and hot isostatic pressing. *Journal of Geophysical Research,* 100**,** 15451-15464.

4D microtomography of brine-assisted healing processes in deformation-damaged rocksalt: A first look

Y. Ji[1*], C. J. Spiers[1], S.J.T. Hangx [1], J.H.P. de Bresser[1], M.R. Drury [1]

[1]Department of Earth Sciences, Utrecht University, the Netherlands;

* y.ji@uu.nl

ABSTRACT: Rock salt formations represent key options for storage of natural gas, hydrogen, and compressed air energy, and for storage or disposal of radioactive waste. At depths beyond a few tens or hundreds of meters, undisturbed halite-dominated (>90%) rock salt deposits are usually impermeable and have very low porosity. However, as a result of excavation, near-field microcracking and associated dilatancy occur in rock salt, increasing porosity and permeability. The connectivity of a brine- or water-vapour-filled microcrack network in deformation-damaged salt, is expected to decrease over time, partly due to dissolution-precipitation healing. Here, we employ 4D (i.e., time-resolved 3D) microtomography to study the long-term evolution of dilated grain boundary and microcrack networks developed in deformation-damaged natural salt by such brine-assisted processes. We found substantial microstructural modification or "healing" over periods of days to a few months. Cracks and dilated grain boundaries became crystallographically faceted, necked, discontinuous, and disconnected, and often migrated to "recrystallize" the material, producing an increase in tortuosity and a decrease in connectivity of the crack network. The magnitude and rate of associated permeability reduction and its evolution with time remain to be determined in future studies.

1   Introduction

By virtue of its low permeability and high ductility, rock salt has long been identified as a favorable host rock for solution-mined oil and gas storage caverns and for radioactive waste repositories (e.g., Langer 1993; 1999). Driven by the growing urgency to transition to non-fossil energy sources, current interest in salt is also fast expanding towards construction and re-use of solution-mined caverns for large-scale energy storage in the form of hydrogen and compressed air.

To evaluate the long-term performance and safety of all such systems and abandoned salt-production caverns, a quantitative understanding is needed of the coupled mechanical behavior and transport properties of salt. Extensive experimental data exist on the creep behavior of intact salt rock (e.g., Carter et al. 1993; Hunsche & Hampel 1999), on the development and mechanical closure of microcrack damage (Alkan et al. 2007), and on compaction creep of salt backfill material (Hansen et al. 2014). These have been cast into constitutive models that are widely applied in geomechanical simulations of storage systems and repository behavior (e.g., Hampel et al. 2010). The predictions of such simulations are crucial for evaluating the timescale for closure and ultimate sealing (to natural salt permeabilities) of boreholes and backfilled openings, for example. Not yet included, however, are the effects of crack and pore healing by dissolution-precipitation processes. These are known to occur in salt when small amounts of brine or adsorbed water are present and are expected to dominate permeability reduction in the late stages of convergence of boreholes and backfilled cavities, i.e., when deviatoric and effective mean stresses and associated strain rates are low (Houben et al. 2013). They may also play a role in controlling permeability evolution under the low deviatoric and effective stress conditions expected in the roof region of abandoned brine caverns.

Under such conditions of low deviatoric and low effective stress, the connectivity and contiguity of brine-filled or water-film-coated grain boundaries, triple junctions, pores, and microcracks

present in deformation-damaged or granular salt are expected to decrease over time by internal mass transfer involving dissolution, diffusion, and precipitation of salt - at least up to fluid pressures (P) of around 75 MPa and temperatures (T) around 100℃ (Lewis & Holness 1996). The driving force for this type of healing process is the tendency to reduce the total interfacial energy by reducing the salt-brine interfacial area, in the approach to an equilibrium state defined by characteristic dihedral wetting angles at salt-salt contacts. Provided porosity lies below a geometric threshold of 4-5%, determined by the equilibrium dihedral angle for the salt-brine system (Ghanbarzadeh et al. 2015), such healing processes are expected to cause a slow decrease in the permeability of salt, depending on pressure-temperature conditions.

The progress of these dissolution-precipitation processes has been directly observed over periods of a few days in cleavage-crack healing experiments performed on single crystals of NaCl in an optical cell, at room temperature and pressure with controlled relative humidity (Houben et al. 2013). Crack contraction rates measured in these experiments demonstrated that healing was controlled by diffusion through adsorbed water/brine films. Similar optical observations have been made on grain boundary healing in static annealing experiments on deformed potash salts (Urai 1987; Schenk & Urai 2004). Pore reconfiguration by dissolution-precipitation transfer is also implied by the end results of the experiments on granular salt plus brine mixtures performed by Lewis & Holness (1996) and Ghanbarzadeh et al. (2015), in which mean dihedral angles were measured after hydrostatic annealing at elevated P-T and zero Terzaghi effective stress conditions for several days. These studies respectively employed petrographic imaging and X-ray micro-computed tomography (µCT). Advanced µCT imaging (Cnudde & Boone 2013; Ji et al. 2015) has also been applied to the characterization of pore and inclusion arrays in natural rocksalt (Thiemeyer et al. 2014; 2015; Burliga & Czechowski 2010) and to timelapse imaging of fine, granular salt undergoing compaction creep by pressure solution (e.g., Renard et al. 2004; Macente et al. 2018). However, we know of no µCT imaging work on the long-term progress of crack healing and pore reconfiguration by solution transfer processes in either coarse granular salt (e.g., backfill) or in plastically deformed and dilated salt rock of the type expected in the walls of converging openings.

In this paper, we report a series of novel healing experiments performed on plastically pre-deformed and dilated (cracked) samples of coarse natural rock salt, using time-lapse µCT imaging. Our goal was to capture evidence for the healing processes operating under brine-saturated, room P-T conditions, over times up to six months, and to obtain insight into the progress and rate of these processes.

2 Methodology

2.1 General approach

The present experiments were conducted on natural polycrystalline rocksalt at room temperature and atmospheric pressure. Small samples were mechanically deformed, damaged, and dilated under unconfined conditions, flooded with saturated brine at atmospheric pressure, and hermetically sealed. In this way, newly generated cracks and dilated grain boundaries were exposed to saturated salt solution and subject to the effects of dissolution, diffusion, and precipitation – under conditions of zero effective stress. The healing process thus initiated was imaged at different stages (in time-lapse mode employing increasing time intervals) using an X-ray CT microscope (µCT tests), as illustrated in Figure 2.

2.2 Sample preparation for CT imaging - specifics

Polished cylinders of Leine rocksalt (Leinesteinsalz from the German Zechstein, grain size 1-4 mm) measuring 3.5-6.4 mm diameter and 7.9-14 mm length were first deformed in unconfined axial compression to create microcrack damage alongside 2.5% to 6.8% of plastic deformation. The microcrack dilatancy obtained corresponded to several percent of intergranular crack and grain boundary porosity, with occasional transgranular cracks also being present. The deformed samples were then jacketed in an FEP (fluorinated ethylene propylene) heat-shrink sleeve and CT scanned in the lab-dry condition. The sample-jacket assembly was then suction-flooded with saturated brine and located in a PEEK (polyether ether ketone) polymer capsule or "bottle". The vessel-sample assembly was subsequently sealed by adding a rubber sheet and plug, as gaskets, and a screw-on PEEK closure-lid. In the mm thickness range used for constructing the PEEK vessels, PEEK is essentially X-ray transparent, allowing maximum resolution to be obtained, in conjunction with the small sample dimensions. The sample assembly and associated components used are illustrated in Fig. 1.
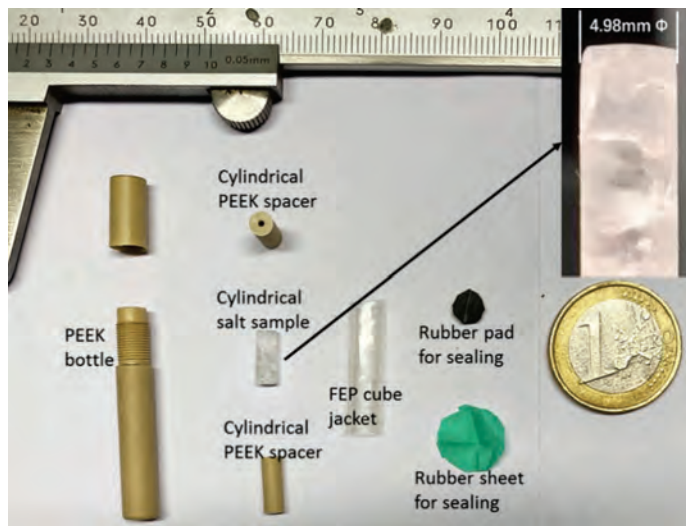
Figure 1: Sample assembly used for µCT. Note the cylindrical rocksalt sample of 4.98mm diameter and the accessories needed to encapsulate the sample for scanning in the brine-saturated condition. In the upper right corner is an enlarged view of the sample.

2.3 X-ray Computed Microtomography

Healing/imaging experiments were conducted on three deformed/cracked rocksalt samples plus added brine, as described above (samples XLSS02, XLSS05, XLSS06 – see Table 1). For control purposes, one intact sample (XLSS00) and one deformed sample (XLSS01) were imaged immediately after preparation, without adding brine (dry). CT imaging was performed using a ZEISS Xradia 610 Versa 3D X-ray Microscope located in the Multi-scale Imaging and Tomography Facility (MINT) at Utrecht University. Multiple series of projections were acquired for each sample. The number of projections per scan was varied from 2001 to 4501 to achieve a high signal-to-noise ratio within acceptable scanning duration. Image reconstructions were done using the "Reconstructor Scout-and-Scan" software developed by Zeiss, employing pixel sizes ranging from 380nm to 7µm. We used incident X-rays generated using a voltage of 60 kV and 6.5 W power or 50kV and 4.5 W power, combined with a source filter to optimize the transmittance of the projection images. As a result, the grey level contrast between solid salt grains, saturated brine and air was maximized and clearly distinguishable in the reconstructed images.

Table 1: List of samples presented in this study. Wet signifies brine flooded.

sample name	diameter (mm)	original length (mm)	deformed length (mm)	plastic strain (%)	condition/ healing time (days)	CT voxel size (micron)
XLSS00	6.40	14.00	intact	intact	dry	7 and 1.75
XLSS01	4.95	11.00	10.25	6.82	dry	5 and 0.8
XLSS02	4.95	12.90	12.25	5.04	Wet/70	5.6
XLSS05	3.70	9.40	9.15	2.66	Wet/264	4, 2 and 0.4
XLSS06	3.50	7.90	7.70	2.53	Wet/120	3.7, 1.85, 0.76 and 0.38

To capture the evolution of healing in each sample studied, a series of CT scans were performed on each sample at gradually increasing time intervals (timelapse imaging). A first scan was conducted on each sample before brine addition, i.e. on the deformed/ cracked, dry sample. The second scan was conducted immediately after brine-flooding and capsule sealing. Subsequent scans of wet samples were performed at gradually increasing time intervals from one day, three days, one week, one month, and up to six months. By doing so, we managed to capture the 4D (i.e. time-resolved 3D) healing process occurring in the damaged rocksalt samples.
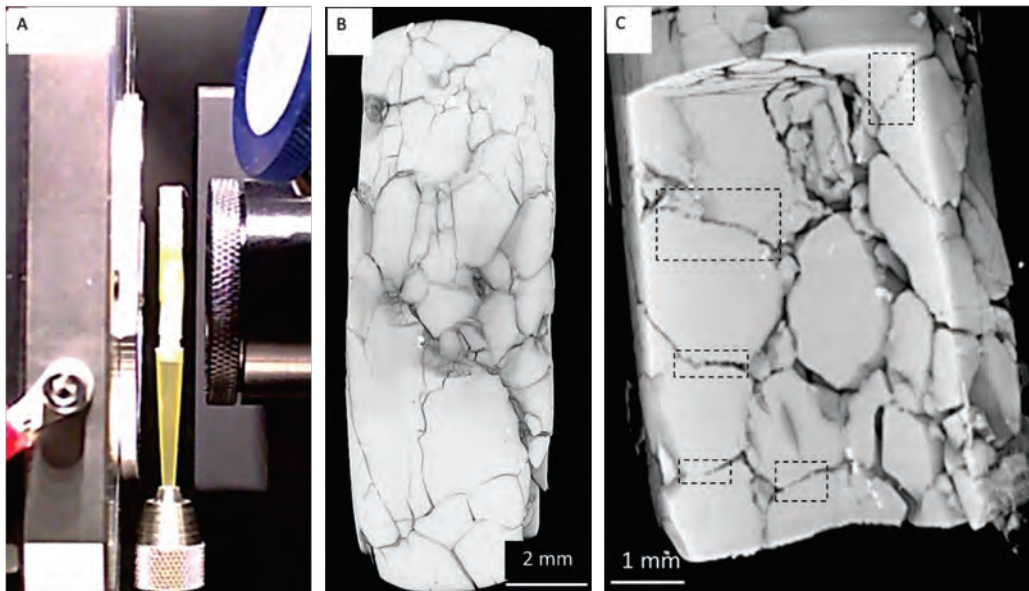
Figure 2, Use of μCT to image a rocksalt sample. (A) An FEP-jacketed rock salt cylinder (5 mm diameter) being scanned in X-ray CT microscopy. (B) Typical 3D CT image of a cracked salt sample (dry, Sample XLSS02). (C) Reconstructed CT image obtained 13 days after driving saturated brine through a deformation-damaged salt cylinder; note the inter-, intra-, and transgranular cracks (SampleXLSS02).

3   Results

The CT imaging results obtained are illustrated below in Figures 3 to 5. Undeformed samples showed intact grains and undilated grain boundaries decorated with fluid inclusions (Figure 3A). Old, healed cracks were also visible. Samples that were deformed only and not (yet) impregnated with saturated brine showed wide, sharply defined grain boundary cracks, and occasional intra- and transgranualr cracks, that were clearly connected throughout the samples, providing high permeability pathways (Figure 3B). No change was observed in these microstructural features in samples that were stored in a dry environment, at least over periods up to five months. After introducing brine, the microstructure started to change and a wide variety of healing phenomena were observed. In the first a few days, we saw a change in surface roughness on the outside of the samples. Their smooth, polished, outer surface became irregular or wavy, with an amplitude of 0.05 to 0.2 mm within a few weeks (Figure 5).
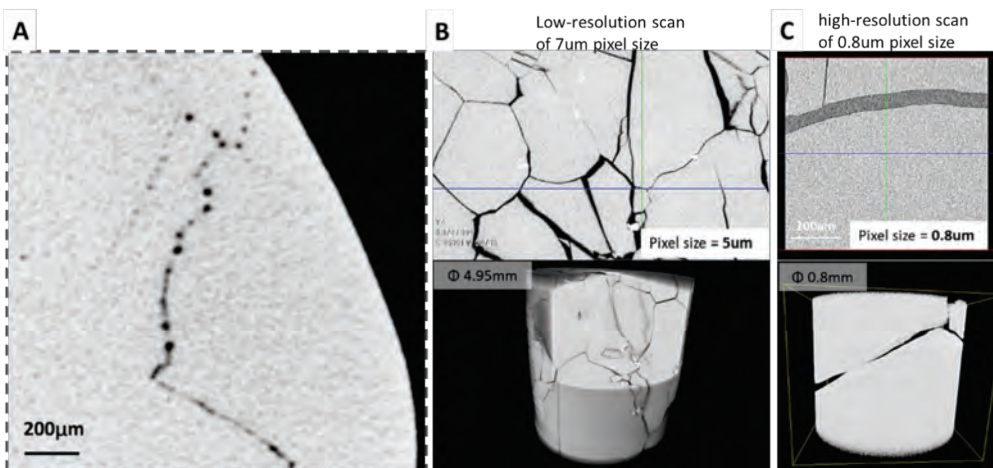
Figure 3: µCT images showing the undeformed Leine rocksalt starting material (A) and axially compressed samples (B) and (C). (A) Grain boundary with fluid inclusions in the undeformed starting material. Healed cracks are also visible. (B) Intergranular and transgranular cracks formed after axial deformation of samples XLSS01, but before brine addition and the onset of healing processes. (C) A subvolume in (B) using a zoom-in high-resolution (800nm per pixel) scan.

Within one day of adding brine and on-going in the subsequent days and weeks, we observed widespread crystallization, overgrowth, and surface reconfiguration within the deformation-induced cracks and pores. Some grains grew topotactically into adjacent pores and cracks, or "ate into" their neighbours by grain boundary migration (i.e., migration of dilated grain boundaries and cracks), forming stepped, idiomorphic (100) cube faces in both cases (Figures 4 and 5). As healing time increased further, most of the deformation-induced cracks and deformation-dilated grain boundaries became more tortuous. This was due to a) the development and progressive coarsening of a zig-zag morphology reflecting the tendency for migrating boundaries and open crack walls to adopt stepped, low energy (100) crystal forms, and b) an accompanying tendency for dilated boundaries and cracks to neck down into less well-connected arrays of pores and inclusions, often as the (001) steps growing on opposing crack walls impinged upon each other (Figures 4 to 6). Significant crack and pore reconfiguration was observed over periods of 2-3 weeks, with major changes occurring in the longest runs (3 months), which showed markedly increased tortuosity and reduced (2D) connectivity (Figures 4 - 6).
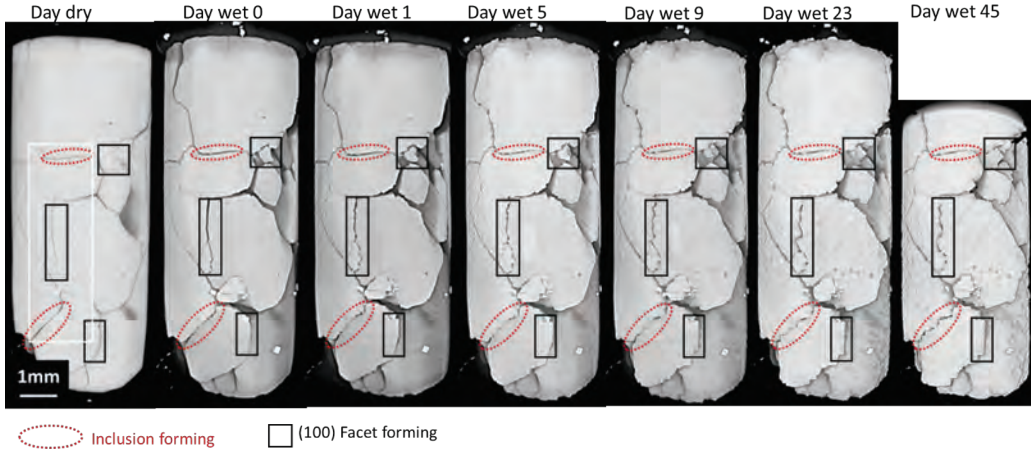
Figure 4: μCT images showing the evolution of the crack network in a pre-cracked sample over 45 days of healing. Sample number XLSS06. Salt is in grey, voids (pores and cracks) are in black. Red dashed ellipses mark the regions with cracks becoming disconnected and inclusions forming. Black rectangles show regions of grain boundary (or crack) migration. These data show clear modification and disconnection of the crack network over time, inevitably resulting in a decrease in permeability. Over the maximum test duration of 4 months, even larger changes were observed.
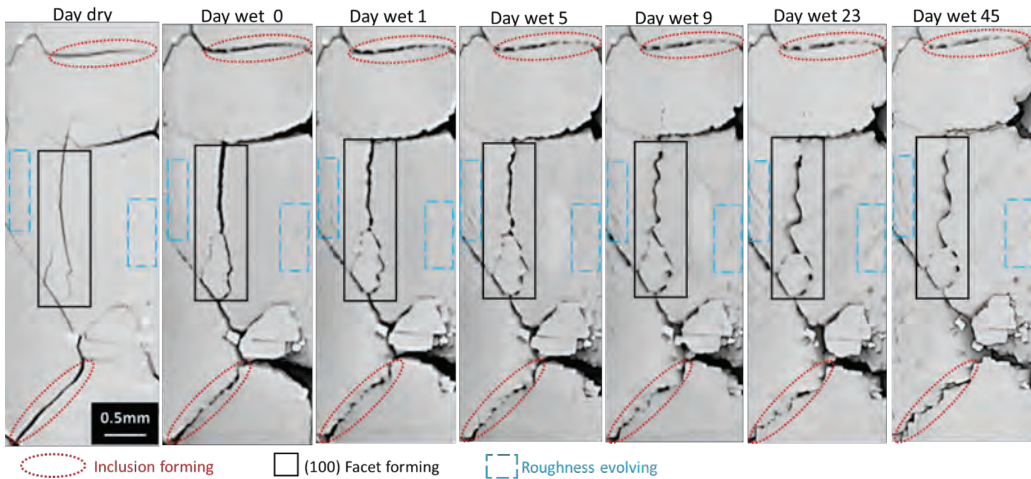
Figure 5: Enlargement of the subregion marked with the white rectangle in Figure 4. Salt is grey, voids (pores and cracks) are black. Red dashed ellipses mark dilated, brine-filled grain boundaries that are becoming disconnected due to necking down of the fluid film to form an island-channel structure and ultimately isolated inclusions. Black rectangles show sites of marked crack migration with local necking of the internal fluid film to form more isolated inclusions (lower portion). Blue rectangles mark the area of roughness evolving.
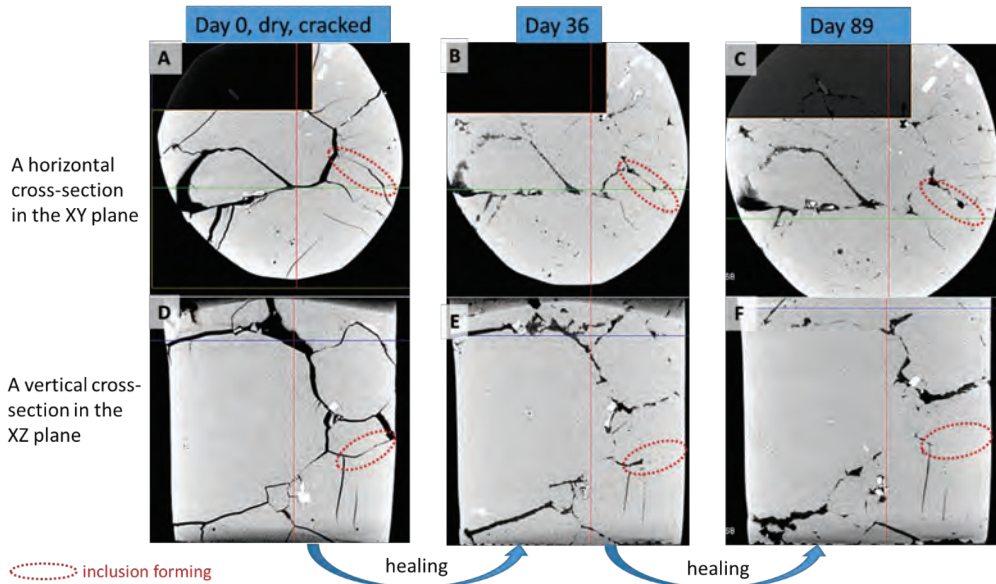
Figure 6. Reconstructed CT images showing crack network evolution in a deformation-damaged rock salt sample in the initial dry condition (left), after 36 days of healing following brine addition (center), and after 89 days of healing (right). Sample number XLSS05. Salt in grey, voids (pores and cracks) in black. (A), (B) (C) are horizontal cross-sections orientated normal to the cylindrical sample axis. (D), (E), (F) are vertical cross-sections orientated parallel to the cylindrical sample axis. Red dashed ellipses mark regions containing cracks that are becoming disconnected due to the formation of inclusion arrays. Local grain/interface boundary migration is also visible.

4. Discussion and Conclusions

This study reports high-resolution X-ray CT imaging of the evolution of grain boundary and microcrack healing processes occurring in plastically deformed and microcrack-damaged rocksalt under brine saturated conditions. The experiments were conducted at room temperature and pressure over periods up to six months, with the aim of elucidating the dissolution-precipitation processes that are believed to dominate crack/pore healing and permeability reduction in salt when deviatoric and effective mean stresses are low, e.g. in the late stages of convergence of boreholes and backfilled cavities.

We observed several phenomena in the CT tests, after addition of brine. Besides roughening of the outer surfaces of the samples, idiomorphic (100) topotactic overgrowths developed on the walls of larger pores and wide cracks. Other dilated grain boundaries and trans/intragranular cracks served as sites for migration of the brine-filled boundary or crack such that one side advanced at the expense of the other, again with idiomorphic (100) forms dominating. Perhaps most importantly from the perspective of permeability reduction, most cracks, both grain boundary and intra/transgranular, became more tortuous and less well connected with healing time, due to the development of a (100)-controlled, zig-zag, surface-step morphology combined with step impingement and necking down of the internal fluid film to form (incipient) inclusion arrays.

This necking down of dilated grain boundaries and cracks to form (incipient) inclusion arrays is qualitatively consistent with the results of the crack healing experiments on cleaved single crystals of NaCl reported by Houben et al. (2013) and with the concept of surface area/ energy reduction by dissolution-precipitation transfer. The topotactic overgrowth features and (100)

steps or faceting that we observed on dilated grain boundary and trans/intragranular crack surfaces, which did not show wholesale migration, were presumably caused by local surface energy minimization over crack walls. In other words, initially irrational, high energy crystallographic (crack) surfaces became reconfigured into stepped (100) surfaces, which have the minimum surface energy in NaCl (Bruno et al. 2009).The dissolution step of this process may also have been enhanced by release of dislocation-stored strain energy induced by the plastic deformation suffered by the samples. In the case of grains consuming portions of their neighbours, our interpretation is that strain-induced boundary migration involving dissolution-precipitation transfer across dilated grain boundaries and cracks occurred, driven by differences in dislocation stored energy related to plastic deformation, with surface energy minimization or kinetic factors again favouring the formation of (100) surfaces at migrating interfaces. This follows from direct comparison with brine-assisted grain boundary migration seen in dense rock salt deforming by dislocation mechanisms under confined, non-dilatant conditions (Urai et al. 1986; Peach et al. 2001; Ter Heege et al. 2005; Pennock et al. 2006).

Conceptual models put forward by previous researchers (e.g. Houben et al. 2013) predict that crack healing should produce isolated or only partly connected pores with reduced surface area, by two processes: i) dissolution and precipitation driven by surface area/energy reduction, and ii) growth of new, strain free crystals (grain boundary migration) over pre-existing brine-filled cracks, again by dissolution-precipitation phenomena but driven by release of stored dislocation strain energy. Our experimental results show clear evidence that both of the above mechanisms substantially modify the pore, crack and grain microstructure of the deformed and dilated salt within a few weeks to months.

We note that (100) faceting of migrating interfaces was much more prevalent than observed in the studies of equilibrium dihedral angle development in the salt-brine system, as a function of P and T (up to 200 °C and 200 MPa), reported by Lewis & Holness (1996) and Ghanbarzadeh et al. (2015). These authors equilibrated loose, fine salt (analytical reagent, 0.2-0.4 mm grain size cubes) with brine, at zero Terzaghi effective stress, and obtained a sintered microstructure of well-rounded grains and well-defined dihedral angles. By contrast, equilibrium was clearly not reached in our experiments as the microstructure continued to evolve even after 2-3 months. We infer that this reflects the lower temperature, coarser grain size and wider pore/crack spacing (i.e. slower diffusion rates) characterizing our experiments, as well as the fact that our samples were plastically deformed (i.e. charged with dislocation-stored energy) and not subjected to intial grain dissolution and "rounding" by heating to elevated temperatures. The implication is that the equilibrium state seen in the above dihedral angle experiments cannot be reached without total recrystallization of our samples -or perhaps not at all due to the intervention of some intermediate meta-stable equilibrium state characterized by local equilibrium in the pore network only. This draws the applicability of previous equilibrium diahedral angle datato plastically deformed and dilated salt rock into question regarding the prediction of pore connectivity in deformed rock salt. The applicability of the mean dihedral angle data reported by Lewis and Holness (1996) to the computation of pore connectivity (i.e. of the percolation threshold) and permeability is also open to question purely because the strong anisotropy of surface energy evidenced in our experiments is not accounted for (e.g., Laporte & Provost 2000).

We suggest that studies of plastically deformed and dilated/cracked rock salt samples can better simulate the evolution and final healed state of crack and grain boundary networks, as developed in the walls of converging galleries and boreholes, than mean dihedral angle experiments on synthetic granular samples. Our results show that, in the early stage of healing, relatively planar, brine-filled grain boundary and trans/intragranular cracks become more tortuous due to (100)- controlled overgrowth and grain boundary migration by dissolution-precipitation transfer. Cracks and dilated grain boundaries become crystallographically stepped, necked/irregular, discontinuous and disconnected, and can migrate to "recrystallize" the material. For crack porosities of a few percent, the associated increase in tortuosity and decrease in connectivity and contiguity of the fluid pathways within dilated grain boundaries

and cracks must concomitantly reduce crack network permeability. However, the magnitude and rate of permeability reduction and its evolution with time remain to be determined.

Though preliminary, the present results indicate that substantial healing occurs in plastically deformed and dilated/damaged rock salt in periods of weeks to months at room temperature, when brine saturated. They offer a starting point for the development and testing of new microphysical-thermodynamic models for healing by dissolution-precipitation processes and are expected to be relevant not only to plastically deformed and dilated rocksalt but also to plastically compacted salt backfill. In future, we plan to conduct experiments with longer healing times to capture the formation of inclusions and the further disconnection of the crack network. We also plan to conduct CT experiments at higher temperatures and effective stress states that better simulate the conditions in converged boreholes, backfilled openings and salt cavern walls. A crucial further step will be to determine the permeability evolution that accompanies the dissolution-precipitation healing, either by direct measurement or by fluid dynamics computation (Arns et al. 2004) based on CT characterization of the evolving crack and grain boundary network.

Acknowledgements

References

ALKAN, H., CINAR, Y. & PUSCH, G. 2007. Rock salt dilatancy boundary from combined acoustic emission and triaxial compression tests. Int. J. Rock Mech. Min. Sci. 44(1), 108–119.

ARNS, C.H., KNACKSTEDT, M.A., PINCZEWSKI, W.V. & MARTYS, N.S. 2004. Virtual permeametry on microtomographic images. J. Pet. Sci. Eng. 45(1), 41–46.

BRUNO, M., AQUILANO, D. & PRENCIPE, M. 2009. Quantum-Mechanical and Thermodynamical Study on the (110) and Reconstructed (111) Faces of NaCl Crystals. Cryst. Growth Des. 9(4), 1912–1916.

BURLIGA, S. & CZECHOWSKI, F. 2010. Anatomy of hydro-carbon-bearing zones, hydrocarbon provenance and their contribution to brittle fracturing of rock salt in the Klodawa Salt Structure (central Poland). In Solution Mining Research Institute Spring 2010 Technical Conference, pp. 125–134.

CARTER, N.L., HORSEMAN, S.T., RUSSELL, J.E. & HANDIN, J. 1993. Rheology of rocksalt. J. Struct. Geol. 15(9), 1257–1271.

GHANBARZADEH, S., HESSE, M.A., PRODANOVIĆ, M. & GARDNER, J.E. 2015. Deformation-assisted fluid percolation in rock salt. Science (80-.). 350(6264), 1069–1072.

HAMPEL, A., GUNTHER, R.M., SALZER, K., MINKLEY, W., PUDEWILLS, A., LEUGER, B., ZAPF, D., STAUDTMEISTER, K., ROKAHR, R., HERCHEN, K., WOLTERS, R., LUX, K.-H., SCHULZE, O., HEEMANN, U. & HUNSCHE, U. 2010. Benchmarking of Geomechanical Constitutive Models For Rock Salt. 44th U.S. Rock Mech. Symp. 5th U.S.-Canada Rock Mech. Symp., ARMA-10-287.

HANSEN, F.D., POPP, T., WIECZOREK, K. & ST, D. 2014. *Salt Reconsolidation Principles and Application.*, Sandia National Lab.(SNL-NM), Albuquerque, NM (United States),p.

HOUBEN, M.E., TEN HOVE, A., PEACH, C.J. & SPIERS, C.J. 2013. Crack healing in rocksalt via

diffusion in adsorbed aqueous films: Microphysical modelling versus experiments. Phys. Chem. Earth, Parts A/B/C 64, 95–104.

HUNSCHE, U. & HAMPEL, A. 1999. Rock salt — the mechanical properties of the host rock material for a radioactive waste repository. Eng. Geol. 52(3), 271–291.

LANGER, M. 1993. Use of solution-mined caverns in salt for oil and gas storage and toxic waste disposal in Germany. Eng. Geol. 35(3), 183–190.

LANGER, M. 1999. Principles of geomechanical safety assessment for radioactive waste disposal in salt structures. Eng. Geol. 52(3), 257–269.

LAPORTE, D. & PROVOST, A. 2000. Equilibrium geometry of a fluid phase in a polycrystalline aggregate with anisotropic surface energies: Dry grain boundaries. J. Geophys. Res. Solid Earth 105(B11), 25937–25953.

LEWIS, S. & HOLNESS, M. 1996. Equilibrium halite-H2O dihedral angles: High rock-salt permeability in the shallow crust? Geology 24(5), 431–434.

MACENTE, A., FUSSEIS, F., BUTLER, I.B., TUDISCO, E., HALL, S.A. & ANDÒ, E. 2018. 4D porosity evolution during pressure-solution of NaCl in the presence of phyllosilicates. Earth Planet. Sci. Lett. 502, 115–125.

RENARD, F., BERNARD, D., THIBAULT, X. & BOLLER, E. 2004. Synchrotron 3D microtomography of halite aggregates during experimental pressure solution creep and evolution of the permeability. Geophys. Res. Lett. 31(7).

SCHENK, O. & URAI, J.L. 2004. Microstructural evolution and grain boundary structure during static recrystallization in synthetic polycrystals of Sodium Chloride containing saturated brine. Contrib. to Mineral. Petrol. 146(6), 671–682.

THIEMEYER, N., PUSCH, M., HAMMER, J. & ZULAUF, G. 2014. Quantification and 3D visualisation of pore space in Gorleben rock salt: constraints from CT imaging and microfabrics. Zeitschrift der Dtsch. Gesellschaft für Geowissenschaften 165(1), 15–25.

THIEMEYER, N., HABERSETZER, J., PEINL, M., ZULAUF, G. & HAMMER, J. 2015. The application of high resolution X-ray computed tomography on naturally deformed rock salt: Multi-scale investigations of the structural inventory. J. Struct. Geol. 77, 92–106.

URAI, J.L. 1987. Development of microstructure during deformation of carnallite and bischofite in transmitted light. Tectonophysics 135(1), 251–263.

URAI, J.L., SPIERS, C.J., ZWART, H.J. & LISTER, G.S. 1986. Weakening of rock salt by water during long-term creep. Nature 324(6097), 554–557.

Direct tomographic observation of brine percolation into MgO-shotcrete material

Kulenkampff, Johannes

[1]Helmholtz-Zentrum Dresden-Rossendorf, Germany

* j.kulenkampff@hzdr.de

ABSTRACT: Heterogeneity and tightness of the barrier demand particular sensitive and long-term measuring methods, as well as spatial resolution of small details. For this reason, we developed a guard-ring surface-packer for process tomography of brine migration into barrier material with positron-emission-tomography (PET). Based on radiolabeling, this method is extremely sensitive, non-destructive and without retroaction. As an example for transport in the engineered barrier, we investigated injection of [^{22}Na] NaClsat – solution from a fluid reservoir with a diameter of 20 mm into the contact zone of adjacent MgO-shotcrete layers. The driving pressure was 0.2 MPa, which caused intrusion of 1 mL of solution over a period of 260 d. The overlay of the temporal sequence of PET images and the structural CT image shows that deeper penetration (> 10 mm) occurred predominantly along one single pathway that was predetermined by the pore network structure. Second, we observed a slowly propagating diffuse tracer front that encompassed only a small portion of the injected fluid. Although the permeability of the material is very low (1e-20 m^2), the major portion of the brine propagates through a strongly localized migration channel and thus may reach a penetration depth of 50 mm, beyond the predictions based on assumed homogeneous flow through the material.

1   Introduction

Practical experience in salt mining has been gained over many centuries of underground salt exploitation. However, design of repositories for hazardous material in salt and proofing long-term safety is still challenging, which is exemplified by 40 years of Saltmech conferences. One crucial challenge is measurement and interpretation of permeability, being the critical parameter for the tightness of geological and engineered barriers. It is generally understood as a porous media parameter that relates fluid flow to driving pressure and that is controlled by pore structure (Kuhlman & Matteo 2018). However, in extremely tight material, the conception of permeability as a parameter of the bulk barrier material should be revised, because in some cases conductive pore structures are hardly detectable, even though hydraulic testing might suggest fluid losses and thus non-zero fluid injectivity. This could be caused not only by homogeneously distributed micro- or nanopores, but also by localized anomalies, like fracture systems or local lining-up of voids. In the latter case, the heterogeneity of the fluid propagation field could cause small volumes travel rather fast over long distances. In order to provide a method for experimental observation of such heterogeneous transport processes, we developed the GeoPET method (Gründig et al. 2007; Kulenkampff et al. 2016). A first application of this method on tracer propagation along a contact seam between rock salt and concrete was reported in Jantschik et al. (2018).

Our present application concerns laboratory testing of flow-field heterogeneities at MgO-shotcrete barriers. MgO-based building material is one option for long-term stable dam and seal constructions in salt mines, because it has favorable chemical properties in contact with salt brines, shows no shrinking, and is characterized by self-sealing characteristics (Freyer et al. 2015). These properties are mandatory requirements for the safety of underground repositories in salt rock over long periods. According to Popp et al. (2018), MgO-concrete is the most versatile construction material in salt-mines, generally featuring superior properties than other construction materials with more limited applicability, like crushed salt, salt concrete, bentonite, or bitumen. Compared to mass concrete, the shotcrete method largely reduces the

initial temperature load during curing, but causes layered and inhomogeneous structuring of the material. Interruptions of the spraying procedure each 10-20 cm are technically required, and cause contact surfaces or joints of the spraying sections (BAG) that could be potential transport pathways. In order to evaluate the contribution of transport along such a contact surface to the overall permeability, we applied our GeoPET during long-term injection of labelled brine.

The common application of GeoPET is on cylindrical samples with diameters between 30 and 100 mm that are enclosed in a plastic pressure vessel or cast in epoxy. Fluids labelled with a positron-emitting tracer are injected into one end plane of the cylinder and extracted at the other end. When the tracer is a long-lived radionuclide, this procedure has to be conducted in a safely enclosed system, in order to avoid hazardous contaminations. However, in this example the drill core had to be extracted orthogonally to the shotcrete joints, which thus complicated injection in parallel direction. Also, preparation of this hard and brittle material is difficult, because machining has to be conducting with air flushing. We thus removed plane-parallel calottes from the cylindrical cores by dry saw cuts (as shown in Figure 2) in order to produce planes for fluid injection and developed an efficient surface packer system for injection through the flat surface.

2 Methods

2.1 Material

In 2008, the test dam GV2 had been erected as shotcrete construction in the framework of the F&E project CARLA (GTS 2010; Popp et al. 2018) in the Teutschenthal salt mine near Halle/Saale, Germany. Core analysis and in-situ tests had been conducted on the dam within the MgO-SEAL project (Arendt et al. 2020), yielding permeability values between 10^{-20} and 10^{-16} m^2. The specimen investigated here has been extracted in 2019 after ageing over more than 10 years. Our focus was the joint zone of spraying sections that could be suspected as possibly conductive zones.

The material, MgO concrete "D4" (5-1-8 binder phase: 5 $Mg(OH)_2$ – $MgCl_2$ – 8 H_2O; sand-gravel aggregates) is characterized in the references. It is resistant against Mg-containing salt brines that are expected in the Carnallite-bearing environment, but not stable in pure NaCl-solutions. Nevertheless, in order to simplify the radioactive labelling procedure, we conducted our experiment with concentrated NaCl-brine, because the small fluid volume was expected to equilibrate rapidly in contact with the MgO-material without significantly affecting its integrity.

2.2 GeoPET - µCT

The two tomographic modalities serve different purposes: µCT provides a density image of the material that is essentially an image of the internal structure. Detectability of structural features is primarily controlled by spatial resolution of the µCT. In contrast, PET images the spatial distribution of the applied radiotracer in the material. The sensitivity of detection of a small number of decaying tracer atoms is extremely high, providing higher than pico-molar sensitivity in each voxel, and the voxel size represents mainly the reference volume for quantification. Significant tracer concentration is detected with PET even when it is located in pores far below the resolution of µCT, as long as the count rate originating from tracer atoms is significantly above the background noise.

The typical PET application takes advantage from µCT in two respects: µCT provides the structural boundary conditions that are required for advanced process characterization, and it is used for constructing the attenuation and scatter cross section image that is required for PET correction.

The typical size of specimens requires a powerful µCT-scanner, like our Nikon XT H 225 equipped with a 2000·2000 pixel 16-Bit Varex flat-panel detector. We apply the OEM-software CTPro3D for tomographic reconstruction, including beam-hardening correction and initial filtering. Apart from tomographic imaging, we use the fast radiography modus for measuring the level of the fluid reservoirs.

The PET-scanner ClearPET by Elysia-Raytest is a biomedical scanner with a maximum field-of-view of 163 mm. However, the maximum sample diameter is limited to ca. 100 mm by the strong attenuation and scattering of the dense material. The spatial resolution is set by the voxel size of 1.15 mm, which is nearly the fundamental physical limit – the mean free path length of the positron – which is in the order of 1 mm.

The scanner records all potential annihilation photons from the positron decay of the PET-tracer. The detection positions of coinciding events from this large data set define lines-of-response for tomographic reconstruction. The tomographic reconstruction of tracer concentration is based upon the open-source STIR-package (Thielemans et al. 2012). It includes sensitivity normalization, attenuation and scatter corrections. Attenuation and scatter corrections require a tomogram of the mass attenuation coefficients (attenuation map) which is derived from the µCT-image of the complete setup. The attenuation map is co-registrated with a preliminary uncorrected PET-image and then resampled to the size and resolution of the PET-image. The registration-step – a tedious manual procedure, because both images are fundamentally different - is crucial for the resulting PET image quality, because registration errors could cause wrong corrections and potentially strong artefacts, i.e., conspicuous regular patterns with ring or line shape. A less conspicuous and unavoidable level of PET-imaging artefacts is due to reconstruction errors and noise.

We applied ^{22}Na as PET-tracer. This long-lived radionuclide (decay time 2.602 a) is commercially available or can be produced with our cyclotron CYCLONE 18/9 (IBA, Belgium). A tiny volume of the tracer solution is added to the carrier solution, which is saturated NaCl-brine.
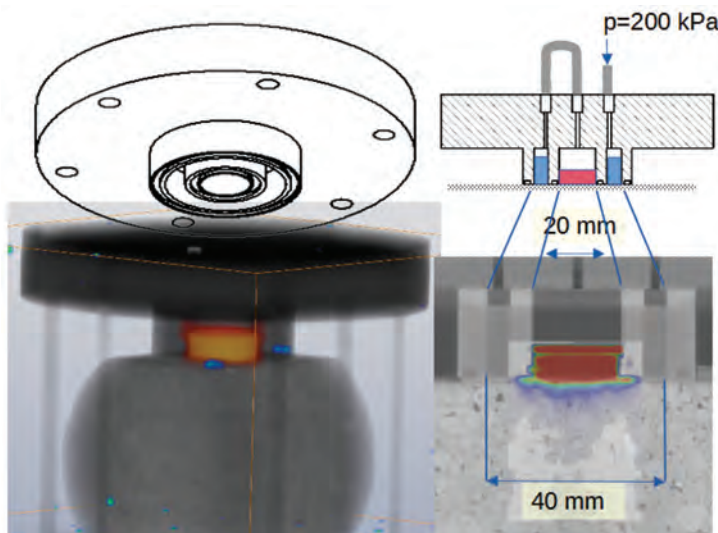
Figure 1: Left: Volume rendering of the PET-µCT-overlay of the system, with active reservoir in orange, inactive reservoir invisible, PET-CT-marker (point sources, blue) serving for image registration. Right: Cross section with dimensions of the surface packer and indicated fluid levels of the labelled (red) and inactive (blue) brine.

2.3 Surface Packer

The purpose of our process tomographic study is to visualize the major features of the advective transport process that underlies permeability. It is meant to reveal whether diffuse infiltration or punctual propagation is present. The temporal evolution of the intrusion pattern indicates whether there is a change of shape of the transport pathways, e.g. due to corrosion and/or precipitation/dissolution, or if the progress of the brine front is declining due to fluid equilibration and self-sealing of pores. The matrix of the concrete is composed of grains surrounded by MgO-binder that we assume as tight material, and we expected the most permeable structures along concrete joints and therefore developed a method to contact these with a small two-chamber surface packer system.

The setup is shown in the GeoPET/µCT-overlay in Figure 1. The cylindrical central chamber has a volume of 5 mL for labelled brine, the external ring chamber has a volume of 15 mL for inactive carrier solution at the same pressure. The outer chamber serves as a guard ring that provides axial symmetry of the driving pressure field, thus a cylindric flow field for the labelled fluid from the central chamber; and it also acts as a safeguard preventing uncontrolled discharge of radioactive tracer. Both chambers are sharing one single 500 mL gas bottle with He-gas set to 0.2 MPa as pressure reservoir. Use of He delimits effects of gas dissolution in the brine.

The tightness of the system was tested over 24 h before tracer injection with inactive brine, and no significant fluid loss or leakage was observed. This test is required as safety measure in order to prevent spill of the long-lived radionuclide. The subsequent tracer injection thus was onto the prewetted sample surface.

2.4 Procedure

The central chamber was filled with 2.8 mL of saturated NaCl-solution, labelled with 3.25 MBq ^{22}Na$^+$ and the outer chamber contained 10 mL of salt brine without tracer, leaving a gas-filled headspace in both chambers as safety measure. Then, the gas bottle with a He-gas at 0.2 MPa was connected, and the pressure was maintained over the whole duration of the experiment (with temporary interruptions during lock-down periods forced by the pandemic situation). After 8 months, the experiment was terminated because of gas breakthrough from the guard cell during an unsupervised period. Nevertheless, the experimental period was adequate for achieving significant results.

Over a period of 8 months, we monitored the progress of the fluid into the sample with GeoPET, and the descent of the fluid level in the reservoir with X-ray radiography. In total, 28 PET-frames were recorded with increasing time intervals.

The fluid levels in the reservoirs were determined with X-ray radiography (Figure 4). These images are cone-beam projections and thus geometrically distorted and blurred by 3D-effects. Nevertheless, they can be calibrated by the known dimensions of the cell. With this calibration, we achieved a volume resolution of ca. 30 µL that enables to monitor the temporal injection rate.

3 Results

3.1 Structural image

The µCT-image was segmented with focus on porous structures. The majority of these pores with sizes above the resolution of 50 µm are bubble-shaped apparently unconnected pores. Larger pores are usually found at the aggregate-grain surfaces. In earlier µCT-investigations,

performed on a number of different specimens collected from drill-hole samples, we observed an increase of fines, reduction of aggregate sizes, and smaller pores in BAG-zones. These features are less pronounced in the present sample, the sample is rather homogeneously structured and the BAG is hardly distinguishable (Figure 2). However, some larger but very flat voids with diameter in the order of a few millimeters that are possibly related to the BAG were hit by the saw cut making the injection plane. One of these voids is a groove that reaches a depth of ca. 6 mm and apparently connects to deeper pore space along grain boundaries.
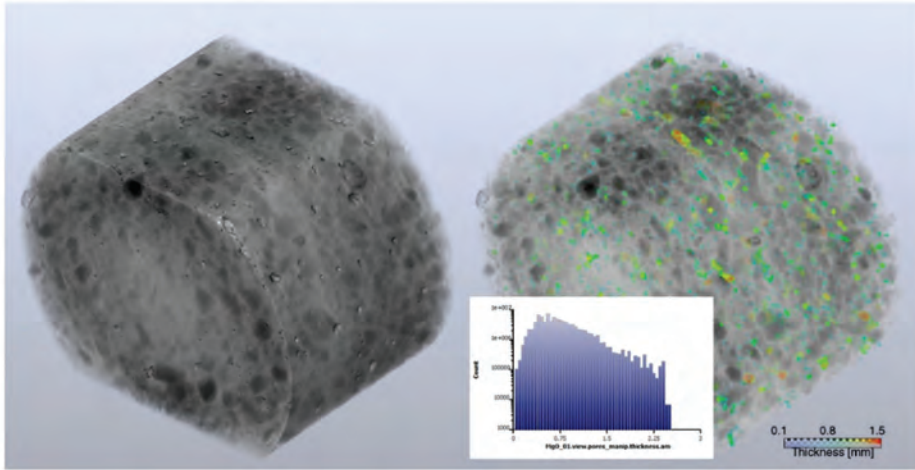
Figure 2: µCT of the whole sample. Right: External surface with indication for BAG as zone with less aggregate. Left: Thickness map computed after segmentation of pores representing the pore size distribution.

3.2   Process

The PET-images are showing slow intrusion of the labelled brine into the sample volume. During the first days we observed local progress with a penetration depth hardly exceeding PET resolution. An initial uniform apparent increase of activity within the sample has to be attributed to the background that essentially is due to the portion of uncorrected scatter. The intrusion pattern becomes more significant with time (Figure 3), its penetration depth gradually increases to ca. 5 mm, reaching deeper near the groove. Finally, the progress appeared to stagnate, but the activity within the affected volume still was increasing gradually.

Activity never was observed near the guard ring volume or in zones near the sample surface, confirming the proper function of the guard ring concept and safe conditions with respect to radiation protection.
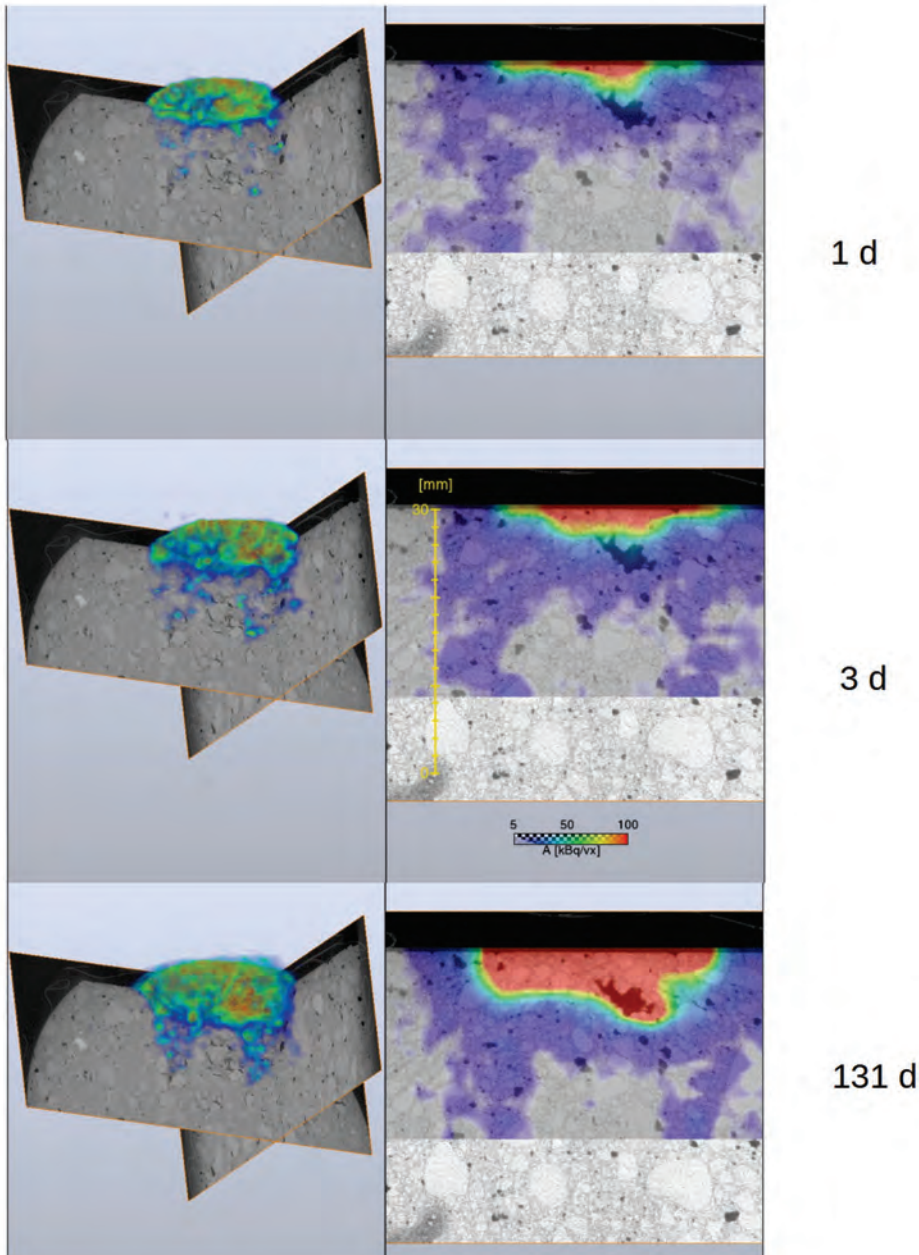
Figure 3: Development of the activity pattern, 3 frames out of 28. Left: volume renderings showing irregular intrusion surface, right: cross sections. Injection from top (reservoir not shown), propagation downwards.

In order to quantify the injected volume V_{act}, we only considered the portion of activity that appeared inside the MgO-body. V_{act} can be computed from the measured activity, because with the known activity concentration of 1.2 MBq/mL it is directly proportional to activity. The total activity in the MgO-sample was computed by integration over a cylindrical control volume from 1 mm below the sample surface with a depth of 50 mm. The superficial layer is excluded from the calculations because it is biased by the activity in the reservoir.
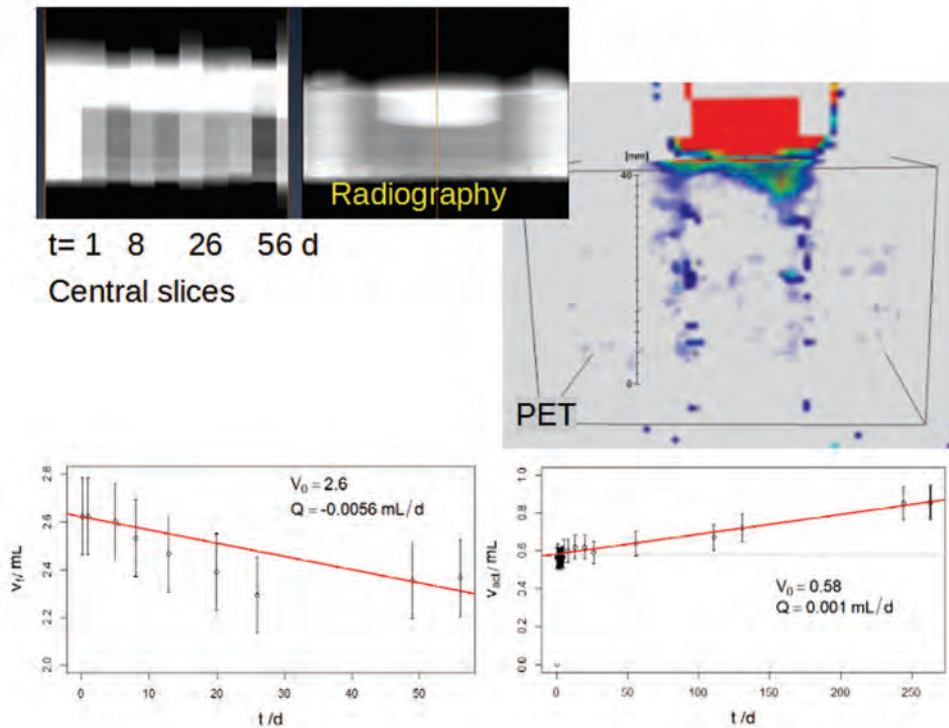
Figure 4: Injected volume calculated from radiography and from PET-activity. Left: μ-radiography (projection) of the central fluid reservoir (decrease of central slices with time and final cross section), below time dependence of the fluid level. Right: One example PET-slice with integration volume of the intruded activity, below intruded fluid volume calculated from the total activity in the integration volume versus time. The color scale was enlarged compared to Fig. 3 for this overview – red is the maximum injected activity concentration and blue is near the detection threshold.

The time series of V_{act} (Figure 4) shows an initial apparent intrusion of 0.58 mL. This initial step is partly caused by blurring and scattered radiation that projects radiation from the reservoir into the material, and partly resulting from initial intrusion into mm-sized voids. During the course of the process, V_{act} increased steadily over 200 days with a rate of 1.05 μL/d. The uncertainty of this quantification is dominated by square root error of the decay process and is in the order of ±10%. Assuming a cylinder with the diameter of the central chamber of 20 mm, and a length of 50 mm as sensitive volume of permeability, we estimate a brine permeability of 0.9e-20 m².

The PET-volume V_{act} is somewhat lower than the injected volume V_i that was computed from the decreasing level in the reservoir measured with radiography. The flow rate from this volume V_f is 5.5 μL/d during the first two months. This flowrate would suggest a permeability of 4.1e-20 m². Unfortunately, the radiography measurements had to be interrupted after these two months, before a more significant volume was injected.

This difference between V_{act} and V_i could have two reasons: Underestimation of the mass attenuation coefficient, which would imply too low activity readings in the sample volume, or stronger superficial infiltration into the superficial layer that was excluded from the activity integration. Both effects would reduce V_{act}.

The low permeability could be an underestimate for three reasons. Firstly, it was impossible to maintain the constant pressure of 0.2 MPa during the unsupervised lock-down periods, thus a lower mean pressure around 0.15 MPa appears more realistic. Secondly, the permeability calculation is based on an oversimplified homogeneous cylinder geometry, and consequently, the pressure gradient is underestimated. Thirdly, small salt crystals in the fluid reservoir are visible in the final µCT-image that could be an indication for dissolution and recrystallization processes caused by the non-equilibrium between NaCl-brine and MgO-material. This self-sealing could block further fluid intrusion. On the other hand, solid state and grain boundary molecular diffusion of ^{22}Na$^+$-cations should not be ruled out as additional transport process that does not rely on fluid mobility.

4   Conclusions

In the present example, the major brine propagation largely followed pre-existing connected pathways but barely dispersed into their vicinity. There are indications for deeper reaching diffuse traces down to ca. 50 mm, but these are less obvious and would require additional investigations. The punctual penetration depth of 10 mm does not exceed the estimated depth that can be computed from reasonable assumptions for porosity and the injected volume. This example confirms that common permeability and porosity measurements are applicable for fluid penetration estimates in such tight barrier material. Moreover, the PET images indicate that the transport path is mainly determined by a pre-existing pore network along grain boundaries, possibly related to the BAG. The computed permeability value is at the lower end of core and in-situ measurements conducted on the same material. This could be an effect of its self-sealing characteristics with unequilibrated brines which should be studied possibly further.

The general ability of GeoPET/µCT to quantify transport into tight material could be demonstrated. It can be conducted at constant driving pressure; in contrast to common brine permeability measurements, it does not require a signal from the outlet – and not necessarily a stable pressure supply (which unfortunately was the case). The quantitative imaging of tracer activity concentration directly yields the effective volume that is affected by the transport process. Apart from this practical benefit, it yields in-depth information on the transport process that is hardly achievable with other methods, i.e., the local penetration rate within the sample, the spatial and temporal evolution of the penetration depth and the shape of the intrusion pattern.

Acknowledgements

References

Arendt, J., Freyer, D., Grafe, F., Gruner, M., Müller, B., Popp, T., Wilsnack, T. & Kudla, W. 2020. MgO-Spritzbeton: Verhalten bei Angriff von MgCl2-Lösung ("MgO-SEAL"). Final Report No. 02E11435, TU Bergakademie Freiberg, available via TIB Hannover.

Freyer, D.; Gruner, M. & Popp, T. 2015. Zusammenhang von Chemismus und mechanischen Eigenschaften des MgO-Baustoffs. Freiberger Forschungshefte E 15, TU Bergakademie Freiberg, ISBN 978-3-86012-516-8.

GRÜNDIG, M., RICHTER, M., SEESE, A. & SABRI, O. 2007. Tomographic radiotracer studies of the spatial distribution of heterogeneous geochemical transport processes. Applied Geochemistry, 22, 2334–2343.

GTS 2010, EDS. KNOLL, P.,FINDER, M. & KUDLA, W. Entwicklung eines Grundkonzeptes für langzeitstabile Streckendämme im leichtlöslichen Salzgestein (Carnallitit) für UTD/ UTV, Teil 2: Erprobung von Funktionselementen : zusammenfassender Abschlussbericht. Report No. 02C1204, available via TIB Hannover.

JANTSCHIK, K., KULENKAMPFF, J. & MOOG, H.C. 2018. Investigation of the flow along the contact seam between salt cement and rock salt. The Mechanical Behavior of Salt; Proc. 9th Conference, Hannover, 261–273.

KUHLMANN, K.L. & MATTEO, E.N. 2018. Porosity and Permeability: Literature Review and Summary. The Mechanical Behavior of Salt; Proc. 9th Conference, Hannover, 291–303.

KULENKAMPFF, J., GRÜNDIG, M., ZAKHNINI, A. & LIPPMANN-PIPKE, J. 2016. Geoscientific process monitoring with positron emission tomography (GeoPET). Solid Earth, 7, 1217–1231.

POPP, T., FREYER, D., SALZER, K., RÖLKE, C. & GRUNER, M. 2018. Geochemical and hydro-mechanical characterization of MgO-based ("Sorel") building materials for engineered barrier systems (EBS) in salt formations. The Mechanical Behavior of Salt; Proc. 9th Conference, Hannover, 305–320.

THIELEMANS, K., TSOUMPAS, C., MUSTAFOVIC, S., BEISEL, T., AGUIAR, P., DIKAIOS, N. & JACOBSON, M.W. 2012. STIR: software for tomographic image reconstruction release 2. Physics in 990 Medicine & Biology, 57(4): 867.

Microstructure and permeability of vein-bearing Upper Permian anhydrite rock (Gorleben-Bank, Germany)

Michael Mertineit[1], Michael Schramm[1], Hua Shao[1], Benjamin Paul[1], Jürgen Hesser[1], Jörg Hammer[1†], Gernold Zulauf[2]*

[1]Federal Institute for Geosciences and Natural Resources (BGR), Stilleweg 2, 30655 Hannover, Germany;
[2]Institute for Geosciences, Goethe-University Frankfurt, Altenhöferallee 1, 60438 Frankfurt/Main, Germany

* michael.mertineit@bgr.de

ABSTRACT: The permeability of the Gorleben-Bank (z3OSM), a strongly deformed vein-bearing anhydrite rock layer, was measured in situ in three boreholes of the former Gorleben exploration mine, Germany. The corresponding drill cores were investigated for their microstructures and their mineralogical properties. The veins cutting through anhydrite rock consist of halite, kieserite, carnallite, sylvite and small amounts of polyhalite. Subgrains with a size of 100 ±40 µm are omnipresent in halite of the veins and of the surrounding salt rocks. The corresponding paleodifferential stresses (2.0 +1.0/-0.5 MPa) are consistent with published values. The hydraulic borehole tests were carried out using nitrogen gas and in form of pulse tests. The permeability obtained for the Gorleben-Bank is generally <10^{-20} m², independent of the amount, size, orientation and mineralogical composition of healed fractures. Similar values for permeability were obtained from adjacent salt rocks. The results of the present study suggest that pervasive pathways for brines are lacking in the anhydrite rocks as most of the open fractures are healed.

1   Introduction

Investigations of salt rocks are important for several economic and technical purposes. In Germany, Upper Permian (Zechstein) salt rocks of the Gorleben salt dome were investigated from 1979-2000 and 2010-2012 in great detail. The rock composition is characterized by stratigraphically and locally varying amounts of anhydrite layers, the latter with thicknesses of a few mm to several 10 m (Bornemann et al. 2008). In the German Site Selection Act for a final repository for high-level, heat generating radioactive waste (StandAG 2017), a low hydraulic conductivity of the barrier system (host rock and geotechnical barrier) is a strict requirement. The lowest limit is 10^{-10} m/s, but favored values are <10^{-12} m/s (§24, section 3, annex 1, StandAG), which correspond to a permeability of 10^{-19} m². Thus, investigations on the permeability of different host rocks and further site-specific analyses play a crucial role in the assessment of the possible host rock and, in the future, of a specific repository site for high-level radioactive waste. The permeability of rock salt was determined in laboratory and in situ experiments (e.g. Peach 1993; Popp et al. 2007; Bräuer et al. 2011; Warren 2017). In general, undisturbed rock salts are characterized by very low permeability values of <10^{-20} m², but these values increase in the excavation damage zone (EDZ; Popp et al. 2007, Bräuer et al. 2011) or in anhydrite rocks (Peach 1993), where brittle behavior results in open or mineralized tension and shear fractures. Results concerning the deformation behavior of rock salt obtained from laboratory and field studies were published by many working groups (e.g. Carter et al. 1993; Jackson & Hudec 2017). Important deformation mechanisms in diapiric rock salt are dislocation creep and fluid assisted grain boundary migration (e.g. Thiemeyer et al. 2016; Jackson & Hudec 2017). Pressure solution was often observed in experimentally deformed rock salt (e.g. Urai & Spiers 2007), and is triggered by fluid phases situated along grain or phase boundaries. The mechanical behavior of anhydrite rocks and halite-anhydrite composites were investigated in different studies. In experiments at higher temperatures and confining pressure, crystal plastic flow occurred (e.g. Dell'Angelo & Olgaard 1995). Dependent on the experimental setup and deformation conditions, brittle-ductile behavior of anhydrite was observed (e.g. Peach 1993; Zulauf et al. 2009, 2010). Evidence for brittle-ductile behavior was also found in naturally deformed anhydrite rocks, where solution-precipitation creep, bulging,

grain boundary migration recrystallization, twin boundary migration, twinning and kinking of anhydrite were determined as important deformation mechanisms (Zulauf et al. 2010; Mertineit et al. 2014, 2015; Thiemeyer et al. 2016). Anhydrite rocks in rock salt are often fractured and boudinaged (Bornemann et al. 2008; Jackson & Hudec 2017).

The formation and deformation structures of the so-called Gorleben-Bank (z3OSM), a cm to dm-thick anhydrite rock layer, were described by Bornemann et al. (2008), Kühnlenz et al. (2014), Mertineit et al. (2014, 2015) and Hammer et al. (2016). In the present study, the results of in situ hydraulic borehole tests are combined with microstructural and mineralogical findings. As boudinage and fracturing of anhydrite rocks in rock salt matrix plays a significant role for pathways of fluids, the results of the present study will be of interest for a large number of workers dealing with salt rocks and their use as barrier rocks.

2   Geological setup and Methods

The Gorleben-Bank (z3OSM) is an anhydrite rock layer with a thickness of mostly <10 cm and maximal 66 cm (Kühnlenz et al. 2014) and forms the middle part of the Orangesalz (z3OS). The Gorleben-Bank was subdivided in seven zones (Bornemann et al. 2008; Kühnlenz et al. 2014). Zone I consists mainly of halite/carnallite, zones II, V & VI of anhydrite with impurities of insoluble material and halite, and zone VII is a halite/anhydrite composite. Zone III consists of clay, organic matter, siliceous components and fine-grained anhydrite and halite. Open veins caused by bedding-parallel fracturing of zone III were mineralized with carnallite and/or halite; this mineralization is defined as zone IV. The Gorleben-Bank is frequently boudinaged and fractured, the infill of open fractures consists of halite and/or carnallite (Bornemann et al. 2008; Kühnlenz et al. 2014; Mertineit et al. 2014, 2015). Brine and gas, released from the Gorleben-Bank during mining activities, were frequently observed and were usually limited to few cm^3 to m^3 (Bornemann et al. 2008).

Most Gorleben-Bank outcrops are located within the infrastructure area of the former Gorleben exploration mine (Fig. 1). The outcrops at the 820-m and 840-m level of the former exploration mine were differently affected by a domal structure within the salt dome (Fig. 1). Outcrops at the 880-m and 930-m levels were not influenced by this domal structure.
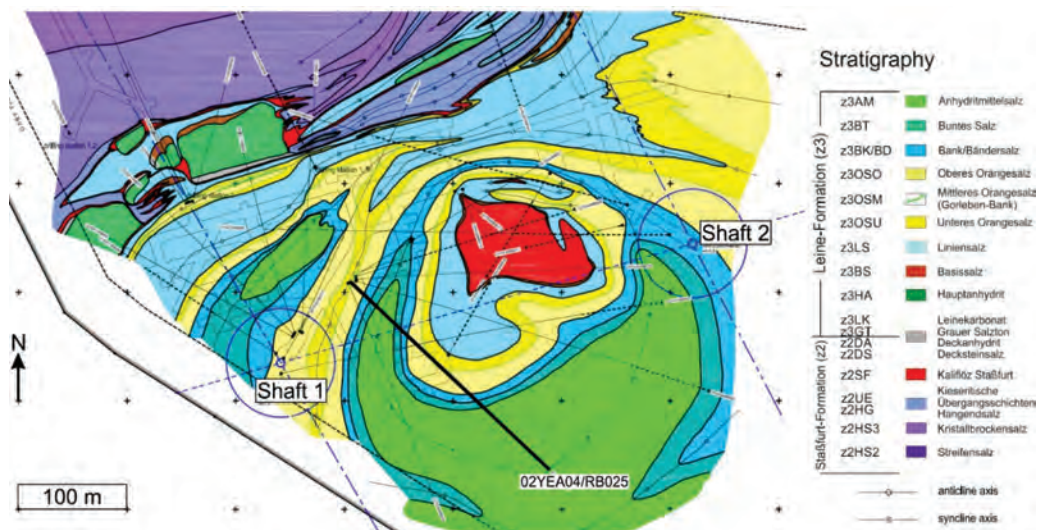
Figure 1: Geological map of the study area, located on the 840-m level of the former Gorleben exploration mine. From Bornemann et al. (2008), modified.

Samples of rock salt of the lower and upper Orangesalz (z3OSU and z3OSO) and of anhydrite rock of the Gorleben-Bank were collected from three horizontal drill cores gathered at the 820-m, 880-m and 930-m level of the former exploration mine (Fig. 4). The drillings were carried out to analyze the permeability of the Gorleben-Bank and adjacent rock salt in situ.

The drillings were carried out to a depth of 34 - 37 m each, with a diameter of the borehole of 98 mm and a diameter of the drill cores of ca. 65 mm. Each drilling cuts through the Gorleben-Bank for two times. Additionally, drill cores of the drilling 02YEA04/RB025 (840-m level; Fig. 1) were investigated for their structural and mineralogical properties.

Sampling was carried out by cutting pieces of the drill core. Microfabrics of halite and anhydrite rocks were analyzed using thin and thick sections. For analyses of halite microfabrics, thick sections were etched for ca. 45 sec with slightly unsaturated NaCl-brine (Zulauf et al. 2009). In all samples halite showed subgrains, whose size can be used for paleopiezometry according to equation (1) (Carter et al. 1993; Schéder & Urai 2005):

$$d = 215 * \sigma^{-1.15} \qquad (1)$$

with d = subgrain diameter [μm] and σ = differential stress [MPa].

The distribution of different components was analyzed in 3D by X-ray computer tomography (CT; Philips Brilliance 6-slice CT at the Neuroradiologic Department of the Frankfurt University Clinic) of whole drill cores of a length of max. 15 cm. The obtained 2D raw data images (up to 347) were restacked, and 3D models of the samples were generated by implementation of volumetric models into the software "Smoooth". The effective voxel size is ca. 0.5*0.5*0.8 mm, that represents the resolution limit.

For permeability measurements, hydraulic borehole tests were carried out using a double packer system (Glötzl exDMA; Paul et al. 2012). As test fluid, at normal conditions chemical inert nitrogen gas was used by pulse tests, which are appropriate for constraining the permeability of tight rocks (Bräuer et al. 2011). The test intervals have a length of 1.20 m and were chosen after a visual assessment of the corresponding drill cores. The injection pressure was set at 0.5 MPa, and the pneumatic packers were inflated with a pressure of constantly 3 MPa, which then sealed the test interval. Measurements include pressure and temperature within the packed-off interval, flow-rate of the test fluid into the test interval, pressure of the packer, as well as temperature, air pressure and air moisture in the mine gallery. The results were evaluated by comparing the measured data with results of numerical modelling (for details of the processing procedure, the reader is referred to Zaretzki et al. 2013). The permeability tests were carried out a few days after the borehole completion.

Since the length of the test interval (1.20 m) is considerably higher than the thickness of the Gorleben-Bank (max. 15 cm), permeability values were not solely measured for the Gorleben-Bank, but also covering the adjacent rock salt z3OSO and z3OSU. Hence, reference permeability measurements were performed in the adjacent rock salt formations z3OSO, z3OSU, and z3BK/BD. Thus, the results of the test interval including the Gorleben-Bank were compared with those without the Gorleben-Bank according to the rule of mixture for transmissibility by following equations (Hammer et al. 2016):

$$K_{total} * L_{total} = K_{OSU} * L_{OSU} + K_{OSM} * L_{OSM} + K_{OSO} * L_{OSO} \qquad (2)$$

With measured $K_{total} = K_{OSU} = K_{OSO}$:

$$K_{total} * L_{total} = K_{total} * L_{OSU} + K_{OSM} * L_{OSM} + K_{total} * L_{OSO} \qquad (3)$$

$$K_{total} * (L_{total} - L_{OSU} - L_{OSO}) = K_{OSM} * L_{OSM} \qquad (4)$$

$$K_{total} * L_{OSM} = K_{OSM} * L_{OSM} \qquad (5)$$

$$K_{total} = K_{OSM} \tag{6},$$

with K = permeability [m^2] and L = length of the specific stratigraphic unit (subscript) within the test interval [m]. For abbreviations of the stratigraphic units, see Fig. 1.

3   Results

The investigated anhydrite rocks of the Gorleben-Bank are between 3 cm and 15 cm thick. The anhydrite rocks (zones V and VI) are grey with black seams. The rocks consist of fine-grained anhydrite (grain size ≤50 μm) with minor amounts of halite and insoluble material (magnesite, hematite, polyhalite, phyllosilicates, organic matter), often enriched in seams, which are oriented parallel to bedding. In these areas, the grain size of anhydrite is particularly small (partially <25 μm; Fig. 2a). Large anhydrite crystals (max. 0.5 mm) show a distinct shape preferred orientation with the long axis parallel to bedding (Fig. 2b). At the interface anhydrite rock-rock salt, some anhydrite crystals show a narrow seam of polyhalite.
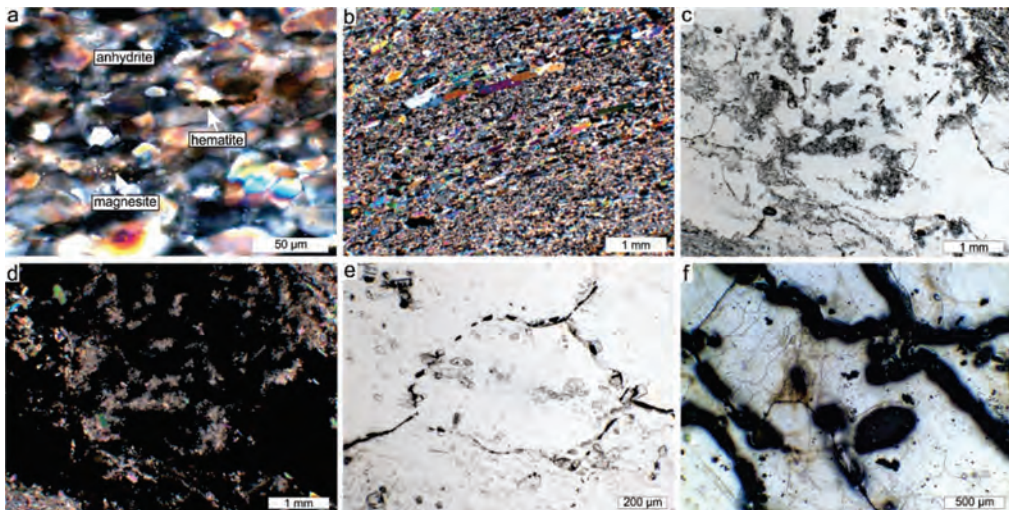
Figure 2: Microphotographs of anhydrite rock of the Gorleben-Bank (z3OSM) and rock salt. a) Detail of a seam, with enrichment of insoluble material. Note small grain size of anhydrite, # polarizers. b) Overview of fine-grained anhydrite rock of zone V/VI. Larger anhydrite crystals are oriented parallel to bedding, # polarizers. c) Highly impure rock salt of zone VII. Impurities consist of anhydrite and polyhalite, // polarizers. d) Same image as in c), but under # polarizers. e) Halite crystal of z3OSO. Grain boundaries are decorated with anhydrite crystals and fluid inclusions, // polarizers. f) Subgrains in halite of z3OSM, zone VII. Surficial impurities are caused by the etching of the thick section, // polarizers.

Space between single anhydrite layers of zone VII consist of highly impure, orange halite and occasionally carnallite, anhydrite and polyhalite (Figs. 2c, d). The grain boundaries of halite are decorated with fluid inclusions and small anhydrite crystals, seldom hematite. The grain size of halite is up to 1 cm; most grains are 0.2 - 0.4 mm in size. The grains are elongated with the long axis parallel to bedding.

Rock salt of the z3OSU and z3OSO, respectively, is grey to orange and shows fewer impurities. The grain boundaries are decorated with small anhydrite crystals and fluid inclusions (Fig. 2e). The grain size is 1-2 cm, locally elongated grains occur, but most grains show a more or less isometric shape. Subgrains with a size of 100 ±40 μm are omnipresent in halite (Fig. 2f), pointing to paleodifferential stresses of 2.0 +1.0/-0.5 MPa.

Extension fractures cut through the whole rock sequence, or taper off after few mm within the anhydrite rock. The fractures have a width of up to 3 cm and most are oriented subperpendicular to bedding (Figs. 3a-d) or bedding-parallel (Fig. 3e). The filling consists of halite and/or carnallite, the latter reaching a grain size of 1 cm (Figs. 3e, f). Halite grain boundaries are decorated with high amounts of fluid inclusions, but many halite crystals also contain intracrystalline fluid inclusion trails. Some carnallite crystals show intense twinning.
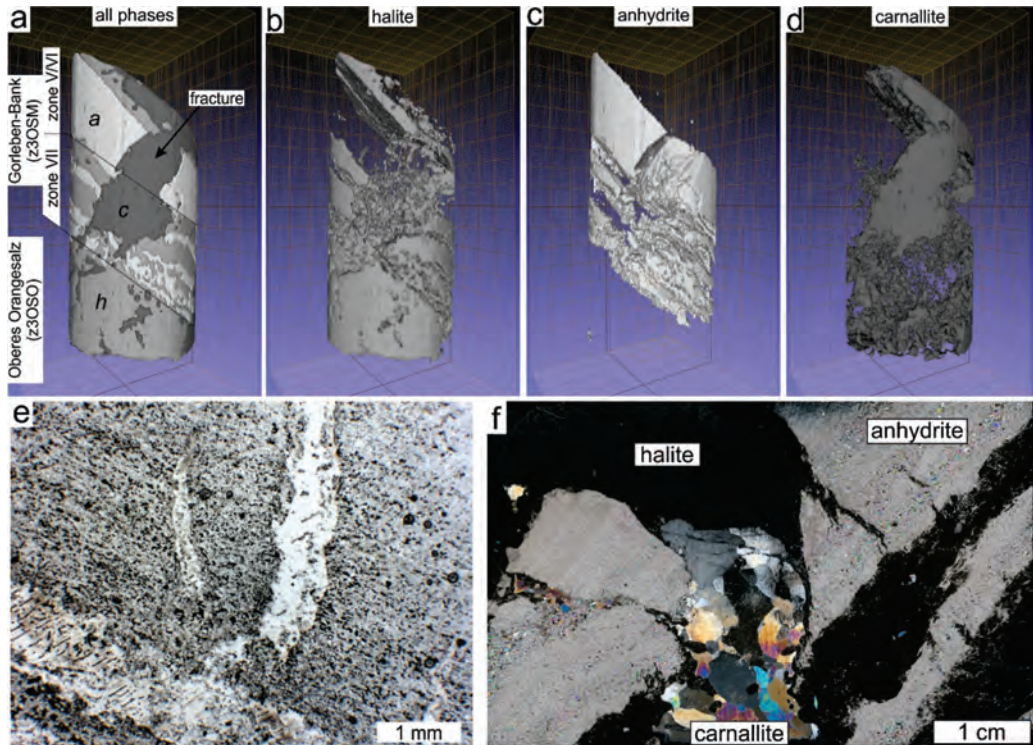
Figure 3: Healed fractures in rock salt and anhydrite rock. a-d): CT-images of the drill core 03YEA02/RB754, depth 9.70 - 9.80 m. Note healed fracture, crosscutting the Gorleben-Bank. Core diameter = 6.5 cm. a) 3D-model, displaying all phases (white: anhydrite (*a*), light grey: halite (*h*), dark grey: carnallite (*c*)). b) Same image as in a), but with grey scale, representing halite. c) Same image as in a), but with grey scale, representing anhydrite. d) Same image as in a), but with grey scale, representing carnallite. The fracture infill consists of both, halite and carnallite. Carnallite is also present in the z3OSO and the z3OSM. e) Bedding-parallel and subperpendicular to bedding oriented, halite healed fractures in fine-grained, impure anhydrite rock. Halite in fractures contains high amounts of fluid inclusions, // polarizers. f) Carnallite healed fracture in fine-grained anhydrite rock, # polarizers.

For in situ permeability tests, most measurements show an expected low decrease in pressure over time of <0.02 MPa (0.2 bar), corresponding to permeability values of $<10^{-20}$ m^2 (Figs. 4b-d). Some data reveal an initial decrease, followed by a weak increase of the pressure, but the overall trend shows a slight temporal decrease of pressure. In the borehole 01YEA02/RB753, at two places small amounts of entered brine were detected. For this reason, the measurements had to be interrupted. In single measurements, the pressure increased slightly by max. 0.02 MPa (RB753-1a_10.5, RB755-3_28.6, RB755-2_30.8; Figs. 4b, d). Repeated analyses after a period of five months revealed an expected trend for the curve and a slight temporal decrease in pressure (RB753-1a_10.5). Unfortunately, it was not possible to analyze the test intervals RB755-3_28.6 and RB755-2_30.8 again due to the discontinuation of the Gorleben exploration program.
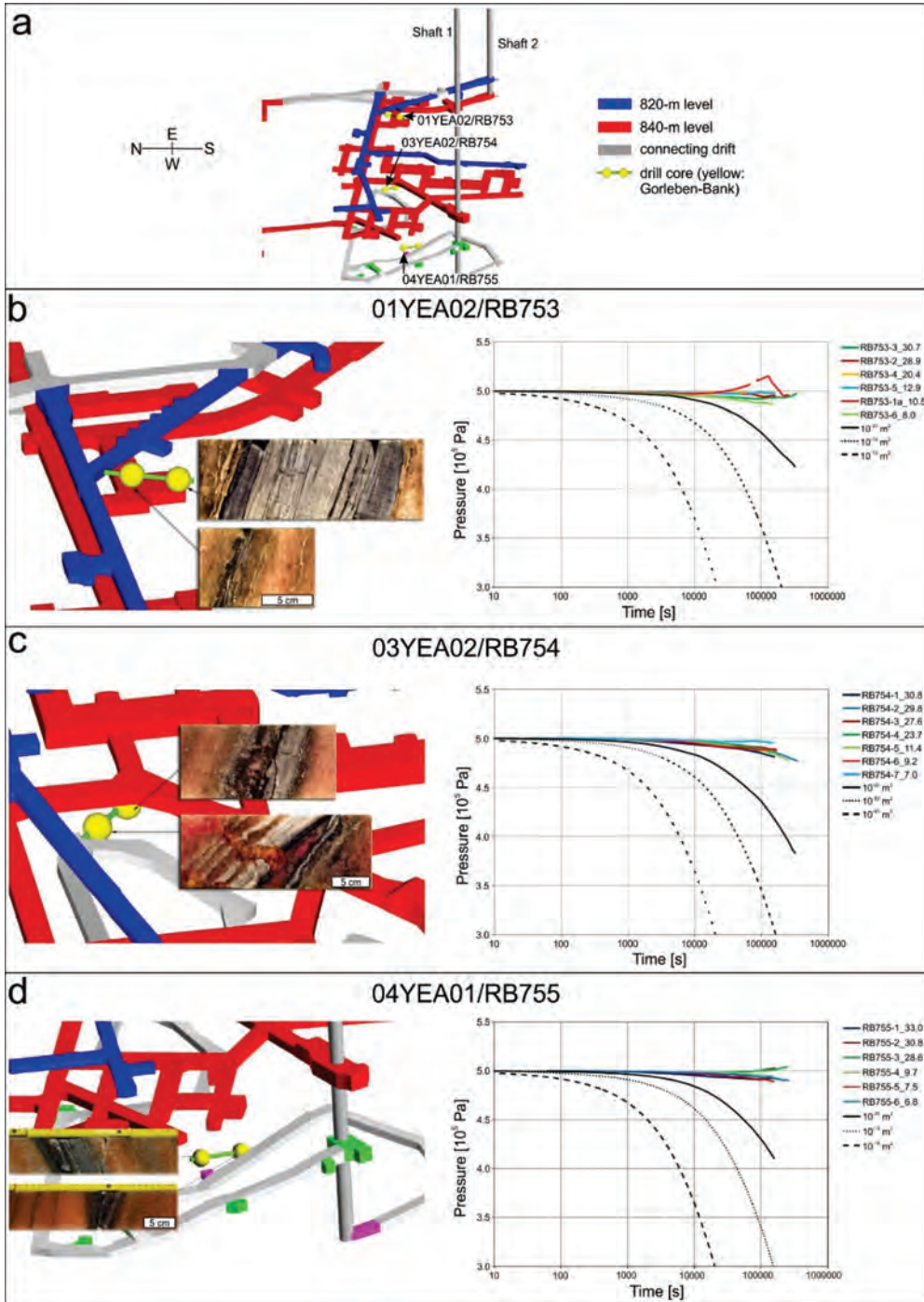
Figure 4: a) Position of the investigated boreholes in the former Gorleben exploration mine, oblique view. The distance between the shafts is ca. 400 m. b) - d): Detail of a) (left) and measured (coloured lines) and calculated (black lines) pressure flow of test intervals (right). The injection pressure is normalized to 0.5 MPa. From Hammer et al. (2016), modified.

4   Discussion

In the investigated Gorleben-Bank drill cores, the anhydrite rocks show similar deformation structures. Especially the zones V and VI display a small grain size of <50 µm and high amounts of insoluble material, pointing to solution-precipitation creep as dominant deformation mechanism. Larger anhydrite crystals do not show internal deformation structures indicating crystal plasticity (e.g. twinning, undulatory extinction, subgrains) as observed in other Gorleben-Bank outcrops (Mertineit et al. 2014, 2015 Hammer et al. 2016). One reason, which could explain the lack of such microstructures, might be the relatively low layer thickness. In thin beds of anhydrite rock of the Gorleben-Bank (thickness <~3 cm) solution-precipitation creep seems to be the dominant deformation mechanism (Mertineit et al. 2014).

Brittle deformation of anhydrite rock of the Gorleben-Bank is documented by fractures, which are mineralized with halite and/or carnallite. CT data reveal a complex intergrowth of both mineral phases, and show that the entire volume of previous open space of the fracture is now filled with secondary phases. However, this is the case for the investigated drill cores, but (limited) brine inflow connected to the Gorleben-Bank at different positions in the former exploration mine show that this is not always the case (e.g. Bräuer et al. 2011).

In all investigated samples, halite shows subgrains, indicating dislocation creep as important deformation mechanism in halite. The mean size of 100 ±40 µm corresponds to paleodifferential stresses of 2.0 +1.0/-0.5 MPa, which is in line with published data of the z3OS in the Gorleben salt dome (Mertineit et al. 2014; Hammer et al. 2016). Halite in fractures also shows subgrains of more or less the same size, indicating that opening and filling of the fracture was succeeded by even younger deformation stages.

The calculated values for permeability ($<10^{-20}$ m^2) correspond to data published for the Gorleben salt dome (Bräuer et al. 2011), but also to values obtained from other salt structures (Bräuer et al. 2011; Popp et al. 2007; Warren 2017). In Gorleben, for most stratigraphic units of the upper z2-Formation and the lower z3-Formation (except the Hauptanhydrit, z3HA), a permeability between $5*10^{-22}$ m^2 and 10^{-20} m^2 was determined. In a strongly deformed domain covering the units z3OS and z3LS, where the rock salt contains numerous open fractures filled with halite and carnallite, the permeability varies considerably between $5*10^{-21}$ m^2 and 10^{-18} m^2 (Bräuer et al. 2011).

Although the permeability could not be analyzed solely for the Gorleben-Bank due to the restricted dimensions of the measuring probe and the low thickness of the Gorleben-Bank, it can be assumed that the permeability values are of the same order of magnitude with that of the adjacent rock salt. Although anhydrite rock of the Gorleben-Bank tends to develop fractures during deformation due to its brittle behavior (e.g. Mertineit et al. 2015), the permeability values suggest that anhydrite rock is gas-tight like intact rock if the open fractures are filled with secondary fluid-derived phases.

The slight temporal pressure increase or fluctuations in some borehole tests can be explained by a low inflow of gas and brine. The exact position of the inflows could not be localized, but they are not restricted solely to the Gorleben-Bank. The volume of these fluid inflows is limited, and the discharge occurred fast, as the repeated measurements of permeability after five months exhibit an expected temporal decrease in pressure without any fluctuations.

5   Conclusions

- Anhydrite rocks were deformed in the plastic-brittle deformation regime, where solution-precipitation creep and fracturing are the dominant deformation mechanisms.

- Halite was deformed in the viscous deformation regime by subgrain formation and fluid-assisted grain boundary migration. Precipitation of halite and carnallite in open fractures is succeeded by younger deformation events.

- Anhydrite rocks of the Gorleben-Bank show the same values for permeability compared to those obtained from adjacent rock salt ($<10^{-20}$ m^2), indicating, that pervasive pathways for brine or gas are lacking.

Acknowledgements

References

BORNEMANN, O., BEHLAU, J., FISCHBECK, R., HAMMER, J., JARITZ, W., KELLER, S., MINGERZAHN, G. & SCHRAMM, M. 2008. Description of the Gorleben Site Part 3: Results of the geological surface and underground exploration of the salt formation. Bundesanstalt für Geowissenschaften und Rohstoffe, Hannover, 211 p.

BRÄUER, V., EICKEMEIER, R., EISENBURGER, D., GRISSEMANN, C., HESSER, J., HEUSERMANN, S., KAISER, D., NIPP, H.-K., NOWAK, T., PLISCHKE, I., SCHNIER, H., SCHULZE, O., SÖNNKE, J. & WEBER, J.-R. 2011. Description of the Gorleben Site Part 4: Geotechnical exploration of the Gorleben salt dome. Bundesanstalt für Geowissenschaften und Rohstoffe, Hannover, 184 p.

CARTER, N.L., HORSEMAN, S.T., RUSSEL, J.E. & HANDIN, J. 1993. Rheology of rocksalt. Journal of Structural Geology 15, No. 9/10, 1257-1271.

DELL'ANGELO, L.N. & OLGAARD, D.L. 1995. Experimental deformation of fine-grained anhydrite: Evidence for dislocation and diffusion creep. Journal of Geophysical Research 11/B8, 15425-15440.

HAMMER, J., MERTINEIT, M., PAUL, B., HESSER, J. & SHAO, H. 2016. Einzelfragen der Barriereintegrität: Auswirkungen von halokinetischen Deformationsprozessen auf Ausbildung und Permeabilität der Gorleben-Bank. Ergebnisbericht Projekt Gorleben, Bundesanstalt für Geowissenschaften und Rohstoffe, Hannover, 70 p.

JACKSON, M.P.A. & HUDEC, M.R. 2017. Salt tectonics – Principles and practice. Cambridge University Press, 498 p.

KÜHNLENZ, T., SASSNOWSKI, M., HAMMER, J., MINGERZAHN, G. & KUTOWSKI, J. 2014. Evaluation of mapping results of the textural features of the Gorleben-Bank within the Gorleben salt dome, Germany. Z. Dt. Geowiss. (German J. Geosci.), 165 (1), 63-76.

MERTINEIT, M., HAMMER, J., SCHRAMM, M. & ZULAUF, G. 2014. Deformation of anhydrite rocks (Gorleben-Bank, z3OSM) in a high-strain domain of the Gorleben salt dome, Germany. Z. Dt. Geowiss. (German J. Geosci.), 165 (1), 49-62.

MERTINEIT, M., HAMMER, J., SCHRAMM, M., KNEUKER, T., THIEMEYER, N. & ZULAUF, G. 2015. Deformation of thin layered anhydrite rocks within the Gorleben salt dome, Germany. In: ROBERTS, L, MELLEGARD, K. & HANSEN, F. (eds.): Mechanical behavior of salt VIII Proceedings of the 8th Conference, 99-107, Taylor & Francis Group, London.

PAUL, B., HESSER, J., KUNZ, H., LEGE, C., FLENTJE, R., NOWOTNY, D. & SANCHEZ-HERRERO, S. 2012. Geotechnische Instrumentierung und Messungen der BGR: Stand 2011. Zwischenbericht, Bundesanstalt für Geowissenschaften und Rohstoffe, Hannover, 156 p.

PEACH, C.J. 1993. Deformation, dilatancy and permeability development in halite/anhydrite composites. In: GHOREYCHI, M., BEREST, P., HARDY JR., H.R. & LANGER, M. (eds.): The Mechanical behaviour of Salt: Proceedings of the 3rd Conference. Trans Tech Publications, 153-166.

POPP, T., WIEDEMANN, M., KANSY, A. & PUSCH, G. 2007. Gas transport in dry rock salt – implications from laboratory investigations and field studies. In: WALLNER, M., LUX, K.-H., MINKLEY, W., HARDY JR., H.R. (EDS.): The Mechanical Behavior of Salt – Understanding of THMC Processes in Salt. Taylor & Francis Group, London, 17-26.

SCHLÉDER, Z. & URAI, J.L. 2005. Microstructual evolution of deformation-modified primary halite from the Middle Triassic Röt Formation at Hengelo. The Netherlands, International Journal of Earth Sciences 94, 941-955.

Standortauswahlgesetz vom 5. Mai 2017 Gesetz zur Suche und Auswahl eines Standortes für ein Endlager für hochradioaktive Abfälle (Standortauswahlgesetz – StandAG) 2017. BGLG. I.S. 2808.

THIEMEYER, N., ZULAUF, G., MERTINEIT, M., LINCKENS, J., PUSCH, M. & HAMMER, J. 2016. Microfabrics and 3D grain shape of Gorleben rock salt: Constraints on deformation mechanisms and palaeodifferential stress. Tectonophysics 676, 1-19.

URAI, J.L. & SPIERS, C.J. 2007. The effect of grain boundary water on deformation mechanisms and the rheology of rocksalt during long-term deformation. In: WALLNER, M., LUX, K.-H., MINKLEY, W., HARDY JR., H.R. (eds.): The Mechanical Behavior of Salt – Understanding of THMC Processes in Salt. Taylor & Francis Group, London, 149-158.

WARREN, J.K. 2017. Salt usually seals, but sometimes leaks: Implications for mine and cavern stabilities in the short and long term. Earth-Science Reviews 165, 302-341.

ZARETZKI, B., SHAO, H. & HESSER, J. 2013. Geotechnische Bewertung der Erkundungsbereiche: Permeabilitätsmessungen: Stand 2011. Ergebnisbericht, Bundesanstalt für Gowissenschaften und Rohstoffe, Hannover, 123 p.

ZULAUF, G., ZULAUF, J., BORNEMANN, O., KIHM, N., PEINL, M. & ZANELLA, F. 2009. Experimental deformation of a single-layer anhydrite in halite matrix under bulk constriction Part 1: Geometric and kinematic aspects. Journal of Structural Geology 31, 460-474.

ZULAUF, G., ZULAUF, J., BORNEMANN, O., BRENKER, F., HÖFER, H., PEINL, M. & WOODLAND, A. 2010. Experimental deformation of a single-layer anhydrite in halite matrix under bulk constriction, Part 2: Microfabrics and deformation mechanisms. Journal of Structural Geology 32, 264-277.

Theme 2: Laboratory testing

Insights from an experimental campaign on rock salt and implications at the cavern scale

Laura Blanco-Martín[1]*, Mejda Azabou[1a], Ahmed Rouabhi[1], Faouzi Hadj-Hassen[1], Grégoire Hévin[2]

[1]MINES ParisTech, PSL University, Centre de Géosciences, France; [2]Storengy, France; [a]Currently at Storengy, France

* laura.blanco_martin@mines-paristech.fr

ABSTRACT: The design of underground facilities in rock salt requires a correct characterization of the rock as a first step, which is usually performed at the laboratory scale using samples of a given size, constrained by the drilling equipment in the field and by the size of the experimental devices in the laboratory. Rock salt often contains impurities of different nature, which may rise representativity problems if the size of the tested samples is smaller than the representative volume element of the rock mass. An improper characterization of the rock in the laboratory may lead to an improper design of underground facilities. These two aspects are illustrated through an experimental campaign and subsequent computations at the cavern scale. In order to evaluate heterogeneity, different measurement techniques should be used in laboratory tests, covering different spatial scales within the samples. The use of two design criteria at the cavern scale is also discussed and proves that design criteria embedded at the constitutive level overcome the limitations of external criteria applied during post-processing of the cavern simulation results. Hence, the use of constitutive laws that reproduce laboratory data and yield pertinent long-term predictions is of utmost importance.

1   Introduction

Rock salt is a potential storage and disposal medium because of several assets, including very low permeability and porosity in the undisturbed state and relatively high thermal conductivity as compared to other shallow-crustal rock types (Hardin & Voegele 2013). Additionally, rock salt is ductile and, if the stress state is propitious, it has the potential to seal and heal technically induced fractures (Hou 2003; Hunsche & Hampel 1999). Because of these favorable characteristics, leached salt caverns have been used since the late 1940s to store hydrocarbons and other substances such as helium, compressed air and wastes (Thoms & Gehle 2000). Large-scale hydrogen storage in salt caverns is being considered in several countries worldwide in the context of the energy transition (Tarkowski 2019). Additionally, non-heat-generating nuclear waste is being stored at the WIPP site, and the disposal of heat-generating nuclear waste is under investigation (Blanco-Martín et al. 2015; MacKinnon et al. 2012). Chemo-toxic waste is disposed of in abandoned mines in salt in Germany since 1972 (Fahland & Heusermann 2012).

When designing underground excavations – in rock salt or any other rock – it is common practice to first characterize the rock behavior at the laboratory-scale. Then, the observed rock behavior is modeled using constitutive laws, whose parameters are fitted on the basis of the laboratory test results. As the next stage, the underground excavations are designed combining the constitutive laws and parameters determined at the laboratory scale with a well-established design methodology. During operation of the underground facilities, model parameters are recalibrated when possible using *in situ* data, and long-term predictions are updated.

Laboratory characterization is therefore an important step in the design of underground openings, as is the determination of constitutive laws and design methodologies; these three aspects have been widely investigated for rock salt, which exhibits time-dependent behavior. Regarding laboratory characterization, extensive literature exists on experimental results,

comprising both short-term (strength) and long-term (creep) tests (Azabou 2021; DeVries et al. 2005; Düsterloh et al. 2015; Herchen et al. 2018; Roberts et al. 2015; Salzer et al. 2015; Tijani et al. 2009). The duration of some creep tests is in the order of a few years (Bérest et al. 2019; Günther & Salzer 2012); while this time scale is considered a success at the laboratory (applying the loadings over long time scales is challenging and expensive), such a duration is negligible compared to the time scales that are relevant in the field. In fact, laboratory tests allow exploring the stress and temperature ranges that are expected underground, but their duration is inherently shorter than the relevant *in situ* time scales (up to millions of years in the case of nuclear waste disposal). Therefore, when analyzing underground facilities, temporal extrapolation of the laboratory data is unavoidable.

Owing to the lack of uniqueness, many constitutive laws have been proposed over the past decades to reproduce the time-dependent behavior of rock salt (Azabou et al. 2021a; Cristescu 1993; Gährken et al. 2018; Günther and Salzer 2012; Hampel 2015; Heusermann et al. 2003; Julien 1999; Khaledi et al. 2016; Lux et al. 2018; Odqvist 1974; Munson 1997). The laws differ in the features they consider, and how they are accounted for (transient, stationary and tertiary creep, reverse creep, damage, dilatancy, healing, stress triaxiality, effect of the mean stress, tensile viscoplastic deformation…). The constitutive laws should be able to reproduce laboratory data accurately. Also, the quality of the long-term extrapolations at the field scale depends on the capability of the constitutive laws to provide pertinent long-term predictions.

Two main methodologies exist for salt cavern design. In the first methodology, numerical computations of the underground facilities are performed, and the results are analyzed using some design criteria (*e.g.*, no dilatancy, see for instance DeVries et al. 2005 or Minkley et al. 2016). Many dilatancy criteria are available; they define a boundary in the stress space between the contracting and dilating behavior of rock salt. The major drawback of this method is that the constitutive laws used in the numerical computations are often based on creep tests, whereas the dilatancy criteria are based on short-term (strength) tests. Hence, inconsistencies in the parameter sets may arise, as the two types of tests have different time scales. In addition, the criterion is fixed in the stress space, regardless of the evolution of the loading rate, the mean pressure or the stress state. In the second methodology, the design criterion is embedded within the constitutive law, which is based and fitted simultaneously on strength and creep tests (Labaune et al. 2018). In this case, the onset of dilatancy, which evolves as the mean pressure, the loading rate or the stress state changes, is used as a design threshold.

The target of this paper is twofold. First, we show that material heterogeneity affects the representativity of the laboratory samples and may lead to an improper rock characterization, which in turn affects the computations at the cavern scale. Second, we show the differences between the two cavern design methodologies described above. To analyze the laboratory data and perform the cavern simulations, we use a constitutive law that attempts to give more pertinent long-term predictions than well-known transient or steady-state creep laws.

2 Experimental results

Rock salt crystals have different sizes, and rock salt deposits often contain impurities of different nature (Speranza et al. 2016). Material heterogeneity leads to a wide range of representative volume elements (RVE) among different rock origins. Ideally, laboratory work should be performed on samples that meet the RVE size; however, this is impractical as the drilling equipment in the field and the experimental devices in the laboratory cannot be adapted easily to different sample sizes. In order to illustrate the effects of specimen representativity and material heterogeneity on the characterization of the behavior of rock salt at the laboratory scale, we show results of an experimental campaign performed at the Geosciences Department of Mines ParisTech. The tested samples have a diameter of 65 mm and a height

of 130 mm. They contain impurities with an average size of several mm. Figure 1 shows three of the tested samples, cored within 7.5 m from each other.
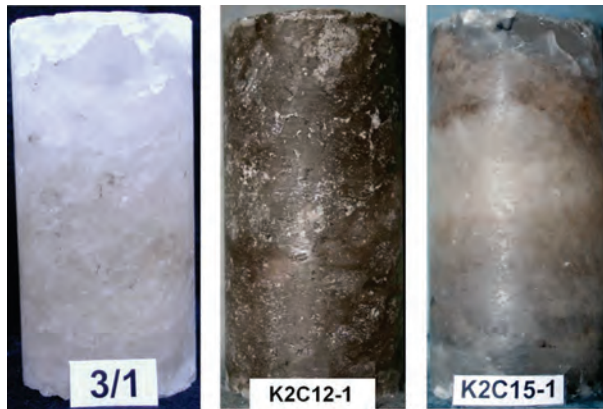
Figure 1: View of three of the rock salt samples tested, having different impurity content. Coring depths from left to right are 1298.5, 1303.5 and 1306 m.

2.1 Experimental set-up

A typical cell for short-term and long-term tests is displayed in Figure 2. The tests can be performed at ambient or greater temperatures (up to 80 °C). Short-term tests are performed using servo-controlled testing machines that allow conducting the tests under either controlled strain rate or controlled pressure rate. Creep tests are performed in a temperature-controlled underground room (18 ±1 °C). To ensure stability over long time periods, the axial and lateral pressures are applied via bladder accumulators.
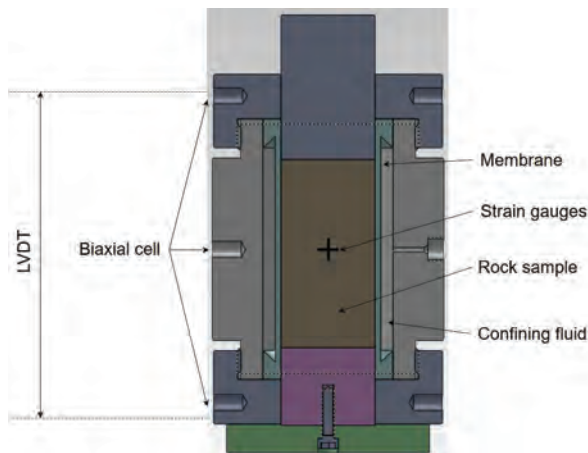
Figure 2: Cutaway view of the biaxial cells used to perform the tests. Local and axial global measurement techniques are displayed.

In short-term tests, deformation is measured locally and globally. The interest of capturing the sample response at different spatial scales will be highlighted below. Locally, two pairs of strain gauges (axial and circumferential, see Figure 2) are placed at the center of the specimen, diametrically opposed. Globally, the axial displacement of the sample is measured using LVDT sensors, and the volume variation of the confining fluid is measured by means of an injector. The combination of these two measurements permits to compute the global hoop strain (Rouabhi et al. 2019). In creep tests, the axial global deformation of the sample is measured

using LVDT sensors (note that recently, the creep cells have been equipped with strain gauges; however, the tests shown here were performed before the use of such equipment).

2.2 Experimental campaign

Sixteen short-term tests and twelve creep tests have been conducted on samples cored at depths between 1224 and 1472 m. The short-term tests have been performed at ambient temperature and under constant axial strain rate ($\dot{\varepsilon}_{ax} = 2 \cdot 10^{-6}$ s^{-1}). The confining pressure, P, is kept constant during each test. Four values have been applied to different samples: 5, 10, 17 and 20 MPa. When possible, the same loading conditions are applied to samples from the same and different facies to evaluate repeatability and material heterogeneity. Creep tests have been performed at temperatures between 50 and 70 °C, with stress deviators $D=Q-P$ (Q is the axial pressure) up to 15 MPa. Several loading stages are applied to each sample, at increasing and decreasing values of D. Figures 3 and 4 show some typical results (note that compression is positive). All tests have been performed under compressive conditions, i.e., $Q>P$.
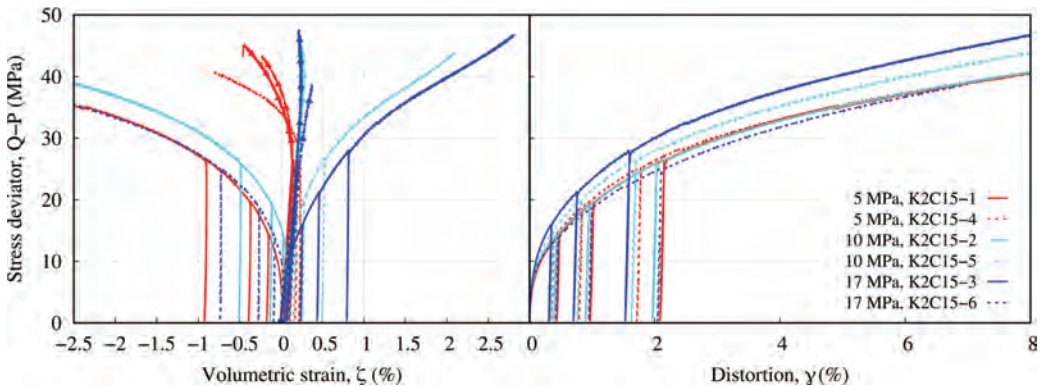
Figure 3: Results of six short-term tests performed at $\dot{\varepsilon}_{ax} = 2 \cdot 10^{-6}$ s^{-1} and three different confining pressures (each test is repeated twice). The samples are cored between 1306 and 1307 m. In the left-hand side plot, lines with symbols correspond to global volumetric strains and lines without symbols correspond to local volumetric strains.
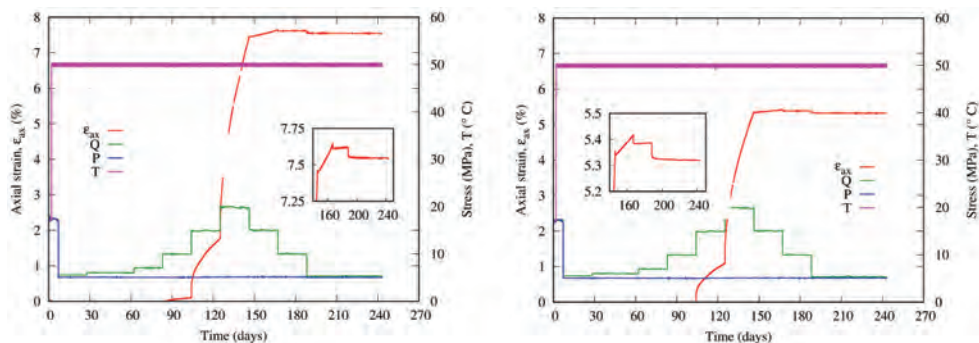
Figure 4: Results of two long-term tests performed at 50 °C (same loading stages for both tests). The samples are cored between 1303.5 and 1303.8 m. The initial, one-week sample consolidation phase at $3C=2P+Q=51$ MPa is visible in the plots. The enlarged views correspond to the strain recorded during the stages in which the stress deviator decreases.

2.3 Some comments on the test results

Figures 3 and 4 show significant scattering among tests that were conducted under equivalent conditions but using different samples. Moreover, as it can be seen in Figure 3, for a given sample the volumetric response measured using local and global techniques can be very different (for instance, in one of the tests performed at P=10 MPa, the local measurements suggest that the sample remained within the contracting domain throughout the test, whereas the global measurements indicate a switch to the dilation domain at a stress deviator of 40 MPa). These differences exceed the limits of natural variability and are related to some kind of heterogeneity. The differences in the measurements are particularly important for the volumetric strains, given their small values as compared to the distortion strains (note that differences between global and local deviatoric data are within experimental error limits). It should be noted that the volumetric strains are particularly important because the dilatancy threshold is used as a criterion for salt cavern design.

There could be several explanations to the observed anomalies. The first one is related to the contact between the platens and the sample, which induces non-homogeneous stress and strain fields within the specimens, particularly close to the upper and lower ends. However, as investigated in Rouabhi et al. (2019), this explanation alone is not sufficient to explain the recorded anomalies. Another possible explanation is material heterogeneity: depending on the placement of the strain gauges with respect to the heterogeneities (such as impurities), their response could be very different from the global measurements (Azabou et al. 2021b). This suggests that the samples may not be representative of the salt rock mass, as their size seems to be smaller than the RVE.

3 Constitutive modeling

3.1 RTL2020 constitutive law for rock salt

The RTL constitutive law is based on the Lemaitre creep law (Tijani et al. 1983) and has been augmented with additional terms to better reproduce the time-dependent response of rock salt. The current version, RTL2020, is fully detailed in Azabou et al. (2021a), and here we only recall its main features. The total strain rate tensor reads

$$\underline{\dot{\varepsilon}} = \underline{\dot{\varepsilon}}_{el} + \underline{\dot{\varepsilon}}_{th} + \underline{\dot{\varepsilon}}_{vp} \tag{1}$$

where $\underline{\dot{\varepsilon}}_{el} = \frac{1+\nu}{E}\underline{\dot{\sigma}} - \frac{\nu}{E}tr\left(\underline{\dot{\sigma}}\right)\underline{1}$ is the elastic strain rate (E is Young's modulus and ν is Poisson's ratio), $\underline{\dot{\varepsilon}}_{th} = \alpha_{th}\dot{T}\underline{1}$ is the thermal strain rate (α_{th} is the linear thermal expansion coefficient), and the viscoplastic strain rate $\underline{\dot{\varepsilon}}_{vp}$ is given by

$$\underline{\dot{\varepsilon}}_{vp} = \sqrt{\frac{3}{2}}\dot{\gamma}_{vp}\underline{N} - \frac{1}{\sqrt{3}}\dot{\zeta}_{vp}\underline{I} \tag{2}$$

where $\dot{\gamma}_{vp} = \sqrt{2/3}\left\|\underline{\dot{\varepsilon}}'_{vp}\right\|$ ($\left\|\underline{\dot{\varepsilon}}'_{vp}\right\|$ is the norm of the deviatoric component of the strain rate tensor), $\dot{\zeta}_{vp} = -tr\left(\underline{\dot{\varepsilon}}_{vp}\right)$, $\underline{N}$ is a unit tensor that defines the deviatoric flow direction and $\underline{I} = 1/\sqrt{3}$. Eq. (2) shows that the viscoplastic strain rate has a deviatoric component and a volumetric component. The deviatoric component is defined by two mechanisms:

$$\dot{\gamma}_{vp} = \dot{\gamma}_L + \dot{\gamma}_R \tag{3}$$

with $\dot{\gamma}_L$ a transient mechanism of Lemaitre's type, and $\dot{\gamma}_R$ a transient mechanism inspired from Munson-Dawson (Munson 1997) and limited by $\bar{\gamma}_R = \left(\frac{q}{A_1}\right)^{n_1}$ ($q = \sqrt{3/2\underline{\underline{\sigma'}}:\underline{\underline{\sigma'}}}$ is the von Mises equivalent stress [$\underline{\underline{\sigma'}} = \underline{\underline{\sigma}} + p\underline{\underline{1}}$ is the stress deviator and $p = -tr\left(\underline{\underline{\sigma}}\right)/3$ is the mean stress]):

$$\dot{\gamma}_L = \alpha \exp\left(\frac{A_R}{\alpha}\left(\frac{1}{T_r} - \frac{1}{T}\right)\right)\left(\frac{q}{A_2}\right)^{n_2} \gamma_L^{1-\frac{1}{\alpha}} \qquad (4)$$

$$\dot{\gamma}_R = \begin{cases} A(1 - \gamma_R/\bar{\gamma}_R)^n \gamma_L^{1/\alpha} & if \quad \gamma_R \leq \bar{\gamma}_R \\ -B(\gamma_R/\bar{\gamma}_R - 1)^m \gamma_L^{1/\alpha} & if \quad \gamma_R \geq \bar{\gamma}_R \end{cases} \qquad (5)$$

where α, A_2, n_2, A_R, T_r, (T_r is the reference temperature at which A_R is determined), A, n, B, m, A_1 and n_1 are material parameters. Note that $\gamma_L^{1/\alpha} = \exp\left(\frac{A_R}{\alpha}\left(\frac{1}{T_r} - \frac{1}{T}\right)\right)\left(\frac{q}{A_2}\right)^{n_2}$. Note also that the second mechanism $\dot{\gamma}_R$ allows to model reverse (or inverse) creep, which can be observed in the laboratory if $\dot{\gamma}_{vp} < 0$. The combination of these two transient mechanisms allows to reproduce laboratory data satisfactorily; more importantly, it can yield long-term predictions that lie between those of well-known transient and steady-state creep laws. The volumetric component is defined by

$$\dot{\zeta}_{vp} = \phi\left(\underline{\underline{\sigma}}, T, \gamma_{vp}\right)\dot{\gamma}_{vp} = z\frac{\langle p/N_z\rangle^{n_z} - \gamma_{vp}}{\langle p/M_z\rangle^{m_z} + \gamma_{vp}}\dot{\gamma}_{vp} \qquad (6)$$

where z, n_z, N_z, m_z and M_z are material parameters. Note that when $\dot{\zeta}_{vp} = 0$, there is a transition from contractancy to dilatancy (dilatancy threshold).

3.2 Modeling of laboratory tests

The experimental results have been analyzed with RTL2020. Figures 5 and 6 compare experimental and fitted results for the tests displayed in Figures 3 and 4. A single parameter set has been used for the whole experimental campaign, which explains the misfit observed individually for some tests. Overall, the comparison is quite satisfactory. Note that two parameter sets have been determined for the volumetric part: one is based on local measurements and the other is based on global measurements. Both parameter sets will be used to perform cavern simulations in the next section. Table 1 lists the obtained parameters.

Table 1: Model parameters fitted from laboratory results (the unit system is such that strain is in □m/m, stress in MPa, time in days and temperature in K).

E	ν	α_{th}			
31200	0.30	29			

A	B	n	m	A_1	n_1
146.41	2.13·10⁻⁹	2.99	3.48	0.29	2.11

α	A_2	n_2	A_R	T_r	
0.45	0.5	5.76	2212.39	289.55	

z_{glo}	$n_{z,glo}$	$N_{z,glo}$	$m_{z,glo}$	$M_{z,glo}$	
0.11	2.34	0.24	4.99	2.80	

z_{loc}	$n_{z,loc}$	$N_{z,loc}$	$m_{z,loc}$	$M_{z,loc}$	
0.50	2.48	2.23	1.23	0.05	
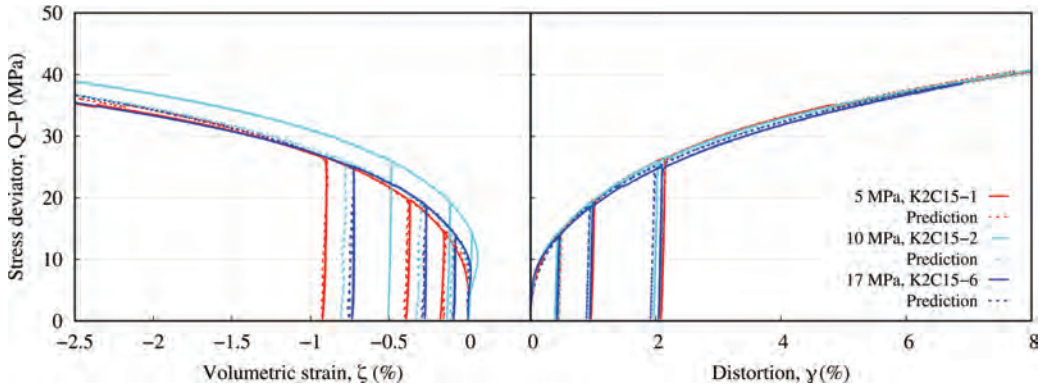
Figure 5: Comparison between experimental results and RTL2020 predictions for the short-term tests. In the left-hand side plot, lines with symbols correspond to global volumetric strains and lines without symbols correspond to local volumetric strains.
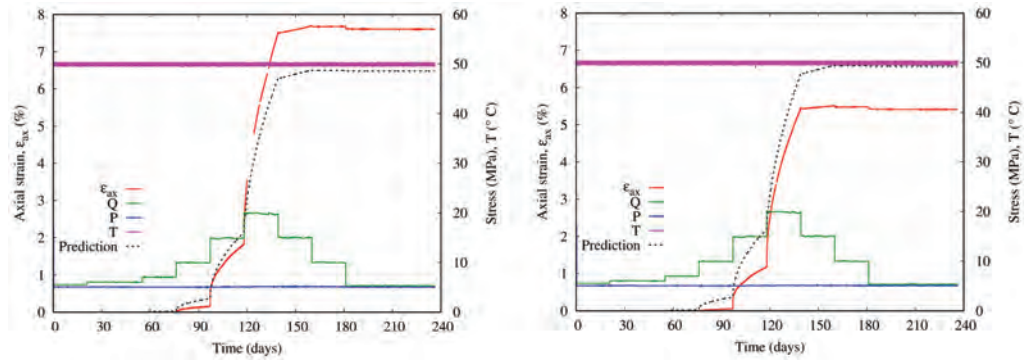

Figure 6: Comparison between experimental results and RTL2020 predictions for the long-term tests.

3.3 Cavern design methodologies based on laboratory tests

As explained in the Introduction, two design methodologies exist based on the dilatancy criterion. In the first methodology, the criterion is determined by plotting in the p-q plane the dilatancy thresholds (here defined as $\dot{\zeta}_{vp} = 0$) obtained in different short-term tests, and by fitting such thresholds with a linear or nonlinear function. Figure 7 displays the experimental dilatancy thresholds obtained in the short-term campaign and the fitted dilatancy criterion. For the illustrative purposes of this paper, a linear criterion is selected. The fitting yields (in MPa):

$$q = 1.23p + 8.18 \tag{7}$$

In the second methodology, the dilatancy criterion is embedded within the constitutive law, and no additional fitting is required. The parameters in Table 1 (volumetric part) hold.
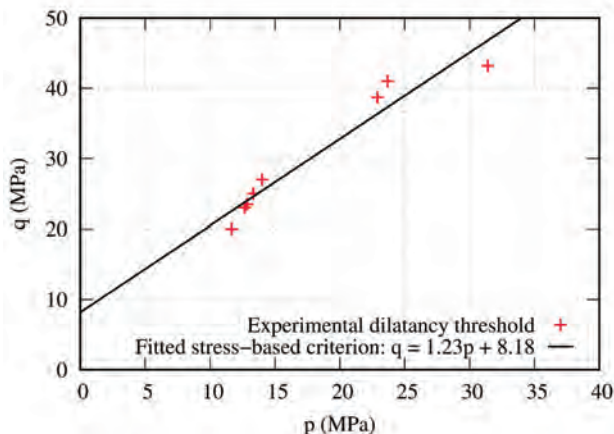
Figure 7: Onset of dilatancy (defined as $\dot{\zeta}_{vp} = 0$) determined from the short-term tests and fitted linear dilatancy criterion.

4   Implications at the cavern scale

We consider seasonal storage of CH_4 in an isolated cavern having an initial volume of 191000 m^3. The sump, filled with brine, represents about 43000 m^3. The cavern is 145 m high, and its top is at a depth of 1430 m. The profile of the cavern is shown in Figure 8. Two FEM axisymmetric simulations are performed including the leaching (3 years) and debrining phases (3 months), followed by 40 years of cycling. The simulations differ in the parameter set used for the volumetric part (both sets are shown in Table 1). At the cavern wall, the applied pressure varies between P_{max} = 24 and P_{min} = 12 MPa.

Figure 8 shows the isovalues of $\dot{\zeta}_{vp} = 0$ at different times obtained in the two simulations. As it can be seen, the global parameter set predicts a smaller extent of the dilatancy zone than the local set: 25 m vs.150 m. In both cases, during the cycling phase the extent of the dilatancy zone around the cavern increases rapidly initially and then tends to stabilize over time, which is beneficial from a design perspective. However, the local parameter set predicts an important extent of the dilatancy zone during the leaching phase. The differences obtained in these simulations are important for cavern design (e.g., spacing between caverns), and show the importance of accurate laboratory measurements and rock characterization.

The results of the simulation that uses the global parameter set are also analyzed using the stress-based dilatancy criterion. In this case, the simulation results are post-processed and the dilatancy areas are those verifying Eq. (7). Since the minimum cavern pressure P_{min} remains quite high (note that 20% of the initial *in situ* stress is about 7 MPa), the stress-based criterion predicts no zones affected by dilatancy around the cavern, which is quite a different result than that provided by the use of the strain-based criterion embedded in the constitutive law.
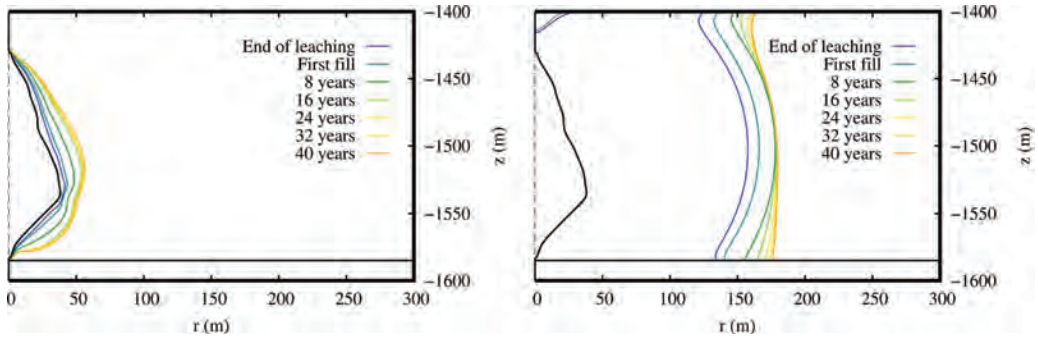
Figure 8: Isovalues of $\dot{\zeta}_{vp} = 0$ obtained using the global (left) and local (right) parameter sets for the volumetric component of RTL2020. The horizontal line at z=-1590 m represents the bottom of the salt layer (clay layer underneath).

5 Discussion and conclusions

Not using specimens that meet the RVE size may lead to an improper characterization of the rock at the laboratory scale, which in turn may lead to an improper design of the underground facilities. This has been illustrated through an experimental campaign and subsequent simulations at the cavern scale. Several measurement techniques should be used in the laboratory, at different scales within the sample (local, global, hybrid): this not only mitigates possible malfunctions of the equipment, but it also allows identifying heterogeneities in the strain and the stress fields. To overcome material heterogeneity and associated representativity issues, a methodology that combines experimental and numerical work has recently been proposed (Azabou et al. 2021b, c): starting from non-representative samples tested at the laboratory, it uses a virtual laboratory to reproduce the measured response and to determine the RVE size, on which the parameters of a constitutive law can be fitted.

Another important aspect is the design criterion used. Stress-based criteria are determined from short-term tests (stress state at the onset of dilatancy). They are applied during post-processing and are fixed in the stress space; this means that they do not evolve as the mean pressure, the loading rate or the stress state changes around the cavern. In turn, design criteria embedded at the constitutive level such as the strain-based criterion presented in this paper, are based on both short-term and long-term tests, and evolve as the mean pressure, the loading rate or the stress state changes around the cavern; therefore, they have less limitations than the stress-based criteria. Thus, the use of a pertinent constitutive model is crucial: it should reproduce laboratory data accurately and yield pertinent long-term predictions. For this purpose, model parameters should be recalibrated based on *in situ* data when possible.

Acknowledgements

References

AZABOU, M. 2021. Modélisation et prédiction du comportement macroscopique du sel gemme dans le contexte du stockage souterrain. PhD Thesis, MINES ParisTech, 150 p.

AZABOU, M., ROUABHI, A. & BLANCO-MARTÍN, L., HADJ-HASSEN, F., KARIMI-JAFARI, M. & HÉVIN, G. 2021a. Rock salt behavior : From laboratory experiments to pertinent long-term predictions. Int. J. Rock Mech. Min., 142, 104588.

AZABOU, M., ROUABHI, A. & BLANCO-MARTIN, L. 2021b. Effect of insoluble materials on the volumetric behavior of rock salt. J. Rock Mech. Geotech. Eng., 13(1), 84–97.

AZABOU, M., ROUABHI, A. & BLANCO-MARTÍN, L. 2021c. On the Representativity of Rock Salt Specimens During Laboratory Tests. Rock Mech. & Rock Eng., 14 p.

BÉREST, P., GHARBI, H., BROUARD, B., BRÜCKNER, D., DEVRIES, K.L., HÉVIN, G., et al. 2019. Very Slow Creep Tests on Salt Samples. Rock Mech. & Rock Eng., 52, 2917–2934.

BLANCO-MARTÍN, L., RUTQVIST, J. & BIRKHOLZER, J.T. 2015. Long-term modeling of the thermo-hydraulic-mechanical response of a generic salt repository for heat-generating nuclear waste. Eng. Geol., 193, 198–211.

CRISTESCU, N.D. 1993. A General Constitutive Equation for Transient and Stationary Creep of Rock Salt. Int. J. Rock Mech. Min., 30(2), 125–140.

DEVRIES, K.L., MELLEGARD, K.D., CALLAHAN, G.D. & GOODMAN, W.M. 2005. Cavern Roof Stability for Natural Gas Storage in Bedded Salt. Respec, Rapid City, SD (Rep. DE-FG26-02NT41651, 191 p).

DÜSTERLOH, U., HERCHEN, K., LUX, K.-H., SALZER, K., GÜNTHER, R.-M., MINKLEY, W., et al. 2015. Joint Project III on the comparison of constitutive models for the mechanical behavior of rock salt III. Extensive laboratory test program with argillaceous salt from WIPP and comparison of test results. The Mechanical Behavior of Salt; Proc. 8th Conference, Rapid City, SD, 13–21.

FAHLAND, S. & HEUSERMANN, S. 2012. Measurement and calculation of rock stress in the Morsleben repository. The Mechanical Behavior of Salt; Proc. 7th Conference, Paris 2012, 193–200.

GÄHRKEN, A., DEVRIES, K.L. & STAHLMANN, J. 2018. Advanced development of the constitutive model TUBSsalt for rock salt regarding the influence of Lode angle effects. The Mechanical Behavior of Salt; Proc. 9th Conference, Hanover 2018, 479–496.

GÜNTHER, R.-M. & SALZER, K. 2012. Advanced strain-hardening approach: a powerful creep model for rock salt with dilatancy, strength and healing. The Mechanical Behavior of Salt; Proc. 7th Conference, Paris 2012, 13–22.

HAMPEL, A. 2015. Description of damage reduction and healing with the CDM constitutive model for the thermos-mechanical behavior of rock salt. The Mechanical Behavior of Salt; Proc. 8th Conference, Rapid City, SD, 2015, 301–310.

HARDIN, E. & VOEGELE, M. 2013. Alternative Concepts for Direct Disposal of Dual-Purpose Canisters. Sandia Natl. Lab., Albuquerque, NM (Rep. SAND2013-1710P, 53 p).

HERCHEN, K., POPP, T., DÜSTERLOH, U., LUX, K.-H., SALZER, K., LÜDELING, C., et al. 2018. WEIMOS: Laboratory Investigations of Damage Reduction and Creep at Small Deviatoric Stresses in Rock Salt. The Mechanical Behavior of Salt; Proc. 9th Conference, Hanover 2018, 175–192.

HEUSERMANN, S., ROLFS, O. & SCHMIDT, U. 2003. Nonlinear finite-element analysis of solution mined storage caverns in rock salt using the Lubby2 constitutive model. Comput. Struct., 81(8), 629–638.

HOU, Z. 2003. Mechanical and hydraulic behaviour of rock salt in the excavation disturbed zone around underground facilities. Int. J. Rock Mech. Min., 40, 725–738.

HUNSCHE, U. & HAMPEL, A. 1999. Rock salt – the mechanical properties of the host rock material for a radioactive waste repository. Eng. Geol., 52, 271–291.

JULIEN, M. 1999. Une modélisation constitutive et numérique du comportement rhéologique du sel gemme. PhD Thesis, Ecole Polytechnique de Montréal.

KHALEDI, K., MAHMOUDI, E., DATCHEVA, M. & SCHANZ, T. 2016. Stability and serviceability of underground energy storage caverns in rock salt subjected to mechanical cyclic loading. Int. J. Rock Mech. Min., 86, 115–131.

LABAUNE, P., ROUABHI, A., TIJANI, M., BLANCO-MARTÍN, L. & YOU, T. 2018. Dilatancy criteria for salt cavern design: a comparison between stress- and strain-based approaches. Rock Mech. & Rock Eng., 51, 599–611.

LUX, K.-H., LERCHE, S. & DYOGTYEV, O. 2018. Intense damage processes in salt rocks – a new approach for laboratory investigations, physical modelling and numerical simulation. The Mechanical Behavior of Salt; Proc. 9th Conference, Hanover 2018, 47–67.

MACKINNON, R.J., SEVOUGIAN, S.D., LEIGH, C.D. & HANSEN, F.D. 2012. Towards a defensible safety case for deep geologic disposal of DOE HLW and DOE SNF in bedded salt. Sandia Natl. Lab., Albuquerque, NM (Rep. SAND2012-6032, 62 pp).

MINKLEY, W., MÜHLBAUER, J. & LÜDELING, C. 2016. Dimensioning principles in potash and salt: stability and integrity. Rock Mech. & Rock Eng., 49(11), 4537–4555.

MUNSON, D.E. 1997. Constitutive model of creep in rock salt applied to underground room closure. Int. J. Rock Mech. Min. Sci., 34(2), 233–247.

ODQVIST, F.K.G. 1974. Mathematical theory of creep and rupture. Oxford, Clarendon Press.

ROBERTS, L.A., BUCHHOLZ, S.A., MELLEGARD, K.D. & DÜSTERLOH, U. 2015. Cyclic Loading Effects on the Creep and Dilation of Salt Rock. Rock Mech. & Rock Eng., 48, 2581–2590.

ROUABHI, A., LABAUNE, P., TIJANI, M., GATELIER, N. & HÉVIN, G. 2019. Phenomenological behavior of rock salt: on the influence of laboratory conditions on the dilatancy onset. J. Rock Mech. Geotech. Eng., 11(4), 723–738.

SALZER, K., GÜNTHER, R.-M., MINKLEY, W., NAUMANN, D., POPP, T., HAMPEL, A., et al. 2015. Joint Project III on the comparison of constitutive models for the mechanical behavior of rock salt II. Extensive laboratory test program with clean salt from WIPP. The Mechanical Behavior of Salt; Proc. 8th Conference, Rapid City, SD, 3–12.

SPERANZA, G., VONA, A., VINCIGUERRA, S. & ROMANO, C. 2016. Relating natural heterogeneities and rheological properties of rocksalt: new insights from microstructural observations and petrophyisical parameters on Messinian halites from the Italian peninsula. Tectonophysics, 666, 103–120.

TARKOWSKI R.2019. Underground hydrogen storage: Characteristics and prospects. Renew. Sust. Energ. Rev., 105, 86–94.

THOMS, R. & GEHLE, R. 2000. A brief history of salt cavern use. 8th World Salt Symp., The Hague, 207–214.

TIJANI, M., HADJ-HASSEN, F. & GATELIER, N. 2009. Improvement of Lemaitre's creep law to assess the salt mechanical behavior for a large range of deviatoric stress. 9th Int. Symp. Salt, Beijing, 135–147.

TIJANI, M., VOUILLE, G. & HUGOUT, B. 1983. Le sel gemme en tant que liquide visqueux. ISRM Conference, Melbourne, 241–246.

WEIMOS: Creep of rock salt at low deviatoric stresses

Christoph Lüdeling[1]*, *Ralf-Michael Günther[1], Andreas Hampel[2], Junqing Sun-Kurczinski[3],
Ralf Wolters[3], Uwe Düsterloh[3], Karl-Heinz Lux[3], Savaş Yıldırım[4], Dirk Zapf[4], Svenja Wacker[5],
Ida Epkenhans[5], Joachim Stahlmann[5], Benjamin Reedlunn[6]*

[1]Institut für Gebirgsmechanik GmbH (IfG), Leipzig, Germany; [2]Hampel Consulting, Mainz, Germany; [3]Technische Universität Clausthal (TUC), Germany; [4]Leibniz Universität Hannover (LUH), Germany; [5]Technische Universität Braunschweig (TUBS), Germany; [6]Sandia National Laboratories, Albuquerque, NM, USA

* *christoph.luedeling@ifg-leipzig.de*

ABSTRACT: The vast majority of rock salt creep tests have been conducted at deviatoric stresses above 6 MPa, yet the long-term behaviour of waste repositories, mines and caverns is dominated by creep below 6 MPa. Steady-state creep in this range is very slow (around 10^{-6}/d or lower) and is easily overwhelmed by other effects, such as dilatancy and long transient phases. Hence, a careful experimental approach was developed to measure creep at low stresses that includes

- an isotropic compression step to consolidate the sample,
- high confining stresses to avoid dilating the sample during deviatoric stress steps,
- elevated temperature in the first deviatoric stress step to speed up transients,
- and several temperature steps to obtain several creep rates and activation energies from a single sample. Since dislocation microstructure depends only weakly on temperature, there are essentially no new transients in the later load stages.

We discuss the procedure in detail and present a long-term creep test (duration almost five years) at 4 MPa that validates the procedure. These tests should help calibrate rock salt constitutive models and derive parameter sets for creep laws, and hence allow them to predict long-term structural performance with greater confidence.

1 Introduction

The long-term behaviour of excavations in salt formations is dominated by creep at deviatoric stresses below, say, 6 MPa. For waste repositories, in particular, this has implications for drift convergence (see e.g. Hampel et al. 2022) – which affects the behaviour of geotechnical barriers such as crushed salt backfill and drift seals – and for large-scale stress redistributions which affect the geological barrier by lowering the minor principal stress and possibly allow allowing fluid transport via pressure-driven percolation (see e.g. Kock et al. 2012).

However, experimental data is scarce in this region because creep tests on rock salt are predominantly conducted at higher stresses (see e.g. Salzer et al. 2015; Mellegard, Pfeifle 1993). Pioneering work on the creep of natural rock salt in the low-stress range has been done by Bérest et al (2017, 2020; see also Gharbi et al. 2020), but the amount of available data does not currently allow a comprehensive characterisation of the low-stress creep properties of specific rock salt varieties. Furthermore, considerable scatter and uncertainties exist, e.g. about pre-existing damage, the influence of external humidity and the question of stationarity. Nevertheless, it seems clear that rock salt creeps faster at low stress than would be expected from a pure Norton-type creep law such as BGRa (Hunsche & Schulze 1995),

$$\dot{\epsilon}_{\text{Norton}} = A\, e^{-\frac{Q}{RT}} \sigma^n, \tag{1}$$

with $n = 5$. Figure 1 summarises stationary creep rates for some rock salt varieties in the range from 40 MPa to 0.1 MPa. For stresses of a few MPa, creep rates generally are in the range of $\dot{\epsilon} \sim 10^{-6}$/d (i.e. around 10^{-11}/s).

This is consistent with microphysical analyses of creep mechanisms. At moderate and high stress, creep of rock salt is dominated by intracrystalline dislocation motion, with comparatively steep stress dependence. At lower stresses, it has been shown (Urai et al. 1986; Schleder, Urai 2005) that fluid-assisted dissolution-precipitation processes, such as pressure solution and dynamic recrystallization, become the main creep mechanisms. Spiers et al. (1990) derived the creep rate for pressure solution creep to be similar to Eq. (1), but with a linear stress dependence, i.e. $n = 1$.

While the stationary creep of rock salt has often been modelled using a single-component power law such as Eq. (1), current state-of-the-art constitutive models (see e.g. Lüdeling et al. 2018; Reedlunn et al. 2022) contain more complex creep laws that allow for enhanced creep rates at low stress. On the other hand, the lack of a proper experimental data base means that the creep laws can only be partially validated, and necessary parameters cannot be firmly determined.
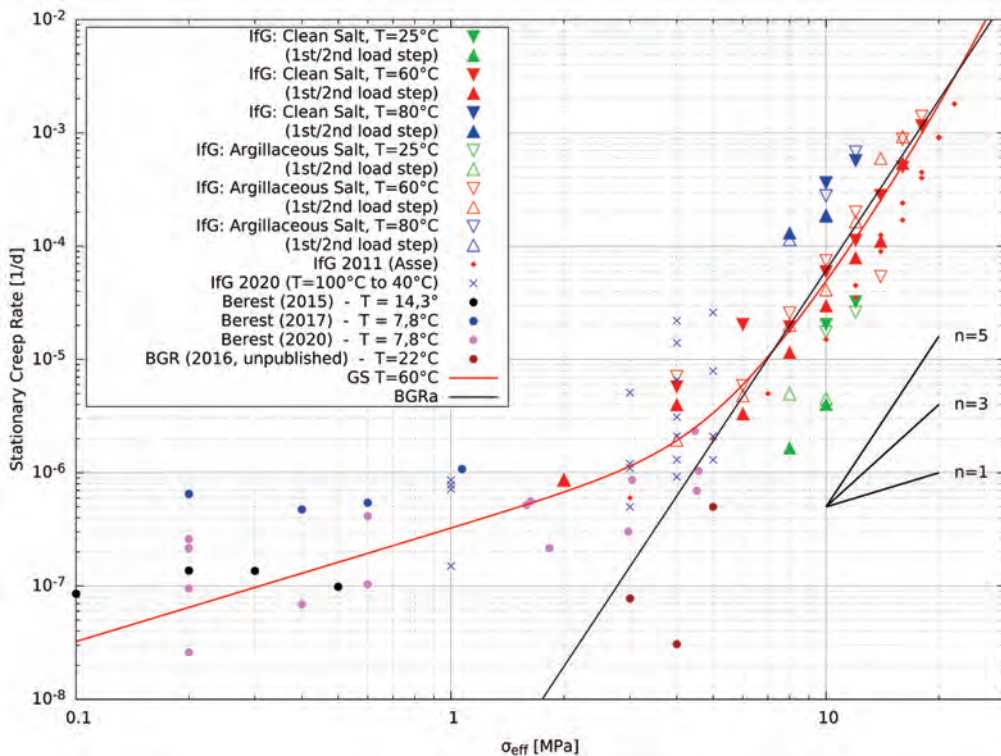
Figure 1: Stationary creep rates for various rock salt varieties (modified from Herchen et al. 2018). The triangles indicate measurements on WIPP salt from joint project III (Salzer et al. 2015). Note that the Bérest and BGR tests used different salt varieties. The solid lines indicate the BGRa law (black) and the Günther-Salzer model (three-component power law, red).

In the WEIMOS research project, creep at low stress is one of the work areas. In this paper, we present an improved creep test procedure to accurately determine creep rates and their temperature dependence at low stress.

2 Key problems in and strategies for identifying "true" creep

In lab tests, the stationary creep of rock salt, in particular for the small rates at low stresses, is easily overwhelmed by other effects, both from external influences and the internal structure of the salt. Generally, the disturbances will increase the measured creep rates, i.e. the stationary rates will be overestimated.

The mechanical disturbances during sample preparation generically introduce a small amount of dilatancy, generally in the order of $\epsilon \sim 10^{-3}$, to the specimen. Similarly, end face roughness with amplitude of a few hundredths of a millimetre corresponds to, for samples of length 120 mm, a deformation in the range of $\epsilon \sim 10^{-4}$ to $\epsilon \sim 10^{-3}$. Note that for a (measured) creep rate of $\dot{\epsilon} = 10^{-6}$/d, a spurious deformation of $\epsilon = 10^{-3}$ implies more than 10^3 d before the actual creep stage of the salt is reached.

In addition, a temperature fluctuation of 1 K corresponds to several weeks of creep at $\dot{\epsilon} \sim 10^{-6}$/d; however this is a reversible effect and may be corrected for if one assumes the temperature fluctuation is uniform throughout the sample.

It is currently an open question whether rock salt forms micro-cracks (dilates) under low uniaxial compressive stresses. If it does, the dilation will contribute to the measured creep rate. Furthermore, if the sample is not shielded, humidity from the ambient air can access the interior of the specimen via (pre-existing or newly generated) micro-cracks and speed up any fluid-assisted creep processes (Hunsche, Schulze 2002; Bérest et al 2020).

Finally, the low rates mean that any transient stage takes a long time. (Note that "transient" and "stationary" creep phases are, in particular, a feature of the dislocation microstructure, while dissolution-precipitation creep plausibly does not have a pronounced transient stage.) Hence, creep tests will be very time-consuming, and it is nontrivial to ascertain that a stationary stage has been reached.

To address these problems, some general strategies have been developed:

The first is to perform creep tests in a triaxial setup with high confining stress, e.g. 20 MPa. The triaxial cell will isolate the sample from external humidity and allow for controlled sample temperatures independent of the ambient conditions. The confining stress suppresses dilatancy generation during the creep stage.

Additionally, triaxial tests enable an initial isotropic consolidation phase to heal the pre-existing damage and crush the end face asperities. It was found in Günther et al. (2015) that consolidating the samples for ten days at 20 MPa greatly reduced the intersample scatter at deviatoric stresses above 10 MPa. For lower deviatoric stresses, longer consolidation phases are to be expected.

To reduce the required test durations, it is recommended to exploit temperature effects. A higher temperature accelerates creep deformation and thus speeds up the transient phase, such that the stationary stage is reached faster. Elevated temperatures are usually closer to the rock temperatures in mines, and many applications, such as disposal of heat-generating waste, require knowledge of the temperature dependence of stationary creep rates. Tests at different temperatures, or with several temperature stages, can be used to derive the activation energies.

As we discuss in the next two sections, an understanding of the basic creep mechanisms is helpful to develop suitable test procedures and to obtain reliable creep rates.

3   Procedure at moderate and high stress

We briefly discuss the procedure of Günther et al. (2015) to determine stationary rates at higher stresses, say, above 8 MPa, where dislocation creep dominates. Hence, one can exploit the transient creep behaviour to obtain both upper and lower bounds for the stationary creep rate.

The key point is that transient creep reflects the evolution of the dislocation microstructure towards an equilibrium state that is determined by the applied stress. Thus, after a stress increase, creep rates are initially high and subsequently reduce (the sample hardens, normal transient creep). After a stress decrease, on the other hand, the material is over-hardened, so creep rates are initially low and increase over time (inverse transient creep). In other words, the stationary rate is approached from above and below in normal and inverse transient creep, respectively.

Thus, in a series of two-stage creep tests with unloading, e.g. at $18\,\text{MPa} \rightarrow 16\,\text{MPa}$ and $16\,\text{MPa} \rightarrow 14\,\text{MPa}$, both normal and inverse transient creep occur at 16 MPa, and the creep rates bound the stationary rate from both sides (see Figure 2).
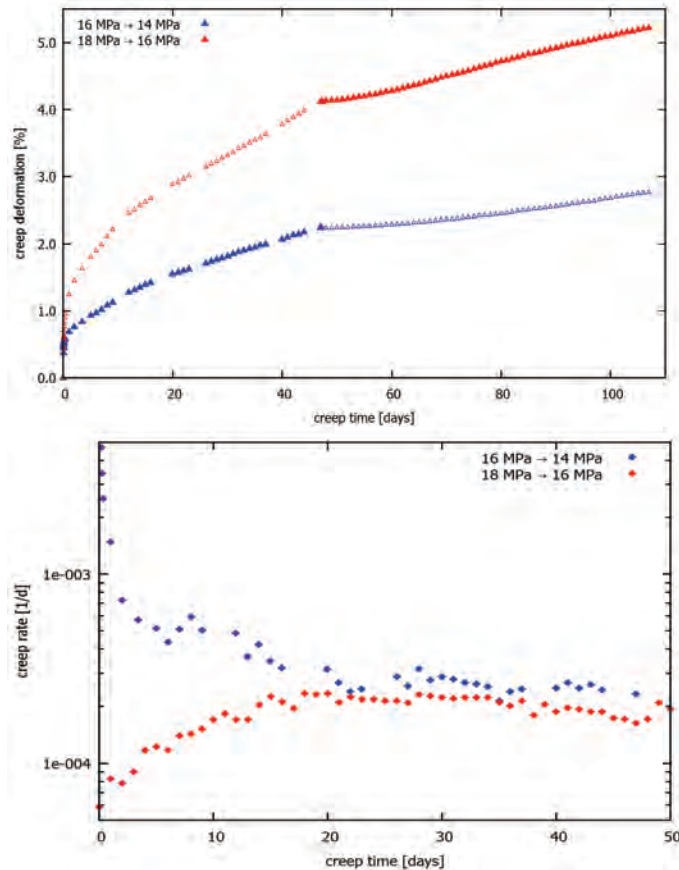
Figure 2: Determination of stationary creep rates (after Günther et al. 2015). Top panel: Deformation versus time for two-stage creep tests with 16 MPa and 14 MPa (blue, lower curve) and with 18 MPa and 16 MPa (red, upper curve). Note that the solid symbols show creep at 16 MPa with normal and inverse transient creep. Bottom panel: Creep rates for the 16 MPa stages; the values converge to the stationary rate.

The majority of tests is performed at elevated temperature (e.g. 60°C) to speed up the transient phases, and the activation energies are determined from supplementary tests at, e.g., 30°C and 80°C.

All tests are conducted as triaxial tests at 20 MPa confining stress and include an isotropic consolidation phase of ten days.

4 Modified procedure for small stress

Based on the understanding of creep mechanisms discussed in Section 1, it becomes clear that the procedure discussed in the previous section is only partially appropriate to stresses below 8 MPa. While the consolidation phase and the accelerating influence of higher temperatures can be carried over, the two-stage tests with unloading are not helpful: Practically, an unloading by 2 MPa becomes too large for stresses of only a few MPa, and significantly smaller load steps, such as 0.2 MPa, are experimentally challenging. Conceptually, the change of the dominant creep mechanism from dislocation motion to dissolution-precipitation processes implies much smaller transients and smaller stress exponents, so that the intersample scatter is likely to overwhelm the signal. Hence, the underlying motivation to use the transient creep stages to bound the stationary rates does not apply anymore.

In the WEIMOS project, we have adapted the approach for stresses above 8 MPa (Günther et al. 2015) to measure creep rates at low deviatoric stress:

- For the reasons discussed above, we use triaxial tests at high confining stress.
- Pre-existing damage is reduced in an initial isotropic consolidation phase. It is recommended to monitor the creep rate and to continue the consolidation until the rate is small enough (e.g., significantly smaller than the expected creep rates in the first deviatoric load step).
- The consolidation phase and the first load stage are conducted at high temperature to speed up healing and transient creep, i.e. the evolution of the dislocation microstructure.
- The specified load is held until a stationary state is reached.
- In subsequent phases, the load is kept constant, and the temperature is reduced in steps of 20 K. Since the dislocation structure only weakly depends on temperature, essentially no new transients occur, and later stages can be comparatively short.

With this procedure, we obtain several stationary rates, at fixed stress and several temperatures, from a single specimen. The time-consuming transient stage is accelerated by the initially high temperature and only happens once.

5 Long-term creep test TCC34

We have performed a long-term creep test (TCC34) using the procedure discussed in the previous section. Sample material is clean salt from the Waste Isolation Pilot Plant (WIPP), see Figure 3, sample diameter and length are 60 mm and 120 mm, respectively.
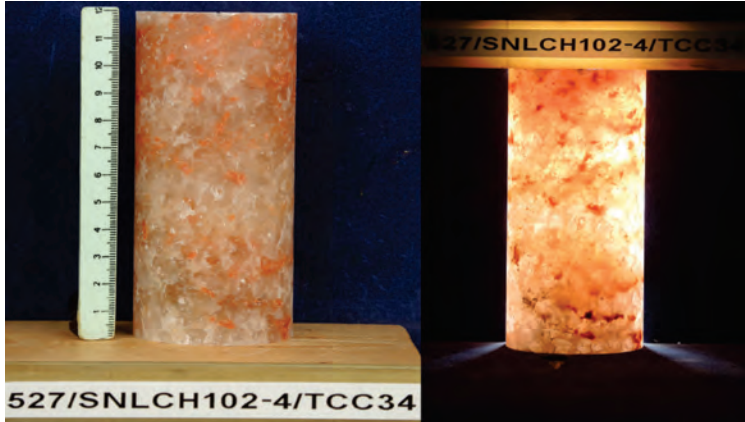
Figure 3: Sample for TCC34 ("clean salt" from WIPP; representative grain sizes in the range of several millimetres to a centimetre)

The test has been running for almost five years and is still ongoing. It started with two consolidation stages at an isotropic stress of 20 MPa at 298 K and 393 K, with durations of about 50 and 80 days. The load of 4 MPa was applied by raising the axial stress (keeping the confining stress at 20 MPa), the initial loading stage at 393 K ran for approximately 110 days. In the following stages, temperature was reduced to 373 K, 353 K, 333 K, and 313 K. To validate the underlying procedure, a number of steps was repeated afterwards – a temperature increase to 333 K, a further isotropic stage and another loading at 4 MPa, and two temperature stages at 353 K and 373 K. The development of (true or logarithmic) strain over time is plotted in Figure 4. (In Figure 4 and later plots, dashed lines indicate isotropic-stress stages, solid lines stages with 4 MPa of deviatoric stress, and colours denote the temperature).
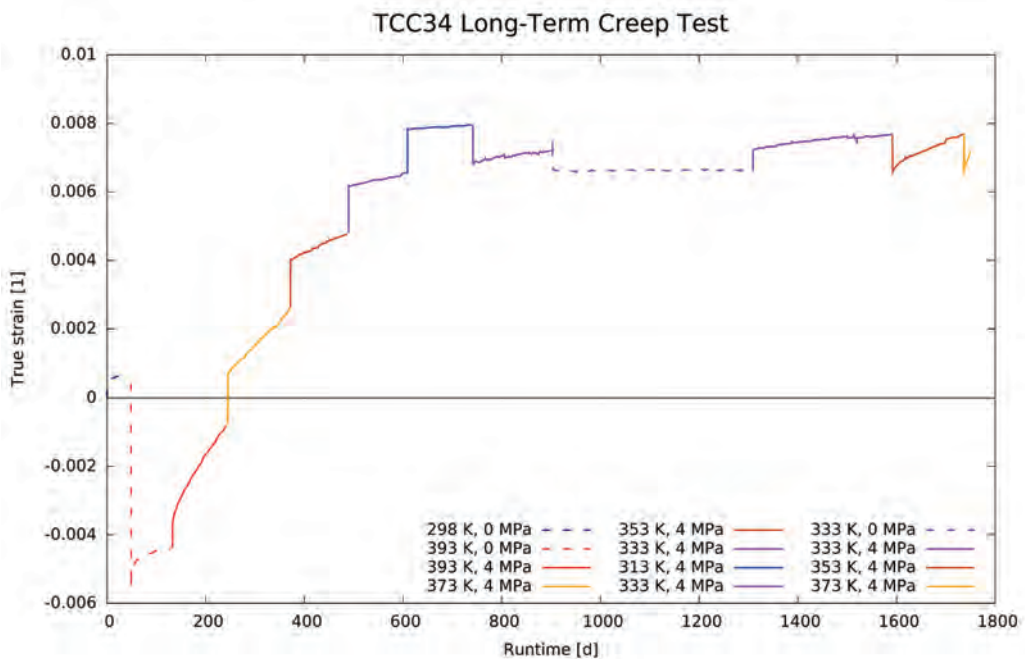
Figure 4: Deformation over time for TCC34.

In Figure 4, the deformation jumps at the points where the temperature changes due to the thermal expansion of sample and cell (the temperature changes take approximately seven hours). In Figure 5, the same data is plotted with temperature correction, showing only the creep deformation of the sample. Note that over 1750 days, the sample has accumulated a deformation of slightly more than 1%. The temperature dependence of the creep rate is clearly visible.
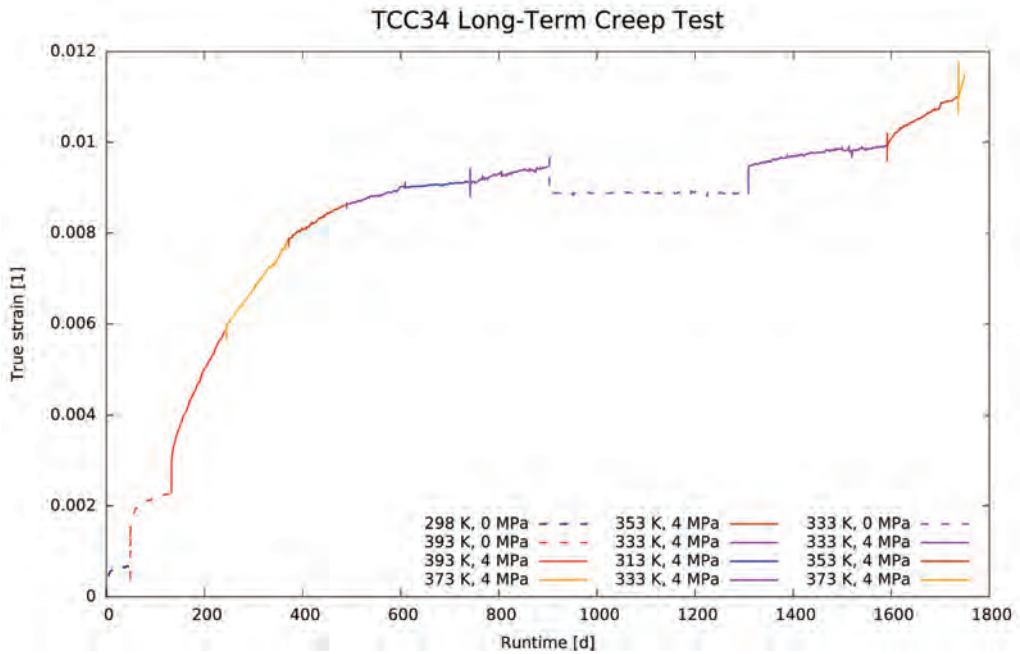
Figure 5: Temperature-corrected data for TCC34

To check the validity of the test procedure, we first analyse the isotropic phases. Figure 6 shows the consolidation and the second isotropic stage from $t = 903$ d to 1309 d. At the end of the consolidation phase, i.e. after more than 120 days, there is still a residual creep rate of 3.4×10^{-6}/d $= 3.94 \times 10^{-11}$/s. Note, however, that this is at 393 K, and the stationary rate in the following load step is an order of magnitude larger at 2.04×10^{-5}/d $= 2.36 \times 10^{-10}$/s. In the second isotropic phase, there is no significant deformation anymore (note the small scale on the vertical axis in the right panel of Figure 6).
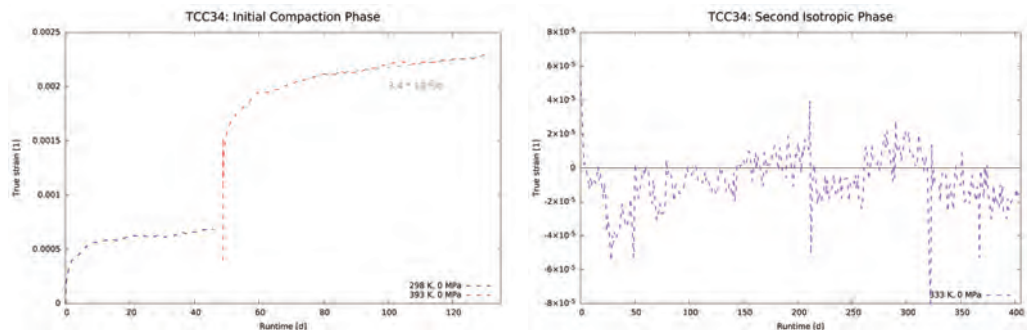
Figure 6: Isotropic phases of TCC34. Consolidation (left) and second phase (right).

During the test, there were two completed creep phases at $353\,\text{K}$ and three at $333\,\text{K}$. We should expect very similar creep rates with small transients; Figure 7 shows the results of the temperature stages, relative to the strain and time at the beginning of a given stage. The diagrams show that the individual stages line up well for both cases, except for a short transient phase of about 20 days for $353\,\text{K}$.
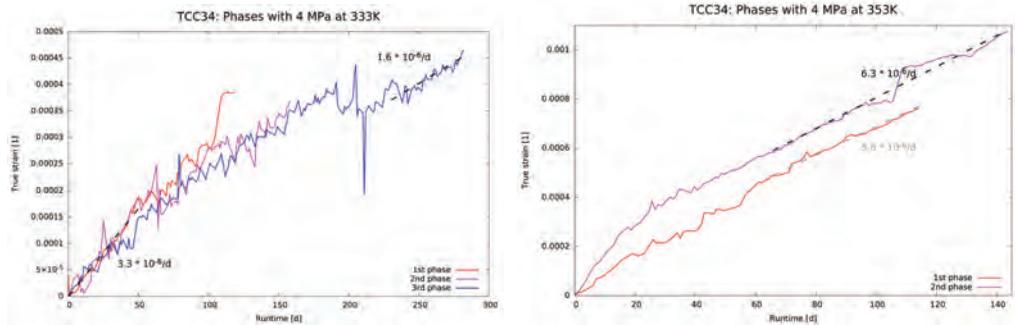
Figure 7: Phases with 333K (left), 353K (right)

We summarise the creep rates in Table 1.

Table 1: Creep rates at deviatoric stress of $4\,\text{MPa}$ for different temperatures from long-term test TCC34

Temperature	Stationary creep rate	
K	$10^{-6}/d$	$10^{-11}/s$
393	20.4	23.6
373	15.0	17.4
353	6.3	7.29
333	1.6	1.85
313	0.96	1.11

To assess the temperature dependence, the Arrhenius plot is shown in Figure 8. The data points are to a good approximation described by a straight line corresponding to an activation energy of $42\,\text{kJ/mol}$. Note that a value of $54\,\text{kJ/mol}$, as it is often assumed for dislocation creep, is clearly disfavoured by the data. This is consistent with the transition from dislocation to dissolution-precipitation creep, for which an activation energy of $25\,\text{kJ/mol}$ has been determined (in artificial crushed salt; Spiers et al. 1990). This, together with the clear transient phase in the first load stage, suggests that for a deviatoric stress of $4\,\text{MPa}$ in the temperature range considered here, rock salt could be in the transition region where both dislocations and dissolution-precipitation contribute to creep deformation.
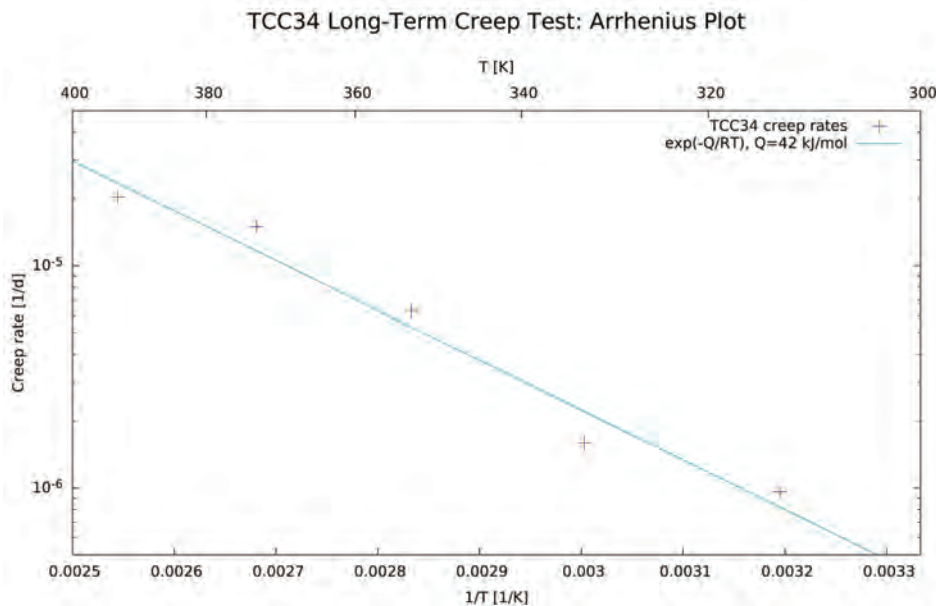
Figure 8: Logarithmic plot of the stationary creep rates versus inverse temperature. The temperature dependence of the creep rates is well described by an Arrhenius term with activation energy of $Q = 42$ kJ/mol.

6   Conclusions and Outlook

The long-term behaviour of waste repositories in rock salt, as well as that of mines and caverns, is dominated by creep at low deviatoric stresses, below, e.g., 6 MPa (Herchen et al. 2018; Hampel et al. 2022). However, the creep behaviour of natural rock salt is not well tested, and creep laws cannot be properly validated, in this range.

It is expected that for low stress, the dominant creep mechanism changes from dislocation motion to grain-boundary dissolution-precipitation processes (Carter et al. 1993; Hunsche, Schulze 1994; Urai et al 1986; Schleder, Urai 2005), which show a weaker stress and temperature dependence. The currently available data supports enhanced creep rates at low stress. However, data is scarce, and there are considerable uncertainties. Hence, while modern constitutive models include creep laws that allow for larger low-stress creep rates, a reliable derivation of parameter sets for specific rock salt varieties is currently not possible.

In this paper, we have presented an experimental procedure to measure creep rates at low stress. The key ingredients are

- triaxial tests at high confining stress to suppress dilatancy,
- an initial long isotropic compaction phase at high temperature to consolidate the sample,
- a first deviatoric load stage at high temperature to accelerate the transient phase,
- and subsequent temperature reduction steps at constant deviatoric stress to obtain several stationary creep rates from one sample.

Since the dislocation structure, which is primarily responsible for transient creep, only weakly depends on temperature, the later load stages show essentially no new transients. This test procedure should allow for a faster and more reliable determination of creep rates and

activation energies in the low stress regime and thus help to validate creep laws and determine parameter sets. The long-term geomechanical behaviour of excavations in rock salt can thus be predicted with greater confidence.

We have performed a long-term test at a deviatoric stress of 4 MPa. The results show that repeated stages are consistent and that there are only small transient phases. The test thus validates the proposed procedure.

Acknowledgements

References

BÉREST, P., GHARBI H., BROUARD B., HOFER G., STIMMISHER S., BRÜCKNER D., DE VRIES K. & HÉVIN G. 2017. Very Slow Creep Tests as a Basis for Cavern Stability Analysis. SMRI Research Report RR2017-1

BÉREST, P., GHARBI, H., BROUARD, B., HOFER, G., STIMMISHER, S., BRÜCKNER, D., DE VRIES, K., HÉVIN, G., URAI, J., SPIERS, C. & PEACH, C. 2020. Very Slow Creep Tests as a Basis for Cavern Stability Analysis – Phase 2. SMRI Research Report RR2020-1

CARTER, N.L., HORSEMAN, S.T., RUSSELL, J.E. & HANDIN, J.1993. Rheology of rocksalt. Journal of Structural Geology 15(9/10):1257-1271

GHARBI, H., BÉREST, P., BLANCO-MARTÍN, L. & BROUARD, B. 2020. Determining upper and lower bounds for steady state strain rate during a creep test on a salt sample. Int. J. Rock Mech. Min. Sci.

GÜNTHER, R.M., SALZER, K., POPP, T. & C. LÜDELING, 2015. Steady-State Creep of Rock Salt: Improved Approaches for Lab Determination and Modelling. Rock Mech Rock Eng 48, 2603–2613 (2015).

HAMPEL, A., LÜDELING, C., GÜNTHER, R.M., SUN-KURCZINSKI, J.Q., WOLTERS, R., DÜSTERLOH, U., LUX, K.H., YILDIRIM, S., ZAPF, D., WACKER, S., EPKENHANS, I., STAHLMANN, J. & REEDLUNN, B. 2022. WEIMOS: Simulations of two geomechanical scenarios in rock salt resembling structures at WIPP. In: S. Hangx et al. (eds.), The Mechanical Behavior of Salt X. (this volume)

HERCHEN, K., POPP T., DÜSTERLOH, U., LUX, K.H., SALZER, K., LÜDELING, C., GÜNTHER, R.M., RÖLKE, C., MINKLEY, W., HAMPEL, A., YILDIRIM, S., STAUDTMEISTER, K., GÄHRKEN, A., STAHLMANN, J., REEDLUNN, B.& HANSEN, F.D. 2018. WEIMOS: Laboratory Investigations of Damage Reduction and Creep at Small Deviatoric Stresses in Rock Salt. In: S. Fahland et al. (eds.), The Mechanical Behavior of Salt IX.

HUNSCHE, U. & SCHULZE O. 1994. Das Kriechverhalten von Steinsalz. Kali und Steinsalz 11 (8/9) 1994

HUNSCHE, U. & SCHULZE, O. 2002. Humidity induced creep and its relation to the dilatancy boundary. In: N.D. Cristescu, H.R. Hardy, Jr. & R.O. Simionescu (eds.): Basic and Applied Salt Mechanics, Proc. 5th Conf. on the Mechanical Behavior of Salt, Bucharest/Romania, 1999, pp. 73-87, Swets & Zeitlinger (A.A. Balkema Publishers), Lisse, ISBN 90 5809 383 2.

KOCK, I., EICKEMEIER, R., FRIELING, G., HEUSERMANN, S., KNAUTH, M., MINKLEY, W., NAVARRO, M., NIPP, H.K. & VOGEL, P. 2012. Integritätsanalyse der geologischen Barriere. Bericht zum Arbeitspaket 9.1. Vorläufige Sicherheitsanalyse für den Standort Gorleben. GRS-

286. ISBN 978-3-939355-62-5. Gesellschaft für Anlagen- und Reaktorsicherheit (GRS) mbH, Köln.

LÜDELING, C., K., SALZER, R.M., GÜNTHER, A., HAMPEL, S., YILDIRIM, K., STAUDTMEISTER, A., GÄHRKEN, J., STAHLMANN, K., HERCHEN, K.H., LUX, B., REEDLUNN, S., SOBOLIK, F.D. & HANSEN, S.A. 2018. WEIMOS: Joint project on further development and qualification of the rock mechanical modelling for the final HLW disposal in rock salt Overview and first results on tensile stress modelling. In: S. Fahland et al. (eds.), The Mechanical Behavior of Salt IX.

MELLEGARD, K.D. & PFEIFLE, T.W. 1993. Creep Tests on Clean and Argillaceous Salt from the Waste Isolation Pilot Plant. Contractor Report, SAND92-7291, RE/Spec Inc., Rapid City, May 1993

REEDLUNN, B., ARGÜELLO, J.G. & HANSEN F.D. 2022. A Reinvestigation into Munson's Model for Room Closure in Bedded Rock Salt. International Journal of Rock Mechanics and Mining Sciences. (Accepted)

SALZER, K., GÜNTHER, R.M., MINKLEY, W., NAUMANN, D., POPP, T., HAMPEL, A., LUX, K.H., HERCHEN, K., DÜSTERLOH, U., ARGÜELLO, J.G. & HANSEN, F.D. 2015. Joint project III on the comparison of constitutive models for the mechanical behavior of rock salt, II. Extensive laboratory test program with clean salt from WIPP. L. Roberts, K. Mellegard & F. Hansen (eds.): The Mechanical Behavior of Salt; Proc. 8th Conference, South Dakota School of Mines & Technology, Rapid City, SD, USA, 26-28 May 2015, 3-12, Taylor &Francis Group, London, ISBN 978-1-138-02840-1.

SCHLEDER, Z. & URAI J.L. 2005. Microstructural evolution of deformation- modified primary Halite from Hengelo, the Netherlands. International Journal of Earth Sciences 94(5-6): 941-956.

SPIERS, C.J., SCHUTJENS P. M. T. M., BRZESOWSKY R. H., PEACH C. J., LIEZENBERG J. L. & ZWART H. J. 1990. Experimental determination of constitutive parameters governing creep of rocksalt by pressure solution, in: Deformation Mechanisms, Rheology and Tectonics, edited by R. J. Knipe, and E. H. Rutter, Geol. Soc. Spec Publ., 54, 215–227, 1990.

URAI, J.L., SPIERS, C.J., ZWART, H.J. & LISTER, G.S. 1986. Weakening of Rock Salt by Water During Long-Term Creep. Nature 324: 554-557

A composite flow law for wet polycrystalline halite to capture the transition from dislocation creep to solution-precipitation creep

N. Muhammad[1]*, J.H.P. de Bresser[2], C.J. Peach[2], C.J. Spiers[2]

[1][1]Center for Advanced Studies in Physics, GC University Lahore, Pakistan; [2]Experimental Rock Deformation Laboratory, Department of Earth Sciences, Utrecht University, the Netherlands

* nawazmuhammad@gcu.edu.pk

ABSTRACT: For wet or dry polycrystalline halite, the creep behaviour observed in laboratory experiments at relatively high temperatures and strain rates is generally considered to be controlled by dislocation mechanisms. For fine grained wet materials at low temperature and strain rates, solution-precipitation creep is suggested to dominate. We studied if the transition between these mechanisms can be observed in laboratory experiments, and if so, at what strain rate. We used synthetic and natural wet polycrystalline halite (starting grain sizes ~0.3 and ~4.0 mm, respectively), and deformed these in multiple strain rate step experiments at *in situ* PT conditions of 50 MPa and 125 °C. We also applied the stress relaxation technique, to achieve strain rates approaching 10^{-9} s^{-1}. For higher stresses and strain rates, we found a power law stress exponent *n~11*, while towards lower stress and strain rate, the *n*-value decreased to ~1. This transition took place over the strain rate interval 10^{-8}-10^{-9} s^{-1}. We interpret this behaviour as a transition from glide-controlled dislocation creep at high *n* to solution-precipitation creep at *n~1*, made possible by grain size adjustment through fluid-assisted dynamic recrystallization. We defined a first-order creep law combining a power law and a solution-precipitation law to cover the transition.

1   Introduction

The mechanical behaviour of halite has been studied extensively before in the laboratory; both for dry (<10 ppm by weight) and wet (>10 ppm by weight) conditions, at different temperatures and pressures (Heard 1972; Heard & Ryerson 1986; Wawersik & Zeuch 1986; Spiers et al. 1990; Senseny et al. 1992; Peach et al. 2001; Ter Heege et al. 2005a). For dry conditions, Carter & Hansen (1983), suggested dislocation climb process as rate controlling mechanism, Franssen (1994) concluded that at laboratory strain rates and relatively low temperatures, 250-450 °C, the behaviour is best explained by climb-controlled dislocation creep with climb itself being governed by diffusion through dislocation cores, while at higher temperatures, 500-780 °C, lattice diffusion-controlled creep is dominant. Muhammad (2015) performed pressure stepping tests to investigate the creep behaviour of dry halite in the temperature range 22-350 °C, where a transition was observed from glide to dislocation climb. For wet conditions, several authors have suggested that under laboratory conditions of temperature 23-500 °C, dislocation creep is the main mechanism controlling creep (Heard 1972; Heard & Ryerson 1986; Carter et al. 1993) while other authors concluded that if grain size is small and temperature is low, solution-precipitation creep plays an important role (Spiers et al. 1990; Urai et al. 1986). Ter Heege et al. (2005b) argued based on an experimental study that in wet polycrystalline halite, both dislocation and solution-precipitation mechanisms might contribute to the overall deformation, provided that microstructural modification processes such as dynamic recrystallization and grain growth can take place freely.

Salt rocks in nature are wet rather than dry (Roedder & Bassett 1981; Urai 1983). The creep of these salt rocks usually occurs at strain rates in the range of 10^{-8} to 10^{-15} s^{-1} (Heard 1972; Van Eekelen 1981; Jackson & Talbot 1986). To fully understand the creep behaviour of halite under natural conditions, it thus is of importance to not only know, in general, which mechanisms may control creep of halite, i.e. dislocation vs. solution-precipitation mechanisms, but also to be able to constrain the strain rates under which a given mechanism prevails. The

strain rates relevant for *in situ* deformation, 10^{-8} to 10^{-15} s^{-1}, are difficult to achieve in laboratory experiments. However, one way of approaching such slow strain rates is to perform stress-relaxation experiments (Rutter & Mainprice 1978). In this technique, strain rates as slow as 10^{-9} s^{-1} can be achieved by allowing the stress on a sample to relax through plastic deformation. The experiments are time consuming but result in valuable data regarding creep behaviour at low stresses and slow strain rates.

2 Method

2.1 Sample preparation

In this study, synthetic as well as natural salt samples were used. All samples were manufactured such that they became cylindrical with length in the range of 80-85 mm and diameter 35-36 mm. The synthetic rock salt sample (halite1) was prepared in the laboratory starting from analytical grade NaCl powder from Merck, with an average particle size of 200-400 μm. The powder salt was cold pressed in a hardened steel, piston-cylinder assembly. The powder was axially pressed at 200 MPa for 20 minutes. The resulting cylindrical sample was sealed in a Viton rubber sleeve and was put in a silicone oil pressure vessel for annealing under 100 MPa confining pressure and a temperature of 150 °C for one week. The sample thus obtained had a theoretical density (mass to volume ratio) of 99.5%. For more details about the sample preparation technique, see (Peach 1991). Two natural halite samples (halite2 and 3) were prepared from 'Speisesalz' cores. These cores came from the Asse mine, Germany, and were taken from the ~800 m gallery level and from a depth of > 3 m inside the horizontal gallery wall (Peach 1991, Urai et al. 1987). The samples had a grain size in the range of 3-10 mm. The constituents of the cores were mainly halite (> 98%), a small amount of poly-halite ($K_2SO_4.MgSO_4.2CaSO_4.2H_2O$; ~1%), and some minor quantity of anhydrite. To create a deliquescence condition in our samples, comparable to that at *in-situ,* all samples were moisturized with water < 0.5 wt.% using atomizer in a chamber and carefully measured for its mass increase. These samples were further sealed in 1.0 mm thick polymer "ethylene propylene diene monomer (EPDM)" jackets to avoid contamination of the samples by the confining medium (silicone oil) used in the deformation apparatus.

2.2 Deformation apparatus

The apparatus used for this study was the so-called "Shuttle Vessel" of the experimental rock deformation (HPT) laboratory at the department of Earth Sciences at Utrecht University, also used in a second study of us in this volume The Shuttle Vessel machine is an internally heated 100 MPa confining pressure vessel mounted on a standard 100 kN Instron 1362 loading frame with an electro-mechanical servo-controlled positioning system. The machine is provided with a (Instron standard, +/-50 mm) linear variable differential transformer (LVDT), but to come to an accurate measurement of the sample deformation, a second LVDT (0-25 mm range, H.F. Jensen, Denmark) was installed at the top of the vessel and near the sample. This was done to reduce the effect of the elastic distortion of the apparatus and measure accurately the shortening of the sample, especially during stress relaxation, where very limited natural strain in the order of 0.001 is to be monitored. The temperature was measured by thermocouples at two locations inside the vessel; one was positioned close to the middle of sample and, the other was at the top of the sample. K-type thermocouples were used, which are accurate within ±1 °C. The confining pressure was created by using silicone oil which is kept at constant pressure within ±0.1 MPa using a servo pump. Measurement of the pressure was done using a diaphragm pressure transducer (Teledyne 2403, 100 MPa range). The triaxial apparatus used is very sensitive to the environmental conditions. Therefore, it was carefully calibrated for the effect of pressure and temperature on the load cell.

2.3 Experiments

In total three multistep experiments were performed; one on synthetic (halite1) and two on natural (halite2 and 3) samples. A typical experiment consisted of a few steps at constant strain rate, in the range 5×10^{-5} to 5×10^{-8} s^{-1}. During the constant strain rate part of the test, the sample was deformed until a steady (or near steady) state of stress was reached. Then the piston was arrested and the stress on the sample was allowed to relax until the diminishing force on the sample reached the limits of the load cell resolution. The duration of each relaxation step was a few days.

The synthetic sample, halite1, was deformed by a 3-step repetitive strain rate of 5×10^{-7} s^{-1}, for a natural strain of 0.01-0.03 per step and each step was followed by stress relaxation. The natural samples, halite2 and 3, were tested in a seven strain rate steps (5×10^{-5}, 5×10^{-6}, 5×10^{-7}, 5×10^{-8}, 5×10^{-7}, 5×10^{-6}, 5×10^{-5} s^{-1}), and the relaxation was followed the constant strain rate parts of 5×10^{-6}, 5×10^{-8} and 5×10^{-6} s^{-1}. The experiments were performed at 125 °C sample temperature and 50 MPa confining pressure (a value where dilatancy/microcracking is suppressed, Peach 1991).

2.4 Data acquisition and processing

The data containing pressure, temperature, load, and position (LVDT_1 and 2) were logged throughout the test. The stress on the sample was calculated from the load values by assuming constant volume deformation, correcting the instantaneous change in area value for progressive change in length of the sample. The cumulative strain (shortening) of the sample was calculated as the natural strain, i.e. the natural logarithm of the ratio of the final length and the initial length (shortening taken as positive). The data acquired during stress relaxation was analysed with a dedicated code to produce the plastic strain rate of the sample.

The stress relaxation technique is based on the following. During deformation at constant rate (imposed by a moving piston), some energy gets stored inside the material as elastically stored energy. During relaxation, when the loading piston is arrested, this energy is dissipated through plastic deformation of the sample. Additionally, the elastically stored energy inside the active part (under force) of the machine also dissipates through the plastic strain of the sample, so the data also need to be corrected for the stiffness of machine. To calculate the sample straining, we take the simple assumption that the stress is proportional to strain, provided that other physical conditions (confining pressure, temperature, microstructure) are constant (Rutter & Mainprice 1978). The strain rate at any instant will then be proportional to the stress relaxation rate, with the elastic (Young's) modulus of sample as a constant of proportionality.

The measured total displacement "x_{total}" (from LVDT_2) can be written as the sum of the sample deformation (elastic + plastic) and elastic distortion of apparatus

$$x_{total} = x_{sample} + x_{apparatus} \qquad (1)$$

After differentiating time and normalizing this equation using the instantaneous length of the sample, the following relation of plastic strain rate of the sample is obtained:

$$\dot{\varepsilon}_{plastic} = \dot{\varepsilon}_{total} - \frac{1}{E_{sample}}\left(\dot{\sigma}_{sample}\right) - \frac{1}{L_t}S\left(\frac{\partial F}{\partial t}\right) \qquad (2)$$

where,

$\dot{\varepsilon}_{plastic}$ = plastic strain rate of sample [s^{-1}]
$\dot{\varepsilon}_{total}$ = total strain rate measured by LVDT_2 [s^{-1}]
E_{sample} = Young's modulus of sample [MPa]
$\dot{\sigma}_{sample}$ = sample stress relaxation rate [MPas^{-1}]
L_t = instantaneous length of sample [m]
S = machine stiffness correction constant [mN^{-1}]
$\left(\frac{\partial F}{\partial t}\right)$ = rate of change of force [Ns^{-1}]

3 Results

3.1 Stress vs natural strain and time

The synthetic salt sample, halite1, was deformed in three steps using a similar strain rate of 5×10^{-7} s^{-1}. In each step, the sample was deformed through a very limited amount of natural strain of 0.015-0.02. The stress-strain curve of Figure 1a shows that steady state was not reached in any of the three steps, but the strain hardening rate appears to decrease with increasing strain.

The natural salt samples, halite2 and 3 were deformed in 7-steps (see Table 1 for details), adding 0.025-0.03 strain at each step. The strength of the natural halite samples is almost twice that of the synthetic salt, at strain rate 5×10^{-7} s^{-1}. Steady state was not reached in any of the strain rate steps. The rate of strain hardening differed depending on the strain rate and appeared higher at the higher rates. For the slowest deformation step, 5×10^{-8} s^{-1}, a few stick slip events, due to high friction between deformation piston and seal, were also observed, as seen by the irregular nature of the stress-strain curve.

Although the hardening rate per individual step in strain rate could be established, for both the synthetic and the natural samples, the data were insufficient to uncover a robust trend in changing hardening rate when going from one strain rate to the other. This hampered reliable extrapolation to higher strain, preventing a comparison of differential stress as a function of strain rate at the same strain. Thus, in Table 1, only the values of the differential stress at the end of each step are given.

Table 1: Mechanical data

Sample	$\dot{\varepsilon}$ [s^{-1}]	ε_a	σ [MPa]
Halite1	5×10^{-7}	0.01	7.7
	5×10^{-7}	0.03	8.7
	5×10^{-7}	0.05	9.2
Halite2	5×10^{-5}	0.04	22.6
	5×10^{-6}	0.07	21.9
	5×10^{-7}	0.11	16.0
	5×10^{-8}	0.13	13.1
	5×10^{-7}	0.15	15.7
	5×10^{-6}	0.17	20.3
	5×10^{-5}	0.21	21.1
Halite3	5×10^{-5}	0.04	21.8
	5×10^{-6}	0.07	20.9
	5×10^{-7}	0.10	15.3
	5×10^{-8}	0.13	11.9
	5×10^{-7}	0.16	15.2
	5×10^{-6}	0.18	19.5
	5×10^{-5}	0.22	21.9

$\dot{\varepsilon}$ is the deformation strain rate
ε_a is the natural axial strain at the end of the particular step
σ is the differential stress value at the end of the deformation step

(a)　　　　　　　　　　　　　　(b)
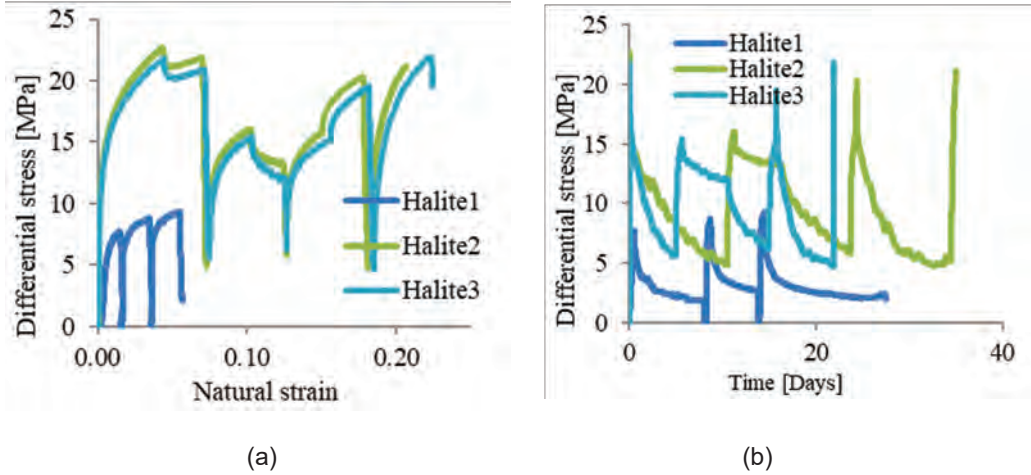
Figure 1: Strain rate stepping deformation of halite samples showing differential stress against a) natural strain and b) time

3.2　n-value for natural halite

The dependence of the differential stress on the strain rate for the natural halite samples (Fig. 2) was tested by applying a conventional power law creep of the type $\dot{\varepsilon} = A\sigma^n$, where $\dot{\varepsilon}$ is the strain rate, σ is the flow stress, and A and n are constants. Since both halite2 and 3 presented substantial strain hardening, any estimate of the constants A and n can only give a first-order impression of the creep behaviour of the material. The data were divided into two parts, for both halite2 and 3; step1 to step4 (decreasing strain rate) and step4 to step7 (increasing strain rate). Linear regression analysis in log-log space resulted in high n-values, ranging 10.8-13.6 (Figs. 2(a-b)). Note that the strain rate is the independent variable, but it is shown as dependent in the Figure 2 (i.e. on Y-axis) to compare with the stress relaxation curves (Figs. 3(a-c)).

(a)　　　　　　　　　　　　　　(b)
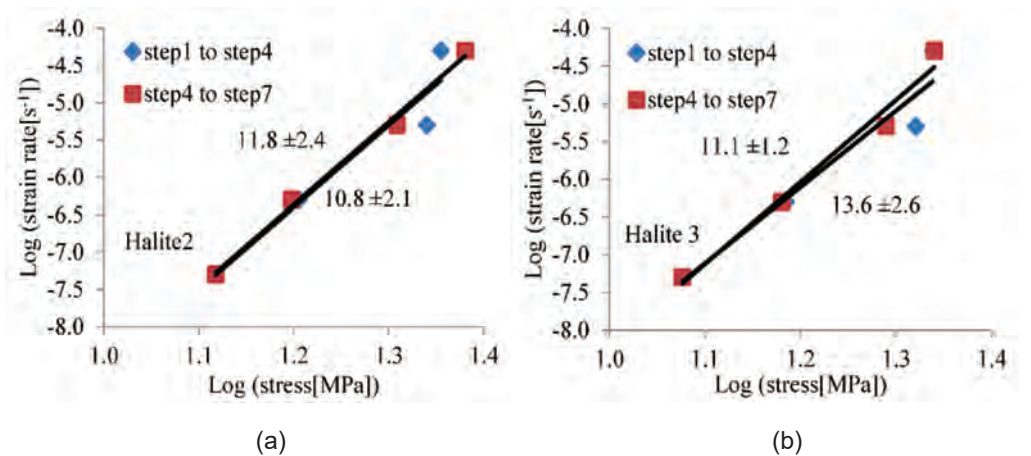
Figure 2: Log-log plot of strain rate vs. differential stress using the maximum differential stress values at the end of each step. Best fit lines to the data of **a)** halite2 and **b)** halite3, represent power law fits, with corresponding n-values indicated.

3.3 Stress relaxation

The stick slip events between deformation piston and seal were more conspicuous during stress relaxation than during deformation. Such events caused great noise in the signal of the measured displacement and, hence, resulted in substantial scatter in calculated strain rate, so the mode values were used instead. Moreover, the relaxation behaviour of all samples appeared identical and we have selected only three as representatives. These are plotted in Figures 3(a-c). The steady state/maximum stress values obtained at the end of each strain rate deformation steps are marked in the graphs along with the projected slopes representing
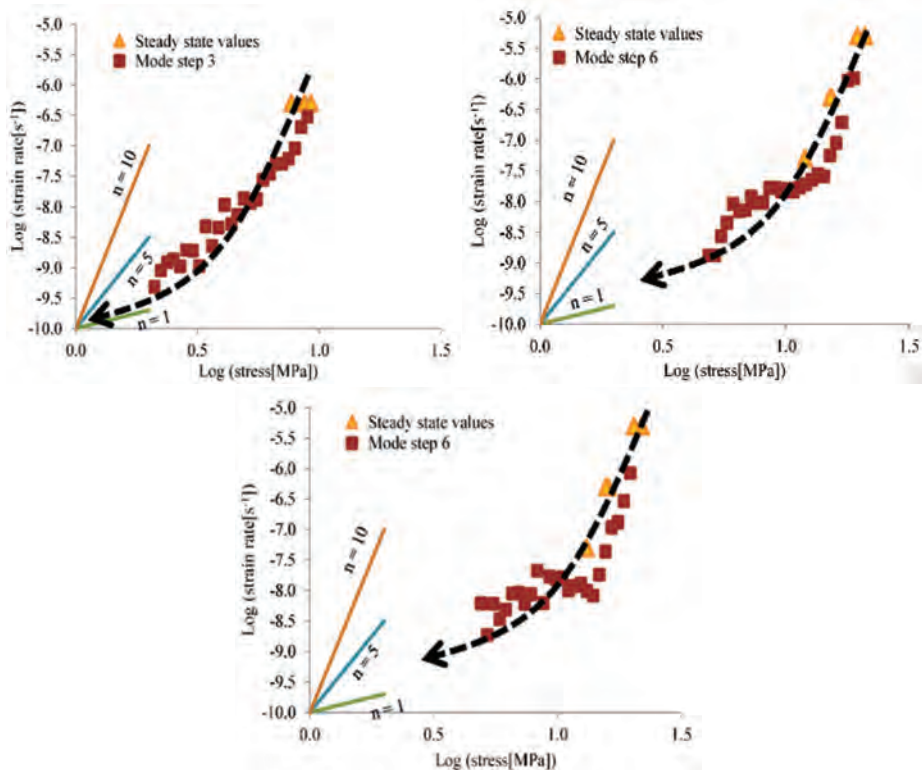
Figure 3: Log-log plot of strain rate vs. differential stress including the results of stress relaxation steps. Closed triangles are the steady state/maximum differential stress values obtained at the end of each step, closed squares are the mode values of the calculated strain rate data. Three slopes representing the n-values of 1, 5 and 10 are included to be compared with the trend during relaxation, represented by the free-hand drawn dashed line. Top left: halite1, Top right: halite2, Bottom: halite3

the stress exponent n-values ($n = 1$, 5 and 10) according to scale. Generally, the graphs show that the calculated plastic strain rate at the start of each relaxation period fits to a trend with high n-value (>10), implying that the stress is not very sensitive to strain rate. Progressively, the sensitivity increases and the corresponding n-value approaches $n = 1$ for lower stress and slow strain rate values near end of each relaxation step. A free hand dashed-line drawing, showing trend of relaxation is also plotted along to show the expected trend during relaxation.

4 Discussion

The aim of this study was to investigate if a transition can be observed from creep behaviour of halite governed by dislocation mechanisms to creep behaviour controlled by a solution-

precipitation mechanism, and if so, what the conditions of this transition are in terms of strain rate. Below, we will discuss our observations and compare the strength of the halite and its change with decreasing strain rate with the mechanical behaviour established in other studies.

4.1 *n*-value

Fitting the stress-strain rate data obtained during the constant strain rate parts of the multi-step experiments to a conventional power law creep of the type $\dot{\varepsilon} = A\sigma^n$ resulted in a value for *n* larger than 10. Although steady state was not fully reached during the steps, the decrease in strain hardening rate is such that the high *n* values are likely to remain robust at higher strains. Microphysical models for creep controlled by dislocation climb generally result in power law creep equations (Muhammad 2015), but the values for *n* usually range 3-4.5 for climb controlled by lattice diffusion, or up to 6.5 in case of climb controlled by dislocation core (pipe) diffusion (Franssen 1994; Carter et al. 1993; Urai et al. 1987). The value of *n* > 10 appears to rule out climb control for the creep behaviour of wet polycrystalline halite for the conditions tested. Rather, a glide or cross-slip controlled creep model may apply (Spiers et al. 1986). Muhammad (2015) presented results on dry rock salt and showed a low sensitivity of the stress on the strain rate like the wet halite reported here, at comparable conditions of temperature and pressure, at 125 °C and 50 MPa. For the dry halite, it was concluded that a glide mechanism (Weertman 1957; Poirier 1985) rather than a cross slip mechanism (Auten et al. 1973; Skrotzki et al. 1981) controls flow at the given conditions. We infer that the conclusion regarding glide control also holds for the current wet halite.

The stress relaxation behaviour of the wet halite (Figs. 3(a-c)) shows that the *n*-value gradually decreases with decreasing stress and strain rate, reaching ~1 at strain rates below 10^{-8} s^{-1}. This trend is observed in both synthetic and natural halite samples. This strongly suggests that a transition takes place towards grain size sensitive (GSS) creep (Spiers et al. 1990; Ter Heege et al. 2005a; Ding et al. 2021).

If we compare our work with previous studies on halite by using their flow laws (Heard 1972; Wawersik & Zeuch 1986; Ter Heege et al. 2005a; Carter et al. 1993) for 125 °C, we see in Figure 4a that the current data on natural halite2 and 3 have got the upper limit by Wawersik et al. (Wawersik & Zeuch 1986) (unknown water content) and Ter Heege et al. (2005a) (wet), whereas Carter et al. (1993) (dry) gives the lower bounds. The data of synthetic sample halite1 show weaker behaviour and lie in approximation of Wawersik & Zeuch (1986)] and Ter Heege et al. (2005a).

(a) (b)
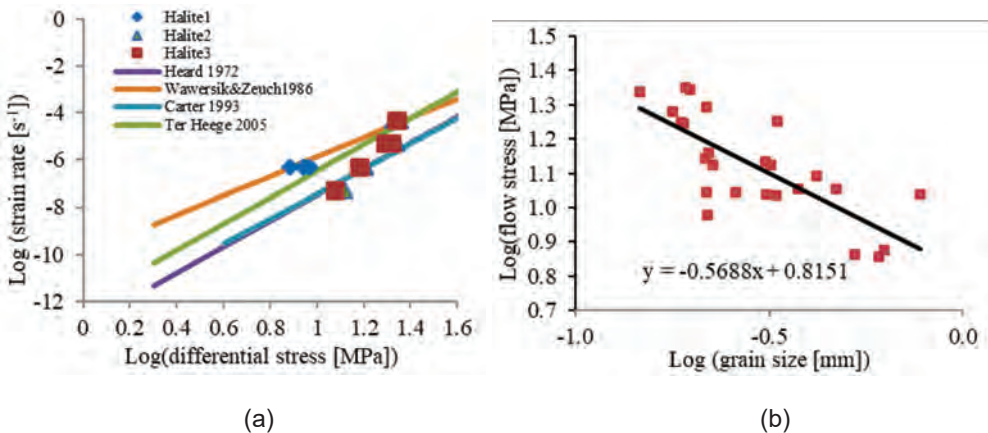
Figure 4: a) Log-log plot of strain rate vs. differential stress, comparing the current results with the results of previous studies on wet and dry halite at 125 °C. (Heard 1972; Wawersik & Zeuch

1986; Carter et al. 1993; Ter Heege et al. 2005a), b) Log-log plot of differential stress vs. grain size for wet synthetic halite (Ter Heege et al. 2005b)

4.2 Composite flow law

Provided physical conditions (like pressure and temperature) are fixed, the microstructure of the sample may be expected to remain constant during stress relaxation with limited straining (Rutter & Mainprice 1978) while processes such as dynamic (syn-deformational) recrystallization and grain growth are likely to affect the microstructure during deformation that results in substantial increase in strain. The relaxation data show that the dependence of strain rate on stress approaches linearity at low stress and slow strain rate, which observation has been used above to suggest that grain size sensitive behaviour might play a role.

We thus consider if the flow behaviour of wet halite can be described by a composite flow equation of grain size insensitive (GSI) and grain size sensitive (GSS) behaviour

$$\dot{\varepsilon} = A^* \sigma^n + B^* \sigma d^{-p} \tag{3}$$

where $\dot{\varepsilon}$ is the strain rate, σ the differential stress, A^* and B^* are constants at a given temperature, n is the stress exponent, d is the grain size and p is the grain size exponent.

To evaluate Equation (3), we need to estimate what the grain size was during deformation of our halite samples. We do this by using a conventional piezometric relation, allowing predicting what the dynamically recrystallized grain size was at a certain stress value (De Bresser et al. 2001)

$$d = K \sigma^{-m} \tag{4}$$

where K and m are material and mechanism specific constants. This relationship between stress and recrystallized grain size is generally assumed to be independent of temperature, although that there is evidence that this assumption is not generally valid.

Ter Heege et al. (2005b) established a piezometric relation between the grain size d and differential stress σ by measuring the grain size of experimentally deformed synthetic halite
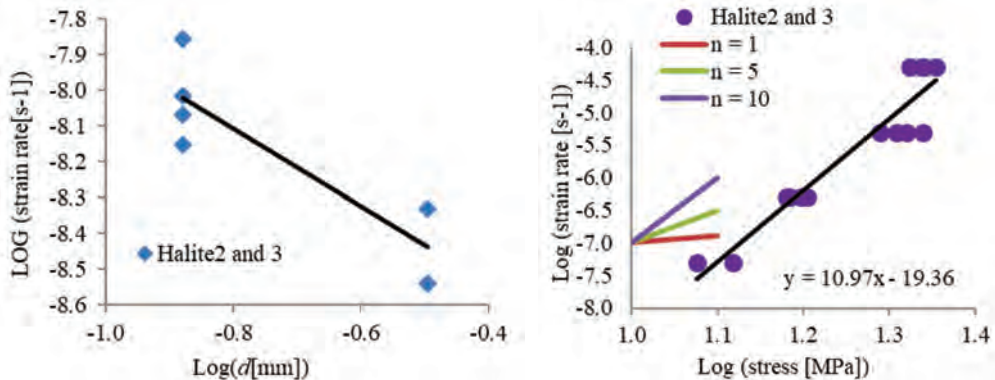
Figure 5: a) Strain rates picked from relaxation curves at fixed stress value (σ =6.3[MPa]) against the recrystallized grain size calculated using the piezometer relation of Eq. 5, b) Log-log plot for conventional power law ($\dot{\varepsilon} = \sigma^n$). The slope of the curve represents the stress exponent n-value. Three slopes lines corresponding to n = 1, 5 and 10 are also projected according to scale. The slope of halite2 and 3 combined data is very high (i.e. $n \sim 11$).

samples. The data by the authors are shown in the Figure 4b along with the best fit linear trend. The halite samples tested here (halite2 and 3) are natural salt samples, but we assume that

the same piezometer relation holds at current conditions of temperature and pressure; 125 °C and 50 MPa respectively.

Using the slope and intercept values of the best fit line in Figure 4b, we obtained values for K and m as 27.1 and 1.75 respectively, so the Equation (4) reduces to

$$d = 27.1\sigma^{-1.76} \tag{5}$$

The values of d represent the grain sizes at the end of the constant strain rate parts of the experiments, and hence, the grain sizes at the start of the relaxation parts. Assuming now that the microstructure remains constant during relaxation, these are the grain sizes applicable at the behaviour at $n \approx 1$. This allows us to estimate the p-value of Equation (3), in which stress is linearly dependent on strain rate. Taking logarithms and simplifying Equation (3), we get

$$log\dot{\varepsilon} = (logB^* + log\sigma) - plogd \tag{6}$$

or

$$log\dot{\varepsilon} = intercept - plogd \tag{7}$$

To keep the intercept part of this equation as a true constant, a fixed value of log stress (0.8) was selected (i.e. 6.3 MPa). For this fixed value of stress, log strain rate values were picked from the stress relaxation curves (Figs. 3(b-c)). Note that halite1 was not used in this analysis being different. The selected strain rate values are thus plotted against the calculated grain size d values in Figure 5a.

Regression analysis revealed a p-value of 1.1 (±0.3). This p-value supports the hypothesis that during stress relaxation, grain size sensitive (GSS) creep might play a role. It is well known that (GSS) solution-precipitation mechanisms may play an important role in the creep of fine-grained halite, creep (Spiers et al. 1990; Raj 1982; Schutjens 1991; Cox & Paterson 1991). According to these authors, a p-value of about 1 suggests, that the rate controlling step in the process will be dissolution or precipitation rather than diffusion. Accordingly, we infer that dissolution/precipitation-controlled pressure solution processes dominate the creep of wet halite at low stress and slower strain rate, at 125 °C.

Now using the intercept value of the best fit line in Figure 5a, the unknown constant B^* gets the value of 1.68×10^{-10} (MPa^{-1} mm$^{1.1}$ s^{-1}), so the GSS creep equation becomes

$$\dot{\varepsilon}_{GSS} = 1.68 \times 10^{-10}\sigma d^{-1.1} \tag{8}$$

For the GSI part of Equation (3), we assume that conventional power law is applicable; plotting the steady points of halite2 and 3, against the deformation strain rates (Figure 5b), the values of n and A^* come out to be ~11 and 4.365×10^{-20} s^{-1} MPa^{-11}, so the GSI part can be written as

$$\dot{\varepsilon}_{GSI} = 4.365 \times 10^{-20}\sigma^{11} \tag{9}$$

The GSS flow law (Eq. 8) is based on the calculated grain size - strain rate data at $\sigma = 6.3$ MPa under the assumption that there is no influence of GSI flow at that condition. So, the GSS flow law (Eq. 8) is the right-handed end member of the composite description of Equation (3). Its trends for four different grain sizes are plotted in Figure 6a, where the trend for the steady state data (halite2 and 3) is included, as described by Equation (9). Equation (9), however, cannot simply be regarded as the left-hand (GSI) end member of the composite flow law (Eq. 3), since grain size sensitive behaviour might have influenced the steady state creep without realizing it. We thus took the data of halite2 and 3 from Table I and fitted them to Equation 3, using the established values for n, p and B^* and applied non-linear regression. This resulted in a value of 6.42×10^{-20} (MPa^{-11}s^{-1}) for A^*. The composite flow law (Eq. 3) now can be written

$$\dot{\varepsilon} = 6.42 \times 10^{-20}\sigma^{11} + 1.68 \times 10^{-10}\sigma d^{-1.1} \tag{10}$$

The trend lines in Figure 6b show that the influence of grain size is effective at lower stresses and strain rates. For higher stresses, these curves satisfy the steady state points, whereas on lower stress/strain rates, these trends satisfy the data picked from relaxation curves. So, the composite flow law gives a complete picture of the creep characteristics of natural wet halite

samples, in two regimes of GSI ($n \sim 11$) and GSS ($n \sim 1$) that gradually pass into each other on higher stress and faster strain rate side.
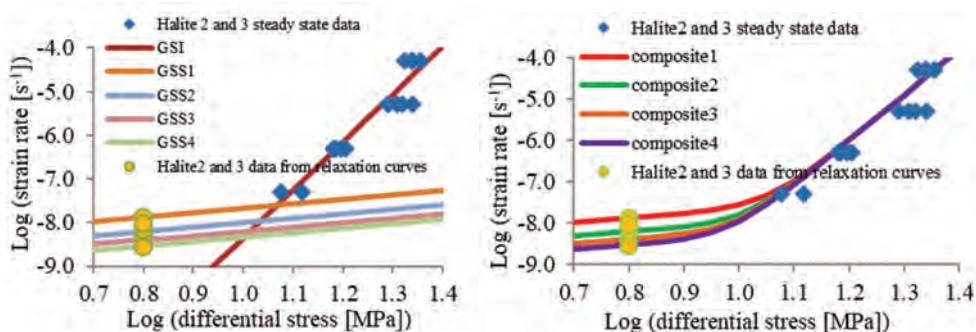
Figure 6. a) Log-log plot of strain rate and differential stress showing the predicted trends for GSS creep applying Eq. 8 for different grain sizes (GSS1, 2, 3 and 4 for d = 0.1, 0.2, 0.3 and 0.4 mm respectively), satisfying the lower stress and slower strain rate data. Note that higher grain sizes are lower in strain rates. The trend for GSI creep applying Eq. 9, satisfies the steady state values of constant deformation data, b) Log-log plot of strain rate and differential stress showing the predicted trends applying the composite creep Eq. 10, for a grain size of 0.1 mm (composite1), 0.2 mm (composite 2),0.3 mm (composite 3) and 0.4 mm (composite 4).

5. Conclusions

The main research question addressed in this study was if a transition can be observed, in wet polycrystalline halite, from creep behaviour governed by a (grain size insensitive) dislocation mechanisms to creep behaviour controlled by a (grain size sensitive) solution-precipitation mechanism, and if so, what the conditions of this transition are in terms of strain rate.

The experiments on the synthetic and natural halite samples at a confining pressure of 50 MPa and temperature of 125 °C revealed that at faster strain rates and higher stresses, dislocation creep (GSI) plays its role, which can be described by a conventional power law creep equation with n = 11. With such a high value, dislocation climb is unlikely to be rate controlling, but a dislocation glide mechanism should be considered. During the stress relaxation parts of the experiments, the n-value decreased to ~1 and a grain size sensitive creep mechanism, most probably pressure solution, becomes operative with the dissolution/precipitation step as rate controlling, as revealed by an analysis of the grain size exponent of creep ($p \sim 1$), using a flow equation of the type $\dot{\varepsilon} = B^*\sigma d^{-p}$.

The transition from (presumably) glide controlled dislocation creep with high power law n-value to grain size sensitive creep at $n \sim 1$, at 125 °C, occurs at a strain rate of about 10^{-9} s^{-1}. So, at slow strain rates ~10^{-9} s^{-1}, at a depth equivalent to an overburden/hydrostatic pressure of 50 MPa, grain size sensitive creep mechanism plays a more important role than dislocation mechanisms.

Acknowledgements

References

AUTEN T.A., DAVIS L.A. & GORDON R.B. 1973 Hydrostatic pressure and the mechanical properties of NaCl polycrystals. Philosophical Magazine, 28, 335-341.

CARTER N.L. & HANSEN F.D. 1983 Creep of rocksalt. Tectonophysics, 92(4), 275-333.

CARTER N.L., HORSEMAN S.T., RUSSELL J.E. & HANDIN J. 1993 Rheology of rocksalt. Journal of Structural Geology, 15 (9-10),1257-1271.

COX S.F.& PATERSON M.S. 1991 Experimental dissolution-precipitation creep in quartz aggregates at high temperatures. Geophysical Research Letters 18.8: 1401-1404.

DE BRESSER J.H.P., TER HEEGE J.H. & SPIERS C.J. 2001 Grain size reduction by dynamic recrystallization: can it result in major rheological weakening? International Journal of Earth Sciences, 90(1), 28-45.

DING J., CHESTER F.M. CHESTER J.S., X. SHEN & ARSON C. 2021 Coupled brittle and viscous micromechanisms produce semibrittle flow, grain-boundary sliding, and anelasticity in salt-rock."Journal of Geophysical Research: Solid Earth 126, no. 2.

FRANSSEN R.C. 1994 The rheology of synthetic rocksalt in uniaxial compression. Tectonophysics, 233(1), 1-40.

HEARD H.C. 1972 Steady-State Flow in Polycrystalline Halite at Pressure of 2 Kilo bars,"Flow and Fracture of Rocks, 191-209.

HEARD & RYERSON F.J. 1986 Effect of Cation Impurities on Steady-State Flow of Salt,"Mineral and Rock Deformation: Laboratory Studies: The Paterson Volume, 99-115.

JACKSON M.P.A. & TALBOT C.J. 1986 External shapes, strain rates, and dynamics of salt structures," Geological Society of America Bulletin 97.3: 305-323.

MUHAMMAD N. 2015 Deformation and transport processes in salt rocks: An experimental study exploring effects of pressure and stress relaxation. Utrecht Studies in Earth Sciences, 84, 1-275.

PEACH C.J. 1991 Influence of deformation on the fluid transport properties of salt rocks," Geologica Ultraiectina, 77, 1-238.

PEACH C.J., SPIERS C.J. & TRIMBY P.W. 2001 Effect of confining pressure on dilatation, recrystallization, and flow of rock salt at 150 °C. Journal of Geophysical Research: Solid Earth (1978–2012) 106.B7: 13315-13328.

POIRIER J.P. 1985 Creep of crystals: high-temperature deformation processes in metals, ceramics and minerals. Cambridge University Press.

RAJ R. 1982 Creep in polycrystalline aggregates by matter transport through a liquid phase," Journal of Geophysical Research: Solid Earth (1978–2012)87. B6: 4731-4739.

ROEDDER E. & BASSETT R.L. 1981 Problems in determination of the water content of rock-salt samples and its significance in nuclear-waste storage siting. Geology 9, no. 11: 525-530.

RUTTER E.H. & MAINPRICE D.H. 1978 "The effect of water on stress relaxation of faulted and unfaulted sandstone," Pure and Applied geophysics 116.4-5: 634-654.

SCHUTJENS P.M.T.M. 1991 Intergranular pressure solution in halite aggregates and quartz sands: an experimental investigation. Geologica Ultraiectina, 76, 1-233.

SENSENY P.E., HANSEN F.D., J.E. RUSSELL J.E. CARTER N.L. & HANDIN J.W. 1992 Mechanical behaviour of rock salt: phenomenology and micromechanisms", International journal of rock mechanics and mining sciences & geomechanics abstracts, vol. 29, no. 4, 363-378.

SKROTZKI W., FROMMEYER O. & HAASEN P. 1981 Plasticity of polycrystalline ionic solids. physica status solidi (a), 66 (1), 219-228.

SPIERS C.J., URAI J.L. LISTER G.S. BOLAND J.N. & ZWART H.J. 1986 The influence of fluid-rock interaction on the rheology of salt rock," Commission of the European Communities, Luxembourg.

SPIERS C.J., SCHUTJENS P.M.T.M., BRZESOWSKY R.H., PEACH C.J., LIEZENBERG J.L. & ZWART H.J. 1990 Experimental determination of constitutive parameters governing creep of rocksalt by pressure solution. Geological Society, London, Special Publications 54, 215-227.

TER HEEGE J.H., DE BRESSER J.H.P. & SPIERS C.J. 2005a Rheological behaviour of synthetic rocksalt: The interplay between water, dynamic recrystallization and deformation mechanisms. J. Struct. Geol. 27, 948-963.

TER HEEGE J.H., DE BRESSER J.H.P. & SPIERS C.J. 2005b Dynamic recrystallization of wet synthetic polycrystalline halite: dependence of grain size distribution on flow stress, temperature and strain," Tectonophysics 396.1: 35-57.

URAI J.L. 1983 Water assisted dynamic recrystallization and weakening in polycrystalline bischofite. Tectonophysics 96.1: 125-157.

URAI J.L., SPIERS C.J. ZWART H.J. & LISTER G.S. 1986 Weakening of rock salt by water during long-term creep," Nature; 324(6097): 554-7.

URAI J.L., C.J. SPIERS C.J. PEACH R.C.M.W. FRANSSEN & J.L. LIEZENBERG 1986 Deformation mechanisms operating in naturally deformed halite rocks as deduced from microstructural investigations," Geologie en Mijnbouw 66, no. 2: 165-176.

VAN EEKELEN H.A., HULSEBOS T. & URAI J.L. 1981 Creep of bischofite. The Mechanical Behavior of Salt: Proceedings of the First Conference Held at the Pennsylvania State University, University Park, Pennsylvania, Gulf Pub Co.

WAWERSIK W.R. & ZEUCH D.H. 1986 Modeling and mechanistic interpretation of creep of rock salt below 200 ºC," Tectonophysics, 121(2), 125-152.

WEERTMAN J. 1957 Steady-State Creep of Crystals. J. Applied Physics, 28(10), 1185-1189.

Flat-bedded rock salt – a mechanically anisotropic material?

Ida Epkenhans[1], Volker Mintzlaff[1], Sven Fachinger[1], Svenja Wacker[1], Eugen Daumlechner[1], Joachim Stahlmann[1]*

[1]Institute for Geomechanics and Geotechnics, Technische Universität Braunschweig, Germany

* i.epkenhans@tu-braunschweig.de

ABSTRACT: Rock salt is considered to be an isotropic material. However, flat-bedded rock salt shows a layering that has sedimentary origin, which may influence the mechanical behavior of the rock. To estimate the impact of the structural anisotropy on the mechanical behavior, a series of triaxial compression experiments on two facies of rock salt originating from the mine "Borth" in Rheinberg (South-Western Central European Basin, North-Western Germany) were performed by the Institute for Geomechanics and Geotechnics of Technische Universität Braunschweig. Test specimens were prepared with layering horizontal and vertical to the axial loading direction. The results show, that the peak stress values lie in a comparable range in both test series. However, the peak stress occurs at a higher strain during low confining pressure tests on horizontally layered samples. The paper presents the results of the performed tests and argues that, based on these results, an anisotropic mechanical behavior can be assumed with respect to the failure strain.

1   Introduction

Rock salt is widely considered as an isotropic material (e.g. regard to mechanical behavior, Hansen et al., 2016) and therefore most constitutive models represent it isotropic (e.g., Hampel et al. 2016). Consequently, numerical simulations of potential depositories are conducted using these models, even for depositories in flat-bedded rock salt formations (Bollingerfehr et al. 2018). However, being a sedimentary rock in origin, rock salt may show a distinct layering. As a result, the variation of e.g. crystal size may be greater between different layers than within one layer. Therefore, a mechanical anisotropy can be expected.

According to (Langer, 1981) rock salt under mono-axial load "is distinctly anisotropic to strength. With increasing isotropic pressure, the anisotropy to strength decreases greatly whereas the anisotropy to deformation on fracture is retained, although it is also reduced ". Unfortunately, no further information regarding to the type of salt (except that it is Na3β-Leinesalz) or detailed test results can be found. Uniaxial compression tests on flat-bedded salt with load directions parallel and perpendicular to bedding direction were e.g. performed at high strain rates up to approximately 50 s^{-1} by (Bauer et al. 2019). The authors identified an anisotropy in strength depending on the bedding direction. No current publications of triaxial compression tests on bedded salt with load directions parallel and perpendicular to bedding direction have been published to our knowledge.

The Institute for Geomechanics and Geotechnics of the Technische Universität Braunschweig has performed in total 48 triaxial compression tests on flat-bedded rock salt. The tests were performed on two types of samples, varying the bedding direction in relation to the load direction, with the aim to determine the mechanical anisotropy of flat bedded rock salt. So far, only macroscopic examinations have been performed.

2 Background

2.1 Geological setting of the Borth mine

The Borth mine is located in the north-western part of North-Rhine-Westfalia in Germany. It is operated by the K+S Minerals and Agriculture GmbH and capable of mining 2.000.000 tons of rock salt annually.

Geologically, the mine is situated on the edge of the Central European Basin in the Niederrhein Basin. The rock salt formation is the Werra formation, which facies and thickness are influenced by synsedimentary rift structures. Therefore, the depth and thickness of rock salt vary over small distances to a great extent. On horst structures, the thickness of the rock salt is less than 100 m or even 0 m, in graben structures like in Borth, the thickness is up to 450 m. On the Borth site, the overall thickness is about 185 m (Reinhold & Hammer 2016). The rock salt lies between coal-bearing carboniferous footwalls and overlying anhydrite and lime stones of the Zechstein formation and clay and silt stones of the Buntsandstein formation (see Figure 1).
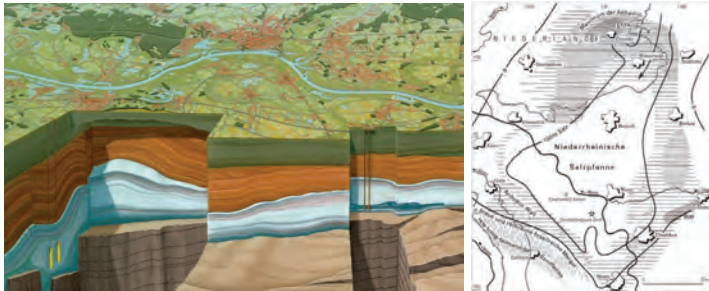
Figure 1: Left: Sketch of the geological profile of the Niederrhein Basin (Borth mine is on the left side), Right: Salt thickness of the Werra Formation in the Niederrhein Basin with the location of the Borth salt mine (Becker et al. 2014).

2.2 Samples

The former esco company (now a part of K+S Minerals and Agriculture GmbH) kindly provided the Institute for Geomechanics and Geotechnics of Technische Universität Braunschweig with two blocks of rock salt in 2017 (Block 2017) and 2020 (Block 2020). The blocks were obtained in a depth between 750 and 950 m. Block 2017 is a lightly orange colored layered rock with small crystals (size up to 10 mm, mean size about 5 mm). Small impurities of brownish clay are present in some samples. Block (2020) is colored white with very few grayish impurities. The crystal size on average is about 10 mm with some crystals of 50 mm. The bigger crystals tend to be longer than they are wide in the direction of the sedimentary layers. Both blocks show no visible cracks. The specimens were obtained using a lathe. After the preparation, they were stored in airtight sealed bags until testing. The height of the samples is 100 mm, the diameter is 50 mm. Figure 2 gives an overview of some samples. Density and water content of the samples were measured and no significant differences between the two blocks in regard to these parameters were found. Density was around 2.15 g/cm³, water content around 0.05 % for both blocks.

Figure 2: Obtained samples from Block (2017) (lightly orange colored) and Block (2020)

The tested samples are classified according to their stratification, following Figure 3. For samples with a horizontal layering the abbreviation 'Bo-01-xx' is used, where 'Bo' stands for the mine Borth, '01' stands for the orientation of the layering and 'xx' is a continuous numbering. In the following text, the terms 'samples with horizontal layering' or 'horizontal samples' describe a sample with layering as shown in Figure 3 (left). 'Samples with vertical layering' are being treated analogously.
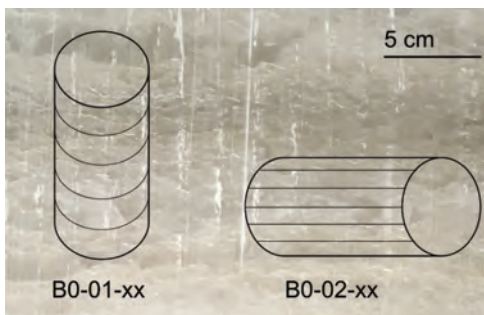
Figure 3: Prepared samples with a horizontal layering (left) and a vertical layering (right) from the Salt Mine Borth (Block 2020)

3 Methodology

3.1 Test equipment

The test series was performed using a hydraulic triaxial rock press by Walter+Bai, which is capable of applying an axial load of 3 MN and a confining pressure up to 80 MPa. The triaxial cell is designed for a sample diameter of 50 mm. During the tests, the stresses (axial load and confining pressure) and the deformations of the test specimen are measured. All tests were performed at room temperature.

3.2 Test sequence

Before testing the sample its height, diameter and weight is recorded. The obtained sample is then pressed into a rubber jacket and inserted into the test cell. The piston and the bottom are enclosed by the rubber jacket; therefore, no oil can reach the sample. After inserting the prepared sample into the test cell, the cell is being filled with oil which is used to apply a confining pressure to the specimen, and an axial load is applied by moving the stamp down on the piston, which transfers the force on the sample.

The test starts with a consolidation phase that lasts for 15 hours. In the consolidation phase, the sample is exposed to a nearly isotropic stress regime with an axial stress of 40.5 MPa and confining pressure of 40 MPa. The difference of 0.5 MPa is necessary to prevent penetration of the oil into the rubber jacket. Stresses of 40 MPa are approximately twice as high as the stresses to which the specimen was subjected in the rock due to the depth of the mine. During the consolidation phase microcracks, which may have occurred during the extraction of the sample, are expected to close. The stresses of the consolidation phase are applied with a stress rate of 0.01 MPa/s.
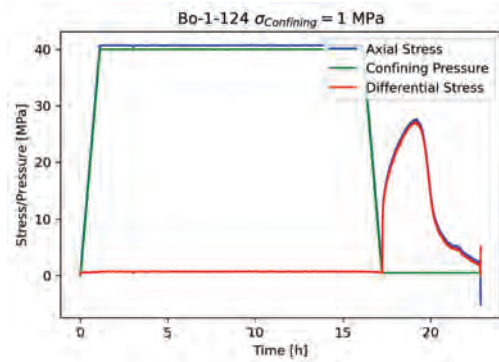
Figure 4: Exemplary test sequence for test Bo-01-124

After the completion of the consolidation phase, the axial compression phase starts. At first, the confining pressure is reduced to the intended value for the following phase with a stress rate of again 0.01 MPa/s. The axial stress is reduced in parallel to the confining pressure so it is always 0.5 MPa higher than the confining pressure. When the intended confining pressure is reached, the compression of the sample begins. The test is strain-controlled with a strain rate of 1E-5 s^{-1} which corresponds to a speed of 0.001 mm/s. The test ends when an axial deformation of 2 mm is reached.

Figure 4 illustrates the test sequence for the test Bo-01-124 as an example. Table 1 gives an overview of the tests which were performed on samples of the two blocks at different confining pressures. The tests are performed under different confining pressures. By varying the confining pressure, a failure boundary can be determined.

Table 1: Overview of the lab tests at samples from Block 2017 and Block 2020

confining pressure [MPa]	0.1	0.5	1.0	1.5	2.0	5.0	10.0	20.0
Block 2017	-	8	8	4	2	2	2	2
Block 2020	2	6	6	6	-	-	-	2

4   Results

In the following, all tests are summarized and the consolidation and compression phase of the test series Block (2017) and Block (2020) are analyzed. The main objective is to analyze the difference between horizontal and vertical layers.

4.1 Test series Block 2017

4.1.1 Consolidation phase

Figure 5 shows the axial strain and the strain rate over time during the consolidation phase for the test series Block 2017. The test results of samples that have a horizontal layering are colored blue, the tests with vertical layering are colored green. The graphs of samples with horizontal layering scatter more than samples with vertical layering. However, on average the horizontal samples show a larger strain and a higher strain rate than the vertical samples. At the end of the consolidation phase the axial deformation of the horizontal samples on average amounts to 0.042 mm and of the vertical samples to 0.032 mm. By implication, the axial strain of the horizontal-layered specimens is approx. 30 % higher than the vertical-layered specimens.

At the end of the consolidation phase, the strain rate does not reach zero. On average, the strain rate is 2.5E-9 s^{-1} for vertical and horizontal samples of this test series.
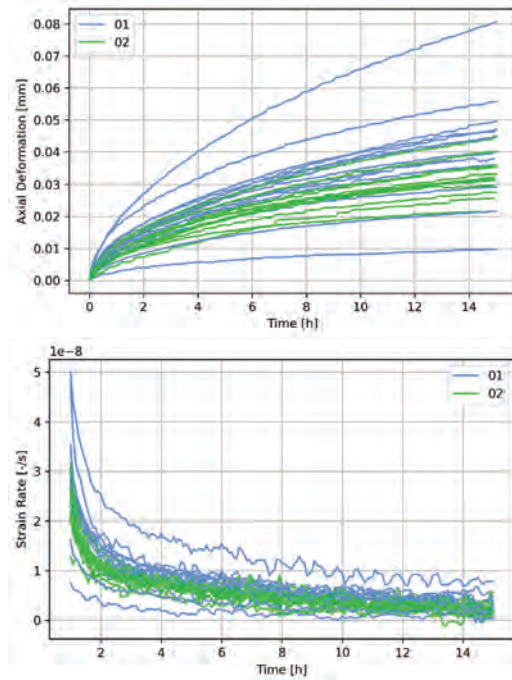
Figure 5: Axial deformation and strain rate over time (test series Block 2017); blue (01): specimen with horizontal layering, green (02): specimen with vertical layering

Table 2: Overview of average failure points and max. differential stress reached of test series Block 2017

confining pressure [MPa]	horizontal layering		vertical layering	
	failure strain	failure stress	failure strain	failure stress
0.5	0.078	39.70	0.060	37.85
1.0	0.102	43.28	0.078	41.91
1.5	0.141	50.68	0.111*	30.83*
2.0	0.115	46.89	0.119	47.48
confining	max. reached stress		max. reached stress	
5.0**	54.00		61.59	
10.0**	64.67		71.56	
20.0**	78.96		76.49	

* without outlier
** no failure

4.1.2 Compression phase

In Figure 6 the results of the tests performed on Block (2017) can be seen for the different confining pressure levels. The stress-strain curves are shown on the left side and the associated failure points are depicted on the right.
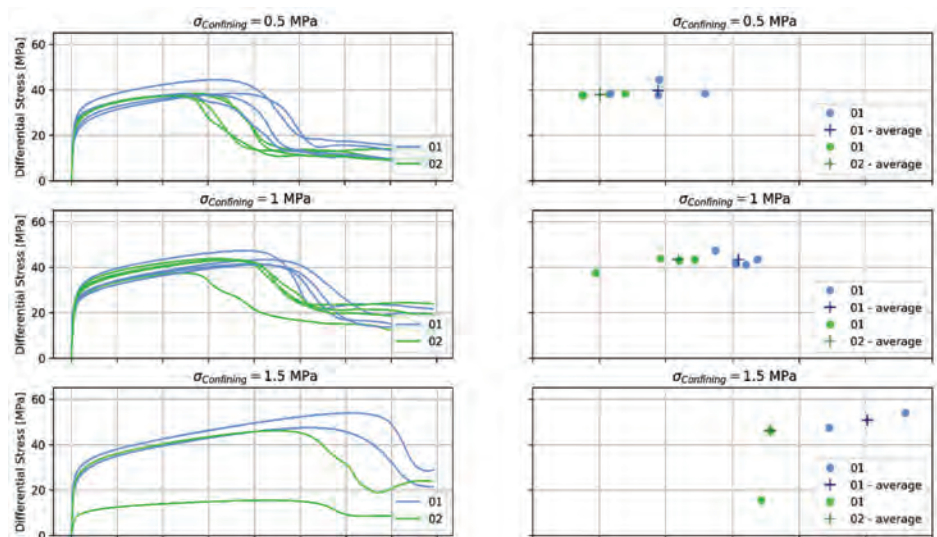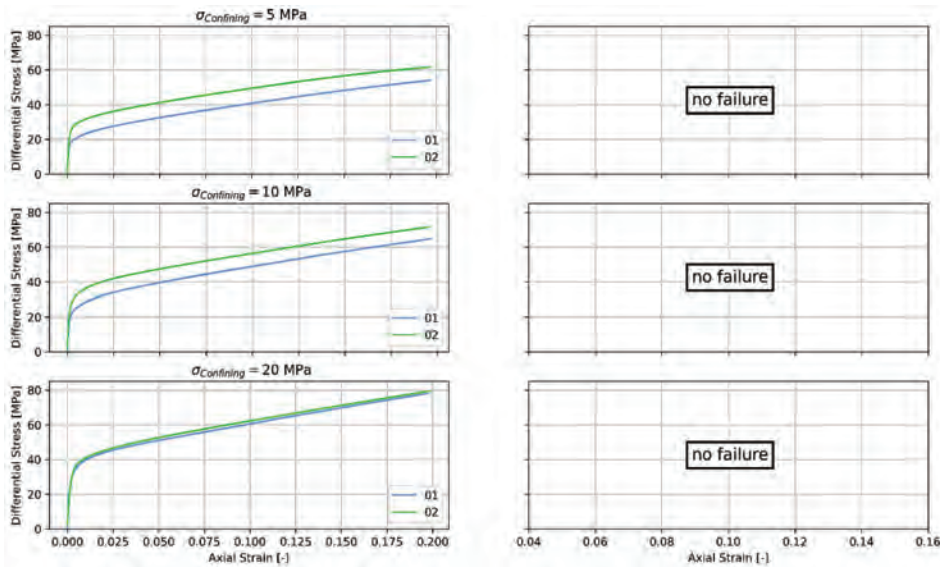
Figure 6: Stress-strain diagram (left) and failure points (right) at different confining pressures (test series Block (2017)); blue (01): specimen with horizontal layering, green (02): specimen with vertical layering

For low confining pressures, 0.5 and 1.0 MPa, the stress-strain curves for all specimen are close together. However, the failure behavior is different for horizontal and vertical test specimens. The samples with horizontal layering fail at higher strains and some at higher stresses. On average, the horizontal samples fail at a strain of 0.078 and differential stress of 39.70 MPa while the vertical samples fail at 0.060 and 37.85 MPa (0.5 MPa confining pressure). At a confining pressure of 1.0 MPa, similar behavior of the failure points can be observed compared to 0.5 MPa confining pressure. The results of failure points for different confining pressures are listed in Table 2.

At a confining pressure of 1.5 MPa, one outlier for the vertical sample can be identified. This sample fails at a relatively small differential stress. The horizontal samples however fail at relatively large stresses and strains. The average values of the failure stress and strain are higher than for a confining pressure of 2.0 MPa. But in general, the behavior is similar to the tests at the low confining pressures (0.5 and 1.0 MPa).

At a confining pressure of 2.0 MPa, the failure behavior is the opposite. The specimen with vertical layering reaches a higher stress level and breaks at a higher strain than the specimen with horizontal layering. However, the difference is very small, the stress-strain curves during hardening are almost identical and the failure points are close together.

At high confining pressures (5.0 to 20.0 MPa) failure is not being reached during the test. The stress-strain behavior looks similar for all three confining pressures. The samples with vertical layering reach a higher stress level already at the beginning of the compression phase. With increasing confining pressure, the difference regarding the differential stress gets smaller.
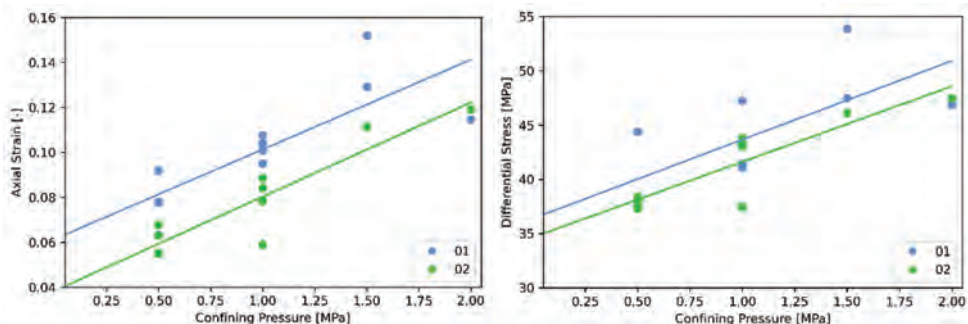
Figure 7: Failure points in terms of axial strain (left) and differential stress (right) over confining pressure (test series Block 2017); blue (01): specimen with horizontal layering, green (02): specimen with vertical layering

Considering all failure points for the different confining pressures in one chart, a failure boundary for failure strain and failure stress can be estimated. As a starting point, failure boundaries were determined with a linear approach over all failure points. In Figure 7 the failure points and failure boundaries in terms of axial strain (left) and differential stress (right) for the horizontal and the vertical samples can be seen. It has to be taken into account, that more tests at low confining pressures were performed and therefore these results dominate the shape of the boundary. The failure points at higher confining pressures have to be determined and following the selection of the initial function has to be verified with more tests.

Nevertheless, it can be seen, that the boundaries of the horizontal samples are located above the boundaries of the vertical samples. For low confining pressures, the horizontal samples fail at higher differential stresses and axial strains than the vertical samples. At 1.0 MPa confining pressure for example, the axial failure strain of the vertical samples is 20 % lower and the differential stress is 5 % lower than the corresponding values of the horizontal samples.

4.2   Test series Block 2020

4.2.1   Consolidation phase

Figure 7 shows the axial strain and the strain rate over time during the consolidation phase for the test series Block 2020. The curves for the horizontal samples (blue lines) show a higher axial strain and a higher strain rate. At the end of the consolidation phase, the axial deformation of the horizontal samples is on average 0.063 mm and of the vertical samples 0.030 mm. So on average, the axial strain of the horizontal specimens is twice as high as of the vertical specimens.

The consolidation seems to be not completed after 15 hours, since there is still a not negligible strain rate at the end of the phase of about 2.92 E-9 s^{-1} for both test samples.
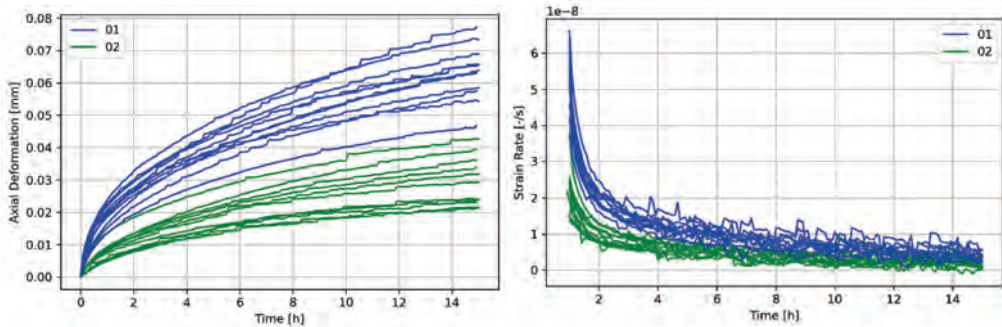
Figure 8: Axial deformation (left) and strain rate (right) over time (test series Block 2020); blue (01): specimen with horizontal layering, green (02): specimen with vertical layering

4.2.2 Compression phase

In Figure 8 the results for the compression phase of the tests which were performed on Block (2020) under different confining pressures can be seen.

In the hardening phase, the curves of the tests which were performed under a confining pressure of 0.1 MPa are close together. Though the failure behavior shows differences. The sample with horizontal layering fails at a higher strain and higher stress than the sample with vertical layering.

At a confining pressure of 0.5 MPa curves of the vertical samples show a smaller scattering than the curves of the horizontal samples during the hardening process. On average, the samples with vertical layering reach higher failure stress of 35,54 MPa but a lower failure strain of 0.069 than the horizontal specimens (31.45 MPa and 0.072). One vertical sample fails at a relatively large strain in comparison to the other two vertical samples.
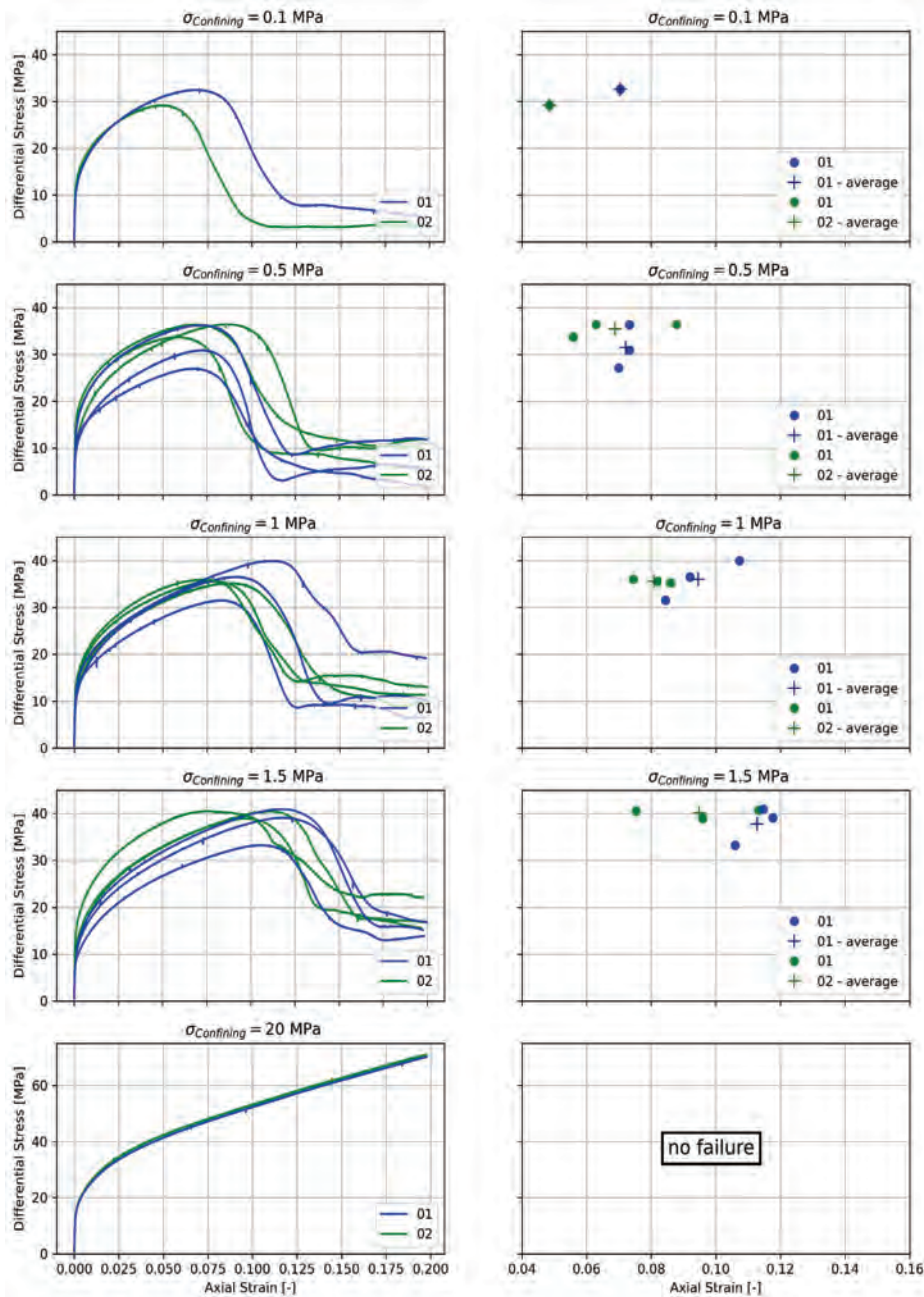
Figure 9: Stress-strain diagram (left) and failure points (right) at different confining pressures (test series Block 2020); blue (01): specimen with horizontal layering, green (02): specimen with vertical layering

For confining pressures of 1.0 and 1.5 MPa, the curves of the vertical samples show a larger gradient of the hardening process compared to the horizontal samples. Therefore, the vertical samples reach larger stresses at smaller strains. They also fail at smaller strains than the horizontal samples, compare to Table 3. At 1.0 MPa confining pressure the average failure stresses of the vertical and horizontal samples are very close together, at 1.5 MPa the vertical samples show slightly larger failure stresses at smaller strains.

Table 3: Overview of the average failure points of test series Block (2020)

confining pressure [MPa]	horizontal layering		vertical layering	
	failure strain [-]	failure stress [MPa]	max. strain [-]	failure strain [-]
0.1	0.070	32.63	0.049	29.18
0.5	0.072	31.45	0.069	35.54
1.0	0.095	36.02	0.081	35.60
1.5	0.113	37.78	0.095	40.07
confining pressure [MPa]	max. reached stress [MPa]		max. reached stress [MPa]	
20.0*	70.16		70.92	

* no failure occurs

At a confining pressure of 20.0 MPa, there is no failure of the specimens. The stress-strain curves for both tested specimens are almost identical. The vertical sample shows minimal higher stress for the associated strain than the horizontal sample.
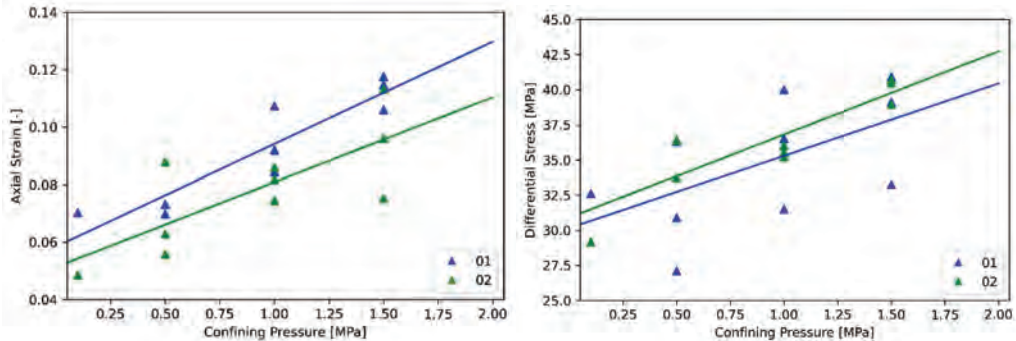
Figure 10: Failure points in terms of axial strain (left) and differential stress (right) over confining pressure (test series Block (2020)); blue (01): specimen with horizontal layering, green (02): specimen with vertical layering

In Figure 10 the estimated failure boundaries for axial strain and differential stress are shown. Again, it has to be taken into account, that more tests were performed at low confining pressures, so the course of the boundary at high confining stresses and the selection of the initial function of the boundaries has to be checked once more tests were executed.

For the Block (2020), the failure boundary for axial strain of the horizontal samples is also located above the boundary of the vertical samples. The failure boundary in terms of differential stress of the horizontal samples however is located below the boundary of the vertical samples. For 1.0 MPa the failure strain of the vertical samples is about 15 % lower, the failure stress is about 4 % higher than the corresponding values horizontal samples.

4.3 Comparison of test series Block 2017 and Block 2020

4.3.1 Consolidation phase

Figure 11 provides an overview of both the test results of Block (2017) and Block (2020) to validate whether the results are comparable. The horizontal samples are still colored blue, the vertical colored green. The tests conducted at Block (2017) are visualized with solid lines and the tests from Block (2020) with dotted lines.
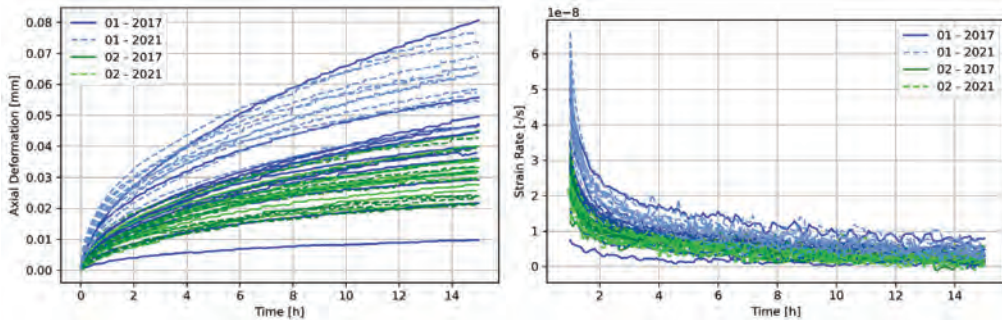
Figure 11: Axial deformation (left) and strain rate (right) over time for both test series; blue (01): specimen with horizontal layering, green (02): specimen with vertical layering

All in all, the results of the test series Block (2020) scatter less. Furthermore, the axial strain curves of the old and the new results of the vertical samples are very close together. The horizontal samples of Block (2020) in average show larger axial strains than the samples of Block (2017). The strain rates of the old and the new tests are very similar. In general, the horizontal samples show a larger axial strain and a higher strain rate compared to the vertical samples. On average, the axial deformation at the end of the consolidation phase is 0.051 mm for the horizontal samples and 0.031 mm for the vertical samples.

4.3.2 Compression phase

Figure 10 provides a compilation of stress-strain curves and failure points for all tests that were examined on Block (2017) and Block (2020) which show a failure of the samples.

At the beginning of the compression phase, the samples show elastic behavior. This elastic phase is followed by hardening until the sample fails. In comparison, the differential stresses, which are reached during the elastic phase, are larger in the test series Block (2017) than in the tests performed on Block (2020), while the hardening modulus is lower.
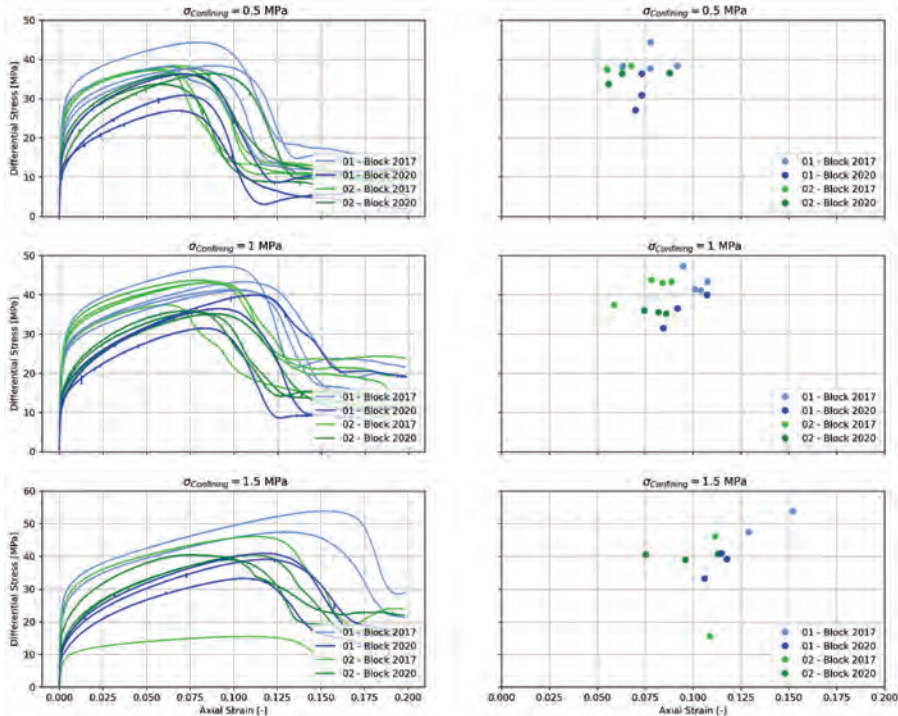
Figure 12: Stress-strain diagram (left) and failure points (right) at different confining pressures (both test series); blue (01): specimen with horizontal layering, green (02): specimen with vertical layering

In conclusion, the tests on Block (2017) show a larger stiffness, but a small hardening, and in total, the reached stress level is higher than for the series Block (2020). Therefore, the failure stresses of the older series are higher. The failure strains of the vertical samples are similar for both test series, whereby the horizontal samples of the older test series show slightly higher strain values. Especially at a confining pressure of 1.5 MPa, the failure strains of the horizontal samples are higher at Block (2017) than at Block (2020).

4.4   Evaluation of the results

4.4.1   Consolidation phase

The results of the consolidation phase clearly show an anisotropic behavior. The horizontal samples show larger axial strains and therefore higher strain rates in both series Block (2017) and Block (2020). The quantity of the axial strain however differs slightly for the horizontal samples between old and new tests.

The strain rate does not reach zero at the end of the consolidation phase. Therefore, the consolidation of the test specimen is not completed after 15 hours. An uncompleted consolidation has an influence on creep tests in which the steady-state creep rate has to be determined. If the consolidation is uncompleted, steady-state creep can be influenced by further consolidation or remaining damage. Therefore, consolidation should be continued until the rate is small enough, especially for creep tests at small deviatoric stresses (Lüdeling et al. 2022). The influence of the uncompleted consolidation on the compression test should be evaluated in further tests.

4.4.2 Compression phase

The results of the tests, which were performed on Block (2017) showed, that at low confining pressures (0.5-1.5 MPa), the horizontal samples fail at higher strains and stresses compared to the vertical samples. At confining pressures of 2.0 MPa and higher the number of tests performed is too low to provide a definite prediction of the mechanical anisotropy of the salt samples. However, the tests indicate that there might not be any detectable anisotropy above a certain confining pressure level in terms of stress-strain behavior.

Overall, the hypothesis can be made that at low confining pressures the horizontal samples fail at higher strains and stresses. For medium and high confining pressures this does not apply respectively no statement can be made.

In 2021 a new test series Block (2020) was started, which is not finished to date. The first results show that the samples of the test series Block (2017) demonstrate a larger stiffness. Also, a lower stress level was reached in the tests at Block (2020) compared to the tests at Block (2017).

The different results may be explained by the fact that even though the test specimens originate from the same mine they were obtained in different locations in the mine. Purely optically the samples look different (see Figure 2). Furthermore, the macrostructure differs. The grain size in the new samples is bigger than in the old ones. According to (Mouritz 2012) strength of polycrystalline materials is increased with a decreasing grain size.

The results of the tests at Block (2020) confirm the established hypothesis from the test series at Block (2017) that the horizontal samples fail at higher strains. A difference of 15 to 20 % in failure strain is significant. The results in terms of the reached stresses at failure are however ambiguous. The horizontal samples fail not necessarily at higher stresses. Also, the difference between the failure boundaries in terms of differential stress of the vertical samples is just around 4 to 5 %, so maybe in terms of differential stress, there is no anisotropy in failure behavior. For 20.0 MPa the results for both the Block (2017) and the Bock (2020) series are very similar, there is no anisotropic behavior detectable while failure was not reached.

An explanation for the first hypothesis that the horizontal samples fail at higher strains than the vertical samples could be that the tested samples are composed of two regions, layers and layer boundaries, while both have their own stiffness and strength.

In terms of the higher failure strains at the horizontal samples at low confining pressures the direction of the layer boundary in relation to the load direction is important. For the vertical samples, layers and boundaries are parallel to the direction of axial stress, which is higher than the confining pressure. Because one region (layer or boundary) has a higher stiffness, load transfer applies primarily in that region while the other region is loaded less. Therefore, the axial strain is essentially influenced by the region with the higher stiffness. For the horizontal samples the direction of both regions is perpendicular to the axial stress, load transfer applies in both regions. Hence, axial strain is influenced by the stiffness of both regions. The accumulated axial strain is essentially influenced by the smaller stiffness which causes higher deformations.

5   Conclusions

The Institute for Geomechanics and Geotechnics has performed triaxial compression tests on two facies of flat-bedded rock salt. The tests were performed by varying the bedding direction in relation to the load direction, with the aim to determine the mechanical anisotropy.

In conclusion, an anisotropic behavior is visible in the triaxial compression tests on flat-bedded rock salt. This applies especially to the consolidation phase, in which the conditions for every

performed test are the same. For the compression phase, which was performed with different confining pressures, the test results under low confining pressures present an anisotropic mechanical behavior with respect to the failure strain. The scope of testing at medium and high confining pressures has to be increased.

Since the differences between the test series leaves questions unanswered, the stratification-dependent behavior in terms of failure stress should be evaluated as well. Therefore, further evaluation methods and test methods would be useful. According to e.g. (Moslehy et al. 2022) unconfined strength, grain characteristics play an important role for an anisotropic behavior. Therefore, microscopic investigations should be performed.

The determination of the volume strain of the specimen can be used to verify microcrack closure in the consolidation phase and to detect potential anisotropic dilatancy behavior of the samples. Changes of oil volume were measured during all tests, but still have to be evaluated. The test framework conditions of all tests are currently reviewed again and necessary corrections will be made.

References

BAUER, A. J., SONG, B. & SANBORN, B. 2019. Dynamic compressive strength of rock salts. International Journal of Rock Mechanics and Mining Sciences, 113, 112–120.

BECKER, F. BRÄUNING, A. HAGENGUTH, G., STEINWELLER, M.& WREDE, V. 2014. Salz und Sole im GeoPark Ruhrgebiet. GeoPark Themen. GeoPark Ruhrgebiet e.V.

BOLLINGERFEHR, W., BERTRAMS, N., BUHMANN, D., EICKEMEIER, R., FAHLAND, S., FILBERT, W., HAMMER, J., KINDLEIN, J., KNAUTH, M., LIU, W., MINKLEY, W., MÖNIG, J., POPP, T., PRIGNITZ, S., REINHOLD, K., SIMO, E., THIEMEYER, T., VÖLKNER, E. & WOLF, J. 2018. Concept developments for a generic repository for heat-generating waste in bedded salt formations in Germany, 2018.

HANSEN, F.D., KUHLMAN, K.L. & SOBOLIK, S. 2016. Considerations of the Differences between Bedded and Domal Salt Pertaining to Disposal of Heat-Generating Nuclear Waste. Sandia National Laboratories, Albuquerque, Report SAND2016-6522R.

HAMPEL, A., HERCHEN, K., LUX, K.-H., GÜNTHER, R.-M., SALZER, K., MINKLEY, W., PUDEWILLS, A., YILDIRIM, S., ROKAHR, R., MISSAL, C., GÄHRKEN, A. & STAHLMANN, J. 2016. Verbundprojekt: Vergleich aktueller Stoffgesetze und Vorgehensweisen anhand von Modellberechnungen zum thermo-mechanischen Verhalten und zur Verheilung von Steinsalz.

LANGER, M. 1981. The rheological behaviour of rock salt, The mechanical behavior of Salt, Proc. 1st Conference, Pennsylvania State University, 1981.

LÜDELING, C., GÜNTHER, R.-M., HAMPEL, A., SUN-KURCZINSKI, J., LUX, K.-H. YILDIRIM, S., ZAPF, D., WACKER, S., EPKENHANS, I., STAHLMANN, J. & REEDLUNN, B. 2022. WEIMOS: Creep of Rock Salt at Low Deviatoric Stresses. The Mechanical Behavior of Salt; Proc. 10th Conference, Utrecht 2022, (this volume).

MOSHLEY, A., ALSHIBLI, K. A. & TRUSTER, T.J. 2022. Influence of Temperature and Crystal Orientation on Compressive Strength of Rock Salt Using a Newly Developed High-Pressure Thermal Cell Rock Mechanics and Rock Engineering, 55, 91–108.

MOURITZ, A. P. 2012. Introduction to aerospace materials. Oxford, Woodhead Publishing Limited.

REINHOLD, K. & HAMMER, J. 2016. Steinsalzlager in den salinaren Formationen Deutschlands. German Journal of Geology, 167 (2/3),167-190.

WEIMOS: Shear behaviors of bedded salt clay seams and their impact on disposal room porosity

Steven R. Sobolik[1]*, Chet Vignes[1]*, Stuart Buchholz[2], Evan Keffeler[2], Benjamin Reedlunn[1]*

[1]Sandia National Laboratories, Albuquerque, NM, USA; [2]RESPEC, Rapid City, SD, USA;

* srsobol@sandia.gov

ABSTRACT: This paper presents laboratory experiments on clay seams in-between layers of salt, and simulations of WIPP disposal rooms that include clay seams. The experiments involved two series of direct shear tests. The first test series was performed on representative core samples from a potash mine near the WIPP. These natural geologic contacts had intergrown halite crystals, and their residual shear strengths were like that of intact salt. The second test series involved artificial clay seams prepared by mixing brine with bentonite, placing the clay between two cylindrical salt specimens with grooved contact surfaces, and hydrostatically consolidating the assembled specimen. The artificial clay seam residual shear behavior was similar to that of a saturated, highly consolidated, clay. Thus, these weak and strong residual strengths likely bound the actual shear behavior of clays seams in bedded salt. The bounds were then used in simulations that probe the sensitivity of WIPP disposal room porosity to clay seam shear behavior. Weaker clay seams accelerated the decrease of room porosity within the first 300 years but had minimal impact on final room porosity.

1 Introduction

Sandia National Laboratories (SNL) is responsible for modeling the long-term behavior of the Waste Isolation Pilot Plant (WIPP), a permanent disposal site in bedded salt for defense-generated transuranic waste. In addition, SNL participates in extensive international collaborations to better understand the behavior of salt for potential spent nuclear fuel repositories. One key subject area for the modeling of the mechanical behavior of emplacement drifts is the influence of inhomogeneities, specifically interfaces between the host salt and other in situ materials such as clay seams within bedded salt. The potential increases in closure rate, roof collapse, and permeability near and along these inhomogeneities are thought to be first-order effects. Despite their importance, characterizations of the peak and residual shear strengths, and permeability of interfaces in salt are extremely rare in the published literature. Minkley & Mühlbauer (2007) documented direct shear laboratory tests on carnallite and salt blocks under varying normal and shear loads and shear velocities, but they did not perform experiments on clay seams.

This paper presents results from laboratory experiments and numerical simulations involving clay seams. The experiments measured the mechanical behavior of a clay seam as it was sheared. Two series of laboratory direct shear tests were performed (Sobolik et al. 2019 & 2020; Keffeler et al. 2021): one involved clay seams from a potash mine near the WIPP, the other involved artificial clay seams. These tests were performed as part of the US-German Collaborative Joint Project WEIMOS (2016 – 2019; "Further Development and Qualification of the Rock Mechanical Modeling for the Final HAW Disposal in Rock Salt") (Lüdeling et al. 2018). The numerical simulations used the test results to investigate the impact of clay seam shear behavior on the short-term and long-term porosity of disposal rooms at the WIPP.

2 First series of shear tests on interfaces

An initial series of laboratory direct shear tests was performed on several samples of materials assumed to be typical of WIPP emplacement rooms (Buchholz 2019; Sobolik et al. 2019). Samples with halite-anhydrite and halite-polyhalite interfaces were included in this test series,

but this paper will focus on the samples with halite-clay interfaces and pure salt samples. The direct shear test method was designed to measure the complete shear stress-strain curve and characterize the following mechanical properties:

- Intact normal and shear stiffness
- Dependence of shear yield, ultimate, and residual strength on normal stress
- Residual normal and shear stiffness

Sample collection was conducted in a salt-potash mine in the Permian Basin in New Mexico. These samples were to be drilled from the floor of an inclined drift at the mine. Cores were drilled using a concrete coring rig with a diamond bit core barrel having dimensions of 300 mm in diameter and 560 mm long. Several cores were drilled from the floor as planned, but nearly all exhibited damaged seams or interfaces, making them unsuitable for testing. As a result, a determination was made to extract cores horizontally from the rib. This procedure was much more successful; several intact cores were extracted for all the desired interface types.

Four-inch (100-mm) diameter cylindrical specimens were subcored from the field core using a vertical mill. Bright-Cut NHG metal working fluid was used as a lubricant during subcoring to prevent washing of the evaporite materials. The long axes of the subcores were oriented perpendicular to the geologic interface to the extent possible. The subcores were trimmed so that the specimen length on either side of the interface was between 50 and 76 mm. Total specimen length did not exceed 152 mm. The specimens were then cleaned using an alcohol-based degreaser. The interface between the halite layer and the clay section was somewhat well-defined visually when looking at the exterior surface of the sample. In addition to the cores obtained from the Permean Basin mine, RESPEC obtained sections of nominally 4-inch (102-mm) diameter core from a Prairie Evaporite storage well in Alberta, Canada. These samples were used for the initial tests to qualify the test conditions and procedures.

The shear tests were performed using a rock direct shear testing machine designed and fabricated by RESPEC (see Figure 1 for a schematic). It has an axial and shear load capacity of 30,000 pounds (130 kN) each. The machine consists of shear boxes (that hold the test specimen), a normal load ram, a shear load ram, and hydraulic controls. The shear displacement δ is measured by using a linear variable displacement transformer (LVDT). The shear load S is controlled by a mechanical-over-hydraulic intensifier that advances the shear load ram at a set displacement rate. The normal load N is controlled by a pressure regulator that maintains N within 1 percent of the set point. Both maximum shear strength and residual shear strength were determined for each rock type. The tests were conducted at several normal and shear loads up to expected in situ pre-mining stress conditions, and at a single shear velocity of $\dot{\delta} = 0.01$ in/min (0.0042 mm/sec). This shear velocity is currently the slowest capable on this direct shear machine (and much faster than the $\dot{\delta} = 0.00005$ to 0.002 mm/sec used by Minkley & Mühlbauer), so these tests were unable to evaluate potential velocity-dependent shear stress evolution. The tests were performed while holding the load normal to the interface constant. Each test used one of four different normal loads, which corresponded to nominal normal stresses of $\Sigma = 3.4$, 6.8, 10.3, 16.6 MPa.

Regardless of the rock type (i.e., with or without contacts), the specimens behaved and broke like solid salt rock. The tests tended to follow a similar pattern – an increase of shear stress until a break occurred, followed by a sudden drop in stress to an eventual residual value. Figure 2 plots shear stress vs. shear displacement for the tests performed on halite-clay contact samples. The stresses were calculated using the original cross-sectional area of the interface. See Table 2 in Sobolik et al. (2019) for the peak nominal shear stress and residual nominal shear stress from each experiment.
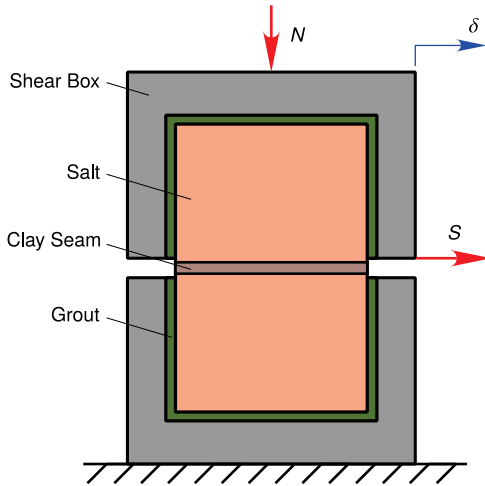
Figure 1. Schematic of direct shear test setup.
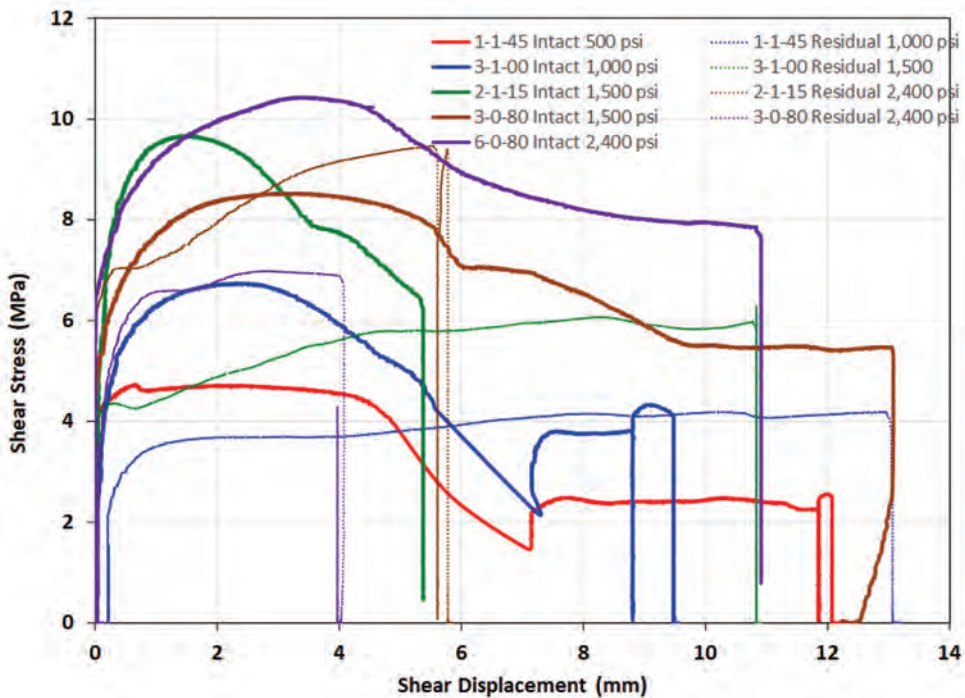
Figure 2. Shear stress vs. displacement for Halite-Clay shear tests.

3 Second series of shear tests on artificial clay seams

A series of laboratory experiments was performed that consisted of fabricating consolidated clay seams within salt (predominately halite) and performing direct shear tests on those clay seams. These tests were conducted at several normal and shear loads up to the expected in

situ pre-mining stress conditions, and at the same single shear ram advancement velocity of 0.01 in/min (0.004 mm/sec).

A total of eight artificial clay seam specimens were created. The salt on either side of the clay seam was from the same set of cores extracted for the earlier interface shear tests. A full description of the test procedure is included in Sobolik et al. (2020) and Keffler et al. (2021). The specimen preparation method is summarized as:

1. 4-inch (108 mm)-diameter by approximately 3-inch (76 mm)-long salt cylinders were subcored from the 12-inch-diameter core obtained from the potash mine near WIPP.
2. A series of 1.3-mm-deep circular grooves were machined, radially spaced ~6 mm apart, into one face of each subcore, as shown in Figure 3.
3. Bentonite powder was mixed with saturated salt (halite) brine to a fresh-water moisture content (by weight) of approximately 60 percent.
4. A 6-mm or 12-mm-thick layer of the bentonite-brine mix was applied to the grooved surface of a subcore. A second subcore was placed onto the bentonite-brine mix with the grooved surface facing the bentonite-brine mix. This assembly constituted an unconsolidated test specimen.
5. The unconsolidated test specimen was wrapped in filter fabric and placed into a consolidation vessel. The specimen was protected from the confining oil using neoprene jackets, and the platens were vented to the atmosphere.
6. The test specimen was consolidated under an isostatic stress of 20 MPa (nominal) at 21 degrees Celsius (°C) for 14 days. (For comparison, the lithostatic pressure at the WIPP horizon is approximately 14.8 MPa.) Excess pore fluid from the bentonite mixture was expelled through the vents.
7. The consolidated test specimen was removed from the consolidation vessel, and the diameter of the clay seam was measured. The consolidated test specimens were coated in clear acrylic to protect them from the encapsulation grout used in the shear boxes. An example photograph of a consolidated specimen is provided in Figure 3.

Four of the specimens had pre-consolidation seam thicknesses of 6 mm, and the remaining four had pre-consolidation seam thicknesses of 12 mm. The post-consolidation seam thicknesses were approximately 1.6 mm and 4.8 mm for the 6- and 12-mm pre-consolidation seam thicknesses, respectively. After the shear tests, clay chips from the specimens were tested for moisture content; this ranged from 13 to 17%. Post-test examination also revealed that there was no asperity-to-asperity contact between the two machined ends of the salt at the seam.

Shear tests were performed at three normal loads that corresponded to nominal normal stresses of 3.4, 6.8 and 10.3 MPa (500, 1000, 1500 psi). The data from each test were analyzed to determine the following:
- Pretest normal stiffness
- Pretest shear stiffness
- Peak shear strength
- Shear strength at 0.75 inch (19 mm) of shear displacement (a proxy for residual strength)
- Posttest shear stiffness
- Posttest normal stiffness.

For the study of seam shear behavior, the peak and residual shear strength are of highest importance. Nominal stresses were calculated using the original shear area of the specimens. One source of error was the shear displacement δ, causing the top half of the specimen to protrude over the bottom half. The maximum shear displacement reached as high as 20 mm (0.80 inch). This overhang led to a decrease in modified cross-sectional area A_δ available to resist the normal and shear loads. This modified cross-sectional area can be calculated as the overlap between two offset circles as:

$$A_\delta = (\theta - \sin\theta)\left(\frac{d_0}{2}\right)^2, \theta = 2\cos^{-1}\frac{\delta}{d_0},$$
(2)

Figure 3. Photographs of grooves machines into salt sample, and consolidated test specimen.

where d_0 is the initial specimen diameter. Nevertheless, the nominal normal and shear stresses were calculated assuming the initial area of the specimens $A_0 = \pi \, d_0^2 \, / \, 4$. The error that results from assuming constant area is negligible for the intact portion of the tests as shear displacement is small prior to exceeding the ultimate shear strength of the specimens. For the portions of the intact tests after seam fracture (ultimate shear strength), the shear displacement and area loss are larger; neglecting the changing area resulted in roughly 15-25% errors in calculated stresses at the end of the test. In the Mohr-Coulomb strength criterion fits discussed below, calculations of shear stress calculated with original and modified contact area are compared.

Figure 4 plots the shear stress versus shear displacement curves for the intact sample tests 6A/6B and 7A/7B, which were performed at a nominal normal stress of 6.83 MPa for the 6-mm and 12-mm pre-consolidated seams, respectively. For the plots in Figure 4, two values are plotted for shear stress: the blue curves represent shear stress calculated with the original seam contact area, A_0, calculated with the average original seam diameter d_0; and the orange curves represent the shear stress calculated using the modified contact area reduced by the shear displacement, A_δ.

In the initial analysis of all eight tests using the original seam contact area, two tests at most appeared to have achieved a residual shear stress through 19 mm shear displacement. After recalculating the shear stress based on the displacement-reduced contact area, four tests appear to have achieved a residual stress: Tests #8, #2, #4, and #7. It is unclear why the other tests failed to reach a residual stress condition.

While calculating the shear stress using the displacement-reduced contact area indicated that four of the shear tests reached a residual shear stress, that same method changes the calculation of the normal stress during the test. As the normal force remains essentially constant, the reduction in area causes an increase in normal stress on the contact area by about 33%. This is a curious result, because there is no corresponding increase in the shear stress with increasing Cauchy normal stress. This result complicates the notion that the shear tests actually reached a residual shear stress and somewhat skews any analysis of the shear behavior. For now, the post-test analysis simply utilizes the final shear strength measured at 19 mm of shear displacement. A summary of the measured peak and residual shear stresses for all the tests is listed in Table 1, with shear stress values at $\delta=19$ mm based on the modified contact area A_δ.
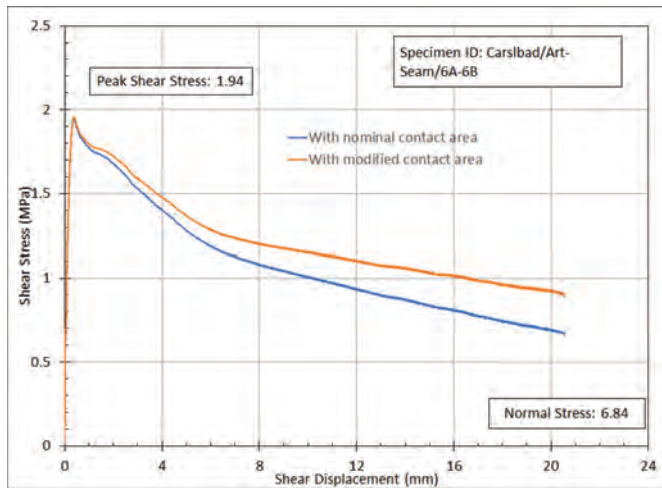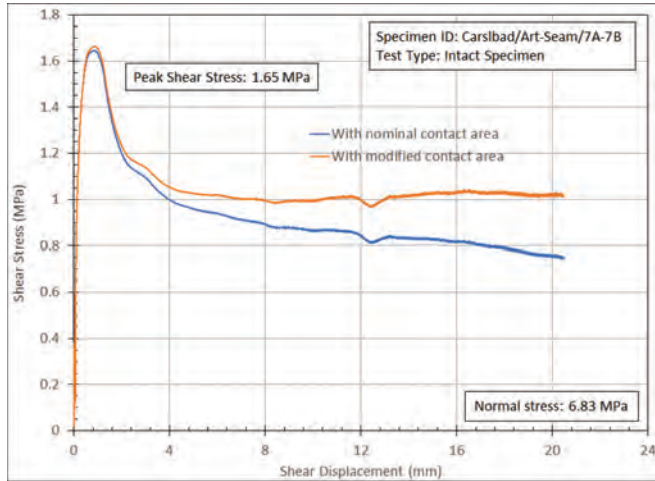
Figure 4. Shear Stress vs. Shear Displacement for Nominal Normal Stress of 6.89 MPa, pre-consolidation seam thicknesses of 6 mm (top), 12-mm (bottom)

Table 1. Direct shear testing strength results for artificial seam samples.

Specimen/ Test ID	Pre-Consolidation Seam Thickness (mm)	Nominal Normal Stress, psi (MPa)	Peak Nominal Shear Stress, psi (MPa)	Shear Stress, psi (MPa), at 0.75" (19 mm) Displ.
1A-1B	6	504 (3.47)	140 (0.97)	96 (0.66)
2A-2B	6	1494 (10.3)	325 (2.24)	161 (1.11)
3A-3B	12	1000 (6.89)	215 (1.48)	76 (0.52)
4A-4B	12	507 (3.50)	277 (1.91)	104 (0.72)
5A-5B	12	1487 (10.3)	427 (2.94)	155 (1.07)
6A-6B	6	992 (6.84)	282 (1.94)	136 (0.94)
7A-7B	12	990 (6.83)	239 (1.65)	149 (1.03)
8A-8B	6	496 (3.42)	234 (1.61)	144 (0.99)

4   Interpretation of test data

The experimental data was analyzed using the Mohr-Coulomb shear strength criterion. This criterion is defined as

$$T = \Sigma \tan \Theta + S_0 \tag{1}$$

where T is either the peak shear stress at failure or the residual shear stress, Σ is the normal stress on the shear surface, Θ is the friction angle, and S_0 is the cohesion strength. All stresses in (1) are taken as nominal stresses (force divided by original cross-sectional area) for simplicity. The friction angle and cohesion strength were fit, in a least squares sense, against the set of tests on each specimen type.

The peak and residual nominal shear stress measurements versus the nominal normal stress, the Mohr-Coulomb fits, and the associated Mohr-Coulomb parameters are shown in Figure 5 and 6. The simple fits reasonably capture each interface type. Notably, the cohesion strength is non-zero in all cases, suggesting the interfaces have a non-zero shear strength at zero normal stress.
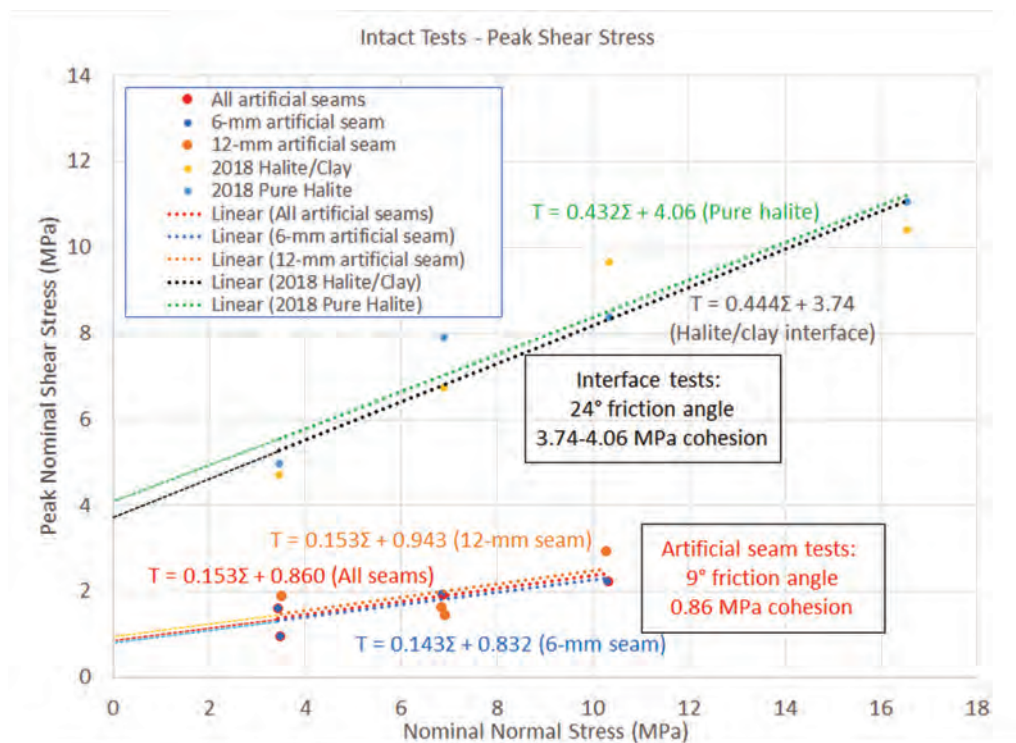
Figure 5. Peak shear stress as function of normal stress, halite interface tests and artificial seam tests.

Figures 5 and 6 show the natural clay seams had shear strengths like that of pure salt, meaning the clay interspersed in the natural clay seams did not weaken the salt. Presumably, a more distinct natural clay seam without intergrown halite crystals would exhibit substantially lower shear strengths. Efforts to extract such seams are ongoing.

Figure 5 and 6 also show the artificial clay seam shear strengths were much lower than those from the previous salt interface tests. The residual strength friction angle is 22.7 / 1.6 = 14 times smaller in the artificial clay seams than the diffuse natural clay seams. For an additional reference point, a friction coefficient of 0.2, which is equivalent to $\Phi = 11.3°$ and $S_0=0$, has historically been assumed in WIPP geomechanical analyses.
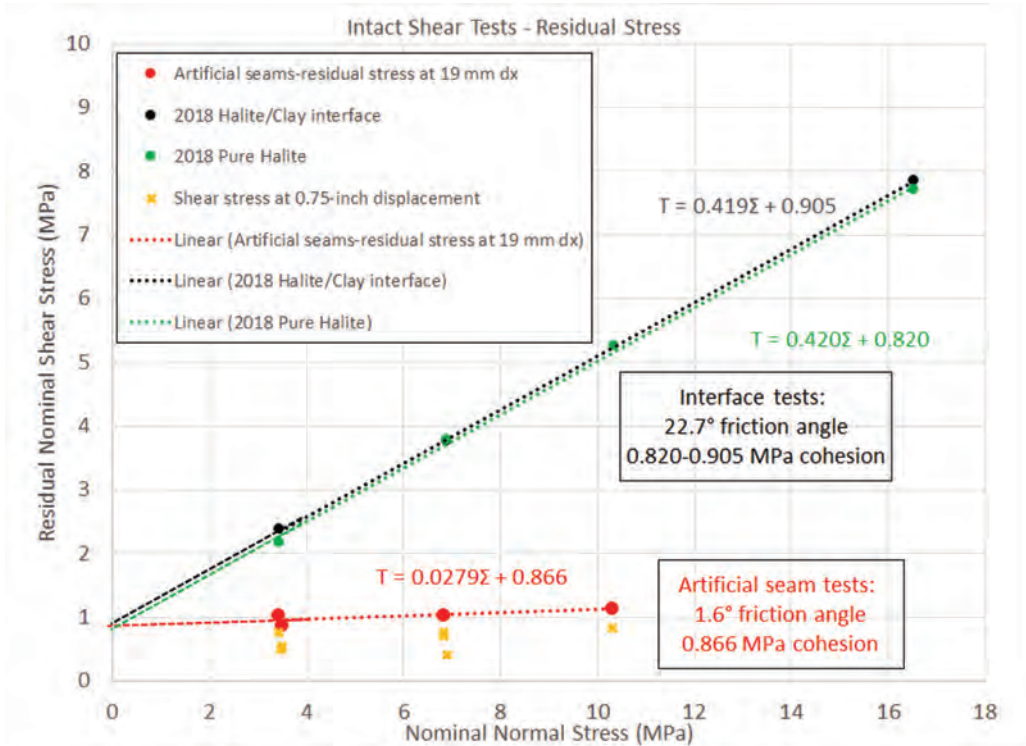
Figure 6. Residual shear stress as function of nominal normal stress, natural halite interface tests and artificial seam tests.

The softness of clay and small asperity size in the artificial clay seams may explain the low Mohr-Coulomb parameter measurements, particularly the friction angles. When examining the collection of artificial seam tests, it was surprising that the 6-mm and 12-mm artificial seams underwent approximately the same behavior, with similar Mohr-Coulomb cohesion and friction angle values. This suggests that the tests may be measuring the shear strength of the clay, rather than the shear strength of a rougher clay-salt interface where the salt must deform somewhat to permit sliding. It is assumed that no salt asperity-to-salt asperity contact occurred during shearing and the behavior was likely dominated by the saturated, consolidated, clay properties. This conclusion is supported by the calculated values of the Mohr-Coulomb constants. Clays (especially over-consolidated clays) typically exhibit non-zero cohesion. The values of cohesion in Figure 6 are larger than most references cite for clays (for example, Ladd & Edgers, 1972), but not dramatically higher. Direct shear tests on clay-only samples would help determine if the clay does, in fact, dominate the shear response.

5 Application to geomechanical analyses

Clay seam sliding at the WIPP site has historically been modeled using Coulomb friction, and the same simple approach is continued herein. Coulomb friction is defined as

$$\tau = \sigma \tan \theta \qquad (2)$$

where τ is the Cauchy shear stress at the interface, σ is the Cauchy normal stress on the interface, and θ is the residual strength friction angle.

This approach ignores the intact peak strength and assumes sliding occurs as soon as the shear stress at the interface reaches the residual shear strength τ. The intact peak strength is assumed to be important only upon room excavation when cracks first form in the clay seams.

The remainder of the room closure period will involve crack propagation and sliding along the clay seam. It could be worth trying to incorporate crack propagation, which generally requires less stress than initiation, into a model, but the propagation behavior has not been quantified. Accordingly, it is prudent to assume the propagation strength is equal to the residual strength to begin with.

Expression (2) is similar to (1) except $S_0 = 0$ and the shear and normal stresses are Cauchy stresses. A model with non-zero cohesion strength may be attempted in the future, but if $S_0 = 0$, then the distinction between nominal and Cauchy stresses becomes less relevant because $\theta = \Theta = \tan^{-1}(\tau/\sigma) = \tan^{-1}(T/\Sigma)$.

The Coulomb friction model assumes sliding is a rate independent process, but there may be a shear rate dependence similar to that found by Minkley & Mühlbauer (2007). The experimental shear velocity of 363 mm/day is multiple orders of magnitude above clay seam shear velocities around rooms at the WIPP. WIPP clay seam shear velocities have not been directly measured, but the sliding within one day is not noticeable, so these velocities are probably well beneath 1 mm/day. Future clay seam shear experiments will hopefully include shear velocity sensitivity studies.

Another consideration is whether fluid pressure within an in-situ clay seam would support some of the normal stress, thereby reducing the effective normal stress applied to the clay material. This effect might be significant if the clay provided the majority of the clay seam strength, but, most likely, sliding causes asperities on either side of a clay seam to interlock and supply the bulk of the shear resistance.

The simple clay seams constitutive model in Eqn (2) was utilized in finite element simulations similar to those in Stone (1997), which predicted disposal room porosity over time. Figure 7 shows a schematic of the boundary conditions, stratigraphy, and idealized, homogeneous, block of waste within both upper and lower horizon disposal rooms at the WIPP. This disposal room is long and slender, allowing a plane-strain approximation at room mid-length. Disposal room porosity was computed as

$$\phi = \frac{V_R - V_S}{V_R} \tag{3}$$

where V_R was the current volume of the room (void space plus solid waste) and V_S was the volume of solid waste within the room. Any gas within the room was allowed to escape, so that the gas pressure remained zero. The most important deviations from Stone (1997), for the purposes of this paper, are these simulations included the 12 clay seams shown in Figure 7 and used an updated waste constitutive model calibration.

The two seams closest to the room are Clay F and G. Clay Seam F is generally several inches wide and resembles the interfaces from the first series of lab tests. Clay Seam G is a thin distinct clay layer that resembles the artificial seams from the second series of lab tests over a few centimeters, yet still exhibits centimeter undulations over spans of several meters. The other clay seams near WIPP are still being studied, but they are expected to be somewhere between Clay F and G. Consequently, Clay F's friction coefficient was set to the upper bound from the shear tests (tan θ = 0.42), while all other clay seams were varied between the lower and upper bounds from the shear tests (tan θ = 0.0279 to 0.42) (see Fig. 6). The simulations were run with a coarse mesh to get a preliminary understanding of the clay seam sensitivity.
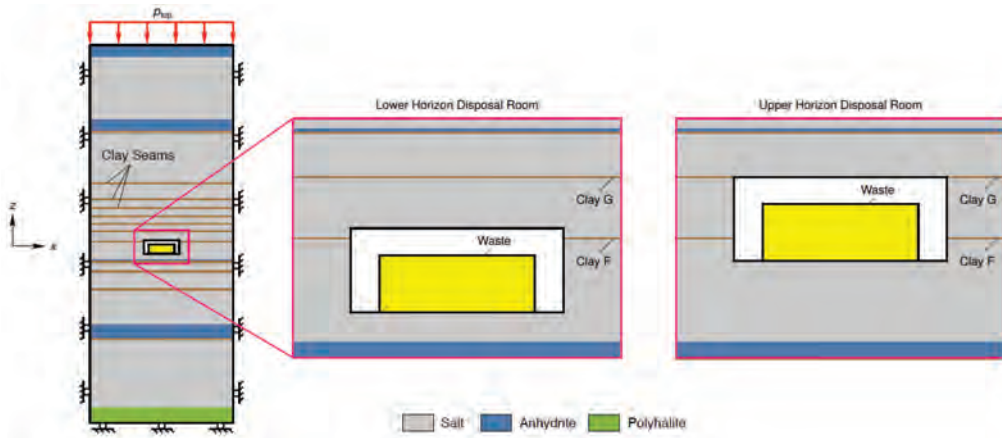
Figure 7. WIPP disposal room simulation boundary conditions and idealized stratigraphy, including seam locations for upper and lower horizon disposal rooms.
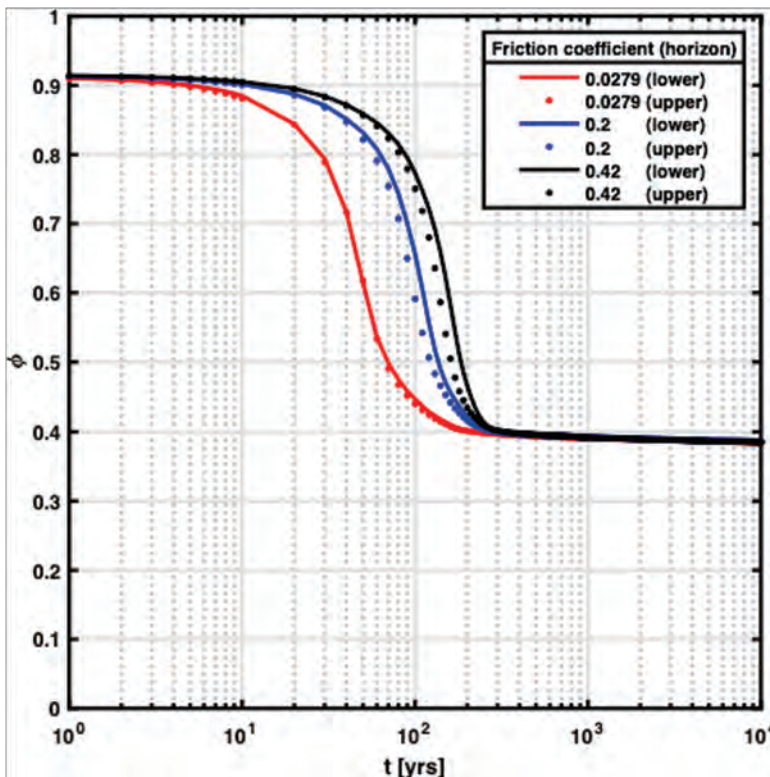
Figure 8. Upper and lower horizon disposal room porosity histories, assuming no gas trapped in the room. The friction coefficient tan θ was varied for all seams except Seam F.

Figure 8 shows the room porosity for upper and lower room configurations for several different friction coefficients for all clay seams, except Clay F. For times less than 300 years, the room porosity is quite sensitive to the clay seam sliding. At 70 years, the porosity varies between approximately 0.5 and 0.85 when the clay friction coefficient is varied from tan θ = 0.0279 to 0.42. At ~300 years, however, the waste is highly compacted and begins to supply resistance comparable to the far-field lithostatic pressure. As the waste pressure starts to balance with

the salt pressure, the clay seam shear stresses asymptote to approximately 0.38 and the room porosity becomes insensitive to the clay seam friction coefficient.

6 Conclusions

Eight samples of salt with artificial clay seams of two different thicknesses were subjected to displacement-controlled direct shear tests at three different normal loads. The tests ran according to procedure, and both maximum shear strength and final shear strength were determined for each test. The test results were similar in that a peak stress was achieved at which the seam broke, and the shear stress lowered through continual shearing. Although none of the tests achieved a true residual stress plateau, the final shear stresses reasonably conformed to Mohr-Coulomb behavior. The Mohr-Coulomb parameters were similar to those of a highly consolidated, saturated, clay, which is to say they were quite low compared to direct salt surface contacts.

These artificial clay seam results and previous direct shear test results on salt with diffuse clay interfaces appear to provide lower and upper bounds for the expected strength of clay seams from the WIPP site. These results will hopefully be precursors to tests on relevant clay seams from the WIPP site (probably Clay Seams F and G). Some potential improvements for future shear tests would be to reduce the shear velocity to something closer to expected in situ rates, use larger diameter samples for more asperity interlocking, and take the evolution of the contact area into account.

The upper and lower bounds from the direct shear tests were used in simulations of waste compaction due to disposal room closure at the WIPP. This preliminary study found disposal room porosity was sensitive to clay seam sliding behavior during the first 300 years, yet became insensitive afterwards.

References

BUCHHOLZ, S.A. 2019. Technical Letter Memorandum RSI/TLM-190, Direct Shear Testing of Bedded Interfaces and Clay Seams, RESPEC, Rapid City, SD, January 11, 2019.

HANSEN, F.D., SOBOLIK, S.R. & STAUFFER, P. 2016A. Intermediate Scale Testing Recommendation Report, FCRD-UFD-2016- 000030 Rev. 0, SAND2016-9041R, Sandia National Laboratories, Albuquerque, NM.

HANSEN, F.D., STEININGER, W. & BOLLINGERFEHR, W. 2016B. Proceedings of the 6th US/German Workshop on Salt Repository Research, Design, and Operation. FCRD-UFRD-2016-00069. SAND2016-0194R, Dresden, Germany, Sept. 2015. Sandia National Laboratories, Albuquerque, NM.

HANSEN, F.D. STEININGER,W. & BOLLINGERFEHR, W. 2017. Proceedings of the 7th US/German Workshop on Salt Repository Research, Design, and Operation, SFWD-SFWST-2017-000008. SAND2017-1057R, Arlington, VA, Sept. 2016, Sandia National Laboratories, Albuquerque, NM.

KEFFELER, E.R, BUCHHOLZ, S.A. & SOBOLIK, S.R. 2021. Direct Shear Testing of Consolidated Artificial Clay Seams in Salt. ARMA 21-1566. Presented at 55th US Rock Mechanics/Geomechanics Symposium held in Houston, Texas, USA, 20-23 June 2021.

LADD, C.C. & L. EDGERS, 1972. Consolidated-Undrained Direct-Simple Shear Tests on Saturated Clays. Department of Civil Engineering, Massachusetts Institute of Technology, Cambridge, Res. Rept. R72-82, No. 284, 1972, 354 pp.

LÜDELING, C., SALZER, K., GÜNTHER, R. M., HAMPEL, A., YILDIRIM, S., STAUDTMEISTER, K., GÄHRKEN, A., STAHLMANN, J., HERCHEN, K., LUX, K.H., REEDLUNN, B., SOBOLIK, S., HANSEN, F.D. & BUCHHOLZ, S.A. 2018. WEIMOS: Joint Project on further development and qualification of the rock mechanical modeling for the final HLW disposal in rock salt. Overview and first results on tensile stress modeling. Proceedings of the 9th Conference on the Mechanical Behavior of Salt (Saltmech IX), 12-14 Sept. 2018, Hannover, Germany. Eds.: S. Fahland, J. Hammer, F.D. Hansen, S. Heusermann, K.-H. Lux & W. Minkley, published by BGR Hannover, ISBN 978-3-9814108-6-0, pp. 459-477.

MINKLEY, W. & M MÜHLBAUER, J., 2007. Constitutive Models to Describe the Mechanical Behavior of Salt Rocks and the Imbedded Weakened Planes. Wallner, M., K-H Lux, W. Minkley, H.R. Hardy, eds. The Mechanical Behavior of Salt: Understanding of THMC Processes in Salt. Taylor & Francis/Balkema, Leiden, The Netherlands.

SOBOLIK, S.R., KEFFELER, E.R, BUCHHOLZ, S.A., BORGLUM, S. & REEDLUNN, B., 2019. Shear Behavior of Bedded Salt Interfaces and Clay Seams. ARMA 19-040. Presented at 53rd US Rock Mechanics/Geomechanics Symposium held in New York, NY, USA, 23-26 June 2019.

SOBOLIK ,S.R., KEFFELER, E.R, & BUCHHOLZ, S.A., 2020. Shear Behavior of Artificial Clay Seams within Bedded Salt Structures. SAND2020-11959, Sandia National Laboratories, Albuquerque, NM, USA.

STONE, C.M. 1997. Final disposal room structural response calculations. SAND97-0795, Sandia National Laboratories, Albuquerque, NM, USA.

Rate-dependent behaviour of fracture propagation in salt rock

Andreu Escanellas[1*], Eduardo Cámara[1], Joaquín Liaudat[2] and Ignacio Carol[1]

[1]ETSECCPB, Universitat Politècnica de Catalunya, Barcelona

[2]Geo-Engineering section, TU Delft, The Netherlands

* andreu.escanellas@upc.edu

ABSTRACT: This paper describes an on-going experimental and numerical modelling research project on salt rock specimens. The experimental part of the study consists of a number of Mode I fracture tests with the WST (Wedge-Splitting Test) configuration, which are performed at different loading rates and complemented by a series of standard uniaxial creep tests. The preliminary WST results show a greater mechanical fracture work accompanied with lower force peaks, for the slower tests. As a first attempt to represent the experimental results, an in-house Finite Element model has been used, which combines an inviscid discrete fracture approach with a Maxwell chain model for the continuum material. The simulations show a decrease of the mechanical work needed for opening the fracture and higher peak force, as foreseen by the ongoing experimental results, but not with the same intensity, which seems to indicate that work dissipation may not be caused exclusively by the bulk viscosity.

1   Introduction

The long-term deformations and stability of underground salt/potash mines are mainly determined by the viscous behaviour of the saline rock mass. As tunnels are excavated, deviatoric stresses are induced around the tunnel cross section, leading to the development of creep strains in the salt rock. Traditionally, it has been assumed that the main consequence of the creep deformation is the loss of serviceability of the mine due to the time-dependent convergences that progressively reduce the excavated cross-section. However, the development of creep deformations is associated to a progressive redistribution of stresses, which has the potential of inducing cracking and fracture in the salt rock, especially if discontinuities are already present in the rock mass. Consequently, a tunnel cross-section that is perfectly stable after the excavation may approach failure collapse as time goes by due to the propagation of fractures.

Because creep-fracture interactions have been often neglected, mine engineers have traditionally addressed the creep behaviour and the mechanical strength of the salt rock separately. On one hand, the creep behaviour is typically considered through simple visco-elastic models which make it possible to estimate the convergence rate and the possible effect on the tunnel serviceability. On the other hand, mechanical strength issues may be treated in ways similar to other rock materials, via strength criteria defined in the stress space. However, significant tunnel collapses have indicated that this approach may not be on the safe side (Whyatt & Varley 2008).

To the best of the authors' knowledge, very little has been published on the fracture mechanics of salt rock and the interaction between creep and fracture. Along this line, this paper describes an on-going experimental and numerical modelling research project which is carried out at UPC (Barcelona) on salt rock specimens from the mines in the region of Bages in Central Catalonia, Spain.

The experimental part of the study consists of a number of Mode I fracture tests at different loading rates, complemented by a series of standard uniaxial creep tests. The fracture tests were performed with the Wedge Splitting Test (WST) setup (see, e.g. Brühwiler & Wittmann 1990), at four different opening rates with the purpose of assessing the time dependency of parameters such as the tensile strength and the fracture energy.

In the numerical part of the study, the WST were simulated in order to aid the test interpretation and planning as suggested elsewhere (Liaudat et al. 2015). For this purpose, an in-house Finite Element model is used which allows to simulate WST within the discrete fracture approach.

2   Experimental evidence

2.1   Samples

The salt rock samples come from the Cardona saline formation. This formation, belonging to the Catalan potassium basin, formed between the Superior Eocene and Oligocene, when the Pyrenees rose, closing the oceanic communication of the mass of water that occupied what nowadays is the Ebro Valley. This closure gave place to a potent sedimentary series, where the layer of Halite can reach a thickness of more than 100 m.

Samples were extracted from Halite layers crossed by the mines in this region. Grain size range from <1 up to 20 mm, with no visible joints or preferential orientations. For the creep tests, cylindrical bore hole samples of 50 mm in diameter and 100 mm length were used. For the WST, prismatic blocks of 150x150x150 mm^3 were cut.

2.2   Standard creep Tests

2.2.1   Methods

The aim of these creep tests is to aid the interpretation of the WSTs presented in the following Section 2.3, by assessing the uniaxial creep behaviour of the material. For this purpose, cylindrical samples were tested under three different load levels: 2.5 MPa, 5 MPa and 10 MPa. Since the WST at the lowest loading rate required approximately 12 hours, a total duration of the creep tests of 7 days was deemed sufficient for this study.

The vertical constant load was applied using an oedometer bench setting. Vertical displacements were recorded via LVDT transducers (±2.5 mm, lineal error < ±0.1\%) aligned with the oedometer loading axis.

2.2.2   Results

Figure 1 shows the creep curves obtained in two different representations. The top plot shows the complete deformation curves, i.e. including the initial elastic deformation, in natural time scale. The bottom plot shows the steady state creep deformation, i.e. after deducting the initial elastic deformation, in logarithmic time scale.

Observing the bottom plot at the end of the tests, it is apparent that the time-dependent strain obtained for 5 MPa is approximately twice the strain obtained for 2.5 MPa. Therefore, creep for compressive loading under 5 MPa may preliminary be considered as proportional to the applied load level, i.e. the linear creep assumption may be valid. In contrast, the creep obtained for 10 MPa is about 6 times the creep observed for 5 MPa, and consequently, for the purpose of the current study, creep under uniaxial stress of 5 MPa may be considered preliminarily as linear creep This limit value of 5Mpa for the linear range of creep seems to be in agreement with other experimental observations in similar time ranges, e.g. Wang et al. (2022).
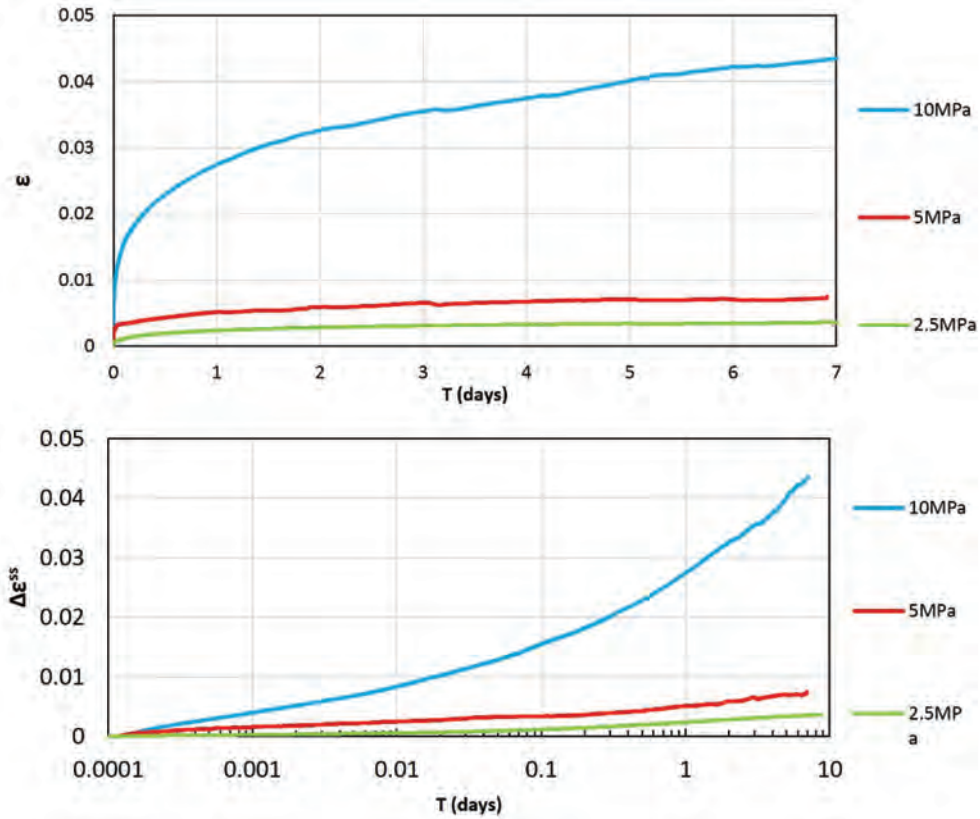
Figure 1: Uniaxial creep curves for three different load levels. Top, complete deformation (ε) curves in natural time scale. Bottom, steady state creep (Δε^{ss}) curves in logarithmic time scale.

2.3 Wedge Splitting Tests (WST)

2.3.1 Methods

The WST is a method to generate stable fracture propagation in quasi-brittle materials, e.g. rock or concrete, to determine fracture mechanics parameters in mode I such as the fracture toughness or the specific fracture energy (e.g. see Brühwiler & Wittmann 1990). The specifics of the setup used for this study are schematically depicted in Figure 2 (left). A rectangular notch and a groove are cut in the cubic specimens in order to apply the splitting force and to localise the fracture. A pair of steel L-profiles equipped with roller bearings is affixed to both sides of the notch. Lateral opening displacement of the rollers is imposed through a wedge moving vertically down. From the $F_H - COD$ (Horizontal splitting force – Crack Opening Displacement) response of the specimen, the specific fracture energy is determined. Moreover, with this setting, the tensile strength can also be derived via numerical back analysis.
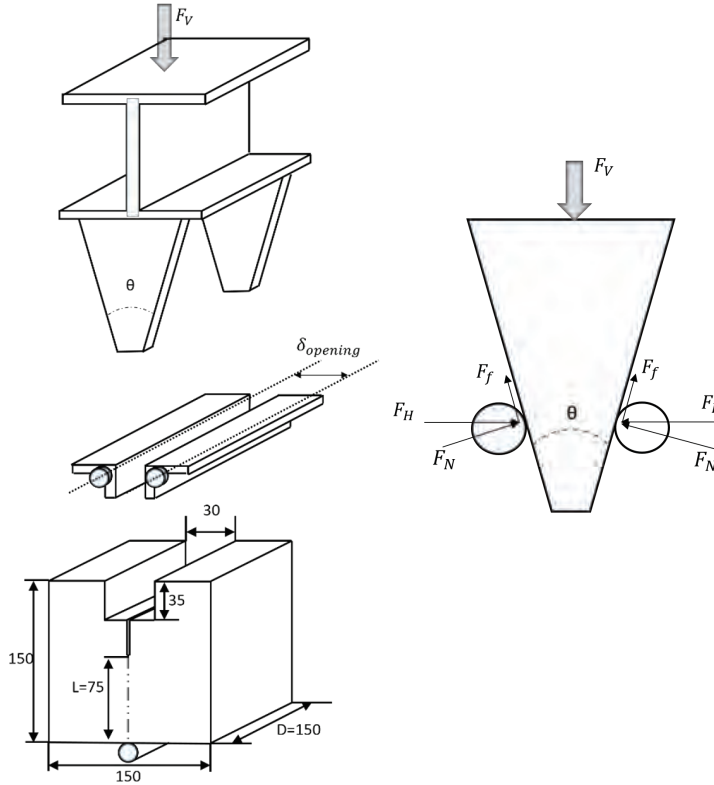
Figure 2: Wedge Splitting Test setup (left) and graphical force decomposition at the wedge-roller bearing contacts (right).

Figure 2 (right) shows a free body diagram of forces on the wedge. The horizontal force applied to the specimen is calculated by means of Equation (1), where F_V is the vertical load applied, θ is the wedge angle and μ is the coefficient of friction between wedge and roller.

$$F_H = \frac{1 - \mu tan\varphi}{2(\mu + tan\varphi)}$$

(1)

If the fracture process is stable, the mechanical work required to create a unit area of fracture ($\tilde{G}_f^I$ [J/m²]) can be obtained from the $F_H - COD$ response of the specimen using Equation (2), where A_f is the surface of the ligament area ($A_f = L \cdot D$, as in Figure 2).

$$\tilde{G}_f^I = \frac{1}{A_f} \int_0^\infty F_H \, dCOD$$

(2)

For a material with negligible creep deformation, $\tilde{G}_f^I$ can be identified with the specific fracture energy of the material G_f^I, a rate-independent material parameter. In the case of salt rock, in contrast, part of the invested mechanical work will be spent in creep deformations and, consequently, $\tilde{G}_f^I$ is expected to be a rate dependent value.

The testing system used consisted of a loading frame, a load cell, two displacement measurement devices and data acquisition equipment:

- Loading frame – ELE Digital Tritest 100 (loading capacity 500kN). Load cell – UtilCell 610 (nominal load 25 kN, linearity error < ±0.25\% F.S.) with signal conditioning amplifiers Krenel CEL/M010.

- Displacement measuring devices – Two LVDT displacement transducers RDP GT2500, ±2.5mm (linearity error < ±0.1\% F.S.), with signal conditioning amplifiers RDP S7AC, were used in the axis of the horizontal splitting force, one on each side of the specimen (COD1 on side 1, COD2 on side 2).

- Data acquisition – ELE automatic data acquisition unit.

2.3.2 Results

In order to investigate the effect of the loading rate on the $F_H - COD$ response curve, four WSTs were performed with different COD rates, namely: 5, 0.625, 0.078 and 0.011 mm/min. The obtained curves are given in Figure 3. It can be readily appreciated in this plot that as the COD rate decreases, the peak value of the F_H decreases but the area under the curves (the spent mechanical work) increases.
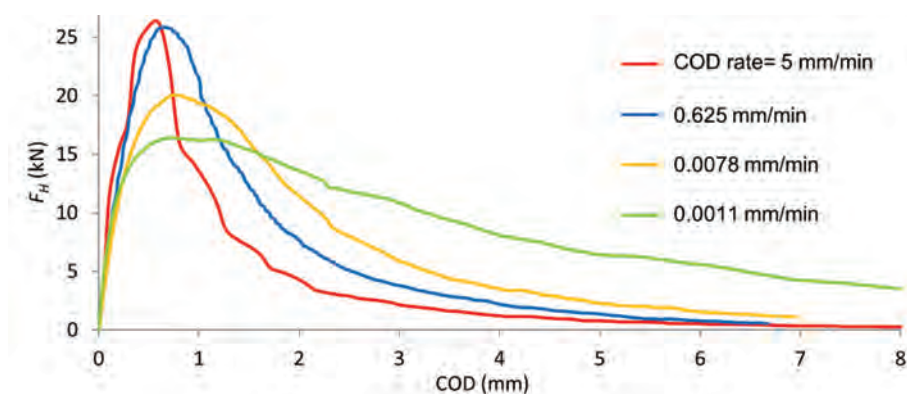
Figure 3: Wedge Splitting Test curves for different COD rates.

3   Discussion

As a first (simplest) interpretation, the observed effect of the COD rate on the WST curves could be attributed solely to the development of creep deformations in the bulk material. In order to tests this hypothesis, the performed WSTs are simulated with a Finite Element numerical model, as has been done before for other types of rock by some of the authors (Liaudat et al. 2015; Liaudat et al. 2017).

3.1   The numerical model

The model consists of continuum elements for the bulk of the salt rock, while the fracture is represented via zero-thickness interface elements pre-inserted along the fracture path, which are equipped with a mechanical constitutive law based in the non-linear fracture mechanics theory (Carol et al. 1997). This constitutive law has an analogous structure to traditional elasto-plasticity theory using a yielding surface in the stress plane as a criterion for fracturing. The parameters that describe the yielding surface (F) depend on the fracture work (W^{cr}) as history variable. Thus, when fracture work reaches the value of the fracture energy of the material (G_f^I), tensile strength has totally vanished. The main aspects of this law are summarised in Figure 4.
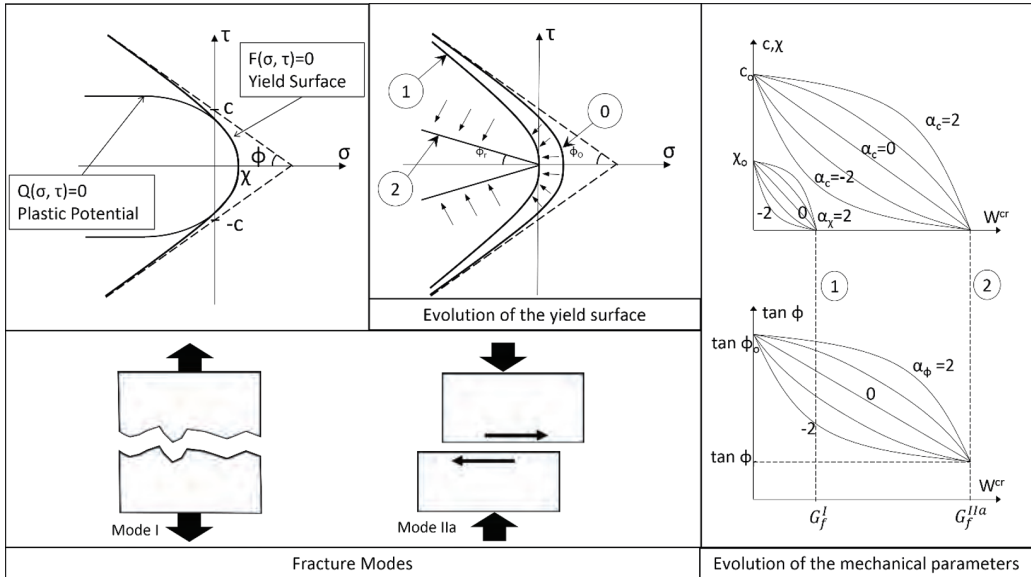
Figure 4. Fracture-based elasto-plastic constitutive law for interface element. After Carol et al. (1997). Being c, shear strength, χ, tensile strength, ϕ, internal friction angle, G_f^I, fracture energy in mode I, G_f^{IIa} fracture energy for mode IIa, α_c, α_χ and α_ϕ, shape parameters for the evolution of mechanical parameters.

The FE mesh and boundary conditions used for the calculations are depicted in Figure 4. The geometry corresponds to the cross section of a generic specimens of 150x150 mm. The dark blue elements represent the loading plates, and the magenta elements are used to represent the compliance of the loading system. The red arrows represent the imposed horizontal displacements.
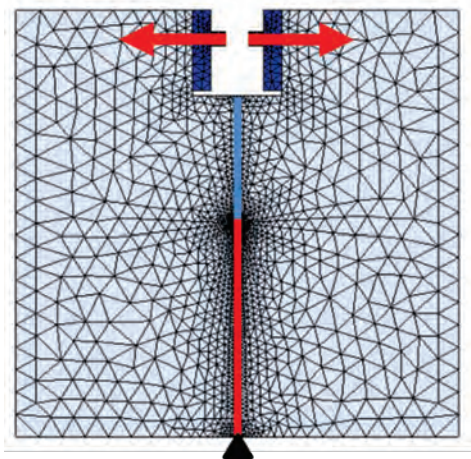
Figure 5: Finite Element mesh and boundary conditions of the problem.

In order to calibrate the parameters of the fracture constitutive law, a first simulation is performed of the WST test with highest loading rate, by using linear elasticity for the continuum elements representing the salt rock. This corresponds to assuming that in this fast loading

case viscous deformations are very small and may be neglected, which may be only approximate but is a simple first approach to determine fracture parameters. Figure 5 shows the experimental WST curve for the highest COD rate together with the fitted numerical curve, using elastic parameters $E = 900$ MPa, $\nu = 0.3$. The calibrated parameters are the tensile strength $\chi_0 = 3.15$ MPa and the specific fracture energy $G_f^I = 400$ J/m². The rest of the constitutive parameters are not relevant since shear stresses cannot be developed due to the symmetry of the problem.
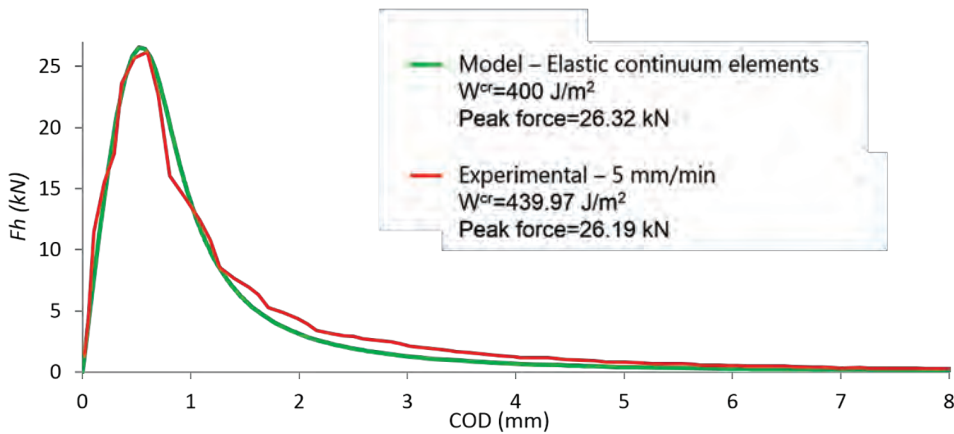
Figure 6: Wedge Splitting Test curves: experimental for 5 mm/min COD rate and numerical modelling using a linear elastic law for representing the salt rock.

Once theese parameters have been calibrated, a second set of simulations have been performed using a Maxwell chain visco-elastic constitutive law for the continuum elements representing the salt rock, in order to reproduce the creep behaviour reported in Section 2.2. This combination of visco-elastic continuum elements and rate-independent interface element has been previously proposed by López et al. (2001) for modelling combined creep and cracking in concrete. The visco-elastic law parameters were obtained by fitting the data from the uniaxial creep tests under 2.5 MPa (Section 2.2) using the method proposed by Bažant (1982).

Figure 6 shows the WST curves obtained with the model for the four experimental COD rates. For comparison, the experimental WST curves are plotted (in grey dashed lines) together with the numerical curves. Both the numerical and experimental WST results are summarised in Figure 7 in terms of the peak splitting force (F_H) and the apparent fracture energy ($\tilde{G}_f^I$) as functions of the COD rate.
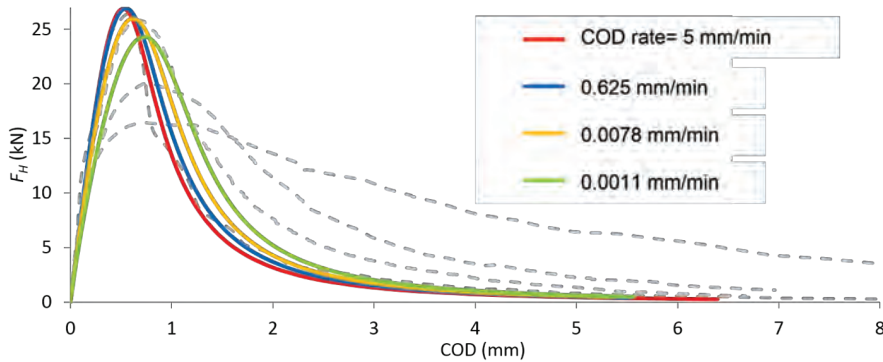
Figure 7: Numerical Wedge Splitting Test curves for different COD rates using a visco-elastic constitutive law for representing the salt rock. The dashed lines correspond to the experimental curves in Figure 3.
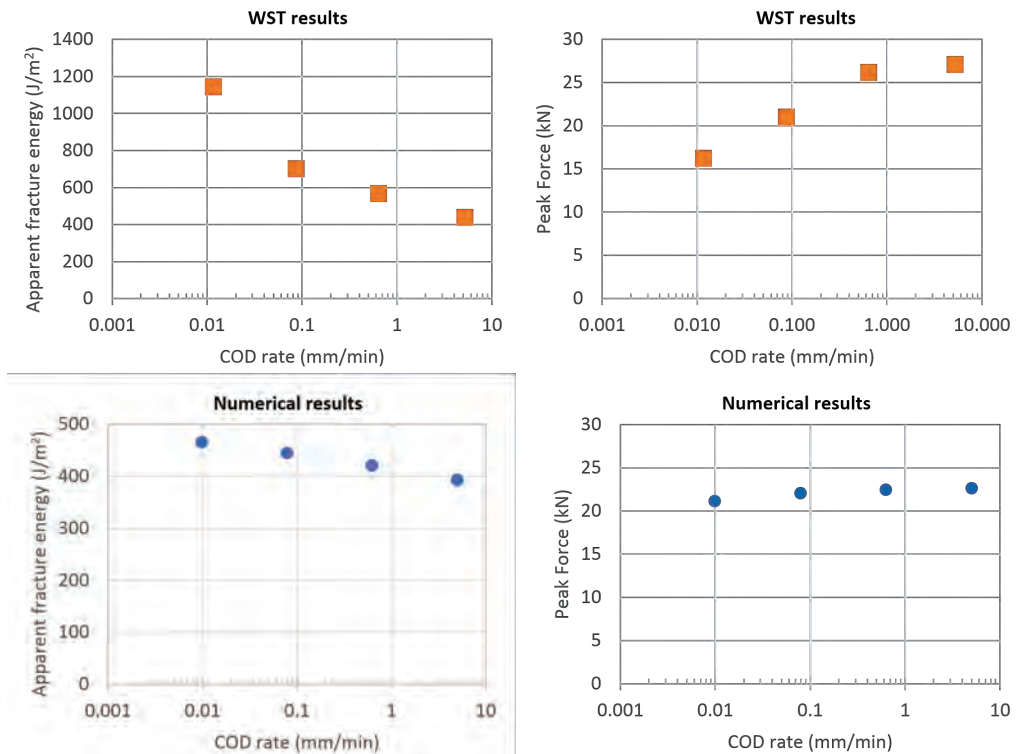
Figure 8: Peak horizontal force (F_H) and apparent fracture energy ($\tilde{G}_f^I$) as a function of the COD rate. Top, experimental results. Bottom, numerical modelling results.

In Fig. 6 and 7, it can be observed that the numerical model was able to qualitatively reproduce the main trends observed in the experiments, i.e. the reduction of the peak splitting force and the increase of the apparent fracture energy for decreasing loading rates. However, the model failed to quantitatively capture the experimental response. This analysis seems to indicate that the effect of the loading rate on the WST cannot be attributed solely to the creep deformations of the saline rock on both sides of the fracture path, and that the loading rate could have an effect on the development of the fracture itself. In the proposed numerical modelling approach,

introducing that effect would require a new rate-dependent constitutive law for the interface elements which would combine fracture/damage and viscous behaviour.

4   Concluding remarks

- The effect of the loading rate on the development of Mode I fractures in salt rock is being investigated by means of WST tests with different COD rates.
- Preliminary results indicate that the peak splitting force decreases, and apparent fracture energy increases as the COD decreases. Further testing is needed to confirm these trends and assess the variability of the results.
- Numerical modelling analysis of the experimental results seems to indicate that these effects cannot be only attributed to the development of creep deformations in bulk salt rock, and that the viscous effects would need to be introduced in the discrete fracture law as well.

Acknowledgements

References

BAŽANT, Z. 1982. Mathematical models for creep and shrinkage of concrete. Creep and Shrinkage in concrete structures, New York, NY: John Wiley & Sons, 1982, pp. 263-256.

BRÜHWILER, E. & WITTMANN, F.1990. The wedge splitting test, a new method of performing stable fracture mechanics tests. Engineering Fracture Mechanics, vol. 35, 117– 125.

CAROL, I., PRAT, P. C. & LÓPEZ, C. M. 1997. Normal/Shear Cracking Model: Application to Discrete Crack Analysis. Journal of Engineering Mechanics, 123(8), 765–773.

LIAUDAT, J., GAROLERA, D., MARTÍNEZ, A., CAROL, I., LAKSHMIKANTHA, M. R. & ALVARELLOS, J. 2015. Numerical modelling of the Wedge Splitting Test in rock specimens, using fracture-based zero-thickness interface elements. E. Oñate, D. R. J. Owen, D. Peric, & M. Chiumeti (Eds.), XIII International Conference on Computational Plasticity - Fundamentals and Applications (COMPLAS XIII), pp. 974–981. International Center for Numerical Methods in Engineering (CIMNE).

LIAUDAT, J., GAROLERA, D., CAROL, I., LAKSHMIKANTHA, M. R. & ALVARELLOS, J. 2017. Avoiding fracture instability in Wedge Splitting Tests by means of numerical simulations. E. Oñate, D.R.J. Owen, D. Peric & M. Chiumenti (Eds.), XIV International Conference on Computational Plasticity. Fundamentals and Applications (COMPLAS XIV), pp. 514-521. International Center for Numerical Methods in Engineering (CIMNE), Barcelona.

LÓPEZ, C. M., CAROL, I. & MURCIA, J. 2011. Mesostructural modeling of basic creep at various stress levels. Creep, Shrinkage and Durability Mechanics of Concrete and other Quasi-Brittle materials, 101-106.

WANG J., ZHANG Q., SONG Z., FENG S. & ZHANG Y. 2021 Nonlinear creep model of salt rock used for displacement prediction of salt cavern gas storage, Journal of Energy Storage 48

WHYATT, J. & VARLEY, F. 2008. Catastrophic Failures of Underground Evaporite Mines. Proceedings of the 27th International Conference on Ground Control in Mining; July 29 - July 31, 2008, Morgantown, West Virginia. Peng S.S., Mark C, Finfinger G.L., Tadolini

S.C., Khair A.W., Heasley K.A., Luo-Y, eds., Morgantown, WV: West Virginia University, 113–122.

WEIMOS: Laboratory investigation and numerical simulation of damage reduction in rock salt

R. Wolters[1], J.Q. Sun-Kurczinski[1], U. Düsterloh[1], K.-H. Lux[1], R.-M. Günther[2], C. Lüdeling[2], A. Hampel[3], S. Yildirim[4], D. Zapf[4], S. Wacker[5], I. Epkenhans[5], J. Stahlmann[5], B. Reedlunn[6]*

[1]Technische Universität Clausthal (TUC), Germany; [2]Institut für Gebirgsmechanik GmbH (IfG), Leipzig, Germany; [3]Hampel Consulting, Mainz, Germany; [4]Leibniz Universität Hannover (LUH), Germany; [5]Technische Universität Braunschweig (TUBS), Germany; [6]Sandia National Laboratories, Albuquerque, USA

* ralf.wolters@tu-clausthal.de

ABSTRACT: Damage reduction (healing) of rock salt is one of four laboratory research topics in joint project WEIMOS. Damage reduction is important for long-term safety of nuclear waste repositories in rock salt because it is directly linked to the time span needed for geotechnical barriers and the surrounding rock salt to reach long-term hydraulic tightness. In the WEIMOS damage reduction laboratory tests, which have been performed by TUC, samples of natural salt have first been damaged to specific values of dilatancy. Afterwards, the reduction of dilatancy at different temperatures and stress conditions has been observed over several months using high-precision measurement devices. Overall, four damage reduction test series with 34 damage reduction tests on Asse-salt and 10 damage reduction tests on WIPP-Salt in total have been performed within the WEIMOS project. Based on the test results, each project partner improved the damage reduction formulation within their constitutive models. These improved models were then used to simulate the damage-evolution around an emplacement drift, with increasing damage during the open drift phase and decreasing damage after including a sealing dam construction within the emplacement drift. This paper will present exemplary lab test results as well as selected simulation results.

1 Introduction

1.1 Some general comments about the WEIMOS project

Between 2004 and 2016, within three joint projects funded by the German Federal Ministry for Education and Research as well as the German Federal Ministry for Economic Affairs and Energy, the project partners documented and compared their constitutive models for rock salt with simulations of typical underground scenarios (2D and 3D). In back-calculations of laboratory test results the partners studied the ability of the individual models to describe relevant mechanical phenomena in rock salt, and compared model predictions against each other and against in situ measurement data. Within this series of joint projects, the first two projects focused on the investigation of basic deformation phenomena under various influences, e.g. transient and steady-state creep, damage-induced creep and dilatancy evolution, short-term strength and creep failure, post-failure behavior (Schulze et al. 2007; Hou et al. 2007; Hampel et al. 2010). Joint project III was a US-German collaboration in which selected benchmark calculations were performed to check and compare the various modeling approaches of the partners regarding the ability to describe the temperature influence on deformation as well as first approaches for the modeling of damage reduction and healing behavior of rock salt (Hampel et al. 2018; Hampel et al. 2015; Salzer et al. 2015; Herchen et al. 2016).

Following these joint projects, the WEIMOS project started in 2016 to further develop and improve the rock mechanical modeling approaches as well as the numerical simulation tools used by the different project partners in the context of long-term repository behavior analyses for a repository in rock salt mass. Based on the previous joint projects, four topics were identified by the partners for a necessary further development of the physical modeling. The

topics are the deformation behavior at small deviatoric stresses (Work Package 1 (WP 1)), the influence of temperature and stress state on the damage reduction behavior (WP 2), the deformation behavior resulting from tensile stresses (WP 3), and the influence of rock inhomogeneities (layer boundaries, interfaces) on deformation behavior (WP 4). Finally, the progress in the first three work packages (WP 1) to (WP 3) shall be demonstrated with simulations of complex 3D-models that characterize a sealing element situation of a final repository system (Virtual Demonstrator I (VD I)) as well as of a 3D-model of several parallel drifts (Virtual Demonstrator II (VD II)) (WP 5). The development of the partners' constitutive models is based on the laboratory work and common theoretical considerations. The laboratory work of WEIMOS consists of tests to investigate the damage reduction behavior and the rock salt deformation behavior at small deviatoric stresses (WP 2 and WP 1). The laboratory tests for the project were conducted by TUC (WP 2) and IfG (WP 1).

Preliminary WEIMOS results were already shown at the 9th Conference on the Mechanical Behavior of Salt (SaltMech IX) in 2018, e.g. Herchen et al. (2018) and Lüdeling et al. (2018). Within this volume, some selected final results of the WEIMOS project will be shown, focusing on the results of the latest damage reduction test series as well as on some selected numerical results at VD I.

1.2 Motivation to investigate damage reduction processes in rock salt

For the final disposal of heat-generating radioactive waste in deep geological rock salt formations, a safety analysis must demonstrate the long-term, complete containment of the waste in the host rock for the protection of the biosphere. Safety analysis simulations must reliably describe the temperature-dependent behavior of the host rock and the long-term tightness of rock salt within drift/shaft contour areas, especially in the nearfield of geotechnical barriers. This tightness depends on damage processes, which mainly take place during the excavation and operational phase of the open drifts and shafts, and damage reduction processes, which mostly occur after the operational phase. Against this background, the WEIMOS project is the latest in a series of joint projects that strive to develop and compare numerical tools for the design and analysis of repositories, and other underground openings, in rock salt formations. These tools include the physical constitutive models, techniques to determine the salt-type specific parameter values, models of underground structures, and methods to evaluate simulation results.

The damage and healing processes are significant parts of the integrity analysis for the demonstration of the containment-providing rock zone (CRZ) and especially in simulations with respect to the tightness of geotechnical barriers which consider the development of the excavation disturbed/damaged rock zone (EDZ, DRZ). Generally, "damage" involves the formation of microcracks and results in reduced load-bearing capacity, volumetric strains (dilatancy), and permeability (Peach et al. 1996; Popp et al. 2001). "Damage reduction" or "healing" at first reduces dilatancy by a closure of opened microcracks and subsequently may restore mechanical strength by a recovery of cohesion with a regeneration of bonds between microcrack surfaces.

Both for lab tests and for many constitutive models, dilatancy is the main parameter characterizing rock salt damage. Hence, in this paper we focus on volumetric strains as the measure of damage and healing; further research is needed regarding the regeneration of mechanical strength and impermeability (Lüdeling et al. 2015).

Because of the secondary permeability evolution within the EDZ, a well-supported "healing" approach in the constitutive models would help to more realistically assess the long-term performance of geotechnical barriers. The healing of the EDZ after the installation of a sealing element depends on the stress state in the surrounding rock mass. This stress state evolves with time, and it is influenced by the creep behavior of the rock salt mass and the stiffness of the sealing structure, e.g. a concrete structure (hard inclusion) or crushed salt (soft inclusion).

Thus, reliable experimental data for the influence of temperature and stress state on the damage reduction are of urgent need for developing improved healing approaches.

2   Laboratory investigations of damage reduction in rock salt

2.1   Description of test machine and test procedure

The damage reduction tests of the WEIMOS project have been performed at TUC laboratory using the test equipment shown in Fig. 1. Their design is characterized by the four modules axial piston, pressure chamber, thick-walled tube and base plate. A constructive peculiarity of these triaxial cells in comparison to conventional systems with an external load frame construction is the integration of the axial pressure generation into the triaxial cell.
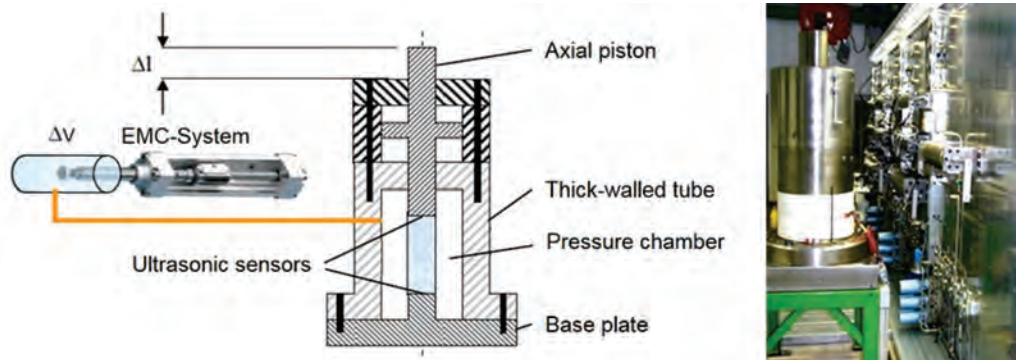
Figure 1: Sketch and picture of the test machine

Sample dimension were $15\,cm$ diameter and $30\,cm$ length. Material was rock salt from the Asse deposit in Germany and the WIPP site in the United States.

The dilation of a salt sample is measured to infer the amount of damage during a test. The dilatancy parameter is the main quantity for the damage and healing approaches in the constitutive models of each partner. In general, dilation measurements during damage reduction tests are a big challenge because the tests have to be performed over a long test period at high pressures with very high resolution and stability – volume changes of approx. $1\,ml$ over several months have to be accurately monitored including their time-dependent evolution during that time period. External impacts such as room temperature fluctuations, hydraulic oil compressibility, and test machine stiffness can have large influences on the test results and have to be considered. For these reasons, four high-precision test machines at the TUC were additionally equipped with an electromechanical cylinder system (EMC system) to measure even very small volumetric deformations of the salt samples. An EMC-system, which is measuring volume changes using a rotating screw to move a piston within an oil chamber, is much a more precise measurement device than the typically used dilatancy measurement cylinders, which are also measuring volume changes using a moving piston, but where the movement of the piston is controlled by an oil pressure within a second hydraulic oil chamber, because oil creeping effects between both oil chambers along the edge of the piston with possibly very high volume rates are avoided at an EMC-system.

The basic aim of the damage reduction tests performed during the WEIMOS project was to first damage the samples by a deviatoric stress above the dilatancy boundary and then observe the gradual damage reduction under various non-dilating conditions. In the context of this paper focusing on the latest damage reduction test series ($\rightarrow$ series 4), these specific tests were performed according to the following five steps:

(1) After installation of the test specimen into the triaxial test cell, the cell was heated up to the intended test temperature and an isotropic stress level of $\sigma_r = \sigma_z = 30\,MPa$ was applied for 5 days. The aim of this 1st phase was the reduction of damage induced by the core drilling, the transport and/or the test specimen preparation (recompaction and tempering phase).

(2) At the end of the recompaction and tempering phase, 3 unloading-loading-cycles were applied, each with a simultaneous decrease of axial stress and confining pressure down to $\sigma_r = \sigma_z = 2\,MPa$, followed by a simultaneous increase of axial stress and confining pressure up to $\sigma_r = \sigma_z = 30\,MPa$ again. This 2nd phase provides information about the test machine compression and extension stiffness, as well as of the hydraulic oil compressibility.

(3) At the beginning of the 3rd phase, the confining pressure was lowered down to $\sigma_r = 2\,MPa$, while the axial stress was held at $\sigma_z = 30\,MPa$. This triaxial compression stress state, which according to Düsterloh et al. (2015) as well as according to Salzer et al. (2015) is significantly above the rock salt dilatancy boundary of approx. $20\,MPa$ for $\sigma_r = 2\,MPa$, was held fixed during the damage phase. The damage phase ended as soon as a volumetric strain value of approx. $\varepsilon_{vol} \approx 1-1.5\,\%$ was reached. According to Schulze et al. (2001) the induced microcracks should have been mainly oriented in the axial direction at the end of this damage phase. This phase generally lasted several days up to two weeks.

(4) During the 4th phase of the test, the confining pressure was slowly increased with a pressure rate of $\dot{\sigma}_r = 2\,MPa/d$ until the intended confining pressure level of the healing phase is reached. Then, the axial stress was immediately set to the intended axial stress level of the healing phase. At the end of the 4th test phase, the 1st invariant of the stress tensor always was at $I_1 = 43\,MPa$, while the deviatoric stress was different from test to test, but always below the dilatancy boundary.

(5) The 5th test phase is the healing phase, where the axial stress and confining pressure have usually stayed constant for several months or even longer periods of time. Nevertheless, within some of the performed damage reduction tests the axial stress and/or confining pressure were changed during the healing phase due to different reasons.

2.2 Discussion of testing experiences and some selected laboratory test results

During the first 2.5 years of the WEIMOS project, the damage reduction laboratory tests were designed to quickly collect test data for different loading conditions during the healing phase. This way, the project partners should be enabled to develop and improve their physical modeling approaches for damage reduction in rock salt already at an earlier stage of the project. To achieve this goal, the laboratory tests were performed on four similarly constructed test machines using a common EMC system at the same time. The EMC-system had to be switched all the time between the four test machines.

The same loading conditions were used on all four test machines during the 1st damage reduction test series, but different confining pressures on the four test machines for the 2nd and 3rd damage reduction test series to get test results for different loading conditions as fast as possible. Unfortunately, the setting of four different confining pressures during the 2nd and 3rd damage reduction test series made lots of the tests of the 2nd and 3rd damage reduction test series fail. It showed that the controlling of the switching process of the common EMC-system is much more difficult at different confining pressures than at an equal confining pressure for all of the four test machines. Therefore, afterwards, a 4th healing test series was performed

with same loading conditions on the four test machines. The 4th healing test series itself includes seven subseries (subseries 4a to 4g), each with four tests – one on each test machine. The subseries had different loading conditions among each other, but same loading conditions on all four samples within each subseries. The general test conditions of this 4th test series are described in the previous section. A more detailed description of the test conditions may be found within the final report of the WEIMOS-partner TUC (Lux et al. 2022).

Fig. 2 shows some exemplary test results of the 3rd and 4th damage reduction test series (sample A → 3rd test series / sample B → test series 4a / sample C → test series 4b / sample D → test series 4c) focusing on the test phases 3 (damage), 4 and 5 (healing) and especially on the dilatancy reduction at different stress conditions. All of these four samples have been investigated at a test temperature of $T = 35\,°C$. A more comprehensive overview of the test results may also be found within the final report of the WEIMOS-partner TUC (Lux et al. 2022).

Clearly, the dilatancy reduction took place much faster when the confining pressure is first slowly increased (4th test phase) than when the confining pressure is later fixed (5th test phase). Nevertheless, the dilatancy reduction did not start immediately with the beginning increase of confining pressure respectively mean stress, but there was a small timely delay, so the dilatancy reduction started when the confining pressure respectively the mean stress reached a certain level. This might be an indicator for a damage reduction, which starts as soon as the stress state falls below the dilatancy boundary, or even an indicator for the existence of a healing boundary, which could be near to or exactly at the dilatancy boundary.
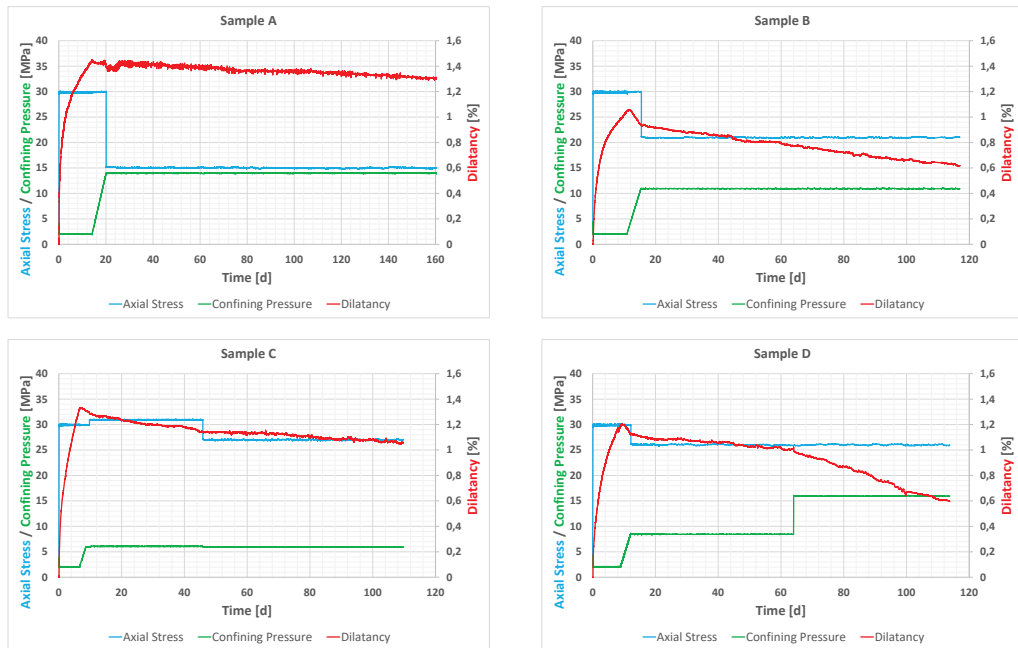
Figure 2: Exemplary test results of the 3rd and 4th damage reduction test series focusing on the dilatancy reduction at different stress conditions

Sample A and sample B both had an isotropic stress of $14.3\,MPa$ during the healing phase, but sample B had a 10-times larger stress difference than sample A. Despite the larger stress difference, dilatancy reduced faster on sample B than sample A. The stress states on sample C and sample D changed during the healing phase: decreasing the axial stress during the healing phase (sample C) resulted in a slower dilatancy reduction, while increasing the confining pressure during the healing phase (sample D) resulted in a faster dilatancy reduction.

The faster dilatancy reduction observed after increasing the confining pressure on sample D was expected. The triaxial compression during the damage phase induced primarily axially oriented microcracks, while the hoop stress due to the confining pressure during the healing phase was oriented mainly normal to the microcrack planes, so the closure of the predominantly axially oriented microcracks should be more efficient at a higher confining pressure.

In contrast, it was surprising that the greater deviatoric stress applied to sample B, compared to sample A, seemed to enhance the closure of microcracks. Perhaps larger deviatoric stress caused more creep, which accommodated the closure of rough microcrack surfaces. Further experiments are needed to confirm this unexpected result. Reducing the axial stress during the healing phase on sample C reduced both the deviatoric and isotropic stress. The decreased deviatoric stress may have contributed the slowing of dilatancy reduction in sample C, but it cannot be definitively proven. Besides, the slower dilatancy reduction observed at decreased axial stress on sample C might also be explained by the assumption, that there are also some more or less horizontally oriented microcracks within the sample which are closed less efficiently at lower axial stresses.

3   Some recommendations for modeling damage reduction in rock salt

Summarizing the results of the healing lab tests shown in the previous section as well as the results of the other healing lab tests performed during the WEIMOS project and described in Lux et al. 2022, it may be concluded, that the damage reduction process occurring in rock salt is a quite complex process to model and simulate. For not only qualitatively, but also quantitatively accurate physical modelling and numerical simulation, highly developed modern constitutive models for rock salt should include all the different dependencies of the dilatancy reduction rate on the different stress states which might be relevant in an excavation damaged zone around underground openings of a repository, a mine or other geotechnical constructions built in salt rock mass.

The distinction of different dilatancy reduction rates occurring at different stress conditions seems to need a modelling approach that considers the orientation of damage-induced microcracks. Therefore, during the WEIMOS project, the different project partners have improved their constitutive models by including a physical modelling approach for the damage reduction process based on the results of the performed healing lab tests. A specific explanation of these different approaches cannot be given within this paper but will be written in the final WEIMOS report of each project partner.

4   Numerical simulations of damage reduction in rock salt

According to Hampel et al. (2022), the achieved status of modeling of damage reduction and healing with the different constitutive models was demonstrated with simulations on the so-called Virtual Demonstrator I (VD I). These simulations were performed by each project partner.

VD I represents a square-cut drift in salt rock mass which is totally open for the first 30 years after its excavation. During this open drift phase, an excavation damaged zone (EDZ) occurs within the nearfield of the drift contour. 30 years after excavation of the drift, a dam structure was built into a part of the drift. During the following decades due to the creep behavior of the surrounding salt rock mass, the minimum principal stress within the EDZ around the dam starts to increase. This increase caused the damage-induced dilatancy around the dam to decrease while the dilatancy continues to increase around the open part of the drift.

Fig. 3 shows the numerically simulated evolution of the damage-induced dilatancy around the drift as a contour plot for different time points within the TUC simulation of VD I. The dilation starts in the nearfield of the drift corners immediately after the drift excavation. One year after

drift excavation, the damage-induced volumetric strain (dilation) is already higher than $0.1‰$ at the whole drift contour. The dilation continues to increase around the open drift and reaches approx. 6% in the nearfield of the drift corners and approx. 0.4% at the center of the drift roof 30 years after drift excavation. At this time, the dam is built into the front part of the drift. Afterwards, the dilation starts to decrease around the dam reaching dilatancy values below $0.1‰$ almost in the whole area around the dam 10 years after dam installation, while the dilation continues to increase in the still open part of the drift reaching more than 20% at the center of the drift roof 60 years after drift excavation.
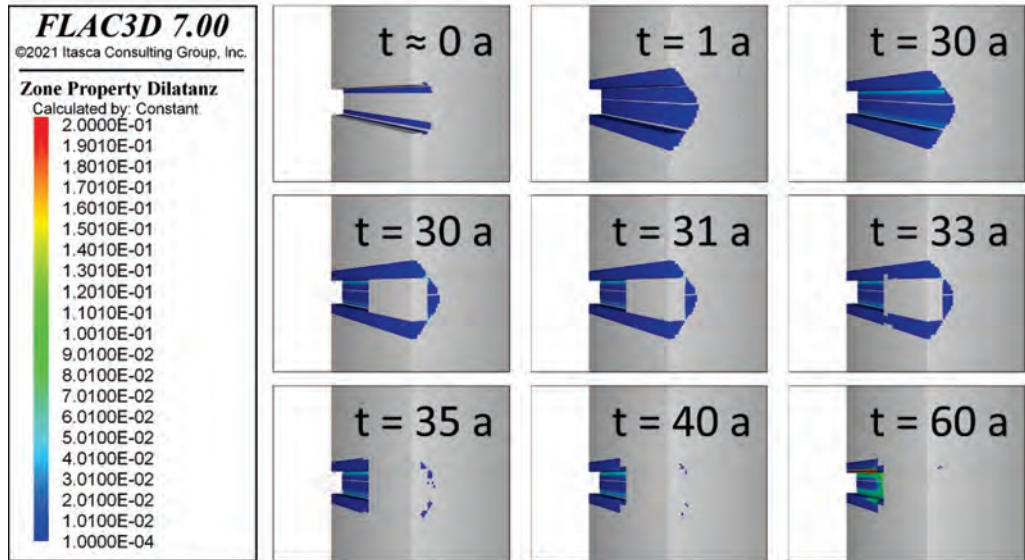
Figure 3: Numerically simulated evolution of the damage-induced dilatancy around the drift in the TUC simulation of VD I

Although 44 healing lab tests in total have been performed within the WEIMOS project, only a subset of them were successful, so the results can only be seen as a preliminary data base for the damage reduction behavior respectively the healing behavior of rock salt. Having this in mind, the different project partners of course have each developed different approaches for physical modelling of damage reduction in rock salt, have added them to their own constitutive models and have implemented them into their constitutive model codes used for numerical simulation of the rock salt behavior. For this reason, it is not very surprising, that the time period needed to reduce the dilatancy around the dam to very low dilatancy values differs significantly between the project partners, as it may be seen from Fig. 4, which is also shown in Hampel et al. (2022).
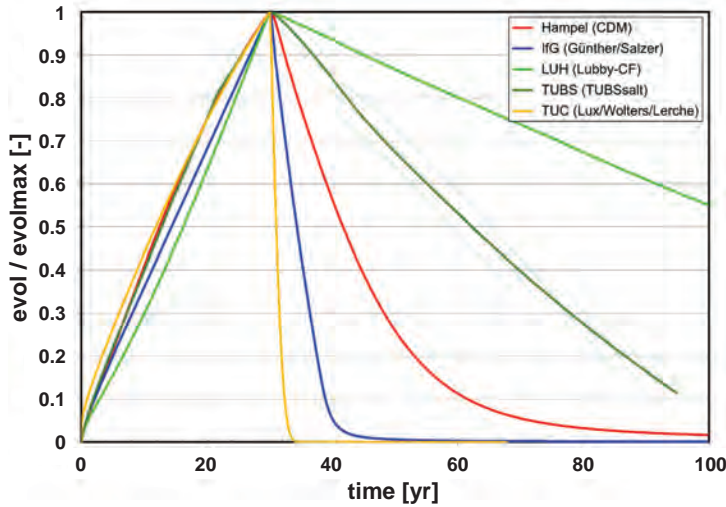
Figure 4: Time-dependent evolution of damage-related dilatancy at the middle of the roof above the dam of VD I, normalized by the maximum value after 30 years from simulations of the partners with their constitutive models

5   Conclusions

Within the WEIMOS joint research project, a significant number of damage reduction lab tests were performed on rock salt to provide the project partners with an adequate lab test data base for development and/or improvement of their physical modelling approaches concerning the damage reduction process in salt rock mass. Not very much surprisingly not every lab test worked as intended, but the less successful lab tests helped to improve the general knowledge concerning the further performance of damage reduction lab tests, while the successful lab tests helped to improve the understanding of various dependencies of the dilatancy reduction rate on dilatancy and stress state, especially on minimum principal stress and mean stress. As expected, increasing the confining pressure accelerated the dilatancy reduction. Unexpectedly, at an isotropic stress of $14.3\,MPa$ with a stress difference of $10\,MPa$ the dilatancy reduction rate was higher than at an isotropic stress of $14.3\,MPa$ with a stress difference of $1\,MPa$. Further investigations are needed to confirm this – at least at first view – surprising observation.

Based on the successful lab tests, the project partners have improved their constitutive models for consideration of the damage reduction process using the WEIMOS lab test data as an indicating preliminary data base. This further improvement of the constitutive models may be seen as a new significant milestone in the context of confidence building into numerical analyses regarding the long-term behavior of backfilled repository drifts in salt rock mass.

Nevertheless, more experimental investigations concerning the damage reduction process in salt rock mass are needed to further improve the understanding of the damage reduction process in salt and to diminish the remaining differences between the project partners' long-term dilatancy reduction predictions that resulted from the numerical simulations of VD I and could not be solved till the end of the WEIMOS project.

References

DÜSTERLOH, U., HERCHEN, K., LUX, K.-H., SALZER, K., GÜNTHER, R.-M., MINKLEY, W., HAMPEL, A., ARGÜELLO, J.G. & HANSEN, F. 2015. Joint project III on the comparison of constitutive models for the mechanical behavior of rock salt, III. Extensive laboratory test program with argillaceous salt from WIPP and comparison of test results. In L. Roberts, K. Mellegard & F. Hansen (eds.): Proc. of the 8th Conference on the Mechanical Behavior of Salt (SaltMech VIII), South Dakota School of Mines & Technology, Rapid City, SD, USA, 26-28 May, Taylor & Francis Group, ISBN 978-1-138-02840-1.

HAMPEL, A., GÜNTHER, R.-M., SALZER, K., LÜDELING, C., MINKLEY, W., PUDEWILLS, A., YILDIRIM, S., STAUDTMEISTER, K., ROKAHR, R., GÄHRKEN, A., MISSAL, C., STAHLMANN, J., HERCHEN, K., LUX, K.-H., REEDLUNN, B., ARGÜELLO, J.G. & HANSEN, F.D. 2018. Joint Project III on the Comparison of Constitutive Models for the Mechanical Behavior of Rock Salt: Modeling of the Temperature Influence on Deformation at WIPP. In S. Fahland, J. Hammer, F.D. Hansen, S. Heusermann, K.-H. Lux & W. Minkley (eds.): Proc. of the 9th Conference on the Mechanical Behavior of Salt (SaltMech IX), Hannover, 12-14 September 2018, Bundesanstalt für Geowissenschaften und Rohstoffe (BGR), ISBN 978-3-9814 108-6-0.

HAMPEL, A., GÜNTHER, R.-M., SALZER, K., MINKLEY, W., PUDEWILLS, A., LEUGER, B., ZAPF, D., STAUDTMEISTER, K., ROKAHR, R., HERCHEN, K., WOLTERS, R., LUX, K.-H., SCHULZE, O., HEEMANN, U. & HUNSCHE, U. 2010. Benchmarking of Geomechanical Constitutive Models for Rock Salt. Proc. 44th U.S. Rock Mechanics Symposium, Salt Lake City, 27-30 June 2010, ARMA10-287. American Rock Mechanics Association (ARMA).

HAMPEL, A., GÜNTHER, R.-M., SALZER, K., MINKLEY, W., PUDEWILLS, A., YILDIRIM, S., ROKAHR, R., GÄHRKEN, A., MISSAL, C., STAHLMANN, J., HERCHEN, K. & LUX, K.-H. 2015. Joint project III on the comparison of constitutive models for the mechanical behavior of rock salt, I. Overview and results from model calculations of healing of rock salt. In L. Roberts, K. Mellegard & F. Hansen (eds.): Proc. of the 8th Conference on the Mechanical Behavior of Salt (SaltMech VIII), South Dakota School of Mines & Technology, Rapid City, SD, USA, 26-28 May, Taylor & Francis Group, ISBN 978-1-138-02840-1.

HAMPEL, A., LÜDELING, C., GÜNTHER, R.-M., SUN-KURCZINSKI, J.Q., WOLTERS, R., DÜSTERLOH, U., LUX, K.-H., YILDIRIM, S., ZAPF, D., WACKER, S., EPKENHANS, I., STAHLMANN, J. & REEDLUNN, B. 2022. WEIMOS: Simulations of two Virtual Demonstrators. Proc. of the 10th Conference on the Mechanical Behavior of Salt (SaltMech X), Utrecht, July 2022 (this volume).

HERCHEN, K., DÜSTERLOH, U. & LUX, K.-H. 2016: Verbundprojekt: Vergleich aktueller Stoffgesetze und Vorgehensweisen anhand von Modellberechnungen zum thermo-mechanischen Verhalten und zur Verheilung von Steinsalz (TV 5: TUC). Final report, BMWi-FKZ 02E10820, Lehrstuhl für Deponietechnik und Geomechanik, Technische Universität Clausthal, Clausthal-Zellerfeld.

HERCHEN, K., POPP, T., DÜSTERLOH, U., LUX, K.-H., SALZER, K., LÜDELING, C., GÜNTHER, R.-M., RÖLKE, C., MINKLEY, W., HAMPEL, A., YILDIRIM, S., STAUDTMEISTER, K., GÄHRKEN, A., STAHLMANN, J., REEDLUNN, B. & HANSEN, F.D. 2018. WEIMOS: Laboratory Investigations of Damage Reduction and Creep at Small Deviatoric Stresses in Rock Salt. In S. Fahland, J. Hammer, F.D. Hansen, S. Heusermann, K.-H. Lux & W. Minkley (eds.): Proc. of the 9th Conference on the Mechanical Behavior of Salt (SaltMech IX), Hannover, 12-14 September 2018, Bundesanstalt für Geowissenschaften und Rohstoffe (BGR), ISBN 978-3-9814 108-6-0.

HOU, Z., WOLTERS, R., DÜSTERLOH, U., ROKAHR, R., ZAPF, D., SALZER, K., GÜNTHER, R.-M., MINKLEY, W., PUDEWILLS, A., HEEMANN, U., SCHULZE, O., ZETSCHE, F. & HAMPEL, A. 2007. Comparison of advanced constitutive models for the mechanical behavior of rock salt - results from a joint research project, II. Numerical modeling of two in-situ case studies and comparison. In K.-H. Lux, W. Minkley, M. Wallner, and H.R. Hardy, Jr. (eds.): Basic and Applied Salt Mechanics; Proc. of the 6th Conference on the Mechanical Behavior of Salt (SaltMech VI), Hannover, Mai 2007, Taylor & Francis (Balkema).

LÜDELING, C., GÜNTHER, R.-M., KNAUTH, M. & MINKLEY, W. 2015. Healing of Rock Salt Damage and Applications. ARMA15-698.

LÜDELING, C., SALZER, K., GÜNTHER, R.-M., HAMPEL, A., YILDIRIM, S., STAUDTMEISTER, K., GÄHRKEN, A., STAHLMANN, J., HERCHEN, K., LUX, K.-H., REEDLUNN, B. & HANSEN, F.D. 2018. WEIMOS: Overview and First Results on Tensile Stress Modelling. In S. Fahland, J. Hammer, F.D. Hansen, S. Heusermann, K.-H. Lux & W. Minkley (eds.): Proc. of the 9th Conference on the Mechanical Behavior of Salt (SaltMech IX), Hannover, 12-14 September 2018, Bundesanstalt für Geowissenschaften und Rohstoffe (BGR), ISBN 978-3-9814 108-6-0.

LUX, K.-H., WOLTERS, R., SUN-KURCZINSKI, J.Q. & HERCHEN, K. 2022. Verbundprojekt: Weiterentwicklung und Qualifizierung der gebirgsmechanischen Modellierung für HAW-Endlagerung im Steinsalz (WEIMOS) (Teilprojekt E: TUC). Final report, BMWi-FKZ 02E11446, Lehrstuhl für Geomechanik und multiphysikalische Systeme, Technische Universität Clausthal, Clausthal-Zellerfeld.

PEACH, C.J. & SPIERS, C.J. 1996. Influence of crystal plastic deformation on dilatancy and permeability development in synthetic salt rock. Tectonophysics, 1996, 256(1):101-128.

POPP, T., KERN, H. & SCHULZE, O. 2001. Evolution of dilatancy and permeability in rock salt during hydrostatic compaction and triaxial deformation. Journal of Geophysical Research Solid Earth, 2001, 106(B3):4061-4078.

SALZER, K., GÜNTHER, R.-M., MINKLEY, W., NAUMANN, D., POPP, T., HAMPEL, A., LUX, K.-H., HERCHEN, K., DÜSTERLOH, U., ARGÜELLO, J.G. & HANSEN, F.D. 2015. Joint project III on the comparison of constitutive models for the mechanical behavior of rock salt, II. Extensive laboratory test program with clean salt from WIPP. In L. Roberts, K. Mellegard & F. Hansen (eds.): Proc. of the 8th Conference on the Mechanical Behavior of Salt (SaltMech VIII), South Dakota School of Mines & Technology, Rapid City, SD, USA, 26-28 May, Taylor & Francis Group, ISBN 978-1-138-02840-1.

SCHULZE, O., HEEMANN, U., ZETSCHE, F., HAMPEL, A., PUDEWILLS, A., GÜNTHER, R.-M., MINKLEY, W., SALZER, K., HOU, Z., WOLTERS, R., ROKAHR, R. & ZAPF, D. 2007. Comparison of advanced constitutive models for the mechanical behavior of rock salt - results from a joint research project. I. Modeling of deformation processes and benchmark calculations. In K.-H. Lux, W. Minkley, M. Wallner, and H.R. Hardy, Jr. (eds.): Basic and Applied Salt Mechanics; Proc. of the 6th Conference on the Mechanical Behavior of Salt (SaltMech VI), Hannover, Mai 2007, Taylor & Francis (Balkema).

SCHULZE, O., POPP, T. & KERN, H. 2001. Development of Damage and Permeability in Deforming Rock Salt. Engineering Geology 61 (2001).

Investigation of fluid transport in rock salt under repository-relevant conditions – the PeTroS project

Christoph Lüdeling[1], Dirk Naumann[1], Wolfgang Minkley[1]*

[1]IfG Institut für Gebirgsmechanik GmbH, Germany

*christoph.luedeling@ifg-leipzig.de

ABSTRACT: In rock salt, fluid transport can occur under dilatant conditions, or if fluid pressure above the minor principal stress can open pathways (pressure-driven percolation). Recently, high permeabilities in rock salt have been postulated under certain conditions, in particular, at high stresses and temperatures. We investigated fluid transport in natural rock salt drill cores at five points under supposedly permeable conditions that are plausibly relevant for a repository for heat-generating nuclear waste. Experiments included several stages of fluid pressure up to almost the confining stress, and a final fluid breakthrough phase with fluid pressure above the minor principal stress. Both nitrogen and saturated NaCl solution were used as test fluid. Fluid breakthroughs were observed at all conditions when the fluid pressure exceeded the minor principal stress. Some samples showed flow already below the minor principal stress, with permeabilities in the order of 10^{-20} m^2 or below, likely due to the small size and pre-existing sample damage. However, a stable permeability over longer times was not observed in any of the experiments. Intriguingly, no experiments with (wetting) brine showed any initial permeability. The claims of permeable rock salt were thus not confirmed.

1   Introduction

Rock salt is generally considered to be impermeable in its undisturbed state. This view is supported by examples of fluids isolated in or below salt strata over geological times, and by the extensive technical use in salt and potash mining and cavern storage. Its strong isolation potential also forms the basis for the use as host rock for repositories for toxic and nuclear waste. On the other hand, there are numerous cases of barrier failures in mines and caverns around the world. It is thus necessary to confirm the barrier properties in the entire range of conditions that may plausibly occur, e.g., in the context of the disposal of heat generating waste. This entails understanding the fluid transport mechanisms that are active in rock salt and the conditions under which rock salt can lose its hydraulic integrity.

There have been claims in the literature (Lewis & Holness 1996; Ghanbarzadeh et al. 2015) that rock salt becomes permeable at high pressure and temperature because of a reduction of the equilibrium dihedral angle that makes the pore network connected; the supposedly permeable region includes conditions that may be relevant for the disposal of heat-generating waste.

We report on laboratory measurements of fluid transport (nitrogen and NaCl solution) that do not confirm this prediction (Minkley et al. 2020). We conclude that the dihedral angle does not play a significant role for the hydraulic integrity of rock salt barriers.

2   Fluid transport in rock salt and criteria for barrier integrity

2.1   Established fluid transport mechanisms

Fluid flow through rock masses and soils is often modelled using Darcy's law. The conceptual basis is the laminar flow through an existing, static pore space network, whence the flow is

$$q \sim \kappa \, \Delta P \tag{1}$$

i.e. it is proportional to the difference in fluid pressure between input and output times the permeability κ which is a constant parameter characterising the material.

Rock salt, on the other hand, is a polycrystalline viscous material with low permeability, which in its natural state does not sustain a connected pore space in which bulk water can flow: Creep deformation of the grains will close grain boundaries, and pressure gradients are different in the rock mass and in bulk fluids. Hence, the equilibrium state is one where the stress state in the rock mass is close to isotropic, and fluids are enclosed in isolated pores, with fluid pressure equal to the average stress in the rock mass. Rock salt thus has a vanishing (Darcy-type) permeability in the undisturbed state.

However, there are two fluid transport mechanisms in rock salt that are known and verified in lab and field situations:

- Stresses exceeding the dilatancy boundary lead to the formation of microscopic defects that can accumulate and coalesce into larger fractures. These cracks act as secondary porosity, turning rock salt into a porous medium; macroscopically, this porosity manifests itself in an increase in volume, i.e. dilatancy. Due to the preferred orientation of the cracks forming in a deviatoric stress state, even small amounts of volumetric strain can form connected pathways, so that less than one percent of dilatancy can cause permeabilities in the order of $10^{-17} \, \mathrm{m}^2$ (Popp et al. 2001; Urai et al. 2008; Peach et al. 1996).
- If fluid pressure exceeds the normal stress on a grain boundary (plus, potentially, a tensile strength), the fluid can open a flow path, in the process of pressure-driven percolation (Minkley et al. 2012). Hence, there is a threshold pressure below which there will be no flow. If the threshold is exceeded, the fluid will predominantly open grain boundaries where the normal stress is low. In a rock mass, this corresponds to a directed motion orthogonal to the minor principal stress. It is important to note that both the threshold and the preferred direction are not parameters of the rock, but depend on the stress state.
  We should point out that the name "percolation" is applied to other possible modes of fluid transport that do not share these properties. Pressure-driven percolation derives its name from percolation theory which deals with the connectivity of graphs, and the percolation threshold (expressed in terms of fluid pressure and rock stress) is analogous to the percolation threshold as link occupation probability, as it divides connected and non-connected graphs, i.e. intact and failed barriers.

2.2 Barrier integrity criteria

The fluid transport mechanisms discussed in the previous section can be translated into criteria to assess the hydraulic integrity of a rock salt barrier.

The dilatancy criterion requires that there is a sufficiently thick barrier left in which there is no dilatancy. Note that damage is cumulative, so that dilatancy persists even if the current stress state is below the dilatancy boundary. (It is by now clearly established that dilatancy can be "healed" under appropriate conditions (Lüdeling et al. 2015; Herchen et al 2018; Wolters et al. 2021). However, the quantitative understanding is still limited, so healing effects are generally conservatively neglected in barrier integrity assessments.)
Dilatancy is mostly generated in the vicinity of excavations (the excavation damage zone, EDZ) with a range of few metres. Thus, dilatancy alone can impact hydraulic integrity only if the barrier is rather thin; a permeable EDZ will, however, negatively affect the function of drift or shaft seals.

Pressure-driven percolation can be modelled in hydromechanically coupled simulations (Minkley et al. 2013; Knauth, Minkley 2014; Knauth 2018; Zill et al. 2021) alternatively, its effects on barrier integrity can be captured by the minimal stress criterion which requires that the ratio of minor principal stress and fluid pressure exceeds one,

$$\eta_{\min} = \frac{\sigma_{\min}}{p_{\mathrm{fl}}} > 1 \tag{2}$$

in a sufficiently thick part of the barrier to exclude pressure-driven percolation.

The minimal stress criterion does not take into account the directed nature fluid transport by pressure-driven percolation and is thus a conservative simplification.

Since creep convergence of excavations or thermal expansion due to heat-generating waste can change the stress state throughout the entire barrier, pressure-driven percolation potentially has a much larger range than dilatancy-based permeability (see e.g. Kock et al. 2012; Bollingerfehr et al. 2018 for applications to nuclear waste repositories).

2.3 Hypothetical further mechanisms

The generation of permeability via dilatancy and pressure-driven percolation are the only fluid transport mechanisms that have been shown to have practical relevance for barrier integrity. However, there have been claims in the literature of additional fluid transport mechanisms; we will discuss two such hypotheses.

The first hypothetical mechanism (Lewis & Holness 1996) is related to the textural equilibrium of rock salt with the included brine. The idea is that the pore space connectivity is controlled by dissolution-precipitation processes that try to minimise the surface energies, resulting in a dihedral angle that depends on pressure and temperature. For high p and T, the equilibrium angle is smaller than $60°$, resulting in a connected pore space network with significant porosity (Lewis and Holness (1996) estimate permeabilities of $10^{-16}\,\mathrm{m}^2$ or more for rock salt with porosities of approximately 1%). For significantly larger angles, the fluid is supposed to occur in disconnected pores, and consequently there is zero permeability (see Figure 5). This claim is based on the measurement of dihedral angles in synthetically compacted halite-brine mixtures, with sample size of several millimetres. Ghanbarzadeh et al. (2015) have repeated the analysis and obtained tomographic images of the pore space network. The actual permeability has not been determined. In the undrained compaction experiments, the stress state was fully isotropic, i.e.

$$\sigma_{\min} = \sigma_{\max} = p_{\mathrm{fl}} \tag{3}$$

such that there is no creep deformation and the system is precisely at the percolation threshold, $\eta = 1$. Such a situation suppresses the major deformation and fluid transport mechanisms, and it is not possible on the scale of a geological barrier (i.e. several tens to hundreds of metres) due to the different pressure gradients in brine and rock.

The second hypothesis (Ghanbarzadeh et al. 2015) posits that even for dihedral angles above $60°$, where the pore space consists of isolated pores, dynamic recrystallisation, grain-boundary wetting and stretching of inclusion into grain-boundary films provide a fluid transport mechanism ("deformation-assisted percolation") whenever deviatoric stresses in the order of $1\,\mathrm{MPa}$ or more are present. This, in particular, would apply across large parts of the geological barrier of mines and waste repositories, where stress redistributions due to excavations and waste-generated heat alter the initial near-isotropic stress state. However, the mechanism itself is specified rather vaguely, and estimates of an associated (effective) permeability or transport rates are not given. The evidence is limited to observations of hydrocarbons in regions where the dihedral angle is well above $60°$ in oil wells in the Gulf of Mexico.

The conceptual basis of deformation-assisted percolation has been questioned by Sinn et al. (2018), where it was shown that mass transfer by dissolution-precipitation processes will completely prevent the formation of permeable fluid pathways by inclusion stretching and that recrystallisation and grain boundary wetting will not produce a detectable permeability.

3 Natural and technical analogues

There are numerous examples for the isolation potential of salt formations from geological and technical processes. Additionally, the analysis of failure cases has identified the relevant fluid transport mechanisms (see Minkley et al. 2020 for a discussion of examples and references). Here, we present two cases that are pertinent to the hypothetical transport mechanisms discussed above.

3.1 The BAS-2 cavern

The solution mining cavern BAS-2 in the Netherlands is in a depth range of $2500\,\text{m}$ to $3000\,\text{m}$; rock temperature is $97°\text{C}$, and the undisturbed lithostatic stress at the roof (which may be modified by the solution mining activities) is about $55\,\text{MPa}$. The conditions are thus in the transition zone according to Figure 5, where a connected pore space network may develop and the hydraulic integrity of the rock is not guaranteed. Note that around the cavern sump, pressure and temperature will be higher, i.e. further toward the supposedly permeable region.

The pressure build-up after plugging has been monitored (van Heekeren et al. 2009). Brine pressure was increased to approximately $40\,\text{MPa}$ at abandonment. Subsequently, pressure quickly rose to about 95% of the lithostatic stress and continued to slowly increase. Pressure buildup is due to the creep deformation of the host rock which tries to eliminate the deviatoric stress by cavern convergence; it is counteracted initially by the infiltration of brine into the damaged cavern contour, and in the long term by pressure-driven percolation at the roof, which keeps the brine pressure at the minor principal stress. Surface subsidence has practically stopped after abandonment, indicating a stress state around the cavern that is close to isotropic equilibrium. The BAS-2 cavern does not give any indication of a loss of hydraulic integrity of the rock salt.

3.2 The Altmark test

An integrity test was performed by GDF SUEZ in an abandoned gas well in the Altmark region in Germany; the well crossed a rock salt stratum, and the aim of the test was to demonstrate the tight sealing of the well by the rock salt to allow subsequent CO_2 sequestration (Wundram 2014). Depth of the seal was $3096\,\text{m}$, rock temperature was about $127°\text{C}$. Thus, the conditions are fully in the permeable region according to Figure 5.

Fluid pressure below the salt was raised in several step until breakdown pressure. After the breakdown, pressure drops again and a shut-in pressure develops without further injection of gas. In the test, breakdown occurred at $73.4\,\text{MPa}$, and a constant shut-in pressure of $71.8\,\text{MPa}$ – slightly above the computed lithostatic pressure – was observed.

The constant pressure is in good agreement with the minor principal stress, given by the lithostatic pressure. If rock salt would have developed a high permeability, the pore pressure should be closer to a halmostatic pressure with a gradient between fresh water and saturated brine.

4 Laboratory Tests of Fluid Transport under High Pressure and Temperature

4.1 Test Conditions

To test the hypothesis of a connected pore space network in the permeable region of Figure 5, we have measured the permeability of natural rock salt under appropriate pressure and temperature conditions. A test matrix of five p-T combinations was defined:

- Pressure of $p = 18$ MPa with temperatures of 160°C and 180°C
- Pressure of $p = 36$ MPa with temperatures of 140°C, 160°C and 180°C

These conditions are plausibly relevant for a repository for heat-generating nuclear waste in depths of 500 m to 1000 m. (Note that in the VSG and KOSINA studies for a repository in domal and bedded salt, a maximum temperature of 200°C at the canister surface was assumed.) They are in the "transition" and "permeable" regions of Figure 5.

According to Ghanbarzedeh et al. (2015), the low residual humidity of rock salt can form a connected pore space that allows the migration of non-wetting fluids, such as hydrocarbons. Thus, at each p-T point, the permeability was measured by both nitrogen and saturated NaCl solution ("brine"). As a wetting fluid, brine should enhance the formation of a connected pore network; however, it is technically more demanding due to its corrosive nature.

There were thus ten test conditions. A few tests were repeated, so that 13 tests were performed in total.

4.2 Sample material

The samples were prepared from German Zechstein (Staßfurt and Leine) rock salt. Drill cores were selected from the Bernburg (bedded salt, eight samples), Teutschenthal (bedded salt, one sample), Asse (domal salt, two samples) and Gorleben (domal salt, two samples). The material was mostly relatively pure halite with average grain size below 10 mm; the Gorleben samples showed some visible anhydrite impurities.

4.3 Test setup and procedure

The basic principle of the test is shown in the left panel of Figure 1: A cylindrical sample (200 mm length, 100 mm diameter) is loaded in a triaxial cell with confining and axial stress. Fluid is applied via a pressure chamber at the end of a lined borehole; any migrating fluid is collected via wire mesh at the outside of the sample. The fluid can flow in an axial or radial direction according to the stress state. (One test was performed with an "axial flow" setup with two short boreholes at each end of the sample.)
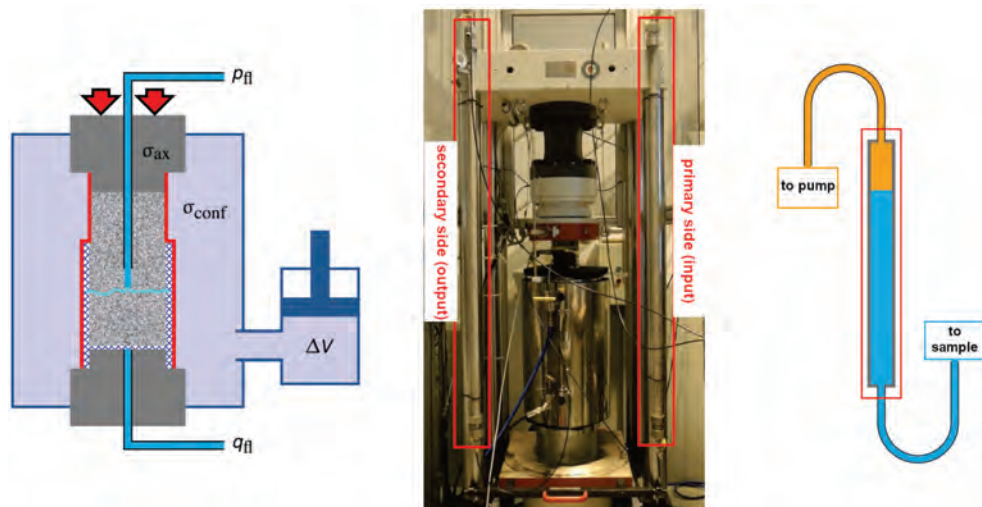
Figure 1: Left: Sketch of the permeability test setup. Centre: Servohydraulic test rig D2000 with sample in the heated triaxial cell and hydraulic separators installed. Right: Sketch of the hydraulic separator with oil (yellow) and brine (blue).

The confining pressure was applied via a silicon-based oil that was heated externally to the required temperatures. A temperature sensor in the cell (close to the sample) was used for temperature control.

For the nitrogen tests, the gas pressure was applied using a gas cylinder and a compressor ("Maximator") to boost the pressure to the required level. On the secondary side, gas flow was measured with flowmeters. From the gas pressures p_{in} and p_{out} and the flow rate q, an effective permeability K can be determined by

$$K = q\,\eta \cdot \frac{p_{\text{out}}}{\frac{1}{2}(p_{\text{in}}^2 - p_{\text{out}}^2)} \cdot \frac{1}{\pi h} \cdot \ln\frac{R}{r} \;.$$

Here, R is the sample radius, r and h are radius and height of the pressure chamber, and η is the viscosity. We have assumed a purely radial flow from the pressure chamber, which is consistent with the flow paths found by coloured tracer fluid. The viscosities were taken constant at the specified test conditions; since the viscosity increases with pressure, the resulting permeabilities are overestimated, and the analysis is conservative in this respect.

We should point out that the permeability determined in this way is not a constant parameter intrinsic to the material, as it is usually assumed in Darcy's law, Equation (1). (Recall from the discussion in Section 2.1 that the permeability of undisturbed rock salt is essentially zero.) Rather, it is an effective quantity that is specific to the current conditions; in particular, it strongly depends on the stress state in the rock and the fluid pressure (or, equivalently, the effective stress).

There is one caveat to this statement: Small amounts of mechanical damage can lead to significant Darcy-type permeability in the network of microcracks. An initial dilatancy in the order of 10^{-3} is often generated during core drilling and sample preparation, with an associated permeability in the order of 10^{-21} m^2 to 10^{-20} m^2.

The brine tests used a very precise spindle pump ("Quizix") which is equipped with two reservoir cylinders of $22\,\text{ml}$ volume each. The pump uses a low-viscosity silicon oil as medium; the fluid pressure is transferred to the brine in vertical stainless steel pipes that acted as hydraulic separators (see Figure 1, centre and right panels). The sample was evacuated to expel any gases and flooded with brine in the test initialisation, before the temperature was applied. A small constant pressure of $0.3\,\text{MPa}$ was maintained at the secondary side; flow was detected be the reaction of the axial stress to fluid flow due to the infiltration of the brine into the sample, by refills of the pump cylinders, and, for moderate or larger flow rates, by the increase in pressure on the secondary side.

The solubility of halite increases by about 20% from 25°C to 180°C and only weakly depends on pressure (IUPAC 1991). The primary side contains about half a litre of brine, only a small amount of which is actually heated inside the cell. During the heating of the sample, at most a few cm^3 of rock salt can be dissolved, which would increase the permeability; the results are thus conservative in this regard.

The test procedure generally comprised three stages:

i. In the initialisation, the test conditions are applied. First, the triaxial cell is heated at the specified temperature for approximately eight hours to ensure a uniform temperature throughout the sample. Afterwards, the desired isotropic stress is applied.

Note that in the nominally isotropic stages, the axial stress is always slightly higher than the confining stress (up to $2\,\text{MPa}$) to avoid lifting the axial platens off the sample.

ii. In the isotropic flow stage, fluid pressure is applied and the flow is determined for several pressure stages, keeping the fluid pressure below the minor principal stress.

In different tests, the second stage lasted from several hours to up to 144 hours.

Note that the experiments reported by Ghanbarzadeh et al. (2015) used equilibration times of 120 hours.

iii. Finally, a fluid breakthrough is triggered by a reduction of the minor principal stress: The test rig is switched to strain control, and the sample is axially extended with a prescribed rate of $2.5 \times 10^{-6}/s$ or $2.5 \times 10^{-7}/s$. Consequently, the axial stress decreases below the fluid pressure. Note that the minor principal stress is thus acting in the axial direction, so that pressure-driven percolation naturally produces a radial fluid flow. (In the first tests, the axial stress was lowered with a constant stress rate.)

The procedure was slightly varied in individual tests. After the fluid breakthrough, the samples were unloaded (fluid pressure, axial and confining stress) and left to cool down to room temperature.

An alcohol-based coloured tracer fluid was injected into the pressure chamber with about 0.3 MPa to qualitatively visualise localised flow paths (if they have not closed during the unloading and cool-down phase).

4.4 Results

Here, we will present the result of three tests to illustrate the key results. All tests are described in detail in Minkley et al. (2020).

4.4.1 Test 1b ($180°C$, 36 MPa, Nitrogen)

In Test 1b, a sample from the Bernburg deposit was equipped with a central pressure chamber. The test was performed at $180°C$ and 36 MPa, i.e. in the "permeable" region.

Figure 2 shows the evolution of stress, pressure and flow. The stress in the sample was initialized to 36 MPa, and the gas pressure was raised in steps of 13 MPa, 24 MPa, 29 MPa, and 34 MPa. No flow was detected (note that at about $t = 4.9$ h, the flowmeter was changed to one with a larger range and consequently larger noise). The jitter in the flow signal showed a small increase in the last pressure stage (34 MPa); the measured flow can be bounded from above by approximately 0.4 ml/min, which is significantly below the rated resolution of the flowmeter and likely again just noise. The derived permeability of about 10^{-22} m^2 thus indicates the lower limit of the measurable permeabilities in this setup.

Overall, we do not observe any clear indication of nonvanishing permeability in the" permeable" region.
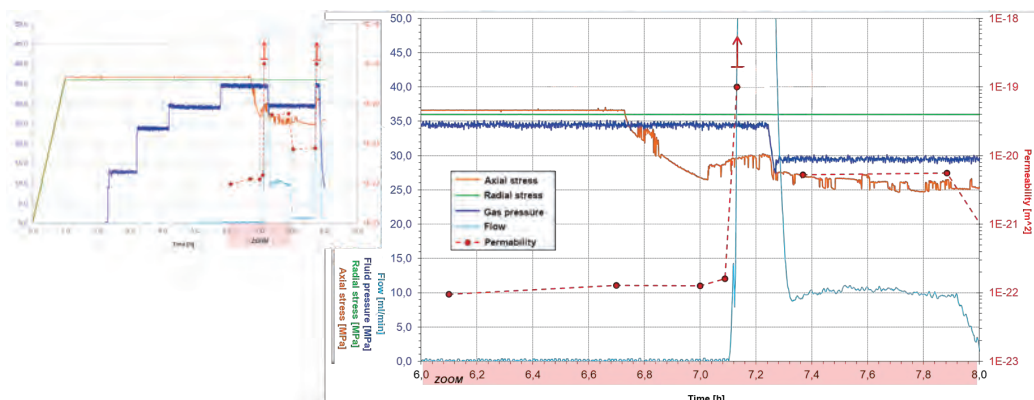
Figure 2: Evolution of pressure, stress and flow in Test 1b. Small panel (left) shows the complete test, the large panel (right) shows a detailed view of the first breakthrough phase.

To initiate pressure-driven percolation and trigger a breakthrough, the test mode was changed by strain-controlled extension at about $t = 6.72$ h (see Figure 2, right panel, for a close-up of the first breakthrough stage). The axial stress first reduced to 26.5 MPa (at $t = 7.02$ h), at which point it started to rise again to 30 MPa. This indicates the initial generation of flow paths and migration of the gas into the sample, whence the axial stress reacts to the gas pressure. Consequently, at $t = 7.1$ h, the breakthrough occurred, and gas flow increased very strongly, exceeding the measuring range of the flowmeter of 500 ml/min. At this point, gas was vented from the secondary side by a safety valve. The permeability during the breakthrough was thus higher than 10^{-19} m^2. The axial stress was approximately constant during the breakthrough.

After approximately six minutes, the gas pressure was lowered to 29.5 MPa. As a consequence, the axial stress dropped, and the gas flow reduced to 10 ml/min, corresponding to a permeability of about 4.5×10^{-21} m^2; at about $t = 8$ h, the flow further dropped to 1 ml/min (permeability 7.5×10^{-22} m^2) without a change in the boundary conditions, i.e. at fluid pressure several MPa above the minor principal stress. This indicates the closure of the pressure-generated pathways, possibly due to the reduction of the gas pressure along the flow paths.

At $t = 8.7$ h, the gas pressure was increased to 35 MPa, leading to an immediate increase in the axial stress and a second gas breakthrough. Tracer injection showed localized flow paths near the height of the upper end of the pressure chamber.

4.4.2 Test 2 (180°C, 36 MPa, Brine)

At the same pressure and temperature as Test 1b, Test 2 (see Figure 3) was performed with brine on a sample from the Asse mine. Here, brine pressures of 20 MPa and 33 MPa were applied for 24 h each in the isotropic stage. No indications of fluid flow were observed.

In the right panel, Figure 3 shows a zoom of the breakthrough stage of the test: Strain-controlled extension was activated at $t = 51$ h, and the axial stress dropped to 30 MPa within an hour. Before the pressure on the secondary shows a reaction, the reduction of the slope of the axial stress near $t = 52$ h indicates the beginning of fluid percolation. The apparent drop of fluid pressure from $t = 52.1$ h to 52.25 h indicates the refill of the primary-side cylinder of the Quizix pump, showing that brine is injected into the sample (the output valve is closed during this time, so that the pressure acting in the sample does not actually vanish). The spike in the output pressure at $t = 52.3$ h marks the fluid breakthrough, which establishes a hydraulic connection between primary and secondary side. After a second refill, the system is in a quasi-stationary stage; the close connection between brine pressure and axial stress indicates a constant flow through the sample (note also the secondary-side refill around $t = 53.4$ h).
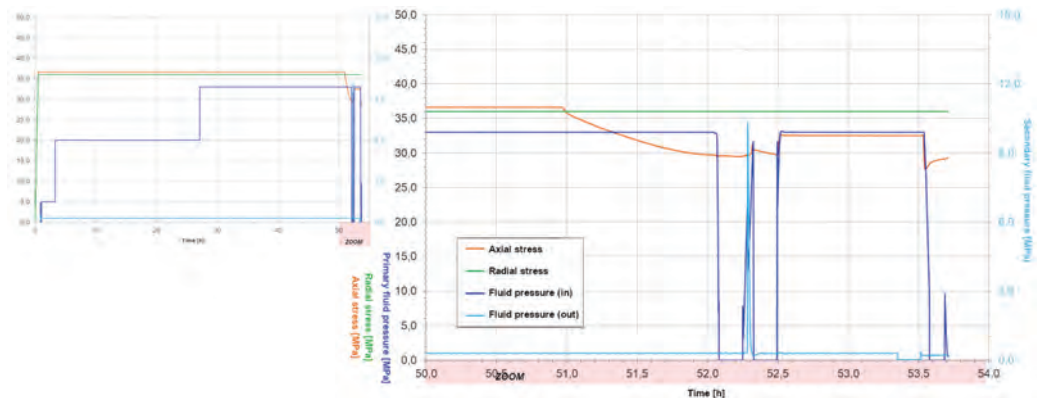
Figure 3: Test 2: Complete test (left) and detailed view of the breakthrough phase (right)

This test was performed at the most "permeable" conditions with wetting fluid. Nevertheless, no flow was detected below the minor principal stress for $48\,h$. Only after the percolation threshold was exceeded, pressure-driven percolation started and caused the fluid break-through.

4.4.3   Test 9 (160°C, 18 MPa, Nitrogen)

Finally, we briefly discuss Test 9, which was conducted at the least "permeable" conditions according to Figure 5, in the transition region, with nitrogen as test fluid. The sample from the Bernburg deposit was prepared in an "axial flow" configuration with two short boreholes at the end faces. To ensure an axial flow direction, the axial pressure increased to 20.2 MPa.
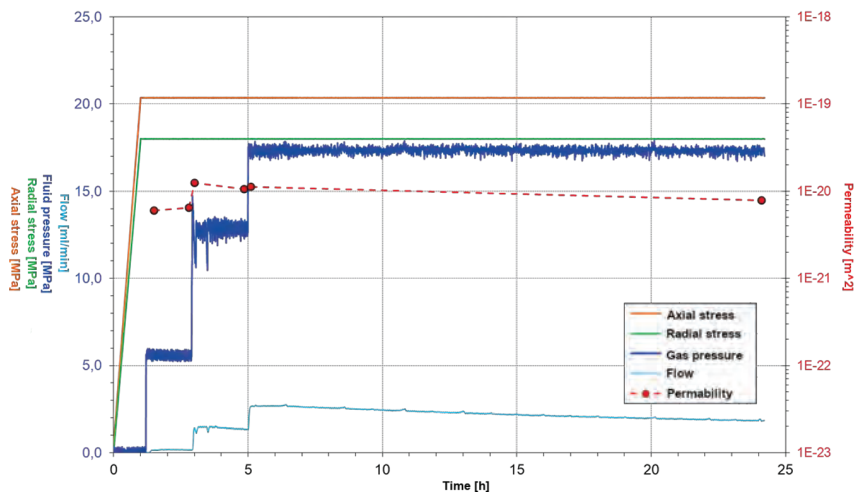
Figure 4: Evolution of pressures and flow in Test 9 (160°C, 18 MPa, nitrogen)

Gas pressure stages of $6\,MPa$, $12\,MPa$ and $17\,MPa$ were applied (see Figure 4). In the first stage, the flow was small and near the sensitivity limit of the flowmeter, at $12\,MPa$ a flow was clearly observed, and it increased after the next pressure increase. During this stage, the flow decreased from $2.7\,ml/min$ to $1.8\,ml/min$. The tracer injection showed no visible flow paths. The sample showed a Darcian flow with an approximately constant permeability of about $10^{-20}\,m^2$, and without obvious localised flow. Since the flow reduced by about a third in $19\,h$, it seems plausible that the flow is caused be preexisting damage that partially healed during the test.

5   Summary and Discussion

It has been claimed in the literature that rock salt becomes permeable in the Darcian sense under high pressure and temperature due to the generation of a connected pore space network in textural equilibrium of halite and brine. This includes conditions potentially relevant for the disposal of heat-generating nuclear waste.

We have presented the first measurements of permeability under repository-relevant and supposedly permeable conditions. These results complement the tests performed in the KOSINA project (Liu et al. 2018; Minkley et al. 2018) that also probed the "permeable" region at temperature close to $100°C$ and pressures up to $95\,MPa$.

Tests were performed on samples of natural rock salt form German Zechstein deposits. Five points in p-T space were selected that plausibly cover the conditions relevant for a repository

or heat-generating waste in a depth of $500\,\mathrm{m}$ to $1000\,\mathrm{m}$. As test fluids, both nitrogen and brine (saturated NaCl solution) were used for each point.

Some samples showed a Darcy-type flow for fluid pressures below the minor principal stress; permeabilities were in the range of $10^{-22}\,\mathrm{m}^2$ to $10^{-20}\,\mathrm{m}^2$. These values can be reasonably interpreted as effects of pre-existing sample damage from sample preparation and the small sample size. Note that the fluid needs to flow along a distance of about $4.5\,\mathrm{cm}$, corresponding to less than ten grain diameters. Hence, even a small loosening of the grain contacts can allow fluid motion. Permeabilities in this range are regularly observed in lab tests at lower pressure and temperature (Popp et al. 2007; Minkley et al. 2013). This interpretation is supported by the fact that the flow decreased under constant boundary conditions, i.e. that the damage reduced in an isotropic stress state.

Note also that the initial permeabilities did not systematically depend on the dihedral angle, and were not observed in tests with brine, although the wetting fluid should favour the generation of a connected pore network.

A constant or increasing permeability over longer times, as would be expected for (the formation of) a stable connected equilibrium pore space, was not observed in any test.

Under all conditions, a fluid breakthrough could be observed when the fluid pressure exceeded the minor principal stress. Pressure-driven percolation was thus confirmed as the major fluid transport mechanism, also in the supposedly permeable region.
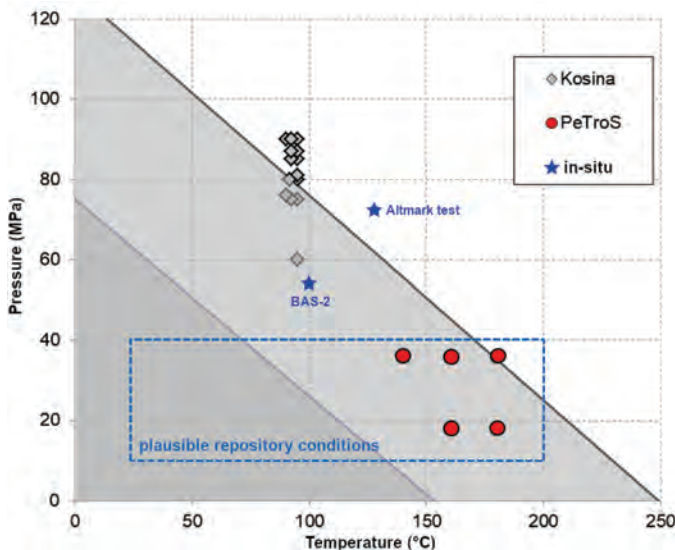
Figure 5: Regions in pressure-temperature space where, according to static pore-scale theory, rock salt is impermeable (dark grey) or permeable (white), with a transition region in light grey (after Lewis & Holness 1996). Symbols indicate lab and in situ tests of the permeability hypothesis; a stable connected pore space was observed neither in the supposedly permeable nor the transition region.

Figure 5 summarises the laboratory test results, as well as the technical large-scale tests at Altmark and BAS-2. For all points, no Darcian permeability was detected. The predictions of the static pore-scale theory are thus refuted. While the additional mechanism of deformation-assisted percolation (Ghanbarzadeh et al. 2015) is hard to test directly, the results presented here cast doubt on the observational basis, since pressure-driven percolation was not taken into account. For waste repositories, we can conclude that the isolation properties of rock salt

persist in the high p-T region, and that dilatancy and pressure-driven percolation (minimal stress criterion) determine barrier integrity. From a geomechanical point of view, a temperature of $180°C$ in the rock mass around the waste canisters does not pose a threat to complete containment. Generally, higher temperatures accelerate creep and healing processes, leading to a smaller EDZ and less violations of the minimal stress criterion.

Acknowledgements

References

BOLLINGERFEHR, W., BERTRAMS, N., MINKLEY, W., BUHMANN, D., MÖNIG, J., EICKEMEIER, R., TILL POPP FAHLAND, S., PRIGNITZ, S., FILBERT, W., REINHOLD, K., HAMMER, J., SIMO, E., KINDLEIN, J., THIEMEYER, T., KNAUTH, M., VÖLKNER, E., LIU, W. & WOLF, J. 2018. *KOSINA Concept developments for a generic repository for heat-generating waste in bedded salt formations in Germany Synthesis Report.*

GHANBARZADEH, S., HESSE, M.A., PRODANOVIĆ, M. & GARDNER, J.E. 2015. Deformation-assisted fluid percolation in rock salt Science 350.6264

HERCHEN, K., POPP, T., DÜSTERLOH, U., LUX, K.-H., SALZER, K., LÜDELING, C., GÜNTHER, R.-M., RÖLKE, C., MINKLEY, W., HAMPEL, A., YILDIRIM, S., STAUDTMEISTER, K., GÄHRKEN, A., STAHLMANN, J., REEDLUNN, B. & HANSEN, F.D. 2018. WEIMOS: Laboratory Investigations of Damage Reduction and Creep at Small Deviatoric Stresses in Rock Salt. In: S. Fahland et al. (eds.), The Mechanical Behavior of Salt IX.

IUPAC 1991. Solubility Data Series 47: Alkali Metal and Ammonium Halides in Water and Heavy Water. IUPAC SDS 47. Editors R. Cohen-Adad and J.W. Lorimer. Available at

KNAUTH, M. & MINKLEY, W. 2014. Modeling of the mechanical and hydraulic behavior of salt rocks on a discontinuum-mechanical basis. In: 48th US Rock Mechanics / Geomechanics Symposium 2014, Vol. 2, 2014:1385–1394.

KNAUTH M. 2018. Diskontinuumsmechanische Modellierung von Salzgesteinen [Ph.D. thesis]. Freiberg, Germany: TU Bergakademie Freiberg; 2018.

KOCK, I., EICKEMEIER, R., FRIELING, G., HEUSERMANN, S., KNAUTH, M., MINKLEY, M., NAVARRO, M., NIPP, K.H. & VOGEL, P. 2012. Vorläufige Sicherheitsanalyse Gorleben (VSG), AP 9.1: Integritätsanalyse der geologischen Barriere, GRS-286, 2012, https://www.grs.de/node/1647

LEWIS, S. & HOLNESS, M. 1996. Equilibrium halite-H_2O dihedral angles: High rock-salt permeability in the shallow crust? Geology 24(5)

LIU, W., KNAUTH, M., EICKEMEIER, R., FAHLAND, S., MINKLEY, W. & POPP, T. 2018. TM- und THM-gekoppelte Modellberechungen zur Integritätsanalyse der geologischen Barrieren in fllach gelagerten Salzformationen – Ergebnisse aus dem Vorhaben KOSINA. BGR, IfG, Hannover 2018

LÜDELING, C., GÜNTHER, R.-M., KNAUTH, M. & MINKLEY, W. 2015. Healing of Rock Salt Damage and Applications. Paper ARMA15-000698 at the 49 th US Rock Mechanics / Geomechanics Symposium, San Francisco, USA, 2015

MINKLEY, W., KNAUTH, M. & WÜSTE, U. 2012. Integrity of salinar barriers under consideration of discontinuum-mechanical aspects. Mechanical Behavior of Salt VII, Paris, France, 16-19 April 2012, 469 – 478, Taylor & Francis Group, London, ISBN 978-0-415-62122-9

MINKLEY, W., KNAUTH, M. & BRÜCKNER, D. 2013. Discontinuum-mechanical behaviour of salt rocks and the practical relevance for the integrity of salinar barriers. In: Pyrak-Nolte LJ, Chan A, Dershowitz W, Morris J, Rostami J, eds. Proceedings of the 47th US Rock Mechanics/Geomechanics Symposium. ARMA; 2013.

MINKLEY, W., BRÜCKNER, D. & LÜDELING, C. 2018. Percolation in salt rocks. In Fahland, S. et al. (editors), The Mechanical Behavior of Salt IX: Proceedings of the 9th Conference on the Mechanical Behavior of Salt (SaltMech IX), Hannover, Germany, 12-14 September 2018, BGR 2018 (ISBN: 978-3-9814108-6-0)

MINKLEY, W., LÜDELING, C. & NAUMANN, D. 2020. Überprüfung des perkolationsgetriebenen Transports von Fluiden im Wirtsgestein Steinsalz unter Bedingungen für ein Endlager (PeTroS). Report B IfG 73/2017, BfE-RESFOR-006/20/. urn:nbn:de:0221-2020112023854, Institut für Gebirgsmechanik GmbH. Available at

PEACH, C. J. & SPIERS, C. J. 1996. Influence of crystal plastic deformation on dilatancy and permeability development in synthetic salt rock. Tectonophysics. 1996;256(1):101–128.

POPP, T., KERN, H. & SCHULZE, O. 2001. Evolution of dilatancy and permeability in rock salt during hydrostatic compaction and triaxial deformation. J Geophys Res Solid Earth. 2001;106(B3):4061–4078

POPP, T., WIEDEMANN, M., KANSY, A. & PUSCH, G. 2007. Gas transport in dry rock salt – implications from laboratory investigations and field studies. In: Proceeding of the 6th Conference on the Mechanical Behavior of Salt (SaltMech VI), Hannover 2007. Taylor & Francis, London, 2007

POPP, T., WEISE, D., SALZER, K. & WIEDEMANN, M. 2012. Hydraulic integrity of highly soluble carnallite bearing salt rocks. The Mechanical Behavior of Salt; Proc. 7th Conference, Paris 2012, 131-141.

SINN, C.J.A., GIACOMEL, P., PEACH, C.J., HANGX, S.J.T. & SPIERS, C. 2018. Effects of Plastic Deformation on the Transport Properties of Rocksalt. Mechanical Behavior of Salt IX, Hannover 2018

URAI, J.L., SCHLÉDER, Z., SPIERS, C.J. & KUKLA, P.A. 2008. Flow and transport properties of salt rocks. In: Dynamics of Complex Intracontinental Basins: The Central European Basin System. Springer Berlin; 2008:277–290.

VAN HEEKEREN, H., BAKKER, T., DUQUESNOY, T., DE RUITER, V., MULDER, L. 2009. Abandonment of an extremely deep Cavern at Frisia Salt. SMRI Spring 2009 Technical Conference, 27 - 28 April, Krakow, Poland

WUNDRAM, L. 2014. Langzeit-Bohrungsverschluss: Konzeptentwicklung, numerische Modellierung und feldtechnische Erprobung [PhD thesis]. Dissertation TU Clausthal

ZILL, F., LÜDELING, C., KOLDITZ, O. & NAGEL, T. 2021. Hydro-mechanical continuum modelling of fluid percolation through rock salt, International Journal of Rock Mechanics and Mining Sciences, Volume 147, 2021, 104879, ISSN 1365-1609,

Creep behaviour of bischofite, carnallite and mixed bischofite-carnallite-halite salt rock at *in situ* conditions

N. Muhammad[1]*, J.H.P. de Bresser[2], C.J. Peach[2], C.J. Spiers[2]

[1]Center for Advanced Studies in Physics, GC University Lahore, Pakistan; [2]Experimental Rock Deformation Laboratory, Department of Earth Sciences, Utrecht University, the Netherlands

* nawazmuhammad@gcu.edu.pk

ABSTRACT: To accurately predict cavern convergence and subsidence caused by solution mining of K- and Mg-bearing salt bodies, a good understanding of the creep behaviour of bischofite, carnallite and mixed salts rocks is required. We studied the mechanical properties of these materials aiming to produce flow laws that can be applied at *in situ* conditions. We performed triaxial deformation experiments on natural polycrystalline samples of bischofite, carnallite (starting grain size ~5 mm), and their mixtures with halite, at *in situ* PT conditions of 40 MPa and 70 °C. All deformation tests were done in strain rate stepping mode, with intervening stress relaxation to reach low strain rates. We found that carnallite is 4-5 times stronger than bischofite, and that bischofite-carnallite-halite mixtures are stronger than carnallite. The constant strain rate parts of the multistep experiments allowed dislocation creep laws to be defined for bischofite and carnallite at relatively high stress, with a power law stress exponent n~5. During stress relaxation, n changes to ~1 at a strain rate of ~10^{-9} s^{-1}. This is interpreted as reflecting a change from dislocation creep at the faster strain rates to solution-precipitation behaviour at slow strain rate, mediated by changing grain size.

1   Introduction

The salt deposits at Veendam (northern part of the Netherlands) are mainly composed of the evaporites bischofite, carnallite and halite in the form of layers and mixtures, with sulphates in minor quantities. In order to solution mine the caverns, it is important to know the rheology of the different salts at *in situ* conditions, so that the rate of inflow into the caverns as well as surface subsidence can be predicted. The strain rate of such salts in underground mines is normally in the range of 10^{-8} to 10^{-15} s^{-1} (Heard 1972; Van Eekelen et al. 1981; Jackson & Talbot 1986) which is a rate that cannot be achieved easily in laboratory scale experiments. However, laboratory experiments can be used to define a flow law that allows extrapolation to *in situ* conditions. In order to perform such extrapolation in a reliable manner, good understanding of the deformation mechanism of the material is needed, so that the characteristics of the flow law can be related to the microphysical mechanism controlling creep.

Van Eekelen et al. (1981) and Urai (1983) have tested the creep behaviour of bischofite at a fixed confining pressure of 28 MPa, in the temperature range of 40-80 °C, with varying water content including dry samples. The authors suggested that a conventional power law of the type $\dot{\varepsilon} \sim \sigma^n$, relating strain rate $\dot{\varepsilon}$ to stress σ, can be used to describe the flow behaviour of bischofite, as long as two regimes were defined, one at low and one at relatively high differential stress. The flow laws of the two regimes show different values of the power law stress exponent n, namely 1.5 and 4 for the low and high stress regime, respectively. However, the nature of the two regimes was not fully understood and accordingly, a good basis for establishing the rate of inflow relevant in the case of cavern evolution associated with solution mining is still missing.

The creep properties of dry and wet carnallite have been studied by Urai (1985), by performing triaxial deformation experiments at a temperature of 60 °C, using a range of strain rates and confining pressures. Urai (1985) proposed a conventional power law for steady state creep of wet carnallite with stress exponent n = 4.8±0.1. The strength of carnallite was found to be substantially higher than that of bischofite. It is yet unknown what the rheology of mixtures of

bischofite and carnallite is like, and which of these salts dominates creep in a mixture. Also, halite, both as natural single and poly-crystals and as artificially prepared dense aggregates, has been studied before for its creep properties under dry and wet conditions (Heard 1972; Heard & Ryerson 1986; Wawersik & Zeuch 1986; Urai et al. 1986; Spiers et al. 1990; Senseny et al. 1992; Carter et al. 1993; Spiers & Carter 1998; Ter Heege et al. 2005b; Muhammad et al. 2012). Also, for this material, a conventional power law appears to describe the behaviour well. For wet salt, the proposed stress exponent *n* lies in the range of 4.1 to 5.7, in the temperature range of 23 to 400 °C.

In the current work, we have performed triaxial deformation experiments on polycrystalline natural samples of bischofite, carnallite and their mixture with halite, at *in situ* conditions of confining pressure 40 MPa and at a fixed temperature of 70 °C. All deformation tests were done in strain rate stepping mode, with several steps being followed by stress relaxation (Rutter & Mainprice 1978), with the aim to achieve strain rates as low as ~10^{-9} s^{-1}, approaching the natural strain rates in salt caverns.

2   Method

2.1   Sample preparation

The natural cores of bischofite, carnallite and their mixture with halite (mixture1: halite 65%, carnallite 4%, bischofite 14%, mixture2: halite 30%, carnallite 37%, bischofite 19%), extracted by Nedmag Industries Mining & Manufacturing B.V. during the so-called TR9 drilling project, were provided with 100 mm diameter and 1 m length, along with the description. The cores were first cut down to rectangular rods of about 100 mm length and 50 mm diameter using a hand saw. These rods were then shaped down to samples with the required dimensions of 35 mm diameter and 85 mm (average) length, using SiC papers. Since the salts under investigation are hygroscopic, the samples were prepared in a low humidity room with relative humidity (R.H.) < 15% to control the water content. Natural salts in general are wet (Roedder & Bassett 1981; Urai 1983). In order to create a deliquescence condition in our samples, comparable to that at *in-situ* conditions, the samples were first equilibrated with air with R.H. > 30% (Urai 1985; Christov 2009) and, in parallel, carefully measured for increase in weight by water absorption. This was followed by wrapping up the samples in a double layer of perforated glass fibre sheet (0.3 mm starting thickness) creating an equilibrated humid environment around the sample. These wrapped samples were further sealed in 1.0 mm thick polymer "ethylene propylene diene monomer (EPDM)" jackets to avoid contamination of the samples by the confining medium (silicone oil) used in the deformation apparatus.

2.2   Deformation apparatus

The apparatus used for this study was the so-called "Shuttle Vessel" of the experimental rock deformation (HPT) laboratory at the department of Earth Sciences at Utrecht University. The Shuttle Vessel machine is an internally heated 100 MPa confining pressure vessel mounted on a standard 100 kN Instron 1362 loading frame with an electro-mechanical servo-controlled positioning system. The machine is provided with a (Instron standard, +/-50 mm) linear variable differential transformer (LVDT), but to come to an accurate measurement of the sample deformation, a second LVDT (0-25 mm range, H.F. Jensen, Denmark) was installed at the top of the vessel and near the sample. This was done to reduce the effect of the elastic distortion of the apparatus and measure accurately the shortening of the sample, especially during stress relaxation, where very limited natural strain in the order of 0.001 is to be monitored. Further details can be seen in Muhammad (2015).

2.3 Experiments

In this study, multistep experiments were performed. A typical experiment consisted of a few steps at constant strain rate, in the range 10^{-5} to 10^{-8} s^{-1}, interrupted by periods of stress relaxation. During the constant strain rate part of the test, the sample was deformed until a steady (or near steady) state of stress was reached. This usually required about 2-4% of shortening. Then the piston was arrested and the stress on the sample was allowed to relax until the diminishing force on the sample reached the limits of the load cell resolution. The duration of each relaxation step was a few days. The experiments were performed at 70 °C sample temperature and 40 MPa confining pressure for *in situ* conditions.

2.4 Data acquisition and processing

The data containing pressure, temperature, load, and position (LVDT_1 and 2) were logged throughout the test. The stress on the sample was calculated from the load values by assuming constant volume deformation, correcting the instantaneous change in area value for progressive change in length of the sample. The data acquired during stress relaxation was analysed with a dedicated code to produce the plastic strain rate of the sample.

$$\dot{\varepsilon}_{plastic} = \dot{\varepsilon}_{total} - \frac{1}{E_{sample}}\left(\dot{\sigma}_{sample}\right) - \frac{1}{L_t}S\left(\frac{\partial F}{\partial t}\right)$$ (1)

where,

$\dot{\varepsilon}_{plastic}$ = plastic strain rate of sample [s^{-1}]
$\dot{\varepsilon}_{total}$ = total strain rate measured by LVDT_2 [s^{-1}]
E_{sample} = Young's modulus of sample [MPa]
$\dot{\sigma}_{sample}$ = sample stress relaxation rate [MPas^{-1}]
L_t = instantaneous length of sample [m]
S = machine stiffness correction constant [mN^{-1}]
$\left(\frac{\partial F}{\partial t}\right)$ = rate of change of force [Ns^{-1}]

The second term of Equation 1 contains the Young's modulus E of the sample material. Unfortunately, its value for bischofite and carnallite is not reported in literature. We thus

Table 1. Elastic modulus of the specimens

Sample	ρ [kg m^{-3}]	V_p [m s^{-1}]	V_s [m s^{-1}]	N	G [GPa]	E [GPa]
Carnallite	1600*	3938	1988	0.33	6.3	16.8
Bischofite	1600*	4312	2037	0.36	6.6	18.0
Mixture	1600*	3970	2207	0.28	7.8	19.8
Halite	2100*	--	--	--	--	39*

ρ: density of the material
V_p: longitudinal component of velocity (measured)
V_s: shear component of velocity (measured)
v: Poisson's ratio (calculated)
G: shear modulus (calculated)
E: Young's modulus (calculated)
*From literature

Determined these values for the material tested, by performing ultra-sonic time of flight sound velocity measurements on unconfined samples of bischofite, carnallite and the mixture under study, using the facilities at Technical University Delft (see Table 1).

3   Results

3.1   Mechanical data

The mechanical testing was done on a total of ten samples including three samples of bischofite, five samples of carnallite and two samples of their mixture with halite. The differential stress vs natural strain and time are plotted in Figure 1. The relaxation behaviour of all the salts was found to be nearly same so only three representative plots (bischofite5, carnallite2 and mixture1) of differential stress vs time are given here. The mechanical results of bischofite, carnallite and mixture samples, along with the experimental conditions have been tabulated in Table 2, where the differential stress values obtained at the end of each step are given. Since the main aim of this study is to produce a flow law to be applied at *in situ* conditions, we will assess how the obtained mechanical data fit to conventional power laws (Van Eekelen et al. 1984; Urai 1983; Ter Heege et al. 2005b), describing grain size insensitive (GSI – dislocation) creep and/or grain size sensitive (GSS – diffusion/pressure solution) creep, as given below

GSI:
$$\dot{\varepsilon} = A^* \sigma^n \qquad\qquad (2)$$

GSS:
$$\dot{\varepsilon} = B^* \sigma d^{-p} \qquad\qquad (3)$$

where $\dot{\varepsilon}$ is the strain rate, A^* is a substituted constant term for $A\exp(-Q/RT)$, where A is constant (for constant temperature), Q is the activation energy, R is the gas constant, T is the absolute temperature, B^* is also constant at a given temperature T, σ is the flow stress of the sample, n is the stress exponent, d is the average grain diameter, p is the grain size exponent.

3.1.1   Flow behaviour

All stress values obtained at the ends of the constant strain rate steps (Table 2), approaching steady state, are plotted against corresponding deformation strain rates in Figure 2a. Note that the dependent variable (stress) is plotted along the x-axis in this figure, to allow easier comparison with the relaxation data presented below. For bischofite, the best fit linear

Table 2: Test conditions and results of constant deformation parts

Test sample	$\dot{\varepsilon}$ [s^{-1}]	σ [MPa]	Experiment duration [days]	Test sample	$\dot{\varepsilon}$ [s^{-1}]	σ [MPa]	Experiment duration [days]
Bischofite5	10^{-5}	5.3	24	Carnallite1	10^{-5}	20.8	44
	10^{-6}	3.8			10^{-6}	13.2	
	10^{-7}	2.3			10^{-7}	9.0	
	10^{-8}	1.2			10^{-8}	5.5	
	10^{-7}	2.2			10^{-7}	9.0	
	10^{-6}	3.4			10^{-6}	14.0	
	10^{-5}	5.0			10^{-5}	24	
Bischofite6	10^{-6}	3.2	21	Carnallite2	10^{-5}	21.5	40
	10^{-6}	3.8			10^{-6}	13.4	
	10^{-5}	5.7			10^{-7}	9.0	
	10^{-5}	5.5			10^{-8}	5.2	
	10^{-7}	2.3			10^{-7}	9.0	
Bischofite7	10^{-5}	5.2	56		10^{-6}	14.5	
	10^{-6}	3.4			10^{-5}	24.3	
	10^{-7}	2.1		Carnallite3	10^{-5}	28.1	3
	10^{-8}	1.2			10^{-6}	18.8	
	10^{-7}	2.0			10^{-7}	11.1	

	10^{-6}	3.5		Carnallite4	10^{-5}	17.4	6
	10^{-5}	5.3		Carnallite5	10^{-5}	21.9	24
	10^{-6}	3.5			10^{-6}	13.8	
	10^{-6}	3.5			10^{-7}	9.4	
	10^{-5}	5.5			10^{-8}	6.1	
	10^{-5}	5.3			10^{-7}	10.2	
					10^{-6}	15.2	
					10^{-5}	23.8	
Mixture1	10^{-5}	25.7	42	Mixture2	10^{-5}	24.9	25
	10^{-6}	26.1			10^{-6}	21.6	
	10^{-7}	23.2			10^{-7}	16.8	
	10^{-8}	20.6			10^{-8}	10.8	
	10^{-7}	23.3			10^{-7}	16.7	
	10^{-6}	27.7			10^{-6}	21.1	
	10^{-5}	33.3			10^{-5}	25.2	

$\dot{\varepsilon}$ is the deformation strain rate
σ is the differential stress value at the end of the deformation step

regression (in log-log-space) resulted in $n = 4.8\pm0.2$ when applying the conventional power law of Equation (2). The steady state stress values have also been used to calculate n-values (cf. Eq. 2) for every individual step in strain rate of experiments bischofite5-6-7. The resulting values are plotted in Figure 2b. The n-value changes from about 6 at the higher stress to about 4 at the lower end of the stress range. This shows that a simple power law of the type of Equation (2) might not be applicable to the full data set for bischofite.

Five carnallite samples were tested and their stresses vs. natural strain data (Table 2) are shown in Figure 1b. Carnallite1 and 2 were both 7-step strain-rate stepping tests with three relaxation periods after constant strain rate deformation steps at 10^{-6}, 10^{-8} and 10^{-6} s^{-1},
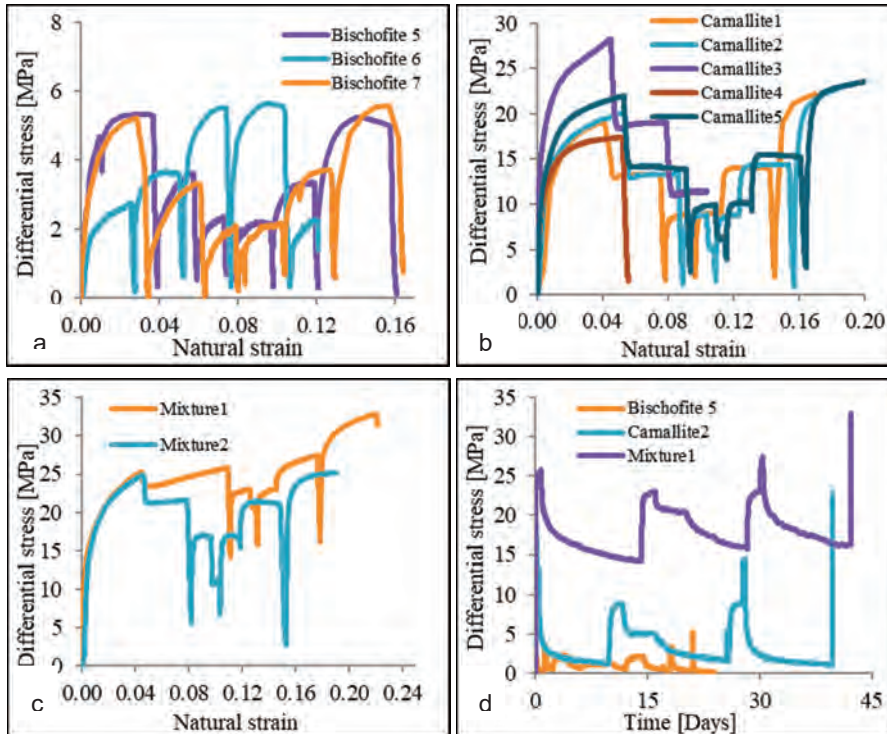
Figure 1. Mechanical data; differential stress vs. natural/true strain for bischofite (a), carnallite (b) and mixtures (c), and differential stress vs. time for three representative samples (d)

respectively. Carnallite3 was a 3-step stepping test without relaxation, carnallite4 was a single step deformation test followed by stress relaxation, and carnallite5 was a repeat experiment of carnallite 1 and 2. The samples showed strain rate sensitivity of stress, and strengths at the end of similar (repeat) strain rates were slightly higher for steps at higher total strains (see Table 2). The strengths of carnallite1, 2 and 5 are in good agreement with each other, demonstrating good reproducibility. Carnallite3 was comparatively too strong when compared with carnallite1, 2 and 5 at similar strain rates, while carnallite4 was found to be slightly weaker than the other samples. All stress values obtained at the end of the constant strain rate steps (Table 2), approaching steady state, are plotted against strain rate in Figure 2a. Best fit linear regression (in log-log-space, Fig. 2b) resulted in $n = 5.1 \pm 0.3$ when applying the conventional power law of Equation (2).

Two multistep experiments were performed on mixed bischofite-carnallite-halite samples. Mixture1 was a 7-step strain-rate stepping test with three relaxation periods after constant strain rate steps at 10^{-6}, 10^{-8} and 10^{-6} s^{-1}, respectively (see Table 2). The sample showed strain hardening in all constant strain rate steps, except for the one at the lowest rate. Mixture2 was also a 7-step strain-rate stepping test with three relaxation periods (Table 2), following the same sequence of steps as applied in mixture1. Mixture 2 was found to be weaker than mixture 1, and did not show the strain hardening as observed in mixture 1, but rather approached steady state stress behaviour in individual steps (Figure 1c). At the end of the
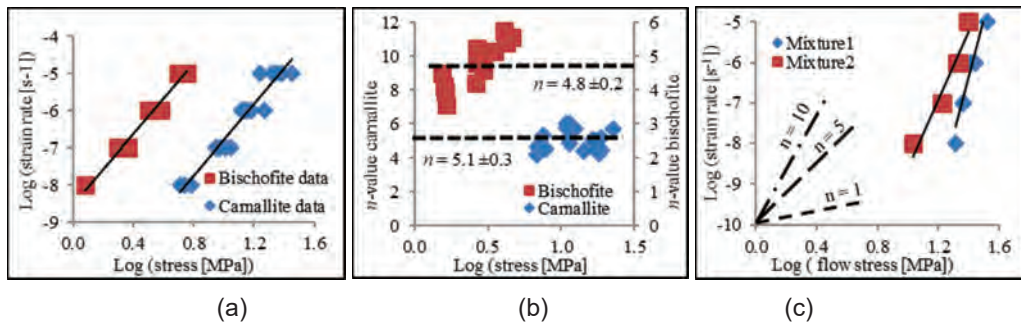
Figure 2. a) Steady state stress values of bischofite and carnallite samples against the strain rate on log space, b) n-value at different steady state stress values in bischofite and carnallite, c) n-value at different steady state stress values in mixture

experiment, the sample was taken out of the testing machine and localized strain along the pre-existing carnallite band was observed. This localized shear strain at the carnallite band most probably caused some leakage of the rubber jacket in the final stage of the experiment, which allowed some silicone oil to effuse through jacket and contaminate the sample. The sensitivity of stress to strain rate of the two mixtures is illustrated in Figure 2c, plotting the stress values at the end of each step as a function of strain rate, again with strain rate along the y-axis. The Figure 2c quite clearly illustrates the hardening behaviour of mixture1 and shows that the sensitivity of the differential stress to strain rate is rather low (high n-value), whereas the flow behaviour of mixture2 does not follow a linear trend in log-log space. Expressed using the power law n-value (Eq. 2), the trend is from $n \sim 10$ at the higher stress and faster strain rate, to $n \sim 5$ at lower stress and slower strain rate.

3.1.2 Stress relaxation

The stress relaxation results obtained are plotted in Figures 3a-c. The steady state stress values obtained at the end of each strain rate step are included in the graphs and form the starting points for relaxation. Moreover, the relaxation behaviour of all samples appeared identical and we have selected only three representative curves i.e. bischofite5, carnallite2 and

mixture1. Results at similar strain rate are combined. Generally, the graphs of bischofite and carnallite show that the evaluated plastic strain rate at the start of each relaxation fit to a trend with relatively high n-value ($n \sim 5$), implying that stress is relatively insensitive to strain rate. During relaxation then, the stress-strain rate sensitivity gradually increases and the n-value appears to approach $n = 1$ near the end of each relaxation step. Strikingly, the individual relaxation curves, starting at a particular strain rate and gradually decreasing in strain rate, do not pass through the steady state values obtained during the constant strain rate parts at lower rates. If compared at the same strain rate, the strength of the material during relaxation is always less than that during the constant strain rate part.

The stress relaxation data of mixtures are shown in Figure 3c. The steady state values obtained at the end of each deformation step are included in the graphs and from the starting points of relaxation. For comparison, similar strain rate steps are combined. At start of relaxation, the n-value is high ($n > 10$) showing steep slope, implying that the stress is relatively insensitive to strain rate. During relaxation then, the n-value decreases and appears to approach $n = 1$ near the end of each relaxation step. Distinctly, mixture1 relaxation curve progressively, passes through the steady state points obtained during deformation steps, pointing that the mixture2 shows weaker behaviour during relaxation than during deformation.

4 Discussion

4.1 Mechanical behaviour

The stress strain plots of the three salts tested; Figures 1(a-c), showed that these materials have different strengths for similar strain rates and temperature. Bischofite was found the weakest in the series. Carnallite appeared stronger than bischofite and the mixture was found even stronger than carnallite. If we compare our work with previous studies on halite by Heard (1972), Wawersik & Zeuch (1986), Carter (1993) and Ter Heege et al. (2005a), we see (Figure 4a) that the upper limit (highest stress at a given strain rate) is constrained by the flow law by Heard (1972 - confined tests on polycrystalline natural halite aggregates) at the temperature of 70 °C. Carnallite is weaker and lies around the flow law given by Wawersik & Zeuch (1986), whereas the bischofite is clearly the weaker end in the family. The data set on the mixtures is not extensive enough to allow a meaningful definition of the creep behaviour in terms of GSS creep cf. Equation (3).

(a)   (b)   (c)
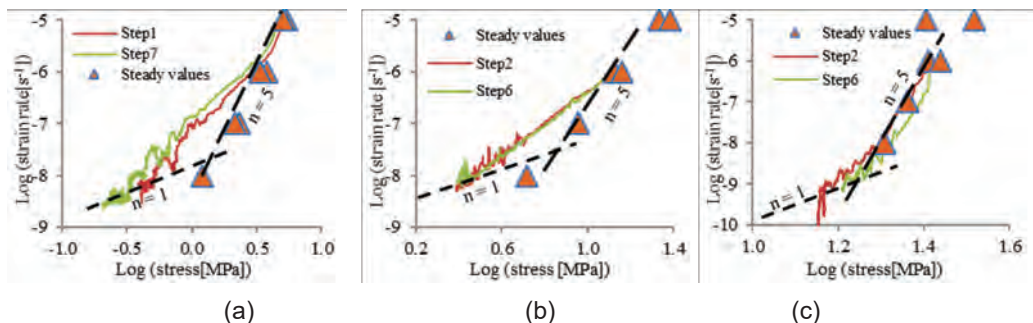
Figure 3. Stress relaxation curves a) bischofite5, step1 and step7 $\dot{\varepsilon} = 10^{-5}$ s^{-1}, b) carnallite2, step2 and step6 $\dot{\varepsilon} = 10^{-6}$ s^{-1}, c) mixture1 step2 and step6 $\dot{\varepsilon} = 10^{-6}$ s^{-1}
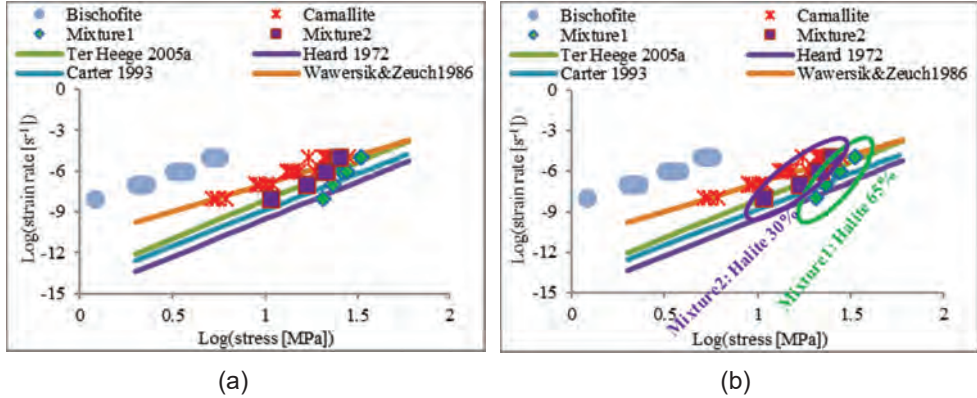
Figure 4 a) Projected curves for flow laws of wet halite from previous studies, b) steady state values comparison of bischofite, carnallite and mixture (with halite% composition)

4.2 Composite flow law

The basis for determining composite flow laws were the data obtained during the deformation at constant strain rates, providing near steady state stresses, and the analysis of the relaxation curves under the assumption of constant structure. We will now evaluate if combining GSI and GSS creep in the form of a composite creep law is of added value. We start from:

$$\dot{\varepsilon} = A^*\sigma^n + B^*\sigma d^{-p} \tag{4}$$

Since our study did not systematically involve experiments on materials with different grain sizes, we explore the possible role of GSS creep using predictions on the basis of recrystallized grain size piezometers for the salts under consideration. In a recrystallized grain size piezometer, the size of the grains is directly related to the differential stress (e.g. Twiss 1977, Shimizu 2008, De Bresser et al. 2001) according to:

$$d = K\sigma^{-m} \tag{5}$$

where K and m are material and mechanism specific constants.

Van Eekelen et al. (1981) measured the recrystallized grain size in a number of bischofite samples experimentally deformed at 60 °C. We used their data to calibrate the values for K and m in Equations (5) and (4.11) by simply applying

$$d = K(\sigma)^{-1/slope} \tag{6}$$

The resulting piezometric relation for bischofite (with d in mm) is:

$$d = 4.725\sigma^{-1.15} \tag{7}$$

Using the piezometer of Equation (7), we can now estimate the recrystallized grain size at any stress, under the assumption the dynamic recrystallization was fully effective at the conditions imposed. We have done this for the average stresses relevant for our bischofite samples at the start of the relaxation periods, after steps at constant strain rate of 10^{-5}, 10^{-6}, 10^{-7} and 10^{-8} s^{-1}. The role of grain size can now be further evaluated by; i) assuming that during relaxation the grain sizes will remain the same, ii) and that a GSS creep law of the type of Equation (3), with $n = 1$, applies at the final stages of relaxation, i.e. at the very slow strain
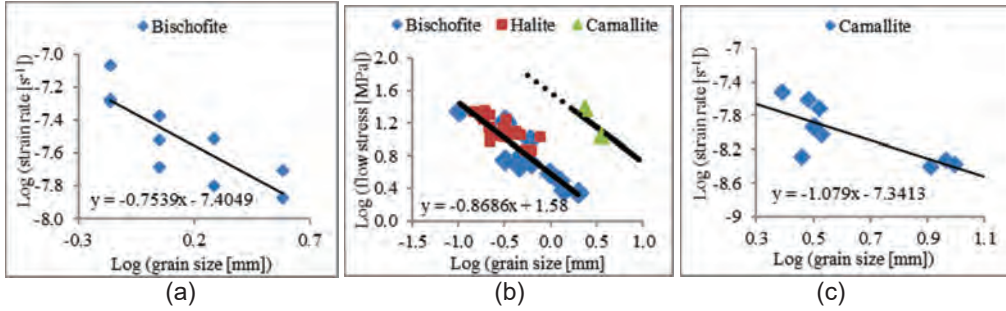
Figure 5. a) Bischofite Log strain rate values picked from relaxation curves at similar stress of 1.0 MPa, b) carnallite measured grain sizes in log space with halite and bischofite, c) strain rate values picked from relaxation data plotted against stress equivalent grain size from piezometer

rates. This allows calculating the *p*-value (Equation 3). Taking logarithm and simplifying the Equation (3) we get

$$log\dot{\varepsilon} = intercept - plogd \qquad (8)$$

The intercept includes the stress and is only a constant if data are considered at single value of stress. For this, we picked $\sigma = 1.0$ MPa (i.e. $Log\sigma = 0$) in the stress relaxation curves (Figure 3a), determined the strain rate values at the various relaxation curves, and plotted the results, in log-log space (cf. Eq. 8, see Fig. 5a), against the evaluated grain sizes. Then using Equation (8), the grain size exponent '*p*' can be determined as from the slope of the best fit line (Figure 5a). As is clear from the Figure 5a, the scatter is quite substantial, so the resulting value for *p*, 0.8 ±0.2, must be regarded as only a crude estimate. Nevertheless, the result confirms the suggestion that grain size sensitive behaviour is likely to play a role in the flow behaviour of bischofite, at least during the relaxation.

A possible mechanism controlling flow in this GSS regime is dissolution or precipitation-controlled pressure solution creep (e.g. Spiers et al. 1990, Schutjens 1991). According to these studies, the inter-granular pressure solution creep (IPS) is a serial process comprising of three steps; dissolution of material at high stress zones, transportation via diffusion to lower stress zones and precipitation at low stress zones. The slowest of these will determine the creep rate. The creep rate is inversely related to the grain size ('d^{p}'), where $p = 1$ and 3 are the sensitivities of the rate controlling mechanism to grain size, defining interface dissolution/precipitation and diffusion respectively.

Using the intercept value of the best fit line (Fig. 5a), the unknown constant B^* of Equation (3) was calculated to be 3.94×10^{-8} (MPa^{-1} mm$^{0.8}$ s^{-1}). Hence, the GSS flow law for bischofite at 70 °C, with grain size *d* in mm, is

$$\dot{\varepsilon}_{GSS} = 3.94 \times 10^{-8}\sigma d^{-0.8} \qquad (9)$$

No recrystallized grain size piezometric relation is available in the literature for carnallite. We plotted our grain size data of two carnallite samples as a function of stress together with the data for halite (Ter Heege et al. 2005b) and bischofite (Van Eekelen et al. 1981) in Figure 5b. Bischofite and halite follow very comparable trends, but the grain size of carnallite at a given stress is substantially larger than that of halite and bischofite. We assumed that the trend observed for halite and bischofite also holds for carnallite, coming from the same family of materials. We thus suggest that the recrystallized grain size Piezometric relation for carnallite (Fig. 5b) is:

$$d = 65.92\sigma^{-1.15} \qquad (10)$$

Now doing the same exercise for carnallite as carried out for bischofite, applying Equations (3) and (8) under the assumption of constant structure (grain size) during relaxation, we can obtain a crude estimate for the *p*-value for carnallite. We picked $\sigma = 4.0$ MPa (i.e. $Log\sigma = 0.6$) in the

stress relaxation curves (Figure 5b), determined the strain rate values at the various relaxation curves, and plotted the results, in log-log space against the values for the grain size,
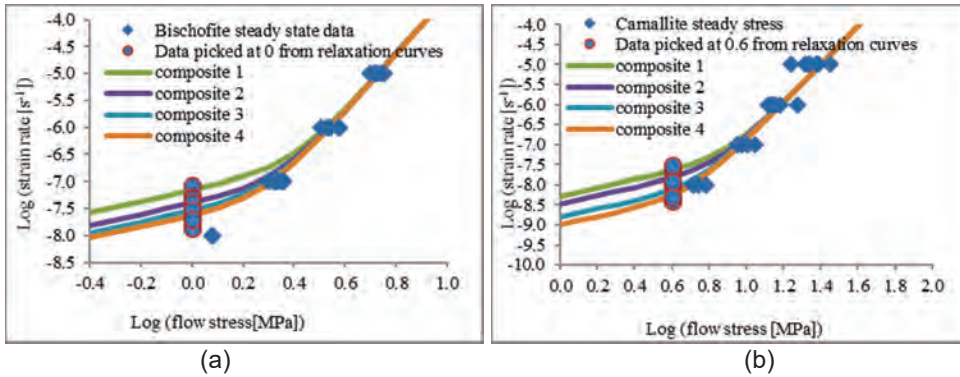
Figure 6. Trends resulting from the composite GSI + GSS flow law covering the steady state behaviour (diamond data points) as well as the gradual decrease in *n*-value during relaxation (from *n* ~ 5 to *n* ~ 1 when going towards low stress and strain rate), a) bischofite, b) carnallite

see Figure 5c. The resulting value for *p* was: 1.0 ±0.26. Using the intercept value of the best fit line (Figure 5c), the unknown constant *B** of Equation (3) was calculated to be 1.01×10^{-8} (MPa^{-1} mm$^{1.0}$ s^{-1}). Hence, the GSS flow law for bischofite at 70 °C, with grain size *d* in mm is

$$\dot{\varepsilon}_{GSS} = 1.01 \times 10^{-8} \sigma d^{-1.0} \tag{11}$$

Equation (4), however, cannot simply be regarded as the sum of the GSI and GSS creep laws defined separately, since grain size sensitive behaviour might have influenced the steady state creep while this was not considered in performing the best fitting exercise. In other words, the established GSI creep law might not hold for the complete stress – strain rate range covered. We assume now that at the highest stress, GSI creep is robust. Regression analysis taking only the data into account at strain rate 10^{-6} and 10^{-5} s^{-1}, i.e. at the higher stresses, then results in $n = 5.4 \pm 0.4$ for bischofite and $n = 5.3 \pm 0.7$ for carnallite. Using these new values for the stress exponent *n*, holding for the GSI part of the composite Equation (4), and taking the established GSS flow equations, non-linear regression best fitting resulted in values for *A** of Equation (4).

For bischofite:

$$\dot{\varepsilon} = 1.1 \times 10^{-9} \sigma^{5.4} + 3.94 \times 10^{-8} \sigma d^{-0.8} \tag{12}$$

For carnallite:

$$\dot{\varepsilon} = 3.70 \times 10^{-13} \sigma^{5.3} + 1.01 \times 10^{-8} \sigma d^{-1} \tag{13}$$

The trends representing composite flow for bischofite: (for a grain size of 0.5 mm (composite1), 1.0 mm (composite 2), 1.5 mm (composite 3) and 2.0 mm (composite 4)) and carnallite: (for a grain size of 2 mm (composite1), 3 mm (composite 2), 6 mm (composite 3) and 9 mm (composite 4)) following Equations (12) and (13) are shown in Figures (6a-b).

The trend lines in Figures (6a-b) show that the influence of grain size is effective at lower stresses and strain rates. For higher stresses, these curves satisfy the steady state points, whereas on lower stress/strain rates, these trends satisfy the data picked from relaxation curves. Hence, the composite flow laws give a complete picture of the creep characteristics of bischofite and carnallite, in two regimes of GSI (*n* ~ 5) and GSS (*n* ~ 1) that gradually pass into each other.

Conclusions

Deformation experiments were conducted on bischofite, carnallite and mixed bischofite-carnallite-halite samples obtained from natural cores. Main aim was to produce constitutive flow laws that can be applied at *in situ* conditions. The experiments were carried out at a confining pressure of 40 MPa and a temperature of 70 ºC. The experiments were multi-step tests consisting of constant strain rate parts and stress relaxation parts. The flow laws developed are mainly on the basis of mechanical data, microstructural work is for future.

The main findings are:

1. Carnallite is 4-5 times stronger than bischofite. The bischofite-carnallite-halite mixtures, at their turn, are stronger than carnallite, and hence also stronger than bischofite. We infer that the difference in strength from one mixture to the next is best explained by differences in halite wt. %.
2. The constant strain rate parts of the multistep experiments allowed defining (dislocation/grain size insensitive GSI) creep laws for bischofite and carnallite.
3. For bischofite as well as carnallite, we observed that during stress relaxation, the conventional power law stress exponent in the creep laws changes from ~5 at 10^{-5} to ~1 at 10^{-9} s^{-1}. This is interpreted as reflecting a change from grain size insensitive (GSI) dislocation creep at the faster strain rates to grain size sensitive (GSS) behaviour at slow strain rate.
4. If during deformation of bischofite and carnallite the microstructure is continuously being reworked, some balance might develop between the GSI and GSS mechanisms, at the boundary between the creep regimes. The established single GSI flow laws then form solid descriptions of the creep behaviour of these materials. In cases that effective microstructural modification cannot be assumed, as for example during transient creep in the walls of salt caverns, the composite creep laws form better descriptions.

Acknowledgements

References

CARTER, N.L., HORSEMAN, S.T., RUSSELL, J.E. & HANDIN, J. 1993. Rheology of rocksalt. Journal of Structural Geology, 15 (9-10), 1257-1271.

CHRISTOV, C. 2009. Isopiestic Determination of the Osmotic Coefficients of an Aqueous $MgCl_2$ + $CaCl_2$ Mixed Solution at (25 and 50) °C. Chemical Equilibrium Model of Solution Behavior and Solubility in the $MgCl_2$ + H_2O and $MgCl_2$ + $CaCl_2$ + H_2O Systems to High Concentration at (25 and 50) °C J. Chem. Eng. Data, 54, 627–635.

DE BRESSER, J.H.P., TER HEEGE, J.H. & SPIERS, C.J. 2001. Grain size reduction by dynamic recrystallization: can it result in major rheological weakening?. International Journal of Earth Sciences, 90(1), 28-45.

HEARD, H.C. 1972. Steady-State Flow in Polycrystalline Halite at Pressure of 2 Kilo bars. Flow and Fracture of Rocks, 191-209.

HEARD, H.C. & RYERSON, F.J. 1986. Effect of Cation Impurities on Steady-State Flow of Salt,Mineral and Rock Deformation: Laboratory Studies: The Paterson Volume, 99-115.

JACKSON, M.P.A. & TALBOT, C.J. 1986. External shapes, strain rates, and dynamics of salt structures. Geological Society of America Bulletin 97.3: 305-323.

Muhammad, N. 2015. Deformation and transport processes in salt rocks: An experimental study exploring effects of pressure and stress relaxation. Utrecht Studies in Earth Sciences, 84, 1-275.

Muhammad, N., Spiers, C.J., Peach, C.J. & De Bresser, J.H.P. 2012. Effect of confining pressure on plastic flow of salt at 125 °C. In: Bérest, P., Ghoreychi, M., Hadj-Hassen, F., and Tijani, M. eds. Mechanical behaviour of salt VII, CRC press, 57-64.

Roedder, E. & Bassett, R.L. 1981. Problems in determination of the water content of rock-salt samples and its significance in nuclear-waste storage siting. Geology 9, no. 11: 525-530.

Rutter, E.H. & Mainprice, D.H. 1978. The effect of water on stress relaxation of faulted and unfaulted sandstone. Pure and Applied geophysics 116.4-5: 634-654.

Schutjens, P.M.T.M. 1991. Intergranular pressure solution in halite aggregates and quartz sands: an experimental investigation. Geologica Ultraiectina, 76, 1-233.

Shimizu, I. 2008. Theories and applicability of grain size piezometers: The role of dynamic recrystallization mechanisms. J. Struct. Geol. 30, 899-917.

Spiers, C.J., Schutjens, P.M.T.M., Brzesowsky, R.H., Peach, C.J., Liezenberg, J.L. & H.J. Zwart, H.J. 1990. Experimental determination of constitutive parameters governing creep of rocksalt by pressure solution. Geological Society, London, Special Publications 54, no. 1: 215-227.

Spiers, C.J. & Carter, N.L. 1998. Microphysics of Rocksalt Flow in Nature, The Mechanical Behaviour of Salt IV. Proceedings of the Fourth Conference. M. Aubertin, H. R. Hardy Jr., Trans. Tech., Clausthal-Zellerfeld, Germany, 115–128.

Ter Heege, J.H., De Bresser, J.H.P. & Spiers, C.J. 2005a. Rheological behaviour of synthetic rocksalt: The interplay between water, dynamic recrystallization and deformation mechanisms. J. Struct. Geol. 27, 948-963.

Ter Heege, J.H., De Bresser, J.H.P. & Spiers, C.J. 2005b. Dynamic recrystallization of wet synthetic polycrystalline halite: dependence of grain size distribution on flow stress, temperature and strain," Tectonophysics 396.1: 35-57.

Twiss, R.J. 1977. Theory and applicability of a recrystallized grain size paleopiezometer. Pure and applied Geophysics 115, 227-244.

Urai, J.L. 1983. Water assisted dynamic recrystallization and weakening in polycrystalline bischofite. Tectonophysics 96.1: 125-157.

Urai, J.L. 1985. Water-enhanced dynamic recrystallization and solution transfer in experimentally deformed carnallite. Tectonophysics, 120(3), 285-317.

Urai, J.L., Spiers, C.J., Zwart, H.J. & Lister, G.S. 1986. Weakening of rock salt by water during long-term creep. Nature 324, 554–557.

Van Eekelen, H.A., Urai, J.L. & Hulsebos, T. 1981. Creep of bischofite. In Prodeedings of the 1st Conference on the Mechanical Behavior of Salt, Pennsylvania, USA. Trans. Tech., Clausthal-Zellerfeld, Germany.

Wawersik, W.R. & Zeuch, D.H. 1986. Modeling and mechanistic interpretation of creep of rock salt below 200 °C. Tectonophysics, 121(2), 125-152.

Theme 3: Geological isolation systems and geotechnical barriers

Evaluation of current knowledge for building the Safety Case for salt-based repositories

*Jacques Grupa[*1], Thomas Schröder[1], Kelvin Browning[1], Arjen Poley[1]*

[1]NRG, The Netherlands

* grupa@nrg.eu

ABSTRACT: Over the past 50 years in the Netherlands much effort has been devoted to the geologic disposal of radioactive waste in rock salt. Examples of such efforts are contained in the framework of the ICK, OPLA, CORA, and OPERA research programmes. Additional work has been done in several EU Framework projects like EVEREST, BAMBUS, PAMINA, and THERESA, and other research efforts. In these programmes and projects, safety assessments and detailed analyses have been performed for generic repository designs in rock salt in order to show that radioactive waste may safely be disposed of, i.e. the waste can be isolated from our living environment. The results of the "*Evaluation of current knowledge for building the Safety Case for salt-based repositories*" (Hart et al. 2015) will be presented, with a focus on the processes that drive the isolation of the waste: salt creep and crushed salt compaction. This knowledge has been developed over time by theoretical research, laboratory testing (a.o. in the HPT laboratory in Utrecht), and field testing (mainly in the underground laboratory in the Asse II salt mine). In this paper, it is elaborated how that knowledge has been applied in the safety studies for geologic disposal in rock salt.

1   Introduction

Over the past 50 years, much effort has been devoted to the geologic disposal of radioactive waste in a rock salt formation. Several national research programmes were performed in the Netherlands, e.g. ICK (1979), OPLA (1989); CORA (2001), and many research projects were conducted within EU Framework programmes, e.g. EVEREST (1997), BAMBUS (1999), BAMBUS-II (2004), PAMINA (2011), or THERESA (2012). Likewise, large research programmes on disposal in rock salt have been executed in Germany, to support the Safety Case for a planned repository in Gorleben, and the US, in support of the Safety Case for WIPP. In all these programmes and projects, safety assessments and detailed analyses have been performed in order to show that radioactive waste may safely be disposed of in rock salt isolating the waste from our living environment.

However, due to political developments in Germany and the U.S. (e.g. Gorleben Moratorium), in the last 20 years' research on radioactive waste disposal in rock salt somewhat lost its focus. The recently finalized Dutch research programme OPERA (OPERA, 2017) concentrated mainly on disposal in poorly indurated clay, however, a single project was devoted on wrapping up the current status on disposal in rock salt: "*Evaluation of current knowledge for building the Safety Case for salt-based repositories*" (Hart et al. 2015a & 2015b). That project concluded that presently a substantial amount of knowledge on rock salt is available. The main conclusion of that report was that, although currently in the Netherlands certainly a few 'loose ends' have to be tied off before a quantitative safety assessment for a radioactive waste repository in rock salt could be performed, in general sufficient knowledge and experience exist to realize a first generic Safety Case for such a repository design with reasonable efforts. Within said project, also a roadmap towards such a Safety Case for a repository in rock salt was developed (Hart et al. 2015b), and currently in the Netherlands a follow-up programme is being performed (COVRA, 2020).

For the knowledge gaps identified, Hart et al. (2015b) proposed actions on how to address these on the short term. A number of topics related to these safety relevant processes are summarized in Table 1.Table 1: Recommendations with respect to knowledge gaps related to safety relevant processes as identified in OPERA (adapted from Hart et al. 2015b)

(Thermo)mechanical	Geochemical, salt-related	Geochemical, super-container-related
Enhancement of the understanding of physical processes, amongst others convergence and any effects of the presence of brine, which control the efficiency of granular salt compaction especially with respect to humidity effects	To inventarize which mineral dissolution processes can be of principal interest considering the anticipated size of a Dutch disposal concept compared to the size and (chemical) composition of available rock salt host formations in the Netherlands	Analysing CSH corrosion processes in saturated brine, their influence on radionuclide solubility and mobility, and assessing existing uncertainties, through an evaluation of existing literature on CSH in saline environments. Since potential corrosion and degradation reactions depend on the composition of the brine, the studies should carefully consider the source of the brine in the Dutch situation
Enhancement of the understanding of the porosity development during the compaction process as well as the correlated permeability, which adds to the understanding of reaching a complete isolation of the disposed waste	To judge, based on the previous inventory, whether the range of expected mineral interactions is sufficiently well covered by existing experiments	If necessary, establishing an experimental programme of critical parameters and processes based on the outcome of the modelling study
		It is therefore recommended first to clarify constructional aspects of cementitious barriers and their role in the safety concept
	The elaboration of non-equilibrium reaction kinetics in a saline system, still being in an initial state due to the lack of many reaction parameter values, may be taken forward	Additionally, from the point of view of process understanding of corrosion of cementitious barriers in a salt environment, it is recommended to consider the ease of assessment as an important design criterion, thus focusing as much as practically eligible on the current knowledge of the involved materials as well as the relevant processes and their remaining uncertainties

2   Implementation of a radioactive waste repository: The Safety Case methodology

The fundamental safety objective when demonstrating the safety of radioactive waste disposal is to protect people and the environment from harmful effects of ionizing radiation (IAEA, 2006). Furthermore, radioactive waste must be managed in such a way as to avoid imposing an undue burden on future generations; that is, the generations that produce the waste have to seek and apply safe and practicable solutions for its long term management. The preferred strategy for the management of all radioactive waste is to contain it and isolate it from the accessible biosphere.

There is no fixed recipe for the compilation and maintenance of a Safety Case for the disposal of radioactive waste, since the purpose and context of the Safety Case may differ from country to country. However, it is generally agreed that a Safety Case should constitute all relevant safety aspects of a geological repository, and that it evolves as time progresses towards the implementation and subsequent closure of the site. The Safety Case for final disposal involves several principal elements, as depicted in Figure 1.

The present methodologies for the execution of performance assessments in geological disposal are for a significant part based on, but not solely limited to the ideas that have been developed in the EU project PAGIS (Performance Assessment of Geological Isolation Systems; Storck 1988), a collaborative research program of the European Union. The safety assessment consists of the following steps:

1. Definition of safety relevant scenarios.

2. Evaluation against safety and reliability requirements.

3. Analyses of relevant processes and development of conceptual models.

4. Nuclide transport and dose calculations.

5. Evaluation against safety and reliability requirements.
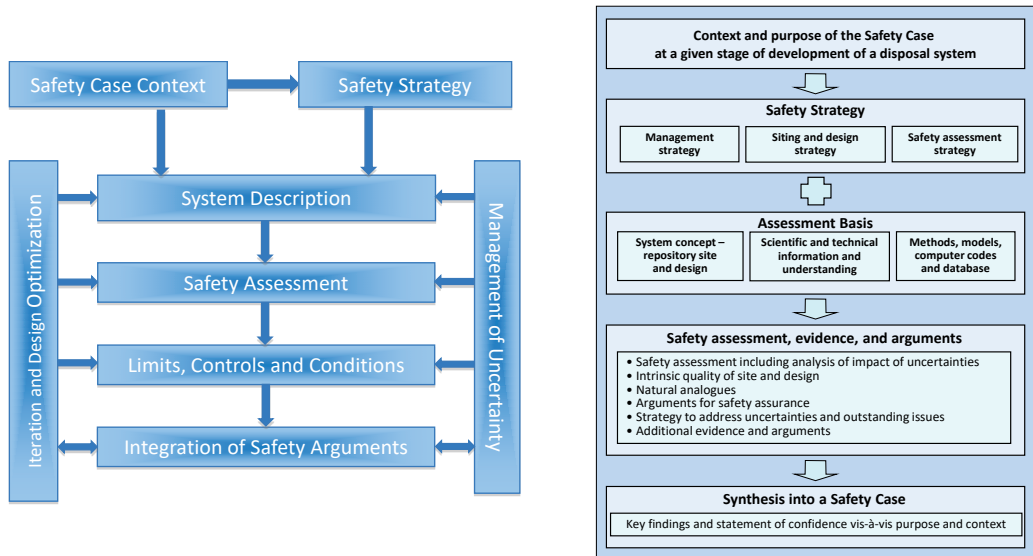
Figure 1: General elements and structure of a Safety Case for final disposal of radioactive waste (left: IAEA, 2012; right: adapted from NEA, 2004).

The safety case methodology is an iterative process required to build confidence and demonstrate safety of a repository. During the different disposal stages, the current state of the art is periodically evaluated, and the outcomes of safety assessments are used to direct further research, if necessary. In course of time, it can also be established which processes and related model parameters are critical for long-term safety, and might require more experimental or scientific support. In this manner, research efforts are directed in a structured manner, aimed at reduction of uncertainties that may relevantly affect long-term safety.

3   Understanding of the geo-mechanical behaviour of rock salt: where do we stand now?

Halite rock salt is an interesting candidate as host formation for a radioactive waste repository. It is often found in accessible depths in large formations, it easily minable, mined volumes are self-supporting, and easily maintained. Any mined openings in the rock salt are healed due to creep of the rock salt under stress differences (self-healing property), i.e. by differences between local rock pressure and internal pressure in a mined volume. As result, in time any material stored in a mined volume in rock salt will become completely isolated by the rock salt.

A radioactive waste repository in rock salt principally exists of mine works – shafts, working areas and connection galleries and waste disposal volumes – galleries, boreholes or cells. The mine works will successively be backfilled and sealed at closure of the repository, while the waste disposal volumes will be sealed during operation of the repository once waste has been emplaced. The objective of these seals is to shield personnel during repository operation, but also to contribute to the long-term isolation of the waste. The radioactive waste itself is contained in waste type specific containers. For the more hazardous high-level waste these are rigid enough to endure the lithostatic pressure and provide isolation for a long time (hundreds to thousands of years).

One of the considered sealing methods is the application of blocks of precompacted salt grit resulting from the earlier mining operation as per the Metro-1 disposal concept (e.g. Heijdra & Prij 1997). The advantage of using salt grit is that in that way no unnecessary foreign material is introduced into the salt formation and that due to salt creep of the surrounding salt, the salt grit will be compacted until it is indistinguishable from the surrounding host rock. Compaction

of salt grit mainly depends on the effective pressure in the salt grid, its porosity and its moisture content: the larger the effected pressure, the higher the porosity or moisture content, the faster the compaction (Zhang & Grupa 2006). Here, effective pressure is essentially the difference between external and internal pressure (air or brine pressure!) plus internal compaction resistance.

3.1 *From process description to performance assessment model*

A disadvantage of a precompacted salt grit seal is that it will remain permeable for several decades, i.e. will not be able to prevent accidentally intruding brine turned ground water from entering a sealed disposal cell nor potentially contaminated brine to be squeezed out of the cell. In safety assessments modellers apply various models for convergence of rock salt around open mined volumes and compaction of salt grit, which is often applied to backfill such volumes. In the Netherlands, physics- and geometry-based models are applied. To analyse convergence of mined volumes, a model developed by Prij (1991) is used. In that model it is assumed that convergence of a mined volume V is related to the volume itself:

$$\frac{d}{dt}V(t) = -\alpha \cdot A \cdot e^{\frac{-Q}{RT}} \left(\frac{\alpha \cdot p_{eff}}{m}\right)^m \cdot k \cdot V(t) \tag{1}$$

in which k is the normalized convergence rate. For the compaction of salt grit, models based on research by UU are applied (Spiers et al. 1988). In the NFR-PRO project (Zhang & Grupa, 2006) compaction creep of salt grit was modelled to occur by two independent mechanisms working in parallel, namely:

- (dislocation coupled) recrystallization creep

- pressure solution creep

A phenomological model was provided in Schléder et al. (2004):
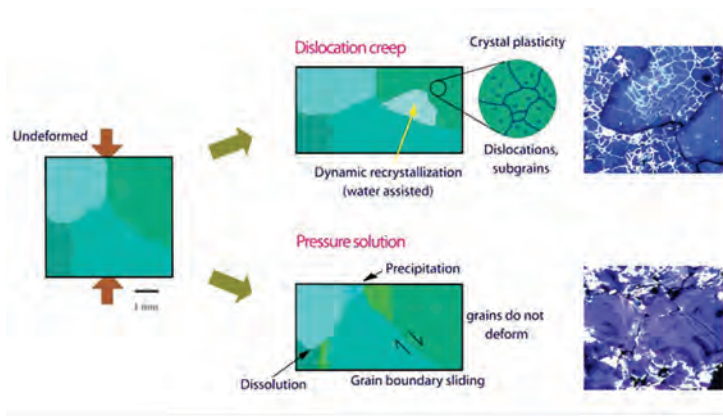
Figure 2: Deformation mechanisms of (dislocation-coupled) recrystallization creep and pressure solution creep

Zhang and Grupa proposed a mathematical model addressing both creep processes in terms of volumetric strain rate $\dot\varepsilon$ that was further elaborated in Schröder et al (2008) by

$$\dot\varepsilon[s^{-1}] = Q\dot\varepsilon_{ps} + \dot\varepsilon_{recr} = Q \frac{A_{ps}}{T \cdot d_g^2} \cdot g(\phi) \cdot \sigma + \frac{B_{recr}}{d_g^2} \cdot e^{-\frac{dH}{RT}} \cdot h(\phi) \cdot \sigma^5 \tag{2}$$

where σ is stress in [MPa]. The geometry-related functions $h(\phi)$ and $g(\phi)$ are defined by

$$h(\phi)[-] = \frac{\phi^{1.5}}{\left(1 - 1.20899 \cdot \sqrt[3]{\phi^2}\right)^{15}} \tag{3}$$

$$g(\phi)[-] = \phi \frac{1 + 3.5\phi}{\left(1 - 1.20899 \cdot \sqrt[3]{\phi^2}\right)^2} \frac{\sqrt[3]{\phi}}{\left(1 - \sqrt[3]{\phi}\right)} \tag{4}$$

with ϕ the porosity of the salt grid. A_{ps} and B_{recr} are parameters fitted to measured strain rates (Figure 3). Likewise, a permeability-porosity relation was implemented based on the NF-PRO 'pore healing model' (Zhang & Grupa 2006):

$$k[m^2] = \begin{cases} F_{47} * \phi + F_{09} * (\phi - F_{46})^n & \phi \geq F_{46} \\ F_{47} * \phi & \phi < F_{46} \end{cases} \tag{5}$$

The porosity value where the salt grit is assumed to become impermeable is also referred to as the "percolation threshold porosity" and was determined experimentally in the NF-PRO project at about 3% (Zhang & Grupa 2006). Other reported values for the percolation threshold porosity are between 1% (Grupa & Houkema 2000) and 5% (Poley 2007). While complete impermeability by pore healing is claimed at the "percolation threshold porosity", for the safety calculation conservatively a minimum permeability was assumed, also acknowledging that providing evidence for impermeability will be difficult or impossible. Again, model parameters were derived from measured values (Figure 3), and a distributed parameter set was generated that covers experimentally determined values (Table 2). Finally, a model representation was implemented in the performance assessment model EMOS (Storck et al. 1990; Schröder 2008). The resulting parameter values and their distributions for the above equations are summarized in Table 2. For more details, see Schröder et al. (2009).
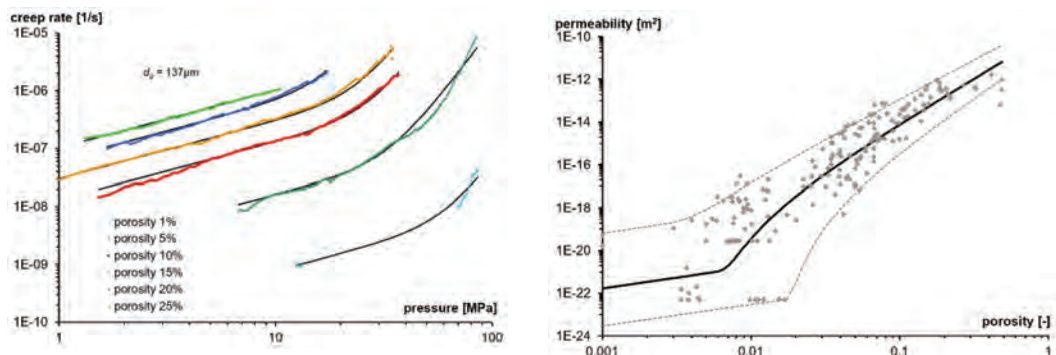
Figure 3: Left: Measured strain rate as a function of applied stress (Zhang & Grupa, 2006) for brine-saturated samples. Right: Measured (Spiers et al. 2005) vs modelled data for the permeability-porosity relation (Schröder et al. 2009). Dashed curves represent the 95%-confidence interval (upper and lower boundaries).

Table 2: Parameter intervals and assumed sample distributions

parameter	best fit	lower boundary	upper boundary	sample distribution
pressure creep constant A_{ps} [μm^2·K/(MPa·s)]	0.83	0.22	3.11	log-uniform
recrystallization creep constant B_{recr} [μm^2/(MPa^5·s)]	204	16.68	2501	log-uniform
permeability parameter F_{09} [m^2]	$1.39 \cdot 10^{-10}$	$3.43 \cdot 10^{-11}$	$5.62 \cdot 10^{-10}$	log-normal
exponent n [-]	4.18	3.67	4.69	normal
threshold porosity F_{47} [m^2]	$1.70 \cdot 10^{-19}$	10^{-26}	$2.95 \cdot 10^{-21}$	log-uniform, 25% of sample
		$2.95 \cdot 10^{-21}$	$6.31 \cdot 10^{-17}$	log-uniform, 75% of sample
threshold permeability F_{46} [-]	0.0050	0.00079	0.0016	log-uniform, 2.5% of sample

3.2 Assessing the performance of a salt grit plug

One of the safety relevant barriers in a salt-based radioactive waste repository is the sealing plug of a disposal cell, consisting of precompacted salt grit (e.g. Heijdra & Prij 1997). As discussed in the previous chapter, due to convergence of the host rock, the porosity and permeability of the plug will slowly decrease until, eventually, the permeability becomes extremely low and the "percolation threshold porosity" may be reached due to the breakdown of the pore network. As part of an exercise on testing different sensitivity analysis tools in the EU project PAMINA, 1000 calculations for a precompacted salt grit disposal cell plug configuration were performed, covering the parameter space shown in Table 2 (Schröder et al. 2009). Figure 4 depicts the evolution of such a plug in absence of brine, considering the uncertainties summarized in Table 2 and assuming an initial porosity of 0.3.
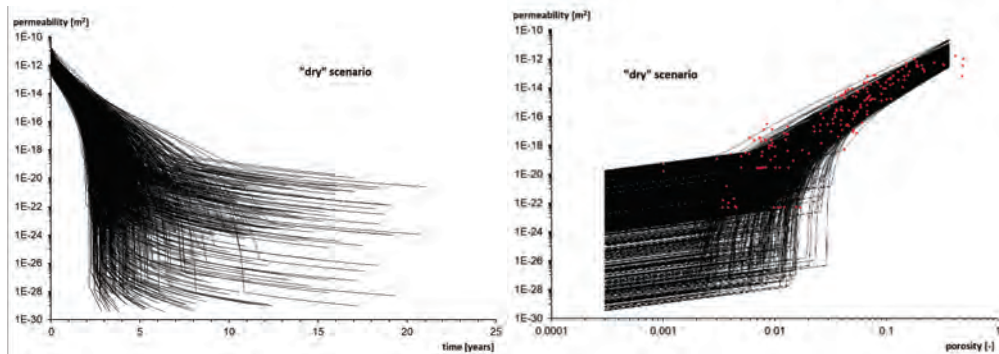
Figure 4: 1000 calculated seal permeability evolutions (left) and porosity-permeability relations (right) in absence of brine (Schröder et al. 2009). Red diamonds are experimentally measured values by Spiers et al. (2005).

Figure 4 shows that in absence of brine ("dry"), in most cases the permeability decreases rapidly within the first 10 years. The minimum permeability that is reached on the long term is mostly affected by the parameter F_{47} that defines the linear relation between porosity and permeability at low porosities (Eq. 5). Note, however, that calculations were stopped when a porosity of 0.0003 was reached, i.e. in all cases the decrease of porosity and permeability will continue, although with a decreasing rate. It can be concluded that if dry conditions can be maintained over a period of 20 years, permeability values $<10^{-20}$ m^2 are achieved.

In PAMINA, also the so-called abandonment scenario was analysed ("wet"). In that scenario, it is assumed that for external reasons a radioactive waste repository, with the waste filled disposal cells properly closed with a precompacted salt grit plug, will be abandoned before

final closure. This will result in flooding of the repository and build-up of relevant, convergence inhibiting brine pressures inside the repository. Consequently, brine will intrude through the initially permeable plugs into the waste containing disposal cells. In course of time, brine will be pressed out of the disposal cells. Figure 5 (left) depicts the resulting seal permeability evolutions considering an initial porosity of 0.3.
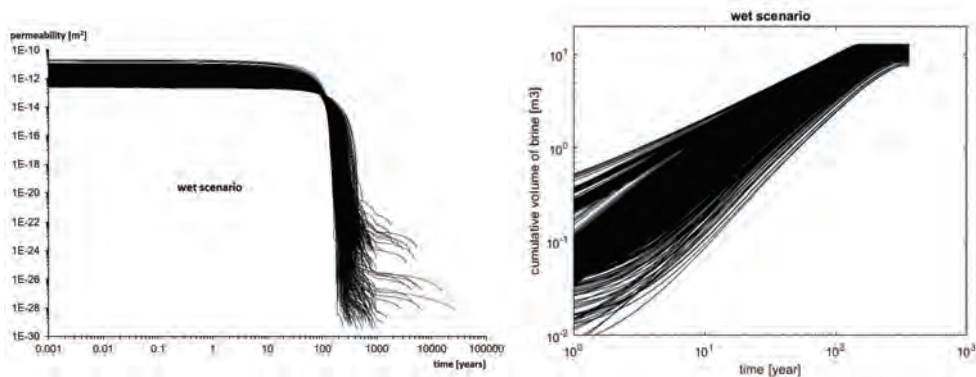
Figure 5: 1000 calculated seal permeability evolutions (left) and cumulative volumes of brine pressed out of a disposal cell (right) in the abandonment scenario.

3.3   Evaluation and lessons learned

The development of a Safety Case is an iterative activity, requiring periodic evaluations of whether sufficient knowledge is available to provide confidence on the long-term safety. The question of interest for this paper is: do we have sufficient understanding on the creep- and compaction behaviour of salt grit? To evaluate this question fully, a model representation of a disposal concept and the surrounding geosphere has to be built, considering all barriers that contribute to safety. Furthermore, relevant future evolutions that may occur and the pathways that eventually may lead to human exposure have to be established. Since long-term safety depends on several barriers, failure of a single barrier, such as the disposal cell plug, does not necessarily lead to impairment of the long-term safety. E.g. as long as the containers isolate the waste, the brine pressed out of a disposal cell will be uncontaminated. Likewise, even in case of flooding and failure of the waste container, the waste matrix will only slowly release radionuclides, hence limiting potential exposure. In most evolution scenarios, there will also be a shaft seal and additional dams within the repository that will isolate repository sections where disposal activities have been completed, further reducing potential emissions of contaminated brine. I.e. a statement on safety can only be made by evaluating the overall system.

However, even without a full evaluation of the disposal system, the performance calculations of a generic disposal cell as conducted in PAMINA showed that most uncertainties noted have little effect on the plug's sealing function: in case of the absence of brine, extensive compaction takes place within two decades, reducing the permeability by more than 6 orders of magnitude. In case of the intrusion of saturated brine, compaction takes longer, since the pressure of the brine that enters the disposal cell will counteract convergence of the surrounding host rock. However, model calculations show that after about 200 to 300 years, most brine is pressed out of the cell (Figure 4). If containers fulfil their containment function in the first 300 years, no relevant radioactive releases are expected. On the long-term (>300 years), the uncertainty on the plug's behaviour is mostly related to the parameter F_{47} that defines the linear relation between porosity and permeability at low porosities, hence is directly related to the assumptions that are made on the porous network breakdown at low porosities.

3.4 How to decrease uncertainties (is our model good enough?)

One of the main drivers for research on geological disposal is to reduce remaining uncertainties on safety relevant processes. From the above it is clear that any improvement/refinement of the creep-behaviour model does not directly lead to less uncertainty for the long-term risk without further evaluation of container failure rates, dissolution rate for the waste matrix, and detailed modelling of the overall radioactive waste repository. A key issue, however, is the ability to provide experimental evidence whether or not a total healing of a salt plug can be reached, both for a "wet scenario" and in absence of brine.

Uncertainties on the future evolution may also be reduced by introducing additional barriers, e.g. a watertight bitumen layer in front of the plug that is stable long enough to provide dry conditions while the plug is compacted (few decades). Uncertainty could also be reduced by in-situ monitoring of e.g. pressure build-up in the disposal cell, stress/strain behaviour of the plug, or the presence (or absence) of brine. In the last decade, sufficient expertise has been built up in the nuclear sector to allow safe wireless data transmission of monitoring data over safety relevant barriers, e.g. disposal cell plugs, section dams or through several hundreds of meters of host rock (Schröder 2019). However, it needs to be considered that in an abandonment case, monitoring would be of limited value since correcting actions may not be applicable. Relevant uncertainties might also be addressed by full-scale experimental work, preferably in a suitable environment (Underground Research Laboratory). In this particular case, the Dutch policy of long interim storage may allow for experiments over a relevant period of time to provide further evidence on the closure of a plug under dry conditions, if necessary.

4 Conclusions and outlook

In the present paper, the current knowledge for building the Safety Case for salt-based repositories is shortly summarized. It was evaluated in more detail whether current understanding of the creep and compaction behaviour and the porosity-permeability relation is sufficiently well understood, and how remaining uncertainties can be addressed. The evaluation started from phenomenological models and its mathematical formulation, through the parameterization by experimental data and its implementation into a modelling code, to evaluation of uncertainty analyses of a (relevant) case scenario. It should be noted that the structural approach followed can be repeated when triggered by new insight on the topic, or when new experimental data (or other interpretations of current data) comes available. The evaluation is based on a case study, however, to provide better answers, more complete input by a Safety Case - as currently planned for 2024 - is needed. The Safety Case is a strong tool for pointing out remaining uncertainties and evaluating necessary future actions. It should be noted that remaining uncertainties can be addressed in several ways, with improved process models or parameterization only being one of the ways to reduce uncertainties.

References

GRUPA, J.B. & HOUKEMA, M. 2000. Terughaalbare opberging van radioactief afval in diepe zout- en kleilagen - Modellen voor een veiligheidsstudie. NRG Report 21082/00.33017/P.

HART, J., PRIJ, J., VIS, G-J., BECKER, D.-A., WOLF, J., NOSECK, U. & BUHMANN, D. 2015a. Collection and analysis of current knowledge on salt-based repositories, OPERA report OPERA-PU-NRG221A.

HART, J., PRIJ, J., SCHRÖDER, T.J., VIS, G-J., BECKER, D.-A., WOLF, J., NOSECK, U. & BUHMANN, D. 2015b. Evaluation of current knowledge for building the Safety Case for salt-based repositories, OPERA report OPERA-PU-NRG221B.

HEIJDRA, J.J. & PRIJ, J.. 1997. Concept ontwerp terughaalbare berging in steenzout: eindrapport 1996 METRO 1. ECN report ECN C 96 087.

IAEA, 2006. Fundamental Safety Principles, IAEA Safety Standards Series No. SF-1, IAEA, Vienna

IAEA, 2012. The Safety Case and Safety Assessment for the Disposal of Radioactive Waste, Specific Safety Guide No. SSG-23.

NEA, 2004. Post-closure Safety Case for Geological Repositories: Nature and Purpose. NEA Report No. 3679.

POLEY, A.D. 2007. Modelling of compaction and permeability of salt grit. NRG note 21952/07.82374.

PRIJ. J. 1991. On the design of a radioactive waste repository, PhD-thesis, University of Twente.

SCHLEDER, Z., BURLIGA, S. & URAI, J.L. 2004. Comparison of halite microstructures from different tectonic settings: implications for deformation mechanism, fluid flow and rheology. Presentation RWTH Aachen.

SCHRÖDER, T.J. 2008. PAMINA task 2.1.D – Update model parameters for sensitivity analysis. NRG Note 2.1952.21/08.88799, Petten.

SCHRÖDER, T.J., HART, J., COSTESCU-BADEA, A. & BOLADO LAVIN, R. 2009. Techniques for Sensitivity and Uncertainty Analysis - Analysis of a repository design in a rock salt formation, PAMINA Milestone Report M2.1D.7, NRG-21952/09.95945.

SCHRÖDER, T.J. (ED.). 2019. Wireless data transmission systems for repository monitoring. Modern2020 Deliverable D3.2.

SPIERS C.J., ET AL. 2005. Buffer/backfill in salt (long-term compaction, additives, precompacted bricks). NF-PRO Meeting.

STORCK, R., BUHMANN, D., HIRSEKORN, R.P., NIES, A. & RAUSCH, H. 1990. EMOS: Programmpaket zur Langzeitsicherheitsanalyse eines Endlagers für radioaktive Abfälle - Version 4. GSF-Bericht 90.

STORCK, R., ASCHENBACH J, HIRSEKORN R.P, NIES A, STELTE N, 1988. Performance Assessment of Geological Isolation Systems (PAGIS) - Disposal in salt formations EUR 11778 EN.

ZHANG, X. & GRUPA, J. 2006. NF-PRO deliverable 3.5.7 – Compaction behaviour and permeability of low porosity compacted salt grit (dry and wet). NRG Report 21146/06.77412/P.

Disposal of radioactive waste in rock salt: long-term research programme

Jeroen Bartol[1], Marja Vuorio[1],*

[1]COVRA, The Netherland;

* *Jeroen.bartol@covra.nl*

ABSTRACT: In 2021, COVRA launched a new long-term research programme on the deep geological disposal of radioactive waste. For disposal in rock salt, the following salt topics will be addressed: long-term evolution of the permeability-porosity of the backfill and excavation damage zone, past diapirism and subrosion rates in the Netherlands, availability of brine in (bedded) salt, setting up a database with properties of rock salt, mapping of the Röt Formation. Though the long-term research programme has just started, the first results have been obtained for the diapirism and subrosion rates in the Netherlands. These results showed that the external uplift and subrosion rate of the Anloo, Hooghalen, Schoonloo, and Gasselte-Drouwen diapir varied since the Late Cretaceous between 0.0034-0.021 mm/year and 0-0.08 mm/year respectively.

1   Introduction

Radioactive substances and ionizing radiation are widely used in medicine, industry, agriculture, research, education, and electricity production. These activities generate radioactive waste. The current policy in the Netherlands is that radioactive waste is collected, treated, and stored for at least 100 years above ground at the Central Organisation For Radioactive Waste (COVRA Fig. 1). Long-term storage has multiple advantages. Heat producing high-level waste will, for example, cool to a temperature at which it will be easier to handle. Additionally, there will be more time to do research into the best management options and learn from experience abroad (Ministry of infrastructure and the Environment 2016). However, storage is only temporary and all radioactive waste in the Netherlands is intended for (permanent) deep geological disposal in 2130 in either rock salt or poorly indurated clay (Ministry of infrastructure and the Environment 2016).

Figure 1: High level radioactive waste is currently stored in the HABOG building

While disposal of radioactive waste is still 100 years away, COVRA recently started a continuous long-term research programme on the geological disposal of radioactive waste (Verhoef et al. 2021). This programme will run for at least 30 years and its agenda will be updated every five years. The outputs of the research programme will be used as input for a cost estimate of a deep geological repository and a safety assessment. The latter is a quantitative assessment of the post-closure safety of a disposal facility. Together, they form the foundation of the safety case: an integration of arguments and evidence that quantify and substantiate the safety, and the level of confidence in the safety, of the geological disposal facility (IAEA 2012). Here, we will present the content and the first results of the long-term research programme focusing on rock salt. More specifically, we will discuss the results from Lauwerier (2021) on the uplift and subrosion rate of Anloo, Hooghalen, Schoonloo, Gasselte-Drouwen and the status of the safety assessment.

2   Past and present research programmes

The current long-term research programme is not the first research programme on the disposal of radioactive waste in rock salt in the Netherlands. The first research programme, ICK, started in 1972 and ran until 1979 (Fig. 2). This programme was followed by the OPLA (1984-1993; e.g. Commissie Opberging te Land 1989) and the CORA research programme (1996-2001; e.g. Grupa & Houkema 2000; Poley 1999). Between these research programmes, a gap of respectively five (ICK – OPLA) and three (OPLA – CORA) years exist during which research activities on disposal were very limited. Consequently, the research infrastructure weakened in these (inter-research) periods while earlier collected knowledge had to be recovered at the start of a new research programme. Therefore, COVRA decided to set up a continuous long-term research programme that will run for at least 30 years (Verhoef et al. 2021). This approach guarantees the continuity of the programme which will help to strengthen nuclear knowledge infrastructure, specifically on disposal, in the Netherlands.
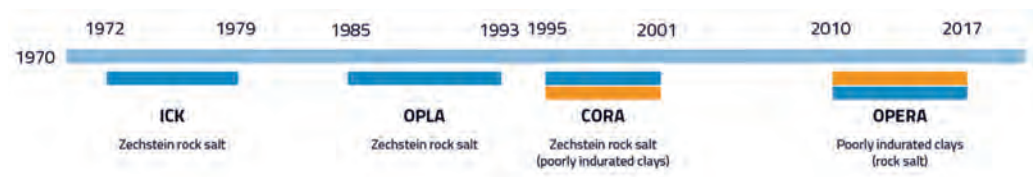
Figure 2. Overview of previous research programmes from Verhoef et al. (2021).

This long-term research programme started in 2021 and will last until at least 2050. For disposal in rock salt, the long-term research programme will first focus on the host rock and the engineered barrier (e.g. waste packages, Verhoef et al. 2021). Prioritisation of the tasks within this research programme is based on three drivers. These are the (1) confidence in long-term safety, (2) disposability, and (3) the cost of disposal. Not all tasks can be prioritized by drivers and some are selected because they provide a unique opportunities to collaborate or support strategic policy needs. The emphasis of these drivers may change over time when certain knowledge or information is obtained or policies change. The prioritization is revaluated during different stages of the long-term research programme.

The results of the long-term research programme will be used for the safety assessment and a cost estimate. Based on the current disposal concept (Bartol et al. In progress) and the prioritization of the research, six salt-specific tasks (Verhoef et al. 2021) will be completed during the first stage of the long-term research programme. These salt specific tasks are:

- long-term evolution of the permeability-porosity of the backfill and excavation damage zone
- past-present diapirism and subrosion rates in the Netherlands,

- safety assessment,
- availability of brine in (bedded) rock salt,
- setting up a database with properties of rock salt and
- mapping of the Röt Formation.

As the long-term research programme started in 2021, most tasks have not started yet, or are at early stages and therefore do not have results available yet. An exception is a task on the past-present diapirism and subrosion rates in the Netherlands. Here, we will discuss the result of this task and the upcoming safety assessment.

3   Diapirism and subrosion

Different processes like subrosion and diapirism can affect a repository in rock salt. Subrosion is the dissolution of salt due to groundwater flow around and over a salt dome. Diapirism also referred to as external uplift, on the other hand, is the upward movement of salt (e.g. Hudec & Jackson 2007) in reference to the mother (bedded) salt layer. Both subrosion and diapirism could result in the release of radionuclides into the biosphere. Subrosion, for example, reduces the natural rock salt barrier which could eventually result in the destruction of the repository and consequently the release of its content into the biosphere. Diapirism, on the other hand, could potentially bring a repository to the surface where it could release its content. As the radioactivity of waste will decay over time, both subrosion and diapirism do not necessarily pose a problem as long as the radioactivity of the waste is low enough when released into the biosphere (e.g. Prij et al. 1993; Verhoef et al. 2017). It's therefore important to determine the diapirism and subrosion rates of salt domes in the Netherlands. As part of our research programme, the subrosion and diapirism rate were determined by Lauwerier (2021) for four diapirs in the Lower Saxony basin (Fig. 3; Anloo, Hooghalen, Schoonloo, Gasselte-Drouwen) and three different periods (Late Cretaceous, Paleocene-Oligocene, Eocene-Recent) based on the quantitate analysis of peripheral sinks (Zirngast 1996). Peripheral sinks, also referred to as salt withdraw basins, are sedimentary sinks close to a salt dome that result from the movement of salt towards the salt dome. Hence, the volume of these peripheral sinks equals the volume of salt that moved from the source to the salt dome (V_{In}). Together with estimates on the current and past volumes of salt domes ($V_{Salt\ dome}$), the subrosion rate is determined by subtracting the volume of salt that moved to the salt dome (V_{In}) from the estimated total volume of a salt dome at a specific time ($V_{Salt\ dome}$) divided by the time interval. The diapirism rate is calculated by dividing the volume of salt that moved to the salt dome (V_{In}) by the estimated width of a salt dome during a specific time interval. #

A different trend is observed for the subrosion rates of the Anloo, Hooghalen, Schoonloo and Gasselte Drouwen diapir (Fig. 4). For the Anloo, Hooghalen, and Schoonloo diapir, the subrosion rate increases from around 0 mm/year in the Late Cretaceous to 0.02 mm/year in the Palaeocene-Oligocene (Schoonloo) or Eocene-Recent (Anloo, Hooghalen). In contrast, the difference in the subrosion rates between the Paleocene- Oligocene and Eocene-Recent is significant (≈ 0.02 mm/year) for these three diapirs. In contrast, the Gasselte-Drouwen diapir shows again a different trend: the highest subrosion rates were found to be during the Late Cretaceous and the lowest during the Eocene-Recent period. In addition, the subrosion rate of this diapir was significantly higher (up to four times) than that of the three other diapirs.

Overall, the strongest salt movement in this area occurred during the Late Cretaceous while it was limited during the Paleocene-Recent period. The Late Cretaceous movement of salt could be related to the Late Cretaceous-Late Eocene (partial) inversion of the Lower Saxony basin during the Sub-Hercynian inversion phase (Remmelts et al. 1993). If true, this suggests a correlation between the salt movement and the intraplate stresses and differential loading (e.g. Hudec and Jackson. 2007; Rijks Geologische Dienst 1988). The subrosion rates, in contrast, appear to be the highest from the Eocene onwards. This is possibly related to the uplift of the salt dome. Hence, the higher the salt dome, the higher the subrosion due to the exposed

surface. However, other processes also play a role like, for example, groundwater flow patterns, stratigraphy and the saturation of the ground water flow with respect to salt (e.g. Glasbergen 1989).
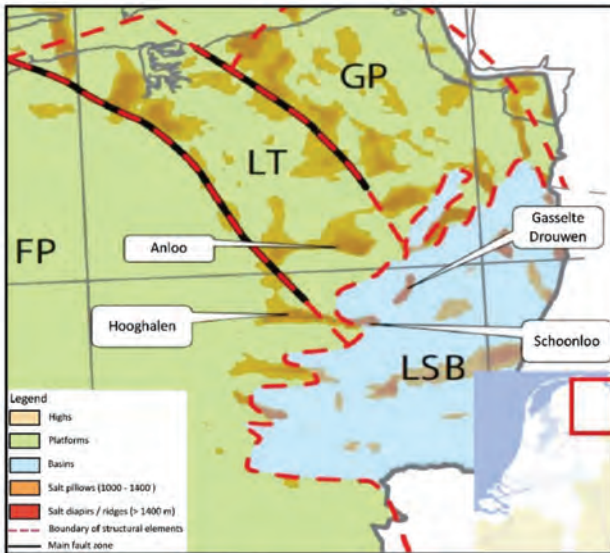
Figure 3: Location of the salt domes. FP: Friesland platform; LT: Lauwerszee Through; GP: Groningen Platform; LSB: Lower Saxony Basin; DH: Figure is from Ten Veen et al. (2012); Lauwerier (2021).
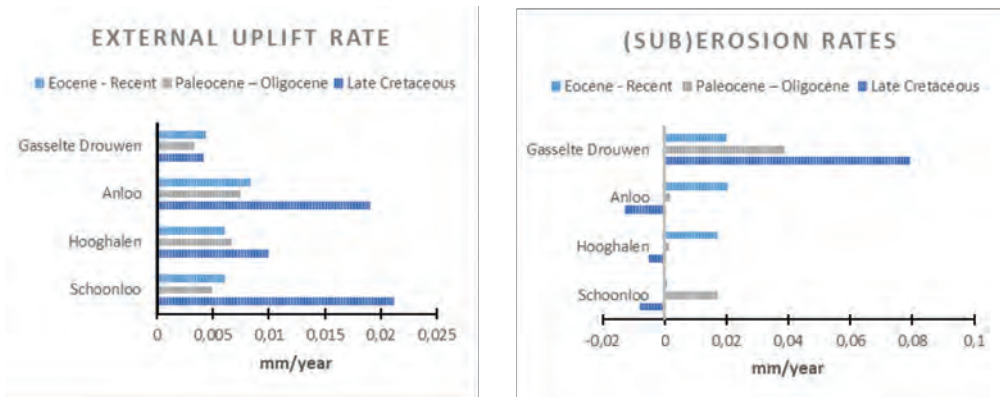
Figure 4: For the Anloo, Hooghalen, Schoonloo, Gasselte Drouwen diapir, the external uplift rate is shown on the left and the subrosion on the right. Note Gasselte Drouwen salt dome has a different trend compared to the other salt domes. Also note the negative subrosion rates for the Anloo, Hooghalen and Schoonloo diapir. This negative erosion rate is possibly a result of the method used and suggest that the subrosion rate was close to or even zero. Figure from Lauwerier (2021).

4   Safety assessment

The results of the long-term research programme, including the subrosion and external uplift rate, will be used in a safety assessment.

A safety assessment is normally done for the expected evolution of the repository and an altered scenario(s) (e.g. Verhoef et al. 2017). An altered scenario can, for example, be a container that fails much earlier than anticipated. For a repository in salt, it has been shown that there are no radiological consequences within a million years after the closure of the repository when a repository evolves as expected (e.g. Bollingerfehr et al. 2018). Therefore, the focus of the safety assessment in the next rock salt safety case expected in 2025 will be on an altered scenario. In this safety assessment, it will be assumed that the seals in the shafts connecting the repository will surface will fail after 1000 years (Stein et al. 2021). Consequently, groundwater will enter the repository but will eventually be squeezed out due to salt creep. For this model, the results of long-term evolution of the permeability-porosity of the backfill and excavation damage zone and the database with properties of rock salt will be used as input for the safety assessment. The observations of the past subrosion and external uplift rates will also be used in the current safety assessment to gain a first-order idea about the impact of these processes. However, models that simulate subrosion and external uplift are expected to be incorporated at a later stage as these have yet to be developed and validated against observations.

This safety assessment will not only be done for a generic Dutch repository, but also a generic one with different types of waste from different countries (Stein et al. 2021). This is done as part of international research and model comparison collaboration: DECOVALEX. Participation in DECOVALEX helps to compare different models, approaches, and outcomes. The first results are expected in 2022 and the results in 2023.

5   Conclusions

While disposal is still over 100 years away, COVRA started a new long - term research programme in 2021. For disposal in rock salt, research will initially focus on the host rock and engineered barrier (e.g. container) and its results are used as input for a cost estimate, and a safety assessment: a quantitative assessment of the post-closure safety of a repository in rock salt. Together, they are the basis for a rock salt safety case. While the long-term research programme has just started, its first result on the uplift and subrosion rate of the Hooghalen, Schoonloo, Gasselte Drouwen diapir varied since the Late Cretaceous between 0.0034 - 0.021 mm/year and 0 - 0.08 mm/year respectively.

References

Bartol, J., Vuorio, M., Neeft, E. & Verhoef, E., In progress. Outline of a disposal concept in domal salt.

Bollingerfehr, W., Bertrams, N., Buhmann, D., Eickemeier, R., Fahland, S., Filbert, W., Hammer, J., Kindlein, J., Knauth, M. & Wenting, L. 2018. Concept developments for a generic repository for heat-generating waste in bedded salt formations in Germany. Synthesis Report (BGE TEC 2018-13). BGE TECHNOLOGY GmbH.

Commisie Opberging te land 1989. [OPLA] Onderzoek naar geologische opberging van radioacief afval in Nederland; Eindrapport fase 1, Den Haag.

Glasbergen, P. 1989. Veiligheid evaluatie van opbergconcepten in steenzout; subrosieberekeingen (eindrapportage deelrapport 7)

Grupa, J.B. & Houkema, M. 2000. [CORA] Terughaalbare opberging van radioactief afval in diepe zout en kleiformaties. Modellen voor een veiligheidsstudie., 196.

Hudec, M.R. & Jackson, M.P.A. 2007. Terra infirma: Understanding salt tectonics, Earth-Science Reviews, pp. 1-28.

IAEA 2012. The safety case and safety assessment for the disposal of radioactive waste (No. SSG-23).

Lauwerier, W. 2021. The evolution of the Zechstein salt diapirs in the north-eastern Netherlands, https://www.covra.nl/en/downloads/eindberging-20202025/.

Ministry of Infrastructure and the Environment 2016. The national programme for the management of radioactive waste and spent fuel, p. 61.

Poley, A.D. 1999. Concept ontwerp terughaalbare opslag van radioactief afval in diepe boorgaten in steenzout (Torad-B). pp. 1-54.

Prij, J., Blok, B.M., Laheij, G.M.H., Van Rheenen, W., Slagter, W., Uffink, G.J.M., Uijt De Haag, P., Wildenborg, A.F.B. & Zanstra, D.A. 1993. [OPLA 1A] PROSA PRObabilistic Safety Assessment final report.

Remmelts, G., Muyzert, E., Van Rees, D.J., Geluk, M.C., De Ruyter, C.C. & Wildenborg, A.F.B. 1993. [OPLA phase 1a] Evaluation of salt bodies and their overburden in the Netherlands for the disposal of radioactive waste: b. salt movement.

Rijks Geologische Dienst 1988. Geologische inventarisatie en ontstaansgeschiedenis van zoutvoorkomens in Noord- en Oost-Nederland. Rijks Geologische Dienst.

Stein, E.R., Jayne, R., LaForce, T. & Leone, R. 2021. DECOVALEX-2023 Task F Specification Revision 7: Spent Fuel and Waste Disposition.

Ten Veen , J. H., Van Gessel, S. F., & Den Dulk, M. (2012). Thin-and thick-skinned salt tectonics in the Netherlands; a quantitative approach. Netherlands Journal of Geosciences, 91(4), 447-464.

Verhoef, E., Neeft, E., Bartol, J., Vuorio, M., Scholten, C., Buitenhuis, A., Veen, G.V.D., Chapman, N. & McCombie, C. 2021. COVRA's Long-term research programme for geological disposal of radioactive waste., p. 89.

Verhoef, E.V., Neeft, E.A.C., Chapman, N. & McCombie, C. 2017. Opera safety case.

Zirngast, M. 1996. The development of the Gorleben salt dome (northwest Germany) based on quantitative analysis of peripheral sinks. Geological Society, London, Special Publications 23.

Influence of selected model parameters for integrity analysis of disposal of heat-generating waste in bedded salt

Wenting Liu[1], Ralf Eickemeier[1], Jan Thiedau[1]*

[1]Federal Institute for Geosciences and Natural Resources (BGR), Germany

*Wenting.Liu@bgr.de

ABSTRACT: To analyze the long-term barrier integrity of bedded salt formations, numerical models of a generic repository for heat-generating nuclear waste were developed (Liu et al. 2019). This study focuses on comparing the influences of selected model properties and material parameters. Under consideration of the thermal loading caused by disposal of heat generating nuclear waste, three sets of numerical investigations have been carried out, including variation of mesh density, model dimension and material stiffness of selected geological layers. Thermal (T) and thermomechanical coupled (TM) modeling has been conducted by using the finite element method. The results are discussed in this paper.

1   Introduction

With the restart of site selection for a repository for heat-generating radioactive waste in Germany (StandAG 2013 & 2017), all potential host rocks are being evaluated for suitability as a nuclear-waste repository. BGR makes further investigations on flat-bedded rock salt formations in Germany, to improve their understanding and reevaluate the data contained in previous studies. On behalf of the former Federal Ministry for Economic Affairs and Energy (BMWi), investigations of bedded salt have been launched in the framework of the R&D project BASAL ("Distribution and properties of flat-bedded rock salt horizons in Germany"). These investigations focus on the enhancement of the database containing the data on the distribution, characterization and repository-relevant properties of bedded salt. As part of the project, numerical calculations were carried out to investigate the influence of selected model parameters for integrity analysis of disposal of heat-generating waste in bedded salt.

This paper describes three investigations, including one thermal (T) and two thermomechanical coupled (TM) simulations. All of them were conducted using the FEM code JIFE (Faust et al. 2016). The thermal calculation is carried out to investigate the influence of mesh density on temperatures in near and far field of disposal area. One of the TM coupled simulations analyzes the effects of model dimensions on the temperature and thermally induced displacements. By varying the Young's modulus of two geological, we investigate the impact of the stiffness of these layers on the evaluation of the barrier integrity based on the fluid pressure criterion.

2   Numerical simulation of disposal of heat-generating waste in bedded salt

To establish a practicable generic model for the flat-bedded salt, twelve homogeneous layers were taken into considernation. These homogeneous layers haven been developed and described by Völkner et al. (2017). The overburden is composed of three homogeneous zones: Quaternary (Q), Tertiary (T) and Bunter (S). Seven homogeneous zones form the geological host rocks: Aller rock salt (NA4), the so-called Anhydritmittelsalz (AM3), Ronnenberg potash seam (K3), Leine rock salt (NA3), main anhydrite (A3), Staßfurt potash seam (K2) and Staßfurt rock salt (NA2). Two homogeneous zones of anhydrite/carbonate (A2/C2) and Underlying Red (R) form the Basement. For simplification reasons, the thickness in each homogeneous layer is assumed to be constant. The overburden, the basement and the main anhydrite layer were assumed to be elastic. The rock salt was considered ductile with steady-state creep and

dilatant behavior, which are the most relevant deformation processes over the long-term in the far-field of the salt barrier.

For all the modeling in this study, an initial temperature at rock surface is according to the average annual temperature in the Northern Germany 8.5°C. A temperature gradient of the rocks is 3°C per 100 m of depth increase. The pressure gradient was defined as 0.022 MN/m3 for all homogenous zones. The following mechanical boundary conditions were specified: no x-displacement (horizontal) on the left and right boundaries of the model; no y-displacement (vertical) on the bottom of the model; no z-displacement on the entire model. For thermal boundary conditions: under consideration of the thermal loading of high-level waste (HLW) in the case of drift disposal (Bertrams et al. 2017), time-dependent heating power was assigned to certain points in the homogeneous zone NA2 at a repository depth of 700 m below sea level. Disposal drifts were not taken into account in the models.

3 Variation of mesh density

3.1 Model setup

To investigate the influence of mesh density on temperature in both the near and far field of disposal area, five 2D models with different meshes of the same geometry were developed and thermal simulations of heat transport are carried out with these models. Figure 1 depicts the numerical 2D models with sections through the near field of disposal area and location marks of the disposal drifts (yellow points).
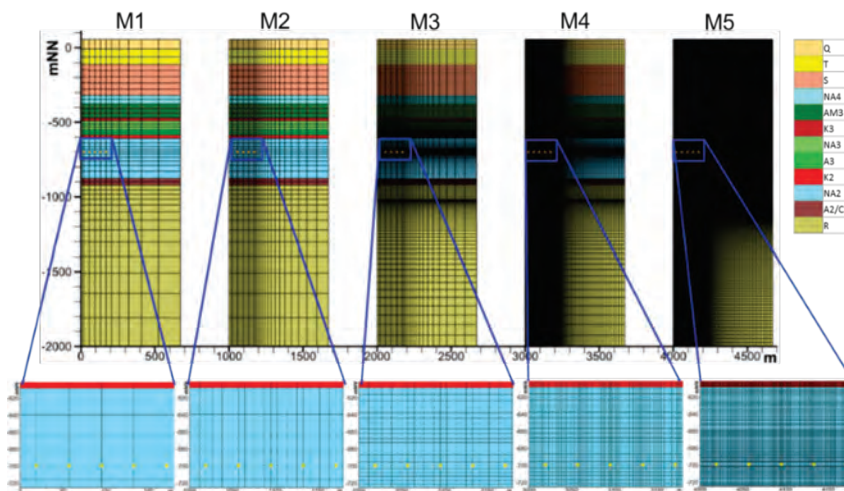
Figure 1: Numerical 2D models with different mesh densities

Due to the symmetry existing at the emplacement center, only half of the model width of 670 m and depth of 2060 m had to be created. By varying the mesh density, from very coarse, to coarse, medium, fine and very fine, different numbers of linear quadrilateral elements with four nodes were generated. The first model (M1) with a very coarse mesh has only 500 elements, the second (M2) has 1500, the third (M3) and the fourth (M4) have 6300 and 25000, respectively. The last model (M5) with a very fine mesh has 98000 quad elements.

3.2 Comparison of modeling results

Due to the thermal loading of High Level Waste (HLW), temperature of the rock mass increases quickly in all model variants, especially in and around the disposal area. Figure 2 shows the temperature development of all model variants in the center of the disposal area (Point A) and in some selected points, located directly above and below the center (Points D, E and G). The curves with same color but different line styles indicate the values of same observation locations in the different models. The time history of temperatures for the points above and below the center of the disposal area are practically identical. Only at point A in the first model (M1) the temperature maximum is a bit lower than the maxima of the other variants. In the first model, a maximum temperature of 118°C is reached after 190 years in the center of the disposal area (point A), whereas in the other variants a maximum of 120°C develops already after 180 years. The reason for this difference is probably due to the lack of grid points in the vicinity of the simulated heat sources (model M1): Between Points A and B (locations of the heat sources), there is only one finite element created.
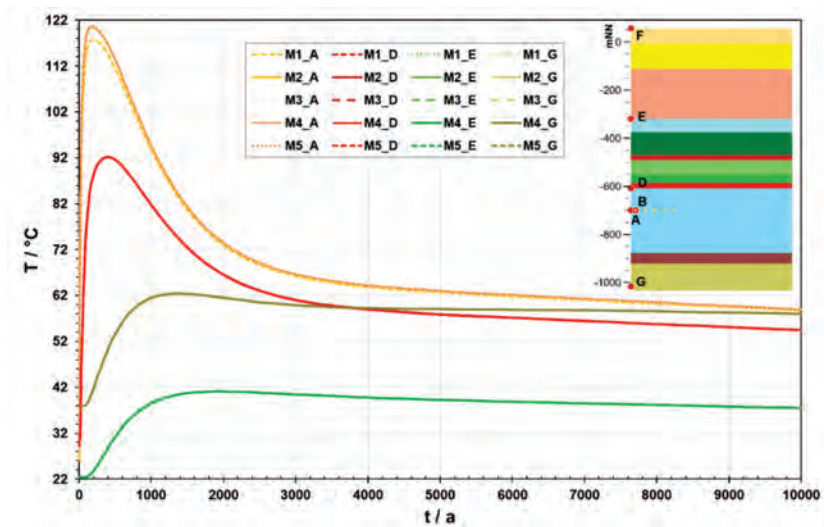
Figure 2: Comparison of calculated temperatures at selected points of all variants

Figure 3 depicts the calculated temperature of rock salt at the level of the repository depth after 180 years. With increasing mesh density from M1 to M5, the temperatures at the points of heat sources increase by 4.5°C in each case. In the models with finer mesh discretization, higher temperatures can also be observed in the vicinity of the points of the heat sources. However, in the far field, the curves of temperature are very similar. At a distance of 10 m from the outermost point of the heat sources, the temperature difference in M4 and M5 is less than 0.05°C. At a distance of 30 m, the difference is less than 0.01°C. Similar results have been indicated in M2 and M3. The temperature difference is less than 0.05°C at a distance of 40 m from the outermost point of the heat sources and less than 0.01°C at a distance of 140 m.
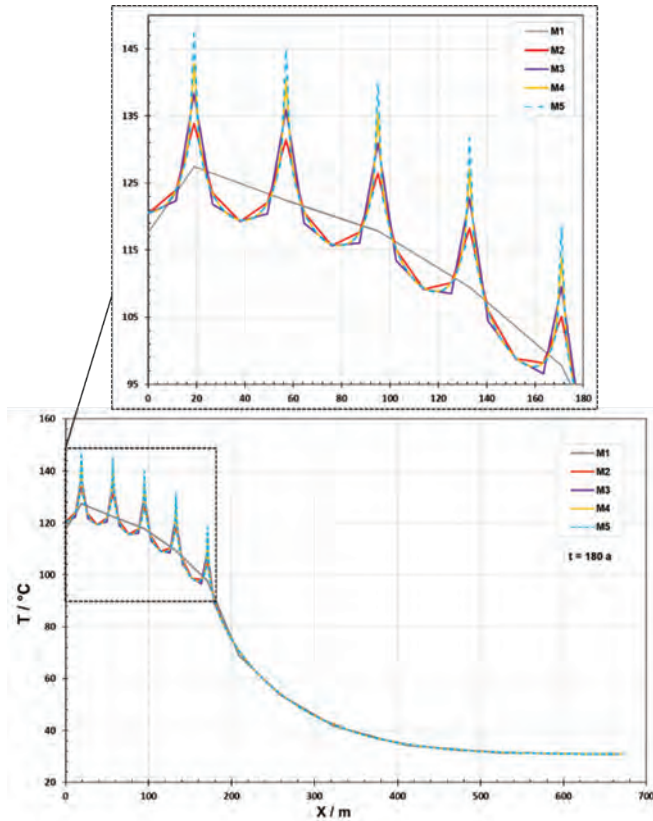
Figure 3: Comparison of calculated temperatures at the level of the repository depth after 180 years

3.3 Discussion

The results of the thermal calculations show temperature differences mainly at the simulated heat sources and in their vicinity. By varying the mesh densities of the 2D models, the calculated temperatures are different mainly in the very near field of disposal area. With increasing mesh density, the temperatures at the points of heat sources increase by 4.5°C in each case. Higher temperatures in the models with finer discretization can also be observed in the vicinity of the heat sources. However, in the far field, the values are almost the same, although there are large differences of mesh densities between the five variants. The curves of temperature are practically identical in the far field, for instance at the top of the salt barrier (Figure 2, point E). The comparison between different model variants indicates that, at a distance of 10-40 m from the outermost point of the heat sources, the temperature difference is less than 0.05°C. At a distance of 30-140 m, the difference is less than 0.01°C.

4 Variation of model dimensions

4.1 Model setup

To study the influence of model dimension on temperature and displacement results in both the near and far field of waste disposal area, three variants of 2D models were selected and thermomechanical coupled modeling has been carried out. The first variant (V1) is a basic

model, which has a width of 2.5 km and a depth of 2.5 km. By varying the model dimension, the second model (V2) is smaller and the third variant (V3) is a larger model. Table 1 gives an overview of the model dimensions. However, variation of the model dimensions only changes the distance from disposal area to the bottom and outer edge of the model. The depth of the simulated disposal areas and the thickness of the overburden and rock salt layers remains constant in all variants. Beside the point, all the models have a same fine mesh discretization. For instance, the basic model has 158500 quad elements.

Table 1: Width and depth of different model variants

2D Models	Model dimension / km	
	width	depth
Variant 1 (V1, Basic model)	2.5	2.5
Variant 2 (V2)	1.5	1
Variant 3 (V3)	4	4

4.2   Comparison of modeling results

Figure 4 shows the temperature development of all model variants at the center of the disposal area (Point A) and at the top of the salt barrier (Point E). The curves with same line style but different colors demonstrate the values at the same observation locations in the different models.
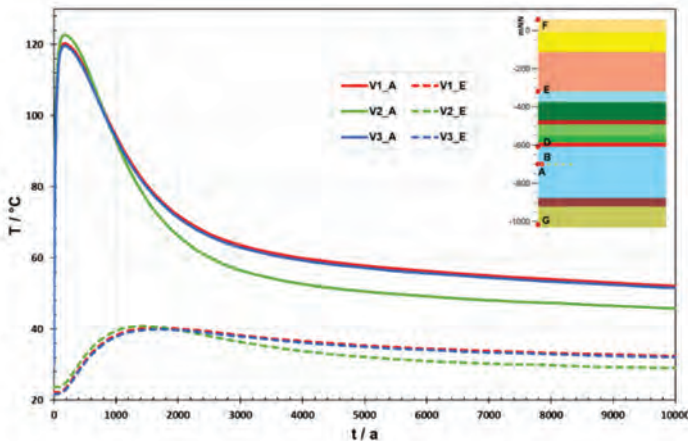
Figure 4: Comparison of calculated temperatures of all variants at the center of the disposal area and at the top of the salt barrier

At both locations, the green curves of temperature in the second model (V2) behave differently than the other two curves (red V1 and blue V3). At point A, the center of disposal area in models V1 and V3 reaches a maximum temperature of 120°C after 180 years, in the smaller variant V2 it reaches a maximum of 123°C at the same time. At the top of the salt barrier (Point E), a maximum temperature of 40°C is reached after 1600 years in models V1 and V3 and already after 1460 years in model V2. However, at both points after reaching the max. values, the temperature drops more quickly in V2 than in the other two variants, so that at the end of the observation period of 10000 years, the temperatures at both locations in model V2 stay lower than in the others.

Due to the temperature increase, thermally induced deformation leads to an uplift of the rocks above the repository. Figure 5 compares calculated vertical displacements at the top of the salt barrier (Point E) and at ground surface (Point F) above the center of emplacement area. The curves of the basic model V1 and the larger variant V3 behave at both locations in a very similar way. The green curves of the smaller model V2 behave in the same way at the beginning, but reach their peak earlier and decrease more quickly until the end of the observation period of 10000 years. In the case of V1 and V3, a maximum vertical displacement of 1.7 m is observed at the top of salt barrier (Point E) after 1000 years. In model V2 it reaches the peak value of 1.6 m already after 750 years. At the ground surface (Point F), the maximum uplift in models V1 and V3 is 1.6 m after 1100 years, in model V2 is 1.5 m after 830 years.
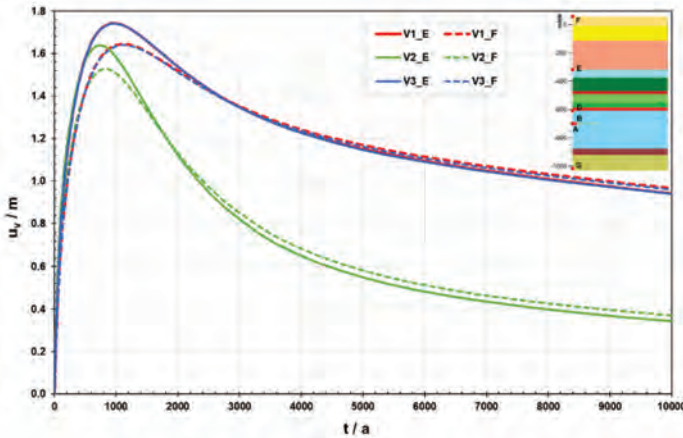
Figure 5: Vertical displacement at the top of the salt and at the surface

4.3 Discussion

The reason for the difference of vertical displacement between models V2 and V1/V3 is due to the limitation of the model dimensions. Regarding to the boundary condition of the 2D models (see chap. 2), the displacements perpendicular to the model bottom and the model outer edges are fixed. Therefore, the uplifts in V2 are limited due to its small dimension and therefore reach their maximum values 250 - 280 years earlier and after that, they drop faster. At the end of the observation period, the difference in vertical displacement between models V2 and V1/V3 remains at about 0.6 m.

Overall, according to the results of the basic model V1 und the lager model V3, both the temperature and vertical displacement, show good agreement in these models. This confirms that the chosen dimension for the basic model is sufficient for this kind of numerical calculations and that the larger models do not produce significantly different results. At the same time, the different thermal and mechanical behaviors of the V2 model indicate that this smaller variant V2 is unsuitable and should be increased in size to avoid the influence of small model dimensions.

5 Variation of material stiffness

The thermal expansion caused by the heat-generating waste induces an uplift above the repository. The uplift of the rocks leads to a reduction of horizontal stresses, especially in the Bunter overburden, at the top of the salt barrier. The barrier integrity of bedded salt is assessed by using the fluid pressure criterion. When the minimum principal stress in the salt barrier drops below the hydrostatic pressure, the fluid pressure criterion is violated.

5.1 Model setup

To investigate the impact of material stiffness on the evaluation of the barrier integrity based on fluid pressure criterion (BMU 2010; Heusermann et al. 2017), variations of Young's modulus of two geological homogeneous layers have been conducted. The Bunter layer was selected because it is much thicker than the other layers in the overburden. The main anhydrite was selected because it is the only layer assumed to be elastic in the host rocks (see chap. 2). In basic model (V1), the Young's modulus of Bunter (S) layer is 15 GPa and the Young's modulus of main anhydrite (A3) is 60 GPa (Kock et al. 2012). In the second variant (V2), the Young's modulus of S is reduced to 1.5 GPa, the Young's modulus of A3 remains constant. In the third variant (V3), the Young's modulus of S is the same as in the basic model V1 whereas the value of A3 is reduced to 0.6 GPa.

5.2 Results

5.2.1 Comparison of modeling results

Figure 6 compares the minimum principal stress after 74 years between the basic model (V1) and the second and third model variants (V2 & V3). Compressive stresses are negative and tensile stresses are positive.
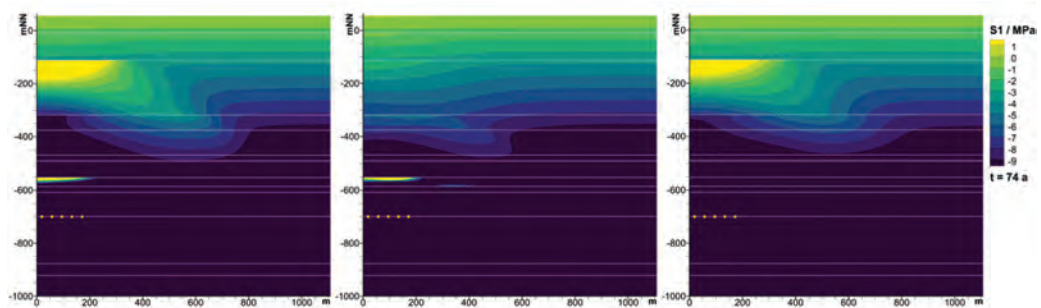
Figure 6: Minimum principal stresses in models V1 (left), V2 (middle) and V3 (right)

In model V1, a reduction of the minimum principal stresses can be observed in the bunter overburden and the main anhydrite directly above the disposal area. At the top of the salt barrier the minimum principal stresses is also reduced, but the location is not directly above, but at least 125 m away from the center area. In the case of V2, the minimum principal stresses are reduced at the top of the salt barrier and in the main anhydrite layer. The decrease of the minimum principal stresses in Bunter overburden itself becomes less noticeable than in the basic model V1. In the case of V3, due to the reduction of the stiffness of A3, a significant reduction of the minimum principal stress does not occur in this layer. However, the change of the Young's modulus of A3 does not have a noticeable effect on the stresses at the top of salt barrier.

The fluid pressure criterion is violated in the zones of the salt barrier, where the minimum principal stress drops below the hydrostatic pressure. Figure 7 shows violated zones (yellow) and less affected areas due to the reduction of the minimum principal stress (light blue), which are located at the top of the salt barrier after 74 years. The violated zone develops only in the basic model. In case of V2, the affected area is located directly above the center area, but in the V1 and V3, these areas are both 200 m away from the center.
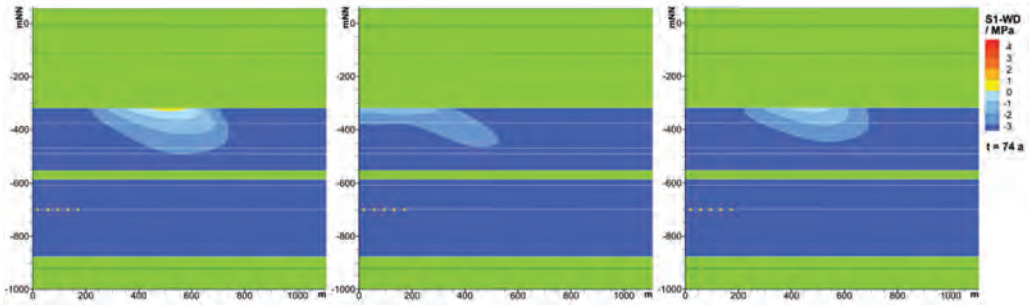
Figure 7: Violation of fluid pressure criterion in models V1 (left), V2 (middle) and V3 (right)

5.2.2 Comparison with FLAC3D

Besides the modeling carried out with the FEM code JIFE, a simulation with the same input data and model setup of the basic variant (V1) is conducted with the FDM code FLAC3D, which enables a comparison of the calculation results between different numerical modeling software. Figure 8 compares the calculated minimum principal stress after 74 years between JIFE and FLAC3D.
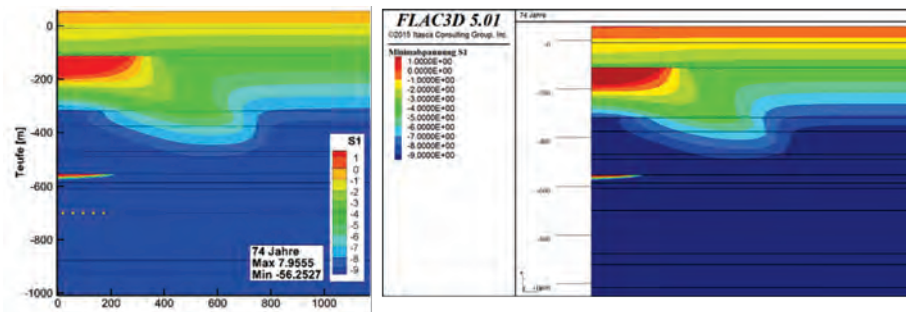
Figure 8: Minimum principal stress in models V1 with JIFE (left) and with FLAC3D (right)

The results of the simulation in FLAC3D show also a reduction of the minimum principal stresses in the Bunter overburden and the main anhydrite directly above the disposal area. At the top of the salt barrier, the reduction is located not directly above the center area, which agrees well with the areas calculated with JIFE.

5.3 Discussion

The calculation results indicate that the variation of the Young's modulus of Bunter overburden has a great impact on the stress field in the layer itself and at the top of salt barrier. Therefore, violation of the fluid pressure criterion is located in different areas, in case of high or low stiffness of Bunter layer. When the stiffness of S is reduced, the fluid pressure criterion is violated directly above the center of disposal area. Variation of the Young's modulus of main anhydrite has no significant influence on the assessment of barrier integrity of the bedded salt.

6 Conclusions

In the framework of the R&D project BASAL, three sets of exemplary calculations have been carried out focusing on investigations of the influence of selected model properties and

material parameters. Thermal (T) and thermomechanical coupled (TM) simulations have been performed.

The first set of the simulations investigates the influence of mesh density on temperature in both near and far field of disposal area. The results show temperature differences mainly at and in the vicinity of the simulated heat sources. In the far field, the temperatures are very similar. The model M1 with a very coarse mesh is not acceptable due to the lack of elements between the heat sources. For further investigation in both near and far field of the disposal area, the fine mesh of M3/M4 is recommended.

By varying the model dimension, the comparison between the basic model and the larger model shows a good agreement of temperature and vertical displacement results. The results of the smaller model show significant differences to the other models. The uplifts in the smaller variant are limited and reach their Maximums 250 - 280 years earlier. The value drops faster. At the end, the difference of vertical displacement between V2 and V1/V3 is still 0.6 m. Therefore, the dimension of the smaller model is not suitable for the modeling to analyze the long-term barrier integrity of bedded salt.

The last simulations investigate the impact of the stiffness of selected geological layers on the evaluation of the barrier integrity. The calculation results indicate that; the material stiffness of competent geological layers has a significant influence on the analysis of barrier integrity of the bedded salt. The variation of the Young's modulus of Bunter has a great impact on the stress field in the layer itself and at the top of salt barrier. Regarding the fluid pressure criterion, the shape and the location of violated areas are changed. However, the variation of the Young's modulus of the main anhydrite has no significant. For further investigations, a well-founded knowledge of elastic parameters is critical for integrity analysis.

Generally, the numerical investigations within the BASAL project contribute to creating well-established FEM models for the evaluation of the long-term integrity of the bedded salt barrier.

Acknowledgements

References

Bertrams, N.J., Bollingerfehr, W., Filbert, W., Prignitz, S. & E.K. Simo, 2017. Technische Konzepte für ein Endlager in flach lagernden Salzformationen – Ergebnisse aus dem Vorhaben KOSINA. DBE TECHNOLOGY GmbH, TEC-12-2017-AP; Peine.

BMU 2010. Sicherheitsanforderungen an die Endlagerung wärmeentwickelnder radioaktiver Abfälle. - Bundesministerium für Umwelt, Naturschutz und Reaktorsicherheit. Stand 30. September 2010.

Bollingerfehr, W., Bertrams, N., Buhmann, D., Eickemeier, R., Fahland, S., Filbert, W., Hammer, J., Kindlein, J., Knauth, M., Liu, W., Minkley, W., Mönig, J., Popp, T., Prignitz, S., Reinhold, K., Simo, E., Thiemeyer, T., Völkner, E. & Wolf, J. 2018. KOSINA - Concept developments for a generic repository for heat-generating waste in bedded salt formations in Germany. BGE TECHNOLOGY GmbH, BGE TEC 2018-13; Peine.

Faust, B., Krüger, R., Lucke, A. & Tertel, S. 2016. JifeMP Java application for Interactive Nonlinear Finite-Element analysis in MultiPhysics. Benutzerhandbuch für JIFE 5.1.1; Berlin.

Heusermann, S., Fahland, S. & Eickemeier, R. 2017. Geomechanical stability and integrity of nuclear waste disposal mines in salt structures. In: Rock Mechanics and Engineering (Ed.:

X.-T. Feng). Vol. 3: Analysis, Modelling and Design. p. 513–547; CRC Press, Taylor & Francis Group.

KOCK, I., EICKEMEIER, R., FRIELING, G., HEUSERMANN, S., KNAUTH, M., MINKLEY, W., NAVARRO, M., NIPP, H.-K & VOGEL, P. 2012. Vorläufige Sicherheitsanalyse Gorleben - Integritätsanalyse der geologischen Barriere. Abschlussbericht zum Arbeitspaket 9.1, GRS-286, Gesellschaft für Anlagen- und Reaktorsicherheit (GRS) mbH, Köln, 2012.

LIU, W., EICKEMEIER, R. & FAHLAND, S. 2019. Thermomechanical analysis of the long-term barrier integrity in bedded salt formation. 53rd US Rock Mechanics / Geomechanics Symposium, Jul 2019, New York City. (American Rock Mechanics Association).

STANDAG 2013. Gesetz zur Suche und Auswahl eines Standortes für ein Endlager für Wärme entwickelnde radioaktive Abfälle und zur Änderung anderer Gesetze (Standortauswahlgesetz StandAG). Deatscher Bundestag.

STANDAG 2017. Gesetz zur Suche und Auswahl eines Standortes für ein Endlager für hochradioaktive Abfälle (Standortauswahlgesetz - StandAG). Deatscher Bundestag.

VÖLKNER, E., KÜHNLENZ, T., HAMMER, J. & GAST, S. 2017. Entwicklung generischer geologischer Modelle für flach lagernde Salzformationen - Ergebnisse aus dem Vorhaben KOSINA. Bundesanstalt für Geowissenschaften und Rohstoffe (BGR); Hannover.

Hydromechanical integrity of HAW-repositories in bedded and domal salt - Commonalities and differences as implications for a site selection process in Germany

Till Popp[1], Ralf-Michael Günther[1], Dirk Naumann[1]*

[1]Institut für Gebirgsmechanik GmbH (IfG), Friederikenstraße 60, D-04279 Leipzig, Germany

* *till.popp@ifg-leipzig.de*

ABSTRACT: Since 2013, the search for a site for a repository for high-level radioactive waste has started again in Germany. For many decades, the development of repository concepts and safety analyzes for a repository in a salt dome was prioritized in Germany. The aim of a comparative site selection process is to find a site by 2031 that offers the best possible safety for the containment of high-level radioactive waste (HLW) for a period of 1 million years. Demonstration of long-term safety absolutely requires the systematic proof of the barrier integrity, mainly regarding geological and geomechanical aspects. Compared to clay and crystalline rocks salt rocks, especially as "salt pillow" have important safety advantages: (1) Sufficient thickness of the Stassfurt rock salt (several 100m thick); (2) A natural multi-barrier system through lithological alternation of clay / salt rocks, which is extremely robust against external influences (e.g. erosion, leaching, earthquakes); (3) geologically simple (easily predictable) geological and structural situation.

1   Introduction

In Germany the Site Selection Act for a repository for heat generating radioactive waste and spent nuclear fuel was issued in July 2013 and amended in Mai 2017 (StandAG 2017). This act directs the selection process for a repository site in Germany that best ensures the repository safety for a demonstration period of one million years. This requires the existence of generic repository concepts as well as suitable safety and demonstration concepts for all potential host rocks (salt, claystone and crystalline rocks) in Germany.

Due to their unique properties, including tightness and plastic deformability, as well as mineral natural resources, salt formations have been investigated and used, both in Germany and worldwide for decades of mining of potash/halite bearing salt and, especially, for energy storage (e.g. as gas storage caverns). However, the structure and composition of salt deposits are not uniform, as shown in Figure 1.

As pointed out by Hansen et al. (2016) the extent to which bedded and domal salt formation types differ in characteristics important to high-level radioactive waste (HLW) disposal is a somewhat unanswered question. In the early 1980s, a reference concept for the disposal of heat-generating radioactive waste and spent nuclear fuel was developed, but only for salt domes. Since 1977 the Gorleben salt dome has been investigated regarding its suitability as a final HAW-repository, but during the new site selection process the site has been identified as not future-oriented due to the properties of the cap rocks (BGE 2020). Although since 1987 in the US, nuclear waste disposal in the US has concentrated on bedded salt (i.e. the WIPP-site), at least in 2015 the R&D project KOSINA was launched in Germany to investigate the technical feasibility and safety of a generic repository for HAW in such formations (Bollingerfehr et al. 2018).

Because neither a salt dome nor bedded salt seems to have such great advantages that it immediately becomes the ideal candidate, the individual pros and cons have to be evaluated regarding setting, geologic history and forth-coming evolution. Thus, in addition to simple geometrical features, e.g. lateral extension, depth and thickness, also other aspects such as

lithological variability or robustness against thermo-hydro-mechanical loadings may play a significant role.

In the following, after a brief description of the geologic and lithologic characteristics of the various salt formations the favourable properties of bedded salt will be illustrated based on practical experiences from mining activities. In addition, results from the numerical analysis of the integrity of the geological barriers performed in the framework of the KOSINA-project will be presented. Finally, as outcome, recommendations for safety margins to risk areas, e.g. the borders of the respective geological structure or carnallite intercalations will be given.
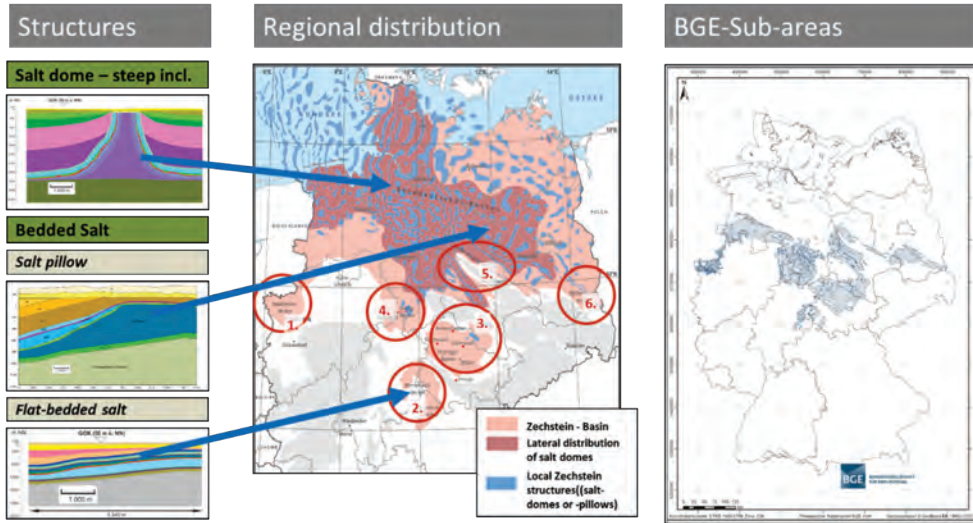
Figure 1: Salt structures in the central Zechstein basin in Germany: (left) Structural pheno-types, (middle) regional distribution (numbers indicates local sub-basins), (right) potential sub-areas for a further site search, as identified in the 1st site selection step (BGE 2020).

2   Lithological commonalities and differences between bedded and domal salt

Salt formations occur frequently in Germany in the following individual formations of the stratigraphic units: Rotliegend, Zechstein (both Permian), Röt, Muschelkalk, Keuper (all Triassic), Malm (Upper Jurassic) and Tertiary (Palaeogene) (e.g. Reinhold et al., 2014). In this study only the subdivision Zechstein is considered, which is the most widespread salt in the Northeast German Basin (NEGB). Seven cycles of Zechstein salt, z1 – z4 (with distinct salt thickness) and z5 – z7 (mostly clastic sediments: sand-silt-mudstone-pelite) were deposited after a series of marine transgressions and regressions during the Upper Permian (e.g. Zhang et al. 2013). The z1 (up to 300 m) locally developed in a lagoon environment. The thick z2 (over 500 m) was widely deposited in the whole basin. The z3 and z4, followed by the z5 – z7 decreased progressively in thickness, composition and distribution.

Within one evaporation cycle of seawater the main mineral composition represents the progressing evaporitic conditions, resulting in alternating sequences of lithological and mechanical different salt rocks (which are characterized by a significant thickness) (e.g. Warren 2016). Firstly, (after sedimentation of a clastic clay-foot) carbonates were precipitated, subsequently followed by sulfates (anhydrite/gypsum). When salinity of seawater reached 10 to 12 times of the normal seawater, halite ($NaCl$) starts to precipitate reaching primary thicknesses from 200 m to over 600 m (in the central parts of the basin), until finally potassium-magnesium salts generate from supersaline water.
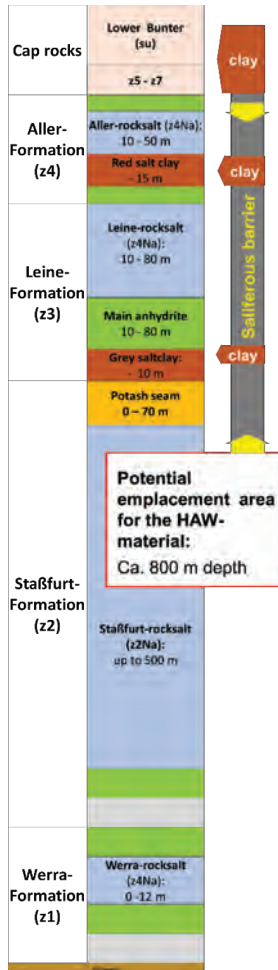
Property		Bedded Salt		Domal salt / salt diapir
Subtype		Flat bedded salt	Pillows	
Host rock formation	Lateral extent	Large	Sufficient	Sufficient
	Thickness	Limited	Significant	large
	Geology	Simple	Lateral inhomogeneous	Complex
	Uniformity / bedding	• Anhydrite/clay layering • Salt clay inter-beddings		• Homogenized salt portions
Cap rocks / overburden (main features)		• Intact cap rocks with overlaying clay rocks • In the lower part dry		• Disturbed • Often water bearing
Host rock: Petro-physical properties (main features, data base)		Anisotropy ➢ Mechanical /hydraulical weakness planes ➢ Scarce data sets		Isotropy ➢ Low permeability ➢ Comprehensive rock-mech. data
Fluid path way scenarios (related to the main structural elements)		• Horizontal bedding: ➢ lateral fluid flow due to sulfate/clay layers		• Steep inclined foliation: ➢ Fractured „Main Anhydrite" ➢ Dissolution of the potash seam

Figure 2: Properties of salt formations in relation to the main structural phenotypes as indicated in Figure 1.

Figure 3: Lithostratigraphy of the Zechstein (Late Permian) in the subherzynian depression (Harz-foreland, i.e., Saxony-Anhalt (D). The different colours refer to the specific lithological rocks, i.e., blue = rock salt, orange = potash salt, brown = salt clay, green = anhydrite, grey carbonate.

As a consequence, flat-bedded salt formations include laterally extensive deposits of halite, but also other evaporates (e.g. anhydrite and potash rocks, such as carnallite, polyhalite and sylvite) which are layered sequentially as deposited and, additionally, altered by diagenetic differentiation due to fluid movements (Figure 2). Argillaceous salt layers are only present as massive layer at the base of z3 (Grauer Salzton) and z4 (Roter Salzton). Thereby, it is worth to note that the various rocks are characterized by significant different rock-mechanical behaviour, whereby no unique description is possible due to different acting hydro-mechanical and humidity random conditions, e.g. rock salt can be stronger or weaker than other evaporites. Following Jackson & Hudec (2017), the rock-mechanical behaviour of the various salt rocks can be characterized, as depicted in Figure 4, from low- to high-strength resp. brittle-ductile behaviour.

In the following geological times halokinesis (the process of flowing and rising of salt) occurs when the differential pressure of stress exceeds the strength within the salts, although the individual relevancy of the underlying driving mechanism is still under debate, e.g. buoyancy-induced salt-movements are triggered by some tectonic impact (e.g. Pollok et al. 2020). In

addition, due to the visco-plastic behaviour of salts (e.g. as described for the Thuringian basin, Bachmann et al. 2008), their layers usually act as a decoupling horizon between the substratums and the covers, resulting in the formation of different salt structures, such as salt pillows and salt diapirs. While rock salt in salt domes (type: steep inclined bed) is particularly common in Northwest Germany, flat bedded salt rocks (type: flat-bed) and in parts of Northeast Germany salt pillow structures (type: salt pillow) dominate (Figure 1).
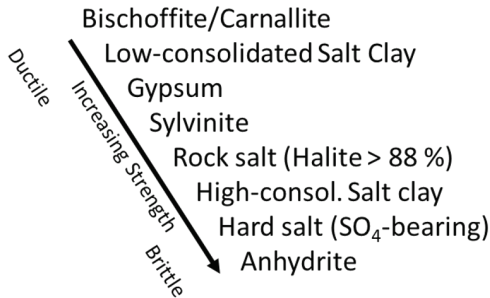
Figure 4: Order of various salt rocks, corresponding to their rock strength.

Salt pillows are dome-like structures (brachyanticlines) which developed, preferably during the Zechstein, as a result of the migration of salt into the structure (Pollok et al. 2020). A crucial aspect of the genesis of these structures is the accumulation of rock salt by the lateral inflow and accumulation of the most easily mobilizable parts of a salt sequence (frequently the rock salt horizons belonging to the Stassfurt Formation). During the course of the accumulation, the younger, less creepable salt rocks in the evaporitic sequence, as well as the cover rock, become domed upwards. However, in contrast to salt domes the bulging of the structure and its overburden layers is not accompanied with the formation of crest faults.

This is an important advantage compared to salt domes (e.g. compared to the Gorleben site) because due to non-water bearing caprocks (in East and Central Germany: the clay-silt-bearing sediments of the z5-z7 and lower Bunter) subrosion (salt dissolution in contact with groundwater) becomes unlikely. In addition, as documented briefly in Figure 3, bedded salt formations seems to be simpler regarding their internal structure but textural effects may control some hydro-mechanical properties, e.g. fluid flow.

3   Demonstration of the Long-term integrity of the geological barrier

The emplacement of heat-generating high radioactive waste gives rise to temperature changes in the rock mass which itself causes stress and deformation changes, and can diminish the integrity of the geological barrier. Thus, the question arises whether thermo-hydro-mechanical induced stresses, which occur over time as a result of the forecast behaviour of the geologic repository system, could violate the integrity of the barrier during the specified verification period. The impact of the heat generating radioactive waste on the long-term barrier integrity of the bedded salt is usually analysed numerically based on computer simulations. A potential loss of salt barrier integrity can occur due to the following three main processes (e.g. Minkley et al. 2010):

- mechanical damage due to transgression of the dilatancy boundary which acts mainly in the excavated damage zone (EDZ) ⇨ Near field (decimetres up to several metres)
- convergence and thermo-mechanical induced stress re-distribution. These processes depend on the size of the underground excavations and the impact of temperature

induced stresses due to the thermal rock expansion accompanied with extensive up-lift development ⇨ Far field (decametre up to several hundred meters)

- fluid pressure driven creation of hydraulical pathways along discontinuities in the micro- and macro-scale in the rock salt (grain boundaries, bedding planes) at fluid pressures > minimal principal stress, i.e., σ_{min} ⇨ Far field

To evaluate the long-term integrity of the salt barrier, two safety criteria, the dilatancy criterion and the fluid pressure criterion, have to be considered (BMU 2010):

- Dilatancy criterion: The integrity of the rock salt barrier is guaranteed if rock stresses do not exceed the dilatancy boundary. If the deviatoric stress exceeds this boundary, microcracks will form and will cause progressive damage and permeability of the rock salt.
- Fluid pressure criterion: The integrity of the barrier is guaranteed if the hydrostatic pressure of an assumed column of brine extending from the ground surface to depth of the considered location of the salt body contour (e.g. top of the salt formation) does not exceed the minimum principal stress at that point.

Using this approach, in the last decade comprehensive analysis of THM-processes on the barrier integrity related to disposal of heat-generating radioactive waste were performed by IfG and BGR on domal salt (site study Gorleben – VSG, Kock et. al. 2012) and bedded salt (generic study – KOSINA; BGR 2018). IfG used for THM-coupled 2D modelling the DEM programs UDEC & 3DEC and BGR for the TM-coupled 3D modelling the FEM program JIFE. Neglecting the impact of the repository concept, e.g. vertical borehole- or drift-disposal, in both cases, i.e., modelling of the bedded salt and the salt dome, the results of the numerical calculations show the effect of thermal expansion. As a result of the deformation, the horizontal stresses at the top of the salt barrier were reduced and the fluid pressure criterion was locally violated, as shown for the bedded salt in an up to < 60 m thick zone (Figure 5). According to the reduction of horizontal stress, the pressure-driven fluid percolation in the THM-coupled modelling acts in a vertically aligned direction with a penetration depth similar to the violation depth of the minimum principal stress criterion analysed in the continuum mechanical analyses. However, this effect of criteria violation is only associated with the thermal pulse occurring in the first few 1000 years and will diminish with time due to salt creep.
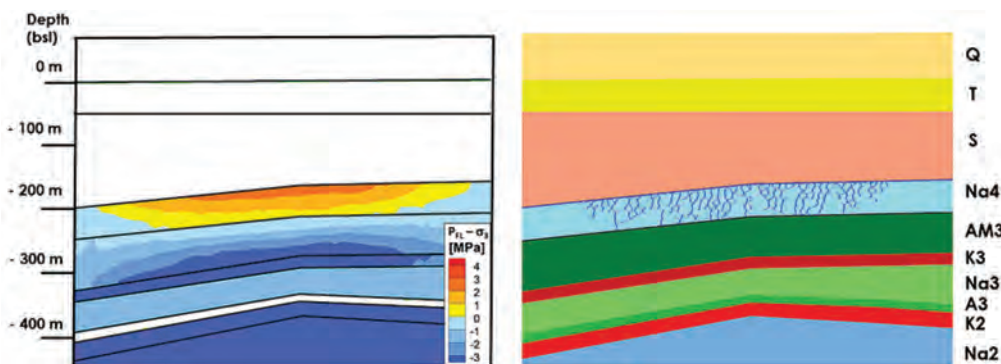
Figure 5: Case study KOSINA - bedded salt; Comparison of violation area of the minimum principle stress criterion (left) and the area, where pressure-driven percolation occurred in the coupled thermo-hydro-mechanical calculations (right, dark blue structure) for vertical borehole disposal in a salt pillow structure (taken from Bollingerfehr et al. 2018).

4   Robustness of the saline barrier under dynamic loading

Although the long-term integrity of HAW-repositories in salt was demonstrated, independently from the structure (bedded – KOSINA, Boolingerfehr et al. 2018 - or domal salt – VSG, Kock et al., 2012) it is worth to note that the integrity of the salt barrier is also preserved under dynamic loadings. In the Teutschenthal mine long-lasting and intensive potash salt extraction was carried out until 1982. Because the load-bearing carnallitite-pillar system was assessed as unstable, backfill measures are being performed for stabilization of the remaining underground openings (see Popp et al. 2018). However, a rock burst (the 3rd - earlier events happened in 1916 and 1940) occurred on September 11, 1996 (RB 1996) at 05:36 CEST. As depicted in Figure 6a, b during a chain reaction-like collapse the entire eastern working area with an extension of approx. 2.5 km² at a depth of 620 m - 770 m failed (Minkley 2004).
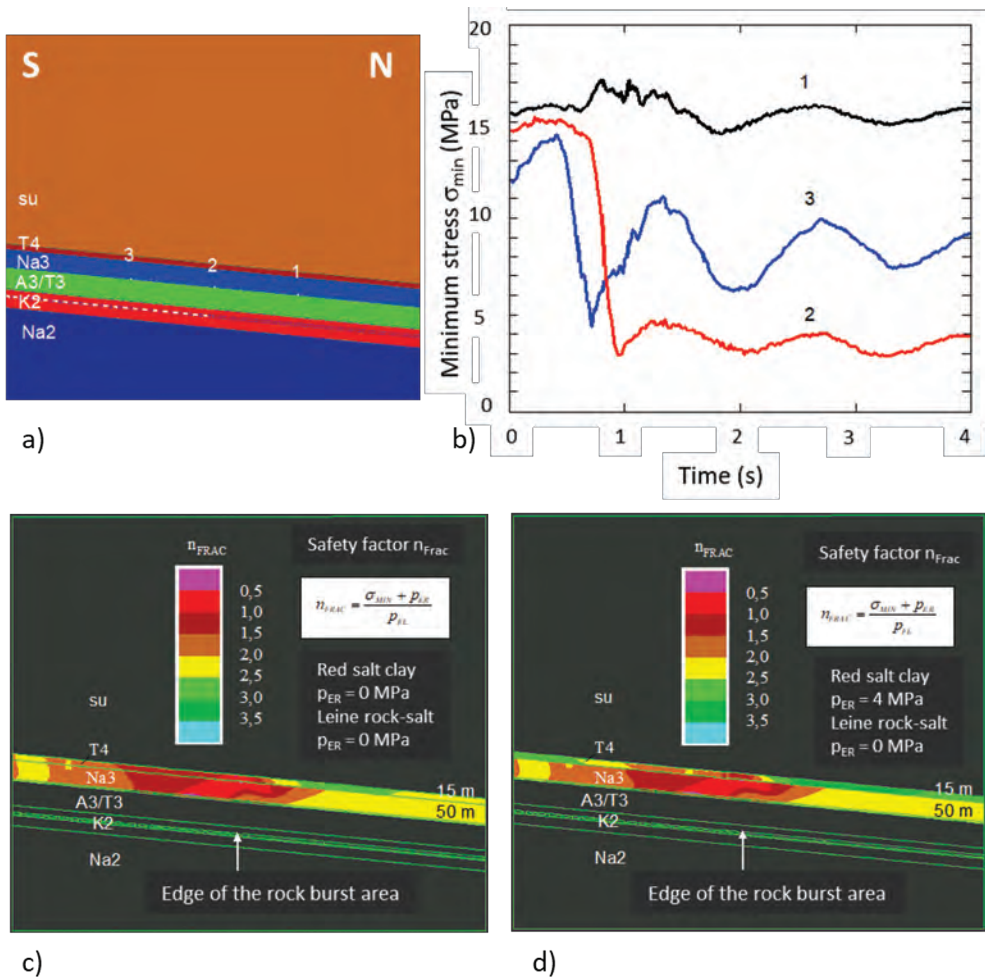
Figure 6: Numerical back analysis of the rock burst Teutschenthal 1996 (modified after Minkley et al., 2010). a) N-E-section through the collapsed East-Field; b) Temporal variation of the minimum stresses at the top edge of the Leine-rock salt at three observation points, indicated in (a); Safety factor frac criterion 4 seconds after rock burst without (c) and with (d) hydraulic tensile strength in Red Salt Clay

As a result of the rock burst with a local magnitude of around 5, the geological hanging wall barrier consisting of red salt clay (z4T) and Leine-rock salt (z3Na), above the collapsed eastern working area, was exposed to a total subsidence of 1.3 m, of which 0.5 m occurred in a few seconds during the rock burst. Despite this considerable unloading effects in the water protecting salt-barrier (here Na3 = z3NA), no water entered the underground salt openings, although the minimum-stress criterion was violated, as shown in Figure 6c, d.

This could ultimately only be explained by the effect of a lithological multi-barrier consisting of rock salt and Red Salt Clay as horizontal layer elements in the geological barrier. Short term lab-tests on red salt clay samples using brine as injection medium demonstrated that the clay could tolerate significant fluid over-pressurisation, in contrast to rock salt (Minkley et al. 2013). Exceeding the minimum stress results not in tensile macro-fractures (as confirmed in recent field tests) but a moderate increase of rock permeability of up only order is apparent, probably due to "pathway dilatation" processes. In addition, self-healing capacities are obvious, which generally helps to maintain the integrity of natural and technical (i.e., bentonite) barriers.

5   Tightness of salt / safety margins and optimal repository depth

Under undisturbed conditions, in principle all lithological different salt rocks (e.g. rock salt, potash and anhydrite) are liquid- and gas-tight, as demonstrated by natural analogues (e.g. by CO_2-deposits in the Werra region, Minkley et al. 2010) and lab- and field measurements (e.g. Popp et al. 2014). On the basis of practical experience from gas storage in salt caverns, a permeability of $\leq 10^{-22}$ m^2 is defined as tight. However, as argued by Warren (2017) locally salt bodies may become leak, as evidenced by the loss of a number of salt mines due to uncontrolled floods, the rapid creation of solution dolines atop subcropping salt masses and to black salt haloes around highly pressurized hydrocarbon reservoirs. Although the reasons of integrity loss have to be individually analysed with respect to integrity criteria and geology (see chapter 4) definition of safety margins to risk zones is the prerequisite to avoid such leakages in terms of both mine safety and waste storage. For example, the hydrate bearing-carnallite starts to dehydrate at temperatures > 100°C, depending on the confinement of the respective potash sections (Popp & Kern 1993). Thus, depending on the time dependent developing temperature field a minimum safety distance of, at least, 50 m between the repository areas and the potash seam is recommended, as estimated, e. g. in the framework of the safety concept of the preliminary safety analysis of the Gorleben-site (Mönig et al. 2012).

 As deduced from mining legal rules, the experiences from flooded mines and safety considerations in the framework of salt mining and mine closure activities (e.g. Minkley et al. 2010) Figure 7 summarizes the respective recommendations to relevant risk areas.
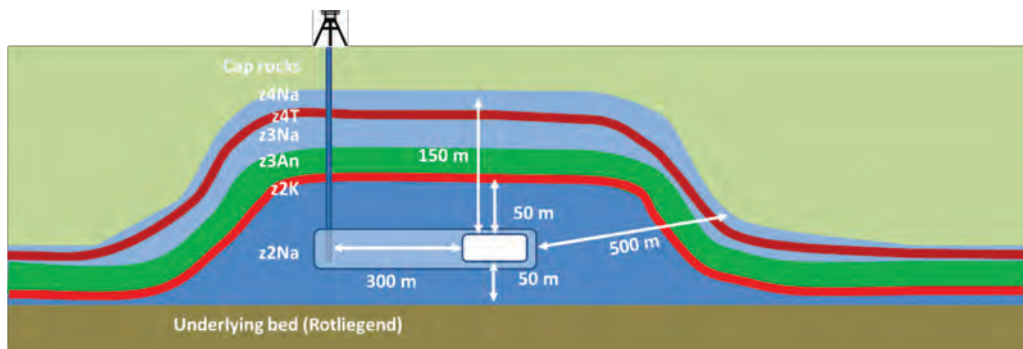
Figure 7: Recommendations for safety distances in bedded salt ("salt pillow").

Regarding a reasonable minimum depth of the repository observations of Herbert & Schwandt (2007) give valuable hints, who analysed statistically water inflows from the past occurred in salt mines (mostly in Eastern Germany, e.g. in the Stassfurt region). Their findings suggest that in depths > 800 m ingress of fluids becomes unlikely because no open fissures in the main anhydrite and in adjacent rock salt areas may exist due to the effect of lithostatic stress.

As maximum depth, a limitation of the depth to ≤ 1200 m is recommended, corresponding to a maximum rock temperature of approx. 50°C, to ensure safe working conditions underground and to limit the convergence of underground openings.

6   Conclusions

Salt formations, i.e., both, domal and bedded salt deposits, are in principle suitable for construction of a HAW-repository, if sufficiently thick and spatially large rock salt portions are available. Nevertheless, it has to mentioned that also a combination of the advantages of both favoured host rocks, i.e., the unique isolation capacity of rock salt as well with the water tightness and absorption capacity of clay formations (e.g. the Red Salt Clay, z4T as well as in the z5 - z7 and the Lower Bunter, see below) against radionuclides, can significantly improve the barrier properties. The flat bedded Zechstein salt deposits in Germany represent already an advanced natural geological multi-barrier-system consisting of rock salt and clay horizons, as demonstrated by the technical analogue "rock burst 1996 - Teutschenthal". In addition, clay horizons in the hanging wall of the respective salt formation are favourable in the long term because they act as water protecting layer and counteract possible subrosion.

In addition, the following recommendations apply for a site selection process

- The repository area (EWG) is to be set up in a spatially large and homogeneous part of rock salt. Rock salt is defined here as an almost mono-mineral rock with a halite content > 88%, which means that it can be clearly distinguished from neighboring rock units, such as anhydrite or potash salt. Lithological anhydrite inclusions, which can be locally up to about 1 m thick, are to be regarded as a natural component of the rock salt.
- Based on the present state of knowledge, the Stassfurt rock salt (z2Na) in the form of a salt pillow (cf. KOSINA project) is estimated to be the presumably most favorable storage horizon or part of a salt structure. Advantages regarding rock salt intercalations in other Zechstein sequences include large thicknesses and absence of intercalated potash seams.
- To minimize the risk of a potential water inflow, the depth of the repository should be at least 800 m depth.
- To ensure mining manageable boundary conditions (e.g. low convergence, limited temperature), the maximum repository depth should be 1,000 - 1,200 m.
- When selecting potential repository sites, safety distances justified by mining and long-term safety, e.g. to a water-bearing overburden, to potential fault zones or carnallite seams, must be respected in order to avoid potential pathways. The minimum permissible distance to the potash seam is 50 m (to avoid thermal induced dehydration processes).
- Qualified and robust hydro-mechanical long-term analyses of barrier integrity can already be helpful in the context of preliminary safety analyses for site selection. Verified numerical calculation tools and suitable rock parameter sets of the lithological rock units are available to check the established failure criteria, (1) dilatancy and (2) minimum stress criteria.
- The methodological procedure of the integrity verification within the framework of a safety analysis for repositories of HAW waste or for underground storage sites for chemical-toxic waste as well as for backfill-mines with environmentally hazardous waste materials is qualitatively the same.

Acknowledgements

References

BACHMANN, G. H, EHLING, B. C, EICHNER, R. & SCHWAB, M. 2008. GEOLOGIE VON SACHSEN-ANHALT, SCHWEIZERBART'SCHE VERLAGSBUCHHANDLUNG.

BGE 2020. Zwischenbericht Teilgebiete gemäß § 13 StandAG, Bundesgesellschaft für Endlagerung, Peine, Stand 28.09.2020.

BOLLINGERFEHR, ET AL. 2018. KOSINA Concept developments for a generic repository for heat-generating waste in bedded salt formations in Germany, BGE TEC, 2018-13.

BGR 2018. TM- und THM-gekoppelte Modellberechnung zur Integritätsanalyse der geologischen Barrieren in flach Lagernden Salzformationen - Ergebnisse aus dem Vorhaben KOSINA. – BGR; Hannover.

BMU 2010. Bundesministerium für Umwelt, Naturschutz und Reaktorsicherheit (BMU): Sicherheitsanforderungen an die Endlagerung wärmeentwickelnder radioaktiver Abfälle. Bonn, Stand: 30. September 2010.

HANSEN, F.D., KUHLMANN, K.L. & SOBOLIK, S. 2016. Considerations of the Differences between Bedded and Domal Salt Pertaining to Disposal of Heat-Generating Nuclear Waste. Sandia National Laboratories, July 7, 2016, FCRD-UFRD-2016-000441, SAND2016-6522R.

HERBERT, H.-J. SCHWANDT, A. 2007. Salzlösungszuflüsse im Salzbergbau Mitteldeutschlands - Er-fassung und Bewertung der chemischen und physikalischen Analyseergebnisse. GRS – 226, ISBN 978-3-939355-00-7.

JACKSON, M.P.A. & HUDEC, M.R. 2017. Salt Tectonics - Principles and Practice. Cambridge University Press; ISBN: 978131678639.

KOCK, I., EICKEMEIER, R., FRIELING, G., HEUSERMANN, S., KNAUTH, M., MINKLEY, W., NAVARRO, M., NIPP, H.-K. & VOGEL, P. 2012. Integritätsanalyse der geologischen Barriere. Bericht zum Arbeitspaket 9.1, Vorläufige Sicherheitsanalyse für den Standort Gorleben. GRS-286, ISBN 978-3-939355-62-5, Gesellschaft für Anlagen- und Reaktorsicherheit (GRS) mbH: Köln.

MINKLEY, W. 2004. Gebirgsmechanische Beschreibung von Entfestigung und Sprödbruch-erscheinungen im Carnallitit. Schriftenreihe des Institutes für Gebirgsmechanik – Band 1, Shaker Verlag Aachen.

MINKLEY, W., POPP, T., SALZER, K., GRUNER, M. & BÖTTGE, V. 2013. Hydro-mechanical properties of the Red Salt Clay (T4) – Relevancy of the minimum stress criterion for barrier integrity. Physics and Chemistry of the Earth, Parts A/B/C. Available online 3 June 2013 http://www.sciencedirect.com/science/article/pii/ S1474706513000545.

MINKLEY, W., WÜSTE, U., POPP, T., NEUMANN, D., WIEDEMANN, M. & BOBINSKY, J. 2010. Beweissicherungsprogramm zum geomechanischen Verhalten von Salinarbarrieren nach starker dynamischer Beanspruchung und Entwicklung einer Dimensionierungsrichtlinie zum dauerhaften Einschluss, BMWi-FKZ: 02C1264, IfG-Institut für Gebirgsmechanik GmbH, Leipzig, 31.01.2010.

MÖNIG, J., BUHMANN, D., RÜBEL, A.,WOLF J., BALTES B. & FISCHER-APPELT, K. 2012. Sicherheits- und Nachweiskonzept. Bericht zum Arbeitspaket 4, Vorläufige Sicherheitsanalyse für den Standort Gorleben. GRS-277, ISBN 978-3-939355-53-3, Gesellschaft für Anlagen- und Reaktorsicherheit, Köln, Juni 2012.

POLLOK, L., HAMMER, J., FLEIG, S. & MUSMANN, P. 2020. Salinarstrukturen – Entstehung, Außenformen und Internbau. – In: Deutsche Stratigraphische Kommission; Koordination/Redaktion: Paul J. & Heggemann, H. (Hrsg.): Stratigraphie von Deutschland XII - Zechstein. – Schriftenr. Dt. Ges. Geowiss., Heft 89:559-593; Berlin.

POPP, T., MINKLEY, W., FILLINGER, E. & BOETTGE, V. 2018. Closure of the Teutschenthal backfill mine - About the challenge to elaborate a geomechanical safety concept in salt formations. In: The Mechanical Behavior of Salt IX; Proceedings of the 9th Conference on the Mechanical Behavior of Salt (SaltMech IX), Hannover, Germany, 12-14 September 2018 (ISBN 978-3-9814108-6-0), 385-402.

POPP, T., MINKLEY, W., WIEDEMANN, M. & SALZER, K. 2014. Gas-pressure induced integrity of salt formations. In: R. Shaw (ed.). Gas Generation and Migration in Radioactive Waste Repositories. Geological Society. London, Special Publications, 415, 107-122.

POPP, T. & KERN, H. 1993. Thermal dehydration reactions characterized by combined measurements of electrical conductivity and elastic wave velocities. Earth Planet. Sci. Lett., 120: 43-57.

REINHOLD, K., HAMMER, J. & PUSCH, M. 2014. Verbreitung, Zusammensetzung und geologische Lagerungsverhältnisse flach lagernder Steinsalzfolgen in Deutschland – Zwischenbericht: 98 S.; Berlin / Hannover (Bundesanstalt für Geowissenschaften und Rohstoffe.

STANDAG 2017. Bundesministerium der Justiz und für Verbraucherschutz (BMJV): Gesetz zur Suche und Auswahl eines Standortes für ein Endlager für Wärme entwickelnde radioaktive Abfälle (Standortauswahlgesetz – StandAG) vom 5. Mai 2017 (BGBl. I S. 1074), das zuletzt durch Artikel 2 Absatz 16 des Gesetzes vom 20. Juli 2017 (BGBl. I S. 2808) geändert worden ist.

WARREN, J. K. 2016. Evaporites: A Compendium. Berlin: Springer, 1854p. ISBN 978-3-319-13511-3.

WARREN, J. K. 2017. Salt usually seals, but sometimes leaks: Implications for mine and cavern stabilities in the short and long term. Earth-Science Reviews 165 (2017) 302–341.

ZHANG, Y., KRAUSE, M. & MUTTI, M. 2013. The Formation and Structure Evolution of Zechstein (Upper Permian) Salt in Northeast German Basin: A Review. Open Journal of Geology, 2013, 3, 411-426.

Derivation of a non-local criterion to assess functionality and robustness of rock salt barrier

Michael Rahmig[1], Christian Lerch[1], Nina Müller-Hoeppe[1], Mirko Polster[1], Thomas Schröpfer[2], Beatrix Stielow[2]

[1]BGE TECHNOLOGY GmbH, Germany; [2]BGE, Germany;

* Michael.Rahmig@bge.de

ABSTRACT: To rate rock salt barrier integrity, two local criteria are typically used – the dilatancy and the fluid pressure criterion. However, these local criteria are not suitable to assess the rock salt barrier as a whole. So, even if both criteria are locally exceeded, a tight rock salt barrier may be preserved if an intact rock salt envelope remains that encloses the mine openings. Thus, a non-local criterion of effective barrier thickness is proposed as a criterion for containment capability. The effective thickness of the intact rock salt barrier evolves as a function of time, taking into account present and future uncertainties. The influence of different technical concepts on barrier integrity can be assessed. The effective thickness of the intact rock salt barrier is defined as the shortest distance that a fluid must theoretically pass to intrude from the surrounding, potentially water-bearing rock into the mine openings and comprises different sections that may either be interconnected or may be intersected by one or more possible flow paths. The advantage of the use of this non-local criterion of effective thickness is its capability to describe rock salt barrier performance by a single comprehensible quantity regarding geology and the mine openings that implicitly covers the dilatancy and fluid pressure criteria.

1   Introduction

In Germany, rock salt is one potential host rock formation to dispose of heat-generating radioactive waste. In the case of HLW disposal, a new repository mine will be excavated in an undisturbed rock formation. It is required to demonstrate the safe containment of the radioactive waste in a containment providing rock zone (CRZ), to optimize the repository concept with respect to safety, and to make a statement on the robustness of the safety functions of the repository system (BMU 2010), (BMU 2020).

For the disposal of low- and intermediate-level radioactive waste (LILW), former salt mines were used in Germany in the past, e.g. the LILW Repository Morsleben. Presently, the Morsleben Repository is under licensing for closure. Within the licensing process, it was recommended (ESK 2013) to include aspects of the above-mentioned legal requirements (BMU 2010). The licensing authority requests for the Morsleben Repository a statement on the containment capabilities of the host rock as well as on the robustness of the repository system, including the geologic rock salt barrier. Furthermore, technical measures are checked in order to optimize the safety functions of the repository system. This contribution focuses on the safety functions of the rock salt barrier – its containment capabilities and robustness – taking into account the safety functions´ time dependence and related uncertainties.

Undisturbed rock salt is tight. However, rock salt loses its tightness if the dilatancy or the fluid pressure criterion is exceeded. From a mathematical point of view, the dilatancy and the fluid pressure criteria are suitable to analyse the rock salt barrier´s integrity locally. Nevertheless, a statement on the safety function of the rock salt barrier as a whole is not possible because a pointwise integrity loss is not of safety relevance if no continuous pathway to water-bearing geologic structures is created (Bollingerfehr et al. 2018). In this case, the rock salt barrier conserves its containment capability.

Furthermore, within the rock salt barrier, locations exceeding the dilatancy or the fluid pressure criterion vary with time. Despite their importance, the dilatancy and the fluid pressure criteria are not suited to serve as a measure for the rock salt barrier´s safety function and its robustness. Therefore, a new non-local criterion was derived – the effective barrier thickness – a single scalar value that allows to assess the evolution of the rock salt barrier´s containment capability with time and to include uncertainties as well. Furthermore, the effective thickness can be used to optimize the repository concept, especially the backfilling concept in the case of the Morsleben Repository. The procedure to evaluate the effective thickness is described below.

2 Theoretical background

2.1 Definition

The effective thickness of the intact rock salt barrier is defined as the shortest distance that a fluid must theoretically cross in intact salt (dilatancy or fluid pressure criterion not exceeded) to intrude from water-bearing geologic structures into the mine openings. The effective thickness may comprise different sections, because potentially, it is intersected by one or more isolated geologic structures (e.g. different geologic strata) without reliable barrier properties.

2.2 Fundamentals

In order to determine the rock salt barrier´s effective thickness, the rock mass volumes of integrity loss must be identified. For this purpose, the dilatancy and the fluid pressure criteria are applied. Equ. (1) and Equ. (2) give the quantitative approaches for both criteria, which are applied to compute numerical examples. Remarkably, the procedure to evaluate the effective barrier thickness shows flexibility as different quantitative representations of both criteria can be applied. The dilatancy criterion denotes the limit state where micro-cracking occurs, as in this case, the salt becomes permeable. In this contribution, the dilatancy criterion according to Cristescu/Hunsche Equ. (1) (Cristescu 1998), which describes the micro-crack boundary, is used.

$$allowed \ \frac{\tau}{\sigma_*} \leq -0{,}01697 \left(\frac{\sigma}{\sigma_*}\right)^2 + 0{,}8996 \frac{\sigma}{\sigma_*} \ ;$$

$$sign \ convention: compressive \ stress \ with \ plus \ sign,$$

$$tensile \ stress \ with \ minus \ sign$$

(1)

with

$$\tau: octahedral \ shear \ stress \ \tau = \frac{1}{3}\sqrt{(\sigma_1 - \sigma_2)^2 + (\sigma_2 - \sigma_3)^2 + (\sigma_3 - \sigma_1)^2}$$

$$\sigma: mean \ stress \ \sigma = \frac{1}{3}(\sigma_1 + \sigma_2 + \sigma_3)$$

$$\sigma_*: normalization \ stress \ \sigma_* = 1 \ [MPa]$$

The fluid pressure criterion describes the limit state where the grain boundaries of rock salt open due to the pressure of the intruding fluids. Thus, it is required that the fluid pressure is lower than the sum of the least principal compressive stress σ_3 that is acting in the rock mass and the tensile strength of rock salt (Kock et al. 2012). In rock salt, grain boundary separation does not occur if the pressure situation meets the fluid pressure criterion. This is the process that enables fluid migration. In practice, the tensile strength is often neglected (is set to 0 Pa).

In addition, it is often neglected that the stress component acting perpendicular to the flow direction and the least principal stress are not identical. Furthermore, in this contribution, the fluid pressure used to determine the effective barrier thickness results from a conservative approach – a hypothetical liquid column to the ground surface and the liquid density, see Equ. (2) for quantitative values.

$$allowed\ p\ < \sigma_3 \qquad\qquad (2)$$

with

$$p: depth\ specific\ brine\ pressure\ p = 0{,}0126\frac{MPa}{m}z_T$$
$$z_T: depth$$
$$\sigma_3: least\ principal\ compressive\ stress\ \sigma_3$$

2.3 Procedure to determine effective thickness

After the rock mass volumes of integrity loss have been identified, the procedure to determine the effective barrier thickness consists of five steps. The volume/area of investigation is defined by step 1 to 4, Figure 1 to 4, while the effective thickness is evaluated in step 5, Figure 5:

1) Marking of the volumes/areas where liquid is present or the presence of fluid is expected, e.g. potentially water-bearing surrounding rock (LEA-liquid expected area).

2) Marking of the volumes/areas where the presence of liquid should be avoided, e.g. mine openings assigned to the disposal area (LAA-lquid avoided area).

3) Marking of the volumes/areas within the rock salt barrier where the dilatancy or fluid pressure criterion is exceeded (CEA-criteria exceeded area).

4) Marking of isolated but potentially permeable geologic structures, e.g. (jointed anhydrite blocks) (PPA-potentially permeable area).

5) Calculation of the effective thickness of the intact rock salt barrier by searching the shortest distance a fluid must theoretically pass.
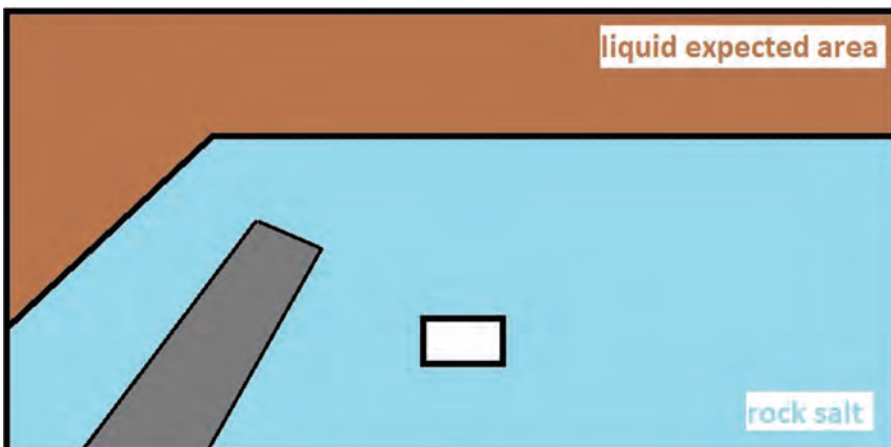
Figure 1: Schematic illustration – step 1
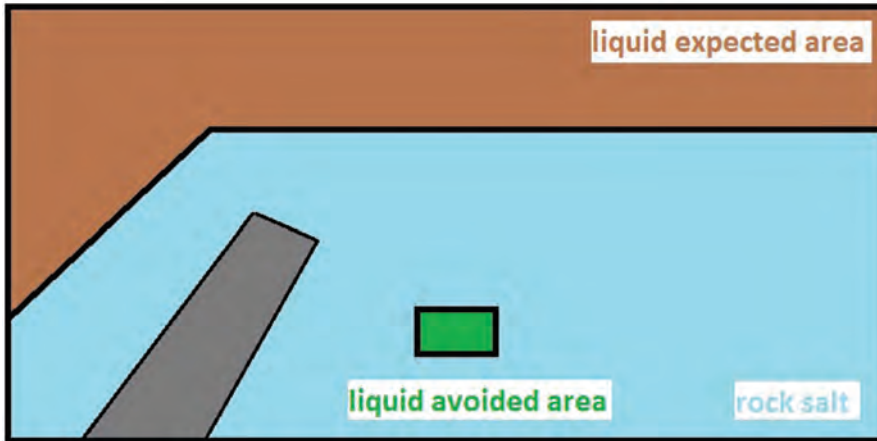
Figure 2: Schematic illustration – step 2
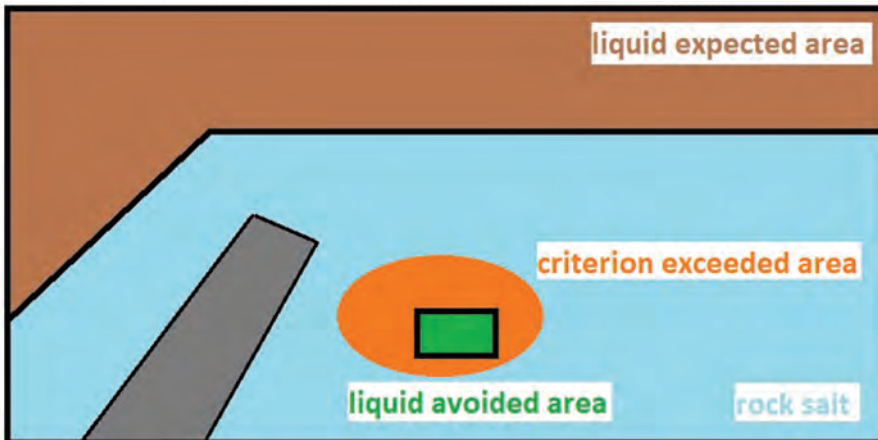
Figure 3: Schematic illustration – step 3
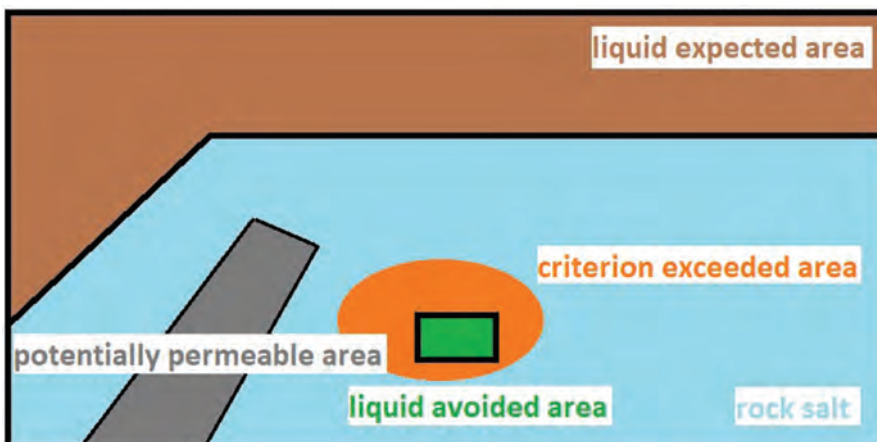
Figure 4: Schematic illustration – step 4
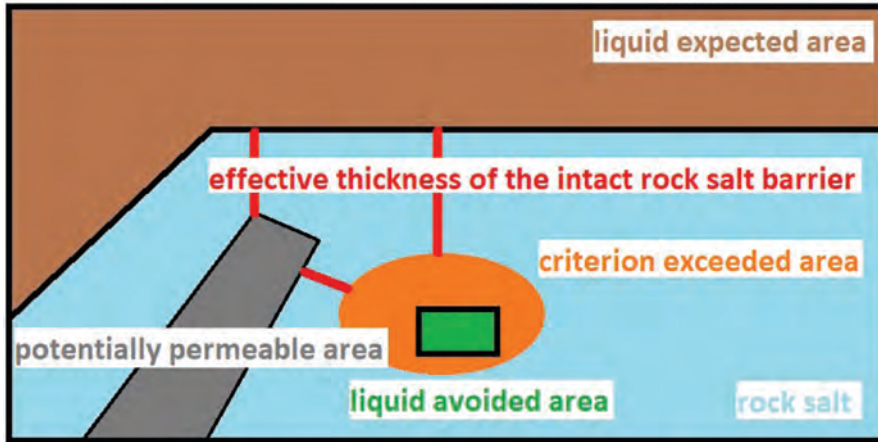
Figure 5: Schematic illustration – step 5

Figure 5 shows two representations of effective thickness between LEA and LAA. As LAA is fully enclosed by CEA, the outer boundary of CEA, the area, in which one of the criteria according to Equ. (1) and Equ. (2) is exceeded, is relevant for the purpose of the calculation. One representation runs continuously through the barrier, the other is a representation, in which the effective thickness of the barrier consists of two sections. In the example shown here, the continuous case leads directly to the top of the salt dome, while the second case is intersected by a (potentially) permeable layer of jointed anhydrite.

From all possible representations of active thickness, the relevant one is selected by calculating the minimum thickness – the effective thickness – of the intact rock salt barrier quantifying the shortest distance of intact rock salt that a fluid must theoretically cross to intrude from the LEA into CEA. In the case of the example in Figure 5, the continuous case is the minimum effective thickness of the barrier because it is slightly shorter than the sum of the two parts of the intersected one

Although the algorithm is shown using a 2D example, it is also applicable to 3D structures.

2.4   Procedure to capture time dependence of effective thickness

The procedure to capture time-dependent effective thickness is straight forward. The effective thickness is calculated at different times and displayed as a graph of effective thickness versus time. For illustration, a generic model is selected, which represents a simplified cross section of a mine structure in the Morsleben Repository (Wolf et al. 2019).

The structure considered in this work is a possible mine configuration at the edge of a salt dome, Figure 6. The surrounding rock, together with the cap rock, is assumed to be the LEA. The structure of the salt dome itself consists of different salt layers. In addition, anhydrite is present in this generic cross section, which is folded and blocked due to the uplift of the salt within geologic timescales.

Mine excavations are located both above the western anhyrite and east of the eastern anhydrite. The excavation is a process with interruptions and lasts several years up to decades. In this model, excavation starts on the eastern side of the anhydrite. Later on, the excavations above the anhydrite start. First, the opening on the lowest floor is excavated. This is followed by the excavation of the next, higher lying opening. This process is continued until the opening on the highest floor is finished. The openings to the east of the anhydrite are already backfilled with crushed salt shortly after their excavation.The excavations above the anhydrite are backfilled with concrete, again starting at the lowest floor and continuing to higher levels.

The modelled backfilling is based on a conceivable realistic backfilling plan. This means that it takes a while after the backfilling of an opening to prepare the mine for the next backfillling of an opening. So there is a time difference between the individual backfillings.

It is assumed that all these excavations are connected to the emplaced waste, thus, they are the LAA. PPAs are below the excavations. In this example, they have no effect on the effective rock salt barrier.

The material models used are linearly elastic for the overburden, the anhydrite, and the backfill (western opening), while they are elastic-viscoplastic for the rock salt and elastic-poro-viscoplastic for the backfill (eastern opening). Note: In this example the choice of the viscoplastic constitutive model is of minor significance. In other cases, however, the uncertainty caused by its choice may affect the effective barriere thickness significantly.

The calculations have been carried out with the ITASCA code FLAC3D.

The surface of the liquid column is located 120 metres above sea level, which is equal to the ground surface; the salt table is located 140 metres below sea level.
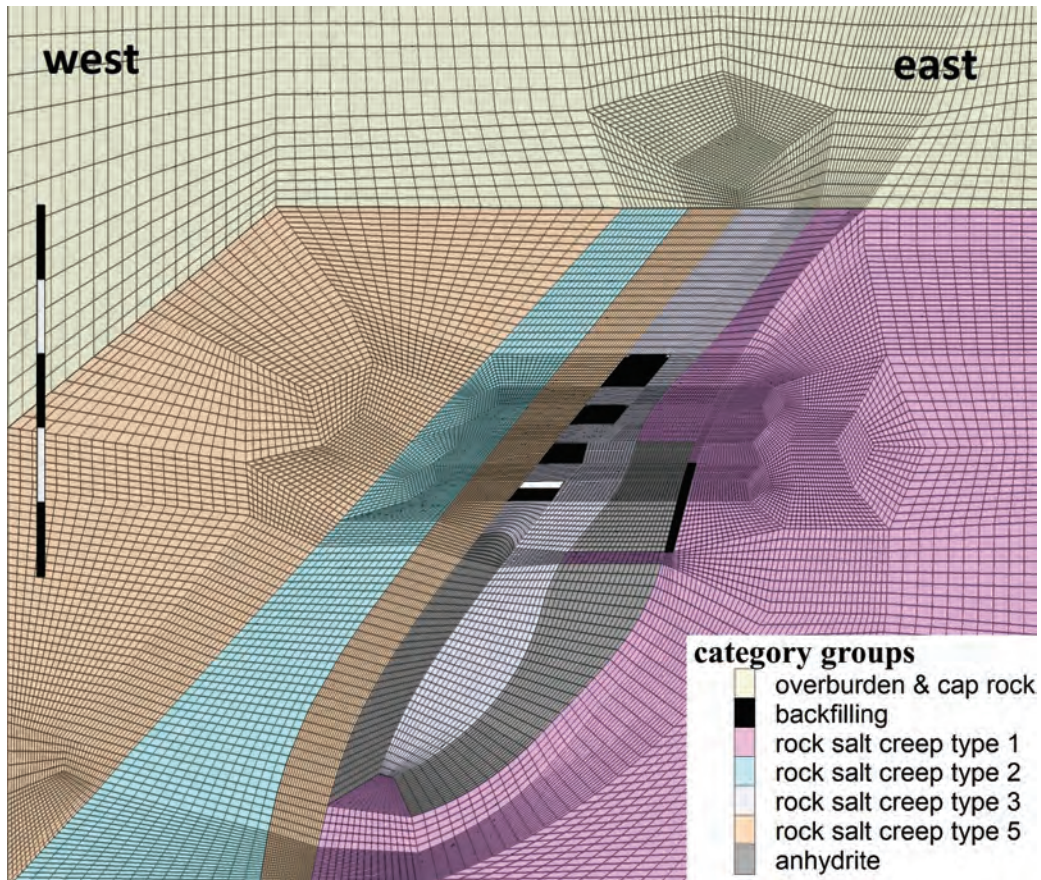
Figure 6: Generic model of the mine situation (cross-cut)

Figure 7 shows the time-dependent evolution of the effective thickness of the intact rock salt barrier for the generic model, taking into account different points of time when the backfilling measure is started in order to allow a conclusion about the time needed until the barrier effectiveness is regained. It illustrates the depletion and the recovery of the rock salt barrier in a descriptive way. The effective thickness is calculated first when excavating the first mine opening. The subsequent decrease of the effective barrier thickness is primarily driven by the following excavations. After this excavation process, the rock salt barrier´s effective thickness

decreases further caused by the visco-plastic behavior of rock salt. How much of the effective barrier thickness remains, depends on the depth of the excavation as well as on several more items, for instance the geology, the related geotechnical properties or material behavior (Wolf et al. 2019).

With a backfilling measure and the resulting backfill pressure, the function of the barrier can be improved. The rate of improvement depends, among others, on the backfill material used.

Hence, this procedure is useful to assess the success of the backfilling measure by the increase of effective barrier thickness with time. Furthermore, this method demonstrates the valuable effect of an early point of time for backfilling to ensure that the integrity of the barrier meets the requirements. It is noticeable that the effective salt barrier´s thickness never reaches its starting value again. The reason for this is the mine configuration. When calculating the starting value, there is only one excavation on the lowest floor. After terminating the mine operations, the highest floor is relevant for the value of the effective rock salt barrier. This is the cause for the difference between the starting value and the final value.
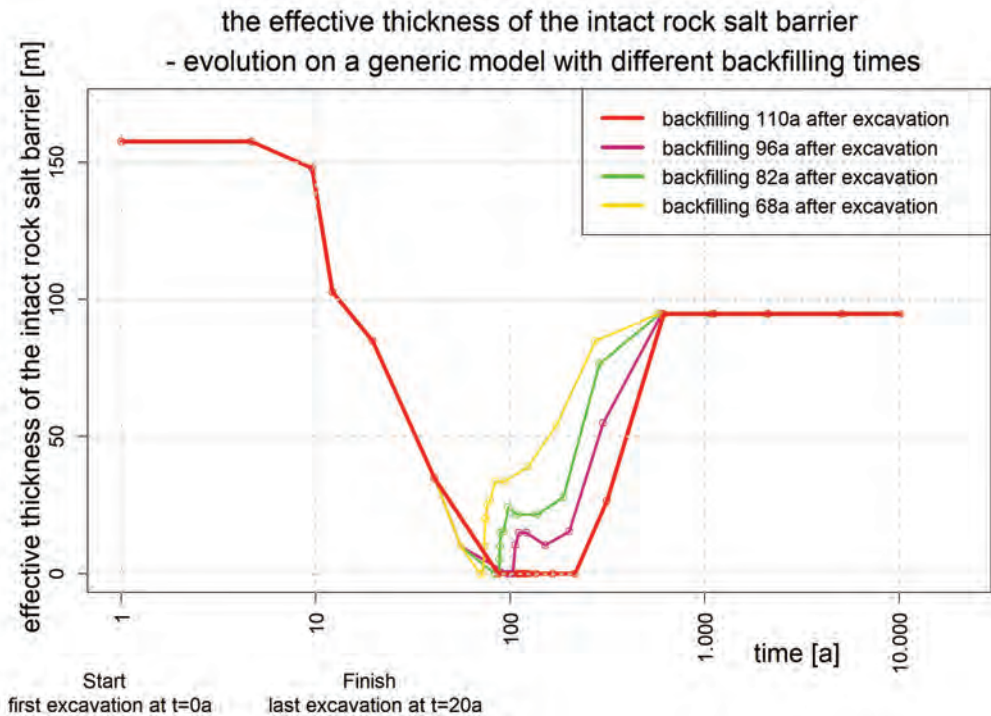
Figure 7: Containment capability of the rock salt barrier over time using the non-local effective thickness criterion

In addition to the backfilling concept, which served to illustrate the application of this procedure, further applications may appear in evaluating different mine geometries with respect to geology, type, and implementation of construction work or the choice of construction materials and their effect on the effective rock salt barrier. This applies also to the design and layout of a repository mine for heat-generating waste.

3   Application of this procedure – further examples of use

The procedure may be applied to additional fields of interest, which are briefly listed below.

3.1 Effective rock salt barrier thickness as a tool to assess uncertainties

Obviously, this procedure can be used to assess the influence of uncertainties on rock salt barrier performance by varying uncertain quantities and calculating the effective thickness versus time in each case. The result is a set of curves that show the range of barrier containment capability versus time. This procedure allows the identification of the most significant uncertainties and consequently, it is possible to investigate how to mitigate the effects of the most significant uncertainties on the rock salt barrier´s safety function. A conclusion on robustness taking into account containment may be drawn.

In this contribution, this aspect is not discussed in detail as results have been published recently (Wolf et al. 2019).

3.2 Optimization of technical solutions

The procedure allows a standardized comparison of the effects of different backfilling concepts on the effective rock salt barrier. It is even possible to rate the influence of different technical solutions with this simple method.

The evaluation of the valuable effect of an early point of time for backfilling was already mentioned, Figure 7. Furthermore, the degree of backfilling was investigated. Again, the generic model from chapter 2 was used for calculation. The modelled excavation process corresponds to the sequence described in chapter 2. Three backfilling concepts were investigated.

The backfilling concept 1 is the backfilling from Figure 6 in chapter 2. In concept 2, the projected degree of backfilling has been reduced by approximately 40% (based on the total backfill quantity) compared with concept 1. Concept 3 comprises a full backfilling. The backfilling concepts are illustrated in Figure 8.
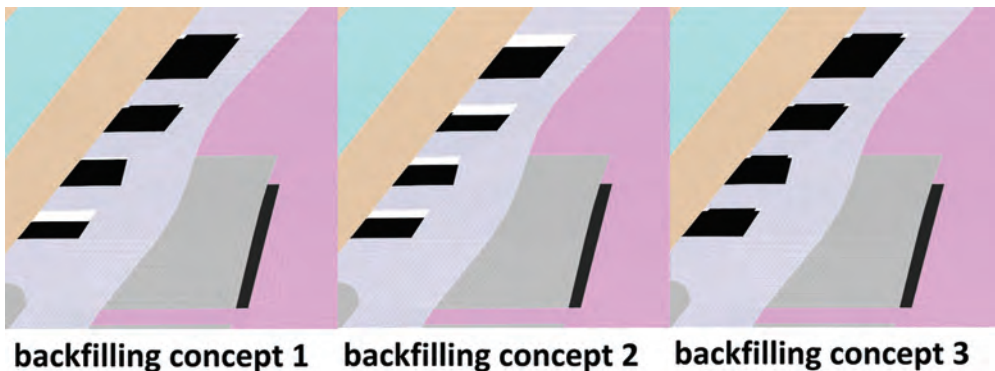
Figure 8: Comparison of the different backfilling concepts

Concepts 1 and 3 are suitable to re-establish the rock salt barrier permanently within a short period, Figure 9. Concept 3 accelerates this process compared with concept 1. Concept 2 re-establishes the rock salt barrier for a short period of time. After that, the effective barrier thickness becomes zero again over a much longer period than that considered here. Thus, concept 2 is not suitable to re-establish the rock salt barrier permanently.

In a further step, the cavities whose backfilling shows the maximum effect on the barrier´s safety function may be evaluated. Or the effect of backfilling specific cavities may be rated against the additional amount of barrier thickness that can be achieved.
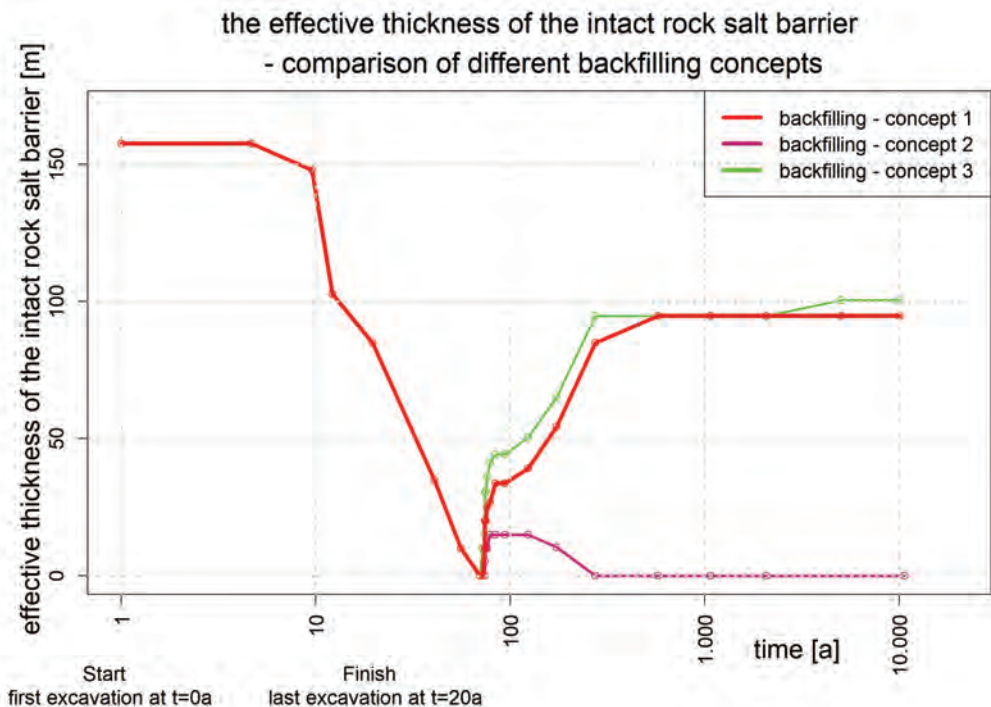
Figure 9: Comparison of three different backfilling concepts

3.3 Influence of external actions and far field events

When taking into account external actions, e.g. glaciation or far field events like earthquakes, the effective barrier thickness may again serve as a quantity to describe the influence of these actions on barrier safety function and to make a statement on the rock salt barrier containment capacity versus time. Multiple future repository system evolutions can be captured, while their influence on the rock salt barrier´s safety function and the robustness of the rock salt barrier can be assessed by a single quantity.

3.4 Comparison of different salt formations for HLW/SF disposal

In Germany, a new site selection process was started in order to identify the site that offers the best possible safety for the disposal of heat-generating HLW and SF.

Potential host rock formations are crystalline rock, clay, and salt. In accordance with the legal requirements, the site with the best possible safety has to be identified from a large number of potential sites that meet the minimum requirements and the weighting criteria according to the site selection act (StandAG 2020). Thus, it is necessary to compare different sites. In the case of salt, this even includes different salt formations – domal and bedded salt.

The stepwise site selection process has to meet high requirements. It must be transparent and comprehensible. At the same time, it undergoes extensive public participation. Naturally, the criteria describing the safety functions of a site must rely on a sound scientific and technical basis. However, it is helpful if these safety-related criteria are easy to understand.

The effective thickness of a rock salt barrier does not describe all aspects of the containment capability of a site and its robustness over time. However, it could support the site selection process by offering the possibility to compare rock salt formations among each other, taking

into account future potential evolutions and repository designs, the latter maybe based on a conceptual modular planning.

4 Summary and Conclusion

The so-called effective rock salt barrier denotes the area/volume that is decisive for the containment capacity of a radioactive waste repository. It is the "envelope" that offers resistance against fluid intrusion. To rate the rock salt´s integrity, two criteria – the dilatancy and the fluid pressure criterion – are currently applied. Both criteria allow a statement on the local loss of tightness in space and time. Whether this local loss of tightness induces a continuous pathway, however, cannot be detected without a systematic procedure.

This contribution presents a procedure that also takes into account the dilatancy and the fluid pressure criterion, but additionally simplifies the rating of the evolution of the rock salt barrier´s functionality as a whole, using a single quantity – the effective barrier thickness. It also allows showing the evolution of the rock salt barrier over time using the same single quantity.

Furthermore, this unique quantity can be used to optimize repository containment capability with respect to uncertainties, technical measures, and site-specific conditions in a transparent way.

5 References

BMU, 2010. Bundesministerium für Umwelt, Naturschutz und Reaktorsicherheit, Sicherheitsanforderungen an die Endlagerung wärmeentwickelnder radioaktiver Abfälle vom 30.09.2010

BMU, 2020. Bundesministerium für Umwelt Naturschutz und nukleare Sicherheit, Verordnung über Sicherheitsanforderungen und vorläufige Sicherheitsuntersuchungen für die Endlagerung hochradioaktiver Abfälle vom 6. Oktober 2020, (BGBl. 2094)

BOLLINGERFEHR, W., BERTRAMS, N., BUHMANN, D., EICKEMEIER, R., FAHLAND, S., FILBERT, W., HAMMER, J., KINDLEIN, J., KNAUTH, M., LIU, W., MINKLEY, W., MÖNIG, J., POPP, T., PRIEGNITZ, S., REINHOLD, K., SIMO, E., THIEMEYER, T., VÖLKNER, E. & WOLF, J. 2018. KOSINA - Concept developments for a generic repository for heat-generating waste in bedded salt formations in Germany; BGE TEC 2018-13BGE TECHNOLOGY GmbH, Peine.

CRISTESCU, N.D. & HUNSCHE, U. 1998. Time Effects in Rock Mechanics, In: Desai, C.S.; Krempl, E. (Hrsg.): Wiley Series in Materials, Modelling and Computation. Chichester: John Wiley & Sons, 1998

ESK, 2013. Stellungnahme der Entsorgungskommission; Langzeitsicherheitsnachweis für das Endlager für radioaktive Abfälle Morsleben (ERAM); 31.01.2013

KOCK, I., EICKEMEIER, R., FRIELING, G., HEUSERMANN, S., KNAUTH, M., MINKLEY, W., NAVARRO, M., NIPP, H.K. & VOGEL, P. 2012. Integritätsanalyse der geologischen Barriere. Bericht zum Arbeitspaket 9.1, Vorläufige Sicherheitsanalyse für den Standort Gorleben, GRS-286, Gesellschaft für Anlagen- und Reaktorsicherheit (GRS) mbH, ISBN 978-3-939355-62-5: Köln, GRS.

STANDAG, 2020. Standortauswahlgesetz vom 5. Mai 2017 (BGBl. I S. 1074), das zuletzt durch Artikel 1 des Gesetzes vom 7. Dezember 2020 (BGBl. I S. 2760) geändert worden ist

WOLF, J., POLSTER, M., STIELOW, B., MÜLLER-HOEPPE, N.& WOLLRATH, J. 2019.Treatment of Uncertainties with Respect to Geomechanical Modelling to Demonstrate Structural Stability and Integrity of the Geologic Barrier of a Radioactive Waste Repository in Rock Salt, BGE und BGE Technology, Ninth International Conference on Sensitivity Analysis of Model Output (SAMO-Conference), Barcelona.

Design and performance assessment of engineered barrier systems in a salt repository for HLW/SNF

Eric Simo[1,3]*, Edward N. Matteo[2], Kristopher L. Kuhlman[2]; Richard S. Jayne[2];
Paola León Vargas[1]; Philipp Herold[1]; Andree Lommerzheim[1]; Andreas Keller[1]

[1]BGE TECHNOLOGY GmbH, Germany; [2]Sandia National Laboratories, USA, [3]TU Freiberg, Germany

* eric.simo@bge.de

ABSTRACT: BGE TECHNOLOGY GmbH (BGE TEC) and Sandia National Laboratories (SNL) developed and jointly tested a methodology for the safety assessment of engineered barrier systems (EBS) for a high-level waste/spent nuclear fuel (HLW/SNF) repository in salt. Long-term isolation in such a repository is provided by a multi-barrier system including natural and engineered barriers. The salt provides the natural barrier, whereas the engineered barriers are different sealing components installed in the repository. The developed methodology is tested via a generic repository concept that is situated in a generic bedded salt formation. Based on this, a global model was generated, including relevant stratigraphic layers and underground openings of the repository. BGE TEC used this model to perform the integrity assessment of the shafts and drift sealings as main parts of the EBS. Simultaneously, SNL conducts the radiological performance assessment (PA). Both parts interact by an optimization of the EBS based on PA simulations and EBS-parameters. For this purpose, sensitivity analyses were incorporated into the PA simulation. This contribution presents the modeling and methodological approach used for BGE TEC and SNL for the design and performance assessment of EBS.

1   Introduction

RANGERS is an acronym for "Methodology for design and performance assessment of geotechnical barriers in a HLW repository in salt formations". It is an ongoing joint project between BGE TECHNOLOGY GmbH (Germany), hereafter BGE TEC, and Sandia National Laboratories (US). It aims to develop a methodological approach to design EBS and how to handle them in the course of performance assessments in repositories in salt. The EBS design and construction methodology is based on the existing knowledge and experience of BGE, BGE TEC, Sandia, and others. The methodology will then be tested on a generic repository system in Germany. Four project sub-goals are formulated:

- Compilation of existing knowledge and experience in the design of geotechnical barriers and compilation of new concepts and technologies on the subject of geotechnical barriers.

- Development of a methodology based on the state of the art in science and technology for the design and verification of geotechnical barriers.

- Preliminary design and verification of the geotechnical barrier system for selected repository systems based on the developed methodology.

- Comparison of design results according to the new methodology with results of previous design and assessment.

The current priority roadmaps of the US Department of Energy Office of Nuclear Energy (DOE-NE) Spent Fuel and Waste Science and Technology (SFWST) campaign as well as of Federal Ministry for Economic Affairs and Energy of Germany highlight the value of international collaboration. BGE TEC and Sandia envisage therefore a deep collaboration in the project. The expertise of BGE TEC on modeling-based design of the EBS will be used to dimension the generic repository. The expertise of Sandia on performance assessment of large repository

systems will be used to analyze the propagation of radionuclide through the engineered barrier systems and geochemical evolution of the generic repository design.

The current work summarizes the developed methodology for the design and verification of geotechnical barriers and describes the subsequent modeling concept necessary for the application of the proposed methodology. Finally, some numerical applications based on a generic bedded salt formation will be discussed.

2   Methodology

Based on international methodological standards, the evolution of HLW/SNF repositories in salt formations is analyzed in terms of a safety assessment, which means an assessment of the total system performance (IAEA 2012; NEA 2014). Safety and the safety demonstration concept for salt repositories take full credit for the favorable properties of salt formations, including low permeability and porosity, high thermal conductivity, and self-healing behavior (Bollingerfehr et al. 2016), (Fischer-Appelt 2013). The German repository concept is based on the safe containment of radioactive waste within the containment providing rock zone (CRZ), which requires the EBS (including the crushed salt backfill) to seal the perforation of the geological barrier by the mine excavations (BMU 2020). The long-term safety of the mined excavations will be ensured by backfilling them with crushed salt. Crushed salt acquires its sealing capacity through compaction due to the convergence of the underground openings. Convergence is accelerated by waste heat and by humidity in the repository and water content in the host rock. Eventually crushed salt backfill will reach the same mechanical and hydraulic properties as the intact salt host rock. Until this time, the EBS ensures the waste isolation.

The present methodology summarizes all aspects of design and integrity assessment of the EBS, as well as their treatment in an eventual integrated performance assessment. Starting from the regulatory framework, a safety concept is defined. This is a basis for the development of repository and sealing concepts for the selected geological site. The evolution of the resulting repository system can be analyzed through preliminary analysis of the Features, Events, and Processes (FEP) catalogue, which includes all properties and possible evolutions that may occur in the repository system over the performance period.

While a comprehensive FEP analysis is not usually performed until after a site has been selected and characterized, the RANGERS methodology includes it, since there are aspects of EBS performance that can be studied by means of a focused preliminary FEP analysis using EBS-relevant FEPs. Ultimately, process models, based upon numerical models and experiments, are used to assess the integrity of the EBS as well as its impact in the integrated performance assessment simulations. For this purpose, the link between the (preliminary) FEPs and performance assessment is a key aspect of the proposed methodology. Based on the FEPs, the relevant loads (disturbances) affecting the EBS can be identified for the integrity assessment. The relevant processes have also to be modelled and considered in the performance assessment. FEP interactions are described in scenarios. The relevant scenarios impacting the EBS and the repository can be derived from the FEP catalogue. A different procedure is provided for human intrusion impacts that are analyzed by stylized or "what if" type scenarios.

A reference scenario and two alternative scenarios were identified in the specific FEP analysis carried out for RANGERS. The reference scenario implies the EBS (i.e., shaft and drift seals) retains its function over 50,000 years, what is considered up to the next ice age in Germany (Müller-Hoeppe et al. 2012). It is expected that the hydro-geologic and topographic conditions will change significantly at the next ice age, so that an accurate prediction of the geochemical composition of the inflowing waters becomes impossible. The first alternative scenario involves the shaft seal losing its function but drift seals retaining their function. In the second alternative scenario, the opposite is assumed: the drift seals lose their function and the confinement of

the emplaced waste relies solely on the shaft sealing system. For each of these scenarios, three different cases for fluid migration are assumed:

- Case 1: Water flows from overburden through the shaft seal to the disposal zones
- Case 2: Gas migration inside the repository from corrosion of the casks
- Case 3: Water source inside the repository from inter-/ intragranular salt solutions

At this stage, numerical modeling is being performed to assess the integrity of the EBS and its impact on the integrated performance assessment (PA) simulations. For this purpose, the link between the two kinds of assessment is a key aspect of the proposed methodology. The main idea is to increase the physical realism of the repository PA simulations by comprehensive and specific analyses of the behavior of the EBS under thermal-hydrological-mechanical and chemical (THMC) conditions. The results of these analyses can be considered in the PA modeling, thus increasing realism and reducing the material and model uncertainties describing the EBS in the PA model. Figure 1 gives an overview of the proposed methodology.
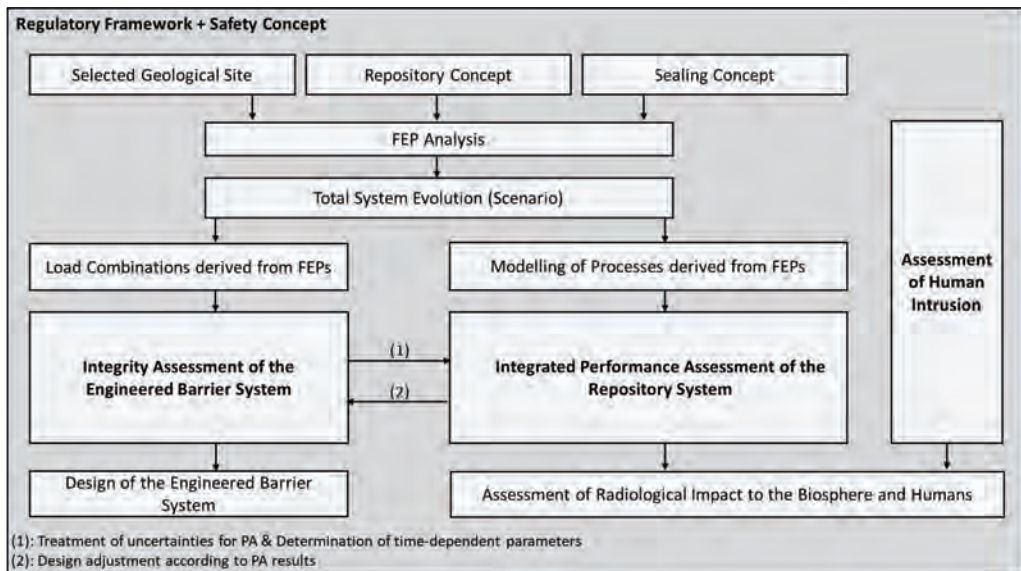
Figure 1: Methodology for the design and performance assessment of the EBS in a salt repository.

3   Modeling and verification concept

3.1   Integrity assessment of the Engineered Barrier System

Because the EBS is an engineered structure, the procedure for EBS performance assessment can rely on adequate regulations or recommendations. In Germany, the EBS is seen as a set of civil engineering structures, and their adequate design has to be verified by a technical proof in accordance with EUROCODE and respectively with its national implementations DIN EN 1997-1 and DIN EN 1990, (Müller-Hoeppe et al. 2012). The EUROCODE is a semi-probabilistic, reliability-oriented safety assessment concept using partial factors. In the USA, the Building Code Requirements for Structural Concrete (ACI 318-14) can be considered for the design of the EBS in compliance with other local regulations. The aim is to verify the required level of reliability of EBS construction by verifying that the loads acting on the structure do not exceed the inherent strength or resistance of the structure. For the specific integrity assessment of the EBS, the demonstration of sufficient hydraulic resistance (demonstration of

tightness) and the demonstration of the sufficient load bearing capacity (structural integrity) must be verified individually. Additionally, assessment of constructability must be included, due to the uniqueness of EBS as structure. For the demonstration of the tightness, the contact zone between seal and surrounding rock, as well as the excavation-damaged zone in the surrounding rock, must be considered in addition to the constructed barrier itself. Demonstration of structural integrity requires individual assessment of structural stability, crack limitation, and deformation limitation. For soil-based components, the filter stability must also be verified. The functional lifetime of the EBS significantly exceeds the usual functional lifetime of conventional civil engineering structures (50 to 100 y). To ensure applicability of the EUROCODE over the functional time of 50,000 years, a long-term stability criterion is introduced. This criterion assesses how the materials and components of the EBS may deteriorate over time in each material. Example phenomena affecting the long-term performance of the EBS materials include creep and shrinking in concrete, the geochemical evolution of the repository system or the effect of temperature. The overall verification concept for the EBS is summarized in Figure 2.
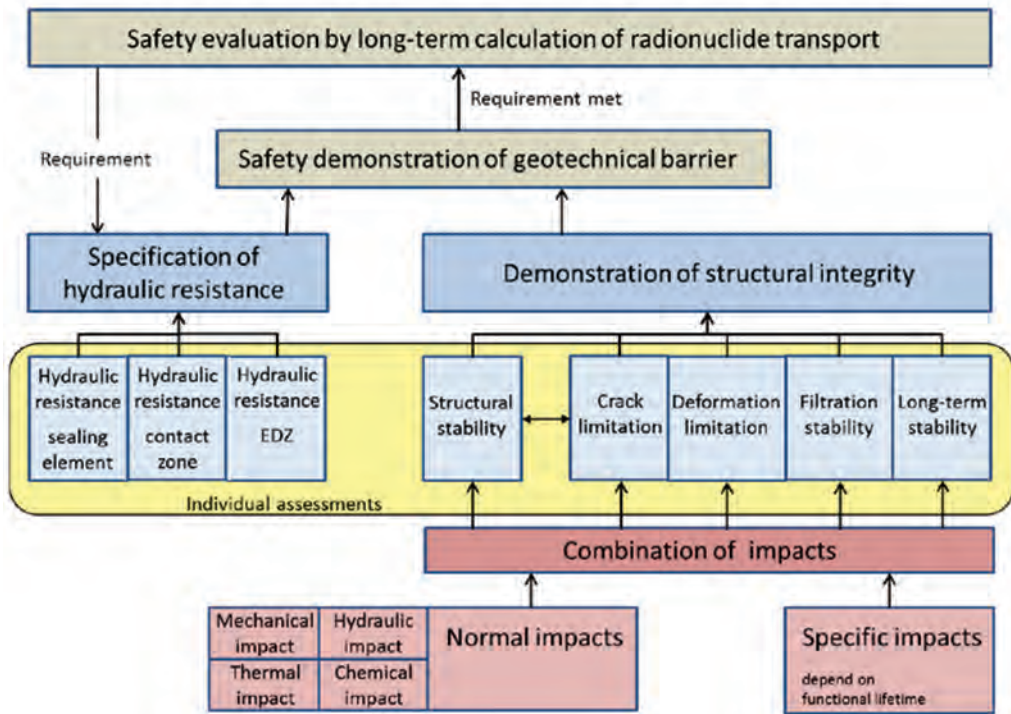
Figure 2: Verification concept for the integrity assessment of EBS based on German Regulatory Requirements (Müller-Hoeppe et al. 2012).

Due to the complexity of the processes taking place within the repository system, the determination of mechanical, thermal, hydraulic or chemical loads acting on the repository can only be carried out through numerical modeling. To verify the assessment criteria mentioned above, a methodological modeling approach has been developed within project RANGERS. In this regard, each possible scenario evolution case derived from the specific FEPs is considered a verification case. Based on the understanding of the processes considered in the scenarios, one determines the processes necessary to assess each of the criterion of the verification concept. For instance, the assessment of the hydraulic resistance of the EBS can obviously be derived by analyzing the hydraulic evolution of the repository system. The hydraulic resistance is verified when the resulting flow rate within the EBS stays below the limit set in the German repository safety concept (in the US, regulations do not apply to individual

system components). Processes can be combined if concurrent processes may affect the criterion under consideration. This is for example the case when compaction of crushed salt leads to a decrease of permeability in the system. In this case, the effect of the compaction in the assessment of the hydraulic resistance can be considered explicitly through coupled hydro-mechanical analyses or implicitly through the consideration of permeability and porosity due to compaction in the hydraulic analyses. The swelling behavior of bentonite can be considered similarly. Several individual assessments can be carried out simultaneously in the process modeling, once the material properties have been evaluated. This is for instance the case for the sealing element, the element-host rock contact zone, and EDZ, which are usually part of a single numerical model. When the material constitutive models allow, individual structural integrity assessments can also be combined. Following these reflections for each considered scenario, a simulation matrix can be constructed, connecting the scenarios (or the FEPs) with the assessment criteria coming from the verification concept (or the building codes). Such a matrix is presented in Figure 3 for the generic repository system analyzed within RANGERS.

	Specification of hydraulic resistance			Demonstration of structural integrity				
	Hydraulic resistance -sealing element	Hydraulic resistance -contact zone	Hydraulic resistance -EDZ	Structural stability	Crack limitation	Deformation limitation	Filtration stability	Long-term stability
Reference Scenario: The EBS retains its function over 50000 years								
Case 1: Water flow from overburden through the shaft to the disposal zones	H: determination of flow rate and passing time (constant permeability) HM: including compaction of crushed salt (time dependent permeability)			TM: structural analysis of the EBS components			No modelling intended	C: determination of geochemical stability of the sealing elements against water/brine T: temperature effects on EBS-materials
Case 2: Gas production inside the repository from corrosion of the casks	HM: crushed salt compaction under gas pressure build up			No modelling intended			No modelling intended	No modelling intended
Case 3: Water source inside the repository from inter-/ intragranular salt solutions	H: determination of flow rate and passing time (constant permeability) HM: including compaction of crushed salt (time dependent permeability)			TM: structural analysis of components inside the drift (concrete abutments)			No modelling intended	**Geochemical analysis:** determination of geochemical stability

BGE TEC	SANDIA

Figure 3: Modeling matrix for the integrity assessment of the EBS.

3.2   Integrated repository system performance assessment

To carry out PA simulations of the repository, the identified scenarios must be broken down into process groups affecting the components of the EBS and the geological barrier. Examples of processes derived from the scenarios include: advection and diffusion phenomena (linked to alteration of the EBS and to radionuclide transport), compaction of crushed salt, creep of salt, and heat propagation in the repository. The impacts of considering such processes in the PA must carefully be considered. Because of the large model domain, long time scales, and the need for uncertainty quantification in PA simulations, not all processes can be explicitly included. Sometimes separate process models must be used to understand the evolution and importance of key parameters over time, and how these effects can be best presented in PA. The current approach for Geologic Disposal Safety Assessment (GDSA) Framework in the US (LaForce et al., 2020) builds upon previous salt reference cases (Sevougian et al. 2016) for deep geologic disposal of defense-related HLW and SNF. Subsequent developments to the GDSA framework make it now possible to assess most of the relevant processes in a single numerical model (LaForce et al. 2020; 2021; Nole et al. 2021). Processes accounted for in the conceptual model include waste package degradation, waste form (UO_2) dissolution, equilibrium-controlled radionuclide sorption and precipitation/ dissolution, radioactive decay and ingrowth in all phases (aqueous, adsorbed, precipitate), coupled heat and fluid flow, and radionuclide transport via advection and diffusion. Implicit mechanical effects are not yet considered in GDSA PA simulator, but are part of process modeling (TOUGH-FLAC). Due to the massively parallel nature of PFLOTRAN (Hammond et al. 2014) it is possible to represent

the repository system with a high level of geometric and configurational complexity. The conceptual framework for the salt reference case focuses on the components of the engineered barrier and the natural barrier and assumes an undisturbed scenario outside the repository zone. In the same way alternative scenarios can be assessed.

Building on this background, the RANGERS project is deriving all relevant processes from the FEPs and scenario evolution that should be considered in the process modeling. Similar to the integrity assessment of the EBS, the different scenario evolution cases are assumed separately as verification cases. Here, concurring scenario evolution cases can be combined, depending on the capabilities of the simulator used. In PFLOTRAN, water and gas flow within the repository can explicitly consider the effects of gas production in the repository. For each analyzed verification case or combined cases, the target criteria assumed for the PA must be verified. Following the German regulations (BMU 2020, para 4), the safe containment of radionuclides in a repository should be demonstrated by assessing the mass of radionuclides discharged through the essential barriers. The mass fraction of radionuclides leaving the CRZ must stay below 10^{-4} cumulatively and 10^{-9} annually for the verification period. For spent fuel and high-level waste in the US, rather than a simple mass fraction, most recent regulations stipulate a maximum annual dose (15 mrem/yr before 10,000 years and 100 mrem/yr after) to a hypothetical exposed future individual (DOE 2008). Additionally, a groundwater protection standard is included to protect drinking water. In Germany, exposures due to discharges of radionuclides are negligible if the estimated additional effective dose for individuals of the population is at most in the range of 10 mSv (1,000 mrem) per calendar year, and for the deviating evolutions, the estimated additional effective dose for individuals of the population does not exceed 100 mSv per calendar year (BMU 2020 para 7).

4   Numerical applications

To test the developed methodology, a generic repository system is considered. The selected generic geological formation is a salt pillow formation developed within the project KOSINA (Bollingerfehr et al. 2018). Within this formation, a repository has been located where the salt formation is thickest. The repository planning assumes a maximum temperature of 200 °C at the surface of the waste casks. To meet this temperature requirement, the repository has been thermally designed to optimize the spacings between the drifts and between the disposal casks within the drifts. The resulting repository system is represented in Figure 4. The engineered barrier systems of this repository consists of four horizontal closure systems installed in the main drifts near sealing the two emplacement wings and of two shaft closure systems installed in both shafts. Each of these horizontal closures is 500 m long and is divided into two abutments made of magnesia (i.e., Sorel) concrete with a length of 50 m. In between the abutments, the 400 m long backfill seal is made of a mixture of crushed salt and clay, which itself seals after reconsolidation and compaction, taking over the long-term sealing function of the repository. For up to 50,000 years, the concrete abutments should limit any potential fluid migration within the repository mine and should protect the crushed salt seal against hydromechanical loads. The shaft closure system is made of several material following the concept of diversity and redundancy. The shaft closure is redundant to the drift closure. The sealing elements made of Sorel concrete, salt clay, and bentonite ensure the diversity and the redundancy of the closure system. If one seal loses its function, other seals made of different material will significantly reduce the chance that the same deficiency occurs in multiple elements.

Two simulation cases will be discussed in the following to illustrate the proposed methodology.
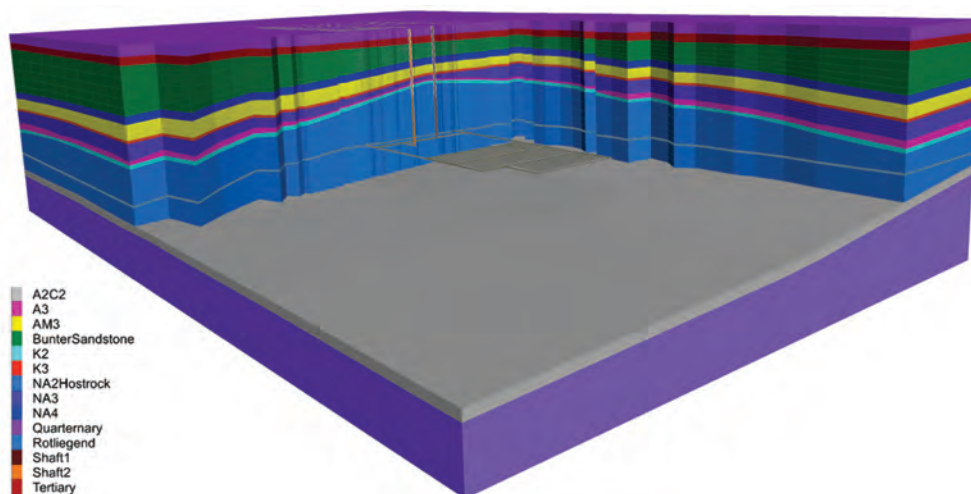
Figure 4: Generic repository system of a salt pillow formation used in RANGERS.

4.1   Verification of the long-term stability of EBS-components based on thermal simulation

High temperature can affect the long-term performance of the EBS materials. As part of the assessment of the long-term stability criterion, the temperature evolution in the repository is evaluated, see Figure 3. The numerical model for this assessment includes a detailed representation of the whole repository system with dimensions of several km on each side. The thermal load has been homogenized in each drift based on the heat power of the radioactive waste disposed in the drift. A more detailed analysis at the level of drift where each component within the drift is discretized have been performed during the thermal design of the repository. Due to the homogenization and reduction in the ability to represent steep temperature gradients between the cask and surrounding material, the maximum temperature in the homogenized drift is about 130°C compared to 200°C at the surface of the cask when individual disposal casks are represented in the numerical model. Nevertheless, this discrepancy only occurs in the nearfield and the developed numerical model is believed to be precise enough for the temperature evolution in the far field. Figure 5 shows the thermal evolution of the system after 500 years, by which time the repository mine has reached its maximum. In the figure, one can see how the heat propagates through the geological formation. This propagation is asymmetric between the two emplacement fields due to the different heat power of the different families of radioactive waste emplaced in the repository.

The evaluation of the temperature evolution in the engineered barriers is shown in Figure 6. In the first 1,000 years the maximum temperature increase in the shaft is about 5 °C. In the drift seal a maximum temperature increase of 20 °C occurs around 400 years. The drift seal starts subsequently to cool down reaching a temperature increase of less than 15 °C after 1200 years near the emplacement field. In regard to the long-term stability of the EBS components, one can conclude that due to the negligible temperature increase in the EBS, the temperature evolution will not endanger the long-term stability of the geomaterials used in the EBS. For instance, the sealing properties of clays and bentonite do not deteriorate when exposed to temperature up to 100 °C (Villar et al. 2020). Rock salt from bedded salt formation in Germany with a water content of 0.02 up to 2% - only shows disintegration ("decrepitation") linked to the formation of microcracks above approx. 250 °C, (Bräuer et al. 2016). Sorel and salt concretes are stable up to 90 °C. This temperature limit increases with the *in situ* confining pressure that is to be expected in repository conditions. Higher confining stress will reduce the development of fractures.
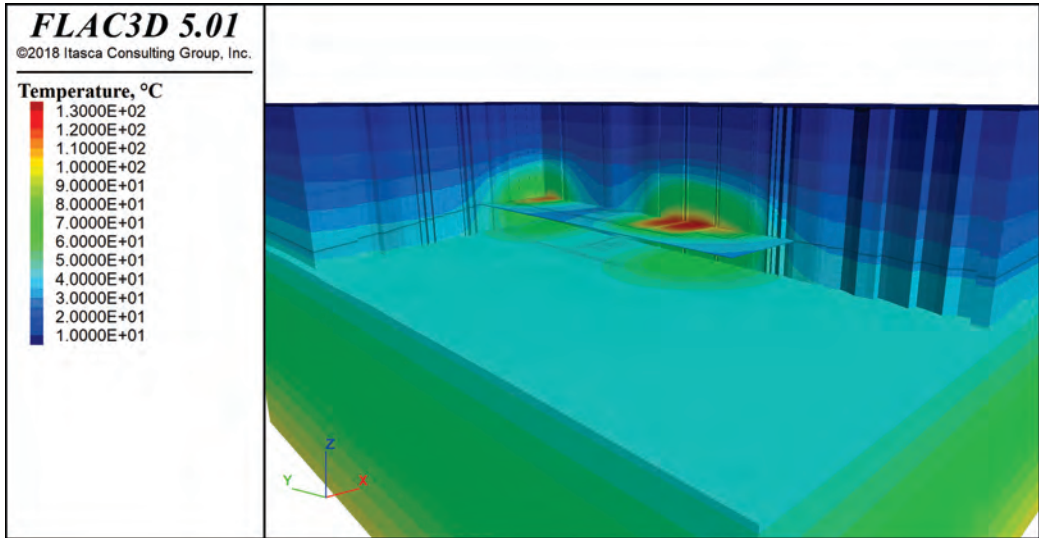
Figure 5: Thermal evolution in the repository system at 500 years.
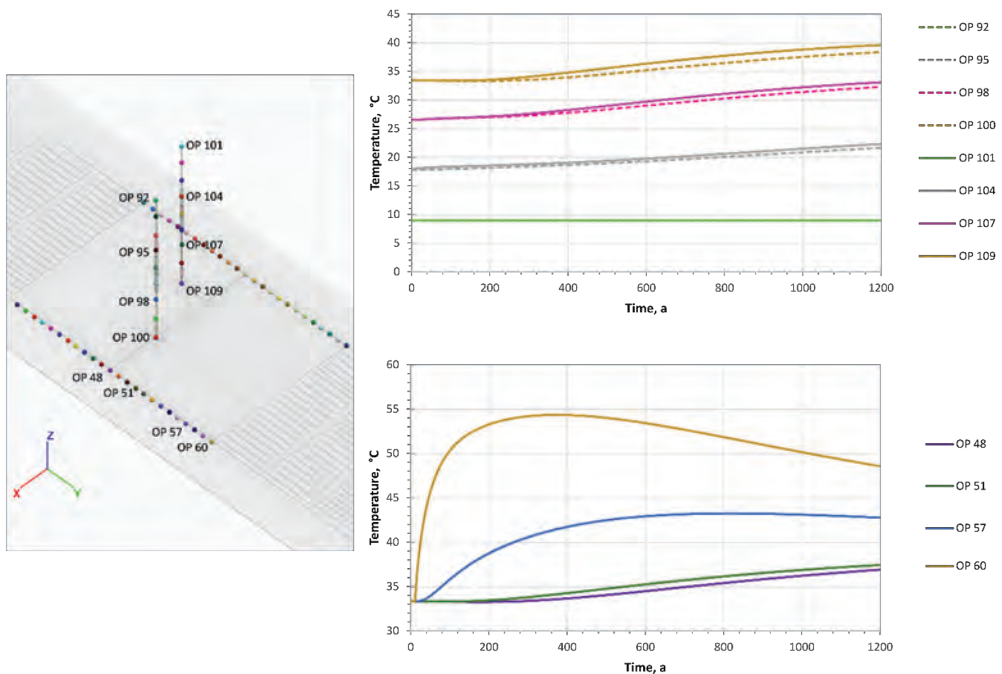
Figure 6: Evolution of the temperature in the shaft and drift closure systems.

4.2 Preliminary long-term evolution of the repository system for the reference scenario case

For a realistic PA, a coupling between the integrity assessment and the integrated performance assessment has been proposed in the methodology, see Figure 1. The coupling consists of determining the time dependent hydraulic behavior of the EBS components upon thermomechanical loads that occur due to the compaction of the salt host rock. These time-dependent parameters will then be used to describe the hydraulic behavior of the EBS in the scope of the performance assessment. This approach is useful as mechanical processes are

challenging to efficiently include in the PA due the long timescale of such simulations, and the typical requirement of uncertainty quantification through Monte Carlo, requiring numerous model runs.

In this context, thermal-mechanical analyses of the compaction of the crushed salt backfilled in the working mines of the repository have been realized. The simulations are based on the same numerical model shown in Figure 4 as well as on the thermal analyses in Figure 4 into incorporation of mechanical effects. The behavior of crushed salt is described by a visco-plastic model (Bertrams et al. 2020). The BGRa model is used to describe the creep behavior of rock salt (Bertrams et al. 2020). The resulting compaction of crushed salt (i.e., change in porosity from initial value of 0.35) at 100 years is depicted in Figure 7. The porosity distribution is a function of the thermal evolution at each location. Generally, the higher temperature correlates with higher compaction. With the determined porosity, the permeability in the repository can be determined. Both data will be subsequently used in performance assessment simulations.
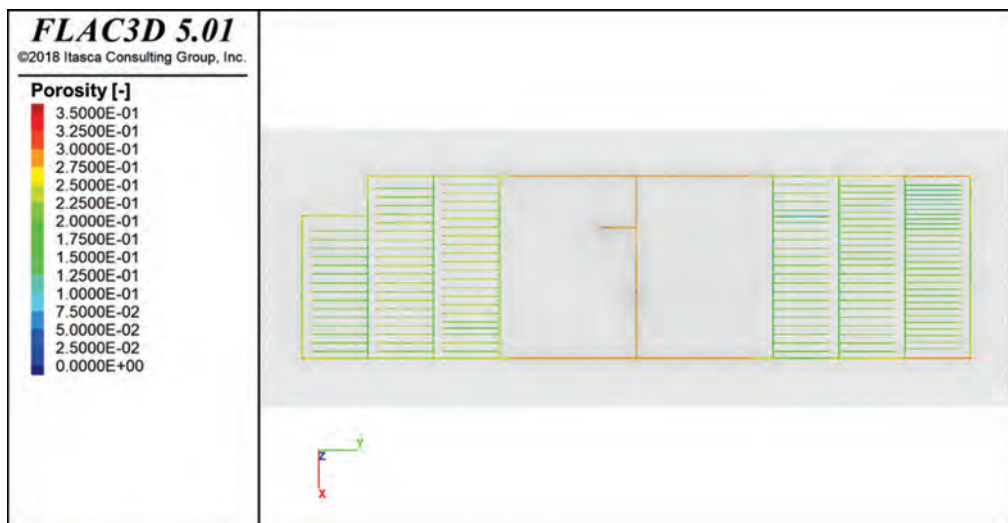
Figure 7: Porosity distribution in the drift system backfilled with crushed salt at 100 years

The results of the thermal-mechanical simulation, giving porosity through time will be included as inputs to PFLOTRAN, which will compute the thermal-hydrological response of a system on the same solution mesh, with the same thermal sources, and the specified porosity from the results of the thermal-mechanical model. Decreases in porosity lead to increases in both gas and liquid pressure, and since gas is more compressible than liquid, the liquid saturation tends to increase.

5   Conclusion

Within the framework of the project RANGERS a methodology for the generic design and performance assessment of EBS in a repository in salt has been developed. The methodology consists of a workflow to assess the integrity of engineered barrier systems in repositories in salt. The consideration of the EBS in the scope of integrated performance assessments is also part of the proposed methodology. To apply the methodology, a modeling and verification concept is proposed. The methodology is currently being applied on a generic repository system in a bedded salt formation. Based on this, a global model was developed to carry out different numerical assessments that have been derived from the application of the modelling concept. Two of these assessments have been presented in this work. Further assessments

will be carried out in the next phase of the project to completely design the EBS according to the regulations in force. The role of the EBS and the uncertainties concerning their treatment in the scope of performance assessment will be also investigated.

Acknowledgements

References

BMU (GERMAN FEDERAL MINISTRY FOR THE ENVIRONMENT, NATURE CONSERVATION AND NUCLEAR SAFETY) 2020. Verordnung über Sicherheitsanforderungen an die Endlagerung hochradioaktiver Abfälle (EndlagerSiAnfV). Bonn: BGBl, Teil I, No. 45, 14.10.2020.

BOLLINGERFEHR, W., BUHMANN, D., DÖRR, S., FILBERT, W., GEHRKE, A., HEEMANN, U., KELLER, S., KRONE, J., LOMMERZHEIM, A., MÖNIG, J., MRUGALLA, S., MÜLLER-HOEPPE, N., RÜBEL, A., WEBER, J.R. & WOLF, J. 2016. Evaluation of methods and tools to develop safety concepts and to demonstrate safety for an HLW repository in salt. TEC-15-2013-AB, Peine: DBE Technology GmbH.

BERTRAMS, N., BOLLINGERFEHR, W., EICKEMEIER, R., FAHLAND, S., FLÜGGE, J., FRENZEL, B., HAMMER, J., KINDLEIN, J., LIU, W., MAßMANN, J., MAYER, K.-M., MÖNIG, J., MRUGALLA, S., MÜLLER-HOEPPE, N., REINHOLD, K., RÜBEL, A., SCHUBARTH-ENGELSCHALL, N., SIMO, E., THIEDAU, J., THIEMEYER, T., WEBER, J.R. & WOLF, J. 2020A. RESUS: Grundlagen zur Bewertung eines Endlagersystems in flach lagernden Salzformationen bei einer höheren Auslegungstemperatur. Gesellschaft für Anlagen- und Reaktorsicherheit (GRS) gGmbH, Köln, GRS-570, ISBN 978-3-947685-56-1, August 2020.

BRÄUER, V., DOHRMANN, R., ENSTE, G., FAHLAND, S., GRÄSLE, W., HAMMER, J., HERTZSCH, J.-M., HESSER, J., HEUSERMANN, S., KAUFHOLD, S., LANDSMANN, B., MAßMANN, J., MERTINEIT, M., MRUGALLA, S., SCHÄFERS, A., SCHRAMM, M., SCHUSTER, K., SÖNNKE, J., STADLER, S., STÜHRENBERG, D., WEBER, J.R. & WEITKAMP, A. 2016. Beratung der Kommission „Lagerung hoch radioaktiver Abfallstoffe" gemäß § 3 Standortauswahlgesetz : Antworten der Bundesanstalt für Geowissenschaften und Rohstoffe zum Pflichtenheft „Literaturstudie Wärmeentwicklung-Gesteinsverträglichkeit", K-MAT 55, Bundesanstalt für Geowissen-schaften und Rohstoffe (BGR), Hannover.

BOLLINGERFEHR, W., BERTRAMS, N., MINKLEY, W., BUHMANN, D., MÖNIG, J., EICKEMEIER, R., POPP, T., FAHLAND, S., PRIGNITZ, S., FILBERT, W., REINHOLD, K., HAMMER, J., SIMO, E. KINDLEIN, J., THIEMEYER, T., KNAUTH, M., VÖLKNER, E., LIU, W. & WOLF, J. 2018. KOSINA - Concept developments for a generic repository for heat-generating waste in bedded salt formations in Germany. BGE TEC 2018-13, Peine: BGE Technology, GRS, BGR and IfG.

DEUTSCHES INSTITUT FÜR NORMUNG 2010 DIN EN 1990. - Eurocode: Grundlagen der Tragwerksplanung. Deutsche Fassung, Berlin: Beuth Verlag.

Deutsches Institut für Normung 2009 DIN EN 1997. - Eurocode 7: Entwurf, Berechnung und Bemessung in der Geotechnik – Teil 1: Allgemeine Regeln. Deutsche Fassung, Berlin: Beuth Verlag.

DOE (U.S. Department of Energy) 2008. Yucca Mountain Repository License Application. DOE/RW-0573, Update No. 1. Docket No. 63-001. Las Vegas, Nevada: U.S. Department of Energy, Office of Civilian Radioactive Waste Management. DIRS 185814 ACC: MOL.20081023.0041.

Fischer-Appelt, K., Baltes, B., Buhmann, D., Larue, J. & Mönig, J. K. 2013. Synthesebericht für die VSG – Bericht zum Arbeitspaket 13. Vorläufige Sicherheitsanalyse für den Standort Gorleben. GRS-290, Köln: Gesellschaft für Anlagen- und Reaktorsicherheit mbH (GRS).

Hammond, G.E., Lichtner, P.C. & Mills, R.T. 2014. Evaluating the performance of parallel subsurface simulators: An illustrative example with PFLOTRAN. Water Resources Research, 50 (1), 208-228.

IAEA 2012 The Safety Case und Safety Assessment of the Disposal of Radioactive Waste. IAEA Safety Standards. Spec.Safety Guide No. SSG-23, Vienna: International Atomic Energy Agency.

LaForce, T., Basurto, E., Chang, K., Jayne, R., Leon, R., Nol, M., Perr, F. & Stein, E. 2021. GDSA Repository Systems Analysis Investigations in FY2021. SAND2021-11691 R, Albuquerque: Sandia National Laboratories.

LaForce, T., Chang, K.W., Perry, F.V., Lowry, T.S., Basurto, E., Jayne, R., Brooks, D., Jordan, S., Stein, E., Leone, R. & Nole, M. 2020. GDSA Repository Systems Analysis Investigations in FY2020. M2SF-20SN010304052, Albuquerque: Sandia National Laboratories.

Müller-Hoeppe, N., Buhmann, D., Czaikowski, O., Engelhardt, H.-J., Herbert, H.-J., Lerch, C. & Xie, M. 2012. Integrität geotechnischer Barrieren Teil 1: Vorbemessung. Bericht zum Arbeitspaket 9.2. Vorläufige Sicherheitsanalyse für den Standort Gorleben. GRS-287, Peine, Braunschweig: DBE TECHNOLGY GmbH, Gesellschaft für Anlagen- und Reaktorsicherheit (GRS).

NEA 2014. The Safety Case for deep Geological Disposal of Radioactive Waste: 2013 State of the Art. Symposium Proc. 7-9, October 2013, Paris: Radioactive Waste Management, NEA/RWM/R(2013)9.

Nole, M., Leone, R., Park, H., Paul, M., Salazar, A., Hammond, G. & Lichtner, P. 2021. PFLOTRAN Development FY2021. SAND2021-8709 R, Albuquerque: Sandia National Laboratories.

Sevougian, S. D., Stein, E. R., Gross, M. B., Hammond, G. E., Frederick, J. M. & Mariner, P. E. 2016. Status of Progress Made Toward Safety Analysis and Technical Site Evaluations for DOE Managed HLW and SNF. SAND2016-11232R, Albuquerque: Sandia National Laboratories.

Stormont, J. C. 1987. Small-Scale Seal Performance Test Series "A" – Thermal/Structural Data through the 180th Day. SAND87-0178, Albuquerque: Sandia National Laboratories.

Vaughn, P., Sevougian, S. D., Hardin, E. L., Mariner, P. E. & Gross, M. B. 2013. Reference Case for Generic Disposal of HLW and SNF in Salt. Albuquerque: Waste Management Symposia.

Villar, M.V., Armand, G., Conil, N., de Lesquen, Ch., Herold, Ph., Simo, E., Mayor, J.C., Dizier, A., Li, X., Chen, G., Leupin, O., Niskanen, M., Bailey, M., Thompson, S., Svensson, D., Sellin, P. & Hausmannova, L. 2020. D7.1 HITEC. Initial State-of-the-Art on THM behaviour of i) Buffer clay materials and of ii) Host clay materials. Deliverable D7.1 HITEC. EURAD Project, Horizon 2020 No 847593. 214 pp.

Compaction of crushed salt for safe containment – Overview of phase 2 of the KOMPASS project

Larissa Friedenberg[1]*, Jeroen Bartol[3], James Bean[7], Oliver Czaikowski[1], Uwe Düsterloh[4], Ann-Kathrin Gartzke[5], Suzanne Hangx[8], Ben Laurich [5], Christian Lerch[2], Svetlana Lerche[4], Johanna Lippmann-Pipke[5], Wenting Liu[5], Christoph Lüdeling[6], Melissa Mills[7], Nina Müller-Hoeppe[2], Till Popp[6], Ole Rabbel[6], Michael Rahmig[2], Benjamin Reedlunn[7], Christopher Rölke[6], Christopher Spiers[8], Kristoff Svensson[5], Jan Thiedau[5], Bart van Oosterhout[8], Kornelia Zemke[5], Juan Zhao[4]

[1]Gesellschaft für Anlagen- und Reaktorsicherheit (GRS) gGmbH, Germany; [2]BGE TECHNOLOGY, Germany; [3]COVRA, Netherlands*; [4]Clausthal University of Technology (TUC),* Germany; [5]*Federal Institute for Geosciences and Natural Resources (BGR),* Germany; [6] *Institut für Gebirgsmechanik GmbH (IfG),* Germany; [7] *Sandia National Laboratories,* USA; [8] *Utrecht University,* Netherlands;

* larissa.friedenberg@grs.de

ABSTRACT: The KOMPASS project strives to improve the scientific basis behind using crushed salt for long-term isolation of high-level nuclear waste within rock salt repositories. Efforts to improve the prediction of crushed salt compaction began during the first phase of the KOMPASS project (KOMPASS-I, 2020). The second project phase (KOMPASS-II) just started in 2021. Its aim is foremost to quantify the effect of isolated experimental influencing factors on the compaction. Such influencing factors are for instance temperature, moisture or the chosen stress path. Used methods are laboratory tests, microstructural investigations and numerical simulations.

1   Introduction

In Germany, rock salt formations are possible host rock candidates for a repository for heat-emitting radioactive waste. Their safety concept includes a multibarrier system consisting of the geological barrier salt and geotechnical seals ensuring the safe containment. Due to its favorable properties and its easy availability (mined-off material), crushed salt is considered for backfilling of cavities and sealing measures in drifts and shafts. With time the creep of the surrounding rock salt leads to crushed salt's compaction due to convergence. Thereby, its initially high porosity in the range of 30 % - 40 % is thought to be reduced to a value comparable to the porosity of undisturbed rock salt (≤ 1 %). The compaction behavior of crushed salt is rather complex as it involves thermo-hydro-mechanical (THM) coupled processes (Kröhn et al. 2009; Hansen et al. 2014). Influencing factors are material intrinsic properties, like mineralogy, grain size distribution and humidity, as well as environmental conditions such as temperature, compaction rate or stress state. The current process understanding has some important gaps with respect to the material behavior. Thus, the experimental database and the numerical modelling need to be extended and validated, especially in low porosity ranges. Within the first phase of the KOMPASS project (KOMPASS-I) efforts to improve the prediction of crushed salt compaction began and are followed up in the second phase (KOMPASS-II) beginning in the middle of 2021.

2   Investigation work in KOMPASS-II

The KOMPASS project comprises working areas of experimental investigations, microstructural examinations and numerical simulation, all strongly connected to each other. The laboratory investigations serve to improve process understanding regarding the material behavior depending on various boundary conditions. Additionally, examinations on micro-scale are performed, relating microstructures to deformation mechanism, estimating the influence of

humidity by observing dissolution/precipitation processes and to create a basis to compare crushed salt compacted in laboratory and in-situ. Therein, varying abundancies of microstructural deformation indicators are related to variations in the experimental compaction conditions.

Furthermore, the planning of the laboratory program servers the second aim of considering the numerical needs for model improvement.

2.1 Experimental investigations

Basis for the experimental investigation is the KOMPASS reference material which was specified in the beginning of the project (KOMPASS-I 2020). With the determination of an easily available and reproducible reference material generic investigations are possible independent from site-specific material conditions, like lithological composition and grain size distribution. Crushed salt representing the Staßfurt-sequence in a bedded Zechstein salt formation with an optimized grain size distribution was chosen (Figure 1).
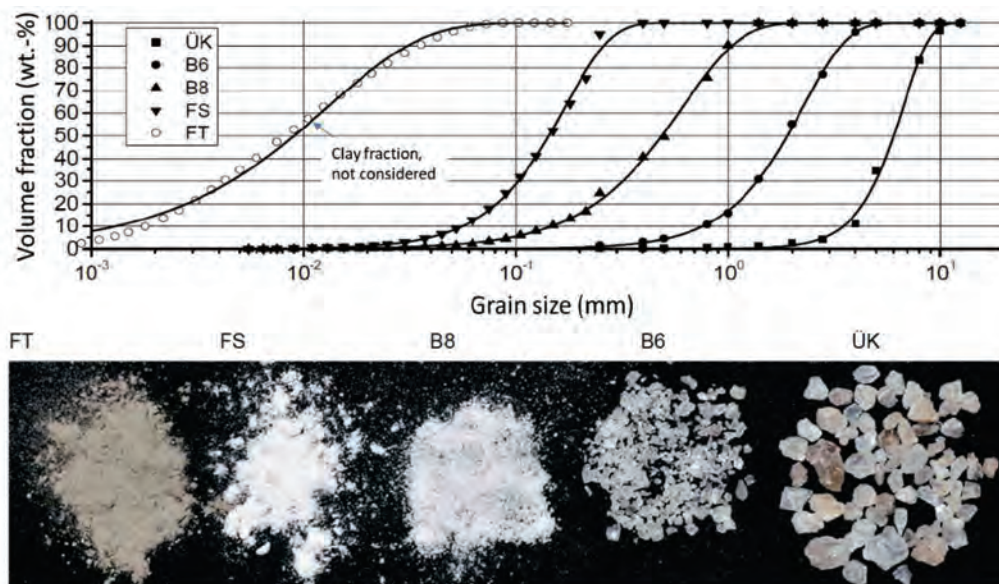
Figure 1:Salt grain fractions and grain size distribution of the KOMPASS reference material (Glaubach et al. 2016)

2.1.1 Pre-compaction methods

Within KOMPASS-I two new pre-compaction methods were developed. In general, pre-compaction aims to rapidly produce cohesive samples from the lose reference material within days to weeks. The samples are desired to exhibit a low porosity and a natural grain structure, such that they can subsequently be used for long-term, in-situ realistic THM investigations that commonly last for month to years. Without the rapid pre-compaction procedure, experiments with in-situ like strain rates would even last for tens of years before reaching the desired small porosity states.

First, there is the plane-strain compaction method developed by the TUC, where fixed end plates and an increasing radial confining pressure simulate the radial compaction of crushed salt due to drift convergence (Figure 2a). Second, the IfG applied a so-called "Big-compaction cell" with a diameter-to-height ratio of 0.5 facilitating the controlled pre-compaction of a

significant sample with a specified porosity. From this large sample, several subsamples were taken with different orientations and geometry (Figure 2b).
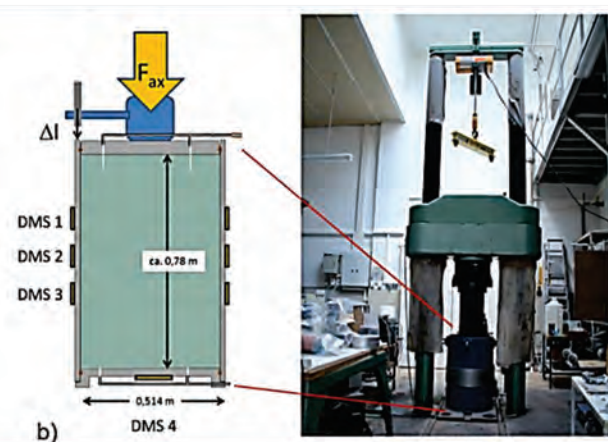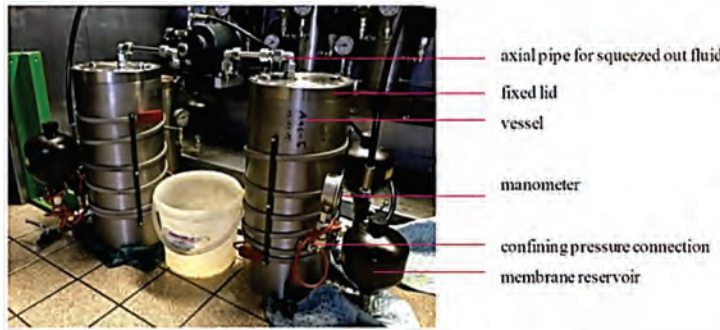
Figure 2: Pre-compaction methods developed in KOMPASS. a) Plane-strain compaction cell of TUC, b) "Big-compaction cell" of IfG (KOMPASS-I 2020)

Both methods are able to successfully produce various specimen varying in water content, time and applied stress (Figure 3). In the next step (KOMPASS-II), it is required to establish of reproducible and predictable correlations between stress regime, test duration, moisture and the respective target tensity.
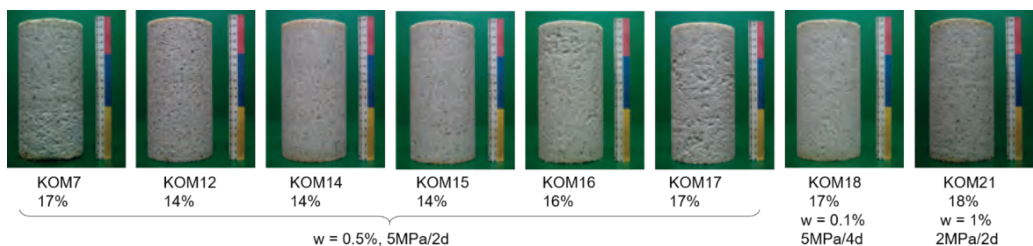
Figure 3: Successfully produced pre-compacted crushed salt specimen with the plain-strain approach – water content and confining pressure below

2.1.2   Long-term compaction experiments

Systematic investigations of crushed salt compaction and hydraulic behavior are needed to demonstrate its long-term tightness as backfill. Therefore, an extended laboratory program for the systematical analysis of the THM-coupled behavior of crushed salt was elaborated aiming at the factors influencing compaction behavior (Figure 4). These are:

▪   Porosity

▪   Stress regime (isotropic, deviatoric)

▪   Moisture content

▪   Stress geometry (isotropic, TC/UC or TE conditions)

▪   Test method (strain-controlled vs stress controlled)

▪   Pre-compaction method

Besides testing pre-compaction methods, due to project specific time restrictions prioritized experiments were chosen and first experiments are already executed within KOMPASS-I. One long-term experiment was started within KOMPASS-I by TUC and executed over 750 days continuing within KOMPASS-II. It comprises five different influencing factors and therefore, covers a wide range of planned experiments (Düsterloh et al. 2022).
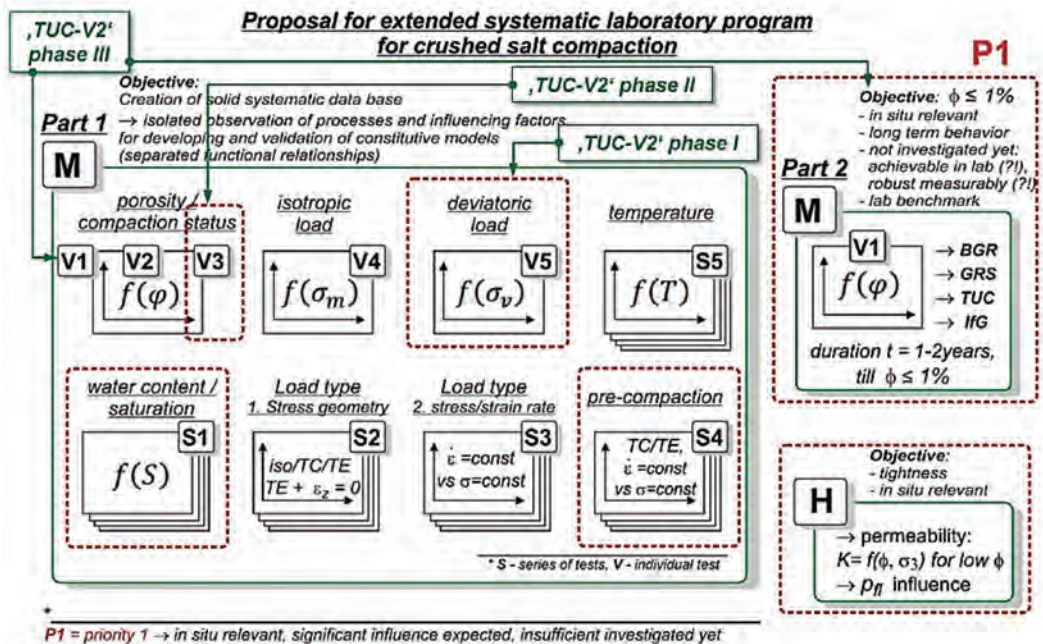
Figure 4: Test program for the systematically analysis of the THM-coupled behavior of crushed salt with prioritization and allocation of the TUC-V2 test (KOMPASS-I 2020)

Especially, the hydraulic behavior and the change of transport properties during the crushed salt compaction is of great importance for the long-term sealing function. Thus, permeability measurements will be performed during or after sample consolidation as part of the laboratory program. However, the measurement and quantification of low porosity ranges is challenging, and therefore part of current research. In the frame of KOMPASS-I, the IfG developed a design for the "New IfG-compaction cell" allowing a record of measurement data during the testing

time and combining parallel measuring methods for determination of porosity and permeability (Figure 5). Realization of this compaction cell is planned within KOMPASS-II.
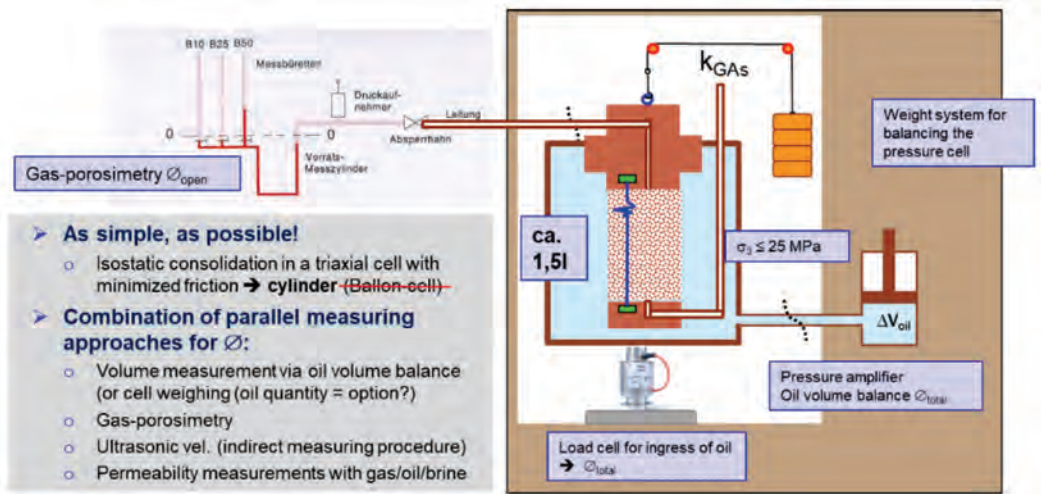
Figure 5: General design concept of the "New IfG-compaction cell" (KOMPASS-I 2020)

2.2   Microstructural investigations

The compaction of crushed salt is facilitated by several microstructural deformation mechanisms, which are well known from former material studies, foremost in the field of rock salt rheology (Hansen et al. 2014; Jackson & Hudec 2017; Spiers et al. 1990; Urai & Spiers 2007). However, each mechanisms' overall contribution to the crushed salt compaction remains yet unknown and varies depending on compaction state and acting material as well as environmental influencing factors. Within KOMPASS-I microstructural investigation methods were established. In KOMPASS-II, the abundancy of microstructural deformation indicators is related to the compaction conditions. Moreover, the micro-structure of samples with and without rapid pre-compaction are compared. The latter samples originating from real-used backfill material in the Sigmundshall mine near Hannover, Germany. Therefore, Figure 6 compares the abundance of microstructural deformation indicators for the raw material, pre-compacted crushed salt and long-term compacted crushed salt. The given quantity is based on subjective impression only and in total 16 thin sections were examined so far. Figure 6 also shows three exemplary micrographs to illustrate indicators for cataclasis (intra-granular fracturing), diffusive mass transfer by pressure solution (flush grain boundaries and deformation at grains' edges) and intracrystalline deformation by dislocation creep (subgrain formation).
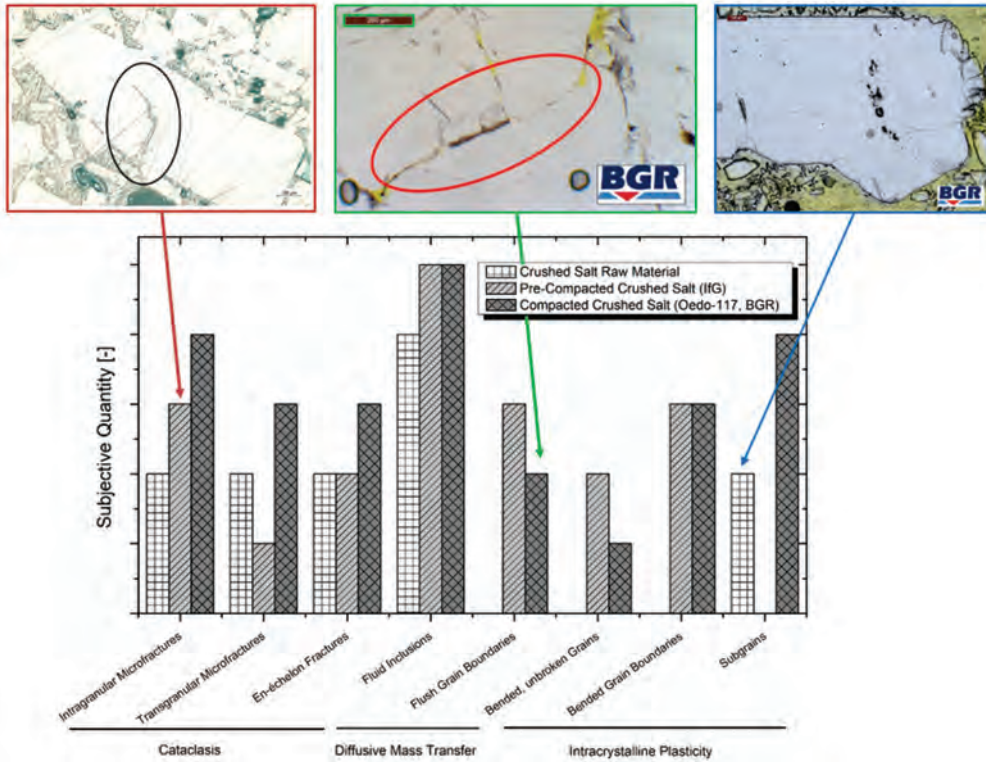
Figure 6: Observed microstructures in different compaction stages of the KOMPASS reference material. Red: intra-granular fracture in pre-compacted material, green: flush grain boundaries in long-term compacted material, blue: subgrains in raw, lose material (fine black lines inside the grain mark the subgrain boundaries). Bottom: subjective quantities of observed microstructures. Note: No subgrains were determined for pre-compacted IfG-samples (Modified after KOMPASS-I 2020)

2.3 Numerical modelling

Several constitutive models for crushed salt are currently in use for numerical simulations. Within KOMPASS-I, a wide range of models are applied and comparatively analyzed (Figure 7), therefore, the models were separated to phenomenological models and models with microstructural grounds (KOMPASS-I).
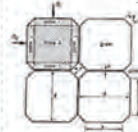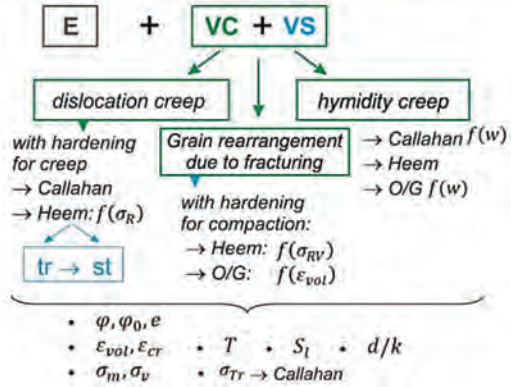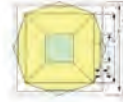
Figure 7: Schematic composition of the material models for crushed salt: basic structures and considered main influencing factors in comparison (KOMPASS-I 2020)

The current available constitutive models were investigated by benchmarking against laboratory data of three long-term triaxial tests. Figure 8 shows an example the differently modelled volumetric strain as well as the actual, measured strain for the long-term multistage test TUC-V2. Additionally, two inset diagrams of the test are given, focusing on strain and strain rate from runtime day 124 to 148 (KOMPASS-I 2020). The detail shows that the deviatoric load phases cause inaccuracies in the recalculation for almost all tested models. From these results and the comparative analysis, the need for further developments is evident. In correlation with the laboratory plans for KOMPASS-II (Figure 4) a systematic model validation of a wide range of influencing factors is possible due to calibration and benchmarking of the crushed salt constitutive models against the long-term compaction tests.
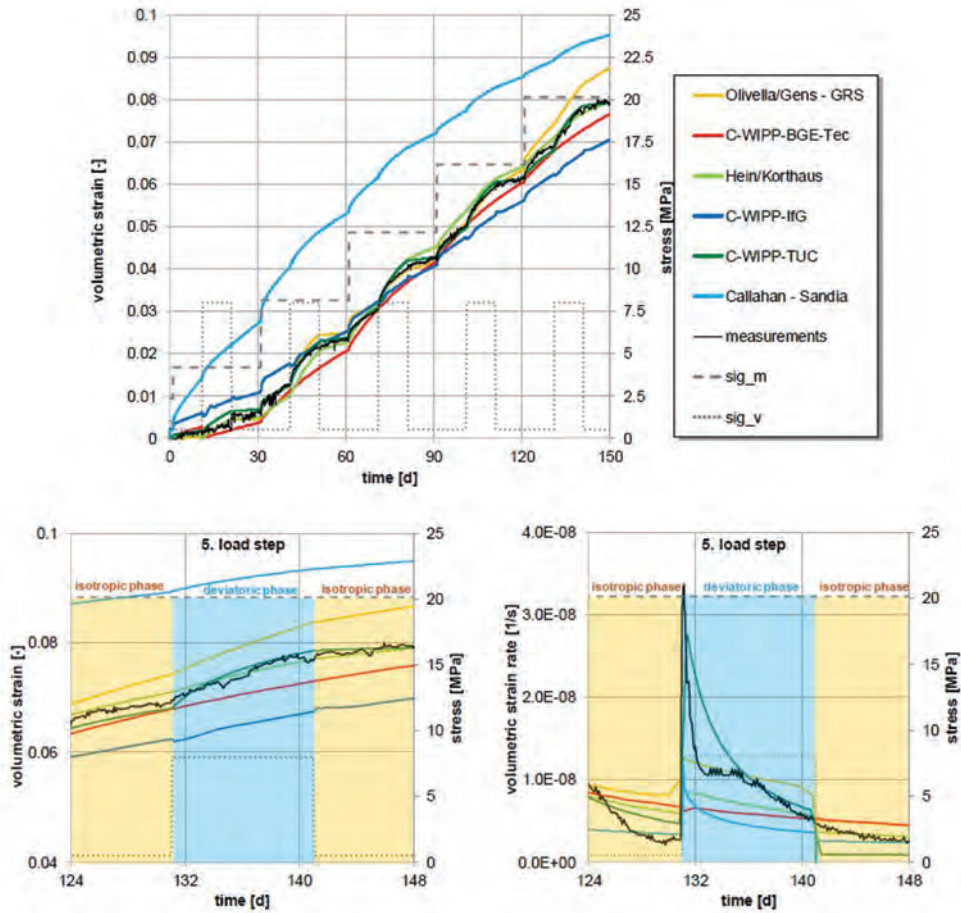
Figure 8: Recalculation results for the long-term multistage test TUC-V2 (KOMPASS-I 2020)

3   Conclusions

Based on the outcomes of KOMPASS-I, the improvement of the scientific basis behind using crushed salt as backfill for high-level nuclear waste is continued in KOMPASS-II. One of the main objectives is the microstructural comparison of grain structure of pre-compacted samples to in-situ compacted material for the verification of the new pre-compaction methods. Additionally, the microstructural methods will be further developed and applied for investigating humidity influence on compaction behavior. Another main objective is the further development of pre-compaction methods and the execution of long-term experiments. In correlation with the laboratory work, calibration and benchmarking will be done for improving the numerical models for crushed salt.

Acknowledgements

References

GLAUBACH, U., HOFFMANN, M. 2016. SCHACHTVERSCHLÜSSE FÜR ENDLAGER FÜR HOCHRADIOAKTIVE ABFÄLLE – ELSA-PHASE 2; Konzeptentwicklung für Schachtverschlüsse und Test von Funktionselementen von Schachtverschlüssen; Teilbericht zum Arbeitspaket §Laborversuche zu den Arbeitsschritten 2.1 bis 2.6 Vorhaben ELSA – Phase 2 (FKZ 02E11193A), TU-BA Freiberg

DÜSTERLOH, U., LERCHE, S. 2021. Methodology of structured development and validation of multiphysical constitutive models using the example of crushed salt compaction under 3D THM load conditions, Interdisziplinäres Forschungssymposium für die Sicherheit der nuklearen Entsorgung, Berlin

DÜSTERLOH, U., LERCHE, S., SARUULBAYAR, N. 2022. Crushed salt compaction – a new approach for the lab test analysis, physical modelling and numerical simulation, Part 1: Development and validation, SaltMechX 2022

HANSEN, F.D., POPP, T., WIECZOREK, K. & STÜHRENBERG, D. 2014. Granular Salt Summary: Reconsolidation Principles and Applications. Fuel Cycle Research & Development; FCRD-UFD-2014-000590. SAND2014-16141R, 2014.

JACKSON, M.P.A. & HUDEC, M.R. 2017. Salt Tectonics Principles and Practice. Cambridge University Press, Cambridge, United Kingdom, 2017. ISBN: 978-1-107-01331-5.

KOMPASS-I 2020. CZAIKOWSKI, O., FRIEDENBERG, L., WIECZOREK, K., MÜLLER-HOEPPE, N., LERCH, CH., EICKEMEIER, R., LAURICH, B., LIU, W., STÜHRENBERG, D., SVENSSON, K., ZEMKE, K., LÜDELING, CH., POPP, T., BEAN, J., MILLS, M., REEDLUNN, B., DÜSTERLOH, U., LERCHE, SV. & ZHAO, J. 2020 Compaction of crushed Salt for the safe Containment. KOMPASS. Gesellschaft für Anlagen- und Reaktorsicherheit (GRS) gGmbH, GRS-608; Köln.

KRÖHN, K.P., STÜHRENBERG, D., HERKLOTZ, M., HEEMANN, U., LERCH, CH. & XIE, M. 2009. Restporosität und -permeabilität von kompaktierendem Salzgrus-Versatz Repoperm – Phase 1. Gesellschaft für Anlagen- und Reaktorsicherheit (GRS) gGmbH, GRS-254, Köln, 2009.

SPIERS, C.J., SCHUTJENS, P.M.T.M., BRZESOWSKY, R.H., PEACH, C.J., LIEZENBERG, J.L. & ZWART, H.J. 1990. Experimental determination of constitutive parameters governing creep of rocksalt by pressure solution. From Knipe, R.J. & Ruter, E.H. (eds) 1990. Deformation Mechanisms, Rheology and Tectonics, Geological Society Special Publication No. 54, pp. 215-227.

URAI, J.L. & SPIERS, C.J. 2007. The effect of grain boundary water on deformation mechanisms and rheology of rocksalt during long-term deformation. Proceedings of the 6th conference on the mechanical behaviour of salt, 'SaltMech6', Hannover, Germany, 22-25 May 2007.

Laboratory and numerical analysis for the simulation of crushed salt compaction behavior

Larissa Friedenberg[1]*, Sebastià Olivella[2], Uwe Düsterloh[3]

[1]Gesellschaft für Anlagen- und Reaktorsicherheit (GRS) gGmbH, Germany; [2]Universitat Politècnica de Catalunya (UPC), Spain; [3]*Clausthal University of Technology,* Germany

* larissa.friedenberg@grs.de

ABSTRACT: The paradigm changes in the safety case for a repository of heat-emitting radioactive waste and the necessity of a qualified prognosis of its long-term behavior results in extended requirements regarding the understanding and modelling of crushed salt compaction behavior for a possible repository in rock salt. In the current state, some uncertainties with respect to the existing database and process understanding of crushed salt compaction still remain, especially for the numerical modelling of the crushed salt compaction process. This paper presents an insight in a PhD work with the objective to improve the numerical simulation of crushed salt compaction with CODE_BRIGHT. First, the role of crushed salt and the necessity of process understanding in its entirety are described in the introduction. In Section 2, the methodologic approach is outlined which includes first numerical studies for characterizing shortcomings (Section 3), and second, an approach for laboratory experiments (Section 4) to gain deeper process understanding.

1   Introduction

Rock salt is considered as a possible host rock formation for the deep geological disposal of heat-emitting radioactive waste in Germany. The safety concept of a repository in rock salt is based on a multibarrier system including the geological barrier salt, geotechnical seals and the backfill material. Immediately after disposal, the sealing function will be provided by the waste matrix, waste casks and geotechnical barriers. In the long-term, the sealing function will be given by the rock salt as geological barrier and the backfilling of open cavities and shafts with crushed salt.

Crushed salt will be used as long-term stable backfilling material due to its favorable properties and its easy availability (mined-off material). The compaction of crushed salt is driven by the creep of the surrounding rock salt resulting in natural compaction by convergence. It is expected that during compaction, the porosity and permeability of crushed salt decreases down to barrier properties comparable to undisturbed rock salt (≤ 1 %).

A qualified prognosis of long-term behavior of crushed salt is needed, which results in extended requirements regarding the understanding of the compaction behavior which is pretty complex and involves several thermo-hydro-mechanical (THM) coupled processes (Kröhn et al. 2009; Hansen et al. 2014). Compaction behavior is influenced by internal properties, like grain size distribution, mineralogy and humidity, as well as boundary conditions such as temperature, compaction rate or stress state. In the current state, some uncertainties with respect to database and process understanding still remain, especially for the numerical reproduction of crushed salt compaction processes.

2   Methodology

The methodological approach is characterized by a combination of laboratory studies and numerical investigations. First, the existing and well documented database about crushed salt was studied with the aim of carving out laboratory tests suitable for the investigation process.

The following THM-coupled long-term tests were estimated to be appropriate for further numerical investigations:

- 3 THM-coupled oedometric tests performed by GRS in frame of the REPOPERM2 project (Kröhn et al., 2017)

- 2 triaxial tests (TK-031 & TK-033) performed by the Federal Institute for Geosciences and Natural Resources (BGR) (KOMPASS-I 2020)

- 1 triaxial test (TUC-V2) performed by the Clausthal University of Technology (TUC) (KOMPASS-I 2020)

These experiments were chosen considering the complex compaction behavior of crushed salt which is influenced by several parameters like internal material properties as well as boundary conditions (Table 1).

Table 1: Influencing factors (KOMPASS-I 2020)

Internal properties	Boundary conditions	
- Grain size distribution	- Temperature	- Isotropic stress path
- Mineralogy	- Compaction rate	- Deviatoric stress path
- Humidity	- Stress state	- Stress geometry
	- Pre-compaction	- Stress type
	- Porosity	

The selected experiments were re-simulated using the finite element (FEM) code CODE_BRIGHT with the objective to determine the quality of numerical reproduction and deficits in the simulation of the crushed salt compaction process. Therefore, the handling of the influencing factors within the numerical approach was considered and compared to the laboratory results. The numerical work is shown in Section 3.

Additionally, laboratory experiments will be performed parallel to the KOMPASS-II project. Within the KOMPASS-I project a synthetic and easily available reference material (KOMPASS reference material) was specified as basis for different experimental investigations (KOMPASS-I 2020). Thus, the influence of some internal material properties as grain size distribution and mineralogy could be neglected and comparability is increased. The crushed salt originates from the Sondershausen mine in Germany representing the Staßfurt-sequence in a bedded Zechstein formation. An optimized grain size distribution was chosen with a maximum grain size of 8 mm (KOMPASS-I 2020).

In KOMPASS-I, an extended laboratory program was developed for an isolated investigation of the various influencing factors which are specified in Table 1 (KOMPASS-I 2020). Parallel to this program, the planned laboratory experiments will investigate the influence of mean stress and deviatoric stress on the compaction behavior of crushed salt. The laboratory approach is presented in Section 4.

3   Numerical approach

3.1   Constitutive model for crushed salt in CODE_BRIGHT

For the numerical modelling, the finite element (FEM) code CODE_BRIGHT developed at the Polytechnical University of Catalunya (Barcelona) is applied. Originally, it was developed on a

new general theory for saline media but generalized with time for modelling THM-coupled processes in porous geological media. The theoretical approach is based on an idealized microstructure arrangement which is composed by a regular arrangement of polyhedrons (Olivella & Gens, 2002). For pre- and post-processing, the GiD system is used which is developed by the International Center for Numerical Methods in Engineering (CIMNE) (Olivella et al., 2021).

The model for crushed salt in CODE_BRIGHT is based on a microscopical approach and is described by an additive approach of elastic, creep and viscoplastic strain rates (Olivella et al. 2021).

$$\dot{\varepsilon} = \dot{\varepsilon}_{el} + \dot{\varepsilon}_c + \dot{\varepsilon}_{vp} \tag{1}$$

For the description of the linear elastic material behavior the generalized Hook's law is used in combination with a variation of Young's modulus with porosity (Olivella et al. 2021).

$$E = E_0 + (\Phi + \Phi_0)\frac{dE}{d\Phi} \geq E_{min} \tag{2}$$

The creep part covers two mechanisms: fluid assisted diffusional transfer (FADT) and dislocation creep (DC) which allows to simulate humidity creep, as well as mechanisms described by dislocation theory.

The FADT mechanism is dominating for low stresses and low temperatures. Its deformation process is based on dissolution and precipitation processes of salt and its migration through the liquid phase. The gradient in the chemical potential induced by differences in stress contacts is the driving force for diffusion, additionally the presence of humidity is an important factor. The implementation in CODE_BRIGHT is based on the extensive studies by Spiers et al. (1986, 1988, 1990) and Schutjens (1991).

The strain rate is computed as

$$\dot{\varepsilon}_{FADT} = \frac{1}{2\eta^d_{FADT}}(\sigma' - p'I) + \frac{1}{3\eta^v_{FADT}}p'I \tag{3}$$

$$\frac{1}{\eta^v_{FADT}} = \frac{16B(T)\sqrt{S_l}}{d_0^3}g^v_{FADT}(e) \tag{4}$$

$$\frac{1}{2\eta^d_{FADT}} = \frac{16B(T)\sqrt{S_l}}{d_0^3}g_d^{FADT}(e) \tag{5}$$

$$B(T) = \frac{A_B}{RT}exp\left(\frac{-Q_B}{RT}\right) \tag{6}$$

$$g^v_{FADT}(e) = \frac{g^2}{(1+e)} \tag{7}$$

$$g^d_{FADT}(e) = \frac{3g^2e^{3/2}}{(1+e)} \tag{8}$$

$$g = \frac{1}{(1-f)^2} \tag{9}$$

$$f = \sqrt{\frac{2e}{3(1-e^{3/2})}} \tag{10}$$

where $\sigma' = \sigma - P_f$ with $P_f = \max(P_g, P_l)$ is the effective stress, $p' = p - P_f$ is the effective mean stress, S_l is the degree of liquid saturation, d_0 is a factor representing the grain size, A_B

is a pre-exponential parameter, Q_B is the activation energy, R is the gas constant, T is the temperature and e is the void ratio.

The DC mechanism groups several strain mechanisms described by dislocation theory due to their representativeness by power-law terms. The most important mechanism referred to this theory is dislocation climb. The strain rate definition is based on the well-known power law for rock salt:

$$\dot{\varepsilon}_{ij}^{DC} = \frac{1}{\eta_{DC}^d} \Phi(F) \frac{\partial G}{\partial \sigma'} \tag{11}$$

$$F = G = \sqrt{q^2 + \left(\frac{-p}{\alpha_p}\right)^2} \tag{12}$$

$$\Phi(F) = F^n \tag{13}$$

$$\alpha_p = \left(\frac{\eta_{DC}^v}{\eta_{DC}^d}\right)^{\frac{1}{1+n}} \tag{14}$$

$$\frac{1}{\eta_{DC}^v} = A(T)g_{DC}^v(e) \quad \frac{1}{\eta_{DC}^d} = A(T)g_{DC}^d(e) \tag{15}$$

$$g_{DC}^v(e) = 3(g-1)^n f g_{DC}^d(e) = \left(\frac{\sqrt{1+g+g^2}}{3}\right)^{n-1} \left(\frac{2g+1}{3}\right) f + \frac{1}{\sqrt{g}} \tag{16}$$

$$A(T) = A_A \exp\left(-\frac{Q_A}{RT}\right) \tag{17}$$

where G is the flow rule, F is the stress function, Φ is a scalar function, n is the power coming from rock salt power law, g_{DC}^v and g_{DC}^d are non-linear functions of void ratio which are part of the viscosities (Eq. 15), A_A is a pre-exponential parameter, Q_A is the activation energy, R is the gas constant and T is the temperature. The definitions for stresses and the geometrical functions g and f are following the explanations addressing the FADT mechanism.

With the addition of a viscoplastic law, irreversible processes changing the structure of the material, like grain reorganization and sliding, are captured, also including material hardening due to compaction (Olivella & Gens 2002). The following set of equations is defined:

$$\dot{\varepsilon}_{VP} = \Gamma \langle \Phi(F) \rangle \frac{\partial G}{\partial \sigma} \tag{18}$$

$$\Phi(F) = F^m \tag{19}$$

$$G = F = q^2 - \delta^2(p_0 p' - p'^2) \tag{20}$$

$$\Gamma = \Gamma_0 \exp\left(\frac{-Q}{RT}\right) \tag{21}$$

$$\delta = \frac{6\sin(\Phi')}{3 - \sin(\Phi')} \tag{22}$$

$$dp_0 = p_0 \frac{1+e}{X} d\varepsilon_v \tag{23}$$

where $\Phi(F)$ is the stress function, G is the flow rule, Γ is the fluidity, m is the stress exponent, δ is the slope of the critical state line, p_0 is a hardening parameter, Γ_0 is the initial value of fluidity, Q is the activation energy, R is the gas constant, T is the temperature, e is the void

ratio, ε_v is the volumetric strain, X is a parameter in the hardening law, p is the mean stress and $q = \frac{3}{\sqrt{2}}\tau_{oct}$ is the invariant.

3.2 Numerical simulation

Within the PhD work the crushed salt experiments mentioned in the beginning of this section were simulated, however, only the results for the TUC-V2 test are presented in this paper.

The TUC-V2 triaxial test was executed by the Clausthal University of Technology using the KOMPASS reference material. It was started within the KOMPASS-I project and is still followed up in the KOMPASS-II project. Primarily, the test was planned for the isolated investigation of deviatoric stress on viscous volumetric deformations and the influence of porosity on viscous shear deformations (KOMPASS-I 2020). The loading history includes 5 load stages with variations between isotropic and deviatoric phases. For the simulation of the triaxial test, an axially symmetric model was chosen (Figure 1). The initial conditions for the sample are presented in Table 2. The values are derived directly from laboratory measurements and are adapted in the numerical model exactly. Due to the constant temperature during the test, the simulation was performed with an isothermal HM-coupling. Hydraulics were included, because liquid saturation is increasing in the sample with decreasing porosity, however, the moisture content in the crushed salt is very low and therefore having only a very small effect on the mechanical compaction. The moisture content in the experiment was chosen corresponding to the in-situ relevant conditions.
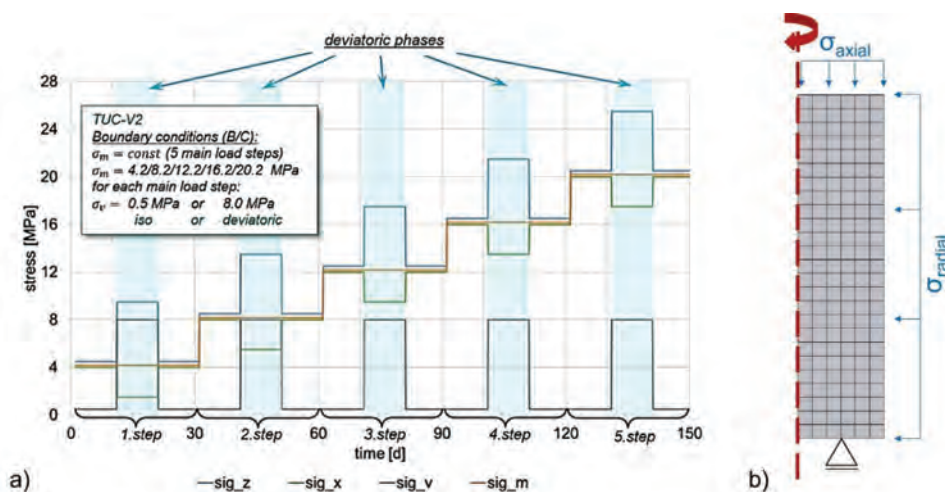
Figure 1:   Multi-stage long-term test TUC-V2. a) Loading history. b) Numerical model (KOMPASS-I 2020)

Table 2:   Initial sample parameters for TUC-V2 derived in laboratory (KOMPASS-I 2020)

Parameter	Unit	Value
Height	mm	180
Diameter	mm	90.1
Porosity	-	16.7
Moisture content	w.-%	0.5
Temperature	[°C]	30

Since no numerical parameter set exists for the KOMPASS reference material yet, initial values for parameters which could not be directly derived from the crushed salt material itself were taken from a simulation of a triaxial test with Asse mine material ("Speisesalz", As z2SP) (Table 3, "Initial"). With these initial parameters the measurement results couldn't be reproduced, because compaction was underestimated especially in the first 60 days of testing time (Figure 2). Therefore, the influence of the various input parameters on the mechanical constitutive equations was determined and parameter improvement was performed. As a result, the parameter set named "Interim" in this paper was compiled, representing the compaction behavior of the sample quite well for 70 days of the test (Figure 2). However, after 70 days, the compaction rate is strongly underestimated with this parameter set. So, further parameter adjustment was performed by improving the pre-exponential parameter A_A in the equation for Dislocation Creep. Actually, A_A is derived directly from the specification of creep class for the crushed salt material (creep class 6, $A_A = 2.08e - 6$), however, in this case the value was not representative for simulating the compaction behaviour and therefore was changed in the final parameter set corresponding to creep class 8 ($A_A = 1.25e - 5$).
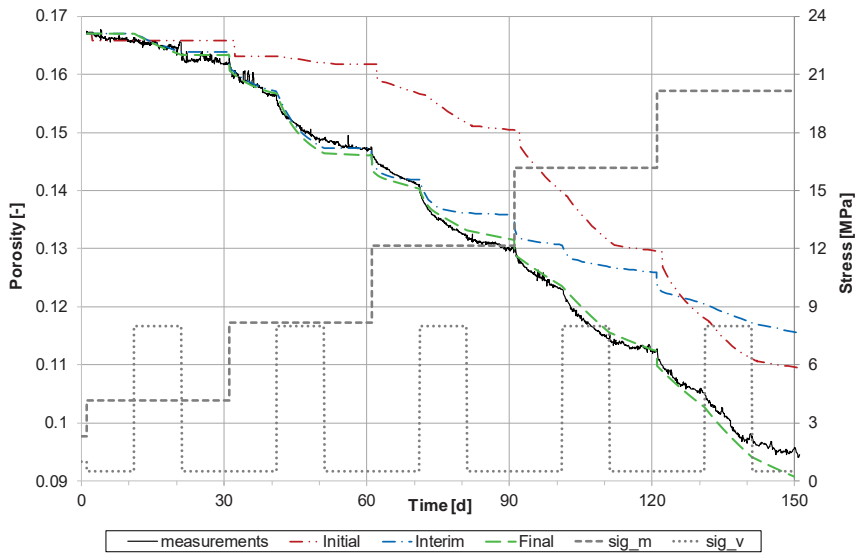
Figure 2: Porosity and stress evolution with time for the TUC-V2 test. Comparison of measurements (KOMPASS-I, 2020) and numerical results with an initial, an interim and a final parameter set.

In general, the porosity decrease could be reproduced quite well using the final parameter set (Figure 2), however, a consideration of the volumetric strain rate shows differences between the numerical values and the laboratory data. Figure 3 shows a good reproduction of volumetric strain rate for both parameter sets, "Interim" and "Final", for the first 60 days of the triaxial test. After 60 days, the accordance between laboratory data and these two parameter sets is getting worse. The initial parameter set shows very large differences to the measurements until 60 days. However, when studying the detail in Figure 4 a nice accordance between the initial parameters and the measurements can be observed up to 90 days.

The results from the numerical simulation of the TUC-V2 test show that with ongoing compaction state, the reproduction of the volumetric strain rate in the numerical model of CODE_BRIGHT is deviating significantly from the measurements. Due to the low moisture content of the crushed salt the influence of hydraulic processes is assumed to be very low and therefore, the issue lies in the mechanical part. In this frame, the FADT mechanism is considered to be a mechanical creep process with hydraulic interactions and therefore is included in the simulation even for this small moisture content.
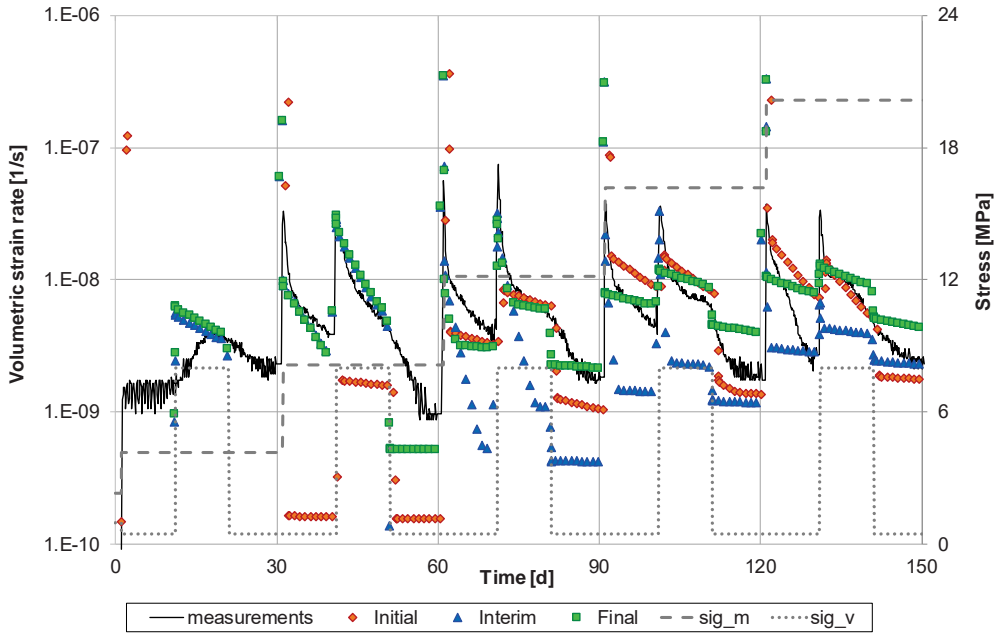
Figure 3:   Volumetric strain rate and stress evolution for the TUC-V2 test. Comparison of measurements (KOMPASS-I 2020) and numerical results with an initial, an interim and a final parameter set.
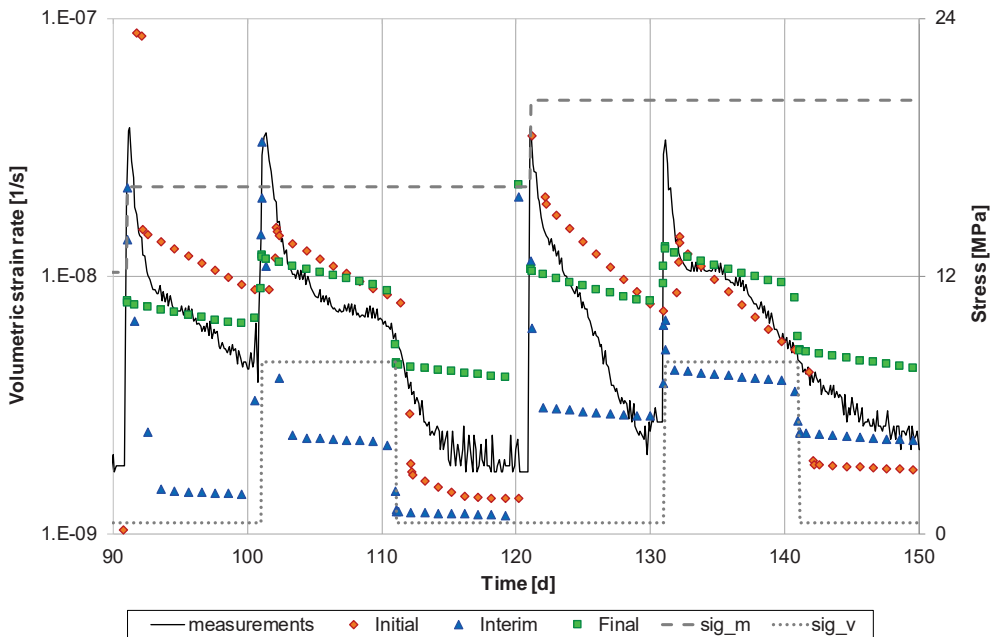
Figure 4:   Detail of volumetric strain rate and stress evolution for the TUC-V2 test. Comparison of measurements (KOMPASS-I 2020) and numerical results with an initial, an interim and a final parameter set.

Table 3:   Parameters for the constitutive modelling of the TUC-V2 test

Parameter	E_0	$\frac{dE}{d\Phi}$	v	d_0	A_B	Q_B	A_A	Q_A	n
	MPa	MPa	-	m	m³s⁻¹MPa⁻¹	J mol⁻¹	s⁻¹MPa⁻ⁿ	J mol⁻¹	-
Initial							2.08e-6		
Interim	1,750	-5,000	0.27	0.008	6e-13	24,530	2.08e-6	54,000	5
Final							1.25e-5		

Parameter	m	Γ_0	Q	p_0	χ	δ	ρ_s
	-	s⁻¹MPa⁻ᵐ	J mol⁻¹	MPa	-	-	kg m⁻³
Initial		0.001		10	0.08		
Interim	3	0.1	54,000	6	0.04	1.4	2160
Final		0.1		6	0.04		

4   Laboratory experiments

For a deeper investigation of the numerical response on changes in mean stress and deviatoric stress and for a possible model improvement, laboratory experiments will be executed within this PhD in collaboration with the KOMPASS-II project. A modified uniaxial testing machine which is capable of testing 5 samples at the same time will be used (Figure 5). Due to the missing possibility of radial deformation measurements and the limited availability of pumps for radial stress application, only 3 crushed salt samples will be testes simultaneously.
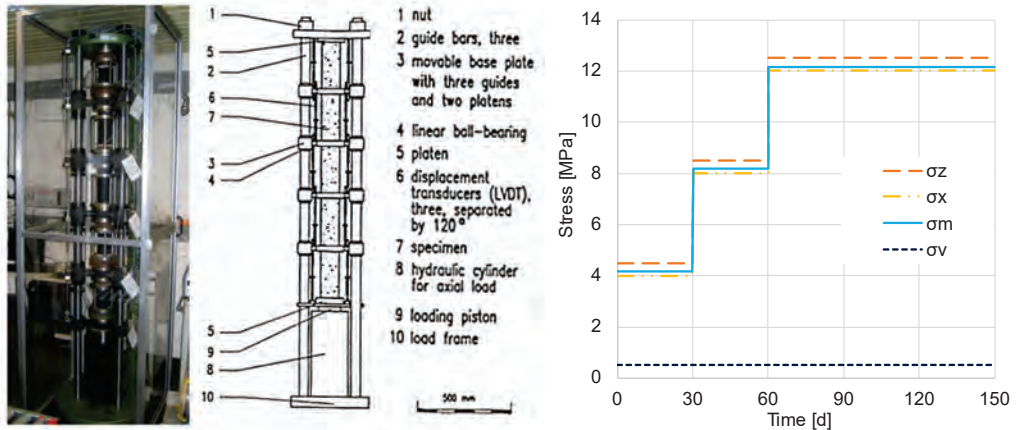
Figure 5:   Left: Rig for uniaxial creep tests. Right: Stress history for the isotropic tests.

Two testing schemes will be executed: one with variation of mean stress under constant deviatoric load (Figure 5) and the other varying deviatoric stress and setting mean stress constant. In order to enable comparability with the TUC-V2 test, the stress history of the laboratory tests will be related to it. The KOMPASS reference material is used for the same reason.

5   Conclusions

The paper presents an approach to the numerical improvement of crushed salt compaction behavior. Shortcomings are identified by re-simulation of triaxial compaction tests which

showed deficits in the simulation of volumetric creep rates. Additionally, an approach for laboratory experiments is presented dealing with an isolated investigation of mean stress and deviatoric stress and their influence on the compaction behavior. The gained process understanding from laboratory studies should be used in future for improving the numerical simulation of crushed salt.

Acknowledgements

References

BOLLINGERFEHR, W., BERTRAMS, N., BUHMANN, D., EICKEMEIER, R., FAHLAND, S., FILBERT, W., HAMMER, J., KINDLEIN, J., KNAUTH, M., LIU, W., MINKLEY, W., MÖNIG, J., POPP, T., PRIGNITZ, S., REINHOLD, K., SIMO, E., THIEMEYER, T., VÖLKNER, E. & WOLF, J. 2018. Concept developments for a generic repository for heat-generating waste in bedded salt formations in Germany. KOSINA project. BGE TEC 2018-13.

HANSEN, F.D., POPP, T., WIECZOREK, K. & STÜHRENBERG, D. 2014. Granular Salt Summary: Reconsolidation Principles and Applications. Fuel Cycle Research & Development

KOMPASS-I 2020. CZAIKOWSKI, O., FRIEDENBERG, L., WIECZOREK, K., MÜLLER-HOEPPE, N., LERCH, CH., EICKEMEIER, R., LAURICH, B., LIU, W., STÜHRENBERG, D., SVENSSON, K., ZEMKE, K., LÜDELING, CH., POPP, T., BEAN, J., MILLS, M., REEDLUNN, B., DÜSTERLOH, U., LERCHE, SV. & ZHAO, J. Compaction of crushed Salt for the safe Containment. KOMPASS. Gesellschaft für Anlagen- und Reaktorsicherheit (GRS) gGmbH, GRS-608; Köln, 2020.

KRÖHN, K.P., STÜHRENBERG, D., HERKLOTZ, M., HEEMANN, U., LERCH, CH. & XIE, M. 2009. Restporosität und -permeabilität von kompaktierendem Salzgrus-Versatz Repoperm – Phase 1. Gesellschaft für Anlagen- und Reaktorsicherheit (GRS) gGmbH, GRS-254, Köln

KRÖHN, K.-P., STÜHRENBERG, D., JOBMANN, M., HEEMANN, U., CZAIKOWSKI, O., WIECZOREK, K., MÜLLER, CH., ZHANG, C.-L., MOOG, H., SCHIRMER, S. & FRIEDENBERG, L. 2017. Mechanical and hydraulic behaviour of compacting crushed salt backfill at low porosities. GRS-450. Gesellschaft für Anlagen- und Reaktorsicherheit (GRS) gGmbH, Köln, 2017.

OLIVELLA, S. 1995. Nonisothermal Multiphase Flow of Brine and Gas Through Saline Media. Tesis Doctoral. Universitat Politècnica de Catalunya, Barcelona.

OLIVELLA, S. & GENS, A. 2002. A constitutive model for crushed salt. Int. J. Numer. Anal. Meth. Geomech., 2002; 26:719-746 (DOI: 10.1002/nag.220).

OLIVELLA, S., VAUNAT, J. & RODRIGUEZ-DONO, A. 2021. CODE_BRIGHT 2021. User's Guide. Universitat Politècnica de Catalunya, Department of Civil and Environmental Engineering, Division of Geotechnical Engineering and Geosciences, Barcelona.

SCHUTJENS, P.M.T.M. 1991. Intergranular Pressure Solution in Halite Aggregates and Quarts Sands: An Experimental Investigation. Thesis. Geologica Ultraiectina, n° 76, Utrecht.

SPIERS, C.J., URAI, J.L., LISTER, G.S., BOLAND, J.N. & ZWART, H.J. 1986. The Influence of Fluid-Rock Interaction on the Rheology of Salt Rock, Nuclear Science and Technology series, EUR 10399 EN.

SPIERS, C.J., PEACH, C.J., BRZESOWSKY, R.H., SCHUTJENS, P.M.T.M., LIEZENBERG, J.L. & ZWART, H.J. 1988. Long-term Rheological and Transport Properties of Dry and Wet Salt Rocks, Nuclear Science and Technology series, EUR 11848 EN.

SPIERS, C.J., SCHUTJENS, P.M.T.M., BRZESOWSKY, R.H., PEACH, C.J., LIEZENBERG, J.L.& ZWART, H.J. 1990. Experimental determination of constitutive parameters governing creep of rock salt by pressure solution, Geological Society Special Publication no. 54: Deformation Mechanisms, Rheology and Tectonics. 215:227.

Crushed salt compaction - a new approach for lab test analysis, physical modelling and numerical simulation

Part 1: Development and validation

Uwe Düsterloh*, Svetlana Lerche, Nachinzorig Saruulbayar

Chair of Geomechanics and Multiphysics Systems, TU Clausthal, Germany

*uwe.duesterloh@tu-clausthal.de

ABSTRACT: This article presents the development, validation and main features of the new constitutive model EXPO-COM for the compaction behavior of crushed salt, which was developed at the Chair of Geomechanics and Multiphysics Systems of Clausthal University of Technology (TUC) within the framework of the joint projects KOMPASS I and KOMPASS II. The methodical analysis of measured data is applied on five selected long-term experiments for the compaction behavior of crushed salt. Two main features of the analysis are first the isolation and quantification of measured values for each influencing factor and second the normalization of processed data for systematic comparative analysis of several experiments with different load histories. Based on the analysis, the process of development, the structure and the mathematical formulation of constitutive model are briefly described. Finally, a successful validation of the model is carried out through accurate simulations of selected tests that are representative of in-situ conditions. For future, the validated ranges for several influencing factors have to be expanded to increase the reliability and robustness of numerical predictions using the new model.

1 Introduction

The conceptual plans in Germany for underground disposal of radioactive waste in rock salt formations are based on extensive backfilling of the remaining cavities with crushed salt after waste emplacement. For the historical and prognostic analysis of the load-bearing behavior and the tightness of a repository in rock salt, it is of special importance to prove, that the compaction progress of the crushed salt backfill is suitable to heal the perforations of the geological barrier created during the underground excavation in the long term in such a way that a safe confinement of the waste is ensured.

Crushed salt as backfill material has been investigated in Germany for decades in projects such as BAMBUS I (1999), BAMBUS II (2002), REPOPERM I (2009), REPOPERM II (2017), but only since the paradigm shift in long-term safety assessment (concept of the isolating rock mass area – ewG-concept) its coupled thermo-hydro-mechanical (THM) behavior at low porosity and the expected low permeability is important for the safety. As recent investigations initiated in this regard can be mentioned for instance KOMPASS I (2020), Müller-Hoeppe & Lerch (2021), Svensson et. al. (2021), Zemke et al. (2021), and Friedenberg et. al. (2021), as well as international contributions such as Lampe et al. (2018). The new constitutive model EXPO-COM from TUC is being developed as a contribution to the continuation of all these investigations within the framework of the joint projects KOMPASS I (2018-2020) and KOMPASS II (2021-2023).

To guarantee reliable, robust and sufficiently realistic statements on the compaction behavior and thus to prove the safe confinement of radioactive waste in rock salt formations, the availability of systematic, comprehensive and sufficiently validated constitutive models is essential. However, the constitutive models for crushed salt, which are based solely on the evaluation of measurements from oedometer tests, require improvements regarding the description in space and time for three-dimensional stress-strain behavior of crushed salt depending on the external load. Evidence for this statement is in particular the fact that even

when same crushed salt materials are used, a back-analysis of compaction tests with a uniform parameter set has not yet been successful if these tests are carried out with different load scenarios, see REPOPERM II (2017) and KOMPASS I (2020). As a consequence, it can be assumed that the compaction behavior of crushed salt, which depends on the loading history and the material properties, is not yet conclusively known. Therefore the compaction behavior of crushed salt must be quantified as a function of the mean stress or the 1st stress invariant, the equivalent stress or the 2nd deviatoric stress invariant, the stress geometry, the stress rate, the porosity, the temperature and the material properties (water content, mineral components, grain size distribution and grain structure).

The lack of a systematic study of the compaction behavior of crushed salt with consequent isolation of the influencing factors is the reason why the currently available constitutive models do not take the corresponding dependencies into account ($\rightarrow$ missing functional relation) or do not take them into account in a sufficiently realistic manner ($\rightarrow$ unsuitable functional relation).

The following Sections document the first development steps for the new constitutive model EXPO-COM.

2 Methodology

In order to systemize and optimize the process of the development of the constitutive model with the above-mentioned requirements, the methodological approach developed and successfully used several times at TUC is applied. The main components of the methodology *SIS-LabPro* and *AQuA-Mod* serve for the model-related optimized planning of experiments to generate a suitable database (*SIS-LabPro*) as well as for the optimized evaluation, development and validation of the constitutive model (*AQuA-Mod*). A detailed explanation for each guideline of the methodical approach and their application based on generalized sketches and diagrams are omitted here with reference to the presentation in safeND-BASE Düsterloh & Lerche (2021).

3 Laboratory database

3.1 Design of laboratory program

The development and validation of a constitutive model require a solid laboratory database. More systematically complete and optimized database allows higher validation status of the model which leads to more reliable and robust statements based on the analysis using the constitutive model. Therefore, a systematic and comprehensive laboratory program was designed for the investigation of the crushed salt behavior, which fulfills the requirements for long-term prediction resulting from ewG-concept. Based on a composition of the expected influencing factors on the compaction behavior of crushed salt, systematized boundary conditions are developed for each test, which allow an isolated analysis of crushed salt compaction corresponding to each influencing factor. An important objective is not only to analyze the effects of individual influencing factors on the crushed salt compaction by varying one parameter while keeping all others constant within a certain test, but also to coordinate the configurations between the tests in a way that they generate a consistent and systematical database together. The experiment TUC-V2 in Section 3.2.3 can be referenced as an example for the test configuration in this regard. Detailed information and explanations on the overall structure of the lab program as well as on the individual test configurations with partly innovative loading histories can be found in KOMPASS I (2020) and the TUC presentation for US-German-Workshop by Düsterloh & Lerche (2021).

3.2   Currently available chosen database

For the development and validation of a new constitutive model for the characterization of crushed salt behavior, following five long-term tests were selected from the currently available database: TK-031 from German Federal Institute for Geosciences and Natural Resources (Bundesanstalt für Geowissenschaften und Rohstoffe, BGR), TUC-V2 from TUC and three tests from German Society for Plant and Reactor Safety (Gesellschaft für Anlagen- und Reaktorsicherheit, GRS) GRS-dry/GRS-0.1%/GRS-wet.

Applied criteria for the suitability of experiments for the systematic analysis of the compaction behavior of crushed salt for the development of the constitutive model are:

1)   the possibility of a clear-cut analysis of test results by isolating individual processes and influencing factors (stress controlled triaxial long-term test with measurement of axial stress and confining stress);
2)   the availability of measured values for all relevant influencing factors;
3)   sufficient amount of measured data for the individual influencing factors (test number and duration);
4)   testing conditions that correspond to in-situ ranges for influencing factors;
5)   the use of a uniform crushed salt material with respect to its composition (grain size distribution, mining location).

The laboratory tests selected for the development of the constitutive model EXPO-COM do not always completely fulfill the criteria mentioned above: criteria 3 and 4 are only partially fulfilled by the test group, since the investigated ranges for several influencing factors are too small in comparison to in situ relevant spectrum and the amount of data is clearly quite limited. Criterion 5 is not met by the selected tests, since the experiments originate from different research projects and were consequently carried out with crushed salt with different grain size distribution and crushed salt location. Therefore, not in each case of test a uniform parameter set can be used to back analyze the selected tests with the new EXPO-COM model. A prerequisite for this possibility is the compliance with criterion 5 already realized in the course of the research work on KOMPASS I and continued in KOMPASS II. The compliance with criteria 3 and 4 will be fulfilled step by step with the help of the laboratory experiments over the course of these projects as well.

The selected database can thus be characterized on the one hand as insufficient for the development and validation of a constitutive model for crushed salt compaction, but on the other hand as the best possible option until completion of the tests planned in KOMPASS II.

3.2.1   *Triaxial compaction test TK-031 from BGR*

Figure 1 shows in a schematic overview the most important information of the test TK-031 used for the analysis. According to the figure, the impact of two influencing factors designated as InF1 and InF2 can be determined on the basis of the measured data as follows:

InF1: dependence between the compaction rate and the porosity,
InF2: dependence between the compaction rate and the mean stress.

With regard to the usability of the measurement, following points should be highlighted:

▪   isotropic boundary conditions for the entire duration of the test,
▪   based on five levels, a sufficient number of stress levels is available to reliably investigate the dependency from mean stress and
▪   based on a test duration of 300 days, is considered as a comparatively long test.
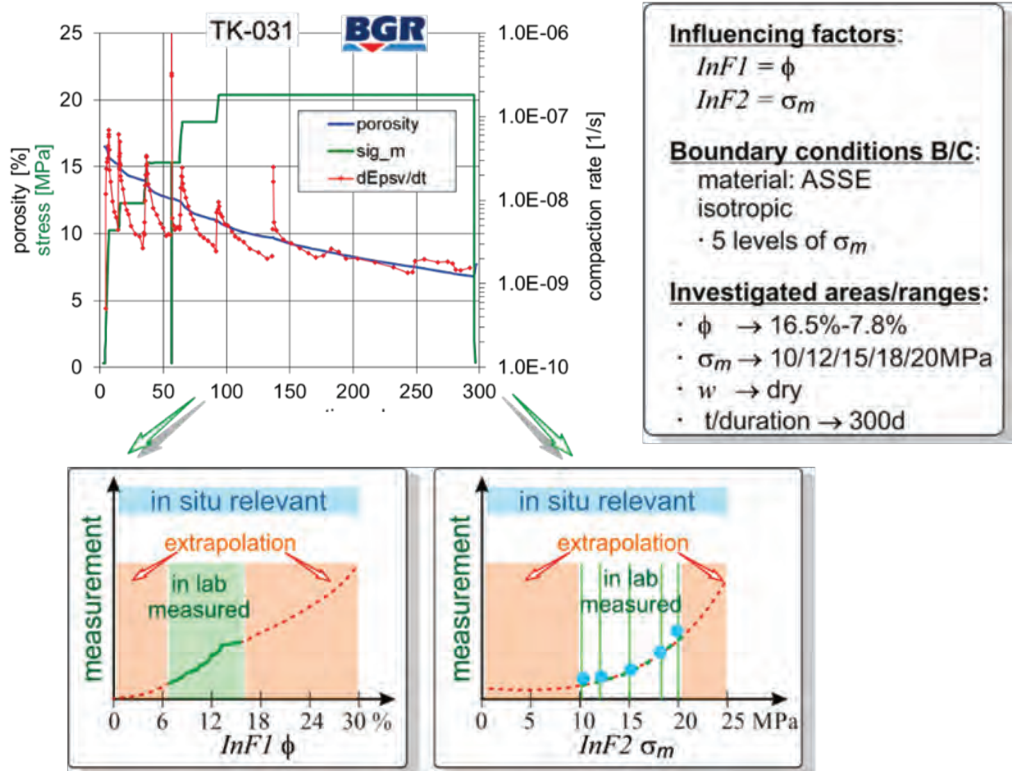
Figure 1: Test TK-031 from BGR – measurements for compaction strain rate and porosity, boundary conditions, intervals for investigated influencing factors in relation to in situ relevant ranges

The disadvantages of the test regarding the intended development and validation of the new constitutive model are:

- minimum mean stress level of σ_m = 10 MPa, so that in situ relevant range for the mean stress from σ_m = 0 MPa to σ_m = 10 MPa is not investigated in this test,
- relatively high final porosity of about ϕ = 6.8%, so that the in situ relevant range has been only partially investigated in this test and finally
- low number of investigated influencing factors: porosity and mean stress.

Detailed information to the test TK-031 beyond the aforementioned characteristics are documented in the final reports to REPOPERM II and KOMPASS I.

3.2.2 Oedometer tests GRS-dry/GRS-0.1%/GRS-wet from GRS

Figure 2 shows in a schematic overview the most important information regarding the tests GRS-dry, GRS-0.1% and GRS-wet used for the analysis. According to the figure, the impact of four influencing factors designated as InF1, InF2, InF3 and InF4 can be individually analyzed based on the measurements of these experiments:

InF1: dependence between the compaction rate and the porosity,
InF2: dependence between the compaction rate and the mean stress ($\rightarrow$ not precise),
InF3: dependence between the compaction rate and the temperature,
InF4: dependence between the compaction rate and the moisture content ($\rightarrow$ not sufficient).

Figure 2: Tests GRS-dry/GRS-0.1%/GRS-wet from GRS – measurements for porosity, boundary conditions, intervals for investigated influencing factors in relation to in situ relevant ranges

With regard to the usability of the measurement, following points should be highlighted:

- high number of investigated influencing factors: porosity, mean stress, temperature and moisture content,
- based on six levels, a sufficient number of axial stress levels is available to reliably investigate the dependency from stress including in situ relevant range of low stress,
- the investigated range for porosity from maximum ϕ = 30% to minimum ϕ = 1-3% represents almost the entire in situ relevant range and
- based on a test duration of 1600 days, in relation to the laboratory tests a very large period generated for the analysis of the long-term behavior.

The disadvantageous characteristics of GRS-dry, GRS-0.1% and GRS-wet for the intended constitutive model development and validation are as follows:

- non-isotropic boundary conditions with missing measurement of radial stress, thus no unambiguous analysis for the stress dependence possible;
- low number of investigated moisture content levels and temperature levels, thus insufficient database to determine or validate reliably the relations in this respect.

Detailed information to the tests GRS-dry, GRS-0.1% and GRS-wet beyond the is documented in the final report to REPOPERM II.

3.2.3   Triaxial compaction test TUC-V2 from TUC

Figure 3 shows in a schematic overview the most important information to the test TUC-V2 used for the analysis. According to the figure, impacts of five influencing factors designated as InF1, InF2, InF3, InF4 and InF5 can be analyzed on the basis of the measured data as follows:

InF1: dependence between the compaction rate and the porosity,
InF2: dependence between the compaction rate and the mean stress,
InF3: dependence between the compaction rate and the temperature,
InF4: dependence between the compaction rate and the deviatoric stress ($\rightarrow$ only one level),
InF5: dependence between the volume-preserving creep rate and the porosity.

With regard to the usability of the measurement, following points should be highlighted:

- high number of investigated influencing factors: porosity (regarding the influence on the compaction), porosity (regarding the influence on the creep), mean stress, deviatoric stress (von Mises) and temperature;
- based on six levels, a sufficient number of stress levels is available to reliably investigate the dependency from stress;
- a relatively wide investigated range for porosity from ϕ = 16.7% to $\phi \approx$ 3%;
- with 750d test-days, a very long test duration for the analysis of the long-term behavior is available;
- due to innovative configuration of load conditions, a possibility to isolate the investigated factors, especially for the dependency of the creep behavior from the porosity and for the dependency of the compaction behavior from the deviatoric stress ($\rightarrow$ The demand of the investigation regarding the dependency of the creep rate from porosity results from analytical benchmark calculations in REPOPERM II research project, which showed significant differences in the predictions depending on the choice of constitutive model and thus deficits with regard to the validation.)

The disadvantageous characteristics of this test regarding the intended constitutive model development and validation are:

- the experimental analysis of the temperature influence is limited to only three load levels in a relatively low interval for the temperature 30°C/50°C/70°C, and thus insufficient database to determine or validate a reliable relation in this respect;
- index-type investigation for the influence of deviatoric stress due to only one level of deviatoric stress, and thus test merely enables the possibility for a sensitivity estimation of the influence, but not (or not reliable) the functional relation in this respect.

Additional information to the analysis of the first three test phases are documented in safeND-BASE Düsterloh & Lerche (2021) and in the final report for KOMPASS I (2020).
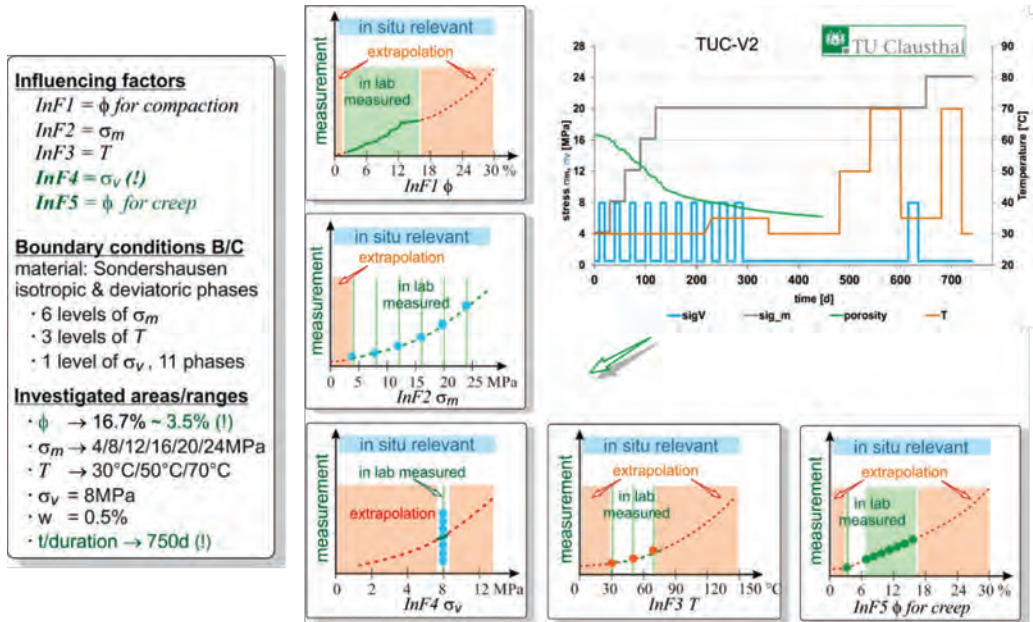
Figure 3: Test TUC-V2 from TUC – measurements for porosity (until 450d), boundary conditions, intervals for investigated influencing factors in relation to in situ relevant ranges

4   Analysis of database and development of the new constitutive model

4.1   Approach for the analysis

One of the basic principles of the analysis of lab database is the preparation of data in such a way that these data are directly and unambiguously applicable for the functional relations used in the already developed constitutive model (for parameter determination). During the development phase, the database must be prepared in such a way that a clear-cut analysis and unambiguously identification of the searched for functional relationships are possible. The measured values are usually available in the form of strain (e.g. axial strain, volumetric strain) as a state variable accumulated over time. However, the constitutive model is formulated in the form of strain rate as a function of different influencing factors (e.g. mean stress, deviatoric stress etc.). For this reason, it is useful and purposeful to first calculate the strain rates from the measured data and then to plot and analyze the rates as a function of the currently investigated influencing factor instead of a function of time. This procedure is independent from the specific assumptions of an individual constitutive model and therefore generally applicable and valid, safeND-BASE Düsterloh & Lerche (2021). Furthermore, the isolation of individual factors is essential in the analysis of a test with several influencing factors (usually the case for effort optimization).

4.2   Practical realization of the isolated analysis of individual influencing factors and the derivation of functional relations

Figure 4 demonstrates the practical realization of the methodology for comparative analysis of the data obtained from the five chosen compaction experiments described in Section 3. Graph (a) of Figure 7 shows the original measurements for the tests shown: green –TUC, blue – BGR, yellow/orange/red – GRS-dry/GRS-0.1%/GRS-wet. In Graph (b) the result of the first step of the database preparation can be seen: the rates are derived from the volume strains and

plotted versus time. In Graph (c) the volumetric strain rates are now plotted versus porosity. Graph (d) depicts the rates normalized with respect to the mean stress (the normalization stress levels are listed in the diagram). Finally, Graphs (e) and (f) present the comparison between the prepared measured values and the analytical curves from the new constitutive model EXPO-COM. In these diagrams, some jumps were intentionally left unnormalized to additionally accent the effects caused by the changes in temperature, deviatoric stress and moisture content.

Lab database: preparation, isolation, normalization for individual and comparative analysis
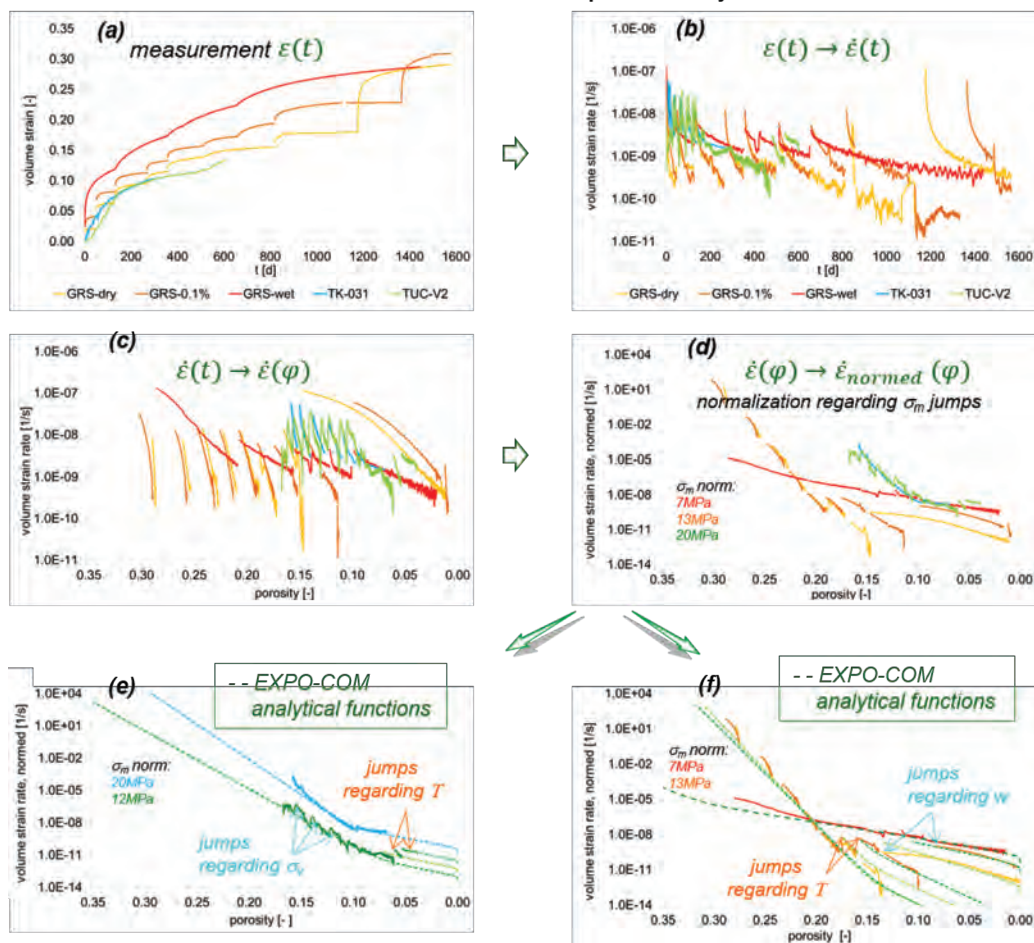
Figure 4: Database preparation for the five chosen tests and comparison of the measurements with the new analytical curves for the dependency of compaction from porosity in the constitutive model EXPO-COM

In this regard, the following should be mentioned in particular:

▪ Regardless of backfill material, moisture content and temperature being different, the tests TK-031 and TUC-V2 show similar behavior with respect to the qualitative as well as quantitative dependence between volume strain rate and porosity. It is therefore to be

expected, that the constitutive model parameters for the characterization of the specimen TK-031 and TUC-V2 will have a similar order of magnitude.

- A comparison of the tests TUC-V2 and TK-031 with the oedometer tests GRS-dry and GRS-0.1% shows significant differences. Therefore, the parameter sets can be expected to differ considerably.
- The influence of temperature on the compaction behavior is similar for both TUC and GRS samples (indicated by similar sizes of jumps).
- The influence of moisture content on the compaction behavior is evidently significant. Clear difference in the inclinations for the dry and wet samples of GRS can be distinguished.
- The difference between the results from GRS-dry and GRS-0.1% is nearly undetectable on the other hand. Considering the previous statements, therefore the dependence on moisture content has to be represented in the model with clearly nonlinear correlations.

As a result of the systematic comparison of isolated standardized dependencies between the strain rate and influencing factors, it was evidently possible to define functional relations that qualitatively and quantitatively represent the changes in compaction rate due to the changes in the respective influencing factor with sufficient accuracy.

5   New constitutive model EXPO-COM from TUC

5.1   Structure and the functional relations of the constitutive model EXPO COM

Based on the analysis of the experimental database as discussed previously, the structure of the generated constitutive model EXPO-COM has been developed, (see Figure 5). The functional relations implemented in the model are summarized in Figure 6.
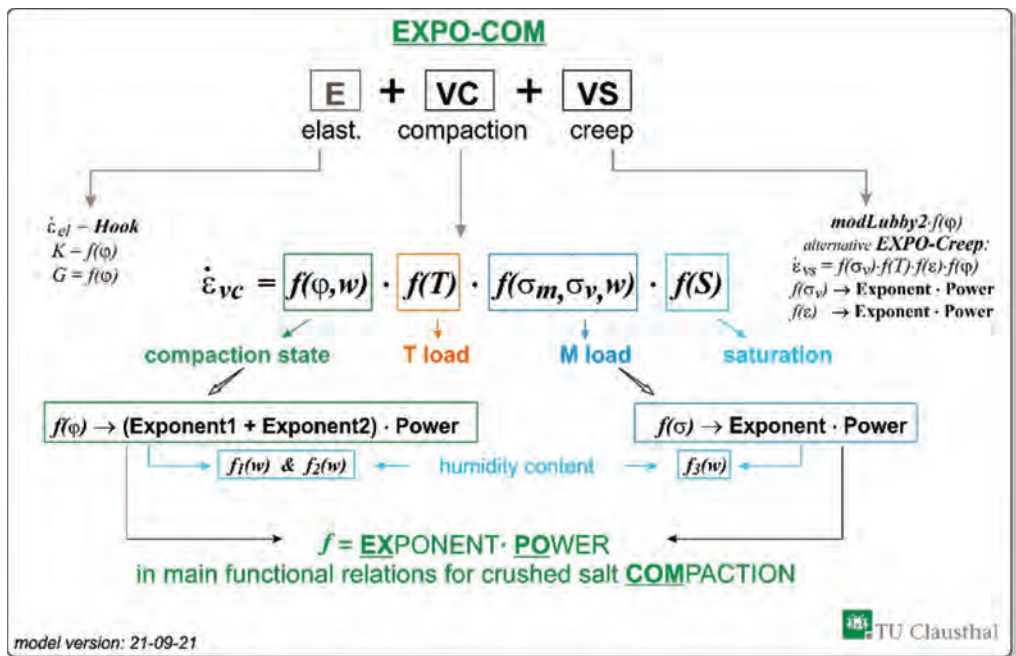
Figure 5: Structure of the new constitutive model EXPO-COM from TUC for the material behavior of crushed salt

The model is originally based on the C-WIPP-model or more specifically, based on a modified C-WIPP model named C-WIPP-TUC-2020 which was developed in the framework of KOMPASS I. According to the description in Figure 5, in contrast to the C-WIPP model with only two influencing factors (mean stress and porosity), all relevant experimentally detected influencing factors are now implemented in the EXPO-COM model – mean stress, porosity, deviatoric stress, temperature and moisture content (exception: grain size distribution). The pre-factors in functional relations regarding the mean stress and porosity C_0^{hm}, C_{1e}^{iso} and C_{2e}^{hm} were formulated as variables dependent from moisture content. Thereby the two main dependencies, expressed by the exponent-power functions to characterize the relations regarding the influencing factors stress and porosity, inspired the name of the new constitutive model. Furthermore, a significant modification is the incorporation of modLubby2 as the creep term into the EXPO-COM model. The term modLubby2 is additionally multiplied by the porosity-function, which is adopted from the accelerated damage part of the constitutive model Lux/Wolters/Lerche (Lux et al. 2018). Supplementary, a new creep term EXPO-Creep is currently being developed for the crushed salt model to describe the transient creep phase more realistically.

A schematic overview of the equations for the essential functional relations characterizing the viscous compaction behavior of crushed salt is shown in Figure 6.
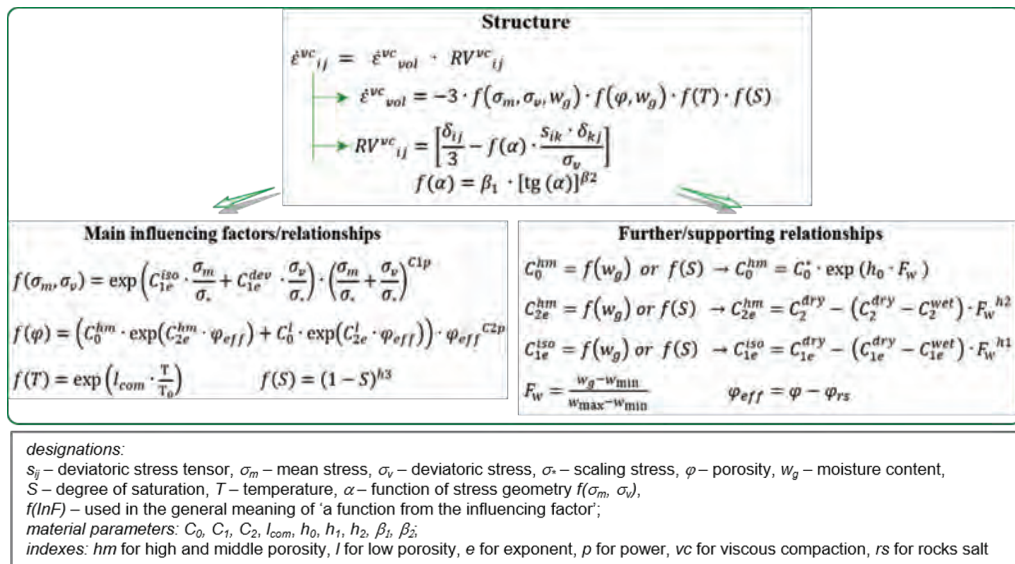
Figure 6: Formulation of the main relationships in the constitutive model EXPO-COM from TUC

The majority of the influencing factors were taken into account as normalized quantities, i.e. without a physical unit. The main functional relations in the model are functions of porosity, stress and temperature. The function of moisture content is built into the coefficients C_0^{hm}, C_{1e}^{iso} and C_{2e}^{hm}. The function of saturation is currently not determined on the basis of experiments but serves only for the plausibility consideration that the compaction process in the moist crushed salt is terminated with the degree of saturation S = 1. Furthermore, the dependence on porosity is realized in terms of effective porosity, where effective porosity is defined as a difference between actual porosity of the crushed salt and minimum reachable porosity that corresponds to the natural porosity of intact rock salt. Consequently, the compaction rate becomes zero when the minimum porosity (ϕ_{rs} of rock salt) is reached and only a deformation rate corresponding to the volume-preserving creep behavior of intact rock salt remains. This ensures a smooth transition between the compaction behavior of crushed salt and the creep behavior of rock salt.

5.2   Back-analysis of the selected laboratory tests to verify and validate the functionality of the new constitutive model EXPO-COM

To demonstrate and verify the functionality of the new constitutive model EXPO-COM, the compaction tests GRS-dry, GRS-wet, TK-031 and TUC-V2 were calculated and the calculation results were compared with the measurement results. The aim of the back-analysis is neither a development of the material model nor a determination of the material parameter set. Rather, the back analysis is intended to show or verify whether the influence of individual factors based on the isolated analysis has been correctly implemented to the extent that the evaluated dependencies are in principle suitable for representing the material behavior observed in the experiment. The result of the back-analysis displayed in Figure 7 demonstrates for example that the calculated porosity evolution agrees comparatively well with the measured porosity evolution.

Although the constitutive model incorporates all influencing factors currently considered to be relevant for the compaction behavior of crushed salt, its validation quality can still be characterized as very heterogeneous. While the influence of mean stress and porosity on the compaction behavior could be validated by several independent tests, the experimental database to ensure sufficiently valid statement regarding the influence of moisture content, temperature and deviatoric stress is not yet available.
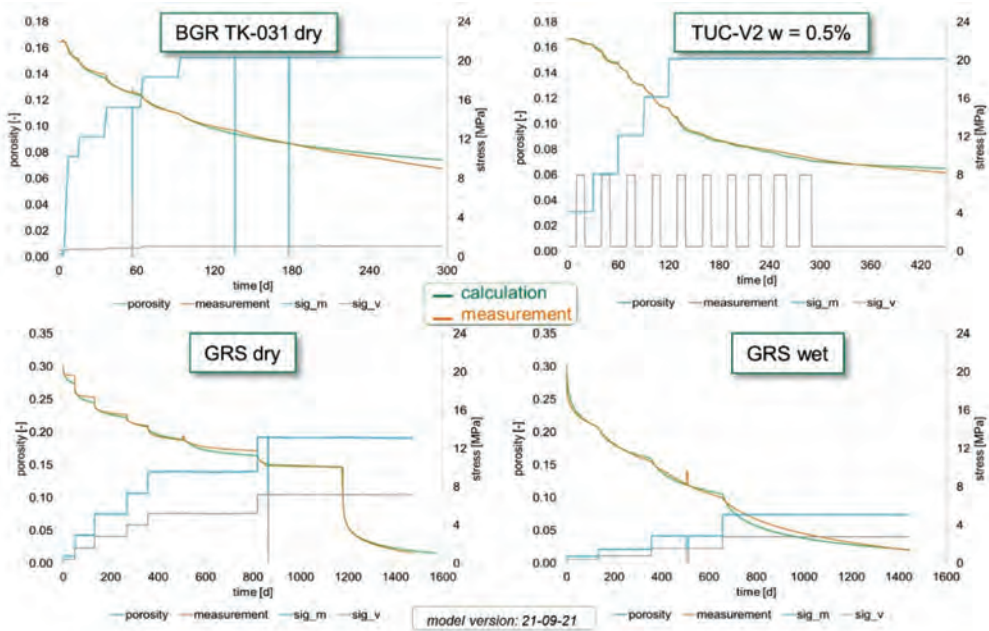
Figure 7: Back-analysis of the selected tests using the new constitutive model EXPO-COM from TUC

In conclusion, the constitutive model EXPO-COM can be considered as successfully validated on the basis of the available laboratory test in principle for almost all in situ relevant influencing factors (with the exception of grain size distribution) but only for a partial range of the in situ relevant load conditions. However, the validation status still requires significant increase by supplementary tests in order to guarantee the robustness and reliability of the model predictions required in the research field of final disposal. The elaboration of the still missing information by suitable compaction experiments is part of the current joint research project KOMPASS II.

6 Summary and outlook

The essential steps of the experimental database analysis and the development of the new constitutive model EXPO-COM were presented. The functionality, capability and current validation status of the constitutive model are determined by the currently available data used in the development-process. By taking into account most relevant factors influencing the compaction behavior of crushed salt and the successful back-analysis of selected tests, the functionality and suitability of the constitutive model for the prognostic analysis of the long-term behavior of repository excavations backfilled with crushed salt in salt formation can be expected. The small amount of suitable tests for the analysis of most influencing factors regarding the compaction behavior of crushed salt has evidently shown the necessity for systematic expansion of the experimental database. In this context, TUC plans investigations regarding the influence of deviatoric stress and moisture content, since these dependencies have been insufficiently investigated by triaxial tests so far.

The next essential step consists in the implementation of the constitutive model in the numerical calculation tools of the FLAC3D software used and in the performance of calculations on the practicability, robustness and stability of the simulation routines on the one hand and on the plausibility and sensitivity of the calculation results on the other. First results in this regard are documented in Part 2 of this article "Crushed salt compaction - a new approach for the lab test analysis, physical modeling and numerical simulation. Part 2: Numerical application".

References

BAMBUS, I. BECHTHOLD, W., ROTHFUCHS, T., POLEY, A., GHOREYCHI, M., HEUSERMANN, S., GENS, A. & OLIVELLA, S. 1999. Backfilling and Sealing of Underground Repositories for Radioactive Waste in Salt. Final Report. - European Commission, nuclear science and technology, EUR 19124 EN, Luxembourg.

BAMBUS II. BECHTHOLD W. SMAILOS E., HEUSERMANN S., BOLLLNGERFEHR W., BAZARGAN SABET B., ROTHFUCHS T., KAMLOT P., GRUPA J., OLIVELLA S. & HANSEN F.D. 2004 Backfilling and sealing of underground Repositories for radioactive waste in salt. Final report. - European Commission, nuclear science and technology, EUR 20621 EN, Luxembourg.

DÜSTERLOH, U., LERCHE, S. & ZHAO, J. 2021. The KOMPASS project, Modelling related experimental aspects, 11th US/German Workshop on Salt Repository Research, Design, and Operation, TUC, Part 2 of the online workshop

KOMPASS I. CZAIKOWSKI, O., FRIEDENBERG, L., WIECZOREK, K., MÜLLER-HOEPPE, N., LERCH, CH., EICKEMEIER, R., LAURICH, B., LIU, W., STÜHRENBERG, D., SVENSSON, K., ZEMKE, K., LÜDELING, CH., POPP, T., BEAN, J., MILLS, M., REEDLUNN, B., DÜSTERLOH, U., LERCHE, S. & ZHAO J. 2020. Compaction of crushed Salt for the safe Containment, Final Report GRS-608, of the joint project with partners GRS, BGE TEC, BGR, IfG, TUC, Sandia, KOMPASS I, FKZ 02E11708A.

LAMPE, B.C., STORMONT, J.C., LYNN, T.D. & BAUER, S.J. 2018. Experimental investigation of the influence of pore pressure and porosity on the deformation of granular salt, International Journal of Rock Mechanics and Mining Sciences, 110, 291-305

LUX, K.-H., LERCHE, S. & DYOGTYEV, O. 2018. Intense damage processes in salt rocks – a new approach for laboratory investigations, physical modelling and numerical simulation. Saltmech IX, 47-67, BGR Hannover.

MÜLLER-HOEPPE, N. & LERCH, CH. 2021. Role of crushed salt in the repository concept, 11th US/German Workshop on Salt Repository Research, Design, and Operation, BGE TECHOLOGY GmbH, Part 2 of the online workshop.

REPOPERM I. KRÖHN, K.-P., STÜHRENBERG, D., HERKLOTZ, M., HEEMANN, U., LERCH, CH. & XIE, M. 2009. Restporosität und -permeabilität von kompaktierenden Salzgrus-Versatz, GRS – 254, ISBN 978-3-939355-29-8.

REPOPERM II. KRÖHN, K.-P., STÜHRENBERG, D., JOBMANN, M, HEEMANN, U., CZAIKOWSKI, O., WIECZOERK, K., MÜLLER, C., ZHANG, C.L., MOOG, H., SCHIRMER, S. & FRIEDENBERG, L. 2017. Mechanical and hydraulic behaviour of compacting crushed salt backfill at low porosities, GRS – 450, ISBN 978-3-946607-32-8.

SAFEND-BASE. U. DÜSTERLOH, U. & LERCHE, S. 2021. Methodology of structured development and validation of multiphysical constitutive models using the example of crushed salt compaction under 3D THM load conditions, Interdisziplinäres Forschungssymposium für die Sicherheit der nuklearen Entsorgung, Berlin.

SAFEND-BASE. FRIEDENBERG, L., BEAN, J., CZAIKOWSKI, O., DÜSTERLOH, U., MÜLLER-HOEPPE, N., LAURICH, B., LERCH, CH., LERCHE, S., LÜDELING, CH., MILLS, M., POPP, T., REEDLUNN, B., STÜHRENBERG, D., SVENSSON, K., ZEMKE, K. & ZHAO, J. 2021. Compaction of crushed salt for safe containment – overview of the KOMPASS project, Interdisziplinäres Forschungs-symposium für die Sicherheit der nuklearen Entsorgung, Berlin.

SAFEND-BASE. SVENSSON, K., ZEMKE, K. & LAURICH, B. 2021. Deformation mechanisms and their microstructural indicators in the compaction of crushed salt as a geotechnical barrier, Interdisziplinäres Forschungs-symposium für die Sicherheit der nuklearen Entsorgung, Berlin.

SAFEND-BASE. SVENSSON, K., ZEMKE, K., LAURICH, B., LIPPMANN-PIPKE, J. 2021. Over 30 years of research on crushed salt as a barrier material: fundamental findings and open questions, Interdisziplinäres Forschungs-symposium für die Sicherheit der nuklearen Entsorgung, Berlin.

WIECZOREK, K., DÜSTERLOH, U., HEEMANN, U., LERCH, CH., LÜDELING, CH., MÜLLER-HOEPPE, N., POPP, T., STÜHRENBERG, D., WOLTERS, R. 2017. Reconsolidation of crushed salt backfill - review of existing experimental database and constitutive models and need for future R&D work. DAEF Stellungnahme, 2017.

Crushed salt compaction - a new approach for lab test analysis, physical modeling and numerical simulation

Part 2: Numerical application

Uwe Düsterloh*, Svetlana Lerche, Nachinzorig Saruulbayar

Chair of Geomechanics and Multiphysics Systems, TU Clausthal, Germany

*uwe.duesterloh@tu-clausthal.de

ABSTRACT: Based on our Part 1 article addressing lab test analysis, development and validation of the constitutive model EXPO-COM from TUC (Chair of Geomechanics and Multiphysics Systems of the Clausthal University of Technology), the practical application of the newly developed approach for the physical and numerical modeling of the crushed salt compaction is demonstrated in Part 2. The focus of the numerical investigation is to verify and demonstrate the following main capabilities of the numerical modeling equipment: functionality, numerical stability and plausibility of the delivered results. The demonstration is based on different functional numerical models (FM) with stylized illustration of the underground cavities filled with crushed salt for two different applications: (a) repository research (single drift with a representative geometry) to demonstrate the features of the constitutive model under different boundary conditions and (b) existing mines (single 3D-chamber characterized by a complex chamber geometry and complex 3D-mine-field) to demonstrate the functionality of the numerical equipment.

1 Introduction

The peculiarity and the novelty in comparison to the decades-long research on the compaction behavior of crushed salt (see e.g. BAMBUS I 1999; BAMBUS II 2004; REPOPERM I 2009; REPOPERM II 2017) is the new functionality of crushed salt, which originated from the recent development in the repository concept. This requires an in-depth understanding of the crushed salt behavior at very low porosity not only in the mechanical but also in the hydraulic sense (see e.g. KOMPASS I final report 2020; safeND-BASE Friedenberg at al. 2021; US-German-workshop Müller-Hoeppe & Lerch 2021). An additional field of development in this respect is the investigation of optimal grain size distribution in crushed salt and the creation of new crushed salt based materials with higher compactibility than the pure crushed salt or alternatively salt cut bricks concept (e.g. projects ELSA II 2020; GESAV 2017; Düsterloh et al. 2018 as well as ongoing projects such as SAVER, KOMPASS II, and the pilot plant test with salt cut bricks - see Düsterloh et al 2021).

As depicted in Figure 1, the necessity to develop or to improve upon a numerical equipment is a typical challenge in the context of numerical analysis of geomechanical problems. The new tasks usually require, in generalized terms, an increase in the range of validity for existing constitutive model or for the numerical modeling approach. This includes, for example, the implementation of new influencing factors that have not been considered so far, or to increase the realism of the results for relevant state variables or influencing factors in certain ranges of relevance (e.g. permeability of crushed salt for low porosity range).

Also, it is well known that a new implementation requires several successive steps to be successfully completed in the forefront. The first essential component is a suitable experimental database. This encompasses the laboratory investigations, in situ measurements but also pilot plant tests as an essential connection element between the two. Pilot tests deliver on one hand the possibility to demonstrate the functionality of the numerical approach and on

the other the technical feasibility of the backfilling procedures in the field. The second essential element is the physical modeling. The suitable constitutive model has to be developed or refined based on the laboratory investigations. Third essential step is the implementation of the constitutive model into a numerical program code and thus the development of a numerical equipment by verifying and validating its functionality and reliability of the statements. Here, the data from the pilot plant test and in situ measurements are required as well.

In order to optimize the workload described above, a methodological approach was developed and successfully applied several times at TUC. Through this method, a practical and functional numerical equipment was developed which is capable of modeling the compaction behavior of crushed salt under different boundary conditions up to nearly full compacted state.

In addition, the functionality of the new numerical equipment was further developed and verified not only in terms of physical aspects but also in terms of geometric aspects: in the context of modeling from geometrically simple underground opening (a drift) to complex underground opening (a chamber) up to a representative 3D mine field consisting of numerous complex chambers with several levels and rows as well as different rock salt types (potash and salt) and backfilling times (early backfilling with short empty standing time or late backfilling with a standing time of several decades). The aim of these numerous different application examples is to make the new numerical equipment functional for modeling as many thinkable in situ situations as possible in future, both from the mining sector and from the field of final disposal.
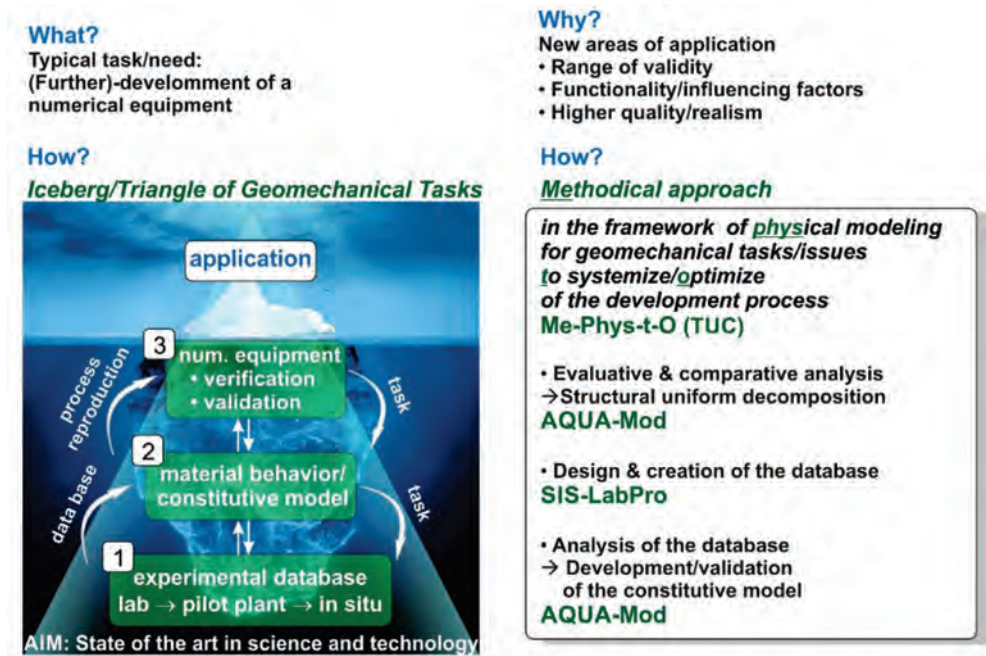
Figure 1: Common workload in the context of numerical investigations related to geomechanical tasks and the methodical approach for optimizing the development process

2 Verification of the functionality for the new constitutive model EXPO-COM

2.1 Structure, features and validation state of the constitutive model

The new constitutive model EXPO-COM developed by TUC in the framework of projects KOMPASS I and II was applied here. This model includes all relevant and so far investigated influencing factors and has been successfully validated by the recalculation of the tests from the available database. A detailed description of the model, its development process and the validation state are avoided here with reference to the Part 1 of the article. The implementation of the model into a numerical equipment and the verification of its functionality under different boundary conditions and for different geometrical configurations are covered in the following Sections.

2.2 Sensitivity analysis for variation of main influencing factors

In this Section, analytical calculations as well as numerical simulations were carried out to test the functionality and the numerical stability of the new constitutive model and the plausibility of the results. Furthermore, the aim was to find out by the use of a sensitivity analysis, which relationships and parameters play the most important role concerning the full compaction time.

Following calculations were done:

1) Analytical calculations (one-zone consideration) for the variation of moisture content and temperature of the crushed salt. The considered zone represents the drift in the depth 500 m surrounded by rock salt with the creep behavior corresponding to the creep class 3 of the well-known constitutive model BGRa, German Federal Institute for Geosciences and Natural Resources (BGR, 2011). Following variations have been investigated:
    - w = 0.03% (dry): T = 30 °C (cold) / 60 °C (warm) / 90 °C (hot) / 120 °C (hot2);
    - T = 30 °C (cold): w = 0.3% / w = 0.5% / w = 0.7% / w = 1% (wet).
    2) Numerical simulations (2D-drift, plane-strain approximation) considering a variation of depth and creep behavior of the surrounding rock salt. Following variations have been investigated:
    - CC3: z = 400 m, 500 m, 600 m;
    - CC5: z = 400 m, 500 m, 600 m.
3) Numerical simulations (2D-drift, plane-strain approximation) considering a variation of the material parameter set to simulate different materials (e.g. different grain size distribution). A detailed description of these tests used for the parameter determination can be found in Part 1 of this article. Following variations have been investigated:
    - parameter set derived from the BGR long-term compaction test TK-031;
    - parameter set derived from the TUC long-term compaction test TUC-V2;
    - parameter set derived from the GRS (German Society for Plant and Reactor Safety) long-term compaction test dry-sample.

A similar variation to series 1 can be referenced to VSG final reports (AP9.2 2012; AP10 2013) or in US-German-workshop presentation from Müller-Hoeppe & Lerch 2021 regarding Gorleben site. However, it has to be emphasized that the variations shown in this article do not refer to any location. Rather, they only serve as a generic example to test the model functionality and do not realistically represent mechanical and thermal load conditions in the repository.

For the calculations in the variation series 1 and series 2, the parameter set derived from the TUC long-term compaction test TUC-V2 was chosen as the reference parameter set. The results of the variation series 1 are depicted in Figure 2. The assumed load history is also

shown in this diagram and derives from the following numerical calculations of series 2. The chosen temperature levels and moisture contents represent possible ranges for relevant conditions in the access drift, crosscut as well as in the emplacement drift.
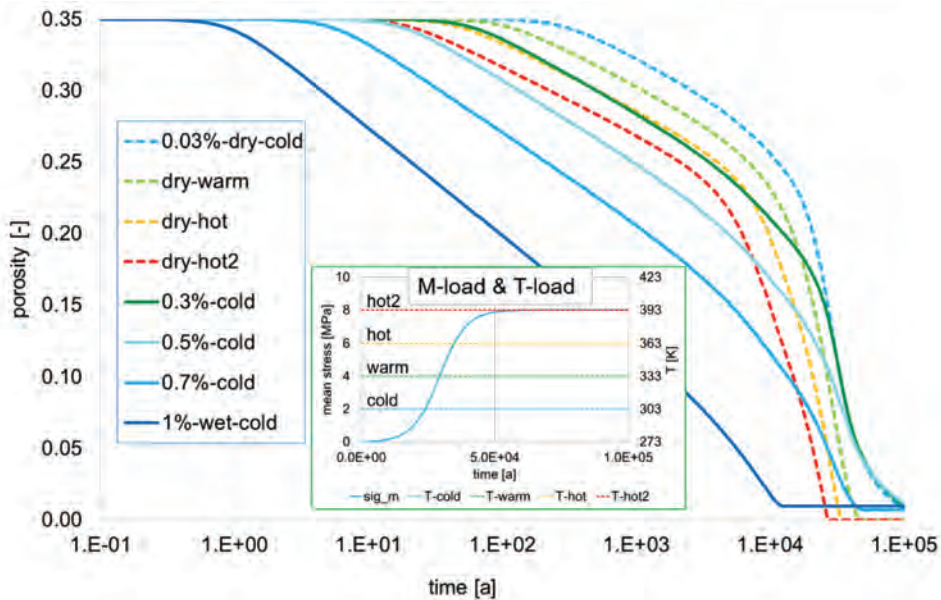
Figure 2: Results of analytical calculations for a zone in a drift with crushed salt backfill considering variation of moisture content and temperature

The curves with variations of moisture content and temperature can be regarded as plausible and meet the expected coherent progress. That is, the higher both, temperature as well as moisture content, the higher the decrease of porosity. Additionally, it is recognizable that, at least with the parameters currently used and with the relationships built into the new constitutive model, the dependence of the compaction behavior from the moisture content is more significant than the temperature dependence, although both dependencies seem to be essential and not negligible.

Figure 3 shows the results of numerical calculations with a 2D-model representing a single drift. The discretization and the dimensions of the drift are shown in the figure as well. The following conditions were used in the simulations: the stratigraphy surrounding the drift was assumed to be rock salt and was taken into account in the model with 30 m dispersion around the drift, the temperature was set at 21.1 °C/ 22.3 °C/ 23.5 °C for respective depths of 400 m/ 500 m/ 600 m, the drift was backfilled one year after the excavation, the crushed salt tied to the intact salt (without interface).
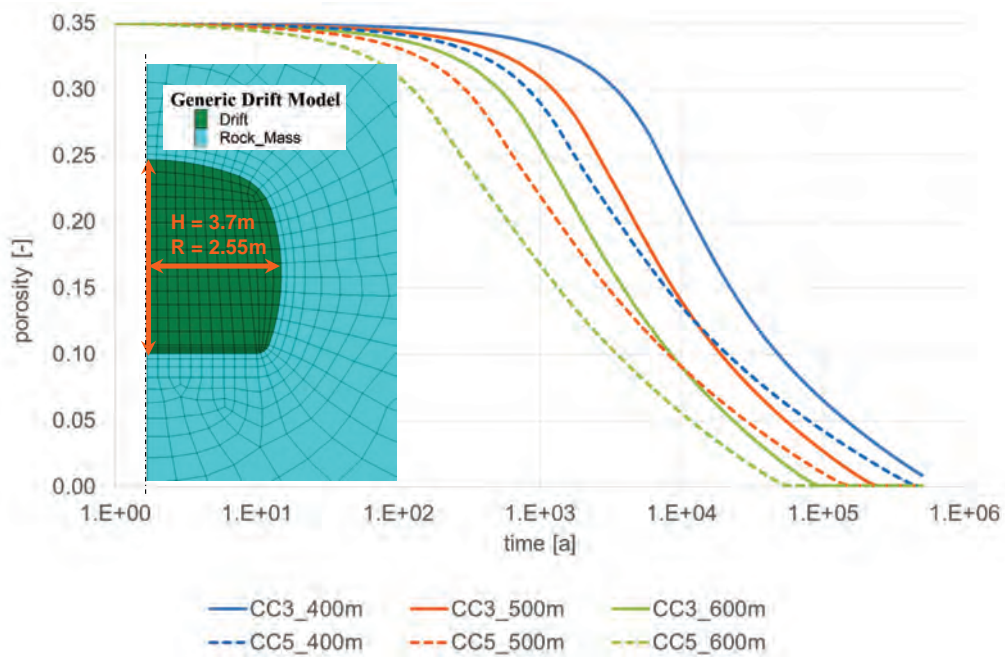
Figure 3: Results of numerical calculations with variation of (a) creep behavior of surrounding rock salt and (b) depth of the drift

The chart shows the progression of the averaged porosity over the cross section of the drift. In similar fashion to Figure 2, the variations of creep behavior of the surrounding rock salt and the depth of the drift deliver plausible results. Both of these varied parameters influence the creep deformation of the surrounding rock salt onto the backfill in the cavity. It can be seen that (a) the depth affects the compaction time similar to the creep class for these certain variation ranges, (b) the constitutive model can respond clearly plausible to both external influences.

Finally, Figure 4 shows results of a variation series with three different parameter sets for dry conditions. The similarity of the curves with the parameter sets derived from TK-031 and TUC-V2 and the significant difference in the curve with the parameter set derived from the GRS test can be clearly identified. These simulations ran with reference boundary conditions: depth of 500m, creep class CC3 for rock salt, crushed salt is backfilled in dry condition 1a after the excavation. Figure 4 additionally shows a chronological sequence of surface plots for the spatial distribution of the minimum principal stress σ_3 in the surrounding rock and the porosity in the backfill. The rock is artificially shown without deformation and in contrast, the drift is shown with the deformations to visually highlight the compaction progress in the crushed salt and the volume changes of the drift. The surface plots are shown merely exemplary for the reference parameter set TUC-V2.
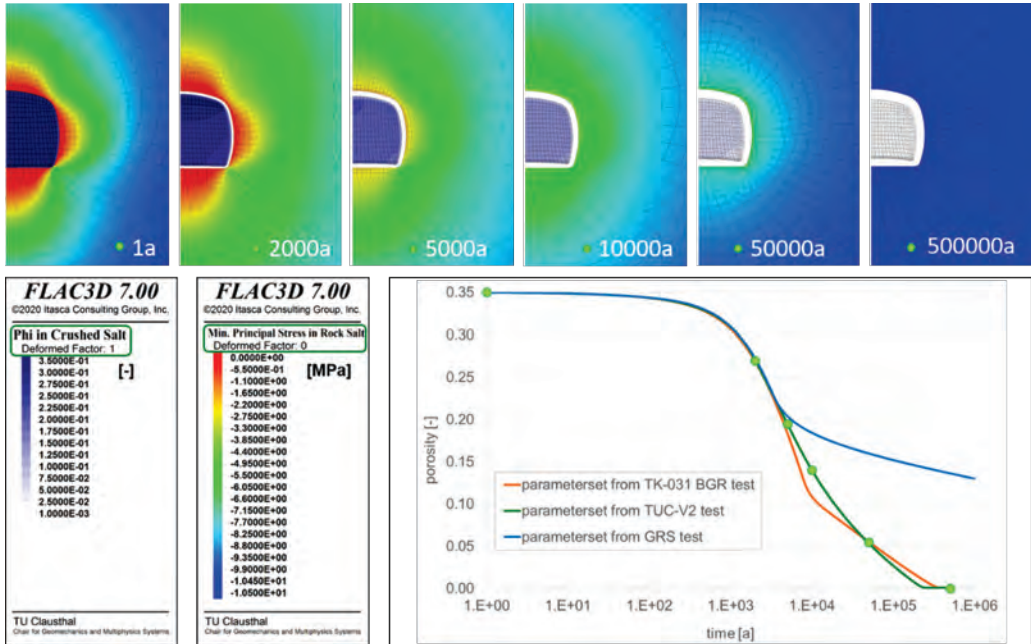
Figure 4: Results of numerical calculations considering a variation of the parameter set for the compaction behavior of crushed salt: average porosity of the drift over time and minimal principal stress in the surrounding rock salt (compressive stresses defined negative)

Based on the surface plots, a quite plausible chronological evolution and spatial distribution of porosity and stress can be seen. Furthermore, the state of full compaction is desirably remarkable, where the porosity in the entire cross section of the drift has decreased to the minimum value given by the constitutive model parameters (0.1%) and the stress in the surrounding rock has reached the primary stress level of 10.5 MPa. This means that the constitutive model is capable of modeling the entire compaction process from loose state to the progressive transition to a fully compacted state with volume-true creep behavior identical to the surrounding rock salt, which is precisely the main objective of long-term analyses.

It is important to emphasize that no quantitative evaluation of the results is presented here, since no realistic end-bearing boundary conditions were explicitly used. The primary focus was rather on examining and verifying the capabilities of the new constitutive model.

3 Development of the numerical equipment for the simulation of crushed salt backfilled chambers with complex geometry

3.1 Procedure for the idealization and discretization

After the first numerical simulations were successfully performed on geometrically simple object (drift), the second step was to continue with the application of the new constitutive model on more complex underground objects. Another important goal of these investigations was the idealization and discretization procedure for highly complex geometry for underground cavities, which enables robust simulations and plausible results for both backfilled and empty cavities. Therefore, in the first step, the variation analysis was performed using a functional model FM-1 with a single chamber at the depth of 600 m with complex geometry and a relevant time period of 100 a of standing empty before backfilling. The simulations were based on the

following conditions: the stratigraphy surrounding the chamber was assumed to be rock salt and was taken into account in the model with 500 m dispersion around the chamber and modeled with Lux/Wolters/Lerche constitutive model, the crushed salt tied to the intact salt (without interface), the temperature was set to 22 °C, the initial stress state at the depth of the chamber was 13 MPa.

Figure 5 shows the original geometry of the chamber selected for the investigations and the individual steps of the idealization and the discretization of the chamber.
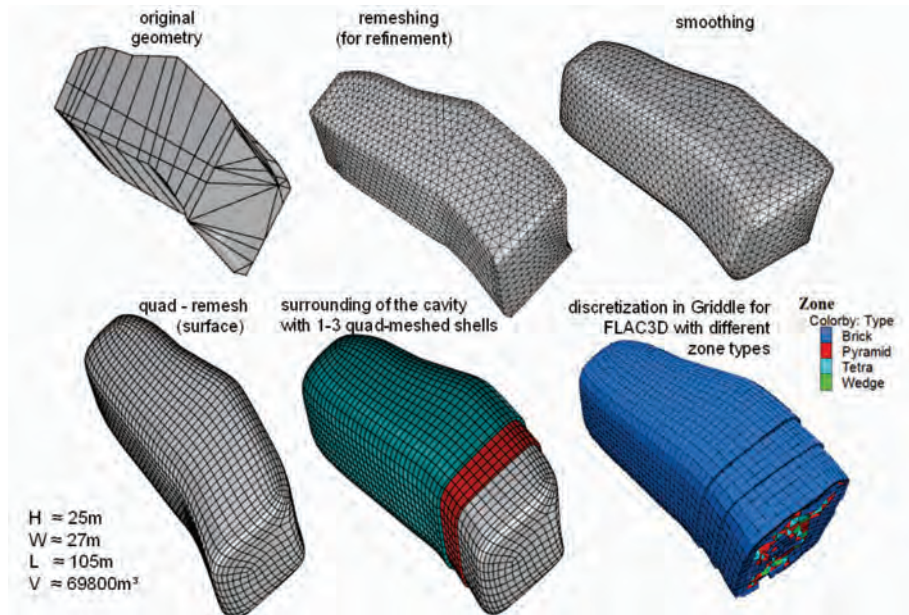
Figure 5: Idealization and discretization steps for a chamber characterized with relatively complex geometry

It can be seen that the original geometry is not suitable for an approximation with an ideal 3D-object (cylinder or cuboid), because it would imply too strong simplification. In this case, a higher degree of reality has been attempted and realized. The procedure was developed with the help of the Software Rhinoceros 7.0 and Griddle 2.0 and contained essentially:

1) Remeshing of the existing comparatively coarse mesh (if the raw data of the geometry is given as mesh) of the chamber surface into a very fine mesh; which keeps the fine details of the chamber contour and allows a better compatibility with the following step.
2) Smoothing of the surface mesh to avoid the sharp edges.
3) Remeshing of the mesh with quads. This step is quite useful when applying FLAC3D for numerical simulations and delivers automatically structured mesh for the surface. This stage is only the pre-step, because the mesh is not volumetrically discretized, yet.
4) Additional idea realized here is the enclosing of the rock surrounding the chamber with only hexahedral zones by avoiding pyramids and tetrahedrons. This ensures a structured mesh with good quality and in most cases also with a targeted fineness mesh in the potential excavation damaged zone EDZ or in relevant and numerically sensitive areas, i.e. serves for numerical stability. These areas with exclusively hexahedral zones are referred to as 'shells'.

5) The last step is the volumetric meshing of each mesh (shells and inside of the chamber) with Griddle 2.0. It can be seen that the discretization inside the chamber is not structured, while the shells (in this case 2 shells) are exclusively meshed with hexahedrons, as desired.

3.2 Development of the functionality for the numerical equipment with the help of one single chamber

To illustrate the effect of the two main mesh optimization steps: smoothing and enveloping with the quad-mesh-shells, three chamber discretization variants were created here (see Figure 7):

V1: without smoothing and without encasing with shells;
V2: with smoothing and without encasing with shells;
V3: with smoothing and encasing with shells (reference).
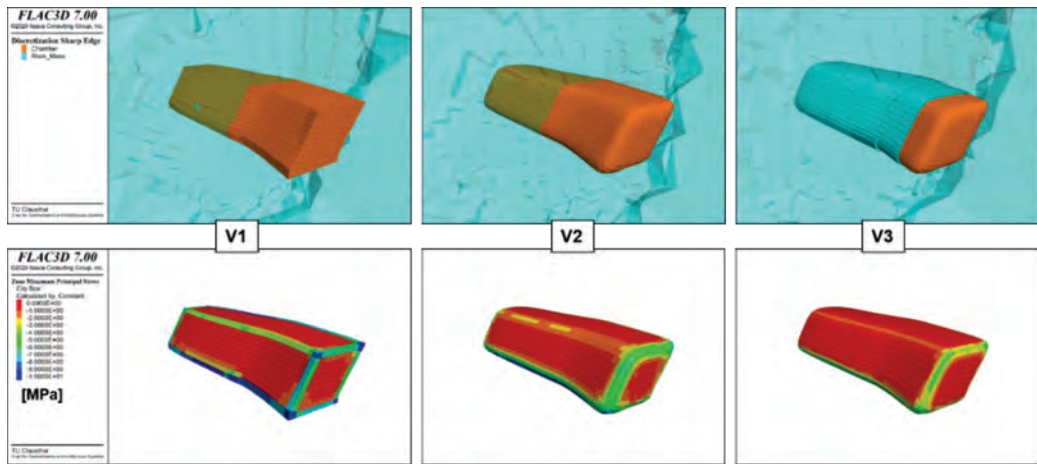
Figure 6: The three variants of discretization for the chamber and the associated distribution of the minimum principal stress at the contour of the chamber immediately after excavation

Test simulations were carried out with all three variants. The discretization effort, calculation time, stability and plausibility of the results were checked. As a result, especially the adverse peaks in the deviatoric stress (essential for rock salt behavior) were representative as an evaluation criterion. Furthermore, the fulfilment of the boundary condition at the chamber contour and the deviations in this respect served as criteria for mesh quality. Figure 6 shows exemplarily the minimum principal stress for all three mesh variants immediately after excavation. It can be seen that the distribution of the stress from variant to variant becomes more homogeneous and the boundary condition is increasingly better fulfilled due to the smoothing and the encasing with hexahedral zones.

Figure 7 shows further simulation results for t = 100 a. The iso-surfaces for the dilatancy distribution in the rock salt around the chamber can be seen for two different values of 1e-4 and 1e-5. Also in the spatial distribution of the damaged area around the chamber, a clear homogenization can be observed in the transition from variant 1 to variant 3.
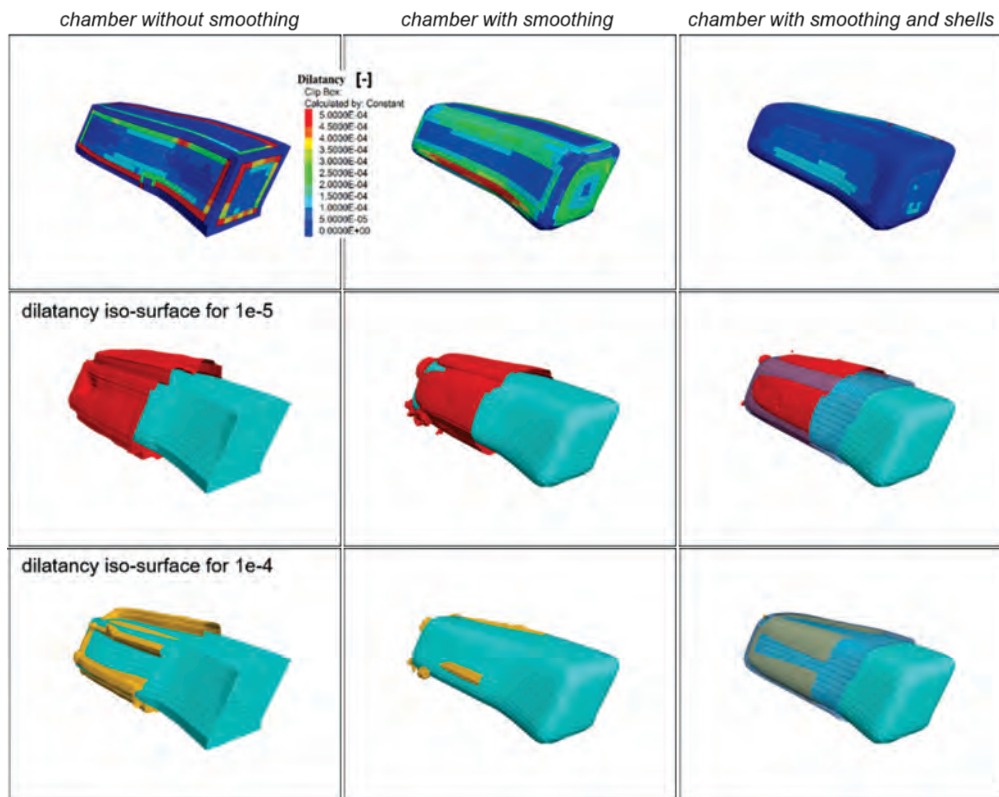
Figure 7: Dilatancy distribution in the rock salt around the chamber and iso-surfaces for the values of 1e-4 and 1e-5 by t = 100 a for three different discretization variants

In a following step, the full backfilling of the chamber with crushed salt after 100 a of empty state was simulated. It has been observed in the test variations that the stability of the simulations after the backfilling can be favored by using the quad-remeshed shells described above, but this time not in the surrounding salt but on the inside of the chamber. Two discretization variants V3 (previously reference) with the outer shells and an additional variant V4 with outer and inner shells were used in comparison. The simulation result after 200 a showed a numerical problem inside the chamber with illegal zone geometry due to the compaction process for variant V3, while variant V4 continued to calculate without any problems, at least for this simulation time, and resulted in a plausible distribution of the porosity in the chamber.

As a final result of the test series with a single chamber, the plots for the chronological progress of the compaction are shown in Figure 8. A plausible evolution of both porosity and mean stress in the chamber until nearly full compaction by 50000 a of total calculated time (or 49950 a of prognostic backfilling time) can be seen. Initial porosity of 30% with moisture content of 0.5% and the reference parameter set (from test TUC-V2) were used for this run.
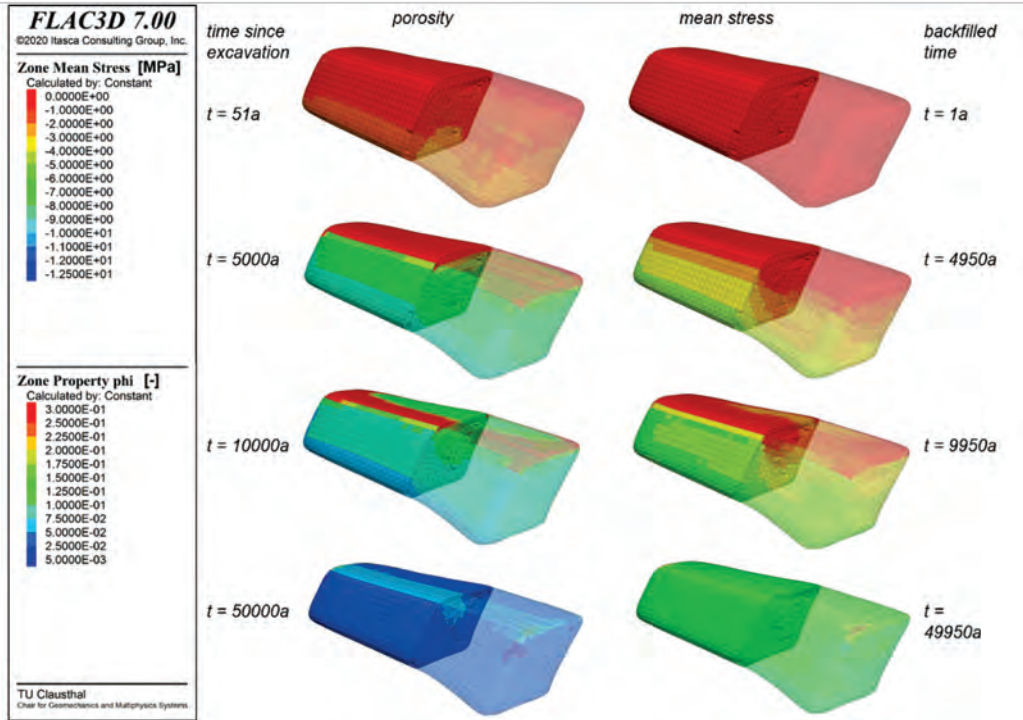
Figure 8: Evolution and spatial distribution of the porosity and the mean stress in the chamber with discretization variant V4 with crushed salt backfill (compressive stresses are negative)

3.3 Demonstration of the functionality for the developed numerical equipment with the help of a complex representative 3D mine

In the last and still ongoing stage, the investigations with the modeling of complex 3D underground structure are carried out. This generic 3D-layout consists of numerous underground excavations with complex geometry (five levels with two rows i.e. four for mirrored consideration as well as different salt types) and different backfilling times (with nearly instantaneous backfill of 1a empty standing time for potash excavations and 50 a for salt chambers). The corresponding discretized model and its dimensions are illustrated in Figure 9.

The first results of this variation series can be seen in the Figure 10 and Figure 11. Figure 10 demonstrates the evolution of porosity and mean stress in the crushed salt backfilled chambers in the potash seam as well as rock salt until 10000 a of simulated time. Although the full compaction state is not reached in the simulated time yet, a plausible tendency is recognizable so far: a significant reduction of the porosity and a corresponding increase of the mean stress. Initial porosity of 30% with dry condition and the reference parameter set (from test TUC-V2) were used.
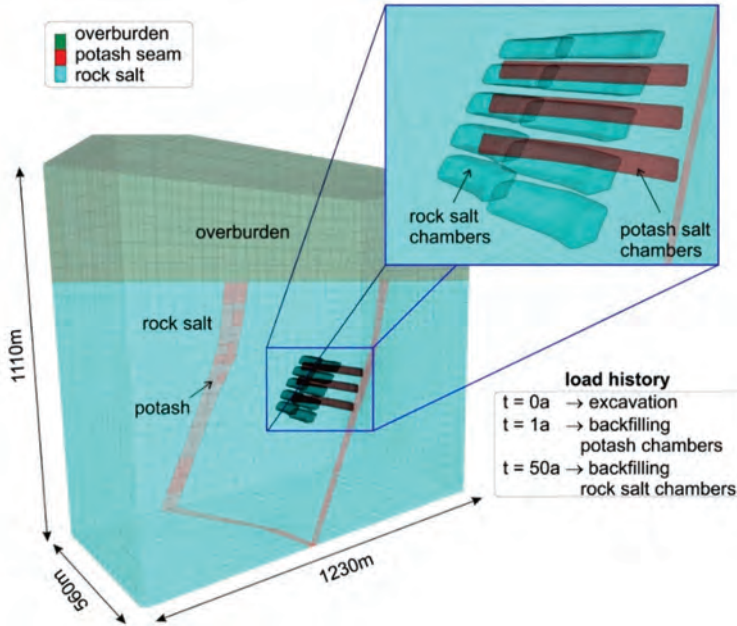
Figure 9: Discretized model for a representative 3D-mine containing numerous underground chambers with complex geometry and 3D-geology
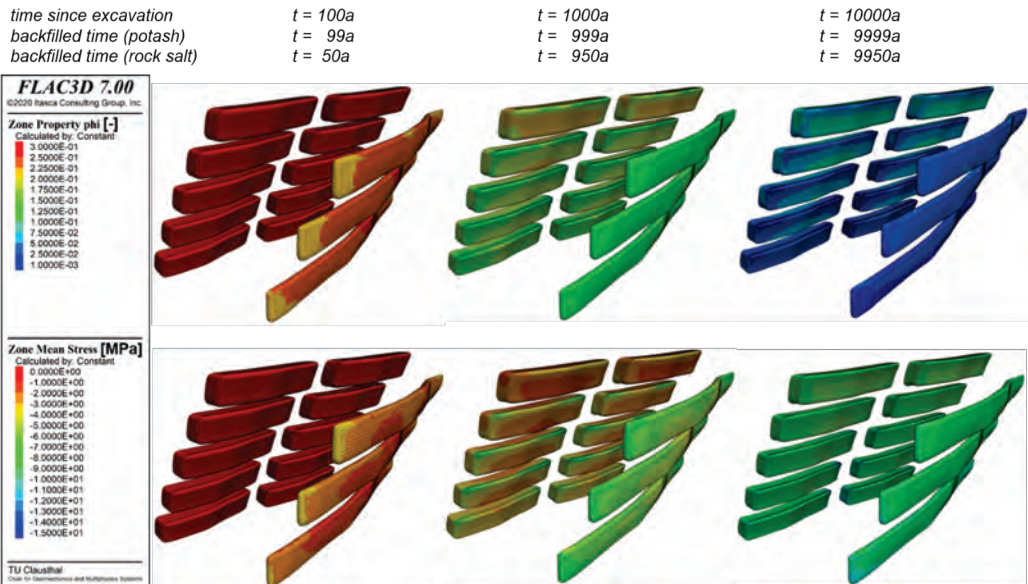
Figure 10: Time evolution and surface distribution of the porosity and the mean stress in the backfilled chambers in potash and in rock salt (compressive stresses are negative)
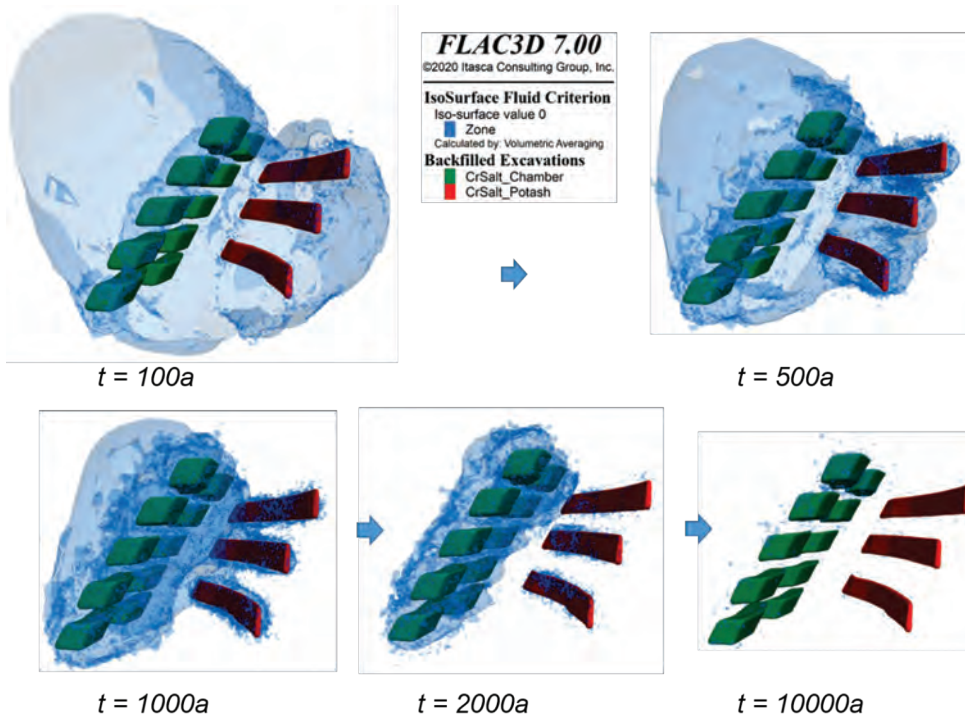
Figure 11: Progressive reduction of the spatial distribution of fluid criterion (iso-surface)

While Figure 10 shows the distribution changes inside the chamber, Figure 11 represents the long-term safety-relevant effects on the surrounding rock. Namely the 3D-areas of the rock mass with the failed fluid criterion $\sigma_3 < p_{fl}$. It can be observed, that the backfill recognizably reduces the areas of the rock mass with failed fluid criterion due to support pressure progressively building up in the chambers.

4 Summary and outlook

In this article, the simulation results of initial application of the new constitutive model EXPO-COM of TUC to describe the compaction behavior of the crushed salt were presented. A common and yet essential challenge to ensure reliable statements for a system analysis is to model geometrically complex underground objects. The TUC drafted an exploitable and practical approach in this regard. In order to demonstrate and verify the functionality of the constitutive model and the robustness and practicability of the developed numerical modeling equipment, the following analytical and numerical variations were carried out:

1)   Analytical calculations for a zone in a drift with variations of temperature and moisture content;

2)   Numerical simulations for a drift (with representative dimensions for radioactive waste repository research) with variations of drift depth, creep behavior of the surrounding rock salt as well as parameter sets for the compaction behavior of crushed salt;

3)   Numerical simulations for a geometrically complex chamber with different discretization variants – 50a long empty state and then backfilled with crushed salt;

4)   Numerical simulations for an extensive 3D model with several chambers with complex geometry excavated in rock salt and in potash salt.

Plausible results were obtained in all four cases. This means, the following objectives were reached:

1)   The constitutive model is functional, responds to all relevant influencing parameters with plausible reactions and provides robust results starting from loose to fully compacted state with the assurance of a smooth transition from crushed salt behavior (compaction + creep) to rock salt behavior (volume-true creep).

2)   The presented numerical modeling equipment gives the possibility to handle geometrically complex but also extensive 3D underground objects in a robust numerically stable way providing plausible results.

Further planned meaningful improvements:

1)   In relation to constitutive model the reliability and realism of the statements need to be increased. This requires further expansion of the laboratory database (planned in KOMPASS II). Furthermore, in situ pilot test must be built to provide suitable measured values to validate the model (planned in SAVER). These future expansions of the data will allow further development and validation of the constitutive model.

2)   In relation to numerical modeling equipment: Similar to the constitutive model, only the functionality of the numerical modeling toolset/equipment has been investigated and developed so far. The realism of the statements can only be achieved and demonstrated in the future by means of a recalculation of a real in situ pilot test construction with suitable measured values.

Acknowledgements

References

BAMBUS I. BECHTHOLD, W., ROTHFUCHS, T., POLEY, A., GHOREYCHI, M., HEUSERMANN, S., GENS, A. & OLIVELLA, S. 1999. Backfilling and Sealing of Underground Repositories for Radioactive Waste in Salt. Final Report. - European Commission, nuclear science and technology, EUR 19124 EN, Luxembourg.

BAMBUS II. BECHTHOLD, W. SMAILOS, E., HEUSERMANN, S., BOLLLNGERFEHR, W., BAZARGAN, SABET, B., ROTHFUCHS, T., KAMLOT, P., GRUPA, J., OLIVELLA, S. & HANSEN, F.D. 2004. Backfilling and sealing of underground Repositories for radioactive waste in salt. Final report. - European Commission, nuclear science and technology, EUR 20621 EN, Luxembourg.

BGR. BRÄUER, V., EICKEMEIER, R., EISENBURGER, D., GRISSEMANN, CH., HESSER, J, HEUSERMANN, S., KAISER, D., D., NIPP, H.-K., NOWAK, T., PLISCHKE, I., SCHNIER, H., SCHULZE, O., SÖNNKE, J., JAN RICHARD, J.-R. 2011. Description of the Gorleben site Part 4: Geotechnical exploration of the Gorleben salt dome

DÜSTERLOH, U., LERCHE, S., DYOGTYEV, O. & FEIERABEND, J. 2018. Langzeitsicheres Abdichtungselement aus Salzschnittblöcken – Bautechnische Realisierung Technikprüfstand mit Durchführung und Auswertung erster Versuche. Abschlussbericht zum BMWi-Vorhaben 02E11425.

DÜSTERLOH, U., LERCHE S. & ZHAO. J. 2021. Pilot plant tests to demonstrate the functionality of sealing elements made of salt cut bricks. Saf. Nucl. Waste Disposal, 1, 117–119.

ITASCA, FLAC3D, VERSION 7.0. Numerical modeling software for geotechnical analyses of soil, rock, groundwater, constructs and ground support. Minneapolis, Minnesota: Itasca Consulting Group.

ITASCA, Griddle Version 2.0. Advanced Meshing Tools for Numerical Modeling

KOMPASS I. Compaction of crushed Salt for the safe Containment, Final Report GRS-608, of the joint project with partners GRS, BGE TEC, BGR, IfG, TUC, Sandia, KOMPASS I, FKZ 02E11708A, 2020.

MÜLLER-HOEPPE, N. & LERCH, C.H. 2011. Role of crushed salt in the repository concept, 11th US/German Workshop on Salt Repository Research, Design, and Operation, BGE TECHOLOGY GmbH, Part 2 of the online workshop.

REPOPERM I. KRÖHN, K.-P., STÜHRENBERG, D., HERKLOTZ, M., HEEMANN, U., LERCH, CH. & XIE, M. 2009. Restporosität und -permeabilität von kompaktierenden Salzgrus-Versatz, GRS – 254, ISBN 978-3-939355-29-8,.

REPOPERM II. KRÖHN, K.-P., STÜHRENBERG, D., JOBMANN, M, HEEMANN, U., CZAIKOWSKI, O., WIECZOERK, K., MÜLLER, C., ZHANG, C.L., MOOG, H., SCHIRMER, S. & FRIEDENBERG, L. 2007 Mechanical and hydraulic behaviour of compacting crushed salt backfill at low porosities, GRS – 450, ISBN 978-3-946607-32-8.

ROBERT MCNEEL & ASSOCIATES: (Rhinoceros 7). SAFEND-BASE. DÜSTERLOH, LERCHE S., ZHAO J. 2021 Pilot plant tests to demonstrate the functionality of sealing elements made of salt cut bricks, Interdisziplinäres Forschungssymposium für die Sicherheit der nuklearen Entsorgung, Berlin,

SAFEND-BASE. FRIEDENBERG, L., BEAN, J., CZAIKOWSKI, O., DÜSTERLOH, U., MÜLLER-HOEPPE, N., LAURICH, B., LERCH, CH., LERCHE, S., LÜDELING, CH., MILLS, M., POPP, T., REEDLUNN, B., STÜHRENBERG, D., SVENSSON, K., ZEMKE, K. & ZHAO, J. 2021. Compaction of crushed salt for safe containment, Berlin.

VSG-AP10. LARUE, J., BALTES, B., FISCHER, M., FRIELING, G., KOCK, I., NAVARRO, M., SEHER, H. 2013. Radiologische Konsequenzenanalyse, Bericht zum Arbeitspaket 10, Vorläufige Sicherheitsanalyse für den Standort Gorleben, GRS – 289,

VSG-AP9.2-Memo. CZAIKOWSKI, O. & WIECZOREK, K. 2012. Salzgruskompaktion – Kalibrierung der in CODE_BRIGHT verwendeten physikalischen Modellansätze zur numerischen Simulation. Memo im Arbeitspaket 9.2, Vorläufige Sicherheitsanalyse für den Standort Gorleben, Gesellschaft für Anlagen- und Reaktorsicherheit (GRS) mbH: Braunschweig,.

VSG-AP9.2. MÜLLER-HOEPPE, N., BUHMANN, D., CZAIKOWSKI, O., ENGELHARDT, H.-J., HERBERT, H.-J., LERCH, CH., LINKAMP, M., WIECZOREK, K. & XIE, M. 2012. Integrität geotechnischer Barrieren Teil 1 Vorbemessung Bericht zum Arbeitspaket 9.2, Vorläufige Sicherheitsanalyse für den Standort Gorleben, GRS – 287,

Pilot plant tests to demonstrate the functionality of sealing systems made of salt cut bricks

U. Düsterloh[1], S. Lerche[2], J. Zhao[3]*

[1]Clausthal University of Technology, Germany; [2]Clausthal University of Technology, Germany; [3]Clausthal University of Technology, Germany

* uwe.duesterloh@tu-clausthal.de

ABSTRACT: To ensure long-term safe confinement of high-level radioactive waste in a repository in saliniferous formations geological barriers in combination with geotechnical barriers are demanded to be permanently tight against fluids. As a consequence, an essential aspect of underground disposal is to demonstrate that connections between biosphere and lithosphere, i.e. shafts, boreholes and drifts, created during the excavation of underground cavities can be sealed sufficiently tightly. An essential element of the sealing system required for this purpose is the shaft closure. All shaft closure concepts developed so far include sealing and support elements in repository shafts, but differ in the arrangement of these construction elements and the materials used for this purpose. To ensure both, redundancy and diversity of a sealing system currently proposed and investigated materials for the construction of sealing elements are: clay/bentonite, asphalt/bitumen, crushed salt and salt-/sorel concrete. In addition to the materials mentioned above, a research project funded by the Federal Ministry for Economic Affairs and Energy is investigating the possibility of integrating a layer of salt cut bricks into the shaft closure system as a long-term sealing element with the option of enabling shortly after installation a long-term healing of the geological barrier. The following article first documents laboratory investigations into the geomechanical-geohydraulic effectiveness of a closure element made of salt cut bricks. For this purpose, chapter 2 presents the development and construction of a test facility able to investigate a cylindrical specimen made of salt-cut bricks characterized by a length of 1,5m and a diameter of 0,75m. Chapter 3 describes work on the configuration and fabrication of salt cut bricks and addresses issues of spatial arrangement of salt cut bricks to avoid axially continuous joints in the specimen. Chapter 4 document special boundary conditions, which have to be consider in case of installing, implementation of tests and removal of large-scale test specimens made of salt cut bricks. Finally, chapter 5 presents the results of mechanically-hydraulically coupled tests to demonstrate and prove the functionality and suitability of sealing elements made of salt cut bricks.

1   Introduction

To guarantee long term safe confinement of high-level radioactive waste perforations respectively disturbances of the geological barrier resulting from excavation of drifts, shafts and boreholes of the repository mine must be compensated by engineered and geotechnical barriers (including crushed salt backfill) until the effectiveness of the geological barrier is restored by long-term convergence processes.

An important element in the closure concept is the shaft closure. The main function of a shaft closure is to prevent water / solutions from entering the repository from the overburden or contaminated solutions from escaping from the repository into the overburden after it has been closed. Within the scope of the proof it has to be proved that the shaft closure system is suitable to show a sufficiently low hydraulic conductivity similar to that of the surrounding rock salt (Kreienmeyer et al. 2008). The surrounding unexcavated saline rock, which is liquid- and gas-tight while maintaining the primary rock pressure, is to be used as a benchmark.

The function of the shaft closure can only be guaranteed by a suitable design with long-term stable closure materials and sealing elements in combination with an early and sufficient regression of the excavation damage zone. Since the excavation of a shaft in depths suitable for a repository generally results in a near-contour excavation damage zone, this indicates that the geotechnical barrier "shaft closure" is characterized by the interaction of technical barriers with the geological environment. The performance of a shaft closure system therefore does not result exclusively from the structural properties of the technical element(s), but is rather dependent on the long-term interactions of the closure structure with the surrounding rock mass (Arbeitskreis 3.1 Zalzmechanik DGGT 2021). All shaft closure concepts developed so far include sealing and support elements in repository shafts, but differ in the arrangement of these construction elements and the materials used for this purpose (Kudla & Herold 2021; Emmerich et al. 2019; Wieczorek et al. 2021; Kudla et al. 2021; Bauer et al. 2019; Engelhardt 2004; Glaubach et al. 2013; IAEA 2013; Kudla et al. 2009; Kudla et al. 2009; Kröhn et al. 2009; Stührenberg et al. 2010; Rothfuchs et al. 2005; Eberth & Müller-Hoepe 2009; Sitz 1981).To ensure both, redundancy and diversity of a sealing system currently proposed and investigated materials for the construction of sealing elements are: clay/bentonite, asphalt/bitumen, crushed salt and salt/sorel concrete. The aim of the following explanations is to show, that in addition to the above mentioned materials, a layer of salt cut bricks is suitable for use as a long-term sealing element with the option of enabling shortly after installation a long-term healing of the geological barrier.

Like the surrounding rock mass, the salt cut bricks consist of natural rock salt. They are profiled according to plan with the aim of minimizing the joint volume as far as possible by means of a cut adapted to the shaft geometry. The joints can optionally be filled either with a supersaturated salt solution, SVV (self-healing backfill) or a molten salt, or they can be brought into contact directly by moistening the salt bricks surfaces. After the salt solution has hardened (cooling of the solution, evaporation of the mixing water), only the air-filled pore space of the crushed salt joint filling or the joint volume resulting from a "mismatching" of individual salt cut bricks is accessible to a reaction, so that the sealing element made of salt cut bricks develops an early supporting pressure against the creeping rock salt mass compared to crushed salt, and has a low initial porosity and already exhibits a high sealing effect in the short term (regression of the excavation damage zone). It can also be assumed that a cohesive bond between the rock mass and the sealing element can already be achieved with the introduction of the joint filling or wetting of the salt cut brick contact surfaces (no or reduced separation surfaces in the contact zone).

In order to answer the question whether sealing elements made of salt cut bricks with joint filling are suitable as a long-term sealing component made of native material for the sealing of repositories and underground disposal sites, large-scale tests on a pilot plant scale are required. Due to the masonry-like characteristics of the sealing elements to be investigated, small-scale laboratory tests on test specimens measuring a few centimeters to decimeters are merely suitable for selected questions of fundamental nature. In contrast, a qualitatively sufficiently reliable analysis of the system behavior requires a test technique that takes into account the size relationships between the crystal grain and the salt cut brick in a manner that is at least sufficiently representative, i.e. a specimen size that clearly exceeds the usual laboratory scale. Essential prerequisites for investigating the geomechanical-geohydraulic effectiveness of a sealing element made of salt cut bricks are thus the development and construction of a pilot plant for analyzing the mechanical and hydraulic material properties of the composite system of salt cut bricks and joint filling, as well as preliminary investigations into the production of salt cut bricks and jointing material ($\rightarrow$ cutting technique/processing of salt cut bricks; production/processability of the joint filling material) and on the spatial arrangement of the salt cut bricks ($\rightarrow$ avoidance of axially continuous joints in the composite system). The work successfully completed in the meantime to ensure that the conditions outlined above are met is documented below in chapters 2 (development and construction of a pilot plant test rig), 3 (production and configuration of salt cut bricks to avoid axially continuous joints) and 4 (special requirements for carrying out the test and for specimen installation

and removal). Chapter 5 finally contains the proof that based on the measurement results of first THM-coupled pilot plant tests it can be stated that a sealing element made of salt cut bricks exhibits a comparatively low permeability of $K < 10^{-18}$ m^2 already after a few months of loading at insitu relevant stresses.

2   Design and construction of the pilot plant test rig

Based on the designs documented in Düsterloh 2014 and Düsterloh et al. 2018, the pilot plant test rig is characterized by a triaxial cell of H = 3.2 m height, D = 1.4 m diameter and a total mass of M = 18 t, Fig. 2.1.

Performance data:

$max\sigma_3$ = 25 MPa

$maxF_{ax}$ = 28 MN

$maxP_{gas-primär}$ = 25 MPa

$maxP_{gas-sekundär}$ = 25 MPa

maxT = 80 °C

$max\Delta u$ = $\pm$ 30 cm

sample size:1,5 m x 0,75 m
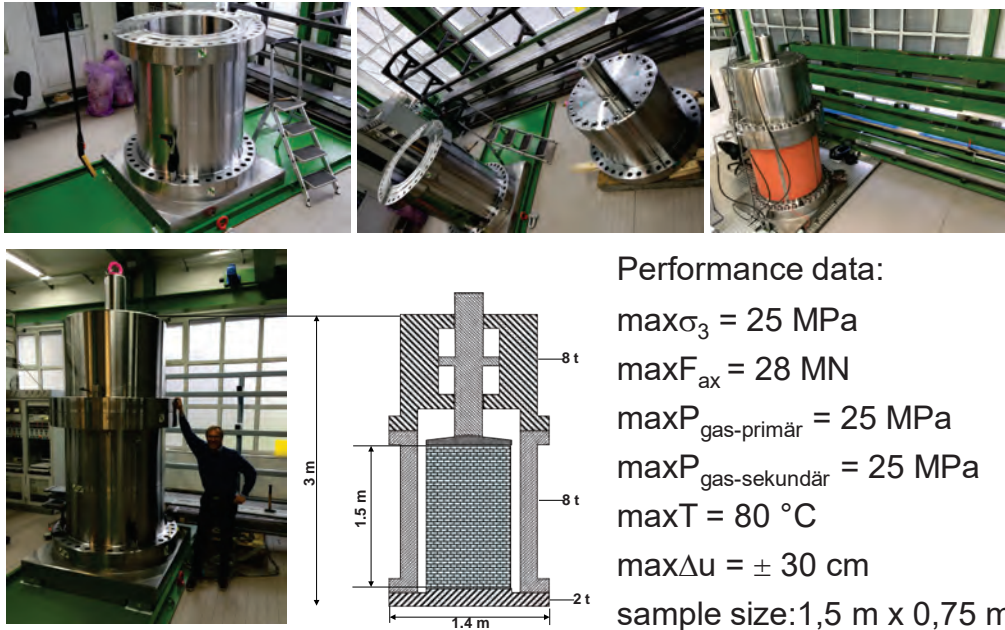
Figure 1: Assembly of triaxial test system designated Dü21

Taking into account the test specimen dimension of l = 1.5 m length and d = 0.75 m diameter, the hook height of the crane runway required for swiveling the triaxial cell in and out during a test specimen change is 4.7 m plus the height of the trolley. Since corresponding spatial conditions were not available in the lab of the Chair for Waste Disposal Technologies and Geomechanics, a two-part construction consisting of a lower and an upper section of the triaxial cell with masses of $M_{triaxbottom}$ = 7.74 t and $M_{triaxtop}$ = 8.37 t was generated. The test rig has a total of five independently controllable hydraulic circuits for axial pressure (0 - 50 MPa), confining pressure (0 - 25 MPa), primary gas pressure (0-25 MPa), secondary gas pressure (0-25 MPa) and fluid pressure (0-25 MPa). The axial pressure is generated by means of a hydraulic power pack and a 7-piston pump. Continuously variable EMC cylinders with the option of high-precision measurement and control of the supplied and discharged volume flows and the specified pressures are used to generate the confining pressure, gas pressure and fluid pressure. The test temperature can be controlled between room temperature and T = 80°C, the maximum available stroke of the axial piston is 60cm.

3 Configuration and production of salt cut bricks - avoidance of axially continuous joints

In view of the large number of possible salt cutting brick configurations a calculation software was developed to determine by calculation the geometry and arrangement of the salt cut bricks for varied joint widths and numbers of cutting bricks, taking into account the requirement of avoiding axially continuous joints. Based on the above mentioned requirements, a 3-layer system according to Figure 2 was generated as the final configuration using the calculation software. Each of the three layer levels is characterized by a height of 10 cm and a rotationally offset of 15° with respect to the respective neighboring layer. As a consequence, the first layer and the fourth layer, the second and the fifth layer, etc. do have an identical configuration (→ numbering of the salt cut brick layers consecutively, starting with the lowest layer). To avoid vertically continuous joints in the area of the central salt cut brick, differently dimensioned central bricks are used. The joint width is assumed to be equidistant in the salt cut brick system (→ horizontal joint thickness = vertical joint thickness). Considering the above specifications, each individual layer plane of the sealing element consists of a prismshaped central piece, characterized by a uniform polygon with flat faces and several prismshaped salt cut bricks positioned centrally around this central piece. To ensure an overall cylindrical geometry of the sealing element respectively test specimen made of salt cut bricks, the salt cut bricks of the outer ring have a rounded outer surface. Based on the configuration outlined above, the result is an orthogonal alignment of the radial forces (confining pressure) acting on the sealing system with respect to the tangential joints.

Preparation of rock salt cut bricks takes place either directly by milling from large-diameter drill cores or from rock salt slabs cut by dividing using a chain saw from the rock salt cut bricks obtained underground by perforation drilling. According to Figure 3 the specimen is generated by a total of 375 salt cut bricks. Approximately 4 m^3 and 9 t of raw salt material were required to produce a specimen / sealing element of l = 1.5 m length and d = 0.75 m diameter (V = 0.66 m^3, m ≈ 1.5 t). The mass of crushed salt generated during salt cut brick production can be estimated to be about 4 t. In addition, there are cutting losses in the order of approx. 3 t.
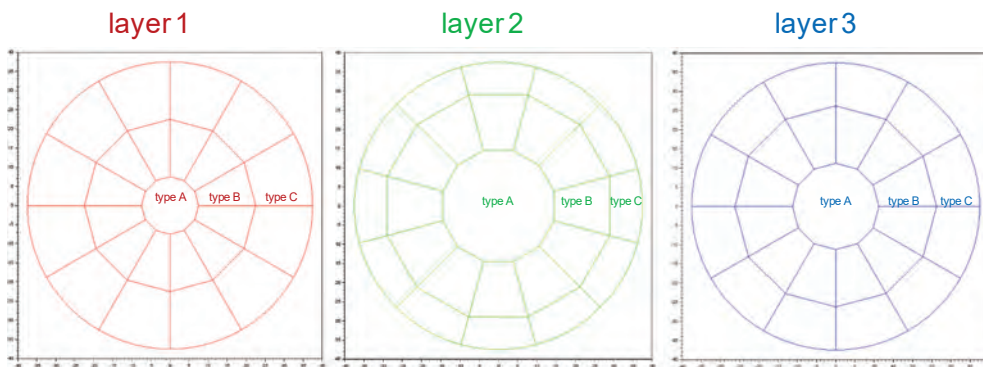
Figure 2: Representation of the base areas of the salt cut bricks (central piece, trapezoid type 1, trapezoid type 2 with rounded outer edge)

Figure 3: Production of salt cut bricks from large-diameter cores and salt plates

4   Preliminary tests - results and experience in carrying out pilot plant tests on test specimens made from salt cut bricks - lessons learned

With regard to the test and calibration trials required following the structural synthesis of the mechanical, hydraulic, electrical and electronic system components outlined in section 2 to test the functionality of transducers and sensors, control and regulation software, hydraulic power unit and hydraulic pump, EMC cylinders and heating tapes, etc., reference is made to (Düsterloh 2014). The installation of a test body is necessary for the realization of the test and calibration experiments. In contrast to classical triaxial test systems, where test and calibration experiments are regularly carried out using a "dummy" made of steel or aluminum, an alternative "dummy construction" had to be selected in view of the dimensions of the test specimens and sealing elements of the pilot plant test rig, which are specified as l = 1.5 m in height, d = 0.75 m in diameter and V = 0.66 m^3 , since otherwise a steel dummy with a mass of 4.6 t and corresponding steel costs would have had to be procured. Consequently, a steel tube with internal stiffening was designed as a dummy and its load-bearing and deformation properties were analyzed numerically (Düsterloh et al. 2018).

To protect the test specimens or the sealing elements made of salt cut bricks against penetration of confining pressure oil a rubber jacket adapted to the planned pressure and temperature boundary conditions is required, analogous to the performance of classical strength and creep tests on cylindrical solid test specimens. Since prefabricated rubber

jackets are not commercially available for the intended pilot plant tests on large test specimens of dimension d = 75 cm, l = 150 cm, the rubber jacket was realized by bonding a 6 mm thick, 2.35 m x 1.58 m NBR mat (Remalin 70-CN) on site. As a result of repeated tests on pressure- and temperature-stable sealing of the specimens, the main requirements for pressure-tight jacketing of the large specimens were:

(a)   Due to the softness of the material, NBR shore grades smaller than 70 lead to a damage of the rubber jacket after a few hours to a few weeks in the area of the salt cut brick limits, depending on the pressure and temperature conditions selected for the tests, with the consequence of oil penetration.
(b)   For successful bonding of the seam, the rubber mat must be ground on both sides and fixed with an overlap of approx. 40 mm - 50 mm.
(c)   In contrast to conventional triaxial tests on small-scale solid test specimens, a tight bond between the rubber jacket and the end-face pressure pieces cannot be achieved by means of one hose clamp each. Instead, the rubber jacket must be bonded over its entire surface to the upper and lower pressure pieces, and the hose clamps must be made in several parts to ensure uniform pressure acting radially over the circumference of the pressure pieces.
(d)   Crystal grain breakouts in the area of the marginal cut brick boundaries must be filled with a suitable material (e.g. Kaloplast) to protect the jacket.
(e)   To test the tightness of the bond, it has proved useful to apply a low gas pressure of approx. 1 bar to the test specimen via the end pressure pieces before installing the specimen in the triaxial cell and before applying the confining pressure, and to apply a leak test agent (leak detection spray) to the bond seams so that any defects in the bond can be identified before the start of the test.
(f)   In contrast to classical tests on small-scale solid test specimens, a system of salt cut bricks weighing about 1.45 tons cannot be removed from the lower pressure piece without further technical aids. Therefore a multipart formwork able to enclose the specimen in place after performing the test, lifted off the lower pressure piece and swung out sideways has been constructed.
(g)   Finally, results of preliminary tests have shown, that continuous extension loading, as practiced in the field of triaxial strength and creep tests on solid test specimens, cannot be directly transferred to the investigation of test specimens made of salt cut bricks. Due to a continuous specimen elongation in case triaxial extension loading a separation of the horizontal joints between the salt cut bricks occure and, as a consequence, the rubber jacket is pressed into the open joints and finally tears open.

To avoid the opening of salt cut brick joints resulting from extension loading, the load in the test is applied by specifying so called plain-strain loading conditions which are characterized by a constant confining stress σ_3 and a hindered axial deformation $\varepsilon_1 \approx 0$. Since $\varepsilon_1 \equiv 0$ cannot be realized in terms of measurement and control, a minimum deformation of u_z = 0.2mm or ε_1 = 0.013% was specified. The axial stress induced by this is oscillating and leads to a test specimen stress that changes continuously between compression and extension (see test evaluations in Chapter 5).

5   Performance and evaluation of pilot plant tests under varied THM loads

The pilot plant test rig described above was used to carry out a permeability test to demonstrate the functional capability of sealing systems made of salt cut bricks. Fig. 5.1 shows the basic test setup of the pilot plant tests as well as the mechanical boundary conditions applied.
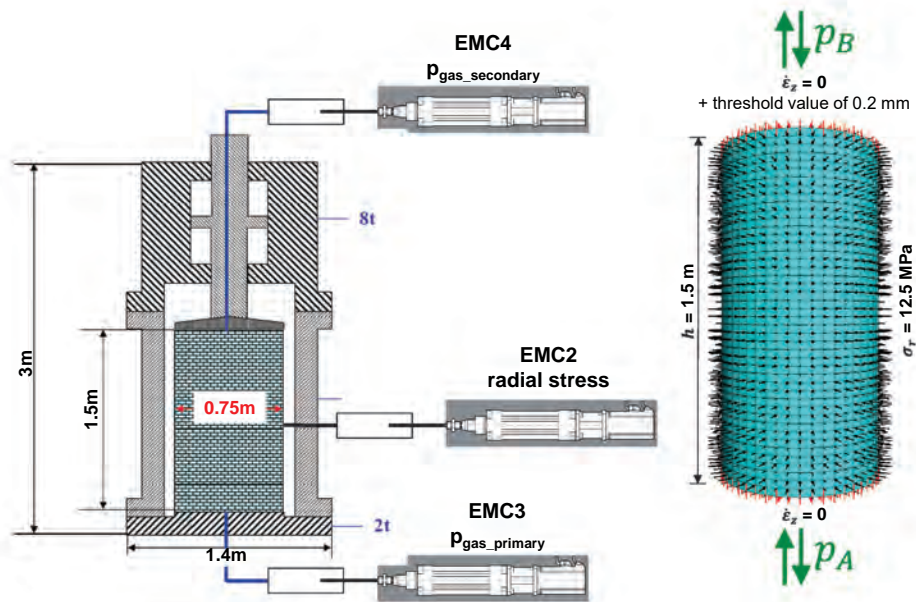
Figure 4: Test setup of the pilot plant tests and mechanical boundary conditions

Mechanical boundary conditions:

With respect to Figure 4 the cylindrical salt cut brick structure was loaded with a constant confining pressure of 12.5 MPa during the test. Axial strains were avoided to a large extent. For reasons of control boundary conditions, an axial deformation-related threshold value of 0.2 mm corresponding to an axial strain of approx. 0.013% ($\rightarrow 0.2\,\text{mm} / 1500\,\text{mm} \cdot 100\%$) was specified at the face of the test specimen. As a consequence of this threshold value, the axial stress is not constant, but oscillates between 7.5 MPa and 17.5 MPa, Figure 5. The axial strain, shown in Figure 5 too, is given by an average value of approx. 0.013% during the entire test run, while the volume strain shows a numerical value of approx. 0.106% at the end of the test run.
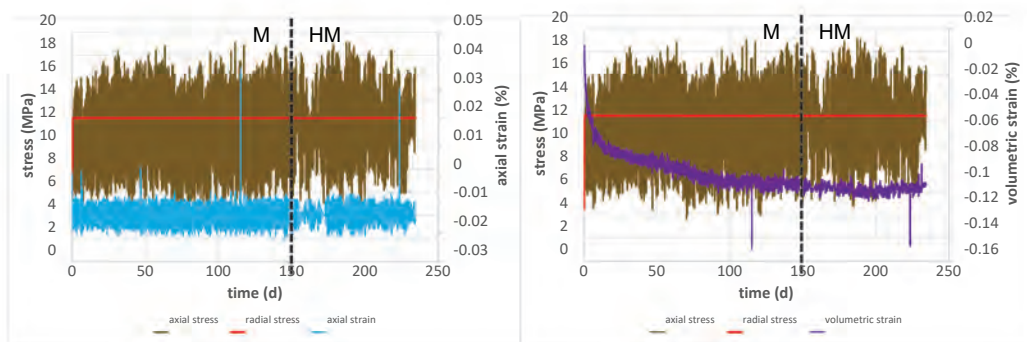
Figure 5: Axial stress, confining pressure, axial strain and volume strain

Thermal boundary condition:

The test temperature was specified at T = 50 °C, the temperature of the EMC cylinders at 30 °C. The lines between the EMC cylinders and the test cell cannot be heated, but also have

only a small volume compared to the overall dimensions of the pilot plant test rig, so that thermal effects in the hydraulic supply lines can be considered negligible.

Hydraulic boundary conditions:

After a test period of 150 days, the test specimen was pressurized with gas (nitrogen) on the primary and secondary sides, with the primary-side gas pressure gradually increased to a maximum of 13 MPa, while the secondary-side gas pressure was set at a constant 0.1 MPa. But, contrary to expectations, no gas volume flow was detected. A clogged sintering plate at the bottom of the test specimen was suspected as the cause for the missing gas flow. Consequently, the lower sintering plate was replaced and the salt cut bricks were perforated in the lowest and uppermost salt cut brick layers according to Fig. 6, each with a 5 cm deep hole corresponding to half the salt cut brick height. With these modifications, the continuation of the test was carried out.
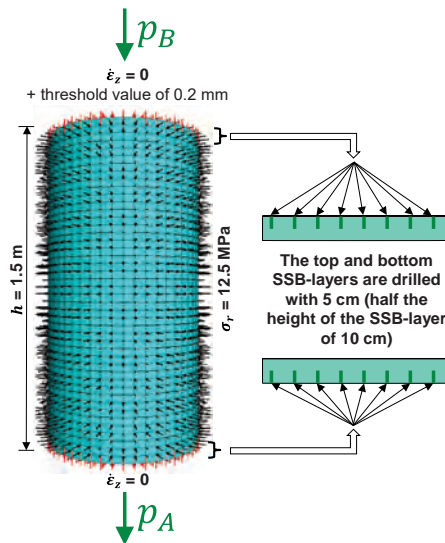
Figure 6: 5 cm deep holes (= half the height of the salt cut brick layer) in the lowest and uppermost salt cut brick layer

Figure 7 documents that the mechanical boundary conditions during the second test period were specified in the first 11 days according to the mechanical boundary conditions during the first 150-day test period. Thereafter, the axial stress was set to a constant 13 MPa until the 30th day of the second test period, i.e. the axial stress is greater than the confining pressure by $\Delta\sigma$= 0.5 MPa, as shown in Fig. 5.4 and Table 1 (Stage I). With respect to Figure 7 the axial strain at the end of 2nd test period is approx. 0.013% and the volume strain approx. 0.025%.
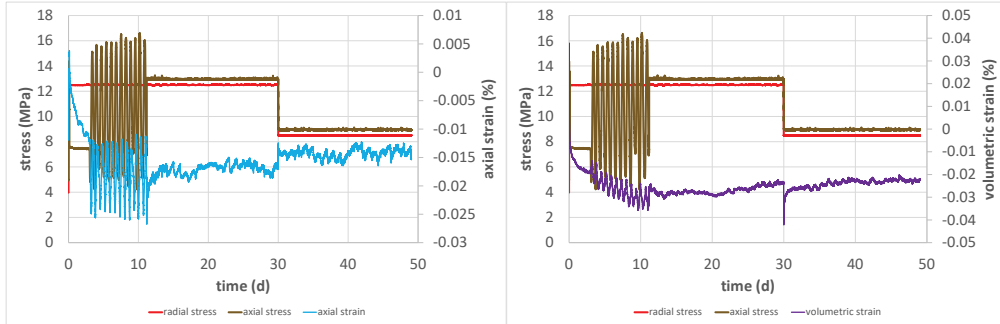
Figure 7: Axial stress, confining pressure, axial strain and volume strain during 2nd test period

The thermal boundary conditions are identical to the thermal boundary conditions within the first test period. In Stage-I, the gas pressures were specified in 10 discrete stages according to Table 1. A graphical plot of the time evolution of the gas pressures is shown in Figure 8.

Table 1: Overview of the mechanical boundary conditions and the primary and secondary gas pressures within the 2nd test period

	$p_{gas\_primary}$	$p_{gas\_secondary}$	σ_r-$p_{gas\_secondary}$		$p_{gas\_primary}$	$p_{gas\_secondary}$	σ_r-$p_{gas\_secondary}$
	MPa	MPa	MPa		MPa	MPa	MPa
σ_r = 12,5 MPa, σ_z = 13 MPa				σ_r = 8,5 MPa, σ_z = 9 MPa			
stage-I-1	0.2	12	0.5	stage-II-1	0.2	4	4.5
stage-I-2	0.2	10	2.5	stage-II-2	0.2	5	3.5
stage-I-3	0.2	8	4.5	stage-II-3	0.2	6	2.5
stage-I-4	0.2	9	3.5	stage-II-4	0.2	7	1.5
stage-I-5	0.2	10	2.5	stage-II-5	0.2	8	0.5
stage-I-6	0.2	9	3.5	stage-II-6	0.2	6	2.5
stage-I-7	0.2	8	0.5				
stage-I-8	0.2	11	1.5				
stage-I-9	0.2	12	0.5				
stage-I-10	0.2	11	1.5				
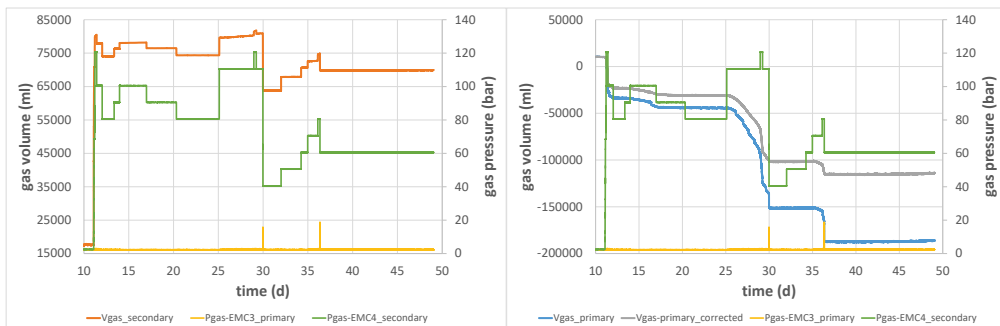
Figure 8: Overall view of gas pressures and gas volumes at the primary and secondary sides during 2nd test period

The primary gas pressure was set constant at 0.2 MPa, while the secondary gas pressure was controlled between 8 and 12 MPa, i.e., set in control increments of 4.5 to 0.5 MPa less

than confining pressure. Each gas pressure loading stage was performed twice as a control. Stage-I was followed by Stage-II, which was conducted until the 50th day of the experiment. Stage-II exhibited a 4 MPa reduction in confining pressure compared to Stage-I, as well as a 4 MPa reduction in axial stress. The secondary gas pressure was also reduced by 4 MPa in Stage-II compared with Stage-I, as shown in Table 5.1, so that the difference between confining pressure and secondary gas pressure was a maximum of 4.5 and a minimum of 0.5 MPa, analogous to Stage-I.

In Fig. 8, the gas pressures and gas volumes measured on the primary and secondary sides during second test period are plotted against the test time. In contrast to the gas volumes observed during the first test period, a clear gas flow is detected. This fact is illustrated by the gas pressures and gas volumes measured on the primary side and secondary side during 2nd test period and is confirmed by the detailed view documented in Figure 9 for stage-I-2 with boundary conditions σ_r / σ_z = 12.5MPa / 13 MPa and $p_{gaspri-mary}$ / $p_{gassecondary}$ = 0.2MPa / 10MPa. From Figure 9, based on the slopes of the measurement curves, a primary-side gas volume rate of about -6931.6 ml/d and a secondary-side gas volume rate of about 128.7 ml/d can be derived, where the gas volume rates refer to a gas pressure of 0.2MPa and 10MPa, respectively.
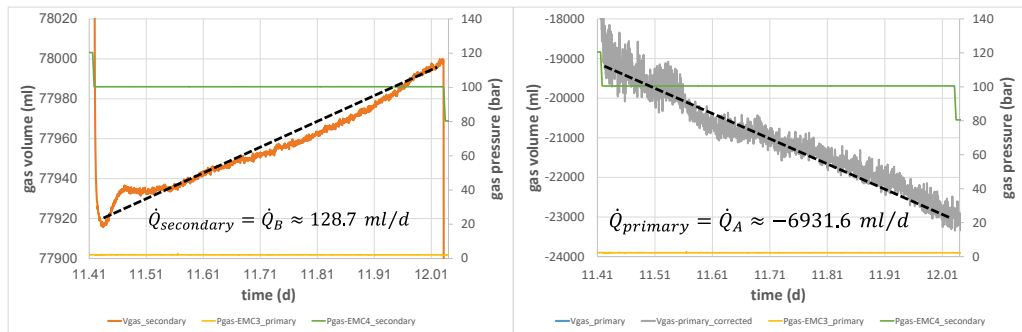
Figure 9: Gas pressures and gas volumes or derived gas volume rates at the primary and secondary sides during 2nd test period

Based on the gas volume rates obtained above, the permeability of the test specimen can be determined using Eq. 1 and 2 as follows:

$$K_A = \frac{2p_A \cdot \dot{Q}_A \cdot \mu_A \cdot L}{A\left(p_A{}^2 - p_B{}^2\right)} \tag{1}$$

$$K_B = \frac{2p_B \cdot \dot{Q}_B \cdot \mu_B \cdot L}{A\left(p_A{}^2 - p_B{}^2\right)} \tag{2}$$

with

$p_A = 0,2\text{ MPa}$, $\quad p_B = 10\text{ MPa}$, $\quad \dot{Q}_A = 6931,6\,\text{ml/d}$, $\quad \dot{Q}_B = 128,7\,\text{ml/d}$, $\quad \mu_A = 1,82 \cdot 10^{-5}\text{ Pa} \cdot \text{s}$, $\mu_B = 2,02 \cdot 10^{-5}\text{ Pa} \cdot \text{s}$, $\text{A} = \pi \cdot \text{r}^2 = \pi \cdot 0,375^2 \approx 0,44\text{ m}^2$ and $\text{L} = 1,5\text{ m}$

As a result, a primary-side permeability of about $2.2 \cdot 10^{-22} m^2$ and a secondary-side permeability of about $2.0 \cdot 10^{-22} m^2$ result for Level-I-2. The mean permeability is approximately $2.1 \cdot 10^{-22} m^2$. Table 2 shows a summary of the gas permeabilities determined analogously for the other stages. The permeabilities are not constant for all experimental stages, but depend on the pressure difference between the confining pressure and the secondary gas pressure. This dependence is visualized in Figure 10. From the semi-logarithmic plot, it can be seen that there is an exponential relationship between the permeability and the pressure difference between the confining pressure and the secondary gas pressure. The greater the pressure difference between the confining pressure and the secondary gas pressure, the smaller the permeability determined. This fact indicates a pressure-driven infiltration of gas from the boreholes into the salt cut bricks. The above hypothesis could be verified by a numerical retrospective analysis with the FTK simulator developed at the chair for Waste Disposal Technologies and Geomechanics.

Table 2: Summary of the permeabilities determined for 2nd test period for different load phases

	$p_{gas\_primary}$	$p_{gas\_secondary}$	σ_r-$p_{gas\_secondary}$	K
	MPa	MPa	MPa	m^2
$\sigma_r = 12.5$ MPa, $\sigma_z = 13$ MPa				
stage-I-1	0.2	12	0.5	4.0E-19
stage-I-2	0.2	10	2.5	2.1E-20
stage-I-3	0.2	8	4.5	5.2E-22
stage-I-4	0.2	9	3.5	9.9E-22
stage-I-5	0.2	10	2.5	7.2E-21
stage-I-6	0.2	9	3.5	1.5E-21
stage-I-7	0.2	8	4.5	2.3E-22
stage-I-8	0.2	11	1.5	3.1E-20
stage-I-9	0.2	12	0.5	2.1E-19
stage-I-10	0.2	11	1.5	3.3E-20
$\sigma_r = 8.5$ MPa, $\sigma_z = 9$ MPa				
stage-II-1	0.2	4	4.5	
stage-II-2	0.2	5	3.5	1.6E-21
stage-II-3	0.2	6	2.5	5.9E-21
stage-II-4	0.2	7	1.5	2.7E-20
stage-II-5	0.2	8	0.5	2.1E-19
stage-II-6	0.2	6	2.5	1.3E-20
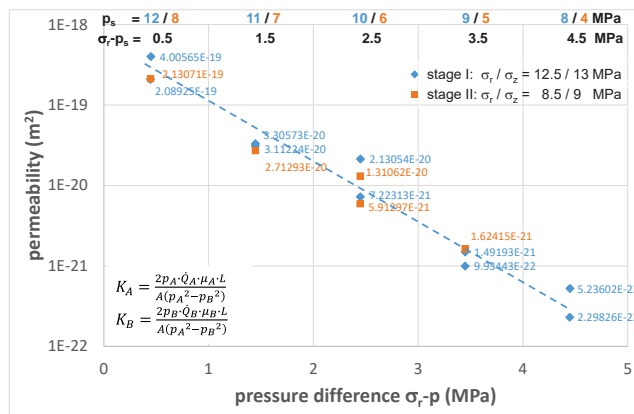
Figure 10: Permeability as a function of the pressure difference between confining pressure and secondary gas pressure for 2nd test period

6   Conclusions and outlook

Based on large-scale laboratory investigations it has been shown that a sealing element made of salt-cut bricks without joint filling generates a high impermeability and support effect under insitu relevant mechanical and thermal stresses within a comparatively short time of a few months. With reference to measurement results documented in Fig. 5.7, it could be clearly demonstrated within the scope of the research project that already after test times of approx. 150 - 200d under insitu relevant stresses, merely a low gas permeability of K = 10-18m^2 to K = 10-22m^2 is measured. As a consequence, it can be stated that a sealing system of salt cut bricks, compared to crushed salt, characterizes a natural material, which is able to seal the shafts of a repository in saliniferous rocks with long-term reliability, both in the short term and in the long term. That is, the compaction times of several tens of years up to several hundred years required for the compaction in case of using crushed salt can be significantly reduced in case of using salt cut bricks.

References

KREIENMEYER, M., LERCH, CH., POSTER, M. & THOLEN, M. 2008. Nachweiskonzept zur Integrität der einschluss-wirksamen technischen Barrieren – Teilbericht (AP 5) zum Projekt ISIBEL "Überprüfung und Bewertung des Instrumentariums für eine sicherheitliche Bewertung von Endlagern für HAW" (BGR, DBE, GRS). DBE TECHNOLOGY GmbH, TEC-15-2008-AP, Peine 2008.

ARBEITSKREIS 3.1, SALZMECHANIK, DGGT 2021. "Kompendium zum Stand von Wissenschaft und Technik bei der Planung und Ausführung geotechnischer Barrieren für Untertagedeponien im Salinargebirge", Clausthal.

DÜSTERLOH, U. 2014. Langzeitsicheres Abdichtungselement aus Salzschnittblöcken - Vorprojekt zur Kalkulation und Qualifizierung der Forschungsarbeiten, FKZ 02 E 11223, Clausthal, Juli 2014

DÜSTERLOH, U., LERCHE, S., DYOGYEV, O. & FEIERABEND, J. 2018. Langzeitsicheres Abdichtungselement aus Salzschnittblöcken - Bautechnische Realisierung Technikumsprüfstand mit Durchführung und Auswertung erster Versuche, FKZ 02 E 11425, Clausthal.

KUDLA, W. & HEROLD, P. 2021. Zusammenfassender Abschlussbericht für das Verbundvorhaben Schachtverschlüsse für Endlager für hochradioaktive Abfälle (ELSA – Phase 2): Konzeptentwicklung für Schachtverschlüsse und Test von Funktionselementen von Schachtverschlüssen, Technische Universität Bergakademie Freiberg und BGE TECHNOLOGY GmbH, 2021.

EMMERICH, K., SCHUHMANN, R., KÖNIGER, F., BOHAC, P., DELAVERNHE, L., WIECZOREK, K., CZAIKOWSKI, O., HESSER, J., SHAO, H., JAEGGI, D., BOSSART, P., HANSMANN, J., GRUNER, M., HOFMANN, M., AURICH, J., RÖLKE, C., POPP, T., DIEDEL, R., SCHELLHORN, M., HÄUßER, S., GLAUBACH, U., WILSNACK, T., KEMPER, G., GARCÍA-SIÑERIZ, J. L., VILLAR, M., GUTIÉRREZ-ÁLVAREZ, C., & IGLESIAS, R. J. 2019. Joint project: Vertical hydraulic sealing system based on the sandwich principle – preproject (Sandwich-VP), Final report, Karlsruher Institut für Technologie (KIT) & Gesellschaft für Anlagen- und Reaktorsicherheit (GRS) gGmbH.

WIECZOREK, K., EMMERICH, K., SCHUHMANN, R., HESSER, J., FURCHE, M., JAEGGI, D., SCHEFER, S., AURICH, J., MAYOR, J. C., NORRIS, S., BIRCH, K., SENTIS, M., GARCÍA-SIÑERIZ, J. L., KÖNIGER, F., GLAUBACH, U., RÖLKE, C. & DIEDEL, R. 2021. Large-scale testing of a sandwich shaft-sealing system at the Mont Terri rock laboratory, Saf. Nucl. Waste Disposal, 1, 133–135.

KUDLA, W., HEROLD, P., ET. AL. 2021. Schachtverschlüsse für Endlager für hochradioaktive Abfälle -ELSA - Phase 2: Konzeptentwicklung für Schachtverschlüsse und Test von Funktionselementen von Schachtverschlüssen, FKZ: 02E11193A/B, Freiberg.

BAUER, J., KREIENMEYER, M., STIELOW, B., SCHRÖPFER, TH. & WOLLRATH, J. 2019. Experiences from an in situ test site for a sealing element in shafts and vertical excavations, Rock Salt, 10. US/German Workshop on Salt Repository Research, Design and Operation, Rapid City, USA.

ENGELHARDT, I. 2004. Experimental and numerical investigations with respect to the material properties of geotechnical barriers, Dissertation, Eberhard-Karls-Universität Tübingen.

GLAUBACH, U., HOFFMANN, M., TEICHERT, TH. & KUDLA, W. 2013. New development of a combined abutment and sealing assembly made of bitumen and gravel. International Conference on the Performance of Engineered Barriers, BGR, Hannover.

IAEA-TECDOC-1718 2013. Characterization of swelling clays as components of engineered barrier systems for geological repositories. Results of an IAEA coordinated research project 2002-2007, IAEA, Vienna.

KUDLA, W., DAHLHAUS, F., GLAUBACH, U., GRUNER, M. & HAUCKE, J. 2009. Diversitäre und redundante Dichtelemente für langzeitstabile Verschlussbauwerke. FKZ 02C1124, TU Bergakademie Freiberg.

KRÖHN, K.P., STÜHRENBERG, D., HERKLOTZ, M., HEEMANN, U., LERC,H CHR. & XIE, M. 2009. Restporosität und -permeabilität von kompaktiertem Salzgrus-Versatz, REPOPERM, Bericht GRS-254.

STÜHRENBERG, D., HERBERT, H.-J. & SALZER, K. 2010. Arteigene Verschlussmaterialien. Workshop Verschlusssysteme in Endlagern für wärmeentwickelnde Abfälle in Salzformationen, GRS-267, Braunschweig.

ROTHFUCHS, T., JOCKWER, N., MIEHE, R. & ZHANG, C.-L. 2005. Self-sealing barriers of clay/mineral mixtures in a clay repository. SB experiment in the Mont Terri Rock Laboratory, GRS-212.

EBERTH, S. & MÜLLER-HOEPPE, N. 2009. Übertragung des Sicherheitsnachweiskonzeptes für ein Endlager im Salz auf andere Wirtsgesteine, FKZ 02E9521, Peine.

SITZ, P. 1981. Untertägige Querschnittsabdichtungen durch Dämme und Pfropfen, Neue Bergbautechnik, 11.Jg., Heft 3.

Theme 4: Analytical and numerical modelling

Deformation patterns in the mechanically stratified evaporites over an active basement fault

Marta Adamuszek[1]*, Marcin Dabrowski[1]

[1] Computational Geology Laboratory, Polish Geological Institute – National Research Institute, Poland

* *marta.adamuszek@pgi.gov.pl*

ABSTRACT: We aim to describe flow patterns that develop in the mechanically stratified evaporite sequence during the basement-involved deformation. We use numerical methods and examine various initial setups, where different lithological profiles of the sequence and vertical offsets along the fault are tested. To better illustrate the impact of layering, we compare our results with the models containing no internal stratification. The results clearly show that the mechanical stratification can have a great impact on the flow pattern initiating heterogeneous deformation within the sequence.

1 Introduction

Low viscosity of rock salt facilitates its flow under a wide range of tectonic conditions. The related intense deformation can lead to the formation of complex internal structures and it also significantly influences the large-scale architecture of sedimentary basins. As a result, many salt-bearing sedimentary basins experience severe deformation, including the development of salt tectonic structures such as salt pillows and diapirs. Basement faulting is widely considered as an important trigger for salt flow and the formation of various salt related structures. The deformation of a salt layer above an active normal fault has been investigated in numerous analogue, analytical, and numerical studies (e.g. Koyi et al. 1993; Vendeville et al. 1995; Burliga et al. 2012; Warsitzka et al. 2015, 2018; Granado et al. 2021). The differential vertical displacement around the tip of a basement fault leads to the formation of forced folds within the salt sequence, and it may also initiate the growth of salt pillows over the footwall. The flow in the salt layer can be approximated by a combination of the Couette and Poisseuille flows (e.g. Warsitzka et al. 2018). The flow is predominantly directed towards the hanging wall during normal faulting. However, with a considerable accumulation of sediments above the subsiding region, the lateral pressure gradient can produce a reverse salt flow towards the footwall region (e.g. Warsitzka et al. 2015). The reactivation of faults during basin inversion may significantly amplify the existing salt tectonic structures. The inversion causes the uplift of the thick sedimentary strata within the hanging wall and the erosion of the elevated parts. Lateral shortening promotes buckle folding causing the growth of salt pillows and further subsidence of the neighbouring synclines. During the inversion stage, the flow in the salt layer is chiefly directed towards the footwall (e.g. Burliga et al. 2012).

In most of the studies, salt deformation models adopt a mechanically uniform evaporite layer. However, evaporites are rarely homogeneous. Thus, we aim to analyse the flow pattern within a mechanically stratified evaporite sequence during deformation over an active basement fault. The model geometry considered in the study is motivated by the geometrical characteristics of salt tectonic structures within the Zechstein salt basin. We carry out a series of numerical simulations to assess the influence of selected parameters. In all cases, basement-involved extension is immediately followed by shortening.

2 Model

2.1 Model geometry and boundary conditions
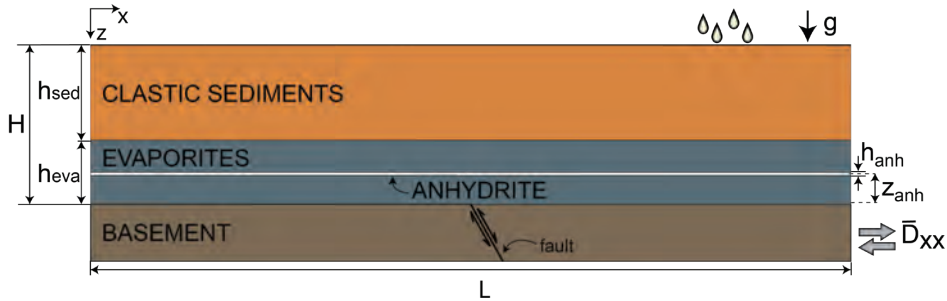
Figure 1: Initial model geometry. Note that the model is not to scale.

The initial model of length L and height H contains a horizontal evaporite bed of total thickness h_{eva} (Figure 1a). The bed is composed of either pure rock salt or rock salt intercalated with an anhydrite layer. The anhydrite layer of thickness h_{anh} is located at position z_{anh} measured from the salt base. The overburden of thickness h_{sed} consists of clastic sediments. A normal fault dipping at 60° is located in the centre of the model within the rigid basement beneath the salt The fault tip is located at x=0 and initial vertical fault offset T is set to 0. The extension activates the basement fault and triggers a vertical and horizontal movement of the hanging wall. As the hanging wall reaches the maximum vertical fault offset T_{max}, the model is subjected to shortening. The extension and shortening take place with a constant rate of deformation, $\bar{D}_{xx}$.

Table 1: Parameters used in the reference model (e.g. S1b)

Parameter	Sym	Unit	Value	Parameter	Sym	Unit	Value
Model length	L	m	40000	Anhydrite thickness	h_{anh}	m	50
Model height	H	m	2500	Anhydrite position	z_{anh}	m	500
Max. vertical fault offset	T_{max}	m	500	Sediment thickness	h_{sed}	m	1500
Rate of deformation	$\bar{D}_{xx}$	s⁻¹	10⁻¹⁵	Salt thickness	h_{eva}	m	1000

We constrain a reference model with parameters given in Table 1. We perform four series of numerical tests to illustrate the role of: a) the presence of the anhydrite layer (S1), b) anhydrite thickness (S2), c) anhydrite position (S3), and d) maximal fault offset (S4) on the flow pattern in the evaporite sequence. In each set, we run three simulations, where we modify only a single parameter in the reference model (Table 2). Note that in each simulation set, model b refers to the reference model.

For the reference model with the maximum fault offset of T_{max}=500 m, the extensional phase lasts ca. 0.45 My and leads to a maximum horizontal extension of 288 m. For T_{max}=250 m, the extension time is shortened to 0.225 My and the maximum horizontal offset is 144 m. Increasing the offset to T_{max}=750 m results in a longer deformation of ca. 0.68 My and causes 433 m of horizontal extension. As the rate of deformation is kept constant, the durations of the extensional and shortening (inversion) phases are equal.

Table 2: Parameters used in the numerical test series. Note that model b is the reference model.

Set	Parameter	Sym	Unit	Tested values		
				Model a	Model b	Model c
S1	Number of anhydrite layers	N	-	0	1	-
S2	Anhydrite thickness	h_{anh}	m	25	50	75
S3	Anhydrite position	p_{anh}	m	250	500	750
S4	Max. vertical fault offset	T_{max}	m	250	500	750

The model extension is implemented by imposing a horizontal velocity v_x to the right boundary and the base of the hanging wall, whereas the vertical displacement is controlled by the dip of the fault and the horizontal velocity, here $v_y = \sqrt{3}v_x$. The velocity changes at each step in order to keep the constant rate of deformation. In the footwall, the horizontal velocity in the left boundary and the base is set to zero. Free-slip boundary conditions are prescribed on the vertical walls and no-slip conditions elsewhere. The top boundary is a free surface and, at the same time, both sedimentation and erosion processes take place. Here, we assume a simplified sedimentation-erosion model and keep the elevation constant. All available sedimentation space is immediately filled with sediments and any uplifted material is instantly eroded. In the model, the temperature is only a function of depth, z, where a temperature gradient is set to 30°/km.

2.2 Material parameters

Densities of rock salt ρ_{eva} and anhydrite ρ_{anh} are constant and set to 2200 kg·m^{-3} and 2900 kg·m^{-3}, respectively. Density of sediments increases exponentially with depth due to compaction according to the relation $\rho_{sed}=\rho_g-(\rho_g-\rho_f)\alpha exp(-\beta z)$, where ρ_g=2640 kg·m^{-3} is the density of solid grains, ρ_f =1000 kg·m^{-3} is the density of fluid, α=0.52 is the surface porosity and β=4.7·10^{-4} m^{-1} is the compaction coefficient. The parameters are chosen to fit the characteristics of siliciclastic sediments. The density is recalculated for the current depth. No decompaction is considered in the model.

Salt and anhydrite follow the Carreau fluid model, for which the apparent viscosity is given by $\mu_{app} = \mu_\infty + (\mu_0 - \mu_\infty)[1 + \xi^2 D_{II}^2]^{(1/n-1)/2}$, where μ_0 and μ_∞ are the characteristic viscosities at zero and infinite shear rate, D_{II} is the second invariant of rate of deformation tensor, n is the stress exponent, ξ is the relaxation time given by $\xi = [A^*/(\mu_0 - \mu_\infty)]^{1/(1/n-1)}$ (see Cornet et al. 2018 for details). The reference viscosity parameter $A^* = A^{-1/n} \cdot exp(Q/nRT)$, where R is the gas constant, A and Q are the material parameters. We model the rheological behaviour of clastic sediments as pseudo-plastic fluid. The frictional yield criterion, given by Byerlee's law, is expressed as $(\sigma_1 - \sigma_3) = \alpha\rho_{sed}gz(1 - \lambda)$, where (σ$_1$-σ$_3$) is the effective principle stress difference, g is the gravity, λ is the pore fluid pressure (e.g. Ranalli 1995 p. 247). In the case of normal faulting, $\alpha = (r - 1)/r$ and, in the case of thrusting, $\alpha = r - 1$, and $r = [(1 + f^2)^{1/2} - f]^{-2}$, where f is the static friction coefficient. In the model, we use λ=0.42 and f =0.85. Rather than using an elastoplastic formulation for the clastic sediments, we locally seek the corresponding equivalent viscosity based on the Carreau model for a stress exponent of 7. The parameters used to characterize rheology of rocks are given in Table 3.

Table 3: Viscosities and related parameters.

Parameter	Sym	Unit	Salt (after Hansen & Carter, 1984)	Anhydrite (after Muller and Bayer, 1978)	Sediments
Pre-exponential parameter	A	MPa^{-n}s^{-1}	$10^{-3.1}$	$10^{1.5}$	-
Activation energy	Q	kJ	10^{17}	10^{21}	-
Power-law exponent	n	-	4.5	2	7
Viscosity at zero shear rate	μ_0	Pa·s	10^{17}	10^{21}	10^{23}
Viscosity at infinite shear rate	μ_∞	Pa·s	0	0	0

2.3 Numerical model

The deformation is studied using the incompressible Stokes equations and a 2D plane-strain finite element model. We use our own numerical code FOLDER implemented in MATLAB (Adamuszek et al. 2016), combined with the MILAMIN (Dabrowski et al. 2008) and MUTILS numerical packages. The model is discretized using high resolution, unstructured triangular computational mesh. A remeshing procedure is applied at each time step. The layer interfaces are advected using a second-order Runge-Kutta method.

3 Results

3.1 Role of the presence of the anhydrite layer

We compare the developing structures at different stages of deformation between the model without the anhydrite layer (S1a) (Figure 2a) and the reference model with a single anhydrite layer in the middle of the evaporite sequence (S1b) (Figure 2b). In both cases, basement normal faulting during the extensional phase causes flexural bending of the overlying evaporites and the overburden. The salt flows towards the hanging wall and smoothens the flexure of the supra-salt sediments. The uplift and bending of the cover over the footwall accompanies the formation of a pillow in the salt layer at some distance from the fault. In S1a, a maximum uplift of 33 m above the initial salt level occurs at x=-4.3 km, whereas in S1b, it is reached at ca. x=-3 km and yields 28 m (Figure 2c). Whilst the extensional deformation naturally leads to the general stretching of all the sedimentary layers in the model, the most pronounced thinning is observed in the fault tip area. Shortening of the sequence leads to the large-scale folds formation in the overburden clastic sediments and the growth of smaller-scale tectonic structures within the evaporites. At the end of the inversion stage, the maximum elevation of the salt pillow reaches 130 m above the initial salt level for S1a, whereas for S1b it is elevated by 90 m (Figure 2d). In both models, the growth of pillow structure is associated with the development of gentle synclines on both sides of the pillow. In S1a model, the subsidence within the synclines reaches ca. 70 m, whereas in S1b the areas neighbouring the pillow subside up to ca. 50 m. In both models, subsidiary pillows form further away from the main pillow structure. In S1b, shortening leads to the folding of the anhydrite layer. The folds concentrate close to the fault tip, in the region of the most intense deformation and a decreased anhydrite layer thickness. A maximum fold amplitude of ca. 50 m and a wavelength of ca. 1500-2000 m are observed.
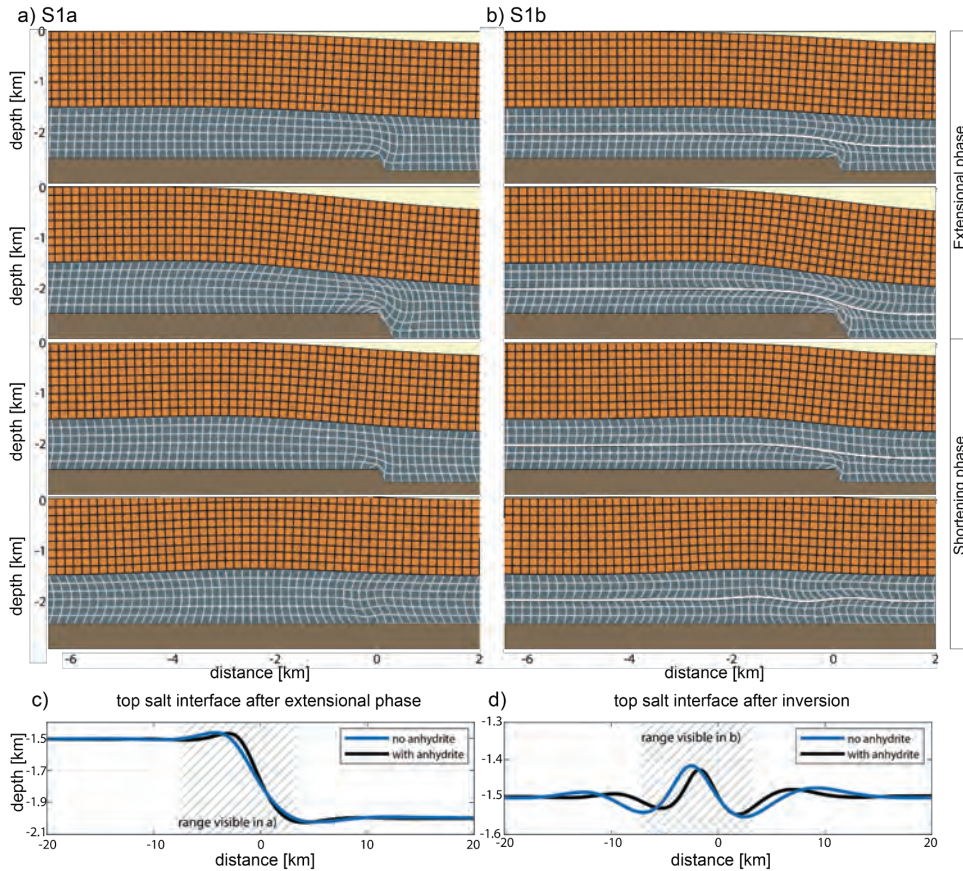
Figure 2: Structure evolution for a) homogeneous rock salt bed (S1a) and b) rock salt bed intercalated by anhydrite (S1b). The overlying grids represent passive markers and illustrate internal salt and overburden deformation. c) and d) compares top salt interface after the extensional and inversion phase, respectively. Note the vertical exaggeration in c) VE=15 and d) VE=35.

During the extensional phase, in S1a, the flow in the overburden is mainly directed towards the hanging wall. The largest velocity magnitude is observed within the evaporite sequence close to the fault tip (Figure 3a). The parabolic flow profile within the evaporite layer, with the maximum velocity close to the centre of the profile, is disturbed by the drag effect at the contact with the overburden sediments. Non-planar geometry of the bottom and top salt interface introduces additional complexity. Nevertheless, the flow can be approximated by the Couette-Poiseuille flow (Figure 3e). At x=-1 km to x=-5 km (profiled in Figure 3d), the horizontal velocity changes its directions along the profiles and the velocity trajectories form a clockwise loop. Further away from the fault tip above the basement footwall, the salt flows exclusively towards the hanging wall (profile c in Figure 3). During the inversion phase, the flow is generally directed towards the footwall, with the largest velocity magnitude detected next to the fault tip (Figure 3a,i). A reverse flow occurs within the salt layer above the footwall at x=-2 km to x=-7 km and the velocity trajectories form a counter clockwise loop (Figure 3a,g,h).
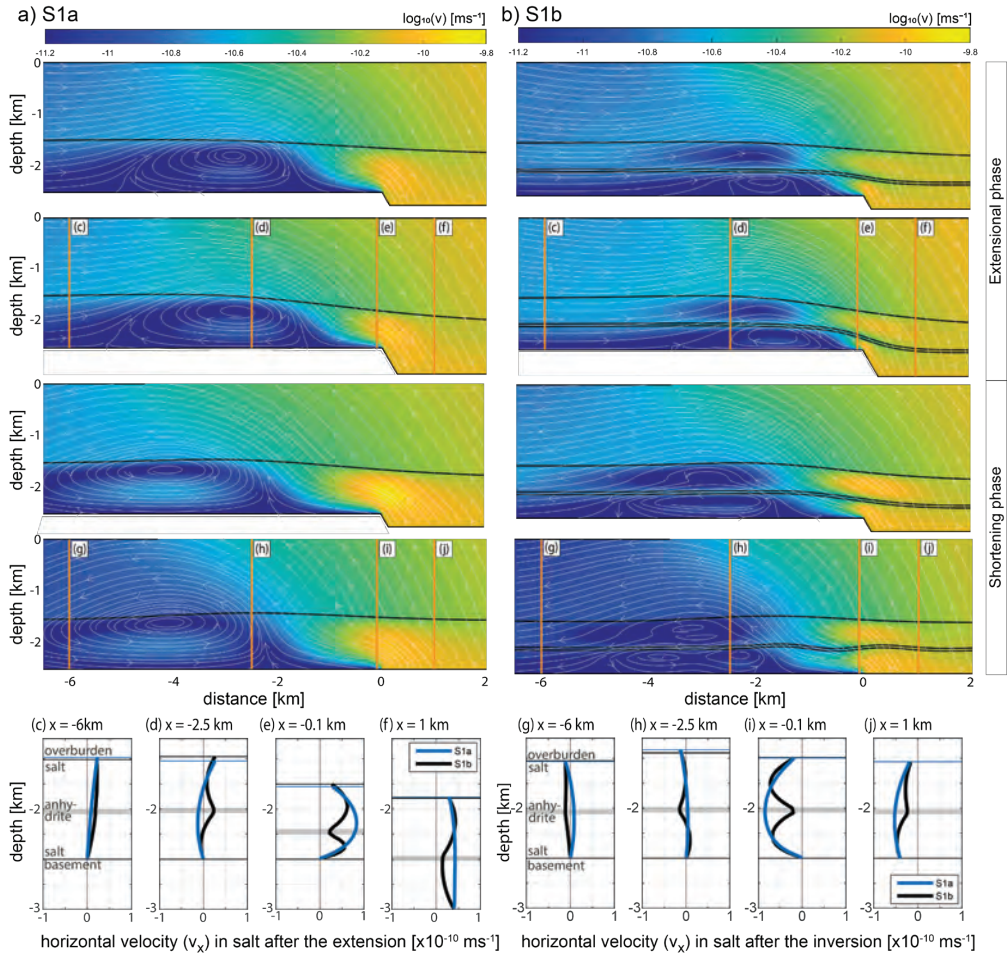
Figure 3: Velocity fields in the models, where the evaporite sediments are represented by a) the homogeneous rock salt bed and b) the rock salt bed intercalated by the anhydrite layer. Logarithm of the velocity magnitude is colour-coded. White lines show streamline flow. c-f) Horizontal velocity profile within the salt bed after the extension. g-j) Horizontal velocity profiles within the salt bed after the inversion. The profile locations at x=-6, -2.5, -0.1, and 1 km are indicated in a) and b).

In S1b, the flow within the salt is channelized into two domains: sub-anhydrite and supra-anhydrite. During the extensional phase, the flow within the salt is generally directed towards the hanging wall (Figure 3b). The largest velocity is observed close to the fault tip at the central parts of the sub- and supra-anhydrite domains (Figure 3e). The maximum velocity value is however much smaller than in the model S1a. From x=-1 km to x=-3 km the velocity significantly decreases in the supra-anhydrite domain, whereas in the sub-anhydrite domain a small back-flow occurs (Figure 3b). The maximum velocity occurs close to the salt-sediment interface and close to the salt-anhydrite interface (Figure 3d). Note that the velocity profiles d and e in Figure 3 show the opposite trends. In the hanging wall, the lowest velocity is observed close to the salt-sediment interface and close to the salt-anhydrite interface (Figure 3f). During the inversion stage, the salt flow is largely directed towards the footwall except for the small areas between x=-5 km and -1 km (Figure 3b,h). The presence of the anhydrite layer slows down the flow above the hanging wall and close to the fault tip (Figure 3i,j), whereas it increases the flow intensity in the footwall area (Figure 3g,h).

3.2 Role of the anhydrite layer thickness
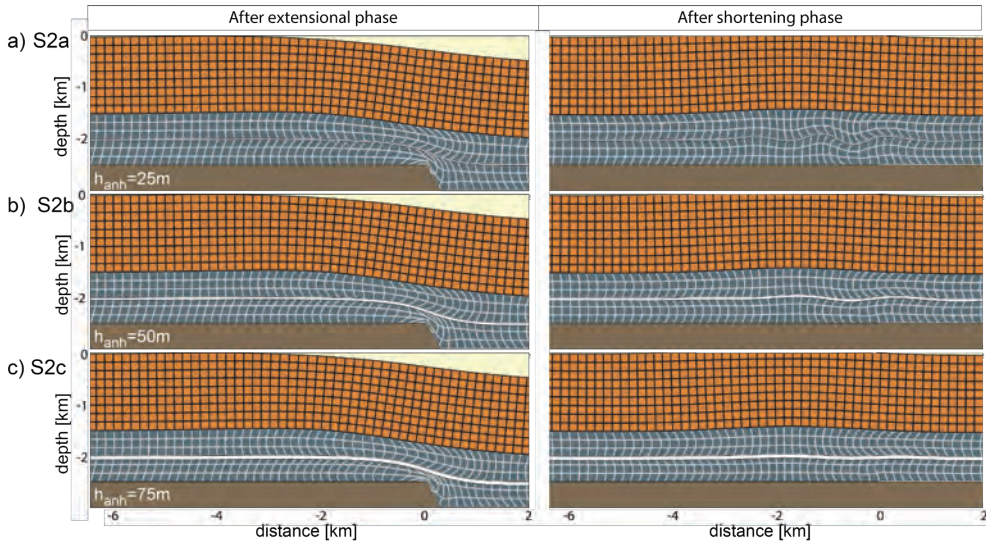
Figure 4 Structure evolution for anhydrite layer thickness of a) h_{anh}=25m, b) h_{anh}=50 m, and c) h_{anh}=75 m.

Figure 4 compares the models with different anhydrite layer thicknesses. In the extensional phase, an increase of the anhydrite layer thickness leads to the development of a slightly smoother and wider monocline over the ramp. During the shortening stage, a thin anhydrite layer forms larger amplitude folds with smaller wavelengths compared to the models with thick anhydrite layers. For S2a, the fold amplitude is 100 m and its wavelength is above 1200 m, whereas for S2c, the amplitude attains 35 m and the wavelength is over 2200 m. The final shape of the pillow structure shows insignificant differences among the models. The height of the pillow reaches 81 m, 72 m, and 70 m for S2a, S2b, and S2c, respectively.

3.3 Role of the anhydrite layer position

Varying position of the anhydrite layer within the evaporite sequence significantly influences the internal flow pattern (Figure 5). Locating the anhydrite layer close to the salt base causes a more intense flow in the supra-anhydrite domain and a more pronounced pillow structure growth, with a narrower wavelength and a higher amplitude. The anhydrite layer positioned close to the top of the salt leads to the formation of smoother and wider monocline within the clastic sedimentary overburden and the development of a least pronounced salt pillow structure. Consequently, it promotes a stronger decoupling of the basement fault and the supra-salt sediments. In this case, the flow is concentrated in the sub-anhydrite domain. The folding of the anhydrite layer is most evident when it is positioned centrally within the salt sequence.
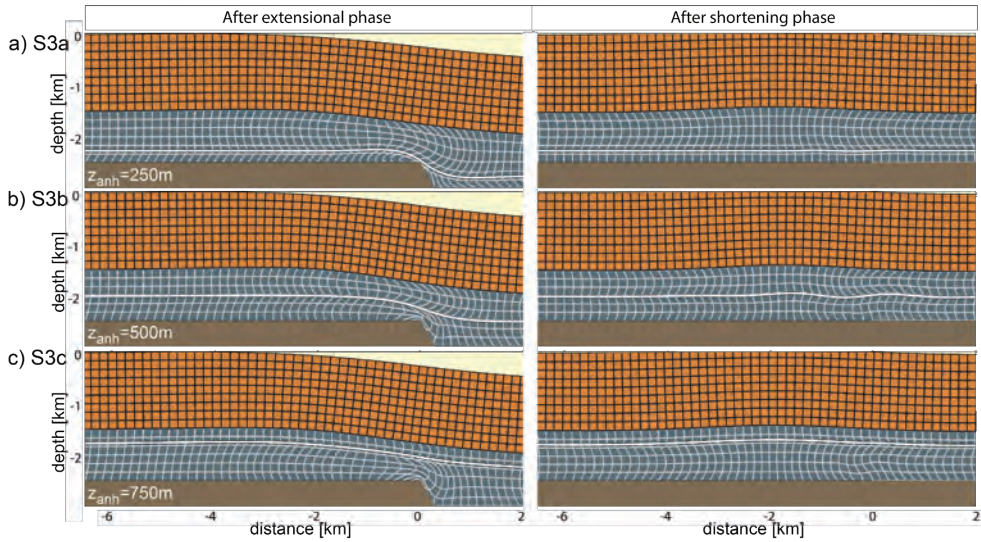
Figure 5 Structure evolution for anhydrite layer position for a) z_{anh}=250m (S3a), b) z_{anh}=500 m (S3b), and c) z_{anh}=750 m (S3c) from the salt base.

3.4 Role of the fault offset
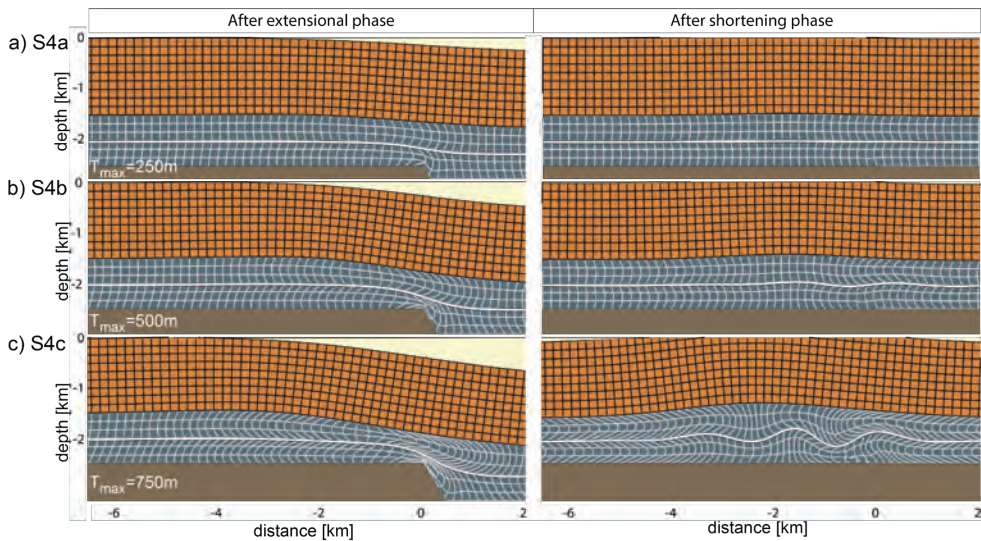
Figure 6 Structure evolution for maximum fault offset of a) T_{max}=250m (S4a), b) T_{max} =500 m (S4b), and c) T_{max} =750 m (S4c).

Increasing the maximum fault offset causes a more intense and longer deformation, which promotes the development of more pronounced internal salt structure (Figure 6). At the end of the shortening stage, folds with an amplitude of over 200 m develop for S4c, whereas in S4a, their amplitude reaches only ca. 10 m. The fold wavelength of ca. 1700 m is similar for all the three models. The large-scale deformation is also more marked for models with a larger fault offset. In S4a, the pillow structure has over 30 m height and 7km width, whereas for S4c it has a height of almost 300 m and a width of ca. 9 km.

4   Discussion and Conclusions

Numerical simulations provide an opportunity to analyse in great details the lateral flow pattern within a salt layer above a basement fault in a region undergoing extension and subsequent shortening (inversion). In the case of a homogeneous salt layer, the evolving velocity fields clearly illustrate that the flow within the salt layer can be approximated as a combination of the Couette and Poiseuille flow types (Figure 3). In both the extensional and shortening stages, we document the areas, which are characterized by flow directions opposite to the dominating flow pattern. The obtained flow pattern is consistent with previous works of e.g. Koyi et al. (1993) and Warsitzka et al. (2015; 2018).

The paper documents the role of the mechanical stratification within the evaporites. On the large scale, such heterogeneity hampers the growth of pillow structures diminishing their height and width (Figure 2). A thick and stiff anhydrite layer generally reduces and channelizes the flow within the salt layer (Figure 4). The location of the anhydrite layer within the salt sequence has a great impact on the relative intensity of deformation within the supra- and sub-anhydrite domains (Figure 5). An asymmetric location of the layer can supress the deformation in one domain and significantly increase the deformation in the other domain. Consequently, mechanical stratification can be a dominating factor responsible for the decoupling of the deformation in salt sequence. Moreover, it impacts on the development of large-scale pillow structures. We suspect that the effect can be reduced if anhydrite layer gets boudinaged during extension.

Varying anhydrite layer thickness insignificantly influences the pillow growth. However, the thin anhydrite layers may promote intense development of the internal structures (Figure 4). In the analysed cases, thinner layers tend to develop folds with larger amplitudes. This can be explained by confinement effects that naturally reduce fold growth. For a general case, the wavelength to thickness ratio is scaled with the viscosity ratio between the anhydrite layer and salt. We expect that in the case of multiple thin layers within the salt, the evaporite sequence should effectively exhibit mechanical anisotropy and can have a more severe impact on the internal salt architecture and the overall shape of salt tectonic structures. Significant variation of the layer thicknesses can lead to development of the polyharmonic folds (Adamuszek et al. 2021).

In our analysis, we focus on the role of anhydrite layer on the deformation pattern within the salt layer. We expect to obtain similar results for the case of other rock types such as carbonates and sandstone, which are characterized by a higher effective viscosity than the rock salt. In contrast, introducing a less competent layers, e.g. bittern salt layer in the sequence, can probably lead to the localized deformation within the bittern salt layer and reduced deformation in the surrounding salt layer. Therefore, we propose that natural evaporitic sequences, which commonly comprises numerous intercalating layers of varying mechanical properties (e.g. Rowan et al. 2019), favour heterogeneous deformation and lead to the development of complex internal geometry.

In our models, the salt structures do not reach the diapiric stage. This is mainly related to the stiff and thick overburden and a relatively short duration of the deformation. We expect that reducing the thickness and strength of the overburden, or/and increasing the fault offset and duration of the deformation processes could result in more pronounced salt structure evolution similarly to the case of a homogeneous salt layer (Warsitzka et al. 2015).

Acknowledgements

References

ADAMUSZEK, M., DABROWSKI, M. & SCHMID, D.W. 2016. Folder: A numerical tool to simulate the development of structures in layered media. Journal of Structural Geology 84, 85–101.

ADAMUSZEK, M., TĂMAŞ, D.M., BARABASCH, J. & URAI, J.L. 2021. Rheological stratification in impure rock salt during long-term creep: morphology, microstructure, and numerical models of multilayer folds in the Ocnele Mari salt mine, Romania. Solid Earth 12, 2041–2065.

BURLIGA, S., KOYI, H.A. & CHEMIA, Z., 2012. Analogue and numerical modelling of salt supply to a diapiric structure rising above an active basement fault. Geological Society, London, Special Publications 363, 395–408.

CORNET, J.S., DABROWSKI, M. & SCHMID, D.W. 2018. Long term creep closure of salt cavities. International Journal of Rock Mechanics and Mining Sciences 103, 96–106.

DABROWSKI, M., KROTKIEWSKI, M. & SCHMID, D.W. 2008. MILAMIN: MATLAB-based finite element method solver for large problems: MILAMIN MATLAB-BASED FEM SOLVER. Geochemistry, Geophysics, Geosystems 9, n/a-n/a.

GRANADO, P., RUH, J.B., SANTOLARIA, P., STRAUSS, P. & MUŇOZ, J.A. 2021. Stretching and Contraction of Extensional Basins With Pre-Rift Salt: A Numerical Modeling Approach. Frontiers in Earth Science 9, 158.

HANSEN, F.D. & CARTER, N.L. 1984. Creep of Avery Island rocksalt. Proceedings of the First Conference on Mechanical Behavior of Salt, Clausthal-Zellerfeld, Germany. Trans Tech Publications. 53–69.

KOYI, H., JENYON, M.K., PETERSEN, K. 1993. The effect of basement faulting on diapirism. Journal of Petroleum Geology 16, 285–312.

MULLER, W.H. & BAYER, U. 1978. The rheological behaviour of polycrystalline Anhydrite. Eclogae Geol. Helv 71, 397–407.

RANALLI, G. 1995. Rheology of the earth, 2. ed. ed. Chapman & Hall, London.

ROWAN, M.G., URAI, J.L., FIDUK, J.C. & KUKLA, P.A. 2019. Deformation of intrasalt competent layers in different modes of salt tectonics. Solid Earth 10, 987–1013.

VENDEVILLE, B.C., GE, H. & JACKSON, M.P.A. 1995. Scale models of salt tectonics during basement-involved extension. Petroleum Geoscience 1, 179–183.

WARSITZKA, M., KLEY, J. & KUKOWSKI, N. 2015. Analogue experiments of salt flow and pillow growth due to basement faulting and differential loading. Solid Earth 6, 9–31.

WARSITZKA, M., KUKOWSKI, N. & KLEY, J. 2018. Salt flow direction and velocity during subsalt normal faulting and syn-kinematic sedimentation—implications from analytical calculations. Geophysical Journal International 213, 115–134.

Influence of THM process coupling and constitutive models on the simulated evolution of deep salt formations during glaciation

Florian Zill[1,2], Wenqing Wang[1], Thomas Nagel[2,3]*

[1]*Department of Environmental Informatics, Helmholtz Zentrum für Umweltforschung GmbH – UFZ, Germany;*
[2]*Geotechnical Institute, Technische Universität Bergakademie Freiberg, Germany;* [3]*TUBAF-UFZ Centre for Environmental Geosciences, Germany*

* florian.zill@ufz.de

ABSTRACT: Rock salt represents a key host rock candidate for deep geological storage of nuclear waste and has been the subject of extensive investigation. To make accurate predictions about the stability and integrity of a repository, a simulation model requires an appropriate representation of the creep behavior of rock salt. On the associated time scales, glaciation periods in particular induce profound changes in mechanical (M), hydraulic (H) and thermal (T) boundary conditions and therefore require further investigation. As part of the AREHS project, we analyse the influence of the coupling of THM physical processes and perform simulations with different coupling schemes (M, TM, HM, THM) for a relevant scenario. Furthermore, we examine the difference in the numerical results between a basic power law creep model and a composite power law that includes both dislocation and pressure-solution creep. The models produce significantly different mechanical responses under glacial loading, highlighting the importance of the pressure solution creep effects at low deviatoric stresses. Due to the simplicity of the model, including hydraulic and thermal coupling had minimal influence in comparison.

1   Introduction

The storage of radioactive waste in underground repositories is widely considered the primary option to isolate nuclear waste from the biosphere for very long time periods. Focusing on Germany, there are three main candidates considered as potential host rocks: clay rock, salt rock and crystalline rock. All three options must be thoroughly examined for their suitability as host rocks in order to be able to select a site which "guarantee[s] the highest possible level of safety over a period of one million years" (Repository Site Selection Act, StandAG) based on the current understanding of the underlying physical processes. This work focusses on rock salt which has been used to store different forms waste as well as fluidic energy carriers (Lux 2009) due to its function as a so-called tight barrier with extremely low permeability.

Bedded rock salt can form underground salt domes over long time periods due to its viscoplastic nature in a process called halokinesis (Kyle, 1991). Such a dome provides easier access to the host rock, due to the material being present at shallower depths and has favorable geomechanical properties due to its high purity. Bedded rock salt more typically contains inhomogeneities in the form of interbeds such as anhydrite, shale, salty mudstones, carbonates, etc. (Liang et al. 2007)

To simulate the mechanical behaviour of rock salt it is common to use viscoplastic material models such as Günther-Salzer (Günther et al. 2015), LUBBY2 (Heusermann et al. 1982) or Minkley (Minkley et al. 2007). The creep behaviour in those aforementioned models replicates experimental results under high deviatoric loading conditions to a good degree. Pressure solution-induced creep is well-known to be the dominating driver for creep at low deviatoric stresses (Urai et al.1986; Spiers et al. 1990) and its importance has been shown many times since (Spiers & Carter 1998; Ter Heege et al. 2005; Urai & Spiers 2007). Only recently this linear creep phenomenon has also been observed in natural salt due to its coarse grain size, confirming the earlier works (Bérest et al. 2019). Considering the conditions in geological salt deposits with prevailing near-isotropic stress states this effect may significantly influence the

outcome of a numerical simulation of long-term creep. Thus, a material model which accounts for this effect should be chosen to capture the physical behaviour observed in experiments.

Glaciation periods are expected to occur within the timeframe to be covered by repository safety assessment (i.e., 1 Ma) and impose significant changes in the mechanical, hydraulic and thermal conditions which could affect barrier integrity (Fischer et al. 2021). Thus, it is of interest to examine the influence of fully coupling these processes. Specifically, we compare simulation results of pure mechanical (M), hydro-mechanically (HM), thermo-mechanically (TM) and thermo-hydro-mechanically (THM) coupled simulations.

2 Modeling Methodology

The overarching idea of this work is to use single-process simulations, whose results act as initial conditions for the glaciation simulations. The initial simulations shall produce the steady-state results for the geothermal gradient, the hydraulic conditions and the stress state. These feed in to the second simulation which models a glacier advancing on top of the domain. Finally, we compare the influence of the different coupled processes on the simulation results and also examine the effect of using either a pure power law-based creep model (BGRa) or a combined power law and linear creep (PLLC) model. Effects of non-linear kinematics are not considered here.

All simulations were performed using the open-source finite element code OpenGeoSys (Bilke et al. 2019).

2.1 Mechanical constitutive model

The BGRa stationary creep model defines the uniaxial strain increment as (Hunsche & Schulze 1994):

$$\dot{\varepsilon}^{cr} = A \exp(-Q/(R\,T)) \left(\frac{\sigma}{\sigma_f}\right)^n \tag{1}$$

Where σ is the von Mises equivalent stress and $A = 0.18\,\mathrm{d}^{-1}, n = 5.0$ and $Q = 54\,\mathrm{kJ/mol}$ are parameters, which are determined by experiments. $R = 8.314462\,\mathrm{J\,K^{-1}mol^{-1}}$ is the universal gas constant and $\sigma_f = 1\,\mathrm{MPa}$ is a reference stress. For the stationary PLLC model, a second Arrhenius term is added to account for creep at low deviatoric stresses believed to be dominated by pressure solution effects (Spiers et al., 1990) which results in a composite creep law used which has been used many times before (Spiers & Carter 1998; Urai & Spiers 2007; Marketos et al. 2016).

$$\dot{\varepsilon}^{cr} = A \exp(-Q/(R\,T)) \left(\frac{\sigma}{\sigma_f}\right)^n + \frac{A_2}{D^3\,T} \exp(-Q_2/(R\,T)) \left(\frac{\sigma}{\sigma_f}\right) \tag{2}$$

The additional parameters were chosen as $A_2 = 6.5 \times 10^{-5}\,\mathrm{m^3 K\,d^{-1}}$, $Q_2 = 24.5\,\mathrm{kJ/mol}$ (Spiers et al., 1990) and $D = 0.05\,\mathrm{m}$, where the latter accounts for the impact of grain size. This combination of parameters results in a model behaviour, which better captures creep rates at low deviatoric stresses compared to the BGRa model as can be seen in Figure 1.
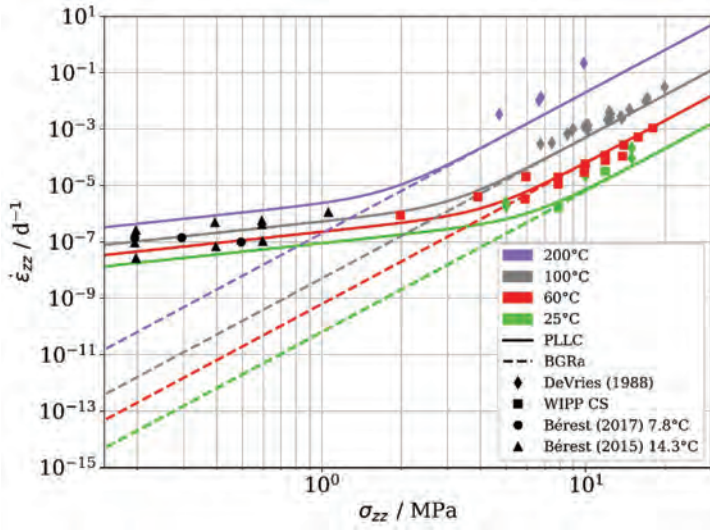
Figure 1: Comparison between PLLC and BGRa models to experimental data of creep rates from uniaxial compression tests on salt samples (amended from Bérest et al. 2019)

2.2 Model geometry

In their report, Bruns et al. (2012) examined the glacial effects on the host rock types clay and salt and their influences on the suitability for hosting a waste repository. Their salt dome model forms the basis of our model geometry. Figure 2 shows the scheme of the discretized model geometry, which extends over a width of 6 km and a depth of 3 km. The given x- and y-coordinates correspond to the points which define the geometry of the rock layers, being from top to bottom: cap rock, side rock, salt rock and bed rock. At the boundaries between salt rock and the other rock layers a finer mesh discretization was applied to better resolve the variable changes at the interface. Two observation points at the bottom of the cap rock, P1 (0 m; -300 m) and P2 (3000 m; -326 m), serve to inspect temporal variable changes.
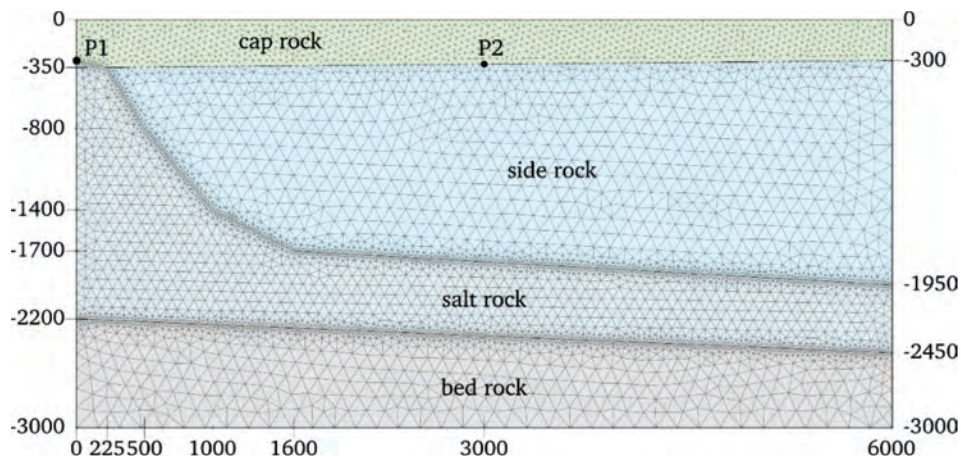
Figure 2: Discretized 2D salt dome model geometry

Boundary conditions

The boundary conditions for the single process simulations are relatively simple and are listed in the following table. For the H-simulation the increased pressure at the right boundary is presumed to be due to the load of a glacier, which is outside the domain of this simulation stage.

Table 1: Boundary conditions for the single process simulations

process	left	right	top	bottom
M (halokinesis)	$u_x = 0$		stress free	$u_z = 0$
T (geothermal gradient)	$\dot{Q} = 0$		$T = 8.5°C$	$\dot{Q} = 65 \text{ mW/m}^2$
H (hydraulic steady state)	$p = -1000 \frac{\text{kg}}{\text{m}^3} g\, z$	$p = -1000 \frac{\text{kg}}{\text{m}^3} g\, z + 1\text{MPa}$	$\dot{m} = 50 \frac{\text{kg}}{\text{m}^2\text{a}}$	no flow

For the glacial crossing simulations, the boundary conditions are shown in Table 2. The glacier has a maximum height of 1 km with a 45° sloped front and is moving in negative x-direction with a speed of 10 m/a beginning at $t = 500$ a. With the height of the glacier $h_g(x, t)$, the density of ice $\rho_{ice} = 900$ kg / m³ and the gravitational acceleration $g = 9.81$ m/s², the vertical traction at the top boundary due to the glacial loading can be calculated.

Since the cooling at the top boundary would not match with the thermal boundary condition for the right boundary, there the imposed temperature is determined as a linear interpolation between the time dependent temperature at the top boundary and the initial temperature at the interface between cap rock and side rock at the right boundary. Below, the temperature remains as the initial value.

Table 2: Boundary conditions for the coupled process simulations

left	right	top	bottom
$u_x = 0$	$u_x = 0$	$\sigma_{zz}(x, t) = -\rho_{ice}\, g\, h_g(x, t)$	$u_z = 0$
$\dot{Q} = 0$	$T = T^*(t = 0)$	$T(t < 200 \text{ a}) = 8.5°C$ In between cooling of 15.5 K/300a $T(t > 500 \text{ a}) = -7°C$	$\dot{Q} = 65 \text{ mW/m}^2$
$p = -1000 \frac{\text{kg}}{\text{m}^3} g\, z$	$p = -1000 \frac{\text{kg}}{\text{m}^3} g\, z + 1 \text{ MPa}$	$\dot{m} = 50 \frac{\text{kg}}{\text{m}^2\text{a}}$	no flow

2.3 Material parameters

The parameters for the different rock layers are given in Table 3. For side rock and bed rock, linear elastic material behaviour is applied. Salt rock employs either the BGRa or the PLLC model. For cap rock, the Mohr Coulomb material model (Marois et al. 2020; Nagel et al. 2017) is applied with a cohesion of 10 MPa and a friction angle of 15 °. The dilatancy angle, transition angle and tension cut-off parameter are all set to zero. Furthermore, Biot's coefficient was set to one in the whole domain. For considering the compressibility of the fluid, a bulk modulus of 2.15 GPa was used.

Table 3: Material parameters for the different rock types as in Bruns et al. (2012)

parameter name	permeability	Young's modulus	Poisson's ratio	density	porosity	thermal expansivity	specific heat capacity	thermal conductivity
symbol	k	E	ν	ρ	ϕ	β_T	c_p	λ_T
unit	m^2	GPa	$-$	$\dfrac{kg}{m^3}$	$-$	$\dfrac{1}{K}$	$\dfrac{J}{kg\,K}$	$\dfrac{W}{m\,K}$
cap rock	10^{-11}	7.7	0.28	1925	0.1	2×10^{-6}	1000	2.0
side rock	10^{-14}	15.6	0.3	2700	0.01	2×10^{-6}	1000	2.0
salt rock	10^{-21}	25	0.25	2140	10^{-6}	4×10^{-5}	860	5.8
bed rock	10^{-17}	15.6	0.3	2700	0.01	2×10^{-6}	1000	2.0

3 Results

This section covers the results of the initial and glaciation simulations and compares the different material models as well as the different coupling schemes.

3.1 T – geothermal gradient

The simulation of the geothermal gradient is governed by a constant geothermal heat flux of 65 mW/m^2 from the bottom and a constant temperature of $8.5°C$ at the top boundary, which corresponds to a mean annual temperature prior to the glaciation. Figure 3 shows the final temperature distribution at the thermal steady state, where the influence of the high thermal conductivity of the rock salt is readily apparent.

temperature

2.8e+02 300 310 320 330 340 350 3.7e+02
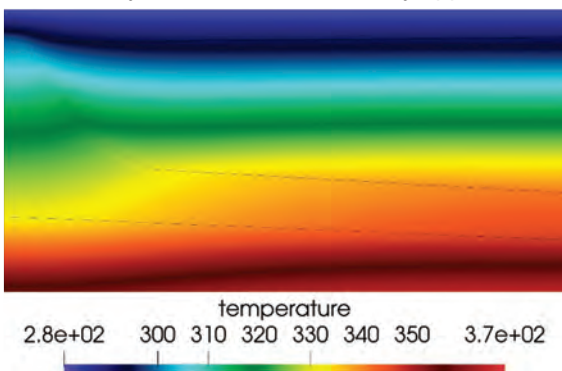
Figure 3: Temperature distribution at thermal steady state prior to glaciation

3.2 M – halokinesis

The initial M-simulation serves to determine the stress state during halokinesis and is solely driven by gravitational loads. The simulation ran for 1 Mio. years for the BGRa and the PLLC model each with the aforementioned boundary conditions. Calculating and displaying the

equivalent von-Mises stress at the last time step gives the results seen in Figure 4. With the PLLC model (left) the equivalent stress in the salt rock is on average $0.2\,\mathrm{Pa}$ and thus low enough to consider the salt formation to be in a quasi-isotropic stress state. With the BGRa model (right) there is still a residual equivalent stress of about $0.3\,\mathrm{MPa}$ in the salt layer. This is due to the slow creep rates at low deviatoric stresses in the BGRa model, translating into a longer time required to reach quasi-isotropy in the simulations. Above the salt dome a stress concentration is induced by the rising salt dome which simultaneously is being released by the Mohr-Coulomb model. At the top part of the side rock there is a higher equivalent stress with the PLLC model.

equivalent von-Mises stress / Pa
2.0e-01   1e+7   2e+7   3e+7   4.5e+07

equivalent von-Mises stress / Pa
3.0e+05   1e+7   2e+7   3e+7   4.5e+07
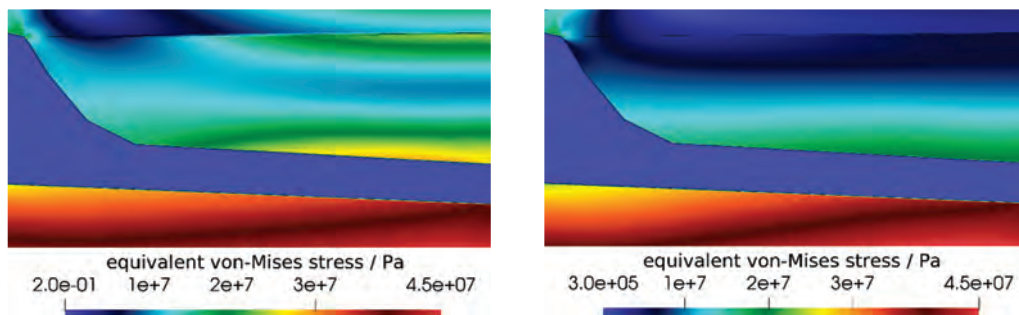
Figure 4: Equivalent von-Mises stress after 1 Mio. years of halokinesis (left: PLLC, right: BGRa)

3.3   H – hydraulic steady state

Regarding the hydraulics, we simulate the model with the given boundary conditions until a steady state is reached. The final hydraulic pressure acts as part of the initial conditions for the coupled simulations. Figure 5 shows the steady state hydraulic head (left) and fluid velocity (right). The arrows indicate the flow direction. Note, that the hydraulic field extends here throughout the salt dome but associated mass flows are very low. Future simulations will also consider modelling the rock salt as tight and eliminating hydraulic fields in the salt formation (TM in salt, THM in surrounding rock).

hydraulic height / m
-4.7e-01   20 30 40 50 60 70 80   1.0e+02

fluid velocity / m/s
9.3e-17 1e-14   1e-12   1e-10   1e-8   2.6e-06
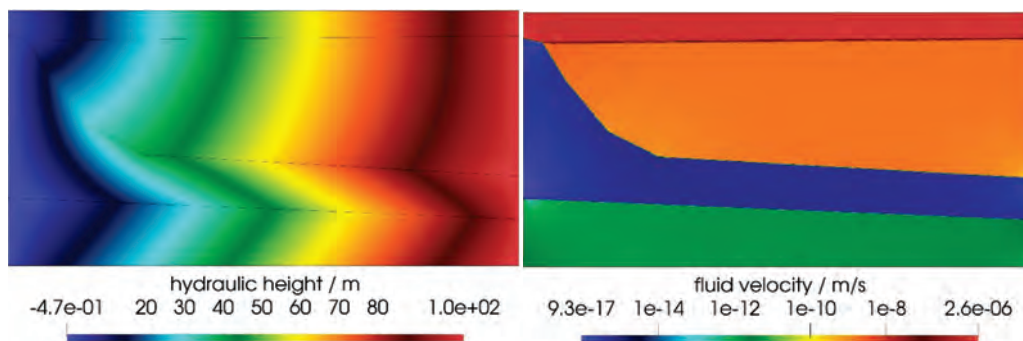
Figure 5: steady state hydraulic height (left) and fluid velocity (right)

Coupled process simulation – glacial loading

With the results from the previous simulations as initial values, we simulate the glacial loading with M, TM, HM and THM coupling schemes, each with the PLLC model. For comparison, only the THM simulation is performed a second time with the BGRa model.

Looking at the observation points P1 and P2 we can observe the vertical movement of the salt formation and the side rock during the simulation time of 1600 years, as shown in Figure 6.
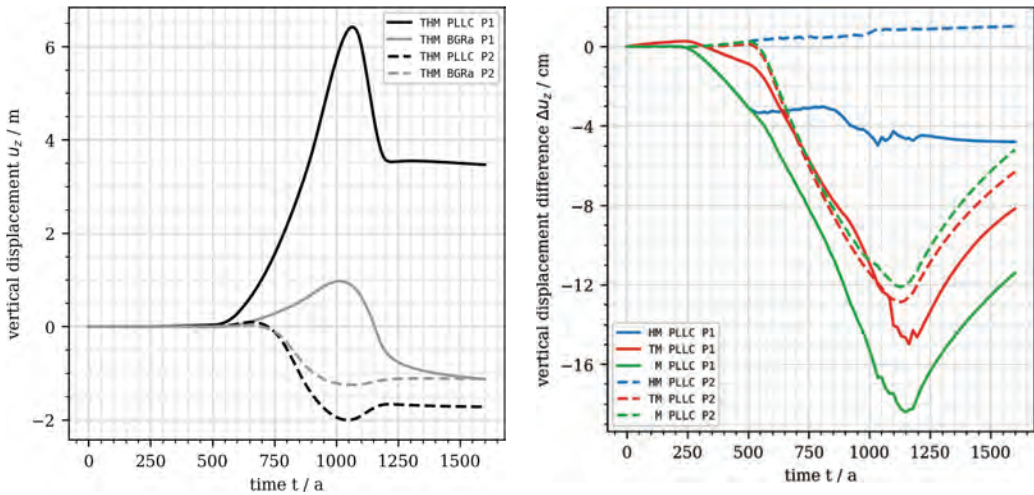
Figure 6: Vertical displacement over time at two observation points for during glacier crossing: comparison between PLLC and BGRa (left) and difference between THM and lesser coupling schemes with PLLC (right)

The glacial load causes the salt rock to creep towards and up the dome at first. When the glacier fully covers the model domain the creep changes direction. Shortly after t = 1000 a, both the uplift of the salt formation and the settlement of the side rock reach a maximum. A strong difference between both material models can be seen, with the maximum lift being approximately 5 times higher with PLLC compared to BGRa. The difference in the settlement of the side rock is not equally significant. Interestingly, at the end of the simulation, the top of the salt dome (P1) remains at an elevated position with PLLC, but with BGRa it results in a lowered final position.

Regarding the different coupling schemes, only minor differences can be seen in the displacement evolution. The HM coupling scheme comes closest to the full THM result with the difference in peak displacement being less than 1%, implying only a minor influence of the thermal coupling. Without the hydraulic coupling, both M and TM differ by a similar amount to the THM result, which is still below 3% at peak displacement.stress principle and volume fraction-dependent phase averaging to obtain effective properties.

The results raise the question, why the influence of the process-coupling is so small in the simulations. An important feature of the analyses without thermal coupling is an adjustment of temperature-dependent material parameters (e.g., of the creep models) for the initial geothermal gradient. In other words, a stationary temperature gradient was imposed while each material point remained locally isothermal. The dynamic thermal coupling is then insignificant, because the simulated temperature variations remain relatively small – below the cap rock the temperature changes stay below 1 K throughout the simulation. Heat transport via fluid motion has also only a negligible effect on the temperature field of the model, since the fluid moves predominantly in the horizontal direction, where there is essentially no temperature gradient for the chosen boundary conditions and density models. Thermally induced density-dependent convection was not considered. The more noticeable influence of the hydraulic coupling can potentially be explained by the action of the effective stress principle and the load-induced fluid flow. In terms of parameterization, simulations without hydraulic coupling were parameterized in terms of total stresses and bulk densities, whereas those

accounting for the fluid employed the effective stress principle and volume fraction-dependent phase averaging to obtain effective properties.
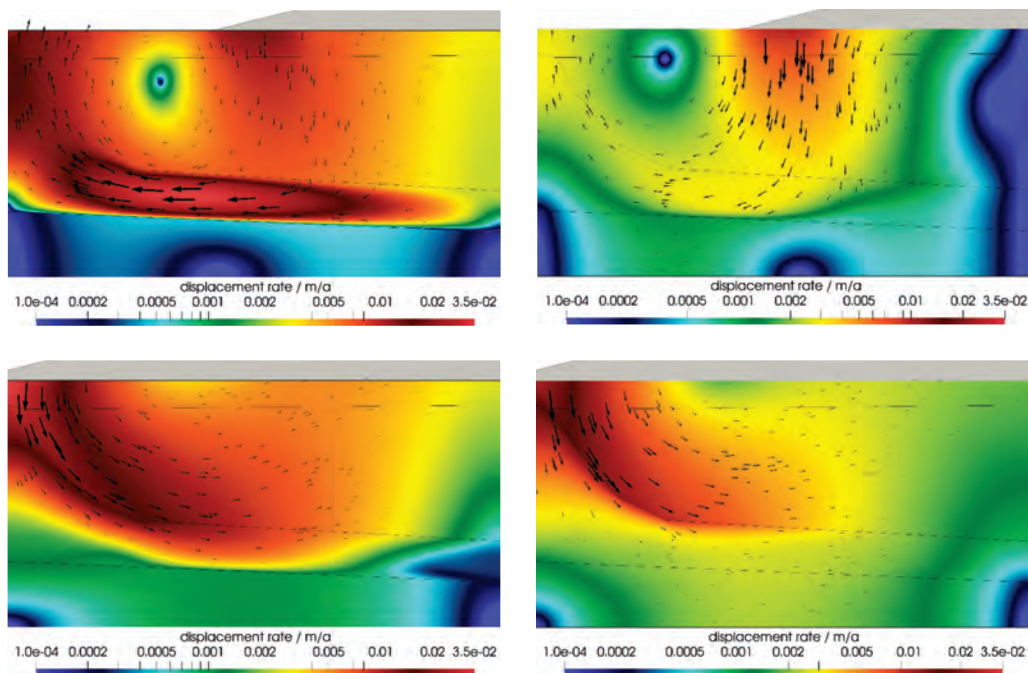
Figure 7: Displacement rate during glacier crossing at 850 a (top) and 1150 a (bottom) with the PLLC model (left) and the BGRa model (right) from THM simulations (glacier scaled 1:4)

In Figure 7 we compare the log-scaled displacement rates of the PLLC model (left) to the BGRa model (right) at $t_1=850a$ (top) and $t_2=1150a$ (bottom). These times roughly correspond to the maxima of vertical displacement rate during the simulation. On top of the model, the glacier is outlined, with the height being scaled 1:4. At t_1 the glacier just passed the right half of the model with the front being at x=2500 m and we can see a clockwise rotational trend in the displacement rate field. The maximum of the displacement rate is located in the center of the salt bed for PLLC and at the cap rock for BGRa, right below the front of the glacier. At t_2, the glacier already fully covers the whole model and the rotational trend is now in counterclockwise direction. With the PLLC model, the displacement rate is slightly higher compared to BGRa. While the stress fields in both models remain very similar, a larger volume of the salt dome is affected by higher creep rates at comparatively low deviatoric stresses when using the PLLC model, highlighting the impact of the pressure-solution component of this model.

4   Conclusions

Being a benchmark study, the chosen model geometry and boundary conditions represent a strongly simplified glacial loading scenario. Despite these simplifications, the simulation results indicate that, in the considered timeframe, taking into account pressure solution creep at low deviatoric stresses has a large influence on the simulation results. This contrasts with results obtained when using power-law models with a single high stress exponent determined from laboratory experiments performed at relatively high deviatoric stresses. These findings highlight the importance of material models, which accurately capture the creep rates at low deviatoric stresses based on experiments in this stress regime (Bérest et al. 2015; Günther et

al. 2015). Such experiments at high temperatures are necessary to improve the accuracy of the material models. The comparison of different coupling schemes for the present simulation model yielded only minor differences. This does not necessarily imply that additional coupling of hydraulic and thermal processes is not important. Rather, the influence of the process coupling could not unfold, because of constitutive assumptions and chosen boundary conditions. Furthermore, the uncoupled simulations were parameterized by considering stationary gradients in temperature and water content, for example. If that is not the case, differences would likely have been larger. Regarding the integrity of potential repositories inside salt domes, this work has served only as a means of benchmarking model formulations. Many more phenomena need to be considered for assessing the impact of glacial loading on the thermal, hydraulic, mechanical and chemical fields in the subsurface. Simulations extending over longer time periods should also study the effect of non-linear kinematics and specific material models for the interfacial behaviour between adjacent rock formations, particularly the rock salt and the cap/side rock. Specific system analyses should furthermore cover a larger model area surrounding the region of interest to avoid unwanted boundary effects.

Acknowledgements

References

BEREST, P., BERAUD, J. F., GHARBI, H., BROUARD, B., & DE VRIES, K. 2015. A Very Slow Creep Test on an Avery Island Salt Sample. Rock Mechanics and Rock Engineering, 48(6), 2591–2602.

BÉREST, P., GHARBI, H., BROUARD, B., BRÜCKNER, D., DE VRIES K., HÉVIN, G., HOFER, G., SPIERS, C. & URAI, J. 2019. Very Slow Creep Tests on Salt Samples, Rock Mech. Rock Eng., 52, 2917–2934

BILKE, L., FLEMISCH, B., KALBACHER, T., KOLDITZ, O., HELMIG, R., & NAGEL, T. 2019. Development of Open-Source Porous Media Simulators: Principles and Experiences. Transport in Porous Media, 130(1), 337–361

BRUNS, J., BOETTICHER, L., DOOSE, H., COTTRELL, M., WOLFF, P., GÜNTHER, R.-M., NAUMANN, D., POPP, T. & SALZER, K. 2012. Glazigene Beeinflussung von Wirtsgesteinstypen Ton und Salz und deren Einflüsse auf die Eignung zur Aufnahme eines HAW-Endlagers.Techn. Ber. Celle: Golder Associates GmbH in Kooperation mit IfG Institut für Gebirgsmechanik GmbH.

FISCHER, U.H., BEBIOLKA, A., BRANDEFELT, J., FOLLIN, S., HIRSCHORN, S., JENSEN, M., KELLER, S., KENNELL, L., NÄSLUND, J.O., NORMANI, S., SELROOS, J.O. & VIDSTRAND, P. 2014. Radioactive wastes under conditions of future ice ages. In: Haeberli, W., Whiteman, C. (Eds.), Snow and Ice-related Hazards, Risks and Disasters. Elsevier, Oxford (812 pp).

GÜNTHER, R.-M., SALZER, K., POPP, T. & LÜDELING, C. 2015. Steady-State Creep of Rock Salt: Improved Approaches for Lab Determination and Modelling. Rock Mechanics and Rock Engineering, 48(6), 2603–2613. https://doi.org/10.1007/s00603-015-0839-2

HEUSERMANN, S., LUX, K.-H. & ROKAHR, R.-B. 1983. Entwicklung mathematisch-mechanischer Modelle zur Beschreibung des Stoffverhaltens von Salzgestein in Abhängigkeit von der Zeit und der Temperatur auf der Grundlage von Laborversuchen und begleitenden kontinuumsmechanischen Berechnungen nach der Methode der finiten Elemente. Schlußbericht zum BMFT/PLE-Forschungsauftrag ET 2011 A, Institut für Unterirdisches Bauen, Hannover, Germany

HUNSCHE, U. & SCHULZE, O. 1994. Das Kriechverhalten von Steinsalz. In: Kali und Steinsalz 11 (8/9), S. 238–255.

KYLE, J.R. & POSEY, H.H. 1991. Halokinesis, cap rock development, and salt dome mineral resources. Developments in sedimentology. Vol. 50. Elsevier. 413-474.

LIANG, W., YANG, C., ZHAO, Y., DUSSEAULT, M.B. & LIU, J. 2007. Experimental investigation of mechanical properties of bedded salt rock. International Journal of Rock Mechanics and Mining Sciences, 44(3), 400–411

LUX, K-H. 2009. Design of salt caverns for the storage of natural gas, crude oil and compressed air: geomechanical aspects of construction, operation and abandonment. Geological Society, London, Special Publications 313.1: 93-128.

MARKETOS, G., SPIERS, C.J. & GOVERS, R. 2016. Impact of rock salt creep law choice on subsidence calculations for hydrocarbon reservoirs overlain by evaporite caprocks. Journal of Geophysical Research: Solid Earth, 121(6), 4249–4267.

MAROIS, G., NAGEL, T., NAUMOV, D. & HELFER, T. 2020. Invariant-based implementation of the Mohr-Coulomb elasto-plastic model in OpenGeoSys using MFront. April.

MINKLEY, W. & MÜHLBAUER, J. 2007. Constitutive models to describe the mechanical behavior of salt rocks and the embedded weakness planes. In: Wallner M, Lux K-H., Minkley W, Hardy H (eds) The mechanical behaviour of salt—understanding of THMC processes in salt: 6th conference (SaltMech6). Hannover, Germany, pp 119–127

NAGEL, T., MINKLEY, W., BÖTTCHER, N., NAUMOV, D., GÖRKE, U.-J. & KOLDITZ, O. 2017. Implicit numerical integration and consistent linearization of inelastic constitutive models of rock salt. Computers & Structures, 182, 87–103.

SPIERS, C.J., SCHUTJENS, P.M.T.M., BRZESOWSKY, R.H., PEACH, C.J., LIEZENBERG, J.L., & ZWART, H.J. 1990. Experimental determination of constitutive parameters governing creep of rocksalt by pressure solution. Geological Society, London, Special Publications, 54, 215–227

SPIERS, C.J. & CARTER, N.L. 1998. Microphysics of Rocksalt Flow in Nature, in The Mechanical Behaviour of Salt IV, Proceedings of the Fourth Conference, edited by M. Aubertin, and H.R. Hardy Jr., pp. 115-128, Trans. Tech., Clausthal-Zellerfeld, Germany

TER HEEGE, J.H., DE BRESSER, J.H.P. & SPIERS, C.J. 2005. Rheological behaviour of synthetic rocksalt: The interplay between water, dynamic recrystallization and deformation mechanisms. Journal of Structural Geology, 27(6), 948–963.

URAI, J.L., SPIERS, C.J., ZWART, H.J., & LISTER, G.S. 1986. Weakening of rock salt by water during long-term creep. Nature, 324, 554–557.

URAI, J.L. & SPIERS, C.J. 2007. The effect of grain boundary water on deformation mechanisms and rheology of rocksalt during long-term deformation. Proceedings of Sixth Conference on the Mechanical Behavior of Salt.

Modeling of the 3D stress state of typical salt formations

Tobias S. Baumann[1,2]*, Boris Kaus[1,2], Anton Popov[1,2], Janos Urai[3]

[1]smartTectonics GmbH, Germany; [2]Johannes Gutenberg University Mainz, Germany; [3]GeoStructures Consultancy, *Netherlands*

* tobias.baumann@smarttectonics.com

ABSTRACT: While salt structures played a central role as traps for hydrocarbons in the oil and gas industry for decades, they also serve as host rocks for salt solution mining, caverns, and other underground storages. Salt rock formations are therefore an important host rock for storing strategic oil and gas reserves, compressed air, and hydrogen and thus an essential part of the energy transition. At the same time, salt formations are currently considered host rocks for the storage of radioactive waste in many countries. Mining processes in the industrial projects mentioned above describe a thermomechanical load and induce stresses in the salt and overburden rocks. The induced stress must be analyzed as it can affect the integrity of the host rock. Together with other natural (e.g., tectonics, glaciation) and anthropogenic (e.g., neighboring caverns) loading events, the behavior of the underground storage becomes even less predictable, and we need the support of thermomechanical models. With the help of these models, we can identify critical parameters and localize characteristic high-stress regions within the host rock. Here, we present an interdisciplinary approach with examples from current studies, in which we include microstructural and lab-scale observations and their uncertainties in the rheological model of the salt rock and compute the stress state for typical salt formations and various scenarios.

1   Introduction

Whenever salt structures serve as host rocks for long-term mining activities such as solution mining or storage of radioactive waste, we initiate a thermomechanical feedback process with the salt structure or at least part of it, which changes the current state of stress before mining ("Ist-Zustand"). The anthropogenic-induced loading can be quite different. Solution mining involves potentially tall caverns that can extend several hundred meters and are filled with cool brine, inducing thermal and mechanical stress in the salt formation. As of today, the role of brine permeation into the host rock and potential hydro-thermomechanical (THM) feedback with the host rock is unclear. A repository with radioactive waste that is partly refilled with different materials introduces a thermomechanical anomaly in the host salt rock formation. Here, the considered timespan is on a different scale (1 Myrs), and long-term processes such as glacial loading and fault reactivation may influence the dynamics of the salt structure and hence the long-term integrity of the geological barrier.

In order to estimate the hydro-thermomechanical feedback, the first step is to constrain the Ist-Zustand as precisely as possible. For this task, the salt structure's geometry is preferably mapped with 3D seismics. We can then integrate the geometrical information with rock properties into the initial conditions of 3D thermomechanical models. By modifying the initial conditions within the uncertainty limits (geometry, rock properties, tectonic boundary conditions), we can compute an ensemble of thermomechanical simulations, the results of which reflect the uncertainty of the actual state of stress and potentially active faults. The 3D aspect is important, because apart from flat-bedded salt layers, pillows, domes are three-dimensional structures with characteristic dynamics. In order to ensure mechanically reliable boundary conditions, the entire salt structure is preferably modeled. While the brittle, poroelastic overburden rock properties are usually known from borehole logs, it is more challenging to determine the creep properties of the salt rocks. At the same time, the long-term, viscous response of the salt rock represents essential information, both for the geoengineering risk analysis (feedback with overburden) and economic reasons related to

cavern abandonment. Starting with the KEM-17 project (Baumann et al. 2019; Brouard et al. 2019; Urai et al. 2019), we combine observations and constraints from different scales to better constrain the salt rock rheology.

We outline the concept of the statistical model for long-term salt creep rheology, which we think is a very useful approach to combine constraints from different scales and to map the associated uncertainties. With its uncertainty limits, the statistical model allows us to derive consistent end-member rheological models, which are used as initial conditions in the thermomechanical models to study the variability of the stress state. Generally, this can be done in a systematic manner to map the effect of the uncertain rheology. In an application section, we show results for specific examples of the 3D stress state regarding the salt rheology, the type of salt structure, and internal heterogeneities.

2 Salt rheology - statistical modeling

Regarding the Ist-Zustand within the salt structure, we need to account for the significant uncertainties in the effective salt rheology. In this section, we summarize our approach to establish a statistical model for the long-term salt creep rheology. Realizations of the statistical model can later be used with 3D THM models to explore the Ist-Zustand credibility ranges.

The total strain rate to describe the long-term creep of rock salt can be additively decomposed into the dislocation and pressure solution creep components, respectively, as follows (e.g., Spiers et al. 1990):

$$\dot{\varepsilon} = \dot{\varepsilon}^{dc} + \dot{\varepsilon}^{ps}. \tag{1}$$

$$\dot{\varepsilon}^{dc} = A_{dc} \exp\left(-\frac{Q_{dc}}{RT}\right) \sigma^n, \tag{2}$$

$$\dot{\varepsilon}^{ps} = A_{ps} \exp\left(-\frac{Q_{ps}}{RT}\right) \frac{\sigma}{TD^m}. \tag{3}$$

In the above equations A_{ps} and A_{dc} denote pre-factors of the creep mechanisms, Q_{ps} and Q_{dc} are the corresponding activation energy parameters, R is the gas constant, T is the temperature, D is the grain size, σ is the effective differential stress (square root of the second invariant of the deviatoric stress tensor), n and m are the dislocation creep and grain size dependence exponents, respectively. It should be noted that the additive creep-law described here can serve as a general description for the long-term creep of rock salt. However, there are several microstructural processes that affect the grain size and the grain boundary activity and can have a critical impact on the effective creep behavior. A prerequisite for pressure solution creep is that the fluid films between the salt grains must not be disintegrated, which is the case if the deviatoric stress is sufficiently high (e.g., van Noort et al. 2008; Drury & Urai 1990; DesBois et al. 2012). Such a critical yield stress adds another layer of complexity to the rheological model and is not yet included here but will be considered in future applications.

Assuming that all parameters in Eq. (2) and (3) are independent, there are six parameters to describe the composite creep. Inferring these parameters in a complete manner may be challenging as the data constraints are usually obtained in the laboratory on a sample scale and relatively fast strain rates. Regular creep tests in the laboratory are usually performed with 1 MPa or higher (strain rates of the order 10^{-10} s^{-1} and higher). With long-term creep experiments in a constant temperature environment, it is also possible to observe strain rates down to 10^{-13} s^{-1} (Berest et al. 2009). However, especially when long-term creep tests are not available, the rheology is extrapolated over 5 to 10 orders of magnitude to strain rates of the actual salt structure (Figure 1a). To overcome the scaling issue, we establish a statistical model in a Bayesian sense and determine the rheology with constraints from various scales. In general, this allows us to include expert knowledge (a priori distributions) and derive credibility ranges for all parameters involved in the additive creep model. For example, the variability of the grain sizes from the microstructural analysis can limit the model variability of the pressure

solution component (Figure 1 a, c). Dome-scale observations, such as the location of anhydrite stringers (Li et al. 2012) or the estimated salt dome rising velocity, allow us to further constrain the effective viscosity of the salt structure. In Figure 1 b-d we demonstrate the statistical modeling approach. In general, using the existing experimental data available, one can construct a cost function that is used to express the likelihood. Here, we use Gaussian error statistics to express the likelihood and use a synthetically generated "laboratory-scale" data set (Figure 1 b) from a "true" model (solid orange line). In the Bayesian approach, we combine the a priori assumptions with the likelihood and determine the posterior distributions for the model parameters (Figure 1 c, d). Technically, this task is performed with a sampling approach, a Markov-chain Monte Carlo method (McMC). The approach is well established, also for the specific application to creep rheology (e.g., Karato & Korenaga 2008). Based on the posterior distribution, one can determine correlation statistics and credibility intervals for the model parameters. Figure 1 b illustrates an example with 20'000 realizations of the statistical creep model, visualized in the stress strain rate diagram, where regions with darker colours represent high posterior probability regions. The variability in the diagram results from the posterior uncertainty ranges of the individual creep parameters (Figure 1 c, d). Figure 1c shows two examples with prior (solid orange lines) and posterior marginal distributions (histograms) of the six model parameters. Generally, we model the priors as Normal distributions adapted from the literature. Here, the grain size prior is a synthetic Normal distribution with a mean grain size of 5 mm. In a specific application, the grain size distribution of a microstructural analysis can serve as a grain size prior. The two-dimensional marginal distributions in Figure 1 d indicate the degree of correlation between some of the individual parameters. This provides important insights into how the creep parameters should be chosen to define consistent end-member rheologies for the site-specific rock salt to be used in thermomechanical modeling.
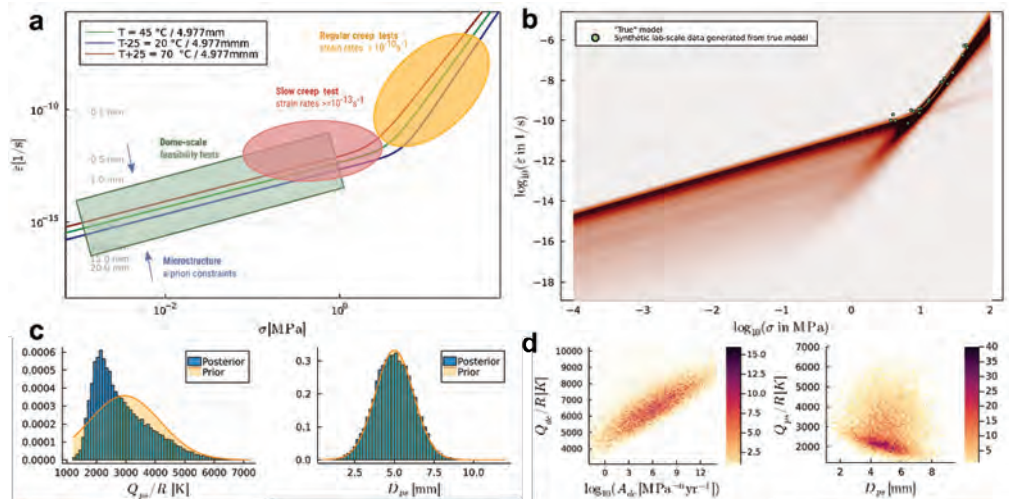
Figure 1: Multi-scale statistical model to describe the effective long-term creep rheology. a) Possible inputs to the statistical long-term creep model, either as a priori constraints or as direct observations from creep experiments. Here, the underlying creep model is an additive creep model with dislocation and pressure solution creep (dashed lines indicate different grain sizes). b) Example result with 20'000 posterior realizations of the statistical model, visualized in the stress strain rate domain with composite creep models (Eq. (1-3)). The posterior probability is higher for darker regions. Solid orange model represents the true model and markers indicate synthetic "lab-scale" data (> 2.5 MPa) generated from the true model with additional noise. c) Example with prior and posterior marginal distributions of two model parameters. Priors are Normal distributions adapted from the literature. The grain size prior is a synthetic Normal distribution. In a specific application, a grain size distribution derived from a microstructural analysis can serve as a prior. d) Example of statistical model results as 2D marginal distribution showing the correlation of the individual creep parameters.

3 Thermomechanical modeling

To compute the Ist-Zustand models, we use a thermo-mechanical code (Lithosphere and Mantle Evolution Model, LaMEM) that is actively developed at JGU Mainz (Kaus et al. 2016) and is available as open-source software. In the following, we describe the governing equations and their numerical implementation in LaMEM.

3.1 Mathematical Description

The model is based on a coupled system of momentum and mass conversation equations, respectively, with velocity (v_i) and pressure (P_{total}) as primary unknowns:

$$\frac{\partial \tau_{ij}}{\partial x_j} - \frac{\partial P_{total}}{\partial x_i} + \rho g_i = 0 \tag{4}$$

$$\frac{1}{K}\frac{DP_{total}}{Dt} + \frac{\partial v_i}{\partial x_i} = 0 \tag{5}$$

Here x_i ($i = 1,2,3$) denote Cartesian coordinates, $\tau_{ij} = \sigma_{ij} + P\delta_{ij}$ is the Cauchy stress deviator, ρ density, g_i the gravity acceleration vector, K the elastic bulk modulus, and $\frac{D}{Dt}$ is the material time derivative, respectively. The visco-elasto-plastic constitutive equation for the deviatoric strain rates is given by:

$$\dot{\varepsilon}_{ij} = \dot{\varepsilon}_{ij}^{el} + \dot{\varepsilon}_{ij}^{vs} + \dot{\varepsilon}_{ij}^{pl} = \frac{\check{\tau}_{ij}}{2G} + \dot{\varepsilon}_{II}^{vs}\frac{\tau_{ij}}{2\eta} + \dot{\varepsilon}_{II}^{pl}\frac{\tau_{ij}}{\tau_{II}}, \tag{6}$$

Where $\dot{\varepsilon}_{ij} = \frac{1}{2}\left(\frac{\partial v_i}{\partial x_j} + \frac{\partial v_j}{\partial x_i}\right) - \frac{1}{3}\frac{\partial v_k}{\partial x_k}\delta_{ij}$ is the deviatoric strain rate tensor, $\dot{\varepsilon}_{ij}^{el}, \dot{\varepsilon}_{ij}^{vs}, \dot{\varepsilon}_{ij}^{pl}$ are the elastic, viscous and plastic components, respectively, $\check{\tau}_{ij} = \frac{\partial \tau_{ij}}{\partial t} + \tau_{ik}w_{kj} - w_{ik}\tau_{kj}$ is the Jaumann objective stress rate, $w_{ij} = \frac{1}{2}\left(\frac{\partial v_i}{\partial x_j} - \frac{\partial v_j}{\partial x_i}\right)$ is the spin tensor, G is the elastic shear modulus, η denotes the viscosity, and the subscript $_{II}$ denotes the square root of the second invariant of a corresponding tensor, e.g. for the deviatoric stress $\tau_{II} = \left(\frac{1}{2}\tau_{ij}\tau_{ij}\right)^{\frac{1}{2}}$. The magnitude of the plastic strain rate ($\dot{\varepsilon}_{ij}^{pl}$) is determined by enforcing the Drucker-Prager yield criterion:

$$\tau_{II} \leq \tau_Y = (P - P_f) \cdot \sin(\phi) + c \cdot \cos(\phi), \tag{7}$$

where τ_Y is the yield stress, P is the dynamic pressure, P_f is the pore fluid pressure, ϕ is the friction angle, and c is the cohesion. Here, we describe the pore fluid pressure P_f as a function of the limiting hydrostatic (P_h) and lithostatic (P_{lith}) pressure and define the pore fluid pressure ratio λ:

$$P_f = P_h + \lambda(P_{lith} - P_h), \tag{8}$$

3.2 Numerical Implementation

We discretize the conservation equations (4) and (5) in space using staggered grid finite differences (Harlow & Welch 1965), as it is a low-order but stable discretisation for (nearly) incompressible fluid flow. To achieve scalability on massively parallel machines we use the distributed arrays (DMDA) and iterative solvers (KSP, SNES) from the PETSc library (Balay et al. 2019). The free surface is implemented using a so-called sticky air approach, which assigns a relatively low but nonzero viscosity to the air phase, together with an appropriate stabilization method to allow for sufficiently large time steps (Kaus et al. 2010). The topography of the free surface is explicitly tracked by an internal 2D grid that covers the entire domain.

We employ a Marker And Cell (MAC) method (Harlow & Welch 1965) to track material properties and implement material advection in a Eulerian kinematical framework. During the advection, the elastic history stresses from previous time step (τ_{ij}^n) are corrected on markers to account for the rigid-body rotation, and then interpolated on the edge and cell control volumes using distance-based averaging to obtain the effective strain rates:

$$\dot{\varepsilon}_{ij}^* = \dot{\varepsilon}_{ij} + \frac{\tau_{ij}^*}{2G\Delta t}, \qquad \tau_{ij}^* = \tau_{ij}^n + \Delta t \left(w_{ik}\tau_{kj}^n - \tau_{ik}^n w_{kj} \right). \qquad (9)$$

The second invariant of the effective strain rate is computed by cross-interpolation and averaging of the missing data (squares of the corresponding components) between all the control volumes. The effective viscosity (η^*) and the updated deviatoric stresses (τ_{ij}) are computed from the effective strain rates, using the standard quasi-viscous expression:

$$\tau_{ij} = 2\eta^*\dot{\varepsilon}_{ij}^*, \quad \eta^* = \min\left[\left(\frac{1}{G\Delta t} + \frac{1}{\eta}\right)^{-1}, \frac{\tau_Y}{2\dot{\varepsilon}_{II}^*}\right] \qquad (10)$$

The discretized coupled system of nonlinear algebraic equations is solved at each time step using the preconditioned Jacobian-Free Newton-Krylov (JFNK) method with line-search as implemented in the PETSc SNES nonlinear solver framework (Balay et al. 2019).

4 Example applications

In the dome-scale part of KEM-17 (Baumann et al. 2019), we addressed the question of the stress state within typical salt structures in the Netherlands before mining. With 3D thermo-hydro-mechanical (THM) modeling, we computed the "Ist-Zustand" (present-day situation and stability) of the salt structures. This was done for typical generic salt structures and included a variety of constitutive relationships and boundary conditions, including the effect of loading and unloading due to thick ice sheets during the Saalian ice age.

Our KEM-17 results clearly show that in addition to variable boundary conditions (tectonics, glacial loading, geometry of the salt structure), the choice of the constitutive relationship (the rheology) of the rock salt and its respective parameters have a decisive influence on the evolution of stress and displacement field. Among other uncertain model parameters, the salt grain size was found to be a key parameter, leading to differences in strain rate (and differential stress) of many orders of magnitude. This effect is well known from microphysical models of pressure solution, and the influence of these parameters will be amplified considering a repository's evolution on a million-year time scale.

Figure 2 illustrates the salt internal stress state of a pillow structure. The blue surfaces represent the top and base salt interface. In between, the maximum differential stress is shown with high stresses visualized with warm colors. The colormap is clipped at 1 MPa to focus on the salt internal differential stress. The model contains interpreted salt-internal heterogeneities, i.e., anhydrite stringers and a thin layer with KMg salt close to the top of the pillow. Here the Anhydrite stringers are modeled as visco-elasto-plastic material with a power-law creep component. The KMg salt is weakened compared to the main Halite (parameters after Baumann et al. 2019). We see that the stress builds up within and in the vicinity of the Anhydrite stringers, whereas the stress is significantly reduced in the weak magnesium salt. Apart from the stress localisations induced by the heavy anhydrite stringers, we consistently encounter a high-stress concentration at the very top of the salt structure. This is also observed when internal heterogeneities are excluded from the model (Figure 3 a, b). Here a dislocation creep end-member rheology is employed, which assumes disintegrated fluid films at the grain boundaries. Under these assumptions, we encounter differential stresses of the order of 1 MPa. (Re-) activated grain boundaries and combined creep mechanism (Eqs. 1-3) of pressure solution and dislocation creep, would lead to decreased stress magnitudes.
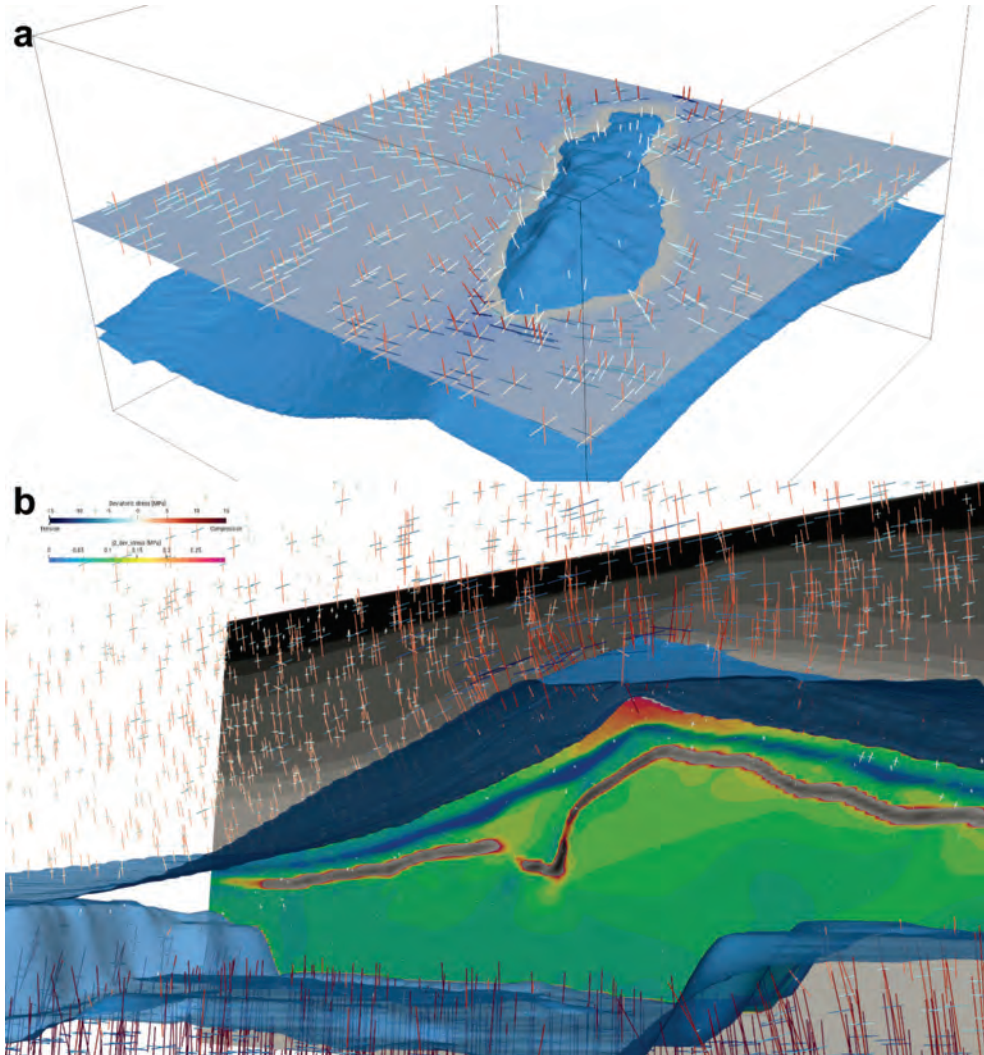
Figure 2: Three-dimensional thermo-hydro-mechanical (THM) model of a salt pillow's present-day situation with heterogeneous internal structures (Baumann et al. 2019). The model has experienced additional load due to temporary ice coverage. Blue surfaces represent Top- and Base-Zechstein. Colors represent deviatoric stress, clipped to the stress ranges inside the rock salt. Warm colors show regions of high deviatoric stress. Crosses are the principal components of the stress tensor, and gray-shaded background colors indicate the geology of the overburden and salt-internal anhydrite stringer.

In Figure 3 a, b, the maximum differential stress is shown on a cross-section orthogonal to the long axis of the dome. As mentioned above, this model has a homogeneous internal structure modeled with two different dislocation creep laws (after Bräuer et al. 2011 (BGRa) and Wawersik & Zeuch 1986). Compared with the less evolved pillow structure, the stresses are lower, although one would expect higher stresses due to the dome geometry.
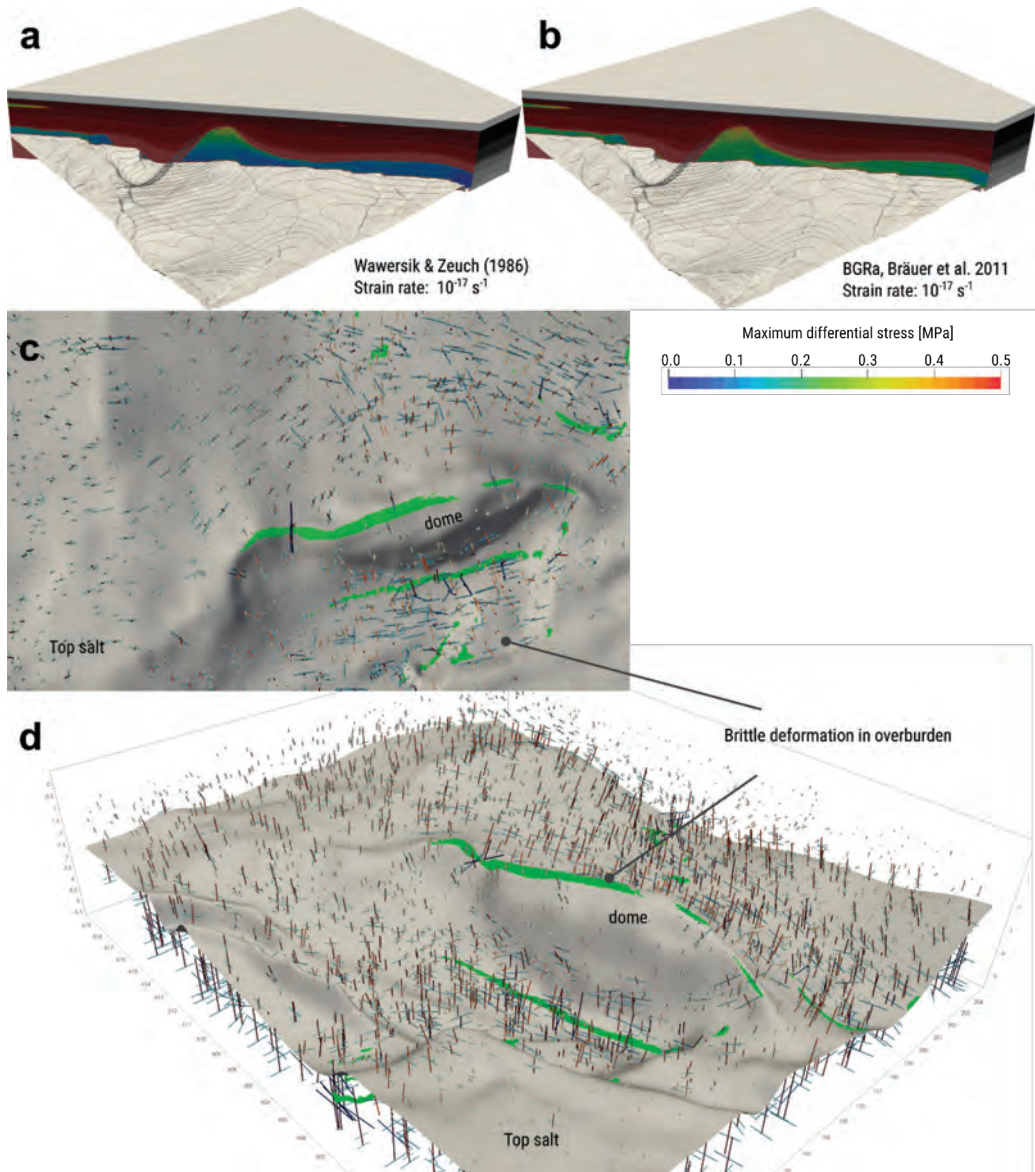
Figure 3: Three-dimensional thermo-hydro-mechanical (THM) model of a salt dome present-day situation without heterogeneous internal structures (Baumann et al. 2019). The models have experienced additional load due to temporary ice coverage. a, b: show maximum differential stress. The colorbar is clipped to the salt internal stress range. c, d: Principal stress directions in the overburden alongside locations of brittle failure (green markers) that are consistent with interpreted normal faults on top of the dome structure.

This emphasizes the impact of internal heterogeneities on the salt-internal Ist-Zustand. The thermomechanical feedback with a cavern field or a radioactive waste repository is likely to be influenced by these heterogeneities too. The cross markers in the overburden and the basement represent the principal stress directions. Here, we see a typical pattern of the stress orientation in the surrounding of steep salt structures, where one of the principal axes turns into the normal direction of the salt surface, which acts as a tangential stress-free boundary. This can also be observed for the more evolved salt dome in Figure 3 c, d. In the top view

(Figure 3c), the sub-horizontal principal stress axes bend around the dome. From the side (Figure 3d), we see that the sub-vertical components gently rotate in a normal direction of the top salt surface. In addition to the stress markers, we also show the model locations where brittle failure occurs (green markers, Figure 3 c, d). The failure pattern follows the ridge of the dome structure. It is a robust feature seen in many of our Ist-Zustand models. It is controlled by the brittle properties of the overburden, which are not as well constrained as the elastic properties. However, in many cases, overburden normal faults are consistently mapped in the seismic interpretation.

5   Conclusions

Handling the long-term creep rheology as a statistical model is a robust description of the effective long-term creep rheology. It allows us to combine expert knowledge and constraints from different scales (micro, cavern, and dome scale) and helps to partly overcome the scaling issue when extrapolating the strain rates observed in the laboratory to natural conditions. The uncertainty and the correlation of the individual parameters can be explored. This provides important insights into how the creep parameters for the thermomechanical models should be chosen to compute the variability of the Ist-Zustand stress state. Dome scale model results predict differential stresses of up to 1 MPa, which can locally be amplified due to the existence of salt-internal heterogeneities. The large-scale pattern of the principal stress directions is a relatively robust model feature primarily affected by the shape of the top salt surface. Our model results demonstrate that brittle failure occurs at distinct locations (the ridge of the salt pillow), often consistent with seismic interpretations of faults in the overburden of salt structures.

References

BALAY, S. ET AL. 2019. PETSc Users Manual. https://www.mcs.anl.gov/petsc.

BAUMANN, T., KAUS, B. & POPOV, A. 2019. Over-pressured salt solution mining caverns and leakage mechanisms. Phase 3 Dome-Scale Report.

BÉREST, P., GHARBI, H., BROUARD, B., BRÜCKNER, D., DEVRIES, K., HÉVIN, G. & URAI, J. 2019. Very slow creep tests on salt samples. Rock Mechanics and Rock Engineering, 52(9), 2917-2934.

BRÄUER, V., EICKEMEIER, R., EISENBURGER, D., GRISSEMANN, C., HESSER, J., HEUSERMANN, S., & SCHNIER, H. 2011. Description of the gorleben site part 4: geotechnical exploration of the gorleben salt dome. Die Bundesanstalt für Geowissenschaften und Rohstoffe.

BROUARD, B. & BÉREST, P. 2019. Over-pressured salt solution mining caverns and leakage mechanisms. Phase 2 Cavern-Scale Report.

DESBOIS, G., URAI, J.L., KUKLA, P.A., WOLLENBERG, U., PÉREZ-WILLARD, F., RADÍ, Z., & RIHOLM, S. 2012. Distribution of brine in grain boundaries during static recrystallization in wet, synthetic halite: insight from broad ion beam sectioning and SEM observation at cryogenic temperature. *Contributions to Mineralogy and Petrology*, *163*(1), 19-31.

DRURY, M.R., & URAI, J.L. 1990. Deformation-related recrystallization processes. Tectonophysics, 172(3-4), 235-253.

HARLOW, F.H., & WELCH, J.E., 1965. Numerical calculation of time-dependent viscous incompressible flow of fluid with free surface: The physics of fluids, v. 8, no. 12, p. 2182-2189.

KAUS, B.J., POPOV, A.A., BAUMANN, T., PUSOK, A., BAUVILLE, A., FERNANDEZ, N., & COLLIGNON, M. 2016. Forward and inverse modelling of lithospheric deformation on geological timescales. In Proceedings of NIC Symposium.

KAUS, B.J., MÜHLHAUS, H. & AND MAY, D.A., 2010. A stabilization algorithm for geodynamic numerical simulations with a free surface: Physics of the Earth and Planetary Interiors, v. 181, no. 1-2, p. 12-20.

KORENAGA, J. & KARATO, S.-I. 2008. A new analysis of experimental data on olivine rheology. J. Geophys. Res. Solid Earth 113.

LI, S., ABE, S., URAI, J.L., STROZYK, F., KUKLA, P. A. & VAN GENT, H. 2012. A method to evaluate long-term rheology of Zechstein salt in the Tertiary. Proc. Mech. Beh. Salt VII, 215-220.

SPIERS, C.J., SCHUTJENS, P.M.T.M., BRZESOWSKY, R.H., PEACH, C.J., LIEZENBERG, J.L., & ZWART, H.J. 1990. Experimental determination of constitutive parameters governing creep of rocksalt by pressure solution. *Geological Society, London, Special Publications*, *54*(1), 215-227.

URAI, J.L., SCHMATZ, J. & KLAVER, J. 2019. Over-pressured salt solution mining caverns and leakage mechanisms. Phase 1 Micro-Scale Report.

VAN NOORT, R., VISSER, H.J., & SPIERS, C.J. (2008). Influence of grain boundary structure on dissolution controlled pressure solution and retarding effects of grain boundary healing. *Journal of Geophysical Research: Solid Earth*, *113*(B3).

WAWERSIK, W.R. & D.H. ZEUCH. 1986. Modeling and Mechanistic Interpretation of Creep of Rock Salt below 200°C. Tectonophysics 121(2–4):125–52.

Unexpected features of salt cavern behavior

Elizaveta Gordeliy[1], Pierre Bérest[1]*

[1]Laboratoire de Mécanique des Solides, Ecole Polytechnique, France

* *elizaveta.gordeliy@polytechnique.edu*

ABSTRACT: Evolution of an idealized spherical cavern leached out from a salt formation can be described by a first order integro-differential equation when constitutive laws such as Norton-Hoff law, Munson-Dawson law (which accounts for transient creep), Marketos-Spiers law (which accounts for pressure-solution creep and dislocation creep) are considered. Such a solution sheds some light on the behavior of salt caverns submitted to various types of loadings. In addition, a moving-boundary formulation, representing progressive cavern creation, is proposed.

1 Introduction

The objective of this paper is to describe a simple numerical tool used to study the behavior of a salt cavern under various types of loadings. For this problem, closed-form solutions are available, at least in the case of a spherical or cylindrical cavern when steady state has been reached. A solution of the transient problem was obtained by Manivannan & Bérest (2019) for a cylindrical cavern in a Norton-Hoff medium.

In this paper, an idealized spherical shape is assumed. The behavior of the salt formation is described by the Norton-Hoff (N-H), Munson-Dawson (M-D, Munson & Dawson 1984), or Marketos-Spiers (M-S, Marketos et al. 2016) law. With such a tool the effects of cavern shape cannot be explored; its main advantage is that it provides insight in some special features of the behavior of salt caverns which result from the highly non-linear character of the strain-rate vs stress relation. The presented results show the significance of the transient rheological creep (resulting from the M-D law) in comparison to the transient "geometrical" creep (resulting from the N-H law), as well as the effect of the inclusion of the pressure-solution creep on the salt cavern behavior, by means of the Marketos-Spiers law. In addition, the spherical cavity approximation greatly simplifies the modelling of solution mining, in which the cavern is created progressively.

2 Spherical cavity approximation

2.1 Constitutive laws

The Munson-Dawson model is defined by the following equations:

$$\dot{\varepsilon}_{ij} = \frac{1+\bar{v}}{E}\dot{\sigma}_{ij} - \frac{\bar{v}}{E}\dot{\sigma}_{kk}\delta_{ij} + \frac{3}{2}A\sqrt{3J_2}^{\,n-1}F(\sqrt{3J_2},\zeta)s_{ij} \qquad \text{(M-D law)} \qquad (1)$$

where σ_{ij} is the Cauchy stress tensor, $s_{ij} = \sigma_{ij} - \sigma_{kk}\delta_{ij}/3$ is the deviatoric stress tensor and $J_2 = s_{ij}s_{ji}/2$ is its second invariant. E and $\bar{v}$ are the Young modulus and the Poisson ratio, respectively. The constant A is a material property and depends on the temperature, $A = A_0\,exp[-Q_{dis}/(RT_R)]$, see Table 1. Function F depends on the internal parameter ζ describing transient creep (see Appendix A). When $F \equiv 1$, the Norton-Hoff law, which includes no description of transient creep, is obtained.

Marketos-Spiers law takes into account pressure solution creep ($B = B_0\, exp[-Q_{ps}/(RT_R)]/T_R$ is function of temperature, see Table 1):

$$\dot{\varepsilon}_{ij} = \frac{1+\bar{v}}{E}\dot{\sigma}_{ij} - \frac{\bar{v}}{E}\dot{\sigma}_{kk}\delta_{ij} + \frac{3}{2}\left(B + A\sqrt{3J_2}^{\,n-1}\right)s_{ij} \qquad \text{(M-S law)} \qquad (2)$$

A spherical hollow cavern is considered whose internal and external radii are a_0 and b_0, respectively. ($b_0 < \infty$ is much larger than a_0, $\gamma = a_0/b_0 = 1/1000$, for instance). It is submitted to a constant external pressure P_∞ (geostatic pressure) and to a varying internal pressure $P_c(t) < P_\infty$. Only small strains and displacements are considered (geometrical changes of the sphere are not taken into account.)

It is convenient to introduce the "deviator" $S = \sigma_{rr} - \sigma_{\theta\theta}$. Note that $|S| = \sqrt{3J_2}$. In Appendix A, it is explained that, in the case of a hollow sphere, when assuming $\bar{v} = 0.5$, deviator evolution in the rock mass can be described by an integro-differential equation (Eq. A8) for the deviator $S(r,t)$. Once $S(r,t)$ is known, the change rate of the cavern's volume V can be found from:

$$\frac{\dot{V}(t)}{V_0}(1-\gamma^3) = \frac{9\dot{P}_c(t)}{4E} - \frac{9}{2}\int_{a_0}^{b_0}(B + A|S(r,t)|^{n-1}F(r,t))S(r,t)\frac{dr}{r} \qquad (3)$$

2.2 Steady state solutions

Internal pressure $P_c < P_\infty$ is constant. Note that steady state implies $F = 1$ and the steady-state solution for M-D and N-H laws are identical. When steady state is reached, $\partial S/\partial t = 0$, and we obtain:

$$S^{ss}(r) = \frac{a_0^{3/n}}{r^{3/n}}\frac{3(P_\infty-P_c)}{2n(1-\gamma^{3/n})} \qquad \text{(N-H law, M-D law).} \qquad (4)$$

For the M-S law, a steady-state solution can be obtained semi-analytically for $n = 2$ or $n = 3$.

3 Numerical implementation

A numerical solution of Eqs. 3 and A8 is obtained as follows. The problem is discretised by choosing a mesh of spatial nodes distributed radially starting at the internal wall of the cavern. The obtained system of non-linear ODE's for $S(r,t)$ (coupled with non-linear ODE's for $\zeta(r,t)$ in case of the M-D law, see Appendix A) is solved using the 4-th order Runge-Kutta method. For this paper, 3000 to 20000 spatial nodes were used.

4 Main results

4.1. Constitutive law parameters

In this section the N-H law and the M-D law are used to simulate the case of an abrupt pressure drop in the cavern. The involved parameters are selected according to Table 1 (the temperature is set to T_R = 318 K, except in Section 4.5). A geostatic pressure, P_∞ = 20.9 MPa (cavern depth is assumed to be 950 m, except in Section 4.5), is applied externally.

Table 1. Parameters values

Elastic	E = 17,000 MPa, $\mu = E/2/(1 + \bar{v})$ = 5667 MPa;
Norton-Hoff	$A(T_R = 318\ K) = 1.61 \times 10^{-6}$ MPa^{-n}yr^{-1}, $\quad n = 3.1$, $\quad A(T_R) = A_0\ exp[-Q_{dis}/(RT_R)]$, Q_{dis}/R = 4100 K, A_0 = 0.64 MPa^{-n}yr^{-1}
Munson-Dawson	$m = 3$, $K_0 = 7 \times 10^{-7}$/MPa^3, c = 0.00902 /K, $\alpha_w = -13.2$, $\beta_w = -7.738$, $\delta = 0.58$
Marketos-Spiers	$$B(T_R = 318\ K) = 10^{-5}\ \text{MPa}^{-1}\text{yr}^{-1}$$ or $B(T_R) = B_0\ exp[-Q_{ps}/(RT_R)]/T_R$, $\quad B_0 = 3.76 \times 10^{-13}/D^3$ (MPa^{-1}s^{-1}K), $\quad Q_{ps}/R = $ 2946.8 K, $D = 0.007\ m$

The parameters for the Norton-Hoff law were taken following Brouard (1998).

4.2. Transient creep after a sudden pressure drop

A constant inner pressure P_0 = 10 MPa was maintained at the cavern wall during a very long period of time before $t = 0$; steady state was reached at $t = 0^-$. At $t = 0^+$, the internal pressure is abruptly decreased to pressure P_c = 5 MPa. Figure 1 shows the "deviator", or $S(r,t) = \sigma_{rr}(r,t) - \sigma_{\varphi\varphi}(r,t)$, for both models. At the cavern wall, the deviator stress decreases ($\partial S(r,t)/\partial t < 0$) to slowly reach its steady state value. (A dilatant criterion, $\sqrt{3J_2} < \bar{a}I_1$, or $|S| < \bar{a}|2S + 3P_c|$, is often used to assess cavern integrity, where I_1 is the first invariant of the Cauchy stress tensor. As $|S|/|2S + 3P_c|$ is an increasing function of S, and S is a decreasing function of time at cavern wall ($r = a_0$), this criterion is more demanding immediately after cavern creation than later.) However, the deviator increases at large distance from the cavern wall as $\partial S(r,t)/\partial t > 0$ there, a consequence of $\int_{a_0}^{b_0}(2\partial S(v,t)/\partial t)(dv/v) = 0$. At the cavern wall, the deviator equals the opposite of the effective stress, $S(a_0,t) = -P_c(t) - \sigma_{\varphi\varphi}(a_0,t)$. In the M-D model the effective stress changes much faster than in the N-H model. In the M-D model, the deviator at the cavern wall drops from 12.8 MPa to 9.4 MPa within 1 day after the sudden pressure drop, and then to 8.6 MPa within 100 days. In the N-H model, there is almost no change in the deviator within 1 day after the sudden pressure drop, and it drops slowly from 12.8 MPa to 9.5 MPa within 100 days. This difference between the two models is due to the "rheological" transient creep, which is included in the M-D law but not in the N-H law. Figure 2 shows the evolution of the cavern volume rate, scaled by the initial cavern volume V_0. A striking fact is that a long transient evolution (more than one century, i.e., much longer than the transient phase observed during a laboratory test) is observed in both models. Steady state volume loss rate before the abrupt pressure drop was $\dot{V}^{ss}/V_0 = -4.2 \times 10^{-4}$yr^{-1}. Steady state volume loss rate at large time after the pressure drop, which is $\dot{V}^{ss}/V_0 = -1.35 \times 10^{-3}$yr^{-1}, is not reached yet one century after the pressure drop. This is remarkable, as Norton-Hoff law includes no transient component. The transient behavior in the Norton-Hoff law results from the slow redistribution of stresses in the rock mass, or "geometrical" transient behavior. The volume rates obtained with the N-H law and with the M-D law become approximately same after about 5 years after the pressure drop, i.e. the most part of the rheological transient creep

in the simulation with the M-D law takes place soon after the pressure drop, while the transient behavior could be attributed to the geometrical creep for times longer than about 5 years after the pressure drop. Note also that, after cavern pressure is lowered from P_0 = 10 MPa to P_c = 5 MPa, transient volume loss rate initially is very fast for the M-D law and is faster by two orders of magnitude than that for the N-H law. Due to the much faster transient stress evolution after the pressure drop (Figure 1), the M-D law predicts a much higher volume loss rate (by two orders of magnitude) in the first few days after the pressure drop, in comparison to the N-H law.

Similarly, it is remarkable that in the case of an abrupt (and large) pressure increase in the cavern, *geometrical* "reverse creep" is observed (cavern volume increases for a while), even if neither M-D nor N-H laws are able to describe *rheological* reverse creep. In addition, following a large pressure increase, the effective stress, or $S(a_0, t) = -P_c(t) - \sigma_{\varphi\varphi}(a_0, t)$, can be tensile (there is a risk of hydrofracturing), even when the final cavern pressure is smaller than the geostatic pressure.
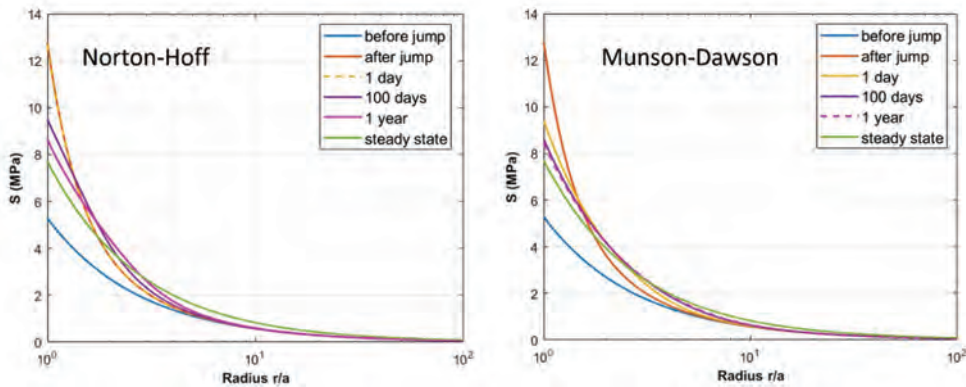
Figure 1. Behavior of $S(r, t)$ obtained with N-H law or M-D law after abrupt pressure drop
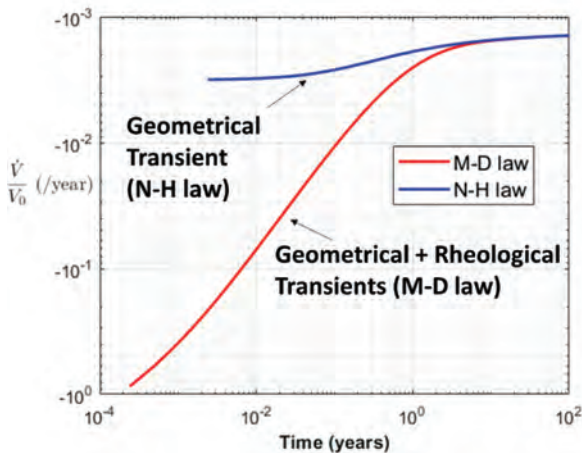
Figure 2. Transient volume rate after an abrupt pressure drop

4.3. Modelling of an *in situ* test

Indeed, the results of modeling of an *in situ* outflow test with the M-D law (Hugout 1988; Bérest et al. 2007) show that the M-D model is capable of capturing a fast transient volume loss after

a sudden pressure drop, as observed in the field. This test was performed in 1982-1983 in the 7500 m³, 950-m deep EZ53 cavern, which is considered currently for hosting a hydrogen pilot plant (HYPSTER project, supported by the European Community). After cavern leaching was completed, the brine pressure in the cavern was kept at 11.4 MPa. On day 93 after end of leaching, the cavern pressure was dropped to 8 MPa. On day 253, the cavern pressure was restored to 11.4 MPa. The measured outflow rate is shown in Figure 3 (left).
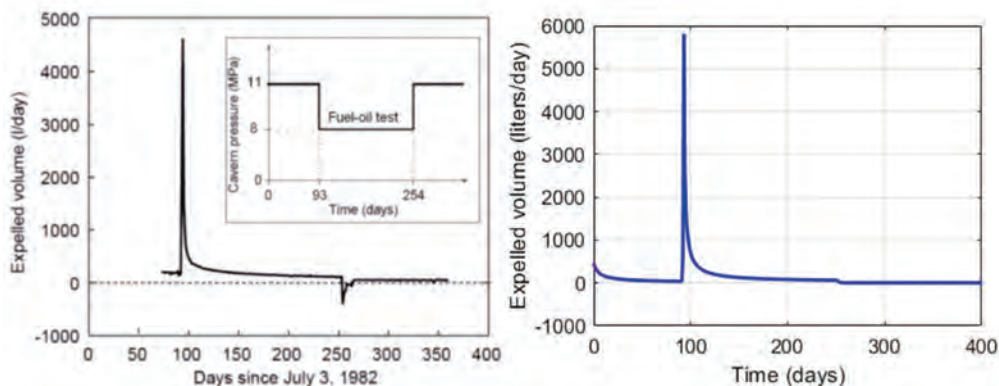
Figure 3. Daily volumes of liquid expelled from the cavern in Hugout's in-situ test (left), and volume loss obtained by modelling the closure of a salt cavern using the M-D law (right) whose parameters were defined in Section 4.1.

The M-D law was used to simulate the volume change due to the pressure schedule following Hugout's test. The leaching phase was simulated by linearly decreasing the cavern pressure. The elastic moduli were set to:

Table 2. Elastic Parameters for the EZ53 test

Elastic Parameters	E = 17700 MPa	μ = 5900 MPa

in order to fit the cavern compressibility, measured by Brouard (1998). Figure 3 shows the daily volumes of liquid expelled from the cavern in Hugout's test obtained in-situ (left), and the volume loss computed with the present model (right). The M-D model is able to capture the sudden significant increase in the volume loss in the few days after the pressure drop. (Note that the M-D model, however, is not able to accurately capture the reverse creep associated with the sudden pressure increase on day 254.)

4.4. Volume loss during pressure cycles
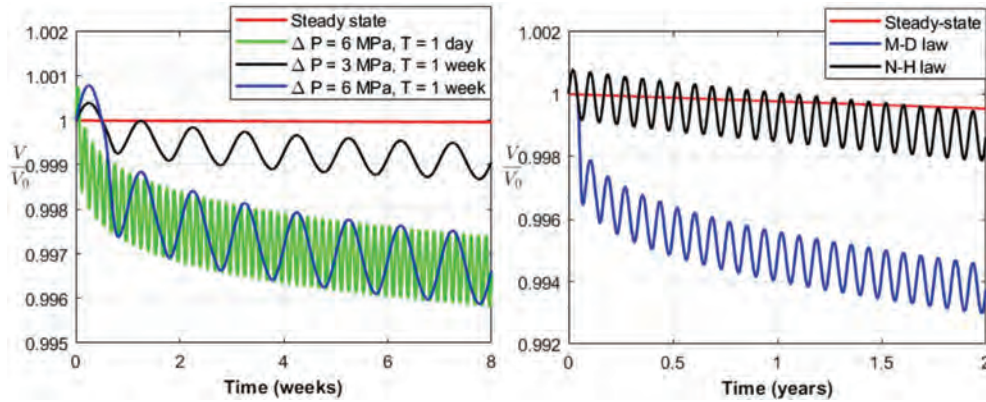
Figure 4: Volume change for a cavern under cyclic pressure. Left: results computed with M-D law for several sets of cycle amplitude ΔP and period T. Right: results computed with M-D law and N-H law for ΔP = 6 MPa and T = 1 month. The steady state solution is computed for the average pressure difference, $P_\infty - P_c$ = 9 MPa.

In this section the M-D law is used to simulate the case of a cyclic pressure change. A constant pressure difference, $P_\infty - P_0$ = 9 MPa, was maintained at the cavern wall during a long time before $t = 0$, such that the steady state was reached at $t = 0^-$. At $t = 0^+$, the cavern pressure is cycled according to $P_\infty - P_c = 9 \text{ MPa} - \Delta P \sin{(2\pi t / T)}$. When pressure cycles are performed, the average volume loss rate is much larger than the loss observed when the average pressure is applied (Figure 4, left). The difference is a function of period T and amplitude ΔP (Lestringant et al. 2010). Influence of the period is relatively small. The M-D law predicts a much larger volume loss than the N-H law (Figure 4, right).

4.5.   Comparison between M-S law and N-H law

We consider next the M-S law, which includes pressure solution creep. The exponent of the non-linear term in the M-S law and in the N-H law is set to $n = 3$. The constant involved in the M-S law is set to $B = 10^{-5}$/yr/MPa. We consider first the steady-state solution as a function of the cavern depth H. Geostatic pressure is $P_\infty = 0.022$ MPa/m $\times H(m)$; cavern pressure is $P_c = 0.012$ MPa/m $\times H(m)$. Figure 5 (left) shows the stress deviator obtained for several cavern depths when rock temperature, $T_R = 318K$, does not depend on depth: H = 200, 500, 1000, 1500, 2000 m. The ratio of the volume rate for M-S law to the rate for the N-H law is larger for shallower depths, see Figure 5 (right). It is more than 20 for a very shallow depth (H = 200 m).

(However, B and A depend on temperature (see Table 1), hence on cavern depth. The value B = 10⁻⁵/yr/MPa corresponds to the temperature $T_R = 318K$ and salt grain diameter $D = 7$ mm, according to the values used for pressure solution creep by Marketos et al. (2016). In fact, when a cavern is shallower, rock temperature is colder, B is smaller, and cavern creep closure is slower than when temperature dependence of B is not taken into account (for depths $H < 996$ m). The opposite is true when the cavern is deeper. This effect can be seen on Fig. 6.)

We then consider a shallow cavern, H = 250 m. The constants B and A, involved in the M-S law, correspond to the temperature $T_R = 291.9K$. The geostatic pressure is P_∞ = 5.5 MPa. Before $t = 0$, the steady state was reached with cavern pressure P_0 = 3 MPa. At $t = 0$, the cavern pressure is abruptly dropped to P_c = 2.5 MPa. Figure 7 (left) shows the behavior of the deviator near the cavern wall. For M-S law, the steady state solution is reached much faster. Indeed, the solution at $t = 9$ years for the M-S law is closer to the corresponding steady state solution than the solution at $t = 100$ years for the N-H law. Figure 7 (right) shows that the volume loss

rate, obtained with the M-S law, is much higher than that for the N-H law – roughly by one order of magnitude.
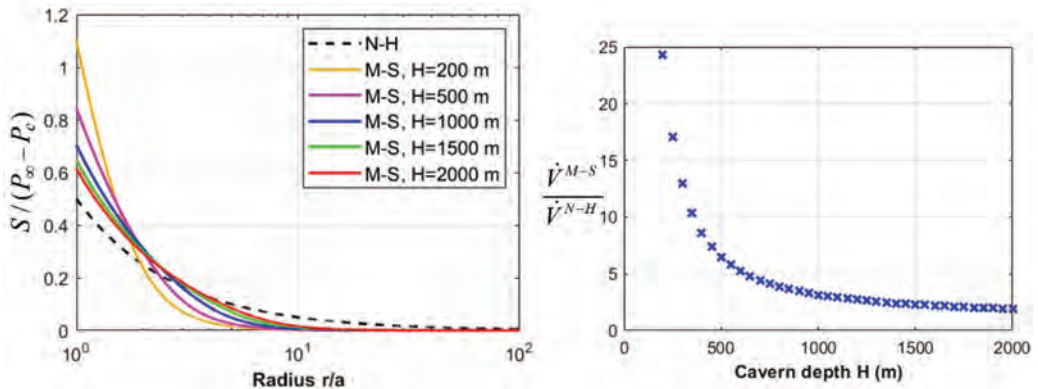
Figure 5: Left: scaled stress deviator $S/(P_\infty - P_c)$, computed using the N-H law and the M-S law for cavern depths: H = 200, 500, 1000, 1500, 2000 m. Right: ratio of the steady state volume rate for M-S law to the volume rate for N-H law, as a function of cavern depth H.
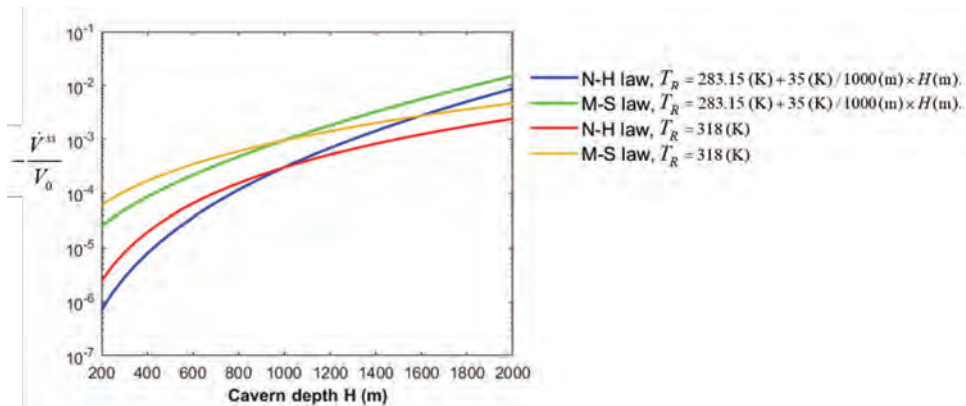
Figure 6. Steady state cavern volume rate when temperature dependence on cavern depth is and is not taken into account. N-H law and M-S law are compared
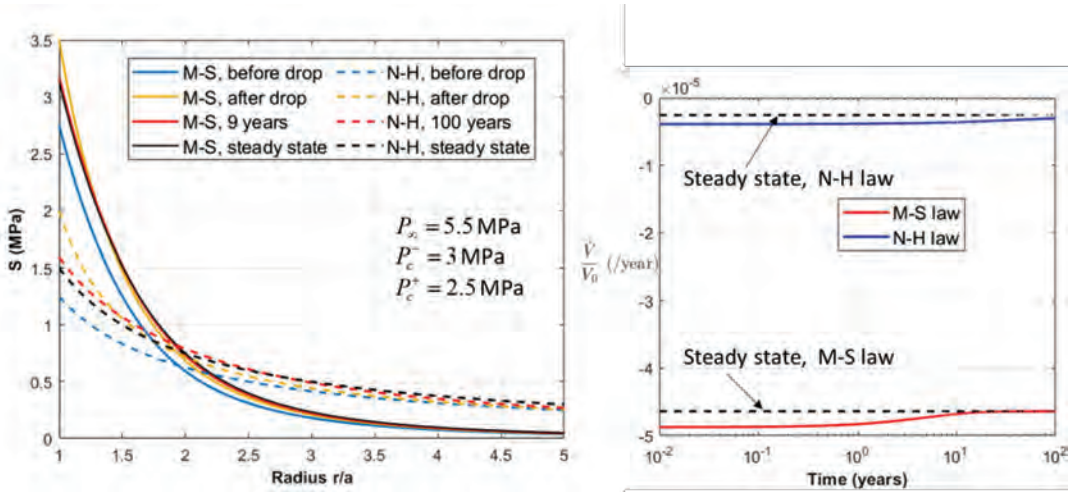
Figure 7. Behavior of $S(r,t)$ (left) and transient volume rate (right) after abrupt pressure drop, for a shallow cavern, H = 250 m. Results are obtained with M-S law or N-H law.

4.6. Solution Mining

Salt caverns are created through solution mining. A wellbore is tapped to the salt formation. Water is injected in the wellbore, brine is withdrawn, cavity grows until its final shape is reached. Brine pressure is applied to the cavern walls. In other words, the cavern wall is a moving boundary. There are different possible methods to describe the solution-mining phase: cavern pressure abruptly decreases from geostatic pressure to halmostatic pressure (method A); pressure decreases linearly (method B, often adopted when performing numerical computations); and progressive creation of the cavern (a moving boundary problem). Generally speaking, the stress distribution obtained when using method A or method B cannot be exact, as there is a competition between stress redistribution due to creep closure and cavern growth due to solution mining, an effect which cannot be accounted for.

The equations describing the moving boundary method are discussed in Appendix B. For the spherical cavern, methods A and B are based on the assumption that the cavern is created instantaneously with its final radius a_0. For the moving boundary method, evolution of the cavern radius $x = x(t)$ results from a physical assumption. For instance it can be assumed that solution mining is performed in such a way that cavern growth rate is constant, or $x^3 = 3Kt$, K is a constant, and $x^2\dot{x} = K$. As an example, we consider a V = 200,000 m³ cavern leached out in one year. At t = 0, the initial cavern of radius $\hat{x}_0$ =0.1 m is created and the pressure at the cavern wall drops to halmostatic pressure, P_c = 11.4 MPa. The final cavern radius after the leaching phase is $\hat{x}_1$ =36.3 m. Figure 8 shows the evolution of the volume loss rate after the leaching phase, and the deviator computed at times t = 0.5 year (half-way through the leaching phase), t = 1 year (end of leaching), and t = 2 years (one year after end of leaching). The results were obtained using the M-D law.

It is seen that during the leaching phase, the methods A and B are not able to capture the behavior of the stress deviator obtained using the moving boundary formulation. At the end of the leaching phase, the method B provides an acceptable approximation for the deviator, but the volume rate is still about twice larger than that obtained with the moving boundary solution. Soon after the leaching phase is completed, the method B provides an acceptable approximation for the volume loss rate as well (from 1.2 years after start of leaching, in this example). On the contrary, there is a notable difference between the solutions for the stress

deviator obtained with the method A and with the moving boundary method even after 2 years since the start of leaching. And it takes a longer time for the volume loss rate obtained with the method A to converge to the result of the moving boundary formulation.
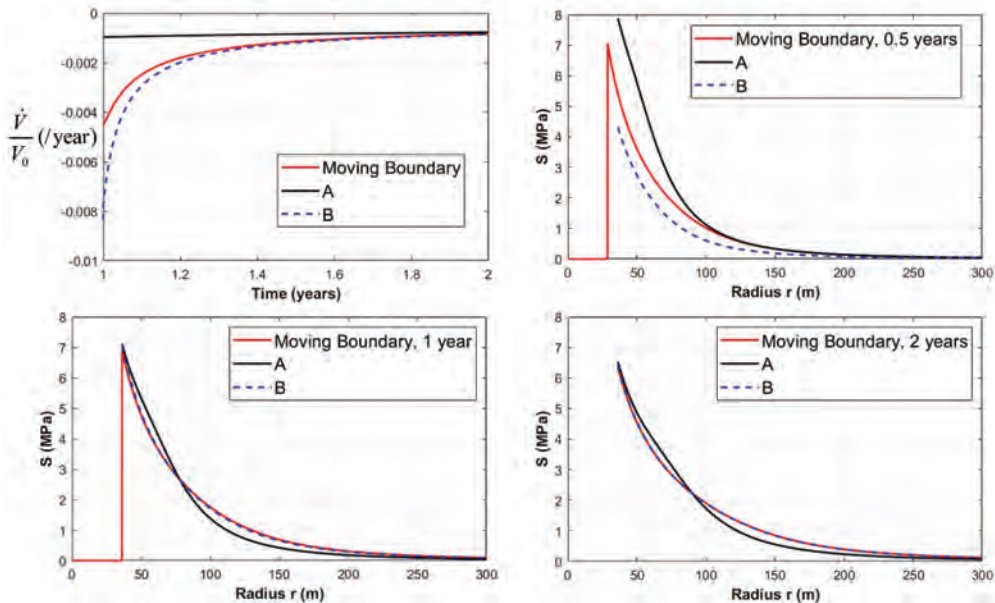
Figure 8. Top-left: Volume rate after leaching phase (x-axis shows time from start of leaching). Top-right: Deviator at 0.5 years after start of leaching. Bottom-left: Deviator at 1 year after start of leaching. Bottom-right: Deviator at 2 years after start of leaching.

5   Discussion

A simple numerical tool was used to assess stresses and displacements in a viscoplastic salt mass in which a spherical cavern submitted to a varying pressure was created. A couple of relatively unexpected results were obtained. Transient evolutions (both "direct" and "reverse") are observed even when the constitutive law (Norton-Hoff) includes no transient component. These transient evolutions are much longer in a cavern than observed during creep tests at the laboratory. After a swift cavern pressure increase, tensile effective stresses develop at cavern wall. In a pressure-cycled cavern, volume loss rate does not depend much on cycle period and the average volume loss rate is much faster when a M-D law (rather than a N-H law) is selected. When progressive cavern growth during leaching is taken into account, stress distribution and volume loss rate are significantly different from what is observed when a simplified model (a fixed geometry and a linear pressure decrease) is selected to describe cavern creation. This simplified model with the linear pressure decrease can provide an acceptable approximation for the volume loss rate only at some (relatively small) time after the leaching phase is completed.

References

BEREST, P., BROUARD, B., KARIMI-JAFARI, M. & VAN SAMBEEK, L. 2007. Transient behavior of salt caverns — Interpretation of mechanical integrity tests. Int. J. Rock Mech. Min. Sci. 44, 767–786

BROUARD, B. 1998. Sur le comportement des cavités salines, étude théorique et experimentation in situ, PhD Thesis, Ecole Polytechnique, Palaiseau, France.

HUGOUT, B. 1988. Mechanical behavior of salt cavities -in situ tests- model for calculating the cavity volume evolution. Hardy RH Jr & Langer M (eds). Proc. 2nd Conf. Mech. Beh. of Salt, Hannover. Trans Tech Pub., Clausthal-Zellerfeld, Germany, 291–310.

LESTRINGANT, C., BEREST, P. & BROUARD, B. 2010. Thermo-mechanical effects in compressed air storage (CAES). Proc. SMRI Fall Meeting, Leipzig, Germany, 29-44.

MANIVANNAN, S. & BEREST, P. 2019. Transient closure of a cylindrical hole in a salt formation considered as a Norton-Hoff medium. Rock Mech. Rock Eng.

MARKETOS, G., SPIERS, C.J. & GOVERS, R. 2016. Impact of rock salt creep law choice on subsidence calculations for hydrocarbon reservoirs overlain by evaporite caprocks. J. Geo. Res.: Solid Earth 121: 4249–4267.

MUNSON, D.E. & DAWSON, P.R. 1984. Salt constitutive modeling using mechanism maps. Proc. 1st Conf. Mech. Beh. of Salt, Penn State University, 717-737.

Appendix

A. Main Equations

The rate of a material point can be written $\underline{v}(r,t) = v(r,t)\,\underline{e}_r$. We introduce the "deviator" $S = \sigma_{rr} - \sigma_{\theta\theta}$. The constitutive law (A1), (A2), the equilibrium condition (A3), the boundary conditions and the initial condition (A4) can be written as follows:

$$\frac{\partial v}{\partial r} = \frac{\acute{\sigma}_{rr} - 2\bar{v}\acute{\sigma}_{\varphi\varphi}}{E} + (B + A|S|^{n-1})SF(S) \tag{A1}$$

$$\frac{v}{r} = \frac{(1-\bar{v})\acute{\sigma}_{\varphi\varphi} - \bar{v}\acute{\sigma}_{rr}}{E} - \frac{1}{2}(B + A|S|^{n-1})SF(S) \tag{A2}$$

$$\frac{r}{2}\frac{\partial \sigma_{rr}}{\partial r} + \sigma_{rr} - \sigma_{\varphi\varphi} = 0 \tag{A3}$$

$$\sigma_{rr}(a_0, t) = -P_c(t), \; \sigma_{rr}(b_0, t) = -P_\infty; \; \sigma_{rr}(r, -\infty) = \sigma_{\varphi\varphi}(r, -\infty) = \sigma_{\theta\theta}(r, -\infty) = -P_\infty \tag{A4}$$

$F = 1$, $B = 0$ corresponds to the N-H model, $F = 1$ to the M-S model, and $B = 0$ to the M-D model. F is defined by the following equations:

$$F(r,t) = exp\left[\Delta(|S(r,t)|)(1 - \frac{\zeta(r,t)}{\varepsilon_t^*(|S(r,t)|)})^2\right] \text{ when } \zeta(r,t) < \varepsilon_t^*(|S|);$$

$$F(r,t) = 1 \text{ when } \zeta(r,t) = \varepsilon_t^*(|S|);$$

$$F(r,t) = exp\left[-\delta(|S(r,t)|)(1 - \frac{\zeta(r,t)}{\varepsilon_t^*(|S(r,t)|)})^2\right] \text{ when } \zeta(r,t) > \varepsilon_t^*(|S|);$$

$$\dot{\zeta}(r,t) = A(F(r,t) - 1)|S(r,t)|^n; \quad \varepsilon_t^*(r,t) = K_0\, exp(cT_R)|S(r,t)|^m \quad \text{and}$$

$$\Delta(r,t) = \alpha_w + \beta_w\, log_{10}(|S|/\mu). \tag{A5}$$

From $\bar{v} = 0.5$ (elastic incompressibility), $v(r,t)/r = a_0^2\dot{a}(t)/r^3$ and (A2) can be rewritten:

$$\frac{a_0^2\dot{a}(t)}{r^3} = \frac{r}{4E}\frac{\partial^2 \sigma_{rr}(r,t)}{\partial r \partial t} - \frac{1}{2}(B + A|S(r,t)|^{n-1})F(r,t)S(r,t) \tag{A6}$$

Eq. (A6) can be divided by r and integrated with respect to r from $r = a_0$ to $r = b_0$. Taking into account $\partial \sigma_{rr}(a_0,t)/\partial t = -\dot{P}_c$, and $\partial \sigma_{rr}(b_0,t)/\partial t = 0$,

$$\frac{1}{3}\frac{\dot{a}(t)}{a_0}(1 - \gamma^3) = \frac{\dot{P}_c(t)}{4E} - \frac{1}{2}\int_{a_0}^{b_0}(B + A|S(v,t)|^{n-1})F(v,t)S(v,t)\frac{dv}{v} \tag{A7}$$

And when combining (A6) and (A7), an integrodifferential equation is obtained for $S = S(r,t)$:

$$\frac{\partial S(r,t)}{\partial t} = -E(B + A|S(r,t)|^{n-1})F(r,t)S(r,t)$$

$$-\frac{a_0^3}{r^3}\frac{3}{1-\gamma^3}(\frac{1}{2}\dot{P}_c(t) - E\int_{a_0}^{b_0}(B + A|S(v,t)|^{n-1})S(v,t)\,F(v,t)\frac{dv}{v}) \tag{A8}$$

The boundary condition results from the definition: $S(r,t) = -r\partial \sigma_{rr}(r,t)/\partial r/2$ or

$$\int_{a_0}^{b_0} 2S(v,t)\,dv/v = P_\infty - P_c \tag{A9}$$

However, (A8) implies $\int_a^b 2\partial S(v,t)/\partial t \ dv/v = -\dot{P}_c$ and it is sufficient that condition (A9) be satisfied at $t = 0$. Eqs. (A7) and (A8) (together with (A5) when M-D law is considered) allow computing the solution.

B. Equations for the Moving Boundary Problem

A spherical hollow cavern is considered whose external radius (fixed) is b_0, where a constant external pressure P_∞ (geostatic pressure) is applied. Its internal radius $\hat{x}(t)$ is a prescribed function of time. It varies from $\hat{x}(t = 0) = \hat{x}_0$ to $\hat{x}(t = t_1) = \hat{x}_1$ (end of solution mining). In most cases, $\hat{x}^2\dot{\hat{x}}(t)$ is constant (salt production rate is constant). For $t > t_1$, $\hat{x}(t)$ is constant, $\hat{x}(t > t_1) = \hat{x}_1$. The internal (varying) boundary, or $\hat{x}(t)$, is submitted to an internal pressure $P_c(t)$. In most cases, $P_c(t)$ experiences a jump at $t = 0$ from P_∞ to a constant figure P_c. When the jump is performed, $\hat{x}(t = 0) = \hat{x}_0$ is very small.

Eqs. (A1) to (A4) still hold except for the first equation in (A4) which must be written as:

$$\sigma_{rr}(\hat{x}(t)) = -P_c(t) \tag{B4}$$

From (A1) to (A3), $\frac{v(r,t)}{r} = \frac{b_0^2 \dot{b}(t)}{r^3}$, where $\dot{b}(t) = v(b_0, t)$ is the displacement rate at the cavern external wall. Eq. (2) can be rewritten (e.g. for M-D law):

$$\frac{b_0^2 \dot{b}(t)}{r^3} = \frac{r}{4E} \frac{\partial^2 \sigma_{rr}(r,t)}{\partial r \partial t} - \frac{1}{2} AS(r,t)|S(r,t)|^{n-1} F(r,t) \tag{B5}$$

Eq. (B5) can be divided by r and integrated with respect to r from $r = x$ to $r = b$. Taking into account $\partial \sigma_{rr}(b,t)/\partial t = 0$, and Eq. (B4):

$$d\sigma_{rr}(x,t)/dt = \partial \sigma_{rr}(x,t)/\partial t + \dot{\hat{x}} \partial \sigma_{rr}(x,t)/\partial r = \partial \sigma_{rr}(x,t)/\partial t - 2\dot{\hat{x}}S(x,t)/x = -\dot{P}_c,$$

$$\frac{1}{3} \frac{\dot{b}(t)}{b_0}\left(-1 + \frac{b_0^3}{x^3}\right) = \frac{\dot{P}_c(t) - 2S(x,t)\dot{\hat{x}}/x}{4E} - \frac{1}{2} A \int_x^{b_0} S|S|^{n-1} F \frac{dv}{v} \tag{B6}$$

And when combining Eqs. (B5) and (B6)

$$\left[-\frac{\partial S(r,t)}{\partial t} - EAS|S|^{n-1}F\right]\left(\frac{a_0^3}{x^3} - \gamma^3\right) = \frac{3a_0^3}{r^3}\left[\frac{\dot{P}_c(t) - 2S(x,t)\dot{x}/x}{2} - EA \int_x^{b_0} S|S|^{n-1} F \frac{dv}{v}\right] \tag{B7}$$

When $\dot{x} = 0$ and $x = a_0$, Eq. (B7) reduces to the case of Munson-Dawson law in (A8).

Single-cavern convergence for an Ellis 2-branch power-law model

Peter A. Fokker[1], Jaap N. Breunese[1]*

[1]TNO – Energy Transition, The Netherlands

* peter.fokker@tno.nl

ABSTRACT: The Ellis model for constitutive behavior, as implemented for rock salt, defines the displacement rate as the sum of a linear term and a power-law term with respect to the deviatoric stress. This combination represents a superposition of dislocation creep and solution-precipitation creep (pressure solution). The linear term constitutes a considerable contribution to the creep rate at small stresses. It must therefore be taken into account when salt cavern closure is considered, in particular at large distances from the cavern wall. In the present contribution we formulate an analytical solution for the quasi-steady-state cavern convergence in a 2D plane strain field. We have compared the outcome with numerical calculations with a Finite Element simulator, with good results. The calculations show that the increased strain rate / shear stress ratio at large distances from the cavern have a profound influence on the cavern squeeze rate, even while the strains and stresses in the cavern vicinity are dominated by the power-law creep branch of the constitutive model.

1   Introduction

The long-term behavior of salt caverns is an important issue now many of them are reaching the end of their operational life times (Bérest et al. 2001). Options for abandonment include pressure control at different levels, well plugging and uncontrolled pressure development, or cavern backfill with solid material. An evaluation of the options calls for an in-depth understanding of the constitutive behavior and the consequences on the long term.

Rock salt is traditionally described by power-law creep, as a proxy for dislocation creep (Li & Urai, 2016). This has proven adequate for many circumstances, including the operation of shallow to medium-depth salt caverns at pressures considerably lower than the virgin stresses. When the cavern pressure is increased, however, the differential stresses decrease and the large decrease of deformation rates predicted by the power-law creep correlations may underestimate the actual rates. While this has been observed in the laboratory for fine-grain-sized synthetic rock salt (Urai et al. 1986; Spiers et al. 1990), this has recently also been demonstrated on larger scales and longer times with natural salt (Bérest et al. 2019).

Pressure solution creep is expected to be the creep mechanism that prevails under low differential stress in natural salt (Spiers et al. 1990; Bérest et al. 2019). It encompasses a linear relationship between deformation rate and differential stress. In the Ellis model, pressure solution creep is combined with dislocation creep. It has been derived for the parallel operation of two creep mechanism by making a superposition of their respective contributions to the shear rate resulting from the same differential stress (Van Keken et al. 1993). The superposition allows a smooth transition from pressure-solution-controlled to dislocation-creep-controlled deformation as a function of the stress and is consistent with microphysical models for the parallel-concurrent operations of two or more independent deformation mechanisms (e.g. Spiers & Carter 1988; Frost & Ashby 1982).

The deviatoric stresses and deformation rates around a salt cavern decrease with increasing distance, simply because of the geometry. As a result, the dominant creep mechanism will also depend on the distance, even under quasi-steady-state conditions. In the present contribution we provide a plane-strain, axially symmetric solution for the mechanical behavior of an infinite salt body around a cylindrical salt cavern under quasi-steady-state conditions, with the Ellis model. The treatment followed is similar to the one by Cornet et al (2017) for the Carreau

model, but it is fully analytic. Application of the solution provides insight in the dependence of cavern squeeze rates on the pressure that is maintained in the cavern.

2   Theory

We want to solve the convergence rate for a salt cavern in which the pressure is smaller than the lithostatic stress. We follow an approach similar to the one by Cornet et al (2017), but employ the Ellis model rather than their Carreau model and we use the more precise formulation of Wang et al (2015).

We consider plane-strain conditions. Because of radial symmetry, the principal stresses are the radial, the tangential, and the vertical stress:

$$\boldsymbol{\sigma} = \begin{pmatrix} \sigma_{rr} & 0 & 0 \\ 0 & \sigma_{\theta\theta} & 0 \\ 0 & 0 & \sigma_{zz} \end{pmatrix} \tag{1}$$

We employ the negative compressive stress formulation. Then, we define the mean stress p, the deviatoric stress tensor s and its second invariant J_2, and for later convenience, the maximum horizontal shear stress τ. q corresponds to the Von Mises stress σ_{VM}. We also define the Von Mises strain rate $\dot{\epsilon}_{VM}$.

$$p = -\frac{1}{3}(\sigma_{rr} + \sigma_{\theta\theta} + \sigma_{zz})$$
$$s_{ij} = \sigma_{ij} + p\delta_{ij}$$
$$\boldsymbol{s} = \begin{pmatrix} \sigma_{rr} + p & 0 & 0 \\ 0 & \sigma_{\theta\theta} + p & 0 \\ 0 & 0 & \sigma_{zz} + p \end{pmatrix}$$
$$J_2 = \frac{1}{2}s_{ij}s_{ji} = \frac{1}{6}\{(\sigma_{rr} - \sigma_{\theta\theta})^2 + (\sigma_{\theta\theta} - \sigma_{zz})^2 + (\sigma_{zz} - \sigma_{rr})^2\} \tag{2}$$
$$\sigma_{VM} = q = \sqrt{3J_2} = \frac{1}{\sqrt{2}}\sqrt{(\sigma_{rr} - \sigma_{\theta\theta})^2 + (\sigma_{\theta\theta} - \sigma_{zz})^2 + (\sigma_{zz} - \sigma_{rr})^2}$$
$$\tau = \frac{1}{2}(\sigma_{rr} - \sigma_{\theta\theta})$$
$$\dot{\epsilon}_{VM} = \frac{1}{\sqrt{2}}\sqrt{(\epsilon_{rr} - \epsilon_{\theta\theta})^2 + (\epsilon_{\theta\theta} - \epsilon_{zz})^2 + (\epsilon_{zz} - \epsilon_{rr})^2}$$

The plane-strain condition implies that the strain rate depends only on the radial velocity and the vertical strain rate is zero.

$$\dot{\epsilon}_{rr} = \frac{\partial v_r}{\partial r}$$
$$\dot{\epsilon}_{\theta\theta} = \frac{v_r}{r} \tag{3}$$
$$\dot{\epsilon}_{zz} = 0$$

The usual assumption of incompressibility, leading to $\dot{\epsilon}_{rr} + \dot{\epsilon}_{\theta\theta} = 0$, allows to solve for the velocity and the strains as

$$v_r = v_R \frac{R}{r}$$
$$\dot{\epsilon}_{rr} = -\dot{\epsilon}_{\theta\theta} = -v_R \frac{R}{r^2}$$
$$\frac{\partial \dot{\epsilon}_{rr}}{\partial r} = 2v_R \frac{R}{r^3} = -\frac{2}{r}\dot{\epsilon}_{rr} \tag{4}$$
$$\dot{\epsilon}_{VM} = \sqrt{3}|\dot{\epsilon}_{rr}|$$

Here, v_R is a constant, signifying the velocity at the cavern boundary, where $r = R$.

We define the apparent viscosity μ_{app} through the relationship between deviatoric stress and strain rate in equilibrium conditions. We will employ a model in which the apparent viscosity only depends on the second stress invariant, q.

$$\dot{\epsilon}_{ij} = \frac{1}{\mu_{app}} s_{ij} \tag{5}$$

Inserting this into the incompressible-flow relationship yields $\dot{\epsilon}_{rr} + \dot{\epsilon}_{\theta\theta} = \frac{1}{\mu_{app}}(s_{rr} + s_{\theta\theta}) = \frac{1}{3\mu_{app}}(\sigma_{rr} - 2\sigma_{zz} + \sigma_{\theta\theta}) = 0$, which relates the vertical to the horizontal stresses and simplifies the stress invariants:

$$\begin{aligned}
\sigma_{zz} &= \tfrac{1}{2}(\sigma_{rr} + \sigma_{\theta\theta}) \\
J_2 &= \tfrac{1}{4}(\sigma_{rr} - \sigma_{\theta\theta})^2 = \tau^2 \\
p &= -\tfrac{1}{2}(\sigma_{rr} + \sigma_{\theta\theta}) \\
\tau &= \sigma_r + p \\
q &= \tfrac{1}{2}\sqrt{3}|\sigma_{rr} - \sigma_{\theta\theta}| = \sqrt{3}|\tau| \\
\mu_{app} &= \frac{\tau}{\dot{\epsilon}_{rr}}
\end{aligned} \tag{6}$$

Because of quasi-steady-state conditions, the equilibrium equation must be obeyed:

$$\frac{\partial \sigma_{rr}}{\partial r} + \frac{\sigma_{rr} - \sigma_{\theta\theta}}{r} = 0 \tag{7}$$

Substituting the expressions in terms of τ and p (Eqs. 2 and 6), the definition for the apparent viscosity (Eq. 4), and the expression for $\dot{\epsilon}_{rr}$ (Eq. 5) we obtain

$$\begin{aligned}
-\frac{\partial p}{\partial r} + \frac{\partial \tau}{\partial r} + \frac{2\tau}{r} &= 0 \\
-\frac{\partial p}{\partial r} + \frac{\partial \mu_{app}}{\partial r} \dot{\epsilon}_{rr} &= 0
\end{aligned} \tag{8}$$

This expression is still independent of the definition of the apparent viscosity.

In the Ellis model (Van Keken et al. 1993; Fokker 1995), the displacement rate is taken to be the sum of a power-law term and a linear term with respect to the deviatoric stress. Physically, this combination represents dislocation creep and solution-precipitation creep (pressure solution), respectively. This sum defines the apparent viscosity (using the notation of Urai et al. (2008))

$$\begin{aligned}
\dot{\epsilon}_{rr} &= \dot{\epsilon}_{DC} + \dot{\epsilon}_{PS} = Ae^{-\frac{Q_{DC}}{RT}} \cdot (2\tau)^n + \frac{B}{TD^m}e^{-\frac{Q_{PS}}{RT}} \cdot 2\tau = \alpha\tau^n + \beta\tau \\
\mu_{app} &= \frac{\tau}{\dot{\epsilon}_{rr}} = \frac{|\tau|}{\dot{\epsilon}_{VM}} = \frac{1}{\beta} \cdot \frac{\tau}{\tau + \gamma \cdot \tau^n} = \frac{1}{\beta + \alpha \cdot \tau^{n-1}} \\
\gamma &= \frac{\alpha}{\beta}
\end{aligned} \tag{9}$$

A and B are the creep strain rate coefficients [1/s], Q_{DC} and Q_{PS} are the activation energies in [J/mol], R is the gas constant (8.314 J/K/mol), T is the ambient temperature [K]; n is the stress exponent for the non-linear creep ($n > 1$). D^m denotes how the pressure solution depends on the grainsize D; the exponent m is 3 for pressure solution. α and β follow from the definition.

As a result, we calculate the second term in the rewritten equilibrium equation (Eq. 8), and this term turns out to have an analytic form:

$$
\begin{aligned}
\frac{\partial \mu_{app}}{\partial r} \dot{\epsilon}_{rr} &= -\mu_{app}^2 \frac{\partial}{\partial r} (\alpha \tau^{n-1}) \cdot \dot{\epsilon}_{rr} = (1-n)\mu_{app}^2 \alpha \tau^{n-2} \frac{\partial \tau}{\partial r} \cdot \frac{\tau}{\mu_{app}} \\
&= (1-n)\mu_{app}\alpha\tau^{n-1}\frac{\partial \tau}{\partial r} = (1-n)\frac{\gamma \cdot \tau^n}{\gamma \cdot \tau^n + \tau}\frac{\partial \tau}{\partial r} \\
&= (1-n) \cdot \frac{\partial}{\partial r} \int \frac{\gamma \cdot \tau^n}{\gamma \cdot \tau^n + \tau} d\tau \\
&= (1-n) \cdot \frac{\partial}{\partial r}\left\{\tau - \tau \cdot {}_2F_1\left(1, \frac{1}{n-1}; \frac{n}{n-1}; -\gamma \cdot \tau^{n-1}\right) + constant\right\}
\end{aligned}
\tag{10}
$$

The last step involves an integration, in which the symbol ${}_2F_1$ denotes the hypergeometric function (Abramowitz et al. 1988).

The formulation of the second term in the equilibrium equation (Eq. 8) as a derivative with regard to the radial coordinate enables its integration. Incorporating the boundary condition that at infinity $p = \bar{p}$ and $\tau = 0$, and using the definition of the stresses in a second step, we obtain:

$$
\begin{aligned}
p &= \bar{p} + (1-n) \cdot \tau \cdot \left\{1 - {}_2F_1\left(1, \frac{1}{n-1}; \frac{n}{n-1}; -\gamma \cdot \tau^{n-1}\right)\right\} \\
\sigma_r &= -p + \tau = -\bar{p} + \tau \cdot \left\{n - (n-1) \cdot {}_2F_1\left(1, \frac{1}{n-1}; \frac{n}{n-1}; -\gamma \cdot \tau^{n-1}\right)\right\}
\end{aligned}
\tag{11}
$$

This equation implies an analytical relationship between the mean stress p and the shear stress τ.

At the inner boundary, $\sigma_r = -p_w$. Therefore, we have

$$
\bar{p} - p_w = \tau_R \cdot \left\{n - (n-1) \cdot {}_2F_1\left(1, \frac{1}{n-1}; \frac{n}{n-1}; -\gamma \cdot \tau_R^{n-1}\right)\right\}
\tag{12}
$$

This equation must be solved for τ_R, which is the deviatoric stress at the cavern rim. That solution is independent of the cavern radius R. Therefore, the solution is not explicitly dependent on the cavern size and it can be scaled. The velocity at the rim is calculated as

$$
v_R = -R\dot{\epsilon}_R = -R\frac{\tau_R}{\mu_{app}} = -R(\alpha\tau_R^n + \beta\tau_R)
\tag{13}
$$

The convergence rate follows immediately:

$$
\frac{1}{V}\frac{dV}{dt} = \frac{2}{R}\frac{dR}{dt} = \frac{2}{R} v_R = -2(\alpha\tau_R^n + \beta\tau_R)
\tag{14}
$$

and the velocity in the full domain, and the strain rates result as

$$
\begin{aligned}
v_r &= v_R \frac{R}{r} = -\frac{R^2}{r}\frac{\tau_R}{\mu_{app}} = -\frac{R^2}{r}(\alpha\tau_R^n + \beta\tau_R) \\
\dot{\epsilon}_{rr} &= -\dot{\epsilon}_{\theta\theta} = \frac{R^2}{r^2}(\alpha\tau_R^n + \beta\tau_R)
\end{aligned}
\tag{15}
$$

The stresses must be determined by inverting the constitutive relationship (Eq. 9).

3   Setup of numerical calculations

We have cross-checked the analytical results with calculations with the Finite-Element code, DIANA (DIANA FEA 2019). The choice of the parameters has been inspired by the salt caverns in the Winschoten salt dome in the North of the Netherlands.
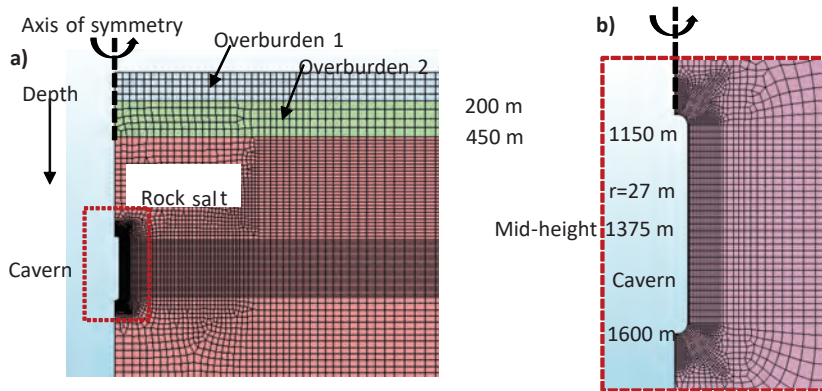
Figure 1: Finite-element mesh used for the cross-validation with the analytical model. Overburden layers are located between the surface and 450 m depth; below that is the salt layer in which the cavern reaches between 1150 and 1600 m depth

An axially symmetric geomechanical model around of a single cavern was constructed, with a model size of 3,000 by 15,000 m (depth and radius). The model boundaries were far enough away from the cavern to exclude boundary effects on the convergence rates. The model layers were meshed using quadratic second-order eight-node quadrilateral ring elements for better solution accuracy. Displacement boundary conditions were imposed to constrain displacements normal to the outer model edge and the model base. A 27-m radius, 450-m height cavern was constructed between 1150 and 1600 m depth, with a volume of about 1 million m^3. Two overburden layers were present to mimic the local geology. Figure 1 shows the geometry.

The material properties for the subsurface layers as used in the finite-element model are listed in Table 1. The salt properties are typical for Netherlands circumstances in the Zuidwending and Heiligerlee locations. The layers have uniform properties.

The material model for rock salt takes into account the quasi-steady-state creep driven by the differential stress, following Eq. 9, combining a power-law branch for the non-linear creep and a linear branch for the pressure solution creep.

Four sets of values were used for the quasi-steady-state creep, referred to as: (i) the non-linear creep variant (NLC); (ii) the low linear creep variant (LLC); (iii) the medium linear creep variant (MLC) and (iv) the high linear creep variant (HLC). The variant (i) is with the non-linear creep branch only, while the variants (ii, iii, iv) are a combination of the non-linear branch and the linear creep branch. The values for the LCC, MLC and HLC have been derived from KBB (2015), IfG (2016) and IfG (2006), respectively. The non-linear part of the equation is much better constrained by lab data, therefore we have chosen a deterministic best fit here, using data from Heiligerlee and Zuidwending (IfG, 2016). Properties of these sets are summarized in Table 2.

Table 1   Material properties used in the Finite-Element model

Layer	Density [kg/m^3]	Young's modulus [GPa]	Poisson ratio [-]	Initial stress ratio σ_h/σ_v [-]
Overburden 1	2050	1	0.25	0.7
Overburden 2	2050	25	0.25	0.7
Rock salt	2179	32	0.26	1.0
Under-burden	2500	25	0.20	0.7

Table 2   Salt creep property values for the 4 salt models. With these parameters, stresses are used in MPa. The temperature used is 317 K at mid cavern depth – ranging from 312 – 323 K from top to bottom.

Model	$A\left[\frac{1}{\text{day}}\right]$	$n\ [-]$	$\frac{Q_{DC}}{R}$ [K]	$\frac{B}{TD^m}\left[\frac{1}{\text{day}}\right]$	$\frac{Q_{PS}}{R}$ [K]
NLC	0.053	5	6495	-	-
LLC	0.053	5	6495	0.0005	3007
MLC	0.053	5	6495	0.003	3007
HLC	0.053	5	6495	0.015	3007

4   Results

To arrive at equilibrium conditions, the Finite-Element runs were started with an initialization of temperature and stress according to the given gradients. Then the cavern was put on halmostatic pressure for 5 years. After that, pressure levels of 56, 70, 80, 90 and 100% of the lithostatic pressure at the top of the cavern (24.33 MPa) were applied, and the simulation was carried on as long as to ensure quasi-steady-state was reached.

Figure 2 and Figure 3 represent results of the stress and strain rate fields versus distance. The Finite-Element calculations were taken at the center depth of the cavern. For the case with only non-linear creep (Figure 2) the agreement is poor. This is related to the very slow, geometrically induced creep (see also Wang et al. (2015) and Manivannan & Bérest 2019). For the Ellis model with medium linear creep parameters, the agreement between numerical and analytical results is excellent (Figure 3). This was also the case for the model with low and high linear creep parameters.
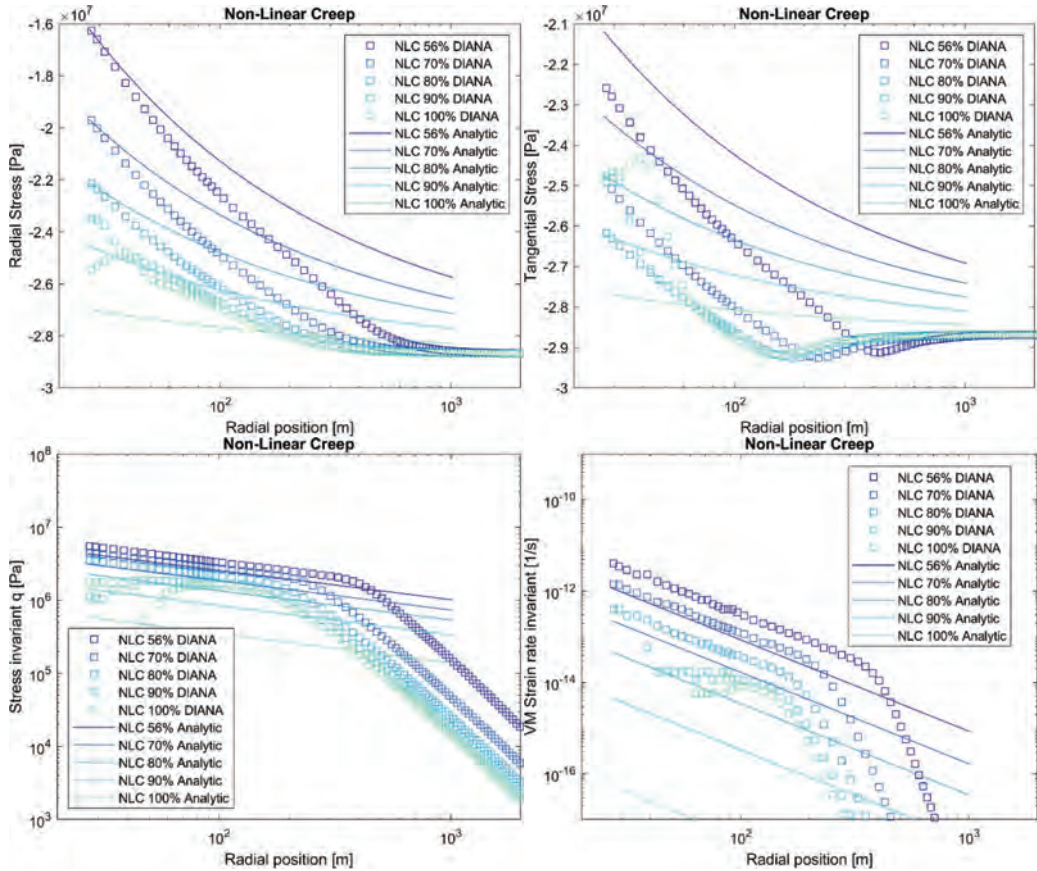
Figure 2: Benchmark results for the case with non-linear creep only. Figures denote the horizontal stresses (radial and tangential); deviatoric stress invariant and Von Mises strain rate invariant. Different colors denote the different cases for cavern pressure. The agreement is poor due to the very slow, geometrically induced creep.

The numerical simulations map a cavern in 3D, meaning that the stress and strain rate curves depend on the height position in the cavern. Thus, part of the mismatch between analytic and numerical results is explained by the fact that there are also vertical displacement rates in the numerical results. These partly compensate the horizontal ones, so the strain rate invariants agree (Figure 3 and Figure 4).

The analytic results also give the volumetric squeeze rate for the prevailing input parameters. To compare them with the numerical results we calculated them as a function of the depth, as both the temperature and the pressure difference are depth-dependent in the Finite-Element calculations. We integrated the results over the height of the cavern in the corresponding numerical simulations and derived in this way a total volumetric squeeze rate. A comparison with the numerical results is provided in Table 3. Again, the results for the power-law model do not agree, but the 80% agreement for the other models is good (given the plane-strain assumption).
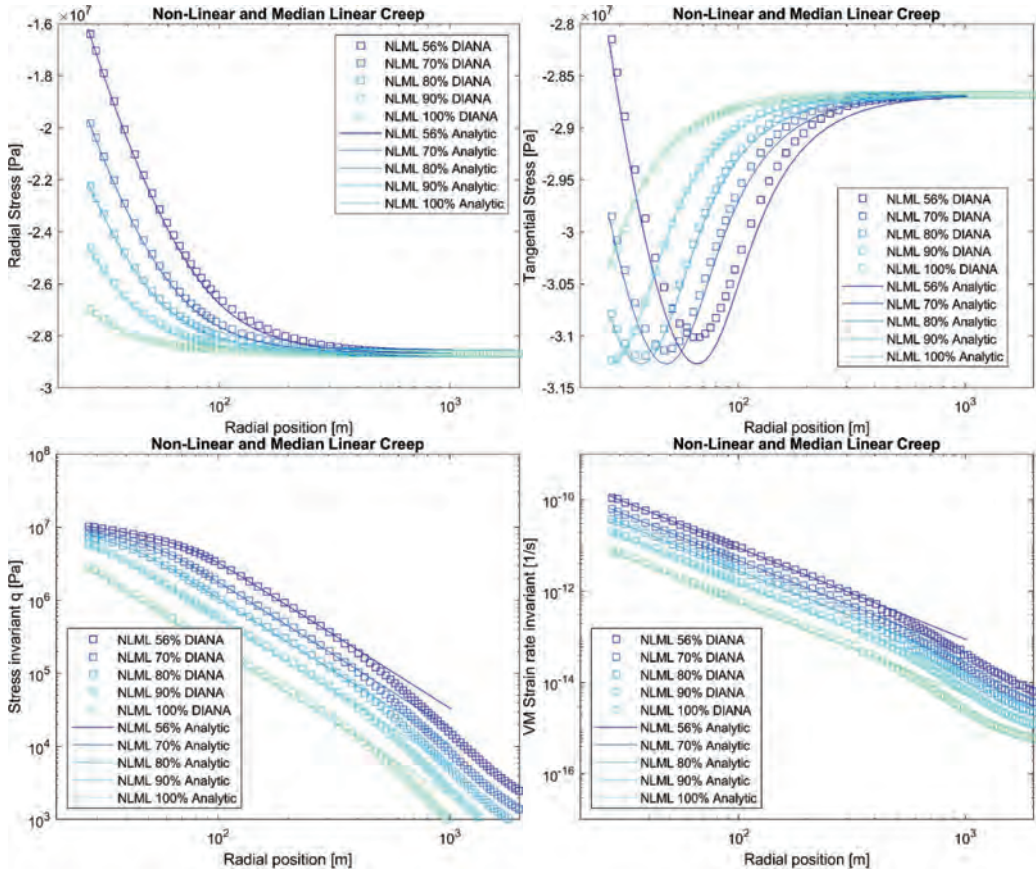
Figure 3: Benchmark results for case with non-linear and medium linear creep with the same coding as in Figure 2. The agreement is good for distances smaller than 500 m.
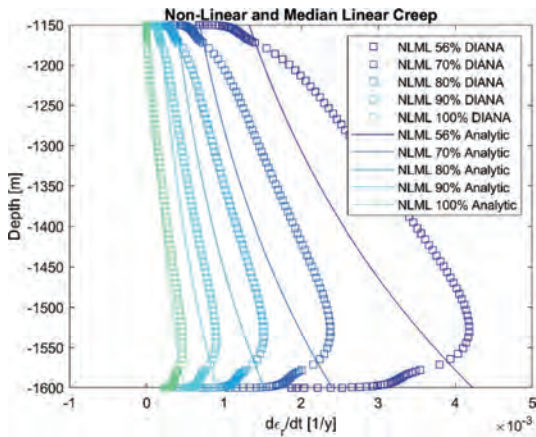
Figure 4: Horizontal strain rates versus depth for the Ellis model with medium linear creep parameters.

Table 3 Comparison of analytical and numerical volumetric squeeze rates for the benchmark cases. The cavern pressure is given as its ratio to the virgin lithostatic stress at the cavern top. Squeeze rates are given as percentage of the total cavern volume per year. The Ellis model employs the combination of non-linear creep and linear creep – results for 3 levels of the latter are represented here.

Model	Pressure / σ_{lith}	Numerical (%/yr)	Analytical (%/yr)
Power law	0.56 (halmostatic)	0.081	0.0063
	0.70	0.016	0.0015
	0.80	0.0033	0.00039
	0.90	0.0013	0.00007
Ellis / low-magnitude linear creep parameters	0.56 (halmostatic)	0.19	0.16
	0.70		0.075
	0.80		0.041
	0.90	0.019	0.020
Ellis / medium-magnitude linear creep parameters	0.56 (halmostatic)	0.63	0.50
	0.70	0.35	0.28
	0.80	0.21	0.17
	0.90	0.11	0.093
Ellis / high-magnitude linear creep parameters	0.56 (halmostatic)	2.1	1.7
	0.70		1.1
	0.80		0.70
	0.90	0.53	0.42

5 Discussion and Conclusions

The two risks to be considered when evaluating salt cavern behavior are the cavern stability and associated leakage risk, and the subsidence resulting from cavern convergence (Breunese et al. 2003).

The present formulation does not give surface movement estimates – it is fundamentally 2-dimensional with no vertical movements. A possible approach, however, is to rely on a nucleus-of-strain concept in which the long-range effect of the cavern convergence is approximated with the effect of two perpendicular horizontal double forces. Such an approach has been shown to give qualitatively similar surface movement signatures as obtained with 2D axially symmetric finite element modelling (Fokker & Osinga 2018).

The main focus of our present work is the behavior of the cavern. For this, the formulation of the analyticsolution for the cavern squeeze rate in a two-branch Ellis salt creep medium enables quick evaluation of dependencies on different parameters. The present study shows a large range of outcomes, spanning two orders of magnitude. The outcome depends on both the cavern pressure and the linear-creep parameters: with the three creep models, an increase of the pressure from 56% to 90% of the lithostatic stress results in a 4-8-fold decrease in squeeze rate. Therefore, only if the creep parameters are constrained better we can provide a trustworthy pressure guideline for cavern abandonment.

We have only considered pressures smaller than the in-situ stress. Larger pressures can develop if the pressure in the cavern is not controlled: the pressure gradient in the cavern, which is smaller than the stress gradient in the surrounding rocksalt, can cause convergence and at the deep cavern parts, and increase the pressure at the shallow parts above the in-situ stress. This is potentially unstable and clearly unwanted, because tensile stresses may cause hydraulic fracturing of the seal and leakage of brine. Further, we have only considered quasi-steady-state conditions. Caverns operating under low pressures cause considerable stress anisotropy around it. Increasing the pressure, even while not reaching the virgin stress, can cause transient stresses which are tensile. A recent large leak during mining operations in Veendam has been attributed to this mechanism (Fokker 2018).

The analysis presented considers infinitely extending layers. As such, the dome structures in which many salt caverns have been leached, are not taken into account. The finite lateral extent of the creeping salt body can be expected to reduce the long-term squeeze behavior, since the induced stresses in the surrounding elastic rock do not disappear. Also, the constitutive model that we employed might not be the complete truth. Care must be taken interpreting our results and extrapolating it to field phenomena. Numerical modelling and ongoing research on material behavior are indispensable for the improvement of the state of the art. The major insight, however, corroborates previous findings: linear creep profoundly influences the cavern squeeze rates and knowledge of its strength is crucial for making reliable estimates for the magnitude of its effect. The analytic formulation formulated here thus forms an important extension of the single-branch power-law-model solutions which were already available (Mahivannan & Bérest 2019). It is important in view of the limited attention that is given to these issues in the current body of literature on the subject.

References

ABRAMOWITZ, M., STEGUN, I. A. & ROMER, R. H., 1988. Handbook of mathematical functions with formulas, graphs, and mathematical tables.

BEREST, P., BERGUES, J., BROUARD, B., DURUP, J. G. & GUERBER, B. 2001. A salt cavern abandonment test. *International Journal of Rock Mechanics and Mining Sciences*, *38*(3), 357-368.

BÉREST, P., GHARBI, H., BROUARD, B., BRÜCKNER, D., DEVRIES, K., HÉVIN, G., ... & URAI, J. 2019. Very slow creep tests on salt samples. *Rock Mechanics and Rock Engineering*, *52*(9), 2917-2934.

BREUNESE, J.N., VAN EIJS, R.M.H.E., DE MEER, S. & KROON, I.C., 2003. Observation and prediction of the relation between salt creep and land subsidence in solution mining—The Barradeel case, paper presented at SMRI Conference, Chester

CORNET, J., DABROWSKI, M. & SCHMID, D.W., 2017. Long-term cavity closure in non-linear rocks. Geophysical Journal International, 210(2), 1231-1243. DIANA FEA, 2019 – last update, DIANA 10.3 User Manual.

DIANA 2019. Diana user's manual, Release 10.3, DIANA FEA BV.

IFG. 2006. Rock mechanical investigations on rock salt from cavern well BAS4. Report for ESCO / Frisia Zout BV (17-10-2006)

IFG. 2016. Rock Mechanical Modelling (incl. history and surrounding caverns) of the Nitrogen Storage Cavern HL-K at Heiligerlee, The Netherlands. Report for Gasunie (28-6-2016)

FOKKER, P. A., 1995. The behaviour of salt and salt caverns. PhD thesis, Delft University of Technology.

FOKKER, P. A., 2018. "Managing pressures in Nedmag caverns to prevent brine leakage during the mining and bleed-off phase and an evaluation of post abandonment cavern behaviour."

FOKKER, P. A.; OSINGA, S., 2018. On the use of influence functions for subsidence evaluation. In: *52nd US Rock Mechanics/Geomechanics Symposium*. OnePetro.

FROST, H. J., & ASHBY, M. F. 1982. *Deformation mechanism maps: the plasticity and creep of metals and ceramics*. Pergamon press.

KBB, 2015. Prediction of Subsidence above Caverns at Heiligerlee, The Netherlands Operation Phase Report on WP2: Applied Subsidence Model Report for Akzo-Nobel (31-8-2015)

LI, S.Y. & URAI, J. L. 2016. Rheology of rock salt for salt tectonics modeling. *Petroleum science*, 13.4: 712-724.

MANIVANNAN, S. & BÉREST, P., 2019. Transient Closure of a Cylindrical Hole in a Salt Formation Considered as a Norton–Hoff Medium. *Rock Mechanics and Rock Engineering*, 52.8: 2701-2707.

SPIERS, C. J., SCHUTJENS, P. M. T. M., BRZESOWSKY, R. H., PEACH, C. J., LIEZENBERG, J. L. & ZWART, H. J. 1990. Experimental determination of constitutive parameters governing creep of rocksalt by pressure solution. *Geological Society, London, Special Publications*, *54*(1), 215-227.

SPIERS, C. J. & CARTER, N. L. 1998. Microphysics of rocksalt flow in nature. In: Aubertin, M., and Hardy, H.R. (eds.): The mechanical behavior of salt, proceedings of the 4th conference, Trans Tech. Publ. Series on Rock and Soil Mechanics, 22, 115-128.

URAI, J. L., SPIERS, C. J., ZWART, H. J. & LISTER, G. S. 1986. Weakening of rock salt by water during long-term creep. *Nature*, *324*(6097), 554-557.

URAI, J. L., SCHLÉDER, Z., SPIERS, C. J. & KUKLA, P. A. 2008. Flow and transport properties of salt rocks. *Dynamics of complex intracontinental basins: The central European basin system*, 277-290.

VAN KEKEN, P. E., SPIERS, C. J., VAN DEN BERG, A. P. & MUYZERT, E. J. 1993. The effective viscosity of rocksalt: implementation of steady-state creep laws in numerical models of salt diapirism. *Tectonophysics*, *225*(4), 457-476.

WANG, L., BÉREST, P. & BROUARD, B., 2015. Mechanical behavior of salt caverns: Closed-form solutions vs numerical computations. Rock Mech. Rock Eng. 48: 2369-2382.

Modeling the behavior of underground structures in a rock salt formation: a coupled Finite Element approach

T.A. Bui [1], G. Cammarata [2], V.C. Kancharla[1], S. Brasile[1]*

[1]*Plaxis B.V., a Bentley Systems company, The Netherlands;* [2]*Bentley Systems Italia S.r.l., Italy*

* *tuan.bui@bentley.com*

ABSTRACT: The behavior of underground structures related to salt strata usually concerns different time scales, both short-term and long-term, during their life cycle. The main factors influencing this behavior include transient boundary conditions and different physics involved (deformation, groundwater flow, thermal effects) as well as nonlinear rock constitutive responses. Finite Element (FE) analysis is a standard and useful tool for considering the aforementioned factors in a unified framework, including time-dependency and multi-physics coupling. In this paper, a fully coupled FE formulation, implemented in the PLAXIS FE package, is presented. Rock time-dependent behavior is modeled by a double power viscoplastic law whereas plastic failure is modeled by Mohr-Coulomb and Hoek-Brown constitutive laws. An implicit integration scheme combined with an automatic adaptive sub-stepping strategy allows reducing computation time while ensuring numerical stability and accuracy. Some numerical examples are performed to demonstrate the efficiency and accuracy of the numerical implementation by analyzing obtained simulation results and comparing them against analytical solution, as well as available measurements and numerical data.

1   Introduction

Modeling the behavior of underground structures in rock formations such as geological storages, waste isolation facilities, etc., is a crucial but challenging task in rock mechanics (Jaeger et al. 2007). On the one hand, most of these applications concern different time scales, including both short-term construction phases (months to years) and long operation and post-closure periods (tens to thousands of years or even longer). On the other hand, the behavior of these structures usually involves high complexities due to time-dependent boundary conditions, complex couplings between different physics (deformation, groundwater flow, thermal effects) as well as nonlinear rock constitutive responses. For the latter, in the case of rock salt, further challenges are expected as both the short and long-term behaviors exhibit nonlinear irreversible responses (Khaledi 2017).

The Finite Element (FE) method becomes a powerful tool to overcome the above challenges and provide reliable analysis and design. This method, formulated on the basis of continuum mechanics, proves to be efficient for large-scale applications as it provides a very good compromise between computational cost and accuracy. However, effective numerical strategies should be implemented both at the global discretization level and material point level to ensure not only the accuracy but also the robustness of the numerical solution.

This paper presents a coupled Thermo-Hydro-Mechanical (THM) formulation implemented in the PLAXIS FE package to address the above-mentioned issues. Such fully coupled scheme proves to be the most realistic for multiphysics simulation, as coupling terms are incorporated in a rigorous way without making any simplifying assumptions. Implicit global integration is employed to allow large global time steps which are convenient for long-term simulations. At material level, constitutive behavior for rock salt is modeled by a viscoplastic double power steady-state creep law in combination with Mohr-Coulomb and Hoek-Brown plastic models. This setup allows describing both the short and long-term rock behaviors. An implicit stress integration along with an adaptive sub-stepping scheme are implemented to ensure numerical stability and accuracy requirements while optimizing computational cost. The efficiency and

accuracy of the implementation are demonstrated by analyzing obtained simulation results and comparing them against available measurements/numerical data.

2 Fully coupled Finite Element framework

PLAXIS FE solver considers a geomaterial as a *3-phases* (solid/liquid/gas) porous medium, as well as the phase change mechanisms (solidification, evaporation) of different species (Bui et al. 2019). In the following, only the principal equations for saturated media usually encountered in rock salt applications are briefly revised. For more details of the general theoretical equations, readers may refer to (Plaxis 2015). As a convention, vectorial and tensorial quantities are denoted in bold, while scalars are in normal character.

2.1 Fundamental balance and constitutive equations

The mass balance equation of the liquid phase writes:

$$\nabla \cdot (\boldsymbol{J_w}) + F_w^{st} = 0; \qquad F_w^{st} = \frac{\partial}{\partial t}(\rho_w) + (\rho_w)\left[\frac{\partial \varepsilon_v}{\partial t} + \frac{1-n}{\rho_s}\frac{\partial \rho_s}{\partial t}\right] \qquad (1)$$

with F_w^{st} the storage term, n the porosity, ε_v the medium volumetric strain and ρ_s, ρ_w the solid and liquid densities, respectively. $\nabla \cdot$, ∇ and $\partial/\partial t$ denote divergence, gradient, and time partial derivative operators, respectively. The liquid mass flux $\boldsymbol{J_w}$ is governed by Darcy's law:

$$\boldsymbol{J_w} = \rho_w(T)\frac{\boldsymbol{K}}{\mu(T)}(\nabla p_w + \rho_w(T)\boldsymbol{g}) \qquad (2)$$

where $\boldsymbol{K}$ is the permeability tensor, μ the dynamic viscosity depending on the temperature T, p_w is the liquid pore pressure while $\boldsymbol{g}$ is the gravity acceleration vector.

The linear momentum balance of the whole porous medium is given by:

$$\nabla \cdot \boldsymbol{\sigma} + \rho \boldsymbol{g} = \boldsymbol{0} \qquad (3)$$

with $\boldsymbol{\sigma}$ the total Cauchy stress tensor and $\rho = (1-n)\rho_s + n\rho_w$ the density of the porous rock.

The energy balance equation for the porous medium can be written as follows:

$$\nabla \cdot (\boldsymbol{J_{Aw}} + \boldsymbol{J_c}) + Q_T + F_T^{st} = 0; \quad F_T^{st} = \rho C_T \frac{\partial T}{\partial t} \qquad (4)$$

where F_T^{st} is the storage term, C_T the rock specific heat capacity with $\rho C_T = (1-n)\rho_s C_s + n\rho_w C_w$ and Q_T the heat source term. The conductive heat flux $\boldsymbol{J_c}$ is governed by Fourier's law:

$$\boldsymbol{J_c} = -\lambda \nabla T \qquad (5)$$

where $\lambda = (1-n)\lambda_s + n\lambda_w$ is the rock thermal conductivity, with λ_s and λ_w the solid and liquid conductivities, respectively. If liquid flow is present, the advective heat flux $\boldsymbol{J_{Aw}}$ is modeled by:

$$\boldsymbol{J_{Aw}} = C_w T \boldsymbol{J_w} \qquad (6)$$

2.2 Discretization

The above equations constitute a coupled system of partial differential equations. For spatial discretization, a standard Galerkin's approach is used. As already mentioned, a coupled numerical scheme is used, meaning that all the degrees of freedom (displacements, pore pressures, and temperatures) are solved simultaneously in the same calculation step. This

scheme, although complex, proves to be the most realistic as no coupling terms are neglected during numerical solving. Triangular elements, either 6-noded (quadratic) or 15-noded (fourth order), are used.

For time discretization, it is well known that any numerical integration scheme should ensure both stability and accuracy conditions (Simo & Hughes 1997. In an explicit integration scheme, the stability condition (boundness of solutions) often requires a very strict time step compared to the accuracy condition, leading to excessive computational costs. Therefore, a global fully implicit scheme is implemented (Plaxis 2015) to ensure unconditional stability, thereby allowing the use of larger time steps subject only to accuracy requirements.

3 Rock constitutive modeling framework

3.1 Constitutive equations

Deformation is assumed to be governed by an effective stress tensor based on poroelasticity:

$$\boldsymbol{\sigma}' = \boldsymbol{\sigma} - \alpha_{Biot} p_w \boldsymbol{\delta} \tag{7}$$

with $\boldsymbol{\delta}$ the second-order identity tensor. The Biot's coefficient is defined as $\alpha_{Biot} = 1 - K'/K_s$ (Coussy et al. 1998), where K_s is the bulk modulus of the solid phase and K' the drained bulk modulus of porous rock.

The rock is modelled as an isotropic thermo-elasto-plastic-viscoplastic material of which the total strain rate is decomposed into an elastic part $\dot{\boldsymbol{\varepsilon}}^e$, a thermal part $\dot{\boldsymbol{\varepsilon}}^{th}$, a viscoplastic creep part $\dot{\boldsymbol{\varepsilon}}^{vp}$ and an instantaneous plastic part $\dot{\boldsymbol{\varepsilon}}^p$, i.e.

$$\dot{\boldsymbol{\varepsilon}} = \dot{\boldsymbol{\varepsilon}}^e + \dot{\boldsymbol{\varepsilon}}^{th} + \dot{\boldsymbol{\varepsilon}}^{vp} + \dot{\boldsymbol{\varepsilon}}^p \tag{8}$$

The following describes the definition of each of these strain components.

3.1.1 Thermo-Elastic strains

The elastic strains obey the classic isotropic linear elastic Hooke's law, i.e.

$$\dot{\boldsymbol{\varepsilon}}^e = \mathbb{D}^{-1} : \boldsymbol{\sigma}'; \quad \dot{\epsilon}_v^e = \frac{1}{K'} \dot{\sigma}'_m; \quad \dot{\boldsymbol{\varepsilon}}_d^e = \frac{1}{2G} \dot{\boldsymbol{s}}; \quad K' = \frac{2(1+\nu)G}{3(1-2\nu)} \tag{9}$$

where $\mathbb{D}$ is the elastic stiffness tensor, G the shear modulus and ν the Poisson's ratio. ϵ_v^e is the volumetric elastic strain, $\boldsymbol{e}_d^e$ the deviatoric elastic strain tensor, σ_m the mean effective stress and $\boldsymbol{s}$ the deviatoric stress tensor. The thermal strain rate is calculated by:

$$\dot{\boldsymbol{\varepsilon}}^{th} = \boldsymbol{\alpha}_T \dot{T} \tag{10}$$

where $\boldsymbol{\alpha}_T$ is the thermal expansion second-order tensor. Note that if isotropic thermal expansion is assumed, $\boldsymbol{\alpha}_T = \alpha_T \boldsymbol{\delta}$ with α_T the linear thermal expansion coefficient.

3.1.2 Viscoplastic strains: Double Power Creep law

In the present model, only steady-state creep strain is considered. This is relatively reasonable considering the large time scale in underground engineering applications (Gunther et al. 2015). The *double power creep* law, a generalized version of the widely used Norton's law (see Fokker 1994), is adopted, i.e.:

$$\dot{\boldsymbol{\varepsilon}}^{vp} = |\dot{\varepsilon}^{vp}| \frac{3\boldsymbol{s}}{2q}; \qquad |\dot{\varepsilon}^{vp}| = A_1^* \left(\frac{q}{q_0}\right)^{N_1} + A_2^* \left(\frac{q}{q_0}\right)^{N_2} \tag{11}$$

where $q = \sqrt{(3/2)\boldsymbol{s}:\boldsymbol{s}}$ is the von Mises shear stress, $|\dot{\varepsilon}^{vp}|$ is the creep strain rate intensity, q_0 is a unit reference stress to render the stress term dimensionless whereas N_1 and N_2 are stress exponent parameters. A_1^* and A_2^* are viscosity parameters depending on the absolute temperature T and are defined as:

$$A_1^* = A_1 e^{\left(-\frac{Q_1}{R}\frac{1}{T}\right)}; \quad A_2^* = A_2 e^{\left(-\frac{Q_2}{R}\frac{1}{T}\right)} \tag{12}$$

in which A_1 and A_2 are two reference viscosity parameters, $R = 8.314\, J.mol^{-1}K^{-1}$ is the universal gas constant, whereas Q_1 and Q_2 are two creep activation energy parameters.

Despite its simplicity, this model allows describing the fundamental features of rock salt steady-state creep behavior, especially the two different responses at different applied stress levels (Gunther et al. 2015). This can be related to the pressure-solution mechanism at low stress and the dislocation mechanism at higher stress (Fokker 1994; Breunese et al. 2003).

3.1.3 Rate-independent plastic strains: Mohr-Coulomb and Hoek-Brown models

The rate-independent plastic strain rate is computed based on the standard plasticity theory with a plastic flow rule and a yield function f satisfying Kuhn-Tucker's conditions:

$$\dot{\boldsymbol{\varepsilon}}^{p} = \lambda \frac{\partial g}{\partial \boldsymbol{\sigma}} \tag{13}$$

$$f\dot{\lambda} = 0, \dot{\lambda} \geq 0, f \leq 0 \tag{14}$$

where g is the plastic potential while λ represents the plastic multiplier.

In this work, two failure criteria widely used in rock engineering are considered: the Mohr-Coulomb (MC) and the Hoek-Brown (HB) model. For the MC model, yield (shear f_{ij}^{MC} and tension surfaces f_{ij}^T) and plastic potential functions are described as follows (Plaxis, 2021):

$$f = f_{ij}^{MC} = \frac{1}{2}(\sigma'_i - \sigma'_j) + \frac{1}{2}(\sigma'_i + \sigma'_j)\sin\phi - c\cos\phi; \tag{15}$$

$$g = g_{ij}^{MC} = \frac{1}{2}(\sigma'_i - \sigma'_j) + \frac{1}{2}(\sigma'_i + \sigma'_j)\sin\psi \tag{16}$$

$$f_i^T = g_i^T = \sigma'_i - \sigma_T; \tag{17}$$

with $i,j = \{1,2,3\}$ and $i \neq j$. Note that σ'_i denotes the i-th principal stress component while c, ϕ, ψ and σ_T are the cohesion, friction angle, dilation angle, and tensile strength, respectively.

For the HB model, the yield and plastic potential functions can be written as:

$$f = f_{13}^{HB} = (\sigma'_1 - \sigma'_3) + |\sigma_{ci}| \left(-m_b \frac{\sigma'_3}{|\sigma_{ci}|} + s\right)^a \tag{18}$$

$$g = g_{13}^{HB} = \left(\frac{-\sigma'_1}{m_b|\sigma_{ci}|} + \frac{s}{m_b^2}\right) - \frac{1+\sin\psi_m}{1-\sin\psi_m}\left(\frac{-\sigma'_3}{m_b|\sigma_{ci}|} + \frac{s}{m_b^2}\right) \tag{19}$$

$$f = f_{12}^{HB} = (\sigma'_1 - \sigma'_2) + |\sigma_{ci}| \left(-m_b \frac{\sigma'_2}{|\sigma_{ci}|} + s\right)^a \tag{20}$$

$$g = g_{12}^{HB} = \left(\frac{-\sigma'_1}{m_b|\sigma_{ci}|} + \frac{s}{m_b^2} \right) - \frac{1+\sin\psi_m}{1-\sin\psi_m} \left(\frac{-\sigma'_2}{m_b|\sigma_{ci}|} + \frac{s}{m_b^2} \right) \tag{21}$$

In the above equations, m_b, a and s are three HB parameters and $|\sigma_{ci}|$ is the uniaxial compressive strength of intact rock. The mobilized dilatancy angle ψ_m is assumed to be linearly decreasing in the compressive zone from its maximum value ψ_{max} (at zero confinement) and vanishing when confinement is higher than a parameter σ_ψ, and, on the other hand, linearly increasing in the tensile zone (limited by the tensile strength σ_t) as follows:

$$\psi_m = \begin{cases} 0, & -\sigma'_3 \leq \sigma_\psi \\ \dfrac{\sigma_\psi + \sigma'_3}{\sigma_\psi}\psi_{max}, & 0 \geq -\sigma'_3 \geq \sigma_\psi \\ \psi_{max} + \dfrac{\sigma'_3}{\sigma_t}(90° - \psi_{max}), & \sigma_t \geq \sigma'_3 \geq 0 \end{cases} \tag{22}$$

3.2 Model implementation

In this paper, the constitutive models are implemented as user-defined models using a user-defined Application Programming Interface (API) allowing the exchange of information with the calculation engine. Knowing all the stresses at time "n", as well as the time increment Δt_{n+1}, total strain increment $\Delta \boldsymbol{\varepsilon}_{n+1}$, and temperature increment ΔT_{n+1}, the effective stress $\boldsymbol{\sigma}'_{n+1}$ needs to be updated based on the relationship between elastic strains and effective stresses:

$$\boldsymbol{\sigma}'_{n+1} = \boldsymbol{\sigma}'_n + \mathbb{D} : \left[\Delta \boldsymbol{\varepsilon}_{n+1} - \Delta \boldsymbol{\varepsilon}_{n+1}^T - \Delta \boldsymbol{\varepsilon}_{n+1}^{vp} - \Delta \boldsymbol{\varepsilon}_{n+1}^{pl} \right] \tag{23}$$

where $\Delta \boldsymbol{\varepsilon}_{n+1}^T$, $\Delta \boldsymbol{\varepsilon}_{n+1}^{vp}$ and $\Delta \boldsymbol{\varepsilon}_{n+1}^{pl}$ are the thermal expansion strain, creep strain, and plastic strain increment, respectively. To solve $\boldsymbol{\sigma}'_{n+1}$, the viscoplastic and plastic strain increments should be integrated from their rate forms described in Section 3.1. As said earlier, fully implicit integration, which is unconditionally stable, is chosen. This produces:

$$\Delta \boldsymbol{\varepsilon}_{n+1}^{vp} = \int \dot{\boldsymbol{\varepsilon}}^{vp} dt = \dot{\boldsymbol{\varepsilon}}_{n+1}^{vp}(\boldsymbol{\sigma}'_{n+1})\Delta t_{n+1} \tag{24}$$

$$\Delta \boldsymbol{\varepsilon}_{n+1}^{pl} = \int d\boldsymbol{\varepsilon}^p = \int d\lambda \frac{\partial G}{\partial \boldsymbol{\sigma}} = \left(\frac{\partial G}{\partial \boldsymbol{\sigma}} \right)_{n+1} \Delta \lambda_{n+1} \tag{25}$$

Equations (23)-(25), together with (14) form a nonlinear system of equations of $\Delta \lambda_{n+1}$ and $\boldsymbol{\sigma}'_{n+1}$ which should be solved iteratively to determine the updated stresses. However, this rigorous procedure is challenging because viscoplasticity is coupled with plastic return mapping, with the latter presenting singularities due to sharp edges in the potential surfaces (Sloan & Booker, 1986). For this reason, a simplified procedure is adopted here where viscoplastic return mapping in Cartesian stress space is done first to obtain a viscoplastic predictor before plastic return mapping is performed in principal stress space using the strategy proposed by (De Borst 1987).

The above implicit scheme presents a great advantage for large-scale applications as large time steps can be used without affecting numerical stability, which is often much more restrictive than an accuracy criterion. For the latter, it is straightforward to prove that the above implicit scheme is first-order accurate, i.e., the viscoplastic strain error is $O(h^2)$, with h the step size. To ensure stability condition, an adaptive substepping procedure is implemented, based on the method proposed by (Mahnken & Stein 1989). The local truncation error corresponding to a global step size h is estimated by comparing the creep strain solution using the full step size with that using two equal half steps of size $h/2$. This helps to estimate the needed number of substeps to fulfil a certain expected accuracy. This algorithm allows adjusting the

substepping depending on the creep level, thus allowing the less creeping material points to be integrated with larger time steps without affecting global accuracy.

4 Numerical examples

In the following, some numerical examples are presented to verify and validate the numerical scheme as well as illustrate the robustness and accuracy of the implementation. In the first two applications (Sections 4.1 and 4.2), we consider the same non-porous rock salt of which the creep parameters are taken from Asse salt (Gunther et al. 2015) while other typical parameters such as elastic, thermal, and density are inspired by (Bottcher et al. 2017) and (Zhu et al. 2017, see Table 1). The MC and HB parameters are calibrated based on another rock salt (Ma, et al., 2013) (see Table 2).

Table 1: Rock salt elastic, creep, and other parameters

G	v	N_1	A_1	N_2	A_2	Q_1/R	Q_2/R	ρ	c_s	λ_S	α_T
8.846 GPa	0.3	6.8	0.02 day^{-1}	2.7	0.05 day^{-1}	7800 K	4800 K	2040 kG/m^3	858.6 kJ/t/°C	5.4 W/m/K	2.8 10^{-5} 1/K

Table 2: Rock salt plastic parameters

c	ϕ	ψ	σ_T	$|\sigma_{ci}|$	m_b	s	a	ψ_{max}	σ_ψ
3.67 MPa	39.6°	20°	1 MPa	22 MPa	25.74	1	0.37	25°	10 MPa

4.1 Isothermal uniaxial relaxation test

For an isothermal uniaxial relaxation test configuration, combining *(8)* and *(9)* yields:

$$\dot{\sigma}_1' = -\dot{q} = E\left(\dot{\varepsilon}_1 - \dot{\varepsilon}_1^{vp} - \dot{\varepsilon}_1^{pl}\right) \tag{26}$$

where $E = 2G(1 + v)$ is the Young's modulus and "1" indicates the loading axis.

The sample is first subject to a fast loading ε_1^{ini} (so that creep is negligible) leading to an initial stress $q^{ini} = -\sigma_1^{ini}$ which can be easily solved using Eq. *(26)* and Eqs. *(15)-(19)* depending on whether MC or HB failure occurs. The solutions are summarized in Table 3.

Table 3: Closed-form solutions for instantaneous loading in uniaxial test

Elastic solution	MC solution	HB solution
$q^{ini} = -E\varepsilon_1^{ini}$	$q^{ini} = \dfrac{2\,c\cos\phi}{1 - \sin\phi}$	$q^{ini} = |\sigma_{ci}|\,s^a$

After the loading phase, ε_1 is kept constant and stress relaxes. Thus, it is expected that plastic strain is not generated during (unloading) relaxation and using Eq. *(11)*, Eq. *(26)* writes:

$$\dot{q} + E\left[\left(\frac{A_1^*}{q_0^{N_1}}\right)q^{N_1} + \left(\frac{A_2^*}{q_0^{N_2}}\right)q^{N_2}\right] = 0 \tag{27}$$

In the case $N_2 = 1$ (pressure solution creep), this nonlinear ordinary differential equation can be solved using some classic techniques (see e.g. Polyanin & Zaitsev 2017), obtaining:

$$\sigma_1 = -q = -\left[\left[\left(q^{ini}\right)^{1-N_1} + \frac{A_1^*}{A_2^*}q_0^{1-N_1}\right]e^{-\frac{(1-N_1)EA_2^*t}{q_0}} - \frac{A_1^*}{A_2^*}q_0^{1-N_1}\right]^{\frac{1}{1-N_1}} \quad (28)$$
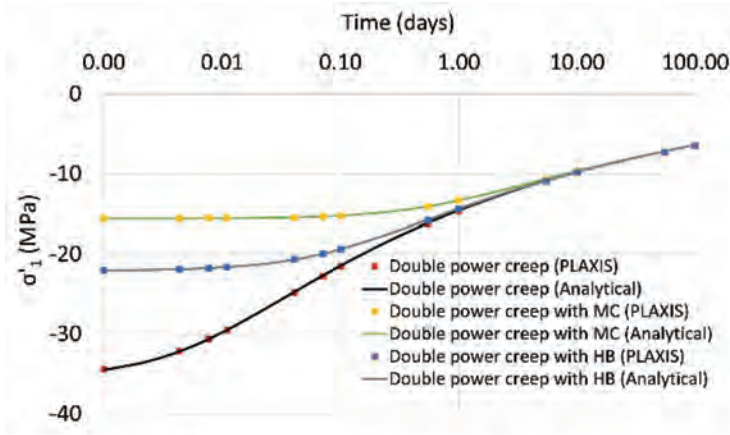
Figure 1: Analytical and numerical simulations of uniaxial relaxation tests

In this example, simulations are performed for the case where $\varepsilon_1^{ini} = 0.15\%$ and the relaxation phase lasts 100 days at a temperature of 60°C. Rock Salt parameters reported in Table 1,2 are used, except for N_2 which is set to 1 to be able to compare with the closed-form solution *(28)*. There is a very good agreement between analytical and numerical results, reporting both instantaneous and relaxation stress results (Fig. 1). It is observed that the adoption of plastic failure mechanisms provide realistic instantaneous stress value, consistently leading to a lower relaxation rate of the relaxation phase"using plastic failure mechanisms limits realistically instantaneous stress value, leading accordingly to a lower relaxation rate of the relaxation phase. Notice that the computation takes less than 3 seconds (laptop assembling and Intel Core i7-8850H CPU @2.60GHz with 6 physical cores and 32 GB of RAM) with only a small number of time steps (10 steps) is needed, illustrating the accuracy and robustness of the implementation, especially the adaptive substepping scheme.

4.2   Salt cavern during its operational life-cycle

A typical gas cavern is modelled throughout its seasonal exploitations. Due to an assumed symmetric geometry, an axisymmetric 2D model is built. The model is extended far enough from the cavern (500m x 500m) to avoid boundary effects (Fig 2a, b). Rock parameters are the ones reported in Table 1,2. Initial lithostatic stresses are initialized with $K_0=1.2$, consistent with the depth range (from 800 to 1300m) in the present study (Brown & Hoek 1978).
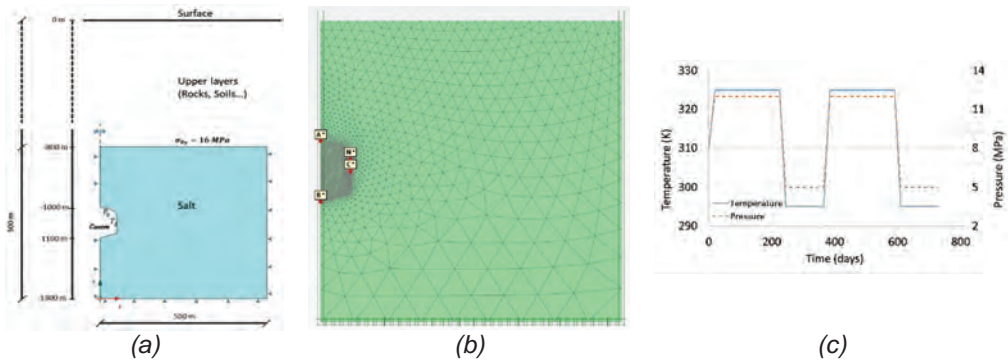
Figure 2: (a) Cavern geometry, (b) Model mesh, (c) Boundary conditions at cavern wall

In this example, solution mining is not modelled but only represented by an initial stress state. Instead, the focus is on typical yearly operational life cycles (Bottcher et al. 2017; Berest 2011), including gas injection (pressurization with heating), gas storing (at maximum pressure and temperature), gas withdrawing (depressurization with cooling), and idling phase (gas stored at minimum pressure and temperature). Instead of modelling complex gas thermodynamic behavior, temperatures and pressures are applied at the cavern wall as simplified boundary conditions, inspired by (Serbin et al. 2015, see Fig. 2c).
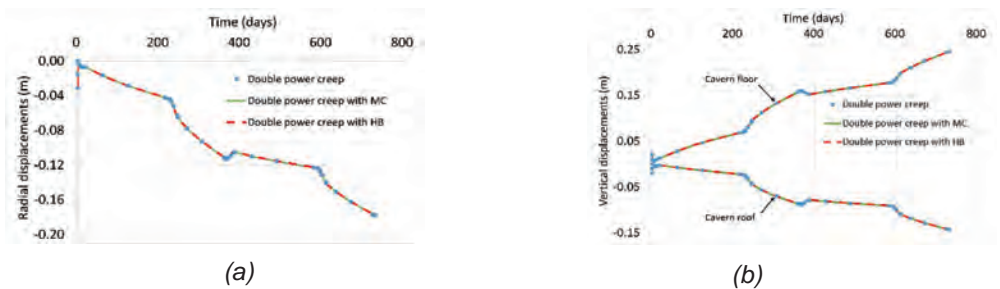
Figure 3: Time evolution of displacements (a) radial (Point C); and (b) vertical (Points A, B)

Moreover, as rock is assumed non-porous, only the thermo-mechanical coupling is considered (Zhu, et al., 2017). Fig. 3(a, b) show the convergence movements due to salt creep at the cavern roof, floor, and wall corresponding to points A, B, C denoted in Fig. 2b, respectively. A volume loss of around 0.9% is roughly estimated after 2 years of operation. Although only rock steady-state creep is considered, transient convergence is still observed due to stress redistribution, as discussed in (Bérest et al. 2017). The highest convergence rate is recorded during idling phases as low gas pressures lead to higher deviatoric stress and creep rate. When accounting for plasticity, displacement changes are negligible. This might be explained by the fact that, in such a case of a very deep cavern, the high in-situ confining pressures, combined with the used strength parameters, only allow failure to occur in a local area of the rock mass. Therefore, stress redistribution due to plastic failure is not significant and creep is the dominating mechanism compared to plastic deformation.

To further analyze material failure, two tangential (to the cavern wall) stress components are plotted for Point N (see Fig. 2b) in the vicinity of the cavern wall, both along the axial direction (parallel to the cavern vertical axis) and out-of-plane (hoop) direction in Fig. 4a. During pressurization, the (compressive) tangential stresses are reduced as the rock mass is pushed

by gas pressure. However, during depressurization, these stresses do not increase, but instead become tensile (Fig. 4a). This may be explained by the accompanying cooling process, where rock shrinkage expands the cavern, resulting in a release of tangential stresses, which is limited by the tensile strength. Fig 4b shows that a small tensile zone (where material points reach tensile failure) appears in the vicinity of the cavern during the 2nd depressurization phase. This may trigger fracturing as reported in the literature (Bottcher, et al., 2017; Berest, 2011).

(a)   (b)
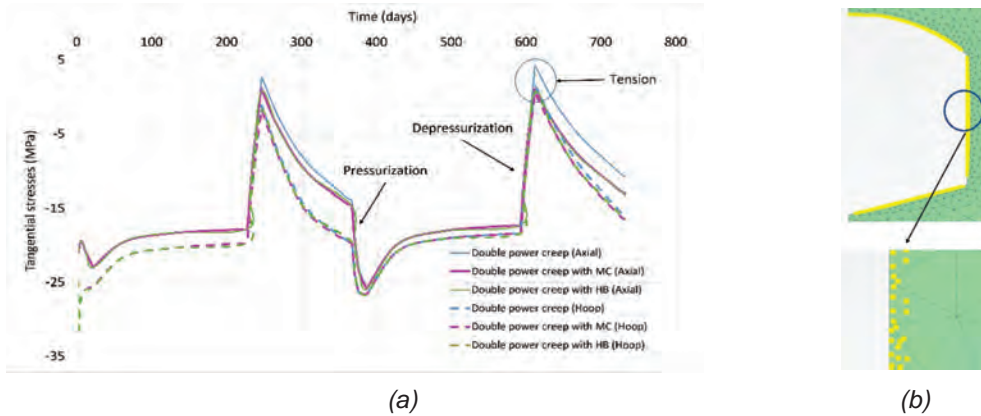
Figure 4: (a) Time evolution of tangential stresses (axial and hoop directions); (b) Failure (tensile) points during the 2nd depressurization phase

4.3   Subsidence analysis for solution mining

In this example, the analysis of a solution mining process performed by (Breunesse et al. 2003) is reproduced. It is noteworthy to emphasize that the purpose of this example is to verify the numerical implementation, thus setup and calibration of the original model (Breunesse et al. 2003), are followed. A 2D axisymmetric model, extending from the ground surface to the depth of 3.6km, is built. The mesh is refined around the mined cavern which is approximated as a cylinder with radius equal to 23m (Fig. 5). The model contains six horizontal elastic rock layers and three creeping rock layers calibrated by the dislocation power creep law. As reported in (Breunesse et al. 2003), pressure solution creep mechanism (characterized by a second branch with $N_2 = 1$) is added to the halite layer. The layer parameters are reported in Table 4.

(a)   (b)
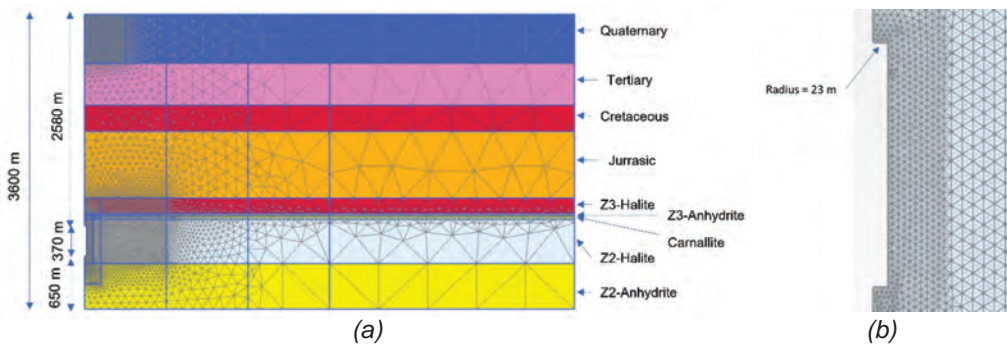
Figure 5: (a) Model geometry and mesh; (b) Zoom at the cavern

Table 4: Layer parameters (reproduced from (Breunese, et al., 2003))

Layer	Depth (m)	E (GPa)	v	N_1	A_1 (day^{-1})	N_2	A_2 (day^{-1})	Q_1/R (K)	Q_2/R (K)	ρ (kg/m^3)
Quarternary	0 - 597	0.125	0.25							1950
Tertiary	597 - 1113	0.125	0.25							2300
Cretaceous	1113 - 1434	5.0	0.25							2250
Jurassic	1434 - 2240	7.5	0.3							2230
Z3 halite	2240 - 2432	11	0.35	3.6	1.71			6206	3007	2185
Z3 anhydrite	2432 - 2462	30	0.35							2900
Carnallite	2462 - 2500	5.5	0.35	4	2	1	-	9021	-	1600
Z2 halite	2500 - 3042	11	0.35	3.6	0.787	1	1.46e-3	6206	3007	2185
Z2 anhydrite	3042 - 3600	25	0.3							2700

Following the procedure described in (Breunese et al. 2003), cavern mining is simulated by increasing the difference between brine and lithostatic pressures from 0 to 26 MPa during 1 year. It is followed by a production phase of 7 years where the brine pressure is kept constant. The subsidence evolution is shown in Fig. 6. It is readily seen that solution mining induces subsidence which continues to evolve during the production phase due to creep convergence. A relatively good agreement between the numerical and measurement data is observed. Moreover, the default computation requires only 32 timesteps, lasting for less than 4 minutes on a laptop assembling and Intel Core i7-8850H CPU @2.60GHz with 6 physical cores and 32 GB of RAM. To demonstrate the efficiency of the implementation, the simulation is repeated using a smaller global step size and thereby a higher total number of steps (302 steps). Due to the adaptive substepping scheme, the computation time increases, albeit not excessively (9 minutes), while relatively similar accuracy is obtained. The reason is that, while nonlinear creeping areas are adaptively and locally substepped to satisfy the targeted accuracy, less nonlinear zones (far from the cavern) can still be accurately integrated with large global time steps, hence saving computation time.
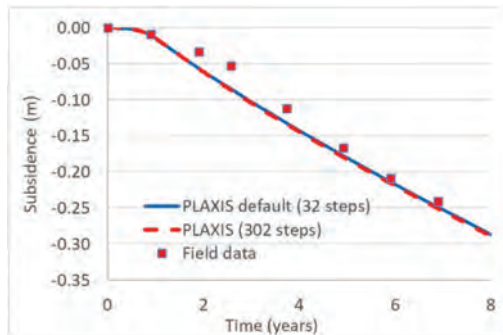
Figure 6: Time evolution of ground subsidence

5 Conclusions

The paper presents a FE approach for the numerical modelling of underground structures in rock salt formation. At the global level, an implicit fully coupled formulation is implemented which allows simulating THM couplings in a rigorous way. At the material level, rock salt is

modelled by a viscoplastic steady-state double power creep law combined with MC and HB plastic models. An implicit stress integration, combined with automatic local sub-stepping, is implemented to ensure numerical accuracy, stability, and robustness. The numerical implementation has been verified by comparing the numerical and analytical solutions for basic relaxation tests. The thermo-mechanical analysis of an underground gas cavern, as well as a solution mining benchmark, are investigated to illustrate the applicability of the numerical approach. It is seen that the power creep model can provide satisfactory outcomes, especially for deformation analysis, while the extended versions with MC and HB failure criteria provide further insights for stress analysis. For future work, other mechanisms, such as transient creep, could be considered.

References

BEREST, P. 2011. Thermomechanical Aspects of high frequency cycling in salt storage caverns. *International Gas Union Research Conference.*

BÉREST, P., KARIMI-JAFARI, M. & BROUARD, B. 2017. Geometrical versus rheological transient creep closure in a salt cavern. *Comptes Rendus Mecanique,* Band 345, p. 735–741.

BOTTCHER, N., GORKE, U., KOLDITZ, O. & NAGEL, T. 2017. Thermo-mechanical investigation of salt caverns for short-term hydrogen storage. *Environmental Earth Science,* p. 76:98.

BREUNESE, J., VAN EIJS, R., DE MEER, S. & KROON, I. 2003. *Observation and prediction of the relation between salt creep and land subsidence in solution mining - The Barradeel case.* Chester, SMRI conference.

BROWN, E. & HOEK, E. 1978. Trends in Relationships between Measured In-Situ Stresses and Depth. *Int. J. Rock Mech. Min. Sci. & Geomech. Abstr.,* Band 15, pp. 211-215.

BUI, T., CASARELLA, A., DI DONNA, A. & BRINKGREVE, R. 2019. *Advanced Thermo-Hydro-Mechanical modelling features for practical applications in energy geotechnics.* Reykjavic, ECSMGE 2019 Proceedings.

COUSSY, O., DORMIEUX, L. & DETOURNAY, E. 1998. From mixtures theory to Biot's approach for porous media. *International Journal of Solids and Structures ,* 35(34-35).

DE BORST, R. 1987. Integration of plasticity equations for singular yield functions. *Computers and Structures,* 26(5), pp. 823-829.

FOKKER, P. 1994. *The behaviour of Salt and Salt Caverns,* Delft: TU Delft .

GUNTHER, R., SALZER, K., POPP, T. & LUDELING, C. 2015. Steady-State Creep of Rock Salt: Improved Approaches for Lab Determination and Modelling. *Rock Mech Rock Eng.*

JAEGER, J., COOK, N. & ZIMMERMAN, R. 2007. *Fundamentals of rock mechanics.* Oxford: Blackwell Publishing.

KHALEDI, K. 2017. *Constitutive Modeling of Rock Salt with Application to Energy Storage Caverns,* Bochum: PhD thesis, Ruhr-Universiy of Bochum.

MAHNKEN, R. & STEIN, E. 1989. Adaptive Time Step control in Creep Analysis. *International journal for numerical methods in Engineering,* Band 28, pp. 1619-1633.

MA, L. 2013. A New Elasto-Viscoplastic Damage Model Combined with the Generalized Hoek–Brown Failure Criterion for Bedded Rock Salt and its Application. *Rock Mech Rock Eng,* Band 46, p. 53–66.

PLAXIS 2015. *Thermal and Thermo-Hydro-Mechanical analysis,* Delft: Plaxis bv.

PLAXIS 2021. *PLAXIS 2D Material Model Manual,* Delft: Plaxis bv.

POLYANIN, A. & ZAITSEV, V. 2017. *Handbook of Ordinary Differential Equations: Exact Solutions, Methods, and Problems.* s.l.:CRC Press/Chapman and Hall.

SERBIN, K., ŚLIZOWSKI, J., URBAŃCZYK, K. & NAGY, S. 2015. The influence of thermodynamic effects on gas storage cavern convergence. *International Journal of Rock Mechanics & Mining Sciences,* Band 79, p. 166–171.

SIMO, J. & HUGHES, T. 1997. *Computational Inelasticity.* New York: s.n.

SLOAN, S. & BOOKER, J. 1986. Removal of singularities in tresca and mohr–coulomb yield functions. *Communications in Applied Numerical Methods,* 2(2), pp. 173-179.

ZHU, C., SHEN, X., ARSON, C. & POUYA, A. 2017. Numerical study of thermo-mechanical effects on the viscous damage behavior of rock salt caverns. *ARMA 17-353.*

Influence of pressure solution and evaporate heterogeneity on the geo-mechanical behavior of salt caverns

Kishan Ramesh Kumar[1][*]*and Hadi Hajibeygi*[1]

[1]Faculty of Civil Engineering and Geosciences, Delft University of Technology, The Netherlands

[*] *k.rameshkumar-2@tudelft.nl*

ABSTRACT: Salt caverns provide large-scale storage volumes for green gases, especially green hydrogen. This makes them quite attractive and feasible for scaling up renewable energy development plans. Accurate characterization of the subsurface properties, specially the nonlinear time-dependent ones under varying gas pressures, plays a major role in safe operations. The present study is focused on studying the influence of pressure solution on the nonlinear deformation of salt caverns. Further a carnallite interlayer was incorporated to study its influence on the deformation in the presence of pressure solution. To this end, we present rigorous finite element computational analyses to model heterogeneous geo-mechanical domain surrounding salt caverns with nonlinear creep deformation, and material heterogeneity.

1. Introduction

To accelerate the transition to renewable energy, it is necessary to scale up the energy storage options. Storage of green gases (e.g., hydrogen) in salt caverns offers a promising large-scale energy storage option for combating intermittent supply of renewable energy, such as wind and solar. Caverns are artificially created by a controlled dissolution mining process within the host rock formation (Donadei & Schneider 2016). They typically hold volumes of about 300,000-500,000 m (Laban 2020), with much larger outliers in the order of a million cubic meters. There are four salt caverns which are operational today for hydrogen storage, of which three of them are salt domes locates in Texas, USA. The fourth one is the relatively small one located in Teeside, UK which acts as a buffer in a shared distribution network for chemical producers and consumers (Hashemi et al. 2021; Laban 2020). Recently a techno-economic study has been conducted in which a system with more than 45 caverns is envisioned to provide a baseload needed to convert a metal manufacturing plant (TATA) to run on hydrogen (Eradus 2022). Note that the study has also envisioned the development of the NorthH2 power plant (https://www.north2.eu/en/), which is expected to be operational by 2030. Salt caverns provide swift deliverability of the stored energy, i.e., have excellent injection and production characteristics compared with porous reservoir rocks, and have strong sealing properties on time scales relevant for underground gas storage (Lord et al. 2014). In the Netherlands, the rock salt layers in the subsurface occur mainly in strata of the Permian Zechstein Group (laid down between approximately 251 and 260 million years ago) and the Triassic Röt Formation (laid down between around 238 and 244 million years ago). The salt is originally accumulated in shallow, restricted salt lakes. Due to the evaporation of the seawater, salt crystals are precipitated to form today's solid rock salt layers. The Zechstein salt rock in the Netherlands has formed in this manner. Today's Dutch salt caverns are mainly the result of salt mining operations. Both purpose-built and existing caverns can potentially be used to store hydrogen or other gases. However, it is first required to conduct safety analysis test of the caverns, under relevant stress ranges, to prevent unfavorable events.

The primary nonlinear deformation physics of rock salts is associated with time-dependent creep processes. Creep is a phenomenon whereby a solid material permanently deforms with time under the influence of persistent mechanical stress. Of critical importance, here, is to predict the resulting evolution of the stress and deformation field over long times, to ensure the safety of the storage facility up to and into abandonment, i.e., potentially over periods of hundreds of years. As shown in Figure 1, after applying an external load, the material generally

goes through three stages of creep at sufficiently low mean stress and high deviatoric stress. These are often called transient (primary or reduced), steady state (secondary or stationary), and tertiary (accelerated) creep stages (Naumenko & Altenbach 2007). The primary creep stage is characterized by a monotonic decrease in the rate of the creep. Secondary creep is characterized by a constant creep rate. The tertiary creep phase, seen when mean stresses are low enough to allow the formation of microscopic cracks, is characterized by micro-crack damage evolution, hence creep acceleration, and ultimately brittle rupture of the material (Betten. 2008). Tertiary creep occurs only when the stresses are above the dilatancy boundary (Cristescu & Hunsche 1992; Hunsche & Hampel 1999). Especially for cavern design, tertiary creep of rocksalt should be avoided at all times when fluids are stored in caverns to prevent accidents.
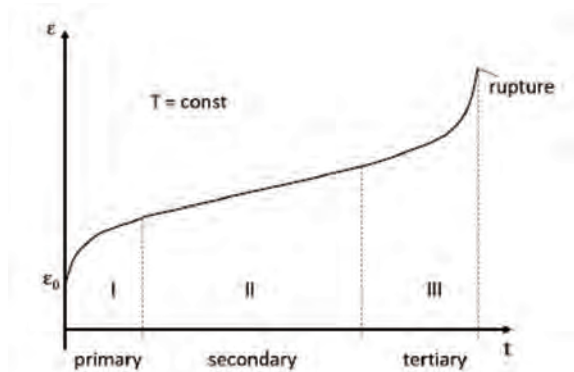
Figure 1: Illustration of the creep response of a material to uniaxial loading under conditions of low confinement that allow ultimate failure. Note the three stages of creep, starting from the initial elastic deformation. The illustration is modified after (Naumenko & Altenbach 2007).

Creep in salt occurs at rates that are significant on short and long engineering time scales at the upper crustal temperatures which typically range from 20-120 ^{0}C, and has been measured in experiments at stresses as low as 0.2 MPa (Bérest et al. 2019). The deformation mechanics are governed by dislocation motion within the crystalline grains and by a range of grain boundary processes.

As explained in the literature (Spiers et al. 1990; Urai et al. 2008), there are two main deformation mechanisms that have been investigated by employing laboratory tests and micro-structural analyses. The first is the dislocation creep mechanism, which in the steady case can be characterized by a power-law dependence of creep strain rate on deviatoric stress and an Arrhenius dependence on temperature. This type of behavior is grain size insensitive, and generally shows stress exponents (n) in the range of 3.5-5.5 and activation energies around 60 kJ/mol (Carter et al. 1993). Exponents in the range 5-7 have also been reported in the literature and may reflect a role of glide or cross-slip controlled dislocation creep, as opposed to climb control which is often assumed to be responsible for exponents of 3-5 (Wawersik & Zeuch 1986). Dislocation creep is favored towards higher stresses and temperatures through its highly nonlinear power-law stress dependence and Arrhenius temperature dependence. The second creep mechanism is solution-precipitation creep or pressure solution. It is a linear viscous creep mechanism that involves stress-driven dissolution-precipitation transfer of salt around water-bearing grain boundaries and is favored in fine-grained materials at low stresses, and temperatures (Spiers et al. 1990).

Different models have been used in the past to model salt flow and geomechanics such as a single power law (Marketos et al. 2016; Muhammad 2015; Ter Heege et al. 2005), the Munson-Dawson model (higher n's only) (Munson 1997; Park et al 2018), Günther-Salzer (which has

been fitted towards n = 1) (Günther et al. 2015), Lux-Wolters (Blanco-Martín et al. 2016; Hou 2003), Lubby2 (Heusemann et al. 1982; Mahmoudi et al. 2015), and the composite model by Hampel (Hampel & Schulze 2007; Hampel & Hunsche 2020). Detailed descriptions can be found in the literature (Ramesh Kumar et al. 2021). A discrete two mechanism flow law, i.e., combining dislocation creep and pressure solution laws of the type proposed by Urai & Spiers (2007), -have been applied in relatively few numerical modelling studies (e.g. Breunese et al. 2003; Cornet & Dabrowski 2018; Orlic et al. 2016).

Heterogeneity of the rock salt may affect the solution mining process, which in turn will also affect the shape of the constructed cavern as well as the evolution of the deformation and stress field. In field-scale cases, salt properties are heterogeneous due to disseminated impurities such as anhydrite or potassium/magnesium salts, shale rocks, bischofite (Jeremic 1994; Ma et al. 2013; Muhammad 2015). Heterogeneity in the geological domain surrounding salt caverns also involves both soluble and insoluble interlayers (anhydrites, potash salts, shale, gypsum, mudstone etc.) (Li et al. 2018; Liang et al. 2007; Liu et al. 2014). Few experimental researchers have attempted to study the impact of heterogeneity in the composition of the rock salt (Luangthip et al. 2017; Muhammad 2015). However very few researchers have studied the impact of heterogeneity in simulations. More precisely, (Wang et al. 2015) showed the effect of heterogeneity by considering only different elastic properties and by considering equivalent elastic modulus. However, very few researchers have studied the impact of heterogeneity employing different elastic and plastic properties and constitutive laws, though the effects of drastically different layer properties might be expected to be large.

This study presents an extension of the recent work of the same authors (Ramesh Kumar et al. 2021) by employing both dislocation steady state creep and linear pressure solution in the entire domain relevant for gas storage (for e.g. H2). Pressure solution has been studied in the past by many researchers (Gratier et al. 2013; Hickman & Evans 1991; Spiers et al. 1990; Urai & Spiers 2007). As a novel contribution, the present work is specifically focused to study the influence of pressure solution in a pure halite domain of the salt caverns in an explicit manner. Note that work to date includes only implicit inclusion of the process within numerical framework. Such inclusion is commonly done by adapting an empirical constitutive model which accounts for the stress sensitivity such that its exponent decreases from around 5 to 1 as the stress is reduced (Günther et al. 2015). Further, we also study the impact of introducing a weak, horizontal carnallite layer around the cylindrical shaped salt caverns by employing both power law and linear pressure solution.

2. Governing equations

Conservation of linear momentum reads

$$\nabla \cdot \boldsymbol{\sigma} = f^b \tag{1}$$

Where the stress, σ, is related to the elastic deformation, ε_{el}, via the Hooke's law, i.e.,

$$\boldsymbol{\sigma} = C : \varepsilon_{el} \tag{2}$$

Here, C is the matrix of elastic coefficients. The total infinitesimal strain, ε_t, is given by the summation of creep strain and elastic strain, i.e.,

$$\varepsilon_t = \varepsilon_{cr} + \varepsilon_{el} \tag{3}$$

which is also related to the deformation, u, according to

$$\varepsilon_t = \nabla^s u \tag{4}$$

The operator in the left-hand-side of the above equation, ∇^s, is the symmetric gradient (Castelletto et al. 2017). The steady state creep strain is then given as a function of stress and temperature, i.e. (Spiers et al. 1990; Urai et al. 2008),

$$\dot{\varepsilon}_{cr} = A(T)\, \boldsymbol{\sigma}^{n1} + B(T)\left(\frac{\sigma}{d^{n2}}\right) \tag{5}$$

Here, the first term in the right hand side is the classical power law which is commonly used in the literature. In this work, we also include the second term in the right hand side which represents the pressure solution. Note that the pressure solution is a linear function of the stress σ. More specifically, the creep strain rate can be stated as,

$$\dot{\varepsilon}_{cr} = A e^{-\frac{Q}{RT}} \sigma_{vM}^{n1-1} \boldsymbol{s} + B\,\frac{\sigma}{d^{n2}} \tag{6}$$

The deviatoric ($\boldsymbol{s}$) and von Mises stress (σ_{vM}) is given by

$$\boldsymbol{s} = \boldsymbol{\sigma} - \frac{1}{3}\delta_{ij}\boldsymbol{\sigma}_{kk} \qquad\qquad \sigma_{vM} = \frac{3}{2}s_{ij}s_{ij} \tag{7}$$

The above creep formulation involves both dislocation creep and pressure solution. The constants $n1$ and $n2$ depend on the material, and d is the grain diameter. Furthermore, the multipliers A(T) and B(T) depend on the material and the temperature of loading.

3. Numerical methodology

A nonlinear finite element approach is developed to study the creep deformation of the salt caverns and their surrounding environment. The discrete system in the space is given by

$$u \approx N u^h. \tag{8}$$

Here $\boldsymbol{N}$ is the shape functions used in the finite element formulation. The shape functions in the local coordinates system are given by (ξ, η), i.e.,

$$N_1 = \xi \qquad\qquad N_2 = \eta \qquad\qquad N_3 = 1 - \xi - \eta. \tag{9}$$

In this work, 2D unstructured triangular mesh is generated to employ finite element methodology. The deformation is stored in the nodes of the triangle and the stress is computed at the integration points. Using the principle of virtual displacements and Gauss divergence theorem, the final discrete equation with unit thickness was obtained. Newton Raphson method is employed to solve for displacement iteratively, in an implicit manner. This allows for unconditionally stable simulation. The nonlinear residual, $\mathfrak{R}^{n+1}$, reads as

$$\mathfrak{R}^{n+1} = \nabla \cdot (C : \varepsilon_{cr}^{n+1}) + f^b - \nabla \cdot (C : \nabla^s u^{n+1}). \tag{10}$$

The objective is to find the deformation at time step n+1. The linearized form of this equation is obtained as

$$\mathfrak{R}^{n+1} \approx \mathfrak{R}^{i+1} \approx \mathfrak{R}^i + \frac{\partial \mathfrak{R}}{\partial u}|^i \delta u^{i+1}. \tag{11}$$

The Jacobian, i.e., $J = \frac{\partial \mathfrak{R}}{\partial u}|^i$, is computed based on the elastic part of the residual equation. Creep term is treated in the right-hand-side. Finally, the iterative linearized system of

$$J^i \delta u^{i+1} = -\mathfrak{R}^i. \tag{12}$$

is solved until the convergence is reached. Further details can be found in the literature (Ramesh Kumar & Hajibeygi 2021).

4. Results

To reflect real-field loading conditions, the cavern's fluid and lithostatic pressure values are such that the fluid pressure is 20% - 80% of lithostatic pressure (Caglayan et al. 2020). In this work, the cavern's fluid pressure is set at 20%. The influence of brine sump located in the bottom of the cavern is ignored. The minimum pressure difference between the cavern's fluid pressure and lithostatic pressure will be at the cavern's roof during the injection; and, the maximum will be at the cavern's bottom during production (see points 1 and 2 in the left Fig. 2). The cavern's fluid pressure, thus, is a function of the overburden rock density, rock salt density and depth of the roof and the bottom of the cavern. The cavern dimensions and constants used in the input parameters are presented in the Table 1. The system is modelled assuming planar 2D domain. Roller boundary condition was imposed at the bottom and the face along the cavern. Traction free Neumann boundary conditions were imposed on the top and the far end face of the geological domain. The density of hydrogen is employed to compute the forces on the cavern walls. Triangular mesh with refinement around the caverns was used for the simulations. A mesh convergence study was also conducted. Consistency and 2nd order accuracy of deformation in the implementation for the elastic domains are confirmed. Most halite rocks in the nature are coarse grained with diameter size varying from 2mm-20mm (Warren et al. 2005). In this work, the grainsize diameter of the rock salt was chosen to be 2 mm. The constitutive parameters chosen for dislocation creep solution was compared with the experimental data (Bérest et al. 2015) to verify the computational framework.
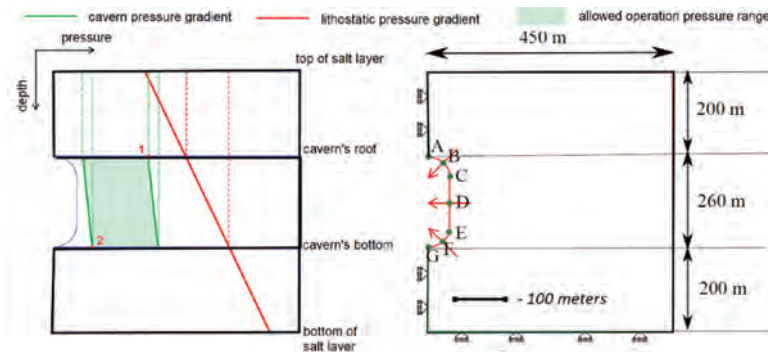
Figure 2: Pressure gradients and safe pressure range within the salt domain (left) and implied numerical model boundary conditions (right) for test cases. The dimensions of the 2D geological domain is shown and the depth of the topmost salt layer from the ground surface is 600 m. Points (A, B, C, D, E, F, G) are located on the caverns wall are depicted to present the results from the numerical simulations. The graph modified after Ramesh Kumar et al.(2021).

Table 1: Parameters employed in the creep formulation for rock salt (halite rock). (Muhammad 2015; Ramesh Kumar et al. 2021; Spiers et al. 1990; Warren et al. 2005)

Rock salt density	2200	A	8e-27
Young's modulus	35 Gpa (Ingraham et al. 2015)	Creep activation energy	51600 J/mol
Poisson ratio	0.25	n1,n2	3.5 , 3
Roof thickness	200 m	B	1e-25
Floor thickness	200 m	Temperature	30 $^{\circ}$C
Depth of top of salt layer	500 m	Diameter of grains	2 to 20 mm

In section 4.1, the entire domain is considered to be pure halite and the influence of incorporating pressure solution is presented. In section 4.2, a carnallite interlayer is incorporated to study the impact of its linear pressure solution behavior on the local deformation.

4.1 Creep under constant loading

In this test case, halite rock is chosen throughout the domain. Creep under constant load with respect to time is imposed. The time-dependent solutions are illustrated in Figure 3, which shows the displacement evolution over time for different grain size diameters and von Mises stress distribution across the domain.

(a)   (b)   (c)

(d)   (e)   (f)

(g)
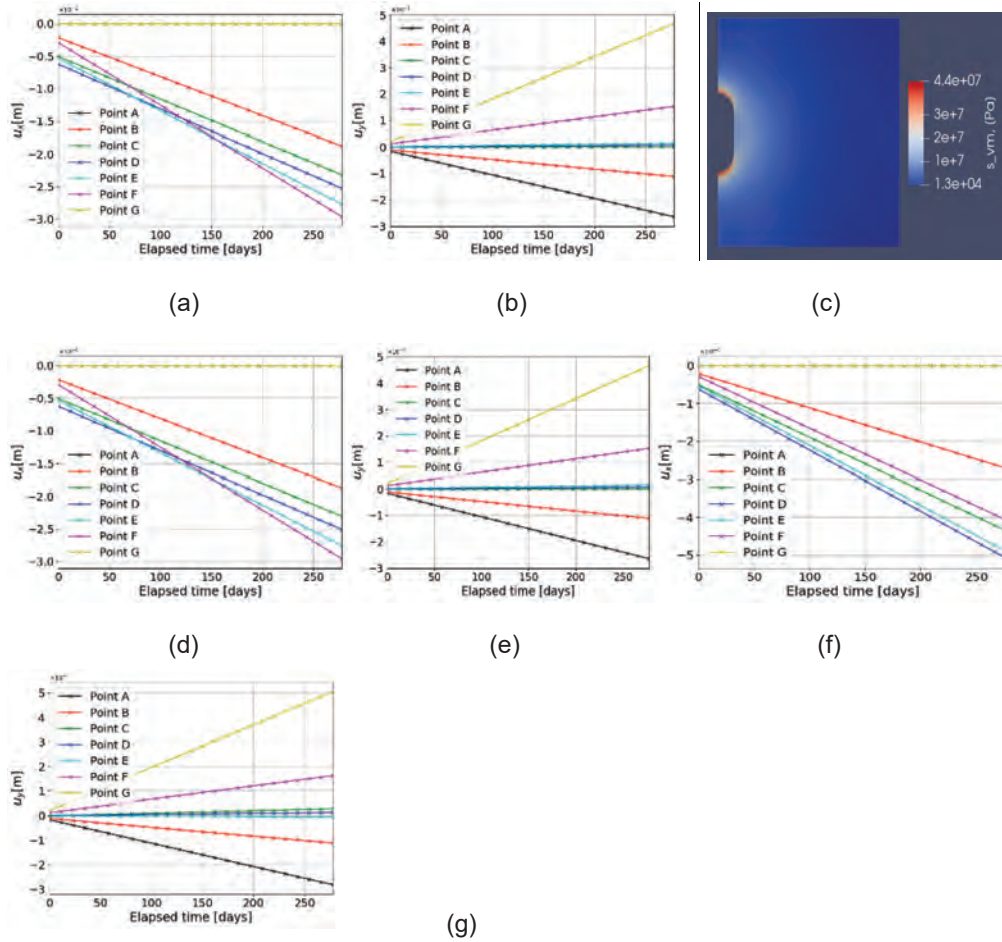
Figure 3: The above shows the illustration of variation of deformation in x and y directions and von Mises stress distribution in presence of pressure solution. Figure (a) and (b) show the variation of deformations with time for grainsize of 10 mm. Accordingly, (d) and (e) show the variation of deformations for grainsize of 5mm, and (f) and (g) for 2mm.

A higher magnitude of displacement is observed around the cavern near larger curvatures at the end of 275 days. This is primarily due to dislocation creep. However, when pressure solution is incorporated, the average change in the percentage of deformation after 275 days is around 0.35 % for 10mm grain size. When Figures 3(a), 3(d) and 3(f) are compared as grain diameter is reducing, the horizontal deformation is increasing especially at points D, C and E. This is because from the stress distribution, as shown in Figure 3(c), lower stresses are observed near central plane of the cavern, i.e., around points D, C and E. These stress values lead to higher magnitudes of deformation, due to the pressure solution, when compared to dislocation creep.

In the following test case, an upper limit threshold of 5 MPa is employed for linear pressure solution. If the stress in the domain is less than 5MPa, linear pressure solution creep will occur along with dislocation solution. Figure 4 shows the deformations after 275 days caused due to linear pressure solution. Figure (4a) and (4b) show the deformations when the linear pressure solution is acting without any stress thresholds. Figure (4c) and (4d) show the deformations when the linear pressure solution is incorporated when the stress is lower than 5 MPa. From Figures (4a) it can be seen that the deformation is higher near the central plane near the cavern

boundaries and slowly reducing in the horizontal direction. However, for Figures (4c), the horizontal deformation higher far off the caverns boundary and the highest magnitude is lower than when the pressure solution is acting in the entire domain.

(a)

(b)

(c)

(d)
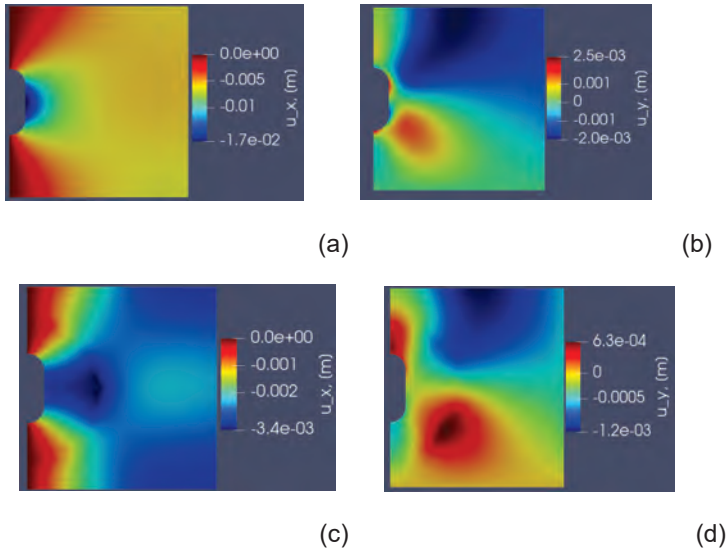
Figure 4: The above illustration shows the deformation caused due to pressure solution. Figure (a) and (b) show the deformation when the pressure solution is acting throughout the domain. Figure (c) and (d) show the deformation when the pressure solution is acting only if the stress is lower than 5 MPa.

4.2 Impact of introducing a carnallite interlayer

(a)

(b)
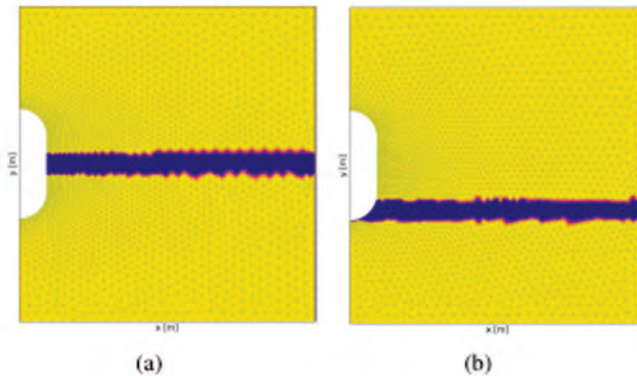
Figure 5: The above contours show the location of a carnallite layer (blue) introduced in to the rocksalt surrounding a hydrogen storage cavern otherwise identical to that shown in Figure 2. The thickness of the carnallite layer is 30 m. Interlayers are located in the central plane as shown in Figure (5a) and near the floor of the cavern as shown in Figure (5b). The test case is modified after the work of (Ramesh Kumar et al. 2021), by introducing pressure solution as a deformation mechanism in the rocksalt and carnallite, alongside power law (dislocation) creep.

In this test case, we examine the change in the deformation when a carnallite layer of thickness 30m is introduced into the rocksalt around a cavern and allowed to deform by power law (dislocation) creep plus pressure solution, using parameters appropriate for this material. The material properties and the constitutive equations chosen for carnallite are presented in Table 2. The grainsize diameter was assumed to be 10 mm. Figure 5 shows the two heterogeneous test cases considered, with interlayer in the central plane and near the floor of the cavern.

Table 2. Properties and steady state constitutive laws employed for carnallite (Muhammad, 2015)

Material	Young's modulus	Poisson ratio	Dislocation creep law	Pressure solution
Carnallite	17 GPa	0.33	2.68e-14 σ^5	$1.01 \times 10^{-8} \sigma d^{-1}$

Figure 6 shows the results when carnallite is incorporated as the additional layer in the central plane of the domain. Properties and constitutive laws employed for halite rocks remain the same as in the previous test case. Figure (6a) and (6b) show the variation of the deformation with time when linear pressure solution of carnallite is incorporated and Figure (6d) and (6e) show the variation of the deformations when linear pressure solution of carnallite is not incorporated.

(a)   (b)   (c)

(d)   (e)

Figure 6: The above illustrates the impact of introducing a carnallite layer at the central plane. Figure (6a) and (6b) show the deformation over time when pressure solution of carnallite is incorporated. Figure (6d) and (6e) show the deformation over time when pressure solution of carnallite is not incorporated. Figure (6c) show the von Mises stress contour of the domain.
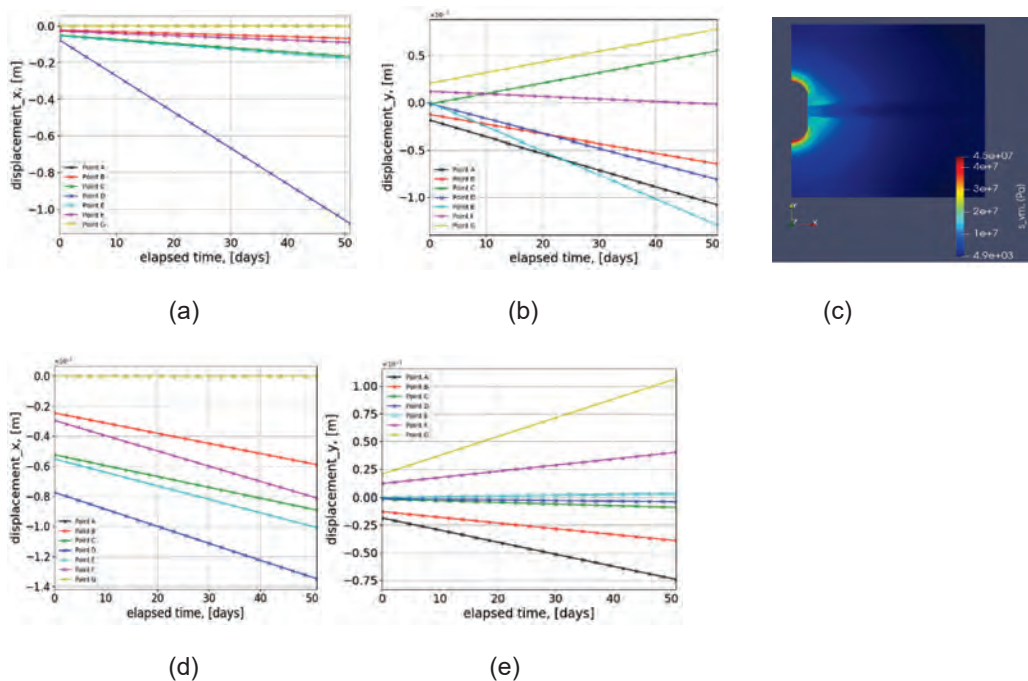
The horizontal deformation at point D has increased by almost 650 % primarily due to the inclusion of pressure solution of carnallite. The maximum increase in deformation when the carnallite (without its pressure solution) is compared with pure halite domain is roughly around 45 %. Deformation at points is very small compared to point D. This is because of lower stresses observed around the central plane of the cavern as seen in Figure (6c).

Similar studies were conducted when the carnallite interlayer was located near the floor of the cavern. Here, the change in deformation caused due to pressure solution when Figure (7a) and (7d) are compared, can be clearly seen in points F, E, D and C. The maximum increase in deformation when carnallite layer (without linear pressure solution) is incorporated compared to pure halite domain is roughly around 300% for point F. Further, the maximum increase in deformation was found to be around 200 % near point F when linear pressure solution of carnallite is incorporated when compared to the domain with carnallite layer (without linear pressure solution). This increase in deformation is lesser when compared to the previous case, i.e., when the interlayer is in the central plane. This is due to the presence of curvature near the interlayer causing higher stresses in the domain.

(a)   (b)   (c)

(d)   (e)
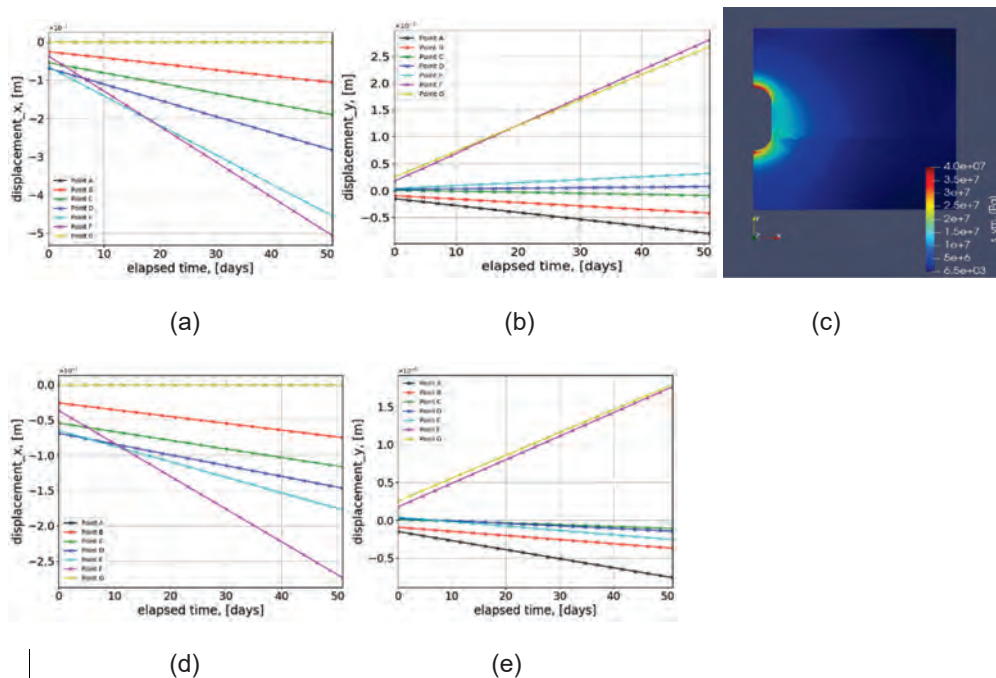
Figure 7: The above illustrates the impact of introducing a carnallite layer near the cavern floor of the model. Figure (7a) and (7b) show the deformation over time when pressure solution of carnallite is incorporated. Figure (7d) and (7e) show the deformation over time when pressure solution of carnallite is not incorporated. Figure (7c) show the von Mises stress contour of the domain.

5. Conclusion

In this work, the influence of incorporating pressure solution in the geological domain on the salt caverns which can be used for energy storage technology is studied using a finite element solver. Cylindrical shaped caverns were chosen to minimize the effect of complex shape and primarily study the influence of pressure solution on the caverns. Homogeneous halite-based

rock salt domain was employed to study the influence of grain size diameter and pressure solution on the time dependent deformation. The higher change in the deformations of the cavern is subject to change depending on the grainsize diameter. Next, a horizontal carnallite interlayer was incorporated in the domain to study the influence of change in plastic properties on the deformation inside the domain. The impact of pressure solution is seen near the cavern. However, due to higher stresses near the cavern, the creep strain caused due to dislocation creep is more pronounced compared to pressure solution. The carnallite layer showed much higher change in the deformation caused by linear pressure solution compared to pure halite. This work shows the importance of studying the local deformation when heterogeneous layers are incorporated, especially when power law and pressure solution are explicitly accounted for.

Future work involves including thermal and (visco)plastic strains to allow for more reliable simulations and sensitivity analyses. Pressure solution needs to be accounted in the future with relevant stress thresholds to study its effect particularly in the far-off heterogeneous fields from the caverns. Since the field test cases are large-scale of the order (km), efficient formulations such as multi-scale formulation would be developed to reduce the computational costs. Better constrained creep laws are needed for carnallite in future, as well as for other materials such as Bischofite and Anhydrite, so that the effects of these evaporate layers can be assessed.

Acknowledgements

References

BÉREST, P., BÉRAUD, J. F., GHARBI, H., BROUARD, B. & DE VRIES, K. 2015. A Very Slow Creep Test on an Avery Island Salt Sample. Rock Mechanics and Rock Engineering, 48(6), 2591–2602.

BÉREST, P, GHARB, H., BROUARD, B., BRÜCKNER, D., DE VRIES, K., HÉVIN, G., HOFER, G., SPIERS, C. & URAI, J. 2019. Very Slow Creep Tests on Salt Samples. Rock Mechanics and Rock Engineering, 52(9), 2917–2934.

BETTEN, J. 2008. Creep mechanics (Third Edition). Springer Berlin Heidelberg.

BLANCO-MARTÍN, L., WOLTERS, R., RUTQVIST, J., LUX, K. H. & BIRKHOLZER, J. T. 2016. Thermal-hydraulic-mechanical modeling of a large-scale heater test to investigate rock salt and crushed salt behavior under repository conditions for heat-generating nuclear waste. Computers and Geotechnics, 77, 120–133.

BREUNESE, J., VAN EIJS, R., DE MEER, S. & KROON, I. 2003. Observation and prediction of the relation between salt creep and land subsidence in solution mining. The Barradeel case. Proceedings SMRI Fall Meeting, Chester.

CAGLAYAN, D. G., WEBER, N., HEINRICHS, H. U., LINßEN, J., ROBINIUS, M., KUKLA, P. A. & STOLTEN, D. 2020. Technical potential of salt caverns for hydrogen storage in Europe. International Journal of Hydrogen Energy, 45(11), 6793–6805.

CARTER, N. L., HORSEMAN, S. T., RUSSELL, J. E. & HANDIN, J. 1993. Rheology of rocksalt. Journal of Structural Geology, 15(9–10), 1257–1271.

CASTELLETTO, N., HAJIBEYGI, H. & TCHELEPI, H. A. 2017. Multiscale finite-element method for

linear elastic geomechanics. Journal of Computational Physics, 331, 337–356.

CORNET, J. S. & DABROWSKI, M. 2018. Nonlinear Viscoelastic Closure of Salt Cavities. Rock Mechanics and Rock Engineering, 51:10, 51(10), 3091–3109.

CRISTESCU, N. & HUNSCHE, U. 1992. Determination of Nonassociated Constitutive Equation for Rock Salt from Experiments. Finite Inelastic Deformations — Theory and Applications, 511–523.

DONADEI, S. & SCHNEIDER, G.-S. 2016. Chapter 6 - Compressed Air Energy Storage in Underground Formations. In T. M. Letcher (Ed.), Storing Energy (pp. 113–133). Elsevier.

ERADUS, D. 2022. The Techno-Economic Feasibility of Green Hydrogen Storage in Salt Caverns in the Dutch North Sea, Delft university of technology.

GRATIER, J. P., DYSTHE, D. K. & RENARD, F. 2013. The Role of Pressure Solution Creep in the Ductility of the Earth's Upper Crust. Advances in Geophysics, *54*, 47–179.

GÜNTHER, R. M., SALZER, K., POPP, T. & LÜDELING, C. 2015. Steady-State Creep of Rock Salt: Improved Approaches for Lab Determination and Modelling. Rock Mechanics and Rock Engineering, 48(6), 2603–2613.

HAMPEL, A. & SCHULZE, O. 2007. The Composite Dilatancy Model: A constitutive model for the mechanical behavior of rock salt. Proceedings of the 6th Conference on the Mechanical Behavior of Salt "SALTMECH6" - The Mechanical Behavior of Salt - Understanding of THMC Processes in Salt, 99–107.

HAMPEL, A. & HUNSCHE, U. 2020. Extrapolation of creep of rock salt with the composite model. Basic and Applied Salt Mechanics, 193–207.

HASHEMI, L., BLUNT, M. & HAJIBEYGI, H. 2021. Pore-scale modelling and sensitivity analyses of hydrogen-brine multiphase flow in geological porous media. Scientific Reports, 11(1), 8348.

HEUSEMANN, S., LUX, K. & ROKAHR, R. 1982. Entwicklung mathematisch-mechanischer Modelle zur Beschreibung des Stoffverhaltens von Salzgestein in Abhangigkeit von der Zeit und der Temperatur auf der Grundlage von Laborversuchen und begleitenden kontinuumsmechanischen Berechnungen nach der Methode d.

HICKMAN, S. H. & EVANS, B. 1991. Experimental pressure solution in halite: the effect of grain/interphase boundary structure. Journal of the Geological Society, 148(3), 549–560.

HOU, Z. 2003. Mechanical and hydraulic behavior of rock salt in the excavation disturbed zone around underground facilities. International Journal of Rock Mechanics and Mining Sciences, 40(5), 725–738.

HUNSCHE, U. & HAMPEL, A. 1999. Rock salt - The mechanical properties of the host rock material for a radioactive waste repository. Engineering Geology, 59(3–4), 271–291.

INGRAHAM, M. D., BROOME, S. T., BAUER, S. J., BARROW, P. C. & FLINT, G. M. 2015. Behavior of Salt from the Bayou Choctaw Salt Dome. In 49th U.S. Rock Mechanics/Geomechanics Symposium (p. ARMA-2015-028).

JEREMIC, M. L. 1994. *Rock Mechanics in Salt Mining* (1st ed., Vol. 1). CRC Press.

LABAN, M. P. 2020. Hydrogen Storage in Salt Caverns: Chemical modelling and analysis of large-scale hydrogen storage in underground salt caverns.

LI, J., SHI, X., YANG, C., LI, Y., WANG, T. & MA, H. 2018. Mathematical model of salt cavern leaching for gas storage in high-insoluble salt formations. Scientific Reports, 8(1), 1–12.

LIANG, W., YANG, C., ZHAO, Y., DUSSEAULT, M. B. & LIU, J. 2007. Experimental investigation of mechanical properties of bedded salt rock. International Journal of Rock Mechanics and Mining Sciences, 44(3), 400–411.

LIU, J., XIE, H., HOU, Z., YANG, C. & CHEN, L. 2014. Damage evolution of rock salt under cyclic

loading in unixial tests. Acta Geotechnica, 9(1), 153–160.

LORD, A. S., KOBOS, P. H. & BORNS, D. J. 2014. Geologic storage of hydrogen: Scaling up to meet city transportation demands. International Journal of Hydrogen Energy, 39(28), 15570–15582.

LUANGTHIP, A., WILALAK, N., THONGPRAPHA, T. & FUENKAJORN, K. 2017. Effects of carnallite content on mechanical properties of Maha Sarakham rock salt. Arabian Journal of Geosciences, 10(149), 1–14.

MA, L. J., LIU, X. Y., FANG, Q., XU, H. F., XIA, H. M., LI, E. B., YANG, S. G. & LI, W. P. 2013. A new elasto-viscoplastic damage model combined with the generalized hoek-brown failure criterion for bedded rock salt and its application. Rock Mechanics and Rock Engineering, 46(1), 53–66.

MAHMOUDI, E., KHALEDI, K., KÖNIG, D. & SCHANZ, T. 2015. Sensitivity analyses on the influence of constitutive parameters on the numerical simulation of the behavior of a cavern in rock salt. Geomechanics from Micro to Macro - Proceedings of the TC105 ISSMGE International Symposium on Geomechanics from Micro to Macro, IS-Cambridge 2014, 2, 933–938.

MARKETOS, G., SPIERS, C. J. & GOVERS, R. 2016. Impact of rock salt creep law choice on subsidence calculations for hydrocarbon reservoirs overlain by evaporite caprocks. Journal of Geophysical Research: Solid Earth, 121(6), 4249–4267.

MUHAMMAD, N. 2015. Deformation and transport processes in salt rocks: An experimental study exploring effects of pressure and stress relaxation (Issue 084). Utrecht studies in earth sciences.

MUNSON, D. E. 1997. Constitutive model of creep in rock salt applied to underground room closure. International Journal of Rock Mechanics and Mining Sciences & Geomechanics Abstracts, 34(2), 233–247.

NAUMENKO, K. & ALTENBACH, H. 2007. Modeling of Creep for Structural Analysis. Springer Berlin Heidelberg.

ORLIC, B., VAN THIENEN VISSER, K. & SCHREPPERS, G.-J. 2016. Numerical estimation of structural integrity of salt cavern wells. ARMA.

PARK, B. Y., SOBOLIK, S. R. & HERRICK, C. G. 2018. Geomechanical Model Calibration Using Field Measurements for a Petroleum Reserve. Rock Mechanics and Rock Engineering, 51(3), 925–943.

RAMESH KUMAR, K. & HAJIBEYGI, H. 2021. Multiscale simulation of inelastic creep deformation for geological rocks. Journal of Computational Physics, 440, 110439.

RAMESH KUMAR, K. MAKHMUTOV, A., SPIERS, C. J. & HAJIBEYGI, H. 2021. Geomechanical simulation of energy storage in salt formations. Scientific Reports, 11(1), 1–24.

SPIERS, C. J., SCHUTJENS, P. M. T. M., BRZESOWSKY, R. H., PEACH, C. J., LIEZENBERG, J. L. & ZWART, H. J. 1990. Experimental determination of constitutive parameters governing creep of rocksalt by pressure solution. Geological Society Special Publication, 54(1), 215–227.

TER HEEGE, J. H., DE BRESSER, J. H. P. & SPIERS, C. J. 2005. Rheological behaviour of synthetic rocksalt: The interplay between water, dynamic recrystallization and deformation mechanisms. Journal of Structural Geology, 27(6), 948–963.

URAI, J. L., SCHLÉDER, Z., SPIERS, C. J. & KUKLA, P. A. 2008. Chapter 5.2 Flow and Transport Properties of Salt Rocks. Dynamics of Complex Intracontinental Basins: The Central European Basin System, 277–290.

URAI, J. L. & SPIERS, C. J. 2007. The effect of grain boundary water on deformation mechanisms and rheology of rocksalt during long-term deformation. Proceedings of the

6th Conference on the Mechanical Behavior of Salt "SALTMECH6" - The Mechanical Behavior of Salt - Understanding of THMC Processes in Salt, 149–158.

Wᴀɴɢ, T., Yᴀɴɢ, C., Sʜɪ, X., Mᴀ, H., Lɪ, Y., Yᴀɴɢ, Y. & Dᴀᴇᴍᴇɴ, J. J. K. 2015. Failure analysis of thick interlayer from leaching of bedded salt caverns. International Journal of Rock Mechanics and Mining Sciences, 73, 175–183.

Wᴀʀʀᴇɴ, J. K., Uʀᴀɪ, J. L., Sᴄʜʟéᴅᴇʀ, Z., Sᴘɪᴇʀꜱ, C. J., Kᴜᴋʟᴀ, P. A., Mᴏʜʀ, M., Sᴄʜᴇᴄᴋ-Wᴇɴᴅᴇʀᴏᴛʜ, M., Mᴀʏꜱᴛʀᴇɴᴋᴏ, Y., Hüʙꜱᴄʜᴇʀ, C., Hᴀɴꜱᴇɴ, M., Mᴀᴢᴜʀ, S., Mᴀɢʀɪ, F., Lɪᴛᴛᴋᴇ, R., Rᴏᴅᴏɴ, S. & Bᴀʏᴇʀ, U. 2005. Flow and transport properties of salt rocks. 248–344.

Wᴀᴡᴇʀꜱɪᴋ, W. R. & Zᴇᴜᴄʜ, D. H. 1986. Modeling and mechanistic interpretation of creep of rock salt below 200°C. Tectonophysics, 121(2–4), 125–152.

WEIMOS: Simulations of two geomechanical scenarios in rock salt resembling structures at WIPP

A. Hampel[1]*, C. Lüdeling[2], R.-M. Günther[2], J.Q. Sun-Kurczinski[3], R. Wolters[3], U. Düsterloh[3], K.-H. Lux[3], S. Yildirim[4], D. Zapf[4], S. Wacker[5], I. Epkenhans[5], J. Stahlmann[5], B. Reedlunn[6]

[1]Hampel Consulting, Mainz, Germany; [2]Institut für Gebirgsmechanik GmbH (IfG), Leipzig, Germany; [3]Technische Universität Clausthal (TUC), Germany; [4]Leibniz Universität Hannover (LUH), Germany; [5]Technische Universität Braunschweig (TUBS), Germany; [6]Sandia National Laboratories, Albuquerque, USA

* hampel@hampel-consulting.de

ABSTRACT: Joint Project WEIMOS (2016-2022) aims to improve geomechanical rock salt models used to analyze high-level radioactive waste disposal in rock salt formations. The project focuses on four research topics: 1) deformation behavior at low deviatoric stresses, 2) damage reduction and healing of rock salt, 3) deformation behavior resulting from tensile stresses, and 4) influence of inhomogeneities (layer boundaries, interfaces) on deformation. The impacts of progress in the first three research areas are demonstrated with simulations of two typical underground scenarios resembling structures at the Waste Isolation Pilot Plant (WIPP): a long open drift with a dam introduced after 30 years (Virtual Demonstrator I), and a vertical slice through part of an underground repository comprising two main drifts and seven emplacement chambers (Virtual Demonstrator II). Each project partner simulated both scenarios with her/his material model, after calibrating it against numerous laboratory tests on WIPP and Asse rock salt. The results show that (1) the higher creep rates at low deviatoric stresses in rock salt, as reliably measured during the WEIMOS project, must be considered in a constitutive model in order to get realistic results for predictions of displacements, convergences, stresses, as well as damage and dilatancy; (2) the constitutive models are able to evaluate damage reduction and healing in the DRZ around a dam now based on an improved experimental basis; (3) tensile stresses have considerable influence on the evolution of damage and dilatancy in the DRZ.

1   Introduction

Reliable constitutive models describing the thermo-mechanical behavior of rock salt are needed for various numerical simulations addressing the design and stability analysis of an underground repository for heat-generating high-level radioactive wastes (HLW) in rock salt, and for the evaluation and proof of the long-term integrity of the surrounding containment providing rock zone (CRZ). Further applications include calculations for the design and operation of caverns for oil and gas storage, as well as for salt mining.

Before WEIMOS, constitutive models were compared in three joint projects starting in 2004. The results show that the considered models accurately describe transient and steady-state creep, evolution of damage and dilatancy and its impact on deformation, damage reduction and healing, creep failure and short-term strength, post-failure behavior and residual strength, all in a wide range of stress states, temperatures, and strain rates (Schulze et al. 2007; Hou et al. 2007; Hampel et al. 2010; Salzer et al. 2012; Hampel et al. 2012; Hampel et al. 2015; Düsterloh et al. 2015; Salzer et al. 2015; Hampel et al. 2016; Hampel et al. 2018; Reedlunn 2018). The studies also identified the following topics in need of further investigation:

1) deformation behavior at low deviatoric stresses,
2) damage reduction and healing of rock salt,
3) deformation behavior resulting from tensile stresses,
4) influence of inhomogeneities (layer boundaries, interfaces) on deformation.

These topics are addressed in Joint Project WEIMOS ("Verbundprojekt: Weiterentwicklung und Qualifizierung der gebirgsmechanischen Modellierung für die HAW-Endlagerung im Steinsalz", English title: "Joint Project: Further development and qualification of the rock mechanical modeling for the final HLW disposal in rock salt"). The project aims to improve the accuracy of rock salt model predictions, especially those associated with the long-term behavior of a final repository system (Lüdeling et al. 2018).

Laboratory tests for topics 1 and 2 were conducted with improved test rigs by the Institut für Gebirgsmechanik GmbH (IfG) and Technische Universität Clausthal (TUC). The experimental technique, performed tests, results and consequences for the modeling were introduced by Herchen et al. (2018) and are updated by Lüdeling et al. (2022) and Wolters et al. (2022). Impacts of progress in the first three research areas are demonstrated with simulations of two typical underground scenarios resembling structures in rock salt from a bedded deposition at the Waste Isolation Pilot Plant (WIPP) in New Mexico, USA. These two scenarios, simulations and results are described in the following chapters. For the fourth topic, Sandia National Laboratories has analyzed a series of shear tests by RESPEC Inc., Rapid City, SD, USA, see Sobolik et al. (2019, 2020, 2022), Keffeler et al. (2021).

Each partner calculated both scenarios with FLAC3D of Itasca Inc. [Itasca 2021] and her or his constitutive model for rock salt (Table 1). The CDM of Hampel models transient and steady-state creep based on the evolution of the deformation microstructure (dislocation density, subgrain structure, Hampel 2015). The evolution of damage, dilatancy and creep failure above the dilatancy boundary is described in dependence of the creep rate. The IfG Günther/Salzer model uses a macroscopic-phenomenological description of hardening, recovery and damage softening. The IfG Minkley model describes salt damage in a plastic formulation with deformation-dependent softening and a two-component yield surface for shear and tensile yielding. The constitutive models of the other partners apply an elasto-viscoplastic concept with a rheological description of transient and steady-state creep by means of modified Kelvin and Maxwell elements, and the plastic flow theory for the modeling of damage-induced strains. All models use different phenomenological formulations for the enhanced creep at low deviatoric stresses, damage reduction (healing) with (LUH, TUC) or without (other partners) assuming a healing boundary below which healing is only possible, tensile damage and tensile failure. Latest versions, that were used in these simulations, are described in detail in the final WEIMOS report comprising individual reports of the partners and a synthesis report (in preparation).

Table 1: Partners and their constitutive models used for simulations of the Virtual Demonstrators with FLAC3D.

Dr. Andreas Hampel	Composite Dilatancy Model (CDM)
Institut für Gebirgsmechanik GmbH (IfG)	Günther/Salzer Model and Minkley model
Leibniz Universität Hannover (LUH)	Lubby-CF
Technische Universität Braunschweig (TUBS)	TUBSsalt_perm
Technische Universität Clausthal (TUC)	Lux/Wolters/Lerche model

2 Virtual Demonstrators and modeling conditions

2.1 Virtual Demonstrator I

Virtual Demonstrator I (VDI) is a model of a long open drift with a dam installed after 30 years (Figure 1). Simulations of VDI demonstrate influences of creep at low deviatoric stresses on the evolution of deformations, stresses and damage (topic 1), and modeling of healing after the installation of a dam (topic 2).

Because of symmetry, the total FLAC3D model comprises only one half of the drift and its environment. The model has a height of 107 m, a width of 26 m, and a depth of 50 m. The simulated half drift is 5.5 m high and 2.75 m wide. The FLAC3D model with open drift consists of 108,000 zones and 115,661 gridpoints, the dam is meshed with 2640 zones and 2730 gridpoints and stretches over a length of 10 m. The corners of the drift are rounded by moving the corner gridpoints about 14 cm into the drift to avoid numerical problems at higher deformation.
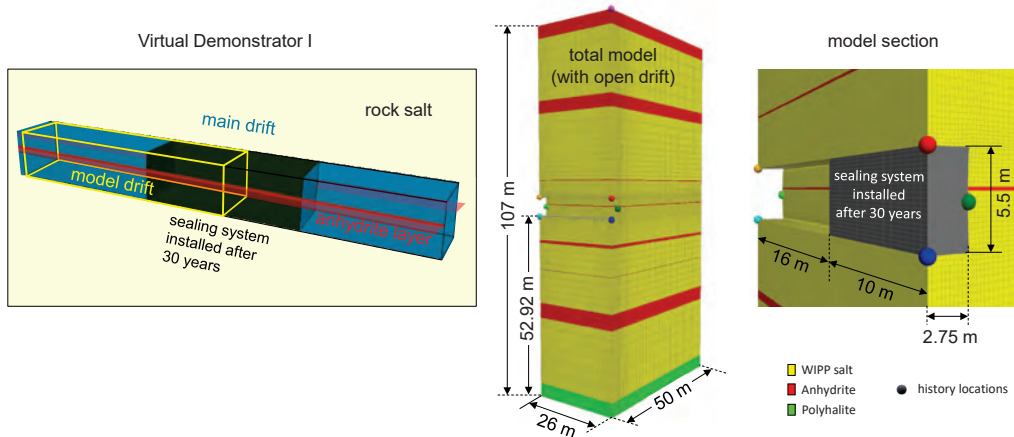

Figure 1: Virtual Demonstrator I simulates part of a long drift with a sealing system (dam) installed after 30 years (left). The central and right pictures show the total FLAC3D model and a model section together with history locations at which various results were recorded.

Three materials are considered in the model according to the stratigraphy at WIPP: rock salt, anhydrite layers, and a polyhalite layer at the bottom, see Figure 1. Clay seams between the layers are not included for simplicity. In the past, a distinction was made between two salt types at WIPP: clean and argillaceous salt (Munson et al. 1989). However, various lab test series of IfG and TUC in the preceding Joint Project III have shown that the deformation behavior of both types is very similar (Hampel et al. 2016; Hampel et al. 2018; Reedlunn 2018). Therefore, the rock salt was treated uniformly as WIPP salt. Those partners who generally use slightly different parameter sets for the two types assumed clean salt. Each partner calculated the FLAC3D models with her or his constitutive model. The parameter values were determined with adjustments of the models to data from lab test series of creep tests, constant strain rate tests, and healing tests conducted by IfG and TUC in Joint Project III and WEIMOS. Furthermore, a density of ρ = 2.17 g/cm^3, shear modulus of 15 GPa and Poisson ratio of 0.265 was used for salt.

The anhydrite was represented with a Mohr-Coulomb model with the following parameter values: density 2.3 g/cm^3, bulk modulus 40 GPa, shear modulus 24 GPa (=> Poisson ratio 0.25), cohesion 2 MPa, and friction angle 30°. The polyhalite layer was described with a power law creep model with density 2.3 g/cm^3, bulk modulus 19 GPa, shear modulus 12 GPa (=> Poisson ratio 0.2391), prefactor 4.5E-11 1/d, and stress exponent 4 (Munson et al. 1990). The dam was modeled in a very simplified manner as an elastic material with density 2.17 g/cm^3, Young modulus 30 GPa and Poisson ratio 0.25. A temperature of 303.15 K and gravitational acceleration of 9.81 m/s^2 was applied throughout the domain. The vertical pressure on the top surface was 13.57 MPa according to the depth of WIPP (2150 ft = 655 m below ground). Roller boundary conditions were applied at all other model surfaces, except the drift surfaces.

Since the whole simulation was performed in large strain mode, most partners treated the drift as filled with a soft elastic material in the first 30 years in order to be able to easily replace the soft material with the dam at t = 30 yr. For the soft material, a Young's modulus of 0.01 MPa, Poisson ratio of 0, and density of 0.01 g/cm^3 were found to be appropriate. Comparisons of simulations with and without the soft material ensured that the soft material did not influence the calculation results. The simulation started with a very small time step (value depends on the respective constitutive model), and damage and dilatancy evolution was switched off in the first day to avoid numerical issues. Then, automatic control slowly increased the time steps ensuring continuously low unbalanced forces in the model. At t = 1 d, damage and dilatancy calculation was switched on.

At t = 30 yr, the soft material was replaced by the elastic material of the dam in the respective section, and the soft material was deleted in the residual drift section. Instead of using a soft material in the drift, the Leibniz Universität Hannover adjusted the dam's gridpoints to the deformed open drift surface manually at t = 30 yr. After the installation of the dam, the simulations were continued until t = 100 yr.

2.2 Virtual Demonstrator II

Virtual Demonstrator II (VDII) reflects a typical underground scenario at WIPP with a vertical slice through part of the waste disposal area (Figure 2). Because of symmetry, the FLAC3D model reflects only one half of the field comprising two open drifts and seven empty emplacement chambers. In contrast to VDI, the vicinity of the main drift was discretized very finely to show results with high resolution. Simulations of this model demonstrate influences of creep at low deviatoric stresses and of heavy shear and tensile damage (topics 1 and 3).

The total FLA3D model has a height of 280 m, a width of 500 m, and an out-of-plane dimension (thickness) of 2 m. It was therefore calculated in plain strain mode imaging infinitely long drifts and chambers in a good approximation to the situation at WIPP. The simulated main drift has a cross section of 8 x 8 m. The second drift at a distance of 26 m has a dimension of 5 x 5 m. The emplacement chambers are 10 m wide and 5 m high and have spacings of 30 m, the left one is 53 m away from the second drift. The total FLAC3D model has 33,309 zones and 39,156 gridpoints. The zone size adjacent to the main drift is only 6.2 x 6.2 cm, and the corners are rounded to avoid numerical problems at higher deformation.
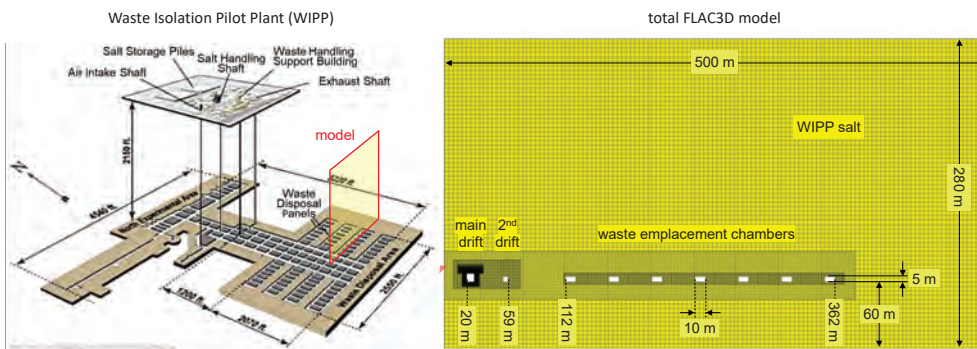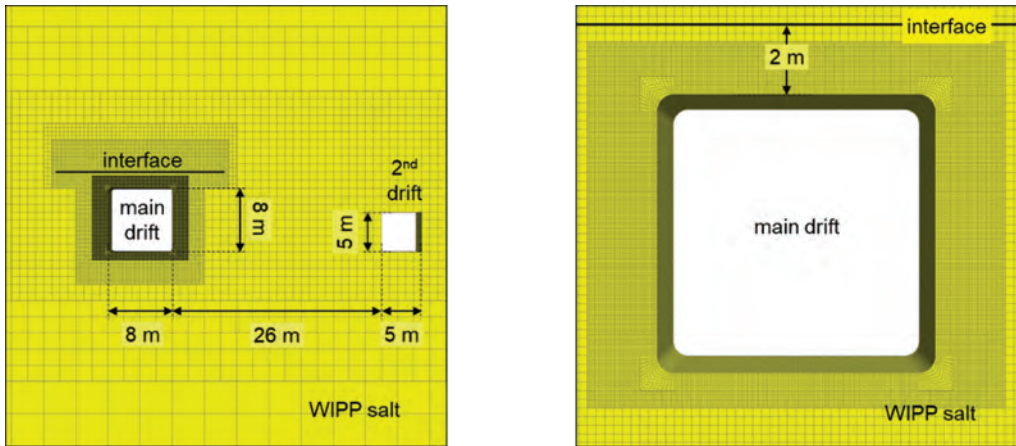
Figure 2: Virtual Demonstrator II resembles a vertical cut through a section of WIPP (top left). The FLAC3D model comprises two drifts and seven open waste emplacement chambers (top right). Bottom: Sections of the FLAC3D model. The simulations focus on the vicinity of the main drift, where the model is meshed with very fine zones. An interface above its ceiling represents a thin clay seam.

An interface of length 21 m and zero thickness represents a thin clay seam 2 m above the main drift ceiling. The following parameters were applied to the interface: cohesion 0.05 MPa, friction angle 15°, residual friction after shear failure 10°, residual cohesion after shear failure 0, tensile strength 0.25 MPa, residual tensile strength after shear or tensile failure 0, normal stiffness 2.5 GPa, and shear stiffness 1.5 GPa. However, simulations with and without the interface showed that it had no visible influence on the simulation results, which is partly a consequence of the limited dimensions of the interface.

The rock salt was again treated uniformly as WIPP salt using the same parameter values as for VDI. A temperature of 303.15 K, a gravitational acceleration of 9.81 m/s^2 and a salt density of 2.17 g/cm^3 was used. The vertical pressure on the top surface was 9.8 MPa. Roller boundary conditions were applied at all other domain boundaries, except the drift and emplacement chamber surfaces. The calculation was performed in large strain mode for a total time of 30 years. As in VD I, the simulation of VD II started with a very small time step, and damage and dilatancy evolution was switched off in the first day to avoid numerical issues. Then, automatic control slowly increased the time steps ensuring continuously low unbalanced forces in the model. At t = 1 d, damage and dilatancy calculation was switched on.

3 Results

3.1 Creep at low deviatoric stresses

In the past, before steady-state creep rates at low deviatoric stresses below 6 MPa could be reliably measured in natural rock salt samples at room temperature, underground scenarios in rock salt were often calculated using a power law creep model with a stress exponent of usually n = 5 for the whole stress range. Figure 3 on the left displays two examples for distributions of equivalent stresses above 6 MPa from a CDM simulation of VDI after 1 day and 1 year. Such higher stresses are only found in small regions around the open drift. In all other regions (left white in the contour plots) equivalent stresses are in the range of low deviatoric stresses below 6 MPa.
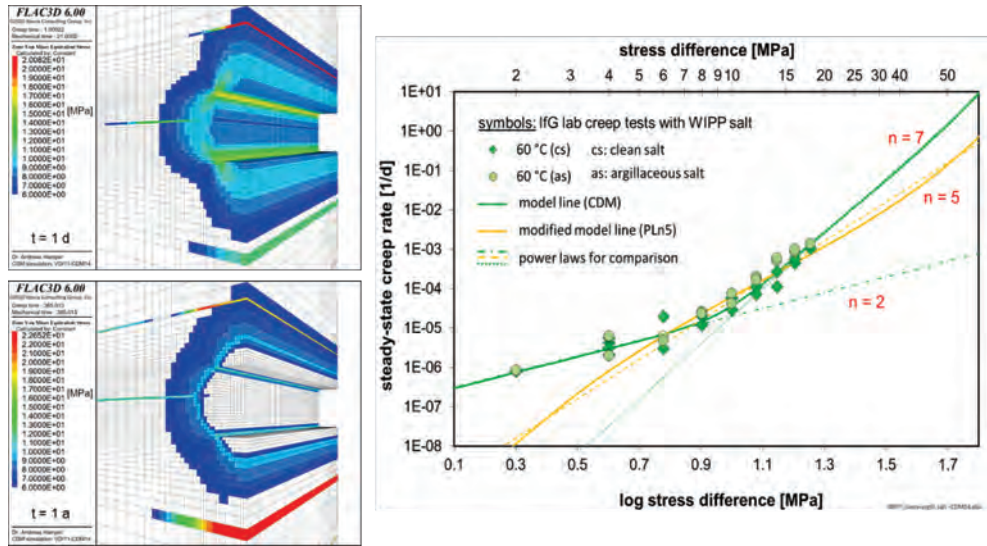
Figure 3: Left: von Mises equivalent stresses in VDI after 1 day and 1 year, displaying only stresses above 6 MPa with colors. Right: steady-state creep rates vs. stress difference from IfG lab tests at 60 C (symbols) and modeled with the CDM constitutive model (full green line). The modified PLn5 model line reflects a power law with stress exponent 5 (full orange line).

Reliable triaxial creep tests with rock salt samples from WIPP clearly confirm that steady-state creep rates in the low stress range are higher than predicted with a power law and stress exponent of 5. WIPP salt cores had grain sizes in the range of 2 to 28 millimetres with an average of 10 millimetres (Reedlunn 2022).

In order to study the influence of these higher creep rates on simulation results, Hampel performed test simulations of VDI and VDII with his CDM constitutive model assuming a modified steady-state creep rate that resembles a power law behavior with n = 5 (PLn5, full orange line in Figure 3 on the right). For this modification, he altered three CDM parameter values for steady-state creep leaving all other parameter values for transient creep, damage and dilatancy evolution, healing etc. unchanged. Figure 3 on the right shows that also the PLn5 curve describes the data points at stress differences at and above 6 MPa quite well. However, it underestimates the measured rates below 6 MPa.

In Figures 4 and 5, results of test simulations of VDI and VDII with PLn5 are compared with those with the original CDM simulation. It is clearly visible that including the higher steady-state creep rates in the low stress range leads to much higher displacements. The displacement in the middle of the ceiling of VDI (Figure 4) after 100 years amounts to 1,74 m with the CDM (a roof fall was not simulated) and only 11 cm with the PLn5, resulting together with the uplifts of the floor in vertical convergences of 3,05 m with the CDM, but only 20 cm with the PLn5. In both simulations, the displacements at the ceiling are higher than at the floor due to the gravitational influence.
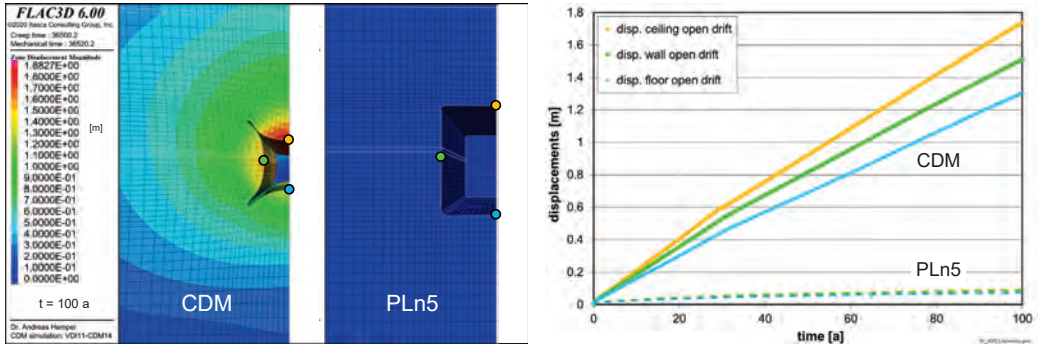
Figure 4: Displacements in VDI at t = 100 years (left) and its time-dependent evolution (right) from simulations with CDM and PLn5, see Figure 3, both at the open drift model side (see history locations of same colors in Figure 1).
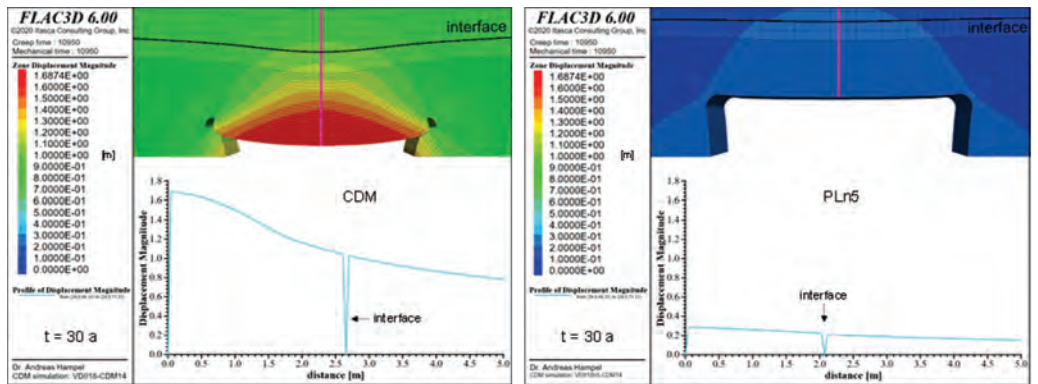
Figure 5: Displacements in VDII above the ceiling of the main drift after 30 years from simulations with CDM and PLn5. The light blue curves display data along vertical profile lines above the middle of the ceiling (pink lines in contour plots), the negative peak stems from the interface opened by about 5 mm.
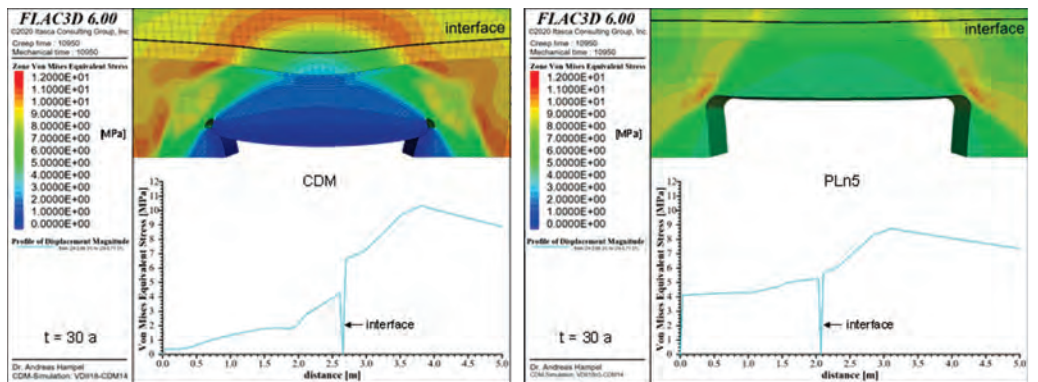
Figure 6: Von Mises equivalent stresses in VDII above the ceiling of the main drift and along the profile lines after 30 years from simulations with the CDM and PLn5.

The displacement in the middle of the main drift ceiling of VDII (Figure 5) is 1,69 m (CDM) and 29 cm (PLn5) after 30 years. The vertical convergences amount here to 2,71 m with the CDM and to only 45 cm with the Pln5. Using a power law and n = 5, the convergence of the open drift would thus be greatly underestimated, progressively increasing with time. Figure 6 shows that the higher steady-state creep rates at low deviatoric stresses in the CDM simulation lead also to a much faster transfer of stresses away from the vicinity of the main drift compared to the simulation with a power law with n = 5 and thus, after some time, to much lower deviatoric stresses in the vicinity of the main drift.

There is a close relation between displacements and damage in salt, because increasing deformation leads to increasing hardening which favors the generation of more and more microcracks, i.e. damage. The opening of microcracks causes damage-related volumetric strains (dilatancy). In experiments as well as in the modeling, dilatancy is used as a measure of damage. Therefore, with a power law with n = 5 not only displacements, but also volumetric strains (dilatancy) are greatly underestimated, see Figure 7. Both contour plots with same scales display volumetric strains above 0.02% after 30 years. In the CDM simulation, the maximum dilatancy at drift corners is 28%, while in the PLn5 simulation it is only 4.8%. The damage vice versa leads to a softening of salt and thus to an increased deformation rate. This interaction between creep and damage enhances the differences between the CDM and PLn5 results. The results clearly underline that the higher creep rates at low deviatoric stresses in rock salt must be described with a constitutive model in order to get realistic results for predictions of displacements, convergences, stresses, as well as damage and dilatancy.
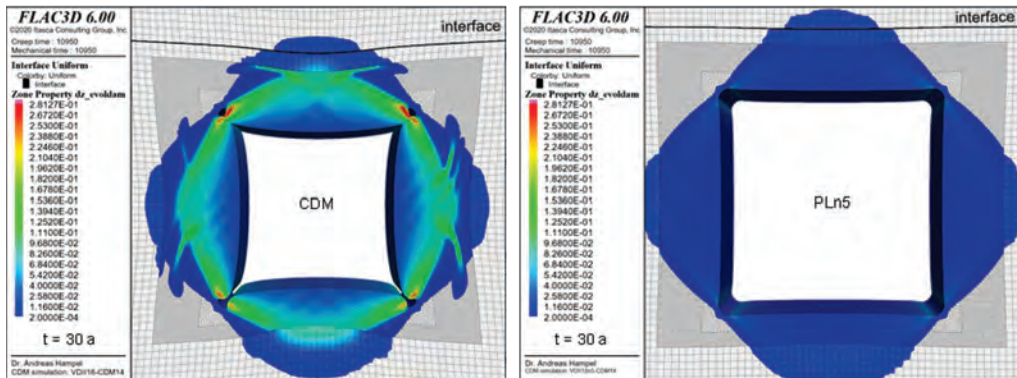
Figure 7: Damage-related dilatancy around the main drift in VDII after 30 years from simulations with CDM and PLn5, see Figure 3.

3.2 Damage reduction and healing

The healing tests in WEIMOS (Wolters et al. 2022) yield a good experimental basis for an improved description of damage reduction in rock salt with constitutive models. The achieved status of modeling of damage reduction and healing is demonstrated with simulations of VDI.

In Figure 8 results of the CDM simulation immediately before the installation of the dam at t = 30 years and at the end of the simulation at t = 100 years are shown. While dilatancy has continued to increase around the open drift in the last 70 years, creep of salt against the dam has led to complete healing of salt around the dam.
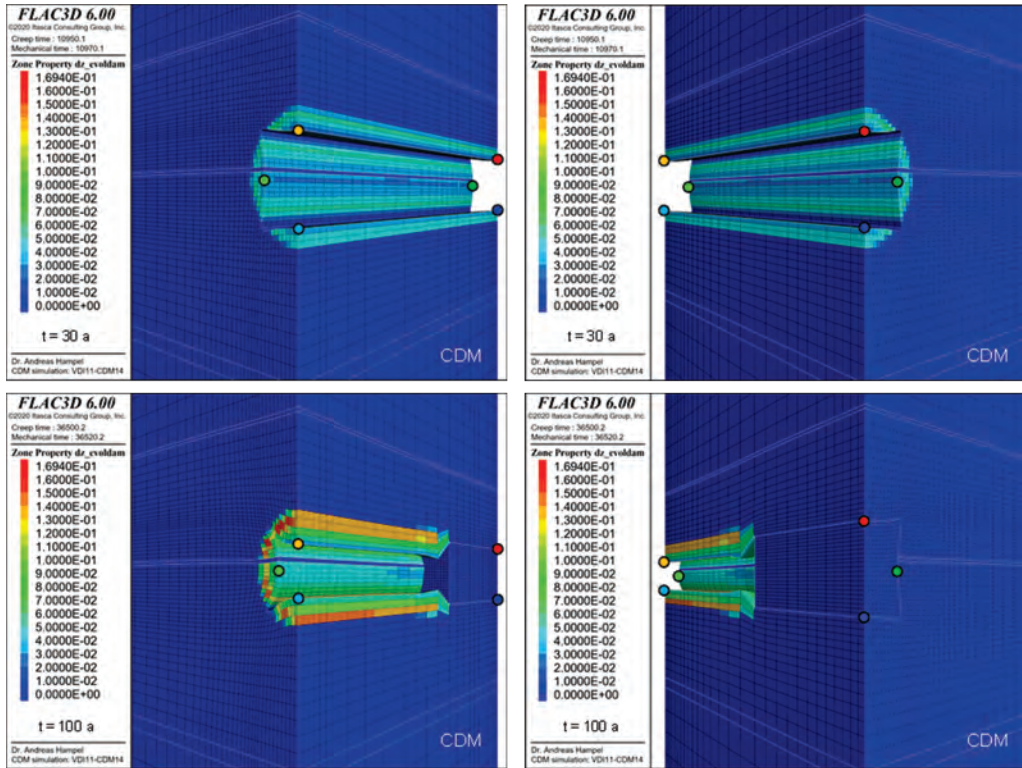
Figure 8: Damage-related volumetric strains (dilatancy) in VDI after 30 years (top) and after 100 years (bottom). Boundaries of the rock layers and dam are indicated with light grey lines, history locations with colored circles, cf. Figure 1.

Figure 9 compares the normalized dilatancy curves at the ceiling above the middle of the dam (red history point) as calculated by the partners with her or his modeling of healing. Although every partner determined the according parameter values based on the same series of healing tests from the TUC lab (Wolters et al. 2022), the dilatancy reduction rates after installation of the dam at t = 30 years still differ. A reason is a big difference in dilatancies achieved after 30 years (evolmax) that comes from differences in the modeling of creep and damage, see Chapter 3.3. Another reason for the different curves are different modeling approaches for healing. Nevertheless, the TUC lab tests in WEIMOS helped to understand and model various dependences of the healing rate on dilatancy, minimum principal stress, and mean stress. More experimental investigations are needed to further understand healing phenomena and reduce the remaining differences.
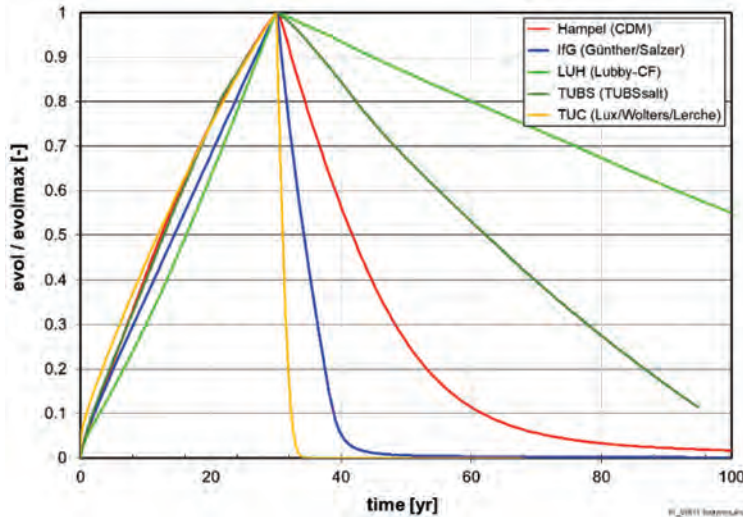
Figure 9: Time-dependent evolutions of damage-related dilatancy at the middle of the ceiling above the dam of VDI (red history point in Figure 8) from simulations of the partners with their indicated models, normalized by maximum values after 30 years.

3.3 Influence of tensile stresses

Influences of tensile stresses on deformation and damage were studied with several VDII simulations. Following a common notation, compressive stresses are negative in FLAC3D. Tensile stresses are thus characterized by positive minimum principal stresses σ_3.

In Figures 10 and 11, results of the partners of the von Mises equivalent stress and of the damage-related dilatancy above the ceiling of the main drift in VDII after 25 to 30 years are compared in contour plots and with a vertical profile line above the middle of the ceiling. Differences between the results partly stem from different amounts of salt deformation around the drift. The more salt creeps into the drift and the more ceiling, walls, and floor are bulged out, the more equivalent stresses are reduced in the immediate vicinity. Furthermore, high damage concentration to small layers in results of IfG and TUC lead to steep increases of equivalent stresses at the same location in Figure 11. In contrast, Hampel calculates a broader damaged rock zone (DRZ), mainly because of a close link between the damage evolution rate and the creep (hardening) rate in the CDM. As a consequence, equivalent stresses are reduced in a broader zone above the ceiling and increase more slowly along the profile line.

The partners use different descriptions of direction-dependent damage. Generally, micro-cracks open mainly in direction of the principal stress component σ_3 that has the smallest absolute value or is even positive in case of tension. As an example, damage and dilatancy evolve only in direction of σ_3 in the Günther/Salzer model of IfG. In contrast, damage evolves mainly in direction of σ_3 in the CDM of Hampel, but evolution in the direction of σ_2 is also possible if the magnitudes of σ_3 and σ_2 are similar. The amount of damage in σ_2 direction depends on the relation of σ_3 and σ_2. The more both stress components are different, the more damage and dilatancy focus on the σ_3 direction.

Figure 12 displays consequences of the modeling of tensile failure. Tensile strength is assumed to be damage-dependent and is therefore described as a function of dilatancy. It starts at a value of 0.7 or 1 MPa for intact salt, see Figure 12, and decreases to zero at a maximum dilatancy of e. g. 2 %. However, as soon as the minimum principal stress reaches the tensile strength, brittle failure is initiated by immediately setting the tensile strength to zero. In addition, TUC models a tensile dilatancy strength similar to a dilatancy boundary in compression. When

σ_3 reaches this curve, the tensile strength begins to decrease faster. This means that damage softening also occurs in tension. In the bottom right diagram of Figure 12, the tensile dilatancy strength of TUC is reached shortly before brittle failure occurs as described above. Contrary to the constitutive models of the other partners, the IfG Minkley model describes salt damage in a plastic formulation with deformation-dependent softening and a two-component yield surface for shear and tensile yielding.
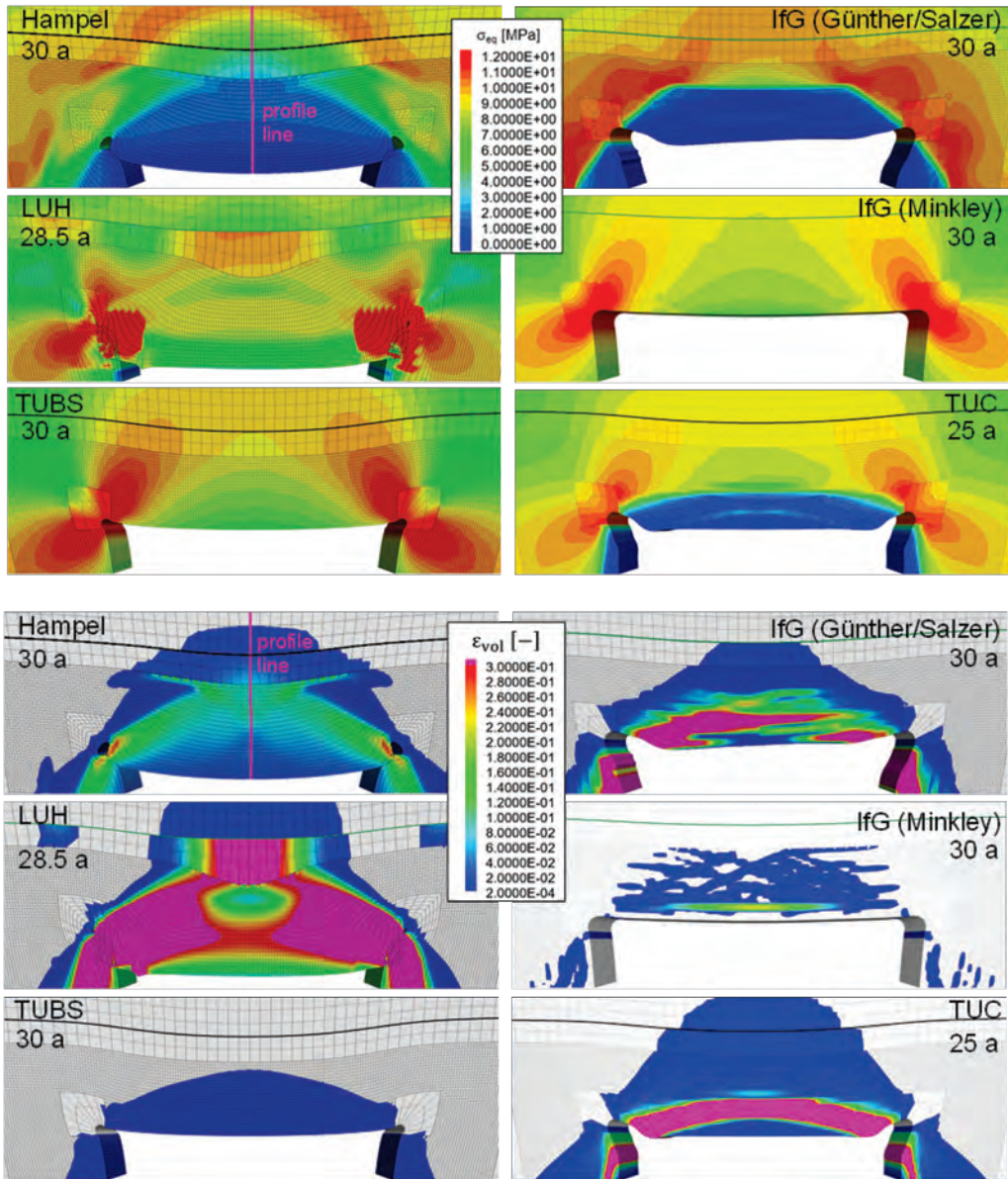
Figure 10: Comparison of von Mises equivalent stresses (top) and damage-related dilatancies (bottom) in a section above the ceiling of the main drift in VDII after 25 to 30 years.
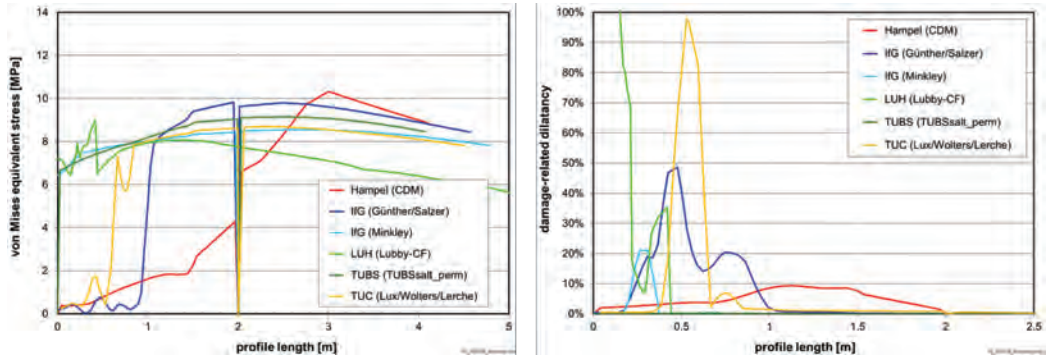
Figure 11: Comparison of von Mises equivalent stresses (left) and damage-related dilatancies (right) along a vertical profile line above the ceiling of the main drift in VDII (pink lines in Figure 10) after 30 years. The abscissa is recalculated to the undeformed model for a better comparison of the curves. The remaining differences underline the need for further research.
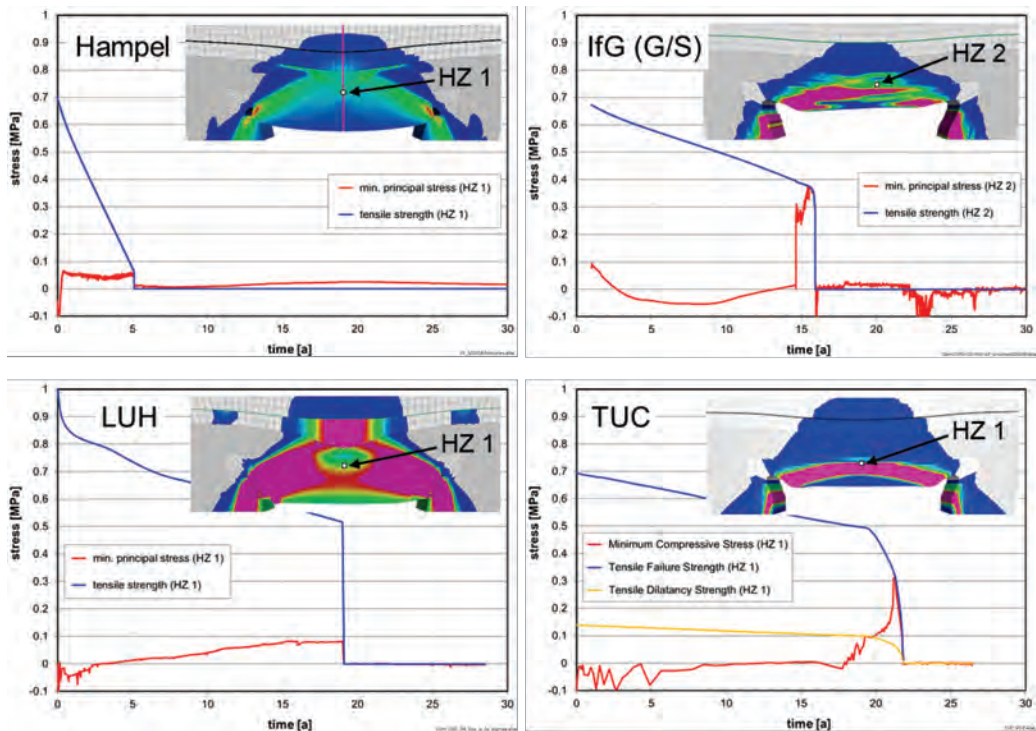
Figure 12: Tensile strength and minimum principal stress at marked history zones (HZ) above the main drift in VDII (cf. Figure 10) from simulations of the partners.

4   Conclusions

In joint project WEIMOS, each partner improved her or his geomechanical rock salt model based on laboratory tests performed by partners IfG, TUC, and Sandia in the following four research areas: 1) deformation behavior at low deviatoric stresses, 2) damage reduction and healing of rock salt, 3) deformation behavior resulting from tensile stresses, and 4) influence of inhomogeneities (layer boundaries, interfaces) on deformation. Impacts of progress in the

first three areas were demonstrated with simulations of two typical underground scenarios in rock salt. Virtual Demonstrator I (VDI) consists of a long open drift with a dam installed after 30 years in a section. Virtual Demonstrator II (VDII) reflects a typical underground scenario at the Waste Isolation Pilot Plant (WIPP) in New Mexico, USA, consisting of a vertical slice through two drifts and seven waste emplacement chambers. Each partner calculated both models with FLAC3D of Itasca Inc. and her or his constitutive model for rock salt. The results of the VDI and VDII simulations clearly underline that the higher creep rates at low deviatoric stresses in natural rock salt, as reliably measured during the WEIMOS project, must be considered in a constitutive model in order to get realistic results for predictions of displacements, convergences, stresses, as well as damage and dilatancy. These quantities would be greatly underestimated using a power law creep model with stress exponent 5 for describing steady-state creep in the whole stress range. Simulations of VDI show that damage reduction and healing in rock salt in the DRZ around a dam are modeled with the constitutive models based on an improved experimental basis. Simulations of VDII have demonstrated that tensile stresses have considerable influence on the evolution of damage and dilatancy. Tensile damage results in higher dilatancy and damage around underground openings and leads to tension failure, which can cause roof falls. Therefore, the influence of even low tensile stresses on deformation, shown in these examples, must not be neglected in model calculations.

Acknowledgements

References

DÜSTERLOH, U., HERCHEN, K., LUX, K.-H., SALZER, K., GÜNTHER, R.-M., MINKLEY, W., HAMPEL, A., ARGÜELLO, J.G. & HANSEN, F.D. 2015. Joint project III on the comparison of constitutive models for the mechanical behavior of rock salt, III. Extensive laboratory test program with argillaceous salt from WIPP and comparison of test results. L. Roberts, K. Mellegard & F.D. Hansen (eds.): The Mechanical Behavior of Salt; Proc. 8th Conference, South Dakota School of Mines & Technology, Rapid City, SD, USA, 26-28 May 2015, 13-21, Taylor & Francis Group, London, ISBN 978-1-138-02840-1.

HAMPEL, A. (2015): Description of damage reduction and healing with the CDM constitutive model for the thermo-mechanical behavior of rock salt. L. Roberts, K. Mellegard & F.D. Hansen (eds.): The Mechanical Behavior of Salt; Proc. 8th Conference, South Dakota School of Mines & Technology, Rapid City, SD, USA, 26-28 May 2015, 301-310, Taylor & Francis Group, London, ISBN 978-1-138-02840-1.

HAMPEL, A., GÜNTHER, R.-M., SALZER, K., MINKLEY, W., PUDEWILLS, A., LEUGER, B., ZAPF, D., STAUDTMEISTER, K., ROKAHR, R., HERCHEN, K., WOLTERS, R., LUX, K.-H., SCHULZE, O., HEEMANN, U. & HUNSCHE, U. 2010. Benchmarking of Geomechanical Constitutive Models for Rock Salt. Proc. 44th US Rock Mechanics Symposium, Salt Lake City, 2010, ARMA10-287, American Rock Mechanics Association.

HAMPEL, A., SALZER, K., GÜNTHER, R.-M., MINKLEY, W., PUDEWILLS, A., LEUGER, B., ZAPF, D., STAUDTMEISTER, K., ROKAHR, R., HERCHEN, K., WOLTERS, R. & LUX, K.-H. 2012. Joint Projects on the Comparison of Constitutive Models for the Mechanical Behavior of Rock Salt - II. Overview of the models and results of 3-D benchmark calculations. P. Bérest, M. Ghoreychi, F. Hadj-Hassen & M. Tijani (eds.): The Mechanical Behavior of Salt, Proc. 7th Conference, Paris, 16-19 April 2012, 231-240, Taylor & Francis Group (Balkema), London.

HAMPEL, A., GÜNTHER, R.-M., SALZER, K., MINKLEY, W., PUDEWILLS, A., YILDIRIM, S., ROKAHR, R., GÄHRKEN, A., MISSAL, C., STAHLMANN, J., HERCHEN, K. & LUX, K.-H. 2015. Joint project III on the comparison of constitutive models for the mechanical behavior of rock salt, I.

Overview and results from model calculations of healing of rock salt. L. Roberts, K. Mellegard & F.D. Hansen (eds.): The Mechanical Behavior of Salt, Proc. 8th Conference, South Dakota School of Mines & Technology, Rapid City, SD, USA, 26-28 May 2015, 349-359, Taylor & Francis Group, London, ISBN 978-1-138-02840-1.

HAMPEL, A., HERCHEN, K., LUX, K.-H., GÜNTHER, R.-M., SALZER, K., MINKLEY, W., PUDEWILLS, A., YILDIRIM, S., ROKAHR, R., MISSAL, C., GÄHRKEN, A. & STAHLMANN, J. 2016. Verbundprojekt Vergleich aktueller Stoffgesetze und Vorgehensweisen anhand von Modellberechnungen zum thermo-mechanischen Verhalten und zur Verheilung von Steinsalz. Final report (synthesis report & individual reports of the project partners in German), BMWi 02E10810-02E10860, link: https://www.tu-braunschweig.de/igb/forschung/salz.

HAMPEL, A., GÜNTHER, R.-M., SALZER, K., LÜDELING, C., MINKLEY, W., PUDEWILLS, A., YILDIRIM, S., STAUDTMEISTER, K., ROKAHR, R., GÄHRKEN, A., MISSAL, C., STAHLMANN, J., HERCHEN, K., DÜSTERLOH, U., LUX, K.-H., REEDLUNN, B., ARGÜELLO, J.G. & HANSEN, F.D. 2018. Joint Project III on the comparison of constitutive models for the mechanical behavior of rock salt: Modeling of the temperature influence on deformation at WIPP. S. Fahland, J. Hammer, F.D. Hansen, S. Heusermann, K.-H. Lux & W. Minkley (eds.): The Mechanical Behavior of Salt IX, Proc. 9th Conference, Hannover, 12-14 September 2018, 427-446, Bundesanstalt für Geowissenschaften und Rohstoffe (BGR), ISB 978-3-9814 108-6-0.

HERCHEN, K., POPP, T., DÜSTERLOH, U., LUX, K.-H., SALZER, K., LÜDELING, C., GÜNTHER, R.-M., RÖLKE, C., MINKLEY, W., HAMPEL, A., YILDIRIM, S., STAUDTMEISTER, K., GÄHRKEN, A., STAHLMANN, J., REEDLUNN, B. & HANSEN, F.D. 2018. WEIMOS: Laboratory investigations of damage reduction and creep at small deviatoric stresses in rock salt. S. Fahland, J. Hammer, F.D. Hansen, S. Heusermann, K.-H. Lux & W. Minkley (eds.): The Mechanical Behavior of Salt IX, Proc. 9th Conference, Hannover, 12-14 September 2018, Bundesanstalt für Geowissenschaften und Rohstoffe (BGR), ISB 978-3-9814 108-6-0.

HOU, Z., WOLTERS, R., DÜSTERLOH, U., ROKAHR, R., ZAPF, D., SALZER, K., GÜNTHER, R.-M., MINKLEY, W., PUDEWILLS, A., HEEMANN, U., SCHULZE, O., ZETSCHE, F. & HAMPEL, A. 2007. Comparison of advanced constitutive models for the mechanical behavior of rock salt - results from a joint research project, II. Numerical modeling of two in situ case studies and comparison. K.-H. Lux, W. Minkley, M. Wallner, and H.R. Hardy, Jr. (eds.): The Mechanical Behavior of Salt, Proc. 6th Conference, Hannover, Mai 2007, 89–98, Taylor & Francis (Balkema), London.

ITASCA 2021. FLAC3D (Fast Lagrangian Analysis of Continua in 3 Dimensions), Itasca Consulting Group, Inc., Minneapolis, MN, USA, www.itascacg.com/flac3d.

KEFFELER, E.R., BUCHHOLZ, S.A. & SOBOLIK, S.R. 2021. Direct Shear Testing of Consolidated Artificial Clay Seams in Salt. ARMA 21-1566. Presented at 55th US Rock Mechanics/Geomechanics Symposium in Houston, Texas, USA, 20-23 June 2021.

LÜDELING, C., SALZER, K., GÜNTHER, R.-M., HAMPEL, A., YILDIRIM, S., STAUDTMEISTER, K., GÄHRKEN, A., STAHLMANN, J., HERCHEN, K., LUX, K.-H., REEDLUNN, B., SOBOLIK, S., HANSEN, F.D. & BUCHHOLZ, S.A. 2018. WEIMOS: Joint Project on further development and qualification of the rock mechanical modelling for the final HLW disposal in rock salt. Overview and first results on tensile stress modelling. S. Fahland, J. Hammer, F.D. Hansen, S. Heusermann, K.-H. Lux & W. Minkley (eds.): The Mechanical Behavior of Salt IX, Proc. 9th Conference, Hannover, 12-14 September 2018, 459-477, Bundesanstalt für Geowissenschaften und Rohstoffe (BGR), ISB 978-3-9814 108-6-0.

LÜDELING, C., GÜNTHER, R.-M., HAMPEL, A., SUN, J.Q., WOLTERS, R., DÜSTERLOH, U., LUX, K.-H., YILDIRIM, S., ZAPF, D., WACKER, S., EPKENHANS, I., STAHLMANN, J. & REEDLUNN B. 2022. WEIMOS: Creep of Rock Salt at Low Deviatoric Stresses. The Mechanical Behavior of Salt, Proc. 10th Conference, Utrecht, July 2022 (this volume).

MUNSON, D.E., FOSSUM, A.F. & SENSENY, P.E. 1989. Advances in resolution of discrepancies between predicted and measured in situ WIPP room closures. Sandia report SAND88-2948, Sandia National Laboratories, Albuquerque, NM, USA.

MUNSON, D.E., JONES, R.L., BALL, J.R., CLANCY, R.M., HOAG, D.L. & PETNEY, S.V. 1990. Overtest for Simulated Defense High-Level Waste (Room B): In Situ Data Report (May 1984 - February 1988). SAND89-2671. Sandia National Laboratories, Albuquerque, NM, USA.

REEDLUNN, B. 2018. Joint Project III on the comparison of constitutive models for the mechanical behavior of rock salt: Reinvestigation into isothermal room closure predictions at the Waste Isolation Pilot Plant. S. Fahland, J. Hammer, F.D. Hansen, S. Heusermann, K.-H. Lux & W. Minkley (eds.): The Mechanical Behavior of Salt IX, Proc. 9th Conference, Hannover, 12-14 September 2018, 447-458, Bundesanstalt für Geowissenschaften und Rohstoffe (BGR), ISB 978-3-9814 108-6-0.

REEDLUNN, B. 2022. A New Rock Salt Constitutive Model with Back Stress and Drag Stress Hardening. The Mechanical Behavior of Salt, Proc. 10th Conference, Utrecht, July 2022 (this volume).

SALZER, K., GÜNTHER, R.-M., MINKLEY, W., POPP, T., WIEDEMANN, M., HAMPEL, A., PUDEWILLS, A., LEUGER, B., ZAPF, D., STAUDTMEISTER, K., ROKAHR, R., HERCHEN, K., WOLTERS, R. & LUX, K.-H. 2012. Joint projects on the comparison of constitutive models for the mechanical behavior of rock salt – I. Overview of the projects, reference mine for 3-D benchmark calculations, in-situ measurements and laboratory tests. P. Bérest, M. Ghoreychi, F. Hadj-Hassen & M. Tijani (eds.): The Mechanical Behavior of Salt, Proc. 7th Conference, Paris, 16-19 April 2012, 221-230, Taylor & Francis Group (Balkema), London.

SALZER, K., GÜNTHER, R.-M., MINKLEY, W., NAUMANN, D., POPP, T., HAMPEL, A., LUX, K.-H., HERCHEN, K., DÜSTERLOH, U., ARGÜELLO, J.G. & HANSEN, F.D. 2015. Joint project III on the comparison of constitutive models for the mechanical behavior of rock salt, II. Extensive laboratory test program with clean salt from WIPP. L. Roberts, K. Mellegard & F.D. Hansen (eds.): The Mechanical Behavior of Salt; Proc. 8th Conference, South Dakota School of Mines & Technology, Rapid City, SD, USA, 26-28 May 2015, 3-12, Taylor & Francis Group, London, ISBN 978-1-138-02840-1.

SCHULZE, O., HEEMANN, U., ZETSCHE, F., HAMPEL, A., PUDEWILLS, A., GÜNTHER, R.-M., MINKLEY, W., SALZER, K., HOU, Z., WOLTERS, R., ROKAHR, R. & ZAPF. D. 2007. Comparison of advanced constitutive models for the mechanical behavior of rock salt – results from a joint research project. I. Modeling of deformation processes and benchmark calculations. K.-H. Lux, W. Minkley, M. Wallner, and H.R. Hardy, Jr. (eds.): The Mechanical Behavior of Salt, Proc. 6th Conference, Hannover, Mai 2007, 77–88, Taylor & Francis (Balkema), London.

SOBOLIK, S.R., KEFFELER, E.R., BUCHHOLZ, S.A., BORGLUM, S. & REEDLUNN, B. 2019. Shear Behavior of Bedded Salt Interfaces and Clay Seams. ARMA 19-040. Presented at 53rd US Rock Mechanics/Geomechanics Symposium in New York, NY, USA, 23-26 June 2019.

SOBOLIK, S.R., KEFFELER, E.R. & BUCHHOLZ, S.A. 2020. Shear Behavior of Artificial Clay Seams within Bedded Salt Structures. SAND2020-11959, Sandia National Laboratories, Albuquerque, NM, USA.

SOBOLIK, S.R., VIGNES, C., REEDLUNN, B., BUCHHOLZ, S.A. & KEFFELER, E.R. 2022. Mechanical Behavior of Bedded Salt Interfaces and Clay Seams Subjected to Shear and Its Importance to Repository Performance Assessment, The Mechanical Behavior of Salt, Proc. 10th Conference, Utrecht, July 2022 (this volume).

WOLTERS, R., SUN, J.Q., DÜSTERLOH, U., LUX, K.-H., GÜNTHER, R.-M., LÜDELING, C., HAMPEL, A., YILDIRIM, S., ZAPF, D., WACKER, S., EPKENHANS, I., STAHLMANN, J. & REEDLUNN, B. 2022. WEIMOS: Laboratory Investigation and Numerical Simulation of Damage Reduction in Rock Salt. The Mechanical Behavior of Salt, Proc. 10th Conference, Utrecht, July 2022 (this volume).

Investigation of the impact of an additional monitoring level above the disposal level in a radioactive waste repository in rock salt

Johann Arne Othmer[1], Jörg Feierabend[1], Karl-Heinz Lux[1], Ralf Wolters[1]*

[1]Chair for Geomechanics and Multiphysics Systems, Clausthal University of Technology, Germany

* johann.arne.othmer@tu-clausthal.de

ABSTRACT: The impact of an additional level for monitoring purposes in a repository for radioactive waste in rock salt mass is investigated. In order to be able to simulate the complex interactions of rock salt, crushed salt, salt concrete and the waste containers, multiphysical simulations were carried out based on a further development of the FLAC3D and TOUGH2 coupled simulator FTK 3.0 with a fully coupled consideration of the geomechanically repository system behavior. Based on the multiphysical simulations for a 1- and 2-level repository mine, difference plots for the dilatancy, porosity and equivalent stress were created, which show the spatial and temporal differences. On the basis of these difference plots, a first characterization of the spatial and temporal impact of an additional monitoring level was carried out.

1   Introduction

The possibility of monitoring the safety-relevant state variables of the geological and geotechnical barriers of a deep geological repository for radioactive heat-generating waste represents a possible information basis for decision-making during the operating and monitoring phase of a repository. Most participants of the stakeholder engagement of the project Modern2020 agreed that monitoring data could play an important role in supporting the dialogue between technical experts and local stakeholders; it could offer the opportunity for local stakeholders to closely follow and check the implementation and performance of the geological repository. This would have the potential to support a long-term dialogue between technical experts and local stakeholders, through which further confidence and trust could be built, White & Scourfield (2019).

Long-term monitoring of a deep geological repository places high demands on the robustness of the measurement technology. With regard to the lifetime of the measurement technology over several decades, however, there are deficits, table 1. In the experiments listed in table 1, primarily classical sensors were used to monitor the pore pressure and the total pressure. In addition, sensors for monitoring the relative humidity, temperature and displacements were also installed. In some cases, optical sensors were also used to monitor the temperature.

In order to react to these deficits in measurement technology, Lux et al. (2017) made the proposal of a drive-over drift about 20 m above the emplacement drift for monitoring purposes. The basic implementation of the measurement technology is carried out during the storage of the waste containers in the emplacement drift. From the monitoring drift, monitoring boreholes can be used to create a connection to the emplacement drift, via which the maintenance or replacement of the defective measurement technology can take place even after the emplacement drift has been backfilled.

Table 1: Behavior of sensors for a selection of experiments at URLs. Acronyms: GTS: Grimsel Test Site; GCR: Galerie Concept Rigide; FEBEX: Full-Scale Engineered Barriers Experiment; SEALEX: Sealing Experiment; MPT: Multi-Purpose Test; POPLU: Posiva Plug; PROTOTYPE: The Prototype Repository, White & Scourfield (2019).

Partner	ANDRA	NAGRA AMBERG	IRSN	SKB	VTT	SKB
URL (country)	Bure (F)	GTS (CH)	Tournemire (F)	Äspö (S)	ONKALO (FIN)	Äspö (S)
Dismantled experiments	GCR	FEBEX				
Ongoing experiments			SEALEX	MPT	POPLU	PROTOTYPE
Duration (years)	6	18	6	5	5	8
Total number of sensors						
Wired/Wireless	-	176/0	149/105	194/33	132/0	328/0
Total/Number of Failed Sensors	134/9	176/108	149/113	277/99	132/20	328/125
% survival rate	93%	39%	24%	56%	85%	61%

In addition, an evidence dependent enlargement can be carried out via additional boreholes. A drive-over drift above the emplacement drift is in principle not a new idea, the use of a drive-over drift for exploration or ventilation purposes was already considered at the planned Gorleben and Konrad repository mines, BfS (2015); BMWi (2008). In order to reduce the penetration of the geological barrier by the monitoring drift, the monitoring drift should be arranged perpendicular to the emplacement drift. The monitoring boreholes may perhaps have a planned diameter of around one meter or even more, which is intended to ensure the accessibility of the measurement technology. These adjustments to the repository concept are intended to enable the monitoring of the repository for decades using the current state of the art measurement technology.

However, the concept of the monitoring drift is related by an additional intervention in the integrity of the geological barrier of the deep geological repository. Especially with the time aspect this intervention in the integrity of the geological barrier and the possible influence on the geotechnical barriers must be examined more closely. First numerical investigations on the coupled thermal-hydraulic behavior of the deep geological repository have shown that the monitoring boreholes have a significant influence on the fluid dynamic processes, since large amounts of pore gas flow from the emplacement drift into the monitoring drift via the monitoring boreholes, backfilled with crushed salt (Lux et al. 2017).

Due to the additional intervention in the function of the safety-relevant geological barrier by the excavation of the monitoring drift and monitoring boreholes, the research question arises what influence this intervention may have on the safety-relevant state variables in the geological and geotechnical barriers in space and time and how this influence could be characterized. In order to characterize this influence, thermal-hydraulic-mechanically coupled simulations are carried out on a 1-level and a 2-level repository model. In addition, a method was developed to show this change in safety-relevant state variables in space and time, the difference plot.

2 Methodology

To answer the research question, two generic local models were set up, Figure 1. A generic local model consists an emplacement drift at a depth of 600 m with 11 containers; the dimensions of the containers correspond to a POLLUX-10 container. The container has a cylindrical shape and is approx. 5.5 m long and has a diameter of approx. 1.6 m, Amelung et al. (2004). The initial heat output of the container is 3.78 kW which corresponds to 0.7 times of the POLLUX-10. The backfill material consists of crushed salt and the sealing structure of salt concrete, local model 1. The second generic local model is supplemented by a monitoring drift and a monitoring borehole, local model 2. This monitoring drift and the monitoring borehole will be kept open for 100 years to monitor the backfilled emplacement drift. After 100 years of monitoring the monitoring borehole will be sealed with salt concrete and the monitoring drift will be backfilled with crushed salt.
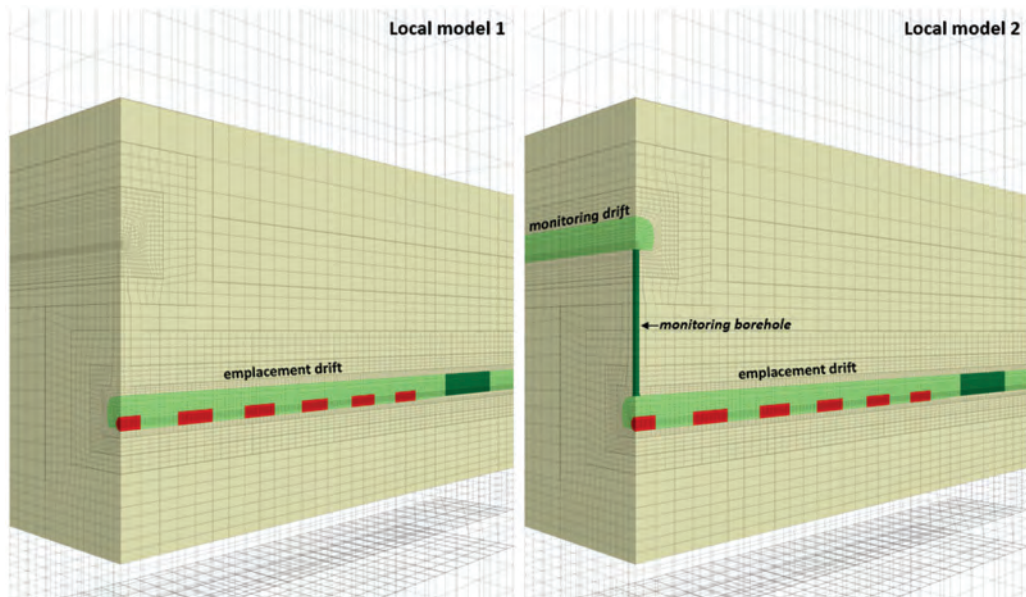
Figure 1: 3-dimensional representation of subareas of the two generic local models without monitoring drift (left) and with backfilled monitoring drift and sealed monitoring borehole (right). Beige = rock salt mass, light green = crushed salt, dark green = salt concrete, red = waste container.

To simulate the mechanical material behavior of rock salt mass and salt concrete, an extension of the elasto-viscoplastic constitutive model *Lux/Wolters/Lerche* was used, which is based on the constitutive model described in Lux et al. (2018). In this constitutive model, transient and stationary creep are taken into account in the sub-model modLubby for the viscoplastic strain rate. The stress dependency of the creep rates is modeled by using a combined exponential and power approach, by which higher creep rates are achieved with lower deviatoric stresses than choosing a pure power approach, such as with the Norton-Hoff model. Additionally, this constitutive model gives the opportunity to vary the creep rates at lower deviatoric stresses between the classic Lubby2 constitutive model (exponential approach) and the classic Norton-Hoff constitutive model (power approach). For the rock salt mass, in addition to the elasto-viscoplastic material behavior, the damage and healing of the rock salt mass were taken into account. In the case of salt concrete, on the other hand, transient creep processes as well as damage and healing were not taken into account. The mechanical material behavior of the crushed salt was simulated with the "CLubby" model. This constitutive model corresponds to the C-WIPP / TUC model from the KOMPASS project (Lerche 2021; Czaikowski et al. 2020).

The description of the viscous material behavior of the crushed salt is based on the constitutive model Lubby2 (Lux 1984). The mechanical material behavior of the container is assumed to be elastic and is described according to *Hooke's* law.

In addition to the mechanical material behavior of the repository system, the thermal and hydraulic processes are also taken into account. For the heat propagation in the generic local models, the thermal process conduction is taken into account. The description of the conduction is based on the *Fourier* approach. In addition to heat propagation, heat sources are also taken into account in the generic local model. The description of the fluid flow in the repository system is based on a *Darcy* flow model generalized to several phases. A more detailed description of the thermal and hydraulic models can be found in Zhao (2017). The material classes used with the associated constitutive models and the input parameters can be found in table 2.

Table 2: Representation of the material classes, associated constitutive models and input parameters of the two generic local models.

Materialgroup		Rock salt		
Constitutive modell		Lux/Wolters/Lerche		
Parameter	density ρ	2170 kg/m^3	a_9	0.577
	Young's modulus E	25000 MPa	a_{10}	1 MPa^{-1}
	Young's modulus E_0	25000 MPa	a_{11}	1
	Young's modulus E_{vol}	2000 MPa	a_{15}	0.3
	Poisson - ratio ν	0.27	a_{12}	8
	$\bar{G}_k$	$2.8 \cdot 10^5$ MPa	C_0	1.933
	k_1	-0.13 MPa^{-1}	Dil_{int}	0.02
	b	-1	Dil_{max}	0.11
	$\bar{\eta}_k$	$4.8 \cdot 10^4$ $MPa \cdot d$	Dil_{min}	0.2
	k_2	-0.12 MPa^{-1}	fc_1	0 MPa
	$\bar{\eta}_m$	$2.02 \cdot 10^{14}$ $MPa \cdot d$	fc_2	0
	m	-0.18 MPa^{-1}	ft_1	5500 $MPa \cdot d$
	l	-0.05 K^{-1}	ft_2	13
	a	-1	n	12
	a_0	0.3	σ_{sut_ZF}	1 MPa
	a_1	0.7	σ_{sik_ZF}	0 MPa
	a_{1_2}	0.8	$\varepsilon_{vol\_iGR\_ZF}$	0
	a_2	11	$\varepsilon_{vol\_aGR\_ZF}$	0.04
	a_3	0.28	initial porosity ϕ_0	0.002
	a_4	0.85	initial permeability K_0	0 m^2
	a_{4_vol}	0.85	initial saturation level $S_{l,0}$	0.5
	a_5	0.065 MPa^{-1}	initial Biot - coefficient α_0	0.002997
	a_{5_vol}	0.05 MPa^{-1}	initial pore gas pressure P_g	σ_{ss}
	a_6	67 MPa	thermal expansion coefficient α_T	$4.20 \cdot 10^{-5}$ K^{-1}
	a_7	37 MPa	initial thermal conductivity λ_0	5.73 $W/(m \cdot K)$
	a_8	0.27 MPa^{-1}	initial specific heat capacity $C_{p,0}$	862 $J/(kg \cdot K)$
Materialgroup		Salt concrete		
Constitutive modell		Lux/Wolters/Lerche		
Parameter	density ρ	1970 kg/m^3	a_8	0.27 MPa^{-1}
	Young's modulus E	23900 MPa	a_9	0.577
	Young's modulus E_0	23900 MPa	a_{10}	1 MPa^{-1}
	Young's modulus E_{vol}	2000 MPa	σ_{sut_ZF}	1 MPa
	Poisson - ratio ν	0.28	σ_{sik_ZF}	0 MPa
	$\bar{\eta}_m$	$1.94 \cdot 10^{15}$ $MPa \cdot s$	$\varepsilon_{vol\_iGR\_ZF}$	0
	m	-0.18 MPa^{-1}	$\varepsilon_{vol\_aGR\_ZF}$	0.04
	l	-0.05 K^{-1}	initial porosity ϕ_0	0.002
	a	-1	initial permeability K_0	0 m^2
	a_4	0.85	initial saturation level $S_{l,0}$	0.5
	a_{4_vol}	0.85	initial Biot - coefficient α_0	0.002997
	a_5	0.065 MPa^{-1}	initial pore gas pressure P_g	0.1013 MPa
	a_{5_vol}	0.05 MPa^{-1}	thermal expansion coefficient α_T	$4.20 \cdot 10^{-5}$ K^{-1}
	a_6	67 MPa	initial thermal conductivity λ_0	5.73 $W/(m \cdot K)$
	a_7	37 MPa	initial specific heat capacity $C_{p,0}$	862 $J/(kg \cdot K)$

Materialgroup	Crushed salt			
Constitutive modell	CLubby			
Parameter	initial density ρ_0	$1660\ kg/m^3$	C_{2p}	0.2
	final density ρ_{end}	$2170\ kg/m^3$	C_3	0.165
	Young's modulus E_0	$650\ MPa$	β_1	3.6
	Poisson - ratio ν	0.27	β_2	1
	η_m	$2.02 \cdot 10^{14}\ MPa \cdot d$	compaction rate$_{max}$	$1.0 \cdot 10^{10}\ d^{-1}$
	m	$-0.18\ MPa^{-1}$	initial porosity ϕ_0	0.235
	l	$-0.05\ K^{-1}$	initial permeability K_0	$1.0 \cdot 10^{-13}\ m^2$
	a	-1	initial saturation level $S_{l,0}$	0.07
	c_m	8	initial Biot - coefficient α_0	1
	C_0	$1.85 \cdot 10^{-17}\ d^{-1}$	initial pore gas pressure P_g	$0.1013\ MPa$
	C_{1m}	$0.66\ MPa^{-1}$	thermal expansion coefficient α_T	$4.20 \cdot 10^{-5}\ K^{-1}$
	C_{1v}	$0.25\ MPa^{-1}$	initial thermal conductivity λ_0	$0.8\ W/(m \cdot K)$
	C_{2p}	151.9	initial specific heat capacity $C_{p,0}$	$862\ J/(kg \cdot K)$
Materialgroup	Container			
Constitutive modell	Elastic			
Parameter	density ρ	$7800\ kg/m^3$	initial saturation level $S_{l,0}$	0
	Young's modulus E	$210000\ MPa$	initial Biot - coefficient α_0	1
	Poisson - ratio ν	0.29	initial pore gas pressure P_g	$0.1013\ MPa$
	initial porosity ϕ_0	0.0001	thermal expansion coefficient α_T	$1.0 \cdot 10^{-7}\ K^{-1}$
	initial permeability K_0	$0\ m^2$	initial thermal conductivity λ_0	$50\ W/(m \cdot K)$
			initial specific heat capacity $C_{p,0}$	$450\ J/(kg \cdot K)$

For the multiphysical simulation of the generic local models, a coupling of the numerical simulators FLAC3D 7.0 and TOUGH3 was used, also called FTK 4.0 simulator. The original coupling of these two simulators is described in more detail in Lux et al. (2015). The FLAC3D 7.0 simulator is used to simulate the mechanical processes and the TOUGH3 simulator is used to simulate the thermal and hydraulic processes. Due to internal limitations within the simulators, a further development of the FTK simulator was carried out, which includes the adaptation of the coupling to the newest software versions FLAC3D 7.0 and TOUGH3. This allows to simulate models with a larger number of zones. With the help of this further developed FTK simulator, thermal-hydraulic-mechanically coupled simulations were carried out.

In order to characterize more closely the safety-related influence of the monitoring drift in space and time, exemplary difference plots for safety-relevant state variables are created on the basis of the generic local models. In order to make this possible, both generic local models must have the same discretization, since the difference in a safety-relevant state variable of local model 1 and local model 2 in space and time can be formed for each zone and each grid point. The difference is formed by subtracting the state variable of the zone of local model 2 from the corresponding zone of local model 1. These differences can be assigned to the respective zones or grid points in a generic local model and thus displayed. In this way, the influence resulting from the monitoring drift can be represented in the form of the difference and characterized spatially and temporally.

3   Results

The time indicated in the result illustrations relates to the time at which the emplacement level is completely backfilled and sealed (t = 0 a). After 100 years of elapsed time the monitoring borehole and drift will be also backfilled and sealed (t = 100 a), Figure 2. In order to characterize the influence of the monitoring drift on the geological and geotechnical barriers, the state variables dilatancy, porosity and equivalent stress are shown as examples of the difference plots in Figures 3 – 5. These figures show the spatial and temporal development of the differences in the respective state variables resulting from the monitoring drift. Negative values correspond to an increase in the state variable due to the additional monitoring level. Positive values correspond to a decrease in the state variable due to the additional monitoring level.
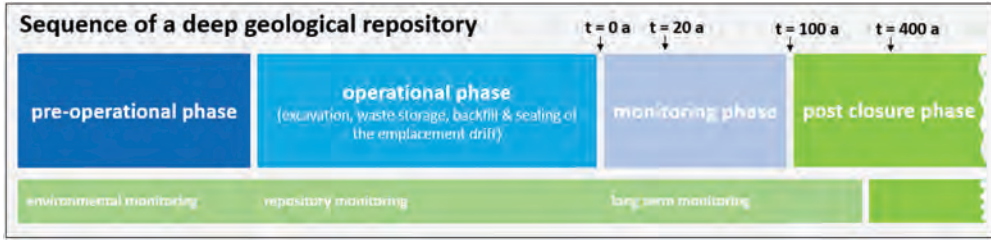
Figure 2: Sequence of a deep geological repository. Arrows indicate the points in time of the simulation results (Figure 3 to Figure 5).
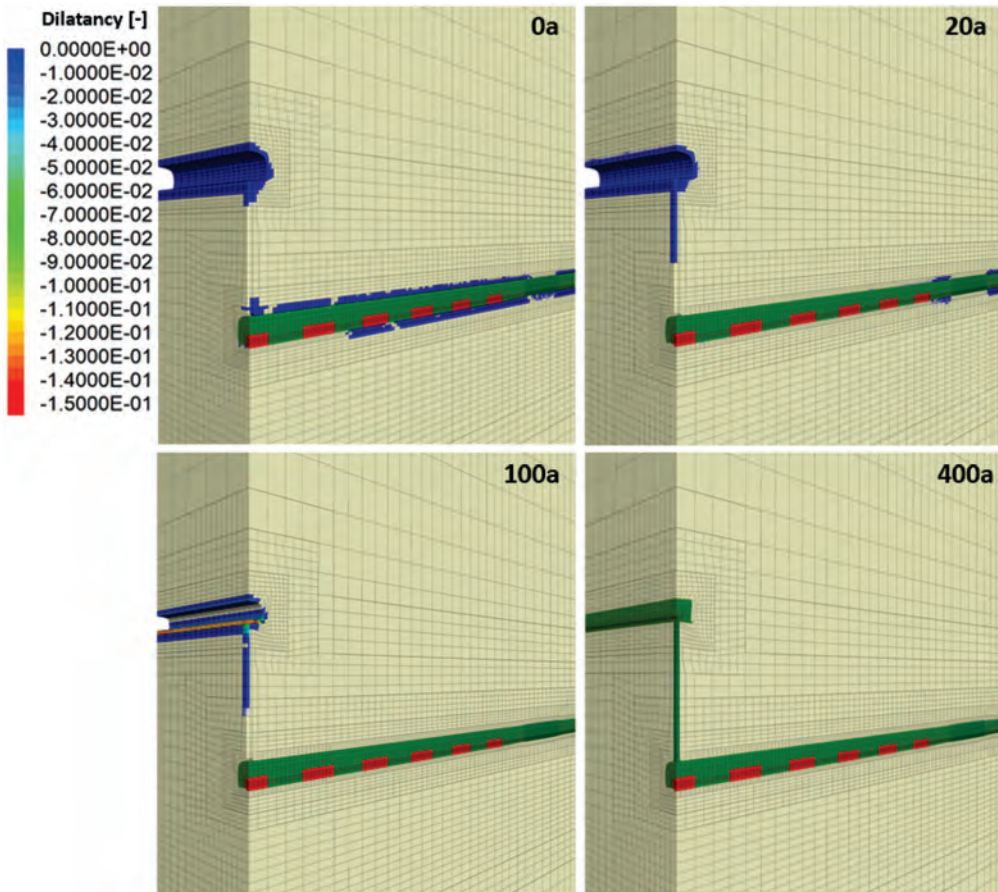
Figure 3: Representation of the differences in the dilatancy $\Delta\varepsilon_{vol}$ of the rock salt mass in space and time resulting from the additional monitoring drift. Negative values correspond to an increase in the dilatancy due to the additional monitoring level.

Figure 3 shows the difference plot of the dilatancy for rock salt mass in the period 0 – 400 years. At time 0 years, differences can be seen in the dilatancy along the contour of the monitoring drift as well as in the area of the crown and bottom in the emplacement drift. 20 years after closure, the differences in the dilatancy $\Delta\varepsilon_{vol}$ in the emplacement drift have almost receded. In the area of the monitoring drift $\Delta\varepsilon_{vol}$ has increased further and has also developed

spatially along the borehole. After 100 years there is no longer any difference in the dilatancy along the emplacement drift. In the monitoring drift, however, $\Delta\varepsilon_{vol}$ reaches its maximum of approx. -0.15. After 400 years of elapsed time, there is no longer any difference in the dilatancy to be observed, $\Delta\varepsilon_{vol}=0$.
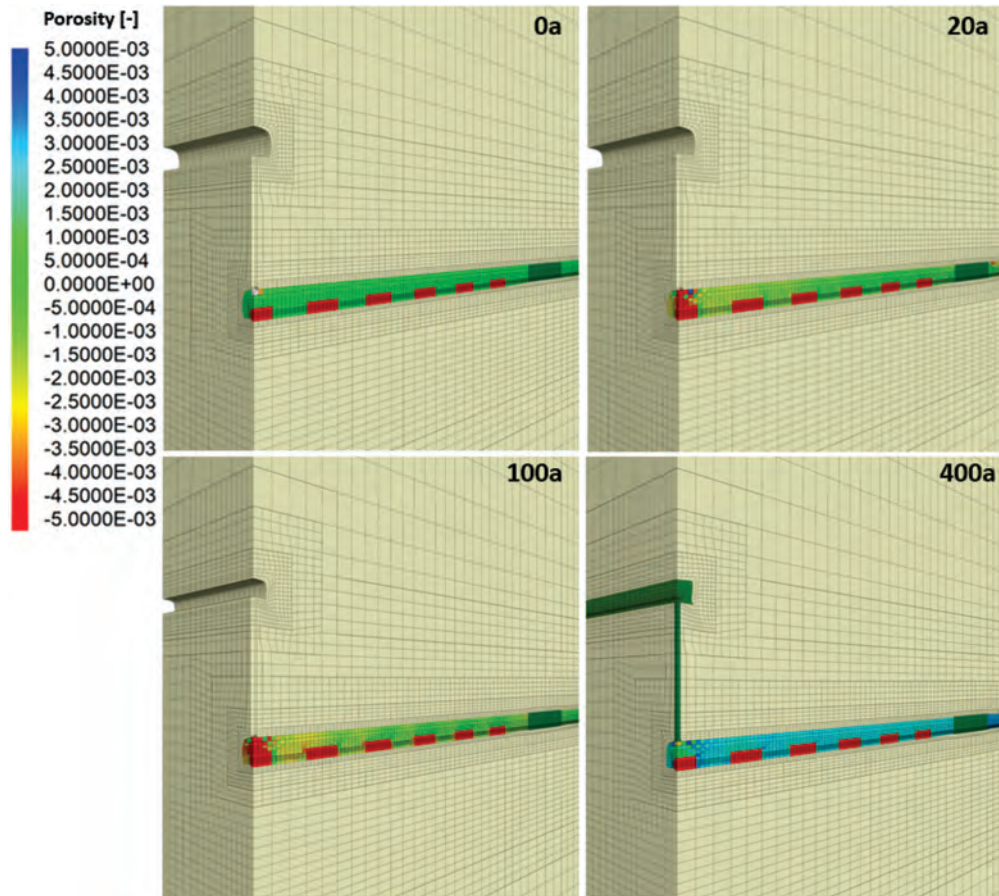

Figure 4: Representation of the differences in the porosity $\Delta\phi$ of the crushes salt of the emplacement drift in space and time resulting from the additional monitoring drift. Negative values correspond to an increase in the porosity due to the additional monitoring level.

Figure 4 shows the difference plot of the porosity in the crushed salt in the period 0 – 400 years. At the time of the backfill of the emplacement level (0 years), there were very slight negative differences in the porosity in the emplacement drift. The negative differences in porosity continue to increase over the next 100 years, especially in the area below the monitoring borehole, where $\Delta\phi$ reach values of approx. -0.005. Positive differences in porosity can be seen 300 years later, which means that the crushed salt is compacted faster due to the monitoring drift. Unfortunately, due to the limited simulation time, no statements can be made about the further development of the difference in porosity beyond 400 years of elapsed time.
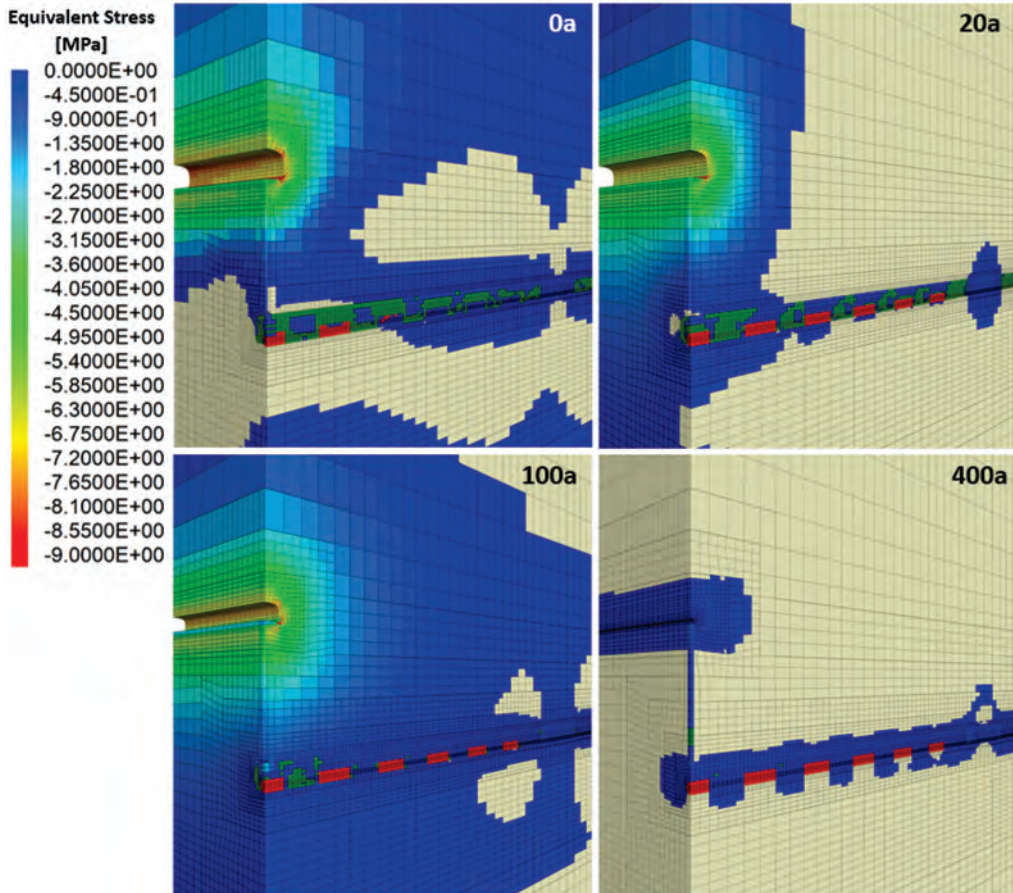
Figure 5: Representation of the differences in the equivalent stress $\Delta\sigma_v$ of the geological and geotechnical barrier in space and time resulting from the additional monitoring drift. Negative values correspond to an increase in the equivalent stress due to the additional monitoring level.

Figure 5 shows the difference plot of the equivalent stress in rock salt mass, crushed salt and salt concrete in the period 0 – 400 years. At 0 years, there are differences in the equivalent stress $\Delta\sigma_v$ in large areas, especially around the monitoring drift, but also in the crushed salt and the salt concrete at the level of the emplacement drift. 20 years later, $\Delta\sigma_v$ have decreased spatially around the emplacement drift, but negative differences are particularly evident in the crushed salt above the waste containers and in the salt concrete. After 100 years, a renewed spatial increase of $\Delta\sigma_v$ around the monitoring drift and emplacement drift can be determined. 400 years after the backfill of the emplacement level, a $\Delta\sigma_v$ of approx. -0.1 to -0.8 MPa can be found in and around the emplacement drift and the monitoring drift. Due to the limited simulation time, unfortunately no statements can be made about the further development of the difference in the equivalent stress beyond 400 years of elapsed time.

4   Conclusions

The difference plots presented in chapter 3 enable the spatial and temporal representation of the additional impacts on the geological and geotechnical barriers caused by the monitoring drift and the monitoring borehole for the in this case exemplary presented state variables. On the basis of these difference plots, an assessment of the additional impacts on selected state

variables of the geological and geotechnical barriers for repository modifications such as the monitoring drift in connection with a monitoring borehole in space and time can be carried out. From the difference plots in Figure 3 to Figure 5, it can be seen that the initial additional dilatancy resulting from the monitoring drift has receded after 400 years. The initially lower compaction in the crushed salt of the emplacement drift also shows after 400 years of elapsed time a higher degree of compaction than in a 1-level repository mine. The large-scale, higher equivalent stresses resulting from the monitoring drift recede significantly in the first 400 years and are then only present very locally in and around the emplacement and monitoring drift. These findings allow an initial assessment of the spatial and temporal influence of the monitoring drift and the future development of the repository system. However, further investigations have to be carried out, which also show the development of the repository over longer periods of time. In addition, the influence of the monitoring drift on the fluid flow has to be investigated, for which other methods are more suitable than difference plots. A safety-related assessment of the influence of the monitoring drift cannot be carried out with the previous results, but in connection with further knowledge about fluid flow processes in the emplacement and monitoring drift, difference plots could give an important contribution to the safety-related assessment of these influence in comparison to the 1-level repository mine as well as the illustration of impacts.

Acknowledgements

References

AMELUNG, P., BOLLINGFEHR, W., FILBERT, W., MÜLLER-HOEPPE, N., POLSTER, M., ZIEGENHAGEN, J., BEHRENS, J., KUTOWSKI, J. & SCHWARZ, T. 2004. Gegenüberstellung von Endlagerkonzepten in Salz und Tongestein (FKZ 02 E 9511) GEIST. Vergleich der technischen Endlagerkonzepte im Wirtsgestein Salz und Ton (A2).

BUNDESAMT FÜR STRAHLENSCHUTZ (BFS) 2015. Konrad - Anlagen unter Tage, 2021.

BUNDESMINISTERIUM FÜR WIRTSCHAFT UND TECHNOLOGIE (BMWI) 2008. Endlagerung hochradioaktiver Abfälle in Deutschland - Das Endlagerprojekt Gorleben.

CZAIKOWSKI, O., FRIEDENBERG, L., WIECZOREK, K., MÜLLER-HOEPPE, N., LERCH, C., EICKEMEIER, R., LAURICH, B., LIU, W., STÜHRENBERG, D., SVENSON, K., ZEMKE, K., LÜDELING, C., POPP, T., BEAN, J., MILLS, M., REEDLUNN, B., DÜSTERLOH, U., LERCHE, S. & ZHAO, J. 2020. KOMPASS. Compaction of crushed Salt for the safe Containment. GRS - 608,

LERCHE, S. 2021. 11th US/German Workshop on Salt Repository Research, Design, and Operation - The KOMPASS project Modelling related experimental aspects, online.

LUX, K.-H. 1984. Gebirgsmechanischer Entwurf und Felderfahrungen im Salzkavernenbau - Ein Beitrag zur Entwicklung von Prognosemodellen für den Hohlraumbau im duktilen Salzgebirge.

LUX, K.-H., LERCHE, S. & DYOGTYEV, O. 2018. Intense damage processes in salt rocks - a new approach for laboratory investigations, physical modelling and numerical simulation - Proceedings of the 9th Conference on the Mechanical Behavior of Salt (SaltMech IX), Hannover, Germany, 12-14 September 2018. pp. 15–35.

LUX, K.-H., RUTENBERG, M., SEESKA, R., FEIERABEND, J. & DÜSTERLOH, U. 2015. Kopplung der Softwarecodes FLAC3D und TOUGH2 in Verbindung mit in situ-, laborativen und numerischen Untersuchungen zum thermisch-hydraulisch-mechanisch gekoppelten

Verhalten von Tongestein unter Endlagerbedingungen. Teil II: Physikalische Modellierung, Kopplung von FLAC3D und TOUGH2 sowie numerische Simulationen. Förderkennzeichen:

LUX, K.-H., WOLTERS, R., ZHAO, J., RUTENBERG, M., FEIERABEND, J. & PAN, T. 2017. TH2M-basierte multiphysikalische Modellierung und Simulation von Referenz-Endlagersystemen im Salinar- und Tonsteingebirge ohne bzw. mit Implementierung einer Möglichkeit für ein direktes Monitoring des längerfristigen Systemverhaltens auch noch nach Verschluss der Einlagerungssohle. Ein Beitrag zur Verbesserung der Robustheit von Sicherheitsfunktionen mit sehr hoher Relevanz im Hinblick auf die Entwicklung von Bewertungsgrundlagen zum Vergleich von Entsorgungsoptionen.

WHITE, M. & SCOURFIELD, S. 2019. Deliverable D6.5: Modern2020 Project Synthesis Repository Monitoring: Strategies, Technologies and Implementation. Work Package 6. Galson Sciences Limited.

ZHAO, J. 2017. Multiphysikalische Prozess- und Systemanalyse für geologische Tiefenlager im Tonsteingebirge in der Nachverschlussphase. Dissertation an der TU Clausthal. Schriftenreihe Lehrstuhl für Deponietechnik und Geomechanik, Institut für Deponietechnik und Geomechanik, Heft Nr. 22, Papierflieger Verlag GmbH, Clausthal-Zellerfeld.

Analyzing Field Data from the Brine Availability Test in Salt (BATS): A High-Resolution 3D Numerical Study

Richard S. Jayne[1]*, Kristopher L. Kuhlman[1]

[1] Sandia National Laboratories, United States

* rsjayne@sandia.gov

ABSTRACT: The disposal of heat generating nuclear waste is a worldwide concern. Salt formations have been investigated as candidate disposal host rocks for heat-generating nuclear waste for decades. However, brine availability is influenced by heat and can affect the evolution of a nuclear waste disposal facility in salt. For example, brine migration is a potential radionuclide transport vector and brine leads to corrosion of waste forms and waste packages. To better understand brine migration in heated salt, he US Department of Energy's generic disposal research campaign is conducting borehole heater experiments are being conducted underground at the Waste Isolation Pilot Plant (WIPP) near Carlsbad, New Mexico. A crucial component of this field test is utilizing numerical models to better understand the system and the data being collected. Meshing and modeling heated, multiphase flow in porous media is a complex and computationally demanding problem. Here we use Voronoi meshing to accurately reproduce the complex 3D geometry of the Brine Availability Test in Salt (BATS) heater test at WIPP. Voronoi elements guarantee accurate fluxes in finite volume simulations, and their distribution is optimized to allow efficient simulation of heat and brine migration during the heating/cooling cycles of the BATS 1a heater test.

1 Introduction

1.1 Background

The United States has investigated disposing of radioactive waste in geologic salt since the 1950s when Hess et al. (1957) recommended direct disposal of liquid reprocessing waste into salt caverns. Since, underground field studies have investigated phenomena that could occur in a mined repository in salt at several sites across the United States, including: Project Salt Vault (Bradshaw & McClain, 1971), Avery Island (Llewellyn 1978; Just 1978; Van Sambeek 1981), Deaf Smith (Pfeifle et al. 1983a; 1983b), and the Waste Isolation Pilot Plant (WIPP) (e.g., Munson et al. 1979a; Krause 1981; Stormont 1984; Molecke & Sorensen 1988; Krumhansl et al. 1991, Franckel et al. 1999; Hardy & Holcomb 2000), which is a deep geologic repository for non-heat generating transuranic defense waste near Carlsbad, NM.

Salt is a potentially effective disposal medium for heat-generating radioactive waste such as spent nuclear fuel due to its low permeability (Beauheim & Roberts 2002) to brine transport and high thermal conductivity relative to other candidate disposal media, such as clay or granite. While undisturbed rock salt has almost unmeasurably low porosity and permeability, upon drift or borehole excavation a damaged region develops surrounding the excavation (Borns & Stormont 1989). This disturbed rock zone (DRZ) around boreholes or access drifts introduces significant changes impacting the near-field transport of brine and gas through the salt (Stormont 1997). The mechanical damage is caused by stress concentration near the excavation, which leads to increased permeability and porosity of the salt through a network of induced fractures which provide high-permeability pathways for brine transport (Kuhlman et al. 2017). Since brine migration is a potential radionuclide transport vector, understanding and characterizing near-field conditions (i.e., DRZ) and processes is an important initial condition to assessing the long-term safety of the system. The development of the DRZ also leads to significant changes to the stress and pore pressure within the salt. Intergranular brine will

migrate towards the low-pressure drift or borehole via the new halo of connected porosity and permeability comprising the DRZ (Figure 1). The addition of heat from a waste package can liberate additional intra-crystalline brine: (1) high temperatures can cause decrepitation (i.e., rupture) of fluid inclusions (Roedder & Belkin 1979) and (2) an elevated temperature gradient drives fluid inclusions to migrate towards the heat source (Roedder & Belkin 1980). Once liberated from within crystals, this fluid becomes more mobile as inter-crystalline brine, which flows through new interconnected fracture network of the DRZ down a pressure gradient. These excavation- and heat-induced changes within the salt cause a near-excavation higher permeability pathway to allow inter- and intra-crystalline brine (enhanced from the introduction of heat) to migrate towards the excavation, leading to a complex short-term and near-field flow system.
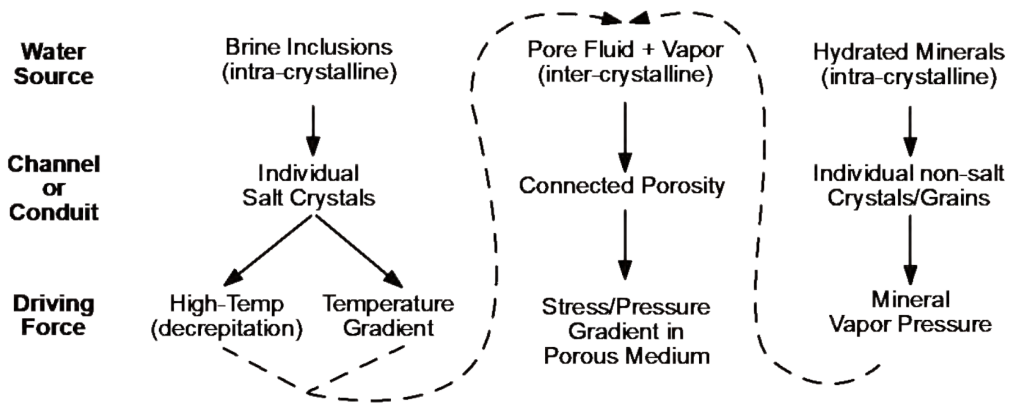

Figure 1. Relations between brine types and flow mechanisms in salt (adapted from Shefelbine (1982)).

1.2 Brine Availability Test in Salt (BATS)

To better quantify the effects of the DRZ and understand how higher temperatures impact brine availability and migration within salt, several heated brine migration tests have been implemented since the 1960s to investigate these engineered systems, including tests as part of Project Salt Vault (Bradshaw & McClain 1971), Avery Island (Llewellyn 1978; Just 1981; Van Sambeek et al. 1983), WIPP (Munson et al. 1997), and Asse II (BMWI 2008). These studies were each different, but they all highlighted the difficulty in studying brine availability and migration within salt and the heterogeneity associated with the DRZ around drifts. Understanding and quantifying heat and mass transport in salt during a salt heater test requires advanced understanding and subsequent complex numerical models of the thermal-hydrological-mechanical system.

The Brine Availability Test in Salt (BATS), hosted at the WIPP courtesy of the US Department of Energy (DOE) Office of Environmental Management, is part of the DOE Office of Nuclear Energy's generic (i.e., non-site-specific) disposal research program. BATS is a meter-scale borehole heater test, with the goals of: (1) improving the understanding of brine availability and brine chemistry in the DRZ for bedded salt; (2) collecting data for validating numerical models, populating constitutive models, and improving process model understanding; and (3) revitalizing in-house expertise at participating institutions in implementing *in situ* experiments in salt (Kuhlman et al., 2017).

The experimental setup for BATS includes two arrays of boreholes, each with a 4-m long, 12-cm diameter horizontal, central heater borehole surrounded by an array of thirteen sub-parallel sampling and monitoring boreholes. One array was heated, the other was monitored at

ambient temperature. In January 2020, the first phase of the BATS heating experiment began. The heater was set to a constant temperature of ~95°C for 28 days, the heater was then shut off and the salt was monitored while cooling for 13 days (Kuhlman et al. 2020). During the 41-day experiment temperature data and brine inflow rate were measured at a high frequency (15-minute averages), along with daily electrical resistivity tomography surveys, continuous monitoring of acoustic emissions, and high-frequency water isotopic and gas composition data by in-drift spectroscopy.

To further understand the field data collected during the BATS field test, we utilize a high-resolution, three-dimensional (3D) thermal-hydrological (TH) model to analyze the temperature distribution within the DRZ and intact salt at WIPP. The finite-volume code PFLOTRAN (Hammond et al., 2014) was used to simulate mass and heat transport within the two-phase (air & water) system. An additional challenge added to this modeling study is the geometric complexity of the BATS field experiment, which is difficult to represent with block hexahedral elements. While hexahedral meshes can be deformed to capture some of the configurational complexity of the field test, the boreholes and drift require some grid cells be badly scaled leading to non-orthogonality (i.e., element faces not perpendicular to the line connecting adjacent element centers) that can cause flux errors in finite volume meshes leading to mass no longer being conserved when fluid flows between elements. To avoid this potential numerical issue, here we use VoroCrust (Abdelkader et al. 2018; 2020), a fully automated Voronoi meshing software that has been adapted to create simulation grids for PFLOTRAN in complex geological systems.

2   Methodology

This study combines Voronoi meshing of the BATS field test and TH numerical modeling to investigate the influence of the fractured nature of the DRZ on brine flow and temperature migration within bedded salt. The current model represents the BATS field experiment, where a 69-cm long interval 2.75 meters deep into in the central borehole (Figure 2) is heated to a constant temperature while temperature is monitored at 66 thermocouples (72 total thermocouples in the heated array, 66 of which produced useable data) grouted into satellite boreholes around the heater (see Kuhlman et al. (2020) for sensor locations and detailed test and data descriptions). Not all 14 boreholes were explicitly meshed, but the permeability and porosity disturbance associated with each excavation were accounted for by superimposing decaying power-law relationship away from the drift (Figure 3). The thermal and hydrological properties of the salt (Table 1) are taken from Jayne & Kuhlman (2020), where a suite of 1D analytical solutions and TH models were utilized in conjunction with Markov chain Monte Carlo methods to constrain the reservoir parameters at the BATS field experiment by matching both temperature and brine flow field data.

Table 1. Model properties for the 3D BATS heater test simulation. Permeability and porosity vary by distance away from the drift and each borehole (see Figure 3).

Reservoir Parameters		Mualem – Van Genuchten Relative Permeability		Van Genuchten Capillary pressure	
Initial Temperature (°C)	29.5	λ	0.6	λ	0.6
Permeability (m²)	Varies	S_{lr}	0.2	S_{lr}	0.2
Porosity (-)	Varies	S_{ls}	1	α (Pa⁻¹)	10^{-6}
Thermal Conductivity W/m°C	Varies	S_{gr}	0.2	S_{ls}	0.999
Heat Capacity J/kg°C	620				

2.1 Voronoi Meshing

The workflow used here to create a Voronoi mesh for PFLOTRAN used two programs; LaGriT (LANL 2017) and Vorocrust (Abdelkader et al. 2018; 2020). LaGrit is a library of mesh generation and optimization tools in two and three dimensions that was used to create borehole- and drift-bounding surfaces for input into Vorocrust. Figure 2A illustrates the surfaces created in LaGriT, which consists of the BATS drift and a single heater borehole (the heater and packer extents are also defined in LaGriT). The model domain only includes a 5 m high by 0.5 m wide section of the drift because the area of interest is the salt surrounding the borehole, but the drift is included as a boundary condition. Vorocrust creates a 3D Voronoi mesh (Figure 2B). Figure 2C and 2D show slices down the center of the model domain parallel to the heater borehole, while Figure 2D is a zoomed-in section of the heater borehole to
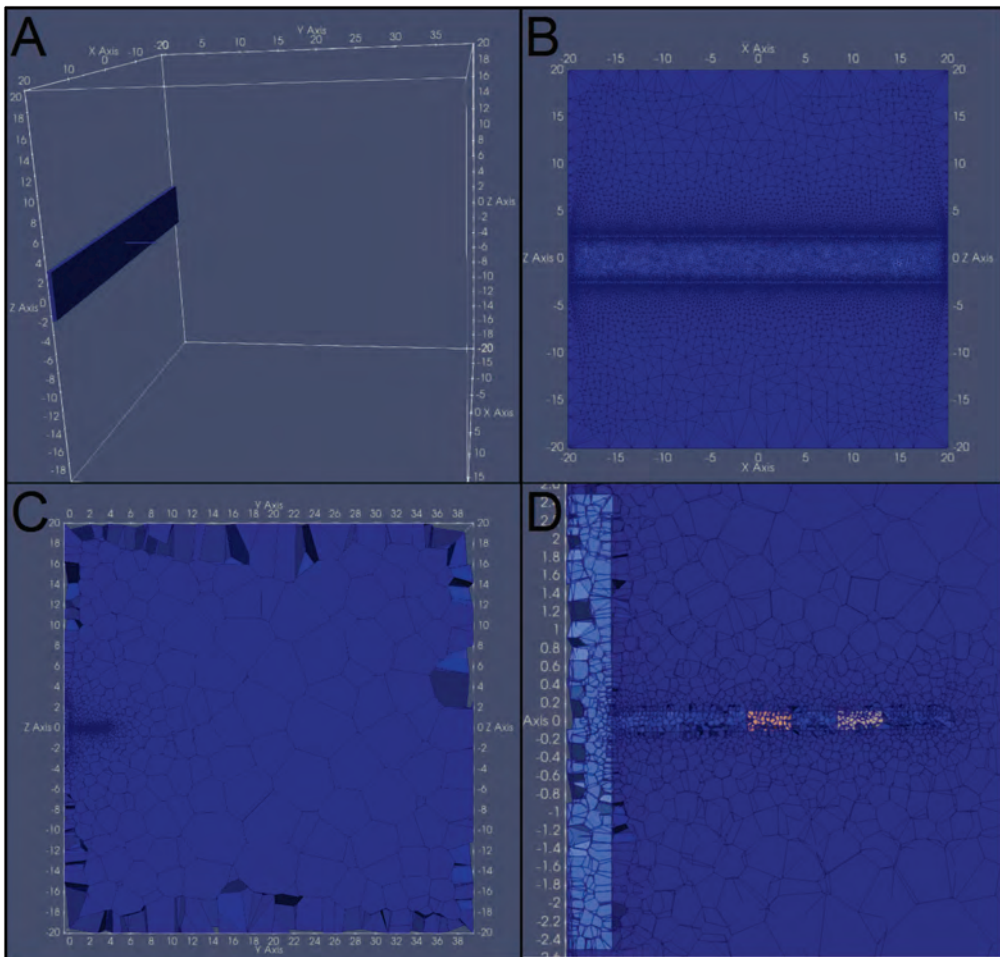
Figure 2. Illustrates the: (A) surface mesh created with LaGrit, featuring a drift and a single heater borehole, (B) an XZ view of the meshed model domain, highlighting mesh refinement around the drift shown in light blue (element boundaries are dark blue lines), (C) a YZ slice through the center of the model domain to highlight areas of high refinement (near the drift and borehole) and the coarsening of the mesh away from areas of interest, and (D) a zoomed in view of the drift, heater borehole, packer location (orange), and heater location (tan).

illustrate the fine mesh within and around the borehole (the smallest element has a volume of 6.0×10^{-6} m³). Vorocrust can resolve the mesh around possibly curved areas of interest while coarsening rapidly away from the area of interest, to reduce the total number of elements and computational burden. Voronoi elements, by construction, are the optimal elements for finite volume simulators, like PFLOTRAN. The current model domain presented is 40 m × 40 m × 40 m consisting of 135,810 elements. Unlike hexahedral meshes, Voronoi meshes do not have a fixed number of connections per element, which leads to a higher connectivity than structured meshes, resulting in more poorly conditioned residual matrices. To address this issue, we used a constrained pressure residual pre-conditioner, which aids with the added numerical challenges associated with a Voronoi mesh (Park et al. 2021).

2.2 DRZ Permeability and Porosity

While thermal, hydrological, and mechanical properties of bedded salt have been studied extensively at the WIPP site and previous salt underground research laboratories, the steep spatial gradient of state variables and material properties across the DRZ (e.g., the pores are air-filled at atmospheric pressure in the drift and brine-filled to lithostatic pressure in far field, as little as 5 excavation radii away – Beauheim & Roberts 2002) makes accurate characterization and simulation of these regions difficult. In numerical studies it is difficult to constrain and/or define the DRZ and intact salt within the model domain and it is commonly handled by considering the DRZ and intact salt to be two separate domains with a sharp boundary between the two. Here we assume that the transition from DRZ to intact salt is gradual and is defined by a decaying power law relationship. Figure 3A illustrates how permeability decays away from the drift by $k = k_0 \left[\frac{r}{r_0}\right]^{-7.5}$, where k is permeability [m²] and k_0 is maximum permeability at the excavation boundary (10^{-14} m²), r is distance from the excavation [m], and r_0 is the excavation radius (drift radius is 2.5 m, borehole radii were 6 and 2.5 cm). The permeability of any element in the model domain was then a superposition of power-law distribution contributions from the drift and all 14 boreholes, based on the distance from each excavation to the element. Similarly, porosity decays away from the drift and borehole (Figure 3B), which is defined by $\theta = \theta_0 \left[\frac{r}{r_0}\right]^{-3.5}$, where θ is porosity, and θ_0 is the highest porosity near the drift (10%).
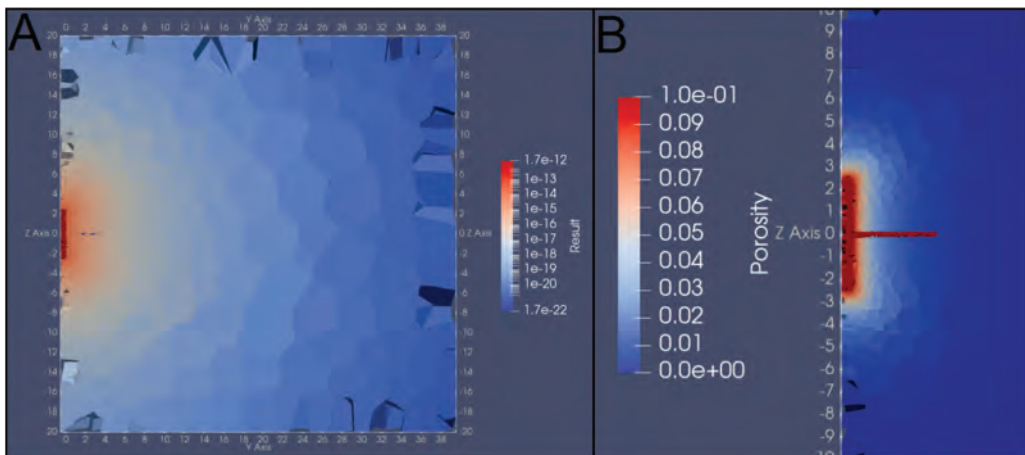

Figure 3. Average permeability and porosity distribution within the DRZ and intact salt. A and B) YZ slice through the center of the domain to show how average permeability (A) and porosity (B) decay away from the drift.

2.3   Thermal Conductivity

Intact salt has higher a thermal conductivity (>6 W m^{-1} K^{-1} at 20°C) than most other rocks and it is strongly temperature-dependent (Raymond et al. 2021; Kuhlman et al. 2020). As temperature increases the thermal conductivity decreases and this can play an important role in accurately modeling a salt heater test. To account for this temperature dependence, we have use a cubic polynomial temperature dependent thermal conductivity model show in Figure 4.

$$k_T(T, S_l) = k_{T,\text{dry}} + \sqrt{S_l}(k_{T,\text{wet}} - k_{T,\text{dry}})[1 + \beta_0 T + \beta_1 T^2 + \beta_3 T^3]$$

where the thermal conductivities at liquid saturation (S_l) of 1 and 0 are $k_{T,\text{wet}} = 7$ W m^{-1} K^{-1} and $k_{T,\text{dry}} = 4.5$ W m^{-1} K^{-1}. The three cubic polynomial coefficients used were -4.53398E-3, 1.41580E-5, and -1.94840E-8, based on fits against thermal conductivity data from BATS cores (Kuhlman et al. 2020).
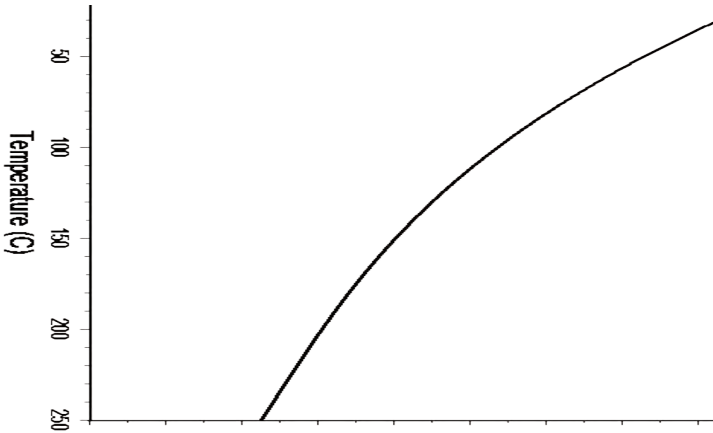

Figure 4. Temperature dependent thermal conductivity model (at full liquid saturation) for intact salt.

2.4   Initial Conditions

The computed initial pressure and saturation profiles for the model domain are shown in Figure 4. To create the initial distribution a preliminary simulation was run with the drifts and borehole set at atmospheric pressure and 99% gas saturation, and model domain was initialized at fully liquid saturated at 12 MPa. The borehole and drift conditions are held constant and the edges of the model domain at $z = 20$ m, $z = -20$ m, and $y = 39.5$ m are no-flow and insulated boundary conditions. To evolve representative initial pressure and saturation conditions for BATS, the preliminary simulation ran to 180 days, which is roughly the amount of time between the BATS boreholes being drilled and the beginning of the heater test, shown in Figure 4.

The results of this preliminary simulation are then used as initial conditions for the BATS heater test experiment. The simulator used for this study is PFLOTRAN (Hammond et al. 2014), an open source, state-of-the-art massively parallel subsurface flow and reactive transport code. The simulation covers 41 days, 28 days where a heater is run at constant temperature (~95°C) and 13 days after the heater is shutoff.
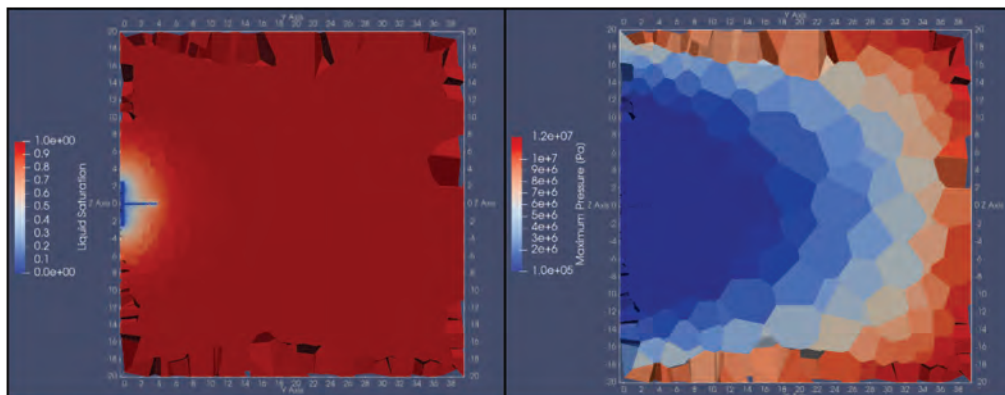
Figure 5. Initial conditions (end of preliminary simulation) for liquid saturation (left) and maximum pressure (right). The YZ slices are parallel to the heater borehole and perpendicular to the drift.

3   Results and Conclusions

The preliminary modeling of the BATS heater test using a 3D Voronoi mesh are illustrated by matching the temperature at six different thermocouples in Figure 6. The six thermocouples chosen were selected based on the proximity of an element center to the location of the thermocouples in the field. Figure 6 illustrates that four of the six thermocouples reproduce the temperatures measured in the field accurately, while the temperature at HE1-TC3 and HF1-TC2 is slightly overpredicted by the current model. While these results are preliminary, they do provide confidence in the current workflow and model conceptualization presented here. Further work on matching brine inflow and the variability of the exponents specifying the permeability and porosity distribution within the DRZ will further the robustness of the current workflow and the heuristic nature of numerical models.
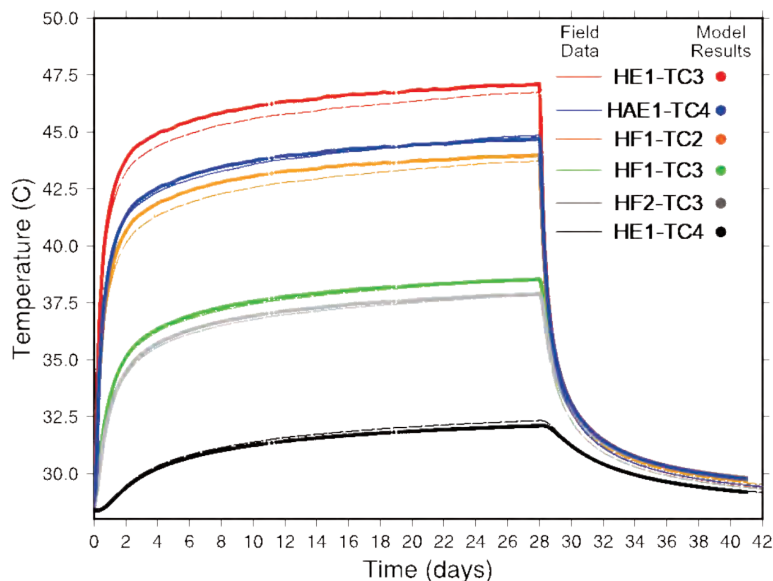

Figure 6. Numerical modeling results for measured temperature at six thermocouples during the BATS heater test.

Acknowledgements

References

ABDELKADER, A., BAJAJ, C.L., EBEIDA, M., MAHMOUD, A.H., MITCHELL, S.A., OWENS, J.D., & RUSHDI, A.A. 2018. Sampling conditions for conforming Voronoi meshing by the VoroCrust algorithm. Leibniz international proceedings in informatics 99.

ABDELKADER, A., BAJAJ, C.L., EBEIDA, M.S., MAHMOUD, A.H., MITCHELL, S.A., OWENS, J.D. & RUSHDI, A.A. 2020. VoroCrust: Voronoi meshing without clipping. ACM Transactions on Graphics (TOG) 39(3):1–16.

BEAUHEIM, R.L. & ROBERTS, R.M. 2002. Hydrology and hydraulic properties of a bedded evaporite formation. J. Hydrol., 259, 66–88.

BRADSHAW, R.L. & MCCLAIN, W.C. 1971. Project Salt Vault: A Demonstration of the Disposal of High-activity Solidified Wastes in Underground Salt Mines; Technical Report ORNL-4555; Oak Ridge National Laboratory: Oak Ridge, TN, USA.

FRANCKEL, C.T., HANSEN, F.D., KNOWLES, M.K., PATCHET, S.J. & REMPE, N.T. 1999. Geotechnical Perspectives on the Waste Isolation Pilot Plant (WIPP); Technical Report SAND99-0618C; Sandia National Laboratories: Albuquerque, NM, USA, 1999.

FEDERAL MINISTRY OF ECONOMICS AND TECHNOLOGY (BMWI) 2008. Final Disposal of High-Level Radioactive Waste in Germany - The Gorleben Project. Technical report, Federal Ministry of Economics and Technology, Berlin Germany.

GUILTINAN, E.J., KUHLMAN, K.L., RUTQVIST, J., HU M., BOUKHALFA, H., MILLS, M., OTTO, S., WEAVER, D.J., DOZIER, B. & STAUFFER, P.H. 2020. Temperature response and brine availability to heated boreholes in bedded salt. Vadose Zone Journal,19.

HAMMOND, G.E., LICHTNER, P.C. & MILLS, R.T. 2014. Evaluating the performance of parallel subsurface simulators: An illustrative example with PFLOTRAN. Water Resources Research 50:208–228.

HARDY, R.D. & HOLCOMB, D.J. 2000. Assessing the Disturbed Rock Zone (DRZ) Around a 655 Meter Vertical Shaft in Salt Using Ultrasonic Waves: An Update; Technical Report SAND2000-0668C; Sandia National Laboratories: Albuquerque, NM, USA, 2000.

HESS, H.H., ADKINS, J., HEROY, W., BENSON, W., HUBBERT, M., FRYE, J., RUSSELL, R. & THEIS, C. 1957. The Disposal of Radioactive Waste on Land, Report of the Committee On Waste Disposal of the Division of Earth Sciences; Technical Report 519; National Academy of Sciences-National Research Council Publication: Washington, WA, USA.

JAYNE, R.S. & KUHLMAN, K.L. 2020. Utilizing Temperature and Brine Inflow Measurements to Constrain Reservoir Parameters During a Salt Heater Test. Minerals, 10.

JUST, R. 1981. Thermal analysis supporting the design of the Avery Island field experiments. Technical Report ORNL/ENG/TM-21; Oak Ridge National Laboratory: Oak Ridge, TN, USA.

KRAUSE, W. 1981. Laboratory-Scale Brine Migration Studies in Southeastern New Mexico Rock Salt; Technical Report RSI-0168; RE/SPEC: Rapid City, SD, USA.

KRUMHANSL, J., STEIN, C., JARRELL, G. & KIMBALL, K. 1991. Summary of WIPP Room B Heater Test Brine and Backfill Material Data; Technical report; Sandia National Laboratories: Albuquerque, NM, USA.

KUHLMAN, K.L., MILLS, M.M. & MATTEO, E.N. 2017. Consensus on Intermediate Scale Salt Field Test Design; Technical Report SAND2017-3179R; Sandia National Laboratories: Albuquerque, NM, USA, 2017.

KUHLMAN, K.L., MILLS, M.M., JAYNE, R.S., MATTEO, E.N., HERRICK, C., NEMER, M., HEATH, J., XIONG, Y., CHOENS, C. & STAUFFER, P. 2020. FY20 Update on Brine Availability Test in Salt; Technical Report SAND2020-9034R, Sandia National Laboratories, Albuquerque, NM, USA.

LLEWELLYN, G. 1978. Thermal responses in underground experiments in a dome salt formation. In Thermal Conductivity 15; Springer: Berlin, Germany, pp. 277–288.

LOS ALAMOS NATIONAL LABORATORY, 2017. Los Alamos grid toolbox, LaGriT.

MOLECKE, M.A. & SORENSEN, N.R. 1988. Retrieval and Analysis of Simulated Defense HLW Package Experiments at the WIPP. MRS Online Proc. Libr. Arch., 127.

MUNSON, D.E. & DAWSON, P. 1979. Constitutive Model for the Low Temperature Creep of Salt (with Application to WIPP); Technical Report SAND79-1853; Sandia National Laboratories: Albuquerque, NM, USA.

PARK, H.D., HAMMOND, G.E., VALOCCHI, A.J. & LAFORCE, T. 2021. Linear and nonlinear solvers for simulation multiphase flow within large-scale engineered subsurface systems. Advances in Water Resources, 156.

PFEIFLE, T.W., MELLEGARD, K.D. & SENSENY, P.E. 1983a. Constitutive Properties of Salt from Four Sites; Technical Report ONWI-314; RE/SPEC: Rapid City, SD, USA.

PFEIFLE, T.W., MELLEGARD, K.D. & SENSENY, P.E. 1983b. Preliminary Constitutive Properties for Salt and Nonsalt Rocks from Four Potential Repository Sites: Technical Report; Technical Report ONWI-450; RE/SPEC: Rapid City, SD.

RAYMOND, J., LANGEVIN, H., COMEAU, F. & MALO, M. 2021. Temperature dependence of rock salt thermal conductivity: Implications for geothermal exploration; Renewable Energy 184:26-35.

ROEDDER, E. & BELKIN, H. 1979. Application of studies of fluid inclusions in Permian Salado salt, New Mexico, to problems of siting the Waste Isolation Pilot Plant. In Scientific Basis for Nuclear Waste Management; Springer: Berlin, Germany, pp. 313–321.

ROEDDER, E. & BELKIN, H. 1980. Thermal gradient migration of fluid inclusions in single crystals of salt from the waste isolation pilot plant site (WIPP). In Scientific Basis for Nuclear Waste Management; Springer: Berlin, Germany, pp. 453–464.

SHEFELBINE, H.C. 1982. Brine Migration: A Summary Report; Technical Report SAND82-0152; Sandia National Laboratories: Albuquerque, NM, USA.

STORMONT, J.C. 1984. Plugging and Sealing Program for the Waste Isolation Pilot Plant; Technical Report SAND84-1057; Sandia National Laboratories, Albuquerque, NM, USA.

STORMONT, J. 1997. In situ gas permeability measurements to delineate damage in rock salt. Int. J. Rock Mech. Min. Sci., 34, 1055–1064.

STORMONT, J., HOWARD, C. & JJK, D. 1991. Changes in Rock Salt Permeability Due to Nearby Excavation. Technical Report SAND91-0269, Sandia National Laboratories, Albuquerque, NM.

VAN SAMBEEK, L. 1981. Dome-Salt Thermomechanical Experiments at Avery Island, Louisiana. In The Technology of High-Level Nuclear Waste Disposal; United States Department of Energy: Washington, WA, USA, p. 100.

Preliminary study on thermomechanical modeling for correlation with microacoustic measurements in the Morsleben repository

Tuanny Cajuhi[1]*, Ralf Eickemeier[1], Sandra Fahland[1], Jan Thiedau[1], Diethelm Kaiser[1], Lars Ceranna[1]

[1]Federal Institute for Geosciences and Resources (BGR), Germany

* tuanny.cajuhi@bgr.de

ABSTRACT: Numerical modeling is an important tool for safety analysis related to radioactive waste disposal. It supports the understanding of strongly coupled processes occurring in the host rock such as excavation and backfilling. The present paper accounts for a thermomechanical modeling approach for simulating the periods before, during and after backfilling of cavity 1an located in the central part of the repository Morsleben. For modeling the behavior of saltcrete M2 used as backfilling material, we consider a simplified and an extended hydration model. The hydration models allow stiffness, temperature and shrinkage developments during backfilling. We find good agreement between the numerical results and the monitored temperature data. Furthermore, we correlate the computed displacements with acoustic emissions recorded in the field. The displacements and the acoustic emissions cloud show similar behavior before, during and directly after the backfilling. The differences at later periods after the backfilling are discussed and indicate further points for (i) differentiated evaluation of acoustic emissions data and (ii) model extension such as the modeling of dilatancy and the coupling with hydraulic effects.

1   Introduction

Numerical modeling is an important tool for safety analysis related to radioactive waste disposal. It supports the understanding of strongly coupled processes occurring in the host rock such as excavation and backfilling. Models can be improved when calibrated and validated with experimental observations. Furthermore, numerical results can help to interpret observations and lead to a more profound system understanding. Thermomechanical modeling is especially relevant to investigations of the salt rock response during loading and temperature changes that can affect the deformability and creep behavior of the rock. Moreover, cracks can nucleate due to e.g. anthropogenic activity such as excavation, which affects the initial condition of the rock, as well as during backfilling. When using cement-based materials such as saltcrete, backfilling causes a temperature rise due to the exothermic hydration (Fahland et al. 2005; Kaiser et al. 2013) and humidity increase in the vicinity of the backfilled cavity (Hesser & Spies 2007). Furthermore, saltcrete creeps like rock salt under a constant load and shrinks (Missal 2019). Shrinkage-induced cracks can impact the integrity of the rock and be path for contaminants. For this reason, its nucleation and behavior must be investigated in detail.

Backfilling activities have been carried out in the former salt mine Morsleben in Germany, which was used to deposit low and medium level radioactive waste (BfS 2016). For preventive stabilization and hydraulic retention, cavities of its central part have been backfilled with saltcrete M2 (BfS 2015). The effects of the backfilling have been monitored with temperature, deformation and acoustic emissions (AE) sensors (Hesser and Spies 2007; Kaiser et al. 2013). Figure 1 shows the considered section of the central part, its geological units and cavities. Detailed information on the geological profile is reported in Viola et al. (1997) and Fahland et al. (2005). This work focuses on cavity 1an, which was backfilled between 24.09.2003 and 25.03.2004 (Figs. 2 and 4). An increase of AE events has been reported. These events are related to property transitions and microcracks. Existing macro-cracks cannot be identified directly via AE, but rather large deformations, crack nucleation and propagation (Becker et al.

2010) are monitored and support the understanding of the crack behavior The combination of AE technique with further experimental measurements, e.g. temperature and displacement, and numerical methods (Kaiser et al. (2013); Hesser et al. (2015); Manthei & Plenkers (2018)) enables a more detailed and quantitative process understanding.

Figure 1: Modeled units of the central part of the Morsleben repository in Germany. Backfilling of cavity 1an occurred between 2003 and 2004. Liniensalz (z3LS), Orange- und Bank-/Bändersalz (z3OS-BK/BD), Hauptanhydrit (z3HA) and other cavities (c) are found in the direct vicinity of cavity 1an.

In this work, we extend the thermomechanical model presented in Fahland et al. (2005) and investigate its response with respect to the monitored temperature and AE measurements before, during and after backfilling. The model extension consists of accounting for the hydration and its effects on the stiffness development, temperature and deformation. We consider a macroscopic, coupled thermomechanical model taking into account the excavation and the periods before, during and after backfilling. Finally, we identify the model limitations and possibilities for extension.

2   Governing equations

In the following, the governing equations of the thermo-mechanical framework are presented. The temporal evolution of the temperature (T) is modeled with the heat equation

$$\dot{T} - \frac{\lambda}{c\rho}\Delta T - \dot{q} = 0, \tag{1}$$

where λ is the heat conductivity, c is the specific heat capacity, ρ is the density and q is the generated heat per volume. The thermal strains (ε^{th}) are calculated with the thermal expansion coefficient α_T as $\varepsilon^{th} = \alpha_T T \delta_{ij}$.

The mechanical stress field is modeled with the momentum balance equation

$$\nabla \cdot \sigma + \rho g = 0, \tag{2}$$

with the contribution of the gravity vector g. In Eq. (2), the mechanical stress σ is computed via the constitutive relation $\sigma = E\varepsilon^{el}$, where E is the elastic modulus and ε^{el} corresponds to

the elastic strains. The total strain ε is given by $\varepsilon = \varepsilon^{el} + \varepsilon^{th} + \varepsilon^{cr} + \varepsilon^{sh}$, where ε^{cr} and ε^{sh} corresponds to the creep and shrinkage strains, respectively.

2.1 Additional constitutive relations

To model the creep behavior of the salt rock and to take into account the hydration process of the saltcrete, additional constitutive relations are used.

2.1.1 Creep of salt units

The Norton law (deviatoric temperature-dependent creep model) is used for computing the creep strains $\dot\varepsilon^{cr}$ as in the following

$$\dot\varepsilon^{cr} = A^* A_0 \exp\left(-\frac{E_A^S}{RT}\right)\left(\frac{\sigma_v}{\sigma^*}\right)^n, \tag{3}$$

where A^* is the dimensionless creep capability related to the reference value $A_0 = 0.18 d^{-1}$. $E_A^\sigma = 54\ kJ\ mol^{-1}$ is the activation energy, R is the universal gas constant, σ_v is the von Mises equivalent stress, $\sigma^* = 1\ MPa$ is the normalizing stress and n is the stress exponent.

2.1.2 Hydration models for saltcrete

In this work, we test a simplified and an extended hydration model. The models differ with respect to the computation of the elastic properties and plasticity. The attributes of each model are explained in the corresponding subsection, while the common formulation of both models (Rostásy & Onken 1992; DBE 2004) is presented in the following.

The hardening of the saltcrete is expressed through the degree of hydration α. The solidification starts at the minimum degree of hydration given by α_0 specific to each mixture. The reaction is completed once the mixture achieves a full degree of hydration $\alpha = 1$, i.e. when there is no available hydration water and the material stiffness is fully developed. The degree of hydration at the effective time or concrete age $\alpha(t_e)$ is computed through

$$\alpha(t_e) = \frac{q}{q_{max}} \tag{4}$$

$$= exp\left[-\left(ln\left(1+\frac{t_e}{t_1}\right)\right)^b\right],$$

where q is the hydration heat with maximum value q_{max}. While t_1 and b are material dependent parameters, $t_e = \int_0^t exp\left[\frac{E_A(T(t'))}{R}\left(\frac{1}{T_0} - \frac{1}{T(t')}\right)\right] dt'$ denotes the effective time. The saltcrete activation energy E_A is computed by

$$E_A(T) = \begin{cases} E_A^0 + e_A(T_0 - T) & \text{if } T < T_o \\ E_A^0 & \text{if } T \geq T_o \end{cases}. \tag{5}$$

In Eq. (5), E_A^0 and e_A are material parameters used to describe E_A before and after the reference temperature $T_0 = 293K$ is reached.

The volume of the mixture (unhydrated solid and water) reduces, i.e. shrinks, due to consumption of hydration water. This phenomenon is called autogenous shrinkage. The strains due to shrinkage ε^{sh} are obtained experimentally and fitted with $\varepsilon^{sh} = \alpha(t_e)\varepsilon^{sh}_{max}$ in analogy to Eq. 4. The incremental form is given by

$$\dot{\varepsilon}^{sh} = \frac{\partial \varepsilon^{sh}}{\partial t} = \frac{\partial \alpha(t_e)}{\partial t_e}\frac{\partial t_e}{\partial t}\varepsilon_{max}^{sh}. \tag{6}$$

2.1.2.1 Simplified hydration model (HydI)

In addition to the formulation presented, the elastic modulus E increases with the advancement of the hydration in analogy to Eq. 4 according to the simple relation

$$E = \alpha(t_e)E_{\alpha=1}, \tag{7}$$

which can be fitted with experimental data. The parameter $E_{\alpha=1}$ corresponds to the ultimate elastic modulus of the fully hydrated saltcrete, i.e. when the hydration is completed.

2.1.2.2 Extended hydration model (HydII)

In the second hydration model (HydII), the stages before and after solidification starts are differentiated (Rostásy & Onken 1992, Faust et al. 2021). The elastic modulus E and Poisson's ratio v are computed as follows

$$E = \begin{cases} E_{liq} = 3K_{liq}(1-2v_{liq}) & \text{if } \alpha \le \alpha_o \\ E_{liq} + (E_{\alpha=1} - E_{liq})h^{\alpha_h} & \text{if } \alpha > \alpha_o \end{cases} \tag{8}$$

$$v = \begin{cases} v_{liq} & \text{if } \alpha \le \alpha_o \\ v_{liq} - \frac{E}{6\left(K_{liq}+\left(\frac{E_{\alpha=1}}{3(1-2v_{\alpha=1})}-K_{liq}\right)h^{\alpha_h}\right)} & \text{if } \alpha > \alpha_o \end{cases} \qquad \text{where } h = \left(\frac{\alpha-\alpha_0}{1-\alpha_0}\right). \tag{9}$$

The parameters E_{liq} and v_{liq} correspond to the liquid properties of the unhydrated concrete. For this reason, E_{liq} is expected to be very small and $v_{liq} \rightarrow 0.5$. Although the influence of E_{liq} and v_{liq} is negligible, their introduction enables to model a continuous transition between the liquid and solid stages, which is of advantage for the numerical solution. The further parameters are obtained experimentally from tensile tests (DBE 2004). The equations are complemented with the plastic flow condition and tension cut-off. For that we utilize the Drucker-Prager yield criterion $f_y = a(\alpha)I_1 + \sqrt{J_2} - k(\alpha) = 0$ with the first $I_1 = \sigma_{ii}$ and second $J_2 = 0.5\sigma_{ij}^{dev}\sigma_{ij}^{dev}$ stress invariants. The parameters evolve with the degree of hydration $a(\alpha) = a_{end}h^{\alpha_{DP}}$ and $k(\alpha) = k_{end}h^{\alpha_{DP}}$.

The tensile f_t and compressive f_c strengths are obtained experimentally and used to compute $a_{end} = \frac{2}{\sqrt{3}}\left(\frac{f_c f_t}{f_c+f_t}\right)$ and $k_{end} = \frac{1}{\sqrt{3}}\left(\frac{f_c-f_t}{f_c+f_t}\right)$. The tension cut-off f_{tco} is activated once the solidification starts $f_{tco} = f_t h^{\alpha_{DP}}$. Accordingly, the yield criterion is extended to account for f_{tco} (Dolarevic & Ibrahimbegovic 2006).

2.2 Numerical solution

The equations are discretized and solved with the Finite Element implementation JIFE 6.1.2. JIFE is a Java based application for Interactive Nonlinear Finite-Element-analysis in MultiPhysics (Faust et al. 2021) developed for BGR. It provides modules for the calculation of geomechanical, thermomechanical and coupled hydromechanical analyses including several nonlinear material models.

3 Numerical simulations

3.1 Model setup and input parameters

The two-dimensional numerical domain presented in this section is based on Fahland et al. 2005. The domain of $620 \times 700 \ m^2$ depicted in Figure 1 is discretized with 6892 quadrilateral elements. Mechanical boundary conditions are imposed to avoid rigid body motion. A temperature gradient is obtained by imposing $T = 290.8 \ K$ and $T = 304.8 \ K$ at the upper and lower model boundaries, respectively. The initial modeled state represents the situation before excavation, hence with all cavities still parametrized like the respective surrounding salt unit, whose material properties are shown in Table 1. The density of the salt is selected as $\rho = 2200 \ kg/m^3$. Then, an instantaneous excavation is carried out followed by a period of 65 years of no load changes in the repository. After that, an instantaneous backfilling with saltcrete M2 is modeled. Note that the boundary nodes of the cavity match the nodes of the surrounding salt unit, i.e. they respond in the same manner. The material properties of the saltcrete were obtained from relevant literature (DBE 2004) and are summarized in Table 2.

Table 1: Material properties of the salt units (Fahland et al. 2005).

Modeled geological unit	Notation	Elasticity		Creep
		Young's modulus [GPa]	Poisson's ratio [-]	A*
Hutgestein (Cap rock)	cr	10	0.27	
Hauptanhydrit	z3HA	30	0.27	
Basal Anhydrit	z2BA	50	0.27	-
Anhydritmittel- und Schwadensalz	z3AM-SS	25	0.27	1/32
Orangesalz	z3OS	25	0.27	1/16
Orange- und Bank-/Bändersalz	z3OS-BK/BD	25	0.27	1/8
Liniensalz	z3LS	25	0.27	1/8
Carnallit	z3SF	25	0.27	10
Hauptsalz, stark verunreinigt durch Anhydrit	z2HS-z3HA	25	0.27	1/16
Hauptsalz	z2HS	25	0.27	1/16

Table 2: Material properties of saltcrete M2 and further constitutive specifications.

Constitutive model	Parameter	Value
Mechanics / Elasticity	ρ	1980 kg/m^3
	K_{liq}	1000 MPa
	ν_{liq}	0.499
	$E_{\alpha=1}$	15350 MPa
	$\nu_{\alpha=1}$	0.33
	α_h	0.667
Thermal	λ	1.14 W/mK
	$c\rho$	21.3125 Wd/m^{3}K
	α_T	4×10^{-5} K^{-1}
Hydration	a	0.66
	b	-1.3425
	t_1	3.2872 d
	q_{max}	1250 J
	α_0	0.263
	E_A	33.5 kJ/mol
	e_A	1.47 kJ/molK
	ε_{max}	-1.12×10^{-3}
Plasticity and tension cut-off (HydIII)	f_c	46.8 MPa
	f_t	2.95 MPa
	α_{DP}	1.5

3.2 General model behavior and comparison with monitored temperature

In the current model, the hydration is accounted explicitly, which enables the assessment of the stiffness development and temperature increase. In the following, the starting time ($t = 0$) refers to the beginning of the hydration. The hydration models HydI and HydII behave similarly with respect to the temperature evolution and shrinkage behaviors. Figure 2 shows the experimentally (exp) and numerically (sim) obtained temperature results in the cavity. The white line represents the approximate location of the sensor chain that monitored the temperature on site. The grid points of the model with positions near the measurement chain were chosen. Then, the experimental and numerical average values were calculated and plotted in the diagram. In the field, the backfilling has been carried out within 6 months in an incremental manner, i.e. the layers of backfilling material were placed one after another. In the numerical model, the backfilling is simulated instantaneously, i.e. the whole cavity is filled in one step, and the maximum temperatures develop at the center of the cavity as depicted in the snapshots of Fig. 2. The initial discrepancy between the results is related to the backfilling procedure. The results show good agreement with respect to the long-term behavior of the backfilling material in the cavity. In addition, the volumetric shrinkage response plotted in the secondary axis of Fig. 2 shows asymptotic long-term behavior ($\varepsilon^{sh} \rightarrow -0.001$) as expected once shrinkage stabilizes. The computed shrinkage shows good agreement with experimental results from literature (DBE 2004).

Once backfilling starts ($t = 0$), model HydI shows a stiffer response ($|u_{\mathrm{max}}| = 0.077 \times 10^{-3}\ m$) in comparison to HydII ($|u_{max}| = 0.13 \times 10^{-3}\ m$). This behavior is related to the elastic modulus, which is larger at the beginning of the hydration in the simplified model since the stages before and after solidification are not differentiated (Eqs. 7 and 8 for comparison). At later steps, the elastic moduli of both models evolve similarly. To take into account the largest deformations and stress development from the start of the hydration, we further describe the behavior of HydII. Once the temperature increases, the saltcrete expands. At the same time, the volume of the hydrating M2 decreases, i.e. shrinks. The maximum displacements are reached at the temperature peak (approximately $t = 28$ days), Fig. 3(a). Afterwards, contraction is induced both due to temperature decrease and shrinkage effects. This behavior is further observed later, e.g. at 20 years as depicted in Fig. 3(b), and is in agreement with the observed asymptotic shrinkage behavior reported in the diagram (Fig. 2). In addition, the maximum principal stresses are shown (Fig.3). The horizontal and vertical stresses are compressive inside the cavity. Positive stresses only develop in the normal direction of the 2D plain-strain model. These might be overestimated due to the chosen approach, i.e. the filled cavity has no resistance in the normal direction. The normal stresses reach the tension cut-off value after approximately 2 years and increase further in the subsequent years (Fig. 3(b)). Additional tests using HydII show a decrease of the maximum tensile stresses when no shrinkage is allowed ($\varepsilon^{sh} = 0$). After 28 days, compressive stresses cover a larger area inside the cavity, since the influence of the tensile stresses reduces, i.e. no shrinkage is taken into account. In the long-term, the maximum principal stress is approximately 5 % smaller in comparison to the models where shrinkage can develop.
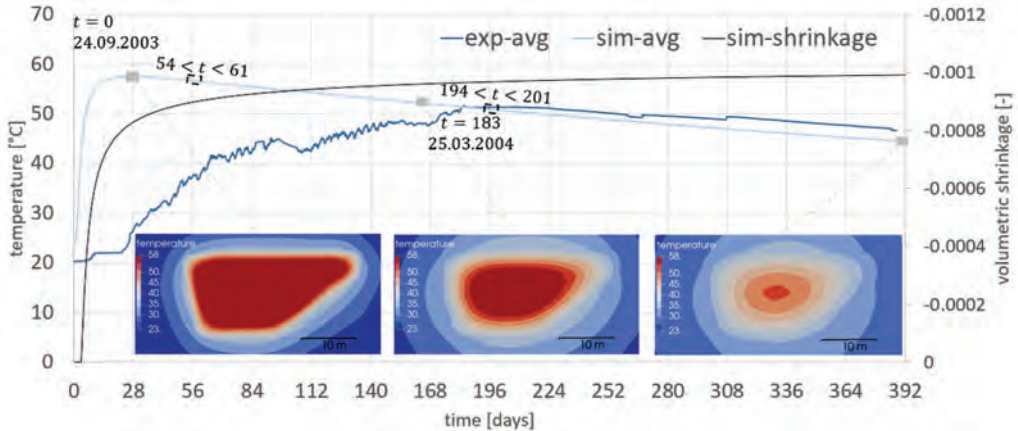
Fig. 2. Temperature evolution in the Cavity 1an. Experimental (dark blue) and numerical (light blue) results show good agreement with respect to the long-term behavior. Snapshots of the simulation results indicate the increase of temperature due to the backfilling. The backfilling starts on 24.09.2003 ($t = 0\ d$) and ends on 25.03.2004 ($t = 183\ d$). The maximum observed temperatures occur at approximately 28 days after the beginning of hydration. The advancement of the hydration reaction induces a decrease in temperature.

(a) 28 days after instantaneous backfilling   (b) 20 years after instantaneous backfilling
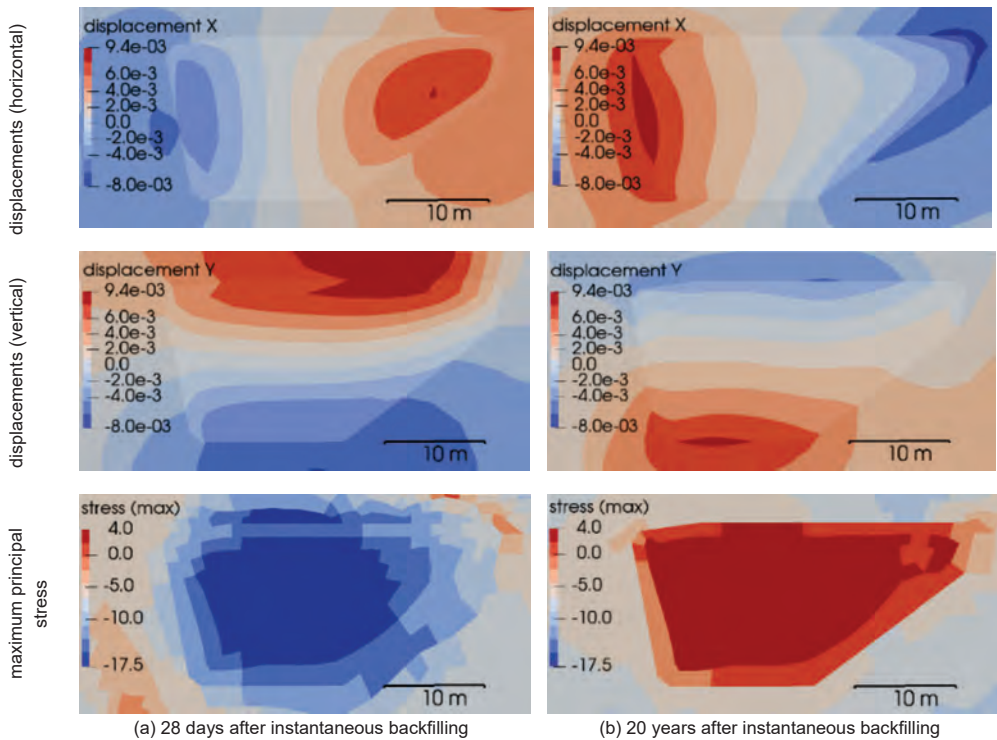
Fig. 3. Horizontal and vertical displacements [mm] and maximum principal stress distribution [MPa] after (a) 28 days and at (b) 20 years since instantaneous backfilling.

3.3 Comparison between monitored AE and numerical results

Before backfilling, the monitored AE activity near the cavity is very low. The cumulative events with magnitude larger than $0\ \mathrm{dB}$ and within 9 months are depicted in Fig. 4(a). A

snapshot of the numerical results directly before backfilling shows that the maximum displacements are very small $\approx -2.6 \times 10^{-9}\, m$ (4(c)). During backfilling, the AE activity increases by a factor of approximately 20 as shown in the cumulative results between 54 and 61 days after backfilling has started (Fig. 4(a) and Fig. 2 for referencing the dates). The displacements, especially the vertical component, increase considerably near the cavity and resemble the shape of the AE cloud (Fig. 4(b,c)). The slight shift of the maximum displacement concentration can be related to the backfilling strategy (instantaneous vs. incremental). The nearly synchronous increase of measured deformation and of AE activity has also been observed in Hesser et al. 2015. Immediately after backfilling ends, the AE activity reduces for 6 weeks (Fig. 4(a)). At the same time, the displacements decrease (Fig. 4(b,c)). Note that the displacements also shift away from the cavity similarly to the AE cloud. An increase of AE activity is reported at later times after the backfilling ends. This behavior can be related to stress redistribution and further, ongoing dilatancy in the cavity roof. The numerical model does not take this process into account. The magnitude of the events is expected to be relatively small in comparison to that observed during backfilling. However, it cannot be quantified with the current plots since the shown values start from a lower bound (0 dB) but are not limited by an upper bound. Experimental tests with saltcrete M2 at laboratory scale also shows small increase of AE activity at later times after hydration (Lay et al. 2021). Moreover, strong changes in the frequency-magnitude distribution (b-values) related to backfilling were observed and associated to the type of loading, time-dependency and heterogeneities, e.g. property transitions, of the salt rock (Köhler et al. 2009), and require another post-processing routine
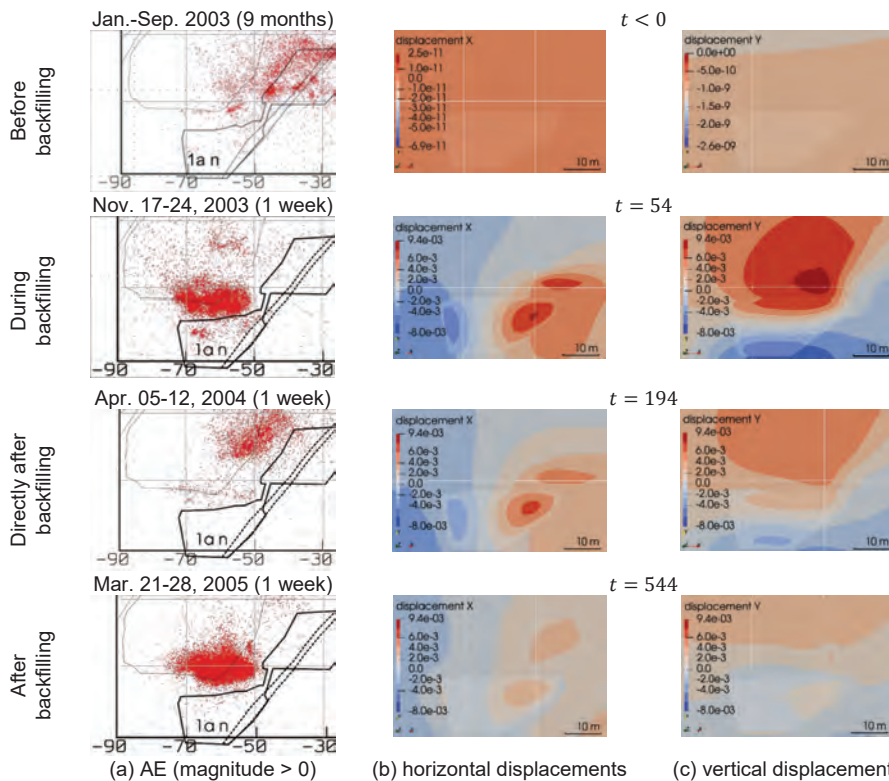

Fig. 4. (a) Monitored acoustic emissions and (b-c) calculated displacements before, during and after the backfilling. The size of the depicted sections is $60 \times 40\, m^2$. The experimental data section is slight rotated (15 degrees) in comparison to the model.

4   Conclusions and outlook

The present paper accounts for a thermomechanical modeling approach considering two hydration models that allow stiffness, temperature and shrinkage developments during backfilling. We model a two-dimensional section of the central part of the Morsleben repository consisting of salt rock, further geological units and cavities. The numerical setup considers the excavation and periods before, during and after backfilling. We focus on the backfilling of cavity 1an with saltcrete M2. This process is modeled instantaneously and the numerical results show satisfactory agreement with the monitored temperature. The consideration of an incremental backfilling approach might reduce the slight temperature differences between the field and numerical data, however this would require a detailed protocol of the backfilling activities and used mixtures. The shrinkage shows asymptotic behavior and is comparable to data provided by the literature. The computed deformation behavior shows good qualitative agreement with the monitored AE data before and during backfilling. The model confirms the increase of AE activity due to an increase of the deformation and in this way assists in understanding the processes and crack nucleation taking place in the rock. The increase of AE at later stages after the end of the backfilling is possibly related to stress redistribution and further dilatancy, and is not reproduced in the numerical model. This indicates the need (i) to carry out additional research related to the behavior of the frequency-magnitude distribution and its evaluation strategy for rock salt, and (ii) to investigate and extend the modeling approach, e.g. consideration of heterogeneities and dilatancy. Further modeling aspects can be taken into account in future research such as the coupling with hydraulic processes. This extension would enable to consider the influence of humidity/concentration changes on the shrinkage behavior, e.g. drying shrinkage, and provide a preliminary understanding on related processes such as shrinkage-induced cracking. Further modeling improvements can be achieved by considering a contact formulation between the saltcrete (backfilled cavity) and surrounding salt unit. This would allow the independent movement of the nodes and its classification, i.e. convergence of the rock salt or shrinkage of the saltcrete. Furthermore, a three-dimensional approach would be advantageous and provide a deeper understanding on the stress response.

Acknowledgements

References

BECKER, D., CAILLEAU, B., DAHM, T., SHAPIRO, S. & KAISER, D. 2010. Stress Triggering and Stress Memory Observed from Acoustic Emission Records in a Salt Mine. Geophysical Journal International, 182, 933-948, DOI 10.1111/J.1365-246X.2010.04642.X

BUNDESAMT FÜR STRAHLENSCHUTZ (BFS) 2015. Hintergründe, Maßnahmen und Perspektiven der Stilllegung (informational government document).

BUNDESAMT FÜR STRAHLENSCHUTZ (BFS) 2016. Endlager Morsleben: Geschichte des Endlagers für radioaktive Abfälle Morsleben (informational government document).

DEUTSCHE GESELLSCHAFT ZUM BAU UND BETRIEB VON ENDLAGERN (DBE) 2004. Verfüllmaterial für Strecken mit hohen Anforderungen. Materialeigenschaften und Materialkennwerte Salzbeton M2 (procedural documentation)

DOLAREVIC, S. & IBRAHIMBEGOVIC, A. 2006. A modified three-surface elasto-plastic cap model and its numerical implementation. Computers and Structures, 85:12, 2007. DOI: 10.1016/j.compstruc.2006.10.001.

FAHLAND, S., EICKEMEIER, R. & SPIES, T. 2005. Bewertung von Gebirgsbeanspruchungen bei Verfüllmaßnahmen im ERAM. Proc. 5. Altbergbau-Kolloquium, Clausthal-Zellerfeld 2005.

FAUST, B. LUCKE, A., HILLMANN, C. & TERTEL, S. 2021. Theoriehandbuch für JIFE 6.1.2 (technical documentation).

Hesser, J., Kaiser, D. Schmitz, H. & Spies, T. 2015. Measurements of acoustic emission and deformation in a repository of nuclear waste in Salt rock. Engineering Geology for Society and Territory, Vol. 6, Pages 551-554.

Kaiser, D., Spies T. & Schmitz, H. 2013. Mikroakustisches Monitoring in Bergwerken zur Bewertung aktueller Rissprozesse. Proc. GeoMonitoring, Hannover 2013.

Köhler, N., Spies T. & Dahm, T. 2009. Seismicity patterns and variation of the frequency-magnitude distribution of microcracks in salt. Geophysical Journal International, Vol. 179, Pages 489-499.

Lay, V., Baensch, F., Johann, S., Sturm, P., Mielentz, F., Prabhakara, P. & Kühne, H. C. (2021). SealWasteSafe: materials technology, monitoring techniques, and quality assurance for safe sealing structures in underground repositories. Safety of Nuclear Waste Disposal, 1, 127-128.

Manthei, G. & Plenkers, K. 2018. Review on in Situ Acoustic Emission Monitoring in the Context of Structural Health Monitoring in Mines. Applied Sciences, 8, 1595, DOI 10.3390/app8091595.

Missal, C.P. 2019. Numerisches Modell zur Entwicklung der Permeabilität von Steinsalz in Abhängigkeit von Schädigung, Fluiddruck und Spannungszustand. Thesis University of Technology Braunschweig.

Rostásy, F.S. & Onken, P. 1992. Wirksame Betonzugfestigkeit im Bauwerk bei früh einsetzendem Temperaturzwang: Forschungsbericht. Institut für Baustoffe, Massivbau und Brandschutz, University of Technology Braunschweig, DOI 10.24355/dbbs.084-201508241614-0.

Viola, S., Heusermann, S. & Wallner M. 1997. Gebirgsmechanische Beurteilung der Integrität der Salzbarriere im Zentralbereich der Grube Bartensleben (technical documentation).

Theme 5: Monitoring and site-specific studies

Progress in the geoscientific exploration of the Asse salt structure as a base for the construction of a new mine for the retrieval of radioactive waste from the Asse II mine

Lukas Pollok[1*], Alja Saßnowski[1], Mareike Henneberg[1], Maximilian Pusch[1], Volker Gundelach[1], Tatjana Thiemeyer[1], Thies Beilecke[1], Ralf Holländer[2]

[1]Federal Institute for Geosciences and Natural Resources (BGR), Germany; [2]Federal Company for Radioactive Waste Disposal (BGE), Germany

* Lukas.Pollok@bgr.de

ABSTRACT: The radioactive waste in the former Asse II salt mine has to be retrieved prior to the legally demanded decommissioning. In this context, the construction of a new mine and shaft is necessary, whereby detailed geological information about the salt structure is indispensable. Knowledge of the evaporite sequence, the internal composition, and the external shape of the Asse salt structure has been significantly enhanced by drill core investigations, borehole measurements, ground penetrating radar, and a new 3D seismic survey in recent years. The combined results indicate a highly complex internal structure with intensely folded Zechstein layers, contradicting earlier geological assumptions about this part of the salt structure. Furthermore, the strong tectonic influence during salt structure development is evidenced by complex structures in the cap rock and overburden, and by the formation of a salt wing on the steep southern flank. Additionally, a considerable narrowing of the salt structure to the southeast reduces the available space for the new mine. Our research shows that planning of waste repositories in complex salt structures has to be based on reliable, site-specific geoscientific data sets to reduce the risk of complications in the construction phase.

1 Introduction

Between 1965 and 1995, the Asse II mine in the southern part of Lower Saxony, Germany, served as an underground rock laboratory to test the handling and storage of radioactive waste in salt repositories. During that time, about 126.000 barrels of low- and intermediate-level radioactive waste were placed in 13 chambers of the about 100-year-old salt mine. In 2009, the Federal Office for Radiation Protection (BfS) decided to decommission the mine, because the combination of continued convergence and the inflow of saline solutions threaten its stability. In 2010, after examining different decommissioning options, it was decided to retrieve the radioactive waste (BfS 2010) and the German Federal Government stipulated this in law in 2013 (AtG 1985).

For this purpose, a new mine, and consequently an additional shaft, specifically designed for the retrieval of the radioactive waste, have to be constructed. In this context, the Federal Institute of Geosciences and Natural Resources (BGR) has been commissioned with the detailed geological investigation of the salt structure by BfS in May 2014 (since 2017 by the Federal Company for Radioactive Waste Disposal (BGE)). Subsequent research on cores from several drilling campaigns has significantly improved the knowledge of the Zechstein evaporite sequence, the internal composition, and the external shape of the Asse salt structure. The combined results of lithostratigraphic drill core investigations, followed by mineralogical-geochemical analyses, geophysical borehole measurements, ground penetrating radar, and a new 3D seismic survey, indicate a highly complex salt structure as well as structural complications in caprock and the sedimentary cover, thereby contradicting earlier geological models (Pollok et al. 2016; Pollok et al. 2019; Saßnowski et al. 2020).

2   Regional geological setting

The NW-SE trending Asse-Jerxheim salt structure is a narrow, ca. 25 km long structure, located in the southern part of the North German Basin (NGB), called the Subhercynian Basin (SB), between the Harz Mountains to the southwest and the Flechtingen basement high (FH) to the northeast (Fig. 1). The salt structure consists of evaporitic rocks of the Permian Zechstein Group that formed in the NGB during alternating periods of seawater influx and high evaporation rates. The Zechstein strata of the NGB reaches up to 1.5 km in overall thickness and has been divided into five to seven formations, depending on basin position during times of deposition (Paul 2020; Käding 2000; Käding 2005). Due to their tectonic setting, a large number of different salt structures, from pillows to diapirs and walls, have formed in the NGB from the Triassic Bunter onwards (e.g. Pollok et al. 2020; Warsitzka et al. 2019).
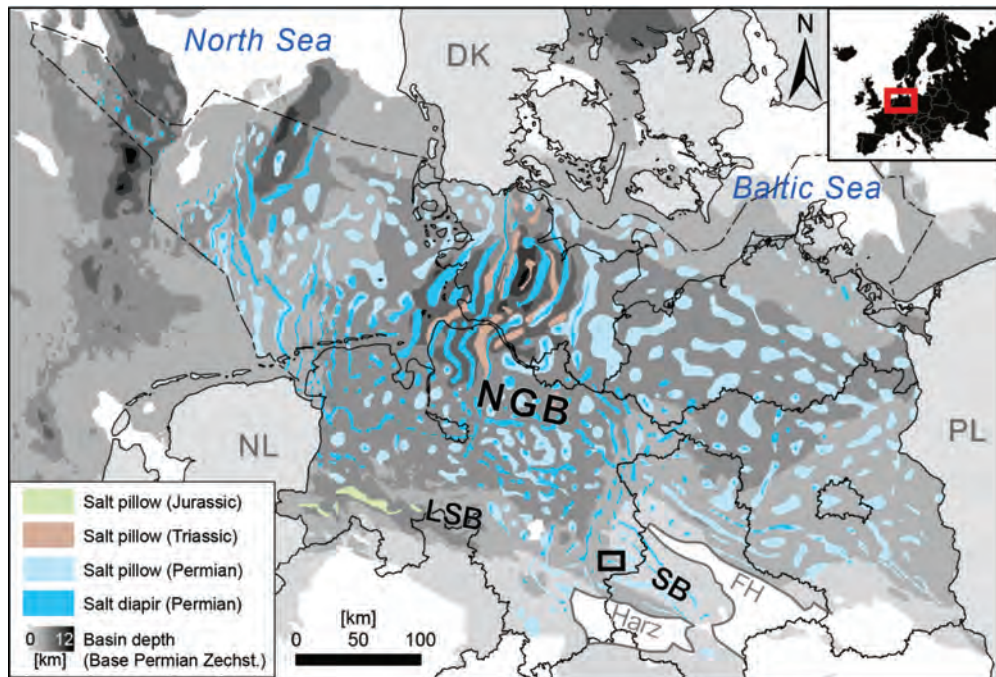
Figure 1: Distribution of salt structures comprising Permian to Jurassic evaporite deposits in the North German Basin (modified after Reinhold et al. (2008), basin depth from Peryt et al. (2010)). The black frame highlights the location of the Asse salt structure. The dashed line marks the German offshore exclusive economic zones. FH: Flechtingen basement high, LSB: Lower Saxony Basin, NGB: North German Basin, SB: Subhercynian basin.

As in many other North German salt structures, the thick rock salt units of the Staßfurt-Formation (z2) were mobilized throughout different tectonic phases forming the Asse salt structure. While the non-chloridic units of the Werra-Formation (z1) remained immobile at the base of the salt structure, the movement of the z2 salt induced the deformation of the overlying Leine- and Aller-Formations (z3 and z4). The overall thickness of the accumulated salt in these formations adds up to about 2 km. The structure received its existing shape by regional compression during the Upper Cretaceous.

3   Methodology

This study uses a combined approach, including drill core investigations, mineralogical and geochemical analyses, geophysical borehole measurements, ground penetrating radar, and

first results from a new 3D seismic survey to gain detailed information on the geological setting of the planned mine and shaft.

Conventional drill core investigations were conducted on cores from eight horizontal underground, as well as five vertical drilling campaigns from the surface (Fig. 2), carried out between 2014 and 2021.
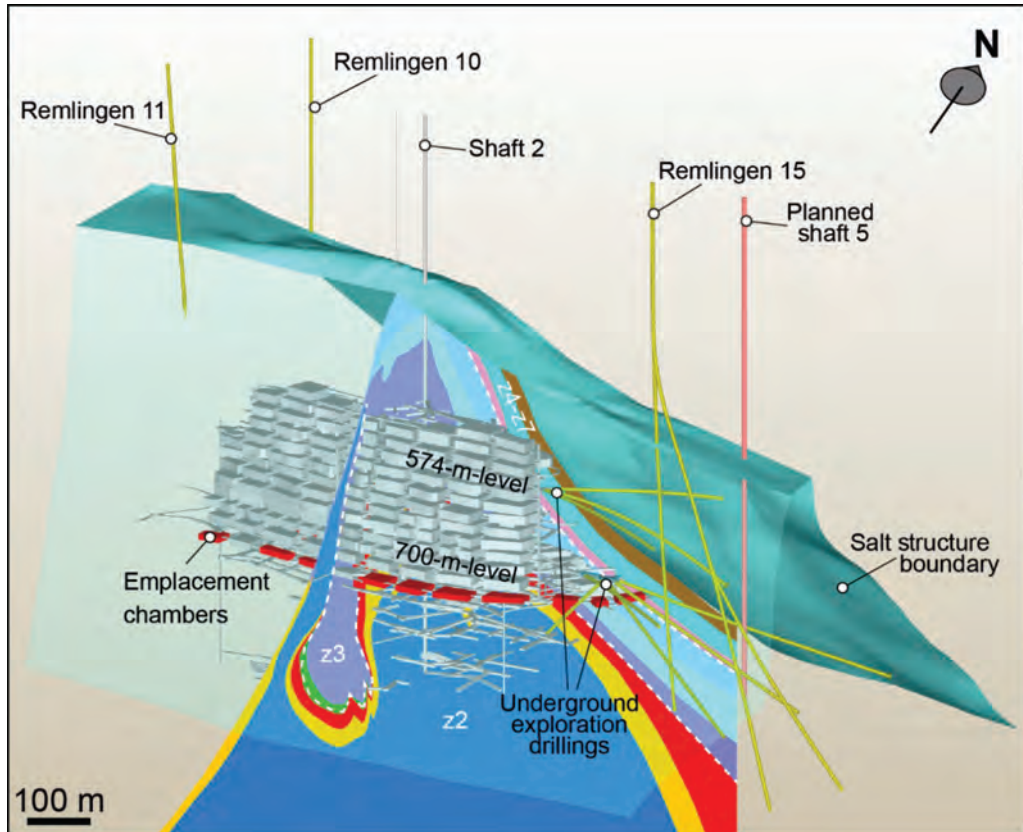

Figure 2: Location of the planned shaft 5, the mine Asse II with its respective shafts 2 and 4, the drill sites of the Remlingen 10, 11, and 15 and its sidetracks as well as the tracks of the underground drill holes.

Geological drill core investigations (Fig. 3) were followed by mineralogical and geochemical investigations by petrographic thin section, x-ray diffraction (XRD), x-ray fluorescence (XRF), inductively coupled plasma optical emission spectroscopy (ICP-OES), inductively coupled plasma mass spectrometry (ICP-MS) as well as stable sulphur and oxygen isotope (δ^{34}S and δ^{18}O) analyses on selected samples. Chosen combinations of analyses depend on sample lithology and the specific questions to be addressed. For details on analytical setups and routines, see Pollok et al. (2016), Pollok et al. (2019), and Saßnowski et al. (2020).

Additional to core-based analyses, geophysical borehole measurements, including acoustic and optical borehole imaging (ABI and OBI), were carried out. ABI and OBI are especially useful for reconstructing the true orientation of a core and thereby its structural elements. Prior to analyses, the image logs are unrolled, oriented to magnetic North and illustrated as 0 to 360° images (Fig. 3). Planar features, e.g., bedding planes, appear as sinus curves, with their maximum and minimum representing dip and azimuth of the planes (Rider & Kennedy 2011).
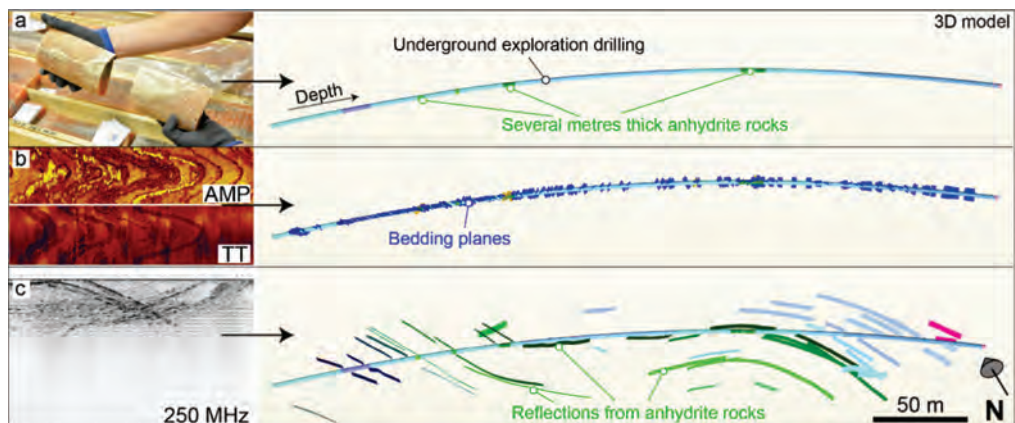
Figure 3: Workflow for combining different exploration methods: a) Detailed drill core investigation leading to a stratigraphic classification of the rocks; b) Acoustic borehole imaging (ABI) log showing the reflected acoustic signal from the borehole wall as amplitude (AMP) and travel time (TT) to the left and structural interpretation of the log to the right; c) Ground penetrating radar (GPR) section indicating spatial orientation of geological strata in the vicinity of the borehole (modified after Gundelach (2017); Pollok et al. (2019)).

Ground penetrating radar (GPR) is another tool used to improve the geological knowledge in structurally complex salt structures. In low-conductive salt, GPR measurements can reach several hundred meters of penetration depth and allow for the detection of geological boundaries and thus structural interpretation of geological features (Fig. 3, Gundelach 2018). Recently, first, preliminary findings of a new 3D seismic survey have added valuable information about the boundaries of the salt structure to our interpretations. Additional results, e.g., on the structure of the sedimentary cover, are expected in 2022, after processing of the data is completed. Based on the collected data, a high-resolution 3D model of the Asse salt structure is currently being developed (Fig. 2 Thiemeyer (2018)).

4   Results and Interpretation

Exploration of the location for the new recovery shaft about 550 m east of the existing shaft 2 started in mid-2013 with drilling of the Remlingen 15 (R 15; Fig. 2) to a total depth of 900 m. First results from this drilling campaign indicated a highly complex internal structure, consisting exclusively of folded units of the z3 (Fig. 4; Pollok et al. (2018); Saßnowski et al. (2018)). These findings prove that the complexity of the salt structure increases significantly more to the southeast than previously assumed (e.g., Klarr et al. (1989)).

Era	Period	Formation	Subformation	Symbol	Underground expl. BH 574-m-level -1	-2	-3	700-m-level -1	-1a	-2	-3	-4	-5	Surface expl. BH R 10	R 11	R 15	R 15-S1	R 15-S2
-	-	-	Caprock	cr														
Triassic	Upper Bunter	Röt 2 (so2)	Röt 2	so2														
		Röt 1 (so1)	Röt 1-Mergelstein	so1/T														
			Röt 1-Deckanhydrit	so1/DA													?	
			Röt 1-Steinsalz	so1/na													?	
			Röt 1-Basalanhydrit	so1/BA														
Permian	Zechstein	Fulda-Formation (z7)	Bröckelschiefer	z7T										?				
		Friesland-Formation (z6)	Friesland-Ton	z6T										?				
		Ohre-Formation (z5)	Ohre-Anhydrit	z5OA										?				
			Unterer Ohre-Ton, Salzbrockenton	z5TU										?				
		Aller-Formation (z4)	Aller-Grenzanhydrit	z4GA														
			Tonbanksalz	z4TB														
			Schnee+Rosensalz	z4SS+z4RS														
			Basissalz	z4BS														
			Pegmatitanhydrit	z4PA														
			Roter Salzton	z4RT														
		Leine-Formation (z3)	Tonmittelsalz	z3TM														
			Schwadensalz	z3SS										?				
			Anhydritmittelsalz	z3AM														
			Buntes Salz	z3BT														
			Bändersalz	z3BD														
			Ronnenberg-Horizont, Banksalz	z3RO+z3BK														
			(Gamma-Linien-) Orangesalz	z3OS														
			(Beta-) Liniensalz	z3LS												?		
			Basissalz	z3BS														
			Hauptanhydrit	z3HA														
			Grauer Salzton	z3GT														
		Staßfurt-Formation (z2)	Gebänderter Deckanhydrit	z2DA													?	
			Decksteinsalz	z2DS													?	
			Kaliflöz Staßfurt	z2SF														
			Kieserit. Übergangsschichten	z2UE														
			Tonliniensalz	z2TS														
			Polyhalitbänkchensalz	z2PS														
			Speisesalz	z2SS												?		
			Hauptsalz	z2HS														

Figure 4: Stratigraphic column of the evaporite units of the Asse salt structure above the basal units of the Werra- and Staßfurt-Formation. Units exposed by exploratory drillings are marked in grey. Boreholes (BH) marked in orange are currently under investigation and represent preliminary results.

Recently, further multi-method investigations on drill cores and boreholes from the 574-m- and 700-m-levels (Fig. 2) are further proof to the existence of strongly folded layers of the z3 to z4 in the central part of the salt structure (Fig. 4; Gundelach (2018); Pollok et al. (2019)). Whereas most of the z3 rocks encountered belong to the middle to upper z3, some of the core intersected parts of the mudstone ("Grauer Salzton", z3GT) and the main anhydritic unit ("Hauptanhydrit", z3HA) at the base of the z3. Distinguishing the z3HA, where only parts of the unit are encountered, from the anhydritic intercalations of the "Anhydritmittelsalz" (z3AM/ah; Fig. 5) is only possible with detailed core examinations in combination with mineralogical-geochemical data (Saßnowski et al. 2018). For example, noticeable amounts of carbonate are a characteristic feature of the z3HA, and while interstices between anhydrite crystals are filled by orange colored halite in the z3AM/ah, they usually contain raspberry red carnallite in the z3HA (Fig. 5). If positively identified, these anhydritic intercalations are shown by characteristic patterns in the georadar measurements and can thus be mapped over long distances into virgin rock areas of the salt structure.

A couple of cores from recent exploration drillings comprise the discordant boundary between the halites of the "Liniensalz" (z3LS) and the potash seam of the z2 ("Kaliflöz Stassfurt", z2SF)

previously known from underground outcrops and a few older drilling campaigns (Klarr 1981). Locally, this boundary could also be traced by GPR measurements.

Close to the southwestern salt flank, preliminary results from the core of two sidetracks (S1 and S2; Fig. 2 and Fig. 4) of the existing R 15 show layers of the z3GT and z3HA occurring repeatedly due to their steep inclination in this part of the salt structure. Next to these basal units of the z3, both the S1 and the S2 encountered the z2SF and adjacent units of the uppermost z2 to lowermost z3. To the Northwest, the Remlingen 10 (R 10; Fig. 2) close to the existing shaft 2 cuts through thick units of the Lower Bunter overlying the uppermost units of the z3 and the siliciclastic to anhydritic basal layers of the z4 (Fig. 4). In contrast, the Remlingen 11 (R 11, Fig. 2), located in the southwestern flank, intersects the Upper Bunter and the anhydrite as well as the halite units of the "Rötdeckanhydrit" (so1/DA) and "Rötsteinsalz" (so1/na), respectively, before reaching halite units of the z2, a thin stringer of the z2SF and finally the z3 (Fig. 4). These results are further evidence for the intrusion of Zechstein salts into the Triassic evaporites and the existence of the salt wing.
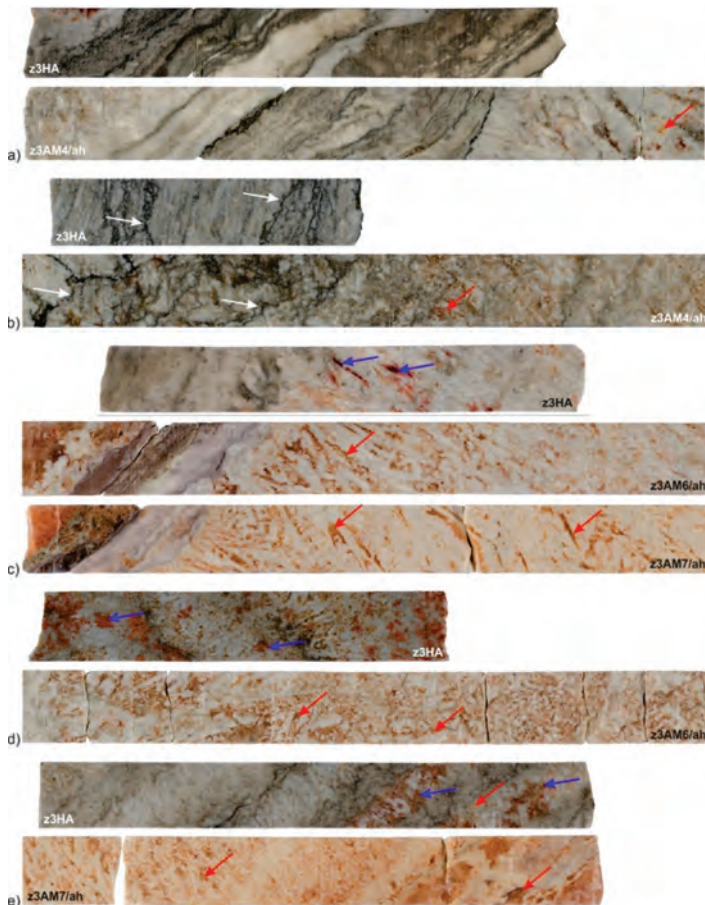
Figure 5: Pictures of bisected cores, highlighting the similarities of the z3HA and the z3AM/ah: a) Light grey anhydrite intercalated with dark grey mudstone in the z3HA and the z3AM4/ah; b) Stylolites (e.g., white arrows) in anhydrite in the z3HA and the z3AM4/ah; c) Sulfate layers preceded by large dove tail anhydrite crystals in the z3HA, z3AM6/ah and z3AM7/ah; d) Chaotically arranged dove tail, as well as smaller, snowflake anhydrite crystals; e) Intercalated anhydrite- (light grey and light orange) and halite-rich (dark orange colored) layers; Interstices are filled by raspberry red carnallite (e.g., blue arrows) in the z3HA and orange to red halite (e.g., red arrows) in the z3AM6/ah and z3AM7/ah. Core diameter is ca. 6.3 cm.

An additional, detailed study on the caprock units of the R 15 (Saßnowski et al. 2020) as well as first preliminary results from the caprock units intersected by sidetrack R 15 S1, R 10 and R 11, indicate that the observed internal complexity of the salt structure also continues into the caprock. Apart from the R 10, the caprock comprises thick, mostly gypsiferous units of the so1/DA, belonging to the evaporitic units of the Upper Bunter. In the R 15, these directly overlie residues of the z3, with no indication that dissolution, erosion and hydration of these units took place in separate events (Saßnowski et al. 2020). While the evaporitic units of the Triassic Upper Bunter have long been known to be directly overlying the salt structure on its southwestern salt flank, their existence in the caprock over the salt structure top was unknown so far (Klarr 1981). However, the provenance of the so1/DA has been proven by stable isotope data that easily distinguish Zechstein and Upper Bunter units. For the Asse salt structure, Zechstein $\delta^{34}S$ (VCDT) values are between 9 ‰ and 14 ‰ in combination with $\delta^{18}O$ values (VSMOW) between 7 ‰ and 15 ‰, whereas the Röt displays $\delta^{34}S$ values between 20 ‰ and 27 ‰ combined with $\delta^{18}O$ values between 13 ‰ and 19 ‰, respectively (Fig. 6; Saßnowski et al. (2020)). In the R 10, hydration of the z4PA and the base of the Lower Bunter could imply dissolution of the halite units of the z4 in this location. However, more detailed investigations are needed to confirm this hypothesis.
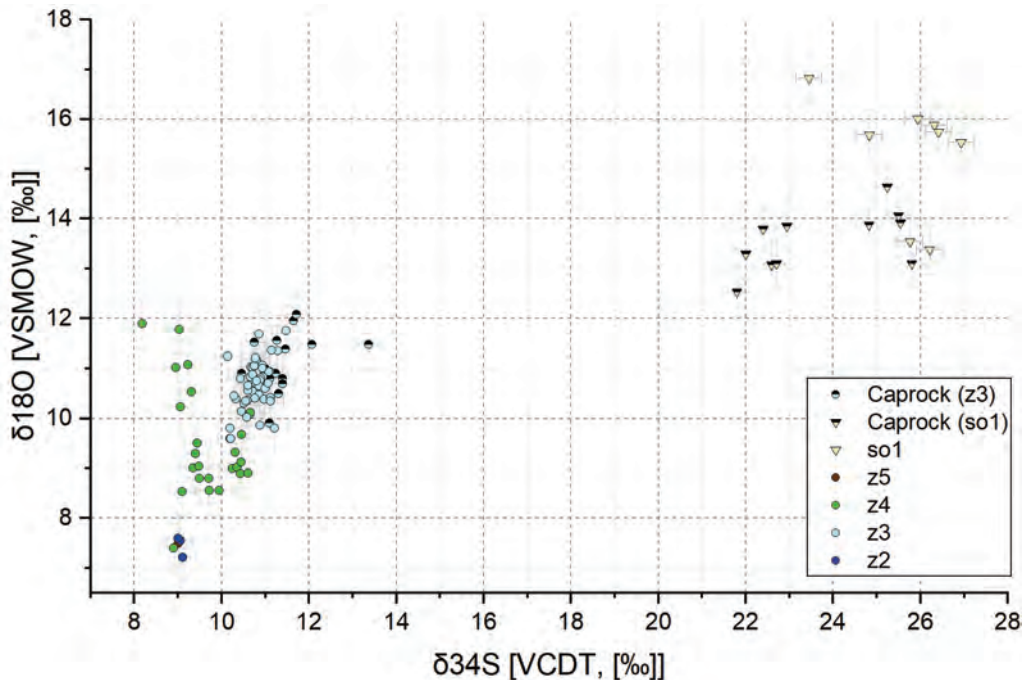
Figure 6: Stable $\delta^{34}S$ and $\delta^{18}O$ isotope data of samples from the Zechstein and Röt units as well as the caprock of the Asse salt structure showing two distinct data clusters clearly differentiating Zechstein from Röt. (modified after Saßnowski et al. (2020)).

5 Conclusions

This case study shows that internal structural styles can change abruptly in salt diapirs. Hence, any planning in complex salt structures, e.g., for the construction of waste repositories, has to be based on geoscientific data sets specifically compiled for the individual salt structure under examination. Suitable geophysical, geological and mineralogical-geochemical exploration methods for rock salt are readily available and have been successfully tested over decades in the Asse and other salt structures. The interpretation of the geological data enables the subsequent construction of 3D geological models of the salt structure interior and thereby the

identification of homogeneous rock salt areas suitable for, e.g., the construction of infrastructure facilities needed for the retrieval of the radioactive waste from the Asse II mine.

The combined results reveal a plunging of the salt structure top and a considerable reduction in salt structure width to the southeast, reducing the available space for the new shaft and infrastructure. First, preliminary results of the 3D seismic survey confirm this interpretation. Final, processed data will be available in 2022 and will contribute to further geologic site characterization and hence 3D modeling in the near future.

References

ATG 1985. Atomgesetz in der Fassung der Bekanntmachung vom 15. Juli 1985 (BGBl. I S. 1565), das zuletzt durch Artikel 1 des Gesetzes vom 10. August 2021 (BGBl. I S. 3528) geändert worden ist - Gesetz über die friedliche Verwendung der Kernenergie und den Schutz gegen ihre Gefahren (Atomgesetz). 42 p.

BFS 2010. Optionenvergleich Asse. Fachliche Bewertung der Stilllegungsoptionen für die Schachtanlage Asse II. Bundesamt für Strahlenschutz, BfS-Bericht 19/10; urn:nbn:de:0221-201004141430, Salzgitter, 225 p.

GUNDELACH, V. 2017. Richtungssensitive Georadar-Bohrlochmessungen in der Erkundungsbohrung EBrg. 574-3. Bundesanstalt für Geowissenschaften und Rohstoffe (BGR), Ergebnisbericht, Hannover, 38 p.

GUNDELACH, V. 2018. GPR Measurements for Spatial Investigations at the Asse Salt Structure. Journal of Environmental and Engineering Geophysics 23 (4), 397-405. doi:10.2113/jeeg23.4.397.

KÄDING, K.-C. 2000. Die Aller-, Ohre-, Friesland- und Fulda-Folge (vormals Bröckelschiefer-Folge) - Stratigraphie und Verbreitung des z4 bis z7 im Zechstein-Becken. Kali u Steinsalz 13 (14), 86-96.

KÄDING, K.-C. 2005. Der Zechstein in der Stratigraphischen Tabelle von Deutschland. News Stratigr 41 (1-3), 123-127.

KLARR, K. 1981. Grundlagen zur Geologie der Asse. Gesellschaft für Strahlen- und Umweltforschung, Institut für Tieflagerung, GSF-Bericht, München, 92 p.

KLARR, K., DÜRR, K., GIES, H., HENSEL, G., KOLDITZ, H., KULL, H., SCHMIDT, M.W., SCHWEINSBERG, A., STEINBERG, S., WALLMÜLLER, R., WALTER, F., BATSCHE, H., CARLS, P. & PAUL, J. 1989. Erstellung von Tiefbohrungen auf der Südwestflanke der Asse. Gesellschaft für Strahlen- und Umweltforschung mbH München, Institut für Tieflagerung, Abschlussbericht, Braunschweig, 404 p.

PAUL, J. 2020. Paläogeographie und Fazies des Zechsteins. In: Deutsche Stratigraphische Kommission; Koordination/Redaktion: Paul J. & Heggemann H, für die Subkommission Perm-Trias, (ed) Stratigraphie von Deutschland XII - Zechstein, 89. Schriftenr. Dt. Ges. Geowiss.. Schweizerbart Science Publishers, Berlin, 41-52.

PERYT, T.M., GELUK, M., MATHIESEN, A., PAUL, J. & SMITH, K. 2010. Zechstein. In: Doornenbal H, Stevenson A (eds) Petroleum Geological Atlas of the Southern Permian Basin Area (SPBA). EAGE Publ., Houten, 123-147.

POLLOK, L., HAMMER, J. & MUSMANN, P. 2020. Salinarstrukturen – Entstehung, Außenformen und Internbau. In: Deutsche Stratigraphische Kommission; Koordination/Redaktion: Paul J. & Heggemann H, für die Subkommission Perm-Trias, (ed) Stratigraphie von Deutschland XII - Zechstein, 89. Schriftenr. Dt. Ges. Geowiss.. Schweizerbart Science Publishers, Berlin, 559-594.

POLLOK, L., SAßNOWSKI, M., HAMMER, J., SCHRAMM, M., MERTINEIT, M. & PUSCH, M. 2016. Geowissenschaftliche Ergebnisse zu den Salinargesteinen der Erkundungsbohrung

Remlingen 15. Bundesanstalt für Geowissenschaften und Rohstoffe (BGR), Zwischenbericht, Hannover, 171 p.

POLLOK, L., SAßNOWSKI, M., KÜHNLENZ, T., GUNDELACH, V., HAMMER, J. & PRITZKOW, C. 2018. Geological exploration and 3D model of the Asse salt structure for SE expansion of the Asse II mine. In: Fahland S, Hammer J, Hansen F, Heusermann S, Lux K-H, Minkley W (eds) The Mechanical Behavior of Salt IX (SaltMech IX), Hannover, 12.-14.09.2018. Federal Institute for Geosciences and Natural Resources (BGR), 753-763.

POLLOK, L., SAßNOWSKI, M., MERTINEIT, M. & SCHRAMM, M. 2019. Geowissenschaftliche Ergebnisse der zwischen 2015 und 2017 gestoßenen geologischen Erkundungsbohrungen auf der 574-m-Sohle (EBrg. 574-1, EBrg. 574-2, EBrg. 574-3). Bundesanstalt für Geowissenschaften und Rohstoffe (BGR), Hannover, 412 p.

REINHOLD, K., KRULL, P. & KOCKEL, F. 2008. Salzstrukturen Norddeutschlands 1: 500 000. Bundesanstalt für Geowissenschaften und Rohstoffe (BGR); Berlin/Hannover.

RIDER, M.H. & KENNEDY, M. 2011. Geological interpretation of well logs. Bell and Brain, Glasgow, 432 p.

SAßNOWSKI, A., SAßNOWSKI, M. & POLLOK, L. 2020. Geowissenschaftliche Ergebnisse zum Hutgestein der Erkundungsbohrung Remlingen 15. Bundesanstalt für Geowissenschaften und Rohstoffe (BGR), Ergebnisbericht, Hannover, 185 p.

SAßNOWSKI, M., POLLOK, L., KÜHNLENZ, T. & HAMMER, J. 2018. Detailed petrographic and structural studies of salt rocks as basis for an internal geological 3D-model of the Asse salt structure (German Zechstein). In: Fahland S, Hammer J, Hansen F, Heusermann S, Lux K-H, Minkley W (eds) The Mechanical Behavior of Salt IX (SaltMech IX), Hannover, 12.-14.09.2018. Federal Institute for Geosciences and Natural Resources (BGR), Hannover, 765-774.

THIEMEYER, T. 2018. Erstellung des 3D-Modells für die Zechstein-Salzhülle der Salzstruktur Asse. Bundesanstalt für Geowissenschaften und Rohstoffe (BGR), Zwischenbericht, Hannover, 58 p.

WARSITZKA, M., JÄHNE-KLINGBERG, F., KLEY, J. & KUKOWSKI, N. 2019. The timing of salt structure growth in the Southern Permian Basin (Central Europe) and implications for basin dynamics. Basin Res 31 (2), 337-360.

Development of comprehensive 3D-models for geomechanical stability proof of the operation phase and the planned radioactive waste retrieval in the Asse II mine

Wolf-Peter Kamlot[1][*], Johannes Kupper[1], Ralf-Michael Günther[1], Grit Gärtner[2], Frank Manthee[2]

[1]Institute for Geomechanics GmbH (IfG), Germany; [2]Federal Company for Radioactive Waste Disposal (BGE), Germany

* peter.kamlot@ifg-leipzig.de

ABSTRACT: The Asse II mine is an over 100 years old salt mine in a steep inclining structure of a salt ridge in which radioactive waste was embedded from 1967 to 1978. Due to instability in a long-term sense, fracturing in the pillars and overhand stopes took place and a brine inflow has been observed since 1988. Considering the Atomic Energy Act (Lex Asse) the mine shall be closed after complete retrieval of all radioactive waste. IfG Leipzig is charged by the BGE, which is the operator of the mine, to give geomechanical expertise. This is mainly done by means of geomechanical modelling. In this article, a three-dimensional model using FLAC3D is presented that focuses on global and local assessment. Selected calculation results on stress development in the mining system and on barrier integrity are given confirming the feasibility of one particular retrieval method at the complicated geomechanical conditions.

1   Introduction

The Asse II mine in Lower Saxony, nearby Brunswick, Germany has experienced a long and varying history. First, it was a commercial salt extraction mine. Then, low-level and intermediate-level radioactive waste was emplaced. After all, comprehensive R&D projects aiming at final disposal of radioactive waste in salt formations took place. Currently, the mine is prepared for closure. Since 2009, the mine is under Atomic Law. The Federal Company for Radioactive Waste Disposal (BGE) is in charge as operator. According to the Atomic Energy Act (§ 57b AtG "Lex Asse") the mine shall be closed after complete retrieval of all radioactive waste, but only if the geomechanical and radiation conditions allow a safe removal and no brine inflow escalation takes place. Following current plans, the retrieval will start in about 2033 and will last several decades. Facing the geomechanical stability problems and on account of the permanent risk of brine inflow escalation, all abandoned openings (drifts, blind shafts and infrastructure rooms) and still open gaps in the backfilled chambers have to be filled using a special Sorel concrete (for more information see Kamlot et al. 2012). IfG Leipzig has developed different modelling concepts and material laws to reproduce and understand the geomechanical processes as revealed by mine surveying (details in Kamlot et al. 2007, 2015, 2018). The bearing elements are mainly characterized by post-failure behavior. They sustain the overburden load with a residual strength only, but under the backfill support. Therefore, it was fundamental to simulate softening (rupturing), dilatancy and creep using a visco-elasto-plastic constitutive law. The IfG Leipzig is charged by the BGE to give geomechanical expertise for the further operation of the mine until retrieval. This article comprises the latest state of model-development by IfG and presents a FLAC3D-model of the whole mine in which for grid generation modern meshing tools were used. Selected calculation results on stress and integrity development validate the feasibility of one particular retrieval method in principle and deliver the basis for the further planning steps.

2 Geology of the Asse ridge

The Asse II mine is situated in an 8 km long ridge, striking from NW to SE. The geology of the Asse ridge is portrayed in Figure 1. The saliniferous layers are visible in the center of the figure, which predominantly comprise rock salt of the Stassfurt, Leine and Aller Formation (blue, violet-blue and cyan color). The carnallitite seam is located in the saliniferous layers of the Stassfurt series (rose color). Between the layers of the Leine and Aller series there is the red salt clay (pink color).
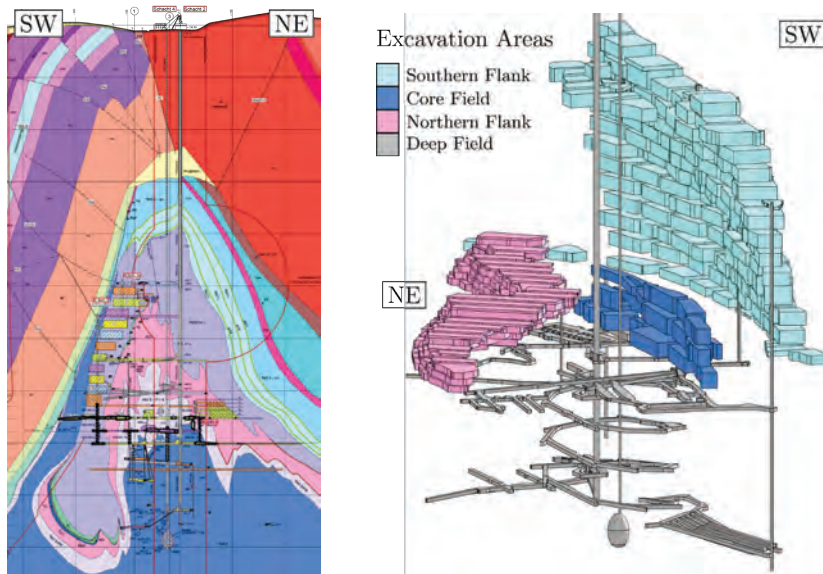
Figure 1: Cross section through the salt ridge in the middle of the NW-SE extension (left) and main mining fields in the Asse II mine (right)

The overburden rocks consist of Triassic Buntsandstein, Muschelkalk and Keuper rocks, followed by Jurassic and Cretaceous rocks. The overburden rocks at the northern edge are older than those at the southern edge. On top of the salt ridge there is a caprock (yellow color).

Due to the close distance of the openings in the upper part of the mine to the overburden (Fig. 1) and the long operation time without backfilling, a loss of integrity of the rock salt barrier to the southern overburden took place. An inflow of brine from the overlaying layers, which are separated tectonically, was first observed in 1988 and is now in the order of 13 m³ per day. The brine is saturated with NaCl and CaSO$_4$, but not with MgCl$_2$. It must be emphasized that the geologic model of the Zechstein and overburden rocks is examined and revised currently.

3 Mining fields and research areas in the Asse II mine

The Asse II mine consists of three mining areas. The first mining area excavated is the carnallitite field at the northern edge of the salt ridge in the Stassfurt series. The excavation of this field took place from 1909 to 1925. This field comprises 25 panels with different lengths across the strike reaching from ca. 40 m to ca. 120 m. The typical width of a panel amounts to ca. 20 m and the pillar between two panels has a width of ca. 10 m. The

maximum heights of the panels amounts to ca. 40 m. This field covers a depth between 750 m and ca. 708 m. The volume of the entire field amounts to ca. 1,000,000 m³. Around 99 % of this volume is backfilled with residues from the factory processing of salt.

The second mining area is positioned at the southern flank. It was excavated in the rock salt of the Leine Formation from 1916 to 1964. The southern flank represents a room and pillar system with 13 levels on top of each other and generally 9 rows of rooms per level. The lowest level is located in a depth of 750 m. The depth of the highest level amounts to 490 m. The typical room length in strike direction reaches 60 m and the width across the strike is 30 m to 40 m. The pillars between two adjacent rooms have widths of ca. 12 m (except for the pillar between the mining rows 4 and 5 with a thickness of ca. 20 m). The overhand stopes between the levels are ca. 6 m thick. The typical height of a room amounts to ca. 15 m. The rooms at the level of 750 m pose a height of ca. 10 m. The volume of the whole field amounts to ca. 3,350,000 m³. The chambers were, after decades of free convergence, partially backfilled during the R&D phase from excavation of single drifts and in a backfilling campaign using pneumatic transportation of granular salt from 1995 to 2004. Today, about 93% of the volume is backfilled (including Sorel concrete in the open gaps above the settled backfill bodies).

A smaller rock salt area was excavated in the center of the salt ridge in the Stassfurt series between 1927 and 1964. This field has also a room and pillar structure with three levels reaching from depths of ca. 775 m to ca. 725 m with a volume of only ca. 450,000 m³. Today, ca. 89% of the volume contains pneumatically backfilled crushed salt and Sorel concrete.

Single drifts and a cavern were excavated below the 800-m-level for research reasons between 1984 and 1992. These excavations belong to the deep field with a volume of ca. 240,000 m³. About 72 % of this volume was backfilled up to today. The excavation structure of the mine is illustrated in Figure 1. Drifts above the 800-m-level used for entrance to the openings are not depicted to maintain clarity.

Low- and intermediate-level radioactive waste is embedded in chambers of the southern flank at 750-m- and 511-m-level and in chambers of the center field at 750-m- and 725-m-level.

4 Comprehensive 3D-model of the Asse II mine

4.1 Model description

The calculation model described in the following represents a significant advancement of the model used for the geomechanical stability proof and forecast of the further operation phase in Kamlot et al. 2018. The model in 2018 covered only the western part of the mine. The shape of the chambers and the geological structure had to be idealized because of limitations of the numerical tools. Nowadays, modern tools are available and using the progress in hardware the complete mine could be reproduced in agreement with the mine map. However, an abstraction of the stratigraphy remains necessary furthermore. This is acceptable because the main focus aims at the interaction of the large openings in the mining system.

In the model in Figure 2, the overburden rocks are divided into layers of Rötanhydrit, Buntsandstein, Muschelkalk, Keuper, Jurassic and Cretaceous rocks. Additionally, the caprock is included. The saliniferous layers are divided into rock salt, carnallitite and red salt clay. A sub-saliniferous layer exists in the underground. Anhydrite accessories inside the saliniferous layers are not incorporated. The rock salt layers are not distinguished between different stratigraphic sequences of the Stassfurt, Leine and Aller series. Following the

requirements of BGE a more detailed stratigraphy can be integrated, if necessary, for evaluation purposes.
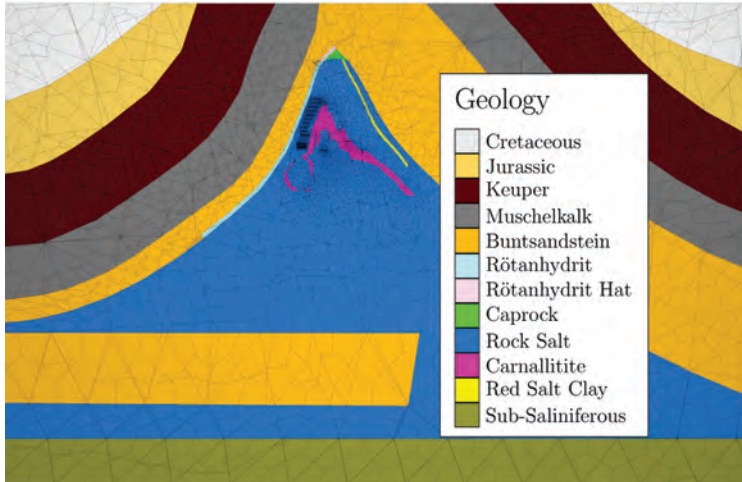

Figure 2: Geological abstraction of the 3D-model

The geomechanical behavior of the overburden rocks is described by an elasto-plastic constitutive law known as Hoek-Brown-Model (Itasca 2017). For the saliniferous layers a visco-elasto-plastic constitutive law, developed by IfG, is used (Günther & Salzer 2007). The backfill from crushed salt is simulated with a Double-Yield-Model (Itasca 2017). In regions backfilled with Sorel concrete an own visco-elasto-plastic material law (Minkley & Mühlbauer 2007) was applied.

The model size is quite large in comparison to the dimensions of the mine. The model dimensions are 6.3 km in across strike direction, 1.6 km in strike direction and 2.5 km in vertical direction (see Figure 3). The model consists of ca. 3.2 million elements. The basic stress state was determined by initializing each element with gravitational forces and solving for equilibrium state subsequently.
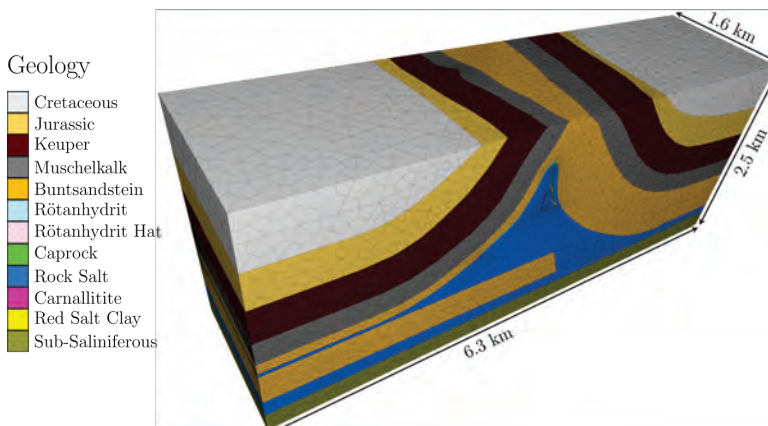
Figure 3: Dimensions of the comprehensive FLAC3D-model

The algorithm of Fast Lagrangian Analysis of Continua in 3D (FLAC3D) was used (Itasca 2017) which is a three-dimensional explicit difference element program. The large model dimensions were necessary to avoid any influence from the boundary conditions. Furthermore, the exaggerated size allows stress redistribution between the southern flank and the overburden rocks which has to be expected because of the high order of excavation. The vertical boundaries and the basis are fixed perpendicular to the edge, and the top is free.
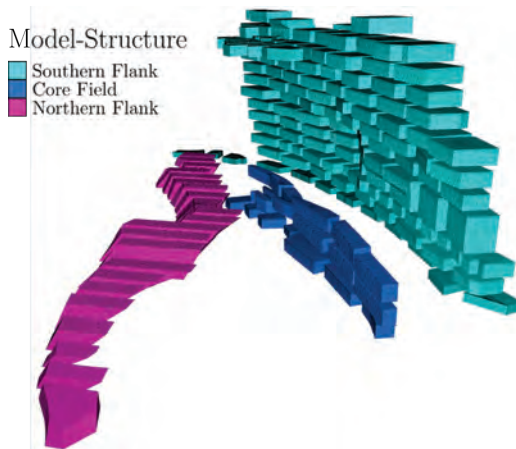
Figure 4: Structure of the three mining fields in the model

The two rock salt mining fields at the southern flank (light blue) and in the centre of the mine (dark blue) are portrayed in Figure 4. The carnallitite field has the magenta color. The model comprises the large rooms and separating pillars only. Excavations below the 775-m-level and all drifts are not part of the model. These simplifications have to be made for getting a compromise between details and calculation time. They are regarded as acceptable because the geomechanical behavior of the mine is governed by the mining fields due to their large excavation volume. On the other hand, the depicted mesh represents a basic discretization for calculation of the primary stress state and the mining history until the present. As already outlined for geology, in dependence on geomechanical questions of the operation phase or focusing on the retrieval process, a finer discretized mesh with drifts can be incorporated in special areas. For such a mesh transformation, the so far calculated stresses, deformations and damages can be transferred into the finer grid (see chapter 4.3).

Similar experiences and a procedure using extended 3D-models of the Asse II mine are described in Lux et al. 2018. A numerical toolkit was developed for increasing the degree of refinement in several phases aiming at calculation of geomechanical behavior (total and local).

4.2   Modelling course

After reaching the primary stress state, the mining history and the backfilling with crushed salt were simulated on basis of the recorded time scales. Recognizing the use of a visco-elasto-plastic material law, it was essential to manage the room excavation and the backfilling gently in many single steps. While calculation, strong disturbances of the equilibrium state in the model have to be restricted (more information about the explicit calculation scheme in Itasca 2017).

In the course of temporal simulation of the mining activities inclusive backfilling it is vital to compare the calculation results at significant locations (e.g. pillar deformation rates) with mine surveying. Only after confirming the correctness of the calculated deformations,

stresses and particularly damaging processes the calculation can be continued. If not, calibrations (mainly in material behavior or in time scale of changing boundary conditions) are necessary. This statement has a special meaning in case of geomechanical prediction for a limited time period under the prerequisite of unchanged system conditions. As outlined above, geomechanical stability of one particular retrieval method has to be evaluated, and the simulated start shall be in 2035.
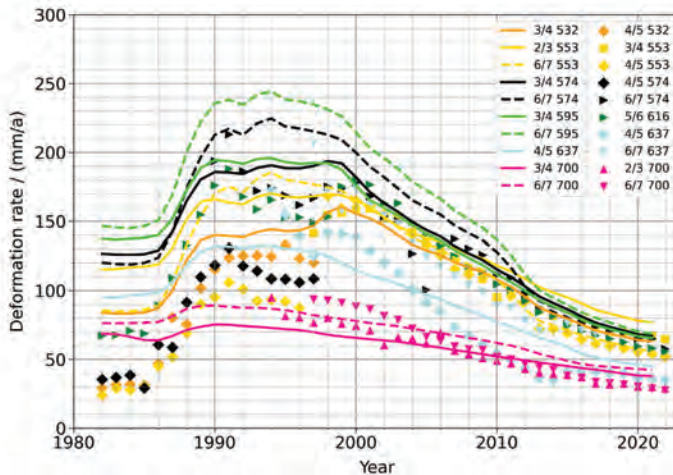

Figure 5: Course of the pillar deformation rates at the southern flank (modeled values with lines, measured values with symbols)

The most important result of mine surveying regarding model verification is the observation of the pillar deformation rates at the southern flank. The pillars are compressed in a horizontal direction as a consequence of the overburden load. As it can be seen in Figure 5, the model describes these deformation rates in general (regarding the tendency and the scattering) very good. The deformation rates increased considerably in the late 80's because of strain-softening processes in pillars and fragmentation in stopes. In the mid 90's, the peak was exceeded and the deformation rates fell down. From 1995 to 2004, the pneumatic backfilling campaign generated increasing reinforcement pressure stabilizing the mining system. Since 2009, the backfilling of small gaps between backfill bodies and chamber roofs with Sorel concrete is been leading to a rate drop down in model and reality. In conclusion, the model is in good agreement with the in-situ measurements and the use for simulation and evaluation of the radioactive waste retrieval is justified.

4.3 Different model meshing in relation to problem formulation

Different degrees of abstraction were used in the modelling course. These models distinguish from each other referring to the model mesh. For solving the primary stress state and modelling the mining activities until 1956, a model with ca. 2.2 million elements was used. For the period from 1956 to 2020, a model with 3.2 million elements came in use. The two models consist of non-structured hexahedral meshes, but the model with 3.2 million elements has a finer mesh in the vicinity of the excavations. A special subroutine was created to transfer all calculated magnitudes (state of stress, deformation and damaging) from the coarser mesh to the finer one. Considering the element midpoints, a mesh related interpolation of the physical field quantities takes place and after reaching a new equilibrium state the modelling course can proceed.
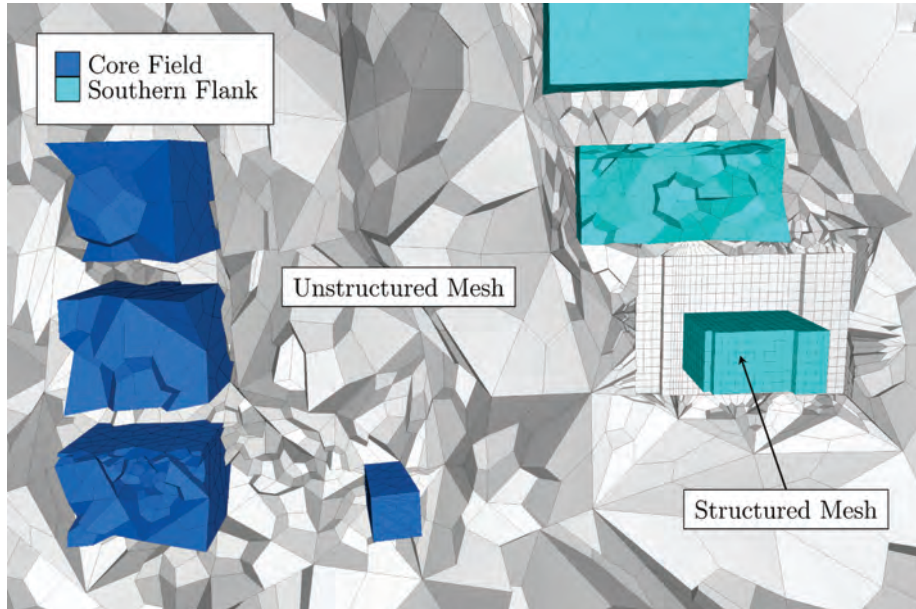
Figure 6: Structured and unstructured hexahedral meshes stitched together

For modelling the retrieval of the radioactive waste, the development of a third model was necessary. The mesh of this model consists of ca. 1.8 million elements. It is composed of two different meshes, one unstructured hexahedral and one structured hexahedral mesh (see Figure 6). The simulation of tunneling with a rectangular shield was only possible within the structured mesh. The two meshes were stitched together by use of special 3D meshing techniques.

5   Retrieval of radioactive waste by use of modified shields

5.1   Description of the procedure of re-excavation

In the study "Alber Geomechanik, IfG Leipzig 2019" the impact of a special retrieval method using shields on stability in the mining system and on integrity of the halite barrier to the overburden was investigated and the feasibility could be confirmed in general. To demonstrate the performance capability of the comprehensive 3D-model, the retrieval sequences shall be reproduced in the following. The description of the process, the technical parameters of the shields and the time schedule of the measure are given in the study. The most radioactive waste chambers are located in the southern flank at the 750-m-level and could be re-excavated in strike direction (see Figure 7).
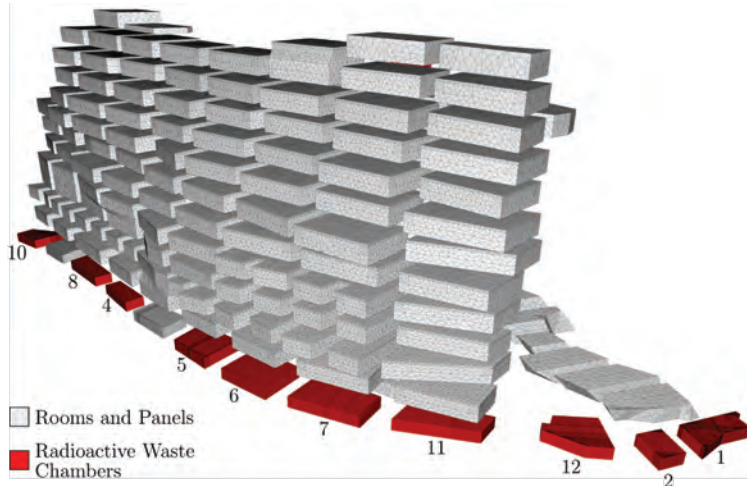
Figure 7: Locations of the radioactive waste chambers at the 750-m-level of the southern flank

In this variant, altogether seven modified excavation shields are set up one after the other in waste-chamber 1. This chamber is previously re-excavated with another retrieval method. After assembling, shield number 1 starts excavation in direction of waste-chamber 2. In the trace of the shield, the pillar between has to be mined as well.
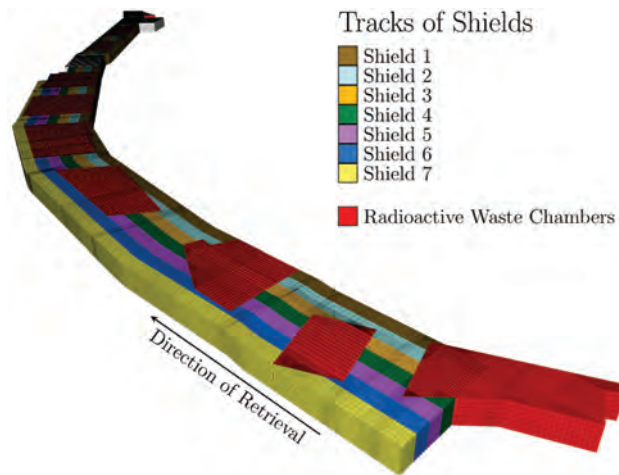
Figure 8: Tracks of excavation shields

After shield 1 has left the pillar between the two chambers, shield number 2 is going to start excavation alongside of the track of shield 1. Afterwards, shields 3 to 7 start excavation in such a way that the tracks of all shields together cover the width of the chambers across the strike. The shields numbers 1 to number 4 continue re-excavation until reaching the last chamber 10 at the edge of the mining field. Contrary to this, the shields number 5 to 7 will be stopped after re-excavating chamber 5. That can be done because the width across the strike of the chambers in western direction amounts only to ca. 20 m and is covered by shields number 1 to 4 (see Figure 8). The width of one shield was drafted in the study by 6 m. After retrieval, the tunnel of each shield is filled by Sorel concrete, but tubes have to be constructed inside for transport and infrastructure reasons.

5.2 Modelling results and assessment

5.2.1 Stress redistribution in a chamber during retrieval of radioactive waste

While re-excavating a chamber the model reveals that the compaction pressure of the backfill body in the whole chamber decreases very quickly after entrance of shield 1 (see Figure 9, compressive stresses positive).
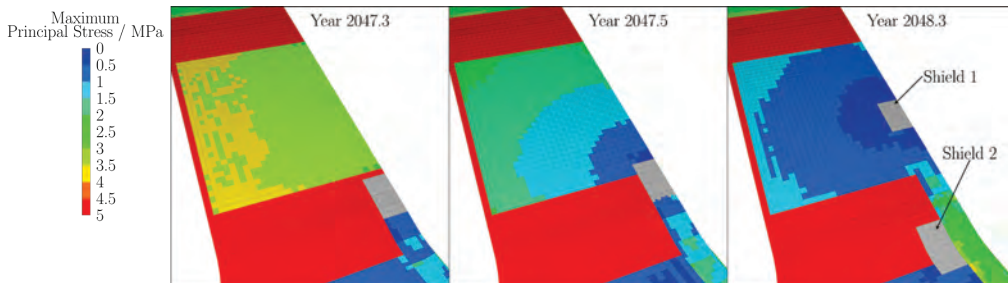
Figure 9: Stress redistribution in chamber 6 during retrieval of radioactive waste

This is a geomechanically important result and has to be regarded in the further planning phases. Due to the reduction of support generated by the backfill, fracturing processes in the stopes above the chambers could be activated.

5.2.2 Evaluation of pillar stability

Figure 10 presents the distribution of maximum principal stress in the pillar between chamber 6 and 7 for two different time points (compressive stresses are positive). At the top of the figure, the corresponding time is year 2035 before start of retrieval. At the bottom of the figure, the corresponding time is year 2048.3 after shield 1 has left the pillar and shield 2 is now pushing his track through this pillar. The comparison of the two stress fields reveals that stress redistributions have taken place. Especially above the excavated and backfilled track of shield 1, stress concentrations have evolved. Within the backfilled Sorel concrete, the compressive stress is still very low. Fortunately, significant strain softening processes were not produced in the model. Therefore, there are no hints of stability problems in the modelled pillar until to this time point. The tracks of the shields are sketched for clarity reasons.

5.2.3 Evaluation of barrier integrity

The evolution of the minimum principal stress at the top of the southern flank for a depth of 451 m nearby row number 3 (at the western part of the flank) is illustrated in Figure 11. As visible, the minimum principal stress begins to rise in the time interval before 2030 when the Sorel concrete filling of the open gaps between backfill and roof in several openings of rows 2 and 4 was simulated. Before, the stress development was characterized by stress interactions in the mining system. There can be stated the most important conclusion, that the retrieval which is in progress since 2035 does not impair this trend of stress increase.
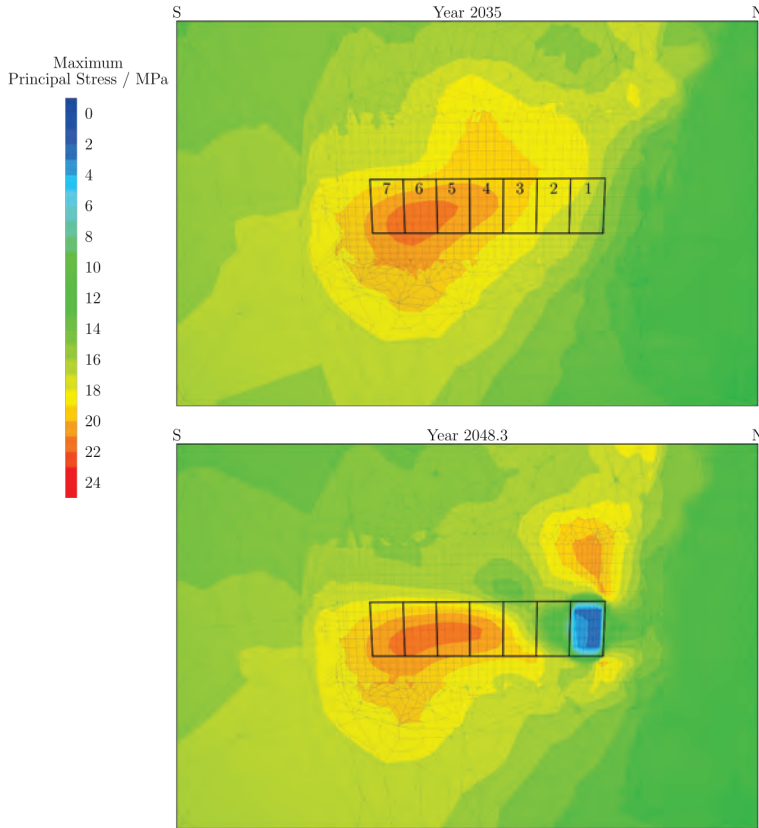
Figure 10: Maximum principal stress in a vertical cut-plane through the pillar between chamber 6 and 7 for two time moments year 2035 and year 2048.3
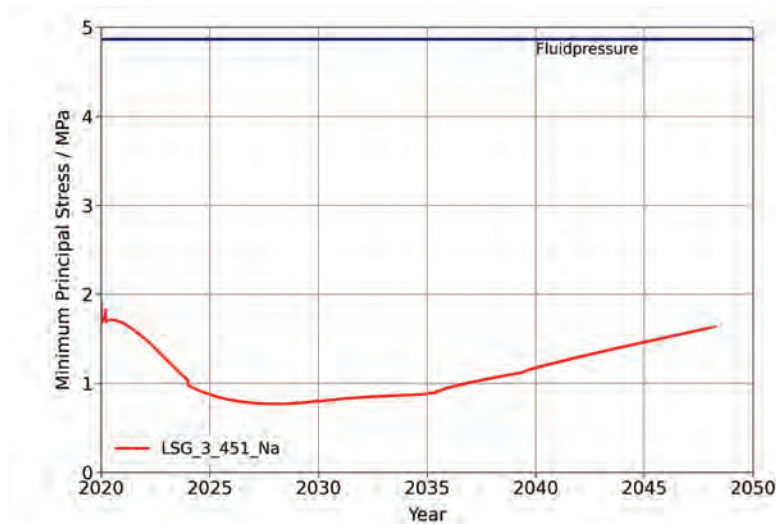

Figure 11: Evolution of minimum principal stress at a depth of 451 m nearby row number 3 of the southern flank

But, for the entire time plotted in Figure 11 the potential fluid pressure, calculated on basis of brine column, exceeds the minimum principal stress. The risk of brine inflow escalation remains present all the time.

Figure 12 presents the development of the maximum and minimum principal stress in the depth of the radioactive waste chambers at two points in the halite barrier 15 m in southern direction of the chamber 6 and the pillar to chamber 7. In the near field, a remarkable influence of the re-excavation can be seen, but the potential fluid pressure does not exceed the minimum principal stress.
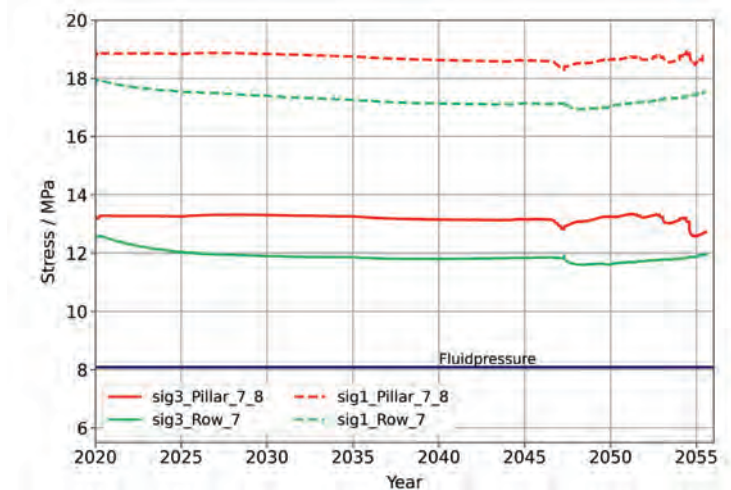
Figure 12: Evolution of maximum and minimum principal stress at a depth of 750 m nearby row number 7 (radioactive waste chamber 6)

6 Summary

IfG Leipzig is involved for about 25 years in giving geomechanical expertise for the Asse II mine. For that, different modelling concepts and material laws have been developed to reproduce and understand the geomechanical processes as shown by mine surveying. In the article, as latest state of model-development, a comprehensive FLAC3D-model of the whole mine is presented. Modern meshing tools for the grid generation were used and a procedure for transmission of calculated magnitudes between grids of different discretization was written. The calculation results until the present are in agreement with the mine surveying. To demonstrate the performance capability of the model, the retrieval sequences of a special method using rectangular mining shields are re-evaluated.

It was found, that the unloading of the backfill while re-excavation has a crucial impact on the roof support of the chambers. Regarding pillar stability, no significant strain softening takes place. The course of re-excavation is slow enough that the backfilled Sorel concrete can harden and is able to bear rock loads again. The geomechanically positive increase of the minimal principal stress in the top of the halite barrier is not impaired by the retrieval. But, the risk of brine inflow escalation remains present all the time. The simulated retrieval method is evaluated as feasible in general. The further planning phases pursue other technical concepts, but the minimal invasive philosophy, which means stepwise re-excavation and fast support, remains valid as well.

References

Kᴀᴍʟᴏᴛ, P., Gÿɴᴛʜᴇʀ, R.-M., Sᴛᴏᴄᴋᴍᴀɴɴ, N. & Gᴀ̈ʀᴛɴᴇʀ, G. 2007. Modelling of strain softening and dilatancy in the mining system of the southern flank of the Asse II salt mine. The Mechanical Behavior of Salt – Understanding of THMC Processes in Salt; Proc. 6th Conference, Hannover 2007, 327-336.

Kᴀᴍʟᴏᴛ, P., Wᴇɪsᴇ, D., Gᴀ̈ʀᴛɴᴇʀ, G. & Tᴇɪᴄʜᴍᴀɴɴ, L. 2012. Drift sealing elements in the Asse II mine as a component of the emergency concept – assessment of the hydro-mechanical functionality. The mechanical behavior of salt; Proc. 7th Conference, Paris 2012, 479-489.

Kᴀᴍʟᴏᴛ, P., Gÿɴᴛʜᴇʀ, R.-M., Gᴀ̈ʀᴛɴᴇʀ, G. & Tᴇɪᴄʜᴍᴀɴɴ, L. 2015. Geomechanical assessment of the Asse II operation phase until radioactive waste retrieval using large 3D-models. The Mechanical Behavior of Salt; Proc. 8th Conference, Rapid City 2015, 389-399.

Kᴀᴍʟᴏᴛ, P., Gÿɴᴛʜᴇʀ, R.-M., Gᴀ̈ʀᴛɴᴇʀ, G. & Tᴇɪᴄʜᴍᴀɴɴ, L. 2018. Geomechanical stability proof of the Asse II mine and forecast of the further development using an extensive 3D-model. The Mechanical Behavior of Salt; Proc. 9th Conference, Hannover 2018, 611-626.

Iᴛᴀsᴄᴀ 2017: Fast Lagrangian Analysis of Continua in 3 Dimensions, User's Guide, www.itascacg.com, ITASCA Consulting Group Inc, Minneapolis, Minnesota, USA.

Gÿɴᴛʜᴇʀ, R.-M. & Sᴀʟᴢᴇʀ, K. 2007. A model for rock salt, describing transient, stationary and accelerated creep and dilatancy. The Mechanical Behavior of Salt – Understanding of THMC Processes in Salt; Proc. 6th Conference, Hannover 2007, 109-117.

Mɪɴᴋʟᴇʏ, W. & Mÿʜʟʙᴀᴜᴇʀ, J. 2007. Constitutive models to describe the mechanical behavior of salt rocks and imbedded weakness planes. The Mechanical Behavior of Salt – Understanding of THMC Processes in Salt; Proc. 6th Conference, Hannover 2007, 119-127.

Lᴜx, K.-H., Dʏᴏɢᴛʏᴇᴠ, O. & Lᴇʀᴄʜᴇ, S. 2018. A contribution with respect to the systematization of the analysis process with exemplary application on the situation existing on the south flank of the ASSE II salt mine (Schacht ASSE II/Südflanke). The Mechanical Behavior of Salt; Proc. 9th Conference, Hannover 2018, 627-648.

Aʟʙᴇʀ Gᴇᴏᴍᴇᴄʜᴀɴɪᴋ, IғG-Lᴇɪᴘᴢɪɢ 2019. Gebirgsmechanische Untersuchung der Auswirkungen der Rückholvarianten „Schildvortrieb mit Teilflächenabbau" und „Teilflächenbau von oben", KZL 9A/23510000/GC/TA/0001/00, Dortmund, Leipzig, 20.05.2019.

Field evidence of salt fracturing and healing in a MgCl₂ cavern field

Peter Fokker[1], Abel Jan Smit[2], Ad Barth[2]*

[1]Nedmag/WEP, Netherlands; [2]Nedmag, NL

* p.fokker@nedmag.nl

ABSTRACT: In the solution mining industry, there has been a long debate whether brine (cavern fluids) can fracture a salt formation with high leakage rates, especially under slow pressure build-up rates. The alternative is leakage via elevated permeation levels via intragranular microfissures. In this way leak-off rates are still an (exponential) function of cavern pressure. A limited test in a German (Etzel) cavern was inconclusive on the mechanism of leak-off. See Brouard (2019) for a summary on leakage tests and incidents.

In 2018, the Nedmag solution-mined cavern system developed a fracture. Nedmag solution-mines bischofite and carnallite from the Zechstein III formations at about 1500 m depth. The caverns are separated from the overburden by the ZE-III-4 and ZE-IV halite formations (Figure 1), and have a roof thickness of about 100 m. Because of a number of reasons, the cavern pressure slowly increased, but still well below 90% of the lithostatic pressure, considered a safe operational cavern pressure. However, a fracture formed, resulting in a leak-off of about 75000 m³ brine and a pressure drop of approximately 30 bars in 2 days. In the days/weeks after the fracture incident, another (estimated) 25000 m³ of brine escaped from the cavern system, mainly driven by creep convergence of the cavern system.
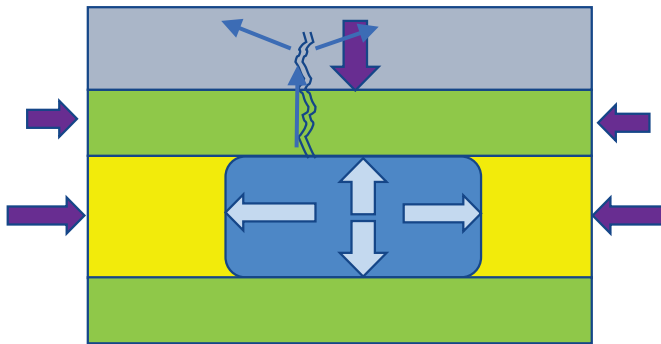
Figure 1: Cartoon of fracture leakage from the cavern system (blue) via the ZE-IV-halite roof (green) towards the overburden (Bunter formation in grey)

The cavern system was monitored by pressure, outflow, subsidence (GPS and Insar) and evaluated using cavern convergence due to salt creep, with historical history matching. It appeared that the fracture most likely closed and stopped leaking after some 2 weeks and remained closed since (for almost 4 years in Jan 2022). It is believed that the fracture mechanically closed, perhaps assisted by cooling crystallization of the saturated magnesium chloride brine, flowing up.

3D Finite Element simulations (using Diana FEA) at the end of 2018 showed that the low fracture gradient, could be explained by strong salt creep of magnesium salts, resulting in subsidence of about 45 cm (100 cm at cavern level) and stress arching above the cavern system, lowering the vertical stress in the midst of the labyrinth by about 8 MPa, which also relaxed the horizontal stresses by (very limited) salt creep in the halite roof by some 5-6 MPa.

1   Introduction

Salt caverns in clean salt are fluid tight, at least within measuring accuracy of gas, brine or oil losses. The exception (apart from leaking via wells) is the situation of fluid pressures that are at or higher than the salt stresses, where fractures may arise. Little field evidence of such large fractures exists or has been reported in open literature. See for instance the reports of Brouard. Limited field tests, like in an Etzel cavern, remained inconclusive on the leakage mechanism, being either a salt mass at elevated permeability (micro-cracks) or via macro-scale (single) fractures. Such a fracture did occur in April 2018 at Nedmag in Veendam.

Nedmag operates a magnesium salt mine near Veendam, solution mining mainly bischofite salt ($MgCl.6H_2O$) and in the past also carnallite ($MgCl.KCl.6H_2O$) at about 1500 m depth. Given the high solubility of bischofite (about 2.5 m^3 per injected 1 m^3 of water, as compared with about 0.15 m^3 of NaCl in halite solution mining) and the limited layer thickness (10-30 m net thickness), caverns expand quickly laterally, mainly in an up-dip direction. Density flow is the main driver for transporting unsaturated brine towards the salt front and transporting saturated brine back to the deepest point in a cavern (Figure 2). A total brine volume of some 7 million m^3 brine was present in a labyrinth type of cavern system (called the cavern cluster) in April 2018. Salt creep related cavern convergence had already resulted in about 7 million m^3 volume reduction (and extra brine production) since 1993, when lower pressure mining became the preferred strategy to near-lithostatic mining, as applied before since 1977. Salt creep had resulted in about 45 cm of subsidence near the mining site.
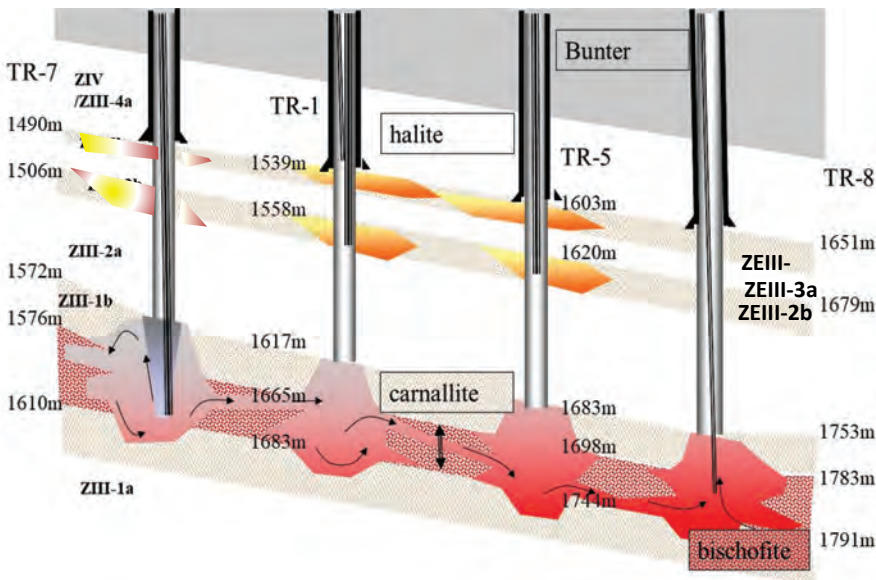

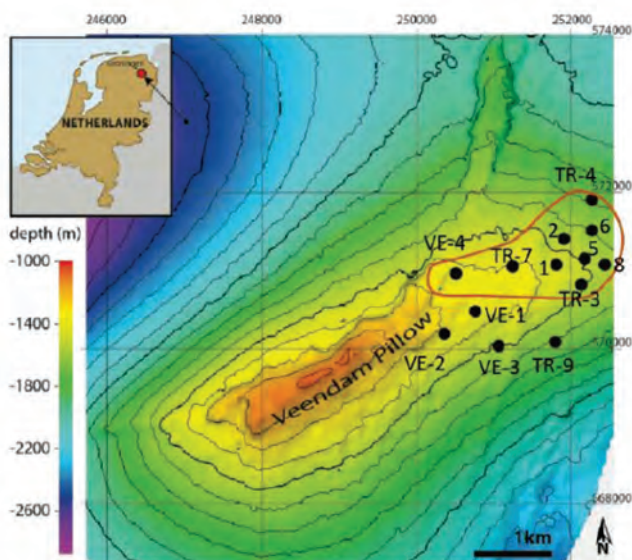Figure 2: Cartoon of cluster with communicating (former) caverns

Figure 3: Depth Map showing Top Salt and the casing shoe position of the wells. The indicative cavern cluster outline is depicted by the red curve.

In April 2018 an unexpected large fracture was formed, linking the cavern cluster (through the salt roof of about 100 m thick) to the Bunter formation, losing about 100 000 m³ of brine volume in a few days, after which the fault closed due to the 35 bar lowered cavern pressures.

Finite element modelling, simulating about 25 years of salt creep, could well explain the fracture by means of (creep assisted) salt stress relaxation in the cap rock, lowering the salt roof horizontal stress and hence the fracture pressure with some 5-6 MPa (50-60 bar).

2   Fracturing of rocks

2.1   Theory and practice

All rocks are brittle under tensile stress. If tensile stress is exerted on any rock, a fracture develops at some stress level, usually starting at a small defect (microcrack, inclusion, internal lamination). For hydraulic fracturing, the situation is a bit more complex, since fluids must enter the microcracks to further wedge-open the micro-crack and form a major crack. Initiating a crack would be difficult in an impermeable rock like salt. Fokker (1995) proved that salt plugs could be hydraulically fractured in the absence of initial cracks at about the tensile strength of the material (using oil, brine and nitrogen as fracturing medium), which is some 2 MPa for clean halite and some 0.6-0.2 MPa for carnallite and bischofite. The tensile strength of anhydrite was not tested in these studies but is higher.

In some cases, especially for slow fracturing processes and rocks with low tensile strength, fracture networks can be formed, rather than single fractures. Inhomogeneous strength, in-situ stress and stiffness levels are the main drivers for fracture networks, but large inhomogeneities are not expected in clean bedded salt, except for layers of anhydrite, that are stiffer and more creep resistant than halite.

Another issue is the effect of fracture closure. In hard rock (carbonates, basalt, cemented sandstone, etc.) a fracture remains a permeable conduit after fracture closing. The fracture

walls do not fit perfectly anymore as a result of small amounts of slip and small chips or broken rock that act as a proppant. Precipitation from passing fluids (usually carbonates and salts) can sometimes clog the fractures or rock healing mechanisms effects come into play, certainly in salts.

2.2 Nedmag fracturing and fracture closing process

The Nedmag cavern cluster was operated for some 10 years at a level of 70 bars below lithostatic (about 80 % of lithostatic) and was steadily (in the course of 9 years) allowed to rise to 50 bars below lithostatic (about 85% of lithostatic), for operational reasons (Figure 4), which was believed to be a safe pressure regimte. In April 2018 an unexpected large fracture was formed, linking the cavern cluster (via an about 100 m thick halite salt roof) to the Bunter (claystone) formation, losing about 100 000 m^3 of brine volume in a few days. The fault most likely closed once the cavern pressure lowered by 30 bar (Figure 5). The fracture remained closed until present day (Jan 2022), while the brine pressures were kept at a much lower pressure than before April 2018, but still at a pressure well above the brine-hydrostatic pressure in the Bunter formation.
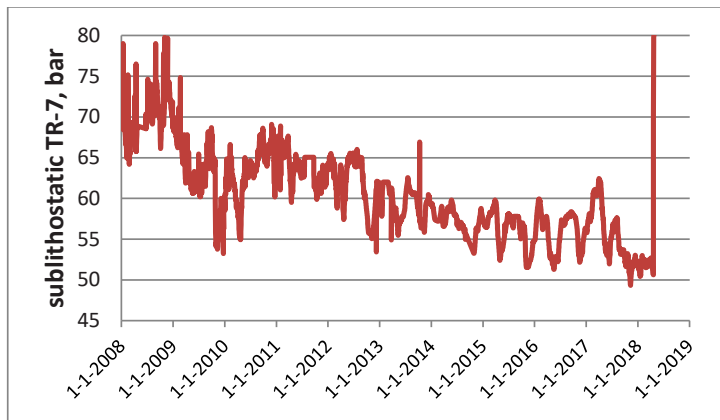
Figure 4: Pressure evolution in cavern cluster. The curve shows the sublithostatic pressure at well TR-7 from 1-1-08 to 1-5-18, a few days after the sudden pressure drop.
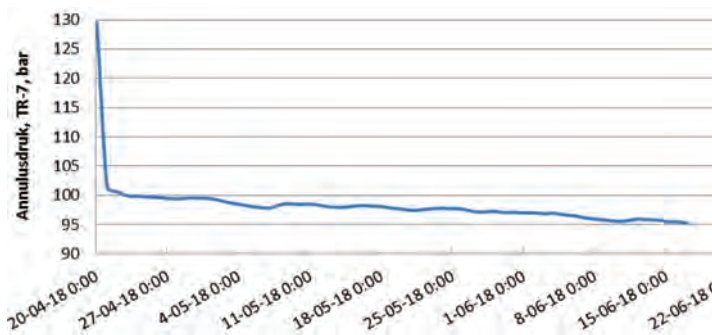
Figure 5: Pressure drop of cavern cluster, as measured via the annular pressure of well TR-7 (in bar). The pressure stabilized at 101 bar, with the further drop to 95 bar until 20-6-18, fully attributed to elevated brine production and stop of water injection.

In the case of Nedmag, several effects may have played a role to quickly stop the cavern leakage. The lowered brine pressure resulted in compressive stresses at the fracture wall. At

the same time, the solubility of magnesium-chloride brine is strongly temperature dependent. This causes cooling crystallisation of salt when flowing through a narrow crack in a salt layer, which is most likely 1-2 degrees cooler than the brine. In order to move away from the fracture closure pressure (and potential fracture reopening pressure some bars above), the pressure was lowered by producing as much brine as possible and stop water injection. This resulted in a further pressure drop of about 5 bars in two months. The cluster pressure was kept constant since that moment (at least until early 2022), producing a squeeze induced dropping flowrate from about 70 m³/h in July 2018 to 40 m³/h in December 2021 (Figure 6). The amount of "free" bischofitic brine, the amount believed to be not enclosed by sump material, dropped from over 2 million cubic metres to slightly less than 1 million cubic metres. This volume was matched with Insar subsidence data, confirming that the fracture is fluid tight.
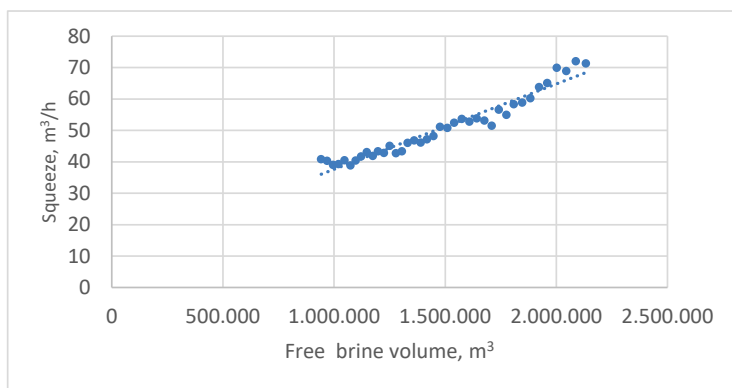
Figure 6: Cavern convergence (salt squeeze) in m³/h as function of the (fitted) open cavern volume in the bischofite section of the cluster. The dots are monthly net production averages over a time span of 3.5 years (July 2018-Dec 2021).

For 2022-2045 a further reduction of cluster volume is planned also by lowering the cluster pressures. It is expected that at these pressures, the 1 million m³ carnallite section (Zechstein III-2b/3b, Figure 2) will contribute to the squeeze (brine) production. The present contribution is marginal. Additional salt dissolution and production is planned from one existing well and from new wells that will be drilled in 2022 and later. The fracturing incident served as a benchmark for cavern pressure management in order to prevent future leakages from the cluster or new caverns.

2.3   Potential leakage effects

The fracturing process has driven 100 000 m³ of brine into the overburden. Fracturing simulators from the oil & gas industry were applied to estimate the fracture dimensions and the potential for fracture growth into the shallow (sweet water) formation. See Smit (2019). Main uncertainty was the leak-off rate into the side walls (and hence the permeability of the overburden). Fracturing into the shallow layers was not found likely. Ground water monitoring (up to 400 m depth) did not show elevated magnesium levels, nor oil (diesel). Diesel was used as blanket control for strip mining (until 1995 in the cluster). Some tens of thousands of cubic metres of diesel are still trapped somewhere in the cluster, though most likely distributed in hundreds of smaller pockets, which may largely remain trapped for ten-thousands of years.

3   Finite Element Simulation

A 3D model (Figure 7) was created from a geological (Petrel) model, applying SKUA-Gocad surface meshing software and DianaFEA Finite Element software for analysis. The magnesium bearing layers (and cavern space within) were modelled separately, but the complexity of mixed salts within the magnesium bearing layers and considerable sump volumes in the caverns had to be neglected. The salt material parameters have been modelled as "averages" of bischofite, carnallite, kieserite and halite parameters.

Bischofite creep dominates the salt creep in the ZE-III-1b layer, whereas carnallite creep dominates the ZE-III-2b/3b layers. The over- and underburden salts are halite creep dominated. Figure 8 shows the top of the ZE-III-1a halite with the meshed bodies of the caverns on top of it, that were cut out of the ZE-III-1b bischofite formation. The new (not yet existing) caverns have been meshed as well for reference and future effects but modelled as lithostatic fluid inclusions for the period 1993-2021.
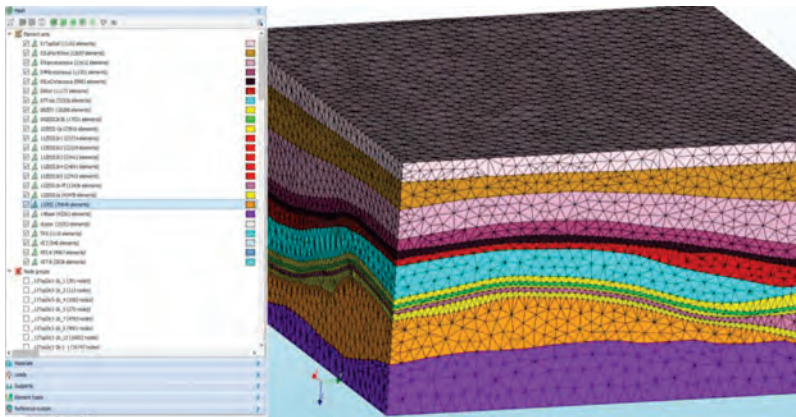
Figure 7: Formations in bird-eye view. Overburden from top to bottom: Top soil (=Upper North Sea), Lower North Sea, Upper- Mid- and Lower Cretaceous, Rot, Trias (Bunter). Yellow layers are ZE-III-IV halite layers, a green carnallite (ZE-III-2b/3b) and maroon bischofite (ZE-III-1b) layer. Beneath in orange the ZE-II in purple is the underburden (ZE-I and Rotliegend).
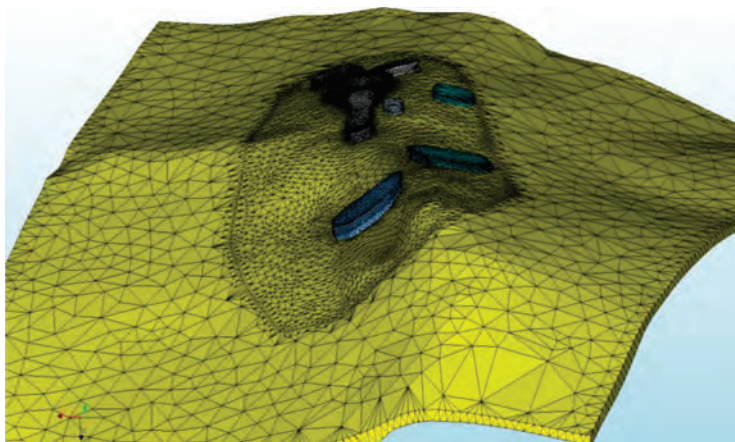

Figure 8: Caverns on top of the underlying ZEIII-1a halite formation, including projections of future caverns

The cavern system was given a realistic pressure history since the mid 90-ies and an increasing trend until 2018. During the low pressure period salt creep resulted in cavern convergence (squeeze in of mainly bischofite) but also resulted in stress arching around the cluster (associated with a subsidence bowl of slightly over 40 cm). The stress arching results in lower vertical stresses in the middle of the cluster (and slightly higher stresses in the flanks to compensate). In an elastic response, stress arching results in elevated horizontal stresses in both the halite roof and in the Bunter formation near the centre. Reduced vertical stresses and increased horizontal stresses result in creep of halite, by which the horizontal stresses slowly drop towards the reduced vertical stress level. Only 1-2 promille of creep is sufficient (in the case of Nedmag) to transfer horizontal stress arching stresses towards the overlying (elastic) Bunter formation. The situation is only slightly reversed by an increased brine pressure level (as evidenced also by the non-reversed subsidence). This halite stress relaxation allows an early break-through (i.e. well below the original lithostatic stress level) of brine through the salt.

The creep parameters of the halite roof are not known from lab tests, but were matched to history match the moment of the incident. They are well within the published range of parameters and test result of the ZE-III-2a halite. Primary creep was neglected in this study (given the slow creep process of decades). Variations (order of magnitude) have been applied for the roof halite creep A-value to arrive at an uncertainty effect (that was determined as low). The average magnesium salt creep parameters (except for the power exponent from literature) have been fitted with the known subsidence development since the 90-ies. Overburden parameters have been fitted somewhat to also create a good conformance with the known shape of the subsidence bowl, but within realistic uncertainty range. Parameters are displayed in Table 1. Figure 9 displays the horizontal stress (Northing) in 2018 at the top of the halite roof (close to the Bunter), prior to the formation of the fracture. The red areas are locations of largest stress drop (of up to 6 MPa) with respect to initial stresses.
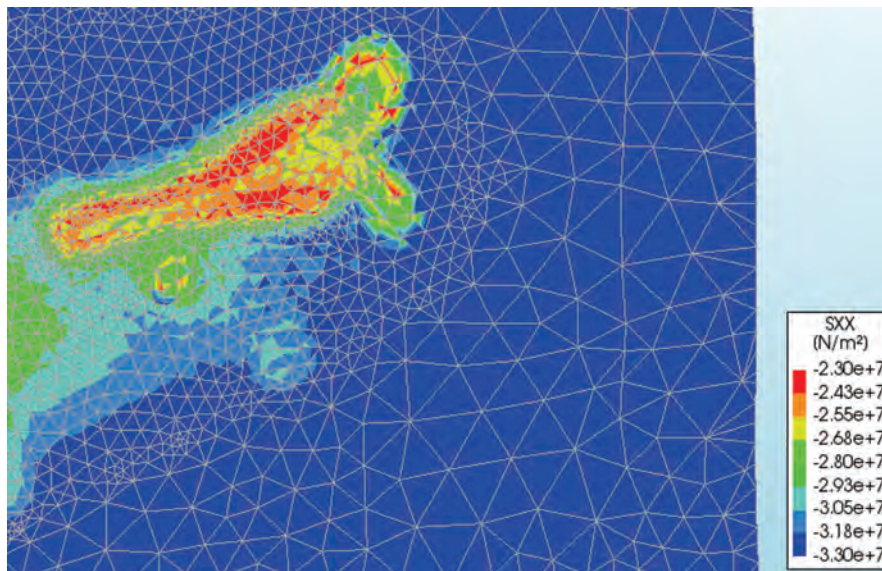

Figure 9: Horizontal (Northing) stresses prior to fracturing 2018 at the top of the ZE-IV salt roof. In the middle, the red area shows a reduced stress of about 23 MPa, whereas the region outside the cavern area has a stress level of about 30 MPa, indicating a stress drop of up to 6 MPa since the start of solution mining.

The critical horizontal stress (picked from a location in the middle section of the cluster roof) has been plotted with fluid pressure evolution. The cavern pressure was extrapolated with a

brine gradient toward the same depth to match fluid pressure with salt stress. It can be seen from Figure 11 that the horizontal stress more or less follows the brine pressure level, but only bounces back slightly when brine pressures are increased again. As soon as the pressure exceeds the salt stress, a fracture is possible, but its formation depending on the tensile stress of salt and existing defects.

This stress relaxation process does explain the fracture process from the cluster at sublithostatic pressure. The sudden pressure drop may be associated with the thin anhydrite layer (base ZE-IV) that has higher strength than halite and postponed the fracturing temporarily. This still a bit speculative for the moment.
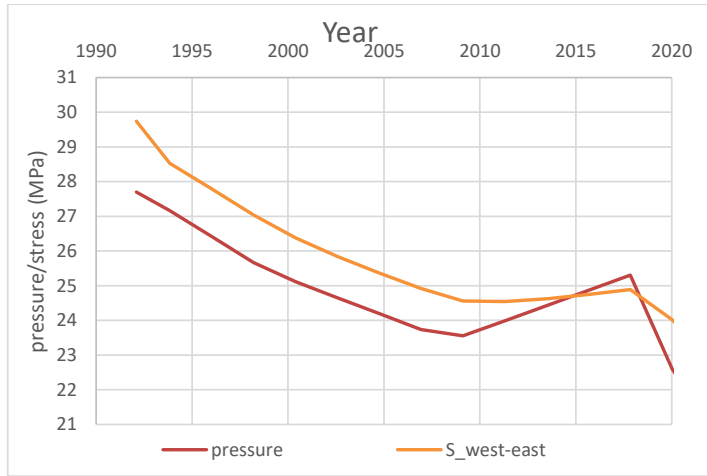
Figure 11 Graph showing cluster brine pressure and minimum horizontal salt stresses at the cavern halite roof as a function of time. Note that since 2015 the pressure exceeded the salt stresses.

Table 1: Rock and Salt parameters as used in 3D Finite Element modelling

3D-modelling:

	density g/cc	Young M GPa	Poisson	n	A /s	K0 Sh/Sv
Quaternary/	2.1	0.5	0.4			0.7
Cretaceous	2.3	5	0.3			0.7
Rot	2.25	9	0.3			0.7
Triassic/Bunter	2.3	12	0.3			0.75
Halite ZE-II	2.2	20	0.3	4	1.E-13	1
Halite ZE-III-IV	2.2	20	0.3	4	1.E-14	1
Carnallite	1.7	3	0.3	2	5.E-13	1
Bischofite	1.7	3	0.3	1.6	6.E-13	1
ZE-I / Rotliegend	2.3	20	0.3			1

4 Future magnesium salt mining

Nedmag has applied a conservative (but easy to implement) approach, where cavern pressures of large (>400 000 m³) caverns will not be allowed to be raised more than 1.5 MPa above the lowest (year-average) pressure of the cavern. This would have prevented the

leakage incident in the cluster and will be a very safe maximum for new and smaller caverns. As a second measure the (connected) cavern volume will not be allowed to grow to the level of the cluster in 2018 (or even close to it). In the later phases of solution mining (and pre-abandonment), the fluid pressure will be lowered to close-to brine hydrostatic pressures, so that salt creep minimises the brine volume, prior to final abandonment.

5   Conclusions

The Nedmag cavern leakage incident proved (perhaps for the first time) that a salt formation can be fractured and can be fractured at levels far below the lithostatic level, in case significant stress arching (and associated subsidence) has occurred. Although the Nedmag situation is most likely not representative of other solution mining or gas storage caverns, it is a situation that cannot be excluded on basis of theory or experience only. The bright side of the incident is that it shows that a fracture also closes and apparently heals in case the pressure is lowered once more.

For Nedmag the incident resulted in an updated mining strategy where cavern pressures will not be allowed to be raised to much higher levels than seen in recent years. In general, this means a slowly dropping cavern pressure from year to year until the cavern is close to brine-hydrostatic (just sufficient to produce brine, given pipeline friction).

References

BÉRÈST, P. 2017. Cavern abandonment issues, Discussion contribution, SMRI Fall 2017 Technical Conference, Münster

BROUARD, B. 2019. Brouard Consulting: Overpressured caverns and leakage mechanisms Phase 2: Cavern scale

BROUARD, B. 2020. (Brouard Consulting, MAP): KEM17 study, Dutch government. Over-pressured salt solution mining caverns and leakage mechanisms, KEM study

DUQUESNOY, A. 2017. Issues concerning the abandonment of deep brine-filled caverns. Discussion paper (revised),SMRI Fall 2017 Technical Conference, Münster, Germany

FOKKER, P.A. 1995. The behaviour of salt and salt caverns, P.A. Fokker, PhD thesis, TU Delft, NL

SMIT, A. 2019. Sudden pressure drop in Nedmag cavern cluster. SMRI Fall Conference Berlin, Germany

URAI, J. 1983. Deformation of wet salt rock, thesis, University of Utrecht, NL.

In-situ analysis of cavern convergence and closure in a complex geological and operational setting

Max Wippich[1]*, Kerstin Künzel[2], Stefan Meyer[2], Dirk Zander-Schiebenhöfer[1]

[1]DEEP.KBB GmbH, Germany; [2]SWKiel Speicher GmbH, Germany

*max.wippich@deep-kbb.de

ABSTRACT: The prediction of cavern convergence that results from the creep of salt rock is an essential information for the operators of gas storage caverns, since convergence has direct influence on the performance of the storage. Therefore, storage operators rely on a continuous analysis of operational data and in-situ measurements. The case study presented is special since

- the cavern is only partially filled with gas and is operated below the maximum cavern pressure
- the cavern interval covers two lithologically very different salt rocks
- the fraction of insoluble components (and the sump volume) is large
- the site is characterized by an anisotropic regional stress field

The history-matching of sonar surveys indicates breakouts at the cavern contour in a preferred direction and convergence perpendicular to that, which leads to increasing ovalisation of cross-sections. At the same time, the sump level has substantially risen during storage operation while the usable open (gas and brine-filled) volume changed by convergence due to salt creep.

An approach is presented that integrates geological, thermodynamical, and rock-mechanical analyses of observed – and partly counteracting – effects. Thereby, the focus was on an estimate of the in-situ creep response with regard to the operational conditions as well as to the different depth sections of the cavern. It is shown that this approach provides a practical tool for the prediction of cavern convergence for the specific cavern considered as well as for other sites.

1 Introduction

Cavern Kiel K103 is part of the Rönne underground storage south of the city of Kiel, which is operated by SWKiel Speicher GmbH (Figure 1). The cavern was solution-mined over a depth range between 1,508 m TVD and 1,870 m TVD in the salt rock of the Honigsee structure. The section of cavern Kiel K103 contains two different types of salt; Rotliegend salt and Zechstein salt. Both lithologies were encountered during drilling of the well and during leaching of cavern K103. Due to the high content of insoluble mudstone in the Rotliegend salt, after the leaching process the open geometrical cavern volume was located within a depth range of 1,508 m to 1,746 m TVD (1,742 m TVD after first gas fill). The entire section below 1,746 m TVD is filled by a cavern "sump" of supposedly very coarse-grained rock fragments.

After leaching, the cavern was only partially filled with gas and the gas/brine interface was at 1,651 m TVD. Since 2014 the cavern was mainly operated for seasonal storage of gas. Three sonar surveys were performed following the initial measurement under gas. After the second measurement under gas, an unexpected high reduction of the gas-filled geometrical volume was observed as well as a change of the general cavern shape and an increase of the brine volume above the sump level.

In order to predict how the cavern volume would develop for the upcoming years of gas storage, the operator required an explanatory model for the observed cavern behaviour and a forecast of a potential future development. In order to identify and to differentiate the effects that contribute to the observed behaviour, an investigation program was launched, which comprised geology, thermodynamics and rock mechanics.
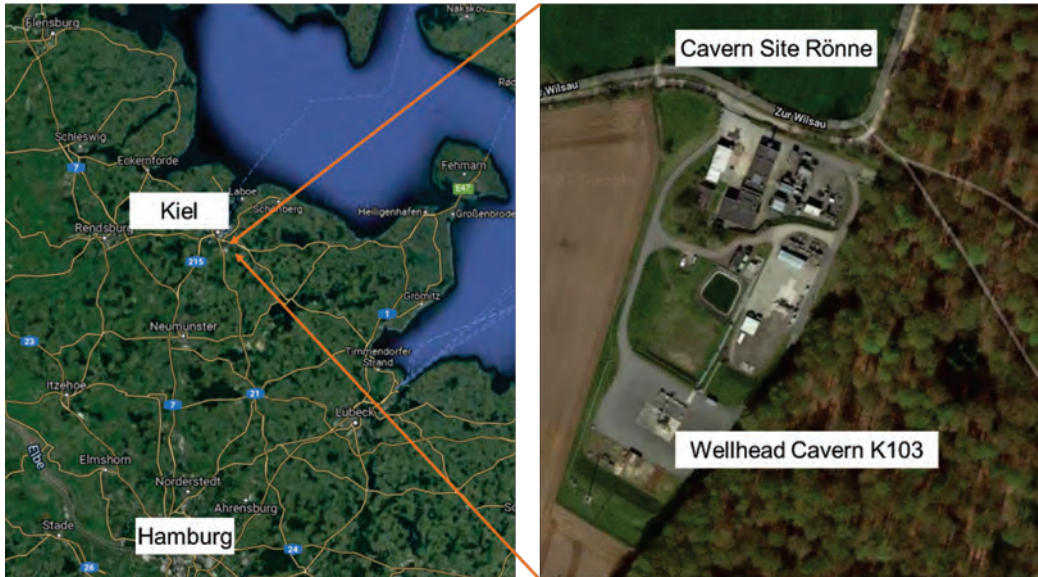
Figure 1: Location of the Kiel-Rönne gas storage site in the north of Germany

2   Observations

The cavern volume was surveyed by four sonar measurements since the beginning of gas storage operation as shown in the diagram in Figure 2. The comparison of the sonar surveys showed that the shape of the cavern has changed over the entire height of the cavern in terms of divergence and convergence in the preferred directions. The cavern shape did expand in a NW-SE direction, whereas the cavern has closed perpendicular to that. In Figure 3, this is illustrated by 3D bodies generated from the sonar data that show the changes that occurred in the time interval of 2017 to 2020. The following main features were identified by the comparison of the sonar measurements:

- Volume increase along the cavern contour due to spalling and rock fall
- Volume loss due to cavern closure (by creep of the salt)
- Rise of the cavern sump level, resulting from fallen rock and from "squeeze-out" of sump material due to closure
- Rise of the brine/gas interface
- Change of the brine volume above the sump level (initially with increasing, later with a nearly constant rate)

These observations raised a number of questions that had to be clarified:

- Why is the observed convergence that high?
- Is there a geological or mechanical background behind the preferred direction of the shape extension (in N-W to S-E direction)?
- Is the creep response possibly triggered by the brine wetting the rock at the cavern wall in the lower part of the cavern?
- Which factors contribute to the observed overall rise of the sump level?
- What could be a reliable forecast of the convergence rate for the upcoming years of storage?
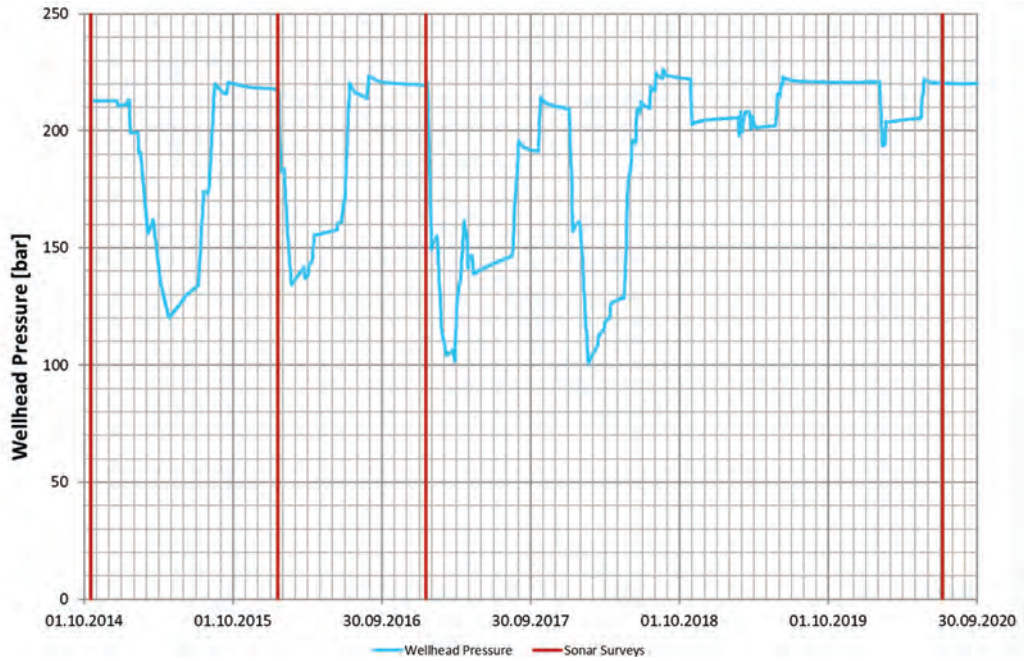
Figure 2: History of wellhead pressure and sonar surveys for cavern K103

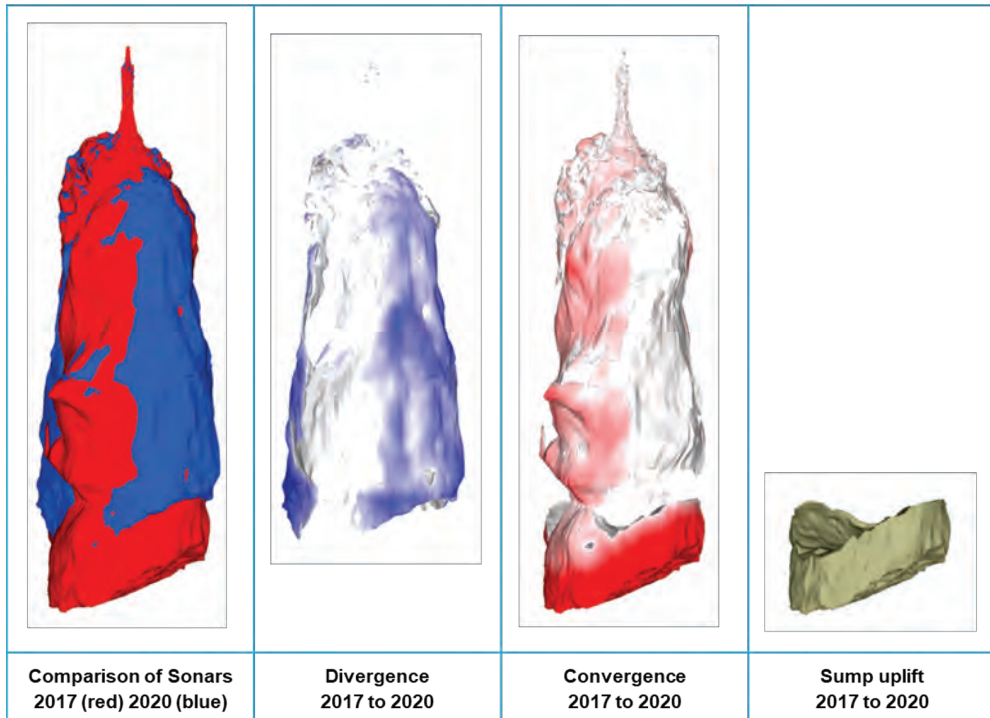| Comparison of Sonars 2017 (red) 2020 (blue) | Divergence 2017 to 2020 | Convergence 2017 to 2020 | Sump uplift 2017 to 2020 |

Figure 3: Modelled 3D bodies demonstrating the observed cavern volume change in the time interval between the sonars in 2017 and in 2020

A multi-disciplinary assessment was thus done consisting of

- a thermodynamic back-analysis of the gas storage period,
- a rock-mechanical analysis of the convergence behaviour,
- an approach of balancing the observed volume losses and volume increase resulting in a convergence prediction tool for future operations, and
- a geological review of the section with special focus on the different salt rocks.

3 Geological analysis

The shape development of cavern Kiel K103 as observed from the echometric surveys from October 2014 to July 2020 suggests that the convergence and divergence volumes that are recognisably linked to different areas of the cavern contour and to preferred orientations are likely to reflect both local and regional geological conditions.

Cavern Kiel K103 is located in the domal Honigsee salt structure, which is a so-called "Doppelsalinar" ("double" salt structure) formed from salt rocks of both the Rotliegend group of the Lower Permian and the Zechstein group of the Upper Permian. This type of structure prevails in the centre of the Permian depositional area, which is roughly bounded by a line from Kiel to Husum in the north and reaches approximately as far as the Hamburg and Bremerhaven in the south. A common, though weakly supported, general model for the formation of these structures suggests that the salt rock of the Rotliegend group occurs in the centre (or along the axis), while the Zechstein salt is to be found along the flanks of the dome.

Cavern well K103 was drilled to a final depth of 1,891.1 m TVD. The well location is in the central part and somewhat east of the main axis of the Honigsee salt structure. From the top of salt at 1,159.3 m TVD to 1,579.1 m TVD the section consists of Zechstein salt, while below Rotliegend salt was drilled. Structural data obtained from drill cores shows shallow to moderately steep dip of 30 to 50° in the Zechstein (measurements were not possible in the largely textureless Rotliegend salt).

The cavern was solution-mined in the interval from 1,888 to 1,508 m TVD. Because of the high average content of non-soluble rock components in the Rotliegend salt, almost half of the height of the leached section was lost to the sump. The geometric volume of the resulting open cavity was determined to be 509,839.8 m³ by the final echometric survey in brine (in February 2012). The cavern sump and the cylindrical part of the cavern are located mainly in the Rotliegend section, whereas the cavern roof is in the Zechstein. Within the Rotliegend part of the well section, two isolated occurrences of Zechstein salt were exposed outside the cavern axis during solution mining: Elevated concentrations of potassium and magnesium in the produced brine as well as an extension of the cavern contour towards SSE (now fully covered by the sump) suggests a portion of Zechstein salt from 1,760 to 1,795 m TVD; a second presumed Zechstein exposure, with a contour anomaly in NE direction, is located between 1,620 and 1,650 m TVD.

The composition, texture and mechanical behaviour of especially the Rotliegend salt are unique to cavern K103 and are considered to be responsible for the shape of the cavity, the sump development and presumably also the convergence behaviour. The Rotliegend salt consists of a mixture of medium to coarse crystalline or fibrous halite and well indurated mudstone with gypsum or anhydrite nodules. The clay minerals in the Rotliegend salt are exclusively non-swellable minerals (illite, chlorite, kaolinite; based on clay mineral analyses on sample material from the neighbouring K102 well). From the openhole density log in well K103, the average content of non-soluble (non-halite) components in the Rotliegend salt was estimated to be 25% vol. This value was also used as a basis for the leaching simulations and led to a realistic model that corresponds to the actual shape and volume development of the

cavity. Density measurements on core samples resulted in mass ratios of clayey material to rock salt of 1:4 to 2:3.

The grain size spectrum of the non-soluble residue from the Rotliegend salt ranges from suspended clay to fist-sized (and most likely much larger) rubble, some of which were produced to surface during solution-mining (Figure 4). Laboratory experiments, although difficult due to the large size of the components, and the observed actual development of the sump during solution-mining suggests a bulking factor of about 1.7. Thus, it can be assumed that the sump had at least initially a pore volume of about 40 %. A clast-supported structure with considerable initial permeability can also be assumed from the fact that in the early construction phase of cavern K103 it was possible to circulate through the sump in direct leaching mode.

Figure 4: Non-soluble components from the Rotliegend salt produced to surface with the brine during solution mining. Red mudstone (left) and anhydrite nodule (right).

The Zechstein salt in the cavern section of K103, by contrast, is rather clean rock salt (>95% halite), which has a texture characterised by a coarse crystalline matrix, in which giant halite monocrystals or "crystal lumps" are interspersed ("Kristallbrockensalz" of the Staßfurt Formation).

In order to characterize the material behaviour of the salt rock in the section of K103, rock-mechanical tests on core samples were carried out by Institut für Gebirgsmechanik (IfG), Leipzig. These tests were performed as triaxial compression (TC) and triaxial extension (TE) tests, respectively. Compared with known other salt rocks, the Zechstein salt in the K103 section shows comparable strengths. For confining stresses greater than 5 MPa, the values are above 40 MPa. For the Rotliegend salt the strength level is about 8 MPa lower compared to the Zechstein salt.

In order to assess the deformation behaviour of the salt, the secondary creep rate versus mechanical stress is plotted as shown in Figure 5. In this diagram, the creep velocities measured for secondary creep are plotted against the differential stress applied in each test. Regression of the measured values yields characteristic curves for the two different salt rocks (Zechstein and Rotliegend salt), which can then be compared with known values for the creep behaviour of other salt rocks. The well-known material law BGRa is shown for comparison (red dashed line in Figure 5). The creep behaviour of the Zechstein rock salt from well Kiel K103 (green line in Figure 5) is then estimated to be somewhat less prone to deformation than the BGRa reference. In contrast, the results for the Rotliegend salt (blue line in Figure 5) is in the expected range.

In fairly good match with the distribution of the two salt rock types along the cavern contour, the observed widening of the cavity at the cavern roof (the divergence volume) is small-scale and patchy, whereas it is rather large-scale and more uniform in the cylindrical part of the cavity above the sump (especially in NNW and SSE direction). The reason for this could be a more plastic Rotliegend salt compared to a Zechstein salt that is less prone to deformation and

reacts more with breakouts and spalling. However, it cannot be ruled out that the different in-situ deformation behaviour is due to the fact that only the upper part of the cavern is filled with gas.
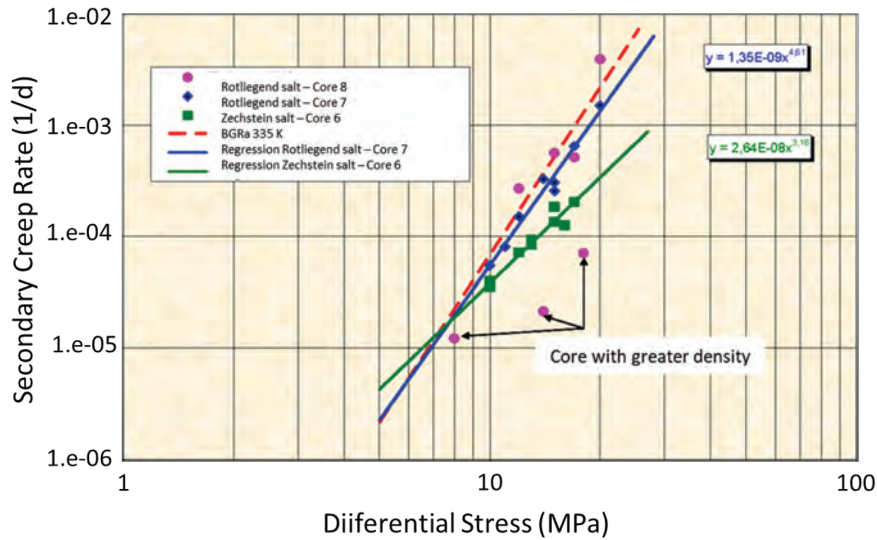

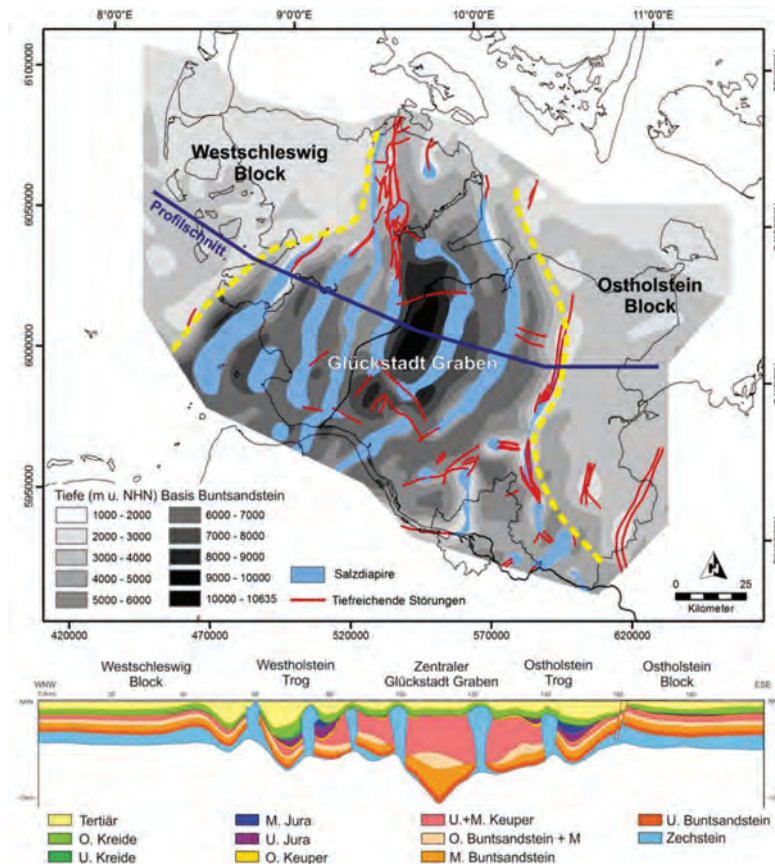Figure 5: Lab-test results from creep tests performed by IfG (2007)

Figure 6: Regional tectonic setting of salt structures of Schleswig-Holstein (from LLUR 2017)

Apparently, the regional geological context also has an impact on the shape development of cavern K103. The long axis of the horizontal sections of cavern K103 runs approximately parallel to the main strike of the Honigsee structure. The Honigsee structure, in turn, is part of a more than 100 km long and about 4 to 6 km wide "salt wall" that extends from Bad Bramstedt north of Hamburg in the south to almost below the Baltic Sea in the north. At the culmination, top of salt lies at a depth of about 1,000 m below surface while the base of the salt is thought to lie at a depth of more than 6,000 m.

The orientation of the elongated overall structure (and that of other salt structures in Schleswig-Holstein) follows the major tectonic trend of the Glückstadt Graben or its eastern marginal fault and is primarily an expression of tectonic activity in the Tertiary in a WNW-ESE to W-E directed stress field (Figure 6). It appears that this stress regime still has an effect today since cavern Kiel K103 obviously converges preferentially in the direction of the regional main tectonic stress, while divergence or breakouts in the contour can be observed perpendicular to it.

4   Thermodynamic analysis with regard to convergence behaviour

The objective of the thermodynamic investigation was to check whether storage operation may have led to unexpected impacts on the cavern contour and to provide general information about cavern volume development over time while considering the creep of the salt. Since the apparent convergence (as can be deduced from consecutive sonar measurements) includes other effects like rock fall, bulking of rock material, rise of the cavern sump level and squeeze-out of sump material, the contribution of the volume changes solely driven by salt creep cannot be determined directly. By history matching of the wellhead pressure general information about convergence driven by salt creep could be derived.

The thermodynamic back-analysis of the gas storage history considered the different parts of the cavern with regard to their content (gas, brine and sump). When applying a uniform dataset for the surrounding salt formation for the analytical convergence formula of VAN SAMBEEK (1992), a reasonable match of the cavern convergence as observed by consecutive sonar measurements could not be achieved with the initial thermodynamic model. However, when considering different creep abilities of the salt during times of operation at low and high cavern pressure, i.e. an accelerated creep at high cavern pressures (i.e. low stressing of the salt rock mass), a good match of wellhead pressure data could be achieved. This point of view was considered in the subsequent rock-mechanical back-analysis of the cavern volume over time.

Finally, with the thermodynamic analysis of the operation history an initial estimate on the general convergence behaviour of the cavern was obtained.

5   Rock mechanical analysis including rock fall and rise of the sump level

The analysis of the volume changes over time with respect to depth (Figure 7) revealed that in the Zechstein salt the divergent behaviour prevails, whereas in the Rotliegend salt below the volume behaviour changes from convergence to divergence as soon as the cavern wall gets again into contact with brine. Since the convergent behaviour is masked by the divergent behaviour, it cannot be deduced from the measurements whether or not the two different lithologies have a different creep behaviour. However, from the comparison of the first measurement under gas in 2014 and the final sonar survey in brine (at the end of leaching) it can be concluded that the convergence rate was almost constant until 2014 (blue line in Figure 7). Therefore, the rock-mechanical analysis of convergence of the cavern caused by the creep of salt was performed with a uniform data set for the creep behaviour of both the Zechstein and the Rotliegend salt in well K103.
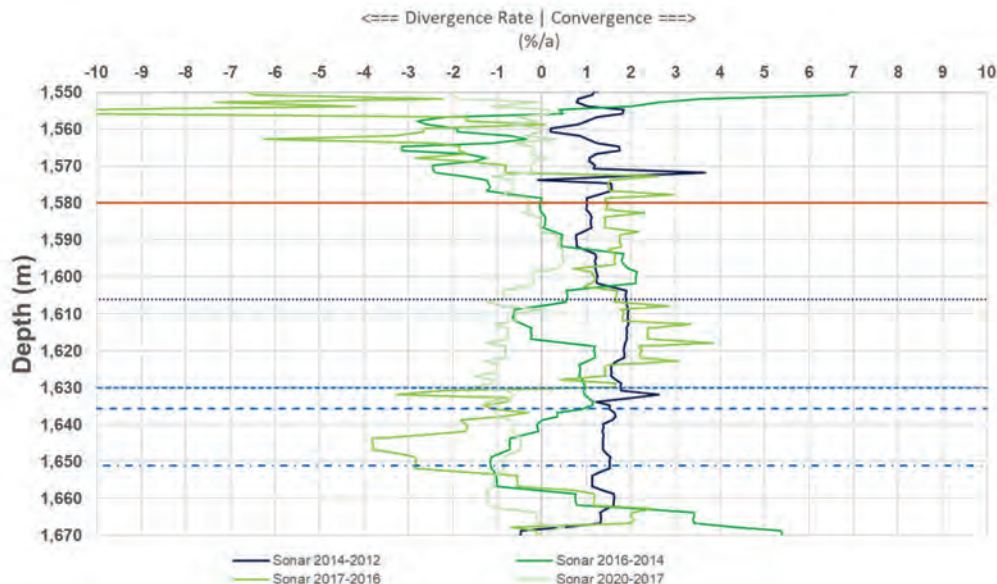
Figure 7: Depth-related volume changes over time, 2012 to 2020

The goal of the overall rock mechanical analysis was to find a balance between the identified different volume changes, back-calculated for the past period, and compare them with the measurements. By back-calculation the following volumes were computed:

- Convergence volume due to salt creep and operating pressures
- Volume of solid material due to rock fall piled up in the sump
- Volume of squeezed-out sump material due to convergence of the sump
- Volume of newly created pore space in the sump

The calculation procedure for the convergence volume considered the results of the thermodynamic analysis. In the rock mechanical analysis, the volume loss due to creep of salt was modelled separately for the three sections of the cavern that are either gas-filled, brine-filled or filled with sump material. A uniform dataset for the analytical creep model was applied. A good match could be found here again when assuming an additional creep mechanism in the low deviatoric stress range. The final approach is shown by the diagram in Figure 8, which also illustrates the contributions from the different creep characteristics in the high and low deviatoric stress range. By this approach, a convergence volume of 61,582 m³ was estimated for the 2017 to 2020 operation period.

A bulking factor was applied to the observed divergence volume as the rock material from contour breakouts piles up in the sump as a debris with a certain pore space. With a bulking factor of 1.6 applied to the divergence volume as deduced from the measurements, an additional sump volume of 13,967 m³ was calculated.

Furthermore, convergence is believed to act on the sump and parts of the still not very well compacted (not very "stiff") sump material are consequently squeezed out into the open cavern volume above. The assumed rise of the sump level by this process was assumed with a volume equivalent of 13,218 m³. Back-calculated and observed volume changes are compared in Table 1. Since the goal of the study was primarily to create a workable prediction tool, the analytical approach of Van Sambeek (1992) was applied. However, the consideration of different mechanisms or creep abilities for the low and the high deviatoric stress range led to a reasonable representation of the cavern volume development over time. Against the

background of the various and partly counteracting influences on the observed cavern volume, the comparison of measured and calculated cavern volumes is in very good agreement for the 2017 to 2020 analysis.
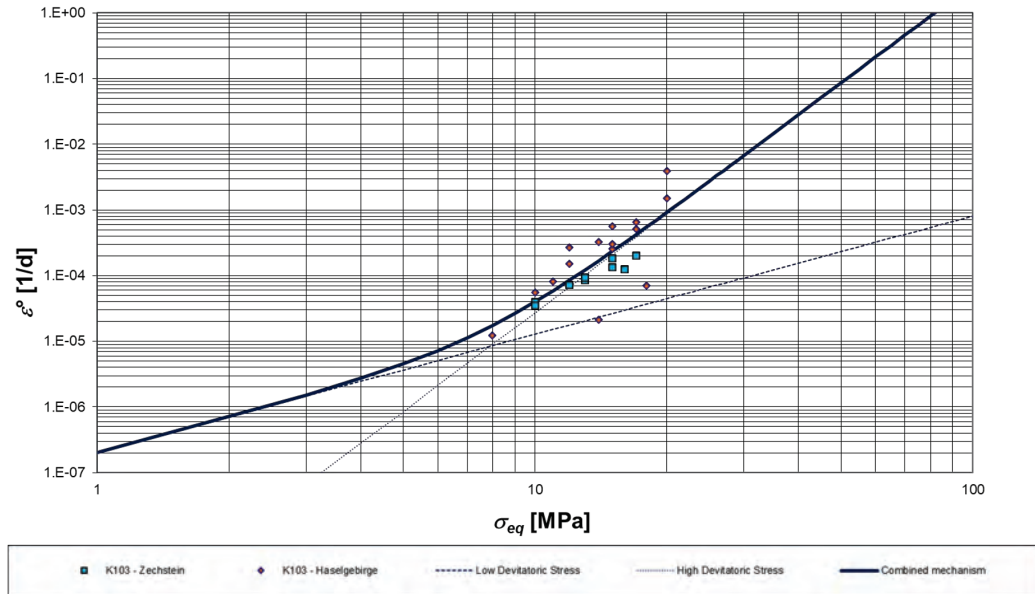

Figure 8: Assumed creep characteristic for rock-mechanical back analysis after calibration of the model

Table 1: Comparison of measured and back-calculated volume changes of cavern K103 during the operation phase of 2017 to 2020

	Total Volume [m³]	Gas-filled Volume [m³]	Brine-filled Volume [m³]	Newly created Sump Volume [m³]
Measurement – Back calculation	-76	-81	5	12,767
Error	0.12%	0.13%	0.47%	17.9%
Volume change (measured)	**-61,659**	**-60,711**	**-948**	**71,515**
Volume change (calculated)	**-61,582**	**-60,630**	**-953**	**58,748**
Convergence Volume (calculated)	-34,357	-34,357		
Brine volume (measured)		953		953
Convergence volume due to rock fall (calculated)j	-13,967	-13,967		37,247
Sump rise (calculated)	-13,218	-13,218		20,549

From the analysis of the cavern volume development over the years of gas storage in cavern K103 (i.e. not only for the period between 2017 and 2020) it can be concluded – from a practical

point of view – that a reliable prediction of the cavern volume behaviour could be made, which was valuable information for the company in order to plan for future gas storage.

6   Conclusions

The observed overall convergence rate of cavern Kiel K103 is not unusually high. The high convergence of the open and usable volume results mainly from the situation that the cavern is only partially filled with gas while its lower part remains brine-filled. To a smaller degree, the loss of gas storage volume is caused by the sump material being squeezed out (as an effect of convergence) and by rock fall in combination with bulking of the debris. Furthermore, the cavern is located at comparably great depth and the rock mass temperature is high at the location. Also, due to technical reasons the cavern is operated below the theoretically possible upper range of pressures.

The deformation of the horizontal cavern cross-sections with a pronounced widening along a NW-SE trend appears to directly reflect a regional tectonic stress field. However, rock mechanical design recommendations are not infringed.

A different deformation behaviour of the two salt rock types, Rotliegend and Zechstein, is suggested by a visual comparison of divergence volumes in different parts of the cavern but could not be quantified based on the more general approach applied. Nevertheless, it is reasonable to assume that the salt creep behaviour differs for high and low stressing, which has to be considered by the applied creep law.

When the cavern wall gets again in contact with brine due to the rise of the gas/brine interface, spalling at the contour was observed in the section of the Rotliegend salt.

The rise of the sump level is not only caused by rock fall, but also largely due to sump material being squeezed out as a result of convergence of the sump.

 Finally, although not all observations could be explained in detail by the model, a practical and robust approach was implemented for the improved prediction of the volume development of cavern Kiel K103 during the upcoming years of gas storage. By history matching, it was possible to identify changes in the overall system as well as specific features such as the in-situ behaviour of the salt rock in contact with brine. Future observations and changes as e.g. convergence, brine and sump level rise, sump compaction, and rock fall can be integrated in the model. Generally, the model can be applied also to other caverns, when comparable site-specific data is available.

Acknowledgements

References

IFG INSTITUT FÜR GEBIRGSMECHANIK GMBH 2007. Gebirgsmechanische Untersuchungen zur Anlage und Dimensionierung der Untergrundgasspeicherkaverne Kiel 103 der Stadtwerke Kiel. - Unpublished

LLUR (Landesamt für Landwirtschaft, Umwelt und ländliche Räume des Landes Schleswig-Holstein, Abteilung Geologie und Boden) 2017. Verbundvorhaben „StörTief": Die Rolle von tiefreichenden Störungszonen bei der geothermischen Energienutzung, Teilprojekt (AP 1.2), 2017.

VAN SAMBEEK, L. 1992. Evaluating Cavern Tests and Surface Subsidence Using Simple Numerical Models. Kyoto: Seventh Symposium on Salt, 1992.

Storage of production brine in potash mine rooms: Investigation of rock mechanical feasibility

J.-P. Schleinig[1], M. Nest, R.-M. Günther[2], M. Günther, H. Zienert, S. Deppe[3]*

[1]K+S Aktiengesellschaft; [2]Institut für Gebirgsmechanik GmbH; [3]K+S Minerals and Agriculture GmbH, Germany

* Jan-Peter.Schleinig@k-plus-s.com

ABSTRACT: Storage in mining rooms is an opportunity to dispose brine from the potash production process. For a comprehensive analysis of the complex rock mechanical behaviour of mine fields under the effects of brine storage K+S and IfG develop an innovative investigation and demonstration concept. The proof of feasibility is based on a stepwise procedure (i) the description of brine-induced effects in the mining horizon, the derivation of their mechanical effects and the development of numerical modelling techniques to investigate these effects, (ii) the application of advanced modelling techniques to evaluate a real potential mining field for brine storage and for an acceptable rock mechanical behaviour and (iii) the development of a monitoring concept to observe the predicted rock behaviour. The study gives an overview of this procedure to establish the basis for a safe brine storage process in rooms of potash and salt mines.

1 Background and Objective

K+S is one of the leading producers of potash fertilizer in the world. The fertilizer is derived from potash salt which is extracted in potash mines mainly by conventional mining methods leading to an underground system of rooms and square pillars (Figure 1).
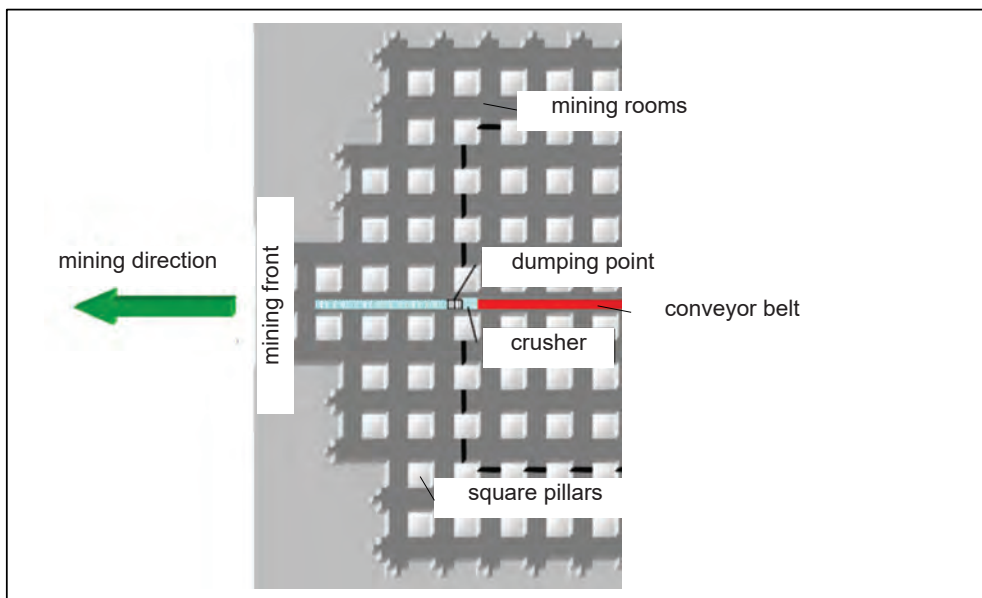

Figure 1: Schematic map of a mining field with square pillars

After processing the potash fertilizer, a production waste brine has to be disposed. One option is brine storage in old mining rooms. This concept is a big challenge in reality and therefore the following presentation focusses on the investigation of brine-induced rock mechanical behaviour of the mining rooms. As a result, a safe brine storing process should be proved. The evaluation procedure includes the following main steps:

- prediction of the expected rock mechanical behaviour by an expert and

- observation of the actual rock behaviour.

The prediction of the rock mechanical behaviour is based on numerical and analytical modelling including the initial mining situation and the mechanical effects of long time brine storage to the mine pillars. The outcome should demonstrate a safe brine storage process and contain the following statements:

- exclusion of mine field collapses: tested by weakening or removing of a pillar in a high stress situation and checking of mine field stability. This conservative approach shows the mining field resistance against dynamic processes.

- prediction of the mining room convergence behaviour - and - based on this:

  - evaluation of stresses in the salt layer barriers between mining rooms and overburden to confirm their integrity (criteria: minimum rock stress and dilatancy criteria) and

  - prediction of surface subsidence bowl development.

The predicted convergence and subsidence behaviour is used to specify a monitoring concept to observe the actual rock mechanical behaviour. Comparable prediction and observation results verify a safe brine storage process. In case of significant differences, causes can be checked and the modelling procedure can be adjusted. On the other hand, hazards can be identified early and countermeasures can be initiated if necessary. Based on practical experiences of brine storage at K+S, special modelling techniques and procedures have been developed for this purpose. This paper presents the main steps of the rock mechanical investigations.

2   Practical Experiences

K+S has practical experiences with flooding of mines in steeply inclined, layered salt sequences. Here the mining rooms are backfilled (mainly with broken rock salt from the fertilizer production) after finishing the mining process. Only few mining rooms and development drifts remain open. The flooding medium (fresh and waste water) is saturated in newly developed caverns which are located in the mine. Saturated brine then flows into the open drifts and mining rooms. Before and during the flooding process, K+S confirms a safe flooding process using the evaluation procedure described in Section 1. An IfG expert predicts the rock mechanical behaviour of the mine (rooms, drifts and caverns) before, during and after the flooding process. Due to the brine saturation, no significant dissolution takes place in the rooms and drifts. Only the mechanical effect of brine penetration in the rock areas around the rooms is modelled by a specific yielding behaviour of these areas. Here, the moisture penetration increases of creep rate of the rock. The modelling results demonstrate a safe flooding process. Based on this K+S verifies the existing monitoring system and adapts it if necessary. Final confidence is added from the fact that previous results of this procedures are similar at different mines: the mechanical response to flooding is smaller in magnitude than the predicted rock behaviour and confirm a safe flooding process (Schleinig et. al. 2019; 2020).

There are only few case studies of brine-storage-induced rock mechanical behaviour in K+S mines constructed in shallow deposits. Only one large-scale brine storage test has been realized in a limited room and pillar area of a potash mine. Here, salt was extracted from two potash horizons with room and pillar mining and square pillars. The brine storage test area lies in the lower mined horizon. The main test objective at that site has been the data collection describing the brine impact on the rock mechanical behaviour. Therefore, various monitoring systems were installed: (i) room convergence and pillar expansion monitoring systems in the brine storage area and (ii) seismic and levelling monument (control point) networks in the open mining level above the test area.

Furthermore, some numerical modelling was done in preparation of this test. The goals are:

- modelling of the initial, air-filled mine field situation and

- advancement of this mine model depending on significant changes observed in the rock mechanical behaviour.

The test has been running more than 12 years and observations show no significant changes in rock behaviour. All results are still in the range of open room conditions and it is impossible to distinguish the rock behaviour in air-filled and brine filled excavation areas. Therefore, no model advancement could be done and the existing measurement results confirm a safe large-scale test procedure (K+S 2021).

The results are also confirmed by the ongoing flooding of the Volkenroda-Pöthen mine (Gessert et. al. 2019). Additional seismic observations show a steady and more or less uniform convergence of cavities since 1996, whereby the rise in the flood level can be traced by a small increase in seismic energy releases.

All presented case studies show that: (i) the predicted rock mechanical behaviour overestimates the actual observed response and (ii) the measurement results show a slow and a more or less uniform convergence process.

3 Advancement of Modelling Techniques

There are many case studies for the evaluation of rock mechanical behaviour in open salt mining rooms with numerical models. Using the Discrete Element Model 3DEC (ITASCA 2016) salt behaviour is described by the mechanical behaviour of the single elements or rock blocks and of the boundaries between the elements or rock blocks. The respective material laws developed by MINKLEY for the elements/rock blocks and by MINKLEY and MÜHLBAUER for the boundaries were tested and used in many calculations for practical projects and describe realistic salt behaviour. Mathematical models for physical processes of primary and secondary creep, as well as plastic failure are well established in numerical codes for the evaluation of rock mechanical behaviour of air-filled (non-flooded) rooms in salt mines (Minkley 2004; Minkley & Mühlbauer 2007). The mechanical behaviour of backfill material, mainly broken rock salt, can also be involved in this calculations. Mine-site-specific rock and backfill material properties were defined by laboratory tests and confirmed during many evaluations in different projects. Summing up, the evaluation of the mechanical behaviour of pillars and pillar areas in air-filled portions of rock salt and potash mines is state of the art.

The integration and evaluation of the hydraulic and geochemical impacts of the brine storage on room and pillar stability and convergence behaviour is a big challenge. Three impacts and the effects to the mechanical behavior have to be evaluated:

(i) Moisture penetration into the rock:

Any brine-pressure-driven percolation is excluded due to the project restriction that the brine pressure must stay below the minimum rock stresses. Hence, only the effects of brine-induced rock penetration and softening take place in the excavation damage zone (EDZ). These processes are defined in the following way: (i) the complete EDZ behind the pillar contour is immediately penetrated with the rise of brine level along the pillar height and (ii) further moisture penetration follows the advancing plastic deformation of the EDZ with a rate of 20 cm/a. The mechanical behaviour of the wetted rock areas includes (i) a reduction of the MAXWELL viscosity of the rock blocks and (ii) a reduction of the contact surface strengths between the rock blocks. No consolidation is taken into account. These effects reduce the load bearing capacity of the wetted rock areas significantly – see IfG (2003)

(ii) Dissolution of sensitive mineral components:

The dissolution behaviour of sensitive mineral components depends on the geological composition of the pillar rock (given by the mining field situation), the composition of brine (mainly defined by the production process) and the possibilities for brine to reach the sensitive mineral components in the pillars. The geological situation of the mining fields described in the following paragraphs is mainly characterized by the composition of hartsalz (kieserite, sylvite and rock salt), carnallitite overlaying hartsalz and sylvinite overlaying hartsalz. The brine composition is adapted to these geological conditions but geochemical equilibrium of all kinds of salt in the rock is not reached in the brine. The brine is:

- completely saturated with NaCl – no dissolution potential,

- nearly completely saturated with carnallite – only a residual dissolution potential has to be taken into account,

- saturated either with kieserite or with sylvinite - there is no equilibrium between components in the brine.

Hence, brine dissolution effects to the pillars have to be evaluated. The relevant parameters for the mechanical effects of dissolution are the brine penetration rate and depth as well as the remaining pore volume after dissolution of minerals. Geological and geochemical experts of K+S give these parameters as input parameter for mechanical evaluation (These input parameters are given preconditions). The general dissolution conditions are defined for:

- Carnallite: The dissolution process follows the brine level rise at pillar surfaces immediately (brine penetration rate is set to its maximum) and completely (up to the maximum penetration depth depending on brine saturation potential in the adjacent rooms).

- Kieserite and Sylvinite: Dissolution of these components results in a kieseritic or sylvine saturation and takes much more time. Penetration rates are defined as 1.0 cm/a for kieserite dissolution and 0.3 cm/a for sylvinite dissolution. As long as both components are reachable for brine, the dissolution process takes place up to complete removal of one of the components.

After dissolution of the sensitive mineral components, a framework of rock salt crystals remains. The maximum pore volume can reach the former volume of the sensitive mineral components in the rocks. The remaining maximum pore volumes are input parameters defined in geological and geochemical studies.

For the evaluation of the rock mechanical behaviour with numerical models, the dissolution process is described with the following physical model. The transition from initial intact rock to the remaining porous rock after dissolution takes place by a change of the rock behaviour from an intact rock behaviour to a backfill material behaviour (Lüdeling et al. 2014; IfG 2020a). This material behaves like broken rock salt without any cohesion or tensile strength conservatively. Based on many laboratory tests, a relationship between backfill material pressure and deformation exists for different backfill densities (respective pore volumes). With this background it is possible to change the mechanical behaviour (intact rock → backfill) in numerical calculations. Depending on the given pore volume after dissolution a suitable backfill behaviour is chosen from the test results. Hence, the dissolution process in rock mechanical calculations can be defined by:

- the penetration rate: describes the transition front rate (intact rock → backfill) in the pillars,

- the penetration depth: describes the elements/blocks in the pillar where transition takes place,

- the behaviour of remaining rock salt structure: behaviour of backfill material depending on its pore volume.

The integration in numerical calculation includes the following conservative approach:

- all mineral parts in pillars which are sensitive for brine dissolution will be removed completely, independent of the actual reachability by brine (reductions of accessible pore volume by convergence, crystallization saturated brine are ignored) – and

- the remaining rock salt crystal structure behaves like a backfill material of loose rock salt. The pore volume is equal to the dissolved volume. This material compacts over time up to intact rock salt density with its mechanical properties.

(iii) <u>Hydraulic brine pressure:</u>

The hydraulic brine pressure depends on the brine density and the height of the overlaying brine volume respectively. In the rock mechanical calculation, the brine pressure is compared with the minimum rock stress regarding the barrier integrity mentioned above in Section 1.

The mechanical effects of these hydraulic and geochemical brine-induced impacts are defined, suitable models are developed and implemented in numerical codes (see references below). These models are tested in numerous calculation runs with single pillar models and a mining field model.

- The single pillar models include various geological configurations, i. e. different kinds of salts (described above) or shear planes in the pillars, various depths and various hydraulic pressures. The results show a plausible pillar behaviour with significant faster pillar convergence rates of brine filled mining rooms compared with open room situations. No pillar collapses are detected for single pillar situations close to reality (IfG 2018a; b; Schleinig et al. 2019; 2020).

- The mining field model is developed to test the stability of calculation runs. Figure 2 (above) shows a mining map with the track of the modelled section. The mining field contains characteristic geological formations and multi-level mining (level boundaries on the left side stand nearly vertical above each other). Due to mining time (middle of the last century) long rooms were constructed. The convergence of the resulting long wall pillar field behaves similar to the typical convergence of square pillar field.

A numerical model is developed for the rock mechanical investigation on the basis of the geological model in figure 2 (below). After successful model calibration using in situ measurement results several calculations are performed to test the developed model techniques with various dissolution rates, solution pressures and brine flooding regimes. The results show:

- Dynamic processes can be excluded, even not in the case of a sudden stop of brine flooding and a provoked pillar failure in carnallitite area.

- Pillar stresses transfer from intact rock to porous rock where sensitive minerals were dissolved by brine.

- First the convergence process during dissolution is faster than under open room condition but later it slow down again. After complete dissolution both compacted porous pillar rock and roof fall material take all stresses supported by brine pressure. Similar to the convergence process the subsidence rate increases after the brine fill in and decreases during and after the load transfer.

- The integrity of the salt barriers between the mining rooms and the biosphere was proven in all variations.

The developed model techniques are able to describe the impacts induced by brine storage in a realistic way. All variations show plausible and comprehensible results. The mining field model is suitable for evaluating the rock mechanical situation of a potential brine storage mining field (IfG 2020b; Schleinig et. al. 2019; 2020).

mining rooms of 1. level
mining rooms of 2. level

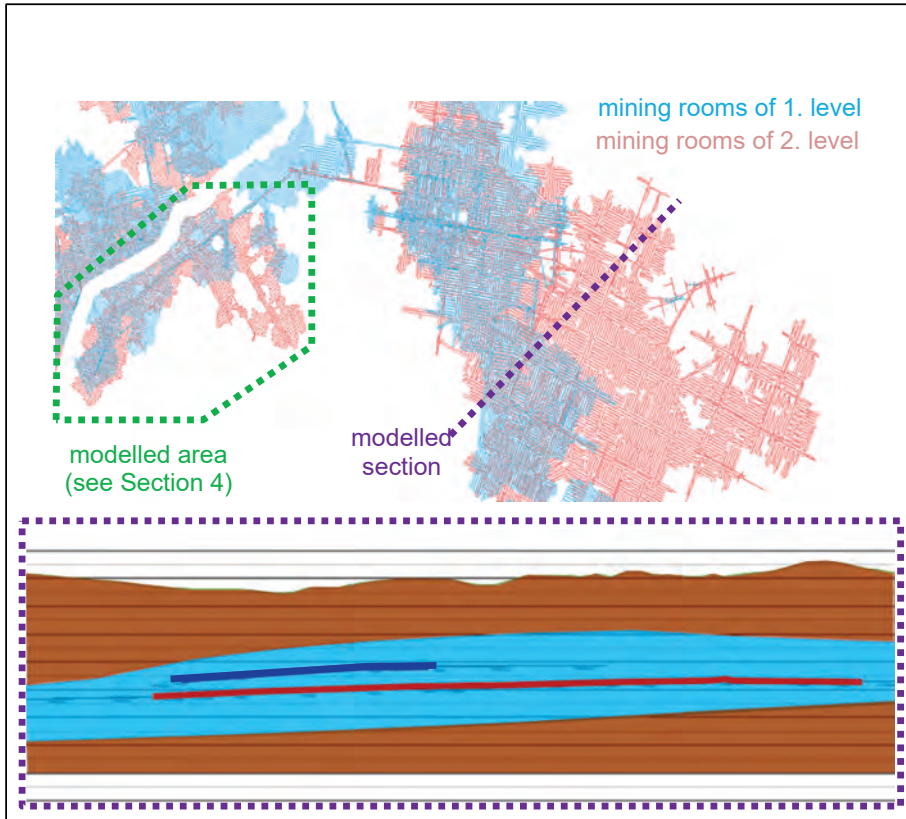modelled area
(see Section 4)

modelled
section

Figure 2: Mine map with room-and-pillars of the upper (blue) and the lower (red) mining level, modelled section and modelled panel (green, see chapter 4) and geological model along with the modelled section: overburden and subsalinar (brown), salinar (bright blue) with upper (blue) and lower (red) potash level which are mined

4 Evaluation of a Potential Mining Field

A room and pillar field is chosen for a potential brine storage and evaluated regarding the feasibility. Here, salt was extracted in two potash horizons (levels) too. Figure 3 shows the situation of this mining field:

(a) Ground view with the upper and lower level of the potential mining field (detail of "modelled section" in figure 2) and the sections and areas for numerical modelling,

(b) Ground view with the brine storage area at the upper level,

(c) Ground view with the brine storage area at the lower level,

(d) Numerical model along the section B.

The geological framework of both levels is comparable to the framework described in Section 3: hartsalz or carnallitite overlaying hartsalz or sylvinite overlaying hartsalz dominate. This is the basis for the facies specific room and pillar design. The level depths vary between 420 m and 720 m. The brine storage areas at the upper and lower level are shown in figures 3 (b) and (c) respectively.

The numerical modelling to evaluate the rock mechanical behaviour is done with 3DEC (Itasca 2016):

(i) 3D strip models (along selected sections and with a width of half a pillar and half a room) representing the general rock behaviour of the whole mining field before, during and after the brine storage and

(ii) additional 3D spatial models to evaluate a specific dissolution behaviour in local areas.

The models include the local geological and mining conditions in a conservative way.

- 3D strip model along section A runs from Northwest to Southeast and covers a relatively wide area of small pillars at the lower mining level. To the south, the mine approaches an area with reduced barrier thickness.

- 3D strip model along section B runs from North to South and covers the steepest level inclination as well as the centrally located small pillars on the lower mining level.

- 3D strip model along section C runs nearly parallel to section A but the mining levels are here at a lower depth. In the North it expands an existing subsidence center above an adjoining open mining field and includes the embedded pillar.

- 3D spatial models D1 and D2 represents local restricted areas where a deeper dissolution process can't be excluded.

The 3D models are based on geological profiles extending from the subsaline units to the surface. Figure 3 (d) shows the developed numerical model of section B for the evaluation of rock mechanical behaviour which is following explained as an example.

The evaluation includes the initial mining situation, the mechanical effects of brine storage to the mine pillars and the long time rock mechanical behaviour. Following the description in Section 1 a safe brine storage process is demonstrated with (i) the exclusion of mining field collapses and (ii) the prediction of the mining room convergence behaviour as the basis for the evaluation of the salt barrier integrity (with the minimum rock stress and dilatancy criteria) and for the prediction of surface subsidence. The brine composition is largely adapted to these geological conditions too and also the general dissolution conditions are comparable to the conditions described in Section 3. The model calculation starts with the initial geological situation and the simulation of the mining history. After that the model is calibrated using in situ measurement data. The processes in the pillars during flooding and storage are simulated as described in Section 3 under the following conditions:

- After initial brine penetration of the existing EDZ the further penetration into salt rocks follows the EDZ development with a rate of 20 cm/a.

- The dissolution in carnallitite unit occurs instantly up to a depth of 0.6 m.

- The kieserite (in hartsalz) and sylvite (in sylvinite) dissolve with a rate of 1 cm/a and 0.3 cm/a respectively.

- Accompanying the rising brine level, a supporting hydraulic pressure acts on the room contours.
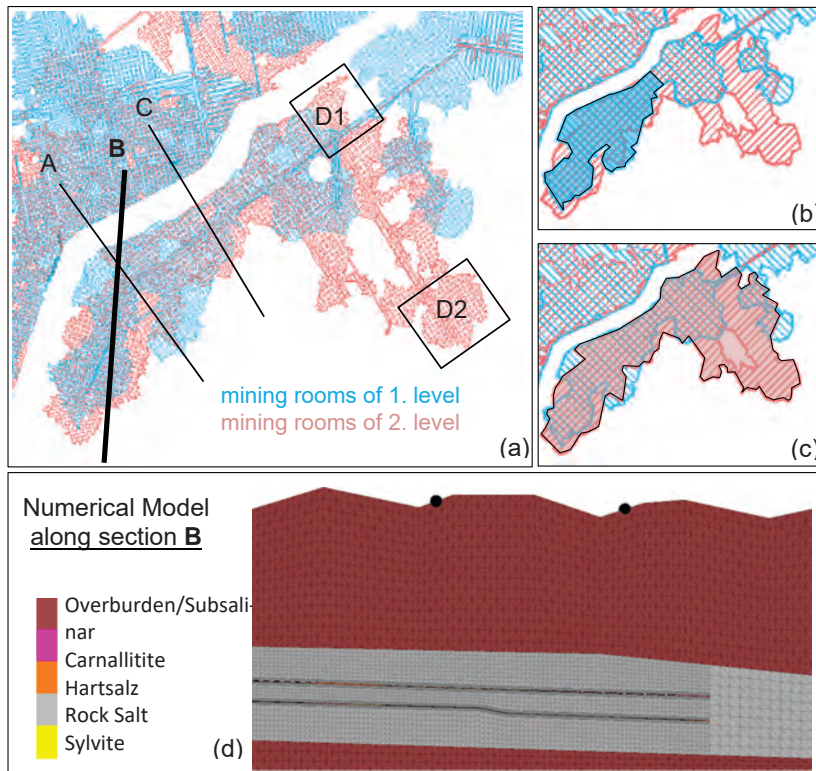
Figure 3: Detailed mining plan with (a) the mine panels (red: upper / blue: lower level) and sections (A, B, C) as well as areas (D1, D2) of numerical models, (b) the brine storage areas at the upper level, (c) the brine storage areas at the lower level (c) and (d) the model B of the rock mechanical investigations

The calculations are done for a time period of more than 1200 years after the start of brine storage. After this time, the moisture penetration and dissolving processes in the pillars are completed. The results can be summarized as follows (IfG 2021a):

- Mining field collapses can be excluded.

- The convergence process runs continuously and smoothly. The convergence rate increases initially and, after the load transfer from intact to porous rock in the pillars, the convergence rate decreases to the previous range of open rooms with some mm/a. The brine stabilizes the rock depending on the level of the overlaying brine volume.

- In the barriers (rock salt units above the potash horizons) the stress distribution and magnitudes fulfill the minimum stress and dilatancy criteria.

- The surface subsidence forms a flat bowl over time above the modelled areas.

As result of these numerical calculations, and based on long time practical experiences, the following recommendations are derived for the design of the accompanying monitoring concept:

- The convergence rate increases to twice of the initial rate at the start of brine storage and decreases later to the previous rate again. Moderately higher rates may occur in situ for limited times. The development of the subsidence rates follows the development of the convergence rates with a time delay.

- Seismic events exceeding a magnitude of 1.0 requires a discussion with experts and exceeding a magnitude of 3.0 requires a general re-evaluation.

The prediction of surface subsidence is restricted of the modelled 3D stripe models and 3D spatial models. More investigations are necessary to get a time depending spatial development of the surface subsidence bowl above the brine storage mining area. The basis is the result of the numerical calculations mentioned above. Only this result contains the impact of brine storage to the rock mechanical behaviour over time. Therefore, the following procedure is developed:

- The calculated convergence rates at different time points are taken from the numerical modelling. Based on comparable mining and geological situations, convergence rates of all mined areas between the numerical models (means between the sections and areas in Figure 3 (a)) are derived. Figure 4 (left) shows a mine map with all areas in the mining field and derived convergence rates for a defined time point: the red values are results of numerical modelling and the blue values between the 3D models are derived convergence rates.
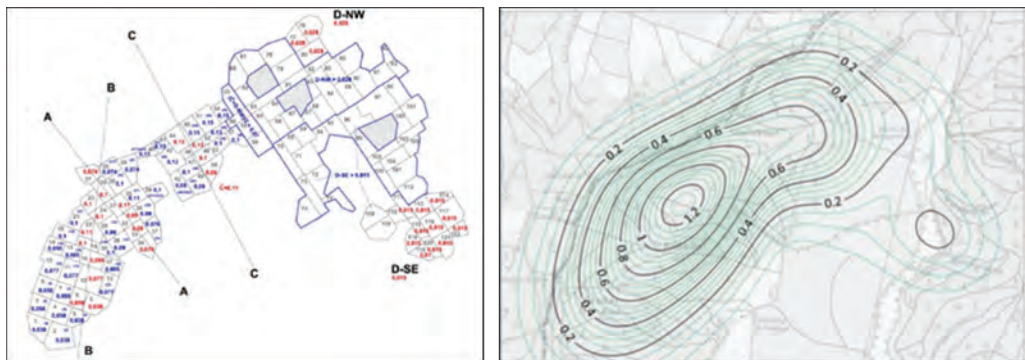
Figure 4: Left: Mine panel with zones of similar convergence rates based on modelling results (red) and derived for comparable geological and design conditions (blue) Right: Surface map with the calculated subsidence bowl contours above the brine filled mining area (3200 years after brine storage)

- All these convergence rates are implemented in an analytical calculation (Schober & Sroka 1983) the subsidence bowl development over time. This program requires the spatially distributed mined volumes and the time-dependent convergence rates to calculate the development of convergence volumes and, following that, the spatial subsidence bowl development using a transition function. Figure 4 (right) illustrates the contours of the predicted subsidence bowl above the brine filled mining area for a time point of about 3200 years (IfG 2021b).

These results show tolerable subsidence behaviour on the surface (predominantly used for forestry and agriculture) and give an orientation for the assessment of later subsidence measurements results (see Section 5). Summarizing all calculation results, the storage of brine in the studies mining panel is feasible regarding the rock mechanical point of view.

5 Advancement of the Monitoring Concept

The monitoring concept contains all observation procedures to determine and document the actual rock mechanical behaviour in and above of the rooms of the potential mining field before, during and after the brine storage process (K+S 2021b). The evaluation of the measurement results regarding the predicted stable conditions of the brine storage (based on expert judgements with numerical and analytical calculations, see Section 4) confirms a safe brine

storage process. Significant divergences can be detected and assessed early in time. The developed monitoring concept contains the following methods:

- Observation of convergence behaviour in brine filled mining rooms: Measuring points will be installed to record the convergence of the brine filled rooms permanently. Figure 5 (right) shows such a point used in the large-scale test area of brine storage for more than 10 years (described above in Section 2). The measuring point consists of 2 displacement sensors which are connected with a special steel bar between and with rock bolts. The bolts are fixed in depths > 1 m above the roof and below the floor. These monitoring points will be located in stations at both mining levels (Figure 5, left: stations 1 to 4). Following the recommendations (see Section 4) and based on practical experience a short-term increase in the convergence rate of up to 20 mm/a after the start of brine storage is acceptable if the convergence rate drops below 10 mm/a again within 3 years. Exceeding observation results requires a new evaluation.

- The existing seismic observation system will be augmented by addition of two seismic stations to evaluate seismic event concentrations at early stages. These additional stations will be installed on the surface above the mining panel. The seismic system is designed to fulfill the recommendations described in Section 4. Therefore, events exceeding a magnitude of 3.0 lead to a temporary stop of flooding and a general re-evaluation of the process.

- The existing levelling control point system for surface subsidence observation is added by further monuments to observe the spatial and time depending development of the subsidence bowl based on the calculation results (see Section 4).
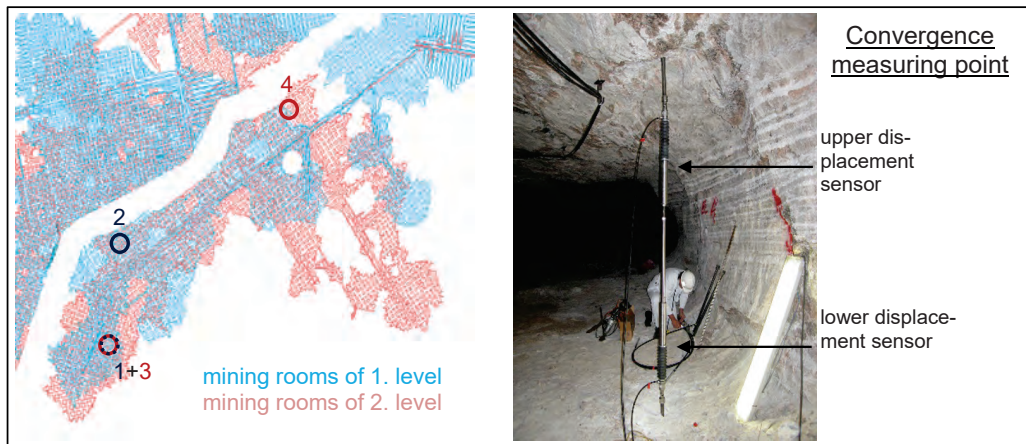
Figure 5: Map of mining field with 4 stations (left: stations 1 and 2 at upper level, stations 3 and 4 at lower level) and a convergence measuring point for use in brine filled mining rooms (right)

The convergence and seismic monitoring system runs permanently and the result evaluation will be done monthly. The subsidence observations are carried out and evaluated annually. Any observation system and evaluation cycle can be adjusted as required. The results of these observations will be summarized in reports and discussed with the rock mechanical experts. It is expected that the observation results agree with the prediction results and confirm a safe and compatible brine storage process.

In summary, both, the prediction of stable and compatible conditions by rock mechanical modelling as well as the verification by a suitable observation program establish the basis for a safe brine storage process in rooms of potash and salt mines.

6 Conclusions

In preparation for the possible storage of waste water of potash production, K+S is evaluating the opportunities to store this brine in rooms of potash and salt mines. Based on practical experiences in potash and salt mines, K+S and IfG are developing a procedure to investigate the rock mechanical behaviour of mine fields under the impact of brine storage. The procedure contains the advancement of numerical modelling techniques in order to investigate the mechanical effects of the brine storage in salt mining rooms and their test in single pillar and mining field models. Beyond that, the new techniques are used to evaluate the suitability of a potential mining field for brine storage. The results show stable field conditions and a convergence behaviour leading to integer barriers. Also based on the convergence behaviour from the numerical modelling, the development of the spatial surface subsidence bowl is calculated with an analytical program. Using practical experiences, the calculation results and the existing monitoring system of the potential brine storage mining field the monitoring concept is advanced by installing further control points. In this way, the conditions are created to evaluate the actual rock behaviour regarding to the predicted rock behaviour. In case of divergences, potential risks can be detected and assessed early in time. Therefore, from the rock mechanical point of view the storage of brine is possible and safe for the environment. The developed procedure of prediction of rock mechanical behaviour by modelling and evaluation of the actual rock behaviour by an advanced monitoring concept likewise provides an integrated and rigorous basis for achieving safe brine storage process in rooms of potash and salt mines.

References:

GESSERT, A., GÖTTERMANN, J., KÖHLER, R., SCHINDLER, A., THOMA, H. & SCHREINER, W. 2019. Die Verwahrung und Sicherung des Bergwerkes Volkenroda / Pöthen durch Flutung mit Haldenlösungen. Proceedings of 48. Geomechanik-Kolloquium, Leipzig, 2019

IFG 2003. Tragfähigkeit des Gesamtsystems der Schachtanlage Asse in der Betriebsphase. Unpublished report of Institute for Gebirgsmechanik GmbH, Leipzig, 2003

IFG 2018a. Gebirgsmechanische Verträglichkeit der Einstapelung von Prozesslösungen an Einzelpfeilern in untertägigen Hohlräumen. Unpublished report of Institute for Gebirgsmechanik GmbH, Leipzig, 2018

IFG 2018b. Untersuchung der gebirgsmechanischen Verträglichkeit der Einstapelung von Prozesslösungen an Einzelpfeilern in untertägigen Hohlräumen in 1100 m Teufe. Unpublished report of Institute for Gebirgsmechanik GmbH, Leipzig, 2018

IFG 2020a. Untersuchungen zum Kompaktionsverhalten von porösem Salzgebirge und gebirgsmechanische Modellrechnungen zum Integritätsverhalten des Markscheidesicherheitspfeiler. Unpublished report of Institute for Gebirgsmechanik GmbH, Leipzig, 2020

IFG 2020b. Baufeldmodellentwicklung zur Bewertung der gebirgsmechanischen Verträglichkeit einer Einstapelung von Prozesslösungen. Unpublished report of Institute for Gebirgsmechanik GmbH, Leipzig, 2020

IFG 2021a. Gutachten zur gebirgsmechanischen Verträglichkeit einer Einstapelung von Prozesslösungen.Unpublished report of Institute for Gebirgsmechanik GmbH, Leipzig, 2021

IFG 2021b. Senkungsprognose . Unpublished report of Institute for Gebirgsmechanik GmbH, Leipzig, 2021

ITASCA 2016. 3DEC V5.20, Itasca Consulting Group, Minneapolis (USA, 2016)

LÜDELING, C. & MINKLEY, W. 2014. A Crushed-Salt Model with Creep, Compaction and Strain-Softening, and Applications to Tailings Heaps. in: Proceedings of the 48th US Rock Mechanics/Geomechanics Symposium, 1-4 June 2014, Minneapolis, Minnesota, USA

K+S 2021a. Versuchsstapel – Bericht für das Jahr 2020, Bewertung markscheiderischer, gebirgsmechanischer und seismischer Messungen. Unpublished report of K+S Minerals and Agriculture GmbH, Unterbreizbach, 2021

K+S 2021b. Lösungseinstapelung, Monitoringkonzept zur gebirgsmechanischen Überwachung. Unpublished report of K+S Minerals and Agriculture GmbH, Kassel, 2021

MINKLEY, W. 2004, Gebirgsmechanische Beschreibung von Entfestigung und Sprödbrucherscheinungen im Carnallitit. Report of Institute for Gebirgsmechanik GmbH, Leipzig, 2004

MINKLEY, W. & MÜHLBAUER, J. 2007. Constitutive models to describe the mechanical behaviour of salt rocks and the imbedded weakness planes. In Proceedings of the Saltmech6, S. 119-127, Taylor & Francis, London, 2007

SCHLEINIG, J.-P., NEST, M., ZIENERT, H. & DEPPE, S. 2019. Einstapelung von Produktionslösungen in untertägige Hohlräume, Konzeptionelles Vorgehen und Gebirgsmechanische Modellentwicklung. Proceedings of 48. Geomechanik-Kolloquium, Leipzig, 2019

SCHLEINIG, J.-P., NEST, M., GÜNTHER, M., ZIENERT, H. & DEPPE, S. 2020. Storage of Production Brine in Rooms of Potash Mines, Mining Field Behaviour: Modelling and Monitoring: Proceedings of 49. Geomechanik-Kolloquium, Freiberg, 2020

SCHOBER, F. & SROKA, S. 1983. Die Berechnung von Bodenbewegungen über Kavernen unter Berücksichtigung des zeitlichen Konvergenz- und Gebirgsverhaltens. Kali und Steinsalz Bd. 8 (1983). Heft 10. S.352-358.

Study of sylvinite heterogeneous creep characteristics and their influence on shaft stability

J. Kazlouski[1,2*], *M.A. Zhuravkov*[2], *S.I. Bogdan*[1]

[1]EuroChem-Project LLC, Russia; [2]Belarusian State University, Belarus

* jkazlouski@outlook.com

ABSTRACT: This paper describes a study of a sylvinite rock mass using the Mohr-Coulomb criterion with an empirical Norton-based combined time hardening creep law. Parameters for empirical creep law were obtained in a series of back-simulations, using field monitoring data from deep potash mine drifts. Following the statistical processing, normal distribution of the primary creep parameter and lognormal distribution of the secondary creep parameter were established. The distributions of these parameters were used to generate two-dimensional auto correlated random fields for stochastic analysis of deep vertical mine shaft by 3 cases: a concrete lining; a concrete lining with a "squeezable" foam layer; no lining. The practical application of this modeling approach made it possible to estimate the expected value of non-uniform mine shafts contour deformations. Analysis shows the unreliability of using a thick "squeezable" (foam) layer for shafts with depths of more than 1000 m.

1 Introduction

The underground construction in salt formations faces the deformations of the structure contour, which increase in a very long time interval and may have unsteady stages. Numerical methods are being actively used in engineering to predict the deformation of the rock mass surrounding underground structures and determine the internal forces, which the lining is subjected to. There are many constitutive models and specialized methods for numerical modelling applications, while the problem of quantifying the irregularity of rock pressure remains yet not sufficiently developed, especially in salt rocks.

The authors noticed the phenomena of asymmetrical deformation of the underground mine workings contours at 1100-1200 m below ground level at Gremyachinsky deposit: the displacements of the opposite walls may vary by 2 or more times. However, the analysis of geological data (strength, inclination, stresses, structure, etc.) indicated homogeneity without any prerequisites for such a displacement difference. It is also known that at the Boulby mine, located in similar conditions, damage to the lining of a mine shaft occurred not only due to high loads, but also their non-uniformity (Kozel 2001). Similar overloads of lining occurred at the Piylo mine, where the back-analyzed pressure exceeded 2 times the total weight of the overlying strata (Kazikaev et al. 2011).

There are various approaches to the study of this phenomenon, for example, through considering perturbations in the initial stress field or the spatial inhomogeneity of its physical and mechanical characteristics (Phoon et al. 1999; Fenton et al. 2008). However, in a particular case, no basis for such approaches have been found. It is proposed to consider the spatial inhomogeneity of the creep function parameters directly within the computational study.

2 Geological and mining situation

The studied sylvinite layer is structurally a monocline, gently dipping from the southwest to the northeast to a depth of 1012 to 1302 m, complicated by low-amplitude (from 50 to 70 m) uplifts. The angles of dip usually do not exceed 5°, in rare cases they reach 9°. The thickness varies from 2.48 m to 20.46 m. The underlying rocks are lithologically represented by carnallite and rock salt (Figure 1).

Mineralogical and petrographic studies have shown that lithologically, sylvinites are composed of alternating layers of sylvin (content of at least 15-45%) and halite. In addition, there are

interlayers and lenses of sylvin-containing rock salt. The boundaries between these types of rocks are rather arbitrary, since all of them are almost completely composed of three minerals - sylvin, halite and anhydrite, which account for at least 98% of the rock mass. According to the results of analysis by ICP-spectroscopy and mineralogical-petrographic studies with quantitative calculations of mineral components, the content of CaSO4 and other insoluble residues at the intersections of the sylvinite layer is in the range from 3.25 to 11.05%.
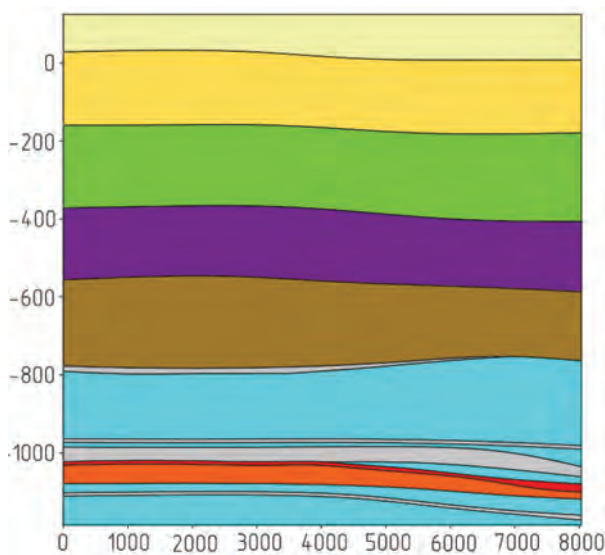
Figure 1: Schematic geological cross-section in the study area. Legend: ☐ – Quaternary and Neogene; ☐ – Paleogene; ☐ – Cretaceous; ☐ – Triassic; ☐ – Permian, Tatarian stage (P$_{23}$, ICS); ☐ – Permian, Kungurian stage, Anhydrite and Dolomite; ☐ – Permian, Kungurian stage, Rock salt; ☐ – Permian, Kungurian stage, Sylvinite; ☐ – Permian, Kungurian stage, Carnallite and Rock salt

Mining at the Gremyachinsky deposit is in its initial stage. Some phenomena and processes require a large amount of research in various scientific areas. In practice, mining works are primarily based on field measurements.

In-situ stress determination was carried out by the Mining Institute UB RAS (Beltukov N.L., 2018) in boreholes using Kaiser effect. According to the data, vertical stress in sylvinite corresponds to γH (24 MPa). The conditions are almost hydrostatic, as the lateral pressure coefficient is in the range from 0.9 to 1.

Field measurements of contour displacements (Figure 2) were carried out in various single drifts and rooms with a different width (from 4 to 6.5 m), depth and geological layers inclination. In-situ strain measurements were also performed but were used only for initial calibration and are not presented in this paper. Some measurement stations were excluded from the analysis due to the influence of local synclines (or anticlines) that increase (decrease) stress levels.

At the time of the study, the following key-reasons for the differences in wall deformation were assumed: 1) changes of the grains/crystals size in space; 2) changes in chemical composition of rock (halite-sylvinite ratio); 3) an influence of halite lenses occasionally encountered during mining operations, but often hidden and difficult to identify. However, none of these factors can currently be determined deterministically. Faced with the challenge of sinking a new shaft, various companies proposed the design of lining backed with a "squeezable" foam layer. To evaluate the possibility of point-loading of such a design and compare it with a conventional rigid-type support, a stochastic analysis was proposed.
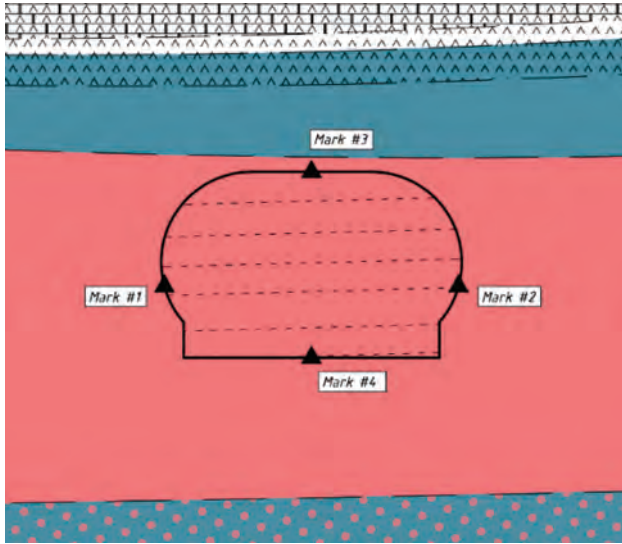
Figure 2: Typical field measurement station (Mark 4 is optional). Contour displacements are measured between marks. Legend: ▨▨▨ – Anhydrite; ▆ – Rock salt; ▆ – Sylvinite; ▨ – Rock salt and Sylvinite; ----- – layers inclination

3   Back-analysis methodology and its results

Due to simplification, it was accepted as part of the preliminary analysis, that total strain ε consist of elastic ε_{el}, rate-independent plastic and rate-dependent (creep) ε_{creep} strains.

$$\varepsilon = \varepsilon_{el} + \varepsilon_{pl} + \varepsilon_{creep}. \tag{1}$$

The plastic behavior is described by a linear Mohr-Coulomb criterion with a non-associated flow rule. Used Mohr-Coulomb's yield surface can be expressed using terms of stress invariants I_1, J_2 and Lode angle θ in the following formulation:

$$f(I_1, J_2, \theta) = -\tfrac{1}{3}I_1 \sin \varphi + \sqrt{J_2}\left(\cos \theta + \tfrac{1}{\sqrt{3}}\sin \theta \sin \varphi\right) - c\,\cos \varphi = 1, \tag{2}$$

where c is the cohesion and φ is the inner friction angle.
In addition to the Mohr-Coulomb criterion, an empirical Norton-type time-hardening creep law was used to describe creep strains:

$$\varepsilon_{creep} = C_1 t^{C_2}\sigma^{C_3} + C_4 t\sigma^{C_5}, \tag{3}$$
$$\sigma = \sqrt{3J_2}, \tag{4}$$

where $C_1 - C_5$ are empirical creep law coefficients.
Creep characteristics were determined by a series of back-analysis, which were performed using finite element method parametrical modelling. The initial stresses were calculated by the method of gravitational loading, considering the inclination of the geological layers, as well as the geometric dimensions of the working and its depth for every in-situ measurement station. The results of parameters calibration and optimization for some marks are shown in Figure 3.
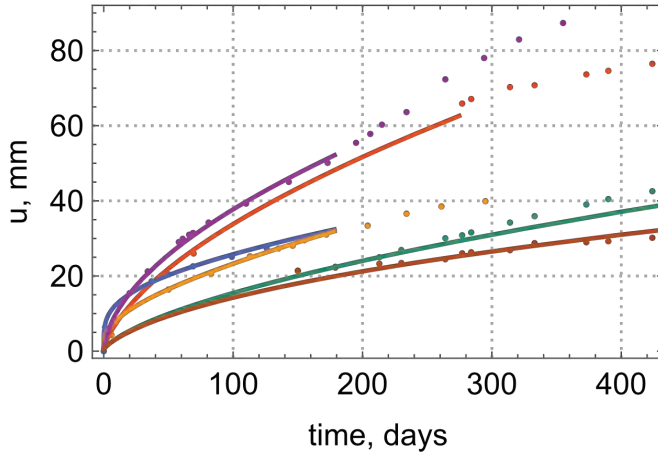
Figure 3: Displacements u (mm) of some monitoring marks: measured (dots) and simulated after back-analysis calibration (solid lines)

During the analysis of the deformation differences of workings there was no obvious reason for such a phenomenon. At the same time, probabilistic approaches are widely used for all types geomaterials since they are characterized by inherent spatial variability of properties (Ma et al. 2014; Mahmoudi et al. 2016). Thus, a stochastic analysis is a common practice (Phoon et al. 1999; Fenton et al. 2008) not only for soils, but also for rocks, and in particular for salts (Mahmoudi et al. 2017; Müller et al. 2018).

Since sylvinite on the site have no significant variability in strength and short-term mechanical properties, it was assumed that the parameters of the creep law are some random functions of coordinates. Since the coefficients C_2, C_3 and C_5 are power-law coefficients, it is exceedingly difficult to include them as functions of spatial variables, because their value directly affects the coefficients C_1 and C_4. But it was found that the coefficients C_2, C_3 and C_5 have similar values for all cases and agree with the value ranges described by many authors (Fokker 1995; Boresi et al. 1963; Hou 1997; Schoenherr et al. 2007). Therefore, their values were taken as non-variable.

The values of the coefficient C_1 are well described through the truncated normal distribution, and the coefficient C_4 – through the lognormal distribution (Figures 4-6). These distributions were taken as initial data for performing further stochastic analysis. A comparison of the back-analysis data with laboratory data is shown in Figure 7. It should be noted that the values of steady-state strain rates according to lab tests are higher due to the presence of primary or tertiary creep effects for all loadings cases.
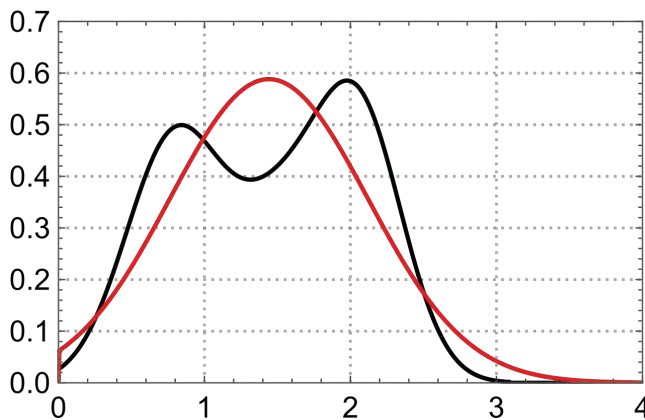

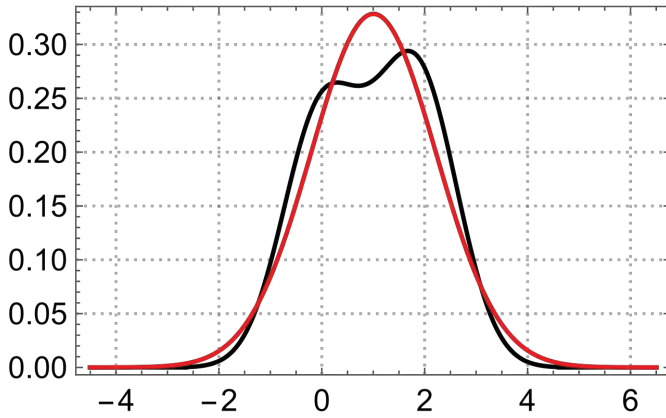Figure 4: Probability density functions of $C_1 \times 10^{14}$

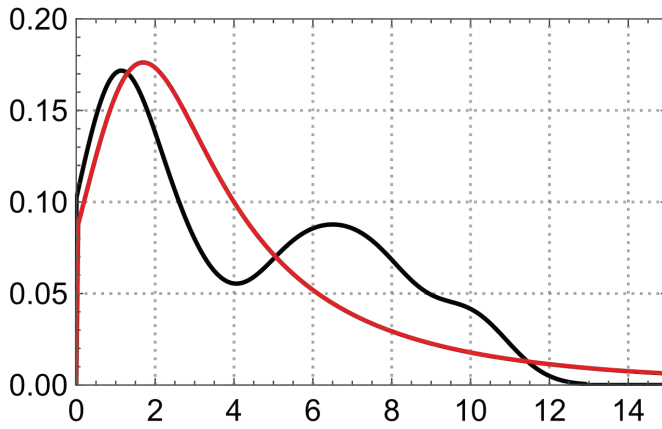Figure 5: Probability density functions of $\ln(C_4 \times 10^{40})$

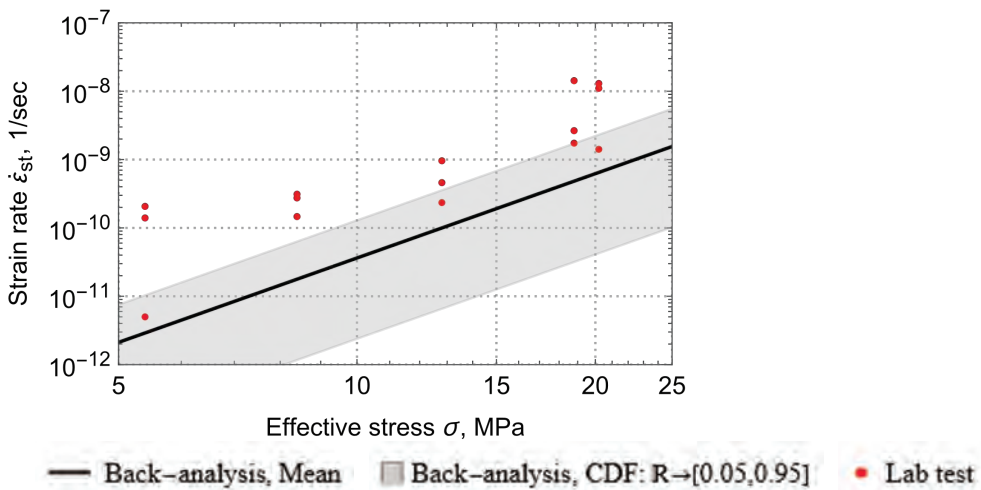Figure 6: Probability density functions of $C_4 \times 10^{40}$

Figure 7: Comparison of steady-state creep strain rates between back-analysis data and lab tests

4 Stochastic analysis methodology

Spatial variability of the coefficients C_1 and C_4 was made with random fields (Figure 8). Random field generation use mean values and variance of variable creep law coefficients and also depend on the correlation structure $\rho(\tau)$. An isotropic model, where correlation lengths θ in both directions are equal ($\theta_x = \theta_y$) the correlation decays exponentially with distance τ, is used (see Eq. 5-6). The value of the correlation length was taken as equal to 6 m because of the significantly different displacements recorded during monitoring, which may indicate the probable proportionality of the coefficient with the dimensions of the mine workings and the zones of the highest stress intensity around them — from 4.4 to 8 m.

$$\rho(\tau) = \sigma^2 \exp\left(-\frac{\tau_x}{\theta_x} - \frac{\tau_y}{\theta_y}\right), \tag{5}$$

$$\rho(\tau) = \sigma^2 \exp\left(-\frac{2\tau}{\theta}\right). \tag{6}$$
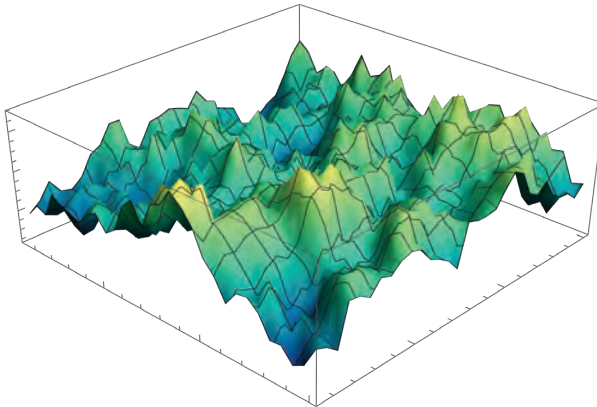
Figure 8: Typical auto correlated (spatially correlated) 2D random field

The stochastic analysis of vertical mine shaft (1200 m deep) in sylvinite was carried for 3 cases:

- **A concrete lining** with a thickness of 0.5 m.
  Rigid support is the most common solution and the most conservative, used on a vertical shaft at Boulby mine in similar conditions (Auld 2019; Jia et al. 2013; Kozel 2001; Williams et al. 2002).
- **A concrete lining** with a thickness of 0.25 m **and a "squeezable" foam layer** with a thickness of 0.25 m.
  A similar construction, but much more massive, was used at Boulby mine as initial lining design (Cleasby et al. 1975; Jia et al. 2013; Kozel 2001; Williams et al. 2002). Also used near shaft junctions at Piylo mine (Kazekaev 2011). Today it is a widely used lining-type in salt mines in Russia (Alymenko et al. 2018; Solov'ev V.A. et al. 2015; Solov'ev V.A. et al. 2017). For "squeezable" layer, a hyperelastic model was used (Figure 9).
- **no lining** or support.
  The option was considered, because the Russian design codes stipulate for the grading of the stability of the mine workings in salt rocks by the magnitude of the wall's displacements.
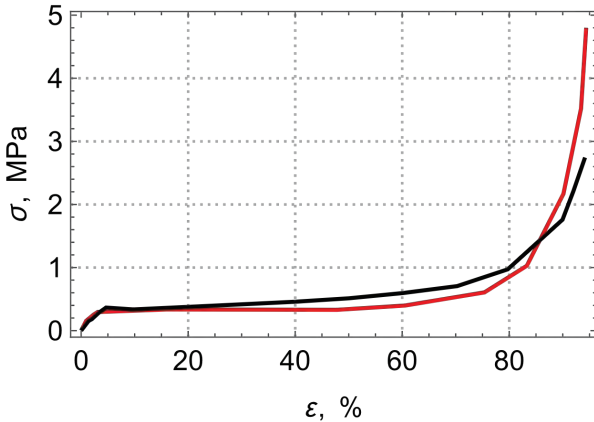
Figure 9: Stress–strain curve of expanded polystyrene foam: red – experimental data (Solov'ev et al. 2017), black – numerical modelling (the Ogden hyperelastic model)

5 Results

For the case of the unsupported mine shaft the results were analyzed at 8 regularly spaced points (virtual marks) on the contour (Figure 10). Resulting radial translations u_i in these points were used to calculate the irregularity of radial displacements with a step of 2 (δ_{90}, with 90°) and 4 (δ_{180}, with 180°) as the maximal ratio δ (Eq. 7-8). Typical deformations pattern is shown in Figure 11.

$$\delta_{90} = \max\left[\frac{u_i}{u_{2+i}}, \frac{u_{2+i}}{u_i}\right] - 1 \tag{7}$$

$$\delta_{180} = \max\left[\frac{u_i}{u_{4+i}}, \frac{u_{4+i}}{u_i}\right] - 1 \tag{8}$$
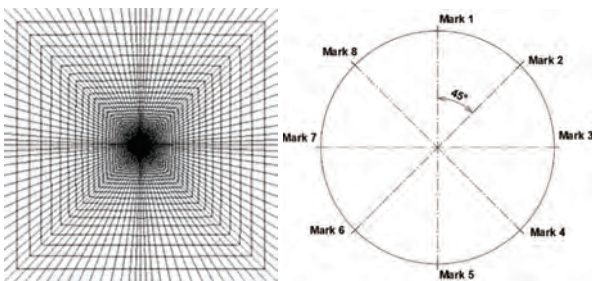
Figure 10: Fragment of finite element model for stochastic analysis (left) and principal scheme of result marks location (right)
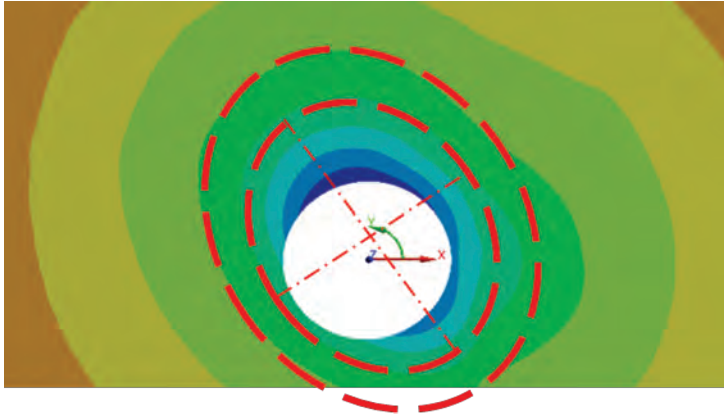
Figure 11: Typical pattern of non-uniform radial displacements and some "idealized" isolines

It was found that both quantities, $\delta_{90°}$ and $\delta_{180°}$, have similar lognormal distributions (see Figure 12). With 95% cumulative probability, the irregularity ratio has maximum values of $\delta_{90°}^{0.95}=70\%$ and $\delta_{180°}^{0.95}=110\%$.

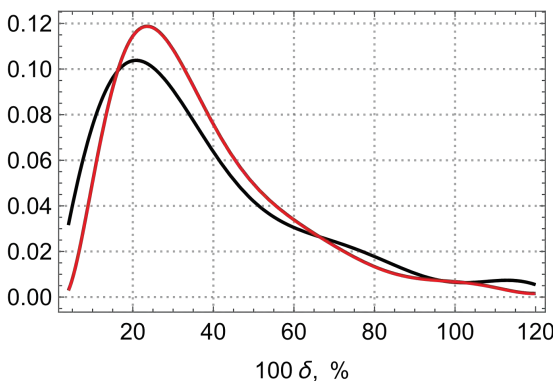Figure 12: Probability density functions of non-uniform displacement indicator δ: black $-\delta_{90°}$; red $-\delta_{180°}$

It should be noted that the accepted in analysis shaft supports are not fully real, but clearly represent the behavior of analogues. The case with a concrete lining was post-processed according to the rising stresses. The obtained distributions at all-time intervals are close to normal (see Figure 13), which means that it is theoretically possible to choose a structure sufficient for the load with a given probability.

The post-processing of a concrete lining with a "squeezable" layer showed, that the resulting stress distribution fields differ significantly from the previous ones. The distribution of forces in the lining is close to normal only at the initial time stages, it is associated with the section with almost no increase in the compression resistance at the compression diagram of the foam. But due to the effect of point-loading, there is a significant increase in the variance of linings inner forces over time and its distribution becomes close to uniform. In this case, the extrema of the stresses in the lining may exceed the values obtained for the lining without a "squeezable" layer. Additionally, it should be noted that there is an effect of uniform displacement from the axis of the entire structure, when "squeezable" layer is used. It indicates the need for the 3D modelling due to the potentially high values of bending moments in longitudinal direction.
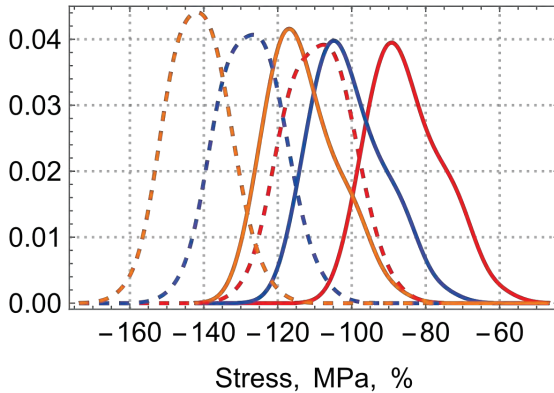
Figure 13: Probability density functions of maximal (solid lines) and minimal (dashed lines) stresses in concrete lining without "squeezable" layer. Red – 5 years, blue – 12.5 years, orange – 25 years
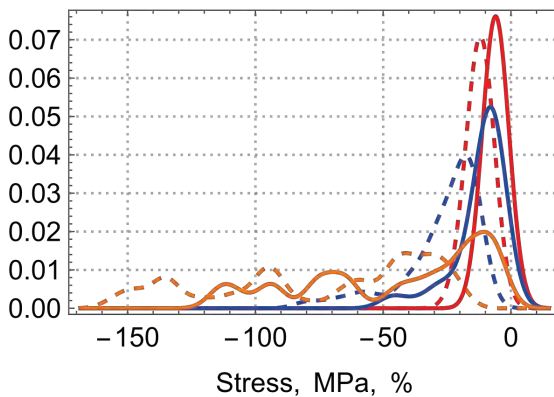

Figure 14: Probability density functions of maximal and minimal stresses in concrete lining with "squeezable" layer. Red – 5 years, blue 12.5 years, orange – 25 years

6   Conclusions

Salt rocks show non-uniform deformation due to creep, which is especially noticeable at depths of more than 1000 m.

According to the presented results of the stochastic analysis, the forces in rigid-type supports without foam layers always have a normal distribution of forces, which makes it possible to design with the required level of reliability.

When a layer of "squeezable" materials such as expanded polystyrene foam is used behind a rigid support, the effect of point loading of the structure appears. This effect, due to the lack of proper reaction at the rock-structure interaction, leads to the appearance of local stress peaks in the lining. The results for such layers have a wide scatter and are close to equiprobable, thus the distribution can be considered as uniform.

Analysis in the plane-strain formulation show that when using a "squeezable" layer, the whole rigid part of structure (lining) receives a certain displacement. This effect requires modeling in three-dimensional formulation even for preliminary analysis due to the bending of the shaft in the longitudinal direction.

The approach shown in the article can be used to predict and quantify pressure irregularities in salt rocks in similar conditions during the construction of new additional shafts, if monitoring data is available at the site.

References

Alymenko, D.N., Solov'ev, V.A., Aptukov, V.N. & Kotlyar, E.K. 2018. Systems of Support for Junctions of Mine Shafts and Roadways in Salt Rocks. Journal of Mining Science, 54(1), 40-47.

Auld, F.A. 2019. Design and Construction of Deep Shaft Concrete Linings in the UK. Proceedings of 4th International Shaft Design and Construction conference, 2019. 1-11.

Beltukov, N.L. 2018. The development of in-situ stress measuring method in boreholes using Kaiser effect (in Russian).

Boresi, A.P. & Deere, D.U. 1963. Creep closure of a spherical cavity in an infinite medium.

Cleasby J.V., Pearse G.E., Grieves M. & Thorburn G. 1975. Shaft-sinking at Boulby mine, Cleveland Potash Ltd. Institution of Mining and Metallurgy, Transactions, 84, , A7-A28.

Fenton G.A. & Griffiths D.V. 2008. Risk Assessment in Geotechnical Engineering.

Fokker, P.A. 1995. The behaviour of salt and salt caverns.

Hou, Z. 1997. Untersuchungen zum Nachweis der Standsicherheit für Untertagedeponien im Salzgebirge.

Jia, Y. D., Stace, R. & Williams, A. 2013. Numerical modelling of shaft lining stability at deep mine. Mining Technology, 122(1), 8-19.

Kazikaev, D.M. & Sergeey, S.V. 2011. Diagnostics and monitoring of the stress state of the lining of mine shafts (in Russian).

Kozel, A.M. 2001. Geomechanical Aspects of Design and Maintenance of Mine Shafts. Book 1 (in Russian).

Ma, J., Wang, Z. & Wu, J. 2014. Probability Distribution Analysis of Rock Salt Creep Parameters Based on Comprehensive Optimal Acceptance Criteria. Key Engineering Materials, 577-578, 561-564.

Mahmoudi, E., Khaledi, K., Miro, S., König, D. & Schanz, T. 2016. Probabilistic Analysis of a Rock Salt Cavern with Application to Energy Storage Systems. Rock Mechanics and Rock Engineering, 50(1), 139-157.

Mahmoudi, E., König, M., Schanz, T. 2017. Probabilistic analysis of a gas storage cavity mined in a spatially random rock salt medium. Computational Methods for Coupled Problems in Science and Engineering, Proc. 7th Conference, Rhodes Island, 2017. 722-733.

Müller, C., Frühwirt, T., Haase, D., Schlegel, R. & Konietzky, H. 2018. Modeling deformation and damage of rock salt using the discrete element method. International Journal of Rock Mechanics and Mining Sciences, 103, 230-241.

Phoon, K.K., Kulhawy, F.H. 1999. Characterization of Geotechnical Variability. Canadian Geotechnical Journal, 36, 612-624.

Schoenherr, J., Schléder, Z., Urai, J.L., Fokker, P.A. & Schulze, O. 2007. Deformation mechanisms and rheology of Pre-Cambrian rocksalt from the South Oman Salt Basin. The Mechanical Behaviour of Salt; Proc. 6th Conference, Hannover, 2007. 167-173.

SOLOV'EV, V.A., APTUKOV, V.N. & KOTLYAR, E.K. 2015. Geomechanical and technological aspects of shaft design improvement in salt rocks (in Russian). Gornyy Zhurnal, 11, 24-28.

SOLOV'EV, V.A., APTUKOV, V.N. & VAULINA, I.B. 2017. Support of Underground Openings in Salt Rocks. Theory and practice (in Russian).

WILLIAMS, A. & AULD, F.A. 2002. Boulby Mine Shaft Lining Design Second Restoration. Mining Technology, 111, 13-27.

Theme 6: Cavern and borehole abandonment and integrity

Finite Element modeling of natural sealing of wellbores in salt using advanced, laboratory-based salt creep laws

Loes Buijze[1]*, Jan ter Heege[1], Brecht Wassing[1]

[1]Applied Geosciences, TNO, Utrecht, The Netherlands

* loes.buijze@tno.nl

ABSTRACT: Using the natural sealing potential of rock salt caprock formations is potentially an economically attractive and safe option for well plugging and abandonment (P&A). Rock salt has excellent sealing capabilities and can be used for P&A by forming a permanent sealing barrier across reamed-out well sections or perforated wells. However, the application of natural sealing by rock salt formations as an abandonment option is not yet common practice; a better understanding of the creep behavior and sealing capacity of rock salt and a quantitative estimate of the timescales required for the wellbore to be fully plugged are needed. In this study the timescales for closure of a reamed-out well section in rock salt are evaluated using finite element modeling, following methods outlined by Orlic et al. (2019). Salt creep is modeled by a two-mechanism steady state creep law, composed of a dislocation and pressure solution branch. Model results show that dislocation creep is dominant in the near-well field and dominates wellbore closure times, whereas pressure solution creep becomes increasingly important for stress relaxation after wellbore closure and in the far-field. Stochastic analysis shows the dislocation creep parameters and temperature to have the largest effect on wellbore closure timescales, and that in many cases wellbore closure occurs within weeks or months.

1   Introduction

As many hydrocarbon fields world-wide are reaching the end of their commercial lifetime, vast numbers of wells will be decommissioned over the coming decades. In the Netherlands for example, thousands of on- and offshore oil and gas wells will be decommissioned over the next 20 years (EBN 2016). The costs associated with plugging & abandonment (P&A) of these wells is estimated at several billions of euros. Innovative P&A techniques are important to reduce these costs and increase the long-term sealing and integrity of the abandoned wells. One innovative approach is to employ the natural sealing potential of caprocks that are penetrated by the wells. Clay-rich and evaporitic rocks exhibit viscoelastic time-dependent deformation (creep) and self-sealing behavior. For abandonment, a section of wellbore can be milled away, allowing the caprock formation to creep into the wellbore and restore the original caprock sealing capacity across the well (Hou et al. 2012; Vrålstad et al. 2019). Rock salt is particularly attractive because it is ductile, self-healing/sealing, has proven its sealing potential and chemical stability, and is a caprock to many hydrocarbon fields in the northwest Europe. A field pilot experiment of natural sealing of a well in rock salt above the Altmark gas field in Germany showed that the original formation integrity was indeed restored across the well (Hou et al. 2012). However, timescales of wellbore closure in rock salt vary significantly as a function of depth, temperature and constitutive creep behavior. Many evaporites, even when ductile and principally suited for natural formation sealing might creep too slow for the application within P&A operations, particularly at shallow depths above 2000 m. Hence it is important to evaluate under which conditions natural sealing by rock salt is a feasible option for well plugging and abandonment, using the appropriate constitutive behavior for salt creep.

Laboratory studies showed that for conditions of interest, two steady-state creep mechanisms may be activated: dislocation creep and pressure solution creep (e.g. Carter et al. 1993; Hunsche & Hampel 1990; Spiers et al. 1990). These can be combined in a two-mechanism creep law, e.g. Fokker (1995), as also recommended by Sinn (2020) and van Oosterhout et al. (2020). Previous modeling studies on natural sealing using this two-mechanism creep law show the expected sensitivity of wellbore closure times to the depth and in-situ temperature

(Orlic & Buijze 2014; Orlic et al. 2019). Orlic & Buijze (2014) show a linear relationship between wellbore radius and the creep rate, and Orlic et al. (2019) furthermore showed that wellbore convergence slows down significantly for open hole sections shorter than 1 – 2 m, and recommended a minimum length of 10 m to achieve maximum convergence rates. However, a limited range of creep parameters was investigated, and several laboratory-based extensions to the two-mechanisms creep law were not yet investigated. Here we build on these previous modeling studies and investigate stochastically the impact laboratory-based creep parameters, including a stress threshold for linear creep.

2 Modeling approach

The timescales for wellbore closure in rock salt were evaluated using a generic Finite Element (FE) model where a section of a well casing along a well penetrating a salt formation has been milled out, allowing the salt to creep into and close this milled interval (following Orlic et al. 2019). An automatic model generator for DIANA FEA v 10.5 was built in Python to effectively model different scenario's.
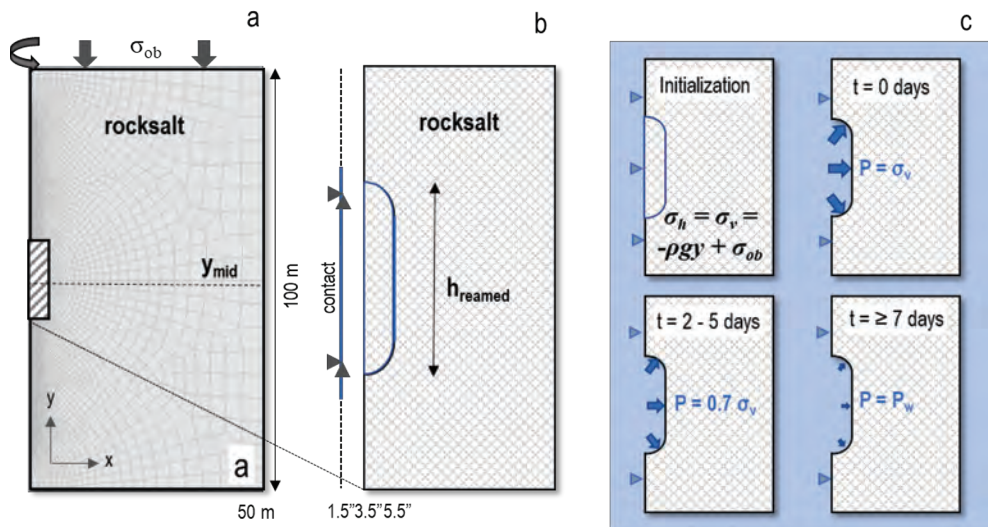

Figure 1 Model geometry and model procedure. a) Model geometry of axisymmetric model (50 x 100 m), with central depth y_{mid} and overburden load σ_{ob}. b) Close-up of wellbore section which is reamed out (not to scale). Blue lines indicate contact elements. c) Modeling procedure, with stress initialization, removal of the salt (reamed out section) and application of pressure along the open wellbore. Triangles indicate translational supports.

2.1 Model setup

An axisymmetric model (50 x 100 m) of a vertical wellbore within a salt formation was used to simulate wellbore closure (Figure 1). In the middle of the wellbore (*r = 3.5"*), an interval of height h_{reamed} (default 10 m) is reamed away to create the open hole section (r_{milled}= 5.5"). A monitoring well (r_{mw} = 1.5") was placed inside the well. The outer well casing/cement was simulated by imposing translational supports along the well-salt interface. The salt formation was modeled using an unstructured mesh, with cell sizes increasing from 0.015 m along the reamed interval to a maximum of 5 m at the outer model boundary (Figure 1a). The vertical edge of the reamed interval and the monitoring well were modeled using linear contact elements (blue lines Figure 1b). The analysis procedure and consists of two phases: (i) a stress initialization phase and (ii) a convergent creep phase (Orlic et al., 2019). Vertical stresses are

initialized in the salt by applying a gravitational load and an overburden load σ_{ob} at the top of the model space (Figure 1a, c), where $\sigma_{ob} = \Delta\sigma_v/\Delta y * (y_{mid} + 50)$. The horizontal stress is initialized through setting $K_0 = \sigma_h/\sigma_v$ to 1, i.e. a hydrostatic stress state. Temperature is computed using the temperature gradient $\Delta T/\Delta y$ and a surface temperature of 10°C. In the second phase the reamed interval was removed, and a pressure load is applied along the edges of the reamed interval instead. Over the first 7 days pressure is stepwise decreased over the first 7 days (Hou et al. 2012, Figure 1c) to 1 MPa, simulating a small layer over brine and N$_2$ in the well to achieve the maximum deviatoric stress along the reamed interval. From t = 0 both elastic and viscous creep deformation of the salt can occur. A tolerance of 1e-7 or stricter is required for the force balance to ensure proper convergence during each time step.

2.2 Salt creep laws: theory & implementation in DIANA

Salt deformation was modeled assuming secondary or steady-state creep of the rocksalt (e.g. Orlic & Buijze 2014; Orlic et al. 2019). A combination of both dislocation creep and diffusion creep was used (Breunese et al. 2003; Cornet et al. 2018; Orlic et al. 2014; Orlic et al. 2019; van Oosterhout, 2021). Here we summarize the equations and implementation in DIANA FEA.
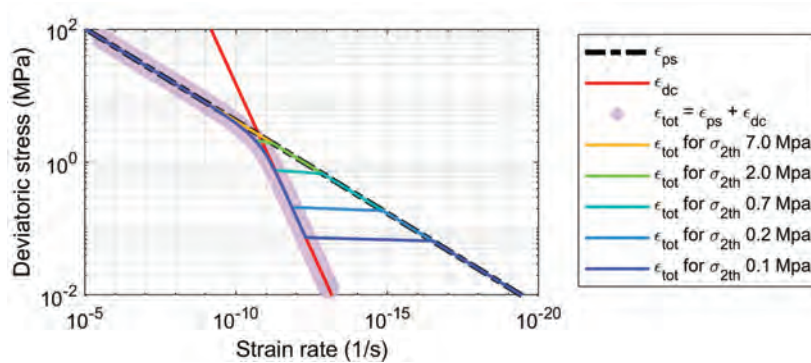

Figure 2 Creep rates for the two-mechanism steady-state creep law using the default parameters (BAS-LLC-HNC), showing the effect of a stress threshold for linear creep.

Secondary creep strain rates for dislocation creep are typically described by an Arrhenius equation power law, also called Norton-Hoff law

$$\dot{\epsilon}_{dc} = A \exp(-\frac{Q}{RT})\sigma^n \tag{1}$$

Where A is the dislocation creep constant (MPa^{-n}s^{-1}), Q (Jmol^{-1}) is the activation energy, R is the gas constant (8.314426 Jmol^{-1}K^{-1}), T is the temperature (K), σ is the deviatoric stress (MPa), and n is the stress exponent. For low deviatoric stresses and/or temperature the role of fluid-assisted mass transfer processes may instead become significant in particular for salt which has a high solubility (e.g. Urai et al. 2008). For diffusion-controlled creep strain rate is linearly related to the stress, as formulated by Spiers (1990)

$$\dot{\epsilon}_{ps} = 5\, V_m\, Z_0 \exp\left(-\frac{Q}{RT}\right)\frac{\sigma}{Td^3} \tag{2}$$

where 5 (molKJ^{-1}) is a numerical constant, V_m (m^{3}mol^{-1}) is the molar volume, R is the gas constant (8.314426 Jmol^{-1}K^{-1}), σ is the deviatoric stress under axi-symmetric loading, $T (K)$ is the temperature, and d is the grain size. Z_0 is the reference effective grain boundary diffusivity and can be determined directly from laboratory measurements (Spiers et al., 1990). Both linear elastic and creep behavior are prescribed in the salt. In DIANA FEA a two-mechanism steady-state creep law is available as a standard material model (Fokker 1995)

$$\dot{\varepsilon} = A_1 \exp\left(-\frac{Q_1}{RT}\right)\left(\frac{\sigma}{\sigma_{ref}}\right)^{n_1} + A_2 \exp\left(-\frac{Q_2}{RT}\right)\left(\frac{\sigma}{\sigma_{ref}}\right)^{n_2} = \dot{\varepsilon}_{dc} + \dot{\varepsilon}_{ps}s \tag{3}$$

Here subscript 1 is used for dislocation creep and subscript 2 is used for pressure solution creep. To link this creep model to the recommended pressure solution equation (2), A_2 can be calculated as follows

$$A_2 = \frac{5\,V_m Z_0 1 \cdot 10^6}{Td^3} \tag{4}$$

Note the cubic dependence on the grain size, and the dependence of A$_2$ on temperature. In addition, a stress threshold σ_{2th} was incorporated in the material model, below which the contribution of the second term in Equation (3) – the pressure solution creep branch - is set to zero (see Figure 2 for the effect of this threshold).

2.3   Input parameters for default scenario and stochastic analysis

The input parameters for the default scenario are the same as used by Orlic et al., 2019 (see Table 1). For the linear elastic behavior, a Young's modulus E of 30 GPa, Poisson's ratio 0.2, and a density of 2180 kgm^{-3} were prescribed. Furthermore, a stochastic analysis was performed to assess the timescales of natural sealing under widely varying conditions. For each simulation, parameters were independently varied by random sampling from predefined distributions (Table 1). Operational parameters included the height of the reamed interval h_{reamed}, and the pressure in the well P_{well}. The latter was fixed here at 1 MPa, the lowest values achievable in the well through for example filling the well with nitrogen (e.g. Hou et al. 2012). For creep parameter A_1 a log-uniform distribution was assumed ranging between 10^{-8} – 10^{-3} MPa^{-n}s^{-1}. The diffusion creep parameter A_2 was computed through equation (4), using V_m 2.7· 10^{-5} m^{3}mol^{-1}, Z_0 (2.79 ± 1.40) · 10^{-15} m^{3}s^{-1} (Spiers et al., 1990), and a grain size with a log-uniform distribution between 2 and 20 mm, in agreement with observations on rock salt cores (e.g. Breunese et al., 2003). Linear regression analysis was performed on the model results to rank the effect of the input parameters on the closure time, first normalizing the input parameter ranges. Note that the stochastic analysis is a generic exercise; in reality creep parameter ranges will be more constrained at a certain location, and parameters can be correlated.

Table 1 Input parameters used for default scenario (BAS-LLC-HNC) and the stochastic analysis. *These values follow from equation (4), see text 2.3. References a) www.nlog.nl, b) Berest & Brouard, 1998, c) Spiers et al., 1990

| Input parameter	Symbol	Unit	Default	Range	Ref.
Depth	y_{mid}	m	-2500	-1700 - -3500	a
Vertical stress gradient	$\Delta\sigma_v/\Delta y$	MPa/km	22	21 – 23	
Temperature gradient	$\Delta T/\Delta y$	K/km	31.3	27 - 35	
Well P during closure	P_{well}	MPa	1	1	
Height of reamed interval	h_{reamed}	m	10	1 - 20	
Dislocation creep parameter	A_1	MPa^{-n}s^{-1}	$2.45 \cdot 10^{-5}$	10^{-8} - 10^{-2}	b
Activation energy disl. creep	Q_1	Jmol^{-1}	51,600	30,000 – 80,000	b
Stress exponent disl. creep	n_1	-	3.6	3 - 7	b
Diffusion creep parameter	A_2	MPa^{-1}s^{-1}	$3.35 \cdot 10^{-8}$	$3·10^{-11}$ - $3·10^{-7}$ *	c
Activation energy diff. creep	Q_2	Jmol^{-1}	25,600	23,500 – 25,500	c
Stress exponent diff. creep	n_2	-	1	1	
Stress threshold diff. creep	σ_{th}	MPa	0	0.02 - 2	
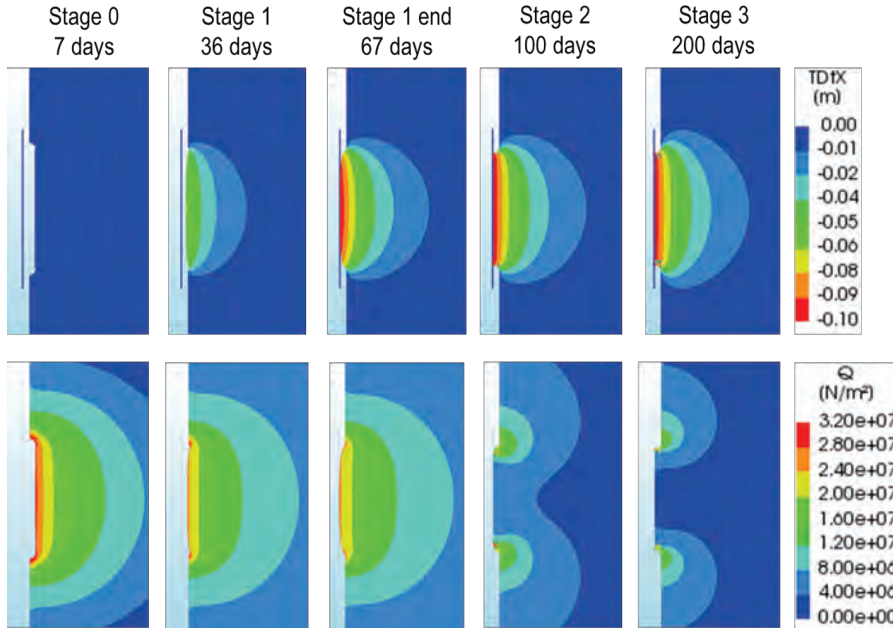
Figure 3 Stages of wellbore closure (see text 3.1 for description of the stages). Color contours indicate horizontal displacement in the salt (top row) and the deviatoric stress (bottom row).

3 Model results

3.1 General behavior: Stages of wellbore closure for default parameters

The closure of the open hole can be divided into different stages characterized by a specific displacement and stress response (Sinn 2020; Van Oosterhout et al. 2020, Figure 3)

- Stage 0 – creation of the open hole and reduction of pressure in the well. For the current loading procedure this stage spans 7 days (see Figure 1c).
- Stage 1 – open borehole convergence. During this stage deviatoric stresses near the open hole are highest, as the pressure along the face of the open hole is much lower than the stress in the salt. The high deviatoric stresses will causes the salt to creep into the open hole section until it touches the monitoring well at time t_c (Figure 3).
- Stage 2 – fully converged borehole with compaction of central zone. Ongoing creep further relaxes the deviatoric stresses around the borehole, until creep rates decrease to very low values. The end of Stage 2 (t_r) is defined as the time for the deviatoric stress at the center of the wellbore wall to reduce to 98% of the maximum value. Stresses near the edges of the reamed interval are higher.
- Stage 3 – fully converged borehole with static healing of the central damaged zone. During this stage creep rates at the center of the reamed interval are very low, and healing can occur (healing is not modeled).
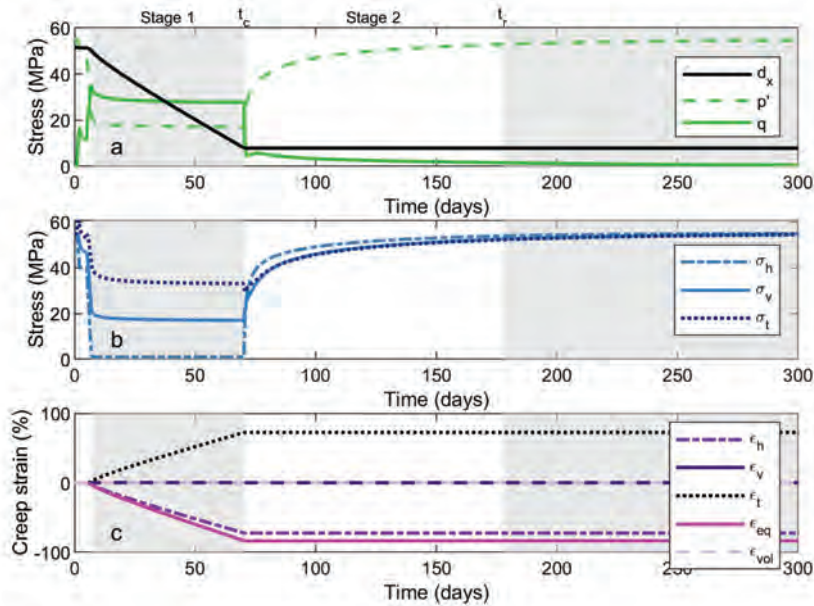
Figure 4 Temporal evolution of displacement, stress, and strain at the center of the open hole wall (at y_{mid} -2500 m). a) Horizontal displacement and stress invariants. Horizontal displacement varies between 0 and -0.10 m. b) Horizontal, vertical, and tangential stress, c) Horizontal, vertical, tangential strains (ε_h, ε_v, and ε_t) and Von Mises strain ε_{eq} and volumetric strain ε_{vol}. Positive values indicate compressive strain.

The initial state of stress is isotropic, with a value of 58 MPa at the depth of the open hole section. During lowering of the pressure in the open hole section, the deviatoric stress q increased stepwise from 0 to 17 MPa (0 - 2 days) and 34 MPa (5 - 7 days), while the mean stress decreased from 58 to 22 MPa (a). Here, only minor creep strain accumulated during Stage 0. After 7 days as P_w = 1 MPa (σ_h = 1 MPa, b), salt convergence rates increased significantly, with horizontal displacement increasing near-linearly. In case no monitoring well would be present (r_{mw} = 1.5"), the time for convergence would be ~37% longer. Convergent creep reduced the deviatoric stress along the open hole section from 34 to 28 MPa. After 67 days' salt first converged onto the monitoring well (d_x -0.10 m); the end of Stage 1. The strains at the open hole wall during this stage exceeded 75%, corresponding to an average creep rate in the order of $1 \cdot 10^{-7}$ s^{-1} over Stage 1. Elastic strains (not shown) are negligible compared to creep strains. After first convergence, the deviatoric stress showed a sharp drop to less than 10 MPa, whereas the mean stress increased rapidly. Ongoing creep further relaxed the deviatoric stress until after 177 days stresses were reduced to ~2 MPa, the end of Stage 2. Creep rates were several orders of magnitude lower than during Stage 1.

Even though the borehole radius is only 5.5" (0.14 m), the presence of the open hole perturbed the stresses up to several m from the borehole (Figure 5). The extent of the stress perturbation increased throughout Stage 1 – see e.g. Figure 5b where the deviatory stress in the direct vicinity of the open hole decreased, but increased at distances >1 m after 10, 40, and 70 days. Deviatoric stresses of 1 MPa were observed at distance over 10 m. Strains of more than 10% were limited to 0.5 m (0.35 m around the open hole).
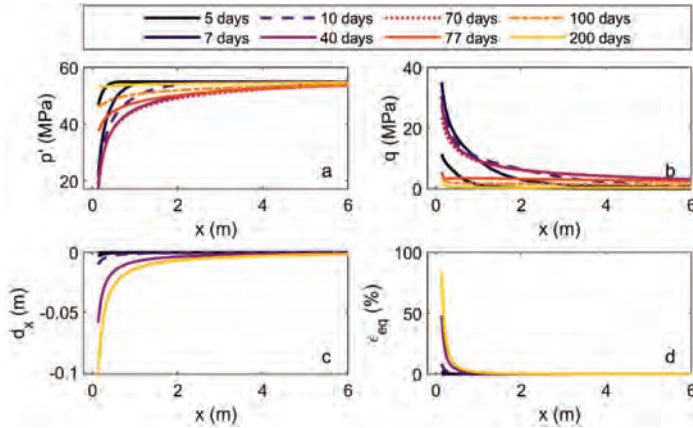
Figure 5 Stress and strains with distance from the borehole, at various points in time. a) mean stress p, b) deviatoric stress q, c) horizontal displacement, d) Von Mises or equivalent strain. Closure occurs after 67 days, see .

3.2 Contribution of pressure solution branch to wellbore closure

Since the deviatoric stresses around the borehole are so large, dislocation creep is expected to dominate. It is however interesting to study the (relative) contribution of pressure solution. To this end we vary A_2 between $2 \cdot 10^{-11}$ to $2 \cdot 10^{-7}$ MPa^{-1}s^{-1}, covering the range expected from the pressure solution creep law of Spiers et al. (1990), for grain sizes 20 to 2 mm (Table 1). The other parameters were kept constant, using the default values for Bas-LLC-HNC.
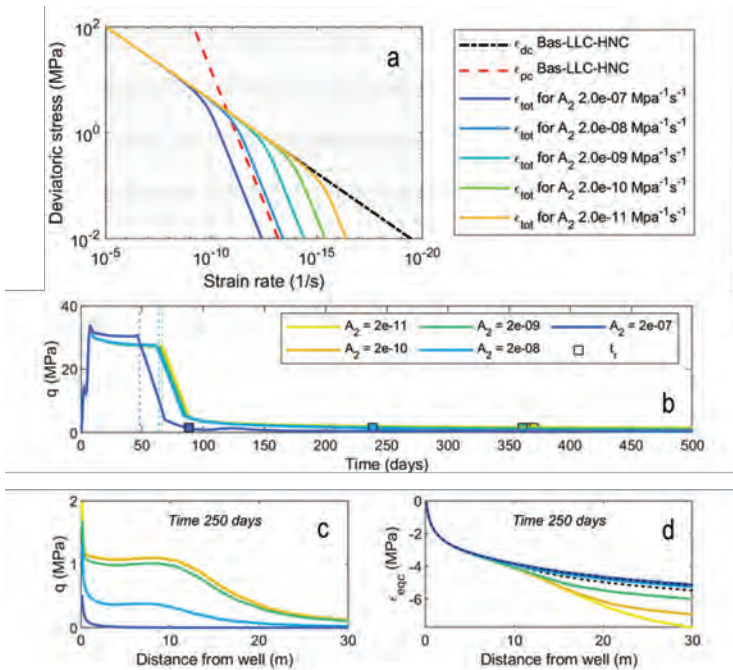
Figure 6 Contribution of pressure solution to wellbore closure (Stage 1) and stress relaxation (Stage 2). a) stress-strain rate map, b) deviatoric stress at wellbore wall, c) deviatoric stress and d) equivalent strain with distance from the well

The effect of A_2 on the wellbore closure time t_c was negligible except for the highest value of $2 \cdot 10^{-7}$ MPa^{-1}s^{-1} (d = 2 mm) which reduced the closure time from 67 days to 56 days. For this value of A_2 pressure solution creep rates dominate the total creep rate at deviatoric stresses of 5 MPa and lower (Figure 6a). Even though deviatoric stresses at the open hole edge are still significantly higher, from 2 m from the well deviatoric stress falls below 5 MPa (Figure 6b). Hence elevated dissolution creep rates at distances > 2 m contributed enough to the total displacement to affect wellbore closure time. Lower values of A_2 causes pressure solution creep to become dominant at lower deviatoric stress, and hence at further distances from the well. This reduces the contribution of the far-field salt to the displacement field, so that closure time is not affected. Hence, wellbore closure times are only affected when pressure solution creep rates in the vicinity of the well are comparable to or faster than those of dislocation creep.

However, the duration of Stage 2 is more affected by pressure solution, compare e.g. A_2 $2 \cdot 10^{-8}$ and A_2 $2 \cdot 10^{-9}$ which give stress recovery times of 240 and 360 days respectively. This effect is visible in the stresses from the near-well field up to distances of 10's of meters from the well (Figure 6c). The effect on recovery time depends however not only on the absolute value of A_2 but also on the dislocation creep parameters. The recovery times for A_2 $2 \cdot 10^{-9}$ to A_2 $2 \cdot 10^{-11}$ are not very different. For these low values, creep rates at stresses down to $0.1 - 2$ MPa, and hence the stress relaxation time t_r, are dominated again by dislocation creep (Figure 6a). Hence, pressure solution creep will impact the duration of Stage 2, but the magnitude of its effect depends on the relative pressure solution creep rates to dislocation creep rates at low stresses, as well as the criterion used to define the end of Stage 2.
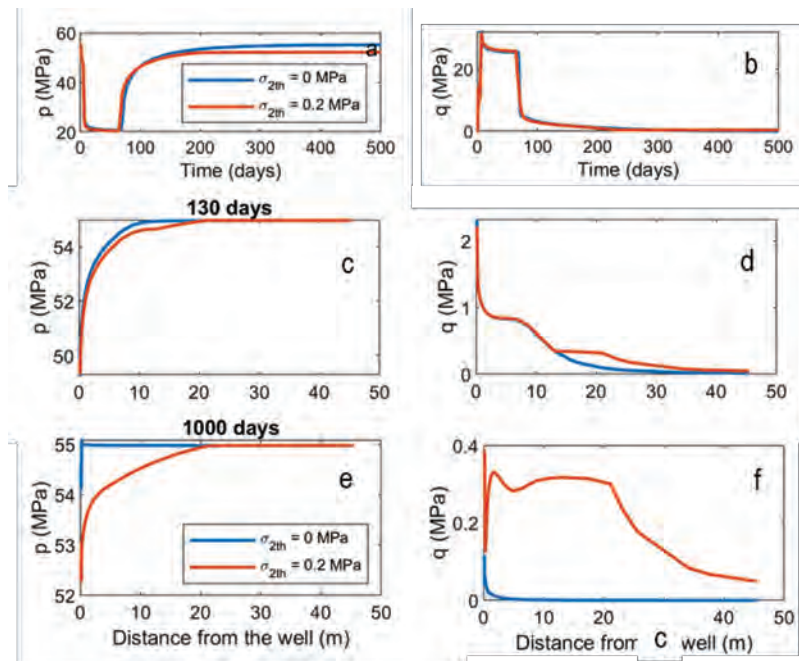

Figure 7 Effect of threshold linear creep on the stresses for default scenario Bas-LLC-HNC. a) mean stress p and b) deviatoric stress q at the open hole wall, c-d) p and q with distance from the well after 130 days, and e-f) p and q with distance from the well after 1000 days.

3.2.1 Effect of stress threshold for pressure solution

Since dislocation creep was the dominant process, the linear creep threshold (default value 0.2 MPa) had only small effect on the wellbore closure time for the default scenario. Also the modeled stresses at the edge of the open hole section were also not affected during wellbore

closure (Stage 1) (Figure 7a, b). The effect of the threshold only became apparent after ~100 days, during Stage 2 (Figure 7c-f), when deviatoric stresses near the wellbore decreased to a level where pressure solution became the dominant creep mechanism (Figure 2). Whereas for the scenario without the threshold the deviatoric stress decayed to zero and the mean stress to the in-situ value, the threshold causes the deviatoric stress to remain at 0.34 MPa ($\sqrt{3}\ \sigma_{2th}$) and the mean stress to remain 1 MPa below its original value (Figure 7d). Eventually the deviatoric stress will decay to zero, due to dislocation creep. However, at deviatoric stresses of 0.2 MPa or lower, dislocation creep rates are orders of magnitudes slower than would be the pressure solution creep rates in absence of a threshold (Figure 2). For the deviatoric stress to fully relax would likely cause years to tens of years

3.3 Stochastic analysis of wellbore closure

The results from the stochastic analysis showed observed closure times t_c ranging from $0 - 10$ days (during or immediately following the creation of the open hole and lowering of well pressure), to timescales of weeks ($10 - 30$ days), months, or even multiple years. For the current input parameter ranges, closure occurred within 10 days for 26% of the runs, $10 - 30$ days for 33% of the runs, $30 - 100$ days for 9% of the runs, $100 - 365$ days for 14% of the runs, and 14% longer than a year.
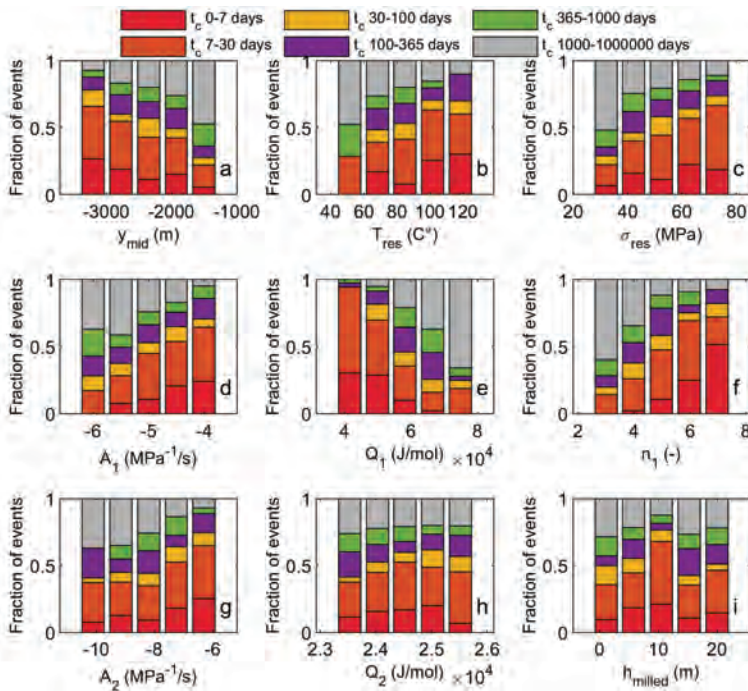

Figure 8 Results of stochastic analysis of closure times using uniformly distributed input parameter ranges. Input parameters are divided into 5 bins. Per bin the fraction of events within a certain closure time range are grouped. a) center depth, b) temperature gradient, c) vertical stress gradient, d) dislocation creep parameter A_1, e) dislocation creep activation energy Q_1, f) dislocation creep exponent n_1, g) pressure solution creep parameter A_2, h) pressure solution activation energy Q_2, i) length of the milled-out wellbore section.
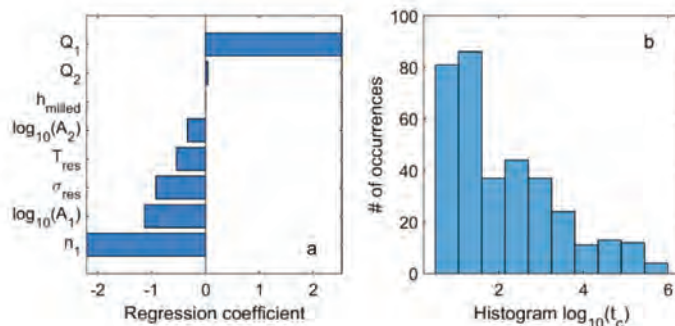
Figure 9 Linear regression results of stochastic analysis. a) Regression coefficients computed for closure times computed in the stochastic analysis, b) Histogram of log(t_c)

Not surprisingly, the dislocation creep exponent n_1 had one of the strongest effects on closure time (Figure 8,). For $n_1 > 6$ more than 50% of simulations reaching full convergence during the first week – i.e. during Stage 0, and for n_1 5 – 6 this was 30% (Figure 8f). Also the activation energy for dislocation creep Q_1, exerted dominant control on the wellbore closure time, as did dislocation creep parameter A_1, and to a lesser extent, the stress and temperature at the reservoir depth. On the other hand, the pressure solution creep parameters Q_2 and A_2 had a smaller effect on closure time, because the dominance of dislocation creep (Section 3.2). Milled casing length also did not impose a strong control on the wellbore closure time.

4   Discussion

The obtained modeling results using the two-mechanism creep law are consistent with previous studies (e.g. Cornet et al. 2018; Orlic et al. 2019), and extends the work of Orlic et al. 2019) by evaluating a broad range of input parameters, to better identify the role of the linear creep component vs. the dislocation component on wellbore closure. Not surprisingly, the dislocation creep parameters had a much stronger effect on wellbore closure times than the pressure solution parameters. This is because the high deviatoric stresses that are present near the open section of the wellbore cause dislocation creep, which has a power law dependence on the deviatoric stress, to be the dominant deformation mechanism. However, pressure solution creep affects the far-field creep and the stress relaxation stage, which may still be important for the sealing capacity of the salt in the open hole section. Also, when pressure in the well is higher (e.g. hydrostatic values instead of 1 MPa), pressure solution creep is expected to become more important.

In the end, not only the convergence time is of interest, but also the time required for wellbore sealing. The high deviatoric stresses near the wellbore wall can cause dilatant micro-cracking in the salt, increasing the permeability and reducing the sealing capacity (e.g. Cristescu & Hunsche 1998; Peach & Spiers 1996). To assess whether dilatancy occurs, a dilation criterion can be considered, e.g. a linear criterion as formulated by Spiers et al. (1988) where dilation occurs for $q \geq 1.44p + 3.5e6$. However, applying this criterion to the stresses shown in e.g. Figure 4a shows that only the salt directly adjacent to the well bore wall (>0.025 m from the open hole wall) falls in the dilatant regime. Mean stress p remains relatively high even though the horizontal component is reduced to P_w (here 1 MPa). In that case dilatancy may not be widespread, and closure time is representative for the sealing timescale. However, other, non-linear dilatancy criteria exist (e.g. Cristescu & Hunsche 1998) for which the dilatant zone will be larger. We recommend future work to focus on incorporating an appropriate dilatancy criterion and enhanced pressure solution laws for dilated salt in the modeling, as recommended in Van Oosterhout et al. 2020. Also, transient creep was not considered in the current study. Model results showed however high strains (>10%) near (<0.35 m) the borehole,

so that transient creep effects (occurring at strains <10%) are expected to have a minor role on the wellbore closure time. However, at larger strains dynamic recrystallization can start to occur, which can cause the grain size to change such that solution precipitation and dislocation creep rates are balanced, leading to enhanced creep rates (ter Heege et al., 2005). It is recommended to incorporate dynamic recrystallization in future analyses of wellbore closure and other applications where strains are large.

In the model assumed uniform salt creep properties were assumed, but in reality salt impurity content varies, and grain size may vary strongly over dm-scales (e.g. Urai et al., 2019). In addition, layers of other (squeezing) salts, for example bischofite or anhydrite may be present, which exhibit faster creep rates than rock salt. The weakest layers may impose a strong control on wellbore closure, possibly reducing wellbore closure times even further. On the other hand, anhydrite or carbonate inclusions in the rock salt formations can lower creep rates and closure times. It is recommended to address the effect of this lithological variability in future studies.

For about 70% of the simulations the timescale for wellbore closure was less than 3 months. The question is what a feasible timescale is for wellbore closure. The hydrocarbon reservoir needs to be isolated from the open hole section of the well into which the salt converges, for example by introducing a bridge plug below the open hole section. If the sealing potential of such a plug can be guaranteed for at least months, leaving ample time for formation of a natural seal in the salt. According to our results, operational aspects that would help reduce closure times are to ream out a long enough wellbore section (>5 m) and to reduce the pressure in the open hole as much as possible. The strong effect of the Arrhenius term (Q_1/RT) also suggests heating of the open hole section could significantly reduce closure times. In particular, for shallow wells, where creep rates are otherwise being low, this could be a solution.

5   Conclusions

Wellbore closure times for natural sealing in a salt formation were evaluated using numerical modeling, with input for salt creep based on laboratory experiments. In the numerical model a milled-out well section was modeled, with a strongly reduced wellbore pressure (1 MPa) along the open hole interval. Main results are summarized here:

- Mean stress decreases and deviatoric stress increases around the open hole driving convergent creep of the salt into the open hole section. For the default creep parameters, the closure time is 67 days. The stress perturbation decays rapidly with distance, affecting a few m around the open wellbore. After full convergence is attained, ongoing salt creep increases the mean stress and decreases the deviatoric stress around the wellbore.
- The high deviatoric stresses around the open hole section cause dislocation creep to be dominant for the timescales for wellbore closure, unless pressure solution creep parameters are such that creep rates approach those of dislocation creep. Pressure solution creep does affect the (final stages of) stress relaxation following closure.
- Stochastic analysis using variable, laboratory-constrained creep parameters showed:
    - Wellbore closure can occur over timescales from 1 day to over thousands of days.
    - For the input parameter ranges used in this chapter, in more than 50% of the simulated scenario's salt converged onto the monitoring well within 1 month.
    - The closure time had the highest sensitivity to the dislocation creep parameter n_1, activation energy Q_1, and length of the milled-out section of well bore.

References

BEREST, P., & BROUARD, B. 1998. A tentative classification of salts according to their creep properties. In Proceeding of SMRI spring meeting, New Orleans, Louisiana, USA, April, pp. 19-22.

BREUNESE, J. N., VAN EIJS, R. M. H. E., DE MEER, S., & KROON, I. C. 2003. Observation and prediction of the relation between salt creep and land subsidence in solution mining. The Barradeel case. In Proc. SMRI Fall Meeting, Chester: United Kingdom, pp. 38-57.

CORNET, J. S., DABROWSKI, M., & SCHMID, D. W. (2018). Long term creep closure of salt cavities. International Journal of Rock Mechanics and Mining Sciences, 103, 96-106.

CRISTESCU, N., & HUNSCHE, U. 1998. Time effects in rock mechanics (Vol. 350). New York: Wiley.

HOU, M. Z., WUNDRAM, L., WENDEL, H., MEYER, R., SCHMIDT, M., KRETZSCHMAR, H. J., SCHMITZ, S., & FRANZA, O. 2011. Developing, modeling and in-situ-testing a long-term wellbore seal in the framework of the CO2-EGR research project CLEAN in the natural gas field Altmark. Energy Procedia, 4, 5291.

HAMPEL, A., & HUNSCHE, U. 2020. Extrapolation of creep of rock salt with the composite model. In Basic and Applied Salt Mechanics, pp. 193-207.

ORLIC, B., & BUIJZE, L. 2014. Numerical modeling of wellbore closure by the creep of salt caprocks. 48th US Rock Mechanics/Geomechanics Symposium, Minneapolis, MN, USA,1-4 June 2014.

ORLIC, B., WOLLENWEBER, J., GEEL, C. R., VANDEWEIJER, V. P., MEEKES, J. A., HEERENS, G. J., & TER HEEGE, J. H. 2019. Formation of a sealing well barrier by the creep of rock salt: Numerical investigations. Proceedings of 53rd US Rock Mechanics/Geomechanics Symposium, New York, USA, 23 – 26 June 2019. ARMA 19-2079.

PEACH, C. J., & SPIERS, C. J. 1996. Influence of crystal plastic deformation on dilatancy and permeability development in synthetic salt rock. Tectonophysics, 256, 1-4, 101-128.

SINN, C. J. A. 2020. Creep behaviour and porosity-permeability evolution in rocksalt under conditions relevant for borehole/cavity convergence and decommissioning. Deliverable Report Phase 0 TKI Rocksalt, Innovation Program Upstream Gas 2016.

SPIERS, C. J., SCHUTJENS, P. M. T. M., BRZESOWSKY, R. H., PEACH, C. J., LIEZENBERG, J. L., & ZWART, H. J. 1990. Experimental determination of constitutive parameters governing creep of rocksalt by pressure solution. Geological Society, London, Special Publications, 54, 1, 215-227.

TER HEEGE, J. D., DE BRESSER, J. H. P., & SPIERS, C. J. 2005. Dynamic recrystallization of wet synthetic polycrystalline halite: dependence of grain size distribution on flow stress, temperature and strain. Tectonophysics, 396(1-2), 35-57.

URAI, J. L.., SCHMATZ, J., & KLAVER, J. 2019. Over-pressured salt solution mining vacerns and leakage mechanisms. Project Report KEM-17, commissioned by State Supervision of Mines.

VAN OOSTERHOUT, B., SPIERS, C. J. & HANGX, S.J.T. 2020. Creep behaviour and porosity-permeability evolution in rocksalt under conditions relevant for borehole/cavity convergence and decommissioning. Deliverable Report Phase 0 Deliverable: Literature Review, Revised Version of Part 3 – Summary and Recommendations. TKI Rocksalt, Innovation Program Upstream Gas 2016.

Integrity of the geological formation barrier -
A comprehensive approach for the assessment of salt caverns

Alexander Raith[1]*, Sven Wille[1], Birgit Horváth[1], Dirk Zander-Schiebenhöfer[1]

[1]DEEP.KBB GmbH, Germany

*alexander.raith@deep-kbb.de

ABSTRACT: The assessment of the long-term integrity of an underground storage is a key factor for its operational safety and economic viability. Since the entire storage system needs to maintain its integrity throughout the operational life and beyond, an integrity assessment of salt caverns should include the borehole and its technical installations, the cavern(s) itself and the surrounding geological formation. The integrity assessment of technical well elements is standard and performed based on systematic approaches. Although there are several approaches to asses most aspects of geological formation barriers around salt caverns, there is no systematic and comprehensive approach for the geological formation barriers comparable to the assessment of the technical well elements. Therefore, we introduce a systematic approach to assess the functionality of the "geological barrier" (storage formation) and "subordinate geological barrier" (e.g. overburden) (Figure 1). The assessment is based on the evaluation of basic influencing factors (i.e. natural permeability, interactions with the cavern fluid, rock mechanical design and operating mode) that need to be considered in different scenarios to evaluate their impact on the geological barrier. All characteristics influencing the geological formation barrier are weighted and combined to generate a comprehensive statement about geological formation tightness and stability. The results can be coupled with the borehole integrity assessment and provide indications for possible measures to improve the storage integrity, to close knowledge gaps, and to identify potential weak elements of the barrier system.

1   Background and motivation

Using salt caverns for energy storage is a well-proven and well-engineered technology. Today, cavern operators are facing challenges like (1) ageing assets in need for workover or abandonment, (2) new operation modes for conventional storages, i.e. high-frequency cycling for natural gas, and (3) new "green" energy carriers to be stored, i.e. hydrogen or CAES. Storage integrity, which includes integrity assessment and integrity management, is an essential part of safe storage. Furthermore, integrity assessment yields valuable information for new projects and existing cavern facilities in order to derive optimization potential, and as a preparatory step for the abandonment phase. Given that some of the stored media may pose a risk to humans and to the environment if storage integrity is breached, it is necessary that efforts are taken to ensure safe and long-lasting containment.

Against this background, the integrity management of storage caverns is increasingly becoming the focus of attention of operators and authorities. This is due to a couple of past incidents of integrity loss as well as to various legal, regulatory and normative standards recently established. In particular, a systematic approach on well integrity and the concept of a mandatory two-barrier well system have become common industry practice.

Generally, the assessment of the integrity of the geological barrier is part of a global concept (Zander-Schiebenhöfer et al. 2016) to identify integrity-related aspects applicable to both technical barrier elements and the geological formation acting as barrier (in short: "geological barrier"). The cavern system as a whole not only comprises the well and its technical installations but also the (salt) formation that surrounds the cavity. To achieve a comprehensive integrity assessment that includes all elements of the cavern system, it is thus

required to focus not only on the technical integrity but also on the geological conditions and an appraisal of the barrier function of the geological formation needs to be added to the overall concept. Further on, unlike the technical barrier, the geological barrier is present and needs to remain functional beyond operational lifetime, also for the time after the abandonment of the cavern storage.

Several fundamental aspects influencing the integrity of the geological formation are commonly assessed (e.g. mechanical stability, permeability, creep behaviour) and huge effort has been undertaken to verify the long-term tightness of rock salt (e.g. research for nuclear waste disposal). What is missing is a practical and systematic approach, customized for salt caverns, that incorporates all aspects and their interaction for a comprehensive and interdisciplinary evaluation that combines all information (from exploration to cavern operation) and different fields of expert knowledge. In the following such an approach will be presented.

2   Definition of terms

Salt caverns are artificially created cavities in salt rock, in which the stored medium (liquid or gaseous) is in direct contact with the surrounding natural geological formation. Unlike a technical structure, the building material cannot be selected in accordance with a pre-defined specification, as it is inherent to the geology at the particular location. Also unlike in many technical structures, failure of the containment cannot be fully monitored and may not be immediately observed. The lack of full monitoring and direct data is commonly addressed by geological and/or geomechanical models, which are therefore a fundamental part of the cavern design. Thus, robust models are required, and lack of robustness is to be compensated by safety margins considered for the cavern design (e.g. dimensions, operation mode).

Integrity means long time mechanical stability and leak tightness. Loss of integrity is the loss of these properties, which may ultimately lead to loss of the stored medium through potential migration pathways of different types and /or the collapse of a cavern. The stored medium may or may not escape to surface. Loss of integrity may result in risks for assets and other protected commodities, for the environment, and for human life.

For salt caverns, the salt formation along the cavern contour represents the primary and only geological barrier to ensure the integrity of the cavity. The salt rock enveloping the cavity must have sufficient tightness and adequate thickness to ensure mechanical stability under the stress conditions of operation. Therefore, the properties to be considered are either primary formation characteristics (lithological, mineralogical, textural and/or structural) or geomechanical features/properties influenced by the geological conditions and the cavern operation.

The primary geological barrier may be supplemented by a secondary barrier that can be provided by a tight cap rock layer directly overlying the salt body or by other sealing layers within the overburden sequence. The secondary barrier does not directly contribute to the integrity of the salt cavern and is not regarded as a component of the storage system itself, but can act as an additional safety element that will prevent leaked media from reaching shallow formations or the biosphere. Therefore, an evaluation not only of the storage formation but also of the secondary barrier can be part of the integrity assessment, if applicable.

Loss of the stored medium can potentially occur through different migration pathways. Potential pathways (in the primary or secondary geological barrier) may be present either due to the primary state of the formation (permeable layers/interbeds, permeable salt, fault planes) or may be "activated" by external feature, processes, or events, such as neotectonics, subrosion, or subsurface operations (e.g. design, operation mode).

To prevent the escape of storage medium from caverns, it is necessary to evaluate the properties of the geologic formation regarding the defined factors influencing their barrier function with a systematic approach in order to maintain its ability to contain the storage medium.

3   Description of approach

Assessment of the integrity of the geological barrier is understood as a structured analysis of the (state of the) barrier and especially the identification of potential pathways that may lead to a loss of leak tightness and ultimately may cause stored medium to escape.

The assessment approach for the geological barrier is based on a three-tier system as displayed in Figure 1 and introduced by Horváth et al. (2021). Two first-tier categories are defined, "geological barrier" (storage formation) and "secondary geological barrier". The assessment is made for both categories, with the focus on the "geological barrier (storage formation)".

The first-tier categories are further broken down into "influencing factors" (second tier) and these into "characteristics" (third tier). The underlying structure of the assessment process is described in the following.

Key elements of the approach are:

- consideration of framework conditions (type of deposit, stored medium)
- "bottom-up workflow" (from single cavern to entire storage)
- parallel acknowledgement of available data base (age, completeness, detail)
- weighting of scores
- flagging of outliers
- flexibility to incorporate site-specific features.

For the first-tier categories "geological barrier (storage formation)" and "secondary geological barrier", the approach investigates the factors that influence the actual state of the barrier. This second tier of influencing factors, which is the essential part of the assessment, considers the natural properties of the formation, the cavern and cavern field design and the operation mode as well as the impact the storage operation may have on the first three factors. The influencing factors are classified into five groups:

- The natural in-situ permeability of the host rock and the material properties, processes and geometries influencing the natural or primary permeability (independent of influences by cavern operation).
- The rock mechanical design of the cavern, influencing the mechanical and hydraulic integrity during cavern operation also influenced by external factors (e.g. neighboring mining operations).
- Influences of chemical or physical interactions of the cavern fluid with the host rock, including dissolution and reaction processes.
- Operation mode of the cavern including cavern pressures and subsequent effects such as cavern convergence and surface subsidence
- Geological barrier in case of failure of primary geological or technical barrier" (only for the secondary geological barrier)
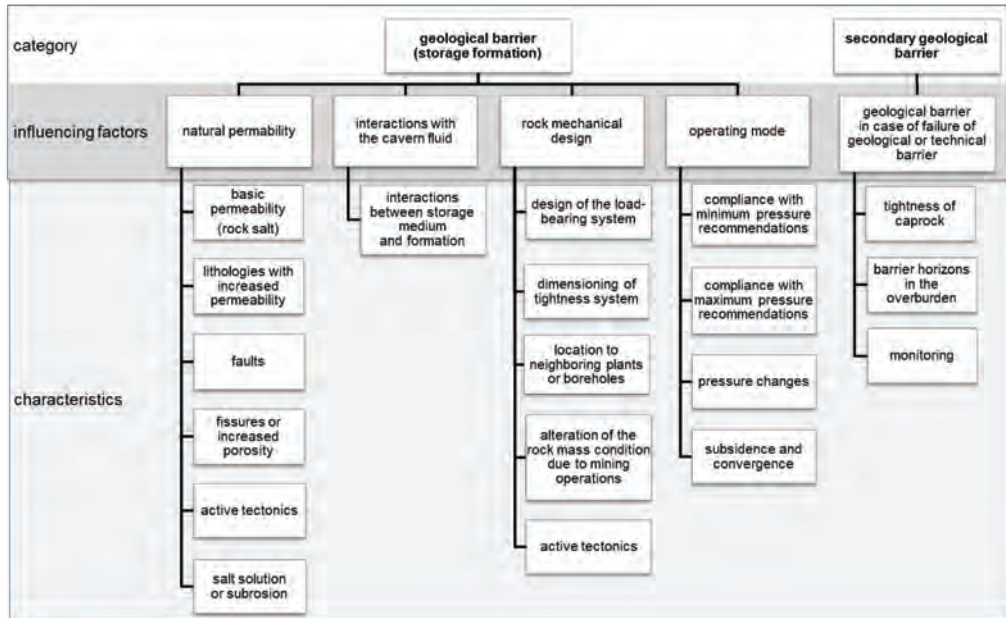
Figure 1: Three-tier approach for the geological barrier assessment

In the third tire, one to six characteristics are subjected to evaluation in five groups of influencing factors (Figure 1). To evaluate these characteristics, a number of subsurface data and operation-related information have to be considered. Therefore, all available and relevant data and models will be compiled. In case no data is available, best estimates or experience-based values can be used, if applicable. To gain robust and reliable results this evaluation also includes an assessment of the age, quality, level of detail and completeness of the data, simplifications and assumptions.

The assessment is carried out bottom-up. At first an assessment is made for every individual cavern considering each of the third-tire characteristic (see Figure 1). For this purpose, the characteristics are evaluated according to a five-stage rating system ranging from "good" to "rather poor" which is based on a detailed evaluation matrix for each of the third-tire characteristic. These evaluation matrixes define how all relevant parameters and aspects are rated. Furthermore, the evaluation of the data quality and completeness is a fundamental part of this assessment. Since the third-tire characteristic evaluation matrixes are rather extensive no detailed description is being given here, but an example is presented in Figure 4.

For better visualization, the classification according to the five-stage rating system is color-coded, with green for "good" through yellow to red for "rather poor". Weighting factors are used to generate a score for each characteristic. After normalization of the individual scores, all characteristics of one influencing factor are also summarized by application of weighting factors. The resulting ratings of the influencing factors are subsequently combined to a final rating of the main category, also using weighting factors.

Since rating scores of several single caverns and characteristics are combined into one figure in the rating process, poor ratings for single caverns may be lost in the overall scores and may no longer be immediately recognizable. Nevertheless, such ratings may be of high relevance as they may highlight very specific flaws or knowledge gaps. To avoid a loss of this information, single poor ratings will be flagged (Figure 2 & 3). For each of the flagged ratings there will be a comment providing insight to the cause and significance of the poor rating.

The final outcome of the integrity evaluation is a report that contains

- comprehensive compilation of all relevant data and documents,
- complete, systematic and site-specific rating of the data and documents,
- description and discussion of individual poor ratings.

The information is condensed into a well-arranged document structure and figures while any problematic aspects are clearly highlighted and described to enable further detailed analysis or measures.

4 Examples

The first example (Figure 2) shows an assessment for the geological barrier of an entire cavern field. Like in Figure 1, the categories "influencing factors" and "characteristics" are arranged from top to bottom.

Right next to each characteristic, a coloured rating is given as an average value for all cavern within the considered cavern field. In case a single value that is part of the characteristics (e.g. rating of a single cavern or parameter) shows a poor rating, it is flagged right next to the rating field. Above the rating of the characteristics, the summarized rating for each influencing factor is given, resulting in the summarized evaluation of the barrier. The coloured illustration is used for better visualization of the assessment result, but behind it there is a numerical scoring and rating system. Thus, the condition of these influencing factors directly reflects the condition of the geological barrier. Adverse conditions in one or more of these influencing factors might therefore state a risk to the integrity of the geological barrier.

Figure 2: Exemplary assessment of a cavern field

The second example (Figure 3) demonstrates the evaluation of one single cavern. While the cavern shows good rating in most of the categories, three categories (see A, B and C in Figure 3) have a lower rating and are thus flagged.
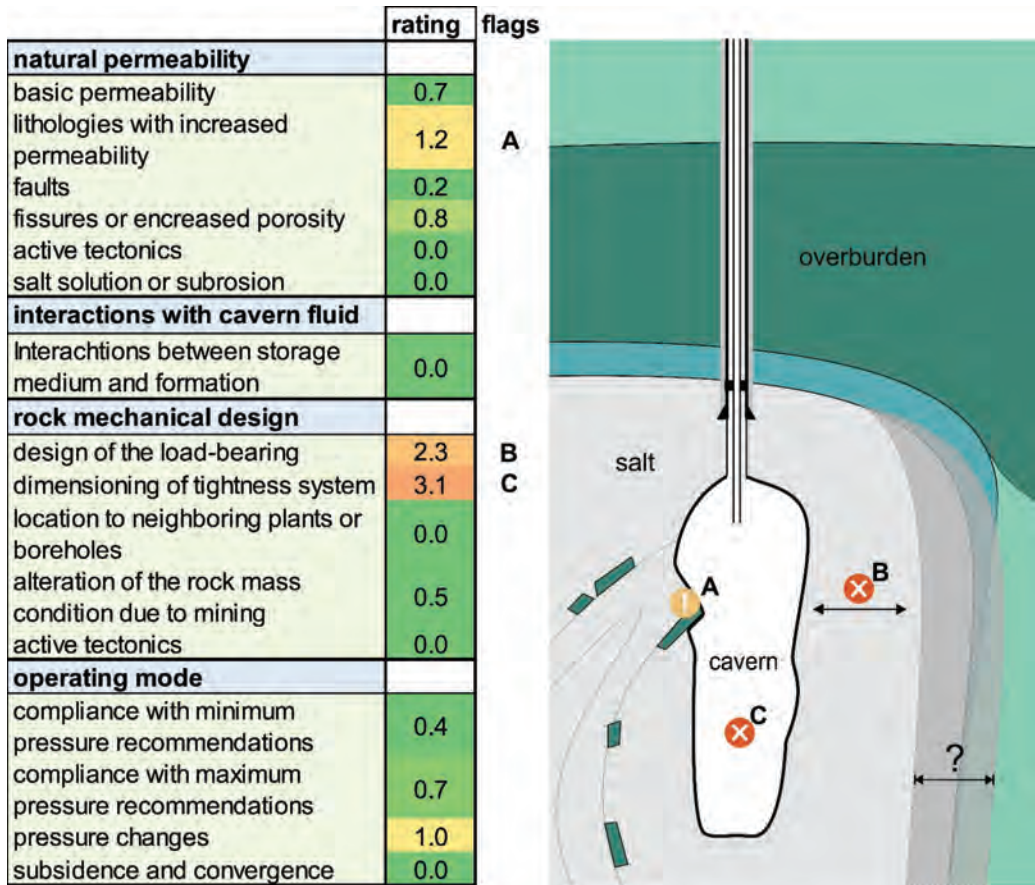
	rating	flags
natural permeability		
basic permeability	0.7	
lithologies with increased permeability	1.2	A
faults	0.2	
fissures or encreased porosity	0.8	
active tectonics	0.0	
salt solution or subrosion	0.0	
interactions with cavern fluid		
Interachtions between storage medium and formation	0.0	
rock mechanical design		
design of the load-bearing	2.3	B
dimensioning of tightness system	3.1	C
location to neighboring plants or boreholes	0.0	
alteration of the rock mass condition due to mining	0.5	
active tectonics	0.0	
operating mode		
compliance with minimum pressure recommendations	0.4	
compliance with maximum pressure recommendations	0.7	
pressure changes	1.0	
subsidence and convergence	0.0	

Figure 3: Evaluation example of a single cavern

A: Natural Permeability – Lithologies with increased permeability

In this case the category is flagged because the cavern is in direct contact with an anhydrite layer that is potentially more permeable than rock salt. Nevertheless, the rating is still rather good since the available data and geological model are sufficient to predict the position and shape of the layer inside the salt body. Based on this geological model and information from a number of additional wells there is sufficient evidence that the anhydrite layer is strongly fragmented. Thus, individual anhydrite blocks are isolated by impermeable salt and do not represent a continuous fluid pathway within or out of the salt body. An example of the evaluation matrix for the characteristic "Lithologies with increased permeability" at the example cavern is given in Figure 4.

Lithologies with increased permeability	5	3	2	1	0
Quality: data					Sufficient data for the structural and stratigraphic interpretations of the relevant lithologies
Quality: structural model					Detailed model of all relevant stratigraphic units surrounding the caverns. Model uncertainties known
Properties of Boundaries		Straight and continuous layer boundaries (potential weaknesses)			
Distance to Cavern	Contact with cavern known or likely				
Continuity of the layer towards a receptor or reservoir					verified: the layer is isolated in salt and not continuous
Permeability			No indications for increased permeability		

Figure 4: Example of the evaluation matrix for "Lithologies with increased permeability". The rating for example "A" is highlighted with grey cells. All rated aspects are combined under consideration of their weighting factor.

B: Rock mechanical design – Design of the load bearing system

In this category the cavern design in the given example is sufficiently described by the available data and by a geomechanical model, so that the derived safety margins for the load bearing system appear to be consistent. However, uncertainties in the underlying geological data and model (here uncertainty of the flank position) are poorly described. In consequence there is a remaining risk that the distance between cavern and flank is smaller than the required safety margin.

C: Rock mechanical design – Dimensioning of the tightness system

The negative rating is caused by the lack of sufficient information. In this case some site-specific data on the formation tightness are available but an appropriate evaluation is missing. The example shows that the assessment of the integrity of the geological barrier highlights problematic aspects of the formation, the available data, data evaluation or design. In case of the evaluation shows that the cavern has a higher geological risk but is unproblematic. In case of B and C the evaluation shows that either data or an appropriate evaluation of the available data is missing. In both cases additional measures can be undertaken to improve the database, and hence the rating.

5   Conclusions

An essential part of cavern design and construction is the demand for long-term cavern integrity, this refers to the property of a cavern well and the cavern itself to provide an effective barrier for containment of fluids. The effectiveness of this (technical) barrier needs to be verified during operation under high and low pressures throughout the whole life cycle of the cavern and during abandonment. In addition to the technical integrity assessment, the geological barrier should also be evaluated. Like the well integrity assessment, the methodology of the assessment of the geological barrier presented here also follows a systematic approach. Once an overall assessment of the geological barrier has been performed, only minor updates need to be made, based on gained operational data or in case of more recent geological findings.

By combining the results of the technical integrity assessment and of the geological integrity assessment, an overall comprehensive integrity assessment is achieved on the basis of which the present storage integrity and its expected development can be evaluated to guarantee third-party protection and long-lasting containment of the storage medium within further operation. Therewith, the possibility is given to take preventive measures, to improve the situation or to derive optimization potential.

The outcome of the evaluation is at first a comprehensive compilation of all relevant data and documents regarding the integrity of the storage formation and a comprehensible, systematic and site-specific evaluation of this data to rate the integrity of a single cavern or cavern field. The aim of the evaluation is to condense the data and information into a well-arranged document and figures while potentially problematic aspects are clearly highlighted and described. Thus, the results of the integrity evaluation can be directly applied to identify topics for detailed assessment and to plan further measures.

Based on the combined and comprehensive integrity assessment hazardous processes and their influencing factors, possible migration pathways can be indicated more easily and thus will support risk assessments and planning of mitigation measures. In case of incidents, the result of the geological barrier assessment can facilitate the identification of potentially active flow paths during route cause analysis. Such an overall comprehensive integrity assessment will also serve as basis for further planning for potential conversions to e.g. to hydrogen storage or for the final abandonment phase of a cavern.

References

Zᴀɴᴅᴇʀ-Sᴄʜɪᴇʙᴇɴʜöғᴇʀ, D., Hᴏʀᴠáᴛʜ, B., Sᴄʜʀᴏᴇʀs-Sᴏɴɴᴇɴsᴄʜᴇɪɴ C. & Aᴄʜᴛ, A. 2016. Systematic Approach for Storage Integrity Assessment of Existing Cavern Storages – SMRI Fall 2016 Technical Conference Paper, Salzburg.

Hᴏʀᴠáᴛʜ, B., Rᴀɪᴛʜ, A.& Zᴀɴᴅᴇʀ-Sᴄʜɪᴇʙᴇɴʜöғᴇʀ, D. 2021. The Geological Barrier – A Key Component of a Comprehensive Integrity Assessment – SMRI Spring 2021 Technical Conference Paper, (Virtual Conference)

Development of surface deformations above salt caverns depending on the abandonment scenario

René Buzogany[1]*, Dirk Zander-Schiebenhöfer[1], Els Wijermars[2], Marinus den Hartogh[2]

[1]DEEP.KBB GmbH, Germany; [2]Nobian B.V., The Netherlands

* rene.buzogany@deep-kbb.de

ABSTRACT: During the operation of salt caverns, the creep behaviour of rock salt leads to a subsurface volume loss (convergence), which is transmitted to the surface and results in a subsidence bowl. The abandonment scenario of a cavern is of high importance for the long-term development of convergence and surface deformations, since the respective abandonment scenario could lead to either very low or moderate deviatoric stresses around the cavern. Subsidence modelling has been carried out for the cavern field in Heiligerlee (eleven brine-production caverns, one gas cavern) using the DEEP.KBB subsidence model, which is based on the established approach by Sroka & Schober (1982) and extended by Buzogany (2019) by differentiating the transmission of cavern convergence inside the salt dome and in the surrounding non-salt rock mass.

For the abandonment phase, three different scenarios were investigated:

- Hard shut-in (plugged cavern)
- Soft shut-in (pressure control at maximum pressure)
- No shut-in (open flow)

To assess if a stable situation is reached within 100 years after the end of the cavern operations, the subsidence and subsidence rates were calculated for up to 200 years after the end of operations. From the operator's prospect, the investigation provided valuable information on the total subsidence as well as the subsidence rates per scenario.

1   Introduction

Monitoring and prediction of surface deformations is an essential task for cavern operators in terms of safety and licensing law. During the operation of salt caverns, the creep behaviour of rock salt leads to a decrease of the subsurface cavern volume. This so-called convergence is transmitted to the surface and results in a subsidence bowl. Since the creep behaviour of rock salt is, inter alia, dependent on the difference between the state of stress in the saline formation and the pressure in the cavern, the abandonment scenario of a cavern is of high importance for the long-term development of surface deformations.

Subject of investigation was the cavern field in Heiligerlee. Solution mining started in the Heiligerlee field at the end of the 1950's. The field configuration of the cavern field is illustrated in Figure 1-1. The cavern field consists of eleven brine production caverns and one gas storage cavern located in a depth range between approx. 700 m and 1,600 m. For the subsidence prediction an extended approach by Sroka & Schober (1982) was applied, which considers the respective location of a cavern in the salt formation with regard to the salt dome edge (Buzogany 2019). Therefore, an azimuthal radius of influence is introduced, which is defined by the combination of two different angles of draw for the salt formation and the surrounding non-salt rock mass.
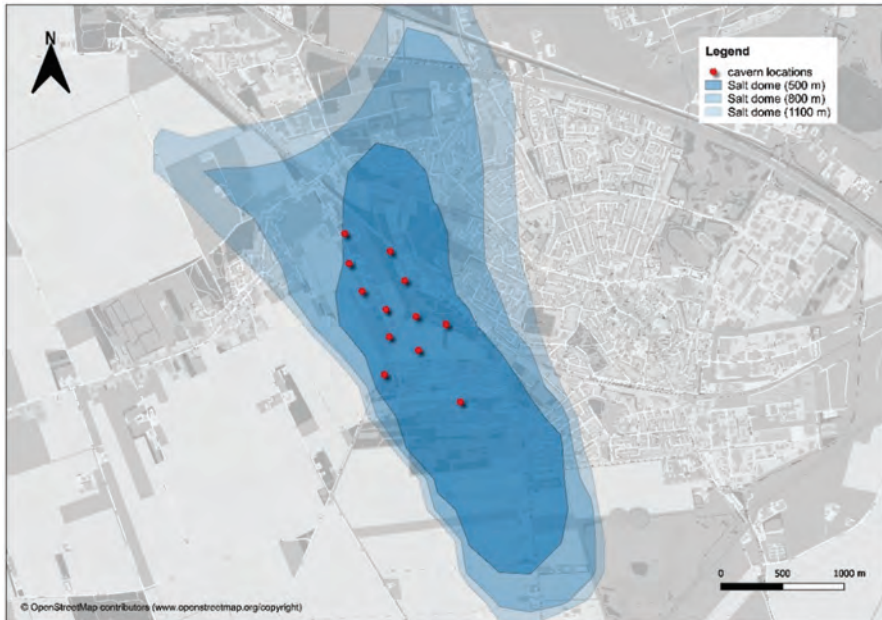
Figure 1-1: Field configuration Heiligerlee

For the abandonment phase, three different scenarios were investigated. The abandonment scenarios differ especially regarding the long-term internal cavern pressure and therefore, in the long-term convergence and subsidence rate. The hard shut-in represents the most common abandonment procedure and results in substantially lower subsidence values than the other scenarios, but it has to be mentioned that brine might infiltrate into the salt formation and even into the overburden over a substantially long period of time. The considered soft-shut-in and no-shut-in scenarios will require long term supervision, monitoring and maintenance and were investigated as alternative scenarios in order to compare abandonment effects.

2   Methodology

Subsidence above salt caverns is generally depending on the subsurface volume loss of the cavern due to the creep behaviour of salt and on the transmission behaviour of these losses through the salt and the overlaying rock layers above the cavern. Therefore, in a first step, the convergence volume of a cavern has to be calculated based on the creep properties of the host-rock material and the operational data of a cavern.

2.1   Convergence

For the description of the creep behaviour of salt, different creep laws have been developed. The BGRa-model is probably the most commonly used creep law in Germany for the long-term calculation of steady-state creep. However, based on laboratory tests, in-situ creep rates in the range of low deviatoric stresses are generally higher than calculated with the BGRa-model (Urai & Spiers 2007) due to the influence of pressure solution creep. Therefore, the BGRc-model according to Equation (1) was used to describe the creep behaviour of rock salt:

$$\dot{\varepsilon}_{eff} = A_1 \cdot \exp\left(-\frac{Q_1}{R_m \cdot T}\right) \cdot \left(\frac{\sigma_{eq}}{\sigma^*}\right)^{n_1} + A_2 \cdot \exp\left(-\frac{Q_2}{R_m \cdot T}\right) \cdot \left(\frac{\sigma_{eq}}{\sigma^*}\right)^{n_2} \tag{1}$$

In contrast to the BGRa, the BGRc is divided into two parts. Through the choice of different structure parameters A_1 and A_2, activation energies Q_1 and Q_2 as well as stress exponents n_1 and n_2, it allows to consider different deformation mechanisms in dependency of the equivalent von Mises stress σ_{eq} and the Temperature T.

Typical stress exponents for pressure solution creep are n= approx. 1 (low deviatoric stresses < 8-10 MPa) and for dislocation creep n= approx. 5 (high deviatoric stresses ≥ 8-10 MPa). However, creep-properties are always specific for the location and have to be determined by creep tests or by monitoring the long-term behaviour of the subsurface volume of a cavern.

The BGRc-model is considering only steady-state creep and its simplicity is suited especially for analytical subsidence prediction models, since the impacts of transient creep or high temperature deviations are very difficult to validate in those models (Berest & Brouard 1998). Since the creep rate is dependent on the equivalent von Mises stress σ_{eq} in the surrounding rock mass, it is important to assess the lithological pressure at cavern depth as well as the internal pressure at all stages in the cavern life cycle. The lithologic stress depends on the density gradient of the local geology (formations), whereas the internal pressure of a cavern during the operational period depends on the storage medium, the wellhead pressure and the cavern temperature. Therefore, internal pressures have to be back calculated based on the operational data of a cavern and predicted based on the operational plans for a cavern.

During the abandonment phase, the internal pressure highly depends on the chosen procedure for the post-operation phase. At this stage, there will be no new media (freshwater injection in case of brine production caverns, gas injection in case of gas caverns) introduced into the cavern and pressure development is mainly driven by temperature effects and the deformation mechanisms in the subsurface.

For the abandonment phase, three different scenarios were investigated:

- Hard shut-in (plugged cavern)
- Soft shut-in (pressure control at maximum pressure)
- No shut-in (open flow)

All of these scenarios considered a fully brine-filled cavern during the abandonment.

2.1.1 Hard shut-in

Directly at shut-in time, the cavern pressure equals the weight of the brine column up to the surface, which is lower than the pressure gradient of the surrounding salt mass. In the following period the cavern pressure will increase due to convergence and finally reach the lithostatic rock mass pressure at the cavern roof. Shortly before reaching the lithostatic rock mass stress, the process of brine infiltration into the rock mass will start as a result of microcrack opening (process of pressure driven percolation (Minkley et al. 2018)), beginning at the cavern surface. This will introduce a secondary induced permeability in the salt, which was originally completely tight.

During the subsequent phase of abandonment, the brine infiltration/percolation or permeation process will continue and spread in the salt, as convergence will still take place in the lower part of the cavern, provoking an overall pressure increase which will be equalized in the upper part of the cavern by brine infiltration. Laboratory experiments performed in various laboratories as well as in-situ tests have shown that the infiltration of brine already occurs when the fluid pressure is slightly below the minimum in-situ stress in the salt mass (e.g. Brouard et al. 2001, Minkley et al. 2013), i.e. the induced secondary permeability was high enough to balance the pressure increase. Therefore, the cavern pressure at the cavern roof can be considered to be slightly lower than the lithostatic pressure during hard shut-in.

For the purpose of convergence calculations, the cavern pressure at the cavern roof is considered to be 1 MPa lower than the lithostatic pressure and the representative cavern pressure in the volumetric centre was derived from the cavern pressure in the cavern roof. Thus, a constant convergence rate can be assumed for the abandonment via hard shut-in. It has to be noted that the influence of brine infiltration on surface subsidence is still not completely clarified. As a conservative assumption for the subsidence prediction, the total convergence volume generated during the hard shut-in will be transmitted to the surface.

2.1.2   Soft shut-in

The second abandonment scenario investigated was the soft shut-in of the caverns. In this scenario, the caverns are initially shut-in when the standstill period begins. Comparable to the first scenario, the pressure inside the cavern will increase due to convergence of the cavern. However, when the maximum allowable pressure at the casing shoe is reached, the pressure is reduced by releasing brine. No infiltration of brine into the overburden will occur, as the cavern pressure will respect the maximum pressure which ensures the geological tightness of the rock mass surrounding the cavern.

A common procedure would be that the cavern will be depressurized by 10 bar after reaching the maximum pressure. Hence, it is assumed that the average cavern pressure during this scenario will be approx. 5 bar lower than the maximum cavern pressure. This value is used for each individual cavern in order to calculate a constant convergence rate for the abandonment via soft shut-in.

2.1.3   No shut-in

In this case the cavern is considered to be "open", which means that brine is constantly being released at the wellhead and no pressure build-up occurs in the cavern. The convergence volume is equal to the released brine volume. The wellhead pressure amounts to atmospheric pressure since brine will flow out freely. The cavern pressure at the volume centre of the cavern, that is used for the calculation of the convergence rate, is only dependent on the pressure caused by the brine column up to surface.

2.1.4   Creep parameters

The chosen creep parameters for the subsidence prediction are visualized in Figure 2-1. Furthermore, the results of creep tests from the Heiligerlee salt dome as well as typical creep rates for salt with low and high creep abilities (creep rates represented by the Lubby2-material law) is presented. Moreover, the representative range of equivalent stresses related to the volumetric centre of a cavern during the different abandonment scenarios as well as during the operational phase is illustrated.

The creep rates in the range of equivalent stresses during operations were fitted based on the development of the open cavern volumes of each individual cavern measured by sonar measurements. For this purpose, the volume development was back-calculated considering

- mined salt volume,
- generated sump volume, which is considered to be still active for convergence,
- wellhead pressures, and
- the location of the caverns in relation to neighbouring caverns, since it is expected that the creep deformation for a cavern located in a cavern field is higher than for a single cavern (Zander-Schiebenhöfer 2007)

Since the equivalent stresses during the operations vary between approx. 5.2 MPa and 19 MPa, the creep rates as derived from lab-tests and from the history match can be

considered to be representative for the dislocation creep mechanism. For the stress exponent n, a value of 5 and 2 was chosen in a higher and lower stress range, respectively. These stress exponents were for example experimentally back-calculated by Günther et al. (2016). However, it has to be mentioned that these stress exponents are primarily calculated for "clean" salt.
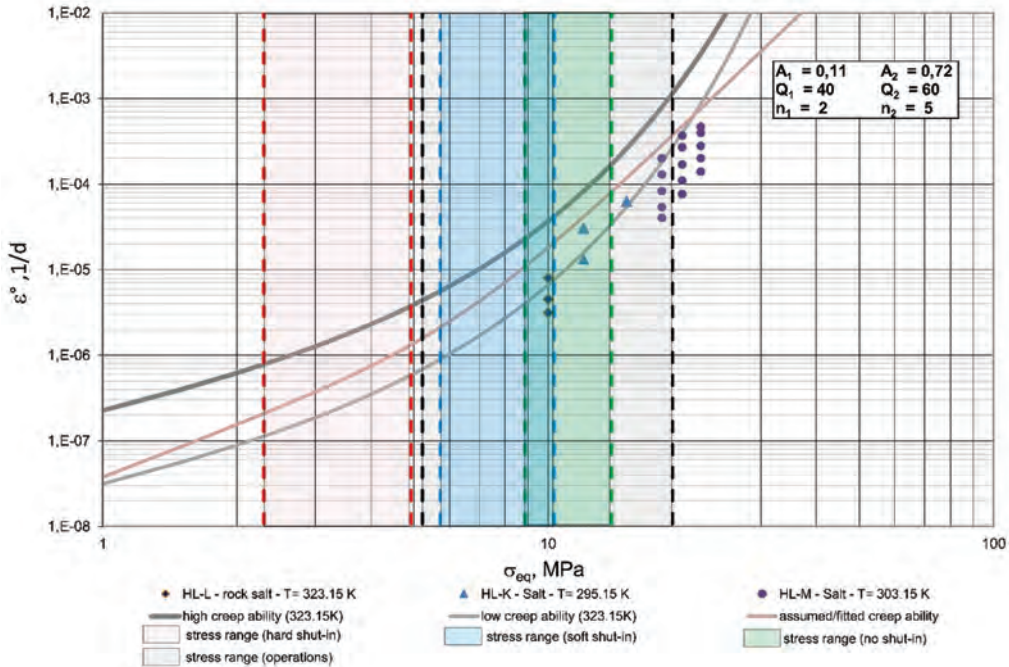

Figure 2-1: Steady-state creep rates vs equivalent stress (calibrated/assumed)

In the lower stress range from 2 MPa to 5 MPa the assumed creep rates were adjusted to the curve characteristic as represented in Figure 2-1 on the left-hand side. Salt creep at low deviatoric stresses has been inter alia recently investigated by Ecole Polytechnique et al. (2020). Therein, based on long-term lab tests as well as long-term tests in the Altaussee Mine in Austria, in a range of 0.2 – 5 MPa, in dependency of the temperature, the pressure solution creep mechanism could be identified as the main creep mechanism. The onset of pressure solution creep is expected to be also dependent on the grain size of salt (Urai et al. 2019). The stress exponent of this creep mechanism is usually assumed with approx. 1. The onset and influence of the pressure solution-precipitation creep is currently not well investigated and therefore uncertainties remain for the modelling. The chosen creep characteristic for low deviatoric stresses during the hard shut-in can be seen as the transitional behaviour between dislocation and solution-precipitation creep, the parameter n was chosen with 2.

2.2 Subsidence

Based on the calculated convergence volume V_{conv}, the subsidence prediction is carried out by using an extended analytical approach of Sroka & Schober (1982). This approach uses a gaussian function defined by a radius of influence to describe the subsidence bowl. It is based on the principle of rotational symmetry. The rock mass structure surrounding the cavern is assumed to be isotropic. In reality, however, anisotropies occur due to the salt dome geometry, different rock layers and faults above caverns.

Therefore, the calculation formula of Sroka & Schober (1982), that generates a circular subsidence bowl on the surface above a cavern, was extended through the introduction of the azimuth φ (Quasnitza, 1988). The azimuth is defined as the horizontal angle between the centre of the cavern and the point, where the subsidence is calculated. The applied modification of the calculation formula of Sroka & Schober (1982) is shown in Equation (2) according to Buzogany (2019) by describing the horizontal shape of the subsidence bowl through a defined number n of radii of influence (see Figure 2-2).

$$s(r,t,\varphi) = a(t) \cdot V_{conv}(t) \cdot \frac{1}{(\frac{1}{n}\sum_{i=1}^{n} R(\varphi=i\cdot(\frac{360}{n})))^2} \cdot exp(-\pi \left(\frac{r}{R(\varphi)}\right)^2) \tag{2}$$
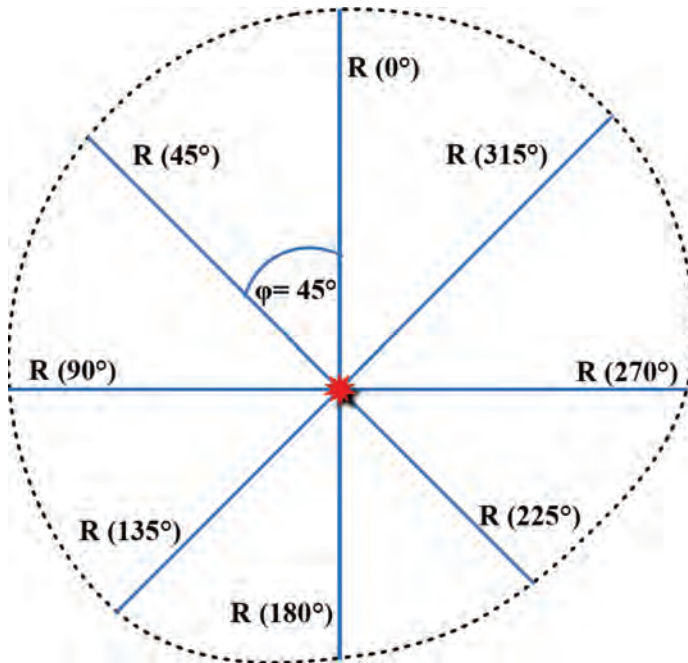
Figure 2-2: Exemplary representation of the subsidence bowl defined by eight radii of influence

Accordingly, the maximum subsidence above the centre of a cavern (horizontal distance cavern centre – calculation point $r = 0$) for a specified point in time t is calculated by considering the average radius of influence R of the total subsidence bowl. The values for $R(\varphi)$ in between a defined number of n sectors are calculated using an elliptical interpolation function. The transmission factor a is conservatively considered to be 1 in this equation. Therefore, all volume losses from the subsurface will be transmitted to the surface.

The variation of the radius of influence is dependent on the distance between the centre of the cavern and the salt dome boundaries. To differentiate the transmission behaviour between the salt dome and the surrounding non-salt rock mass the angle of draw, which represents the angle between the reference point of the cavity and the most distant point of subsidence on the surface, is subdivided into an angle of draw for the salt dome β_S and an angle of draw for the surrounding non-salt rock mass β_N (see Figure 2-3).

As depicted in Figure 2-2, it is generally assumed that the angle of draw of the surrounding non-salt rock mass β_N would be greater than that of the salt rock (Quasnitza 1988). However, this has to be checked against observations. Therefore, the angle of draw for the non-salt rock mass β_N as well as the angle of draw for the salt dome are fitted as modelling parameters to

the measured subsidence values to represent the local specific transmission behaviour of the overburden.

The radius of influence versus depth is expressed by an exponential function. The intersection points between the angle of draw and the salt dome boundaries have to be calculated to evaluate the impact of the surrounding non-salt rock mass.

The distance, which is necessary to ensure that the subsidence of a cavern is not influenced by the salt dome boundaries, is calculated by determining the radius of influence of the caverns in different depths z. The equation is given by Sroka et al. (2017):
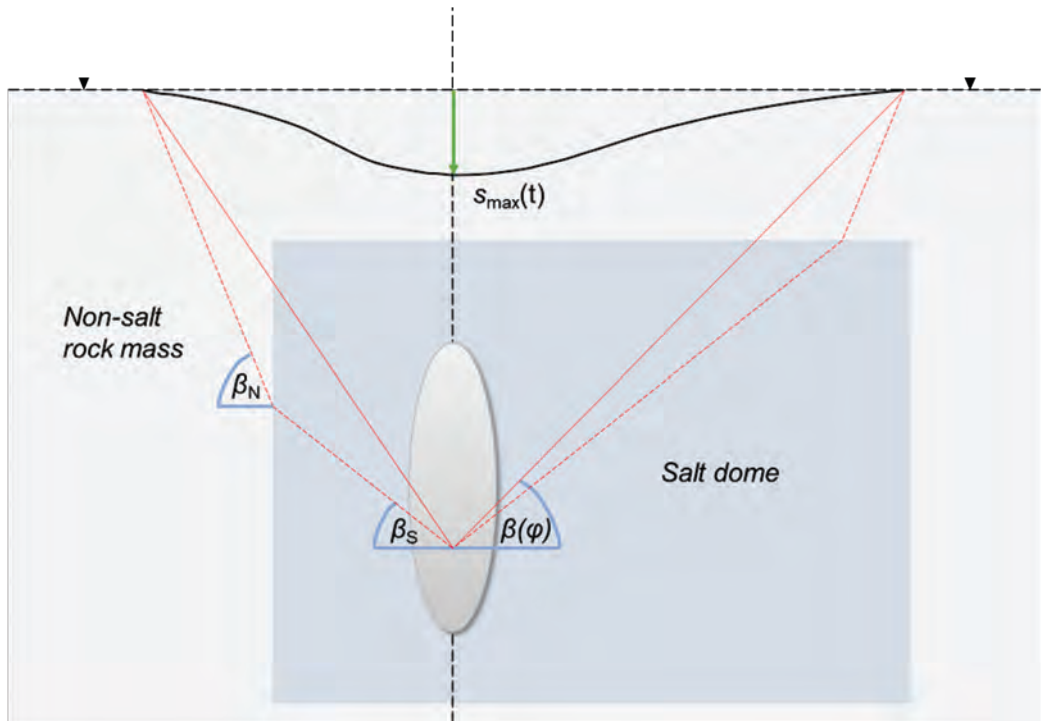
Figure 2-3: Differentiation of the angle of draw (salt dome and surrounding overburden)

$$R(z) = R(0) \cdot \left[\frac{(z_{cav} - z) + c}{z_{cav} + c} \right]^n \tag{3}$$

The parameters c and n represent the cavern roof and the interface coefficient, respectively.

Recommended values for n lie between 0.45 and 0.70 (Dżegniuk et al. 2003). For n a value of 0.5 and for c a value of 1 m was chosen. Since no subsidence below the surface is measured, these values cannot be fitted with measurement results and represent approximations to calculate the function of the angle of draw inside the salt dome.

The calculation of the azimuthal angle of draw $\beta(\varphi)$ is realized by the interpolation between the angle of draw for the salt dome β_S and the angle of draw for the surrounding non-salt rock β_N. As interpolation value the ratio of the height fraction of the function of the angle of draw inside of the surrounding non-salt rock mass Δz_N to the total height of the overlying salt $\Delta z_{S,tot}$ is used.

$$\beta(\varphi) = \beta_S + (\beta_N - \beta_S) \cdot \frac{\Delta z_N}{\Delta z_{S,tot}} \tag{4}$$

With the aim of a better illustration the components of Equation (4) are displayed in Figure 2-4.
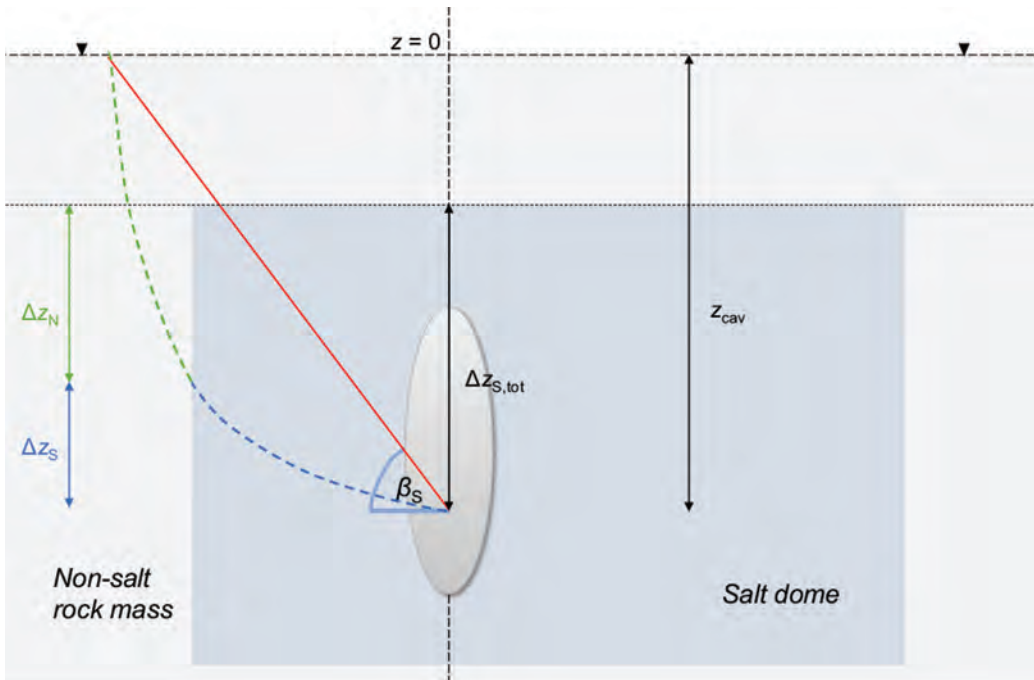
Figure 2-4: Schematic representation of the components of equation (3) and (4)

The calculated subsidence induced by cavern operations was fitted to levelling results. The calibration/validation of the subsidence model against the levelling results is quite complex and a detailed discussion is not being implemented is this article. After a plausibility check of the measurements, the calibration was performed by varying the angle of draw and by a statistical evaluation of the results. Generally, it has to be considered that surface levelling results include all contributions to subsidence. In the Heiligerlee area, these contributions are mainly subsidence due to natural causes, e.g. ground compaction or water management, and due to gas production from gas fields in the Netherlands. These influences have to be taken into account and superimposed with cavern-induced subsidence to assure a reliable calibration process. However, it has to be mentioned that the values for subsidence induced by other sources than cavern operation also include inaccuracies.

In total, 167 benchmark locations, where levelling measurements are available, were considered and initially evaluated whether the levelling results could be utilized for the model calibration. Benchmark locations, where up-lifting was observed or where the predicted subsidence due to other mining activities was already higher than the measured subsidence, were excluded from the calibration of the model. A collection of representative benchmark locations for the model calibration is illustrated in Figure 2-5.

As a conservative approach, the modelled subsidence values have been primarily fitted to represent the development of maximum subsidence values due to cavern operations. In the calibration process the angle of draw for the salt dome β_s and the non-salt rock mass β_N were kept equal, at first. This corresponds to the approach by Sroka & Schober (1982).

The best fit could be achieved with an angle of draw of 35° considering a decrease of the angle of draw of 10°/40a, as proposed by Zander-Schiebenhöfer (2007). The model error amounts to 3.15 % in relation to the maximum subsidence for the centre of the subsidence bowl and 5.75 % for the overall subsidence bowl.

Afterwards, the angle of draw for the salt dome β_s and the non-salt rock mass β_N were varied to achieve a better model quality. A good match could be identified for an initial $\beta_s = 34°$ and

β_N = 36°. The resulting model error amounts to 3.09 % in relation to the maximum subsidence for the centre of the subsidence bowl and 5.72 % for the overall subsidence bowl.

The improvement of the modelling results can be seen as minimal. This might lead to the assumption that the transmission behaviour in the salt dome and the non-salt rock mass is quite similar in the Heiligerlee area.

However, the presented approach shows that by considering inhomogeneities in the influence area of salt caverns the prediction of subsidence can be improved. The presented approach in equation 2 allows to also consider other inhomogeneities besides the differentiation between salt dome and non-salt rock mass. It would be of interest to investigate the improvement of modelling results by considering further geological factors. However, it has to be mentioned that a significant amount of further geological information has to be available and the modelling effort increases.

2.3   Field Situation and Results

The Heiligerlee salt dome extends over an area of approx. 9 km² (in a depth of 1.100 m). The salt dome is oriented in northwest-southeast direction, meaning, distances between caverns and the salt dome boundaries/surrounding overburden are smaller in northeast and southwest direction. Therefore, influences of the overburden on the shape of the subsidence bowl are generally expected in these regions.

Regarding the surface deformations during the abandonment phase of a cavern, the three investigated scenarios differ significantly. Since subsidence and subsidence rates are dependent on the operation mode (high/low pressure, cavern still in operation or already abandoned) of every cavern and can vary considerably depending on time and location, only the development of the maximum subsidence and subsidence rates over time for the centre of the overall cavern induced subsidence bowl are displayed in Figure 2-6. In general, it should be noted, that the caverns will not be abandoned at the same time and therefore, some caverns in the Heiligerlee field will be abandoned while others are still producing brine or storing gas. Thus, the points in time for the first cavern abandonment, the end of brine production and the last cavern abandonment are indicated. Thermal effects are not considered for the pressure development during the abandonment. For the hard-shut-in scenario, a general waiting time of 20 years is considered after the end of operation for the establishment of a thermal equilibrium between brine and rock mass temperature.

2.3.1   Evaluation criterion

Considering current abandonment procedures, the hard-shut-in scenario represents the state-of-the-art. Since the cavern pressure at the cavern roof will rise to slightly below the lithostatic pressure (and therefore exceeds the maximum operational pressure at the last cemented casing shoe), the resulting convergence rate of a cavern is much lower than in the other scenarios. Consequently, subsidence deformations are very small.

The development of subsidence and subsidence rates for the different abandonment scenarios is depicted in Figure 2-6. The shown values are normalized to the final subsidence and final subsidence rate of the "hard shut-in", which are set to be 1 after 200 years of the post-operation phase.

To develop a uniform evaluation criterion in terms of subsidence development, the calculated time-dependent subsidence rates for the different abandonment scenarios will be normalized. Subsidence and subsidence rates calculated for the "hard-shut-in" scenario will be defined as default value. It has to be stated that the calculated subsidence and subsidence rate during the hard-shut-in can be seen as conservative, since the volume losses of the cavern are

directly transmitted to the surface by the model. In reality, brine will be infiltrated into the salt structure, when the cavern pressure exceeds the infiltration criterion of the rock salt. In theory this means, once infiltration started, no volume is lost at subsurface, but will be distributed over a wider area, as long as no brine leaves the salt formation. Based on that, subsidence and subsidence rates would be even lower than calculated.
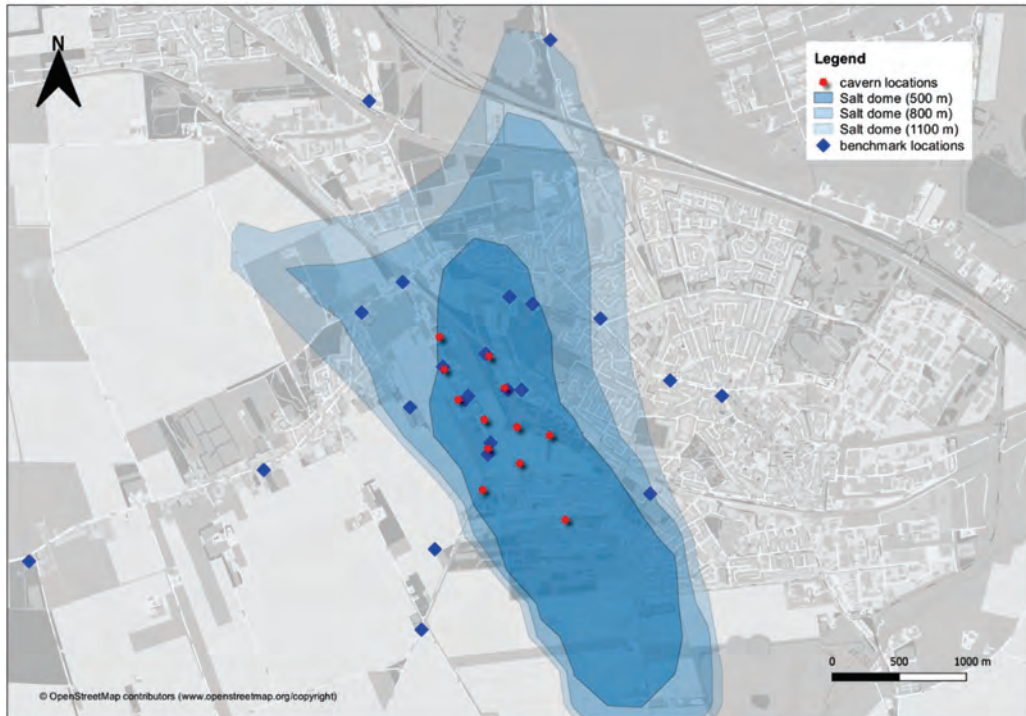

Figure 2-5: Representative benchmark locations for the calibration of the subsidence model

The ratio of the calculated subsidence and subsidence rate per scenario to the calculated subsidence and subsidence rate of the "hard-shut-in" scenario will be formed, to directly compare the scenarios. Since the resulting ratio for the scenario "hard-shut-in" equals 1 over the course of the whole calculation time, values >1 mean that calculated subsidence of the alternative scenario is greater than during the hard-shut-in.

The time-dependent development of this evaluation criterion is displayed in Figure 2-7. Since before the first cavern is abandoned, the operational data for all scenarios are identical, the ratio equals 1 for all scenarios. The differences of the "soft-shut-in" and the "no-shut-in" scenario to the "hard-shut-in" scenario in terms of the development of surface deformations is discussed in the following.

2.3.2 Results for option no shut-in

As illustrated in Figure 2-6, the highest subsidence and subsidence rate are predicted for the "no shut-in" abandonment scenario. While in the other scenarios subsidence rates generated by a single cavern will be reduced during abandonment, in this case, the subsidence rate will increase, because operating pressures will be reduced to atmospheric pressure and brine will flow out of the cavern freely resulting in a lower internal cavern pressure.

At the beginning of the post-operation phase, when all caverns are abandoned, the maximum subsidence rate will be approx. 8 times higher than during the hard shut-in. Since cavern

convergence is directly dependent on the cavern volume, the high volume reduction over time leads also to a high reduction of the convergence and the subsidence rate.

Therefore, after 100 years, the ratio of the subsidence rate during the "no shut-in" scenario to the "hard shut-in" scenario reduces to approx. 7, meaning the absolute value of the subsidence rate reduces faster during the "no shut-in" scenario.
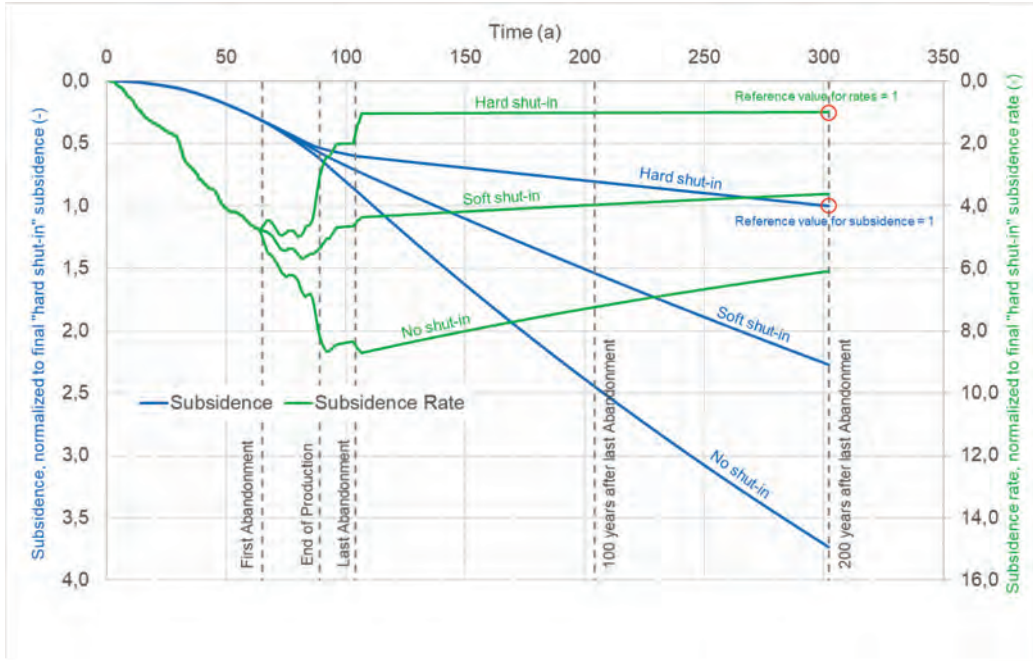
Figure 2-6: Development of subsidence and subsidence rates over time for different abandonment scenarios (normalized to final values of the "hard shut in" scenario)

Since the reduction in subsidence rate implies high convergence, the overall subsidence after 100 years is approx. 3 times higher than during the hard-shut-in scenario. 200 years after the abandonment of the last cavern in the field, the subsidence rate still is approx. 6 times and the maximum subsidence is approx. 3.7 times higher than in the "hard shut in" scenario.

It should be mentioned that in case of no shut-in the cavern will close completely over a longer period of time and practically no brine will remain in the underground, ultimately resulting in higher subsidence in a shorter period of time in relation to the other scenarios.

2.3.3 Results for Option soft shut-in

At the beginning of the post-operation phase, the predicted maximum subsidence rate during the "soft shut-in" scenario is approx. 4 times higher than in case of the "hard shut-in" scenario. While the absolute subsidence rate decreases over time, the ratio to the "hard shut-in" decreases as well, meaning that the decrease in subsidence rate is faster in relation to the "hard shut-in". As also seen during the "no shut-in" scenario, this decrease in the subsidence rate is a result of higher convergence in relation to the "hard shut-in" scenario.

This leads to an increase of subsidence from approx. 1.2 times higher after the last cavern abandonment to approx. 1.9 times higher after 100 years and approx. 2.3 times higher after 200 years.

3   Conclusions

The presented investigation has shown that the abandonment scenario is of essential importance for the long-term development of surface deformation. The key parameter for limiting subsidence is represented by the internal pressure of the cavern, since the convergence rate of a cavern, and in consequence also the subsidence rate, is directly dependent on the differential stress between internal and lithostatic pressure.

In case a cavern will be abandoned under "no shut-in" conditions, meaning brine will flow out freely at the surface, high subsidence rates will be the result, since the differential pressure between the static brine column and the lithostatic pressure will be higher than during the operational phase.

During a "soft shut-in", brine will be released in regular intervals to prevent the pressure from exceeding the maximum pressure. Operating the cavern near its maximum pressure reduces subsidence rates substantially in comparison with the "no-shut-in" scenario.

In relation to the "hard shut-in" scenario, these two scenarios will lead to higher convergence and higher subsidence as well as subsidence rates in short terms. Furthermore, these scenarios require further monitoring and operational effort and therefore, higher expenses for the operators. However, it is expected that no significant amounts of brine will infiltrate into the salt dome and the complete brine volumes will be displaced from subsurface after several thousands of years.

The "hard shut-in" represents the most common abandonment procedure in Europe. For this kind of abandonment, a cavern will be plugged and the well will be cemented, leading to an
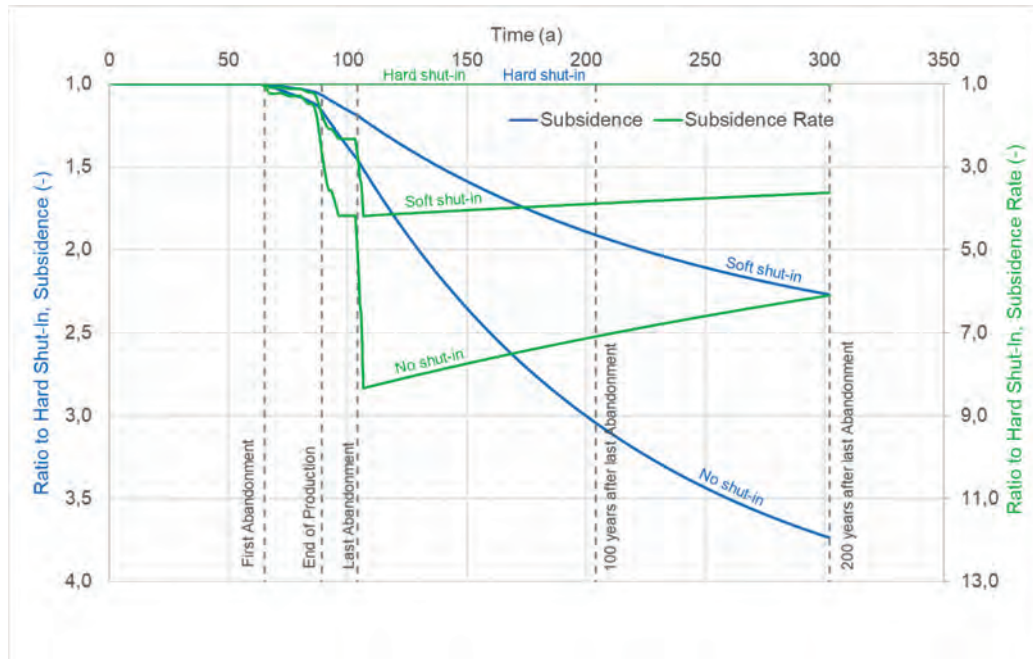
Figure 2-1: Development of subsidence and subsidence rates over time for different abandonment scenarios (in relation to the "hard shut-in" scenario)

isolation of the subsurface volume from the surface. Due to the creep closure, the internal pressure of a cavern will rise until infiltration of brine into the salt formation takes place. This is expected to occur at the cavern roof in a pressure range slightly below the lithostatic pressure. In terms of subsidence, this scenario is most suitable to limit subsidence, since the resulting differential pressure is the lowest out of the three investigated scenarios. However, it should be noted that brine will infiltrate into the salt structure and over a longer period of time,

potentially also into the overburden, which affords the evaluation of potential follow-up processes.

The different abandonment scenarios need to be evaluated in detail for every cavern field, since they implement quite significant differences regarding the subsurface processes, the amount of subsidence generated over time and the operational effort. With the aim of limiting subsidence, the common hard-shut-in represents the most suited abandonment procedure.

Acknowledgements

References

BÉREST, P., & BROUARD, B. 1998. A Tentative Classification of Salts According to their Creep Properties. New Orleans: SMRI Spring Meeting.

BROUARD, B., BÉREST, P., & GREEF, V. D. 2001. Salt Permeability Testing- The Influence of Permeability and Stress on Spherical Hollow Salt Samples. SMRI Research Report RR2001-8.

BUZOGANY, R. 2019. Erweiterung und Validierung eines Modells für die Prognose von Bodensenkungen infolge des Betriebs von Salzkavernen. Masterarbeit. Ruhr-Universität Bochum.

DŻEGNIUK, B., NIEDOJADŁO, Z. & SROKA, A. 2003. Podstawy wymiarowania i eksploatacji szybowych filarów ochronnych. Szkoła Eksploatacji Podziemnej.

ECOLE POLYTECHNIQUE; BROUARD CONSULTING; INSTITUT FÜR GEBIRGSMECHANIK; RESPEC; STORENGY; URAI, JANOS; SPIERS, CJ; PEACH, CJ. 2020. Very Slow Creep Tests As a Basis for Cavern Stability Analysis, Phase 2. SMRI Report RR2020-1.

GÜNTHER, R. M., LÜDELING, C., POPP, T., NAUMANN, D., WIEDEMANN, M. & WEISE, D. 2016. Vergleich aktueller Stoffgesetze und Vorgehensweisen anhand von Modellberechnungen zum thermo-mechanischen Verhalten und zur Verheilung von Steinsalz - Teilvorhaben, 2.

MINKLEY, W., BRÜCKNER, D. & LÜDELING, C. 2018. Percolation in salt rocks. Hannover: Proceedings Mechanical Behavior of Salt IX.

MINKLEY, W., KNAUTH, M., & BRÜCKNER, D. 2013. Discontinuum-mechanical behaviour of salt rocks and the practical relevance for the integrity of salinar barriers. ARMA 13-388, 47th US Rock Mechanics / Geomechanics Symposium.

QUASNITZA, H. 1988. Eine Strategie zur Kalibrierung markscheiderischer Bewegungsmodelle und zur Prädikation von Bewegungselementen. PhD thesis, Technische Universität Clausthal.

SROKA, A., & SCHOBER, F. 1982. Die Berechnung der maximalen Bodenbewegungen über kavernenartigen Hohlräumen unter Berücksichtigung der Hohlraumgeometrie. Kali u. Steinsalz Bd 8, pp. 273-277.

SROKA, A., MISA, R., TAJDUS, K., KLAUS, M., MEYER, S., & FELDHAUS, B. 2017. Forecast of rock mass and ground surface movements caused by the convergence of salt caverns for storage of liquid and gaseous energy carriers. Freiberg: 18. Geokinematischer Tag.

Urai, J., & Spiers, C. 2007. The effect of grain boundary water on deformation mechanisms and rheology. The Mechanical Behavior of Salt - Understanding of THMC Processes in Salt: Proceedings of the 6th Conference (SaltMech6), Hannover, Germany.

Urai, J., Schmatz, J., & Klaver, J. 2019. Over-pressured salt solution mining caverns and leakage mechanisms; Phase 1: micro-scale processes. Project KEM-17.

Zander-Schiebenhöfer. 2007. Kriechverhalten von Salzgestein in der Umgebung von Kavernenfeldern. Kriechverhalten von Salzgestein in der Umgebung von Kavernenfeldern. Gottfried Wilhelm Leibniz Universität: PhD thesis.

CCC - integrated multiscale study of salt cavern abandonment in the Netherlands

Tobias S. Baumann[1], Pierre Bérest[2], Benoit Brouard[2], Martijn ter Braack[5], Marinus den Hartogh[5], Boris Kaus[1], Jop Klaver[3], Paul Oonk[5], Anton Popov[1], Joyce Schmatz[3], Janos L. Urai[4], Els Wijermars[5]*

[1]smartTectonics GmbH, Germany; [2]Brouard Consulting, France; [3]MaP – Microstructures and Pores GmbH, Germany; [4]GeoStructures Consultancy, Netherlands; [5]NOBIAN, Netherlands;

* janos.urai@geostructures.nl

ABSTRACT: The KEM-17 project of the Dutch State Supervision of Mines presented a critical review of concepts of cavern abandonment and related science. It recommended that analyses of cavern abandonment are done as an integrated project, addressing (i) micro-scale physical processes, (ii) cavern scale models based on field scale experiments and numerical models, (iii) the salt dome scale, to model the far field of the salt caverns. The Cavern Closure Consortium (CCC) project is based on this, focusing on the Haaksbergen and Heiligerlee cavern fields in the Netherlands. We build on (i) innovative deformation experiments, integrated with state of the art microstructural analysis to define constitutive equations for deformation and permeation, focusing on the poorly understood domain below 8 MPa differential stress, (ii) numerical finite element models of the cavern field combined with cavern-scale field experiments to define the closure parameters and temperature evolution of the cavern, and (iii) state of the art numerical models at the scale of the whole salt pillow or salt dome to define the "ist-Zustand". All these contributions are closely integrated and will lead to much improved prediction of the evolution of the caverns after closure and abandonment.

1   Introduction

In the KEM-17 project (Baumann et al. 2019; Brouard et al. 2019; Urai et al. 2019), our consortium reviewed the micro- to macro scale aspects of the abandonment of brine-filled solution mining caverns, focusing on the cases where the surrounding salt is of such low permeability that close to lithostatic pressures will develop after abandonment. We proposed an improvement of current methods, using an integration of the state-of the art in materials science, engineering, and numerical modelling. This project follows the main lines of this recommendation and is organized in 5 main Work Packages (Figure 1), many of these involving cooperation by one or more partners. We thus present a novel approach where we integrate materials science, geophysical and engineering approaches, in order to reduce uncertainties in predicting the evolution of abandoned caverns over long time scales.

One critical question asked in this project is whether a close-to lithostatic brine pressure will develop in the caverns after abandonment. We approach this concern by integrating results of microstructural analysis, deformation and permeation experiments, numerical simulation of deformation and permeation at cavern and salt dome scale, and field testing in boreholes and in caverns. Another critical question is if and how the brine will be expelled from the salt formation. We outline the uncertainties and propose ways to reduce this uncertainty and test the predictions.

Finally, in this project, we will present models of the patterns and timescales of brine pressure and brine permeation and discuss strategies for safe abandonment over long term.
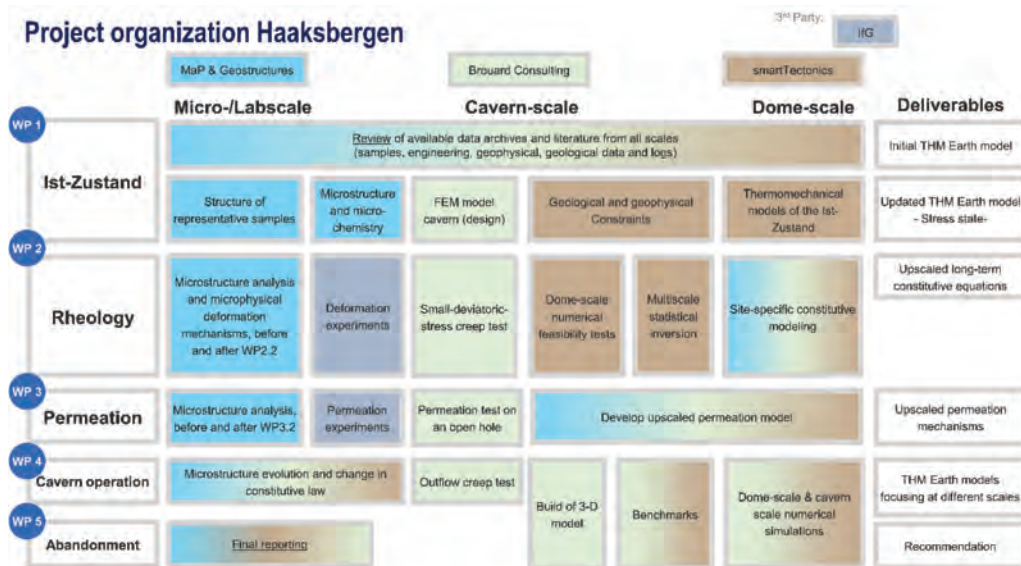
Figure 1: CCC- Project organization Haaksbergen.

Here, we present first results on the future Haaksbergen cavern fields of Nobian, present our preliminary findings and discuss upcoming analyses and cavern- and borehole- scale testing in future wells.

2   Ist-Zustand

The present-day structure and properties of the Haaksbergen pillow were characterised based on an improved geological model, detailed analysis of the drill core and geomechanical modelling. We conclude that Zechstein-1 salt has a deformed and recrystallized microstructure typical of tectonically deformed rock salt, with a median grainsize which varies between 1 and 3 mm (Figure 2), and variable amounts of dispersed and layered Anhydrite. During the evolution of the Haaksbergen pillow it experienced a maximum differential stress of around 2 MPa, and both pressure solution and dislocation creep were active microphysical processes.

Dislocation creep and pressure solution creep were the dominant deformation mechanisms during the formation of the Haaksbergen pillow. Grain boundaries in Halite are equilibrated with non-percolating fluid inclusions, suggesting exceedingly low permeability in-situ. However, polycrystalline Anhydrite in the core is microporous and could form fluid pathways. Based on microstructure, the rock salt's rheology (in the far field of the caverns) can be described by a two-mechanism creep law with a power law part and a change to Newtonian, pressure solution dominated creep at about 8 MPa, predicted using the grain sizes measured.

For numerical modelling, we propose three different mechanical units: (i) Pure Rock Salt - this has the rheology explained above. (ii) Massive Anhydrite - this, we infer at the scale of the cavern operation to be a highly viscous material, with a viscosity about 500x that of the Halite. (iii) Anhydritic Halite which is a fine layercake with effective properties used for modelling: for this we propose a higher viscosity 50x that of Halite.
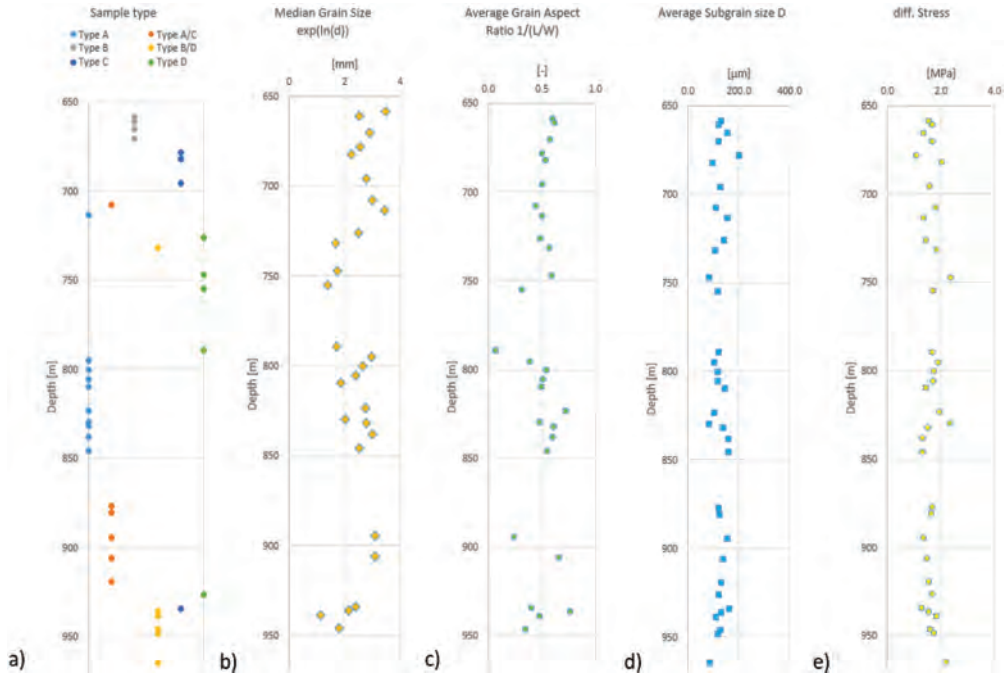
Figure 2: Summary of the results of measurement in relation to litho-classes, the median grain size, the average grain aspect ratio, as well as the subgrain size and the derived differential stress (Schleder & Urai 2005)

2.1 Rheological model to describe the long-term creep of Haaksbergen rock salt

The long-term creep rheology of rocksalt is affected by relatively large uncertainties. Usually, the creep rheology is only inferred from laboratory-scale constraints. With the deformation tests in the laboratory at ~1 MPa or higher, typical strain rates are of the order 10^{-6} to 10^{-9} s^{-1}. Yet, typical strain rates for salt diapirs are of the order 10^{-17} to 10^{-13} s^{-1}. Thus, we need to extrapolate over many orders of magnitude to infer the stress state within a salt dome from lab-scale constraints. We aim to use the complementary expertise of the CCC consortium on different scales (micro, laboratory, cavern, and dome scale) and combine their constraints to derive a consistent long-term creep model for Haaksbergen rock salt with uncertainty intervals.

We develop a long-term rheological model for rock salt that incorporates the first-order effects of grain size kinetics on pressure solution creep and thus on the composite creep law consisting of pressure solution and dislocation components. The new concept introduces additional parameters to the standard long-term rheological model, which are used to parameterize microstructural phenomena of grain size evolution and grain boundary (de-) activation. The total strain rate can be additively decomposed into the elastic, transient, dislocation, and pressure solution creep components, respectively, as follows:

$$\dot{\varepsilon} = \dot{\varepsilon}^{el} + \dot{\varepsilon}^{tr} + \dot{\varepsilon}^{dc} + \dot{\varepsilon}^{ps}.$$

Here, we focus on the *long-term* creep and consider the following two components:

1. Dislocation creep:

$$\dot{\varepsilon}^{dc} = A_{dc} \exp\left(-\frac{Q_{dc}}{RT}\right)\sigma^n, \tag{1}$$

2. Pressure solution creep:

$$\dot{\varepsilon}^{ps} = A_{ps} \exp\left(-\frac{Q_{ps}}{RT}\right)\frac{\sigma}{TD^m}. \tag{2}$$

In the above equations A_{ps} and A_{dc} denote pre-factors of the creep mechanisms, Q_{ps} and Q_{dc} are the corresponding activation energy parameters, R is the gas constant, T is the absolute temperature, D is the average grain size, σ is the effective differential stress (square root of the second invariant of the deviatoric stress tensor), n and m are the dislocation creep and grain size dependence exponents, respectively. Figure 3a illustrates this classical view of the steady-state creep in a stress-strain rate diagram.

Yet, it is known from microstructural observations that pressure solution creep involves various complexities. One complexity is *grain boundary activity*, as pressure solution only operates if the grain boundaries are mobile which requires a connected fluid film to be present. Here, we parameterize this effect using a simplified, stress-dependent activation function ξ, which changes smoothly between 0 and 1. The state $\xi = 1$ corresponds to the fully activated grain boundaries surrounded by connected fluid films. The state $\xi = 0$ describes the situation when the fluid films get disintegrated, and pressure solution creep completely stops (KEM-17). Currently, it is not exactly clear what factor triggers the deactivation. However, various empirical suggestions indicate that it occurs in the case that differential stress drops below a certain low threshold σ_{crit}. We thus propose the grain boundary activity control to be parameterized in the following simplified manner:

$$\dot{\varepsilon} = \xi\,\dot{\varepsilon}^{ps} + \dot{\varepsilon}^{dc}, \tag{3}$$

with ξ being the smooth stress-dependent activation function, given by:

$$\xi = \frac{1}{1+\frac{\sigma_{crit}}{\sigma}}. \tag{4}$$

Figure 3b demonstrates the effect of deactivated grain boundaries at a typical critical stress level.
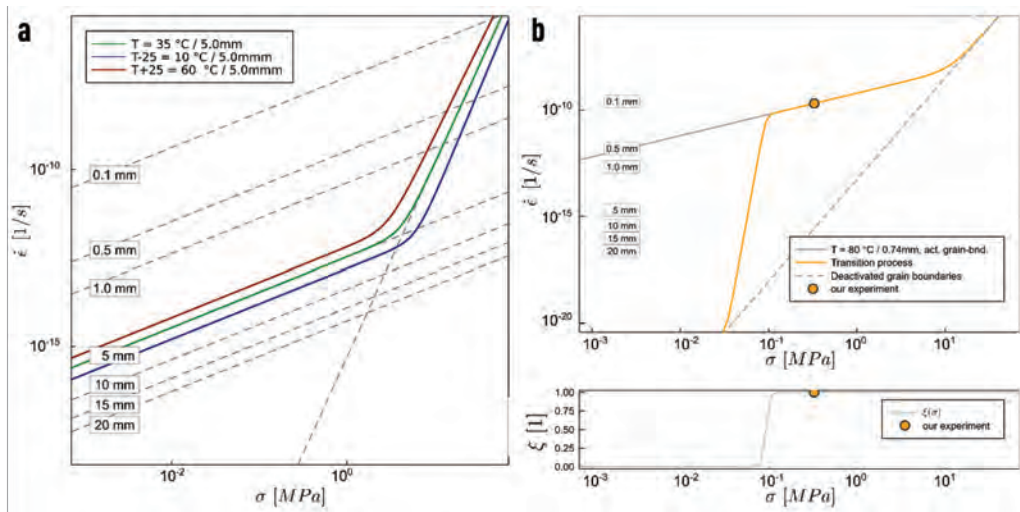
Figure 3: a: Classical stress-strain rate diagram with combined long-term creep composed of dislocation and pressure solution creep illustrated for a constant grain size of 1 mm at different temperatures with parameters from Spiers et al. (1990). Dashed lines correspond to individual creep components, *i.e.*, dislocation creep and pressure solution creep with other dominant

grain sizes b: Combined creep model with critical stress level switch to simulate the deactivation mechanism of pressure solution creep at a critical stress level of $\sigma_{crit.}$=100 kPa. A smoothed logistic function describes the disintegration of the fluid films at this stress level.

Using a Bayesian approach with a Markov chain Monte Carlo (McMC) method allows us to combine expert knowledge (a priori conditions) with measurements. It enables us to quantify the rheology in a probabilistic sense and derive credibility ranges for all model parameters. The approach is well established, also for the specific application to creep rheology (e.g., Korenaga & Karato 2008), even when it has not yet been applied to salt rheology.

We formulated the geometric elements of a geomechanical model to compute both salt pillow-scale and cavern-scale evolution, upscaling the contributions of multiple thin Anhydrite layers in the dominant rock salt section, including realistic long-term rheology of Anhydrite. This model predicts a 3D stress and temperature field of the Haaksbergen pillow which is much more realistic than the strongly simplified assumptions in most current models of cavern abandonment.
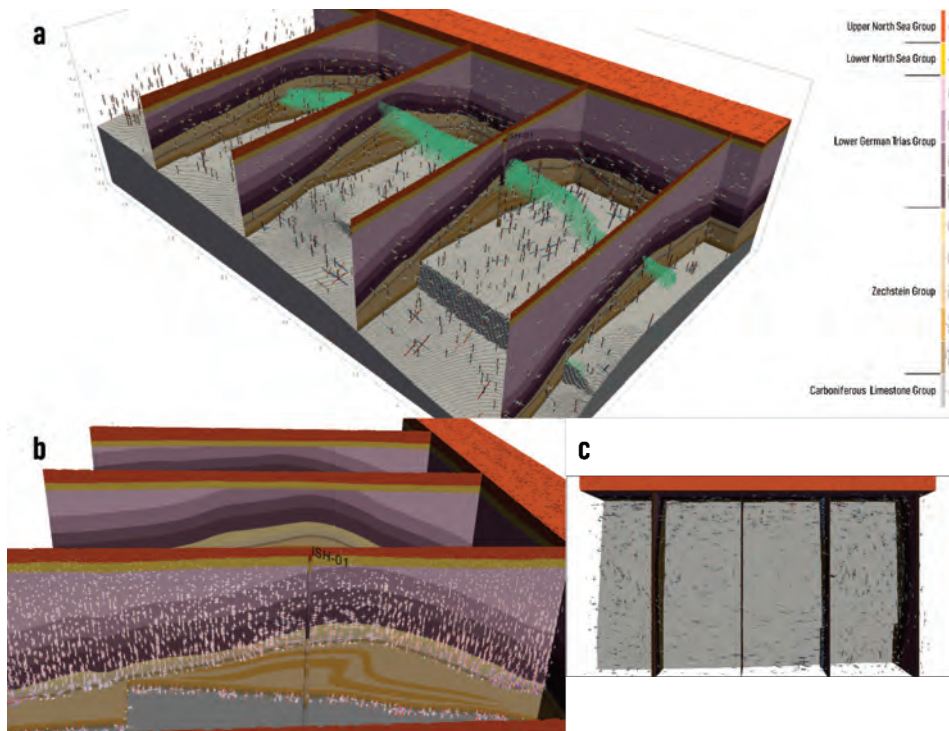
Figure 4: Thermomechanical modelling results on the salt-dome scale. Markers show the principal stress directions of the stress tensors throughout the model domain (a-c). The global pattern of the principal stress directions is primarily driven by the shape of the Top salt surface (b, c). Marker colors indicate the stress magnitude and sense. Green markers in (a) indicate plastic failure. See text for further details.

Although it needs to be confirmed by other end-member model results, our initial results indicate that the large-scale pattern of the principal stress direction is a relatively robust model feature primarily affected by the shape of the top salt surface. Our model results demonstrate that plastic failure occurs at distinct locations (the ridge of the salt pillow, Figure 4), consistent with seismic interpretations of faults in the overburden of salt structures. With the additional scenarios, we will explore the sensitivity of the stresses concerning the uncertain model input (e.g., salt rheology, temperature).

The rheology and permeation of laboratory samples is studied in two world-class facilities: the laboratories of IfG in Leipzig and the laboratory in the Altaussee mine in Austria, both providing unique and complementary data to answer the currently controversial question of the constitutive laws governing rock salt creep at low differential stress and very long-time scales of several years and longer. The samples were characterised extensively with state-of-the art microstructural tools to determine the deformation mechanisms.

The first series of 8 deformation experiments at IfG on wet core samples were set up to investigate the processes in salt close to a cavern, where high differential stress develops during cavern operation followed by long-term deformation at decreasing differential stress during abandonment. Results show that the samples completely recrystallize during these experiments, a process not yet recognised in cavern abandonment studies (Figure 5). Deformation mechanisms are dislocation creep and pressure solution creep and this allowed the results to be incorporated in the constitutive models. Grainsize will affect pressure solution creep rates and can be taken into account in future models of abandoned cavern evolution. Experiments in the Altaussee mine, that operate at even lower differential stress and are much more sensitive and accurate than the ones performed at IfG but last much longer, were set up and started, and are expected to reach stationary creep in several months' time.
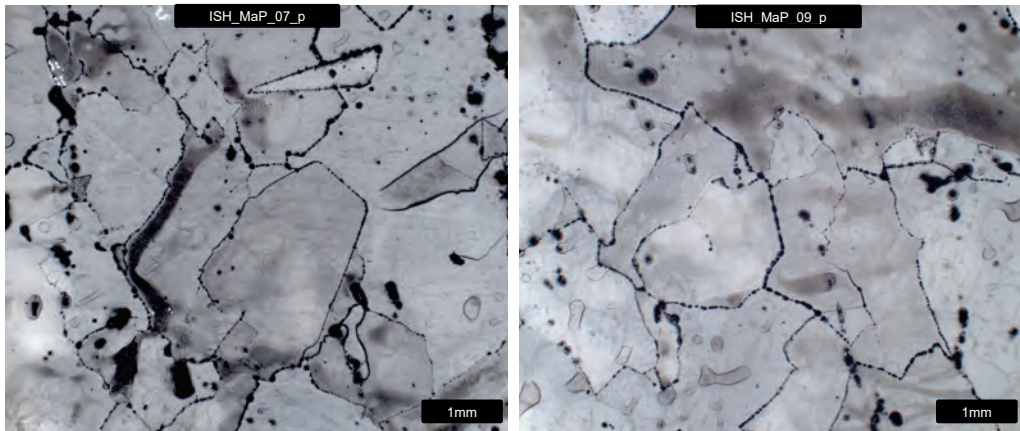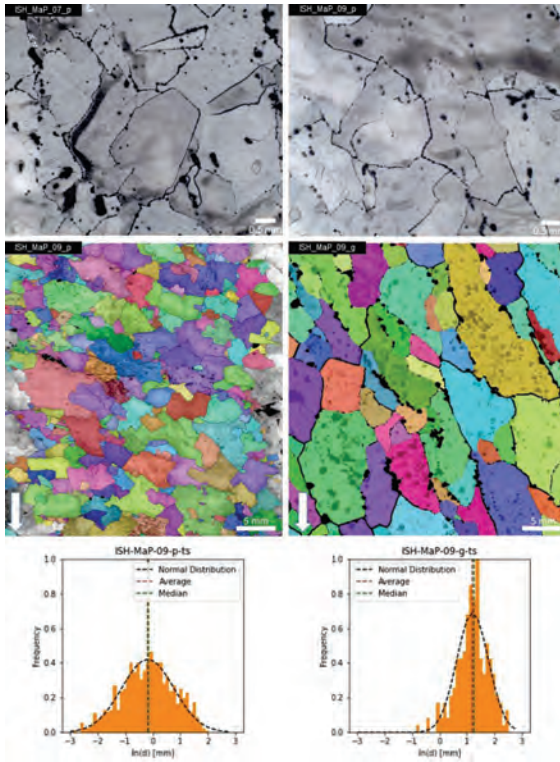
Figure 5: Top images show completely recrystallized microstructure of sample ISH_MaP_07 and ISH_MaP_09. Images underneath show the grainsize reduction of ISH_MaP_09_p (deformed) vs ISH_MaP_09_g (undeformed). This is the first time that salt subjected to stress at the cavern wall is demonstrated to recrystallize.
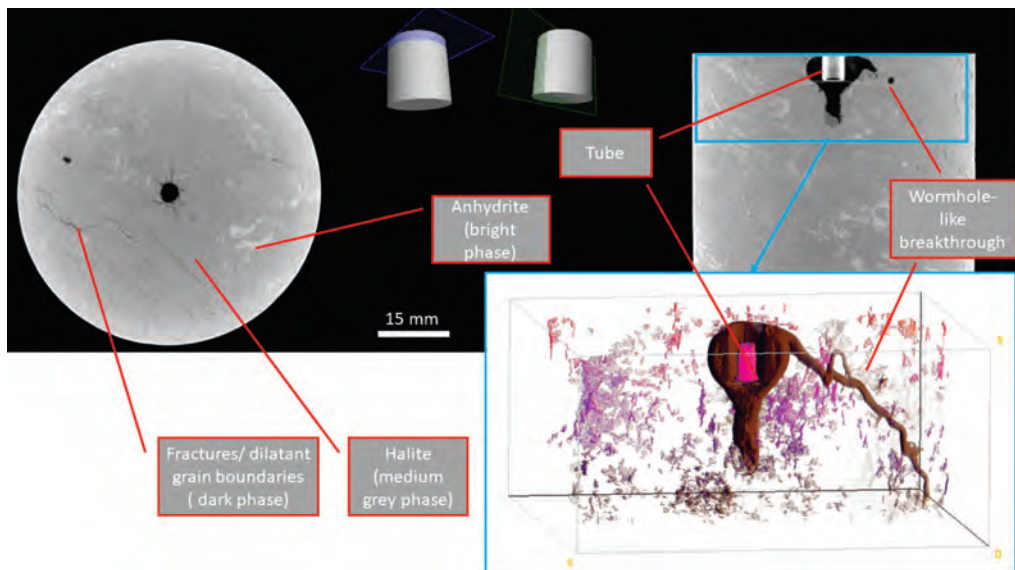
Figure 61: Micro-CT scan of the second permeation sample, showing the preliminary interpretation of fluid pathway during the permeation experiment.

The first permeation experiments with brine as pore fluid are in agreement with what is expected from microstructures: very low permeabilities until the fluid pressure exceeds the minimum stress by a few bars, followed by very rapid increase in permeability and heterogeneous permeation along dilatant pathways (Figure 6), mainly along grain boundaries.

This integrated model of geometry and mechanical properties was combined with the design of caverns by Nobian and implemented in a finite element model to compute the evolution during cavern operation and abandonment (Figure 7).

Because all parameters obtained to date are based on data on sample scale, we will combine these with measurements in the next well. In addition to the planned logging and coring programme, in the open hole it will be critical to measure the in-situ temperature of the salt, as well as the properties of the overburden. To test the properties of the whole salt section, permeation tests in an open hole are required to test the upscaling of the results from the laboratory; doing this is a critical measurement because it is well known that laboratory experiments can underestimate rock mass permeability by orders of magnitude, and miss the presence of permeable layers. We also recommend a pressure build up test in the open hole. Later in the life of the cavern field, the updated and integrated models' prediction must be compared to the results of a several months long, abandonment test ("trial and error test") which can validate the results at the cavern scale.

New drillings offer the possibility to measure the effective permeability at the scale of the caverns. The permeation test that has been proposed (Figure 8) will allow to assess if the formation is perfectly impermeable beyond a zone potentially damaged by the drilling.
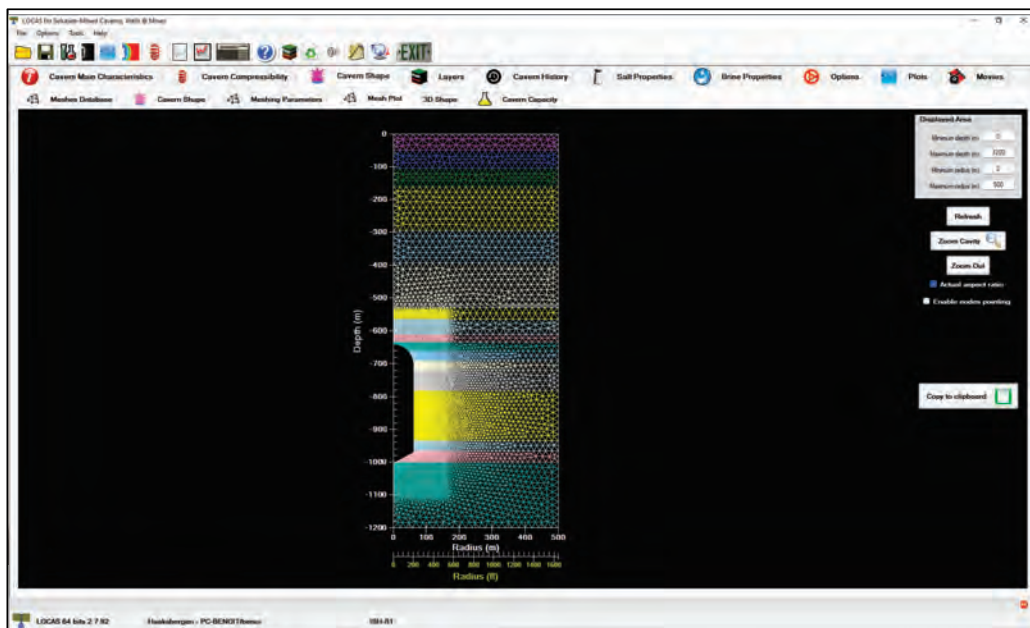
Figure 7: Mesh example [LOCAS software].
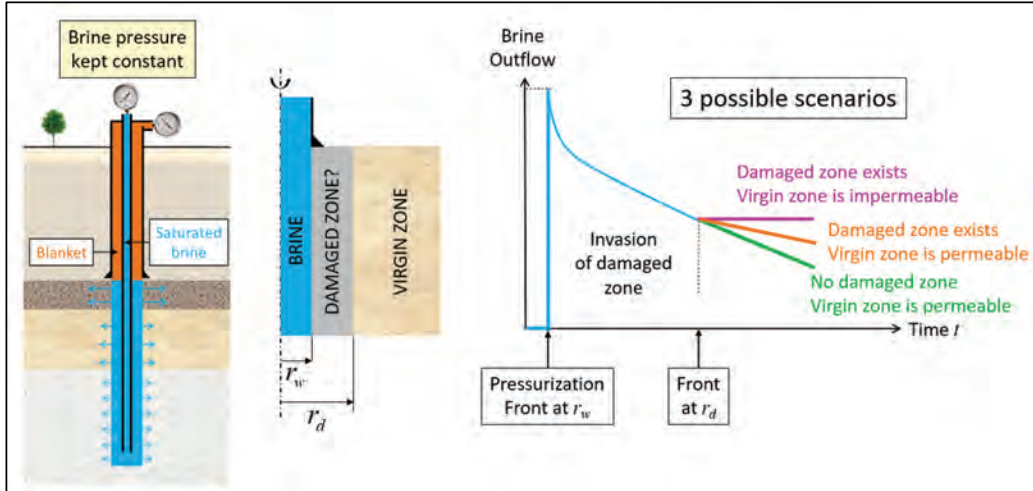
Figure 8: Openhole permeation test.

A more sophisticated permeation test, called WTLog, was also proposed. The WTLog aims at determining a profile of injectivity and permeability along an openhole (Figure 9). Whenever possible, it would be valuable to perform such a test first on the overburden and then along the salt formation.

A more complicated but crucial part of the models concern the predictions of fluid flow after the cavern pressure reaches lithostatic. In the KEM-17 study it was argued that this flow might be localized ("preferential fingering") and we will include aspects of this in our model, but a full, reliable prediction of this will necessarily have to be conservative.
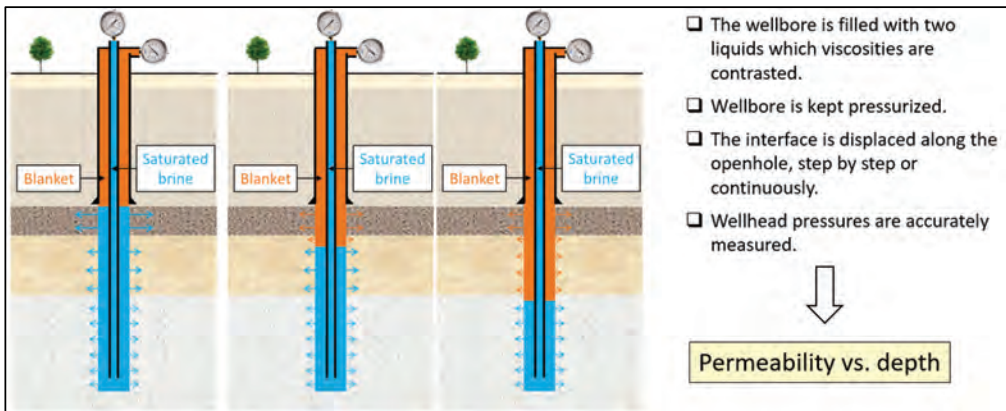
Figure 9: WTLog permeation tests allowing to determine injectivity/permeability as a function of depth along an openhole.

3   Conclusions

At this stage, these results give a good impression of the integrated methods and first results of our approach. However, the results must be considered as preliminary, and the predictions of cavern pressure evolution after abandonment may well change significantly once more results are integrated in the model.

Acknowledgements

References

Urai, J. L., Schmatz, J. & Klaver, J. 2019. Over-pressured salt solution mining caverns and leakage mechanisms. Phase 1 Micro-Scale Report.

Brouard, B. & Bérest, P. 2019. Over-pressured salt solution mining caverns and leakage mechanisms. Phase 2 Cavern-Scale Report.

Baumann, T., Kaus, B. & Popov, A. 2019. Over-pressured salt solution mining caverns and leakage mechanisms. Phase 3 Dome-Scale Report.

Korenaga, J., & Karato, S. I. 2008. A new analysis of experimental data on olivine rheology. *Journal of Geophysical Research: Solid Earth*, *113*(B2).

Schléder, Z., & Urai, J. L. 2005. Microstructural evolution of deformation-modified primary halite from the Middle Triassic Röt Formation at Hengelo, The Netherlands. *International Journal of Earth Sciences*, *94*(5), 941-955.

Spiers, C. J., Schutjens, P. M. T. M., Brzesowsky, R. H., Peach, C. J., Liezenberg, J. L., & Zwart, H. J. 1990. Experimental determination of constitutive parameters governing creep of rocksalt by pressure solution. Geological Society, London, Special Publications, 54(1), 215-227.

The influence of a threshold stress for pressure solution creep on cavern convergence and subsidence behavior – An FEM study

Luuk Hunfeld[1], Jaap Breunese[1], Brecht Wassing[2]*

[1]TNO – Advisory Group for Economic Affairs, the Netherlands; [2]TNO – Applied Geosciences, the Netherlands.

* luuk.hunfeld@tno.nl

ABSTRACT: In rock salt, linear (pressure solution) creep is recognized as an important deformation mechanism under low differential stress conditions (below ~5 MPa), where it takes over from power law (dislocation) creep processes that dominate at higher stresses. In salt caverns, such low differential stress levels occur in the far-field, or following shut-in and abandonment after production stops. It is therefore crucial to incorporate linear creep in numerical simulations assessing cavern behavior. However, theoretical models of pressure solution and microstructural observations suggest that this process does not act below a certain 'threshold' stress, which for rock salt is proposed to lie in the range 0.07-0.7 MPa (Van Oosterhout et al., this volume). By means of numerical finite element (FE) modelling of single-cavern systems, implementing an Ellis-type creep law extended with a user-defined threshold for the linear creep component, we show that pressure solution and its threshold strongly influences creep-induced cavern convergence and subsidence behavior, and should therefore be considered when assessing the effects of salt production or storage applications. Additionally, this threshold may explain certain discrepancies between previous cavern scale modeling studies and field observations (e.g. the rebound predicted for Barradeel by Breunese et al. 2003).

1   Introduction

Salt caverns created for brine production or gas/energy storage tend to converge due to salt creep, creating a gentle subsidence bowl at the surface. This subsidence may cause problems for (ground)water management. The amount of subsidence that can be expected for a given cavern (or cluster of caverns) depends on the mechanical properties of the salt formation, surrounding rock and overlying soil layers, the amount of salt produced, and the rate of salt creep (Fokker 1995).

The creep behavior of rock salt has been studied extensively (e.g. the proceedings of the previous nine conferences on the mechanical behavior of salt). Most of the laboratory experiments are conducted using an applied differential stress in the range 5-20 MPa. Salt creep in this stress domain is typically dominated by dislocation creep processes (Carter et al. 1993), which can be quantified using a power-law function (Norton-Hoff type equation) with a stress exponent typically in the range 3-7 (see Figure 1). These levels of differential stress (hence power law creep behavior) are indeed applicable in the close vicinity of the cavern during typical production conditions, but, as pointed out by Lux & Düsterloh (2015), the stress levels in the far-field surrounding the cavity are well below 5 MPa. In addition, after production is stopped and the cavern pressure rises, the differential stresses surrounding the cavern also diminish over time, as the brine pressure increases due to thermal effects and cavern convergence (e.g. Brouard et al. 2013).

Laboratory data for steady state creep behavior of rock salt at low differential stresses (<5 MPa) are scarce, as they are very difficult to obtain. Field conditions are therefore often modelled by extrapolating the creep laws obtained at higher stresses to low stresses, often without any physical basis. Based on experiments performed on fine-grained synthetic salt, Spiers et al. (1990); Urai & Spiers (2007) have shown that fluid-assisted pressure-solution creep is the dominant deformation mechanism in the low stress domain, with theoretical and experimental evidence suggesting a linear stress dependence (n-value of 1) for this

mechanism (Figure 1). Recently, long-term creep experiments on natural salt samples performed by Bérest et al. (2019) have indeed shown much higher creep rates than what can be expected based on extrapolation of the power law creep laws derived at higher stresses, with a stress exponent (n) close to 1 in the range of 1-5 MPa differential stress. Evidence for a transition of the dominant deformation mechanism from power law creep at high stresses to linear creep at low stresses from laboratory and mine tests has been presented by Campos & Orellana (1996) and Urai & Spiers (2007), and from cavern/field scale observations by Breunese et al. (2003) and Brouard et al. (2013).
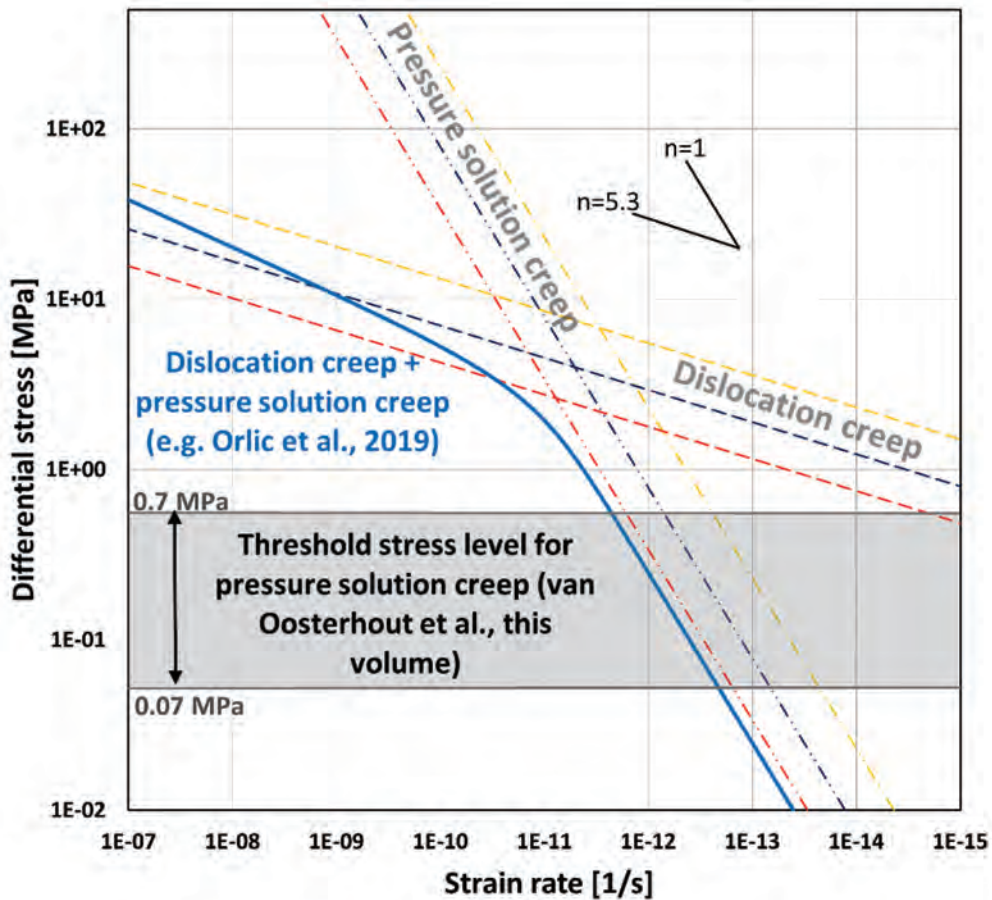
Figure 1: Differential stress versus strain rate plot (log-log scale) showing pressure solution creep laws (Spiers et al. 1990) with stress exponent n = 1, and dislocation creep laws (Carter et al. 1993) with n = 5.3. The solid blue curve indicates a combined power law plus linear creep law (independent from the other models shown), as used by Orlic et al. (2019). The shaded area indicates the range of the threshold stress level for pressure solution creep predicted by Van Oosterhout et al. (this volume).

However, theoretical models of pressure solution creep (Van Noort et al. 2008) and microstructural observations of fluid-filled grain boundaries in rock salt (Urai et al. 2008; Desbois et al. 2012) suggest that below a certain 'threshold' or 'yield' differential stress level, surface energy driven grain boundary healing processes will begin to slow down pressure solution until it ultimately ceases. Building on the above studies, Van Oosterhout et al. (this volume) derived a threshold stress criterion specifically for pressure solution in rock salt, predicting a threshold value in the range 0.07-0.7 MPa differential stress.

In the salt mechanics literature, several constitutive models for steady-state flow of rock salt have been used to model deformation around converging cavities (including solution mined caverns), both in the high stress region, and more recently, at lower stresses (e.g. the proceedings of the nine conferences on the mechanical behavior of salt). These are empirical and phenomenological and lack physical basis for the full range of stresses over which they are applied. Yet several do contain a transition from high n-value creep to low n-value creep, in some cases approaching n=1. The key models that are regarded as standard and have been used widely in the US and German benchmark studies are the Munson-Dawson model (for higher n-value creep only, Munson & Dawson 1979), Günther-Salzer (which has been fitted to n=1, Gunther et al. 2010), Lux-Wolters (Lux et al. 2018), Lubby-2 (Lux 1984), and the Composite Dilatancy model by Hampel (Hampel & Schulze 2017).

A few modelling studies have employed a combined linear (i.e. pressure solution creep) and power law (i.e. dislocation creep) model, based on the underlying physical mechanisms, to model salt flow around and subsidence above caverns or hydrocarbon reservoirs (e.g. Fokker 1995, Breunese et al. 2003; Marketos et al. 2016). However, as far as known to the authors, a threshold stress level for pressure solution creep has not yet been applied in cavern models to date. In this contribution, we investigate the effect of such a threshold stress on creep-induced cavern convergence and subsidence behavior, using a finite element (FE) modelling approach.

2   Numerical model

2.1   Model setup

We used the FE model software package DIANA (DIANA FEA 2018) to construct generic, axisymmetric geomechanical models consisting of 2 overburden layers, a salt layer with a single vertical salt cavern (for simplicity), and a base rock/underburden layer (Figure 2). The model dimensions are 3,000 m (depth) by 15,000 m (radius).

Within this framework, two geometrical model variants were then created. The first model variant (referred to as Model 1, or 'standard' cavern model), is characterized by a relatively thin overburden sequence and thick salt layer (2450 m), with the cavern situated at a depth of 1150 – 1600 m (Figure 2a, b). In the second model variant (referred to as Model 2, or 'deep' cavern model), the overburden sequence is much thicker (2,000 m), and the cavern is situated at 2150-2600 m depth in a salt layer of 900 m thickness (Figure 2c).

In both models, the model boundaries were placed far away from the cavern to avoid edge effects. The model layers were meshed using quadratic second-order eight-node quadrilateral ring elements, which measure 200 m by 200 m far away from the cavern, and gradually refine towards the cavern to a minimum size of 10 by 10 m. The displacement boundary conditions were prescribed to constrain displacements in the direction normal to the outer model edge and the model base. The salt cavern in both model variants has an idealized cylindrical shape with a radius of 27 m and rounded corners to avoid unrealistic stress concentrations (Figure 2b).
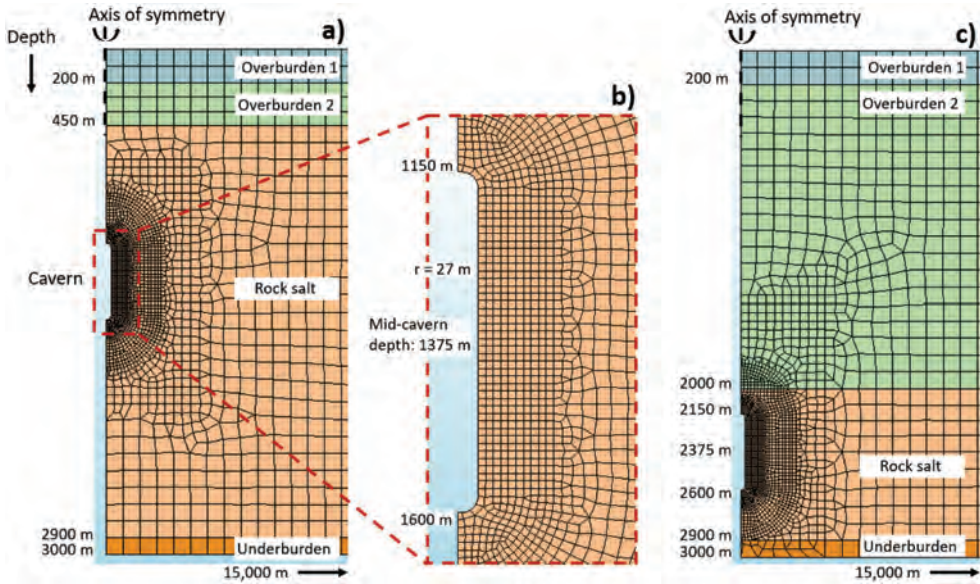
Figure 2: Geometry and mesh for the axisymmetric model setups used. (a) Model 1 (standard cavern setup). (b) Detailed view of the mesh surrounding the cavern in Model 1. (c) Model 2 (deep cavern setup). The cavern volume in both models is approximately 1 M m³.

2.2 Material parameters and constitutive models

All model layers, except the rock salt, were assumed to exhibit purely elastic behavior. Material property values are listed in Table 1 (these apply to both model variants). The model simulations were performed assuming a stationary temperature field (i.e. no temperature changes are considered), based on 10 °C surface temperature and a fixed geothermal gradient of 0.025 °C/m in the case of Model 1 (standard cavern setup), and 0.034 °C/m in the case of Model 2 (deep cavern setup). The temperature at mid-cavern depth in Model 1 (1375 m) and Model 2 (2375 m) is 44.4 °C and 90.8 °C, respectively.

Table 1: Values for material properties used in the models

Layer	Density [kg/m³]	Young's modulus [GPa]	Poisson's ratio	Initial stress ratio K_0*
Overburden 1	2050	1	0.25	0.7
Overburden 2	2050	15	0.25	0.7
Rock salt	2179	32	0.26	1.0
Base rock	2500	25	0.25	0.7

* The initial ratio of minimum to maximum total stress.

Salt deformation was modelled taking into account the steady-state creep deformation driven by differential stresses. The constitutive model for the steady-state salt creep employed here (based on the Ellis formulation – Fokker 1995, see also Spiers & Carter 1998; Cornet et al. 2018) combines (i) a power law (non-linear) branch for dislocation creep and (ii) a linear branch for pressure solution creep:

$$\dot{\varepsilon}_{axial} = A_1 \exp\left(-\frac{Q_1}{RT}\right)\left(\frac{\Delta\sigma}{\alpha}\right)^{n_1} + A_2 \exp\left(-\frac{Q_2}{RT}\right)\left(\frac{\Delta\sigma}{\alpha}\right)^{n_2} \tag{1}$$

where $\dot{\varepsilon}_{axial}$ is the strain rate [1/s], $\Delta\sigma = \sigma_{axial} - \sigma_{radial}$ is the differential stress [MPa]; A_1 and A_2 are the creep strain rate coefficients [1/s], Q_1 and Q_2 are the activation energies [J/mol], R

is the gas constant (8.314 J/(mol K)), T is the temperature [K], α is the reference stress [1 MPa]; n_1 and n_2 are the stress exponents for the non-linear creep ($n_1 > 1$) and the linear creep ($n_2 = 1$), respectively. The two-branch salt material model available in DIANA (i.e. Eq. (1)) was adapted to include a threshold stress level (τ) for the linear branch, which was implemented such that linear creep is switched off in any model element when $\Delta\sigma < \tau$ at the beginning of any timestep in the simulation (and vice versa).

The values used for the salt creep parameters are listed in Table 2. They are constrained (Figure 3) by fitting Eq. (1) to creep data from experiments performed on core material derived from the Strassfurt (Z2) series of the Zechstein group (almost pure halite), extracted from the Zuidwending and Barradeel cavern sites in the north of the Netherlands (Hoelen et al. 2010; Breunese et al. 2003). The lab data were obtained in the temperature range of 40-50°C (Zuidwending - IfG 2007) and 105 °C (Barradeel - IfG 2004 2006). Note that both data sets can be fitted reasonably well with the same set of creep parameters, when accounting for temperature.
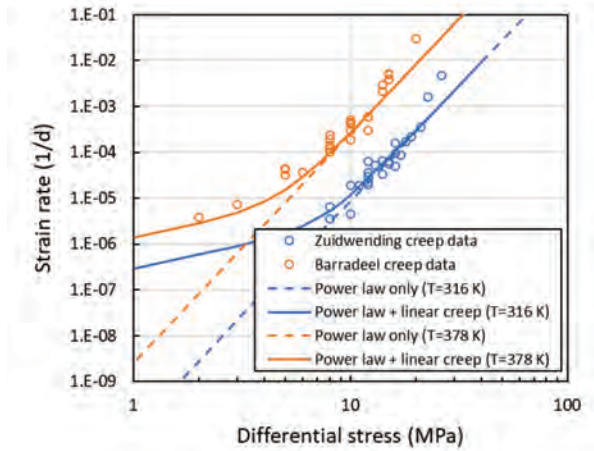
Figure 3: Zuidwending creep data (blue circles) obtained at 40-50 °C (IfG 2007) and Barradeel creep data (orange circles) obtained at 105 °C (IfG 2004, 2006). The power law and power law + linear creep fits based on Eq. (1) use the parameters given in Table 2 (i.e. using the same set of creep parameters but different temperatures).

Table 2: Salt creep parameters (refer Eq. 1) used in the model simulations

Simulation number (model variant)	Power law (dislocation) creep			Linear (pressure solution) creep			
	A_1 [1/day]*	n_1 [-]	Q_1/R [K]	A_2 [1/day]*	n_2 [-]	Q_2/R [K]	Threshold stress (τ) [MPa]
1 (Model 1)	0.075	5	6495	0	-	-	-
2 (Model 1)	0.075	5	6495	0.005	1	3007	0
3 (Model 1)	0.075	5	6495	0.005	1	3007	0.07
4 (Model 1)	0.075	5	6495	0.005	1	3007	0.7
6 (Model 2)	0.075	5	6495	0.005	1	3007	0
7 (Model 2)	0.075	5	6495	0.005	1	3007	0.2

* To convert values to units [1/s], divide values by 8.64E4.

2.3   Loading sequence

In all simulations (using both Model 1 and Model 2), three phases of the cavern's lifetime are modelled (Table 3): (1) the cavern construction phase (0.8 y), where the cavern pressure is changed linearly in time from lithostatic to halmostatic, simulating leaching of the cavity; (2) the brine production phase (10 y), with constant halmostatic pressure; (3) the pressure control phase, where brine pressure is first increased linearly in time over a period of 0.8 y to either 70% of the lithostatic pressure gradient (Model 1, simulating 'soft shut-in') or 100% of the lithostatic pressure (Model 2, simulating 'hard shut-in'), and then held constant at the shut-in level for 50 y.

Table 3: Loading sequence simulated in the model runs (P – pressure inside the cavern)

Phase of cavern's lifetime	Start/end [day]	Duration [day]	[year]	Cavern pressure (values at mid-cavern depth in MPa*)
Cavern leaching	0-300	300	0.8	Lithostatic P (28.8/48.2) to Halmostatic P (16.5/28.5)
Salt production	300-3950	3650	10	Halmostatic P (16.5/28.5)
P-control: P increase	3950-4250	300	0.8	P increase to 70%/100% lithostatic (20.2/48.2)
P-control: P constant	4250-22500	18250	50	Constant elevated P (20.2/48.2)

* Values in black are mid-cavern pressures in Model 1; values in blue (after /) are mid-cavern pressures in Model 2).

2.4   Salt creep settings

The loading sequence presented in Table 3 is applied in the following simulations, using the salt creep settings and model variants as specified below (refer also Table 2):

1) Model 1: Power law creep only (A_2 in Eq. (1) is zero)
2) Model 1: Power law creep + linear creep without threshold ($\tau = 0$ MPa)
3) Model 1: Power law creep + linear creep with low threshold ($\tau = 0.07$ MPa)
4) Model 1: Power law creep + linear creep with high threshold ($\tau = 0.7$ MPa)
5) Model 2: Power law creep + linear creep without threshold ($\tau = 0$ MPa)
6) Model 2: Power law creep + linear creep with intermediate threshold ($\tau = 0.2$ MPa)

3   Results

3.1   Model 1 (standard cavern)

Model 1 was used to estimate the temporal evolution of cavern convergence (Figure 4) and surface deformation (Figure 5) for simulations 1-4 using the creep parameters in Table 2.

3.1.1   Power law creep only

The model run with power law creep only (simulation 1) shows the smallest total reduction in cavern volume (~1.5%, Figure 4) and surface displacements at the end of the simulations (<1mm, Figure 5a). The surface deformation profiles initially show minor uplift above the cavern, until the end of the cavern leaching phase (t = 300 days). This is followed by subsidence during the production phase and pressure control phases, during which a gradually widening subsidence bowl develops (maximum depth ~0.54 mm), with a slight bulge at the center still visible at the end of the simulation.

3.1.2 Power law creep + linear creep without threshold

When pressure solution creep (without threshold) is introduced alongside power law creep (simulation 2), the cavern convergence rate is much larger compared to the power law only case, amounting to a ~33% reduction in final cavern volume (Figure 4). The magnitude of the surface displacements is also much greater (approximately 10-fold, Figure 5). A striking feature in the surface displacement profiles of this run (Figure 5b) is the uplift seen directly above the cavern throughout the entire simulation, while a subsidence annulus develops around this bulge, with its deepest point (~8 mm) located at ~2000 m distance from the symmetry axis.

3.1.3 Power law creep + linear creep with threshold

When a threshold stress for pressure solution creep is applied (simulations 3 and 4), the surface displacement profiles (Figures 5c and 5d) are strikingly different from the other simulations. In these runs, a 'conventional' subsidence bowl (i.e. with its deepest point directly above the cavern) develops without any (significant) uplift at any stage during the simulations. The largest convergence and surface displacements are seen in the run with the low value of the threshold stress (τ = 0.07 MPa, yielding ~31% cavern volume reduction and ~92 mm maximum subsidence at the end of the simulation, versus ~17% and ~18 mm for the τ = 0.7 MPa case). Note that the convergence results in terms of cavern volume reduction are similar for simulation 2 (τ = 0 MPa) and simulation 3 (τ = 0.07 MPa), whilst the shape of the subsidence profiles in these runs is very different. Details of the salt flow behavior in the proximity of the cavern for these two runs are shown in Figure 6.

The spatial extent of the threshold's influence within the salt body surrounding the cavern is visualized in Figure 7 for simulations 3 and 4 (note that these figures would be all red in the case of simulation 2 (no threshold), since the differential stress is larger than zero, and hence pressure solution creep is active, in the entire salt body). In case of the low threshold (0.07 MPa), linear creep penetrates roughly 2-3x further into the salt body compared to the high threshold level (0.7 MPa).
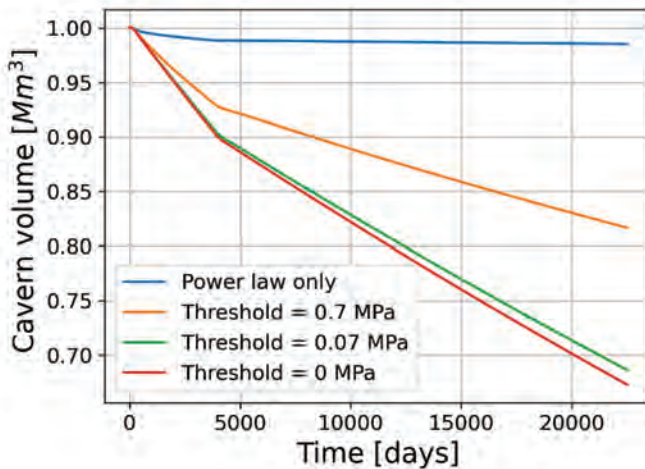
Figure 4: Evolution of cavern volume (in million cubic meters) for all four simulations using Model 1 (standard cavern).
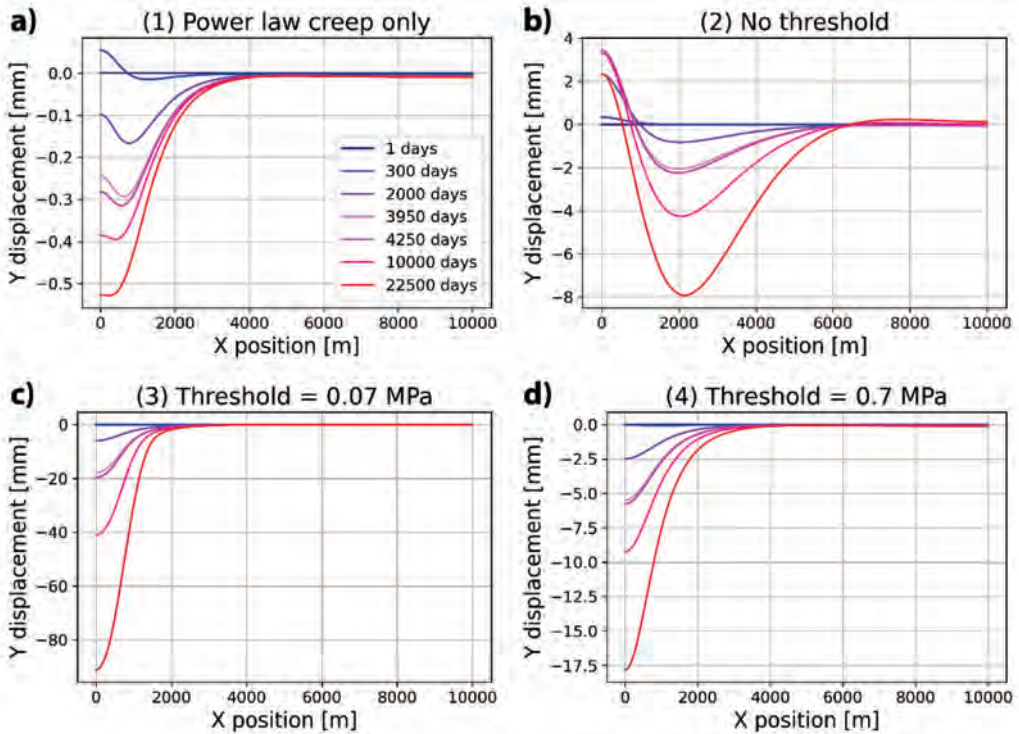
Figure 5: Evolution of vertical surface deformation profiles (Y displacement) above the salt cavern at various time steps (refer Table 3) for all four creep law settings applied in Model 1 (standard cavern). The legend in a) applies to all panels. Note the strongly different scales for the Y-axis.
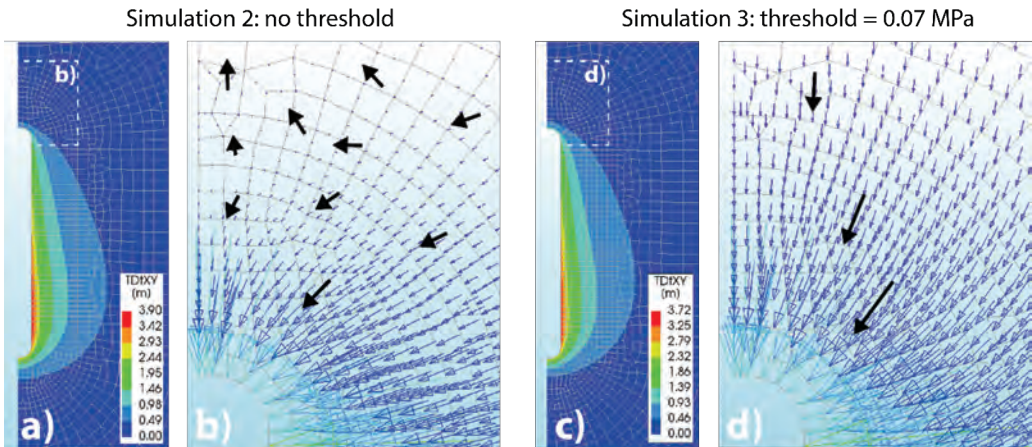

Figure 6: Contour plots and zoomed-in vector plots of the salt flow behavior close to the cavern in terms of total displacement (vector length) for (a, b) simulation 2 and (c, d) simulation 3. The black arrows in the vector plots (panels b, d) in are not to scale.
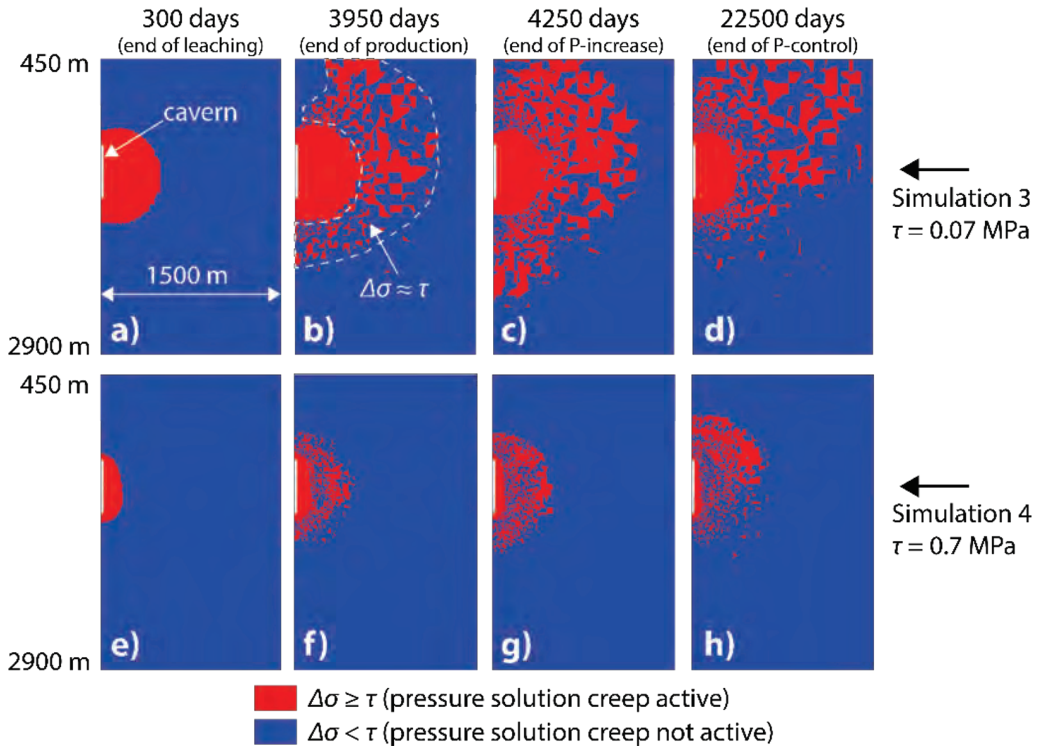
Figure 7: Contour plots indicating in red where pressure solution creep is active (i.e. the differential stress $\Delta\sigma$ is larger than the threshold value τ) in the salt body surrounding the cavern. In the red/blue speckled region (highlighted in panel b), $\Delta\sigma \approx \tau$ and pressure solution is only active in some of the mesh elements. Panels (a-d) show results for simulation 3 (power law creep + linear creep, $\tau = 0.07$ MPa), and panels (e-h) simulation 4 (power law creep + linear creep, $\tau = 0.7$ MPa), both using Model 1 (standard cavern).

3.2   Model 2 (deep cavern)

Figure 8 shows the temporal evolution of surface displacements obtained in simulations 5 and 6, obtained using Model 2 (deep cavern, high temperature).

3.2.1   Power law creep + linear creep without threshold

Without a threshold applied to linear creep (simulation 5), the results show progressive subsidence during the cavern leaching and salt production phases, amounting to almost 8 cm subsidence at its deepest point at the end of the salt production phase. However, as soon as the pressure is increased back to lithostatic during the (hard) shut-in phase, the subsidence bowl gets progressively shallower, with ~60% of the maximum subsidence being recovered after 50 years of (hard) shut-in (i.e. 'rebound'). This is accompanied by a progressive widening and modest uplift at the margins of the subsidence bowl.

3.2.2   Power law creep + linear creep with threshold

When an intermediate level (0.2 MPa) of threshold stress for pressure solution creep is applied (simulation 6), the evolution of surface displacements during the leaching and production phases is qualitatively similar to that observed in simulation 5 (without threshold), but the rebound and widening effects seen in simulation 5 during hard shut-in now vanish. Instead,

the deepest point of the subsidence bowl stays more or less constant during and after shut-in (with only ~2 mm additional subsidence).
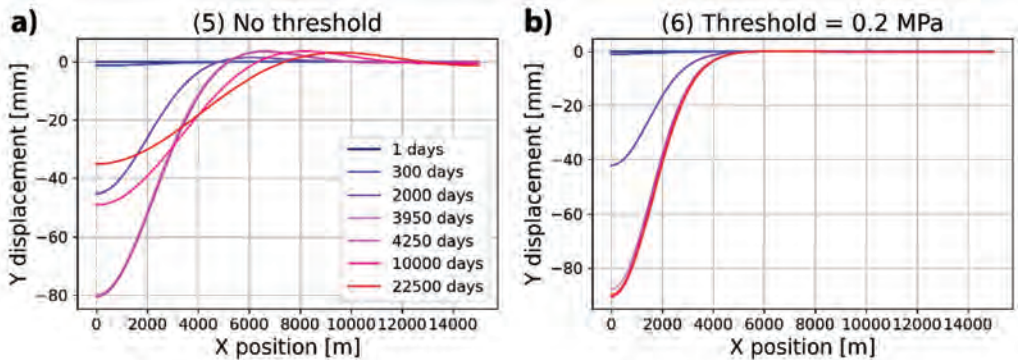
Figure 8: Evolution of vertical surface deformation profiles (Y displacement) above the salt cavern at various time steps (refer Table 3) for the two creep law settings applied in Model 2 (deep cavern). The legend in a) applies to both panels.

4   Discussion

The results presented here clearly show a pronounced effect of linear (pressure solution) creep and a threshold stress level for this mechanism on both creep-induced cavern convergence and subsidence behavior in realistic, single-cavern model setups resembling a 'standard' (~1375 m depth) and a deep (~2375) cavern.

For the geometry and loading sequence adopted in our standard cavern model (Model 1, ~1375 m cavern depth), the contribution of power law creep to salt flow is relatively modest, as evidenced by the limited amount of cavern convergence and surface displacements observed in the simulation with power law creep only (Figures 4 and 5a). When pressure solution is active without a threshold, the rates of cavern convergence and subsidence are approximately 10x higher than observed in the power law only simulation. However, without a threshold for pressure solution, our models show continued uplift directly above the cavern during all model stages, whereas a subsidence annulus develops around this central 'bulge'. We interpret this phenomenon as a result of the 'unlimited' extent of linear creep, which - under the stress and pressure conditions considered here - induces a relatively large volume of salt flow notably in the far-field which cannot be accommodated by the converging cavern only, and is forced to flow upwards near the center of the model above the cavern (Figure 6a, b).

When a threshold stress is applied, the spatial extent of pressure solution creep and hence salt flow induced by this mechanism is much more limited (in the order of 500-1000 m distance from the cavern during the production phase in our simulations - see Figure 7), and the direction of flow within the salt body is converging towards the cavern only (e.g. Figure 6c, d). This results in a subsidence bowl where the deepest point is at the axis of the cavern, which is qualitatively similar to field observations of subsidence above cavern fields in the Netherlands and around the world (e.g. Warren 2016). Similar results will presumably be obtained when the extent of the salt body itself is limited (e.g. simulating a salt dome such as the Zuidwending dome – Hoelen et al. 2010), since this too limits the extent of linear salt creep.

Moving on to deep caverns with relatively high creep rates (due to the increased temperature), our results using Model 2 show that spatially unlimited pressure solution creep (i.e. no threshold) causes rebound and widening of the subsidence bowl following hard shut-in. Similar observations were made by Breunese et al. (2003), who applied a power law creep plus linear creep model in numerical simulations of the deep (~2.8 km) Barradeel caverns (BAS-1 and

BAS-2) located near Harlingen, Friesland (North Netherlands). They concluded that the rapid rates of convergence (~70% of the cavern volume per year) and subsidence (~30 cm in 10 years) observed at Barradeel can only be explained when pressure solution is incorporated. However, the rebound at the center of the subsidence bowl after hard shut-in predicted in their models due to the effects of pressure solution creep, has not been observed in levelling studies and GPS data for the Barradeel caverns to date (Frisia Zout BV 2020). Our simulations for the ~2.4 km deep cavern show that this rebound effect vanishes when a certain threshold stress is applied, in qualitative accordance with the field observations at Barradeel.

5 Factors not considered here

Although not evaluated in the present study, it is likely that the following factors will significantly influence the results of geomechanical model calculations in terms of cavern convergence and surface deformation:

1) the geological representation in the model, particularly horizontal extent of the salt layer (i.e. an infinite horizontal salt layers versus a limited, more dome-like salt structure with non-creeping layers juxtaposed at the sides);
2) single-cavern versus multi-cavern models, where the extent of linear creep, determined by the threshold stress, influences cavern-to-cavern interactions and the overall subsidence response of the cavern field;
3) temperature changes induced by salt production, since both power law creep and pressure solution creep are strongly temperature dependent (Spiers et al. 1990; Carter et al. 1993);
4) the pressure conditions during production and shut-in (Kroon et al. 2003), as this dictates the differential stress around the cavern which drives both creep phenomena;
5) uncertainties in the salt creep model, especially at low differential stresses.

In addition, there are other aspects of salt deformation which are not considered in our model, which are dilatancy and microcrack damage (Urai et al. 2008) and dynamic recrystallization (Peach et al. 2001; Ter Heege et al. 2005), which may accelerate salt creep due to enhanced fluid penetration and grain size reduction effects.

6 Conclusions

We investigated the influence of a threshold stress for pressure solution creep on cavern convergence and subsidence behavior using single-cavern geomechanical FE models, implementing a two-branch constitutive model for combined power law (dislocation) and linear (pressure solution) creep. From our simulations, it becomes clear that pressure solution and its threshold strongly influences cavern convergence and subsidence behavior, not only for deep caverns where creep rates are high, but also for caverns in the more common depth range of ~1200-1600 m. Without a threshold, the application of linear creep alongside power law creep results in surface displacement profiles that are not typically observed in real cavern sites (such as uplift or rebound in the center of the subsidence bowl). Such effects vanish when a threshold stress is applied (varied here in the range 0.07-0.7 MPa, following Van Oosterhout et al. elsewhere in this volume), resulting in conventional subsidence bowls which are qualitatively in accordance with field observations in the Netherlands and elsewhere. We conclude that a threshold on pressure solution creep is to be accounted for in modeling cavern convergence and associated surface deformation, and that this threshold may explain certain discrepancies between previous cavern scale modeling studies and field observations (e.g. the rebound predicted for Barradeel by Breunese et al. 2003). In the present study, we focused on single-cavern behavior for simplicity, but the findings regarding the influence of the threshold stress for pressure solution will also play a role in multiple-cavern fields, following the principles of superposition.

Acknowledgements

References

BÉREST, P., GHARBI, H., BROUARD, B., BRÜCKNER, D., DE VRIES, K., HÉVIN, G., HOFER, G., SPIERS, C.J. & URAI, J. 2019. Very slow creep tests on salt samples. Rock Mechanics and Rock Engineering, 52(9), 2917-2934.

BREUNESE, J.N., VAN EIJS, R.M.H.E., DE MEER, S. & KROON, I.C. 2003. Observation and prediction of the relation between salt creep and land subsidence in solution mining. The Barradeel case. Proc. SMRI Fall Meeting, Chester 2003, 38-57.

BROUARD, B., BÉREST, P., DE GREEF, V., BÉRAUD, J.F., LHEUR, C. & HERTZ, E. 2013. Creep closure rate of a shallow salt cavern at Gelleoncourt, France. International Journal of Rock Mechanics and Mining Sciences, 62, 42-50.

CAMPOS DE ORELLANA, A.J. 1998. Non-associated pressure solution creep in salt rock mines. Series on rock and soil mechanics, 429-444.

CARTER, N.L., HORSEMAN, S.T., RUSSELL, J.E. & HANDIN, J. 1993. Rheology of rocksalt. Journal of Structural Geology, 15(9-10), 1257-1271.

CORNET, J.S.P. 2018. Analytical and numerical modeling of cavity closure in rock salt. PhD Thesis, University of Oslo, Norway.

DESBOIS, G., URAI, J.L. & DE BRESSER, J.H. 2012. Fluid distribution in grain boundaries of natural fine-grained rock salt deformed at low differential stress (Qom Kuh salt fountain, central Iran): Implications for rheology and transport properties. Journal of Structural Geology, 43, 128-143.

DIANA FEA 2018. Finite element program and Users documentation, version 10.1. https://dianafea.com.

FOKKER, P.A. 1995. The behaviour of salt and salt caverns. PhD Thesis, Technical University Delft., The Netherlands.

FRISIA ZOUT B.V. 2020. Uitvoering beheerscyclus van meet- en regelprotocol 'Barradeel-II' over het jaar 2019 - versie 1.3. https://www.sodm.nl

GUNTHER, R.M., SALZER, K., & POPP, T. 2010. Advanced strain-hardening approach constitutive model for rock salt describing transient, stationary, and accelerated creep and dilatancy. 44th US rock mechanics symposium and 5th US-Canada rock mechanics symposium. OnePetro.

HAMPEL, A., & SCHULZE, O. 2017. The Composite Dilatancy Model: A constitutive model for the mechanical behaviour of rock salt. The Mechanical Behavior of Salt; Proc. 6th Conference, Hannover 2007, 99-107.

TER HEEGE, J.H., DE BRESSER, J.H.P. & SPIERS, C.J. 2005. Rheological behaviour of synthetic rocksalt: the interplay between water, dynamic recrystallization and deformation mechanisms. Journal of Structural Geology, 27(6), 948-963.

HOELEN, Q., DIJK, H., WILKE, F. & WIPPICH, M. 2010. Gas storage in salt caverns Zuidwending - The Netherlands. Proc. SMRI Fall Meeting, Leipzig 2010, 241-250.

IFG 2004. Rock mechanical investigations on rock salt from the cavern wells BAS1 and BAS2. IfG Institut für Gebirgsmechanik GmbH, Leipzich.

IfG 2006. Rock mechanical investigations on rock salt from the cavern well BAS4. IfG Institut für Gebirgsmechanik GmbH, Leipzich.

IfG 2007. Rock Mechanical Investigations on Rock Salt from the Zuidwending Gas Storage Site. IfG Institut für Gebirgsmechanik GmbH, Leipzich.

Kroon, I.C., Orlic, B. & Scheffers, B.C. 2003. Abandonment of solution mined salt caverns in the Netherlands. Part 2. Best Practises and methods. NITG 03-172-B.

Lux, K.-H. 1984. Gebirgsmechanischer Entwurf und Felderfahrungen im Salzkavernenbau (Ferdinand Enke Verlag, Stuttgart).

Lux, K.-H. & Düsterloh, U. 2015. From birth to long-term life - main aspects regarding THM-coupled simulation of salt cavern behavior as well as regarding improved salt cavern design with special consideration of rock salt damage. The Mechanical Behavior of Salt; Proc. 8th Conference, Leiden 2015, 273-280.

Lux, K.-H., Lerche, S. & Dyogtyev, O. 2018. Intense damage processes in salt rock - a new approach for laboratory investigations, physical modelling and numerical simulation. The Mechanical Behavior of Salt; Proc. 9th Conference, Hannover 2015, 12-14.

Marketos, G., Spiers, C.J. & Govers, R. 2016. Impact of rock salt creep law choice on subsidence calculations for hydrocarbon reservoirs overlain by evaporite caprocks. Journal of Geophysical Research: Solid Earth, 121(6), 4249-4267.

Munson, D.E. & Dawson, P.R. 1979. Constitutive model for the low temperature creep of salt (with application to WIPP). SAND--79-1853.

Van Noort, R., Visser, H.J. & Spiers, C.J. 2008. Influence of grain boundary structure on dissolution controlled pressure solution and retarding effects of grain boundary healing. Journal of Geophysical Research: Solid Earth, 113(B3).

Van Oosterhout, B.G.H., Hangx, S.J.T. & Spiers, C.J. 2022. A threshold stress for pressure solution creep in rock salt: Model predictions vs. observations. The Mechanical Behavior of Salt; Proc. 10th Conference, Utrecht 2022, this volume.

Orlic, B., Wollenweber, J., Geel, C.R., Vandeweijer, V.P., Meekes, J.A., Heerens, G.J., & Ter Heege, J.H. 2019. Formation of a sealing well barrier by the creep of rock salt: Numerical investigations. 53rd US Rock Mechanics/Geomechanics Symposium. OnePetro.

Peach, C.J., Spiers, C.J. & Trimby, P.W. 2001. Effect of confining pressure on dilatation, recrystallization, and flow of rock salt at 150°C. Journal of Geophysical Research: Solid Earth, 106(B7), 13315-13328.

Spiers, C.J., Schutjens, P.M.T.M., Brzesowsky, R.H., Peach, C.J., Liezenberg, J.L., & Zwart, H.J. 1990. Experimental determination of constitutive parameters governing creep of rocksalt by pressure solution. Geological Society, London, Special Publications, 54(1), 215-227.

Spiers, C.J. & Carter, N.L. 1998. Microphysics of rocksalt flow in nature. In: Aubertin, M., and Hardy, H.R. (eds.): The mechanical behavior of salt, proceedings of the 4th conference, Trans Tech. Publ. Series on Rock and Soil Mechanics, 22, 115-128.

Urai, J.L., Schléder, Z., Spiers, C.J. & Kukla, P.A. 2008. Flow and transport properties of salt rocks. Dynamics of complex intracontinental basins: The central European basin system, 277-290.

Urai, J.L., & Spiers, C.J. 2007. The effect of grain boundary water on deformation mechanisms and rheology of rocksalt during long-term deformation. The Mechanical Behavior of Salt; Proc. 6th Conference, Hannover 2007, 149-158.

Warren, J.K. 2016. Solution mining and salt cavern usage. Evaporites, Springer, Cham, 1303-1374.

Mechanism for the formation of sinkholes above deep salt caverns

W. Minkley[1], C. Lüdeling[1], A. Taghichian[1]*

[1] *Institut for Geomechanics GmbH (IfG), Germany*

* *Wolfgang.Minkley@IfG-Leipzig.de*

ABSTRACT: Sinkholes can develop above deep-lying brine-filled caverns in salt. The basic mechanism is sliding of large columns of rock along overburden joints under the influence of joint fluid pressure. Loss of salt back integrity, i.e. hydraulic connection of the cavern-filling brine to the overburden joints with pressure-driven percolation is the starting point which may lead to sinkhole formation. The sliding of rock columns is linked to the small-scale tectonic fragmentation of the rock mass in the overburden. We present some examples, conceptual and analytical estimates, and results of numerical studies which illustrate the mechanism in single-cavern situations and interacting caverns in cavern fields. In contrast to most situations that are well-described by a continuum simulation approach, sinkhole formation and block sliding instabilities in the overburden are fundamentally discontinuous processes. The overburden is often brittle, so that the shear resistance of joints and fractures is characterised by an adhesive peak strength and subsequent softening. In such cases, hydromechanical coupling is crucial for a stability analysis. Therefore, appropriate constitutive models for rocks and joints and a consistent discontinuous modeling approach are required.

1   Introduction

It is often assumed that sinkholes cannot form above solution mining caverns deeper than about 500 m, as in greater depth, the critical span (i.e. the span at which a cavern becomes unstable) is larger than plausible cavern diameters, and overburden strength is considered sufficient. However, this assumption neglects the effects of fluid pressure and pressure-driven percolation on overburden joints (Minkley et al. 2015). Rock mass generically contains joints and joint sets, which are considerably weaker than the intact rock. Fluid pressure in these discontinuities lowers the effective stress, thereby reducing their shear strength. Thus, the critical spans can be much lower, such that sinkholes with diameters in the order of tens of meters become also feasible. A necessary condition is hydraulic connection of the brine-filled cavern in the salt to the overburden such that the cavern pressure can be transferred to overburden joints.

In a review of sinkholes above solution mining caverns, Bérest (2017) concluded that sinkholes can form when the brine comes into direct contact with the overburden. He developed two conceptual models of sinkhole formation, depending on the geomechanical properties of the overburden. Pertinent to our discussion is the "piston" model, where the cavern ceiling moves upwards into the overburden by partial collapsing until it reaches a strong layer, which then drops as a whole into the cavern as an intact block of rock (the piston). The walls of the resulting sinkhole are straight and vertical to a good approximation. Since the piston itself does not fracture, there is little bulking, and sinkholes can form even over deep caverns.

For a rock sliding instability to occur, the weight of the block must be larger than the maximum retaining forces, which composed of the brine pressure under the piston and the frictional shear forces along the lateral surface. The latter is determined by the coefficient of friction (assuming a rock block bounded by cohesionless joints) and the horizontal effective stress. Here, it is crucial to note that the horizontal stress is commonly lower than the lithostatic stress, and a joint fluid pressure can significantly reduce the resisting shear force, thereby facilitating block sliding (Minkley & Groß 1990) in situations where it is conventionally considered impossible.
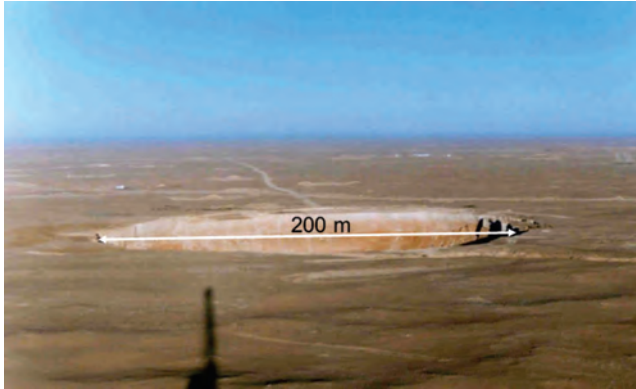
Figure 1: The Haoud Berkaoui sinkhole (Morisseau 2000)

We will briefly review some examples of sinkholes over salt cavities. The Haoud Berkaoui crater (Morisseau 2000; see Figure 1) was formed over a dissolution cavity created in about 550 m depth by an improperly abandoned oil well that caused a hydraulic connection between two aquifers. Bérest (2016) considered it very likely that the circular crater with vertical walls, a diameter of 200 m and a depth of 75 m formed by a sudden drop of a 550 m cylinder of rock above the cavern.
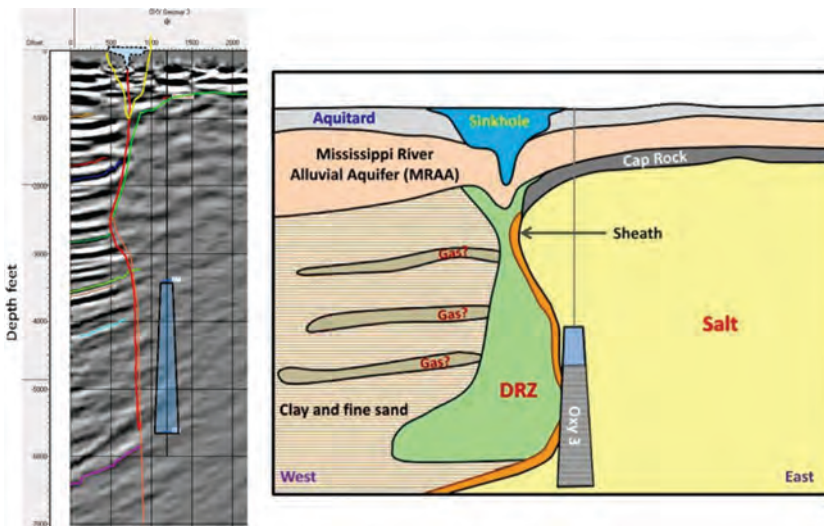
Figure 2: NW-SE Seismic Line with the Oxy3 cavern and the flank of the Napoleonville salt dome (left panel); geological sketch (right panel, van Sambeek 2014)

In 2012, a sinkhole was discovered in Bayou Corne, Louisiana, near the edge of the Napoleonville salt dome (van Sambeek 2014). It turned out that the Oxy3 cavern, mined in a depth from about 1050 m to 1700 m, was closer to the salt dome flank than previously planned. Therefore, its side wall had been breached and sediments flowed into the cavern along the flank. The cavern was essentially filled when the sinkhole appeared at the surface (Figure 2).

Bérest (2017) raised the question of "How did a 1000-1500 m (3000-5000 ft.) high cylinder of rock with an average diameter of a few dozen meters drop into the cavern along the dome edge?" and concluded that this process requires very small or zero cohesion and friction angle.

However, one needs to consider pressure-driven fluid percolation. Taking into account the resulting fluid pressure along the pre-existing mechanical weakness planes (Equation 1), the friction angle recovers a realistic value. In an integrity test in 2010, the Oxy3 cavern at the flank of the Napoleonville salt dome was found to be leaky at high pressure, indicating the presence of fluid pathways. After the cavern was closed and abandoned, pressure-driven percolation along the boundary shear zones could have lowered the effective stress on the weakness planes, enabling the sliding processes.

Similar sinkholes can appear over conventional salt mines if the salt back is lost, or not present at all. Pre-existing weakness planes in the rock mass (e.g. joints, bedding planes, faults) are natural potentials for the sliding to start. The formation of the Neustaßfurt sinkhole in 1975 (Figures 3), during the controlled flooding of the mine, was facilitated by relative shear motion between the Staßfurt potash seam and the anhydrite (Hauptanhydrit) in the hanging wall. In this event, the sliding rock column during the formation of the sinkhole reached a depth of more than 600 m and followed the steeply dipping rock strata. The sinkhole had a diameter of about 100 m (Salzer & Minkley 2005).
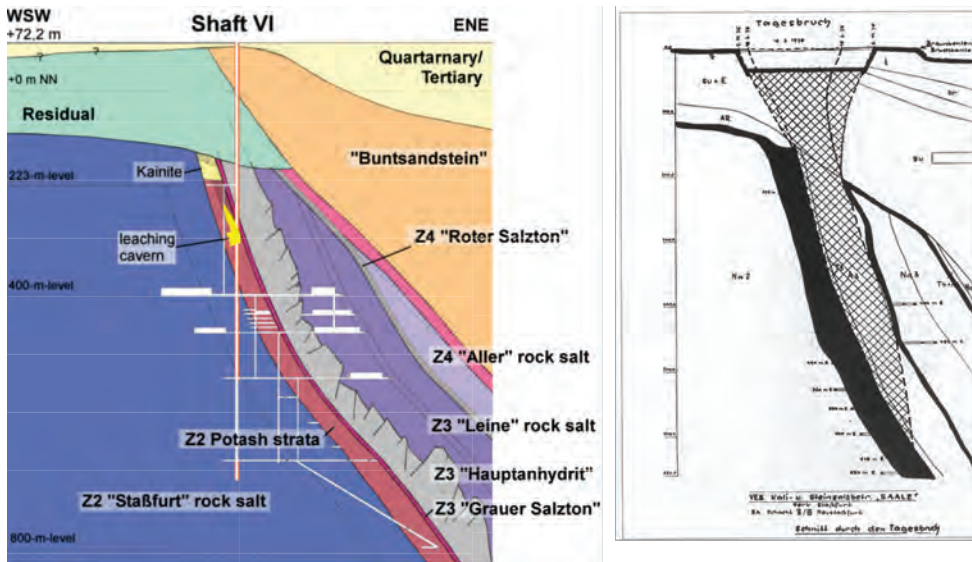
Figure 3: Sinkhole Neustaßfurt 1975: Geological section northeast flank of the Staßfurt Salt Anticline (left), sketch of the sinkhole (right)

2   Conceptual geomechanical model for sinkhole formation over saliferous strata

The development of sinkholes over mined salt formations, both in conventional and solution mining, as presented in the previous section, generically proceeds the following failure sequence:

- In the salt formation, cavities with sufficient volume and span are generated.
- The salt back, i.e. the hydraulic barrier to the overburden, loses its integrity, gets dissolved or breaks into the cavity, or is not present at all.
- The overburden cannot span the (open or brine-filled) cavity without fracturing anymore.
- In the jointed overburden block sliding commences under the influence of joint fluid pressure.

Sinkhole formation is aided by:

- low lateral confinement (e.g. over mining edges or other extension zones),
- joint water pressure and pressure-driven brine percolation over edges of mining panels or caverns (hydrostatic fluid pressure in the overburden, brine pressure in caverns),
- low shear strength on vertical joints, faults or weakness planes in the overburden.

Load limit equilibrium theory allows us to develop a conceptual model of the failure mechanism: If the span of an underground cavity exceeds a critical value, the weight of the overlying column of rock cannot be balanced by the load-bearing forces, which comprise:

- the frictional (shear) force along the circumference of the block, and
- the supporting force at the lower face of the block provided by the brine pressure in the cavern.
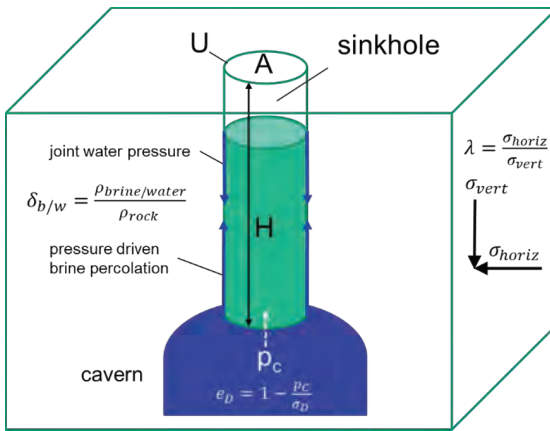
Figure 4: Model for sinkhole formation: Block sliding in the overburden

We assume that the joints that separate the roof column and along which the shear resistance acts are completely traverse the overburden. This is the most critical case and provides a conservative lower bound on stability. Consider a column of rock with cross-sectional area A, circumference U and depth H under the effects of its weight, shear resistance along the boundary and fluid pressure exerted from below by a cavern with internal pressure p_c (geometry and relevant quantities are shown in Fig. 4). Then load limit equilibrium gives the critical ratio of block area and circumference as (Minkley & Groß 1990):

$$\left(\frac{A}{U}\right)_{crit} = \frac{1}{2} \cdot \mu_s \cdot H \cdot \left[\frac{\lambda - \delta_{b/w}}{e_D}\right]$$

(1)

Here, μ_s denotes the static coefficient of friction, λ is the lateral stress coefficient, i.e. the ratio of horizontal to vertical stress in the overburden, $\delta_{b/w}$ denotes the ratio of joint fluid density to rock density and e_D is the factor of cavern underpressure, given by the internal pressure of the cavern and the lithostatic pressure at the cavern roof (Fig. 4). The ratio of area to circumference depends on the shape of the sinkhole and its size. For a circle of diameter D, we have:

$$\left(\frac{A}{U}\right)_{circle} = \frac{1}{4} \cdot D$$

(2)

As an example, a cavern without salt back in a depth of 1000 m and a lateral stress coefficient of $\lambda = 0.6$, $\delta = 0.52$, $e_D = 0.48$ and $\mu = 0.42$ (friction angle $\Phi_R = 23°$, see Fig. 7) results in a

critical ratio of $(A/U)_{crit}$ = 35 m. For a circular sinkhole, under these boundary conditions, we can estimate a diameter of D = 140 m using relation (2), similar to the examples in chapter 1.

Equation (1) immediately shows that for a properly closed cavern where the internal pressure approaches the lithostatic pressure, the underpressure factor e_D tends to zero, and consequently the critical area-circumference ratio goes to infinity. In other words, over a tightly shut cavern in salt rocks, no sinkhole can form.

From Equation (1), the critical ratio of diameter D to height H of a rock column that can slide down is obtained as:

$$\left(\frac{D}{H}\right)_{crit} = 2 \cdot \mu_s \cdot \frac{\lambda - \delta_{b/w}}{1 - \delta_{b/w}} \tag{3}$$

The equation is applied for the case of a cavern with an internal pressure given by a brine or freshwater column (hydrostatic pressure), characterized by the parameters δ_{brine} resp. δ_{water} denoting the ratio of joint fluid (brine or fresh water from an aquifer) density to rock density. For a brine density of ρ_{brine} = 1.2 t/m³ and a mean overburden density of ρ_{rock} = 2.3 t/m³, we have δ_{brine} = 0.52 and δ_{water} = 0.43. Hence, for lateral stress coefficients near these values, $(D/H)_{crit}$ tends to zero, i.e. a rock column of arbitrary diameter can slide since the shear resistance is negated by the fluid pressure (Fig. 5).

We can apply Equation 3 to derive the possible height H of a sliding rock column for a given diameter D. Figure 5 shows the critical ratio of diameter to height, $(D/H)_{crit}$ as a function of the lateral stress coefficient λ. For λ = 0.6 we have $(D/H)_{crit} \approx 0.1$ for brine as the joint fluid, i.e. for D = 100 m, a column of 1000 m could start sliding. For water as the joint fluid $(D/H)_{crit}$ = 0.17 for λ = 0.6 and therefore only a 590 m rock column can slide down according to the limit equilibrium theory. With brine in the joints in the overburden, the fluid pressure is higher compared to water and therefore rock columns larger in height can slide down at the same horizontal confinement. This increases the likelihood that a sinkhole will form above the caverns if brine rises in the joints of the overburden due to pressure-driven percolation.
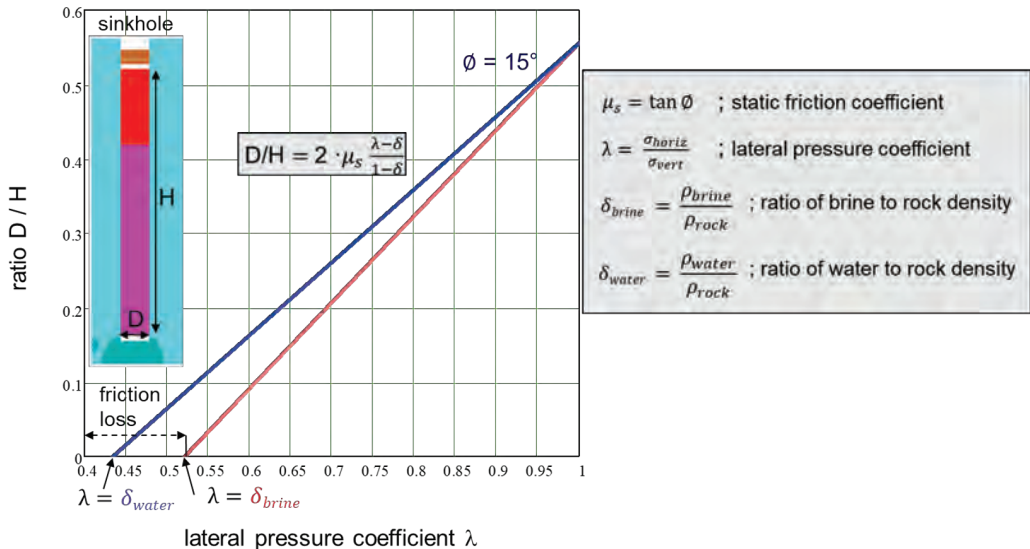

Figure 5: Load limit equilibrium as critical ratio $(D/H)_{crit}$ for block sliding of a rock column with diameter D and height H as a function of the lateral pressure coefficient λ for brine (red line) and water (blue line) as the joint fluid and friction angle Φ = 15°

The block sliding mechanism does not generate significant porosity. Hence, surface sinkholes can appear even for thick overburden. The conceptual model discussed here corresponds to the piston model of Bérest (2017). It is crucial that effective lateral friction is reduced by the joint water pressure and pressure-driven brine percolation (effective stress concept) – only this fluid pressure effect enables sinkholes with diameters of a few tens of meters.

One can plausibly assume that during the sliding process itself, water/brine pressure in the joints changes dynamically, thereby causing hydraulically fractured joints and further reducing or completely removing their shear resistance. Thus, pressure-driven processes cause the chimney-like cylindrical fracture surfaces.

Due to the decisive role of fluid pressure effects along joints, a numerical study of such sinkholes requires discontinuous models together with hydromechanically coupled simulations (Minkley et al. 2012; Knauth & Minkley 2014).

3 Discontinuous modelling and hydromechanical coupling

3.1 Constitutive models for sedimentary rocks and joints

In contrast to some situations that geomaterial simulations can be well described by continuum models, the formation of sinkholes and sliding instabilities in the sedimentary overburden above salt deposits are discontinuous processes. The overburden is usually not viscous, but often brittle and rocks slide along joints and fractures. The shear behavior of these fractures is often characterized by adhesive peaks followed by progressive softening along with hydromechanical coupling, which is critical for stability behavior. Hence, adequate constitutive models for rocks and joints, as well as a consistent discontinuous modelling approach are required.

The visco-elasto-plastic model (Minkley 2004), originally developed for saliferous rock includes elastic, plastic and viscous behaviour of the rock. The nonlinearity of the yield boundary and its dependence on the stress regime cannot be neglected in depth for conventional and solution mining of salt rocks. The yield boundary is given by a nonlinear generalisation of the Mohr–Coulomb criterion (Minkley & Mühlbauer 2007): The yield boundary, expressed as the differential stress at failure, is given by (Fig. 6):

$$(\sigma_1 - \sigma_3)_{\text{fail}} = \sigma_D + \frac{\sigma_{MAX} - \sigma_D}{\sigma_\phi + \sigma_3} \cdot \sigma_3 \qquad (4)$$

Here, σ_1 and σ_3 are major and minor principal stresses. The failure curve is parametrised by the uniaxial compressive strength σ_D, the maximal strength σ_{MAX} and the curvature parameter σ_Φ. In order to take the strain-dependent softening into account, these parameters are functions of the plastic shear deformation ε.

Situations such as block sliding are fundamentally discontinuous and crucially depend on the shear properties of joints and bedding planes. Hence, a comprehensive description of the mechanical behaviour of the jointed rock mass requires adequate models for shear behaviour along discontinuities as well. Therefore, the adhesive shear model (Minkley 1989a; Minkley 1989b) is used to describe the behaviour of discontinuities as joints, bedding planes and other weakness planes. This shear model can simulate:

- velocity-dependent dynamical softening and
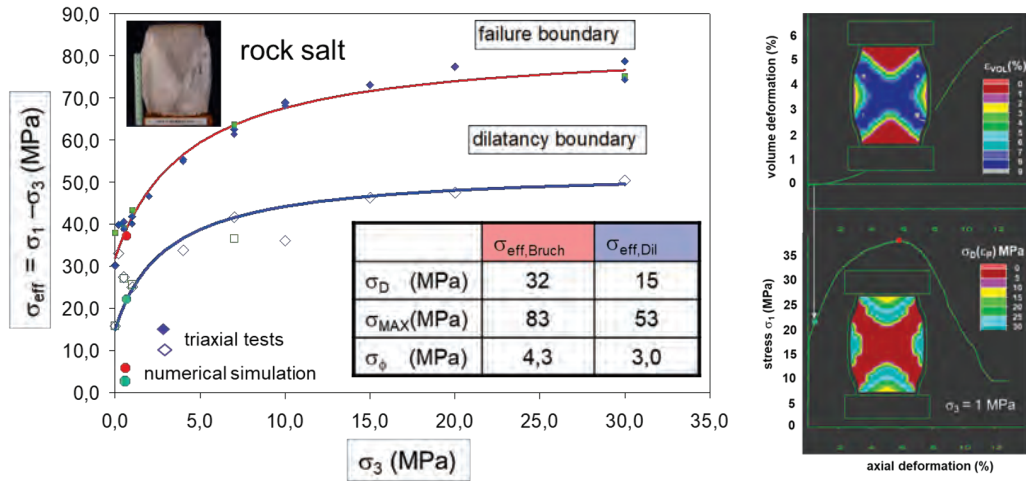- displacement-dependent softening.

Figure 6: Failure and dilatancy boundary for rock salt and fitting with the visco-elasto-plastic model (left) and numerical simulation of a triaxial test (right)

Table 1: Complete set of shear parameters for the adhesive shear model for joints and bedding planes in the overburden of a salt deposit corresponding to Fig. 7

Residual friction angle	ϕ_R	15°
Upslide angle	i_0	18°
Contact strength	σ_K	1 MPa
Curvature parameter	k_1	0.2
Curvature parameter	k_2	0.012
Cohesion	c	1 MPa
Maximum adhesive friction coefficient	$\Delta\mu_{MAX}$	1
Softening distance (Adhesion)	L1	0.001 m
Softening distance (Upslide angle)	L2	0.01 m
Numerical shear model parameter	r	0.01
Velocity factor	b	1,2
Critical shear velocity	V_K	1e-30 m/s
Shear stiffness	K_S	40 GPa/m
Normal stiffness	K_N	50 GPa/m

The peak shear strength is given by (parameters see Table 1):

$$\tau_{peaak} = \tan\left(\emptyset_R + i_0 \cdot \exp\left(-k_2 \frac{\sigma_N}{\sigma_K}\right)\right) \cdot \left(1 + \Delta\mu_{MAX} \cdot \exp\left(-k_1 \frac{\sigma_N}{\sigma_K}\right)\right) \cdot \sigma_N + c \qquad (5)$$

If the maximum shear strength is exceeded, failure and plastic shear displacement occurs. Joint weakening is captured by:

- an instantaneous reduction of cohesion to the residual value
- a decrease of the dilation angle as a function of plastic shear displacement u_s,

$$i_0 \rightarrow i_0 \cdot e^{\frac{-u_s}{L_2}}$$

- a decrease of the adhesive factor as a function of plastic shear displacement u_s,

$$\Delta\mu_{MAX} \rightarrow \Delta\mu_{MAX} \cdot e^{\frac{-u_s}{L_1}}$$

The softening lengths L1 and L2 depend on the rock type and the associated joints and are determined from laboratory experiments.

Table 1 shows a parameter set for the adhesive shear model which was determined from triaxial and direct shear tests on rock specimens of a sedimentary (predominantly sandstone) overburden. In this example, for the softening shear behaviour, the shear strength displacements have been back-calculated in the numerical shear tests for two normal stresses (Fig. 8).
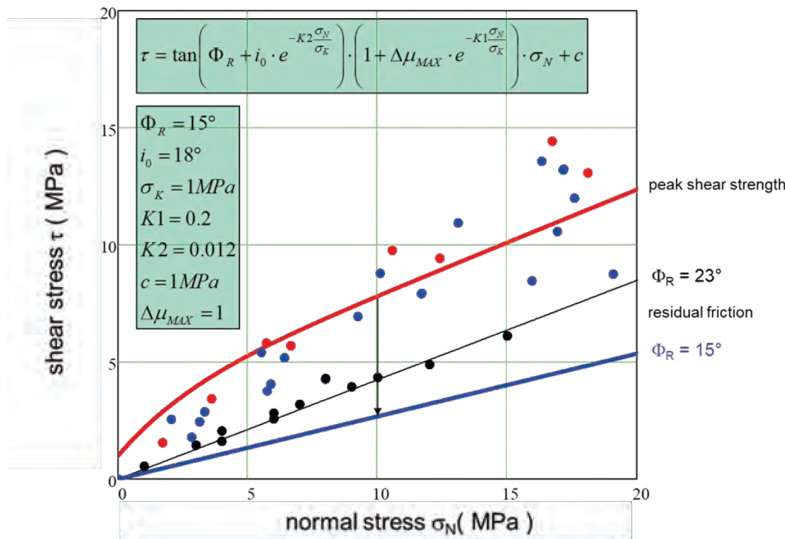
Figure 7: Shear strength for joints determined on shear fracture in the post-failure area by triaxial shear tests on drill cores from the overburden (red dots dry rock, blue dots joint fluid pressure) and fitting with adhesive shear model, black dots direct shear tests
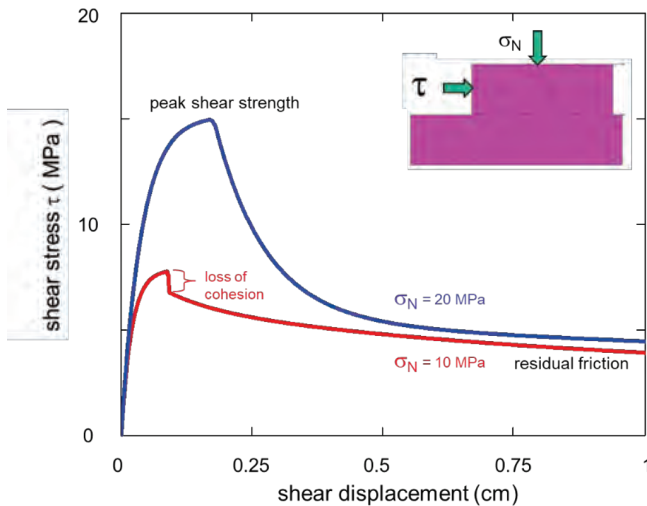
Figure 8: Numerical shear tests with variation of normal stress (σ_N = 10 MPa according to Figure 7, see black pointer). For large shear displacements, the shear strength drops to the residual friction resistance

Thus, the adhesive shear model is characterised by the following properties (Minkley & Mühlbauer 2007):

- Peak shear strength with adhesive friction component
- strain softening by reduction of cohesion and adhesion, modelling the progressive damage of the asperities by plastic shear displacement, and
- dependence of shear strength on the strain rate

This model is universally applicable for joints and discontinuities in sedimentary and salt rocks.

3.2 Examples from Numerical Studies

We will now present a number of examples from numerical simulations that illustrate the mechanism. As previously discussed, block sliding is a fundamentally discontinuous process and is, for relevant depth and rock mass conditions, only possible if fluid pressure on joints is taken into account. Hence, all simulations presented here are hydromechanically coupled discontinuous models, using the discrete-element code UDEC 6 (Itasca 2018) with the user-developed constitutive models (see part 3.1). Rock salt and all joints have been modelled with the visco-elasto-plastic constitutive model and the adhesive shear model, respectively; the overburden has also been treated as a visco-elasto-plastic material but with a very low creep behaviour.

In addition to the constitutive model parameters, an initial state of stress has to be specified in the model. Generally, there is an elastic and a tectonic component to the lateral stress:

$$\lambda = \frac{\nu}{1-\nu} + tectonic \qquad (6)$$
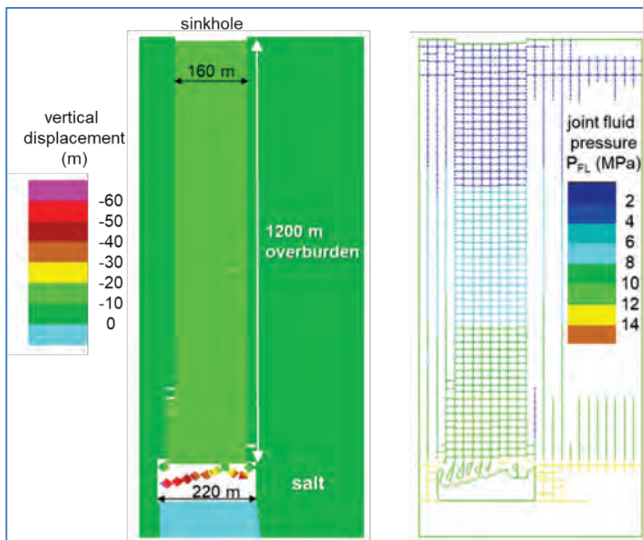
Figure 9: Basic scenario of sinkhole formation with a large-span cavern after the loss of the salt back: A rock column in the overburden has started to slide (left) is modelled with horizontal and vertical joint sets; brine from the cavern percolates along the joints and lowers the effective stress, allowing the rock column to slide

For rocks with Poisson`s ratio of $\nu = 0.33$ the elastic contribution is $\lambda = 0.5$. Large-scale stress surveys show that bedded salt formations tend to decouple the overburden from the recent tectonic stresses in the basement (Groß et al. 1986), since the viscous salt layer mechanically isolates the overburden from the basement. The overburden stress is mainly controlled by the

lithology of the rocks, elastic stiffness contrasts and the regional geology, i.e. (syn)clines and fault zones (Röckel & Lempp 2003).

We first discuss a simple model with a single cavern with the outline (Figure 9): Dimensions are 500x1400 m in the horizontal and vertical directions, respectively; the salt layer is 100 m thick and covered by 1200 m of overburden. The jointing in the overburden is approximated with two orthogonal joint sets (horizontal and vertical) with spacing of 20 m. Continuous vertical joints from the salt horizon to the surface represent a conservative approximation of an in situ joint system, where frictional resistance at overburden joints was set comparatively low with Φ_R = 23° (see Fig 7).

Figure 9 shows the result for a cavern with a span of 220 m and a lateral stress coefficient of λ = 0.5. In case of low-thickness salt bench to the hanging jointed rock, time-dependent softening processes occur under the effect of the brine pressure, which lead to the collapse of the roof layers. The salt back above the cavern has fractured and failed, allowing the brine from the cavern to penetrate along the overburden joints. Brine pressure has developed along the entire joint system above the cavern up to the surface. Consequently, the shear strength is lowered. A column of approximately 160 m width has started to slide down in a piston-like motion. There is essentially no bulking, so the movement in the cavern roof directly translates into sinkhole volume at the surface. (Note that the sliding rock column does not disintegrate although the horizontal joints are inundated).
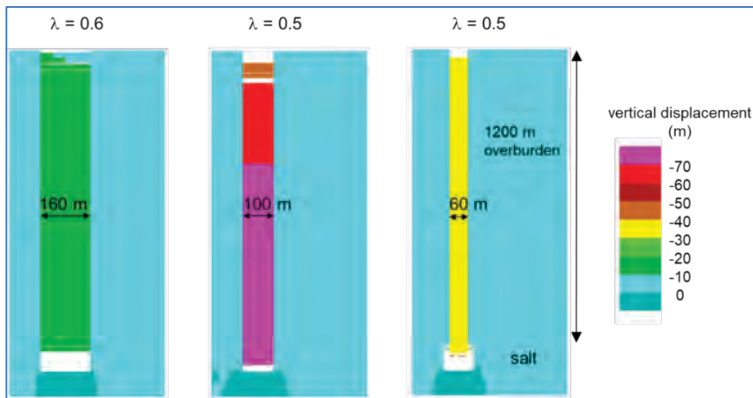
Figure 10: Block sliding and sinkhole formation over the cavern with variation of span and lateral stress coefficient λ, angle of friction $\Phi_R = 23°$

The block sliding instability, i.e. the critical area-circumference ratio, depends on the lateral (confining) stress and the cavern span. To assess the dependence on model conditions, the lateral stress coefficient and the cavern span were varied. The plots in Figure 10 show that block sliding with a width of 160 m still occurs for λ = 0.6, while for λ = 0.5 smaller caverns are unstable as well. The minimal sinkhole width in the model variations was 60 m. For lateral stress coefficients larger than λ = 0.6 block sliding did not occur.

The simplified and conservative models allow to derive necessary conditions for sinkhole formation via block sliding over brine-filled caverns:

- a sufficiently large cavern without salt back, i.e. with hydraulic connection between the cavern and the overburden
- a jointed overburden with moderate to low shear strength
- moderate to low horizontal (confining) stresses in the overburden
- water pressure or brine pressure-driven percolation on the overburden joints

In a cavern field, caverns exert mutual influence due to deformations, stress changes and the alteration of hydraulic conditions. These interactions of neighbouring caverns can contribute to sinkhole formation. In particular, large subsidence over the centre of a cavern field can reduce the lateral stress near the boundary, i.e. at the edge of the subsidence bowl.
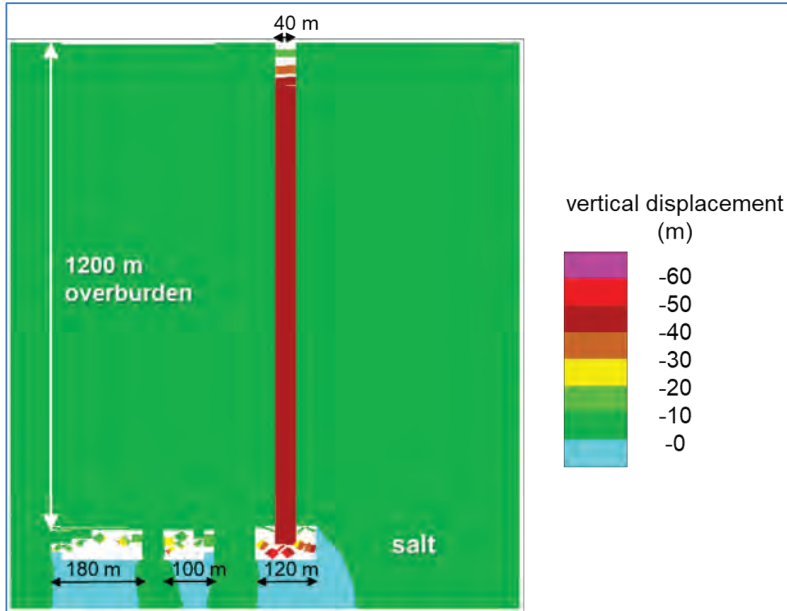

Figure 11: Narrower sliding column due to overpressure in closed cavern with hydraulic connection to the overburden (lateral stress coefficient λ = 0.55, residual friction angle of Φ_R = 23°)

In the model shown in Figure 11, several caverns are modelled with an overburden structure and parameters as before. The lateral stress coefficient has been increased to λ = 0.55, such that a narrow sinkhole would not form by itself. We assume that all caverns have lost their hydraulic barrier, but the cavern on the right has been closed. Thus, the internal pressure is increased by 3.5 MPa. However, due to the hydraulic connection between the cavern and the overburden, the overpressure is transferred to the overburden joint system. Here, it has to be assumed that the overpressure can be, at least temporarily, sustained despite the outflow along the joints. As a consequence, the shear resistance is lowered further, and previously stable rock configurations can start to slide – a narrow sinkhole of width 40 m forms above the third cavern. Recall that in the single-cavern model, minimum sinkhole width was 60 m (Fig. 10, λ = 0.5). The overpressure generated by the temporarily closed caverns, which hydraulically leak at higher pressure, has lowered the critical rock block size.

An analogous failure process occurred during the formation of the sinkhole over the Oxy3 cavern in Louisiana in 2012 (cf. Section 1). The cavern with a depth of 1050 m (from cavern crown to the surface) was also closed, although a tightness test performed before abandoning the cavern in 2010 proved that the cavern was not able to sustain high brine pressures. The seismic analyses of the sinkhole formation (Nayak & Dreger 2014) "indicates the role of fluids in controlling the seismic source processes" and confirm the concept of rock mass sliding combined with fluid-dynamic ruptures caused by pressure-driven percolation.

The fluid pressure on the joints bounding the sliding column dynamically changes during the process (Figure 12), reaching transient pressures of up to triple the hydrostatic pressure in the dynamical simulation. This implies that in-situ joints can be further hydraulically fractured as a result of pressure shocks during the sliding process and that the effective stress is transiently

reduced to zero. Thus, the geomechanical model provides a physical explanation for the generation of vertical chimney-like structures in which entire column of overburden rock can slide down and create sinkholes at the surface: The distinctive chimneys, typical for sinkholes, are formed by pressure-driven shear failure during dynamic rock block sliding in jointed overburden.
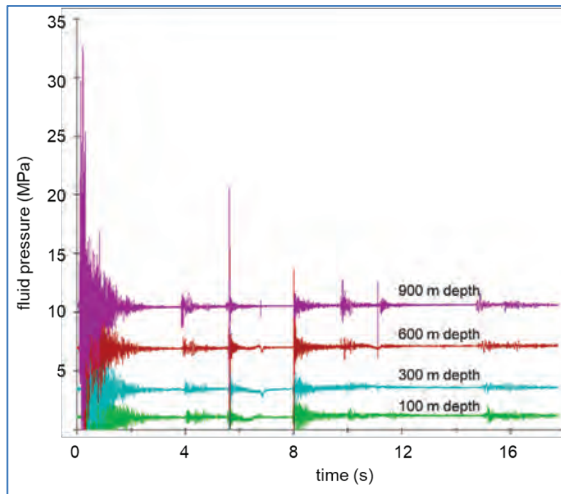

Figure 12: Dynamic evolution of joint fluid pressure at the boundary of the sliding block in the overburden during simulation of a sinkhole. After 16 seconds the rock column has slide down by 35 m

In the case of an inclined dipping joint system in the overburden, the sinkhole may develop farther from the edge of the brine field (Fig. 13). In the calculations, it was assumed that a pressure build-up above the right cavern corresponds to a brine column up to the surface.

A hydrostatic water pressure build-up was assumed in the overburden above the centrally located caverns. In contrast to the previous simulations, a peak shear strength with cohesion/adhesion in the overburden was applied to the joints according to Fig. 7, which decreases to a residual shear strength with the residual friction angle of $\Phi_R = 15°$ after large shear displacements (see shear parameter set Table 1).

In connection with the shear strength reduction due to brine pressure, shear failure occurs at the steeply standing joints above the cavern. Pressure-driven percolation due to cavern creep closure leads to a brine motion into the overburden and the progressive shear softening in the joint system. After breakthrough to the aquifer, a continuous brine or water pressure has built up along the mantle surface of the dipping rock column above the cavern. The outflow of the blanket (diesel, see Fig. 13) in the crater is a clear evidence of a hydraulic connection between the caverns, located at a depth of about 1200 m, and the sinkhole at the surface.

4   Conclusions

We showed that sinkholes are possible for caverns in depths exceeding 1000 m. We presented case histories, analytical estimates and numerical simulations which represent a consistent image of the mechanism. The models provide an explanation for the chimney-like fracture tubes/cylinders in the formation of sinkholes.

The block sliding instability is a hydromechanical process that requires fluid-filled joints in the overburden, where the fluid pressure lowers the effective stress and thus the shear resistance.
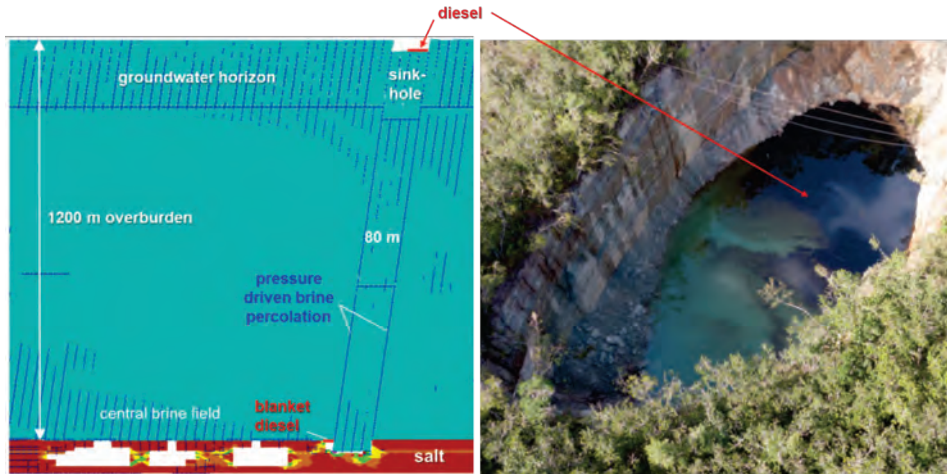
Figure 13: Sinkhole formation over a cavern at the edge of a solution mining field (lateral stress coefficient λ = 0.5, shear parameter set in the overburden according to Table 1, dip of the small-tectonic jointing in the overburden 84°

A necessary condition is the loss of the hydraulic barrier, i.e. a hydraulic connection between the cavern and the overburden, so that brine can permeate the joints by pressure-driven percolation (Minkley et al. 2014).

The process may be aided by dynamic overpressures, e.g. due to rock fall or tectonic events, which fracture remaining rock bridges. Microseismic monitoring systems possibly can track the evolution of the overburden in the cavern roof.

It is important to notice that while the general mechanism is understood, the evolution of specific potential sinkholes where the system is close to a boundary of stability, depends on geological and geotechnical details and cannot be predicted reliably.

In our models, the joint properties (geometry and shear strength) were generally chosen conservatively. In addition, we have not considered chemical alterations in the overburden due to brine such as weathering and dissolution or lubrication of clay-filled joints which cause in general a time-dependent softening behaviour. Therefore, a detailed rock mass assessment is required in each specific case.

References

BÉREST, P. 2017. Cases, causes and classifications of craters above salt caverns. International Journal of Rock Mechanics and Mining Sciences 100, pp. 318–329

GROß, U., MINKLEY, W. & PENZEL, M. 1986. Ergebnisse zur Untersuchung von Gebirgs-spannungszuständen und ihre Anwendung. Proc. Int. Symp. on Rock Stress and Rock Stress Measurement, Stockholm, pp. 531–536

ITASCA 2018. UDEC: Universal Distinct Element Code, Version 6. Itasca Consulting Group Minneapolis, Minnesota, USA. URL: https://www.itascacg.com/software/udec.

JOUSSET, P. & ROHMER, J. 2012. „Evidence for remotely triggered microearthquakes during salt cavern collapse ". In: Geophysical Journal International 191.1, pp. 207–223

KNAUTH, M. & MINKLEY, W. 2014. Modeling of the mechanical and hydraulic behavior of salt rocks on discontinuum mechanical basis. 48thUS Rock Mechanics / Geomechanics Symposium held in Minneapolis, MN, USA, 1-4 June 2014, ARMA 14-7036

MINKLEY, W. 1989a. Festigkeitsverhalten von Sedimentgesteinen im post-failure-Bereich und Gebirgsschlagerscheinungen. Proc. Int. Symp. Rock at Great Depth, Pau. Rotterdam: Balkema Vol. 1, 59 – 65

MINKLEY, W. 1989b. Untersuchungen zur Reibung an Gesteinstrennflächen und Modelle zum Gebirgsschlagmechanismus bei Haftreibungsverlust. Dissertation. TU Freiberg

MINKLEY, W. & GROß, U. 1990. Sliding of blocks in the top rock, a model for rockburst of the regional type. In: Gerlands Beiträge Geophysik 99.5, pp. 487–491.

MINKLEY, W. 2004. Gebirgsmechanische Beschreibung von Entfestigung und Sprödbruch-erscheinungen im Carnallitit. Aachen: Shaker Verlag. ISBN: 3-8322-3495-0.

MINKLEY, W. & MÜHLBAUER, J. 2007. Constitutive models to describe the mechanical behaviour of salt rocks and the imbedded weakness planes. In: The Mechanical Behavior of Salt VI, CRC Press. ISBN: 978-0-415-44398-2

MINKLEY, W., KNAUTH, M. & U. WÜSTE, 2012. Integrity of salinar barriers under consideration of discontinuum-mechanical aspects. In: The Mechanical Behavior of Salt VII. CRC Press. ISBN: 978-0-415-62122-9

MINKLEY, W., KNAUTH, M. & BRÜCKNER, D. 2014. Discontinuum-mechanical behavior of salt rocks and the practical relevance for the integrity of salt barriers. SMRI Fall 2014 Technical Conference, 29 - 30 September 2014, Groningen, The Netherlands

MINKLEY, W., KNAUTH, M., FABIG, T. & FARAG, N. 2015. Stability of salt caverns under consideration of hydro-mechanical loading. Mechanical Behavior of Salt VIII, Rapid City, USA, 26-28 May 2015, 217 – 227

MORISSEAU, J. 2000. Uncontrolled leaching of salt layer in an oil field in Algeria. Tech. rep. SMRI Fall Meeting, San Antonio, TX, USA. Solution Mining Research Institute

NAYAK, A. & D. S. DREGER, 2014. Moment Tensor Inversion of Seismic Events Associated with the Sink-hole at Napoleonville Salt Dome. Bulletin of the Seismological Society of America,

RÖCKEL, T. & C. LEMPP, 2003. Der Spannungszustand im Norddeutschen Becken. In: Erdöl Erdgas Kohle 119.2

SALZER, K. & MINKLEY, W. 2005. Safety Assessment for the Land Surface in the Vicinity of the Potash Shaft Neustaßfurt VI. Post-Mining 2005, November 16-17, Nancy, France

VAN SAMBEEK, L. 2014. Selected Examples of Sinkhole Formation in the United States: Natural and Man-Caused. SMRI Spring 2014 Technical Class. San Antonio, Texas, USA

Theme 7: Energy storage in salt caverns

Underground hydrogen storage in salt caverns in the Netherlands – Storage performance and implications for geomechanical stability

S.F. Van Gessel[1], R.M. Groenenberg.[1], J. Juez-Larré[1], R.A.F. Dalman[1]*

[1] TNO Geological Survey of the Netherlands

* *serge.vangessel@tno.nl*

ABSTRACT: Hydrogen is expected to become an important cross-sectoral energy carrier, providing flexibility through large-scale storage and on-demand production of hydrogen via electrolysis as the proportion of energy produced from intermittent renewable energy sources increases (i.e. wind and solar). van Gessel et al. (2018, 2021) evaluated various scenarios to estimate the need and potential for deploying hydrogen storage capacities in subsurface formations. While there is a need to balance at seasonal timescales, new analyses reveal that optimizing flexibility in the energy system may significantly alter the way storages are used throughout the year. Rather than a single-cycle (seasonal) profile, bi-weekly and monthly cycles, with higher injection and withdrawal rates, may increase the effective utilization of the storages while reducing the capacity needed. Additional long-term (seasonal) storage capacities may be required for strategic reserve or arbitrage purposes. Salt caverns have proven potential for pure hydrogen storage with favourable operational conditions. The estimated maximum practical storage that may be required in the Netherland by 2050 is ca. ~15 TWh, consisting of 60 caverns with a geometrical volume of 1 million m^3 each. This necessitates development of several clusters consisting of multiple salt caverns. Higher storage capacity demands may require additional storage volumes potentially in depleted natural gas fields. Large-scale implementation of cavern storage poses a geomechanical challenge, due to long-term subsidence effects. Additionally, better understanding is needed regarding integrity issues in the near-wellbore area during fast cyclic loading and unloading.

1   Introduction

Future energy systems are expected to adapt to increasing shares of intermittent renewables (wind, solar). In addition to the current seasonal balance of heat demand, this development will result in a growing demand for flexibility on shorter time scales (hourly – daily) to ensure the stability of power grids and to mitigate load-supply variations. Solutions can be delivered by flexible forms of power/heat production, curtailment, response to demand in industrial sectors, improved interconnectivity of the power grid across borders, and various types of energy storage technologies that provide stability, flexibility and adequacy for various time scales, power ranges and sectors.

Hydrogen (both green and blue) is expected to become an important vector in the energy system because it can provide flexibility up to seasonal time scales as well as net zero-emission energy and feedstock for multiple sectors. In the North Sea region, co-location of green hydrogen production with windfarms far offshore may resolve challenges related to transport of electricity over long distances, and can help to balance the intermittent electricity generation patterns of windfarms more cost-effectively by serving as flexible demand, thus avoiding curtailment. Hydrogen can provide high- and low-temperature heat to the industry and built environment, and thereby replace natural gas and coal. Hydrogen can also be used as net zero-emission fuel in transportation vehicles such as heavy duty vehicles, trains and boats. And last but not least, green hydrogen can sustainably decarbonize feedstock demand for various industries by replacing the traditional hydrogen production from hydrocarbons.

The increasing national dependency on secure and affordable supply of hydrogen in the energy system requires large-scale hydrogen storage capacities in order to balance variable load-supply patterns at hourly to seasonal time scales. Salt caverns generally represent a proven and cost-attractive solution to deliver large-scale storage capacities (Kruck & Crotogino 2013).

In this paper we present evaluations of future Underground Hydrogen Storage (UHS) demand in the Netherland and the option to use rock salt formations as the storage sites. Based on these assessments we address the key geomechanical challenges associated with the development and operation of storage caverns.

2 Predicting demand for hydrogen storage

The Dutch National Climate Accord and the ambitions for renewable energy production, with green and blue hydrogen as a pivotal energy carrier, will bring about substantial changes in the energy system in the coming decades. The precise nature and extent of those changes in the future energy system of 2050 are still uncertain. Recent energy scenario studies (Sijm et al. 2020; Berenschot & Kalavasta 2020; Scheepers et al. 2020) present different pathways to reach the minimum emission reduction target of 95% by 2050. Each scenario and study is distinguishable in terms of definitions, criteria and assumptions (e.g. energy supply, energy demand, flexibility solutions, governance models) as well as conditions steering systems modelling (e.g. optimization to lowest marginal costs, CO_2 reduction targets). In all of the evaluated energy scenarios, large-scale hydrogen storage emerges as a pivotal technology from 2030 onwards and with a broad range of estimated capacities in 2050. The key factors that influence the expected demand for hydrogen storage and mode of operation are:

- The total share of intermittent renewable electricity generation from wind or solar.
- The share of natural gas and other fuels to provide flexibility in the electricity system
- The amount of imported hydrogen vs. domestically produced hydrogen
- The sectors in which hydrogen is being used (i.e. power vs transport vs feedstock vs heating)
- The degree to which the combined flexibility solutions are optimized in the energy system
- The consideration of extreme annual weather patterns, which affect energy production (e.g. wind and solar energy deficits) and demand (e.g. extreme cold winters)

While the factors define the minimum required installed storage capacities to balance supply and demand at hourly time scales during the entire year, larger additional storage capacities may be needed to provide strategic reserves in case of supply interruptions due to e.g. geopolitical conflicts, unexpected economic developments or blocking of supply routes (e.g. pipelines, shipping). The demand for strategic reserves was not included in the energy system models. Therefore, this capacity was determined empirically from the ratio of current natural gas and oil storage capacities vs. the total annual demand. In the case of natural gas in the Netherlands and Europe, this is approximately 20-30%. For (crude) oil storage there is an international directive to ensure 90 days of consumption, or in other words 25% of the annual consumption.

Van Gessel et al. 2021 provide a comprehensive assessment of the different energy scenarios and expected large-scale storage capacities for hydrogen and other types of undergrounds energy storage such as green gas storage and compressed air energy storage. Figure 1 shows an overview of the hydrogen storage capacities estimated (balancing and strategic) for the Netherlands in 2050 for each of the studies considered.
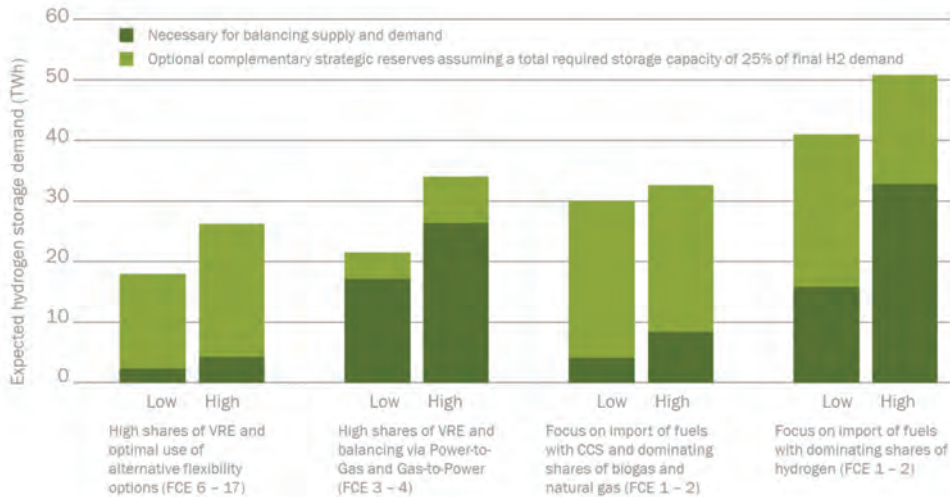
Figure 1: Aggregated summary of estimated demand for large-scale hydrogen storage (installed capacity). FCE = Full Cycle Equivalent (number of full turn-overs of total installed storage capacity per annum). VRE = variable Renewable Energy (wind and solar). After van Gessel et al. 2021.

3   Suitable options for underground hydrogen storage

Salt caverns are globally recognized and deployed as a viable reservoir for the storage of different types of gases and fluids. According to GIE (Gas Infrastructure Europe, 2021) in Europe there are currently 61 operational natural gas storage facilities, each with one or more salt caverns. The total storage capacity (working volume) is 203 TWh. Other typical storage options for salt caverns include crude oil or processed oil products, nitrogen, helium, hydrogen and compressed-air. Hydrogen storage in salt caverns has already been proven and deployed in several sites in UK and US (DBI-GUT, 2017). However, these storages have a mostly static (low-cyclic) mode of operation, while future deployment in a renewable energy system may require fast-cyclic modes.

Based on a comprehensive benchmark study by Kruck and Crotogino (2013), salt caverns are considered to be the most promising, technically advanced and attractive option for the storage of large quantities of hydrogen at high-pressures. Laboratory experiments and practical experiences in existing storages have proven that homogeneous rock salt formations (halite) exhibit a proven tightness for hydrogen gas. In these salt formations the visco-plastic behaviour of rock salt makes that small fracture generated during injection and/or production phases is healed. There are however some factors that can impair the tightness of storage such as the rupture or collapse of surrounding salt formation, presences of permeable interbedded layers intersecting the cavern. These occurrences are generally manageable by prevention or mitigation through detailed geological studies, testing and monitoring, following good salt mining practices and keeping operational pressures and daily draw-downs within safe ranges. Thanks to the fact that rock salt formation does not react with hydrogen, there is a general low risk of geochemical reactions that could jeopardize the quality of the stored hydrogen, or lead to the generation of hazardous/corrosive products (e.g. H_2S). This could only take place in cases were intercalations of non-halite rock formations are present in the salt cavern wall or through microbial contaminations in the remaining brine. But again such hazards can be controlled. Last but not least, salt caverns are flexible and scalable through engineering of

individual caverns (depth, size, shape) and the development of cavern clusters. Although flow is not restricted by a rock matrix (like in porous media), the daily draw down should not exceed certain rates (e.g. 10 bar/day) and the working gas / cushion gas ratio should preferably be higher than 1 in order to minimize risks associated with loss of cavern integrity (Groenenberg et al. 2020). There are several others factors that need to be considered, which may limit the upscaling of dense clusters of caverns. A main point of concern is the fact that salt caverns will converge over time due to salt creep. The rate of salt creep depends among others on the properties of rock salt itself (e.g. Bérest et al. 2019), but also on the depth of the salt cavern, the cavern pressure, the abandonment strategy (after cease of storage operations) and the relative location within the salt dome as well as the distance to other salt caverns. As individual salt caverns typically have much lower storage capacities than porous reservoirs, it is likely that large numbers of caverns, and possibly densely clustered cavern systems, may be needed to realized required capacities. This may lead to several practical limitations such as timely development, significant long-term subsidence in dense clusters and the disposal of brine resulting from salt leaching. These situations may be of particular importance in the Netherlands as salt structures are sparse and mainly concentrated in the eastern and north-eastern parts of the country.

In addition to salt caverns, Kruck & Crotogino (2013) consider depleted gas fields and aquifers as potential alternative for the storage of larger volumes of hydrogen. However, hydrogen storage in porous media has a lower technical readiness level and specific topics still require some research. Heinemann et al. (2021) describe the key technical challenges that need to be resolved including the possible impacts from microbial and geochemical conversion effects, tightness of the seal, multi-phase fluid flow and stress changes on the reservoir formation and intersecting faults.

4   Technical and practical storage capacity assessments in the Netherlands

Van Gessel et al. (2018, 2021) investigated hydrogen storage capacities in salt structures and depleted gas fields in the Netherlands. Figure 2 shows the locations of potentially suitable salt structures, and the estimated technical capacities, assuming cluster of salt caverns, each with a geometrical volume of ~600.000 m^3.

Salt caverns for high-pressure gas storage are typically deployed in homogeneous rock salt (halite) intervals between ca. 1000 and 2000 meters' depth. At shallower depths (<1000 m) the caverns will not be able to withstand the high pressures needed to efficiently operate the storage (assuming a normal lithostatic pressure gradient of 1 Psi/ft). The typical operating pressures for a salt cavern are between ca. 60 and 200 bar (DBI-GUT, 2017). At greater depths (>2000 m), the caverns become less stable as salt creep rates increase significantly.

Van Gessel et al. (2018) evaluated the potential gas storage capacity (working volume) in salt caverns for onshore rock salt intervals within the Zechstein Group. Triassic rock salt intervals were excluded as these appear as relatively thin-bedded formations with little or no domal features. Salt pillars were primarily selected on the condition that the rock salt interval between 1000 and 1500m depth is suitable for the construction of standard caverns (diameter ~50 m x Height ~300 m) with sufficient and safe margin between the top and sides of the salt structure. Additionally, the interval of interest should not have any indications of major anhydrite beds (based on well data and seismic survey data) or other heterogeneities that could prevent the stable construction of the cavern. The maximum theoretical number of caverns was determined by optimizing the placement of caverns in the available rock salt volume, taking into account minimum distances between neighbouring caverns (160m - 210m) and between caverns and the flanks and top of the structure (100m - 150m), following standard salt mining practices (IfG, 2008). The total theoretical number of caverns calculated this way was reduced by a factor 2 to account for local heterogeneities and non ideal subsurface conditions. This

yielded a conservative total number of 321 salt caverns. The hydrogen storage capacity per cavern was determined considering a maximum operational pressure of 180 bar, and a working gas: cushion gas ratio of 1:1 (Juez Larré et al. 2019). This resulted in an estimated working volume of ca. 45 million m^3 of hydrogen per cavern, which is consistent with existing storage caverns for natural gas and hydrogen. All selected salt pillars in the provinces of Drenthe, Friesland and Groningen combined, yield an estimated technically feasible total hydrogen working volume of 14.5 billion m^3 (or 43 TWh). Despite this large potential, van Gessel et al. (2021) conclude that a maximum of 60 caverns of 1 million m^3 each could be realistically constructed between 2030 and 2050. This number considers various practical restrictions such as the time needed to create caverns (ca. 3 to 4 years), not more than 7 to 9 locations, which simultaneously develop caverns, available means to bring produced salt to the market and additional challenges as licensing, exploration and spatial planning. With all that the Netherlands could develop a practical storage capacity of up to ~5 billion m^3 of hydrogen (15 TWh).

Zechstein rock salt (depth >1500m)
- Thickness < 200m
- Thickness 200 – 500m
- Thickness > 500m

Zechstein rock salt (depth 400 - 1500m)
- Thickness < 300m (mounds)
- Thickness > 300m (pillars)

Triassic rock salt (bedded)
- Depth > 500m and/or thickness < 25m
- Depth 400 - 500m, thickness > 25m

Zechstein rock salt, suitability gas storage caverns
- Exsiting gas storage caverns
- Good prospects (pillars)
- Uncertain prospects (mounds)
- Poor prospects (too small, poor salt quality)
- Salt production licenses

Figure 2: (Left) Regional distribution of the Zechstein and Triassic rock salt formations in the Netherlands. (Right) Zoom in of the north-eastern part of the Netherlands. The areas where the Zechstein rock salt has a suitable depth and thickness for the development of salt caverns are coloured in green (pillars). Source: Juez-Larré et al. 2019.

5 Hazards and risks of hydrogen storage

Like other subsurface technologies, underground storage of hydrogen is associated with certain risks that can potentially impact important societal aspects such as health, safety and environment. Van der Valk et al. (2020) took the risks associated with underground natural gas storage (UGS) as a starting point for a risk assessment of underground hydrogen storage.

Experience from past incidents at underground gas storage facilities suggests that the biggest risks arise from failure of the well materials (steels, cement, elastomers) and well interfaces (Evans 2008). Although UGS and underground hydrogen storage have a similar risk profile, important differences arise from the different properties of hydrogen compared to methane.

Hydrogen potentially has a higher likelihood to leak than methane. Due to its small mass and molecular size, hydrogen potentially diffuses more easily through rocks and materials, and along interfaces in wells and surface facilities. The integrity and durability of well completion materials (casing, tubing, packers, wellhead, safety valves, etc.) currently used in UGS wells are not yet fully proven resistant to the higher reactivity potential of hydrogen with other elements. This includes potential toxic and corrosive by-products such as H_2S which may result from geochemical and microbial reactions with rock matrix and formation fluids. Last but not least, large pressure swings on integrity and durability of well materials and interfaces exposed to pure hydrogen are not yet well-enough known (see also next section).

Leakage of hydrogen may have a bigger and more damaging impact. This is in the first place due to the wider flammability range and much lower ignition energy of hydrogen compared to methane. The higher flame propagation of hydrogen potentially results in higher pressures and danger of explosion upon ignition in confined spaces (pressure shock wave). Unlike methane, the combustion of hydrogen is not visible and radiates little (infrared) heat, although it emits substantial ultraviolet radiation. Risks may further increase due to more difficult detectability of hydrogen which could result in leakages remaining unnoticed (e.g. small seepages in confined spaces under buildings).

In order to better understand the risks and how to mitigate them, further research (laboratory experiments, numerical modelling, material testing, pilot-scale field tests) is required in the topics of: a) the long-term durability of rocks and (well) materials (steel alloys, cement, elastomers, etc.) when subjected to hydrogen under an alternating pressure regime that causes mechanical and thermal stresses; b) interactions of hydrogen with rocks, fluids and microbes in reservoirs and their effects on reservoir performance, quality and retrievability of the stored hydrogen, and integrity and durability of materials subjected to products of such interactions (e.g. H_2S). In addition to these research challenges, monitoring techniques and measures are needed which enable quick detection of leakages.

6 Geomechanical challenges related to faster cyclic storage

The highly intermittent energy supply and demand may require hydrogen to be injected into and withdrawn from a cavern at higher frequencies. This may result in important variations in pressure and temperature, which in turn could have adverse effects on the mechanical integrity and stability of the storage complex (cavern, seal, and wellbore). In particular, the amplitude of the variations in combination with the frequency are important parameters because they govern the amount of (geomechanical) stress that is exerted on the rocks, wellbore materials, and interfaces. The amplitude is determined by the volume of gas injected or withdrawn in each cycle, while the frequency by the lapse of time between cycles. Typically natural gas storage (UGS) follows a seasonal usage profile, i.e. one full cycle of charge and discharge. This is known as "full-cycle equivalent" (FCE). Results of a system modelling study by Sijm et al. (2020) indicates that in a future energy system, with production dominated by variable, intermittent renewable energy sources (wind, solar), and an optimal mix of flexibility mechanisms to balance supply and demand, the usage profile of underground hydrogen storage (UHS) may be characterized by higher frequency cycling at larger amplitudes. Figure 3 gives an example of a potential usage profile of an UHS (top graph) compared to an operational (recorded) usage profile of the natural gas storage facility of Zuidwending (cluster of salt caverns) in the Netherlands (bottom graph). Both profiles are based on the wheather profile of year 2015.

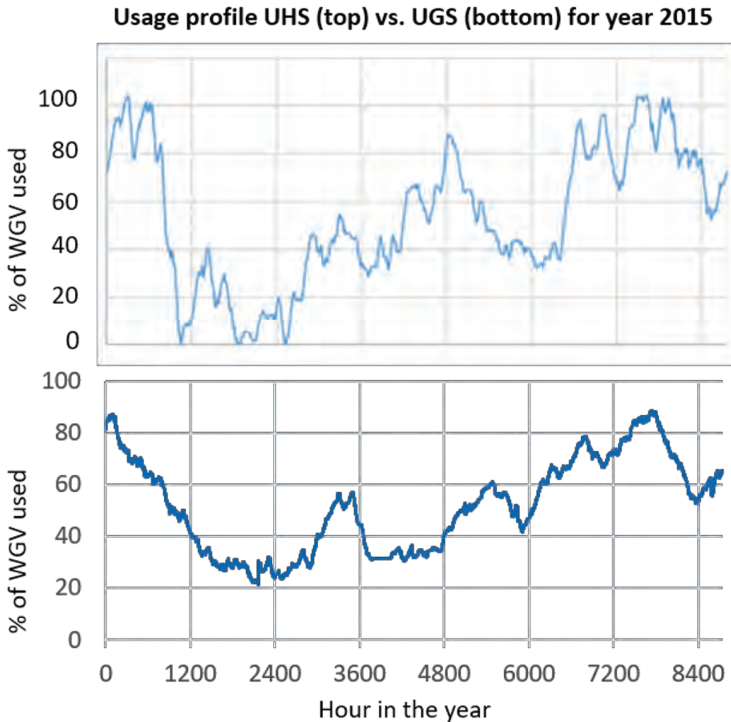**Usage profile UHS (top) vs. UGS (bottom) for year 2015**

Figure 3: Comparison of modeled usage profile of UHS capacity from the LSES study (top; Sijm et al., 2020) with the operational (recorded) usage profile of the natural gas storage facility of Zuidwending in the year 2015 (bottom; data downloaded from EnergyStock.com)

While the natural gas profile of Zuidwending clearly exhibits a typical seasonal profile of withdrawal at fairly constant rate in the winter period (Dec/Jan-March/April), and injection in the spring and summer period (May-October), this is not the case for the UHS profile that exhibits faster cyclicity at higher rates. An analysis of the number of FCE reveals that the standard annual 4 FCE for natural gas for Zuidwending, would be equivalent to 6-14 FCE for the different scenarios modelled by Sijm et al. (2020).

This faster-cyclic storage, i.e., more cycles at higher rates with larger variations in pressures (and temperatures), poses challenges for the stability and integrity of storage reservoirs and wells. In Groenenberg et al. (2020), the effects of faster-cyclic operation, and the extent to which they affect the integrity and stability of salt caverns used for UHS, was assessed by conducting geomechanical numerical simulations (DIANA software) of a salt cavern subjected different FCE's and rates of injection and withdrawal. The results of this work are presented in an accompanying paper by Wassing & Groenenberg (2022).

7   Long-term impacts of subsidence

Large-scale development of salt caverns for hydrogen storage after 2030 (estimated ≤60 caverns) will pose important challenges. Subsidence is one of them, as the selection of salt structures and lay-out of cavern clusters will need to be carefully investigated. Subsidence is caused by the systematic closure of the cavern due to salt creep and lithostatic pressure. It has a surface expression in the form of a gentle subsidence bowl. The rate and magnitude of cavern closure and corresponding subsidence is controlled by the rate of salt creep, the depth

of the cavern, the pressure and temperature conditions during and after the phases of leaching, cyclic storage and withdrawal operation and shut-in, as well as the configuration of caverns in a cluster. From these, the creep rate is perhaps the most uncertain, especially under low deviatoric stress conditions (Bérest et al. 2019 – see also various articles in this issue), which is currently being investigated in new research initiatives. New insights from laboratory experiments under low stress conditions, such as those obtained by Bérest et al. (2019), and theory (e.g. van Oosterhout et al. 2021, this issue) must be taken into account when evaluating the long-term mechanical behaviour of storage caverns and cluster sites. A key challenge here is to unify the observations and theory obtained at the laboratory scale with numerical models and field observations at the cavern scale. In conclusion, the development of storage caverns and assessment of the above aspects requires an integrated approach, where the full life cycle, from initial cavern leaching to abandonment, is considered.

8   Conclusions

It is apparent that hydrogen storage in salt caverns will play a significant role in the energy system of the coming decades. Amongst the main issues that need to be addressed are: the predictability of long-term subsidence in dense cavern clusters and the integrity of the reservoir (cavern), sealing rock formation and wellbore path under fast-cyclic storage operations.

Acknowledgements

References

BERENSCHOT & KALAVASTA 2020. Klimaatneutrale energiescenario's 2050; Scenariostudie ten behoeve van de integrale infrastructuurverkenning 2030-2050. Rapport 61689-Openbaar, maart 2020, pp. 145.

BÉREST, P., GHARBI, H., BROUARD, B., BRÜCKNER, D., DE VRIES, K., HÉVIN, G., HOFER, G., SPIERS, C.J. & URAI, J. 2019. "Very slow creep tests on salt samples." Rock Mechanics and Rock Engineering 52.9 (2019): 2917-2934.

DBI-GUT 2017. The effects of hydrogen injection in natural gas networks for the Dutch underground storages. RVO - Final report

EVANS, D.J. 2008. An appraisal of underground gas storage technologies and incidents, for the development of risk assessment methodology. Health and Safety Executive. RR605 Research Report

GAS INFRASTRUCTURE EUROPE 2021. STORAGE DATABASE, VERSION JULY 2021

GROENENBERG, R., JUEZ-LARRÉ, J., GONCALVEZ, C., WASCH, L., DIJKSTRA, H., WASSING, B., ORLIC, B., BRUNNER, L., VAN DER VALK, K., HAJONIDES VAN DER MEULEN, T. & KRANENBURG-BRUINSMA, K., 2020. "Techno-Economic Modelling of Large-Scale Energy Storage Systems." TNO report 2020 R12004.

JUEZ-LARRÉ, J., VAN GESSEL, S.F., DALMAN, R., REMMELTS, G. & GROENENBERG, R. 2019. Assessment of underground energy storage potential to support the energy transition in the Netherlands. First break, vol. 37-7, p 57-66. Labaune, P., and Rouabhi, A., 2019. "Dilatancy and tensile criteria for salt cavern design in the context of cyclic loading for energy storage." Journal of Natural Gas Science and Engineering 62 (2019): 314-329.

HEINEMANN, N., ALCALDE, J., MIOCIC, J.M., HANGX, S.J.T., KALLMEYER, J., OSTERTAG-HENNING, C., HASSANPOURYOUZBAND, A., THAYSEN, E.M., STROBEL, G.J., SCHMIDT-HATTENBERGER,

C., EDLMANN, K., WILKINSON, M., BENTHAM, M., HASZELDINE, R.S., CARBONELL, R. & RUDLOFF, A. 2021. Enabling large-scale hydrogen storage in porous media – the scientific challenges.: Energy and Environmental Science., 2021, 14, 853

IFG, 2008. Rock-mechanical Appraisal on the Positioning of additional Caverns in the Zuidwending Salt Dome and Safety Distances between Aardgas Storage Caverns. Annex 10 of the Zuidwending storage plan – 2012

KRUCK, O.., & CROTOGINO, F, 2013. "Benchmarking of Selected Storage Options". Hyunder Deliverable 3.3 - Assessment of the potential, the actors and relevant business cases for large scale and seasonal storage of renewable electricity by hydrogen underground storage in Europe.

SCHEEPERS, M., GAMBOA, S., ELODIE JEGU, P., PUPO, L., DE OLIVEIRA, N., RUTTEN, L., VAN STRALEN, J., SMEKENS, K. & WEST, K., 2020. Towards a sustainable energy system for the Netherlands in 2050. TNO 2020 P10338, Final report

SCHREINER, W., LINDERT, A. & BRÜCKNER, D. 2010. "IfG Cavern design concept. Rock mechanical aspects for the development and operation of rock salt caverns." Proc. SMRI Fall Meeting, Leipzig, Germany. 2010.

SIJM, J., JANSSEN, G., MORALES-ESPANA, G., VAN STRALEN, J., HERNANDEZ-SERNA, R. & SMEKENS, K. 2020. "The role of large-scale energy storage in the energy system of the Netherlands, 2030-2050". TNO report 2020 P11106.

TNO & EBN, 2021. Ondergrondse energieopslag noodzakelijk voor toekomstig energiesysteem. TNO-EBN White Paper

VAN DER VALK, K., VAN UNEN, M., BRUNNER, L. & GROENENBERG, R. 2020. "Inventory of risks associated with underground storage of compressed air (CAES) and hydrogen (UHS), and qualitative comparison of risks of UHS vs. underground storage of natural gas (UGS)". TNO report 2020 R12005

VAN GESSEL, S.F., HUIJSKES, T., JUEZ-LARRÉ, J. & DALMAN, R. 2021. Ondergrondse Energieopslag in Nederland 2030 – 2050 Technische evaluatie van vraag en aanbod. TNO report 2021 R11125.

VAN OOSTERHOUT, B.G.A., HANGX, S.J.T. & SPIERS, C.J. 2022. "A threshold stress for pressure solution creep in rock salt: Model predictions vs. observations" 10th Salt Mechanics Conference Proceedings (this issue). 2022

WASSING, B. & GROENENBERG, R., 2022. "Modelling cyclic injection and withdrawal of gas for subsurface energy storage in salt caverns". 10th Salt Mechanics Conference Proceedings (this issue). 2022

Modelling cyclic injection and withdrawal of gas for subsurface energy storage in salt caverns

Brecht Wassing[1*], Remco Groenenberg[1], Jan ter Heege[1]

[1]TNO – Applied Geosciences, the Netherlands

* brecht.wassing@tno.nl

ABSTRACT: The cyclic injection and withdrawal of gas during Compressed Air Energy Storage and Hydrogen Energy Storage in a salt cavern causes variations in the internal cavern pressure and temperature. This can have an adverse effect on the mechanical integrity and stability of the salt cavern. We conducted geomechanical numerical simulations to assess the integrity of salt caverns used for storage. Two axial symmetric geomechanical models of a single storage cavern were constructed in the numerical finite element simulator DIANA: one for CAES and one for HES. Salt deformation was modelled taking into account steady-state creep driven by the differential stress. The constitutive model for the steady-state salt creep used in the simulations combines two different terms: (i) a branch for the non-linear power law creep (i.e. a dislocation creep branch) and (ii) a linear creep branch (i.e. a solution-precipitation creep branch). We investigated the influence of the different scenarios for pressure and temperature cycling on cavern convergence, temperature fluctuations in the cavern wall and cavern integrity. The simulations addressed the potential for tensile failure and dilation of the rock salt in the cavern wall. The implications for subsurface energy storage applications are also discussed.

1   Introduction

Large-scale centralized storage of energy underground is key to ensuring a reliable and secure supply of sustainable energy, as it can provide balancing solutions for seasonal variations in the supply of wind and solar energy and strategic energy reserves. Groenenberg et al. (2020) describe the potential of large scale subsurface energy storage in salt caverns in the Netherlands, mainly in the form of Hydrogen Energy Storage (HES) and Compressed Air Energy Storage (CAES). For a safe and effective application of subsurface energy storage, risks associated with the storage operations need to be identified, assessed and mitigated. Both techniques for energy storage rely on relatively high frequency cycles (intra-daily to daily for CAES up to monthly for HES) of injection and withdrawal of gas from the salt cavern. The cyclic injection and withdrawal of gas causes variations in the internal cavern pressure and temperature, which in turn could have adverse effects on the mechanical integrity and stability of the salt cavern.

In this study, we apply numerical simulations to assess the mechanical integrity of the salt caverns used for storage. We analyze the thermo-mechanical effects of high-frequency daily to monthly cyclic loading on cavern wall convergence and the evolution of stresses in the rock salt near the cavern wall. We built two single-cavern models in the finite element software of DIANA (*DIANA FEA*, 2019), representing: i) a salt cavern used for compressed air storage and ii) a salt cavern used for hydrogen storage. Cavern geometry, stratigraphy and model input parameters and assumptions are representative of Dutch subsurface conditions, and largely based on data available from the underground gas storage sites in the Netherlands (Breunese et al., 2003, IfG, 2011, Van Heekeren et al., 2009, Nederlandse Gasunie, 2012). The full sequence of cavern leaching, cavern debrining, cyclic cavern energy storage operations and maintenance is simulated. The scenarios for storage operations, in terms of storage volumes, frequency and duration of injection and withdrawal cycles, pressure and temperature ranges and maintenance are based on the literature and considerations of current and possible future upscaling of energy storage operations.

2 Geomechanical model of hydrogen and compressed air storage in salt caverns

2.1 Model geometry

We built two axial symmetric geomechanical models of a single storage cavern, one for CAES and one for HES. The stratigraphy of the model is based on the formations found at the Zuidwending salt dome (Nederlandse Gasunie, 2012) and summarized in Table 1.

Table 1: Lithological units (based on stratigraphy at the Zuidwending salt dome)

Layer		Density [kg/m^3]	Young's modulus [GPa]
North Sea Group	Sand and clay		0-115
Caprock	Gypsum, anhydrite and clay		115-200
Zechstein	Rock salt		200-2900
Rotliegend	Sandstone		2900-3000

Both models represent a single cylindrical cavern; cavern dimensions and depth of the cavern for CAES simulations are smaller than for HES simulations. Model dimensions are summarized in Table 2. The well which is used for gas injection and production is vertical and aligned with the symmetry axis of the finite-element model. Model layers are horizontal and meshed with quadratic second-order eight-node quadrilateral ring elements to ensure sufficient solution accuracy. We apply no displacements in the horizontal direction at the vertical boundaries and no displacements in the vertical direction at the lower horizontal model boundary (Figure 2).

Table 2: Cavern dimensions (cylindrical) for CAES and HES

Cavern use	Cavern height (m)	Cavern top (m depth)	Cavern base (m depth)	Radius (m)	Volume (mln m3)
CAES	350	1100	1450	22	0.53
HES	450	1150	1600	27	1.0
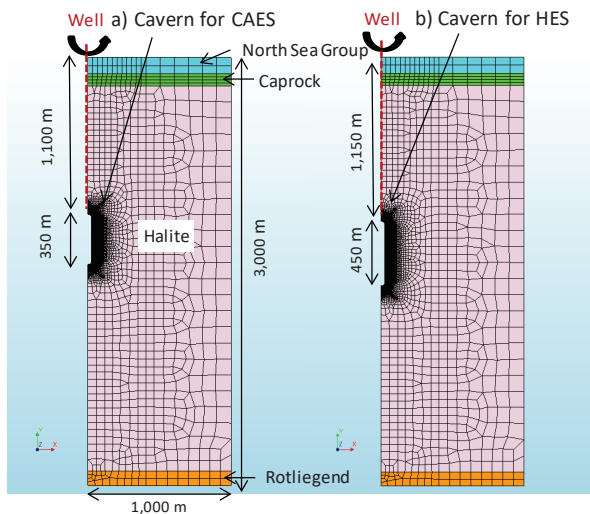
Figure 1: Axial symmetric finite element model of a salt cavern used for a) Compressed Air Energy Storage (CAES) and b) Hydrogen Energy Storage (HES).

2.2 Material properties

The basic driving mechanism for time-dependent deformation (creep) around salt caverns are stress differences in the salt near the caverns and in far field. For modelling salt creep in the Zechstein salt, we use a constitutive model for salt creep in DIANA based on the Ellis formulation (as described in Fokker, 1995). This constitutive model is derived for steady-state creep driven by the differential stress, based on experimental data. The model combines two branches, each describing different deformation mechanisms: (i) a power-law creep branch for dislocation creep with a non-linear relation between stress and strain rate, and (ii) a linear creep branch for solution-precipitation creep:

$$\dot{\varepsilon}_{axial} = A_1 \, exp(-\frac{Q_1}{RT})(\frac{\Delta\sigma}{\alpha})^{n1} + A_2 \, exp(-\frac{Q_2}{RT})(\frac{\Delta\sigma}{\alpha})^{n2} \qquad (1)$$

where A_1 and A_2 are the creep strain coefficients (1/s), $\dot{\varepsilon}_{axial}$ is the vertical strain rate (1/s), $\Delta\sigma = \sigma_{axial} - \sigma_{radial}$ is the differential stress of a triaxial loading test (Pa), Q_1 and Q_2 are the activation energies (J/mol), R is the gas constant, T is the ambient temperature (K), α is the reference stress (Pa), and n_1 and n_2 are the stress exponents for non-linear creep ($n_1>1$) and the linear creep ($n_2=1$), respectively. Note that different pre-exponential factors and (normalized) variables are incorporated in A_1 and A_2 (i.e. A_2 is dependent on grain size, while A_1 is not).

Creep parameters are obtained based on the Zuidwending experimental data (IfG, 2007, Figure 2). The black-dashed line shown in Figure 2 is a power-law fit to the data, which assumes that only non-linear creep is active at all differential stresses. Other experimental data suggest that creep at low differential stress is better fitted if a linear creep branch (grey solid line) is added. Material properties for linear creep are based on previous subsidence studies for the Barradeel site in the Netherlands (Breunese et al., 2003, Van Heekeren et al., 2009). For this study, we use combined non-linear (power law) and linear creep models.
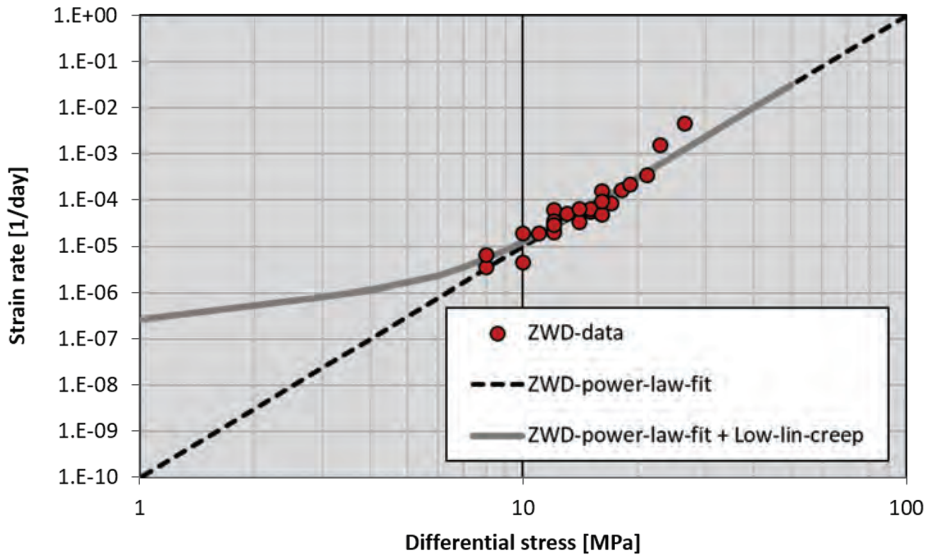
Figure 2. Steady state creep parameters fitted to the Zuidwending experimental data (IfG, 2007, Groenenberg et al., 2020). Black dashed line indicates power-law fit (nonlinear branch only). Grey solid lines represents a combination of a nonlinear and linear creep branch, with linear creep parameters based on data from Barradeel. In this study, we use the combined power-law and low linear creep model.

Creep parameters and parameters for caprock, over- and underburden are summarized in Table 3. We assume linear elastic behavior for all layers other than rock salt.

Table 3a: Material parameters used in simulations

Unit	Density (kg/m^3)	Young's modulus (GPa)	Poisson's ratio (-)	Thermal exp. coef. (1/K)	Heat conductivity (J/day m K)	Heat capacity (J/m^{3}K))
North Sea Group	2050	10	0.25	3e-5	1.71e5	1.84e6
Caprock	2050	15	0.25	3e-5	1.71e5	1.84e6
Zechstein	2179	32	0.26	5e-5	4.28e5	1.84e6
Rotliegend	2200	15	0.20	3e-5	1.71e5	1.84e6

Table 3b: Salt creep properties

Constitutive model	A_1 (1/day)	n_1	Q_1/R (K)	A_2 (1/day)	n_2	Q_2/R (K)	α (MPa)
Rock salt	0.053	5	6495	0.0029	1	3007	1

The salt dilation criterium used to evaluate the integrity of the salt cavern is based on the following expression (De Vries, 2006):

$$\sqrt{J_2} = C\, I_1 \tag{2}$$

Where I_1 is the first invariant of the stress tensor, J_2 is the second invariant of the deviatoric stress tensor, and C is a material constant (value typically near -0.27).

2.3 Load cases for CAES and HES

Cavern response is modelled during 1) cavern leaching, 2) replacement of cavern brine by air/gas, 3) injection and withdrawal cycles during CAES and HES operations and 4) cavern maintenance under atmospheric pressures. Multiple scenarios for cycling are modelled, varying the cycle duration, pressure and temperature ranges for the injection/withdrawal cycles and duration of the maintenance period.

Cavern leaching (CAES and HES). In-situ stresses and temperatures in both models are initialized assuming a horizontal-to-vertical stress ratio $K_0 = 1$ in the Zechstein salt layer and $K_0 = 0.7$ in the other layers. The temperature field is initialized with a thermal gradient of 0.025 °C/m, which is representative for salt deposits in the Netherlands. The leaching phase is modelled by assuming that the cavern is present from the start of simulations. Initially, the pressure inside the cavern is assumed to be equal to the lithostatic stress, simulating in-situ isotropic stresses in the rock salt prior to cavern leaching. Cavern leaching is then modelled by gradually reducing the initial lithostatic pressure inside the cavern to the hydrostatic pressure of brine, i.e. halmostatic pressure (defined with a pressure gradient of 11.8 kPa/m) over the total leaching period. Thermal effects of leaching are caused by injection at temperatures lower (15°C) than the in-situ salt temperature (40-50°C). A thermal boundary condition is applied on the cavern roof, walls and floor to simulate the temperatures in the cavern during leaching, to simulate cooling down of salt in the cavern wall due to injection of cold brine. This cooling down is applied as a linear function of time needed to leach out the storage cavern. The time for cavern leaching is assumed to be 2 years for the smaller CAES

cavern and 3.5 years for the larger HES cavern. Figure 3 shows pressure and temperature evolution at the cavern wall during the cavern leaching phase.
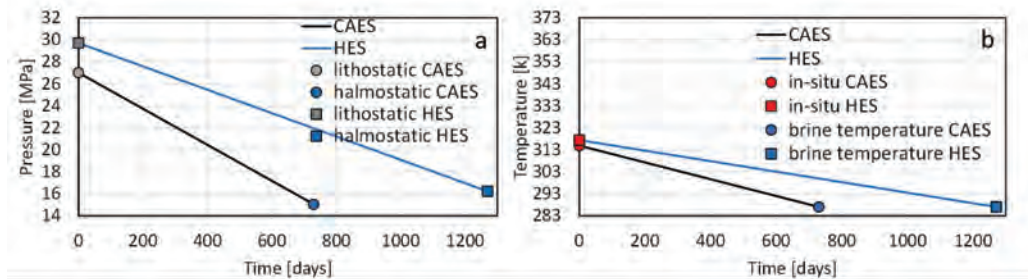
Figure 3. a) Evolution of internal cavern pressure for CAES and HES during cavern leaching, shown at cavern midheight; -1275 m and -1375 m depth for CAES and HES respectively. b) Temperature at the cavern wall during cavern leaching, shown at cavern mid-height.

Debrining, storage operations and maintenance (CAES). We assume cavern debrining takes place immediately after the cavern leaching phase. Compressed air is injected into the salt cavern, while simultaneously removing the brine. The brine is fully replaced by air after 30 days. During debrining, the cavern pressures are gradually decreased from halmostatic to 14MPa. During the leaching phase, the cavern is gradually cooled down by the brine from the in-situ temperature of 40-50°C to 15°C (287°K). During subsequent debrining, the cavern is warmed up again by injection of hot compressed air. At the end of debrining, the temperature of air in the cavern is 40°C (313°K).

We base our estimates of changes in cavern temperature during cycling on the literature data (Nieland, 2008; Düsterloh and Lux, 2010). Fluctuations in gas temperature in the cavern generally depend on rates of pressure rise or decline, the duration of the injection/withdrawal cycles and the temperature of air at the well head. We adopt a change in cavern air temperature of 1.3°C/bar. This means that during injection for every bar pressure increase air temperature increases by 1.3°C, due to compression of the gas. During air withdrawal temperature of the air decreases by the same amount due to expansion of the gas. The adopted value of 1.3°C/bar is representative for short periods of injection and withdrawal that may last from several hours to days, depending on cavern volume and the operating pressure range. Well head injection temperature is 15°C.

For this study, we assume three scenarios for CAES operations. In all scenarios for CAES, we simulate 10 injection and withdrawal cycles, followed by a maintenance period of varying length directly after the first 10 cycles. The pressure in the cavern during cycling varies linearly between a minimum of 140 bar and a maximum of 180 bar, and vice versa. Each injection and withdrawal period lasts 12 hours. In between each injection and withdrawal operation, an idle time of 24 hours is simulated, during which pressures are kept constant at either 140 bar or 180 bar. Temperature of the air in the cavern varies linearly between 40°C and 79°C, which corresponds to the temperature change of 1.3°C/bar as mentioned above. We simulate three scenarios for the length of the maintenance period, i.e. 1, 7 and 30 days. During maintenance, cavern pressure amounts to 1 bar and air temperature is 15°C (see Figure 4).

Debrining and storage operations (HES). Similar as for CAES loading, HES cavern debrining is assumed to take place during 30 days immediately after the leaching phase, with brine being replaced by H_2. During this phase, cavern pressures gradually decline from an initial halmostatic pressure gradient to a uniform pressure of 80 bar at the start of HES cycling. For this study we simulate two scenarios for injection and withdrawal cycles, which are based on

the literature and considerations of current and possible future upscaling of energy storage operations. For both cases, pressures during cycling vary linearly between 80 bar (end withdrawal / start injection) and 180 bar (end of injection / start production). In the first scenario, we assume a duration of one full cycle of injection and withdrawal of one month and simulate 10 cycles in total. In the second scenario, one full cycle of injection and withdrawal lasts one year, with 5 cycles simulated in total. No idle time is modelled for HES. The variations in temperature of the H_2 gas during cycling are based on values obtained from literature (Nieland, 2008). A temperature change of 0.2°C/bar is used to simulate the temperature evolution during the monthly cycles, whereas 0.06°C/bar is used for the yearly cycles. For operational scheme see Figure 5. Well head injection temperature for the monthly cycles is varied between 15°C and 50°C.
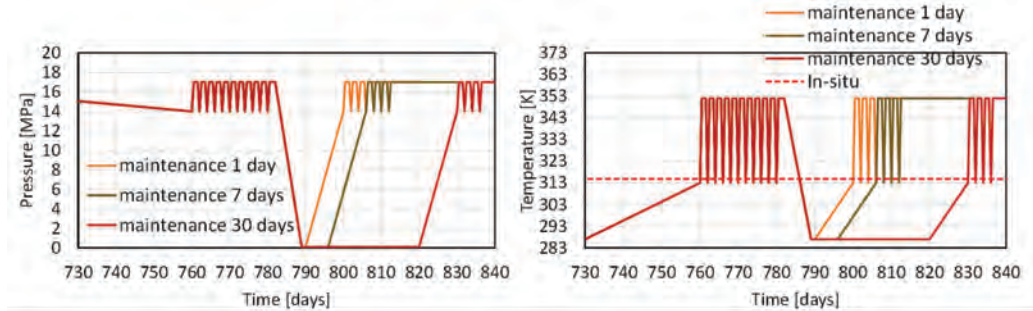
Figure 4. Evolution of internal cavern pressure (a) and temperature (b) for CAES during cavern debrining, cycling operations and maintenance period. Pressures are shown at cavern midheight, i.e. -1275 m depth.
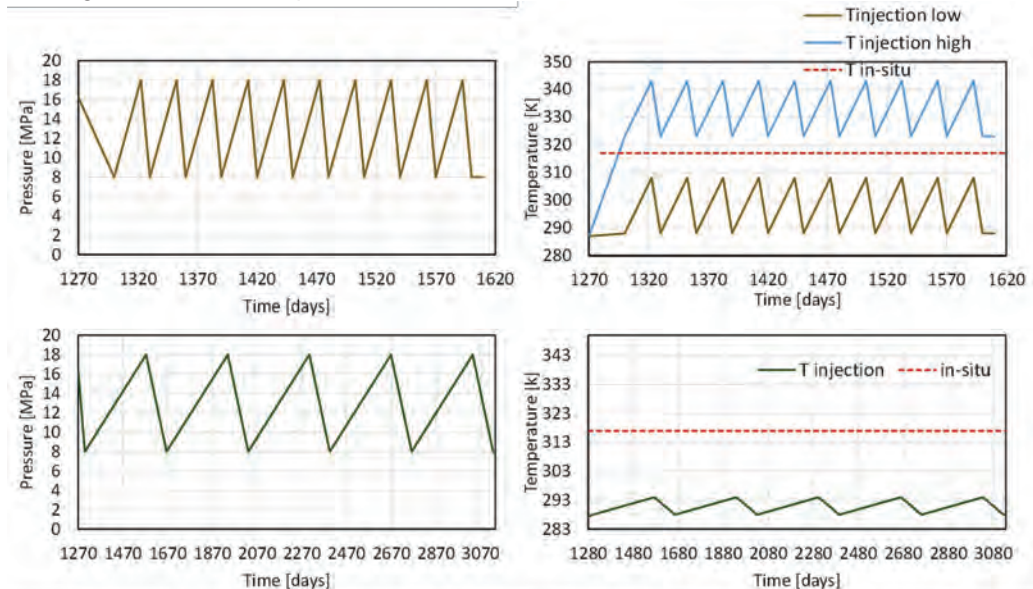
Figure 5. a-b) Evolution of internal cavern pressure and temperature for HES during cavern debrining and cycling operations, monthly cycling; c-d) Pressure and temperature for HES during cavern debrining and cycling operations, yearly cycling. Values are shown at -1375 m depth (cavern mid-height).

3   Model results of CAES and HES storage operations

We investigate the influence of the different phases and scenarios for pressure and temperature cycling on cavern convergence, temperature fluctuations in the cavern wall and cavern integrity. In particular, the potential for tensile failure and dilation of the rock salt in the cavern wall is addressed.

CAES. In Figure 6 we present the results for CAES. We observe a significant cooling of the rock salt some tens of meters into the cavern wall during cavern leaching. This cooling effect is gradually annihilated during subsequent cycling. Cavern wall temperature increases with the number of cycles and increase above in-situ rock salt temperatures in all simulated scenarios for CAES cycling (Figure 6a). We observe temperature fluctuations during cycling which extend approximately 1 m into the cavern wall. During maintenance temperatures in the rock salt around the cavern decrease; the penetration depth of the cooling front into the rock salt increases with the duration of maintenance period. Cycling after maintenance gradually warms up the rock salt. Dilation of rock salt and tensile failure in the cavern wall can occur both due to rapid decompression and cooling during the extraction phase of cycling operations and under low atmospheric cavern pressures during maintenance. Model results show that a longer duration of maintenance period (30 days versus 1 day) promotes cavern convergence (Figure 6b), tensile stressing (Figure 6c and e) and dilation (Figure 6d and f) in the cavern wall. Our model results indicate that the extent of dilation and tensile failure is limited to a thin skin at the cavern wall.
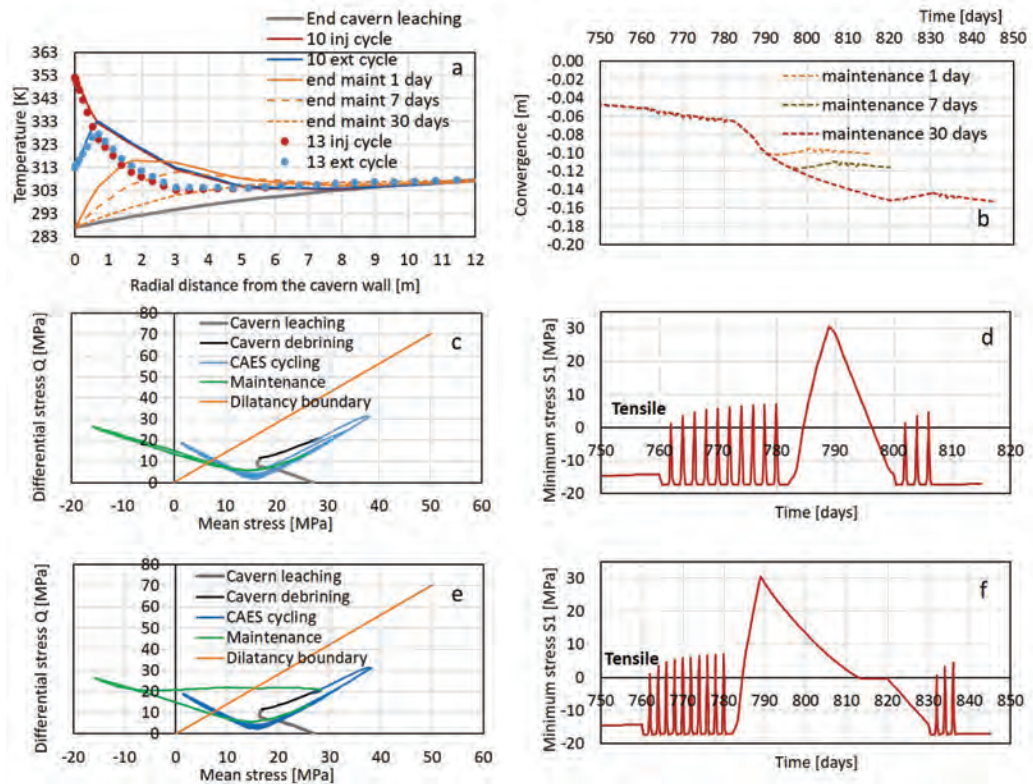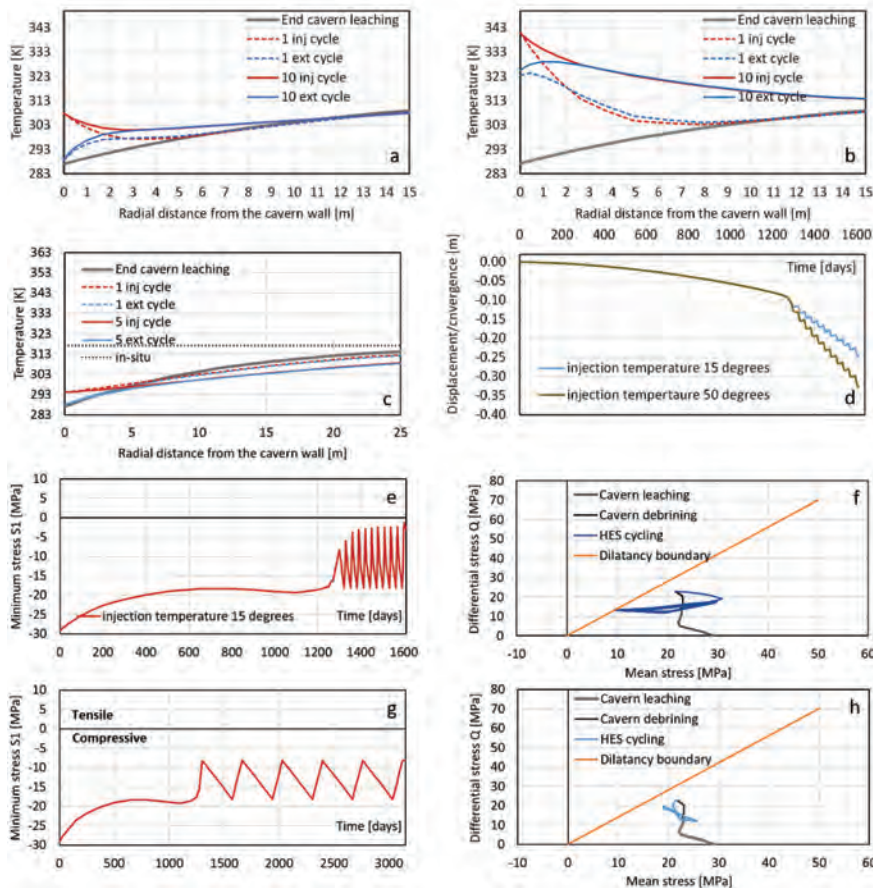

Figure 6. Model results for CAES: a) Temperature at the end of cavern leaching, during cycling and at the end of maintenance. Temperature change during maintenance depends on duration of maintenance period. Small dots present temperature change after 13th cycle, after a maintenance period of 30 days, b) cavern convergence (horizontal displacements) for three

different maintenance periods, c) PQ stress path versus dilation boundary criterium, for a maintenance period of 1 day, d) minimum principal total stress near the cavern wall, for a maintenance period of 1 day, e) PQ stress path versus dilation boundary criterium, for a maintenance period of 30 days, f) minimum principal total stress near the cavern wall, for a maintenance period of 30 days. All plots show values at mid-height cavern depth (-1275 m).

HES. We present similar plots with model results for HES in Figure 7. Again, we observe a significant cooling of the rock salt some tens of meters into the cavern wall during cavern leaching. This effect is partially counterbalanced by heating during HES cycling, specifically for the high wellhead temperature. In contrast to the high-frequency CAES cycles, cavern wall temperatures remain below in-situ temperatures during HES cycling for well head temperatures of 15°C. However, in case of a wellhead injection temperature of 50°C, temperatures in the salt may increase above in-situ temperatures during both the injection and withdrawal cycles. After 10 cycles this heating effect has extended several meters into the cavern wall. The longer monthly and yearly cycles during HES reduce the potential for dilation and tensile stressing in the cavern wall as compared to CAES (Figure 7e-f). We observe that higher wellhead temperatures do affect the amount of convergence (Figure 7d), but only slightly change the potential for tensile failure and dilation in the cavern wall (results not shown here).

Figure 7. Model results for HES a) Temperature at the end of cavern leaching, during monthly cycling and at the end of maintenance for an injection temperature of 15°C; b) temperature at the end of cavern leaching, during monthly cycling and at the end of maintenance for an injection temperature of 50°; c) temperature at the end of cavern leaching, during yearly cycling

and at the end of maintenance for an injection temperature of 15°C; d) cavern convergence (horizontal displacement (m)) for two different injection temperatures, monthly cycles; e) minimum principal total stress near the cavern wall, injection temperature of 15°C, monthly cycles; f) PQ stress path versus dilation boundary criterium for injection temperature of 15°C, monthly cycles, g) minimum principal total stress near the cavern wall, injection temperature of 15°C, yearly cycles, h) PQ stress path versus dilation boundary criterium, injection temperature of 15°C, yearly cycles. All plots show values at mid-height cavern depth (-1375 m).

4 Conclusions

Cyclic injection and withdrawal of compressed air or hydrogen causes variations in the internal cavern pressure and temperature, which in turn could have adverse effects on the mechanical integrity and stability of the salt cavern. Results of the geomechanical numerical simulations in this study indicate that dilation of rock salt and tensile failure in the cavern wall can occur both due to rapid decompression and cooling during the extraction phase of cycling operations, in particular during the short (intra-daily) cycles for CAES and under low atmospheric cavern pressures during maintenance. Dilation and tensile failure may lead to the formation of fractures only in a small area around the cavern wall. Model results suggest that even during maintenance periods, or in extreme cases, when the cavern would experience atmospheric conditions for a prolonged period (like months), the depth of penetration in the cavern wall is limited and is unlikely to jeopardize cavern integrity. However, we note that the constitutive model for salt creep that was used in this study includes the secondary steady state stage of salt creep, but does not include primary creep and does not account for potential effects of failure, damage and accelerating creep rates during the tertiary creep stage. Also, the effect of permeability increase by tensile failure and dilation, and the potential progressive growth of fractures into the salt has not been modelled. Furthermore, during HES operations hydrogen may migrate into the cavern wall and affect properties and creep behavior of the rock salt, which is also not accounted for in this study. Further experimental research is needed to characterize and quantify the salt material behavior when interacting with air or hydrogen at specific CAES and HES energy storage conditions.

References

Breunese, J.N., van Eijs, R.M.H.E., de Meer, S. & Kroon, I.C. 2003. Observation and prediction of the relation between salt creep and land subsidence in solution mining. The Barradeel case. Proc. 5th SMRI (Solution Mining Research Institute) Conference, 5 - 8 October 2003, Chester, United Kingdom.

DeVries, K.L. 2006. Geomechanical analyses to determine the onset of dilation around natural gas storage caverns in bedded salt. Proc. SMRI (Solution Mining Research Institute) Spring 2006 Conference, 30 April - 3 May 2006, Brussels, Belgium.

DIANA FEA. 2019. Finite element program and Users documentation, version 10.3. https://dianafea.com.

DÜSTERLOH, U. & LUX, K.-H. 2010. Some geomechanical aspects of compressed air energy storage (CAES) in salt caverns. Proc. SMRI (Solution Mining Research Institute) Fall 2010 Conference, 3 - 6 October 2010, Leipzig, Germany.

FOKKER, P.A. 1995. The behaviour of salt and salt caverns. PhD thesis, Delft University of Technology.

GROENENBERG, R., JUEZ-LARRÉ, J., GONCALVEZ, C., WASCH, L., DIJKSTRA, H., WASSING, B., ORLIC, B., BRUNNER, L., VAN DER VALK, K., HALJONIDES, VAN DER MEULEN, TH., KRANENBURG-BRUINSMA, K. 2020. TNO-report 2020 R12004. Techno-Economic Modelling of large-Scale Energy Storage Systems.

IFG REPORT 11/2007. 2007. *Rock Mechanical Investigations on Rock Salt from the Zuidwending Gas Storage Site.* IfG Institut fur Gebirgsmechanik GmbH, Report B IfG 11/2007.

IFG REPORT 49/2011. 2011. Case Studies for Cyclic Operated Storage Caverns 'Aardgasbuffer Zuidwending' *NL.* IfG Institut fur Gebirgsmechanik GmbH, Report B IfG 49/2011.

NEDERLANDSE GASUNIE 2012. Gewijzigd opslagplan Zuidwending (Application for gas storage at the Zuidwending salt dome).

NIELAND, J.D. 2008. Salt cavern thermodynamics – Comparison between hydrogen, natural gas, and air storage. Proc.SMRI (Solution Mining Research Institute) Fall 2008 Conference, 13 - 14 October 2008, Galveston, Texas, USA.

VAN HEEKEREN, H., BAKKER, T., DUQUESNOY, T., DE RUITER, V. & MULDER, L. 2009. Abandonment of an extremely deep cavern at Frisia salt. Proc. SMRI (Solution Mining Research Institute) Spring 2009 Technical Conference, Krakow, Poland.

Long-term operational stability analysis of underground storage in horizontal salt cavern with interlayer

Jun Jiang[1,2], Zhengmeng Hou[2,3*], Kepeng Hou[1,2],Wei Sun[1,2], Yanli Fang[3]

[1]Faculty of Land and Resources Engineering, Kunming University of Science and Technology, China

[2]Yunnan Key Laboratory of Sino-German Blue Mining and Utilization of Special Underground Space, China

[3]Institute of Subsurface Energy Systems, Clausthal University of Technology, Germany

*hou@tu-clausthal.de

ABSTRACT: A rock salt cavern is an ideal underground energy storage. Most rock salt deposits in China are thin-layered deposits with interlayers. Therefore, we suggest horizontal rock salt caverns because of much larger storage volumes. Taking the ellipsoidal horizontal single-cavern and double-caverns in rock salt with a single interlayer in the cavern middle as examples, the natural gas storage models were simulated by COMSOL three-dimensional software. The changes of vertical and horizontal displacement, volume convergence and stress-strength-ratio distribution in with different diameter-to-height ratios (N = 1.5, 2.0, 2.5 and 3.0) and operation times (t= 5, 10, 15, 20 years) were analyzed, and the optimal diameter-to-height ratio of N = 2.5 and the optimal pillar width of 100m were determined.

1   Introduction

A rock salt cavern is an ideal underground energy storage. Most rock salt deposits in China are thin-layered deposits, and a horizontal salt cavern has a larger storage volume than a vertical salt cavern (Wu et al. 2005; Xing et al. 2015; Tang et al. 2010). However, Chinese rock salt generally contains some interlayers, such as anhydrite, glauberite and mudstone etc. (Liang et al. 2008; Xing et al. 2014; Wang et al. 2015). In the process of solution mining, the horizontal salt cavern would intersect with the interlayer. How to improve the storage capacity of the rock salt caverns and ensure the safety and stability of the long-term operation have become a hot issue in last 15 years (Yin et al. 2006; Hao et al. 2014; Wu & Shao 2019), e.g. many in-depth studies on the long-term stability of rock salt caverns (Tang et al. 2010; Ma et al. 2017; Wang et al. 2020; Wang et al. 2021; Wu et al. 2019). Huang et al. carried out a numerical analysis on the variation law of shear stress at the interface between rock salt and interlayer. Li et al. (2013) derived the bond constraint stress at the interface, and analyzed the interface shear failure by using the maximum shear stress theory. Li et al. (2014) discussed the effect of interlayer Young's modulus on the stress field around salt cavern and on the interface sliding through numerical analysis. Moghadam et al. (2012) used the finite element method to analyze the effect of interlayer thickness on the shear failure tendency of the cavern wall. Wang et al. (2012) obtained the radial stress and tangential stress formula of the interlayer and rock salt near the contact surface, by increasing or decreasing the local internal pressure, and used the Hoek-Brown criterion to analyze the influence of the internal pressure change on the cavern wall damage. Some scholars have also studied the stability of mudstone interlayers during gas storage operation. Bauer et al. (1998) firstly used the bending theory to study the shear, tensile and other failure modes of the mudstone interlayer on the roof of the salt cavern for gas storage. However, this research did not consider the influence of the horizontal in-situ stress and creep characteristics on the failure mechanism of the mudstone interlayer. Charnavel & Lubin (2002) analyzed the influence of insoluble mudstone interlayers on the final shape of the salt cavern. Bekendam et al. (2003) studied numerically the mechanical mechanism of the roof interlayer collapse of the salt cavern for gas storage, summed up the possible failure modes such as tensile and shear failure of the interlayer, but the study did not carry out a detailed analysis of the failure mechanism of the sandwich (Bekendam & Paar 2002). DeVries et al. (2004) simulated and comprehensively analyzed the influence factors, such as the span, depth, thickness of mudstone interlayer and stiffness of mudstone roof on the operation safety of the salt caverns for gas storage.

At present, most studies focus on the long-term stability of vertical salt caverns and relatively few studies on that of horizontal salt caverns. However, in thin-layered rock salt deposits, the storage capacity of horizontal caverns is much larger than that of vertical caverns [25-28]. Therefore, it is necessary to conduct in-depth research on the feasibility and long-term stability of horizontal salt caverns for energy storage [29-32]. In this paper, we use COMSOL three-dimensional software to optimize the pillar width between horizontal double-caverns and the diameter-to-height ratio of a horizontal single-cavern.

2   Simulation models and parameters

2.1   Shape of rock salt caverns

As mentioned in Section 1, for thin-layered salt deposits with interlayers, vertical caverns cannot achieve high storage capacity. In this case, using a large-span horizontal cavern as the design shape can effectively improve the storage capacity and may solve the problems of stability and tightness of storage caverns as well. However, there are relatively few studies on the long-term stability of horizontal caverns in rock salt. Therefore, the long-term stability of ellipsoidal horizontal caverns (Fig. 1) was simulated and analyzed.
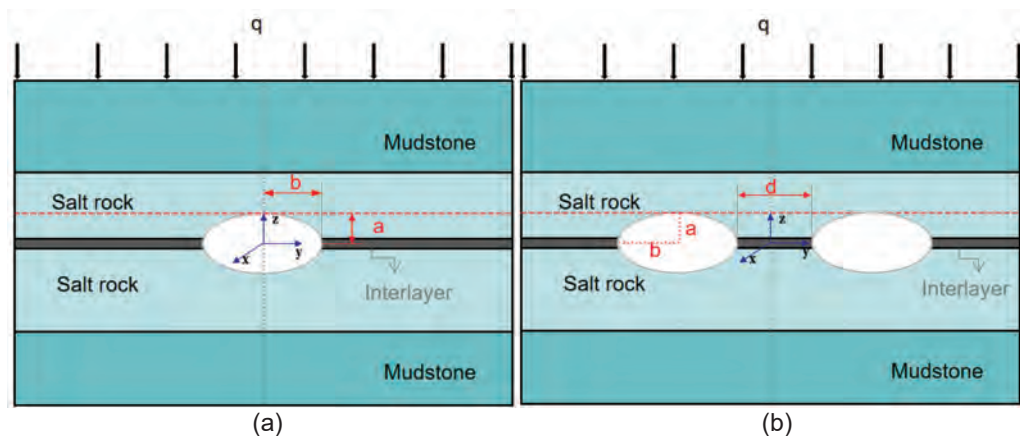
Figure 1: Schematic diagram of simulation models for ellipsoidal horizontal caverns in rock salt with a single interlayer in the cavern middle. (a) Single cavern and (b) Double caverns.

2.2   Geological conditions

The studied rock salt deposit lies in a depth of 1000-1120m, and the upper and lower layers of the rock salt are mudstone with 300 m and 280 m mightiness respectively. The interlayer with a thickness of 4m is located at a depth of 1058-1062m, and the fixed height of ellipsoidal horizontal caverns is 60m (cavern depth: 1030-1090m). The dimensions of the simulation models in the x, y and z directions are 800m, 800m and 700m respectively (Fig. 2). The front, back, left, right, and bottom of the models are constrained in the normal direction, while a 700m depth corresponding overburden pressure of 17MPa is applied to the top of the models.

2.3   Rock mass mechanical parameters

The simulation models consider three kinds of rock mass materials: rock salt, mudstone and interlayer. We use the power creep model (Norton) for rock salt and interlayer, and the Mohr-Coulomb model for mudstone. Table 1 lists the basic mechanical parameters of the rocks (Yu

2012). The interlayer is a kind of soft salt rock, which has a smaller elastic modulus and a higher creep rate than the rock salt.

Table 1: Basic mechanical parameters

Parameters	Density (g/cm^3)	Elastic modulus (GPa)	Poisson's ratio (-)	Cohesion (MPa)	Internal friction (°)	A 10^{-9} [1/h]	n
Mudstone	2.5	10	0.29	6	35	-	-
Rock salt	2.3	6	0.3	3.5	32	8	3.5
Interlayer	2.3	5	0.3	2.5	32	13	3.5

3 Analysis on underground storage stability of horizontal single-salt cavern with interlayer

The fixed height of ellipsoidal horizontal caverns in rock salt is 60m, that is, the short axis (x & z) of the horizontal ellipsoid is 30m, and the size of the long axis (y) needs to be determined, which affected the storage stability of horizontal salt caverns. However, a smaller long axis determines a smaller storage capacity, while a lager span intends a bigger capacity. Therefore, four single-layer horizontal salt cavern models with different diameter-to-height ratios (N=1.5, 2.0, 2.5, 3.0, the fixed height: 60m) were established, and the effects of different diameter-to-height ratios on their long-term stability were analyzed. Relevant scholars have optimized the traditional single-well and single-pipe structure of rock salt underground storage, and proposed a two-well and two-pipe structure. Rock salt underground storage can basically maintain constant pressure during operation to ensure the working efficiency of storage. In order to ensure the compactness of the underground rock salt storage layer, its maximum operating internal pressure generally does not exceed 80% of the overlying formation pressure. Therefore, the internal operating pressure selected in the numerical simulation in this section is 19MPa. Table 2 shows the model parameters for different working conditions.

Table 2: Model parameters and maximal gas storage volumes of horizontal caverns.

working conditions	a(m)	b(m)	N(b/a)	Operation internal pressure (MPa)	Maximal gas storage volume ($10^6 \cdot m^3$)
1	30	45	1.5	19	32.23
2	30	60	2	19	42.98
3	30	75	2.5	19	53.72
4	30	90	3	19	64.47

3.1 Displacement calculation and analysis

Figures 2 and 3 are the cloud plot of horizontal and vertical displacement of the surrounding rock of the horizontal salt cavern (diameter-to-height ratio: 2.5) after running 5a, 10a, 15a, and 20a (a: years), respectively. During the operation of the horizontal single-cavern in rock salt with interlayers, the horizontal displacements on the left and right sides of the surrounding rock are symmetrically distributed, while the maximum horizontal displacement is in the center of the left and right sides. The maximum vertical displacements (-: subsidence; +: uplift) are on top and bottom of the cavern center, respectively. In case of N=2.5, the maximum subsidence at the top and the maximum uplift at the bottom of the rock salt cavern center are -1.51 m and 0.8 m, respectively, after 20 years of operation. Figure 4 shows that the tendency of maximal horizontal displacements during the operation of horizontal rock salt caverns is the same under different diameter-to-height ratio conditions (N=1.5, 2.0, 2.5 and 3.0). Figure 3(d) and Figure 4

show that when the running time is same, the maximum horizontal displacement of the horizontal salt cavern is gradually increasing with the increase of the diameter-to-height ratio. After running 20a, the maximum horizontal displacements of different diameter-to-height ratios of N=1.5, 2.0, 2.5 and 3.0 are 1.51m, 1.61m, 1.83m and 2.14m, respectively. Figure 5 shows the maximal vertical displacements of the horizontal salt caverns (N=1.5, 2.0, 2.5 and 3.0) as a function of the operating time. In case of N≤2, the maximum subsidence of the salt cavern roof does not change much, while the maximum uplift of the cavern floor tends to decrease relatively (Fig. 5a). In case of N>2, the maximum subsidence of the salt cavern roof and the maximum uplift of the cavern floor will increase accordingly (Fig. 5b). Figures 4 and 5 show that the maximum horizontal and vertical displacements of horizontal rock salt caverns are increasing continuously with the operation time. In the initial stage of operation, the roof-settling rate is much faster (Fig. 5a). After the running time exceeds 2a, the settlement of the cavern roof increases linearly with the running time. Figure 5(b) shows that in the initial stage of operation, the floor-uplifting rate is relatively faster. When the running time exceeds 2a, the uplifting rate of the floor is gradually decreased, and increasing linearly with the running time. Figure 5(a) shows that with the increase of N, the roof subsidence of the horizontal single-cavern gradually increases. After 20a operation, the maximal roof subsidence of caverns with N=1.5, 2.0, 2.5 and 3.0 are 1.28m, 1.32m, 1.51m and 1.76m, respectively. Figure 5(b) shows that with the increase of N, the maximum uplift of the cavern floor first decreases and then increases. After running 20a, the maximum floor uplifts with N=1.5, 2.0, 2.5 and 3.0 are 0.8m, 0.75m, 0.8m and 0.91m, respectively.

(a) (b)

(c) (d)
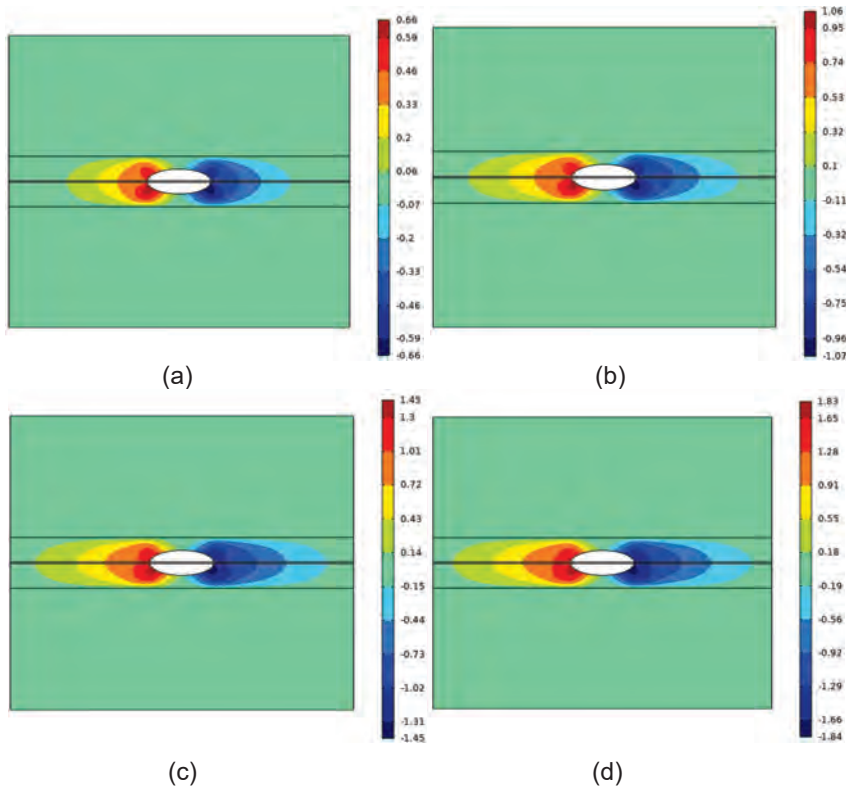
Figure 2: Cloud map of horizontal displacement distributions of surrounding rock of a horizontal single-cavern (diameter-to-height ratio: 2.5) in rock salt. (a) 5a; (b) 10a; (c) 15a; and (d) 20a.
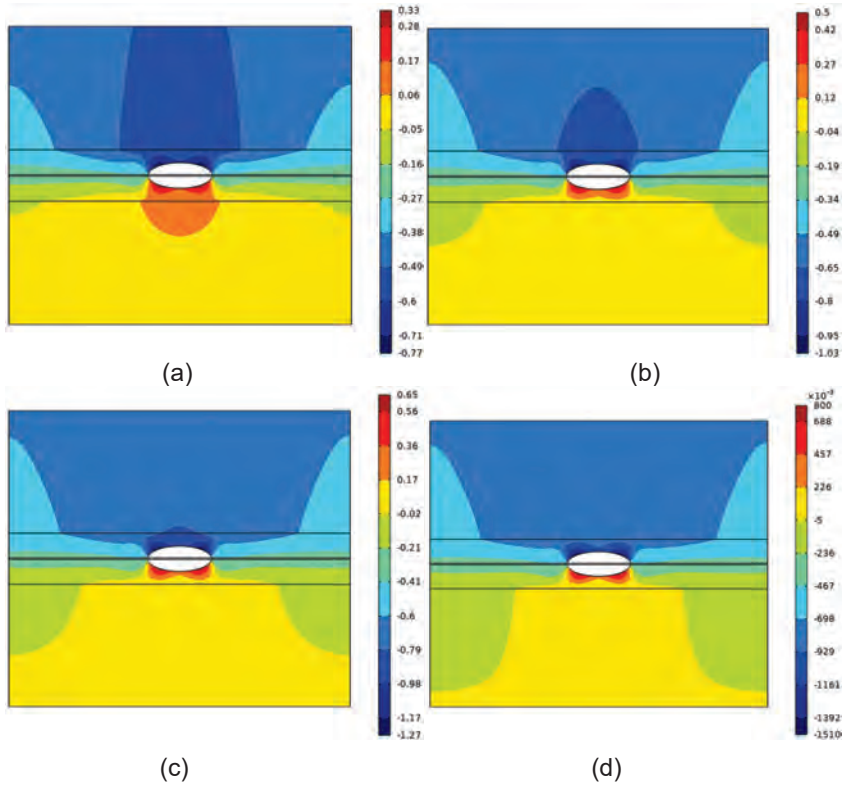
Figure 3: Cloud map of vertical displacement distributions of surrounding rock of a horizontal single-cavern (diameter-to-height ratio: 2.5) in rock salt. (a) 5a; (b) 10a; (c) 15a; and (d) 20a.
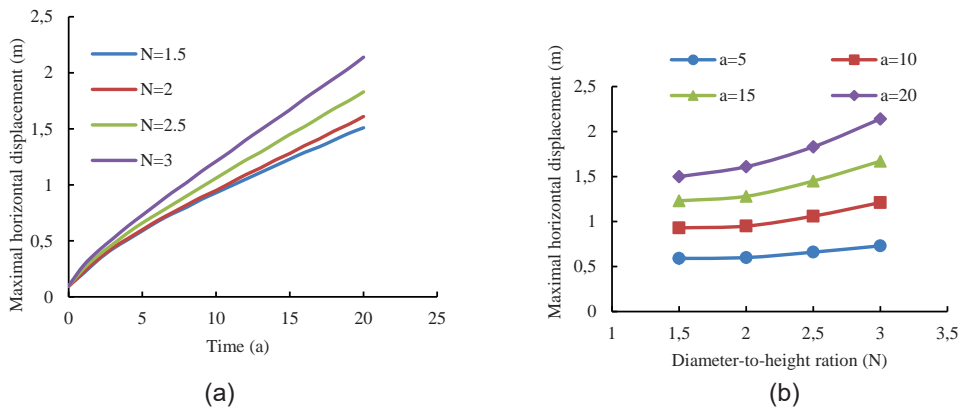
Figure 4: Maximal horizontal displacements with the operation time and the diameter-to-height ratio. (a) Maximal horizontal displacement changing with operation time. (b) Maximal horizontal displacement changing with the diameter-to-height ratio.
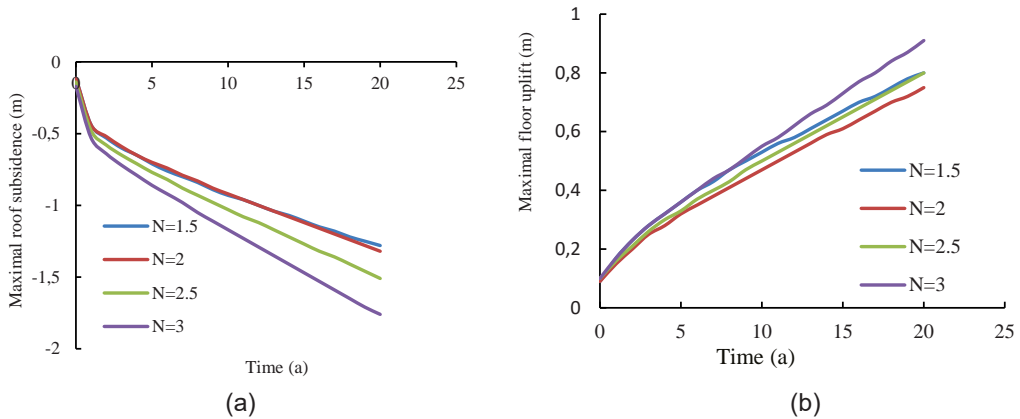
Figure 5: Maximum vertical displacements of horizontal single-caverns (N = 1.5, 2, 2.5, 3) in rock salt with the operation time. (a) Roof subsidence. (b) Floor uplift.

3.2 Cavern convergence

Table 2 shows among others the maximal gas storage volumes of the horizontal salt caverns with four different diameter-to-height ratios. By processing the displacement data of the salt caverns obtained by numerical simulations, the convergences of the rock salt caverns with the running time and the diameter-to-height ratio are calculated, as shown in Fig. 6. The analysis shows that the cavern convergences after running 5 years are 2.505%, 2.896%, 3.185% and 4.106% corresponding to N=1.5, 2.0, 2.5 and 3.0, respectively; 5.796%, 7.188%, 8.341% and 11.591% after running 20 years. According to the utilization criterion of rock salt caverns for gas storage, the cavern convergence after 5a operation must be less than 5%, after 20a operation less than 15%. The calculated cavern convergences in all four cases meet the requirements and are even far below the utilization criterion.
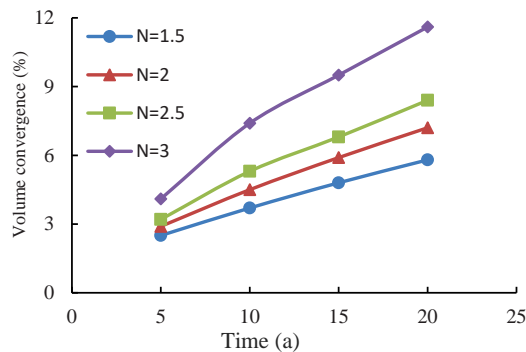
Figure 6：Volume convergences of horizontal single-caverns (N = 1.5, 2, 2.5, 3) in rock salt with the operation time

3.3 Stress-strength-ratio distribution

(a)

(b)

(c)

(d)
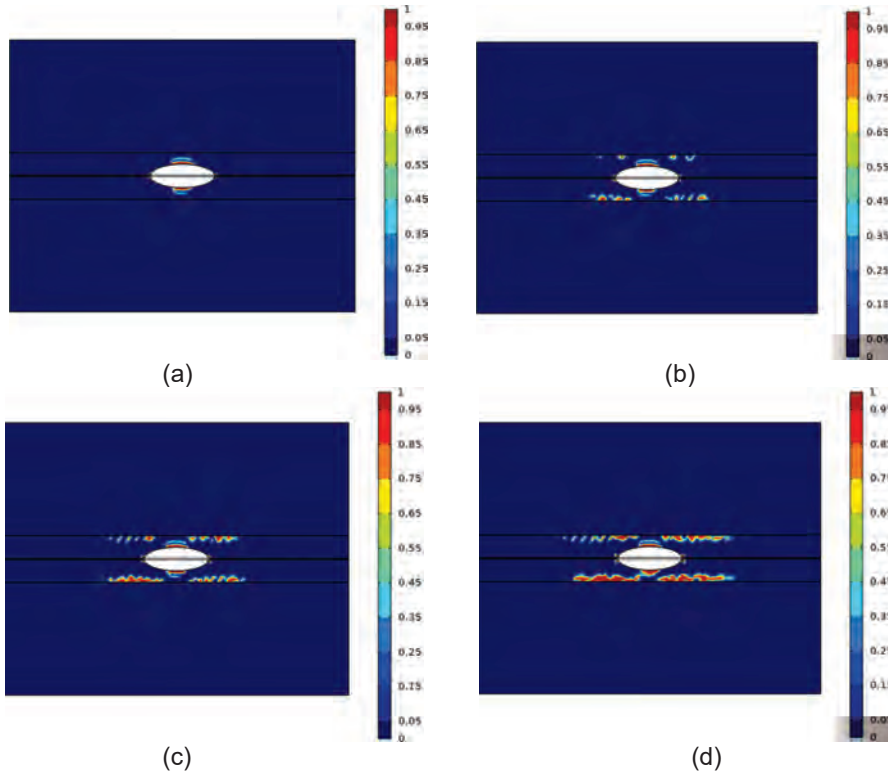
Figure 7: Stress-strength-ratio distributions (> 0.95: plastic zone) of a horizontal single-cavern (N =2.5) in rock salt at different operation times. (a) 5a; (b) 10a; (c) 15a; and (d) 20a.

Figure 7 shows the stress-strength-ratio distributions (> 0.95: plastic zone) of the horizontal single-cavern after running 5a, 10a, 15a and 20a in case of the diameter-height ratio N=2.5. The plastic zone is mainly distributed at the top and bottom of the salt cavern. The stress-strength-ratio at the junction between rock salt and interlayer on the both sides of the salt cavern is also getting bigger and bigger. There is a plastic zone in the interlayer on both sides of the cavern boundary, since its smaller elastic modulus and cohesion shown in Table 1.

(a)

(b)

(c)
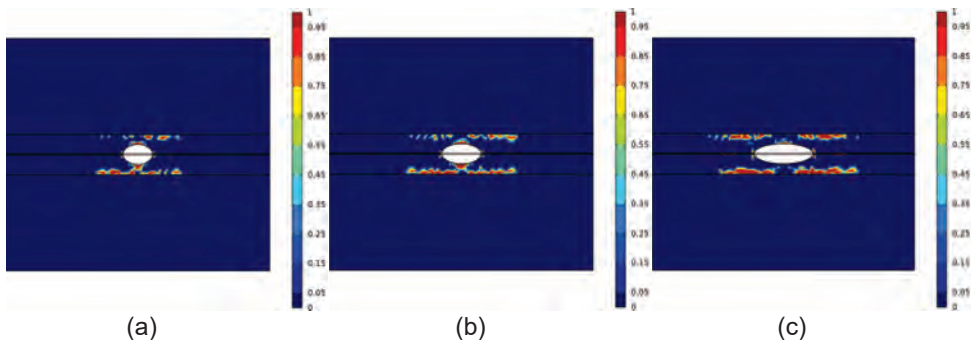
Figure 8: Cloud map of stress-strength-ratio distribution of horizontal single-caverns in rock salt with different diameter-to-height ratios (t = 20a). (a) N = 1.5; (b) N= 2.0; and (c) N = 3.0.

Figure 8 shows the stress-strength-ratio distributions after running 20a of the horizontal salt cavern with N=1.5, 2.0 and 3.0. Combining with Fig. 7(d), it can be seen that with the increase of N, the volume of the plastic zone of the horizontal salt cavern with interlayers after running 20 years is also increasing and the stress-strength-ratio at the junction between interlayer and rock salt increases greatly. When horizontal double-caverns or horizontal multi-caverns are set up, the plastic zone in the interlayer may penetrate the horizontal multi-caverns and affect the stability and especially the tightness of long-term operation. From the above analysis, we can draw the following conclusions: As the diameter-to-height ratio increases, the bigger the convergence of the horizontal salt cavern, the larger the volume of the plastic zone. Therefore, from the perspective of cavern convergence and plastic zone distribution, the larger the diameter-to-height ratio, the worse the stability and the tightness of the horizontal salt cavern. However, the smaller the diameter-to-height ratio, the smaller the storage capacity of the horizontal salt cavern, which affects the economic benefits. Considering the long-term stability and economic benefits of underground salt storage, combined with relevant engineering experience around the world, the suggested ratio of diameter-to-height for a horizontal single-cavern in rock salt can be N=2.5.

4 Analysis on underground storage stability of horizontal double-caverns in rock salt with interlayer

Through the analysis in Section 3, it can be concluded that the optimal diameter-to-height ratio of a single-cavern in rock salt with a horizontal interlayer is N=2.5. However, considering both the economic and safety factors, double caverns or group caverns are mostly simulated. Therefore, the distance between two storage caverns (= pillar size) needs to be considered to ensure its long-term operational stability. This section mainly takes the horizontal double-caverns with a diameter-to-height ratio of N=2.5 as the research object, and analyzes the influence of different pillar widths on the stability of the horizontal double-caverns with interlayers. The pillar widths are 60m, 80m, 100m, 120m, 140m and 160m, respectively.

4.1 Vertical displacement and horizontal displacement

Figure 9 shows horizontal displacement distributions of the horizontal double-caverns in rock salt with interlayers after 20a operation and with the different pillar widths of 60m, 80m, 100m, 120m, 140m and 160m, respectively.

4.2 Cavern convergence

Through the processing and analysis of the surrounding rock displacement data obtained by numerical simulations, the cavern convergences with the operation time under different pillar widths are calculated, as shown in Figure 10. If the pillar width is less than 120m, the cavern convergence of rock salt storage decreases gradually with the increase of the pillar width. If the pillar width is bigger than 120m, the influence of the pillar width on the cavern convergence gradually weakens. The overburden pressure on the pillar will be decomposed to the salt cavern boundary on both sides, which is equivalent to the boundary constraint imposed by the pillar on the salt caverns. As the pillar width increases, the boundary constraints of the salt caverns also increase. Therefore, if the pillar width is larger, the pillar has a significant limiting effect on the deformation of the surrounding rock of the salt cavern on both sides, thereby reducing the convergence of the salt cavern. However, with the decrease of the pillar width, the constraint of the pillar gradually weakens, while the cavern convergence gradually increases. When the pillar width reaches 120m, the cavern convergence of the salt cavern gradually tends to be stable at a same operation time, and the influence of the pillar width on the convergence of the salt cavern becomes weaker.
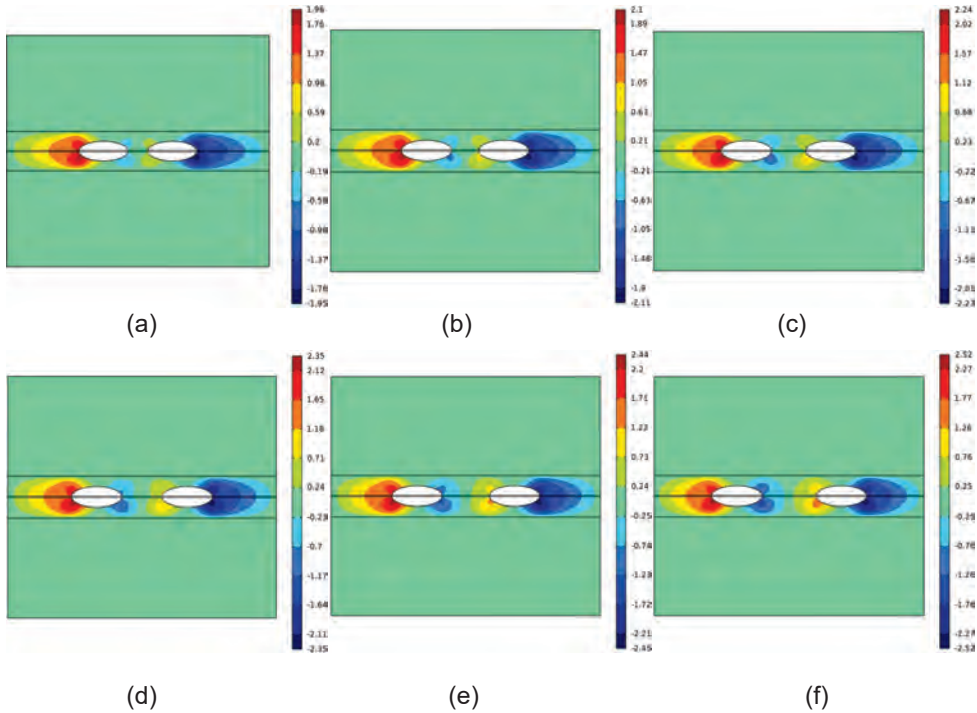
Figure 9: Cloud maps of horizontal displacement distributions of the horizontal double-caverns in rock salt with different pillar widths (t = 20a). (a) 60 m; (b) 80 m; (c) 100 m; (d) 120 m; (e) 140 m; and (f)160 m.
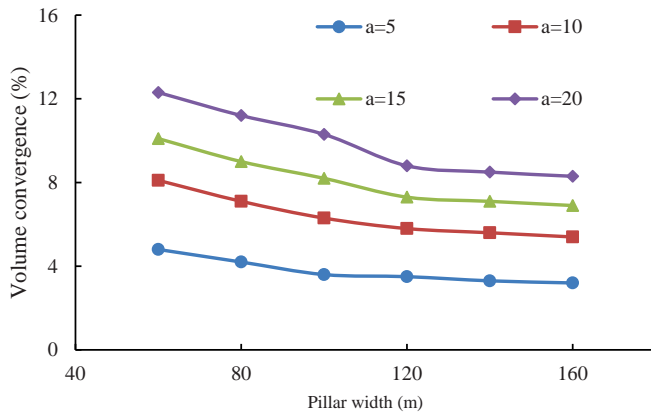

Figure 10: Volume convergences of the horizontal double-caverns (N = 2.5; t = 5a, 10a, 15a and 20a) in rock salt with different pillar widths.

4.3 Stress-strength-ratio distribution

Figure 11 shows the stress-strength-ratio distributions of the horizontal double-caverns (N = 2.5) when the operating time is 20a and the pillar widths are 60m, 80m, 100m, 120m, 140m and 160m respectively. It can be seen that when the width of the salt pillar is less than 80m, the plastic zone (stress-strength-ratio > 0.95) between the salt caverns (= in the pillar) is formed, which affects the long-term stability of the salt caverns. When the pillar width exceeds 100m,

with the increase of the pillar width, the interaction between the salt caverns gradually weakens, and the plastic zones between the salt caverns are independent of each other (not connected). Therefore, from the perspective of the plastic zone distribution of the horizontal double-caverns, the pillar width of the underground double-caverns should not be less than 100m.

In summary, for the horizontal double-caverns with interlayer, with the increase of the pillar width, the cavern convergence decreases. Therefore, from the point of view of controlling the cavern convergence, the wider the pillar, the better. Furthermore, as the pillar width decreases, the interaction between the salt caverns becomes more pronounced. When the pillar width is less than 80m, the plastic zones between the salt caverns are formed and connected, and the salt caverns influence each other, which affects even the short-term stability of the salt caverns. If the pillar width is bigger than 100m, the interaction between the salt caverns gradually weakens, and the plastic zones between the salt caverns are independent of each other. Considering the need for a certain safety reserve, the pillar width between the horizontal double-caverns in rock salt with interlayers can be 120m.
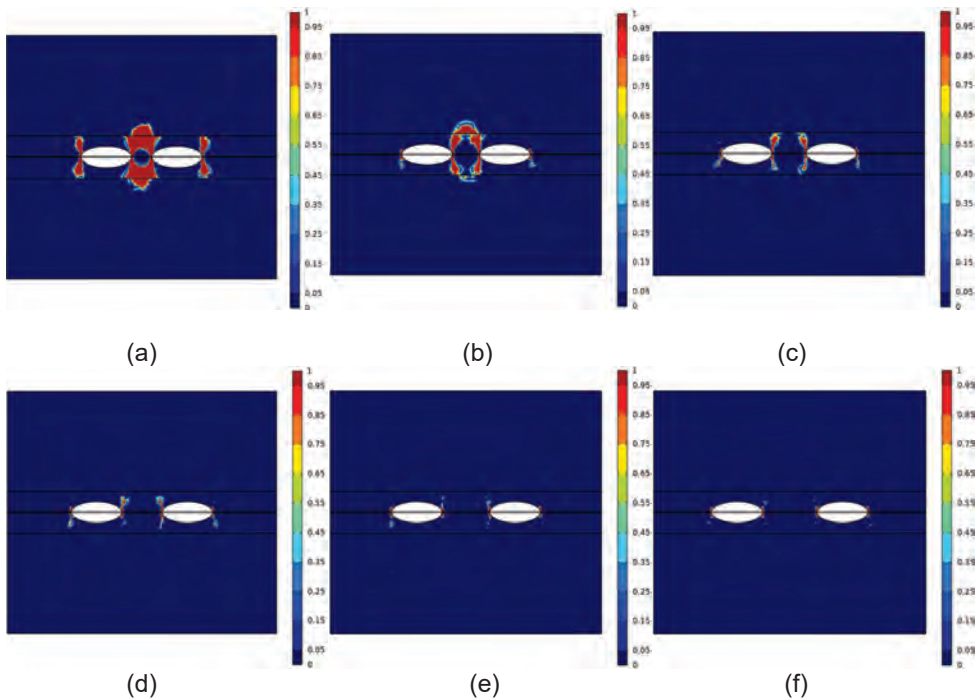
Figure 11: Cloud maps of stress-strength-ratio distributions of the horizontal double-caverns (N = 2.5) in rock salt with different pillar widths (t = 20a). (a) 60 m; (b) 80 m; (c) 100 m; (d) 120 m; (e) 140 m; and (f) 160 m.

5   Conclusions

In view of the characteristics of layered rock salt with multiple-interlayers and small thickness, taking the ellipsoidal horizontal single-cavern and double-caverns in rock salt with a single interlayer in the cavern middle as examples, the salt cavern storage models with different diameter-to-height ratios were simulated by COMSOL three-dimensional software. The changes of vertical and horizontal displacement, volume convergence and stress-strength-ratio distribution with different diameter-to-height ratios and operation times were analyzed, and the optimal diameter-to-height ratio of N = 2.5 and the optimal pillar width of 100m were determined. The main conclusions are as follows:

(1) During the long-term operation of the horizontal single-cavern in rock salt with interlayers, the horizontal displacements on the left and right sides of the surrounding rock are symmetrically distributed, and the maximum horizontal displacement is at the cavern center of both horizontal left and right sides. The maximum displacement in the vertical direction is at the center of the top and bottom cavern. When the running time is same, with the increase of the height-diameter ratio, the horizontal maximum displacement around the horizontal salt cavern is gradually increased. With the increase of operating time, the rate of roof subsidence is gradually decreased. After the running time exceeds 2a, the subsidence of the roof increases linearly with the running time. In the initial stage of operation, the uplift rate of the cavern bottom is relatively faster. When the running time exceeds 2a, the uplift rate of the cavern bottom gradually decreases, and the uplift increases linearly with time.

(2) For the horizontal single-cavern in rock salt with interlayers, as the ratio of diameter-to-height is larger, the volume convergence rate of the salt cavern is bigger and the volume of the plastic zone is larger. From the perspective of volume convergence and plastic zone distribution, the larger the ratio of diameter-to-height, the worse the stability of the horizontal salt cavern. However, the smaller the diameter-to-height ratio, the smaller the storage capacity of the horizontal salt cavern, which again affects the economic benefits. Taking into account the long-term stability and economic benefits of salt cavern for gas storage, combined with relevant engineering experiences around the world, the suggested diameter-to-height ratio of a horizontal single-cavern can be N=2.5.

(3) For the horizontal double-caverns in rock salt with interlayers, with the increase of the pillar width, the cavern convergence of the salt cavern decreases. Therefore, from the point of view of controlling the cavern convergence, the wider the pillar, the better. Furthermore, as the pillar width decreases, the interaction between the salt caverns becomes more pronounced. If the pillar width is less than 80m, the plastic zones between the salt caverns are formed and connected, and the salt caverns influence each other, which affects even the short-term stability of the salt caverns. When the pillar width is bigger than 100m, the interaction between the salt caverns gradually weakens, and the plastic zones between the salt caverns are independent of each other. Considering the need for a certain safety reserve, the suggested pillar width between the horizontal double-caverns in rock salt with interlayers can be 120m.

References

WU, W., HOU, Z. & YANG, C. 2005. Investigations on evaluating criteria of stabilities for energy (petroleum and natural gas) storage caverns in rock salt. Chinese Journal of Rock Mechanics and Engineering, 24(14):2497-2505. (in Chinese)

XING, W., ZHAO, J., HOU, Z., WERE, P., LI, M. & WANG, G. 2015. Horizontal natural gas caverns in thin-bedded rock salt formation. Environmental Earth Sciences 73 (11):6973-6985.

TANG, M., WANG, Z., DING, G. & RAN, Z. 2010. Creep property experiment and constitutive relation of salt-mudstone interlayer. Journal of China Coal Society, 35(1):42-45. (in Chinese)

LIANG, W., YANG, C. & ZHAO, Y. 2008. Physico-mechanical properties and limit operation pressure of gas deposit in bedded salt rock. Chinese Journal of Rock Mechanics and Engineering, 27(1): 22-27. (in Chinese)

XING, W., ZHAO, J., DÜSTERLOH, U., BRÜCKNER, D., HOU, Z., XIE, L. & LIU, J. 2014. Experimental study of mechanical and hydraulic properties of bedded rock salt from the Jintan location. Acta Geotechnica, 9 (1):145-151.

WANG, G., XING, W., LIU, J., HOU, Z. & WERE, P. 2015. Influence of water-insoluble content on the short-term strength of bedded rock salt from three locations in China. Environ Earth Sci 73(11), 2015:6951-6963.

Yin, P., Liu, J. & Yang, C. 2006. Influence of mudstone interlayer on deformation and failure characteristics of salt rock. Chinese Journal of Rock Mechanics and Engineering, 25(12):2461-2466. (in Chinese)

YIN, P., JIANG, W., LIU, J., CHEN, J. & YANG, C. 2007. Direct shear test for layered salt rocks of Yunying salt mine in Hubei province. Chinese Journal of Rock Mechanics and Engineering, 26(9):1768-1771. (in Chinese)

HAO, T., LIANG, W. & ZHANG, C. 2014. Analysis of slippage and fracture characteristic on roof interface of underground horizontal salt caverns. Chinese Journal of Rock Mechanics and Engineering, 33(Supp.2):3956-3966. (in Chinese)

WU, K. & SHAO, Z. 2019. Visco-elastic analysis on the effect of flexible layer on mechanical behavior of tunnels. International Journal of Applied Mechanics, vol. 11, no. 3, Article ID 1950027.

TANG, M., WANG, Z., DING, G. & RAN, Z. 2010. Creep property experiment and constitutive relation of salt-mudstone interlayer. Journal of China Coal Society, 35(1):42-45. (in Chinese)

MA, L., WANG, M., ZHANG, N., FAN, P. & LI, J. 2017. A variable parameter creep damage model incorporating the effects of loading frequency for rock salt and its application in a bedded storage cavern. Rock Mechanics and Rock Engineering, 50(9):2495–2509.

WANG, S., WANG, Q., XU, J. & DING, J. 2020. Effect of freeze thaw on freezing point and thermal conductivity of loess. Arabian Journal of Geosciences13(5):206.

WANG, J., ZHANG, Q., SONG, Z., ZHANG, Y. & LIU, X. 2021. Mechanical properties and damage constitutive model for uniaxial compression of rock salt at different loading rates. International Journal of Damage Mechanics, vol. 30.

WU, F., CHEN, J. & ZOU, Q. 2019. A nonlinear creep damage model for salt rock. International Journal of Damage Mechanics, 28(5):758-771.

HUANG, X., YANG, C. & LI, Y. 2014. Interface shear stress distribution of bedded salt rock considering rheology effect. Chinese Journal of Underground Space and Engineering, 10(3):547-551. (in Chinese)

LIU, W., LI, Y., HUO, Y., SHI, X., XU, B., YANG, C. & LIN, Y. 2013. Analysis of deformation and fracture characteristics of wall rock interface of underground storage caverns in rock salt formation. Rock and Soil Mechanics, 34(6):1621-1628. (in Chinese)

LI, E., TAN, Y., DUAN, J. & WANG, Z. 2014. Effect of change of interbed Young's modulus on the stability of underground storage cavern in bedded salt. Chinese Journal of Underground Space and Engineering, 10(Supp.2):1842-1847. (in Chinese)

MOGHADAM, S.N., MIRZABOZORG, H. & NOORZAD, A. 2012. Stability analysis of caverns excavated in heterogeneous salt formations. Indian Journal of Science and Technology, 5(8):3128-3131.

WANG, W., XU, H. & TONG, Q. 2012. Theoretical analysis of mechanics behavior of cylinder storage cavern in rock salt containing interlayer. Chinese Journal of Rock Mechanics and Engineering, 31(Supp.2):3731-3739. (in Chinese)

BAUER, S., EHGARTNER, B., LEVIN, B. & LINN, J. 1998. Waste disposal in horizontal solution mined caverns considerations of site location cavern stability and development considerations. SMRI Fall Meeting, 33-38.

CHARNAVEL, Y. & LUBIN, N. 2002. Insoluble deposit in salt cavern-test case. SMRI Fall Meeting, 78-82.

BEKENDAM, R. & PAAR, W. 2002. Induction of subsidence by brine removal. SMRI Fall Meeting, 145-149.

Dᴇᴠʀɪᴇs, K., Mᴇʟʟᴇɢᴀʀᴅ, K. & Cᴀʟʟᴀʜᴀɴ, G. 2005. Cavern roof stability for natural gas storage in bedded salt. Rapid City, South Dakota. United States Department of Energy National Energy Technology Laboratory.

Kᴀɴɢ, Y., Fᴀɴ, J., Jɪᴀɴɢ, D. & Lɪ, Z. 2021. Influence of geological and environmental factors on the reconsolidation behavior of fine granular salt. Natural Resources Research, vol. 30.

Wᴀɴɢ, J., Lɪᴜ, X., Sᴏɴɢ, Z., Gᴜᴏ, J. & Zʜᴀɴɢ, Q. 2016. A creep constitutive model with variable parameters for thenardite. Environmental Earth Sciences, 75(6):979.

Wᴀɴɢ, S., Xᴜ, J., Wᴀɴɢ, Q. & Cʜᴇɴɢ, D. 2020. Modeling of wetting deformation of coarse saline soil with an improved von Wolffersdorff model. Bulletin of Engineering Geology and the Environment, 79(9):4783-4804.

Jɪ, W., Yᴀɴɢ, C., Lɪᴜ, W. & Lɪ, M. 2013. Experimental investigation on meso-pore structure properties of bedded salt rock. Chinese Journal of Rock Mechanics and Engineering, 32(10):2036-2043. (in Chinese)

Mᴀ, L., Xᴜ, H., Wᴀɴɢ, M. & Lɪ, E. 2015. Numerical study of gas storage stability in bedded rock salt during the complete process of operation pressure runway. Chinese Journal of Rock Mechanics Engineering, 34(2):4108-4115. (in Chinese)

Cʜᴇɴ, J., Lᴜ, D., Lɪᴜ, W., Fᴀɴ, J., Jɪᴀɴɢ, D., Yɪ, L. & Kᴀɴɢ, Y. 2020. Stability study and optimization design of small-spacing two-well (SSTW) salt caverns for natural gas storages. Journal of Energy Storage, vol. 27:10113.

Hᴜ, B., Sʜᴀʀɪғᴢᴀᴅᴇʜ, M., Fᴇɴɢ, X., Gᴜᴏ, W. & Tᴀʟᴇʙɪ, R. 2021. Roles of key factors on large anisotropic deformations at deep underground excavations. International Journal of Mining Science and Technology, 31(2).

Wᴜ, K., Sʜᴀᴏ, Z., Qɪɴ, S., Wᴇɪ, W. & Cʜᴜ, Z. 2021. A critical review on the performance of yielding supports in squeezing tunnels. Tunneling and Underground Space Technology, 114(1).

Yᴜ, C. 2012. Numerical simulation study on stability of bedded rock salt gas storage. Wuhan Institute of Technology, 17-25.

Energy storage in salt caverns with supercritical CO₂

W. Minkley [1], M. Brandt [1], V. Dostal [2], J. Stepanek [2]*

[1]Institut for Geomechanics GmbH (IfG), Germany; [2]Czech Technical University in Prague (CTU) Department of Energy Engineering, Czech Republic

* Wolfgang.Minkley@IfG-Leipzig.de

ABSTRACT: Energy storage is essential for a supply-secure power grid in the further expansion of the renewable energies, in order to integrate the increasing fluctuating power generation with their low guaranteed power into the energy system. A novel storage technology, an innovative, emission-free cavern storage power plant using supercritical CO_2 as the working fluid in a closed loop is presented. Energy storage with sCO_2 in a salt mine is comparable to a pumped storage power plant with the difference that supercritical CO_2 is used instead of water and the storage does not take place at the surface in an upper and lower reservoir, but in a high- and low-pressure cavern underground in rock salt with a small footprint on the surface. Supercritical CO_2 turbines represent a technical innovation in energy conversion. For the long-term goal of achieving climate neutrality, CO_2 sinks are required for the remaining CO_2 sources from industry and other sectors. The construction of sCO_2 energy storage mines in salt through Carbon Capture, Utilization and Storage can contribute to this.

1   Introduction

With the expansion of renewable energies, primarily wind and solar energy, and the shutdown of base-load generating nuclear power plants by 2022 and coal-fired power plants by 2038 at the latest, the need for storage capacity for electrical energy in Germany is increasing. The rotational energy stored in the turbines and generators with their rotating masses in conventional German large-scale power plants amounts to only about 15 MWh, but it can be called up within 30 seconds (primary regulating power) with a high average power output of about 15 GW (Kneiske et al. 2013). In addition, there is currently still a correspondingly large reserve capacity of rapidly activatable peak-load power plants to ensure the stability and reliability of the power supply. This will change significantly in the future with the shutdown of conventional power plants and the feed-in of renewable energy with an increasing shift in the ratio of secured to non-secured generation capacity. The resulting demand for flexible generation as well as for balancing power makes additional energy storage necessary (Gerhard et al. 2013).

The planned further expansion of volatile renewables, i.e. demand-independent feed-in in Germany, will further increase the discrepancy between electricity consumption and generation. The reason for this is the unsteady power generation, which is not in line with demand, and the relatively low secured power of renewable energies of 1 - 7 % in Germany (Buttler & Spliethoff 2016).

The supply gap between the weather-dependent, fluctuating power generation of renewable energies and consumption is currently still compensated for by base-load generating nuclear energy and controllable gas, lignite and hard coal-fired power plants as well as pumped-storage power plants. There are estimates that the reserve capacity in an electric grid generally needs to be increased by about 200 MW for every 1 GW of additional wind power installed to ensure system stability (Mercangöz et al. 2012). In addition to the development of storage options, the energy supply during hours of low wind and low sun (dark lull) is to be secured by gas-fired power plants. In a recent study by the Deutsche Energie-Agentur (dena 2021) on achieving climate neutrality by 2045, a stock of controllable power plants, primarily consisting of hydrogen-capable combined-cycle gas turbine (CCGT) and peak-load power plants with a total capacity of 50 GW, is considered necessary. In addition, gas-fired power plants that burn

only methane-based gases with a capacity of 9 GW are to remain on the market, mainly fulfilling a reserve function (dena 2021).

This corresponds to a standby power of the backup gas-fired power plants, in the order of magnitude of the electricity consumption generated in Germany today on the basis of an energy mix of coal, natural gas, nuclear energy and renewables. The total installed generation capacity needed to meet the same demand increases substantially as variable renewable generation capacity becomes more widespread. In order to integrate the increasing fluctuating power generation from wind power plants and photovoltaics with their low secured output into the energy system, an expansion of the storage infrastructure is also required. Based on a storage capacity of 7 GW, mainly from pumped hydro storage (PHS), additional storage capacity is needed through new storage technologies. The current dena study prognosticates a storage demand of 15 GW for the year 2045 (dena 2021).
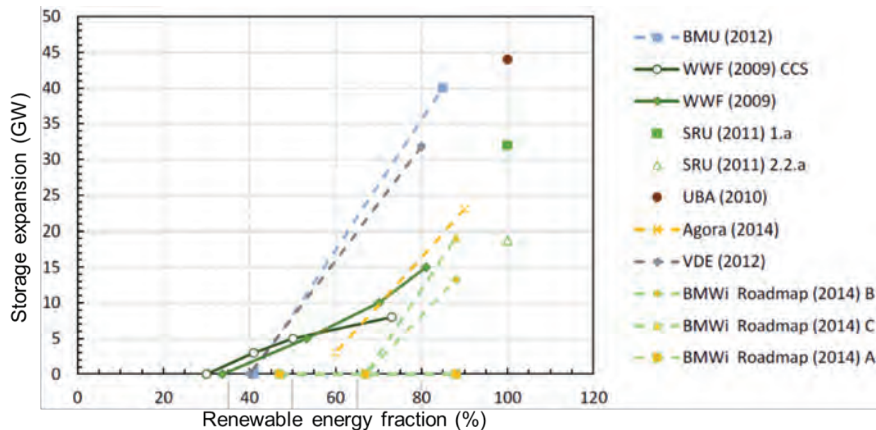
Figure 1: Future storage demand in addition to existing pumped hydro storage (PHS) depending on the share of renewable energies in electricity generation in Germany (Buttler & Spliethoff 2016).

The demand for the addition of storage capacity up to a maximum of 45 GW indicated in Fig. 1 from various studies varies greatly depending on the boundary conditions applied in each case and the assumptions (some of which are not realistic): Flexibilization of the energy system, demand-side management, adoption of European interconnected grid with 80 GW of solar thermal power plants in Spain and North Africa, use of Scandinavian pumped storage, size of installed renewable capacity, level of electricity imports.

With the planned expansion of the installed capacity of wind energy and photovoltaic by a multiple in Germany in order to achieve climate neutrality by 2045 (dena 2021), peak load storage systems will be required to absorb the extreme power generation peaks as far as possible without shutting down and overloading the grid. In the event of generation gaps, peak load storage must step in at short notice to ensure grid stability during the rising gradients (peak load smoothing).

Successfully shaping the energy transition requires the expansion of existing storage solutions and the development of new, efficient storage systems. In addition to battery storage, this will also require large-scale energy storage comparable to pumped hydro storage power plants (Minkley et al. 2021).

2   Storage

The increasing demand for storage with the growing share of renewable energies in electricity generation results, among other things, from the provision of system services (e.g. regulation power) and secured power, absorption of electricity surpluses and balancing between generation and consumption, relief of the electricity grid and avoidance of grid expansion, e.g. through large-scale storage in the north of Germany for balancing the wind energy feed-in (Buttler & Spliethoff 2016).

To compensate for the increasing fluctuating power generation due to the expansion of wind power and photovoltaics, large-scale storage facilities are important for grid stability and security of supply, of which pumped storage power plants are currently the most widely used in Germany (dena 2015).

In Germany, 36 pumped hydro storage plants with power outputs between 1 MW ...1 GW are operated, supplying 4-8 hours of electricity per day with an average efficiency around 70 %. The total pumped storage power is about 7 GW with a total storage capacity of 40 GWh. Pumped hydro storage plants are bound to a certain geomorphology with their upper and lower reservoirs and require a large amount of land for storage volumes of up to more than 10 million m^3. These conditions, which exist only in southern and central Germany, and the major impact on nature make it unlikely that this storage technology will be further extended in Germany.

Better conditions in this respect are offered by underground storage in salt caverns, which requires a small amount of land on the surface, but is related to a specific geology in the underground, such as salt diapirs, which are mainly located in northern Germany. In Germany, various studies and projects have been carried out on electricity storage in salt caverns using brine as the working medium (Häfner & Amro 2013), compressed air (RWE 2012) or chemical storage in the form of a redox flow battery in salt caverns (EWE 2017).

Compressed air energy storage (CAES) in salt caverns is the only technology that has been used on a large scale to date. In Huntorf, compressed air storage in two 150000 m^3 salt caverns has been operated since 1978 together with a gas turbine power plant with a power output of 320 MW and a discharge time of 2 hours at an efficiency of 42% (Crotogino et al. 2001).

To increase the efficiency of CAES, R&D work for an adiabatic compressed air energy storage was carried out in the ADELE project (Moser 2014). The aim was to temporarily store the compression heat in a high-temperature, high-pressure heat accumulator at the surface and to return it to the compressed air after it had been removed from the cavern. The concept proved to be technically extremely challenging and too expensive, so development was discontinued (Zunft 2015).

Energy storage with supercritical CO2 (ESsCO2)

2.1   Starting piont

When sCO_2 is used for energy storage, the problem of strong heating of the working fluid is eliminated and it offers further advantages over compressed air:

- supercritical CO_2 (T > 31°C, p > 7.4 MPa) is an optimal working fluid
- behaves like a gas during expansion and like a liquid during compression
- less work required with compression
- Temperature change in cavern during compression $\Box$p = 1 MPa ca. $\Box$T≈ 1°K
- Density sCO_2 at the high cavern storage pressures 0.5...0.8 g/cm^3
- Efficiency higher than for CAES in conjunction with gas turbines
- compact design of sCO_2 turbine and compressor

R&D is underway worldwide to develop efficient sCO_2 cycles and compact turbines to generate electrical energy from various heat sources such as solar energy, IV generation nuclear reactors and fossil fuels (Brun et al. 2017). The advantage of supercritical CO_2 is its significantly higher energy density, resulting in a much more compact design compared to conventional heat power cycle layouts such as Rankine cycle (Fig. 2). sCO_2 turbines represent a technological innovation in energy conversion and are expected to replace conventional steam turbines as heat engines in the near future, increasing efficiency and reducing water consumption (Persichilli et al. 2012). Europe is lagging behind the USA and Asia in development in this field.
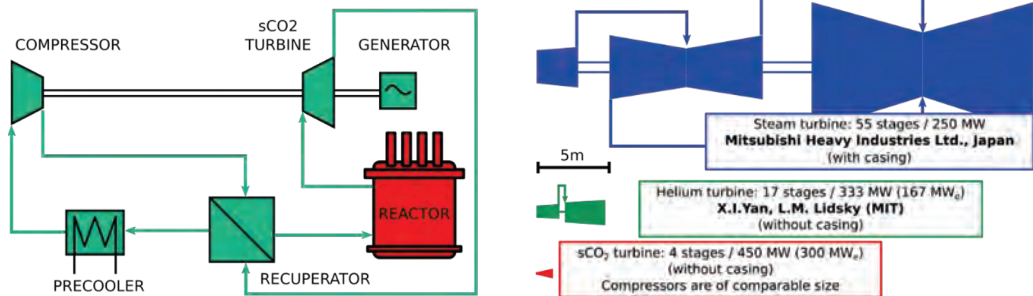
Figure 2: Left: Simple supercritical CO_2 Brayton cycle for a nuclear reactor. Right: Size comparison of steam, helium and supercritical CO_2 turbine (Dostál et al. 2006).

Besides ESsCO2 (IfG 2019), only three research projects are currently known in Europe: sCO2-Flex (EDF, 2019a), sCO2-4-NPP (EDF 2019b), and CARBOSOLA, where an experimental plant in the megawatt power range is to be developed in collaboration with Siemens AG at the Helmholz-Zentrum Dresden-Rossendorf (Gampe et al. 2018). The Federal Ministry for Economic Affairs and Energy (BMWi) is funding the ESsCO2 research project to develop a basic concept for an innovative, emission-free cavern storage power plant using supercritical CO_2 (sCO_2) as the working fluid in a closed cycle (IfG 2019).

2.2 Preliminary investigation results

The basic principle of energy storage is based on two caverns in rock salt (Fig. 3), in which sCO_2 is stored under different pressure and temperature conditions. When there is a surplus of renewable power generation, sCO_2 is compressed in one of the caverns; when there is a demand for energy, sCO_2 flows in the opposite direction and drives a supercritical CO_2 turbine connected via boreholes to the two caverns underground.

Experimental investigations on rock salt cores under pressurization with sCO_2 within the research project ESsCO2 prove that a pressure-driven opening of grain boundaries in polycrystalline rock salt (Minkley et al. 2013) and thus a loss of tightness only occurs when the CO_2 pressure significantly exceeds the minimum principal stress (Fig. 4).

This means that the maximum storage pressure is limited by the minimum principal stress in the salt rock acting in the cavern roof. At a depth of 1500 m, a maximum storage pressure of 30 MPa can thus be applied in the high-pressure cavern. The minimum storage pressure must be above the critical point of 7.4 MPa to maintain the supercritical state of CO_2. This is not a limitation because for caverns in salt rocks, a minimum storage pressure must always be maintained to reduce the volume convergence of the cavern due to creep and to ensure stability (Minkley et al. 2015a).
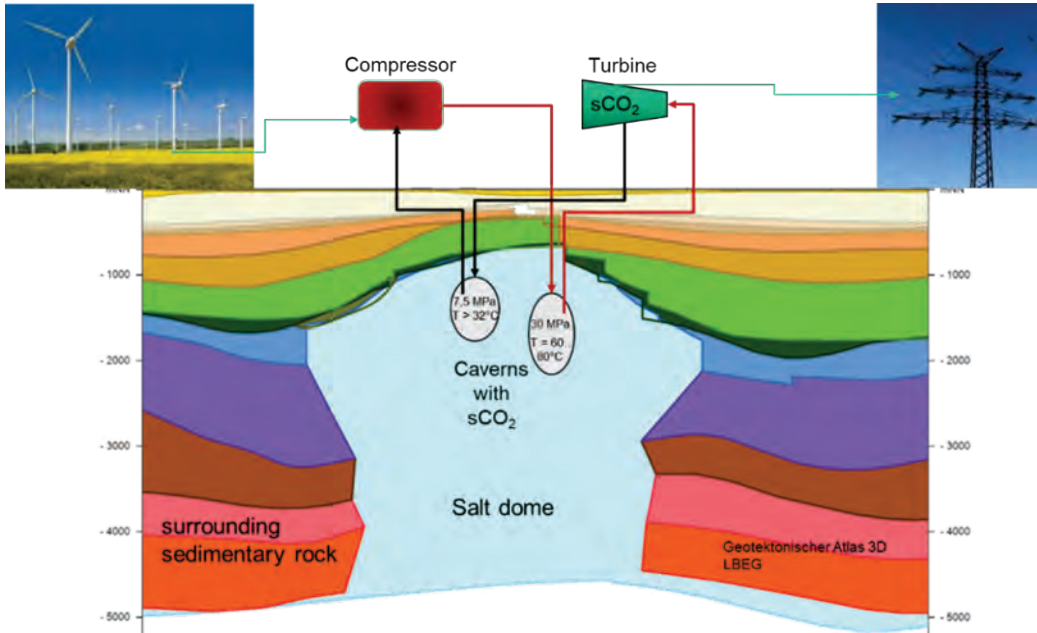
Figure 3: Basic principle for a cavern storage power plant in a salt dome with high-pressure and low-pressure cavern and sCO_2 turbine and compressor at the surface

Calculations for the technical design of the supercritical CO_2 turbine show that the achievable power in relation to the mass flow through the turbine increases with increasing inlet pressure and increasing temperature (Fig. 5). The theoretically achievable peak power of the sCO_2 turbine under the given boundary conditions (p_{in} = 30 MPa, p_{out} = 10 MPa, T = 60°C) is 25 kW/kg/s.
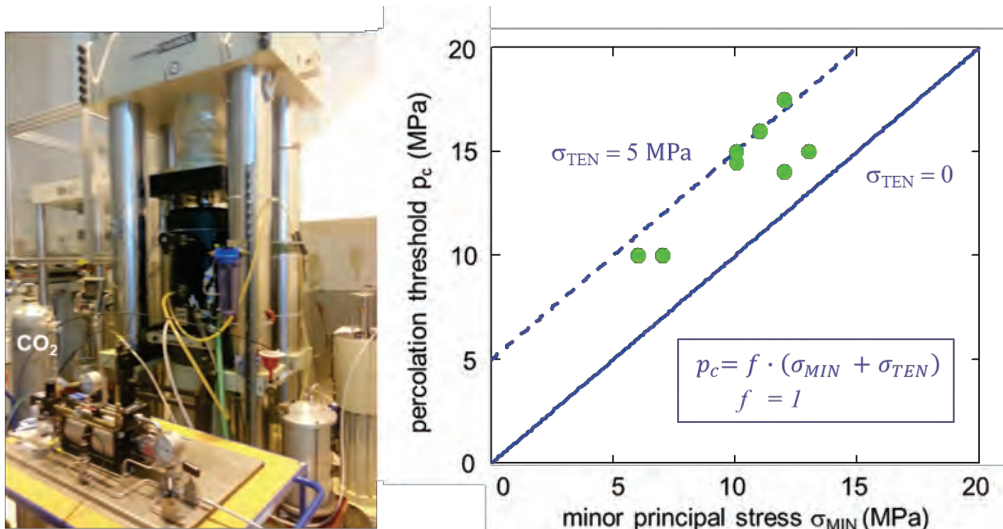
Figure 4: Laboratory tests on the percolation threshold of sCO_2/CO_2 in rock salt in the temperature range 20°C to 80°C: Left; Servohydraulic test system with heatable triaxial cell and CO_2 pressure booster (left foreground), Right; Test results percolation threshold versus minor principal stress
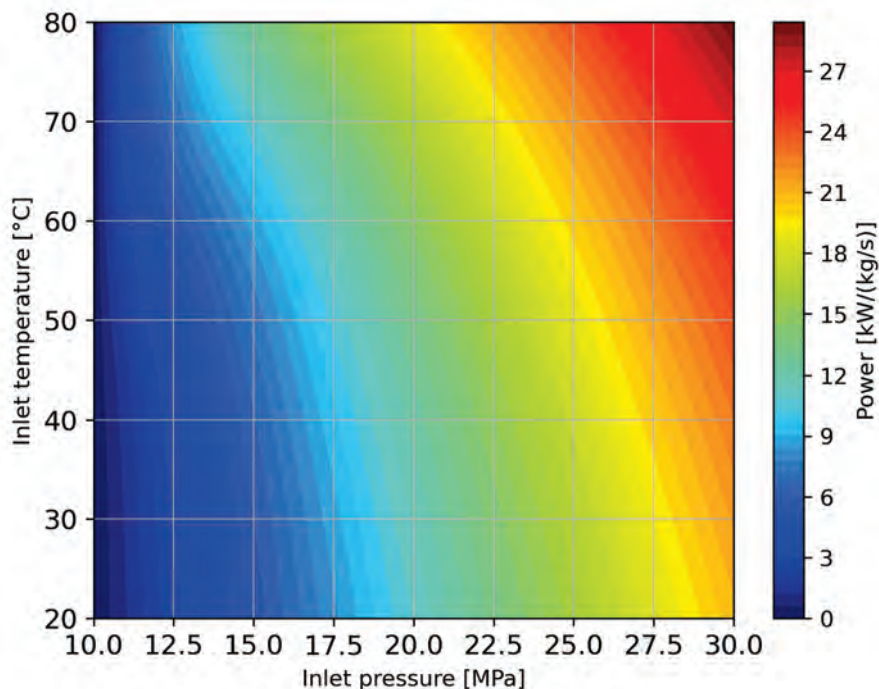
Figure 5: Calculations of theoretical (isoentropic) sCO_2 turbine power as a function of inlet pressure and temperature at a turbine outlet pressure of 10 MPa

At a flow rate of 10000 kg/s, this corresponds to a theoretical peak power of 250 MW. This would assume that the sCO_2 turbine is installed at 1500 m depth and that the pressure drop in the 30" (76.2 cm) pipe from the cavern to the turbine due to friction loss is negligible.
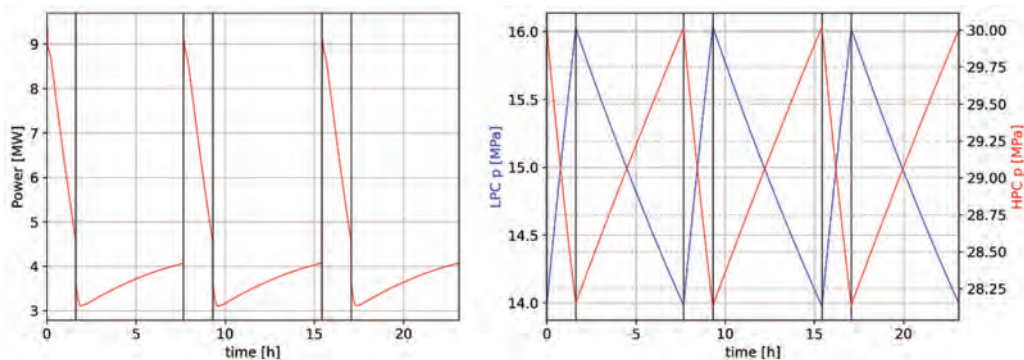
Figure 6: Calculated power for 3 storage cycles for ESsCO2 in salt caverns with sCO2 turbine and compressor at the surface connected by 20" tubing (left). Cyclic pressure changes in caverns (right): HPC at 1500 m (0.8 million m³) and LPC at 800 m (1 million m³) depth

With the sCO_2 turbine located above ground and connecting the high-pressure cavern (HPC) at 1500 m depth and the low-pressure cavern (LPC) at 800 m depth via a 20" (50.8 cm) tube, the calculation yields a peak power of 9 MW (Fig. 6) at a flow rate of 1200 kg/s, taking into account friction- and gravity-induced pressure losses. The gravity-induced pressure drop alone is about 12 MPa and the friction-induced pressure drop is 2 MPa, resulting in an inlet pressure

at the sCO_2 turbine that is reduced by about 14 MPa. During the storage cycles, a sCO_2 mass exchange of less than 5% only takes place between the caverns. The efficiency is about 50%.

3 sCO_2 energy storage mine

In order to exploit the theoretically possible power and efficiency to a large extent, it is advisable to install the sCO_2 turbine and the compressor underground, which significantly minimizes the pressure and energy losses due to gravity and friction by eliminating the kilometre-long pipes to the surface. When installed at a depth of 1000 m in an sCO_2 energy storage mine, a flow rate of 10000 kg/s results in a maximum turbine power of around 100 MW (Fig. 5, p_{in} = 20 MPa, T > 31°C).

The building of sCO_2 energy storage mines (Fig. 7) also offers the advantage that, in addition to the cavern storage facilities, all the technical equipment is located underground. This has the following advantages:

- Increasing the performance and efficiency of energy storage
- Increasing safety by locating all technical equipment underground
- Constant ambient temperature, shorter starting process
- Low footprint on the surface

An sCO_2 energy storage mine with 100 caverns (approx. 1 million m^3 per cavern) in a salt dome built using solution mining could deliver 5 GW of peak power.
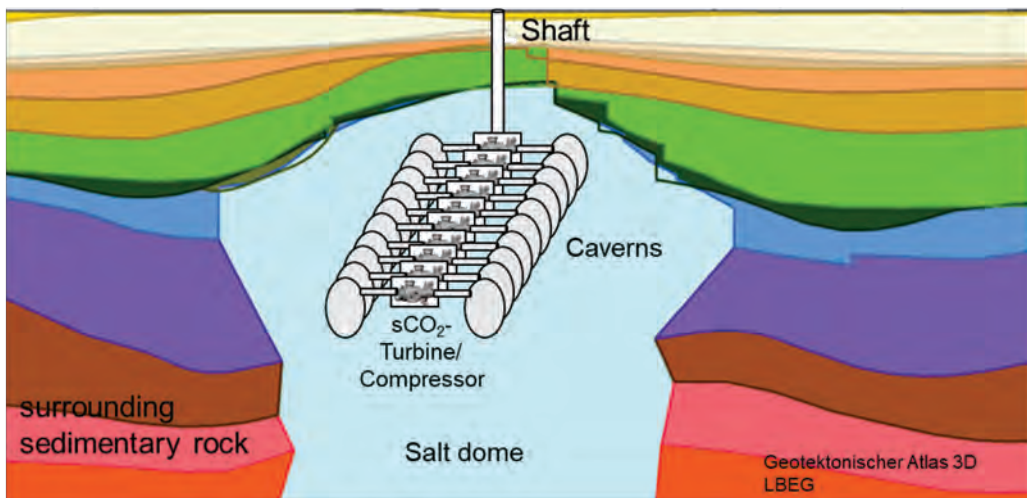
Figure 7: Basic principle of sCO_2 energy storage mine in a salt dome with 20 caverns and a peak power in the 1 GW range

Of the more than 400 salt diapirs (salt domes and salt walls) existing in the subsurface of northern Germany, 240 salt structures were identified in the InSpEE project as potentially suitable for the installation of cavern storage facilities. This provides conditions for adding storage capacity as shown in Fig. 1.

sCO_2 energy storage mines are suitable as peak load power plants and can provide system services such as primary, secondary regulating and minute reserve as well as secured power and have black start capability. Energy storage in salt caverns with sCO_2 in a storage mine has a number of advantages over other storage technologies:

- The efficiency of 50% is higher than that of conventional CAES with gas turbine. This is achieved in particular by the high density of sCO_2, which is 75% that of water at high cavern storage pressures, and lower heat losses during compression.
- Compared to PHS much less land is used because the storage reservoir is located entirely underground, including the generators and compressors in the case of an sCO_2 energy storage mine.
- Suitable sites are located in northern Germany, in the immediate vicinity of the regions where most wind power is also generated on- and offshore, so that the large-scale energy storage systems do not require shutdowns due to grid overloads.
- The salt formations there are already being used to store gas and oil in salt caverns as a strategic reserve.
- The operation principle of ESsCO2 is comparatively simple (for example, compared to adiabatic CAES) and largely builds on existing technology. Prototype turbines and compressors for sCO_2 are being developed and tested in connection with various applications.

Another option for increasing performance and efficiency offers transcritical compressed CO_2 energy storage. Transcritical pressure storage of CO_2 in a closed loop system has the advantage that significantly more energy can be extracted from the storage when the pressure is reduced below the critical point due to the transition from the supercritical state to the gaseous state. When the pressure is reduced to atmospheric, the CO_2 volume increases by a factor of up to 500, as has been the case with CO_2 blowouts in potash mining, see Fig. 9 (Minkley et al. 2015b).

For an adiabatic compressed CO_2 energy storage system with pressure tanks above ground, a round trip efficiency (RTE) of 76% is reported (Manzoni et al. 2021). The heat generated by compressing the CO_2 from atmospheric pressure to the storage pressure, with a temperature rise of several hundred degrees, is stored in a high-temperature heat exchanger regenerator and returned to the CO_2 before it enters the turbine to generate electricity. For underground transcritical pressure storage of CO_2 in salt caverns, the high-temperature heat exchanger can be omitted if the cavern is filled with rock gravel as heat storage material and thus stabilized at the same time. With daily cyclic storage, the process is approximately adiabatic. The energy density for transcritical pressurized storage of CO_2 is more than twice that of CAES (Cao et al., 2020). The volume of the high-pressure storage cavern can therefore be kept relatively small, while the low-pressure storage cavern is significantly larger, depending on the selected storage pressure of several megapascals or atmospheric pressure. Suitable cavities for low-pressure storage of CO_2 are abandoned potash and rock salt mines (Fig. 8), which may have sufficiently large cavity volumes of several tens of millions of m^3 so that the low pressure can be at atmospheric pressure. This has the advantage that nearly the entire mass of CO_2 stored in the high-pressure cavern flows through the expansion sCO_2/CO_2 turbine.

Since CO_2 is heavier than air under normal conditions, CO_2 could only escape from the shafts during the numerous CO_2 breakouts in the Werra potash district (Minkley et al. 2015b and Fig. 9) if the void volume of the mine was smaller than the amount of CO_2 released.
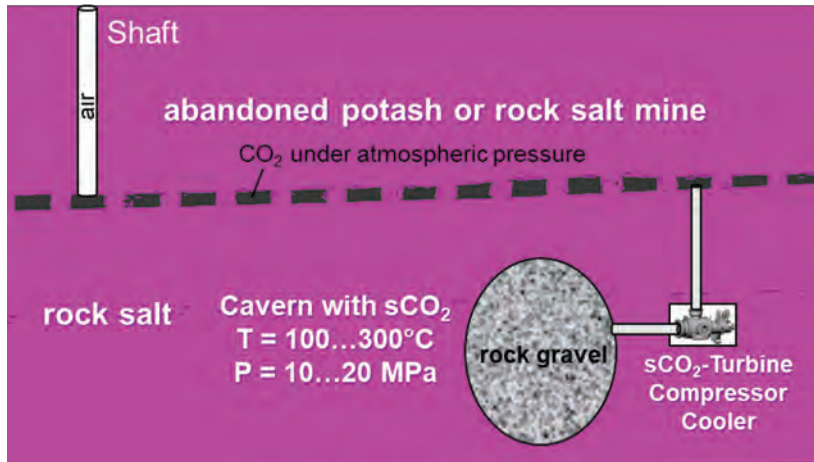
Figures 8: Basic principle of adiabatic transcritical compressed CO_2 energy storage with high-pressure storage cavern and abandoned salt mine as low-pressure reservoir in a closed loop system

The theoretically achievable efficiency of underground adiabatic transcritical pressure storage of CO_2 with expansion turbine is 75% (Bartela et al. 2021).

4   Compressed CO_2 energy storage as CO_2 sink by Carbon Capture, Utilization and Storage

Energy storage with supercritical CO_2 uses carbon dioxide as the working fluid, which can come from fossil fuel energy generation or from industrial production processes. It is therefore Carbon Capture, Utilization and Storage (CCUS). Millions of tons of CO_2 can be stored in an sCO_2 energy storage mine. After decades of use as an energy storage facility, the caverns containing the sCO_2 can be stored in the salt formation with a tight seal for the long term. The impermeability of salt rocks to supercritical CO_2 has been demonstrated by experimental studies (Fig. 4) and natural analogues (Minkley et al. 2015b), such as the high-pressure CO_2 reservoir in the Werra potash region that was trapped by volcanism over millions of years in the Tertiary (Fig. 9). In the case of a large-scale technical development of energy storage with supercritical CO_2 as a working fluid in storage caverns in salt formations, several hundred million tons of CO_2, which corresponds to the current annual carbon dioxide emissions of the energy industry in Germany, can be stored safely over the long term.

The lead study (dena 2021) states that all comprehensive greenhouse gas reduction measures will not be sufficient to achieve climate neutrality in 2045: "In addition, strategies for CO_2 capture and active CO_2 removal are needed to offset unavoidable process emissions or residual emissions, for example in agriculture. This already requires the use of CCU/S by 2030 (2 million tons). By 2045, the need for geological storage of CO_2 increases to 24 million tons annually."

Figures 9: Left: Naturally formed cavern with a volume of approx. 100000 m^3 opened by a blast on 1.10.2013 in the Unterbreizbach mine in which CO_2 originating from Tertiary volcanism was trapped under supercritical conditions over millions of years. Right: CO_2 glacier after a borehole blow-out (CO_2 changes to the solid state at temperatures < -70°C).

In Saxony-Anhalt in Germany, a first project is being planned for the subsequent use of brine caverns in rock salt as CO_2 sinks resp. for carbon capture, storage and utilization. In Europe, a total of 51 CCUS plants/facilities and projects currently exist or are planned, with annual storage of about 50 million tons of CO_2 by 2030 (IOPG 2021).

5 Conclusions

With the planned strong expansion of the installed power of wind energy and photovoltaics in Germany, while abandoning base-load capable and secured energy from nuclear power plants[1] to achieve climate neutrality by 2045, peak load storage will become necessary. Storage facilities must absorb the extreme power generation peaks without shutting down and overloading the grid, if possible, and step in at short intervals when there are generation gaps to ensure grid stability as the gradients increase. According to various studies, in order to compensate for the weather-dependent fluctuations and the low secured power of renewable energies, energy storage facilities with a capacity of 15 ... 45 GW are required in addition to backup gas turbine power plants with a capacity of around 60 GW. The research project Energy Storage with supercritical CO_2 (ESsCO2) serves the development of a basic concept

---

[1] Germany is the only major industrialized nation to have banned by law the technical use and R&D of nuclear power, one of the four natural forces or fundamental interactions gravitation, electromagnetic interaction, weak interaction (weak nuclear power) and strong interaction (strong nuclear power). For a highly complex industrial society in which electric power is becoming the most important energy source, relying exclusively on weather-dependent power generation, which is inherently not base-load capable, and abandoning diversification can lead to a loss of security.

for an innovative, emission-free cavern storage power plant in salt formations with supercritical CO_2 (sCO2) as working fluid in a closed cycle. First results show that with two caverns at a volume of about 1 million m^3 per cavern an energy storage with a power of more than 100 MW can be achieved with underground installation of sCO_2 turbine and compressor. An sCO_2 energy storage mine works on the same principle as a pumped hydro storage power plant (PHS) with the difference that supercritical CO_2 is used instead of water, and storage does not take place on the surface in an upper and lower basin, but in a high-pressure and low-pressure cavern underground in the salt formation, with the sCO_2 turbines and compressors also being installed in the mine to achieve high power. The technology for generating electricity, sCO_2 turbines and compressors, are not niche developments for just one special application. Research is being conducted worldwide on the development of efficient and compact turbines for generating electrical energy from various heat sources such as solar energy, IV generation nuclear reactors and fossil fuels. sCO_2 turbines represent a technical renewal of energy conversion and are expected to replace conventional steam turbines in specific applications as heat engines in the near future.

Electrical energy is generated by wind power, primarily onshore and offshore in northern Germany. Northern Germany is also the location of several hundred potentially suitable salt domes for the construction of sCO_2 energy storage mines.
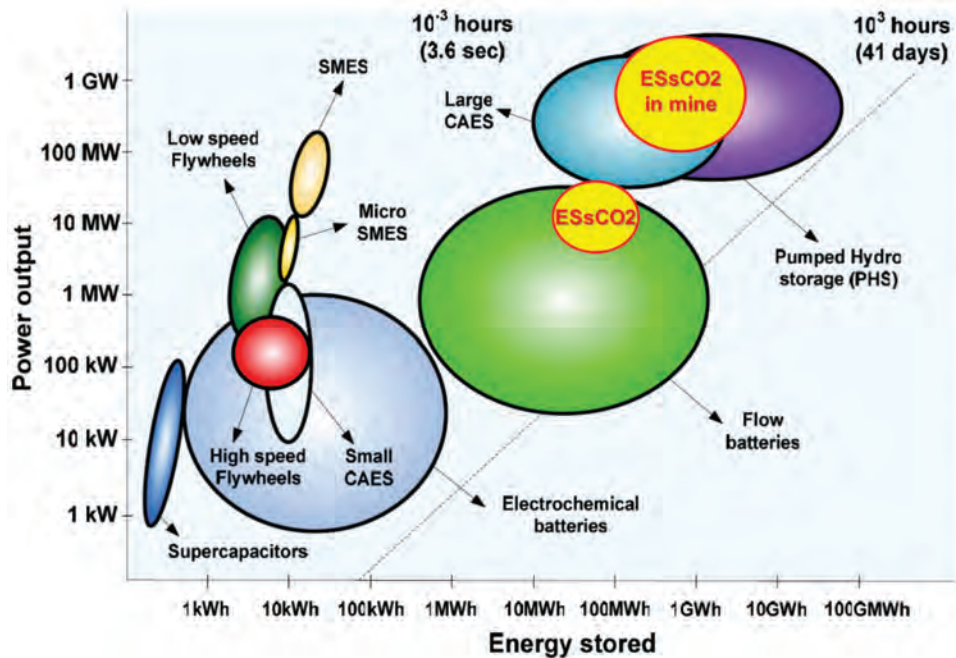
Figure 10: Storage technologies for electricity (San Martin et al., 2011) supplemented: ESsCO2 energy storage with supercritical CO_2 in caverns with aboveground arrangement of sCO_2 turbine and compressor and in mine

In addition, there is the possibility of repurposing or secondary use of some of the currently existing or abandoned brine production caverns in Germany for energy storage with sCO_2. For a single salt dome with 100 caverns (comparable to the Etzel salt dome), this results in a peak storage power in the order of 5 GW and, through Carbon Capture, Utilization and Storage (CCUS), a CO_2 sink of approx. 75 million tons. Energy storage in a storage mine in salt formations using supercritical CO_2 (ESsCO2) is preferable to competing technologies (Fig. 10), such as CAES due to the higher density of sCO_2, lower heat-up during compression, flexibility in the storage pressure range, higher efficiency, and low footprint. ESsCO2 in salt caverns

serves as short-term storage and can also provide regulating power for grid stabilization and, as mechanical pressure storage in conjunction with sCO₂ turbines, has the ability to rebuild the grid (black start). sCO₂ energy storage mines thus contribute directly to stabilizing the power grid and to security of supply. Adiabatic transcritical compressed CO_2 energy storage can achieve round trip efficiencies comparable to pumped hydro storage (PHS). Based on the different possible large-scale compressed CO_2 energy storage variants, a concrete site-specific storage optimization can be performed.

Long-term storage is provided by chemical energy storage of hydrogen (HYPOS 2018) in salt caverns as fuel and propellant and of natural gas or synthetic gas (power-to-X technologies) for electricity generation in gas turbine power plants for bridging days/weeks/months. In the transformation of the energy system, the regulatory framework and legislation must be adapted to the ambitious goals of the energy transition, taking into account not only the generation of renewable energies but also energy storage in the future, to ensure system stability and avoid black outs.

Acknowledgements

References

BARTELA Ł., SKOREK-OSIKOWSKA A., DYKAS S. & STANEK B. 2021 Thermodynamic and economic assessment of compressed carbon dioxide energy storage systems using a post-mining underground infrastructure. Energy Conversion and Management 241, 114279

BRUN K., FRIEDMAN P. & DENNIS R. 2017 Fundamentals and Applications of Superkritical Carbon Dioxide (sCO₂) Based Power Cycles, ELSEVIER, ISBN 978-0-08-100804-1

BUTTLER A. & SPLIETHOFF H. 2016 Kampf der Studien: Eine Metaanalyse aktueller Energie-systemstudien zum Bedarf an Speichern und konventionellen Kraftwerken im Kontext der Annahmen und der historischen Entwicklung. Schriftenreihe Energiesystem im Wandel - Teil II. Technische Universität München, Lehrstuhl für Energiesysteme

CAOA Z., DENGA J., ZHOUA S. & HEA Y. 2020 Research on the feasibility of compressed carbon dioxide energy storage system with underground sequestration in antiquated mine goaf. Energy Conversion and Management 211 (2020) 112788

CROTOGINO F., MOHMEYER K.-U. & SCHARF R. 2001 Huntorf CAES: More than 20 Years of Successful Operation. Spring 2001 Meeting Orlando, Florida, USA 15-18 April 2001

DENA 2015 Ergebnispapier: Der Beitrag von Pumpspeicherwerken zur Netzstabilität und zur Versorgungssicherheit – die wachsende Bedeutung von Pumpspeicherwerken für die Energiewende. Deutsche Energie-Agentur GmbH

DENA 2021 Abschlussbericht dena-Leitstudie Aufbruch Klimaneutralität. Deutsche Energie-Agentur GmbH

DOSTAL V., HEJZLAR P. & DRISCOLL M. J. 2006 High-performance supercritical carbon dioxide cycle for next-generation nuclear reactors. *Nuclear Technology,* p. 265, 154(3) 2006.

EDF 2019a https://www.sco2-flex.eu/

EDF 2019b sCO2-4-NPP based on supercritical CO₂ (sCO₂) for heat removal in nuclear power plants (NPPs). https://www.sco2-flex.eu/sco2-4-npp-kick-off-meeting/

EWE 2017 https://www.ewe.com/en/media/press-releases/2017/06/ewe-plans-to-build-the-worlds-largest-battery-ewe-ag

GAMPE U. ET AL. 2018 Concept and preliminary design of a 600°C + sCO₂ test facility. 2nd European supercritical CO2 Conference, August 30-31, 2018, Essen, Germany

GERHARD S., TRÜMPER S. C. & WEINMANN O. 2013 Qualitative Betrachtung von Lösungs-strategien bei der Integration Erneuerbarer Energien im Elektrizitätsnetz. Konferenz für Nachhaltige Energieversorgung und Integration von Speichern -NEIS 2013- Universität der Bundeswehr Hamburg

HÄFNER F. & AMRO, M. 2016 Energiespeicherung und -bevorratung als nationale Aufgabe. Energiewirtschaftliche Tagesfragen 63. Jg. (2013) Heft 10, S. 48-51

HYPOS 2018 Begleitforschung zur Eignung von Salzkavernen-Untergrundgasspeichern zur geologischen Speicherung von Wasserstoff aus fluktuierenden, regenerativen Quellen (H2-UGS). Teilvorhabenbeschreibung TP4 – Geomechanische In-situ-Untersuchungen und Modellierung. IfG-Institut für Gebirgsmechanik GmbH

IFG 2019 Forschungsprojekt BMWi: Energiespeicherung in Salzkavernen mit superkritisch-em CO_2 (ESsCO2). Verbundkoordination und Ansprechpartner: Dr.-Ing. habil. Wolfgang Minkley, IfG- Institut für Gebirgsmechanik GmbH, 01.01.2019

IOGP 2021 CCUS projects in Europe. Overview of existing and planned CCUS facilities. International Association of Ol & Gas Producers

KNEISKE T. M., BARTH H. & RAAB S. 2013 Untersuchung des Bedarfs elektrochemischer Speicher zur Sicherung der Netzstabilität im Rahmen des Projekts ESPEN. Konferenz für Nachhaltige Energieversorgung und Integration von Speichern -NEIS 2013- Universität der Bundeswehr Hamburg

MANZONI M., PATTI A., MACCARINI S. & TRAVERSO, A. 2021 Adiabatic compressed CO_2 energy storage. The 4th European sCO2 Conference for Energy Systems March 23-24, 2021, Online Conference

MERCANGÖZ M., HEMRLE J., KAUFMANN L., Z'GRAGGEN A. & OHLER, C. 2012 Electrothermal energy storage with transcritical CO_2 cycles. Energy 45 (2012) 407-415

MINKLEY W., KNAUTH M. & BRÜCKNER D. 2013 Discontinuum-mechanical behaviour of salt rocks and the practical relevance for the integrity of salinar barriers. ARMA, 47th US Rock Mechanics Symposium, San Francisco, CA, USA, 23-26 June 2013. Paper ARMA 13-388

MINKLEY W., KNAUTH M., FABIG T. & FARAQ N. 2015a Stability and integrity of salt caverns under consideration of hydro-mechanical loading. Mechanical Behaviour of Salt VIII, Rapid City, USA, 2015, pp. 217-227

MINKLEY W., KNAUTH M., BRÜCKNER D. & LÜDELING C. 2015b Integrity of saliferous barriers for heat-generating radioaktiv waste – natural analogues and geomechanical requirements. Mechanical Behavior of Salt VIII, Rapid City, USA, 26-28 May 2015, 159 – 170

MINKLEY W., BRANDT M., DOSTAL V., STEPANEK J., & LEHMANN J. 2021 Energiespeicherung in Salzkavernen mit superkritischem CO_2. EEK 137 Jg. · Ausgabe 1 | 2021

MOSER P. 2014 Status der Entwicklung des adiabaten Druckluftspeichers ADELE", Leopoldina-Symposium, 6. Februar 2014, Halle

PERSICHILLI M., KACLUDIS A., ZDANKIEWICZ E. & HELD T. 2012 Supercritical CO_2 Power Cycle Developments and Commercialization: Why sCO2 can Displace Steam," Presented at Power-Gen India & Central Asia 2012, 19-21 April, 2012, Pragati Maidan, New Delhi, India

RWE 2012 Druckluftspeicher. Technik-Dialog 2012 der Bundesnetzagentur „Speicher-technologien" Bundeskunsthalle Bonn, 16. März 2012

SAN MARTÍN J.I, ZAMORA I., SAN MARTÍN J.J., APERRIBAY V. & EGUÍA P. 2011 Energy Storage Technologies for Electric Applications. International Conference on Renewable Energies and Power Quality (ICREPQ'11) Las Palmas de Gran Canaria (Spain), 13th to 15th April, 2011

ZUNFT S. 2015 Adiabatic CAES: The ADELE-ING project. SCCER Heat & Electricity Storage Symposium, PSI, Villigen (CH), May 5, 2015

Numerical study of hydrogen storage cavern in thin-bedded rock salt, Anning of China

*Yanli Fang[1], Zhengmeng Hou[1,2] *, Ye Yue[1], Qianjun Chen[1], Jianfeng Liu[2]*

[1] Institute of Subsurface Energy Systems, Clausthal University of Technology, 38678 Clausthal-Zellerfeld, Germany, [2] Sino-German Energy Research Center, Sichuan University, 610065 Chengdu, China

* hou@tu-clausthal.de

ABSTRACT: Since China is leading a significant energy transition to achieve carbon neutrality by 2060, vigorously developing renewable energy is imperative. Hydrogen, a clean and renewable energy, characterized by hydrogen-electricity interchange, will play an important role during the energy transition. However, the development of hydrogen is restricted in China for the limited storage capacity. Compared with ground storage, underground hydrogen storage (UHS) provides a large-scale of capacity without occupying land source. Storing hydrogen in salt caverns is a preferred option for large-scale storage, since rock salt has a high ability of damage healing and characteristics of extremely low permeability, gas tight and inertia with hydrogen. In this paper, the feasibility of UHS storing hydrogen for steelmaking in thin-bedded rock salt Anning was studied. A THM coupled simulator FLAC^{3D}-TOUGH2MP was used to investigate the complex thermodynamic and mechanical behavior of rock salt during the operation. Stability and tightness of salt cavern were studied to evaluate the feasibility. Evaluation criterions of cavern volume convergence, long-term stress to strength ratio at reference depth and gas tightness were applicated. After 30 years' simulation, the stability and tightness analysis showed that the geological conditions of the thin-bedded rock salt Anning are favorable for the UHS in salt cavern.

1 Introduction

In order to achieve the goal of carbon neutrality, it is imperative to vigorously develop renewable energy such as wind power, photovoltaics and energy diversification. However, renewable energy is characterized of randomness, volatility and intermittency, which would inevitably bring challenges to the power balance of the power grid (Mei et al. 2017). The efficient conversion of renewable energy and large-scale energy storage technology provides means to solve problems resulted from power balance, such as wind and solar energy consumption, power peak shaving and valley filling. Among the clean secondary energy, hydrogen is recognized as the most promising secondary energy in the 21st century (Zou et al. 2019). However, the development of hydrogen is restricted in China for the limited storage capacity. Compared with ground storage, underground hydrogen storage (UHS) is favorable offering a large-scale of capacity without occupying land source.

Rock salt is recognized as an ideal medium for underground energy storage due to its extremely low permeability, good creep characteristics and damage recovery properties (Hou, 2003; Hou and Lux 2004; Minkley and Popp 2010). The proven energy that can be stored in salt caverns are hydrogen, natural gas, compressed air and oil. According to International Gas Union (IGU), there are 106 natural gas salt cavern storage and 4 hydrogen salt cavern storage in operation over the world. Besides, the earliest hydrogen salt cavern has been operating safely for nearly 50 years. There are 2 salt cavern natural gas storage in operation in Jintan salt mine of China, while several ones under construction. However, salt cavern hydrogen storage has been implemented in China yet.

Unlike natural gas salt cavern are mainly used for seasonal storage, since hydrogen could be applied in diversified fields, the storage could either be seasonal or be short-term depending on its utilization (Fang et al. 2022). For instance, when hydrogen is used for power generation, it would be seasonal storage. When hydrogen is applied for steelmaking or refuel fuel, it would

be stored for short-term (e.g., hours and days). Since the development of hydrogen in China just in the early stage, hydrogen is currently used for steelmaking and fuel cell fuel. Therefore, a long-term operation stability of hydrogen salt cavern storage for steelmaking is focused in this study. To investigate the complex thermodynamic and mechanical behavior of rock salt during the operation, a THM coupled simulator FLAC3D-TOUGH2MP was used (Figure 1). TOUH2MP is responsible for thermal and hydraulic simulation, while FALC3D is responsible for mechanical calculation.
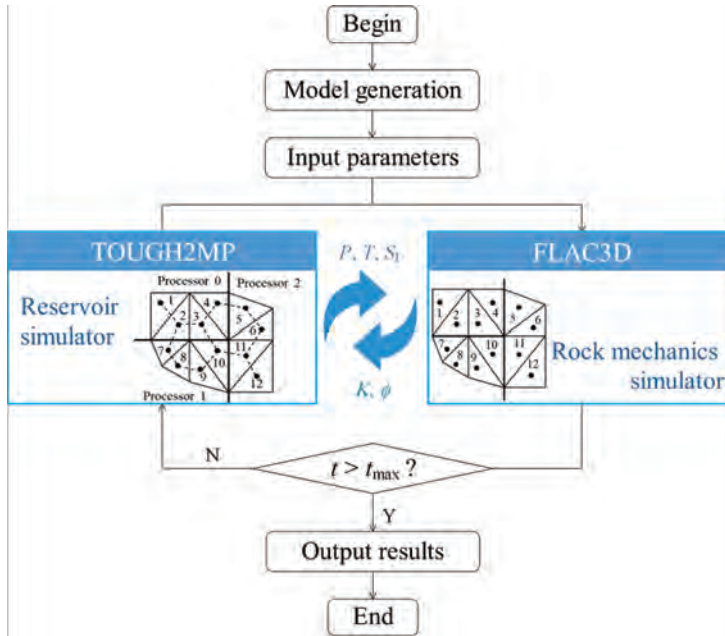
Figure 1: The flow chart of the coupled simulator FLAC3D-TOUGH2MP

Theoretically, the location selection of hydrogen salt cavern should be similar to that of the natural gas salt cavern. Based on the previous studies of different salt mining in China (Liu et al. 2019), Anning salt mine is a potential site for constructing salt cavern. Since there is no existing salt cavern in Anning salt mine, stability and tightness of designed salt cavern were studied to evaluate the feasibility of UHS in this study.

2   Anning salt mining

2.1   Geology conditions of Anning salt mining

Anning Salt Mine is located in Anning Basin, 20 km away from Kunming, the capital of Yunnan Province. The salt ore bed covers an area of 60 km^2, depositing in the upper Jurassic J$_3$an^2 stratum, buried at a depth from 126~960 m. Among of 60 km^2, 1.1038 km^2 has been already recognized to implement salt caverns in the future. The lithological descriptions of Anning salt mine are listed in Table 1. Unlike the pure rock salt in west, most of rock salt in China is bedded and impure. In Anning salt mine, rock salt and glauberite have an associated relationship. The main impurity of Anning rock salt is glauberite, while the main interlayer is mudstone.

Table 1: Properties of the mudstone and interlayer

Period	Epoch	Stratum	Depths (m)	Lithological description
Quaternary	-	Q	0-33	tillage soil
Tertiary	-	N	>75	sandy clay rock
Cretaceous	Middle	K_2g	>146.62	argillaceous sandstone
		K_2t^2	53.36-148.23	calcareous quartz sandstone
		K_2t^1	73.96-148.23	sandy mudstone
		J_3an^3	79.63-147.46	gypsum mudstone, glauberite
	Upper	J_3an^2	362.63-425.46	mudstone, rock salt, Glauberite, Glauberite rock salt
		J_3an^1	127.13-205.31	gypsum mudstone, mudstone, sandy mudstone
Jurassic		J_2l^4	172.07	argillaceous sandstone
	Middle	J_2l^3	14.44	calcareous mudstone
		J_2L^2	302.91	argillaceous sandstone, calcareous mudstone
		J_2L^1	179.38	quartz sandstone
	Lower	J_1L^2	59.15	silty mudstone
		J_1L^1	>55	argillaceous siltstone

2.2   Sealability of caprock

Four ore bodies have been classified from up to bottom in J_3an^2 in Anning Salt Mine. No.4 ore body is located at the top of J_3an^2, mainly composed of thin salt layer and thick glauberite, which claims that the solubility of this formation is poor and not favorable for salt cavern construction. The proposed formation for salt cavern should count from the top of No.3 ore body downwards. Therefore, the caprock of salt cavern is the salt formation (direct caprock) between the top of No.3 ore body and the upper glauberite and gypsum formation (interval caprock) in J_3an^3. The top boundary of the caprock is buried at a depth of 80~460m, and the bottom boundary is buried at a depth of 100~780 m. The thickness of the direct caprock that in the potential area is 38~171 m, and the total caprock thickness is 76~200 m.

2.2.1   Breakthrough Pressure

The value of the closed hydrocarbon column that can be obtained by the size of the breakthrough pressure directly indicates the sealing ability of the caprock. The minimum breakthrough pressure is the minimum pressure required for the gas to break through the overburden. According to the coring test date of ZK2 well (Gou et al. 2013), the minimum breakthrough pressure is 3~14 MPa with a buried depth of caprock varies from 500m to 560m. And the height of closed air column is great than 200 m, which is beyond the thickness of overburden caprock of 185 m. Therefore, the tightness of overburden caprock to close air column is qualified the requirement of salt cavern.

2.2.2   Permeability and porosity

Permeability and porosity of caprock have been investigated in the previous studies (Yang 2016 and Gou et al 2013). The permeability of caprock in ZK2 well is in a range of 2.7 $\times 10^{-18}$ ~ 7.2 $\times 10^{-18}$ m^2, and the porosity varies from 0.8% to 2.1%. It is obvious that the permeability and porosity or caprock in ZK2 well is extremely low and the airtightness is agreeable. With

the respect to tightness of interlayers, the permeability of mudstone interlayer is from 3.5×10^{-18} to 9.87×10^{-18} m², and the porosity is in a range of 1.0% to 7.3%. Since the caprock is composed of rock salt and mudstone and the permeability of mudstone is greater, the real permeability of rock salt for salt cavern should be less than that of caprock. Therefore, an assumed permeability of rock salt in following simulation is supposed as 1.0×10^{-19}.

3   Numerical case study

3.1   Model setup

Based on the actual geological and hydrogeological conditions of Anning Salt mine mentioned above, a salt cavern model had been generated by FLAC 3D. The full cavern is 100,000 m³ with a radius of 25 m height of 60 m. (Fig. 2), buried at a central line of -665 m. This is to avoid constructing cavern between interlayers. As shown in the Figure 2, the whole rock salt formation lies at the depth between -577 m and -930 m, including several mudstone interlayers. The direct cap rock in this case is 58 m which meets the cap rock thickness requirement of 38~171m. Due to the axial symmetry and isotropy of the rock, a quarter model was established to reduce the computation time. The boundary of the entire model in Z axis is between -230 ~ -1230m, which contains 300m mudstone formation above and below salt formation. While in X and Y axis is 500m. The model is finely discretized in the near-field of the rock salt cavern and the interlayer. As the boundary, the bottom surface of this model was vertical-direction fixed, and the other four lateral surfaces were horizontal-direction fixed. To simplify computation, the strata overlying depth of 230 m is simplified to a surface loading.

In order to simulate the process of injection and withdrawn in the salt cavern to investigate the complex thermal and mechanical behaviors of rock salt, a group of extra elements named "air" has been generated. As the name indicates, the group "air" represents the stored hydrogen in salt cavern with a high porosity of 1.0, high permeability of 1.0×10^{-9} m², low Young's modulus of 3.5 MPa and low Poisson's ratio of 0.25. The exact values used for the permeability and deformation modulus of the cavern interior are not important as long as the values are much less than the values for the surrounding rock (Rutqvist et al. 2012). As shown in Figure 2, the group air only contains the elements near the edge of the cavern, from a radius of 24 m to 25m. There is no need to generate too many grids to represent stored hydrogen, because in the TOUGH2 model, the volume of group "air" can decrease to the real cavern volume.
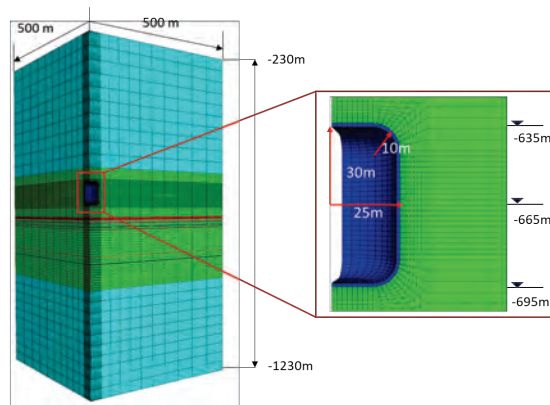
Figure 2: The simulation model based on geological conditions of Anning salt mine

The material properties for the mechanical, hydraulic and thermodynamic simulations are listed in Table 2 and Table 3. The mechanical properties were obtained from the previous studies (Wang et al. 2015). With the respect to mechanical model, Mohr-Coulomb constitutive model

was used to describe the behavior of the mudstone, while the power-law constitute model was applied for the rock salt and the interlayers. As described in the hydrogeological conditions, the salt formation is impervious in Anning scale time. Therefore, fluid infiltration in rock salt is considered in this study. Instead, the pressure and temperature changes during the injection and withdrawn process is notable. Thereby, the initial pore pressure in salt formation was set pretty low just a little greater than atmospheric pressure. Initial temperature was set using a vertical gradient of 0.03 ℃/m and with a constant temperature of 10 ℃ at the ground surface.

Table 2: Properties of the mudstone and interlayer

Properties	Material	
	Mudstone	Interlayer
Density (kg/m³)	2490	2490
Young's modulus (GPa)	22.93	22.93
Poisson's ratio (-)	0.15	0.15
Lateral stress coefficient	0.8	0.8
Internal friction angle (°)	45.4	45.4
Cohesion (MPa)	4.35	4.35
Tensile strength (MPa)	3.19	3.19
Creep parameter A (1/yr)	-	2.30×10^{-8}
Creep Parameter n (-)	-	2.000

Table 3: Properties of the rock salt

Properties	Material	Properties	Material
	Rock salt		Rock salt
Density (kg/m³)	2200	Thermal expansion coefficient (1/ ℃)	3.8×10^{-5}
Young's modulus (GPa)	6.84	Thermal conductivity (W/m ℃)	0.68
Poisson's ratio (-)	0.21	Specific heat (J/ kg ℃)	860
Lateral stress coefficient	1.0	Effective porosity (-)	0.002
Internal friction angle (°)	39.3	Permeability (m²)	1×10^{-19}
Cohesion (MPa)	8.4	Residual gas saturation (-)	0
Tensile strength (MPa)	1.38	Residual liquid saturation (-)	0.1
Creep parameter A (1/yr)	8.89×10^{-7}	van Genuchten, P_0 (MPa)	5.6
Creep Parameter n (-)	2.618	Van Genuchten, m (-)	0.6

In the first five-year before operation, the pressure in cavern was kept constant at 13 MPa for construction.13 MPa was also set as the maximum operating pressure during the injection and withdrawn process. The minimum operating pressure was set as 8 MPa. Normally, the cavern pressure typically varies between 20% and 90% of the in-situ stress at cavern roof depth (Lux et al. 2009; Xing et al. 2014;). In this case, 13 MPa was set as 85% of the in-situ stress, while 8 MPa was determined by simulations. Since the stored hydrogen is used for steelmaking, which means the process injection and withdrawn may change frequently to meet the

steelmaking produce. The supposed injection rate was assumed for 4.0 kg/s for 6 hours at a constant temperature of 25 °C. While the withdrawn rate was assumed as same. 6 hours for maximum operating pressure storage and 6 hours for minimum operating pressure storage (Figure 3). The reason for setting 8 MPa as minimum storage pressure and corresponding - 4.0 kg/s withdrawn rate is upon the simulation results. When the absolute value of withdrawn rate is greater than 4.0 kg/s, the pressure at the end of withdrawn phase is below 8 MPa and the corresponding end temperature is approaching 0°C. Hence, in this case, 8 MPa is the minimum operating pressure.

(a) Pressure change for one day

(b) Injection rates for one day
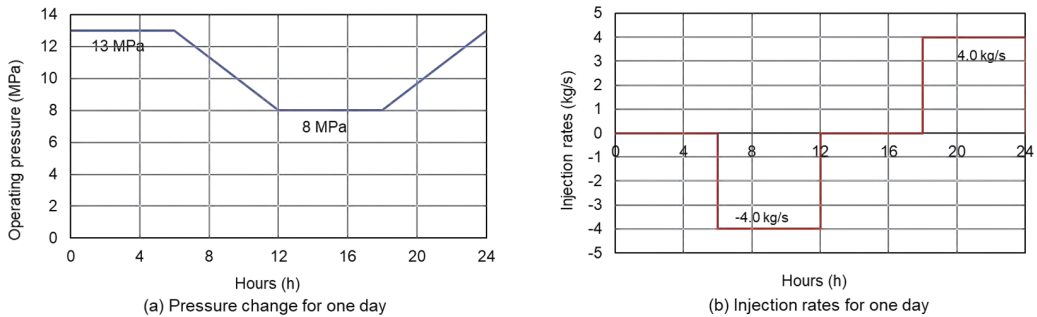
Figure 3: Pressure change in salt cavern and corresponding injection plan

3.2 Evaluation criteria

To investigate the stability and usability of the underground salt cavern, qualified criteria is important. There are three widely used evaluation criteria, namely, stability criteria, airtightness criteria and usability criteria. The maximum stress during the operation of the rock salt cavern often appears at the reference depth of the contour. That is the weakest area of the entire model. For the vertical cavern, the reference depth is at the 1/3 height from bottom or 2/3 height from top (Lux, 1984). Based on the classical design criteria in Lux (1984), Bertram (2000), the following design criteria for the long-term operation of the salt cavern were proposed:

▪ No spalling: The stress-to-strength ratio (the short-term strength of rock salt) at the contour point of the rock salt cavern at the reference depth does not exceed the defined limit value (e.g. 50%). If this is satisfied, there is no spalling.

$$\max cal\eta_{cf} = \frac{\sigma_{eq}(\sigma_1, \sigma_2, \sigma_3)}{\beta} \le 50\% \tag{1}$$

Where max cal η_{cf} is the maximum calculated stress-to-strength ratio at the cavern contour of the reference depth in dimensionless; $\sigma_{eq}(\sigma_1, \sigma_2, \sigma_3)$ is the equivalent stress in MPa; β is the peak strength derived from the short-term tests in MPa.

▪ No creep failure: The effective strain increment at the rock salt cavern contour point at the reference depth does not exceed the defined limit (e.g. 3%) in a storage cycle. If this is the case, there is no creep failure.

In addition, in order to ensure the usability during the long-term operation of the salt cavern, two main requirements were proposed:

▪ The convergence volume of the salt cavern does not affect the normal use of the storage cavern. The volumetric convergence should be less than 5% after 5 years' operation, and it should be less than 30% after 30 years' operation.

▪ The resulted surface subsidence rate and the inclination should not affect the surface structures. The subsidence should be restricted in a controllable range.

3.3 Results

A four-six-phase injection plan has operated in this study, namely, each phase lasts six hours for storage-injection-storage-withdrawn. As described in introduction, in the coupled simulator FLAC3D-TOUGH2MP, TOUGH2 MP is responsible for thermal and hydraulic simulation while FLAC3D is responsible for the mechanical calculation. Figure 4 and Figure 5 shows the pressure and temperature distribution around the cavern for one cycle day. Since fluid infiltration is not focused in this study, only temperature parameters were sent to FLAC3D for creep calculation.

Obeying the regular pattern of temperature in Figure 4 and Figure 5, 30 years' simulation had been performed. The results of cavern volume convergence and stress-to-strength ratio at reference depth were obtained. Fig 6(a) shows the volumetric convergence of the salt cavern during operation. Cavern volume convergence refers to the ratio between the amount of volume change, which is caused by the surrounding rock stress and the cavern internal pressure during the operation process, and the original volume. It can be seen, in the first 5 years, since the pressure is constant at 13 MPa, which is also the maximum operating pressure, the cavern volume shrinks slowly. While after 5 years, when the variable operation begins, the convergence speed of cavern volume is apparently increased. After 30 years' operation, the volumetric convergence of salt cavern is 0.28% much less than the referent convergence of 30%. This satisfies the availability requirements.

(a) Pressure at he end of maximum pressure storage phase

(b) Pressure at the end of withdrawn phase

(c) Pressure at the end of minimum pressure storage phase

(d) Pressure at the end of injection phase
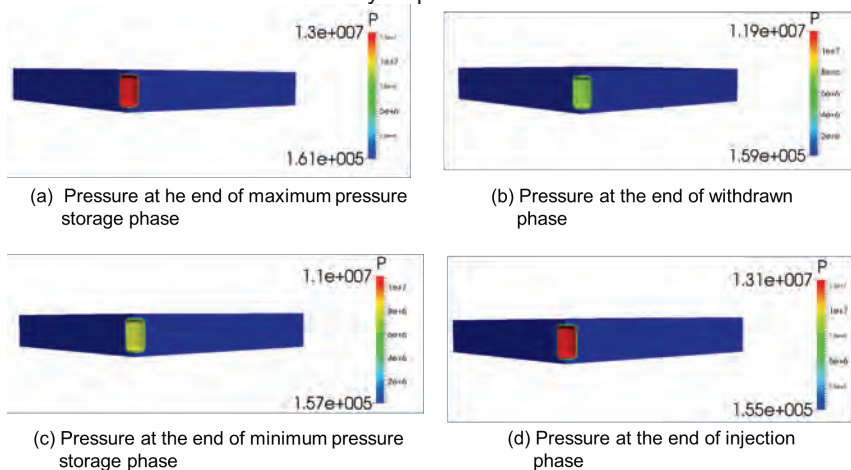
Figure 4: Pressure distribution around cavern in one cycle day

(a) Temperature at he end of maximum pressure storage phase

(b) Temperature at the end of withdrawn phase

(c) Temperature at the end of minimum pressure storage phase

(d) Temperature at the end of injection phase
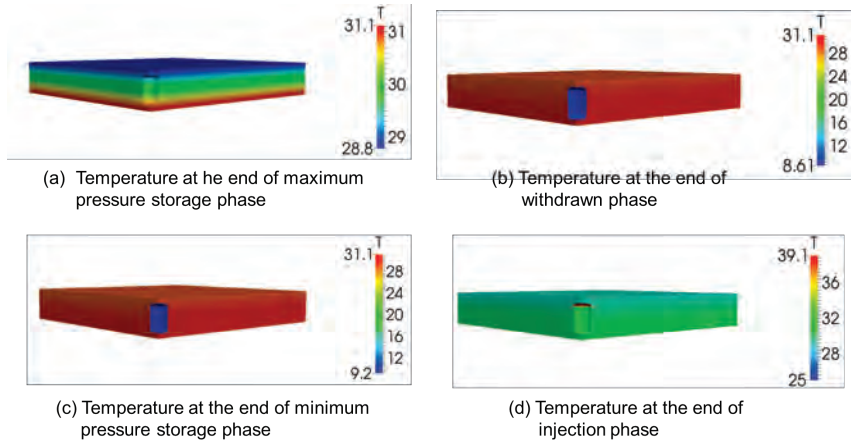
Figure 5: Temperature distribution around cavern in one cycle day

Fig 6(b) displays the temporal evolution of stress to strength ratio (related to the long-term strength) at the cavern contour point at the reference depth. It can be seen, in the first 5 years, since the pressure in salt cavern is constant as 13 MPa, the stress to strength reduces slowly. Then, it increases when the variable operation process begins. Since the pressure is changed as a daily cycle not seasonal cycle, it approximately operating at an assumed average pressure for one day. Obviously, this average pressure is smaller than 13 MPa. Therefore, the stress to strength ratio increases not rapidly, which indicates that the rock salt is adapting that pressure change. After it arrives the maximum average pressure of 10.5 MPa, the stress to strength ratio decreases again. The maximum stress to strength ratio in during operation is 13.34%, which also meets the stability criteria.

(a) Volume convergence (b) Stress to strength ratio
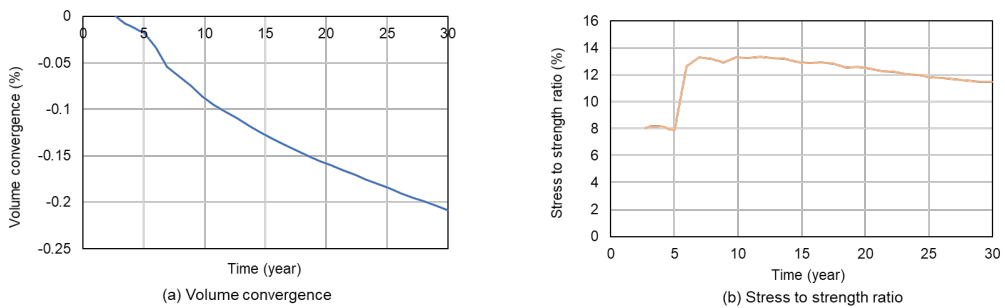
Figure 6: volume convergence and stress to strength ratio during 30 years' operation

With respect to the airtightness requirements, Figure 7 shows the gas saturation after 30 years' operation, gas mainly exists in the "air" elements. Only a few gases infiltrated into the surrounding rock. It proves that the tightness ability of Anning rock salt to close gas in the cavern, which is reliable.
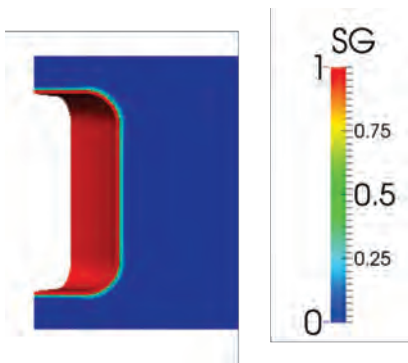
Figure 7: Gas saturation around cavern after 30 years' operation

4   Conclusion and discussion

In this paper, the authors proposed a novel method to simulate the short-term hydrogen salt cavern storage using a coupled FLAC3D-TOUGH2MP simulator. A vertical salt cavern of 100,000 m^3 was designed and simulated based on the actual geological conditions of Anning salt mine. The following conclusions can be drawn:

- The geological conditions of Anning salt mine are favorable for salt cavern construction and operation. It has an extremely low permeability and porosity of caprock, which ensures the prerequisite of airtightness for salt cavern implement.

- The coupled FLAC3D-TOUGH2MP simulator provides means to investigate the complex temperature and pressure change for the short-time storage in salt cavern. TOUH2MP responsible for thermal and hydraulic simulation, while FALC3D is responsible for mechanical calculation.

- After 30 years' simulations, the designed salt cavern meets the useability, stability and airtightness criteria, which proves the potential for UHS in Anning salt mine.

Acknowledgment

References

BERTRAM, J. 2000. Untersuchung zur Weiterentwicklung der Auslegungskriterien für Kavernen im Steinsalzgebirge. ISBN: 3-89720-388-X, Dissertation an der TU-Clausthal.

FANG, Y., HOU, Z. & YUE, Y. 2022. A new concept of multifunctional salt cavern hydrogen storage applied to the integration of hydrogen energy industry. Advanced Engineering Sciences, 2022, 54(1):128-135 (in Chinese).

GOU, Y., WU, Z. & QI, H. 2013. Assessment on the cap rock tightness of the gas storehouse of Anning salt cavern. China well and rock salt, 04(44): 16-19.

HOU, Z. 2003. Mechanical and hydraulic behavior of salt in the excavation disturbed zone around underground facilities. Int. J. of Rock Mechanics and Mining Sciences, 40 (2003):725-738.

HOU, Z. & LUX, KH. 2004. A new coupling concept for the hydro-mechanical interaction of clay stone and rock salt in underground waste repositories. International Journal of Rock Mechanics and Mining Sciences 41:708-713.

LIU, G., JIANG, Y. & YANG, G. 2019. Characteristics of rock salt mines and suitability evaluation of salt cave storages in Yangtze River Economic Zone. Geological Survey of China, 06(05): 89-98.

LUX, KH.1984. Gebirgsmechanischer Entwurf und Felderfahrungen im Salzkavernenbau. Ferdinand Enke Verlag Stuttgart, Germany.

LUX, KH. 2009. Design of salt caverns for the storage of natural gas, crude oil and compressed air: Geomechanical aspects of construction, operation and abandonment. In: Evans D, Chadwick R (eds) Underground Gas Storage: Worldwide Experiences and Future Development in the UK and Europe, Geological Society London, Special Publications, pp 93–128.

MEI, T., GONG, M. & QIN, G. 2017. Advanced adiabatic compressed air energy storage system with salt cavern air storage and its application prospects. Power System Technology ,41(10): 3392-3399.

MINKLEY, W. & POPP, T. 2010. Final disposal in rock salt–geomechanical assessment of the barrier integrity. In: Proceedings of the 44th US Rock Mechanics Symposium (ARMA-10). American Rock Mechanics Association (ARMA), Salt Lake City/Utah, pp 10–492

RUTQVIST, J., KIM, H-M. & RYU, D-W. 2012. Modeling of coupled thermodynamic and geomechanical performance of underground compressed air energy storage in lined rock caverns International Journal of Rock Mechanics and Mining Sciences 52:71-81

WANG, G., XING, W., LIU, J., HOU, Z. & WERE, P. 2015. Influence of water-insoluble content on the short-term strength of bedded rock salt from three locations in China. Environmental Earth Sciences, 73(11), 6951–6963.

XING, W., ZHAO, J. & DUSTERLOH, U. 2014. Experimental study of mechanical and hydraulic properties of bedded rock salt from the Jintan location. Acta Geotechnica, 9(1): 145-151.

YANG, H. 2016. Prediction of favorable construction zones for Anning gas storage. Mater thesis. Southwest Petroleum University, Chengdu.

ZOU, C., YANG, Z. & ZHANG, F. 2019. Strategic role of the synthetic hydrogen production and industry in energy independence of China. Natural Gas Industry, 39(01): 1-10.

Geomechanical analysis of oil storage caverns in salt domes with a low stress creep mechanism added to the M-D model

Steven R. Sobolik[1]*, Tonya S.A. Ross[1]

[1]Sandia National Laboratories, Albuquerque, NM, USA

* srsobol@sandia.gov

ABSTRACT: Sandia National Laboratories has long used the Munson-Dawson (M-D) model to predict the geomechanical behavior of salt caverns used to store oil at the Strategic Petroleum Reserve. Salt creep causes storage caverns to deform inward, thus losing volume. This loss of volume affects the salt above and around the caverns, stresses borehole casings, and creates surface subsidence which affects surface infrastructure. Therefore, accurate evaluation of salt creep behavior drives decisions about cavern operations. Parameters for the M-D model are typically fit against laboratory creep tests, but nearly all historic creep tests have been performed at equivalent stresses of 8 MPa or higher. Creep rates at lower equivalent stresses are very slow, such that tests take months or years to run, and the tests are sensitive to small temperature perturbations (<0.1°C). A recent collaboration between US and German researchers characterized the creep behavior at low equivalent stresses (<8 MPa) of salt from the Waste Isolation Pilot Plant. The M-D model was recently extended to include a low stress creep "mechanism". The results show that the inclusion of low stress creep significantly alters the prediction of steady-state cavern closure behavior and indicates that low stress creep is the dominant displacement mechanism at the dome scale. This paper also describes the changes to predicted stresses and strains that impact cavern and wellbore integrity. The results of the calculations in this paper indicate the need for laboratory creep tests at low equivalent stresses on salt from storage cavern sites.

1   Introduction

The U.S. Strategic Petroleum Reserve (SPR), operated by the U.S. Department of Energy (DOE), stores crude oil in solution-mined caverns in the salt dome formations of the Gulf Coast. There is a total of 60 storage caverns located at four different sites in Texas (Bryan Mound and Big Hill) and Louisiana (Bayou Choctaw and West Hackberry), along with several abandoned or decommissioned caverns. Each cavern is constructed and then operated using a wellbore or wellbores that are lined with steel casings cemented in place from the surface to near the top of the cavern. The West Hackberry salt dome is in the extreme southwestern corner of Louisiana, some 24 km from the Louisiana/Texas border to the west and the Gulf of Mexico to the south. It has an oil storage capacity of about 35×10^6 m³ (222×10^6 barrels) within 21 caverns, and has operated since 1980. Sandia National Laboratories (SNL) has served as a technical advisor on the SPR to DOE since 1980. As part of that responsibility, SNL has long used computational geomechanical models to analyze the viscoplastic, or creep, behavior of the salt in which the oil storage caverns reside. Salt creep causes storage caverns to deform inward, thus losing volume. This loss of volume affects the salt above and around the caverns, puts stresses and strains on borehole casings, and creates surface subsidence which affects surface infrastructure. Therefore, accurate evaluation of salt creep behavior drives decisions about cavern operations. To perform geomechanical computational analyses of the SPR sites, SNL has used the Sierra/Solid Mechanics (2018) finite element code. Sierra/SM has many different constitutive models for viscoplastic behavior, including the Munson-Dawson (M-D) constitutive model for salt. The M-D model was originally developed in the 1980s to predict the thermomechanical behavior of rock salt (Munson & Dawson 1979; 1982; Munson 1998). Since then, it has been used to simulate the evolution of the underground in nuclear waste repositories, mines, and storage caverns for gases and liquids. A recent collaboration between US and German researchers interested in the utilization of salt formations for nuclear waste repositories has recently benchmarked salt creep models against room closure

measurements. The Waste Isolation Pilot Plant (WIPP) in southeastern New Mexico consists of excavated rooms within a bedded salt formation for the permanent storage of transuranic waste. Simulations of Room D at WIPP using the M-D model under-predicted the room's vertical closure rate by a factor of 2.8 at 3.7 years after room excavation (Reedlunn 2016; 2018a). The M-D model numerical implementations in Sierra/SM also ran quite slowly during these simulations. As a result, three enhancements were made to the M-D model in (Reedlunn 2018b). (1) The calculation of equivalent stress was changed to a more generalized formulation proposed by Hosford (1972). (2) New transient and steady-state rate terms were added to capture salt's creep behavior at low equivalent stresses (below about 8 MPa). (3) The M-D model's numerical implementation was overhauled, adding a line search algorithm to the implicit solution scheme. The first enhancement was described in detail in Reedlunn (2018b), but it is the second enhancement, the addition of a low equivalent stress creep component to the M-D model, that is the primary subject of this paper. This newly enhanced M-D model is being called the M-D Viscoplastic model (Sobolik & Ross 2021). The results presented in this paper will show that the inclusion of low equivalent stress creep significantly improves the prediction of steady-state cavern closure behavior.

2   M-D Viscoplastic Model Description

Plastic deformation of intact salt only occurs in the presence of shear stress. Shear stress only occurs when the three principal normal stresses are unequal; such an anisotropic stress state is also called deviatoric stress. Originally, the M-D model utilized the von Mises stress as its equivalent shear stress measure σ_{eq}, but Munson et al. (1989) switched σ_{eq} to the Tresca stress. Both of these formulations are specific instances of a more general formulation for an equivalent stress measure proposed by Hosford (1972). The Hosford stress is given by.

$$\sigma_{eq} = \left\{ \frac{1}{2} \left(|\sigma_1 - \sigma_2|^a + |\sigma_2 - \sigma_3|^a + |\sigma_3 - \sigma_1|^a \right) \right\}^{1/a} \tag{1}$$

where σ_i are the principal stresses and a is a material parameter. For the Tresca equivalent stress, a can be 1 or ∞ (these derive the same values – see Reedlunn (2018b) for derivation), and for von Mises stress, a can be 2 or 4 (also equivalent, see Reedlunn (2018b)). For the calculations using the M-D Viscoplastic model presented in this paper, σ_{eq} was calculated using a value for a of 100 to approximate a Tresca formulation (Sobolik & Ross, 2021).

The original M-D creep model additively decomposed the steady state creep behavior of salt into three "mechanisms" (Munson, 1998). Mechanism 1 is meant to capture dislocation climb, which dominates at high temperatures and low equivalent stresses. Mechanism 2 dominates at low temperatures and medium equivalent stresses, and is the dominant mechanism measured in laboratory creep tests of SPR salts and salts from the Waste Isolation Pilot Plant (WIPP) in southeastern New Mexico. Mechanism 3 is activated at stresses > 20 MPa which is negligible for the stress states experienced at SPR sites and will not be discussed here. A more complete description of the entire model is given in Munson (1998); the equations for Mechanisms 1 and 2 (and which was chosen for Mechanism 0 as explained later) are:.

$$\dot{\varepsilon}^{ss} = \sum_{i=0}^{3} \dot{\varepsilon}_i^{ss} \tag{2}$$

$$\dot{\varepsilon}_i^{ss} = A_i \exp\left(-\frac{Q_i}{RT}\right) \left(\frac{\sigma_{eq}}{\mu}\right)^{n_i} \text{ for } i = 0, 1, \text{ and } 2, \tag{3}$$

where A_i is the creep constant for each mechanism, n_i is the creep exponent, Q_i is the activation energy, R is the universal gas constant, and T is the absolute temperature of the salt. The original M-D model input parameter values for West Hackberry are based on laboratory creep tests using core samples from two boreholes (Munson, 1998); these parameters are shown in Table 1. In addition, for previous SPR geomechanical analyses multiplication factors were applied to the steady-state creep coefficient A_2 for Mechanism 2 in Equation 3, and the

transient creep coefficient K_0. These multiplication factors were used to try to match predictions of surface subsidence and cavern volume closure to historical subsidence data and calculated cavern volume closure from wellhead pressure data using the software CAVEMAN (Ballard & Ehgartner, 2000). For both Bryan Mound and West Hackberry calculations, it was much easier to match the surface subsidence data than the cavern volume closure histories (Sobolik, 2015 & 2018). In particular, it has been difficult to predict match the steady-state cavern closure rate using the M-D model in its original formulation. The M-D model relies on laboratory creep test data to obtain parameters to model steady-state creep behavior. However, nearly all laboratory creep testing has been performed at equivalent stresses of 8 MPa or higher. The primary reason that tests have not been performed at lower equivalent stresses is that the creep rates are very slow so the tests take months or years to run, and they are very sensitive to small temperature perturbations (<0.1°C). Despite these difficulties, several researchers (e.g. Bérest et al. (2005); Bérest et al. (2019); Salzer et al. (2015); Düsterloh et al. (2015)), have reported larger steady-state creep rates at than would be expected from extrapolating rates from higher stresses.

To capture the low equivalent stress behavior, Reedlunn (2018b) added a fourth mechanism to the M-D model. The micro-mechanical mechanism responsible for the creep behavior at low equivalent stresses is probably pressure solution redeposition (J. Urai et al. 2008; Bérest et al. 2019), but Mechanism 0 was given the same mathematical form as Mechanisms 1 and 2 for simplicity. For the extended M-D Viscoplastic model, the addition of the low equivalent stress mechanism (Mechanism 0) is expected to accommodate the creep experienced by the large volume of salt between the caverns existing at that low stress state. Reedlunn (2018) calibrated the parameter values for Mechanism 0 in Eq. (3) against the Salzer et al. (2015) and Düsterloh et al. (2015) experiments on WIPP salt. His values for the Mechanism 0 parameters in Equation 3 are listed in Table 2. Reedlunn used a value of 16 for the Hosford exponent in Eq. 1, which improved computational speed and stability and produced predictions which matched data well; for the calculations performed for this paper a value of 100 was used as it improved computational speed. Due to a lack of currently available test data on SPR salt, these parameters will be used in the extended M-D Viscoplastic model for the SPR.

Table 1: M-D model parameters published for West Hackberry salt (Munson 1998).

Property or parameter	Values
Density, lb/ft^3	144 (2300 kg/m^3)
Elastic modulus, lb/ft^2	648 ×10^6 (31.0 GPa)
Shear modulus, lb/ft^2	259 ×10^6 (12.4 GPa)
Poisson's ratio (dimensionless)	0.25
Primary Creep Constant A_1, sec^{-1}	9.81 ×10^{22}
Exponent n_1 (dimensionless)	5.5
Q_1, cal/mol	25000 (104,600 J/mol)
Secondary Creep Constant A_2, sec^{-1}	1.13 ×10^{13}
Exponent n_2 (dimensionless)	5.0
Q_2, cal/mol	10000 (41840 J/mol)
B_1, sec^{-1}	7.121×10^6
B_2, sec^{-1}	3.55×10^{-2}
σ_0, , lb/ft^2	429 ×10^3 (20.57 MPa)
q (dimensionless)	5335
m (dimensionless)	3.0
K_0 (changed to K_1 in M-D viscoplastic model)	6.275×10^5
c (1/R) (0.009198/1.8)	0.00511
A (dimensionless)	-17.37
B (dimensionless)	-7.738
Δ (dimensionless)	0.58

Table 2: M-D Viscoplastic model low stress steady-state parameters (Reedlunn, 2018b).

Parameter	Value
Low Equivalent Stress Creep Constant A_0, sec^{-1}	56.17
Exponent n_0 (dimensionless)	1.595
Q_0, cal/mol	10000 (41840 J/mol)

Figure 1 shows how the implementation of the low equivalent stress mechanism would change the steady-state strain rate as a function of stress. Strain rate is plotted as a function of equivalent stress for both the original M-D and extended M-D Viscoplastic models, using the original Munson properties for Bryan Mound and West Hackberry salt and the Table 2 properties for Mechanism 0. Also show in Figure 1 are the typical range of stresses at which laboratory creep tests are performed (8-20 MPa), which usually occur within a few feet of the cavern walls, and the lower stress range (1-8 MPa), which occurs in most of the inter-cavern or pillar salt. Even though the strain rates predicted by mechanism 0 are 2-3 orders of magnitude less than strain rates in the normal testing range, those small strain rates over a much larger volume of salt could have profound effects on the overall behavior of the dome.
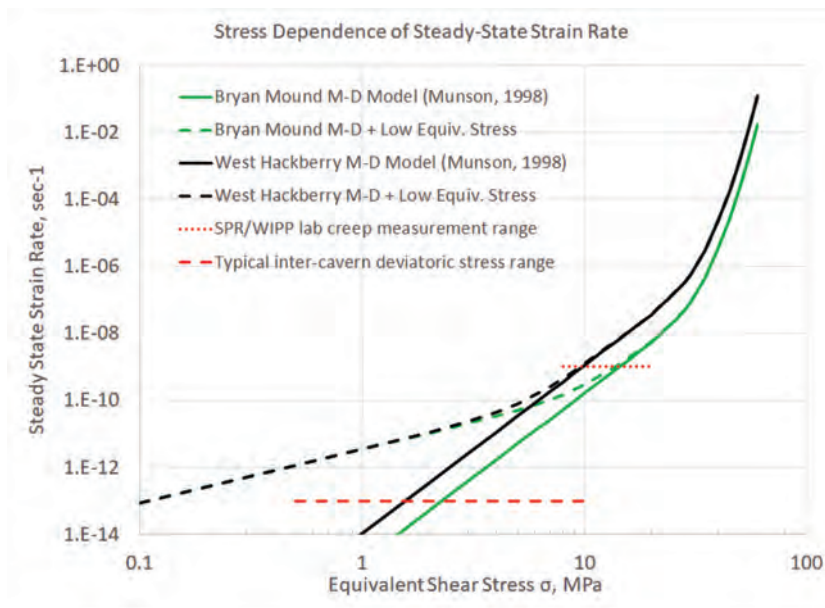
Figure 1: Effect of additional low equivalent stress mechanism in M-D viscoplastic model.

3 Computational Model for the West Hackberry Site

The West Hackberry site consists of 22 caverns. Figure 2 shows the relative locations and geometries of these caverns. The SPR purchased five existing caverns in the early 1980s. These five Phase 1 caverns – Caverns 6, 7, 8, 9, and 11 – were created as early as 1946 and were used for brine production and storage before the SPR took ownership of them. After that time, seventeen other storage caverns (numbered 101 to 117) were created over an eight-year period. The post-1981 caverns were built via solution mining, and all have a generally cylindrical shape (more specifically, frustums with the larger diameter at the top) of approximately 600 m (2000 feet) height and 30-45 m (100-150 feet) in radius. The Phase 1 caverns, however, were originally built for brine production, and thus they were constructed with less concern about the long-term stability of the cavern shape.

The mesh for the geomechanical computational model is illustrated in Figure 3. The left diagram shows the entire mesh used for these calculations, and the right diagram shows the

same view with the overburden and caprock removed to expose the salt formation (in magenta and yellow). The mesh comprises 5.99 million nodes and 5.95 million hexahedral elements. Four material blocks are used in the model to describe the stratigraphic layers: the overburden, caprock, salt dome and sandstone surrounding the salt dome. The overburden is made of unconsolidated sand, and the caprock layer is made of gypsum and limestone. These materials were modeled as elastic materials (Sobolik 2015). The overburden layer is 480 m thick, and the caprock is 120 m in the central portion of the dome. To include the downward contour of the top of the salt dome at its outer perimeter, an outer ring of caprock has a total thickness of 240 m.
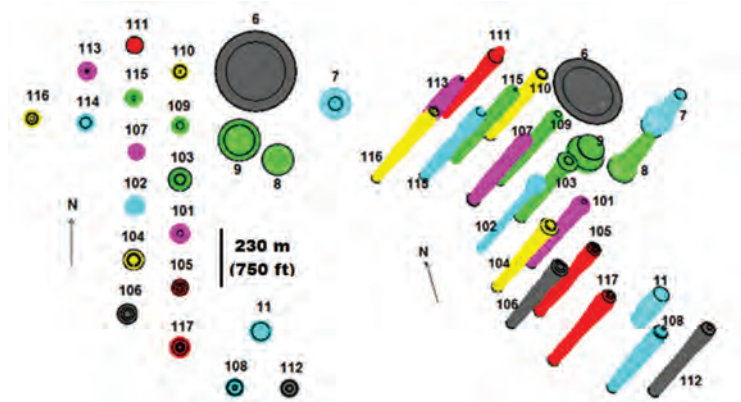
Figure 2: West Hackberry caverns included in the computational mesh (2 views).
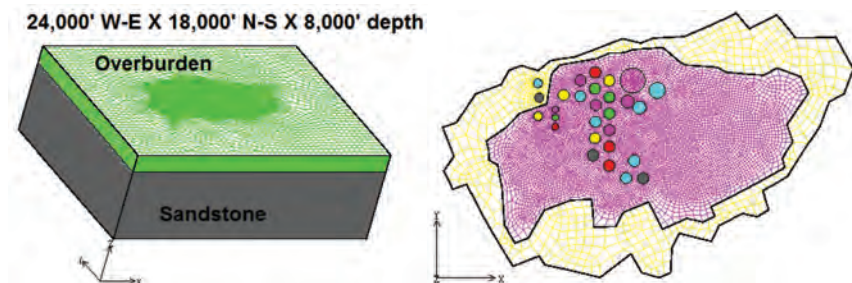
Figure 3: Computational mesh, full-dome West Hackberry model.

4 Predictions of subsidence and cavern closure

This section describes the results of several different sets of model calculations with the geomechanical model of the SPR West Hackberry salt dome for which the salt constitutive model parameters are varied. The results will compare predicted values for cavern volume closure and surface subsidence to values measured at the West Hackberry site.

The classic M-D material properties for West Hackberry (WH) salt were based on laboratory data from core samples, and listed in Table 1. The most recent full-scale simulation of the WH site using the M-D model was performed in 2015 (Sobolik, 2015); for those simulations, multiplication factors were applied to the steady-state creep coefficient A_2 for Mechanism 2 in Equation 3, and the transient creep coefficient K_0. (This is the nomenclature used in the original M-D model – the same coefficient is called K_1 in the M-D Viscoplastic model.) These multiplication factors were applied to the cylinder of salt surrounding each respective cavern, and ranged from 1.21 to 3.20. Figure 4 shows the measured cavern volume closure along with predictions from the 2015 WH model calculations through 2015 (results are for Phase 2

caverns on the east side of the site). For all the figures from this point forward, solid lines are used for measurements, dashed lines for prediction results. Even with a variety of multiplication factors applied to A_2 and K_0 individually for regions around each cavern, it was difficult to match the steady-state closure rate. The large jumps in each closure history represent workovers, which are cavern maintenance periods during which the wellhead pressure is reduced to zero for a period of one to six months (typically three months). During workovers, the transient component is temporarily dominant. These large volume changes help to give a time-averaged prediction of cavern closure that roughly matches the measured values, but this type of match is not desirable. Figure 5 shows the measured surface subsidence at cavern well locations along with predictions from the 2015 WH model calculations. The predicted values match the measured values very well, which in part led to the decision to use the set of parameters applied to the 2015 model.
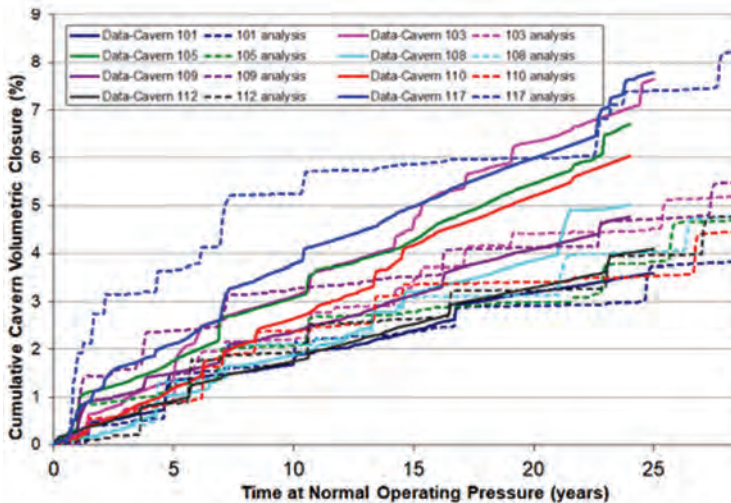
Figure 4: Comparison of West Hackberry predicted cavern closure vs. measurements, 2015 WH M-D properties – dashed lines for predictions, solid lines for data (Sobolik 2015).
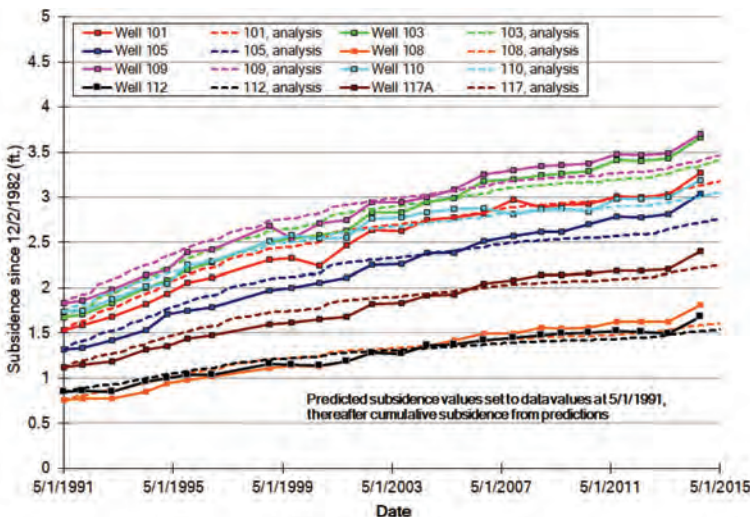
Figure 5: Comparison of West Hackberry predicted surface subsidence vs. measurements, 2015 WH M-D properties – dashed lines for predictions, solid lines for data (Sobolik, 2015).

The use of Mechanism 0 in the M-D Viscoplastic model had a significant effect on predictions of cavern volume closure and surface subsidence at West Hackberry. Figure 6 shows the same measured cavern volume closure as Figure 4, but the predictions utilized Mechanism 0. For these calculations, the A_2 and transient creep K_0 (now renamed K_1 in the new model) multiplication factors are the same as used for the 2015 analysis, with the low equivalent stress Mechanism 0 included, with the Hosford exponent $a=100$. It is obvious that the addition of the low stress creep over a large volume of salt has added greatly to the predicted cavern closure rates. The steady-state closure rates between workovers, as indicated by the slopes of the curves in Figure 6, are much more similar to the measured closure rates. Figure 7 shows the effects of adding the low stress creep mechanism on the predicted surface subsidence. The predicted values are significantly higher than the 2015 predictions and the measured data.
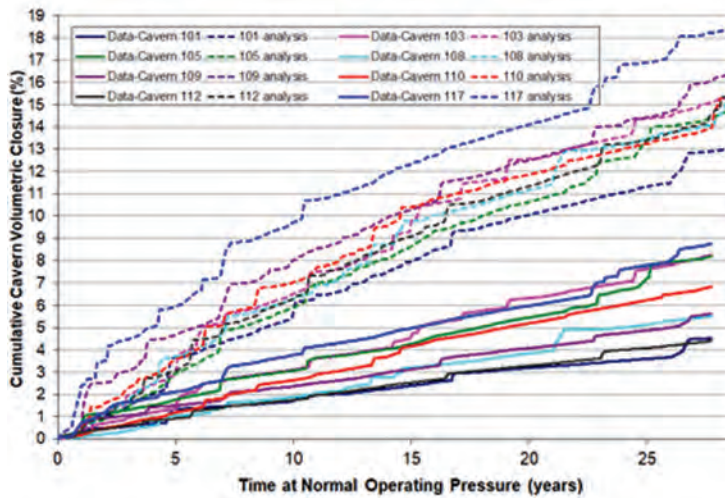
Figure 6: Comparison of West Hackberry predicted cavern closure vs. measurements, 2015 WH M-D properties plus low equivalent stress component (Mechanism 0).
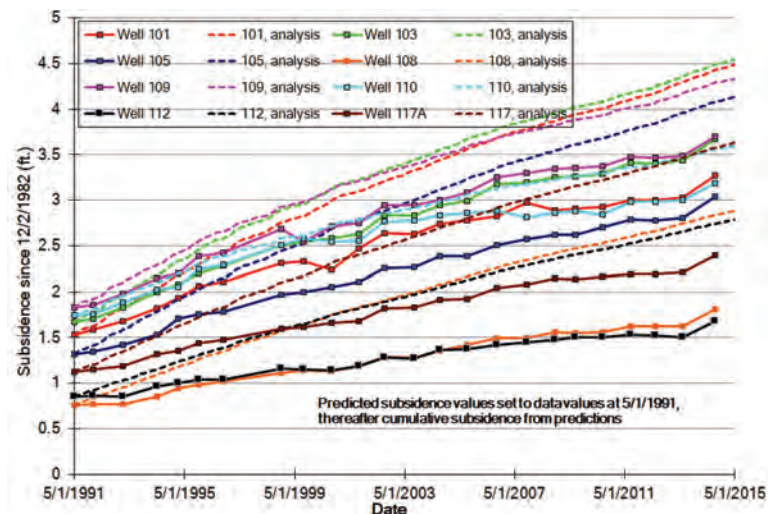
Figure 7: Comparison of West Hackberry predicted surface subsidence vs. measurements, 2015 WH M-D properties plus low equivalent stress component (Mechanism 0).

Because the steady-state creep of the salt has been greatly enhanced by the addition of Mechanism 0, it is now possible to perform new calculations with values of A_2 and K_1 closer to those captured experimentally in Munson (1998), which would better honor the fidelity of the previous laboratory data. A set of calculations was performed with the M-D Viscoplastic model for which all the multiplication factors were removed, thus using the original M-D creep parameters in Table 1 unmodified, along with the Mechanism 0 creep using the parameters in Table 2. Figure 8 shows the results for cavern volume closure. Although the predicted values were indeed somewhat less when removing the previous multiplication factors, the magnitude of the difference is small when compared to the overall magnitudes. This small difference seems to indicate that on a domal scale, the low equivalent stress dominates the overall displacement of salt in the dome. This would potentially be due to the much larger volume of salt between and around the caverns that experiences the smaller stress states, than the volume of the thin skins around the cavern that experience the stress states historically imposed in laboratory creep tests.
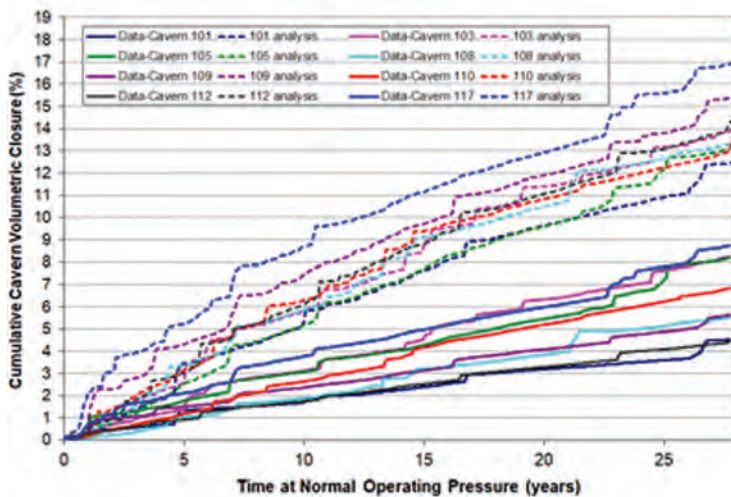
Figure 8: Comparison of West Hackberry predicted cavern closure vs. measurements, original WH M-D properties plus low equivalent stress component (Mechanism 0).

Figure 9 shows contour plots of the predicted equivalent stress in MPa for two vertical slices through the dome. The left slice goes through the approximate center of the cavern field where Cavern 103 is located; the right slice runs through Caverns 107, 9, and 8. These slices are located through the point at which the highest value of equivalent stress is recorded during the calculations, at a point on the bottom lobe of Cavern 9 which is close to Cavern 8 during a workover on that cavern.

It is important to note that the maximum value in Figure 9 is nearly 15 MPa and is small enough in this view to be difficult to see, but only small regions in the immediate vicinity of the caverns experience equivalent stresses over 7.5 MPa. Much larger volumes of salt experience equivalent stresses between 1 and 7.5 MPa. It is the creep of these much larger volumes at lower stresses that has not previously been captured in laboratory creep tests. As the calculations presented here indicate, the deformation of this larger volume may have a more significant effect on the overall deformation of the salt dome and caverns than the higher stressed regions in the walls surrounding each cavern. In addition, the results in Figures 7 and 8 indicate that the Mechanism 0 steady-state parameters for WIPP bedded salt predict higher creep than the WH domal salt may experience, and additional data is required for better parameterizing the transient creep experienced during low cavern pressure activities. Ongoing uniaxial tests of SPR domal salt are currently being performed (Berest, 2022 in progress).
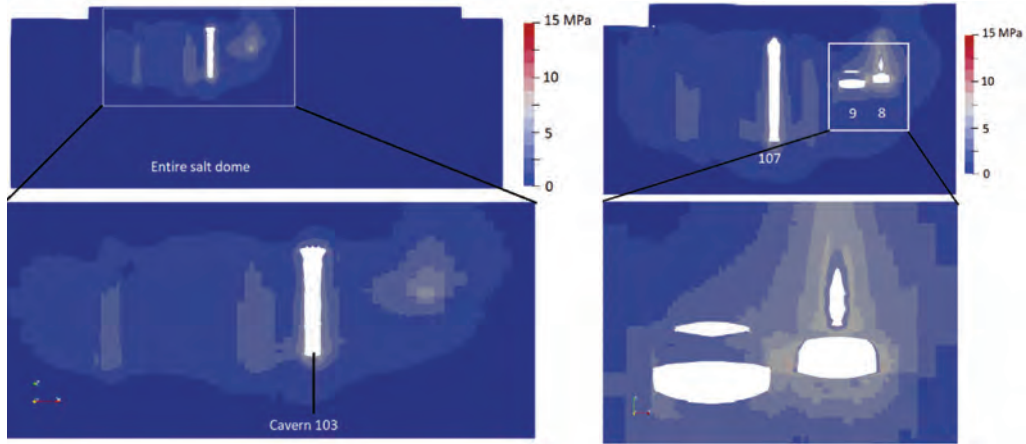
Figure 9: Contour plots of equivalent stresses (in MPa) across two west-east sections near the center of the West Hackberry storage site

5 Implications for predicting cavern integrity

Cavern integrity is dependent upon the evolution of stresses around the caverns, as tensile or high shear stresses can result in tensile fracturing or in dilatant damage resulting in microfracturing and increase in permeability. The potential for fracturing is particularly notable during cavern workovers, when the wellhead pressure is reduced to zero and the differential between cavern oil pressure and in situ pressure of the surrounding salt is at its highest. Figure 10 compares the predicted maximum principal stress (negative numbers represent compression, positive are tension) using the two salt constitutive models for cavern WH-108 at the beginning of a workover, when the stress differential is at its highest. There is some slight difference in the distribution of stresses around the wall of the cavern, but the maximum value is essentially the same for both models (a difference of less than 3%, occurring near the top of the cavern). The pressure in the salt wall reacts to the pressure of the oil equally; the difference in creep models modifies the extent to which the salt deforms in response to the stress. Figure 11 shows a similar plot of the predicted square root of the second invariant J_2 of the deviatoric stress tensor, which is a measure of the shear stress. Higher levels of shear stresses can lead to dilatant deformation of the salt. The difference between models is more pronounced, as the predicted higher shear stresses are spread out over a larger volume for the M-D viscoplastic model. The maximum shear stress values predicted by the M-D viscoplastic model is approximately 30% higher than that predicted by the M-D model, with both occurring near the top of the cavern. This difference in predicted behavior may be important in evaluating the potential for salt falls in the cavern, which has the capacity to damage the hanging string and affect oil-brine interaction in the boreholes.

The effect of the addition of the low equivalent stress component is also apparent when looking at the predicted vertical (axial) strain in the salt along the wellbore casings. It is currently assumed that as the salt deforms alongside the casings, those strains are transmitted through the bond between the salt and cement, and cement with steel casings. One of the evaluation criteria used for predicting damage to steel casings is the onset of plastic deformation at a strain of 1.6 millistrains. Figure 12 shows the predicted vertical strain for a few wellbore locations, comparing results from the M-D and M-D Viscoplastic models. Strain is plotted as a function of the distance from the top of the cavern, going up to the salt /caprock interface. The strains are predicted to be highest near the top of the cavern. Because the displacement of salt is spread out over a larger volume in the M-D Viscoplastic model, the strains near the top

of the cavern are predicted to be smaller, as are the predicted lengths of casing that may exceed the 1.6 millistrain threshold. This difference in the predicted displacements and strains may be highly variable on the property values used for the low stress creep mechanism. Therefore, it is important to obtain laboratory data on which to establish appropriate property values, so that the effect on predicted cavern and casing behavior can be better quantified.
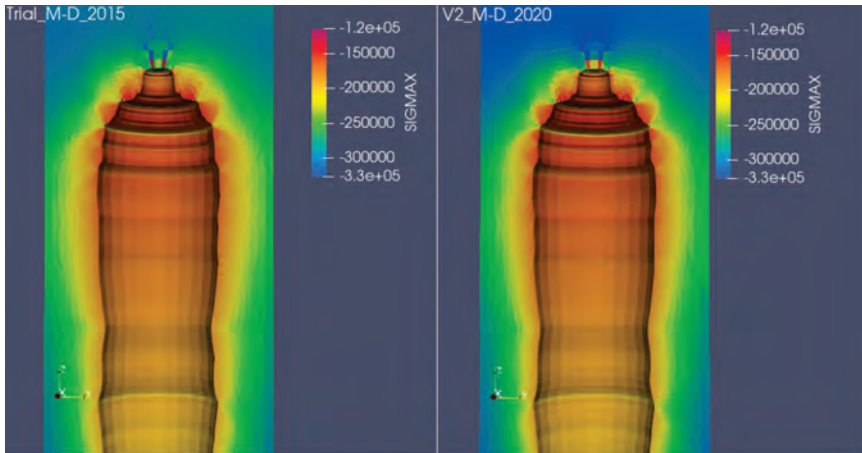
Figure 10: Predicted maximum principal stress (in pounds/square feet) around cavern WH-108 using the M-D model (left) and the M-D viscoplastic model (right).
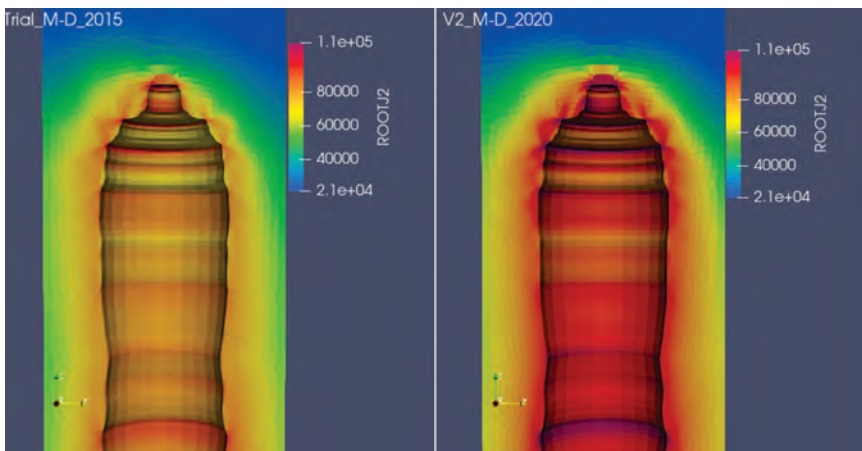
Figure 11: Predicted square root of second stress invariant (n pounds/square feet) around cavern WH-108 using the M-D model (left) and the M-D viscoplastic model (right).
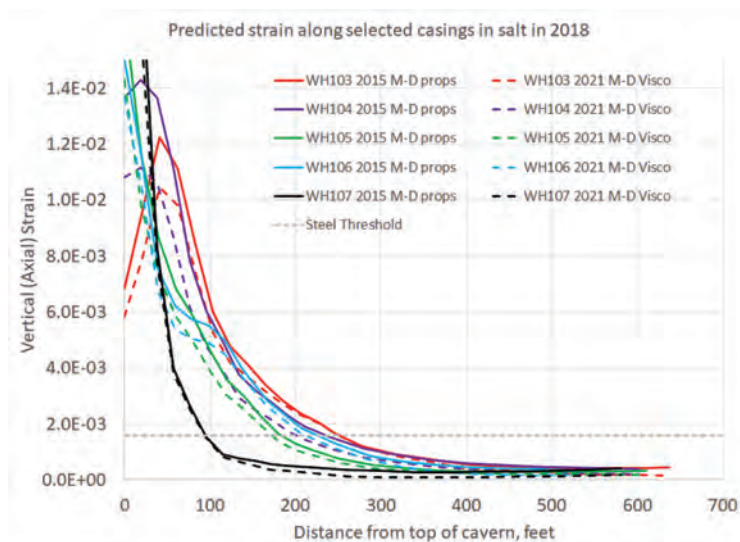
Figure 12: Predicted axial strain along wellbore casings for selected WH caverns using the M-D model and the M-D viscoplastic model.

6   Conclusions

A recent collaboration between US and German researchers characterized the creep behavior of salt at low equivalent stresses (<8 MPa). This research has resulted in an extension of the M-D model that includes a low stress creep mechanism. This extended M-D model, called the M-D Viscoplastic model, has been used in Sandia's geomechanical models for the SPR. The results show that low stress creep is the dominant large-scale displacement mechanism at the dome scale. This discovery indicates the need for laboratory creep tests at low equivalent stresses on salt from storage cavern sites, such as the SPR. This knowledge will help to improve evaluation of storage cavern behavior in salt domes.

Acknowledgements

References

BALLARD, S. & EHGARTNER, B. L. 2000. CaveMan Version 3.0: A Software System for SPR Cavern Pressure Analysis, SAND2000-1751, Sandia National Laboratories, Albuquerque, New Mexico.

BEREST, P., BLUM, P. A., CHARPENTIER, J. P., GHARBI, H., & VALES, F. 2005. "Very slow creep tests on rock samples". In: International Journal of Rock Mechanics and Mining Sciences 42.4, pp. 569–576.

BÉREST, P., GHARBI, H., BROUARD, B., BRÜCKNER, D., DE VRIES, K., HÉVIN, G., HOFER, G., SPIERS, C., & URAI, J. 2019. "Very slow creep tests on salt samples". In: Rock Mechanics and Rock Engineering 52.9, pp. 2917–2934.

DÜSTERLOH, U., HERCHEN, K., LUX, K.H., SALZER, K., GÜNTHER, R.M., MINKLEY, W., HAMPEL, A., ARGÜELLO JR, J. G., & HANSEN, F. D. 2015. "Joint Project III on the comparison of

constitutive models for the thermomechanical behavior of rock salt. III. Extensive laboratory test program with argillaceous salt from WIPP and comparison of test results".In: Proc. 8th Conference on the Mechanical Behavior of Salt. Ed. by L. Roberts, K. D. Mellegard, and F. D. Hansen, pp. 13–21.

HOSFORD, W. 1972. "A generalized isotropic yield criterion". In: Journal of Applied Mechanics, 39.2, pp. 607–609.

MUNSON, D.E. & DAWSON, P.R. 1979. Constitutive Model for the Low Temperature Creep of Salt (With Application to WIPP). SAND79-1853, Sandia National Laboratories, Albuquerque, New Mexico.

MUNSON, D.E. & DAWSON P.R. 1982. A Transient Creep Model for Salt during Stress Loading and Unloading. SAND82-0962, Sandia National Laboratories, Albuquerque, New Mexico.

MUNSON, D.E., FOSSUM, A.F. & SENSENY, P.E. 1989. Advances in Resolution of Discrepancies between Predicted and Measured in Situ WIPP Room Closures. SAND88-2948, Sandia National Laboratories, Albuquerque, New Mexico

MUNSON, D.E. 1998. Analysis of Multistage and Other Creep Data for Domal Salts, SAND98-2276, Sandia National Laboratories, Albuquerque, New Mexico.

REEDLUNN, B. 2016. Reinvestigation into Closure Predictions of Room D at the Waste Isolation Pilot Plant. Tech. rep. SAND2016-9961. Albuquerque, NM, USA: Sandia National Laboratories.

REEDLUNN, B. 2018A. "Joint Project III on the Comparison of Constitutive Models for the Mechanical Behavior of Rock Salt: Reinvestigation into Isothermal Room Closure Predictions at the Waste Isolation Pilot Plant". In: The Mechanical Behavior of Salt IX. Ed. By S. Fahland, J. Hammer, F. D. H. Hansen, S. Heusermann, K.-H. Lux, and W. Minkley. BGR (Federal Institute for Geosciences and Natural Resources). ISBN: 978-3-9814108-6-0.

REEDLUNN, B. 2018B. Enhancements to the Munson-Dawson Model for Rock Salt, SAND2018-12601, Sandia National Laboratories, Albuquerque, NM USA.

SALZER, K., GÜNTHER, R.M., MINKLEY, W., NAUMANN, D., POPP, T., HAMPEL, A., LUX, K.-H., HERCHEN, K., DÜSTERLOH, U., ARGÜELLO JR, J. G., & HANSEN, F. D. 2015. "Joint Project III on the comparison of constitutive models for the thermomechanical behavior of rock salt. II. Extensive laboratory test program with clean salt from WIPP". In: Proc. 8th Conference on the Mechanical Behavior of Salt. Ed. by L. Roberts, K. D. Mellegard, and F. D. Hansen, pp. 3–12.

SIERRA/SOLID MECHANICS 2018. Sierra/Solid Mechanics User's Guide. 4.50. SAND2018-10673. Sandia National Laboratories. Albuquerque, NM, USA; Livermore, CA, USA.

SOBOLIK, S. R. 2015. Analysis of Cavern and Well Stability at the West Hackberry SPR Site Using a Full Dome Model, SAND2015-7401, Sandia National Laboratories, Albuquerque, NM USA. U.S. Strategic Petroleum Reserve.

SOBOLIK, S. R. 2020. Milestone 1.2a2: Geomechanical analysis using MD viscoplastic material model – Bryan Mound (and West Hackberry), Letter to Diane Willard, August 17, 2020, Sandia National Laboratories, Albuquerque, NM USA. U.S. Strategic Petroleum Reserve.

SOBOLIK, S.R. & T.S.A. ROSS, 2021. "Effect of the Addition of a Low Equivalent Stress Mechanism to the Analysis of Geomechanical Behavior of Oil Storage Caverns in Salt," ARMA 21-1127, 55th US Rock Mechanics / Geomechanics Symposium held online in Houston, Texas, USA, 20-23 June 2021.

URAI, J., SCHLÉDER, Z., SPIERS, C. & KUKLA, P. 2008. "Flow and transport properties of salt rocks". In: Dynamics of complex intracontinental basins: The central European basin system, pp. 277–290.

Author Index